CFB 13

VANCOUVER, CANADA

MAY 10-14, 2021

PROCEEDINGS OF THE 13th INTERNATIONAL CONFERENCE ON FLUIDIZED BED TECHNOLOGY

Edited by
Xiaotao Bi, Cedric Briens, Naoko Ellis and Michael Wormsbecker

GLAB Reactor and Fluidization Technologies

CFB13

VANCOUVER, CANADA
MAY 10-14, 2021

Proceedings of the
13th International Conference on Fluidized Bed Technology

Edited by

Xiaotao Bi

The University of British Columbia, Vancouver, Canada

Cedric Briens

Western University, London, Canada

Naoko Ellis

The University of British Columbia, Vancouver, Canada

Michael Wormsbecker

Syncrude Canada, Edmonton, Canada

GLAB Reactor and Fluidization Technologies

Published by GLAB Reactor and Fluidization Technologies, Vancouver, Canada
ISBN 978-1-77136-850-6

Cover design: Social Bubbles in Vancouver, by Kathy Bi

This proceeding is dedicated to Professor John Grace who has exerted great influence on the field of fluidization, and has greatly impacted on the careers of many of us.

Sponsors

BC RESEARCH

Coanda

cpfd

PSRI
Particulate Solid Research, Inc.

GLAB

CFB-13 Organizing Committee

Chair:
Xiaotao Bi – University of British Columbia

Co-Chairs:
Cedric Briens – Western University
Naoko Ellis – University of British Columbia
Michael Wormsbecker – Syncrude Canada Ltd, Edmonton, Canada

Committee Members:
Xiaotao Bi – University of British Columbia
Cedric Briens – Western University
Junnan Chao – University of British Columbia
Naoko Ellis – University of British Columbia
Zhijie Fu – University of British Columbia
John Grace – University of British Columbia
Jing He – University of British Columbia
Allan Issangya – Particulate Solid Research Inc., USA
Eric Dening Jia – Canadian Nuclear Laboratories, Canada
Robert Legros – Polytechnique Montréal
Jim Lim – University of British Columbia
Andres Mahecha-Botero - NORAM Engineering & Constructors Ltd, Canada
Poupak Mehrani – University of Ottawa
Andrew Mezo – Coanda Research & Development Corporation, Canada
Jean Saayman - Powertech Labs Inc., Canada
Milad Taghavivand – University of British Columbia
Jonathan Tyler – Parkland Refining Ltd, Canada
Anthony Wachs – University of British Columbia
Ziliang Wang – University of British Columbia, BC Research Inc., Canada
Michael Wormsbecker – Syncrude Canada Ltd, Edmonton
Lei Zhang – University of British Columbia
Lifeng Zhang – University of Saskatchewan
Siduo Zhang – University of British Columbia

International Advisory Board

PREFACE

Circulating fluidized beds (CFBs) were first applied in the fluid catalytic cracking (FCC) process in the 1940s, while their applications for combustion started in 1970s. As the interest in fast fluidization and the circulating fluidized bed technology increased in 1970s, the first international circulating fluidized bed technology conference was held in Halifax, Canada, in 1985. Since then, the International Conference on Fluidized Bed Technology series has been the forum for both the academia and industrial professionals to showcase their latest research and discoveries, exchange new ideas, stimulate discussions on research challenges and emerging research areas and applications. Since CFB-10 (2011), the scope of the CFB conference has been expanded to include other types of fluidization and applications.

CFB-13 is the 13th conference in a series following the first Zodiac cycle of 12 successful conferences over the past 35 years:

- CFB-1, Halifax, Canada, 1985
- CFB-2, Compiegne, France, 1988
- CFB-3, Nagoya, Japan, 1991
- CFB-4, Hidden Valley, USA, 1993
- CFB-5, Beijing, China, 1996
- CFB-6, Wurzburg, Germany, 1999
- CFB-7, Niagara Falls, Canada, 2002
- CFB-8, Hangzhou, China, 2005
- CFB-9, Hamburg, Germany, 2008
- CFB-10, Sunriver, USA, 2011
- CFB-11, Beijing, China, 2014
- CFB-12, Krakow, Poland, 2017

The CFB-13 conference was originally planned to take place in Vancouver, Canada, in May 2020, as a reflection of the beginning of a new circle of the conference series. Due to outbreak of the global Covid-19 pandemic, the conference was postponed for one year. Although we start to see the containment of the virus spreading with the massive vaccination taking place globally, we believe that it is the collective interest of the fluidization community to have this conference virtually, instead of a further delay.

Following the tradition of the conference series, CFB-13 covers broad topics ranging from fundamentals, modeling/simulations to applications with a particular interest in energy conversion and mitigation of greenhouse gases and criteria air pollutants. Besides the regular technical programs, three workshops on gas fluidized beds with liquid injection, large diameter fluidized beds and modeling/simulation of fluidized beds are organized in parallel to discuss the future research needs in those hot topic areas.

Other activities have been planned to celebrate the accomplishment of the first 12 CFB conference series, which include a historical review given jointly by the convenors of the CFB conference series (Profs. Prabir Basu, Jinghai Li and Joachim Werther), a tribute to 6 fluidization researchers who passed away in the past 5 years (Octave Levenspiel, Frederic Zenz, Daizo Kunii, John Davidson, Owen Potter, Ernst-Ulrich Hartge), and the presentation of fluidization achievement awards to three fluidization researchers who have made outstanding contributions in advancing the fluidization science and CFB technology.

Although the virtual platform of the conference is not ideal, the conference still attracted more than 100 participants, with more than 100 peer-reviewed high-quality papers from both academia and industry. We are proud to present them with this proceeding and wish to gratefully acknowledge the authors, sponsors, reviewers, organizing committee members and all the people who have volunteered generously with their time and efforts to make this conference a great success.

Xiaotao Bi, Cedric Briens, Naoko Ellis, Michael Wormsbecker

TABLE OF CONTENTS

PLENARY LECTURES

HYDRODYNAMICS

MODELING

FLUID BED WITH LIQUID INJECTION

HEAT/MASS TRANSFER

MEASUREMENT & INSTRUMENTATION

DESIGN & SCALE-UP

INDUSTRIAL EXPERIENCE

ELECTROSTATICS

PYROLYSIS

GASIFICATION

COMBUSTION

CO_2 CAPTURE

NO_X/SO_X EMISSION CONTROL

FCC & OTHER PROCESSES

STICKING TOGETHER: IS UNITY STRENGTH?

Lyes Ait Ali Yahia, Andrew Bruce, Ali Ozel, Raffaella Ocone*

School of Engineering and Physical Sciences
Heriot-Watt University, Edinburgh EH144AS, UK

*Email: r.ocone@hw.ac.uk

Abstract

The hydrodynamics of granular flows can be influenced significantly by interparticle forces. Those forces arise from a variety of interactions and factors, such as van der Waals interactions, electrostatics, and presence of liquid. Small amount of liquid can be purposely added or accidentally be present in a number of processes involving solid particles. This paper presents an account of cohesive effects due to the presence of liquid and the rheology of slightly wet particles is studied by means of a commercial rheometer (Freeman FT4 Powder Rheometer). Although an account of the various flow regimes, that can develop in granular materials, is given, specific attention is paid to the transition from the quasi-static regime to intermediate regime (i.e., the regime which develops between the quasi-static regime and the rapid flow regime). Preliminary results show features that can help shed light on the bulk properties of wet granular materials.

Introduction

Granular materials exhibit a broad range of intricate dynamic behaviours. In the chemical and process industries, where those materials are widely handled and produced, studying their hydrodynamics is of critical importance. Indeed, understanding how internal (e.g., particles size and shape) and external (e.g., applied stresses, moisture content) physical properties impact on the flow behaviour of solid particles helps industrial practitioners handle and produce particulates efficiently and less costly.

The physics of granular materials is governed by interparticle, fluid-particle interaction and body forces. Many particulate flows consist of *cohesive particles*, where cohesion can be the consequence of a number of factors. The four mechanisms which can cause cohesion in particulate flows are: chemical bonding, electric charging, liquid bridging and van der Waals forces. Although the totality of those effects plays a relevant role in particle aggregation and flowability, this paper concerns with slightly wet particles in size range of a few hundred microns, hence the predominant cause of cohesion is attributed to the presence of liquid.

The effects of small amounts of liquid on gas–solid systems have been studied experimentally and numerically (e.g., Rauxm and Biance, 2018; Khamseh et al., 2015; Makkawi et al., 2006; Hamrock et al., 2004). Pendular liquid bridges between two particles generate surface tension forces, which provide cohesion between particles, and viscous forces, which act to reduce relative motion between particles. These forces are different when particles are approaching one another as compared to when they are rebounding off one another; indeed, liquid bridges form when particles collide and might persist after particles are no longer in contact. Liquid bridges can be viewed as a mechanism for transferring liquid from wetter to drier particles, and thus liquid introduced to process systems at certain locations can spread throughout the system over time as particles come into contact and mix. The consequent dynamic aggregation results in a distinctive rheological behaviour that is analysed in detail.

The flow of particulate systems depends on the particle concentration and flow velocity. Specifically, two main regimes are usually observed: (1) slow dense flow, usually referred to as “quasi-static flow” and (2) fast dilute flow, usually referred to as “rapid flow” (see Fig. 1).

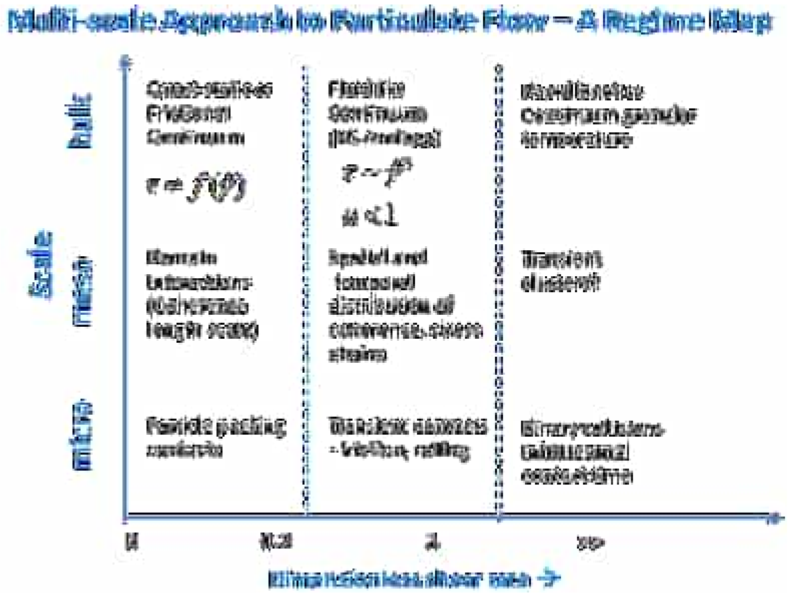

Fig. 1. The regime map and the corresponding stresses (τ). $\dot{\gamma}$ is the shear rate.

Figure 1 gives an account of the flow regimes that can be observed in systems of particles, and whilst regime (1) and (2) are well studied, the so-called intermediate regime, which develops between (1) and (2), is still poorly understood.

The approach taken at Heriot-Watt University to elucidate the regime map is a multi-scale one and a suite of experiments, supplied with simulations at various length scales, is developed to characterise the dynamic behaviour of wet granular material. The results reported in this paper are mainly in the quasi-static regime and at the cross-over, between (1) and intermediate regimes. Although specific emphasis is posed on the cohesion generated by the introduction of a liquid into the granular media, some insight into the role that electrostatic forces play in making powder cohesive is given as well (Kolehmainen, J. et al, 2017 and Sippola et al, 2018).

Experimental Procedure

To analyse the rheological behaviour of powders in the intermediate regime, the Aerated Bed Virtual Couette Rheometer (AB-VCR) is employed. The instrument combines the aeration vessel of the automated Freeman FT4 Powder Rheometer (Freeman Tech.) with a cylindrical cell displaying six blades as shown in Figure 2 ((a) and (b)). The aerated vessel of the FT4 is made of a glass cylinder of 25mm internal radius (R_e: external radius of the Couette configuration) that can hold a volume up to 260 ml. The vessel is attached to an aeration stainless steel base (see Figure 1 (c)) composed of a grid that allows for a uniform distribution throughout the cross section of the injected air at ambient conditions. The air flowing through the vessel is controlled by the FT4 air supply assuring air velocities up to 40mm/s. In this study, the 3D printed cell is 15mm in radius and 70mm in height and is made of plastic material (ABS-M30i – provided by SYS systems 3D Printing).

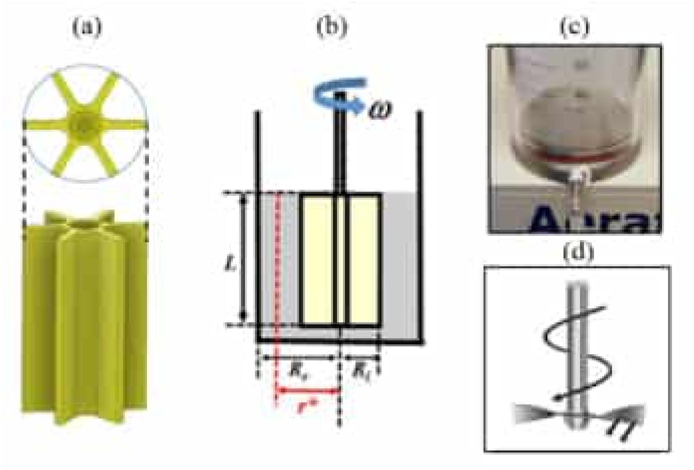

Fig. 2. *(a)* Representative image of the 3D printed Virtual Couette Cell; (b) Schematic view of the assembled AB-VCR with L being the cell's height, ω the rotational speed, R_e, R_i and r^* the external, inner and optimal radii, respectively; (c) aeration base; (d) Conditioning impeller.

The experimental procedure is as follows: the cell moves downward through the material placed in the vessel until it reaches a fixed position. In the present study, the fixed position is assumed to be constant and equal to 1mm, measured from the bottom of the vessel. The granular material under investigation is firstly fluidised at high airflow in order to allow for the cell to move downward; this is to avoid the cell compacting the sample which otherwise causes the device to be overloaded. Once the cell has reached the fixed position, the aeration is stopped and the arm holding the cell starts rotating at a fixed rotational speed, ω. The vessel is filled with enough material to cover the cell up to its upper end. The rotational movement of the cell creates a virtual rotating cylinder of particles comprised between the blades. The torque, T, needed to rotate this cylinder of particles through the remaining bed of particles, is recorded. This procedure is followed while aerating the granular bed from the bottom through the base of the vessel. The shear stress and shear rates are then computed from the torque and the rotational speed, respectively.

This configuration was first tested without aeration using a Newtonian fluid with a known viscosity. It was also tested with aerated and non-aerated dry glass beads powders in the quasi-static regime (Ait Ali Yahia et al, 2020).

Results and Discussion

Monodispersed glass beads (500μm diameter) of known mass, m_s, are mixed with a constant amount (in mass) of silicon oil (viscosity: 10 cST). The mixing occurs within the aerated vessel and the liquid concentration is evaluated as the ratio of the mass of liquid (m_l) to the total mass (m_s+m_l). The FT4 automated conditioning blade (figure 1 (d)) is used to prepare each wetted sample employing the automated conditioning cycles of the FT4. A conditioning cycle comprises a traverse of the rotating blade downward through the sample followed by an upward traverse. For this work the number of conditioning cycles was fix to 20. The automated traverse is used to ensure a homogenous and repeatable distribution of the liquid in the studied powder. It also allows an *in-situ* test, where the AB-VCR shear test (as explained in the experimental procedure) is performed directly on the wet sample after its preparation. Two samples with two liquid concentrations equal to 0.1 and 0.2% were prepared. Experiments were performed with and without aeration (air velocity equal to 40mms^{-1}) and with shear rates ranging from 5 to 22s^{-1}.

The results showed that the shear stress is independent of the shear rate for both dry and wet case, which indicates that even when wet, the studied material remain in the quasi-static regime (see Figure 3). The shear stress obtained with the wet sample was found to be higher than the one obtained with the dry sample and independent of the liquid concentration. The same comments can be made for the aerated case.

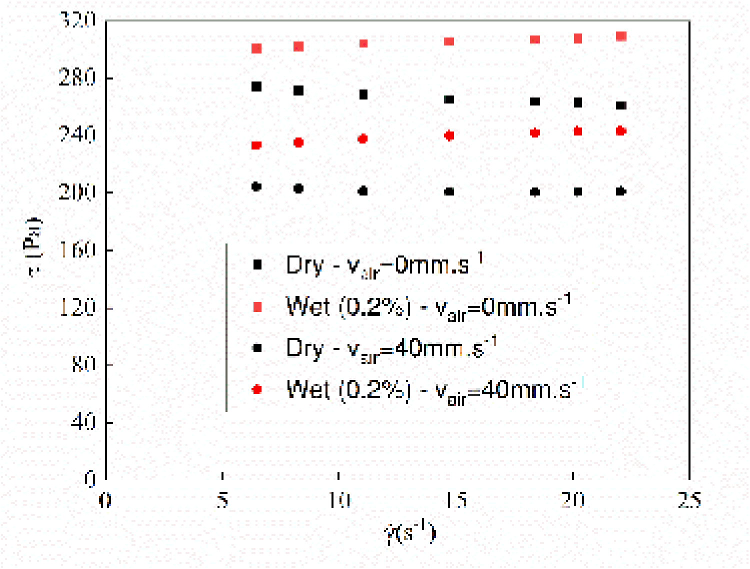

Fig. 3. Shear stress versus shear rate for dry and wet granular media made of glass beads of 500µm diameter.

Additional experiments were performed with smaller particles using water as the wetting agent, with the aim of studying the flowability of wet powders. The experiments were undertaken using the FT4 shear cell, able to determine the stresses which develop in the sheared media, after pre-conditioning (Hare et al., 2015). Table 1 reports the flowability index (see definition below), *ff*, as a measure of powder flowability.

Table 1. Flowability of powders.

<1	Non-flowing
1<*ff*<2	Very cohesive
2<*ff*<4	Cohesive
4<*ff*<10	Easy flowing
>10	Free flowing

Flowability tests were performed and those are reported in Figure 4.

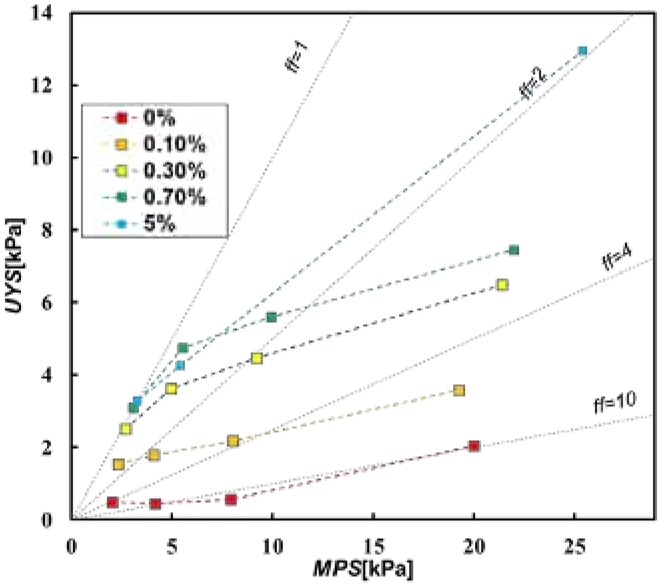

Fig. 4. Flowability chart for glass beads of 106μm diameter.

The flowability index, *ff*, is defined as:

$$ff = \frac{MPS}{UYS} \tag{1}$$

where *MPS* is the major principal stress and *UYS* is the unconfined yield stress. It can be observed that, as the moisture content increase, the flowability decreases. This behavior is as expected showing that water increases cohesion among particles making them less flowable.

Figure 5 reports the experiments for two different powders in the quasi-static regime and how they compare with the correlation presented by Wang et al. (2016)

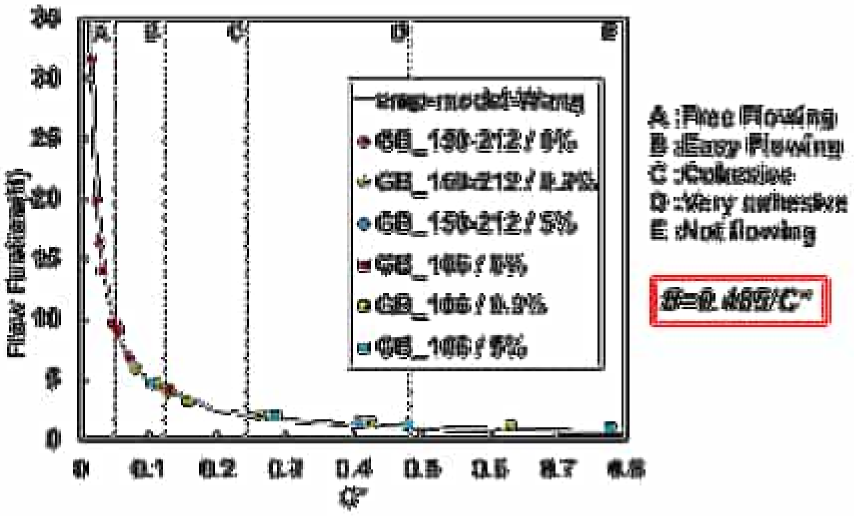

Fig. 5. Flowability as a function of various granular media and variable water content. GB_150-212 indicates glass beads of diameters 150-212μm; GB_106 indicates glass beads of diameter 106μm.

Notation

C^*	Dimensionless cohesion
ff	Flow index
GB	Glass beads
L	Cell's height, m
MPS	Major Principal Stress
m_l	mass of liquid, g
m_s	mass of solid, g
R_e	Cup's Radius, m

R_i	Cell's Radius, m
r^*	Optimal Radius, m
UYS	Unconfined Yield Stress, m
v_{air}	Air velocity, mm.s^{-1}
τ	Shear stress, Pa
$\dot{\gamma}$	Shear rate, s^{-1}
ω	Rotational speed, RPM

Acknowledgment

Financial support from the EPSRC (grant no EP/N034066/1) is kindly acknowledged.

References

Ait Ali Yahia, L., T.M. Piepke, R. Barrett, A. Ozel, R. Ocone, Development of a virtual Couette rheometer for aerated granular material, AIChE J, 2020, accepted for publication

Hamrock, B.J., S.R. Schmid, B.O. Jacobson, Fundamentals of fluid film lubrication, CRC press, 2004

Hare, C., U. Zafar, M. Ghadiri, T. Freeman, J. Clayton, M.J. Murtagh, Analysis of the dynamics of the FT4 powder rheometer. Powder Technol., Pharmaceutical Particle Technology 285, 123–127, 2015

Khamseh, S., J.-N. Roux, F. Chevoir, Flow of wet granular materials: A numerical study, Phys. Rev., 2015

Kolehmainen, J., P. Sippola, O. Raitanen, A. Ozel, C.M. Boyce, P. Saarenrinne, S. Sundaresan, Effect of humidity on triboelectric charging in a vertically vibrated granular bed: experiments and modeling. *Chemical Engineering Science*, *173*, 363-373, 2017

Makkawi, Y. T., P.C. Wright, R. Ocone, The effect of friction and inter-particle cohesive forces on the hydrodynamics of gas-solid flow: A comparative analysis of theoretical predictions and experiments, Powder Technol., 163, 69-79, 2006

Raux, R, A.-L. Biance, Cohesion and agglomeration of wet powders, Phys. Rev. Fluids. 3, 2018

Sippola, P., J. Kolehmainen, A. Ozel, X. Liu, P. Saarenrinne, S. Sundaresan, Experimental and numerical study of wall layer development in a tribocharged fluidized bed. *Journal of Fluid Mechanics*, *849*, 860-884, 2018

Wang, E.Y., S. Koynov, B.J. Glasser, F.J. Muzzio, "A method to analyze shear cell data of powders measured under different initial consolidation stresses," Powder Technol., vol. 294, no. Supplement C, pp. 105–112, 2015

.

DIRECT NUMERICAL SIMULATION OF PARTICLE-FLUID SYSTEMS

Wei Ge[1,2,3,4*], **Qi Chang**[1,4], **Yong Zhang**[1,2,3], **Limin Wang**[1,2,3], **Feiguo Chen**[1,2,3], **Chengxiang Li**[1,2,5]

[1]*State Key Laboratory of Multiphase Complex Systems, Institute of Process Engineering, Chinese Academy of Sciences (CAS), Beijing 100190, China*
[2]*School of Chemical Engineering, University of the Chinese Academy of Sciences, Beijing 100049, China*
[3]*Innovation Academy for Green Manufacture, CAS, Beijing 100190, China*
[4]*School of Chemical Engineering, Tianjin University, Tianjin 300072, China*
[5]*Dalian National Laboratory for Clean Energy, CAS, Dalian 116023, China*

*Email: *wge@ipe.ac.cn*

Abstract

With the continuous development of numerical methods and computational technology, direct numerical simulation (DNS) based on first principles is becoming a powerful tool for exploring the mechanism of particle-fluid systems and providing constitutive correlations for engineering design and simulation methods. To demonstrate this role of DNS for fluidization technology, the relevant studies at IPE, CAS is reviewed in this article, and the future of DNS and its applications is prospected.

Background

It is widely anticipated that turbulence will be the “last” territory conquered in classical physics. However, fluidization researchers should have the right to claim that their field might be conquered even later, as all the difficulties faced in the study of turbulence also presents in their study and the introduction of particles makes the problem much more complicated, not only for their geometries, but also for their hydrodynamic and/or transport boundary layers and the particle morphologies, not to mention the complexity of interfacial reactions.

Both turbulent and particle-fluid flows are characterized by typical multi-scale structures and lack of scale-separation. That means the traditional two-level description with conservation laws at the macro-scale closed by constitutive laws at the micro-scale can no longer be taken for granted, and unveiling the panorama of such multi-scale structures would be fundamental to develop a new framework of modeling. It is certainly impossible for a single experimental or numerical method to reproduce the full spectrum of these structures, but with the continuous progress of computing technology, direct numerical simulation (DNS) is extending to larger scales and becoming a more powerful tool at the bottom of the spectrum.

DNS was first proposed to numerically describe single-phase turbulent flow directly from the Navier-Stokes equation, without resorting to any turbulence models. Literally, it means the Kolmogorov scale or dissipative eddies should be resolved in the simulation and hence the computational cost is incredibly high for engineering problems such as the flow around a commercial aircraft. Therefore, most works have aimed at understanding the flow mechanism and then develop effective models at larger scales, or helping the design and optimization of the mini-systems directly.

Similar scenarios and purposes are found in DNS of particle-fluid systems, as summarized in Table 1 for recent works on gas-solid, liquid-solid, and gas-liquid-solid systems. In periodic domains, drag correlations have been proposed for gas-solid (Hill et al., 2001; van der Hoef et al. 2005; Beetstra et al., 2007; Tenneti et al. 2011; Rong et al., 2013; Rubinstein et al., 2017; Tang et al., 2016b; Liu et al. 2017, 2020) and gas-liquid-solid (Baltussen et al., 2017) flows. In mini-systems with realistic inlet-outlet boundary conditions, Luo et al. (2016) and Tang et al. (2016a) conducted DNS for fluidized beds and the obtained distributions of solid velocity, particle granular temperature, etc. agree well with the experimental measurements. In liquid-solid systems, the particle settling velocities were studied by Pan et al. (2002) and Ozel et al. (2017), which agree well with the PIV (particle image velocimetry) measurement and the correlation of Richardson and Zaki (1954). Moreover, the particle-turbulence interactions have been studied in liquid-solid channel flows (Picano et al. 2015), and the Nusselt number, have been studied in pressure-driven periodic systems (Sun et al. 2015) and realistic fluidized beds (Deen et al. 2012; Feng et al. 2014). Wall-to-liquid heat transfer was also studied in a turbulent liquid-solid system (Ardekani et al. 2018). For reactions, Qu et al. (2019) studied the alkali release in char combustion by coupling mass, heat transfer, and reaction models. In many cases, the particle boundary layer and the lubrication effect are not resolved or even considered yet, so they are not strictly based on first-principles as for single-phase systems, but as long as the flow around the particles are resolved and the particle-fluid interactions are computed by integrating the stress particle surfaces without resorting to any "drag" (in this context, it actually stands for all kinds of interphase forces) correlations, they are all considered as DNS for particle-fluid systems.

The DNS studies at IPE also reflect this state-of-the-art but they have been more directly motivated and then powered by the development of a consistent multi-scale modeling and simulation strategy to particle-fluid systems with the energy-minimization multi-scale (EMMS) method (Li 1987; Li and Kwauk 1994) at the core. These studies have employed four different approaches with different aims at different stages, which are now still in continuous development for new applications, as reviewed in the following sections, respectively.

Pseudo-particle Modeling (PPM) of Gas-solid Flow

As for single-phase turbulence, a major difficulty for multi-scale modeling of gas-solid flow is that, as more variables are introduced to describe the unresolved internal structures in the element considered, not enough equations can be found to close the model and the empirical correlations proposed as alternatives are usually limited to specific conditions and lack of physical explanation. By introducing variational criteria instead, the EMMS model approached the problem in a more general and rational way, but left the task of verifying the criteria, that is, the minimization of mass specific energy consumption rate for suspending and transporting the particles ($N_{st} \rightarrow$min). As no experimental or traditional numerical methods was found to be capable of monitoring the variation of N_{st} in fluidization with sufficient accuracy, we then resorted to Newton's Laws directly and hence proposed PPM (Ge and Li, 1996, 2003a). As illustrated in Fig. 1, PPM is basically a hard sphere molecular dynamics (MD) approach to the simulation of fluid flow, but to take advantage of the efficiency and scalability of synchronized time-driven algorithms, the particles are allowed to overlap slightly in their collisions. The material properties and equation of state of these "pseudo particles" can be well correlated to those of hard spheres by some effective parameters (Chen and Ge 2010), which facilitates the specification of the flow conditions to measure the variation of N_{st} numerically. Fig. 2 shows (Zhang et al. 2005) the typical results from this study which verify that N_{st} indeed approaches minimum as a fluidization bed evolve to its steady state.

As a DNS method, the disadvantage of PPM is the extremely high computational cost and pronounced thermal noise due to its MD nature. The latter is not a big problem for the study of the EMMS model, as only statistical averages are concerned, but obtaining high resolution flow field of macro-scale systems is challenging for this method. However, in recent years, it has found new applications in the study of micro- and nano-systems such as the highly coupled reaction-diffusion-flow processes inside and outside catalytic particles, as shown in Fig. 3 (Zhang and Ge 2016; Li et al. 2017a, 2017b, 2019). At these scales thermal fluctuation is naturally presented and the transport properties are highly dependent on the local geometries and structures, so traditional continuum-based methods are cumbersome to correctly reproduce these features which are, in contrast, inherent to PPM.

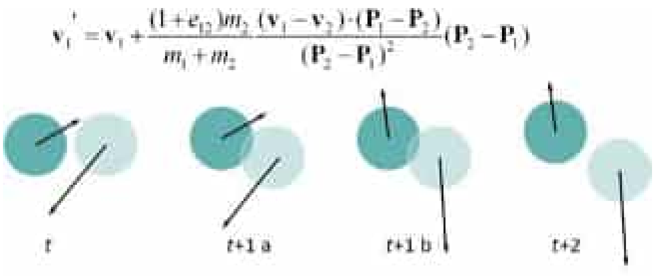

Fig. 1. The basic idea of pseudo-particle modeling (Ge and Li, 1996, 2003).

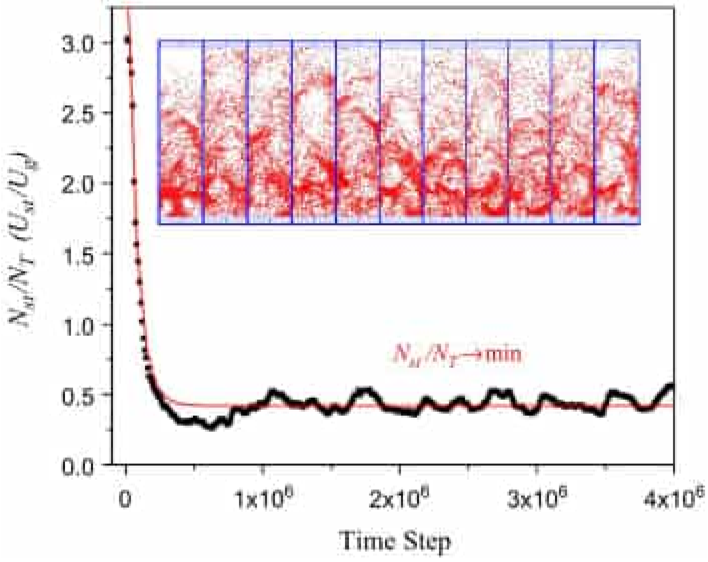

Fig. 2. Variation of N_{st} in a fluidized bed as measured in PPM simulation (Zhang et al. 2005).

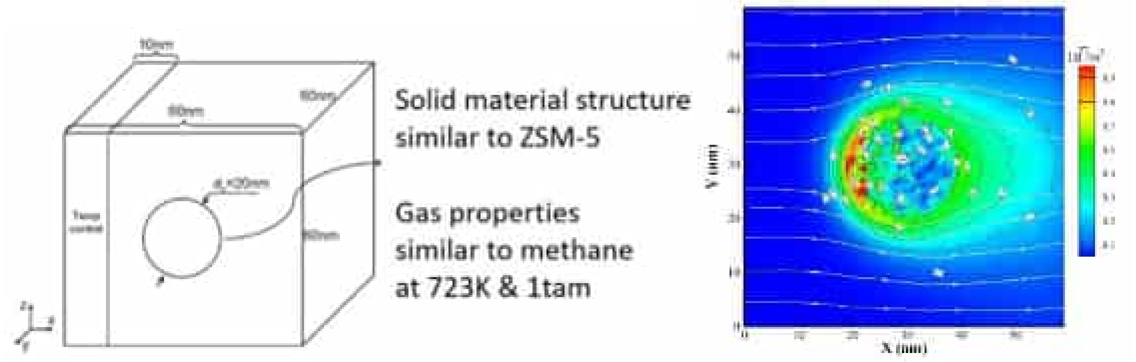

Fig. 3. Flow inside and around a reactive porous particle
simulated using hard sphere MD and PPM (Zhang and Ge 2016, Internal Report).

DNS of Particle-fluid Flow using Macro-scale Particle Methods

Characterizing the multi-scale structures in particle-fluid systems is fundamental to the establishment of their multi-scale models. For example, for the EMMS model, a more reliable correlation for the cluster diameter in fast fluidization has long been a need for improvement. As PPM is inefficient for high resolution simulation, but its algorithmic simplicity is still attracting, seeking a similar particle method at larger scale is a logical choice. We therefore started to integrate the discrete element method (DEM, Cundall and Strack 1979) for the particles to the macro-scale particle methods for fluids, which belongs to the smoothed particle hydrodynamics (SPH, Gingold and Monaghan 1977) family (Ge et al. 2001, 2003b). The particles used in these methods can be understood as a Lagrangian representation of the fluid elements in continuum mechanics, so the computational cost is on the same order of traditional computational fluid dynamics (CFD) methods.

With the help of GPU-based supercomputing, the suspension of thousands to 0.1 million particles in gas flow was simulated in these methods (Tang et al. 2004; Ma et al. 2006, 2009; Xiong et al. 2010). From these numerical studies, the destabilization of uniform suspension to typical heterogenous two-phase structures at the steady state was reproduced. Ma et al. (2009) suggested that a cascaded drafting-kissing-tumbling (DKT) process may explain the forming of clusters, as shown in Fig. 4a, and the slip velocity continues to increase long after the interphase force has balanced the particle weight (see Fig. 4b), demonstrating that the structural evolution is a slow process mainly driven by the hydrodynamic instability rather than particle dynamics (Ma et al. 2009). Anisotropic distribution of the particle velocity and drag force were also found (Ma et al. 2009), which proposes new topics for the kinetic theory of granular flow (KTGF, Lun et al. 1984). Furthermore, the steady-state slip velocity was found to increase with the system scale until sufficiently large (Xiong et al. 2010), however, more cases are needed to confirm this tendency in the future.

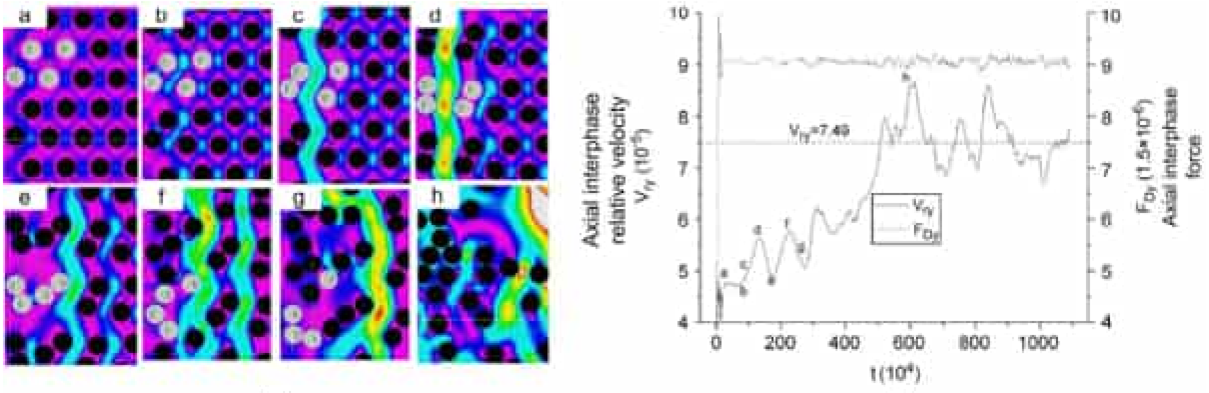

(a) (b)

Fig. 4. Structural evolution of the solid suspension in gas flow (Ma et al. 2009).

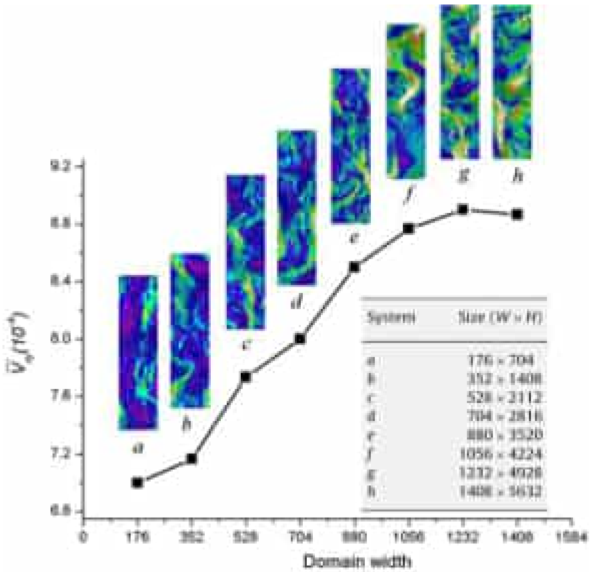

Fig. 5. The dependence of slip velocity on domain size (Xiong et al. 2010).

DNS based on Lattice Boltzmann and Immersed Boundary Methods

In recent years, with the development of computing technology and numerical methods, DNS has become not only an exploration tool for understanding the flow mechanism, but also a practical tool for developing constitutive correlations for larger scale simulation. A typical example is the drag correlations (Hill et al. 2001; van der Hoef et al. 2005; Beetstra et al. 2007) and such studies usually require the simulation of a large number of cases systematically for a huge amount of particles with high accuracy and resolution. For this purpose, macro-scale particle methods are still not favorable. On one hand, as a considerable number of neighboring particles are involved in updating each particle and their trajectories must all be followed, the computational efficiency of these methods is significantly lower than the grid- or lattice-based methods. Moreover, though they are strictly mass-conservative with no numerical diffusion by their Lagrangian nature, their accuracy is limited to 2nd order or even worse at boundaries, and numerical dissipation is high which prevents them from achieving high *Re* numbers.

The lattice Boltzmann method (McNamara and Zanetti 1998) seems to be more suitable in this regard, as the lattice operations are both simple and scalable (explicit, local and additive), which possess the attractions of both grid- and particle-based methods. The difficulty of describing the curved particle-fluid interface on a regular rectangular lattice has been tackled by the immersed boundary method (IBM, Noble and Torczynsk 1998). With this method, we have successfully reproduced the distinctive flow patterns of particulate and aggregative fluidization for liquid-solid and gas-solid systems (Wang et al. 2010), respectively (see Fig. 6). Then with GPU-based supercomputing, the suspension of one million particles suspended in gas flow was simulated on one billion lattice nodes (2D) (Xiong et al. 2012, see Fig. 7), which reproduced the multi-scale heterogenous structures that would present inside a typical computational cell in the CFD simulation for industrial scale fluidized beds. According to this full-range physical pictures, more detailed 3D simulation with higher resolution and accuracy was carried out consequently (Zhou et al. 2014; Liu et al. 2017, 2020), which analyzed the sub-grid scale structure quantitatively. The local particle concentration gradient and its angle to the local slip velocity were confirmed to be the additional variables for correlating the local drag besides the traditionally used slip velocity and particle concentration for uniform suspension. Recently, we obtained a new drag correlation based on a series of large-scale DNS using up to 115,200 freely moving particles (Liu et al. 2020a, see Fig. 8). We employed the local Froude number as a new variable and considered, for the first time, the effect of multi-scale dynamic heterogeneity down to particle-revolved scale.

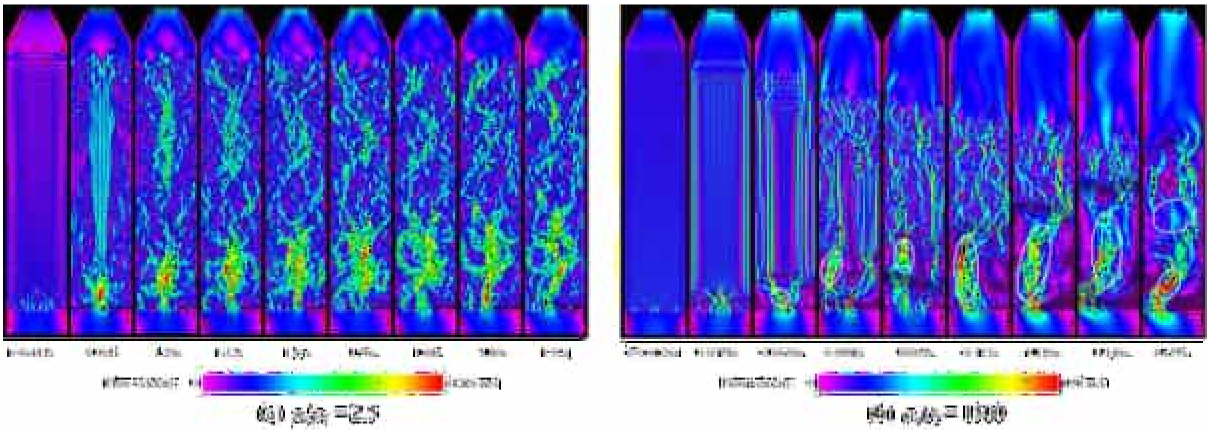

Fig. 6. DNS of gas-solid fluidization: the effect of gas-solid density ratio (Wang et al. 2010).

DNS based on Finite Difference and Immersed Boundary Methods

Though DNS based on LBM-IBM is advantageous in many ways, it also faces difficulties when thermal effect, reactions and phase changes, etc. are to be considered, and for high resolution and high efficiency at the same time, using non-uniform and irregular grid cells maybe inevitable, which is more easily implemented in traditional finite difference or finite volume methods. With this in mind, we also tried to replace the LBM fluid flow solver by a finite difference solver. The first attempt is still based on a staggered Cartesian grid, with a projection-correction method for the velocity-pressure decoupling in the momentum equations. The time propagation is discretized with the 3rd explicit Runge-Kutta method, which has successfully simulated typical bubbling/turbulent fluidization behavior in a 2D small fluidized bed of 24.2×5.82 mm filled with air and 2070 particles of 83.8 μm in diameter and 758.4 kg/m^3 in density (Cui et al. 2020), as shown in Fig. 9.

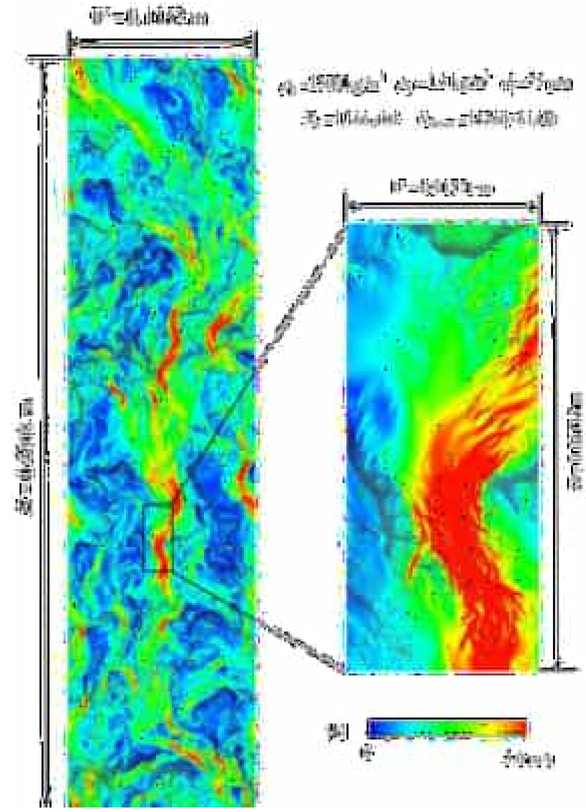

Fig. 7. Multi-scale structure in gas-solid flow reproduced by LBM-IBM (Xiong et al. 2012).

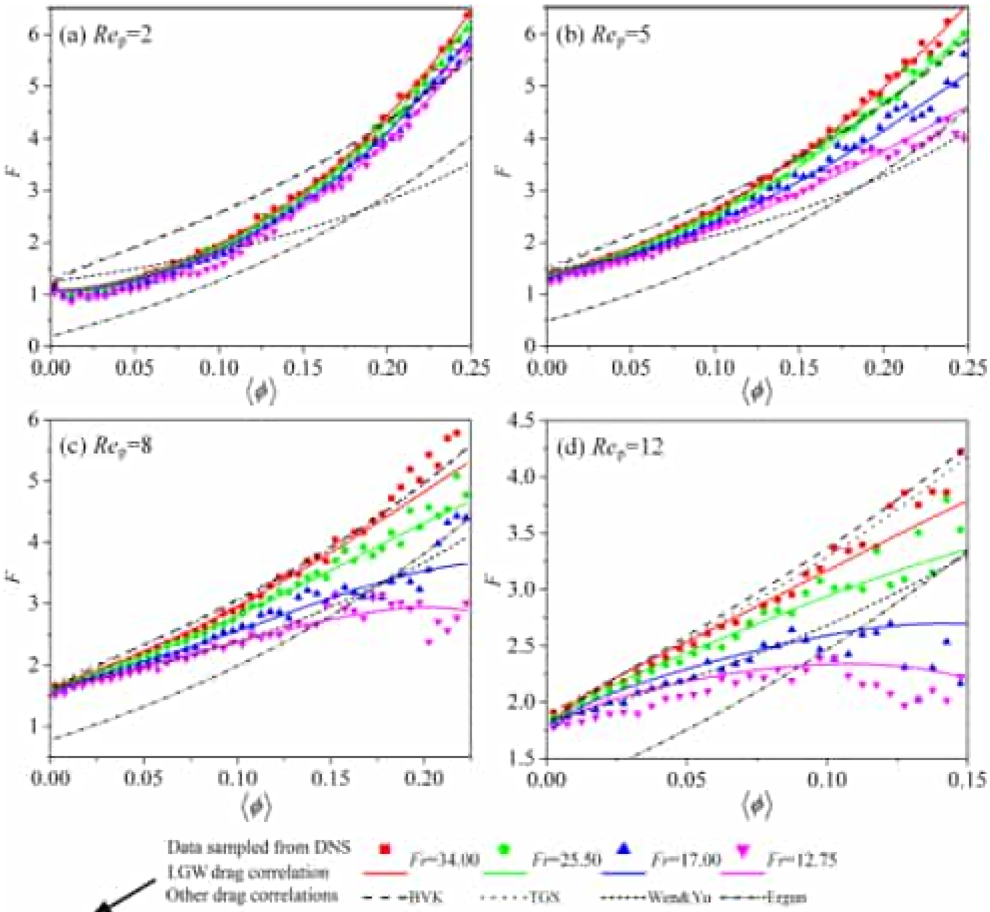

$$F=\frac{1+0.15Re_p^{0.687}}{(1-\langle\phi\rangle)^{3.65}}\left(1-\frac{0.175(1-\langle\phi\rangle)^{1.65}}{Re_{p0}^{0.687}}\ln\frac{Fr_p}{Fr}\right)-\frac{6.06\langle\phi\rangle Re_p^{0.85}}{(1-\langle\phi\rangle)^{5}(Re_{p0}+1)}\ln\frac{Fr_p}{Fr}+\frac{\left(13.36Re_p^{1/4}-1.9(1-\langle\phi\rangle)^{2}(Fr_p+Fr)^{3/8}\right)\sqrt{\langle\phi\rangle}}{(Fr_p+Fr)^{1/8}(1-\langle\phi\rangle)^{4+0.02Fr}}$$

Fig. 8. Correlations for the gas-solid drag from DNS (Liu et al. 2020a).

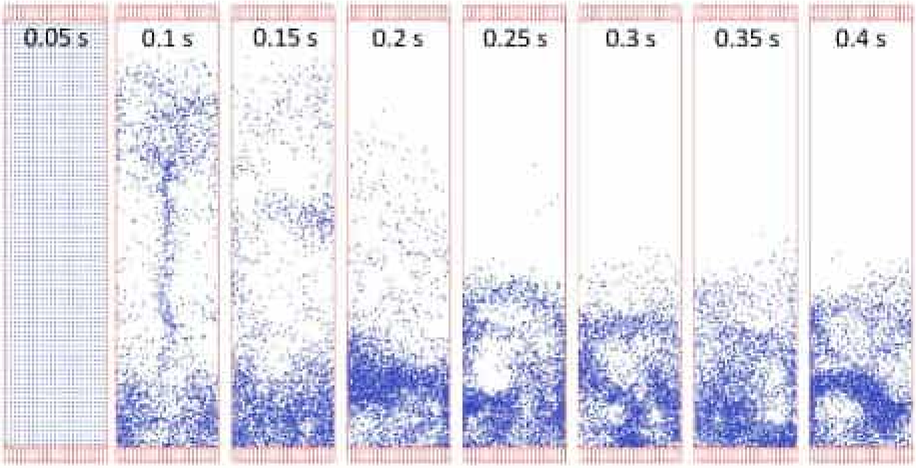

Fig. 9. DNS of gas-solid fluidization using finite difference method and IBM (Cui et al. 2020).

Note that in this implementation the fluid flow is assumed to be incompressible flow, and hence the Poisson equation for the fluid pressure is solved implicitly in iterations with global operations, which is not favorable to large scale parallel computing. This may be inevitable for liquid-solid flow, but for gas-solid fluidization the gas flow can be reasonably considered as weakly compressible and, therefore, more scalable explicit finite difference or finite volume methods can be used.

Prospect and Conclusions

Undoubtedly, DNS has become an important and powerful tool for the study of fluidization, and with the fast development of numerical methods and computing technology, its future capability can be highly anticipated. In fact, computational power will not be the main obstacle, but some fundamental questions are to be answered either by future DNS studies or for more effective use of this numerical tool:

- What is the scale and accuracy of DNS we eventually need to understand and quantify the fluidization process in industries and engineering? We certainly should not expect DNS to reproduce it at commercial scale directly, even if it becomes technologically attainable in a future time. But, on the other hand, an element scale with only thousands of particles is not sufficient also, considering the multi-scale nature of the flow structures and their scale-dependence. Ge et al. (2017) suggested that DNS of fluidization should be conducted up to the meso-scale with multiple clusters or bubbles in the computational domain, which can help to establish and improve the meso-scale models such as the EMMS model, or to provide the constitutive correlations below the meso-scale. This is already a tremendous computational cost, far beyond what we have spent currently. The uncertainty is that how large the meso-scale structures is in commercial systems, and whether they increase monotonously with the system scale? So far, lab experiments and in-situ measurements do not have a decisive answer yet. Other simulation methods at larger scales may have an answer sooner, but as they also need inputs from DNS, large-scale DNS itself may have to be involved in answering this question about it.
- How do we make full use of the DNS results at small scales that are easier to obtain? Some work, including ours, seems to suggest that a statistical description at smaller scale may involve more variables to reflect its local flow structure, which is a challenge to its closure, that is, completeness. Meanwhile, smaller scale means more samples of the same ensemble are needed to find the statistical laws, so smaller scale may not necessarily reduce the total computational cost. Moreover, the statistical descriptions thus obtained are inherently more fluctuating and uncertain when applying to macro-scale dynamics, constituting a further trade-off of its higher apparent resolution. That means, there must be an optimal scale for the coupling between the statistical and dynamical descriptions at the micro- and macro-scales, respectively. How to select the variable set

and how to determine the optimal scale are, of course, very complicated topics theoretically, maybe artificial intelligence, such as machine learning, can play a role, DNS itself could be the exploration tool by accumulating results at different scales.

- Since DNS is not for direct simulation of practical systems, how to design the model systems or elemental domains is a critical problem. Currently periodic domains are widely used, which can effectively suppress the influence of physical boundaries in studying local behavior, but may introduce artificial correlation between the real domain and its images. They are also used very often with additional body force to drive the flow, but our recent study indicated that this treatment may lead to notable difference to the more realistic pressure driven flow (Liu, 2019). Simulating a physically possible system, such as a mini fluidized bed, may avoid such artifacts, but whether the small-scale behavior in such model systems is comparable to that in practical systems is also an open question.
- Technically, developing more accurate and efficient numerical methods is also important for DNS to play a more important role in the study of fluidization and particle-fluid systems. Neither of the four methods we tried previously can be favorable in all aspects. PPM is costly, SPH is not very accurate, LBM is not versatile and FD/FV methods are not so scalable. Therefore, improving different methods for different applications seems to be the logical way forward. On the other hand, coupling different methods in one application could also be fruitful. For example, PPM can be used in the vicinity of the particles to describe the interface reactions with enough details while LBM can be used in the bulk for the flow and transport processes with higher efficiency. In terms of computational methods, adaptive mesh refining and dynamic load balancing are necessary for higher efficiency and new hardware, such as the AI chips should be employed to provide much higher flops.

Finally, multi-scale coupling of DNS and other simulation methods is highly desirable for its numerical improvement and physical setup in case studies. For example, with the development of supercomputing, particle-unresolved Euler-Lagrangian methods will soon be able to simulate full-scale practical systems within reasonable time and cost (Liu et al. 2020b). If DNS can be embedded into the interested locations in runtime to obtain boundary conditions from the evolving neighborhood, we may construct realistic computational domains for the study of reliable micro-scale models. In this sense, DNS is an indispensable component in both concurrent and cascaded multi-scale modeling of particle-fluid systems.

Notation

d_b	bubble diameter, [m]
d_e	particle diameter, [m]
e_{12}	restitution coefficient of pseudo particles, [-]
F	dimensionless drag, [-]
$F_{D,y}$	y-component (vertical) of drag, [N]
Fr	Froude number, [-]
H	system height, [mm]
m_1, m_2	mass of pseudo particles, [kg]
N_p	particle number, [-]
N_{cell}	number of grid cell, [-]
$N_{lattice}$	number of grid cell, [-]
N_T	energy consumption rate for particles, [W kg-1]
N_{st}	energy consumption rate for suspending and transporting particles, [W kg-1]
P_1, P_2	position of pseudo particles, [m]
Re	bulk Reynolds number, [-]
Re_p	slip Reynolds number, [-]
t	time, [s]
U_g	inlet gas velocity (superficial gas velocity), [m s^{-1}]
U_{st}	fluid velocity for suspending and transporting particles, [m s^{-1}]
v_1, v_2	velocity of pseudo particles, [m/s]
V_{ry}	y-component (vertical) interphase slip velocity, [m/s]
W	system weight, [mm]
ρ_f	density of fluid, [kg m^{-3}]
ρ_g	density of gas, [kg m^{-3}]
ρ_s	density of solid equal to ρ_p, [kg m^{-3}]
ρ_p	density of particle equal to ρ_s, [kg m^{-3}]
φ	solid volume fraction

References

Ardekani, M.N., Al Asmar, L., Picano, F., Brandt, L. Numerical study of heat transfer in laminar and turbulent pipe flow with finite-size spherical particles. International Journal of Heat and Fluid Flow 2018. 71, 189-199.

Baltussen, M.W., Kuipers, J.A.M., Deen, N.G. Direct numerical simulation of effective drag in dense gas–liquid–solid three-phase flows. Chemical Engineering Science 2017. 158, 561-568.

Beetstra, R., van der Hoef, M.A., Kuipers, J.A.M. Drag force of intermediate Reynolds number flow past mono- and bidisperse arrays of spheres. AIChE Journal 2007. 53, 489-501.

Chen, F., Ge, W.. Statistical properties of pseudo-particle systems. Particuology 2010. 8, 332-342.

Cui, H., Chang, Q., Chen, J., Ge, W. Particle-resolved simulation study on mesoscale structure and stability in gas-solid fluidization. 2020. Submitted to Chemical Engineering Journal.

Cundall, P.A., Strack, O.D.L. A discrete numerical-model for granular assemblies. Geotechnique 1979. 29, 47-65.

Deen, N.G., Kriebitzsch, S.H.L., van der Hoef, M.A., Kuipers, J.A.M. Direct numerical simulation of flow and heat transfer in dense fluid–particle systems. Chemical Engineering Science 2012. 81, 329-344.

Feng, Z.G., Musong, S.G. Direct numerical simulation of heat and mass transfer of spheres in a fluidized bed. Powder Technology 2014. 262, 62-70.

Ge, W., Li, J. Pseudo-particle approach to hydrodynamics of gas/solid two-phase flow. Li J and Mooson K. Proceedings of the 5th International Conference on Circulating Fluidized Bed. Beijing: Science Press 1996. 260-265.

Ge, W., Li, J. Macro-scale pseudo-particle modeling for particle-fluid systems. Chinese Science Bulletin 2001. 46, 1503-1507.

Ge, W., Li, J. Macro-scale phenomena reproduced in microscopic systems pseudo-particle modeling of fluidization. Chemical Engineering Science 2003a. 58, 1565-1585.

Ge, W., Li, J. Simulation of particle-fluid systems with macro-scale pseudo-particle modeling. Powder Technology 2003b. 137, 99-108.

Ge, W., Wang, L., Xu, J., Chen, F., Zhou, G., Lu, L., Chang, Q., Li, J. Discrete simulation of granular and particle-fluid flows: from fundamental study to engineering application. Reviews in Chemical Engineering 2017. 33, 551-623.

Gingold, R.A., Monaghan, J.J. Smoothed particle hydrodynamics: theory and application to non-spherical stars. Monthly Notices of the Royal Astronomical Society 1977. 181, 375-389.

Hill, R.J., Koch, D.L., Ladd, A.J. Moderate-Reynolds-number flows in ordered and random arrays of spheres. Journal of Fluid Mechanics 2001. 448, 243-278.

Kriebitzsch, S.H.L., van der Hoef, M.A., Kuipers, J.A.M. Fully resolved simulation of a gas-fluidized bed: A critical test of DEM models. Chemical Engineering Science 2013. 91, 1-4.

Li, J. Multi-Scale Modeling and Method of Energy Minimization for Particle-Fluid Two-Phase Flow, Doctor thesis, Institute of Chemical Metallurgy. 1987. Chinese Academy of Sciences, Beijing.

Li, J., Kwauk, M. Particle-fluid two-phase flow energy-minimization multi-scale method, Metallurgical Industry Press. 1994. Beijing.

Li, Y., Zhang, C., Li, C., Liu, Z., Ge, W. Simulation of the effect of coke deposition on the diffusion of methane in zeolite ZSM-5，Chemical Engineering Journal 2017a. 320, 458-567.

Li, Y., Zhao, M., Li, C., Ge, W. Simulation study on the reaction-diffusion coupling in simple pore structures，Langmuir 2017b. 33, 11804-11816.

Li, Y., Zhao, M., Li, C., Ge, W. Concentration fluctuation due to reaction-diffusion coupling near an isolated active site on catalyst surfaces. Chemical Engineering Journal 2019. 373, 744-754.

Liu, X., Wang, L., Ge, W. Meso-scale statistical properties of gas-solid flow — a direct numerical simulation (DNS) study. AIChE Journal 2017. 63, 3-14.

Liu, X., Ge, W., Wang, L. Scale and structure dependent drag in gas-solid flows. AIChE Journal 2020. In press.

Liu, X., Xu, J., Ge, W., Lu, B., Wang, W. Long-time simulation of catalytic MTO reaction in a fluidized bed reactor with a coarse-grained discrete particle method — EMMS-DPM, Chemical Engineering Journal, Volume 389, 2020,

Lun, C., Savage, S.B., Jeffrey, D., Chepurniy, N. Kinetic theories for granular flow: inelastic particles in Couette flow and slightly inelastic particles in a general flow field. Journal of Fluid Mechanics 1984. 140, 223-256.

Luo, K., Tan, J., Wang, Z., Fan, J. Particle-resolved direct numerical simulation of gas–solid dynamics in experimental fluidized beds. AIChE Journal 2016. 62, 1917-1932.

Ma, J., Ge, W., Wang, X., Wang, J., Li, J. High-resolution simulation of gas-solid suspension using macro-scale particle methods. Chemical Engineering Science 2006. 61, 7096-7106.

Ma, J., Ge, W., Xiong, Q., Wang, J., Li, J. Direct numerical simulation of particle clustering in gas-solid flow with a macro-scale particle method. Chemical Engineering Science 2009. 64, 43-51.

McNamara, G.R., Zanetti, G. Use of the Boltzmann equation to simulate lattice gas automata. Physical Review Letters 1988. 61, 2332.

Noble, D., Torczynski, J. A lattice-Boltzmann method for partially saturated computational cells. International Journal of Modern Physics C 1998. 9, 1189-1201.

Ozel, A., Brändle de Motta, J.C., Abbas, M., Fede, P., Masbernat, O., Vincent, S., Estivalezes, J.L., Simonin, O. Particle resolved direct numerical simulation of a liquid–solid fluidized bed: Comparison with experimental data. International Journal of Multiphase Flow 2017. 89, 228-240.

Pan, T.W., Joseph, D., Bai, R., Glowinski, R., Sarin, V. Fluidization of 1204 spheres: simulation and experiment. Journal of Fluid Mechanics 2002. 451, 169-191.

Picano, F., Breugem, W.P., Brandt, L. Turbulent channel flow of dense suspensions of neutrally buoyant spheres. Journal of Fluid Mechanics 2015. 764, 463-487.

Qu, S., You, C. Direct numerical simulation (DNS) of alkali metals released during char combustion. Fuel 2019. 255, 115763.

Richardson, J.F., Zaki, W.N. The sedimentation of a suspension of uniform spheres under conditions of viscous flow. Chemical Engineering Science 1954. 3, 65-73.

Rong, L.W., Dong, K.J., Yu, A.B. Lattice-Boltzmann simulation of fluid flow through packed beds of uniform spheres: Effect of porosity. Chemical Engineering Science 2013. 99, 44-58.

Rubinstein, G.J., Ozel, A., Yin, X., Derksen, J.J., Sundaresan, S. Lattice Boltzmann simulations of low-Reynolds-number flows past fluidized spheres: effect of inhomogeneities on the drag force. Journal of Fluid Mechanics 2017. 833, 599-630.

Tang, D., Ge, W., Wang, X., Ma, J., Guo, L., Li, J. Parallelizing of macro-scale pseudo-particle modeling for particle-fluid systems. Science in China Series B: Chemistry 2004. 47, 434-442.

Tang, Y., Lau, Y.M., Deen, N.G., Peters, E.A.J.F., Kuipers, J.A.M. Direct numerical simulations and experiments of a pseudo-2D gas-fluidized bed. Chemical Engineering Science 2016a. 143, 166-180.

Tang, Y., Peters, E.A.J.F., Kuipers, J.A.M. Direct numerical simulations of dynamic gas-solid suspensions. AIChE Journal 2016b. 62, 1958-1969.

Tenneti S, Garg R, Subramaniam S. Drag law for monodisperse gas–solid systems using particle-resolved direct numerical simulation of flow past fixed assemblies of spheres. International Journal of Multiphase Flow 2011. 37, 1072-1092.

van der Hoef, M.A., Beetstra, R., Kuipers, J.A.M. Lattice-Boltzmann simulations of low-Reynolds-number flow past mono- and bidisperse arrays of spheres: results for the permeability and drag force. Journal of Fluid Mechanics 2005. 528, 233-254.

Wang, L., Zhou, G., Wang, X., Xiong, Q., Ge, W. Direct numerical simulation of particle-fluid systems by combining time-driven hard-sphere model and lattice Boltzmann method. Particuology 2010. 8, 379-382.

Xiong, Q., Li, B., Chen, F., Ma, J., Ge, W., Li, J. Direct numerical simulation of sub-grid structures in gas-solid flow-GPU implementation of macro-scale pseudo-particle modeling. Chemical Engineering Science 2010. 65, 5356-5365.

Xiong, Q., Li, B., Zhou, G., Fang, X., Xu, J., Wang, J., He, X., Wang, X., Wang, L., Ge, W., Li, J. Large-scale DNS of gas-solid flows on Mole-8.5. Chemical Engineering Science 2012. 71, 422-430.

Zhang, J., Ge, W., Li, J. Simulation of heterogeneous structures and analysis of energy consumption in particle-fluid systems with pseudo-particle modeling. Chemical Engineering Science 2005. 60, 3091-3099.

Zhou, G., Xiong, Q., Wang, L., Wang, X., Ren, X., Ge, W. Structure-dependent drag in gas-solid flows studied with direct numerical simulation. Chemical Engineering Science 2014. 116, 9-22.

Table 1. DNS of particle-fluid systems in recent years.

Author(s)	ρ_p/ρ_f	Boundary	Domain size (d_p or mm)	N_p	$N_{cell}/10^6$	d_p/h	Re_p or Re	Description
Hill et al. (2001)	Static	Periodic	5*2.5*2.5d_p	16~2560	~1	1.468~67.6	<<1	Gas-solid; drag law
Beetstra et al. (2007)	Static	Periodic	4*4*4 d_p	54	~0.3	17~26	0~1050	Gas-solid; drag law
Rong et al. (2013)	Static	Periodic	5*5*25 d_p	324~805	5	20	0.002-500	Gas-solid; drag law
Tang et al. (2016b)	500-3000	Periodic	16*16*16	191~859	7	~12	40-900	Gas-solid; drag law
Rubinstein et al. (2017)	10-300	Periodic	12*12*12 d_p	330~990	3	12	≤1	Gas-solid; drag law
Liu et al. (2020)	1153	Periodic	46.8*11.52*0.48	7200-115200	480	20	0-15	Gas-solid; drag law
Baltussen et al. (2017)	2 0.1 (ρ_b/ρ_f)	Periodic	~20*20*20 d_p	60~90 16~150 (N_b)	~2	10 20 (d_b/h)	100 (typical)	Gas-liquid-solid; drag law
Kriebitzsch et al. (2013)	833	Inlet-outlet	14.8*5.6*42	2000	3	10	35.3	Gas-solid fluidiation
Luo et al. (2016)	833	Inlet-outlet	44*10*133.2	9240	6	12	66	Gas-solid fluidiation
Tang et al. (2016a)	2105	Inlet-outlet	100*15*250	5000	3	5	400	Gas-solid fluidiation
Ozel et al. (2017)	1.59	Inlet-outlet	80*80*640	2088	32	12	100	Liquid-solid fluidiation
Pan et al. (2002)	1.14	Inlet-outlet	6.86*203*702.2	1204	3	~10	730	Liquid-solid fluidiation
Picano et al. (2015)	1	Periodic	54*18*27 d_p	10000	100	16	5600	Liquid-solid channel flow; turbulence-particle interaction
Sun et al. (2015)	Static	Periodic	7.5*7.5*7.5 d_p	100	4	40	200	Gas-solid; heat transfer coefficient
Feng et al. (2014)	1.14	Inlet-outlet	102.8*6.85*360	225	5	~17	0.035-0.055	Liquid-solid; heat transfer
Deen et al. (2012)	6.57	Inlet-outlet	20*0.6*40	1296	4	5	33-133	Liquid-solid; heat transfer
Ardekani et al. (2018)	1	Periodic	180*15*15 d_p	5000	2500	30~40	370 (laminar) 5300 (turbulent)	Liquid-solid pipe flows; wall-suspension heat transfer
Qu et al. (2019)	833	Inlet-outlet	350*100	150	3.5	10	130	Gas-solid; heat&mass transfer + reaction

TOWARDS SUSTAINABLE ENERGY AND MATERIALS: CO_2 CAPTURE USING NOVEL NANOSCALE HYBRID PARTICULATE SYSTEMS

Guanhe Rim[1,3], Dongyi Wang[1,3], Valizadeh Bardiya[4], Kyriakos C. Stylianou[4], Berend Smit[4], Donghyun Lee[5], and Ah-Hyung Alissa Park[1,2,3*]

[1]*Department of Earth and Environmental Engineering, Columbia University, NY, USA*
[2]*Department of Chemical Engineering, Columbia University, NY, USA*
[3]*Lenfest Center for Sustainable Energy, Columbia University, NY, USA*
[4]*Laboratory of Molecular Simulation, Institut des Sciences et Ingénierie Chimiques, Valais, Ecole Polytechnique Fédérale de Lausanne (EPFL), 1015 Lausanne, Switzerland*
[5]*School of Chemical Engineering, Sungkyunkwan University (SKKU), 2066 Seobu-ro, Jangan-gu, Suwon, Gyeonggi-do, 16419, Republic of Korea*

Email: ap2622@columbia.edu*

Abstract

A number of novel materials including metal-organic frameworks (MOFs) have been developed to capture CO_2 from various industrial sources. While some recently synthesized MOFs have great CO_2 capture capacity and even water tolerance, large scale application is still debated because the handling of nanocrystalline MOFs powders in a reactor system is very challenging. In this study, millimeter-sized MOFs-bearing porous polymer beads are prepared and the effect of hybrid sorbents on CO_2 capture behaviors are studied in a fixed bed set-up for application in fluidized bed system. Different P_{CO2} gas streams (0.02 – 0.15 atm) are used as the inlet gas and the CO_2 capture conditions are maintained at ambient conditions (25 °C and 1 atm) to obtain CO_2 breakthrough curves. The MOFs bearing polymer beads show higher CO_2 loading compared to the neat polymer beads and bulk MOFs powder (ZIF-8) indicating synergy effect between MOFs and polymer support. The experimental finding shows that this delivery method of MOFs enhances the CO_2 capture capacity as well as provides better handling of MOFs powders for large scale CO_2 capture units ranging from a fixed bed to a fluidized bed.

Introduction

The global atmospheric CO_2 concentration has continuously increased since the industrial revolution due to consumption of fossil fuels such as coal, petroleum oil, and natural gas and reached in 410 ppm level in 2019 (National Oceanic & Atmospheric Administration Research, 2019). It has been identified that the intensification of climate change correlates with the increase in atmospheric CO_2 concentration (Scheffer et al., 2006). The atmospheric CO_2 concentration is expected to further increase at an even faster pace if the current consumption of fossil fuels continues, resulting in global warming of 1.5 °C above pre-industrial levels between 2030 and 2052 (IPCC, 2018). Thus, various solutions have been placed on CO_2 mitigation including the development of carbon capture, utilization and storage (CCUS) technologies (Mission Innovation, 2017; Smit et al., 2014).

In order to develop effective CCUS technologies, the most research and development need to focus on CO_2 capture process which would be the most costly part in CCUS (Patel et al., 2017). The current industrial scale CO_2 capture method is amine solution-base absorption process. The aqueous amine solution is the reason for the high cost due to the intensive energy requirement for the solvent regeneration and the solvents lose over multiple cycle. Adsorption-based solid sorbents, such as metal-organic frameworks (MOFs), are considered as attractive alternatives because of their low energy requirement for sorbents regeneration and recyclability over many cycles (Liu et al., 2012).

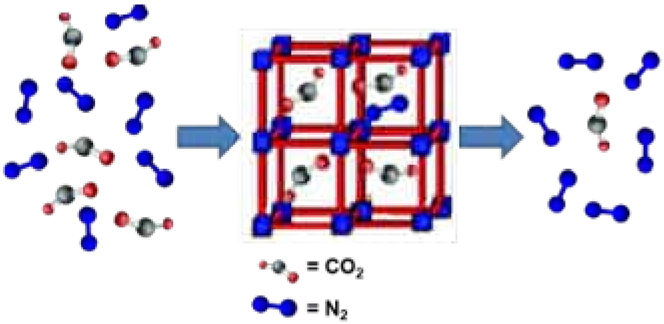

Fig. 1. Schematic illustration of CO_2 capture by metal-organic frameworks (MOFs).

As shown in Fig. 1, MOFs are hybrid materials prepared by metal ions as connectors and organic ligands as linkers. The strong bond between metal ions and organic ligands forms 1D – 3D structures porous frameworks. Due to their unique characteristics, such as high surface areas, structural and chemical tunability, MOFs are excellent candidate for CO_2 capture and separation (Li et al., 2014; Samanta et al., 2012).

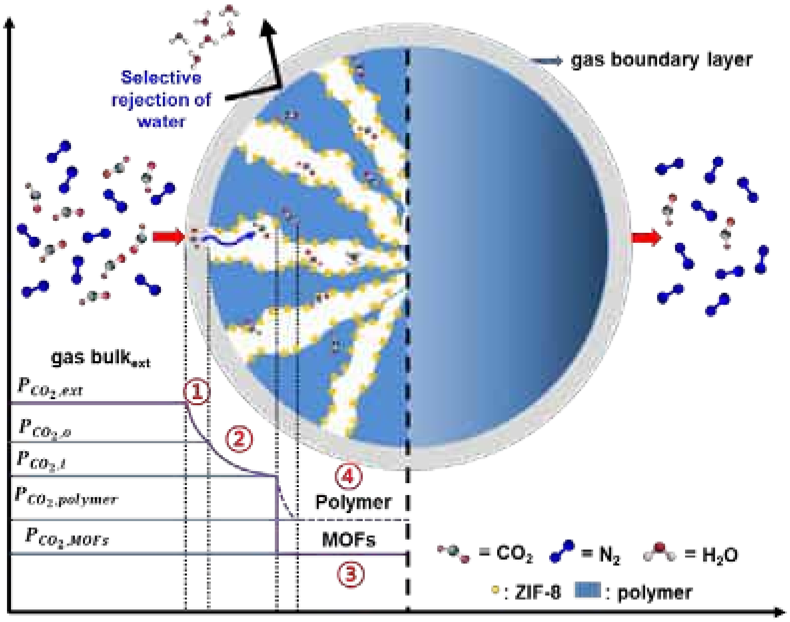

Fig. 2. Overall CO_2 sorption steps by MOF-bearing polymer beads.

However, MOFs are generally synthesized in nano-crystalline powder forms, thus large-scale application is still debated because the handling of nanocrystalline MOFs powders in a reactor system is very challenging. In this study, in order to overcome the handling issues and nanocrystals and fine particles, the nano-crystalline MOF powders (100 – 1000 nm) have been synthesized and mixed with hydrophobic organic polymer solution. The mixture is dropwise added to the coagulation bath to form spherical MOF-polymer composite beads, which we refer to MOFs@polymer depending on the selection of polymer used as the support (Valizadeh et al., 2018) for application in large scale CO_2 capture process. As shown in Fig. 2, zeolitic imidazolate framework (ZIF-8) bearing porous polymer beads were prepared and this millimeter-sized particulate system is expected to provide a better handling of MOFs powders as well as enhanced CO_2 capture behavior resulted from improved CO_2 diffusion through the polymer matrix. The effect of hybrid sorbents on CO_2 capture behaviors are studied in a fixed bed and fluidized bed set-up to demonstrate their applicability in a large-scale CO_2 capture system.

Experimental

The MOFs (ZIF-8) bearing porous polymer beads were synthesized and prepared by the group at Ecole Polytechnique Fédérale de Lausanne (EPFL). The detail synthesis procedures are summarized in their previous work (Valizadeh et al., 2018). As shown in Fig. 3, three hydrophobic polymers: polyetherimide (PEI), polyethersulfone (PES), and polyvinylidene fluoride (PVDF), were employed as the support material for ZIF-8 crystalline powders (100 – 1000 nm). These polymers have been widely used in industry because of their high chemical, thermal, and mechanical stabilities. ZIF-8 nano-crystalline powders were loaded into each porous polymer matrix with a loading of 65 wt%. The synthesized ZIF-8 bearing porous polymer beads had particle diameter of approximately 2 mm and particle density of 370 – 460 kg/m^3, and they were denoted as ZIF-8@PEI, ZIF-8@PES, and ZIF-8@PVDF.

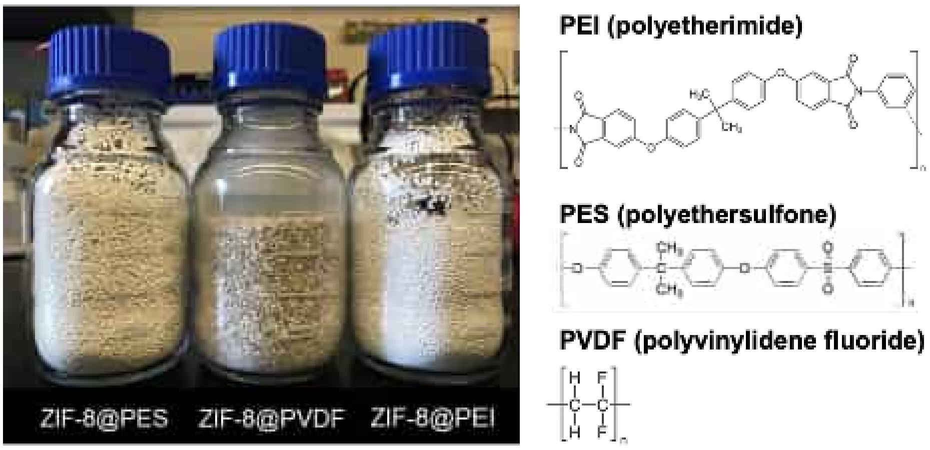

Fig. 3. ZIF-8 bearing polymer beads and chemical structure of PEI, PES and PVDF.

CO_2 single gas adsorption experiments were first performed in a fixed bed system shown in Fig. 4. The adsorption column consists of a 56.25 mm inner diameter acryl column and a porous ceramic gas distributor. In order to conduct CO_2 sorption experiment, the column was filled with neat polymer (base case) or ZIF-8 bearing polymer beads with about 66.23 cm^3 of constant bulk volume. The nano-crystalline ZIF-8 powders dispersed in glass wool were also tested in the same fixed bed system in order to provide the basis for the effect of polymer supports. Since the densities of MOFs@polymer were different, the mass of each loaded sorbent is summarized in Table 1.

The feed gas streams (CO_2 and He) were controlled by mass flow controllers and the CO_2 concentration of feed gas (2, 5, 8, 12, and 15 vol%) was varied by regulating the flow rate of CO_2 and He. The total flow rate of inlet gas stream was always kept at 500 ml/min. Prior to the CO_2 adsorption experiment, the packed sorbents inside the column were purged with He (0% CO_2) for 1 hr. Then, the different P_{CO2} gas streams were injected into the packed column through the 3-way valve and the adsorption took place at T = 25 ^oC and P = 1 atm. During the adsorption experiment, the CO_2 concentration of the outlet gas stream was continuously measured by Non-dispersive infrared (NDIR) gas analyzer to obtain the breakthrough curve as a function of time. A reference breakthrough curve was obtained using 2 mm glass beads, which should not interact with CO_2.

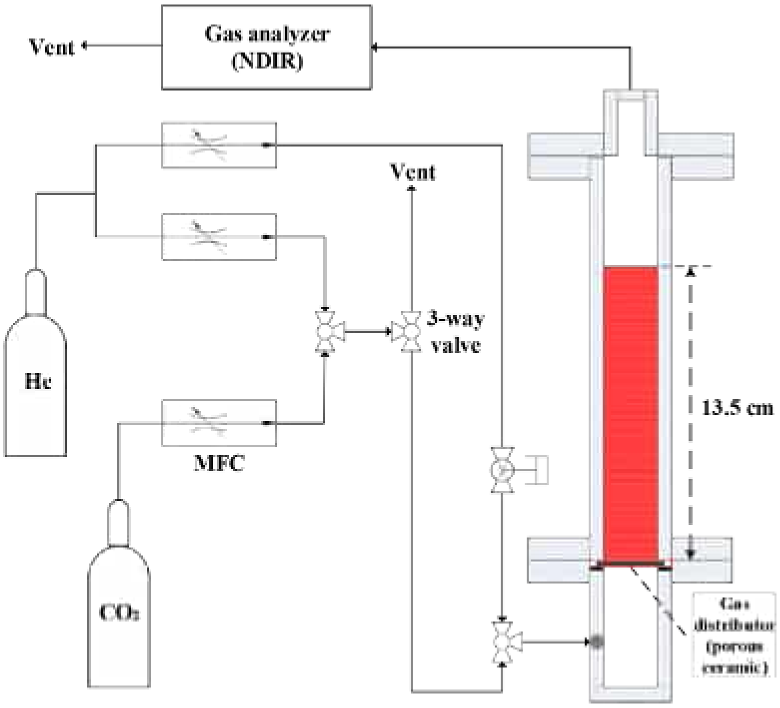

Fig. 4. Schematic diagram of the fixed bed and fluidized bed CO_2 adsorption system for MOF-bearing polymer beads (volume of CO_2 capture zone = 66.23 cm^3).

Table 1. Particle densities and mass of loaded sorbents in the fixed bed system (volume of CO_2 capture zone = 66.23 cm^3).

	ZIF-8	PES		PVDF		PEI	
		Neat PES without ZIF-8	65 wt% ZIF-8	Neat PVDF without ZIF-8	65 wt% ZIF-8	Neat PEI without ZIF-8	65 wt% ZIF-8
Particle density (g/cm^3)	0.95	0.17	0.35	0.33	0.43	0.21	0.37
Mass loading in the fixed bed (66.23 cm^3)	5.7 g (with glass wool support)	6.86 g	13.82 g	13.03 g	16.98 g	8.33 g	14.81 g

Results and Discussion

In order to evaluate the CO_2 capture performance of the ZIF-8@polymer beads, the breakthrough curve of neat polymer and ZIF-8 bearing polymer beads were obtained and are shown in Fig. 5(a) and (b), respectively. As shown in Fig. 5, a longer breakthrough time of ZIF-8@polymer than neat polymer CO_2 indicates that CO_2 capture by sorbents was improved by loading the nano-crystalline ZIF-8 powders inside the porous polymer beads. The equilibrium CO_2 loading (mmol CO_2/g sorbent) of neat polymer and ZIF-8@polymer beads (also bulk ZIF-8 powders) were obtained by integrating the complete breakthrough curve lines and were plotted as a function of P_{CO_2} in Fig. 6(a) and (b), respectively, compared to the equilibrium CO_2 loading of bulk ZIF-8 powders.

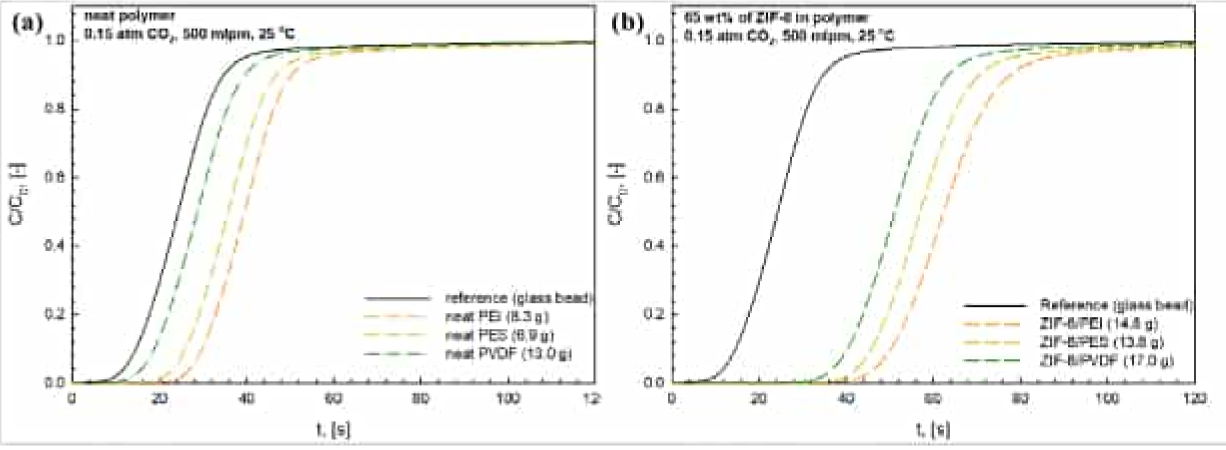

Fig. 5. CO_2 capture breakthrough curve of (a) neat polymer beads and (b) ZIF-8 bearing polymer beads (T = 25 ^oC, P = 1 atm, and P_{CO_2} = 0.15 atm).

Based on these breakthrough curves, the CO_2 capture capacities of the sorbents are determined and the results are shown in Figure 6. As expected, in terms of the unit volume of sorbent particles, CO_2 capture capacity of ZIF-8 was significantly greater than those of neat polymers (Fig. 6(a)) within the given P_{CO_2} range used for this study (0.02 – 0.15 atm). Interestingly, neat PEI and PES polymer beads showed comparable CO_2 capture capacities compared to bulk ZIF-8 powders in terms of per unit mass (Figure 6(b)). This is because the particle densities of neat porous polymers are significantly smaller than that of ZIF-8 (data given in Table 1). Depending on the design of the CO_2 capture reactor (i.e., fixed bed reactor vs. fluidized bed reactor), the volume and mass of the sorbents would play an important role for the process design. While small, PEI and PES can capture CO_2, and thus, they would be better candidates as supporting material for MOFs. PVDF polymer beads showed very low CO_2 uptake capacity, and therefore, it may not be the suitable candidate material for MOFs@polymer. One of the causes of low CO_2 loading in PVDF is its low BET surface area (5 m^2/g) compared to the PEI (11 m^2/g) and PES (12 m^2/g) beads.

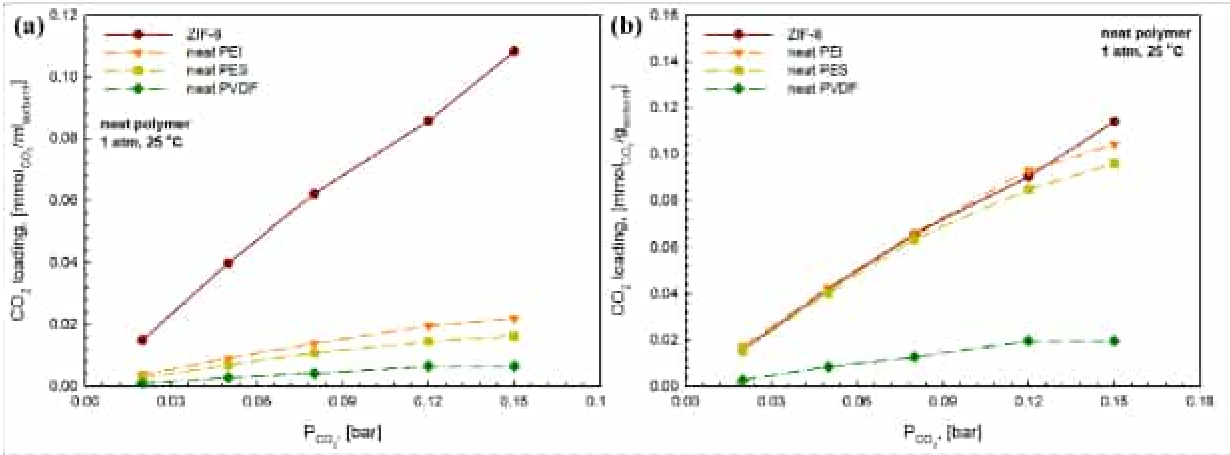

Fig. 6. CO_2 adsorption isotherm of neat polymer beads compared to ZIF-8 nanocrystals at T = 25 ^oC (a) in terms of unit volume and (b)in terms of unit mass.

One of the important questions for CO2 capture by MOFs@polymer was whether these polymers would hinder the CO2 uptake by ZIF-8 embedded in them. As shown in Fig. 7 compared to Figure 6(b), the CO_2 loading of all sorbents were improved by the encapsulated nano-crystalline ZIF-8 powders inside the polymer composites. Among all three ZIF-8@polymer beads, the ZIF-8@PEI exhibited the highest CO_2 uptake (0.15 mmol/g at 0.15 atm

CO_2) and it was even higher than that of the nano-crystalline ZIF-8 powders (0.11 mmol/g at 0.15 atm CO_2). As expected, the ZIF-8@PVDF showed the lowest CO_2 uptake (0.09 mmol/g at 0.15 atm CO_2). The variation in the CO_2 capture capacity with different polymer supports indicates that there is a synergistic effect between ZIF-8 powders and polymer support, and the diffusion of CO_2 molecules through the pores can be tuned with a suitable polymer matrix. Thus, it was concluded that the design of hybrid solid sorbents (ZIF-8@polymer) is very attractive for enhanced CO_2 capture while allowing better handling of nano-crystalline MOFs powders (ZIF-8) in reactor systems.

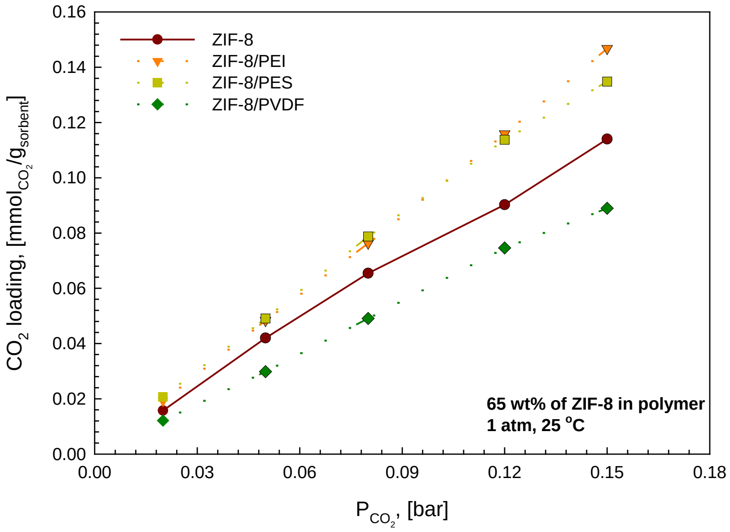

Fig. 7. CO_2 adsorption isotherm of ZIF-8 bearing polymer beads at T = 25 °C.

While a fixed bed reactor system is useful at obtaining breakthrough curves and determining the CO_2 capture capacities of different materials, there are many reactor designs available for gas-solid interactions including CO_2 capture. A fluidized bed reactor is one of the unique systems that can provide excellent heat and mass transfer behaviors. Since the MOFs@polymer particles are light in terms of particle density, we proposed to use a fluidized bed reactor or inject these sorbent particles directly into the duct to capture CO_2.

In order to investigate fluidization behaviors of ZIF-8@PEI beads (selected based on CO_2 capture tests in the fixed bed reactor), the experiment setup shown in Fig 4 was operated at a superficial gas velocity of $U > U_{mf}$ condition. 15 vol% CO_2 in N_2 gas stream was used as a fluidizing gas to simulate a flue gas condition. Based on the Geldart's classification, the ZIF-8@PEI beads having particle diameter of about 2 mm and particle density of approximately 400 kg/m^3 should be Group B particles, that can be readily fluidized (Park et al., 2019). However, as shown in Fig. 8(a), the ZIF-8@PEI beads were quickly de-fluidized and particle agglomeration and wall sheeting were observed. This was due to large static buildup within this particulate reactor system and the low particle density (approximately 400 kg/m^3) did not provide enough weight to overcome the strong electrostatic interparticle forces. Thus, it was clear that a fluidized bed reactor system is not suitable for ZIF-8@PEI sorbent particles.

Interestingly, when He gas was injected as a fluidized gas to purge the captured CO_2 from the ZIF-8@PEI beads, these ultralight ZIF-8@PEI beads quickly became fluidized and particle agglomeration and wall sheeting disappeared (see Fig. 8(b)). It seemed that somehow the particle charge levels were significantly decreased in He (noble gas) environment when compared to mimicked flue gas, resulting in better fluidization quality. Slugging behaviors were detected because of the small column diameter to height ratio but it was still clear that the interparticle forces were significantly lower for ZIF-8@PEI and He system. There are very limited literature exists on the effect of noble gases in electrostatic charging behaviors in particulate systems (Harper and Dufek, 2016; Matsuyama and Yamamoto, 1995). Thus, the effect of He gas on particle charging behaviors in fluidized beds need to be further investigated and the experimental findings will be able to improve the fluidization quality of ultralight particles including ZIF-8@PEI beads.

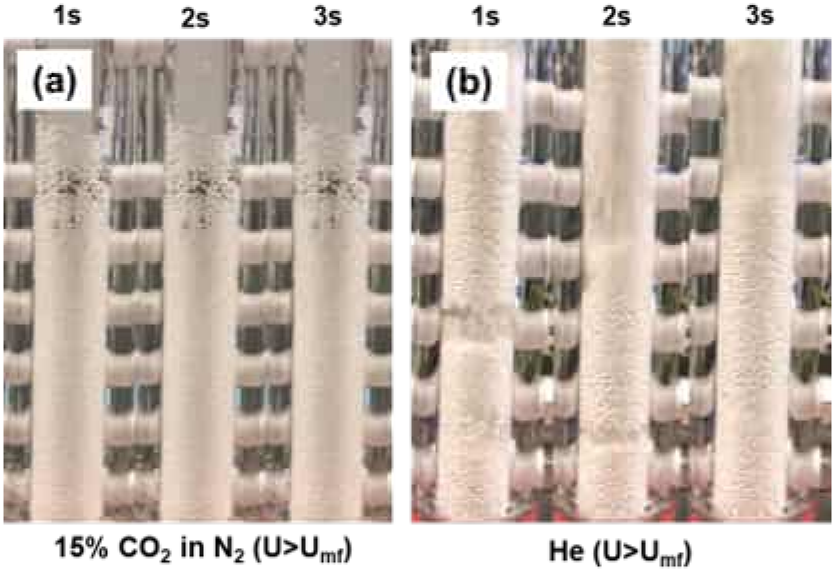

Fig. 8. Fluidization behaviors of of ZIF-8@PEI particles by two different fluidizing gases: (a) 15 vol% CO_2 in N_2 and (b) 100 vol% He.

Conclusions

In this study, a novel delivery method to process nano-crystalline MOFs powders in a large-scale CO_2 capture unit was proposed. Millimeter-sized ZIF-8@polymer beads were prepared with three different hydrophobic polymers (i.e., polyetherimide (PEI), polyethersulfone (PES), and polyvinylidene fluoride (PVDF)) and their CO_2 capture behaviors were studied. It was found that neat PEI and PES can also capture CO_2 while PVDF did not show significant CO_2 loading during the CO_2 capture experiments. Thus, PEI and PES would be better candidates as supporting material for MOFs for CO_2 capture. As ZIF-8 was loaded into these polymer beads, there were synergistic enhancements in their CO_2 capture behaviors. The ZIF-8@PEI beads showed improved CO_2 loadings compared to both neat polymer beads and bulk ZIF-8 powder. This suggested that the diffusion of CO_2 molecules through the porous polymer beads was rapid for our materials and the mass transfer was not limited for the proposed CO_2 capture system. Next, the fluidization behavior of ZIF-8@PEI beads was investigated considering the design of large-scale CO_2 capture units. Based on the Geldart's classification, the ZIF-8@PEI beads were close to group B but these ultralight particles quickly de-fluidized and agglomerated. Wall sheeting was observed due to strong electrostatic inter-particle forces. As He gas was introduced to regenerate ZIF-8@PEI beads, the bed became fluidized without any particle agglomeration and wall sheeting. We suspect that the lower breakdown voltage in He environment reduced the static buildup in these particulate systems, and thus, the fluidization behaviors was improve. The effect of He gas on particle charging behavior in a fluidized bed need to be further investigated for these ultralight MOFs@polymer beads.

Notation

C	CO_2 vol% in outlet gas stream	P	Total pressure, atm
C_0	CO_2 vol% in inlet gas stream	P_{CO2}	Partial pressure of CO_2, atm
T	Temperature, ^oC	t	time, s

Acknowledgment

The authors acknowledge funding support from NSF CBET-1927336 and Saudi Aramco.

References

IPCC, 2018. Special Report, *Global Warming of 1.5 °C.* Intergovernmental Panel on Climate Change.

Niass, T., Kislear, J. Buchanan, M., Svalestuen, J., Park, A.-H. A., DePaolo, D., Powell, J., *Accelerating Breakthrough Innovation in Carbon Capture, Utilization and Storage - Report on the Mission Innovation Carbon Capture, Utilization, and Storage Expert's Workshop*. Department of Energy, United States.

National Oceanic & Atmospheric Administration Research, 2019. *Recent Global CO_2 Trend.* <https://www.esrl.noaa.gov/gmd/ccgg/trends/gl_trend.html>.

Harper, J.M., Dufek, J., 2016. The effects of dynamics on the triboelectrification of volcanic ash. *Journal of Geophysical Research-Atmospheres* 121, 8209-8228.

Li, B., Wen, H.M., Zhou, W., Chen, B.L., 2014. Porous Metal-Organic Frameworks for Gas Storage and Separation: What, How, and Why? *Journal of Physical Chemistry Letter*s 5, 3468-3479.

Liu, J., Thallapally, P.K., McGrail, B.P., Brown, D.R., Liu, J., 2012. Progress in adsorption-based CO_2 capture by metal-organic frameworks. *Chemical Society Reviews* 41, 2308-2322.

Matsuyama, T., Yamamoto, H., 1995. Charge relaxation process dominates contact charging of a particle in atmospheric conditions. *Journal of Physics D: Applied Physics* 28, 2418-2423.

Park, A.-H. A., Zhu, C., Fan, L.-S., Sandvik, P., 2019. Particle Technology. *Kirk-Othmer Encyclopedia*, John Wiley & Sons, Inc.

Patel, H.A., Byun, J., Yavuz, C.T., 2017. Carbon Dioxide Capture Adsorbents: Chemistry and Methods. *ChemSusChem* 10, 1303-1317.

Samanta, A., Zhao, A., Shimizu, G.K.H., Sarkar, P., Gupta, R., 2012. Post-Combustion CO_2 Capture Using Solid Sorbents: A Review. *Industrial & Engineering Chemistry Research* 51, 1438-1463.

Scheffer, M., Brovkin, V., Cox, P.M., 2006. Positive feedback between global warming and atmospheric CO_2 concentration inferred from past climate change. *Geophysical Research Letters* 33.

Smit, B. Park, A.-H. A., Gadikota, G., 2014. The grand challenges in carbon capture, utilization and storage. Specialty Grand Challenge Article. *Frontiers in Energy Research. 2:55.*

Valizadeh, B., Nguyen, T.N., Smit, B., Stylianou, K.C., 2018. Porous Metal-Organic Framework@Polymer Beads for Iodine Capture and Recovery Using a Gas-Sparged Column. *Advanced Functional Materials* 28.

FUTURE APPLICATIONS OF CIRCULATING FLUIDIZED-BED TECHNOLOGY

Filip Johnsson*, **Henrik Thunman, David Pallarès**

Department of Space, Earth and Environment, Chalmers University of Technology
S412 96 Göteborg, Sweden

*Email: filip.johnsson@chalmers.se

Abstract

Considering the climate-change challenge, future thermal and chemical processes must by midcentury be net zero carbon emitting and promote circular processes, phasing out the uptake of fossil fuels from the earth's crust. This paper discusses how circulating fluidized bed (CFB) technology can support such a future. We identify key processes and provide examples of challenges and need for research, demonstration and scale-up. Important CFB applications are both in well-established biomass combustion and gasification, and in novel concepts such as CO_2 capture, plastic recycling and energy storage. It is concluded that large scale implementation of these CFB applications is primarily not a technical challenge but requires stronger climate policy as well as policies promoting a circular economy.

Introduction

Anthropocentric warming of the planet from emissions of greenhouse gases (here expressed in CO_2 equivalents) – in particular from combustion and conversion of fossil fuels – is a major problem faced by mankind. To comply with the Paris Agreement – to limit global warming to well below 2°C – will require strong reductions in carbon dioxide emissions over the coming decades. Although there is a high uncertainty in the equilibrium climate sensitivity (ECS), which describes the long-term temperature increase resulting from a doubling of the atmospheric CO_2 concentration, it seems wise to assume that emissions should be strongly reduced and approach net zero in the middle of the century. Applying different methods, IPCC (2013) has estimated ECS to be in the range 1.5 to 4.5°C (with 66% probability), implying that one cannot rule out that the remaining carbon budget complying with the Paris Agreement, is already almost used up (if ECS is 4.5°C).

The aim of this paper is to discuss the future of CFB technology in a world that complies with the Paris Agreement. We limit CFB applications to *conversion of heterogeneous fuels* and we focus on applications where the CFB technology has the potential to reduce carbon emissions, either directly by lowering stack emissions or indirectly by contributing to circular material systems phasing out the need for using virgin fossil-fuel based feedstocks. For other important CFB applications see e.g. Winter and Schratzer (2013) for a summary.

CFB Advantages and Current Use

CFB technology has been used in the chemical industry for catalytic cracking since the 1940s, in coal gasification since the 1920s and in combustion since the 1980s. A literature search (in Scopus on February 02, 2020) applying the search words "Circulating fluidized bed*" results in 7,230 papers from Year 1973 (Schmidt, 1973) to present. The word combination "Circulating fluidized bed*" AND "review" gives 154 papers, from Year 1979 (Reh, 1979) to present, consisting of a mix of papers reviewing either different applications and aspects of CFB technology or reviews of processes relevant to CFB technology. The dominating part of the works deals with CFB technology in combustion systems applying different types of fuels, with the majority of work still dealing with coal. For an extensive overview of the CFB technology in combustion – including CO_2 capture - and gasification and pyrolysis systems see Scala (2013).

Favorable mixing behavior and high heat and mass transfer are key features of CFB technology, making it possible to maintain an even temperature profile within the reactor. These are features which are important to many chemical processes and in the combustion of solid fuels. Compared to a bubbling (stationary) fluidized bed, the CFB technology adds a higher flexibility in operational conditions. Due to clustering effects in the gas solids suspension, a CFB reactor flow is characterized by high slip velocities, which allows high solids loading to be maintained within the reactor, in particular in the lower part of the reactor. The backmixing is due to a combination of solids clustering and backmixing at the reactor walls. The strong backmixing in vertical gas-solids flow was already observed in the 1940s, as pointed out by Squires (1986), in a review of the history of fluid catalytic cracking in the first proceedings of the CFB conference.

In combustion applications, fuel flexibility is an important feature of the CFB technology, a result of its favorable mixing and high thermal inertia, evening out variations in fuel variations and allowing combustion at a lower temperature than in flame combustion, which is favorable for maintaining low NO_x emissions and allowing for in-bed sulphur removal by means of limestone addition. In combustion for electricity generation, the CFB technology has gone through a strong development from CFB boilers of Megawatt scale in the 1980s to today's CFB power plants of more than 500 MW electric power applying supercritical steam (Cheng et al., 2020). Such upscaling is a challenge with respect to achieving enough heat transfer surfaces and in terms of securing sufficient fuel mixing. Although favorable mixing is a key feature of fluidized beds, this mostly holds for the vertical mixing, whereas the lateral mixing may be a limited factor, in particular in combustion reactors with large cross sections, which will require multiple cyclones and several fuel feed points in order to secure sufficient burnout of the fuel. In summary, fluidized bed combustion is a mature technology applied in large scale utility boilers for electricity production, mainly burning coal, as well as in smaller combined heat and power plants (typically up to some hundreds of MW fuel) burning various low grade fuels such as wood waste from the forest industry and different waste fractions (Johnsson, 2007). The latter type of plants is found in district heating systems (electricity and hot water) and in industrial systems (electricity and steam).

Coal gasification has been applied during oil crisis and war times, e.g. using the high temperature Winkler CFB gasifier which has been applied since 1926. Gasification can operate in either air or oxygen blown modes. Gasification of biomass and waste on a commercial scale has only been applied in a relatively small number of plants, dominated by fuel gas production to be used in downstream application such as lime kilns or heat and power plants. For production of upgraded gas there are even less cases if considering large units including upgrading of the product gas for subsequent use as gaseous or liquid biofuel.

Implications When Limiting Warming to Well Below 2°C

In a climate constrained world there are basically three possibilities for the use of hydrocarbons: to use renewable carbon in the form of biomass, to recycle already available carbon such as in existing plastics and to apply CCS from fossil or biogenic (BECCS) emission sources. As discussed by Johnsson et al. (2018), on the longer run, there are only two options for the future use of fossil-fuels which comply with the climate targets; to leave these in the ground or apply CCS to processes using these fuels, and a combination of these two options. Since there is a certain likelihood that society will have soon emitted more CO_2 than allowed to meet a 2°C warming target, it is likely that on the longer run the world must create net negative emissions requiring Bio Energy CCS (BECCS), i.e. applying CCS to emission sources using sustainable derived biomass (cf. Rogelj et al., 2015, Rogelj et al., 2018). We here assume that it will be politically unacceptable and associated with very high costs to continue using fossil fuels while trying to compensate their emissions with Negative Emission Technologies (NETs) such as BECCS, biochar for soil storage and/or Direct Air Capture (or by some geoengineering), although some residual fossil-fuel emissions from "hard-to-abate-sectors" may be necessary to compensate by means of NETs.

Plastic recycling should be a result of phasing out plastic made from virgin oil over time. It should be mentioned that it is estimated (Geyer et al., 2017) that 60-75% of all plastic that was already produced is still available in nature (in landfills, in the free nature and in the oceans). Thus, phasing out the possibility to produce plastic from new oil will make this plastic a valuable resource, incentivizing “plastic mining”.

With limited biomass resources it is important to maximize the climate benefit of biomass resources while maintaining a sustainable biomass supply, derived from forests or agriculture which sustain or increase the carbon stock in the growing biomass over time. This translates to applying a cascading use (from long lived materials to fuels) and maximizing the substitution effects of the biomass. Residues from forest management, such as stumps, bark and branches can be used as fuels in combustion systems (e.g. in combined heat and power plants), feedstock to “biorefineries”, as additional feedstock in recycled plastic refineries to meet a growing demand for plastic and as feedstock for production of biofuels (e.g. in gasification).

In a future low carbon energy system, there will be high shares of variable renewable electricity (VRE) generation such as wind and solar power. Unless flexibility measures on both supply and the demand sides are created, the value of the VRE will decrease with increased share of VRE (an increasing amount needs to be curtailed). This will increase the need for flexibility in the electricity system, which can be obtained by means of flexible thermal power and by means of energy storage.

Considering the above and limiting this paper to applications for converting heterogenous fuels and feedstocks, it follows that future CFB technology applications in a world complying with the Paris Agreement are possible in 1. *Combustion* using coal with CCS and biomass with and without CCS, 2 *Gasification* and pyrolysis using biomass with and without CCS, 3. *Plastic recycling* and 4. *Energy storage*. Below we discuss the role of CFB technology in these applications and exemplify challenges, need for research, demonstration and scale-up.

Future CFB Applications – Challenges, Research, Demonstration and Scale-up

Combustion

Due to CFB technology being used extensively in combustion of heterogenous fuels, there are good prospects for future applications of this technology, since fuel flexibility and the ability to convert low grade fuels and feedstocks will most likely remain, or be of increasing value, in the future. There will also be an increasing need for flexibility in the load and dispatchable (thermal) power generation and for units to provide systems services such as primary and secondary frequency control. Assuming that VRE with its low running costs will be prioritized in the dispatch of electricity producing units, an increased value of flexibility of thermal power plants can be expected. Important parameters are minimum load level, ramp rate and cycling properties (Agora, 2017, Ye et al., 2019). A potential advantage for CFB technology is from the thermal inertia of the bed solids, which can offer energy storage if charged by extra energy, facilitating hot start ups rather than cold startups (Zabetta et al., 2017) and allowing for low minimum load capability. When applied in a CHP scheme, the CFB technology gives good opportunities for flexibility, since the high thermal inertia facilitates variation in the ratio between power and heat (Anand et al. 2018, Wang et al., 2019) and shifting in load over time, given the different timescales of heat and power (Yao et al., 2018). With respect to future plants these may produce multiple products such as electricity, heat and fuel/chemicals which would further improve flexibility, i.e., to maintain high full load hours, despite a varying electricity market. Yet, this will come at an increased complexity and it is not obvious how such a multi-product “CHP” plant can compete with the chemical industry and refineries when producing bio-based chemicals and fuels.

There is a need to investigate the flexibility performance of CFB plants under different electricity system contexts, applying simulation tools, possibly linked to energy systems modeling with high time resolution (cf. Göransson & Johnsson, 2018). As for operational flexibility and how this is linked to thermal stresses (and O&M), the authors' impression is that requirements are largely empirical and rather conservative because flexibility has not been highly valued. Thus, more tests and research are required to develop a basis for designing flexible CHP and power plants.

When it comes to CO_2 capture, required if fossil fuels are to be used, oxyfuel-fired CFB technologies have been demonstrated successfully at in pilot plants on a Megawatt scale. Thus, it should not be the technology itself which limits the implementation – although there are of course technical issues that must be handled as well as research needs – but rather weak climate policy in terms of the cost to emit CO_2 (see e.g. Nuortimo et al., 2018 and Johnsson et al., 2019). Yet, implementing oxyfuel-fired CFB technology with CCS (as with any other CCS technology) can be assumed to be associated with long lead times. Thus, it is of high importance that demonstration programs are intensified and climate policies strengthened.

When it comes to capture technologies applied to CFB combustion, there are research and demonstration needs in post combustion, oxyfuel combustion and in novel capture technology such as chemical looping combustion. Research in oxyfuel is required to get a better understanding on how basic processes such as heat transfer (see e.g. Seddighi Khavidak et al., 2015), emission formation, combustion dynamics differ from air-fired combustion as well as to develop the technology to higher oxygen concentrations (decreased flue gas recycling) allowing for more compact units (Nuortimo et al., 2018). There is also the alternative to equip existing and new CFB plants with post combustion capture such as amine scrubbing and the calcium looping cycle. Post combustion capture is planned at a waste fired CHP plant in Norway (Fortum Värme, south of Oslo) and at a biomass fired CFB plant in Sweden (Stockholm Exergi, Värtan plant). The latter is a pure Bio-CCS application, yielding negative CO_2 emissions (BECCS). Thus, these units may be early adopters of CCS in the Nordic countries. This would be an important step in demonstrating and scaling up the CCS technology at CHP plants considering the requirements to meet production in heat and electricity with its seasonal characteristics.

Whereas post combustion and oxyfuel combustion can be seen as first generation CO_2 capture technologies, chemical looping technology is a promising capture technology with a potential for significant reduction in the capture cost, either applied as chemical looping combustion (CLC) or in the form of calcium looping cycle as post combustion capture. In the former case, the energy required to capture the CO_2 is more or less removed by not mixing the air and the fuel by means of using an active bed material (metal particles) as an oxygen carrier in a CFB loop with the riser serving as an air reactor and a bubbling bed in the downcomer being the fuel reactor. After the particles have been reduced in the fuel reactor, they re-enter into the air reactor for oxidation. Much of the CLC research has been to characterize suitable oxygen carrier materials (See Lyngfelt 2014 for an overview).

The development of chemical looping combustion has resulted in an understanding of the performance of oxygen carrier materials. From this knowledge it was found that such materials can also be applied in CFB combustion to improve the performance of CFB-boilers burning heterogenic fuels (Thunman et al., 2013). Thus, the oxygen carrier aided combustion (OCAC) concept has been commercially applied in several large-scale boilers. The OCAC concept adds chemical inertia to the thermal inertia of a fluidized bed, thereby evening out fluctuations in local oxygen concentration within the combustion zone as can be seen in Fig. 1 (Lind et al., 2017). Fig. 1 compares silica sand (Fig.1a) and ilmenite (Fig. 1b) as bed material in the Chalmers 12 MW_{th} CFB boiler – shown in Fig. 2 - with respect to oxygen (black curve) and carbon monoxide (red curve). As can be seen there is a clear effect from using an oxygen carrying (ilmenite) bed material, reducing the CO fluctuations and allowing operation with a lower excess air ratio seen from the lower O_2 concentration in Fig. 1b. As a result, the excess air ratio can be lowered while maintaining the combustion efficiency. Although the OCAC development went from research to full scale commercial use in only a few years' time, there are challenges related to controlling the content of the ash components and to lower the use of make-up bed material.

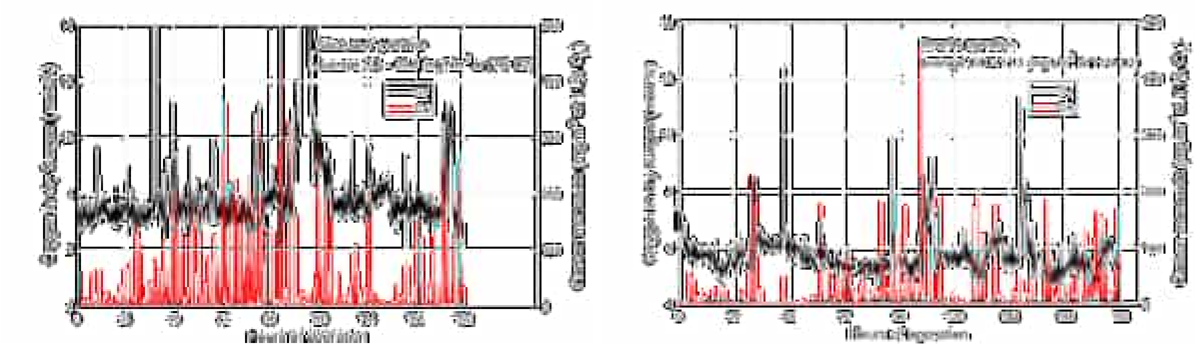
(a) (b)

Fig. 1. Flue gas concentrations of O_2 and CO in the Chalmers 12 MW_{th} CFB boiler operated with silica sand (a) and ilmenite (b) as bed material (from Lind et al., 2017).

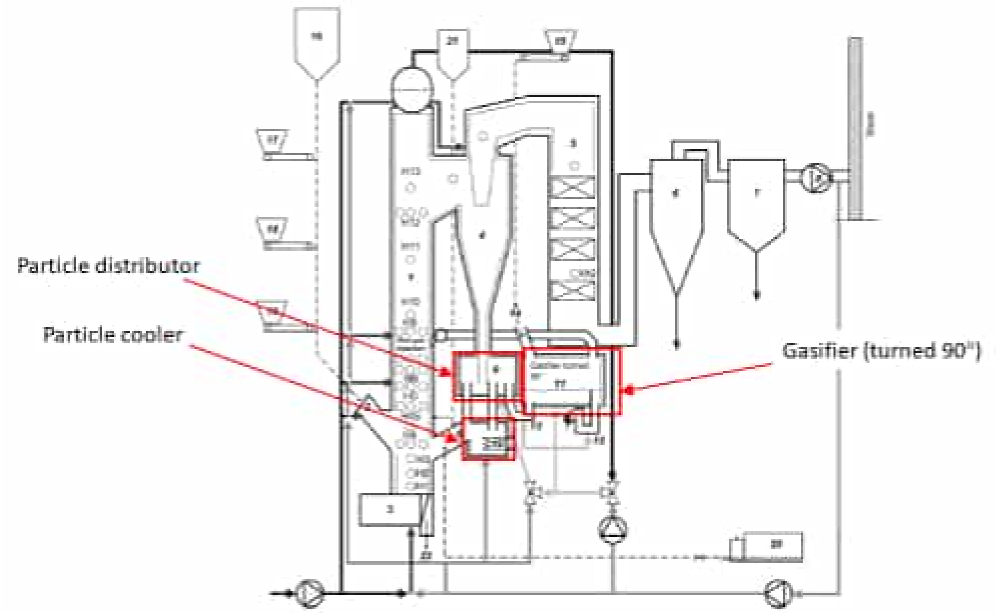

Fig. 2. Chalmers 12 MW_{th} CFB boiler system with an integrated gasifier. By means of using the particle distributor, the gasifier can be by passed operating the CFB as combustor (as is the case in Fig. 1) with solids passing the particle cooler.

Gasification

As indicated above, biomass gasification has so far mostly been used to partly oxidize heterogenous fuels to a fuel gas that can replace fossil fuels in boilers and, in some more advanced cases including gas cleaning from problematic compounds to produce a gas that can be used in a gas boiler with high steam data (i.e. high temperature and pressure). There is obviously a great need to develop gasification technologies for production of more advanced hydrocarbons in gaseous and liquid forms to be used as fuels for transport (road, shipping and aviation) or as feedstock for the chemical industry.

An example of a CFB gasifier is in indirect gasification where a riser – combustor - can be combined with a bubbling bed gasifier in the down-comer in the CFB loop (Larsson et al. 2013, Karl & Pröll, 2018). Fig. 2 shows a schematic of how a steam-blown gasifier is added to the Chalmers 12 MW_{th} CFB, allowing operation both with and without the gasifier. This gasifier was used as part of the development of a 20 MW GoBiGas gasifier in City of Göteborg producing SNG (CH_4) used for transportation fuels (blended into the natural gas network of Göteborg). The dual bed system circulates solids between two beds in which the biomass is converted to a raw gas and then cleaned and upgraded in a methanation section, where the gas is conditioned and synthesized into CH_4 (Thunman et al., 2018). The experiences gained in the GoBiGas gasifier, together with gasifiers in Senden and Güssing, show that it is possible to produce clean hydrocarbons with high utilization times. These experiences have resulted in important knowledge on how to optimize and control the raw gas quality out from the gasifier of dual bed systems so that the produced raw gas can be recovered without clogging the heat exchangers with tars. Provided gasifiers are built of a certain size, the gas cleaning and upgrading processes are commercially available technology (cf. Thunman et al., 2018). The biomass and its ash components must be balanced with the bed material composition to create the right chemical environment for the gasification process. For biomass gasification this can be done by controlling the internal and external circulation of the bed material as well as provide additives of specific ash elements such as potassium, calcium and sulfur to the system (Faust et al., 2019, Berdugo Vilches et al., 2018, Thunman et al., 2018).

The reactor design used for an indirect gasifier of the type shown in Fig. 2 is basically the same as what is used in the above-mentioned combined heat and power systems. It should therefore be a reasonable assumption that the CFB gasification technology has a level of maturity similar to that of commercial CHP plants based on the fluidized bed technology. Thus, the CFB technology can facilitate a fast way to produce renewable fuels for road and aviation transportation (requiring different raw gas treatment steps). This can be further accelerated by integrating such a gasifier in existing CFB plants then requiring supporting infrastructure for gas cleaning (Thunman et al., 2018).

Plastic recycling

Around 90% of all plastic is disposed or incinerated, i.e. only around 10% is recycled. Thermochemical recycling in waste plastic refineries provides an opportunity to close the plastic material cycle. Thunman et al. (2019) show how this can be achieved using the existing petrochemical infrastructure combined with recycling of plastics into monomers using a CFB cracking facility. The energy supply required for the cracking to monomers can be in the form of biomass or fossil fuels with CCS. A CFB gasifier of the type shown in Fig. 2 can be used as the cracking unit. In fact, plastic cracking has already been successfully tested in the Chalmers gasifier. It has been concluded that replacing virgin oil with plastic waste as feedstock for plastic production should be economically favorable (Thunman et al, 2019). To obtain a fully circular system it would require that a value is assigned to the environmental benefits from phasing out plastics produced from virgin oil, such as from sufficiently high pricing of CO_2 emission from waste incineration or from mandatory recycling quotas, which are then increased over time. This would then put a value of existing plastics, creating incentives for collecting already produced plastics (“plastic mining”). In summary, it should be of high importance to show how plastic cracking applying CFB technology can be implemented in existing petrochemical infrastructure and to support demonstration of such technology.

Energy storage

With large shares of VRE – in particular wind power - in future energy systems there is a need to store energy over longer times than what would be possible with batteries or any other day-night storage. A possibility would be to reduce a metal (powder) which is then stored and, later, when needed, oxidized releasing energy. Reduced metals react exothermically when oxidized (by e.g. O_2, H_2O, CO_2), providing molar heat releases higher than that of Carbon (C). After oxidation, the metals can be reduced back through an endothermal reaction driven by H_2, CO or simply heat if using CLOU metals for gaseous oxygen release (CLOU; chemical looping with oxygen uncoupling). The high specific heat of oxidation in some metals offer economic potential to use them as a recyclable “fuels”, which can be transported over long distances (e.g. by ship). Iron is foreseen as a strong candidate for recyclable metal storage due to its relatively low cost and suitable properties (Bergthorson et al. 2015).

The above-mentioned research and experience with oxygen carrier aided combustion (OCAC) have resulted in knowledge of metal oxidation in fluidized beds (Thunman et al. 2013). Replacing carbonaceous fuels with recyclable metal would imply significant advantages by avoiding emissions of fuel-originated pollutants (SO_x, non-thermal NO_x and unburnt gases) and CO_2, as well as ash-melting issues allowing for higher furnace temperature and steam data than what is otherwise typical for CFB combustors (while still maintaining even distribution of the heat flux). As for the reduction step, experience is available from fuel reactors in chemical looping units. CLOU metal composites (Haider et al., 2016) have an advantage in that their reduction only requires heat at a temperature level around 800 ºC, which can be provided by superheaters in district heating plants or produced from electricity during low-price hours (avoiding curtailment of VRE) and thus enabling metals as electrofuels. For non-CLOU metals a reducing agent is required.

To evaluate the above storage application requires significant research efforts with the aim to understand possible heat exchanger setups to cool and store the reduced metal as well as investigating possible particle properties to be used in CFBs for the reduction and combustion steps.

Research of Basic Processes

Although the above CFB applications have their own specific need for research, there are also knowledge gaps which are common to the fluidization technology. Here, we exemplify some important research needs.

To obtain detailed in situ information of reactor processes – such as mixing, gas-solids mass transfer and reaction kinetics - there is a need to develop experimental techniques able to deliver high-quality non-intrusive data with high resolution in space and time. The challenge is to find measurement systems which can withstand the harsh environment within CFB reactors. Most detailed measurements are from small scale reactors of small cross sections. Such can allow for dynamic spatially resolved measurements of gas phase concentrations (Dang et al., 2013). In large CFB reactors at elevated temperatures (e.g. combustors) in-situ solids (e.g. Wiesendorf and Werther, 2000) and gas phase measurements are limited to local probe measurements (e.g. Fernandez et al., 2000). In the case of the gas phase, this would involve significant convolution of the sample before it reaches the detector, thus restricting the information on the dynamics. Non-intrusive tomographic techniques have been applied to smaller geometries (Du et al., ,2002), but for larger units the signal absorption by the bed material becomes a limiting factor together with the number of sensor pairs required to keep a satisfactory spatial resolution. Particle tracking by different means – e.g. radioactive (Stein et al., 2000) and magnetic (Köhler et al., 2017) – can offer detailed spatial insight in the solids flow pattern but density and size of available tracer particles may limit application. Given the limitations for in-situ measurements in large industrial CFB reactors, there is a need to further take advantage of the possibilities offered by fluid-dynamical downscaling of CFB units (Van der Meer et al., 1999, Djerf et al., 2019) which should make detailed time and spatial measurements possible.

Numerical modeling (by means of computational fluid dynamics; CFD) has the potential to be used as design tool for CFB processes. Yet, challenges lie in formulating sub-grid models for the momentum, mass and heat transfer between gas and solids phase. So far, CFD simulations can only be validated against measurements at macroscopic scale. There is also a need to develop experimental methods which can support description of fluid-dynamical characterization of the properties of bed solids (shape and surface roughness). See Pallarès and Johnsson (2013) and Wang (2020) for reviews of CFD for fluidized-bed applications.

The external solids circulation is a key parameter in CFB processes as it is used to control the heat balance in the CFB loop and governs the stoichiometry of reactions in dual fluidized bed systems. Despite its importance, reliable prediction of the external solids circulation still remains a main challenge for CFB design and scale-up, since it requires accurate modeling of the solids population balance as well as of the different solids backmixing phenomena occurring in different fluid-dynamical regions of the riser (entrainment from the bottom region, backmixing at wall layers and backflow at the riser exit). The challenge is further enhanced by the fact that measurements of the solids circulation are difficult, although indirect measurements by means of heat balances may give reasonable estimates (e.g. Rahman et al., 2019). Yet, estimations are often based on assumptions, yielding significant scatter in the estimated values (Edvardsson et al., 2006) and may be difficult to apply for the low solids fluxes (in kg/m^2 s) typically occurring in large industrial CFB units for fuel conversion.

The above-mentioned applications with active bed material require better knowledge of the effective interphase mass transfer between the gas and particle phase. So far studies are restricted to low fluidization velocity (see e.g. Scala, 2007), for which the emulsion phase remains at minimum fluidization conditions and, thus, mass transfer data corresponds to bubble-emulsion gas transfer. Thus, there is a need for mass transfer investigations at higher fluidization velocities representative for CFB conditions with a more complex flow picture. Thus, more research work is needed to develop experimental methods for investigating mass transfer under such conditions.

Conclusions

Future CFB applications in a climate-constrained world are identified together with examples of challenges and need for research, demonstration and scale-up. Possible CFB applications are combustion using coal with CCS and biomass with and without CCS, gasification and pyrolysis using biomass with and without CCS, plastic recycling and in energy storage. It is concluded that large scale implementation of these CFB applications is primarily not a technical challenge but requires stronger climate policy as well as policies promoting a circular economy. Yet, to develop the CFB applications discussed in this work will require a deeper understanding of several key processes related to mixing, gas-solids mass transfer and reaction kinetics.

Acknowledgements

This work is financed by the Swedish Energy Agency.

References

Anand H, Narang N, Dhillon JS. Unit commitment considering dual-mode combined heat and power generating units using integrated optimization technique. Energy Convers Manag 2018;171:984–1001.

Agora Energiewende. Flexibility in thermal power plants - With a focus on existing coal-fired power plants. 2017.

Berdugo Vilches, T, Maric, J, Knutsson, P, Rosenfeld, DC, Thunman, H, Seemann, M. Bed material as a catalyst for char gasification: The case of ash-coated olivine activated by K and S addition (2018) Fuel, 224, pp. 85-93.

Bergthorson, JM, Goroshin, S, Soo, MJ, Julien, P, Palecka, J, Frost, DL, Jarvis, DJ. Direct combustion of recyclable metal fuels for zero-carbon heat and power (2015) Applied Energy, 160, pp. 368-382.

Cheng, L, Ji, J, Wei, Y, Wang, Q, Fang, M, Luo, Z, Ni, M, Cen, K. A note on large-size supercritical CFB technology development (2020) Powder Technology, 363, pp. 398-407.

Dang, TYN, Kolkman, T, Gallucci, F, van Sint Annaland, M. Development of a novel infrared technique for instantaneous, whole-field, non invasive gas concentration measurements in gas-solid fluidized beds (2013) Chemical Engineering Journal, 219, pp. 545-557.

Djerf, T, Pallarès, D, Johnsson, F. 2019. “Evaluation of the fluid-dynamically downscaled model of a utility-scale CFB boiler”. Proc. of the 16th Int. Conf. on Fluidization (Guilin, China).

Du, B, Fan, L-S, Wei, F, Warsito, W. Gas and solids mixing in a turbulent fluidized bed (2002) AIChE Journal, 48 (9), pp. 1896-1909.

Edvardsson, E, Åmand, L-E, Thunman, H, Leckner, B, & Johnsson, F. Measuring the External Solids Flux in a CFB boiler. (2006) 19th Int. Conf. on Fluidized Bed Combustion (p. G-44). Vienna (Austria).

Eriksson T, Alvarez I, Kuivalainen R, et al. Large pilot scale testing of OXY-CFB technology at CIUDEN CO2-Centre and its application to the OXY-CFB 300 Compostilla design. POWER-GEN Europe 2014, Cologne, Germany, June 2014.

Faust, R, Hannl, TK, Vilches, TB, Kuba, M, Öhman, M, Seemann, M, Knutsson, P. Layer Formation on Feldspar Bed Particles during Indirect Gasification of Wood. 1. K-Feldspar (2019) Energy and Fuels, 33 (8), pp. 7321-7332.

Fernandez, MJ, Lyngfelt, A, Johnsson, F. Gas Concentrations in the Lower Part of the Combustion Chamber of a Circulating Fluidized Bed Boiler: Influence of Bed Height (2000) Energy and Fuels, 14 (6), pp. 1127-1132.

Geyer, R, Jambeck, JR, Law, KL. Production, use, and fate of all plastics ever made (2017) Science Advances, 3 (7), art. no. e1700782.

Göransson, L, Johnsson, F. A comparison of variation management strategies for wind power integration in different electricity system contexts (2018) Wind Energy, 21 (10), pp. 837-854.

Haider, SK, Azimi, G, Duan, L, Anthony, EJ, Patchigolla, K, Oakey, JE, Leion, H, Mattisson, T, Lyngfelt, A. Enhancing properties of iron and manganese ores as oxygen carriers for chemical looping processes by dry impregnation (2016) Applied Energy, 163, pp. 41-50.

IPCC (2013). Climate Change 2013: The Physical Science Basis. Contribution of Working Group I to the Fifth Assessment Report of the Intergovernmental Panel on Climate Change [Stocker, T. F., m.fl. (red.)]. https://www.ipcc.ch/report/ar5/wg1/

Johnsson, F, Fluidized bed combustion for clean energy, Proc Fluidization XII, Vancouver, 2007

Johnsson, F, Kjärstad, J, Rootzén, J. The threat to climate change mitigation posed by the abundance of fossil fuels (2019) *Climate Policy*, 19 (2), pp. 258-274.

Karl, J, Pröll, T. Steam gasification of biomass in dual fluidized bed gasifiers: A review (2018) *Renewable and Sustainable Energy Reviews*, 98, pp. 64-78.

Köhler, A, Pallarès, D, Johnsson, F. Magnetic tracking of a fuel particle in a fluid-dynamically down-scaled fluidised bed (2017) Fuel Processing Technology, 162, pp. 147-156.

Larsson, A, Seemann, M, Neves, D, Thunman, H. Evaluation of performance of industrial-scale dual fluidized bed gasifiers using the chalmers 2-4-MWth gasifier (2013) Energy and Fuels, 27 (11), pp. 6665-6680.

Lind, F, Corcoran, A, Andersson B-Å, Thunman, H. 12,000 hours of operation with oxygen-carriers in industrially relevant scale (2017) VGB-Powertech.

Molino, A, Larocca, V, Chianese, S, Musmarra, D. Biofuels production by biomass gasification: A review (2018) Energies, 11 (4), art. no. 811.

Nuortimo, K, Eriksson, T, Kuivalainen, R, Härkönen, J, Haapasalo, H, Hyppänen, T. Tackling boundaries of CCS in market deployment of second-generation oxy-fuel technology (2018) Clean Energy, 2 (1), pp. 72-81.

Pallarès, D, Johnsson, F. Modeling of fluidized bed combustion processes (2013) Fluidized Bed Technologies for Near-Zero Emission Combustion and Gasification, pp. 524-578.

Pröll, T, Zerobin, F. Biomass-based negative emission technology options with combined heat and power generation (2019) Mitigation and Adaptation Strategies for Global Change, 24 (7), pp. 1307-1324.

Rahman, MH, Daniel, L, Shah, U, Bi, X, Grace, JR, Lim, CJ. Estimation of solids circulation rate and char transfer rate from gasifier to combustor in a dual fluidized-bed pilot plant for biomass steam gasification (2019) Particuology, 46, pp. 22-29.

Reh, L. Fluid bed combustion in processing, environmental protection and energy supply (1979) Erdoel und Kohle, Erdgas, Petrochemie vereinigt mit Brennstoff-Chemie, 32 (12), pp. 560-566.

Rogelj, J, Luderer, G, Pietzcker, RC, Kriegler, E, Schaeffer, M, Krey, V, Riahi, K. Energy system transformations for limiting end-of-century warming to below 1.5 °C, *Nature Climate Change* 5, 519–527 (2015) doi:10.1038/nclimate2572.

Rogelj, J., Shindell, D., Jiang, K., Fifita, S., Forster, P., Ginzburg, V., et al. (2018). “Mitigation pathways compatible with 1.5°C in the context of sustainable development,” in Global Warming of 1.5 °C an IPCC special report on the impacts of global warming of 1.5 °C above pre-industrial levels and related global greenhouse gas emission pathways, in the context of strengthening the global response to the threat of climate change Available at: http://www.ipcc.ch/report/sr15/.

Scala, F. Mass transfer around freely moving active particles in the dense phase of a gas fluidized bed of inert particles (2007) Chemical Engineering Science, 62 (16), pp. 4159-4176.

Scala, F., Editor, Fluidized Bed Technologies for Near-Zero Emission Combustion and Gasification, 2013, Woodhead Publishing Series in Energy, ISBN 978-0-85709-880-1 (online).

Schmidt, HW. Combustion of Heavy Oil Fuel in a Circulating Fluidized Bed (in German), (1973) Verfahrenstechnik, 7 (12), pp. 357-362.

Seddighi Khavidak, S, Pallarès, D, Normann, F, Johnsson, F, Ylä-Outinen, V. Heat transfer in a 4-MWth circulating fluidized bed furnace operated under oxy-fired and air-fired conditions: Modeling and measurements 2015) International Journal of Greenhouse Gas Control, 37, pp. 264-273.

Squires, AM. Circulating Fluidized Bed Technology, Proceedings of the First International Conference on Circulating Fluidized Beds, Halifax, Nova Scotia, Canada, November 18–20, 1985.

Stein, M, Ding, YL, Seville, JPK, Parker, D.J. Solids motion in bubbling gas fluidized beds (2000) Chemical Engineering Science, 55 (22), pp. 5291-5300.

Thunman, H, Berdugo Vilches, T, Seemann, M, Maric, J, Cañete Vela, I, Pissot, S, Nguyen, HNT. Circular use of plastics-transformation of existing petrochemical clusters into thermochemical recycling plants with 100% plastics recovery, Sustainable Materials and Technologies, Volume 22, 2019, e00124.

Thunman, H, Lind, F, Breitholtz, C, Berguerand, N, Seemann, M. Using an oxygen-carrier as bed material for combustion of biomass in a 12-MWth circulating fluidized-bed boiler (2013) Fuel, 113, pp. 300-309.

Thunman, H, Seemann, M, Berdugo Vilches, T, Maric, J, Pallares, D, Ström, H, Berndes, G, Knutsson, P, Larsson, A, Breitholtz, C, Santos, O. Advanced biofuel production via gasification – lessons learned from 200 man-years of research activity with Chalmers' research gasifier and the GoBiGas demonstration plant (2018) Energy Science and Engineering, 6 (1), pp. 6-34.

Van Der Meer, EH, Thorpe, RB, Davidson, JF. Dimensionless groups for practicable similarity of circulating fluidised beds (1999) Chemical Engineering Science, 54 (22), pp. 5369-5376.

Wang, J. Continuum theory for dense gas-solid flow: A state-of-the-art review (2020) Chemical Engineering Science, 215, art. no. 115428

Wang J, You S, Zong Y, Træholt C, Dong ZY, Zhou Y. Flexibility of combined heat and power plants: A review of technologies and operation strategies. Appl Energy 2019;252. doi:10.1016/j.apenergy.2019.113445.

Wiesendorf, V, Werther, J. Capacitance probes for solids volume concentration and velocity measurements in industrial fluidized bed reactors (2000) Powder Technology, 110 (1-2), pp. 143-157.

Winter, F, Schratzer, B. Applications of fluidized bed technology in processes other than combustion and gasification, in Scala, F., (Editor), Fluidized Bed Technologies for Near-Zero Emission Combustion and Gasification, 2013, Woodhead Publishing Series in Energy, ISBN 978-0-85709-880-1 (online).

Zabetta, EC, Kovács, J, Eriksson, T, Role and challenges of CFB in a changing energy market, Paper presented at the 12th International Conference on Fluidized Bed Technology, Krakow, Poland, 2017.

Yao S, Gu W, Zhou S, Lu S, Wu C, Pan G. Hybrid timescale dispatch hierarchy for combined heat and power system considering the thermal inertia of heat sector. IEEE Access 2018;6:63033–44. doi:10.1109/ACCESS.2018.2876718.

Ye LC, Lin HX, Tukker A. Future scenarios of variable renewable energies and flexibility requirements for thermal power plants in China. Energy 2019;167:708–14. doi:10.1016/j.energy.2018.10.174.

ADVANCEMENTS IN FLUIDIZED BED COKING TECHNOLOGY AT SYNCRUDE

Mike Wormsbecker*, **Jason Wiens, Jennifer McMillan, Brian Knapper, Craig McKnight**

Syncrude Research Centre, 9421 17 Avenue, Edmonton, Alberta, Canada T6N 1H4

*Email: *wormsbecker.michael@syncrude.com*

Abstract

Syncrude uses FLUID COKING™, a conventional two vessel circulating fluidized bed, as the primary means to convert oilsands bitumen into crude oil. Research activities undertaken over the past 30+ years have led to the commercialization of various technologies that have improved the operability and yield of the process. This paper will summarize research related to circulating fluidized beds, including the commercialized technologies, with supporting data.

Introduction

Syncrude is one of the largest producers of crude oil from oil sands and the largest single source producer in Canada. With a production capacity of 350,000 kbpd, Syncrude has the ability to provide approximately 15% of Canada's total oil requirements. To do this, Syncrude first surface mines the oil sand, then uses a water-based extraction process to separate the raw oil, referred to as bitumen, from the sand. Syncrude upgrades bitumen into a high quality, light sweet crude oil using distillation, three Fluid Cokers, an LC-Finer and hydrotreaters units.

The majority of bitumen conversion at Syncrude is done via FLUID COKING™, an ExxonMobil licensed technology. FLUID COKING™ was developed from the principles of Fluid Catalytic Cracking (FCC). It is a carbon rejection process capable of performing deep conversion on resid feedstocks with Conradson carbon residues > 20 wt%. Its products consist of gas oils, naphtha, non-condensable gases and carbon-based particulate, referred to as fluid coke.

A schematic of the FLUID COKING™ process is shown in Fig. 1. It is a two-vessel circulating fluidized bed comprised of a reactor and burner. Bitumen is atomized with steam through multiple feed nozzles positioned circumferentially around the dense bed portion of the reactor dense bed. Upon contacting with fluid coke, the thermal reaction is initiated, generating short-chained hydrocarbon vapours and a thin layer of coke on the particle surfaces. The hydrocarbon vapours, steam and fluid coke entrained from the bed pass through parallel cyclones. The hydrocarbon and steam enter the scrubber section, which uses fresh feed to recycle unreacted resid to the reactor while also pre-heating the feed. The product vapours and steam that pass through the scrubber are sent to a fractionator prior to hydrotreating.

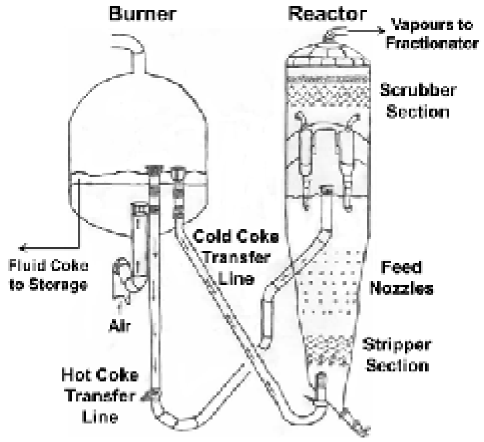

Fig. 1. General Arrangement of a Fluidized Bed Coking Unit.

After reaction, the spent coke must be sent to the burner to be reheated. In order to limit hydrocarbon carryunder to the burner, the fluid coke is passed through a stripper section comprised of multiple rows of chevron-style sheds. Below the stripper is a cone section that contains fluidization steam nozzles and an exit pipe, referred to as a sore thumb, connected to the cold coke transfer line. The burner is fluidized with air to provide combustion conditions. The hot coke is sent back to the reactor via the hot coke transfer line. More coke is generated during the reaction than burned, which means the excess coke must be removed from the system to maintain inventory. The excess coke is quenched with water then sent to storage.

Many operational challenges have occurred since start-up in 1978. These challenges have resulted in a major overhaul of the mechanical design and operational strategy of the Fluid Cokers. This paper will focus on fluidization topics that used a research-based approach to gain fundamental understanding and advance the technology. These areas include hydrodynamic modeling, stripper re-design, sore thumb re-design and jet-bed interaction.

Hydrodynamic Modeling

In order to study hydrodynamic problems at a suitable scale, the ability to scale down a commercial process is required. One of the earliest works describing reactor hydrodynamics was published by Matsen (1996). Here, Matsen illustrates the solids mixing pattern in a commercial FLUID COKING™ reactor. Using the dimensionless parameter scaling approach proposed by Glicksman (1994), the Fluidization Group at UBC designed and operated geometrically and dynamically scaled cold flow reactor models of Syncrude’s Fluid Coker reactors. Song et al. (2004) describe the scaling approach of an approximately 1/20th scale unit. Their work found that a dense annular region with a net downflow of solids surrounded a dilute core of fast-moving upward flowing solids; the same described by Matsen (1996).

This cold flow modeling provided the first glances into the hydrodynamics of the reactor; however, axial and radial voidage profiles and particle velocities only tell part of the hydrodynamic story. As a result, the cold flow model of Song et al. (2004) was re-commissioned to study the solids mixing behavior. Wormsbecker et al. (2012) developed a phosphorescent tracer technique to measure solids mixing in the model. Commercial radioactive tracer studies were done using a zeolite substrate doped with Manganese 56. Both experimental and commercial data sets capture the solids residence time distribution (RTD) and initial break-through of tracer from the top of the dense bed to the top of stripper, with the latter representing the extent of liquid carryunder. Table 1 summarizes these break-through time data. Using the dimensionless scaling parameters of Song et al. (2004), the cold flow model data were scaled up using a dimensionless time parameter; approximately 17 in this case. The result is a close match between the cold flow model and commercial unit. Interestingly, the data also illustrate the stochastic behavior of the bubbling/turbulent fluidized bed and emphasize the importance of collecting statistically relevant data. This is critical when employing computational modeling approaches, including CFD. Witt et al. (2016) illustrate this stochastic behavior through CFD modeling of the cold flow model used above.

Table 1. Comparison of cold flow model and commercial solids tracer data.

Measured break-through times	Reactor cold flow model solids tracer data† (s)	Reactor cold flow model data to commercial scale (s)	Commercial radioactive solids tracer data‡ (s)
Fastest	1.1	19	17
Slowest	2.6	44	50
Mean	1.7	29	32

† (ten repeat tests were conducted); ‡ (seven repeat tests were conducted)

Gas RTDs are equally important to coker performance. The reaction products are maximized when the product vapours are removed quickly from the dense bed to limit over-cracking into non-condensable gases. Using a 1/9th scale cold flow reactor model, a gas mixing study was performed using a helium tracer with thermal conductive detectors (TCDs) to tracer steam flow in the reactor dense bed. No helium was mixed with the air that represents the hydrocarbon vapours generated by the feed. Unfortunately, short time scales associated with fast rising bubbles and dispersion in TCD measurement lines, prevented successful gas RTD measurements. Instead, steady-state helium tracer data were collected. Fig. 2(a) illustrates the tracer concentration relative to the fully mixed concentration exiting the reactor. Similar to the work of Song et al. (2004), there was a distinct core-annular flow structure, with the majority of the tracer gas which represents steam, present in the core of the dense bed and a lesser amount of steam in the annulus. In order to extrapolate gas RTDs from these data, a tanks-in-series modeling approach was used. The model was based in fundamental fluidization correlations for mass transfer and required an assumption of the percent of gas splitting between the core and annulus of air injected through the feed nozzles. Fig. 2(b) shows the comparison between the extrapolated gas phase RTD from the model and a commercial gas tracer RTD that used Argon 41 (half-life of 1.8 hours) as a tracer injected through a nozzle at the top of stripper. The experimental RTD matches commercial data well. Using the tracer data, the reactor Peclet number was calculated to be 5, indicating a large extent of dispersion.

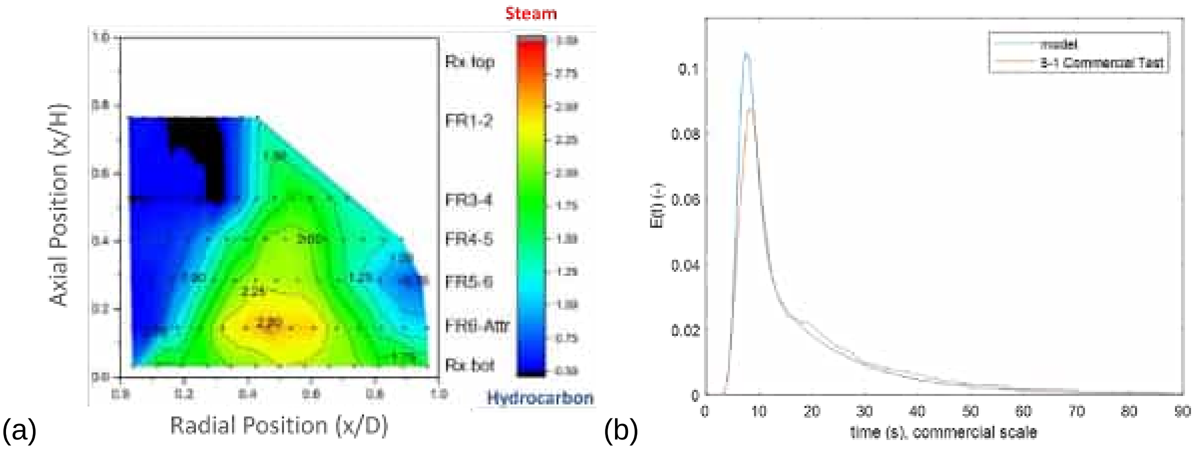

Fig. 2. (a) steady-state helium tracer concentration in a 1/9th scale cold flow reactor model. Data normalized to the fully-mixed helium concentration exiting the system; (b) comparison of cold flow model and commercial gas phase RTD.

Ultimately, the gas and solids mixing studies have confirmed that the geometric and hydrodynamic scaling approach of Glicksman is a suitable approach for studying the hydrodynamics of bubbling/turbulent fluidized bed reactors like those used in FLUID COKING™. This hydrodynamic information has also been used to optimize reactor performance. For example, the solids RTD data show the macro mixing time scales are of the same order of magnitude as the reaction kinetics; as a result, feed injection location plays critical role in liquid carryunder to the stripper. The extent of dispersion shown by the gas mixing study highlights its contribution to the over-cracking of product vapours.

Stripper Re-design

In the late 1990's, Syncrude examined the potential of using coke circulation rate to optimize reactor/burner performance. To satisfy the energy required to thermally crack bitumen, hot coke is provided to the reactor from the burner. For a given bitumen feed rate, this can be accomplished in two ways, a smaller amount of higher temperature fluid coke or a larger amount of lower temperature fluid coke. Based on understanding at the time, higher coke circulation could result in higher liquid product yield. Reactor temperature is also important to avoid rapid agglomeration and defluidization of the bed due to accumulation of liquid, sometimes referred to as "bog". Bogging in turn is controlled by the bitumen feed rate, a factor determined from the coke forming potential of the feed, reactor fluid coke holdup, and the amount of fresh hot fluid coke supplied to the reactor. As a result, higher hot coke circulation would enable a lower reactor temperature to be used for the same bog. Lower reactor temperature would result in reduced over-cracking of liquid products to gas and coke, hence improved liquid yield.

A test was performed on the commercial unit to examine the impact of higher coke circulation (i.e. 100 vs 80 tons per minute as estimated by heat balance). Unfortunately, extensive stripper fouling was observed following only 8 months of operation as reported in Figure 1 of Bi et al. (2005), which resulted in stripper flooding and a reduced circulation rate in order to maintain the system pressure balance. To combat this fouling, they developed a "Steep" shed design (i.e. 30° included angle sheds for the top two rows compared to 90° "Original" sheds) that avoided defluidization hence deposit formation. As suggested by the work, deposit formation appeared to depend on defluidization of wet particles followed by cementation by coke formed from hydrocarbon vapours.

Initial commercial results appeared to suggest great success for the Steep sheds as little deposit was noted at unit turnaround. Unfortunately, the fouling mechanism was not interrupted on the lower Original shed rows, with deposits threatening to block off sufficient area to cause flooding as shown schematically in Fig. 3(a) and in a turnaround photo Fig. 3(b). This result spurred a second stage of stripper development work with UBC as reported here.

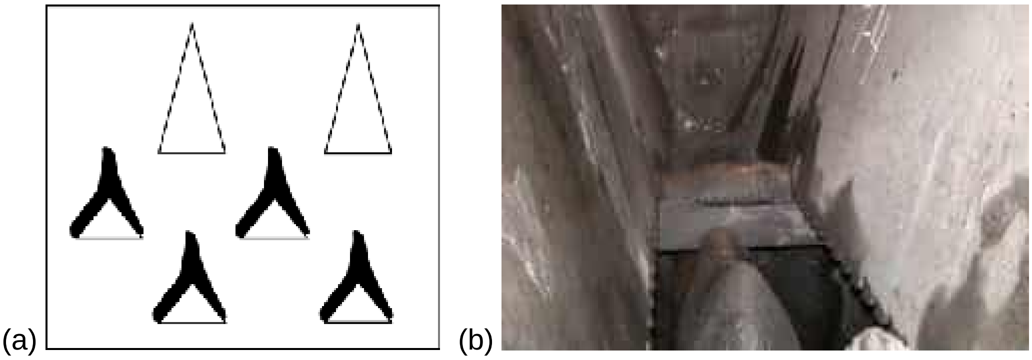

Fig. 3. Steep shed commercial results (a) Schematic of top 3 shed rows with deposit (black); (b) Note foulant growth from below and on cross bracing.

The same UBC column as employed by Bi et al. (2005) was used to screen further options of shed design. As in the previous study, increasing stripper opening for fouling tolerance decreased its efficiency. To span the potential range of efficiency, all shed rows were removed except the bottom two that contained the gas spargers. As shown in Fig. 4, the original eight 90°-included-angle shed row design had the highest stripping efficiency (nearly 99.98% as measured by helium tracer tests) which declined as solids circulation rate (expressed as tons per minute equivalent to commercial circulation) was increased.

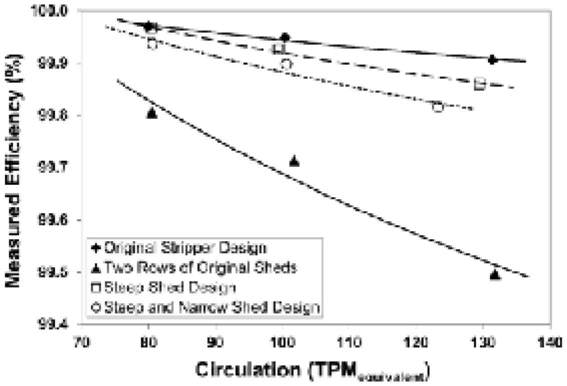

Fig. 4. Stripping efficiencies as a function of solids circulation rate.

In contrast, the two 90° angled shed row case showed the lowest efficiency, ranging from 99.8 to 99.5%, with the impact of circulation having a much larger effect than on the Original design. As expected from the previous work of Bi et al. (2005), the Steep shed design showed marginally lower stripping efficiency compared to the Original design. Commercially, poor stripping efficiency can be observed in the CO boiler, which is downstream the burner. This boiler combusts any remaining fuel components in the burner off-gases with a supplement of natural gas. When stripping efficiency is poor, more fuel components pass from the burner and natural gas makeup to the CO boiler is reduced. This was examined after the Steep shed design was installed, with no observable change noted. Furthermore, the radioactive gas tracer studies mentioned above confirmed the stripper to be operating at relatively high efficiency. Large amounts of radioactive gas were injected at the top of the stripper, but no carryunder to the burner was detected.

Finally, the Steep and Narrow shed (i.e. 60° included angle) design showed even lower stripping efficiency. However, given commercial experience with the steep sheds, high stripping efficiency suggested by the tracer study, and solids tracer work suggesting particles with unreacted liquid feed could always be found at the top of the stripper, it was decided to install the Narrow sheds. Fig. 5(a) shows a schematic of the fouling observed at turnaround and Fig. 5(b) a turnaround photo. The results suggest that the fouling mechanism has been interrupted on the Steep and Narrow shed rows, but not on the lower Original shed. Fortunately, the fouling was not found deeper in the Original shed rows and was contained to a zone of high open area, as shown.

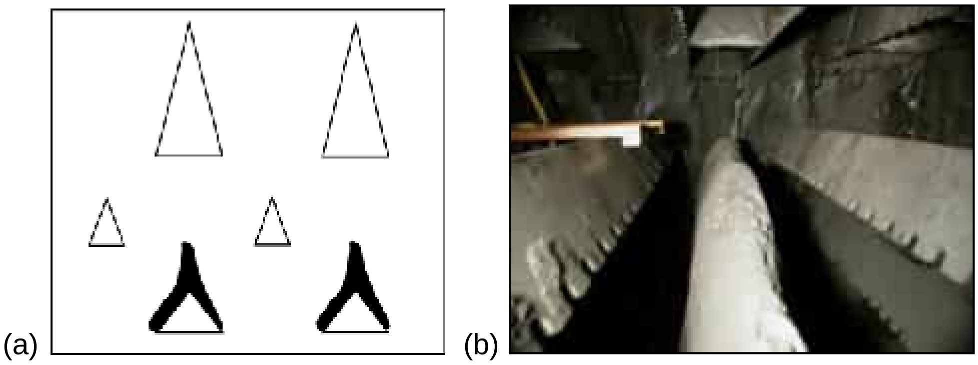

Fig. 5. Steep shed commercial result (a) schematic of top 3 shed rows with deposit (black); (b) Note foulant growth from below and on cross bracing.

The Steep and Narrow shed design has been installed in Fluid Cokers 8-1 and 8-2 since the early 2000's. In addition, Syncrude's newest Fluid Coker, 8-3 also suffered from run lengths limited by stripper fouling when employing the Original shed design and relatively high coke circulation. As a result, 8-3 was also refitted with Steep and Narrow sheds in 2010. Since then, none of the Fluid Cokers have been run-limited by stripper fouling/flooding since employing the Steep and Narrow shed design. However, coke circulation has also been kept to moderate levels (approximately 80 tons per minute) as a precautionary measure.

Work continues on the mechanism of stripper fouling. Defluidization is a required component along with hydrocarbon vapours that form coke in order to cement the deposit in place. However, the origin of wet particles still remains unclear. While unreacted liquid feed on coke particles is obvious from the solids tracer study, recent work suggests that in the presence of hydrocarbon vapour near saturation, liquid can form in the capillaries formed by particle contacts (LaMarche et al., 2016). If this is the case, particle defluidization might also be responsible for wet particle formation, provided hydrocarbon vapour is present at the correct concentration. This might also explain the lack of deposit on lower Original sheds (i.e. 90° with observed defluidization) as hydrocarbons have been stripped by steam by that point. Deconvolution of these effects may help with further stripper improvements.

Sore Thumb Re-design

Sore thumb operability events, referred to internally as sore thumb 'reversals', refer to a loss of pressure build in the cold coke standpipe which restricts cold coke circulation rates and subsequently feed rates must be reduced. Sore thumb reversals are triggered by either reactor thermal cycles that result in spalling of coke foulant off reactor internals which settle in the bottom of the reactor and restrict the flow of coke into the standpipe, or the deposition of coke foulant on the sore thumb itself. More severe reversals are also encountered that result in a complete de-fluidization of bed coke in the bottom cone, referred to as bridging by Senior et al. (1998), thereby resulting in a near complete cessation of circulation.

In the 1990's, differentiating between stripper flooding and sore thumb reversals was also challenging. As a result, sore thumb research was also performed with UBC to further understand these phenomena. The result of this collaboration was a sore thumb design that was customized for the Syncrude Fluid Coker 8-1 and 8-2 geometry. The new sore thumb design utilizes an asymmetric 8° cone; resulting in a similar cage open area and 2.5-times the hat open area compared to the original sore thumb design (similar to modification 'E' in Rusnell et al., 2007). Confirmatory performance testing executed using a fully scaled 1/9th coker model operated at Coanda Research and Development Corporation showed that a commercial equivalent maximum circulation of 160 tons per minute (TPM) could be achieved using the re-designed sore thumb before entering reversal, compared to just 100 TPM with the original design. This increased circulation was attributed to cone's ability to de-gas the solids through the hat of the sore thumb. Photographs of the cold flow model sore thumb designs are shown in Fig. 6. Beyond the re-design, the first stripper-sore thumb ΔP monitoring was implemented.

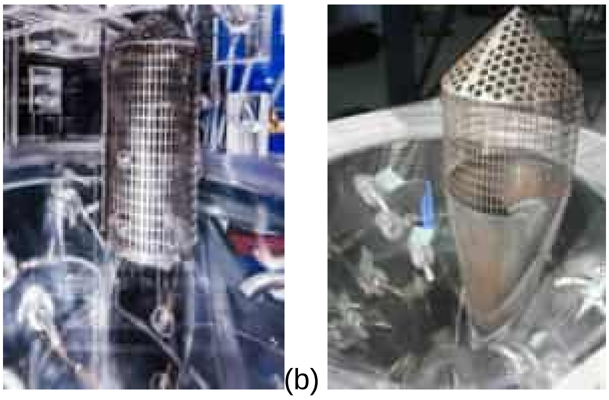
(a) (b)

Fig. 6. Photographs of sore thumb designs tested in a cold flow model (a) original; (b) re-designed.

Fig. 7(a) shows the pressure profiles in the reactor with the original sore thumb operating normally (O-N), the original sore thumb in reversal (O-R), and the re-designed sore thumb at the start of run (RE). A schematic of the instrumentation used to monitor the sore thumb pressure profile is also referenced in Fig. 7(b). The O-N sore thumb indicates a small pressure build across the sore thumb (ΔP_S) and an optimal pressure build across the standpipe (ΔP_D). The pressure build across the sore thumb falls off the optimum pressure build line due to pressure losses caused by acceleration of solids into the standpipe and friction effects from the walls, cage, and standpipe that reduce the pressure build below that expected solely from solids head (Rusnell et al., 2007). In the case of the O-R, there is approximately 5psid pressure loss across the sore thumb (ΔP_S) and a small pressure gain across the standpipe (ΔP_D).

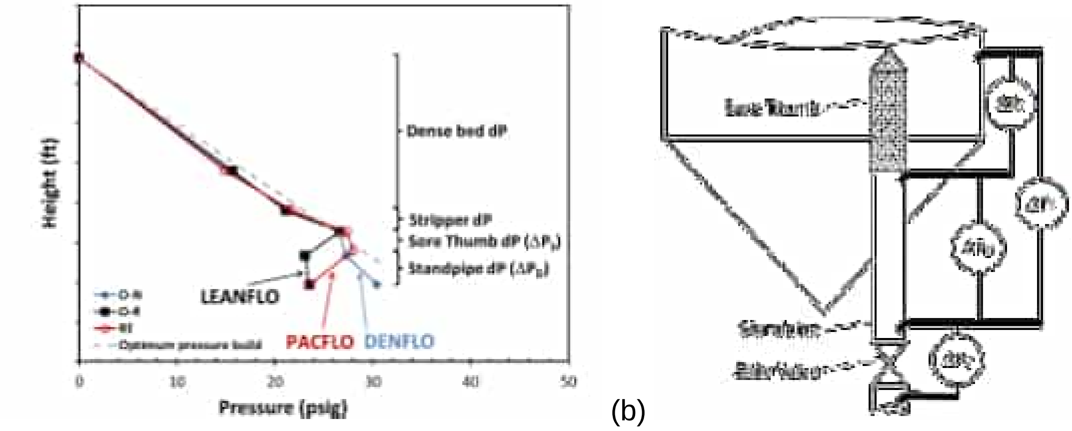

(a) (b)

Fig. 7. (a) Pressure profiles in Fluid Coker reactor for different sore thumb configurations/ operation; (b) Schematic of instrumentation used to monitor pressure profile.

Based on the description of standpipe regimes offered by Klinzing et al. (2010) and Leung & Jones (1978), the original sore thumb standpipe normally operates in the fully fluidized regime ‘DENFLO’, and during a reversal the standpipe operates in streaming flow ‘LEANFLO’. The pressure loss being incurred across the sore thumb (ΔP_S) during a reversal is a consequence of the increased entrainment of steam into the sore thumb and the resulting increases in pressure losses due to particle acceleration and friction across the sore thumb. In the re-designed sore thumb, there is still an inflow of dense solids. However, the pressure loss across the standpipe indicates the packed bed standpipe flow regime (‘PACFLO’) dominates. Packed bed flow indicates that de-gassing is indeed improved.

Understanding the state of health of the sore thumb is beneficial in enabling early interventions such as water lancing so feed rate restrictions can be prevented. In the original sore thumb design, this was identified through reversals. With the re-designed sore thumb starting off in the PACFLO regime, it is postulated that as the run progressed and the sore thumb fouls, gas entrainment into the standpipe will increase. This increase in gas entrainment causes the standpipe to transition from the PACFLO to DENFLO regime. Indeed, this was observed. Fig. 8 shows the reactor pressure profiles of the re-designed sore thumb after significant process upsets. The profiles show that the sore thumb pressure build remains mostly consistent for the duration of the operating cycle, whereas the standpipe pressure build increases after each of the events. Concurrent with an increase in the standpipe pressure build, the slide valve pressure drop also increases. Between the second significant process outage and the near end of run conditions, there is only a small increase in standpipe pressure build. As the end of the operating cycle approaches, no production losses due to sore thumb reversals have been incurred. It is expected that the standpipe pressure build with the re-designed sore thumb will remain in DENFLO and not transition into LEANFLO during its run cycle.

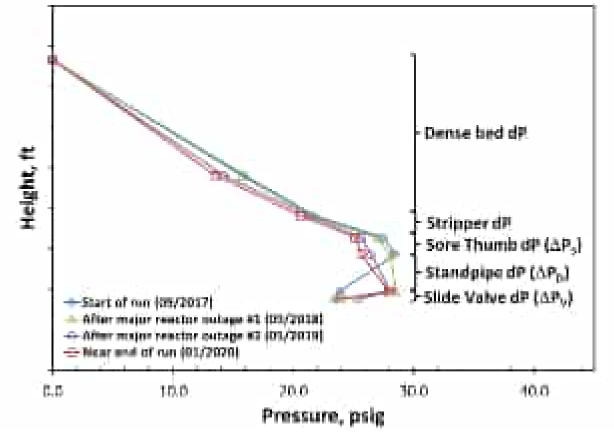

Fig. 8. Pressure profiles in the Fluid Coker reactor using the re-designed sore thumb. Profiles are developed from periods of identical feed rate and solids circulation.

Jet-Bed Interaction

Bitumen is injected into the reactor through steam-assisted atomization nozzles. In order to increase liquid yields and reduce fouling of reactor internals, the bitumen should be spread as evenly as possibly over the particles. This forms a thin liquid film, thus maximizing the contact between the liquid and solids. The original GEN1 feed nozzles used in the reactor were simple geometry nozzles designed in the 1950’s. In the mid 1990’s, Syncrude started a research program with the intent to improve feed nozzle performance. The GEN1 nozzle was tested in open air at the National Research Council (NRC), and results showed that the atomization performance was poor, with most of the liquid exiting the nozzle in large ligaments. Based on mathematical modelling and extensive open spray testing, which used air and water to simulate steam and bitumen, a GEN2 nozzle was developed (Base et al., 1999; Base et al., 2001). The GEN2 nozzle has an improved pre-mixer, which enhances the steam and bitumen contacting while reducing the pulsation tendency of the nozzle. It also has an upgraded nozzle tip geometry that improves atomization.

Concurrently, Syncrude conducted pilot plant experiments in the CANMET facility from 1997-2002. Scaled nozzles operating with the same droplet sizes, velocities and spray angles as the commercial unit, but with a diameter of ¼ the size, were used (Knapper et al., 2003). Samples from the bottom of the reactor were taken to assess the de-fluidization tendencies (bogging) using an index determined from nine different visual and analytical indicators. These results are shown in Fig. 9. A high bogging index corresponded to wet, sticky coke particles that were close to de-fluidizing, whereas a low bogging index corresponded to dry, well fluidized particles. Tests were performed over a range of reactor temperatures at a fluidization velocity of 1 ft/s (0.3 m/s) under good and poor fluidization conditions, where the latter was a result of fluidization steam mal-distribution. The improved atomization performance and reduced pulsation tendency of the GEN2 nozzle had a significant impact on reactor operability. Under poor fluidization conditions the reactor could operate at much lower temperatures for a given bogging index. The impact of fluidized bed mixing was also apparent, as the bogging tendencies of the GEN2 nozzle were only slightly reduced compared to the GEN1 nozzle when operating under good fluidization conditions, and in fact, there was no observable difference in reactor operability between good or poor fluidization conditions when operating with the GEN2 nozzle. These data demonstrate that high fluidization velocities and better solids mixing can compensate for poor feed distribution. In 1999, the GEN1 nozzles were replaced by GEN2 nozzles. Since installation of the GEN2 nozzles, reactor wall coke build-up has been reduced and the reactor liquid yield increased by an estimated 0.7 vol%.

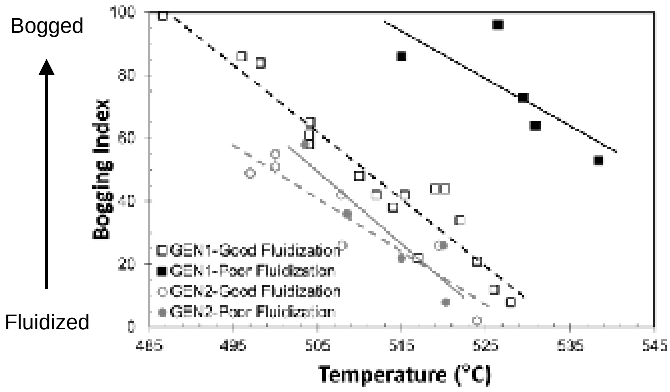

Fig. 9. Effect of Bed Fluidity and Nozzle Geometry on Bogging Tendencies.

With the success of GEN2 nozzle, a 3rd generation nozzle was pursued. The GEN3 nozzle consists of a venturi premixer, which further improves the mixing of the bitumen and steam as well as enhancing the stability of the nozzle spray, and a cloverleaf shaped disperser at the tip of the nozzle that increases the surface area of the spray and draws liquid away from the center of the spray (Chan et al., 2015). During the development of the GEN3 feed nozzle, Coanda R&D Corp developed a novel measurement technique to demonstrate the performance of full scale nozzles in a cold flow fluidized bed model using a liquid fluorescent dye tracer. After tracer is injected, the fluidized bed is slumped, and partitioning plates are rapidly inserted into the bed to section it into thin slices. Images of each section are taken, and based on prior calibration, the concentration of liquid on solids throughout the bed can be determined. This technique was used to estimate the average film thickness on particles, with smaller films corresponding to potential liquid yield increases in the commercial unit. Fig. 10 shows examples of the images obtained with the GEN1, GEN2 and GEN3 feed nozzles at the feed nozzle level, with the corresponding estimated film thickness reduction. GEN3 feed nozzles were installed commercially in 2009. The new feed nozzles helped contribute an additional 1.2 vol% yield uplift. The evolution of coker feed nozzle designs is shown in Fig. 11.

Research has since been directed to understand the interactions between the gas-liquid jet issuing from the feed nozzles and the fluidized bed, termed jet bed interaction (JBI). Cold flow (Mohagheghi et al., 2013), warm flow (Li et al., 2016), CFD (Pougatch et al., 2014) and hot pilot (Stanlick et al., 2017) units show that there are two primary factors affecting JBI

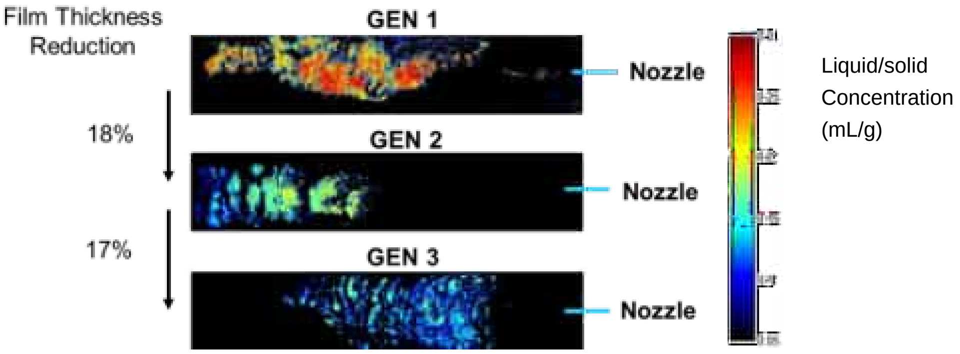

Fig. 10. Examples of JBI Images Obtained with the GEN1, GEN2 and GEN3 Feed Nozzles.

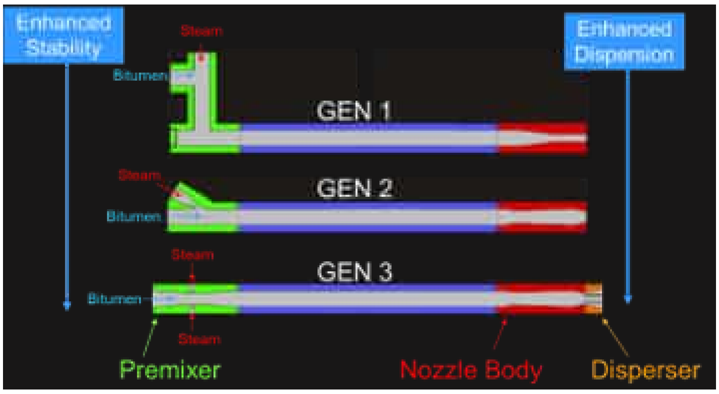

Fig. 11. Evolution of Coker Feed Nozzle Geometry.

performance: (1) fluidized bed properties such as fluidization velocity and particle size; and (2) feed distribution system such as spray shape and size/velocity of the liquid droplets. The effect of fluidization velocity is shown with data from our hot coker pilot (Fig. 12(a)). As with the CANMET facility, but using a 1/5 commercial scale diameter feed nozzle, fluid coke samples were collected periodically and the particle size distributions were measured. When operating at a superficial velocity of 0.6 ft/s, the size and rate of agglomerate formation was less than that obtained at 0.3 ft/s. Similar agglomerate data is shown from the CANMET facility in Fig. 12(b). When operating with a well atomized feed nozzle, the size and rate of agglomerate formation was less compared to a poorly atomized feed nozzle operated under the same fluidization conditions.

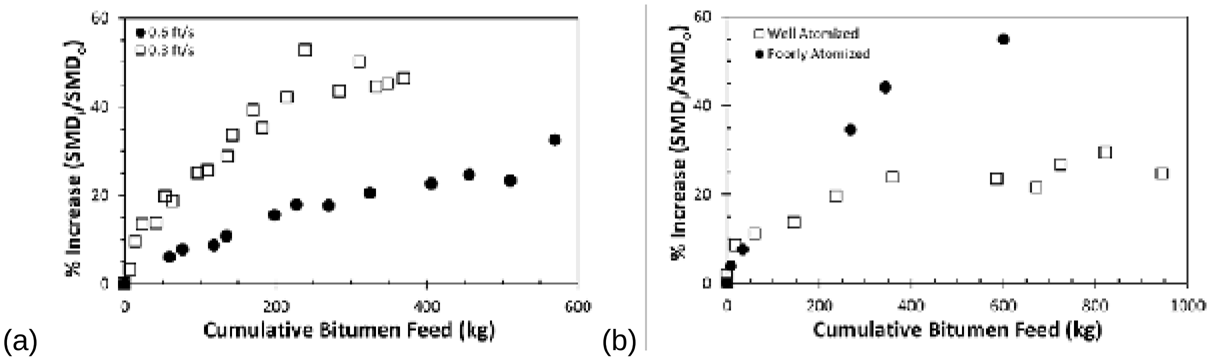

Fig. 12. Agglomerate Growth: (a) Impact of Fluidization Velocity; (b) Impact of Nozzle Atomization.

Conclusion

Through the application of industrial research, Syncrude has made significant technological advancements to its Fluid Coker reactors. Using a systematic hydrodynamic scaling approach, improvements to the stripper and sore thumb designs have been made to reduce the impact of fouling on coke circulation. Similarly, feed nozzle improvements and an understanding of jet-bed interaction have provided yield improvements and reduced fouling of reactor internals.

The result is a higher yield, more reliable process that maximizes the use of the oil sands resource and minimizes its greenhouse gas emission intensity.

Acknowledgements

The authors thank all the academic, government and private industry groups that have contributed to the development of these technologies. Specifically, the authors thank those that participated through the Fluidization Research Centre at the University of British Columbia, ICFAR at Western University, PSRI, and Coanda R&D Corporation.

References

Base, T., E Chan, D Kennett, D Emberley. Nozzle for atomizing liquid in two phase flow. US6003789, 1999

Base, T., E Chan, D Kennett, D Emberley, T McCracken, A Bennett, K Jonasson. Nozzle for atomizing liquid in two phase flow. CA2224615C, 2001

Bi, H.T., JR Grace, CJ Lim, D Rusnell, D Bulbuc, CA McKnight. Can J Chem Eng. 2005. 83, 161-168

Chan, E., B Knapper, E Mueller, J McMillan, J Tyler, D Kiel, R Davuluri. Fluid injection nozzle for fluid bed reactors. US8999246B2, 2015

Glicksman, L.R., MR Hyre, PA Farrell. Dynamic similarity in fluidization. Int J Multiph. Flow. 1994. 20, 331-386.

Klinzing, G.E., F Rizk, R Marcus, LS Leung. Pneumatic conveying of solids 3rd edition, Springer Science and Business Media, 2010

Knapper, B., M Gray, E Chan, R Mikula. Measurement of efficiency of distribution of liquid feed in a gas-solid fluidized bed reactor. Int J Chem React Eng. 2003. 1, 1035

LaMarche, C.Q., AW Miller, P Liu, CM Hrenya. Linking micro-scale predictions of capillary forces to macro-scale fluidization experiments in humid environments. AIChE J. 2016. 62(10), 3585-3597.

Leung, L.S., PJ Jones. Flow of gas-solids mixtures in standpipes, a review. Powder Technol. 1978. 20, 145 – 160

Li, X., A Li, A Gulamhusein, C Brereton, J Grace, CJ Lim, X Bi, M Wormsbecker, C McKnight. A TCD-based technique for experimental study of mass transfer in a gas-solid fluidized bed with liquid injection. Powder Technol. 2016. 290, 83-90

Matsen J.M. Scale-up of fluidized bed processes: principle and practice. Powder Technol. 1996. 88, 237-244

Mohagheghi, M., M Hamidi, F Berruti, C Briens, J McMillan. Study of the effect of local hydrodynamics on liquid distribution in a gas-solid fluidized bed using a capacitance method. Fuel. 2013. 107, 236-245

Pougatch, K., M Salcudean, K Reid, J McMillan. Representation of a small-scale nozzle for gas-liquid injections into a fluidized bed on a large-scale grid. Comput Chem Eng. 2014. 62, 117-124

Rusnell, D., JR Grace, XT Bi, CJ Lim, P Ronan, CA McKnight. Improved standpipe entrance for stable high-flux flow, in: XT Bi, F Berruti, T Pugsley (Eds.), Fluidization XII, ECI, New York. 2007. pp. 161 – 168

Senior, R.C., CG Smalley, E Gbordzoe. Hardware modifications to overcome common operating problems in FCC catalyst strippers, in: LS Fan, TM Knowlton (Eds.), Fluidization IX, Engineering Foundation, New York.1998. pp. 725-732

Song, X., HT Bi, CJ Lim, JR Grace, E Chan, B Knapper, C McKnight. Hydrodynamics of the reactor section in fluid cokers. Powder Technol. 2004, 147, 126-136

Stanlick, C., F Berruti, C Briens, Effect of mixing and vapor residence time on thermal cracking of bitumen in a mechanically fluidized reactor. Fuel. 2017. 200, 481-487

Witt P., Y Feng, Q Wang, J Boulanger. Multiphase CFD modeling at CSIRO. NETL Workshop on multiphase flow science. 2016. Morgantown.

Wormsbecker M., C McKnight, A Mezo, J Mottershead, D Kiel, XT Bi, J Grace. Phosphorescent tracing to study solids mixing in fluidized beds. AIChE Annual Meeting. 2012. Pittsburgh

FLUID BED SYSTEMS FOR CHEMICAL SYNTHESIS AN ENGINEER'S PERSPECTIVE ON DESIGN AND SCALE-UP

Behzad Jazayeri*

Contract Engineer, Irvine, CA 92614, USA

*Email: bjjazayeri@yahoo.com

Abstract

Over 100 fluid bed reactors for chemical synthesis and comparable processes using group A powders have been installed and operated successfully since late 1940s, with some reactors much larger than 7 m (23') ID. The paper discusses developmental milestones leading to their success, the key design differences between chemical synthesis circulating fluid beds and FCC, and author's recipe for successful scale-up. Root causes of typical operational issues of this class of beds are also discussed.

Background

Fluidized bed chemical synthesis reactions convert gas phase hydrocarbons to high value-added products. Reaction is typically limited to around 450 C (840 F). The more common mode of operation is with gas phase oxygen supplied as air, enriched air or oxygen. When using gas phase oxygen, operating pressure is usually limited to around 3 barg (45 psig) due to safety concerns and also because gas phase oxygen reactions are favored by reduced pressure. Higher pressures may be used safely when oxygen is provided in solid form or when there is no oxygen, as occurs in some processes with comparable characteristics such as Sasol circulating or bubbling gas-to-liquid process.

Since mid-1940s, over 100 bubbling, also called fixed fluid bed (FFB), reactors using group A powders have been installed and operated successfully for chemical synthesis and comparable processes across the world. Their success was based on the following developmental milestones:

- Correct overall range for catalyst size (wide size distribution, high levels of 0 – 40 micron)
- Figuring out how to perform research at the lab to get data for scale-up CORRECTLY
- Correct fluidization regime(s) to use
- Proper gas distributor design (many holes distributed evenly with adequate pressure drop)
- Placement of coils inside the reactor and the process and **mechanical** design parameters of the coils

Use of circulating fast fluid bed (CFFB) systems using group A powders for chemical synthesis also dates back to 1940s but their usage has been less successful than FFBs due to more complex design, higher risk when gaseous oxygen is present, and limited window of operation when internal coils are needed (metal erosion). CFFBs have been used or assessed for several types of large-scale processes:

- Gas-to-liquid by iron oxide reduction (solid phase oxygen) – Sasol Synthol process
- Hydrocarbons to oxygenated chemicals by adsorbed oxygen (solid phase oxygen) – DuPont butane to maleic anhydride
- Hydrocarbons to oxygenates with air, enriched air, or oxygen (gas phase oxygen)
- Natural gas to olefins by adsorbed oxygen (solid phase oxygen)
- Natural gas to olefins with air (gas phase oxygen)
- Non-slugging gasification of coal with oxygen (gas phase oxygen) – TRIG^{TM} process
- Conversion of solid waste to chemicals or syngas

Figure 1 below depicts two CFFB systems presented by Jazayeri (2003). The sketch on the left represents the Sasol Synthol process for conversion of syngas to gasoline using iron oxide as catalyst. The iron oxide is reduced as conversion progresses. The sketch on the right is the concept piloted and commercialized by DuPont to convert butane to maleic anhydride using adsorbed oxygen. Both these systems circulate a solid between 2 or 3 vessels, consisting of a riser reactor, a stripper/solid separator, and when required a regenerator.

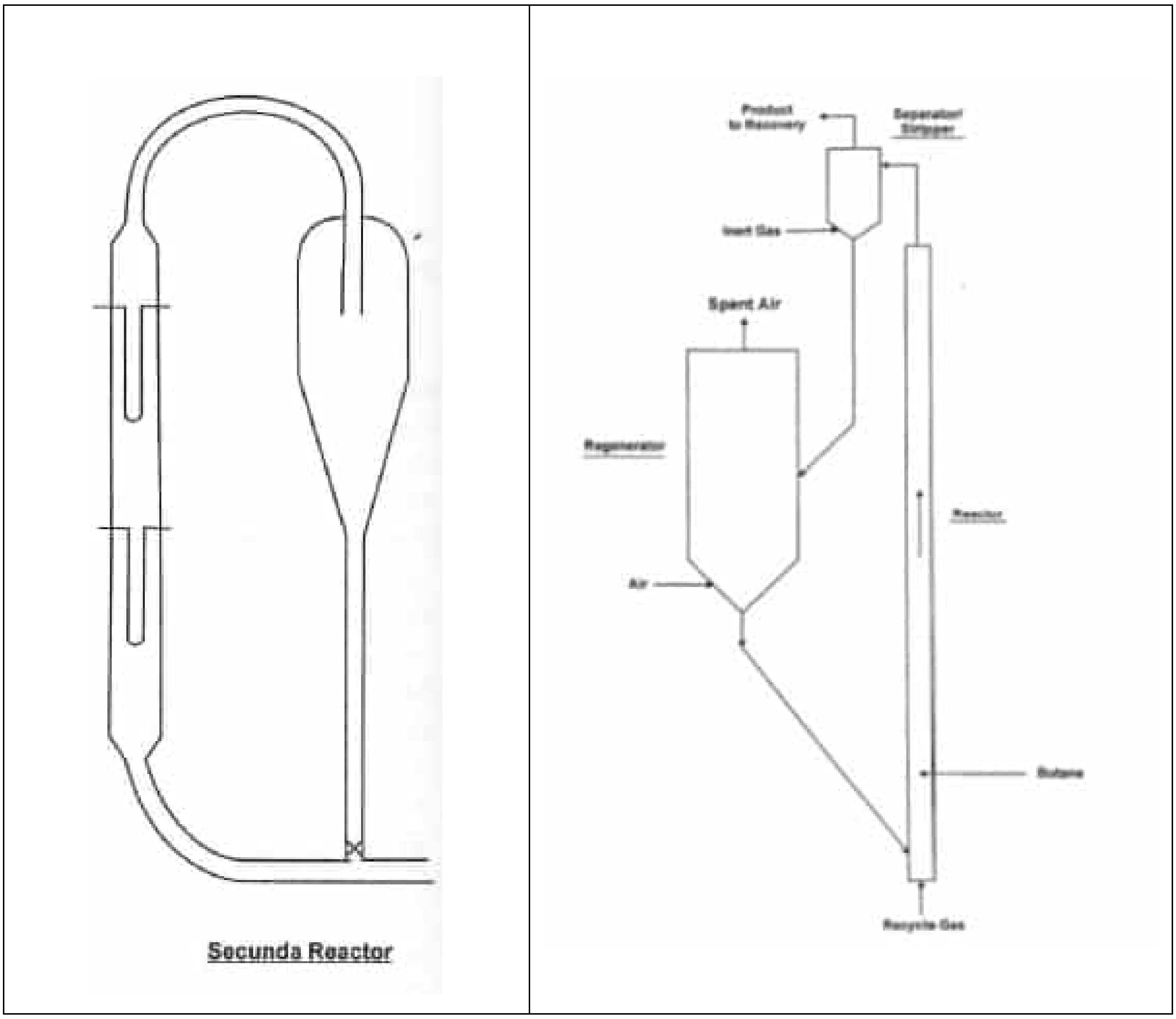

Fig. 1. Examples of CFFBs.

CFFBs have also been assessed both in concept and through demo-scale production plant for conversion of natural gas directly to olefins by most major gas field producers but so far, the economics have not justified further development, the main barrier being process yield.

Jazayeri (2003) has provided excellent accounts of scale-up of several chemical synthesis processes, the Sasol FFB gas-to-liquid process being one such example. The process was bench tested in a 100 barrel/day unit in 1983. Further development was restarted with a 3500 barrel/day demonstration unit in early 1990s when Sasol decided to abandon existing circulating bed concept in favor of FFB concept and commercialized in a 11,000 barrel/day unit in 1995.

CFFB vs FCC

A CFFB has many design aspects similar to that of a Fluid Catalytic Cracking (FCC), which I will refer to as a Circulating Fast Bed (CFB). A **group A powder chemical synthesis**

CFFB will also contain a reactor that operates as a riser, but it should not be designed using FCC design guidelines for the following reasons:

- Use of oxygen gas in the reactor side of CFFB poses safety considerations with respect to design of the reactor in the event of loss of solid circulation. This concern is not present in FCC (deflagration may occur in CFFB reactor due to drop in solid holdup caused by loss of circulation)
- Chemical synthesis catalyst may cost up to \$110/kg (\$50/lb.) with a life of many years compared to less than \$8/kg and a few months life for FCC catalyst. In CFFB, we typically design the unit to minimize attrition. In FCC, attrition of catalyst is not a major design concern
- The diameter ratio of regenerator to standpipe in **modern** FCC units is very large. The ratio in a CFFB with **<u>same size standpipe</u>** is significantly smaller as coke production is much less in CFFBs, or not present at all. Most regenerator standpipe entry designs used in FCC do not translate well to CFFB. Figure 2 below copied from internet shows a “trough” like overflow spent catalyst distributor with horizontal arms, as used in some FFC regenerators. Using an approach like this in a CFFB regenerator would negatively impact fluidization behavior as the size of the trough and its arms would be too large compared to CFFB regenerator ID.

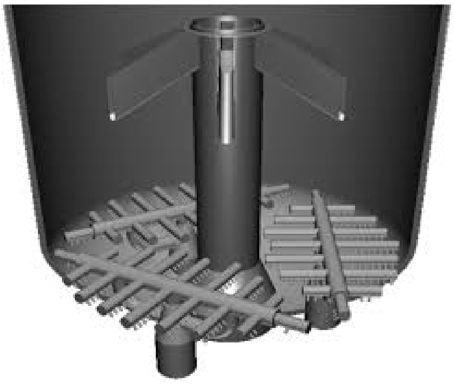

Fig. 2. Spent FCC Catalyst Distributor.

- FCC uses atomized liquid feed in the reactor. CFFB for chemical synthesis is likely to use gas feed which creates challenges on how to mix the feed with circulated catalyst in the reactor bottom, especially if the reaction involves use of oxygen (gas or solid phase)
- FCC reactor is endothermic. FCC regenerator is exothermic and may or may not require heat removal. CFFB may require heat removal in both reactor and regenerator. Use of catalyst cooler commonly used in modern large-scale FCCs is not practical in CFFB reactor side, and often even for the regenerator
- Fast separation of gas and solid at exit of riser in FCC is critical to minimizing gas yield. This separation is not as important in most, if not, all CFFBs
- CFFBs require special considerations on how the reactor exit is connected to cyclones due to high cost of catalyst
- Average density in FCC riser is about 80 kg/m3 (5 lb/ft3). In CFFB, riser density is typically over 160 kg/m3 (10 lb/ft3). CFFB reactor also operates at significantly lower velocity than FCC riser. Moving such a dense mixture vertically up a, say, 30 meter (100’) tall riser at low velocity is not an easy task
- FCC catalyst pores contain high boiling point components that are difficult to strip. CFFB catalyst typically does not have this issue, so stripping in CFFB is generally much easier

Regenerator Temperature Control Options

Approaches to controlling temperature of the regenerator vary depending on the type of process being considered, ranging from external cat coolers for FCC to internal cooling coils, or other approaches, for chemical synthesis.

Riser Solid Holdup

Figure 3 may be used to estimate **CFB** riser solid holdup as a function of velocity and solid flux and applies to solid particle density of about 1100 to 1750 kg/m^3. Obtain volume percent solid (es), from the graph and multiply by particle density. Commercial **CFFBs** typically operate with solid holdup above 10 volume% and fluxes over 300 kg/sqm/sec.

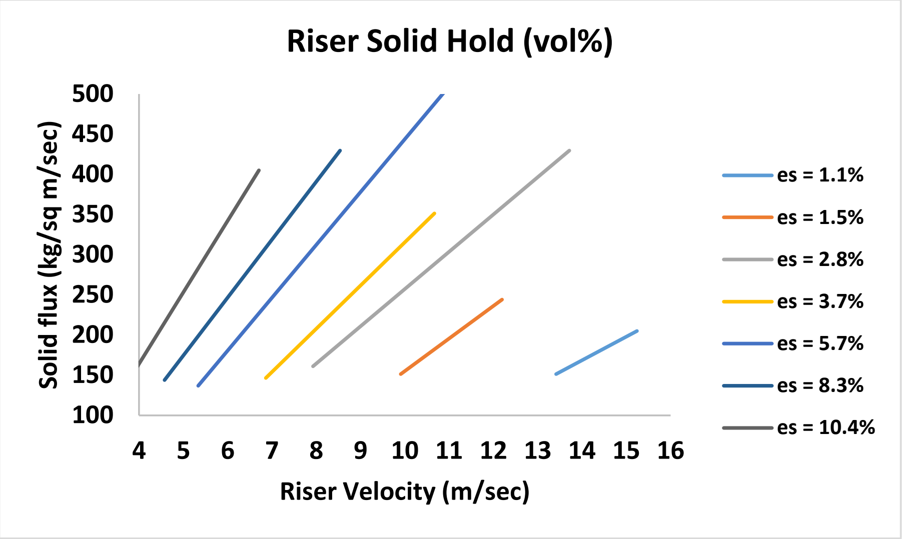

Fig. 3. Riser solid holdup.

Scale-up

My experience suggests there are no “hydrodynamic reasons” to limit the capacity of a fluid bed using group A powder that has “proper solid size distribution; operating velocity and design of internals”. The factors that limit CFFB unit capacities (reactor size) are typically as follows:

- **Plot space**: the structure space (width, length, and specially height) needed to connect three vessels (reactor, stripper, regenerator) together in a CFFB loop becomes excessively large as equipment size is increased
- **Cost factors**: shop fabrication is usually cheaper than field fabrication. Vessel diameters are therefore limited to about 4.5 m (15’) due to over-the-road accessibility with shop fabrication

Since FFBs have a single vessel, the structure height changes only a little with size of reactor. As a result, single train field fabricated FFB reactors of 7 meter (23’) and much larger are commonly used.

The pilot plant, demo plant, or first commercial plant of a new process do not need to be optimal. They need to work reliably and prove the process concept is commercially viable. The optimization can be done by tweaking the second commercial plant. Admittedly this approach may mean having to take some calculated risk. It is the faster approach to demonstrating a new group A based fluid bed process (CFFB, CFB, or FFB). The alternate is to resolve all issues, extending “time to market”, during which engineering, and research hours are spent increasing also “cost to market”. The development of Zsorb low sulfur gasoline process is an excellent example how collaboration between research and engineering and taking some calculated risk can expedite time to market of a new process.

I was part of the team that designed, built, and successfully demonstrated a 6000 barrel/day unit within 16 months of project award allowing ConocoPhillips to license the process before the short window of opportunity disappeared. Engineering started on day 1 based on very limited bench scale data and progressed while bench scale research continued in parallel.

I believe that if the research at the bench scale is done correctly one has all the information needed to design a commercial group A reactor. The only reason for using a pilot plant is to build confidence (a very valid reason) and to verify issues that cannot be addressed at bench scale. Some of these issues often can be addressed at much lower cost using cold mock-ups.

CFD capabilities in modelling gas/solid systems has increased tremendously and will continue to do so. CFD is a **useful tool** for supporting successful scale-up **<u>of a new large-scale</u>** fluid bed reactor using group A powders. Unfortunately, I see some R&D organizations, including very large ones, relying on CFD results too eagerly without asking if the result make any sense. Some even have corporate rules that nothing can proceed without some amount of CFD modeling.

Many papers are written on how solid behaves inside a riser and how this may impact reactor yield and gas backmixing. Many such papers were also written years ago as bubbling beds were being introduced. Obviously, the design of the riser exit can cause recirculation of solid, and therefore gas. But as for the rest of the riser, I will point out that the higher the solid concentration of a riser, the more “well behaved” it becomes. I will also add that even though all chemical plants are designed to operate at full capacity, there will be times when they may have to limp along, sometimes for extended periods, at reduced rates. If one’s new process cannot handle turn down using riser technology, then perhaps, use of a riser is not the best choice?

Our industry does see occasional paradigm shift that allows never used before approaches viable. But I remind you that almost everything you are asked to look at in producing an existing chemical via application of fluidized beds has already been looked at in the past in some form or another.

Recipe for Successful Scale-up

Here is a list of **<u>my</u>** lessons learned for successful commercialization of a new large scale FFB, CFB or CFFB process for chemical synthesis:

- Catalyst with acceptable characteristics is available (given)
- Bench scale research is done correctly. Easier said than done. Many organizations, even some major ones, do not obtain data correctly. The challenges we face is highlighted by use of partial oxidation reactions represented by:

  $$CxHy + O + (N, Cl, etc) = Product + H_2O + COx$$

  Partial oxidation reactions are favored by reduced pressure. The lower the operating pressure, and the lower the concentration of hydrocarbon in total feed, the higher the per pass conversion and per pass yield. Testing such a process using a low pressure or an atmospheric pressure unit and focusing on just adjusting the concentration of the hydrocarbon masks this effect resulting in lower than expected yields when unit is scaled-up in the pressurized pilot/commercial plant.

  Some partial oxidation reactions can also suffer from formation of “color bodies”. These are trace by-product(s) formed in parts per million concentration or less when catalyst is not at its optimal condition. Color bodies must be removed, sometime with great difficulties, to ensure end user product meets the required color specifications (hence “color bodies”). The conditions under which color bodies are formed can only be found by brute force testing at the lab or pilot plant.

Figure 4 below shows impact of reactor size on yield for a group A powder process. The data is masked as it is proprietary and are relative to the smallest unit tested and is at constant pressure, temperature, and gas contact time. It shows yield remains essentially constant as size is increased except at one scale due to hydrodynamics caused by bubbles. Not all group A powder processes show this behavior, that is yield can remain constant as scale goes up.

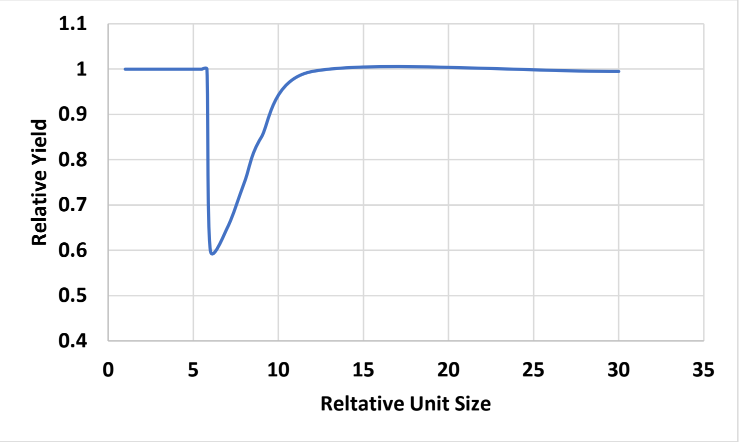

Fig. 4. Impact of Scale on Process Yield.

- Two of my favorite quotes picked up from ex-colleagues: “Do not wish issues away. They tend not to go away and come back to haunt you at the worst possible time!” and “Ignorance is definitely not bliss. Just because we don’t see any issues doesn’t mean there aren’t any!”
- Total engineering approach to design of pilot plant (and first commercial plant). The new reactor is always the “sexy part” and gets the most attention in design phase. But it cannot operate if the front or back end of the process is designed or built poorly and incapable of reliable operation
- Engineering collaboration with research as soon as viability of process is validated in the lab and adequate and repeatable yield data is obtained to start first-pass concept plant design. This exercise often leads to discovery of gaps in research that can then be addressed before committing to pilot plant. These gaps will be eventually discovered and will need to be addressed. Unfortunately, this discovery tends to happen after the engineering firm is hired and staffed up to design the pilot plant. Engineers charging hours will end up working at less than optimal pace while waiting for the missing information increasing project cost, and more importantly, schedule
- Selection of correct engineer for pilot plant design. The “local full service or boutique firm” may be a lower cost option for design and construction phase but may not be the correct choice. Remember, this is fluidization and solid processing! Despite all advancements in the field, still somewhat of a black art. If one has to spend money fixing things before actual steady state pilot plant testing can begin, then any perceived cost saving during design and construction phase may be spent multiple times over. In addition, by that time, the process owner has many operating staff on the payroll waiting around doing little, burning through cash. Not every company has deep pockets to ride through such unfortunate event or ability to re-assign idle operators to other activities
- Correct process and, **as importantly, mechanical** engineering of pilot and first commercial plant reactor, other fluidized vessels, and their internals
- Not spending the correct amount of money. There are reasons why 2” metal seated full port ball valves and actuator cost range from about $3,000 USD to about $25,000 USD (US suppliers’ data only)

Common Operational Issues in Chemical Synthesis Reactors

- ***Poor yield/selectivity caused by***
  - Reaction chemistry not studied correctly/insufficiently
  - Incorrect catalyst size distribution (too coarse/too fine)
  - Incorrect reactor velocity (too low)
  - Poor gas distributor design or damaged distributor
- ***Reactor instability caused by***
  - Reactor velocity too high (high velocity can mean low bed density and runaway reactions)
  - Coil layout too restrictive (solid motion must be reasonably free to dissipate the heat generated)
  - Incorrect distribution of coils within reactor (coils must cover an adequate portion of the reactor)
- ***Catalyst attrition caused by***
  - Catalyst is too soft
  - Incorrect gas distributor design (jet velocity too high)
  - Incorrect cyclone design (cyclone velocity too high)
  - Incorrect gas distributor fabrication/installation or insufficient quality check (either new or repaired)
- ***Catalyst deactivation caused by***
  - Incorrect grid plate design
- ***Erosion of internals caused by***
  - Incorrect placement of internals relative to gas jets
- ***Filter operation caused by***
  - Design filter face velocity too high
  - Design filter cake density too high
  - Design gas inlet pipe layout incorrect
  - Blowback gas temperature too low causing pore plugging

Conclusion

Commercializing a new group A fluid bed process requires extensive research to support catalyst development and prove reaction chemistry but its commercial success ultimately relies on capabilities of the engineers that scale-up and design the first commercial unit for the process. As such, engineering provides a critical and complementary function to research in development of any new multi-phase process, of which fluidization is one of the more important type.

References

Jazayeri, B. Chapter 16, Handbook of Fluidization and Fluid-Particle Systems, Wen-Ching Yang editor, Marcel Deckker Inc, 2003

COLD FLOW MODEL STUDY ON THE OPERABILITY OF A MULTISTAGE-FLUIDIZED-BED COLUMN WITH DEEP BUBBLING BEDS

Andreas Klingler[1*], Christoph Eder[1], Gerhard Schöny[2], Johannes Fuchs[2], Tobias Pröll[1]

[1]*University of Natural Resources and Life Sciences, Department of Material Sciences and Process Engineering, Peter-Jordan-Str. 82, 1190 Vienna, Austria*
[2]*TU Wien, Institute of Chemical Engineering, Getreidemarkt 9/166, 1060 Vienna, Austria*

*Email: *andreas.klingler@boku.ac.at*

Abstract

The operability of a multistage fluidized bed column with deep bubbling beds connected via internal downcomers, originally used as regenerator for a temperature swing adsorption unit, was investigated using a cold flow model. The model consisted of four stages with varying cross sections where each stage was equipped with immersed heat exchanger tubes. The internal downcomers had a high length-to-width ratio and offered the possibility for external aeration at the gap between the downcomer and the fluidized bed stage. The mean particle size of the used bulk material was 650 µm with a bulk density of 550 kg/m³ and are thus classified as Geldart type B powder. The achievable solids circulation rate for varying fluidization numbers was studied in order to attain an operating window. This window was then compared for operation with and without external aeration and showed an increase of solids circulation by 20% and a wider range of possible fluidization numbers. Furthermore, the three operating modes for downcomers (packed moving bed, bubbling bed, slugging bed) were investigated with regard to their pressure fluctuations as possibility for a slug detection system.

Introduction

Multistage fluidized beds have a wide range of application especially in adsorption processes such as a temperature swing adsorption (TSA) process for post-combustion carbon capture as proposed by Pröll et al. (2016) or for the adsorption of volatile organic compounds (VOCs) as investigated by Lv et al. (2019). In addition to the advantages of single stage fluidized beds (e.g. good mixing behavior, high wall-to-bed heat transfer), multistage fluidized have advantages over single stage systems with regard to the maximum sorbent loading that can be achieved. Such multistage fluidized bed systems require solids transport systems guiding the particles between stages. The design of downcomers for the stage-to-stage solids transport and the blocking mechanism caused by the formation of slugs in the downcomers have already been discussed by Eleftheriades and Judd (1978). This early research already discussed the three possible transport regimes for downcomers (packed moving bed, bubbling fluidized bed and slugging bed) and highlights that a moving bed operation is the most desirable operating mode. The formation of slugs does not only inhibit solids transport but also enables the bypassing of large amounts of gas in the downcomer. A more recent publication concerning these issues was carried out by Zehetner et al. (2017). For the purpose of a TSA carbon capture process, this study discussed the different requirements for the necessary contactor columns, that is, adsorber and regenerator (desorber). For an adsorber, where large amounts of raw gas need to be processed, the overall pressure drop of the column has to be as low as possible to keep operating costs at reasonable levels. Therefore, low stage pressure drops and bed heights are required for such an apparatus. However, a desorber, which in the case of a carbon capture process is operated with low-pressure steam, requires a smaller cross section to keep steam consumption of such a column low. The rather large heat of adsorption for CO_2 capture, however, requires a certain amount of heat exchanger area for removal. If the maximum number of stages is limited, a desorber stage will thus have a larger bed height than a stage of the adsorber column. Therefore, deep bubbling beds are necessary in order to meet the mentioned design requirements. While shallow bed columns with internal or external downcomers are well understood, the operation of deep bubbling beds with internal downcomers requires further investigation. Kunii and Levenspiel (1991) already discuss that the crucial physical quantity for the transport regime in a downcomer is the pressure gradient. If the pressure gradient gets too high, bubbles will form. Especially for Geldard B particles, where the bubble size increases over the bed height, this may lead to the formation of slugs and cause a blocking of solids transport. In order to ensure stable operating conditions in each downcomer, a monitoring system may be required. Chen et al. (2020) have investigated the pressure fluctuations at high sampling frequencies (400 Hz) for different operating regimes. The findings showed that the pressure signal and the prevailing frequencies can be used for the identification of the current transport regime in a downcomer.

Based on the aforementioned research articles, the operating window for a multistage fluidized bed column with internal downcomers was investigated. In contrast to previous studies, this study focuses on deep bubbling beds in the stages. The downcomers had a small cross section and high length-to-width ratio and were therefore prone to the formation of slugs. An external aeration (similar to an L-Valve) shall provide an additional degree of freedom for the operation. The influence of this aeration on the operating for the downcomer is discussed. Furthermore, the pressure gradient in two downcomers was measured in order to quantify and discuss pressure fluctuations and to identify the respective operating regime.

Experimental

Experimental Setup

A drawing of the experimental setup is given in Fig. 1. The experiments were conducted with a four-stage-model with differing cross sections (Stage 1 – 150 by 150 mm, Stage 2 and 3 – 170 by 150 mm and Stage 4 – 150 by 180 mm). The downcomer connecting stage 3 and 4 could be partially blocked by a gate valve in order to control the solids transport into the bottom stages while Stage 4 acted as buffer. The weir height of each stage was approximately 450 mm. The inventory of the column was kept constant at 21 kg. The particles used for the experiments had a Sauter mean diameter of 650 µm and a particle density of 850 kg/m³, resulting in a minimum fluidization velocity of 0.12 m/s. The bulk density was 550 kg/m³. Fluidization and external aeration were controlled with six rotameters. Two rotameters were used for controlling fluidization, where one rotameter's air was guided through a bubbler to humidify the air since a low humidity caused electrostatic charging of the material. The bottom stage level was controlled via a slide valve in the standpipe leading into the riser system. From there, particles were conveyed to the particle separator and back into stage 4. Perforated steel plates with openings of 2 mm in diameter were used as gas distributors for each stage. The number of openings varied from 110 in stage 1 to 121 in stage 4. The heat exchanger tubes with a triangular arrangement had a pitch of 30 mm and a diameter of 17 mm. Stage pressure drops, riser pressure drop, windbox total pressure and the pressure drop

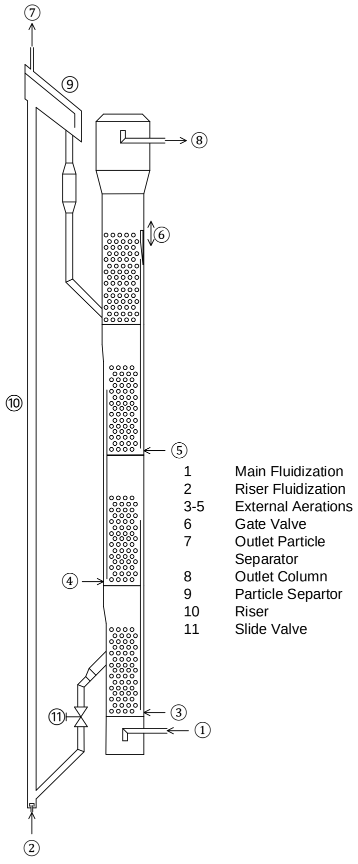

Fig. 1. Schematic drawing of the experimental setup

between particle separator and the freeboard at stage 4 were measured with pressure transmitters (Kalinsky DS2-420) with various ranges. The riser pressure taps were placed at a distance of 1.91 m. Additional pressure drop sensors were installed in the bottom two downcomers at a distance of 106 mm and 1111 mm for the measurement of pressure fluctuations in these downcomers. Pressurized air was used in every experiment for all fluidizations and aerations. At the stage 4 outlet and the particle separator outlet, a filter bag was placed in order to avoid the emission of fine particles.

Experimental Plan

For the investigation of the operating window, a linear correlation between the riser pressure drop and the solids circulation rate (SCR) was determined at a constant riser gas velocity of 5 m/s. Each stationary datapoint was held constant for five minutes. During these five minutes, the filling level of stage 1 was kept at a constant value (100 mm above the solids outlet). The flooding boundary was determined by fully opening the gate valve in the top downcomer and setting the desired fluidization number, starting at approximately 1.3. After recording one datapoint, the fluidization number was increased, which then also increased the maximum solids transport. The opening of the slide valve was set accordingly to maintain a stable filling level in stage 1. The slugging boundary was determined by gradually reducing the SCR with the gate valve in the top downcomer until slugs would form in the downcomer connecting stage 1 and 2. This procedure was identical for experiments with and without external aeration. Experiments with external aeration were carried out with a constant aeration rate of 0.4 Nm^3/h for each downcomer.

For the evaluation of the pressure fluctuations in the bottom two downcomers, the respective downcomer was put into the desired operating regime and the pressure signal was recorded at a sampling frequency of 1 Hz. The relative standard deviation (RSD) was then selected in order to quantify the fluctuations.

Results and Discussion

Operating Window

The operating window of the column is divided into three parts. The packed moving bed regime is characterized by smooth operation and high SCRs. Above the flooding boundary, stable operation is not possible since the transport rate through the column is not high enough leading to an emptying of the bottom stage. When the lower boundary of the operating window is approached, bubbles start to appear in the downcomer. The stable bubbling fluidized bed is a small transition zone due to the tendency of slug formation. A shift between moving bed and slugging can occur leading to inventory swings in the stages connected via the respective downcomer. When the SCR is further reduced, stationary slugging will set in.

A comparison between the operating windows with and without external aeration is given in Fig. 2. The lines depicted in this graph give the limits for stable operation in a moving bed regime in each downcomer. Both windows show a narrow band of stable moving bed operation. However, a comparison shows a significant increase of the maximum SCR for operation with external aeration, especially at low fluidization numbers. The maximum SCR without external aeration is achieved at a fluidization number of 3.3 reaching 1100 kg/h. With external aeration, this maximum is reached at a fluidization number of 3.2. In addition, this SCR is 20 % higher at approximately 1320 kg/h. The flooding boundary without external aeration shows a decrease in SCR when the fluidization number is increased from 3.3 to 3.4. An increase beyond a fluidization number of 3.4 led to the formation of slugs. The maximum fluidization number for operation with external aeration is 3.2 and, therefore, slightly lower than without external aeration. When the maximum fluidization number is exceeded, slugging will occur in the downcomer of stage 1.

Pressure balances shall be used to discuss potential influential factors concerning the transport regime in a downcomer. The pressure balance for a subsystem consisting of two stages n and n+1 and the corresponding downcomer is given in Eqs. (1) and (2).

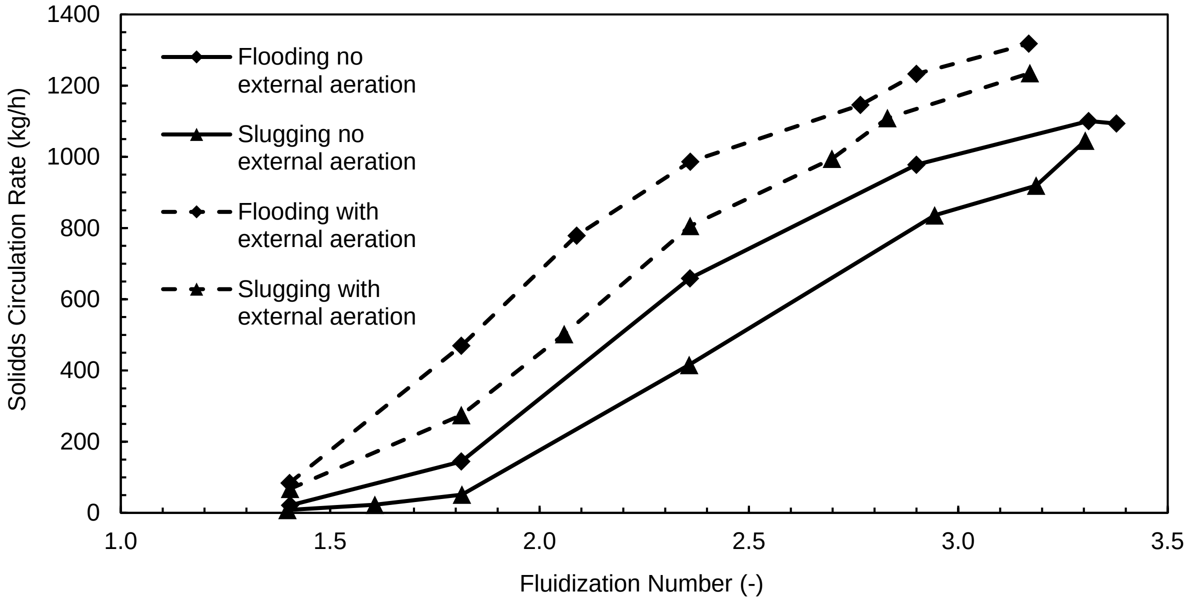

Fig. 2. Comparison of operating windows with and without external aeration

As mentioned before, the pressure gradient in the downcomer is the physical quantity limiting the downcomer. This value shall lie well below the pressure gradient for the fluidized bed at minimum fluidization. In order to keep this gradient low, the pressure drop across the stages or the pressure drop of the gas distributors have to be kept low as well. The reduction of the stage pressure drop however may not be an option due to geometric restrictions. The pressure drop of the gas distributor can be reduced, but there are limits to this. Kunii and Levenspiel (1991) suggest a minimum ratio between distributor pressure drop and bed pressure drop of 0.07 for perforated plates.

$$\Delta p_{DCn} = \Delta p_{Sn} + \Delta p_{GDn+1} + \Delta p_{Sn+1} \tag{1}$$

$$\frac{\partial p_{DCn}}{\partial x} \cdot h_{DC} = \Delta p_{Sn} + \Delta p_{GDn+1} + \Delta p_{Sn+1} \tag{2}$$

The filling level of the downcomer is another parameter which influences the downcomer pressure gradient. However, this parameter cannot be influenced by operating conditions. First experiments show that there is a strong connection between the filling level and the SCR, and it will set according to the mass balance for the downcomer. If the filling level is high enough, the downcomer will be able to equalize the pressure drop in moving bed operation. The gradient itself is created by an upward movement of gas relative to the particles moving down. For a multistage fluidized bed, this means that the amount of gas entering the downcomer is crucial. This aspect can be influenced, e.g., by implementing a controlled aeration in the downcomer area similar to a loop seal or by adapting the gas distributor in this area accordingly.

Downcomer pressure fluctuations

The results for the pressure fluctuation tests are summarized in Table 1 and in Fig. 3 to 5. The data clearly shows that the pressure signal at low sampling frequencies can be used to determine the transport regime in a downcomer. As expected, the RSD for the moving bed is the lowest, closely followed by the bubbling bed. The slugging regime shows significantly higher fluctuations in its signal. The differences in the RSD are significant and therefore suitable to determine the current transport regime. As the distance between the pressure taps is reduced, the fluctuations and the RSD increase. This result is not surprising since a wider distance will show an average over this wider distance leading to a dampening of the signal.

Table 1: Summary of pressure fluctuation experiments

		Downcomer 1	Downcomer 2
Distance pressure taps		106 mm	1111 mm
Moving Bed	Pressure gradient range	7.24	2.25
	RSD	3.55%	1.24%
Slugging	Pressure gradient range	48.87	10.73
	RSD	25.4%	5.3%
Bubbling FB	Pressure gradient range	14.83	no data
	RSD	9.7%	no data

Packed moving bed regime

The moving bed operation only shows minor fluctuations, especially in downcomer 1, where the pressure taps are closer together.

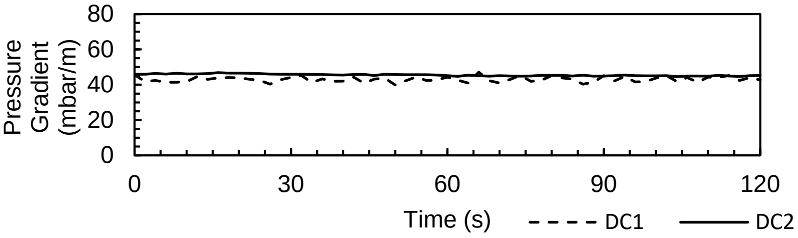

Fig. 3: Pressure signal for the moving bed

Slugging regime

In the slugging regime the Downcomers show significant pressure fluctuations around the mean value.

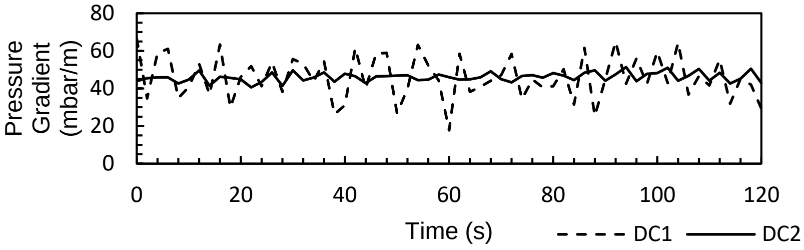

Fig. 4: Pressure signal for the slugging regime

Bubbling fluidized bed regime

Bubbles which do not cover the entire cross section do not inhibit solids transport as significantly as slugs.

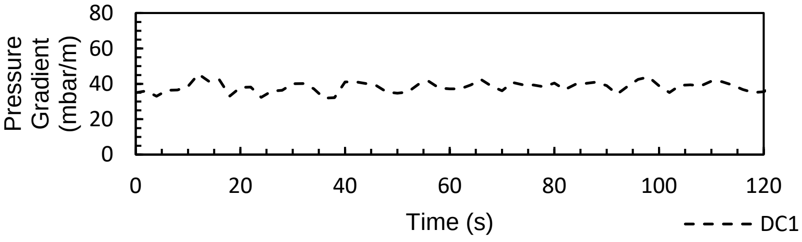

Fig. 5: Pressure signal for the bubbling fluidized downcomer

Conclusions

The results for the operation of this multistage fluidized bed column with internal downcomers in absence of the external aeration have shown that only a small window of moving bed operation is achievable. SCR and the fluidization rate are strongly linked, an aspect which is challenging for the operation of a hot unit under dynamically changing conditions (load, SCR, gas flow rate). Especially with regard to process automation, it is desirable to have a wide operating window where stable automation is possible and flooding does not occur, because the flooding of a hot unit can cause unnecessary down time. External aeration, however, has proven to be a viable option for retrofitting existing columns as well as for future columns. The operating window has shown to widen significantly while the maximum possible solids circulation rate has also increased by 20 %. Looking at, e.g., fluidized loop seals or fluidized downcomers, the filling levels will set according to the governing pressure conditions of the column, yet this is not the case for a moving bed downcomer. It is assumed that the moving bed operating regime is maintained if the pressure gradient is well below the pressure gradient of the fluidized bed. From there, we conclude that the filling level of the downcomer is the critical quantity for moving bed operation. Having a high enough filling level ensures that the downcomer can equalize the pressure drop between the two connected stages and inhibit the bypassing of gas by the formation of slugs. As a design criterion for potential applications of internal downcomers between fluidized bed stages, we recommend a decoupling of fluidization rate for the column and transport rate to be necessary in order to provide enough flexibility for real world applications such as a TSA carbon capture process. This can be reached, for instance, by actively controlling the fluidization of the downcomer area, similar to an approximated J-Valve, or a mechanical valve in each downcomer. In many cases, moving parts are undesirable, since they increase maintenance costs and down time of a plant. We therefore recommend further research into aspects of downcomer geometry (e.g., downcomer length, cross section, gap height between downcomer and stage etc.). In addition to the external aeration, a measurement of the pressure signal in the downcomer can improve the operability of a multistage fluidized bed column. As slugging is detected in a downcomer, the external aeration can be switched off in order to reduce the amount of gas in the downcomer making it possible to regain control over the process.

Notation

RSD	relative standard deviation, -	Δp_{Sn}	pressure drop in stage n, mbar
SCR	solids circulation rate, kg h^{-1}	Δp_{Sn+1}	pressure drop in stage n+1, mbar
Δp_{DCn}	pressure drop downcomer n, mbar	h_{DC}	filling level of downcomer n, m

References

Chen, C., Y. Yang, Z. Huang, J. Sun, J. Wang, Y. Yang. Investigation of particle flow behaviors in a simplified downcomer of multistage fluidized bed, Powder Technology 2020. 375, 292 - 301

Eleftheriades, CM, MR Judd. The Design of Downcomers Joining Gas-Fluidized Beds in Multistage Systems, Powder Technology 1978. 21, 215 - 225

Kunii, D., O. Levenspiel. Fluidization Engineering - Second Edition, Butterworth, Boston 1991,

Lv, X., Y. Zhang, L. Li, W. Zhang, P. Liang. Experimental study of ethanol adsorption using a multistage bubbling fluidized bed, Process Safety and Environmental Protection 2019.

Pröll, T., G. Schöny, G. Sprachmann, H. Hofbauer. Introduction and evaluation of a double loop staged fluidized bed system for post-combustion Co2 capture using solid sorbents in a continuous temperature swing adsorption process. Chemical Engineering Science 2016. 141, 166-174

Zehetner, E., G. Schöny, J. Fuchs, T. Pröll, H. Hofbauer. Fluid-dynamic study on a multistage fluidized bed column for continuous CO_2 capture via temperature swing adsorption. Powder Technology 2017. 316, 528-534

DYNAMIC MODELING OF THE FLUE GAS SIDE OF LARGE-SCALE CIRCULATING FLUIDIZED BED BOILERS

Guillermo Martinez Castilla*, Rubén M. Montañés, David Pallarès, Filip Johnsson

Chalmers University of Technology, Division of Energy Technology, Hörsalsvägen 7B, Gothenburg, 412 96, Sweden

*Email: *castilla@chalmers.se*

Abstract

This paper presents a 1.5D dynamic model of the gas side of large-scale circulating fluidized bed boilers. The model accounts for the solid's hydrodynamics, the fuel conversion and the heat transfer to the waterwalls. The model is validated with industrial data from an 80 MW unit, showing a good agreement between simulation results and measured data. The validated model is used to study the dynamics of the furnace after a load change is introduced. Simulation results show that regions with large concentration of solids are slower to reach steady-state but are less sensitive to load changes.

Introduction

Modeling of circulating fluidized bed (CFB) combustors has been a topic covered by many researchers since the beginning of the technology development, largely driven by the understanding of the combustion process and the generation of pollutants. Simulating the operation of the boiler constitutes a complementary cost-efficient strategy to develop the technology compared to costly approaches based exclusively on empirical testing. According to the review by Basu (1999), there are three levels of models when it comes to predict the behavior of CFB boilers: Level I represents 1D models that assume the entire boiler to behave as either a stirred tank (CSTR) or a plug flow reactor (PFR). Level II models, also called core-annulus models or 1.5D models, split the boiler into two regions in order to capture the internal recirculation of solids and, to some extent, their lateral distribution. Models belonging to Level III describe the combustion process through the Navier-Stokes equation solving a detailed 3D description of the boiler.

Dynamic modeling and simulation represent essential tools for the design of energy conversion units and can be used to study the influence of different process configurations. Dynamic simulations can predict the transient response of the combustor under varying conditions, which can be used for tuning and testing of control strategies and for training plant operators. Furthermore, dynamic models of the combustion side can be integrated into dynamic models of the steam cycle so that the interactions between the flue gas side and the water-steam side can be investigated. Dynamic modeling of power plants acquires special importance when the combustion facilities are subjected to changes due to their integration into markets with increasing penetration of renewables or large variations in heat demand.

Compared to steady-state models of CFB boilers, there is considerably less work published regarding dynamic modeling and simulation. Some works focus on the dynamics of the combustion process itself, e.g., the work by Saastamoinen et al. (2007) predicting the residence times of solids and the char inventory over time. Park and Basu (1997) predicted the char and oxygen concentrations derived from a fuel shift, which was validated against a 0.3 MW_{th} unit. A similar study was carried out in the model presented by Chen and Xiaolong (2006), in which a 410 t/h pyroflow unit was modeled. Several dynamic models have aimed at developing control structures, e.g., Zimmerman et al. (2018), who built up a dynamic model of a CFB waste boiler and concluded that model predictive control showed better performance than PI control.

The aim of this work is to present a dynamic model of the flue gas side of large-scale CFB boilers. The model is general in that the boiler geometry is an input, different fuel types can be introduced, and the empirical expressions used have been derived through the combination of underlying fundamental theory and measurements in several large-scale boilers of different sizes. The model, implemented in Modelica, differentiates between core and annulus regions in the freeboard (i.e. belongs to the Level II according to the classification by Basu (1999)). After validation with operational data from an 80 MW_{th} unit, the model is here applied to predict the transient responses of the main process variables when the boiler load is changed.

Model Description

The model presented in this paper divides the CFB loop into three main parts (represented as red frames in Fig. 1): the furnace, the cyclone and the loop seal. Each of these contains interconnected control volumes. All the control volumes have been modeled as stirred tank reactors (represented as black cells in Fig. 1). Note that the regions known to exhibit a plug flow behavior such as the upper freeboard and the gas flow in the dense bed are modeled as a consecution of N perfectly mixed control volumes.

Dynamic energy and mass balances have been formulated in each of the control volumes for the three phases considered: bulk solids (consisting of a single size class), fuel (containing f conversion classes) and gas (containing g gas species). Fig. 1 also shows the process variables calculated in cell: concentrations of bulk solids (C_s), of each fuel class (C_f) and of each gas species (C_g), and temperatures (T). Note that the wall layers are assumed to contain no gas and therefore only concentrations of solids are computed. The volumes are connected to each other exchanging mass of the three different phases, in the form of three flow variables: fuel mass flow F_f, bulk solids mass flow F_s and gas mass flow F_g. The bulk solids feed into the system as well as the purge of inert solids have been neglected.

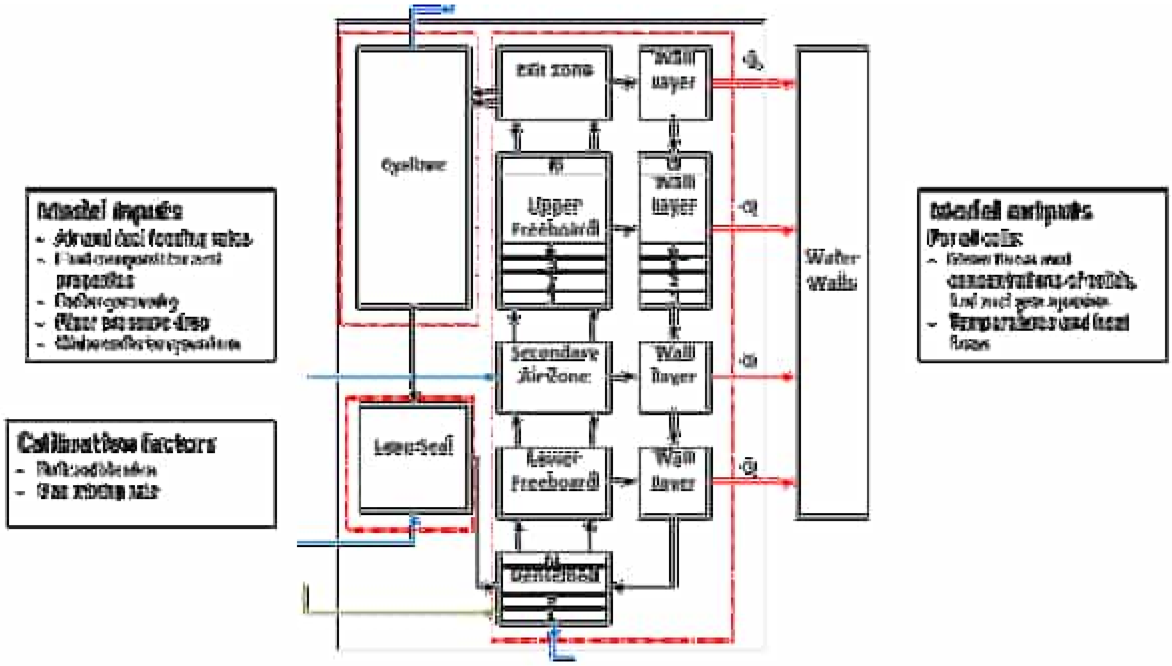

Fig. 1. Schematic diagram of the model (dotted purple line) with cyclone, loop seal and furnace marked with red dots and the control volumes represented with solid line rectangles. The fuel feed is indicated with a green arrow and air inlets with blue arrows. The figure also lists the main inputs and outputs of the model as well as the calibration factors.

The hydrodynamics of the solids phase have been described according to the work by Johnsson and Leckner (1995), complemented with expressions for the solids entrainment from the dense bed as a function of the gas velocity and solids terminal velocity derived from data from (Djerf et al. 2020) the solids net transfer from the core region to the wall layers from Djerf (2020) and the backflow effect at the furnace exit from Djerf et al. (2020).

Regarding the fuel phase, the drying and devolatilization rates are described by a time constant correlated to the fuel particle size. The remaining char is divided into three different conversion classes to account for varying density and size as conversion occurs, which has an impact on the hydrodynamics of the fuel phase.

Nine gas species have been considered: H_2, O_2, CO, CO_2, H_2, H_2O, NH_3, H_2S and heavy hydrocarbons (tar). The model here presented considers three homogeneous reactions (oxidation of carbon monoxide, hydrogen and tar) and one heterogeneous (oxidation of char). The kinetic rates used are taken from Flagan and Seinfeld (1988) and Dryer and Westbrook (1981). The waterwalls are considered as a boundary with given constant temperature, T_w. The wall-layer cells exchange heat with the waterwalls through both convection and radiation according to Eq. (1), where A is the area of the water tubes and h_c is the heat exchange coefficient suggested by Breitholtz et al. (2001) and ε is the emissivity accounting for both the suspension and wall. The net radiative heat exchange between the core region and the waterwalls is accounted through a radiation efficiency coefficient, η_{rad}, according to Breitholtz et al. (2001), which turns radiation into the dominant heat extraction mechanism in the upper furnace.

$$Q_{wall} = h_c \cdot A \cdot (T_{wl} - T_w) + \eta_{rad} \cdot \varepsilon \cdot A \cdot \sigma \cdot (T_c^4 - T_w^4) \tag{1}$$

Model Validation

The model presented here has been validated with operational data from an 80 MW CFB boiler run by Karlstads Energi (Sweden). The boiler has a furnace with dimensions 4.1 x 8.5 x 21 m, two cyclones of 77.5 m^3 each, and a projected area of water tubes of 425 m^2 starting at a height of 5 m from the bottom of the furnace. A steam superheater (SH) is located in the furnace, 11 m above the bottom grid.

A case at design load - 80 MW - has been chosen for validation of the steady-state. The air volume flow into the boiler is 30.6 Nm^3/s, out of which 44% is fed as primary air (corresponding to a superficial velocity of 4.8 m/s), 49% as secondary air and 7% is used to fluidize the loop seal. At design load, the steam-water mixture inside the water tubes has a temperature of 292°C, which is assumed to be the constant wall temperature. The superheater (accounted in the model as heat sink constant at all loads) extracts 2.4 MW. The fuel consists of a mixture of several biomass types which varies frequently in composition. In order to validate the model, a conventional proximate and ultimate analysis of wood chips has been taken from Miles et al. (1995), shown in Table 1, with the average moisture fraction of the reference case (54%).

Table 1. Proximate and ultimate analysis utilized to run the model for validation

Proximate Analysis	Mass fraction (%)
Moisture	54.00
Volatiles	32.00
Char	13.60
Ash	0.40
Ultimate Analysis	
C	50.60
H	5.90
O	43.20
N	0.08
S	0.04

The results from the simulated dynamic model for the design load case are listed in Table 2, where the main process variables of the model are compared with operational data from the reference plant. The industrial data values are averaged over one hour of operation. Deviations between simulated and measured values arise from both errors related to measuring accuracy and to modeling uncertainty. Table 2 shows that all deviations are below 10% with an average error of 3%.

Table 2. Comparison of measured and modeled values of main process variables

Variable	Unit	Reference plant	Model	Deviation
Solids inventory in lower bed	kg	19200	20600	7.3 %
Solids inventory in upper bed	kg	6400	5900	8.9 %
Temperature dense bed	˚C	798	797	1 ˚C
Temperature lower freeboard	˚C	844	830	14 ˚C
Temperature secondary air injection	˚C	834	825	9 ˚C
Temperature close to SH	˚C	839	840	1 ˚C
Temperature at riser exit	˚C	862	860	2 ˚C
Temperature exit of the cyclone	˚C	880	878	2 ˚C
O_2 in exhaust gas	$\%_{vol}$	2.0	2.1	0.1 %-units
CO_2 in exhaust gas	$\%_{vol}$	16.3	15.7	0.6 %-units
H_2O in exhaust gas	$\%_{vol}$	33.5	32.0	1.5 %-units
Heat transferred to furnace walls	MW	45.0	46.9	4.2%

(1) Dynamic Simulations

The model presented in this work is applied to simulate a load reduction from 100% to 75%. In order to be consistent with the operational strategy of the reference power plant, the load changes are modeled as simultaneous decreases in mass flows of fed air and fuel, keeping the air-to-fuel ratio constant at all times. The open-loop (uncontrolled) response of the system is studied by applying load changes in the form of steps and measuring the stabilization time, t_S (the time it takes for a certain variable to be within a ±10% of the new steady-state value after the step is introduced) of the main process variables. The process variables of interest whose responses are tracked are: the dense bed temperature, T_{db}, the furnace exit temperature, T_{exit}, and the heat transferred to the waterwalls, Q_{wall}.

(2) Results and Discussion

The resulting trajectories of the main process variables when a step-down in load at t=0 is introduced are plotted in Fig. 2. The stabilization times of each variable are listed in Table 3.

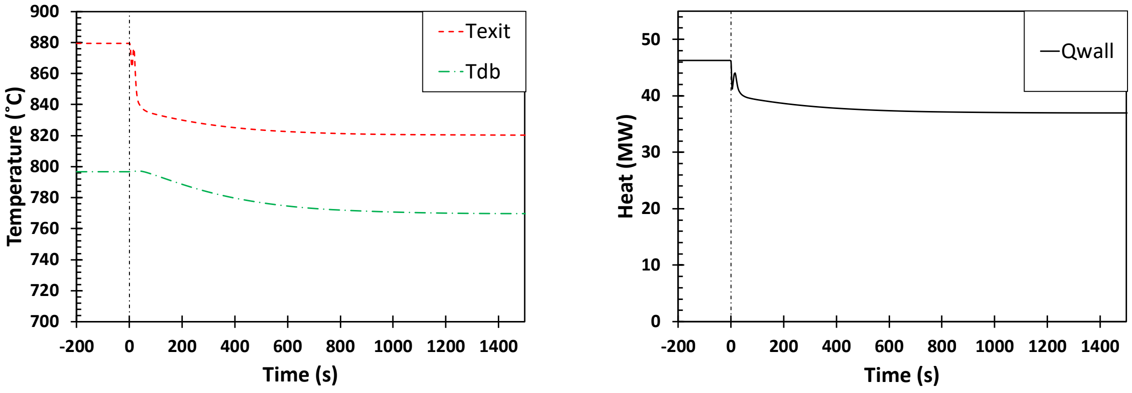

a) Temperatures in the dense bed and exit zone

b) Heat transferred to the waterwalls

Fig. 2. Transient responses of the relevant process variables after a 25% load reduction step change is introduced at t=0 (represented with dotted black line).

Table 3. Stabilization times (time to reach the new steady-state value within a range of ±10%) of the relevant process variables when a 25% load step-down is introduced

Variable	T_{db}	T_{exit}	Q_{wall}
ts (s)	772	360	376

It can be observed that the temperatures (Fig.2.a) in the dense bed and exit region of the furnace drop when the load change is introduced. In the case of the dense bed, the transient towards the new steady-state follows a smooth trajectory in contrast with the abrupt variations observed in the exit zone. Such behavior in the furnace exit is caused by sudden variations in the solid flows when the air velocity is step-changed. The solid flows are found to stabilize after the first 30s of the transient response. Subsequently, the exit region temperature follows a smooth evolution towards its new steady-state. As expected, these trajectories are directly reflected on Q_{wall} (see Fig.2.b), which is first affected by the variations in solid flows and once those stabilize the radiation from the core becomes the driving mechanism. Another interesting aspect that can be extracted from Fig. 2a is the fact that the dense bed temperature presents a smaller relative change between 100% and 80% load than the temperature in the exit region. The reason behind this observation is the difference in heat capacities between the regions, being larger in the bottom of the furnace.

Finally, the stabilization times shown in Table 3 point at the temperature in the dense bed as the variable with the largest stabilization time, also caused by the large heat capacity due to the high concentration of solids. In contrast, the top of the furnace reaches the new steady-state approximately 400 s faster than the bottom region because of its lower inventory of solids and thus lower heat capacity. The heat transfer to the waterwalls stabilizes after 376 s being a direct function of the furnace temperature.

Conclusions

A dynamic 1.5D model of the flue-gas side of large-scale CFB combustors has been presented. The model is built as a combination of tank reactors exchanging mass and energy and can be parametrized for different boiler geometries, fuels and operational parameters. The model incorporates dynamic energy and mass balances of the gas phase, inert solids and fuel phase. The model is successfully validated using data measured in an 80 MW_{th} unit.

The model is applied to investigate the dynamic response of the system when the load is decreased 25% as a step change. Results show the different dynamic behavior of the temperatures depending on the region, being the temperature at the bottom the slowest to reach stabilization. Abrupt responses are observed for some seconds in the temperatures at the top of the furnace, which is also reflected on the heat transferred to the waterwalls. Simulation results show that the temperature changes largely between loads in the regions with lower heat capacity, i.e. the exit zone. Due to its high concentration of solids, the dense bed temperature remains more constant across different load levels.

Future work includes validation of the model for a wider range of load conditions as well as validation of the transients. Further applications of the model range from investigating the sensitivity of the responses to the solids inventory in the system, to the study of the dynamics of the boiler when transient conditions other than load changes occur, such as variations in fuel composition or moisture content.

Notation

Q_{wall}	heat transferred to the waterwalls, MW
T	temperature, ˚C
t	time, s
C_s	solids concentration, kg/m^3
C_f	fuel concentration, kg/m^3
C_g	gas concentration/density kg/m^3

F	mass flow, kg/s
h_c	convective heat transfer coefficient, W/m^2K
ε	emissivity
σ	Steffan-Boltzman´s constant, W/m^2K^4
A	heat transfer area, m^2
η_{rad}	radiation efficiency

References

Basu, P. 1999. “Combustion of Coal in Circulating Fluidized-Bed Boilers: A Review.” *Chemical Engineering Science* 54(22):5547–57.

Breitholtz, C., B. Leckner, and A. P. Baskakov. 2001. “Wall Average Heat Transfer in CFB Boilers.” *Powder Technology* 120(1–2):41–48.

Chen, Yang and Gou Xiaolong. 2006. “Dynamic Modeling and Simulation of a 410 t/h Pyroflow CFB Boiler.” *Computers and Chemical Engineering* 31(1):21–31.

Djerf, Tove. 2020. “Solids Flows in Circulating Fluidized Beds : Explorations of Phenomena with Applications to Boilers.” Chalmers University of Technology.

Djerf, Tove, David Pallarès, and Filip Johnsson. 2020. “Solids Flow Patterns in Large-Scale Circulating Fluidised Bed Boilers: Experimental Evaluation under Fluid-Dynamically down-Scaled Conditions.” *Chemical Engineering Science* 231:116309.

Dryer, Frederick L. and Charles K. Westbrook. 1981. “Simplified Reaction Mechanisms for the Oxidation of Hydrocarbon Fuels in Flames.” *Combustion Science and Technology* 27(1–2):31–43.

Flagan;Seinfeld. 1988. *Fundamentals of Air Pollution Engineering*. Prentice Hall.

Johnsson, Filip and B. Leckner. 1995. “Vertical Distribution of Solids in a CFB-Furnace.” P. 719 in *13th International conference on fluidized-bed combustion*. Orlando.

Miles, T. R., T. R. Jr; Miles, L. .. Baxter, R. Bryers, B. .. Jenkins, and L. Oden. 1995. “Alkali Deposits Found in Biomass Power Plants: A Preliminary Investigation of Their Extent and Nature.” *National Renewable Energy Laboratory*.

Park, C. K. and P. Basu. 1997. “A Model for Prediction of Transient Response to the Change of Fuel Feed Rate to a Circulating Fluidized Bed Boiler Furnace.” *Chemical Engineering Science* 52(20):3499–3509.

Saastamoinen, Jaakko. 2007. “Modelling of Dynamics of Combustion of Biomass in Fluidized Beds.” *Thermal Science* 8(2):107–26.

Zimmerman, Nathan, Konstantinos Kyprianidis, and Carl-Fredrik Lindberg. 2018. “Waste Fuel Combustion: Dynamic Modeling and Control.” *Processes* 6(11):222.

CHARACTERISTICS ON SOUND PROPAGATION IN PACKED BEDS

Yanqin Li[1*], Xuefeng Guan[1], Linghao Xie[1,2], Hailiang Cao[1], Junjie Zhou[1*]

[1] *School of Mechanical and Power Engineering, Zhengzhou University, 100 Kexue Rd Zhengzhou, 450001, P. R. China*

[2] *Department of Physics, Zhejiang University, 38 Zheda Rd, Hangzhou, 310027, China*

*Email: liyq@zzu.edu.cn; zhoujj@zzu.edu.cn

Fund: NSFC, No. 51676175

Abstract

The propagation characteristics of sound waves in a particle-packed bed, in fluidization etc., are not fully clear yet for acoustic monitoring. The acoustic measurement is expected to detect the key parameters such as porosity and information of particle size in the bed. This work discusses the propagation characteristics of sound waves in a particle-packed bed, such as the propagation speed, attenuation, and scattering. A phantom configuration was modeled to simulate the propagation of sound waves in a packed bed. The influence of the sound frequency on the propagation in the bed with certain uniform size was studied, with which an index of the ratio of particle size to acoustic wave number was introduced to define a critical acoustic frequency. When its value is over 1, the sound would be too much attenuated to advance in the bed. It turned out that with increasing the frequency the attenuation increases, while the sound speed in the bed decreases. The results were validated with experiments.

Introduction

The characteristics of sound propagation in a gas-solid phase is interesting and fundamental for related research and applications. Sewell (1910) studied the sound attenuation caused by static rigid particles in a viscous fluid. Further, Lamb (1945) dealt with the sound attenuation related to non-static rigid particles in viscous fluid. And based on that, Urick (1948) modified the attenuation formula proposed by Lamb, under the condition $k \cdot r < 1$. However, Lamb (1945) and Urick (1948) both stated their theories only worked when the volumetric fraction of the particle dispersion is quite small. Once the concentration of particle phase approach 0.1 or higher, related experiment results would deviate remarkably from the theoretical values.

In a later research, Allega and Hawley (1972) combined conservation equations of energy, momentum, and mass, to develop a relative integral formula on sound absorption coefficient which considered the effect of heat conductivity, viscosity, and scattering of particles. Relevantly, Sheng and Hay (1988) proposed an expression of calculating the attenuation coefficient by particle scattering, commonly applied up to now.

Regarding the sound propagation speed in the two phase flow with particle dispersion, there have been also certain researches. Bi *et al*. (1995) and Harris *et al*. (1994) investigated the particle dispersion related pressure wave propagating in fluidized beds, which is of a low frequency of ~10Hz. Roy *et al*. (1990) gave a sound velocity formula for wave propagation in a dense bed. These studies made one assumption that the particles and gas move together (i.e., homogenous). Khawaja *et al*. (2011) and Khawaja (2018) further studied the sound wave propagation in the fluidized bed with CFD-DEM simulation, so that verified the conclusions in the former literature, but made an improvement to consider the slide between the particles and gas. However, the present literature all did not consider relationship of the sound frequency relative to the size of particles. Yet, for the acoustic measurement of the fluidization, such a factor does matter in a remarkable way.

Relevantly, studies on sound propagation in porous media were also performed, which resembles sound waves in fixed beds. However, in porous media, pores totally are not connected thoroughly as in fixed beds. Thus, the sound propagation characteristics would distinguish between the two applications to some extent. Typical works were carried out by Ramakrishnan (1994) and Horoshenkov *et al*. (2016).

In view of such a background, this paper studied the propagation characteristics of sound in a packed bed. For that, we discussed the sound speed and attenuation with varying sound frequency relative to certain particle size and piling structure.

Principle

The sound wave propagation in a fluidized or fixed bed is a nonlinear behaviour, being a complex coupling between characteristics of propagation in gas and solid respectively.

(1) Sound Speed

The sound speeds in a solid and a gas medium are formulated as

$$a=\sqrt{\frac{E}{\rho_s}},\ \text{and}\ c=\sqrt{\frac{dp}{d\rho_g}} \tag{1}$$

respectively. Where, *E* is the elastic modulus of the solid, and *p* is the acoustic pressure in the gas. ρ_s and ρ_g denote the densities of the solid and gas, respectively. And for the ideal gas, the sound speed is $c\approx\sqrt{\frac{\gamma p_0}{\rho_0}}$, where p_0 and ρ_0 are the sound pressure and density in a static gas, respectively.

This paper is focused on the sound propagation in a fixed gas-solid bed. So the sound speed formula, as shown in Eq. (2) that was proposed by Roy *et al*. (1990), approximated in a homogeneous two-phase flow does not fit.

$$c_s=\sqrt{\frac{\rho_g R T_g}{\varepsilon(\rho_s(1-\varepsilon)+\rho_g\varepsilon)}} \tag{2}$$

Where T_g is the gas temperature, and ε the porosity of the gas-solid bed, *R* the specific gas constant. Relevantly, the sound propagation in a fluidized-bed medium is expected to be modeled with Eqs. (3) and (4), proposed by Khawaja (2013), which considers the slips between the particles and the gas phase.

$$c_s=\frac{p_0}{(1-\varepsilon)\rho_s U_{s0}} \tag{3}$$

$$\tau=\frac{4h^2\rho_s}{\pi\mu_p} \tag{4}$$

Where p_0 and U_{s0} are the initial amplitudes of the pressure and particle velocity fluctuations, and *h* is the height of the fluidized medium in the bed, μ_p the effective particle viscosity. The damping time τ depicts the damping of sound in the fluidized bed resulting from particle viscosity. Nevertheless, this formulation may not be valid for fixed beds due to the static particles, instead the sound propagates similar to the propagation in a porous medium.

(2) Attenuation

The attenuation of sound in a fixed/fluidized bed mainly results from factors of two aspects. One is absorption of the gas and particle media respectively. Another is the scattering or refection by the particles in the bed medium. When the particle size is equivalent to wavelength of the sound, enormous scattering happens. And with increasing the sound frequency, sound reflection becomes more and more dominant. At the scattering and reflection regimes, the sound waves can hardly penetrate the particle packed medium. This implies that, with respect to acoustic measurement in such packed medium, the measurement sound frequency should be smaller than a threshold value to avoid too much scattering and reflection effect of sound waves by the particles.

Results and Analysis

To clarify the characteristics of sound propagation in a packed bed, related simulation study was carried out by modeling with a FEM method. And to have a validation, a preliminary experiment was performed.

Air at a temperature of 20℃, and a pressure of 1atm, was used as the fluid medium, with which sound speed c_0 is ~343m/s. Packed particles were solid balls with a radius r = 0.01m, a density of 4000kg/m^3, and a sound speed of 2000 m/s. The material took after applications in an iron shaft furnace, as an illustration of a generalized packed bed. The geometry used a form of cubic with dimensions: 0.2×0.2×0.6m^3. Simulations gave accordant results between boundary condition of hard wall and that of a periodical setting. This shows, fundamentally, such a geometry is able to simulate scenarios of large scales.

Grid independence was tested to achieve a computation mesh fine enough. On the other hand, computation boundaries, expect the one as the plane wave sound source, were set acoustic hard boundary. This was to simulate a circumstance agreeable to the experiment.

(1) Sound Propagation in a Bed with Cubically structured Packing

At first, a simple cubic packing structure between particles was adopted for the simulation, as shown in Fig. 1(a). For reduction of computation, just a quarter of the symmetrical setup geometry was taken. The sound frequency for this scenario was 5kHz. The pressure along the axis, with air medium in which region, is displayed in Fig. 1(b).

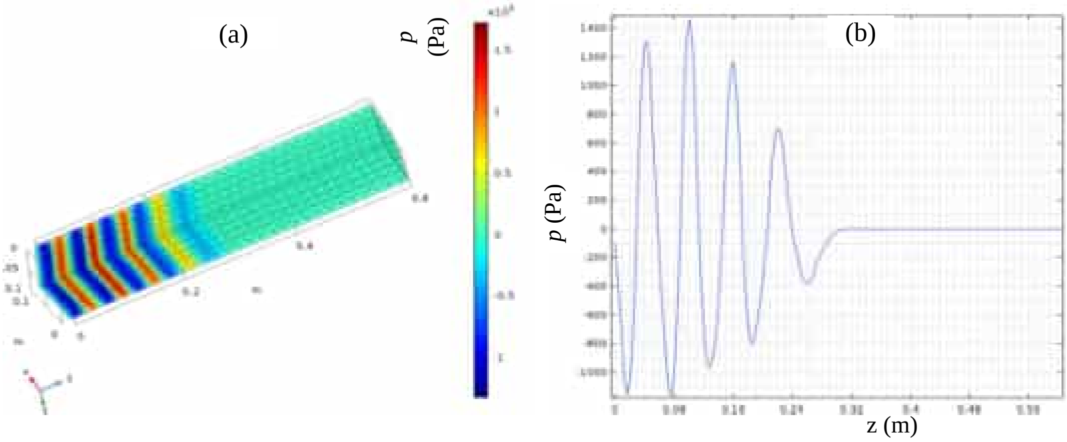

Fig. 1. The pressure distribution in the packed bed, (a), and that along the axis, (b), at 0.001s.

Correspondingly, the sound speed in the packed medium is calculated c_s = 300m/s, which is smaller than that in related pure air as above.

A comparison between different sound frequencies was made to figure out the influence of the frequency to the sound propagation. For a better presentation, the length of the cubic is prolonged to be 2m, with other conditions similar to the previous. The results are given in Fig. 2. Wherein, the images are all snapshot at a time 0.005s instead.

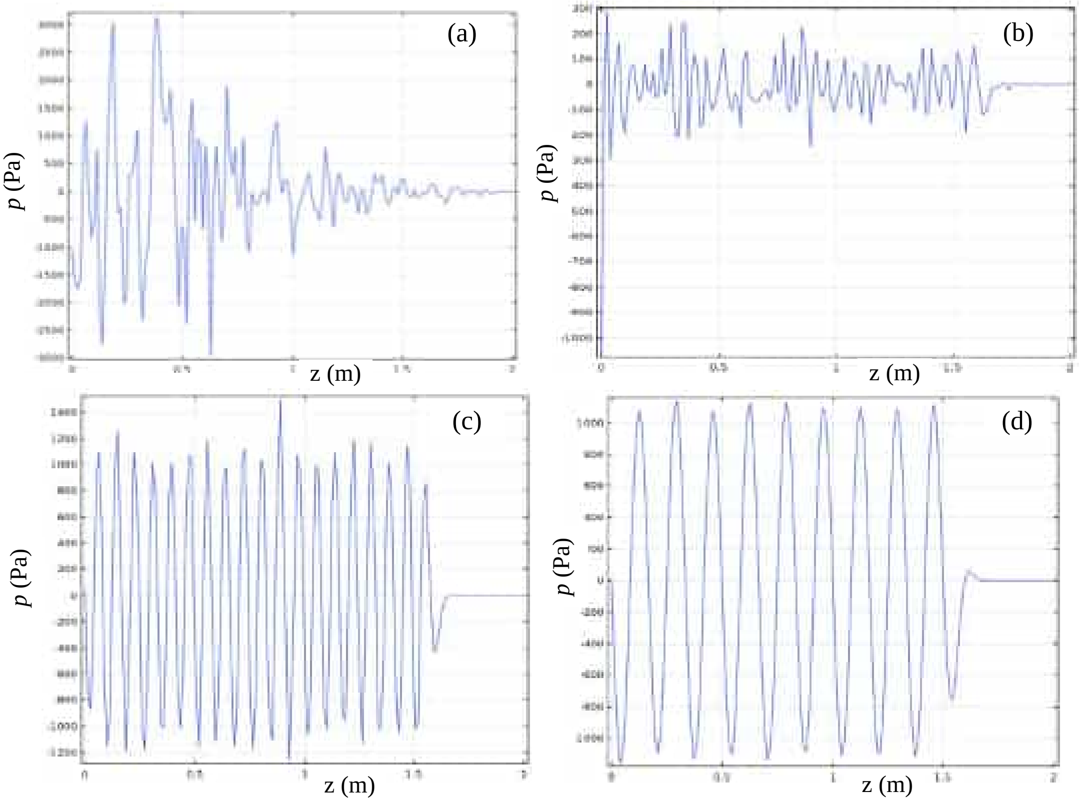

Fig. 2. Sound pressure along the axis for the prolonged geometry relative to Fig. 1, with different frequency: (a) 15kHz, (b) 8kHz, (c) 4kHz, and (d) 2kHz.

It can be seen that, for the same particle parameters, different sound frequencies give similar propagation distance at a similar time. This means that sound waves of different frequencies propagating in the cubic packed medium has a consistent speed, which is calculated ~ 333.3m/s. Note that such a result is for the fixed bed, i.e. particles keep static, comparing to reported models given in the principle section. Nevertheless, the sound speed is distinct to that with a shorter geometry as shown in Fig. 1. This is presumably resulted from the hard end boundary, now that there is only one difference between the two scenarios and further numerical studies showed that length of the packed bed along the z-axis has almost no effect on the sound speed with the end not set as hard boundary.

The result from Fig. 2 shows that at certain larger frequencies, the sound waves appear distorted and attenuate rapidly. More computations with different sound frequencies show that a value ~6kHz can be regarded as such a threshold, f_c, beyond which the sound will distort and attenuate enormously. As such, a characteristic index of a relative particle size, R_c, is defined in this paper to describe the critical frequency, f_c, as Eq. (5)

$$R_c = \frac{2\pi f_c}{c_0} r = \frac{2\pi \times 5500\text{Hz}}{343\text{m/s}} \times 0.01\text{m} \approx 1.0075 \approx 1 \qquad (5)$$

For further confirmation, another configuration of the packed bed was also studied. Relatively, the cubic was set 0.24×0.24×2m^3, and radius of the particles was 0.02m, with other parameters remaining the same. It turned out that such a configuration also gave a similar value of $R_c \approx 1$.

The result shows the index R_c can be taken as the criterion of the relative variation between the particle size and the acoustic frequency. Wherein, *r* can be extended to an equivalent radius of an arbitrarily shaped particle. When $R_c > 1$, i.e. $f > f_c$, the sound would be scattered to attenuate too severely by the particles to advance in the medium.

(2) Influence of Packing Structure and Experiment

Effects of packing structure of particles were studied, and showed interesting results. As stated above, the preceding cases cubically arrange particles with straight through tunnels formed, as shown in Fig. 1(a). With such a defined configuration, the sound speed did not vary with the change of the sound frequency, within the studied frequency scope. Moreover, as shown in Fig. 2, attenuation revealed little changes with the frequency beyond f_c as well.

But comparatively, the result by a packing structure of interlacing particle layers to each other gave a much different conclusion. It turned out that with increasing of frequency, the sound attenuation shows clear increase, while the sound speed decreases. As an illustration, with *r* = 0.01 m, the sound speeds at the frequency of 5 kHz and 10k Hz are computed as 285.66 m/s and 279.35 m/s, respectively. And the attenuation at the latter frequency appears larger correspondingly.

The above conclusion for packing of interlacing layered particles was validated with experiments on a lab-scale fixed bed. A PVC cylinder of ϕ 0.16 m × 0.13 m was taken as the bed container. Spherical glass particles of a uniform radius *r* = 0.007 m act as the bed material, with density 2,500 kg/m^3 and sound speed 3,962 m/s. The sound propagation in the bed was measured for characteristics of the sound speed and attenuation etc. Different sound frequencies were dealt with to validate related conclusions discussed above. Related results see Fig. 3. And simulations with a similar configuration, distinguishing from above, were performed for comparison.

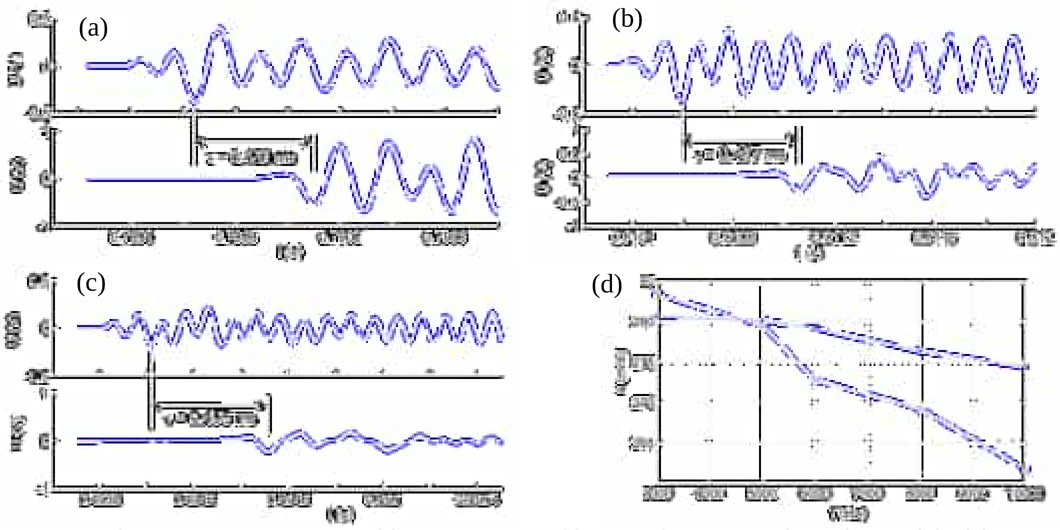

Fig. 3. Experimental results on packing structure of interlacing layered particles. (a)~(c) Acoustic signals at the two ends of the bed, respectively, with sound propagating from the upper end to the lower, and at frequencies of 6, 8, and 10 kHz respectively. The vertical axis, *U*, denotes signal voltage measured. (d) Sound speed at different frequencies, with dot markers for the simulation results and circle markers the experimental results.

In terms of Eq. (5), the critical sound frequency regarding the experimental configuration was calculated as ~7.9kHz beyond which the sound attenuates quickly in the packed medium. It was satisfactorily validated by the experiment as shown in Fig. 3(a)~(c). Note that, since the two acoustic sensors used had different gains, their signal magnitudes were not comparable. Fig. 3(d) gives the comparison between the experiment results and the related simulations, which reveals similar descending trends in between with increasing of frequency. However, the sound speed by simulation shows much slower descending, presumably due to both the not-exact-enough modeling, settings of the simulations, and errors from the measurement.

The conclusion drawn is expected to provide a theoretical reference to the acoustic monitoring for fluidized beds, or related applications, e.g. the gas flow distribution with material inventory in a blast furnace.

Conclusion

Sound propagation in packed media shows complex characteristics. For a generally interlaced packed particle medium with defined configuration, the sound speed would decrease with increasing of the sound frequency, whereas the attenuation would increase. Furthermore, when the frequency get larger than a critical value, the waves will be enormously distorted and attenuated.

Notation

f, f_c	sound frequency and the critical frequency, Hz
$k = 2\pi / \lambda$	angular wave number
ρ_s, ρ_g	solid and gas density respectively, kg/m^3
R_c	index for critical sound frequency, 1
c_0, c_s	sound speed in free air and packed medium, respectively, m/s
μ_p	particle viscosity, Pa·s
r	radius of the particle
ε	porosity of the bed
λ	wave length, m
t, τ	time and flight time, s
E	elastic modulus of solid, Pa

References

Sewell CT. The extinction of sound in a viscous atmosphere by small obstacles of cylindrical and spherical form. Philosophical Transactions of the Royal Society of London, 1910, 210(566): 239-270

Lamb H. Hydrodynamics. Cambridge: Cambridge Univesity Press, 1945

Urick RJ. The absorption of sound in suspensions of irregular particles. The Journal of the Acoustical Society of America, 1948, 20: 283-289

Allegra JR, SA Hawley. Attenuation of Sound in Suspensions and Emulsions:Theory and Experiments.The Journal of the Acoustical Society of America,1972, 51(5B): 1545-1564

Sheng J., AE Hay. An examination of the spherical scatterer approximation in aqueous suspensions of sand. The Journal of the Acoustical Society of America,1988, 83(2): 598-610

Bi, HT, JR Grace, J Zhu. Propagation of pressure waves and forced oscillations in gas–solid fluidized beds and their influence on diagnostics of local hydrodynamics. Powder Technology, 1995, 82(3), 239–253

Harris, SE, DG Crighton. Solitons, solitary waves, and voidage disturbances in gas-fluidized beds. Journal of Fluid Mechanics, 1994, 266, 243–276

Roy, R, JF Davidson, VG Tuponogov. The velocity of sound in fluidised beds. Chemical Engineering Science, 1990, 45(11), 3233–3245.

Khawaja, H., S Scott. CFD–DEM simulation of propagation of sound waves in fluid particles fluidised medium. The International Journal of Multiphysics, 2011, 5(1), 47–60

Khawaja, H. CFD–DEM simulations of two phase flow in fluidised beds. Doctoral dissertation. Cambridge, UK: University of Cambridge, 2013

Khawaja H. Sound waves in fluidized bed using CFD–DEM simulations. Particuology. 2018, 38, 126-133

Ramakrishnan N. Speed of sound in porous materials. Bull. Mater. Sci. 1994. 17(5), 499-504

Horoshenkov KV, G-J Groby, O Dazel. Asymptotic limits of some models for sound propagation in porous media and the assignment of the pore characteristic lengths. J. Acoust. Soc. Am. 2016. 139 (5), 2463 – 2474

FLUIDIZATION OF BIDISPERSE MIXTURE

Harshal Gamit*, S. Srinivas, Manaswita Bose

Department of Energy Science & Engineering, Indian Institute of Technology Bombay,
Powai, Mumbai, Maharashtra 400076, India
*Email:*164170005@iitb.ac.in*

Abstract

The aim of the present work is to understand the minimum fluidization characteristic(s) of different bi-disperse mixtures with various initial configurations. Towards that goal, a laboratory scale cold bed with boro-silicate glass is fabricated. Bed pressure drop along with the physical state of the bed is monitored. Minimum fluidization condition is identified for different types of binary mixtures under various initial configurations. The experimental results show that the initial (u_{if}) and final minimum fluidization (u_{ff}) velocities strongly depend on the initial arrangement of the particles. Small bubbles start appearing in the bed before the entire bed is fluidized. However, there is a difference in the behaviour of the bed when the larger particles are initially configured to be at the top. The bed behaves like a slug immediately after the initial minimum fluidization. Layer inversion is observed following this and the bed is completely mixed when the final minimum fluidization velocity is reached.

Introduction

Fluidization is one of the most widely used unit operations in process industries. During fluidization, the solid particles get suspended in fluid media. Despite the large variation in the size distribution of the particles in actual industrial practice, most of the studies on fluidization are limited to monodisperse systems (Pan et al., 2016). Fluidization and segregation (Di Maio et al., 2012) of binary systems are also investigated in literature using experimental techniques (Brachia et al., 2017), phenomenological modelling (Girimonte et al., 2018), and detailed numerical analysis based on computational fluid mechanics coupled with discrete particle simulations (Tsuji et al., 2014). In a series of articles, Formisani and co-workers have analysed the fluidization of bidisperse system in a great detail (Formisani et al., 2008, Formisani et al., 2011, Formisani et al., 2012, Girimonte et al., 2018). They have proposed a unified model to determine the initial and final fluidization velocities for bidisperse systems (Formisani et al., 2008) and have shown that the fluidization behaviour of the bidisperse mixture depends on the initial configuration of the bed (Formisani et al., 2012). While Formisani and co-workers have used spherical particles of different size and density for performing their experiments, studies involving natural particles have been reported in the recent years. Fluidization and defluidization of biomass and sand particle mixture was investigated by Fotovat et al (2011). Segregation of biomass particles and glass beads in a fluidized bed was investigated by Di Renzo et al. (2015) who concluded that the segregation behaviour depends on the mixture composition. Brachia et al. (2017) investigated the fluidization and segregation behaviour of dried orange peel in different mixtures using alumina particles and quartz sand as the other components. Their studies showed that the bed particles undergo slug fluidization and the orange peel segregates at the bottom during the defluidization.

The objective of the present work is to investigate the fluidization - defluidization behaviour of a binary mixture of particles in a gas-solid fluidized bed and study the influence of the initial configuration on the fluidization behaviour. This includes visual inspection of the bed configuration at different stages of fluidization. To that end, a laboratory scale gas-solid fluidized bed is fabricated with boro-silicate glass. The details of the experimental set-up and the measurement method are discussed in the next section.

Experimental Setup & Methodology

Fig. 1a shows the schematic diagram of the experimental set up. The column is made of a boro-silicate glass pipe with internal diameter of 50 mm. The height of the column is 50 cm. The diameter of the column is chosen to be 100 times that of the larger particles used in the bed to avoid any wall effect on the fluidization behaviour. A dome-shaped outlet section is attached to the top of the column to avoid entrainment of fine solid particles along with the gas. Air is fed through a conical diffuser. The half-cone angle is 13°. A porous distributor plate is used to achieve uniform flow at the inlet of the bed. Air flow rate is measured using a rotameter calibrated by following the standard procedure. The line pressure is controlled with the help of bypass lines. There are three points to measure the pressure drop in the column, (a) across the distributor plate (Points A & B), (b) across the bed (Points B & C), (c) across the distributor plate and the bed (Points A & C). Pressure drop is measured using the pressure transmitter, 11D, Afriso DMU. Pressure drop in the bed is recorded using the data acquisition system (NI 9219). The physical state of the fluidized particles is captured using Nikon DSLR camera (D5200).

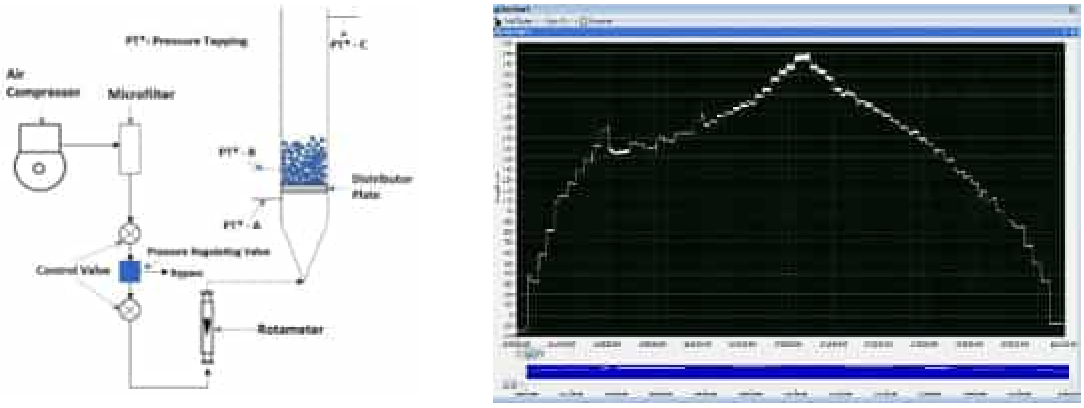

(a) (b)

Fig.1.(a) The experimental set-up; (b) Snapshot of the computer screen during the experimental run

Experiments are performed for binary mixtures of glass particles with different sizes (SMD of 196μm and 550μm). In all the experiments reported in the present work, the ratio of the particle diameter is maintained constant. Also, the total amount of the solid material used in the experiments is kept constant. The volume fraction (X_{FO}) of the constituent particles is varied. Table 1 summarizes the particle properties and all the parameters and configurations used for the current set of experiments, respectively. Experiments are performed for both fluidization and defluidization. Initially, the gas flow rate is slowly increased until the bed is completely fluidized. The air flow rate is then gradually reduced till the bed gets back to the packed state. The pressure drop across the bed is measured for each air flow rate. Signals from the pressure transmitter are recorded at a frequency of 2 Hz (Fig.1b). Pressure drop, once stabilized, is noted and plotted against the superficial gas velocity. The fluidized state of the particles is captured by the DSLR camera simultaneously during the experiment. The height of the bed is obtained from the images of the bed captured.

Experiments are performed for three different initial configurations: (a) homogeneous mixture of the large and the small particles, (b) large particles at the bottom and (c) large particles at the top of the bed. The composition of the mixture is varied by changing the volume fraction of the constituent particles. X_{FO} represents the amount of smaller particles in the mixture.

Table 1 Properties of particles used in the experiments

Property → Particle ↓	Mean diameter (μm)	Sieve size (μm)	Particle (material) density (kg/m^3)	Minimum fluidization velocity (m/s)	Terminal settling velocity (m/s)
Small (black)	196	-220/+180	2500	0.02	2.91
Big (blue)	550	-600/+500		0.17	22.89

Results & Discussion

Homogeneous mixture

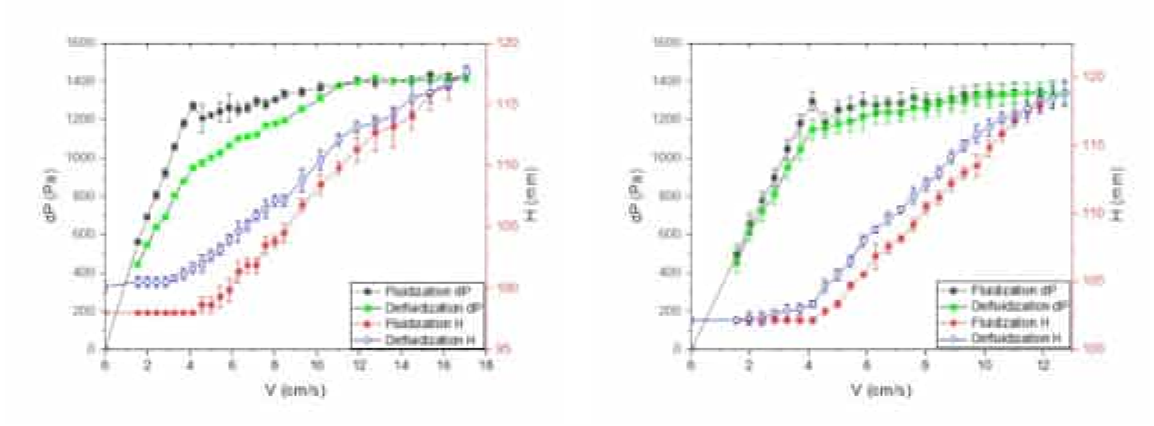

(a) (b)

Fig.2. Bed pressure drop measured using pressure transmitter (AFRISO DMU 11 D) and bed height as a function of the superficial gas velocity for a bed of binary particles with different volume fraction (a) X_{FO} = 0.7, (b) X_{FO} = 0.9

In this case, fully fluidized bed was quenched to ensure the initial condition of homogeneously mixed state for further experiments. Fig. 2a and 2b show the fluidization and defluidization behaviour of two different compositions of binary mixture of particles. For these cases, packed bed voidage value(Ɛ) was 0.38 & 0.4 respectively. The bed pressure drop and the bed height are plotted against the superficial gas velocity. Linear scale is selected for the axes instead of logarithmic scale, as the range of the superficial gas velocity is not too large in laboratory scale experiments. A clear peak in the pressure drop is observed during the initial fluidization of the bed. The pressure drop becomes almost constant after the bed has been completely fluidized. During defluidization, the bed height remains marginally higher than that during fluidization, i.e., during defluidization, the porosity of the bed is slightly higher than that during the fluidized state and consequently, the bed pressure drop is marginally lower. This behaviour is very similar to that observed in fluidized bed of monodisperse particles (Jackson, 2000). The final packed state of the bed has higher voidage than the initial bed. The bed height is observed to have increased by 5 - 6% as compared to the initial state.

Fig. 3a shows the plot of the initial and the final fluidization velocities of the binary mixtures with different compositions obtained from the fluidization curve. The experimentally measured initial and final fluidization velocities are compared with those determined from the correlations proposed by Formisani et al. (2011). There is an excellent agreement between the experimentally measured initial fluidization velocities and that obtained from the correlation. Detailed analysis is required for final fluidization velocity prediction. Fig. 3b and 3c show the snapshots of the fluidized bed during fluidization and defluidization. It is observed that the particles segregate in the bed during defluidization with the larger particles settling down at the bottom of the bed.

(a) (b) (c)

Fig.3. (a) Volume fraction vs. Initial fluidization & final fluidization velocity (b) Completely fluidized homogeneous mixture X_{FO} = 0.7 (c) Final state after defluidization X_{FO} = 0.7

Larger particles at bottom – smaller particles at top

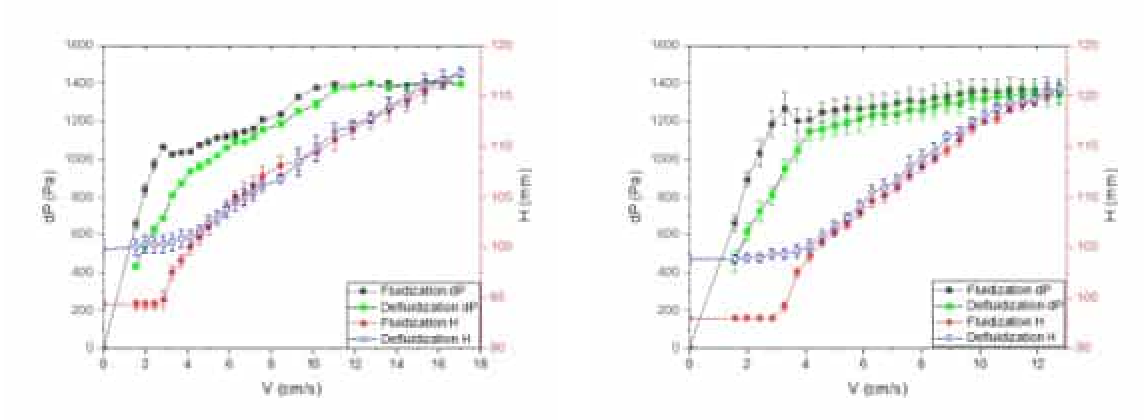

(a) (b)

Fig.4. Bed pressure drop measured using pressure transmitter (AFRISO DMU 11 D) and bed height as a function of the superficial gas velocity for a bed of binary particles with different volume fraction (a) X_{FO} = 0.7(b) X_{FO} = 0.9

The next sets of experiments were carried out for the initial configurations where the larger particles are placed at the bottom. Fig. 4a and 4b show the bed pressure drop and the bed height plotted against superficial gas velocity for a bed of binary particles with different volume fractions. For these cases, packed bed voidage value(ε) was 0.35 & 0.38 respectively. In this case, the peak in the pressure drop during the initiation of the fluidization is not prominent. The smaller particles get fluidized first. The bed pressure drop increases with further increase in the superficial gas velocity before the final fluidization of the entire bed. During defluidization, the bed initially compacts, i.e., the height of the bed is less than that of the fluidized state at that gas velocity. The pressure drop across the bed is higher during the initial phase of defluidization; however, during the final phase of the defluidization, the bed height is marginally higher than that of the initial packed bed.

Fig. 5a plots the initial and the final fluidization velocities of the bed with larger particles at the bottom, obtained from the fluidization curve. The nature of the curve is different from that shown in Fig. 3(a) which was obtained for initially homogeneously mixed particles. The snapshots of the bed captured during fluidization and defluidization are shown in Fig. 5(b) and 5(c), respectively. The bed is observed to get mixed in the fully fluidized state; however, the particles segregate during defluidization. Here, $U_{if,f}$ is initial fluidization velocity of smaller particles & U_{int} (Intermediate velocity) is initial fluidization velocity of the whole bed. At the initial fluidization velocity, only the smaller particles are fluidized, while at the intermediate fluidization velocity, the buoyant weight of the whole bed is balanced by the total drag force and the complete bed is fluidized.

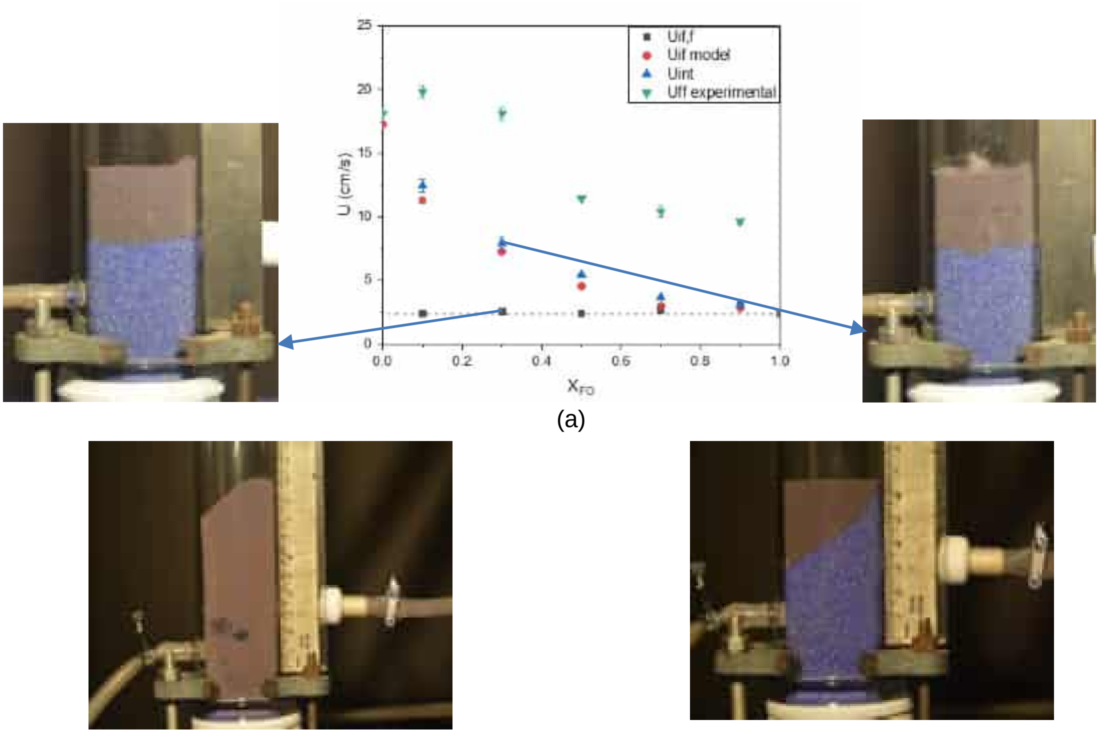

(a)

(b) (c)

Fig.5. (a) Volume fraction vs. Initial fluidization & final fluidization velocity (b) Completely fluidized bed X_{FO} = 0.7 (c) Final state after defluidization X_{FO} = 0.7

Larger particles at top - smaller particles at bottom

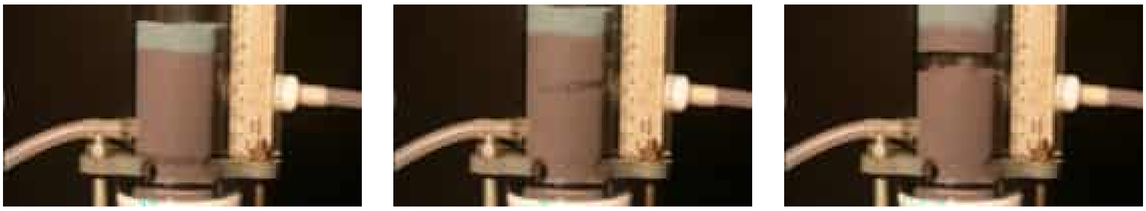

(a) (b) (c)

Fig.6. Progress of slug formation & its movement in upward direction (X_{FO}= 0.85)

Finally, experiments were performed for the initial configuration where the smaller particles are placed at the bottom of the bed. The same volume fractions as in the previous two cases were used; however, the bed behaved quite differently and a slug type fluidization was observed. This was more predominant at higher values of X_{FO}. Fig. 6a to 6c show the slug formation in the bed. Identification of minimum fluidization velocity is quite difficult for this kind of bed configuration. The transition between the initial packed state to the slug regime is quite sharp. Beyond a certain superficial velocity, the bed goes through transition from slug to bubbling fluidization. During defluidization, the particles in the bed undergo segregation with the larger particles settling at the bottom.

Conclusions

Fluidization and defluidization behaviour of binary mixtures are investigated experimentally. It is observed that the fluidization of the bidisperse mixtures is influenced by the initial configurations of the bed. The fluidization behaviour of an initially homogeneous bed (completely mixed) is very similar to that of a monodisperse system; however, for an initially segregated bed, the fluidization behaviour is significantly different. The bed shows smooth transition to a fluidized state for an initial configuration when the large particles are at the bottom; however, for those configurations where the small particles are at the bottom, the bed shows a transition from the packed state to a slug bed. During defluidization, the particles segregate, irrespective of the initial configuration of the bed.

Acknowledgement

Authors thank Mr. Chhotelal Sah Kalwar for design of the setup, Mr. Swapnil Raut & Mr. Rakshit Gadge for their help during experiments.

References

Brachia P., R. Chirone, F. Miccio, M. Miccio, G. Ruoppolo (2017). Segregation and Fluidization Behavior of Poly-disperse Mixtures of Biomass and Inert Particles, *Chemical Engineering Transactions*, 57, 48-54

Di Maio F. P., A. Di Renzo, V. Vivacqua (2012). A particle segregation model for gas-fluidization of binary mixtures, *Powder Technology*, 226, 180-188

Di Renzo A, F. P. Di Maio, R. Girimonte, B. Formisani (2008). DEM simulation of the mixing equilibrium in fluidized beds of two solids differing in density, *Powder Technology*, 184, 214-223

Formisani B., R. Girimonte, T. Longo (2008). The fluidization process of binary mixtures of solids: development of the approach based on the fluidization velocity interval, *Powder Technology*, 185, 97–108

Formisani, B., R. Girimonte, V. Vivacqua (2011). Fluidization of Mixtures of Two solids Differing in Density or Size. *American Institute of Chemical Engineering Journal, 57*, 2325-2333.

Formisani B., R. Girimonte, V. Vivacqua (2012). Fluidization of Mixtures of Two Solids: A Unified Model of the Transition to the Fluidized State, *American Institute of Chemical Engineering Journal*, 59, 729-735

Fotovat B., J. Shabanian, J. Chaouki, J. Bergthorson (2011), Characterization of Fluidization and Mixing of Binary Mixtures Containing Biomass at Low velocities Through Analyzing Local Pressure Fluctuations. *10th International Conference on Circulating Fluidized Beds and Fluidization Technology - CFB 10*

Girimonte R., B. Formisani, V. Vivacqua (2018). The relationship between fluidization velocity and segregation in two-component gas fluidized beds: Density- or size-segregating mixtures, *Chemical Engineering Journal*, 335, 63-73

Jackson R. (2000). The dynamics of fluidized particles, Cambridge monograph on Mechanics

Pan H., X. Z. Chen, X. F. Liang, L.T. Zhu, Z.H. Luo (2016). CFD Simulations of gas-liquid-solid flow in fluidized bed reactors - A review. *Powder Technology*, 299, 235 - 258.

Tsuji T., K. Higashida, Y. Okuyama, T. Tanaka (2014). Fictitious Particle Method: A Numerical Model for Flows Including Dense Solids with Large Size Difference. *American Institute of Chemical Engineering Journal*, 60, 1606 - 1620.

AN EXPERIMENTAL STUDY ON LIMESTONE ATTRITION DURING SULFATION IN A FLUIDIZED BED REACTOR

Dongfang Li[1], Min-Woo Kim[1], Runxia Cai[2], Hairui Yang[2], Chung-Hwan Jeon[1*]

[1] *School of Mechanical Engineering, Pusan National University, Busan, Republic of Korea*
[2] *Department of Energy and Power Engineering, Tsinghua University, Beijing, China*

*Email: *chjeon@pusan.ac.kr*

Abstract

Limestone is widely used as sorbent for in-situ desulfurization in circulating fluidized bed (CFB) boilers. After being injected into the boiler, limestone undergoes calcination and sulfation reactions, as well as fragmentation and attrition process. The attrition of the limestone is investigated in a bubbling fluidized bed reactor during sulfation reaction in the present research. The sulfation conversion rate and attrition rate are obtained. The results show that the sulfation reaction undergoes kinetic-control regime, transition regime and the diffusion-control regime subsequently. The attrition rate decreases along with the sulfation reaction with a great drop in the kinetic-control regime and reaches to stable attrition zone. The formation of $CaSO_4$ shell is investigated with SEM and the layer thickness is found to be non-uniformly distributed. The product layer at the initial kinetic-control stage of the reaction is found to be up to 1μm and is considered to be reason for the great drop of attrition in the kinetic-control regime of sulfation reaction.

Introduction

CFBC (circulating fluidized bed combustion) technology is under fast development for its good fuel flexibility and low cost of emission control. The relative low combustion temperature allows the NO_x emission be lower than that of pulverized coal combustion (Yue, Cai et al. 2017). The availability of in situ desulfurization with limestone as sorbent makes the sulfur capture possible without post-combustion treatment (Anthony and Granatstein 2001). Along with the requirement of high efficiency and low emission of the power generation industry, the large scale and high steam parameter CFB boilers are increasing in number (Lyu, Yang et al. 2017). At the end of 2016, the world first ultra-supercritical CFB boiler, Samcheok plant, consisting four units of 550 MWe boilers, started commercial operation. The plant is designed with in situ desulfurization using limestone as sorbet. The efficiency of desulfurization is significant for not only the cost of power generation, but also the capability of meeting the environmental regulation.

After being injected into the combustors, limestone first undergoes calcination and sulfation as the following reactions. Along with chemical reaction, limestone undergoes fragmentation and attrition results in the change of the size distribution of the particles. Fragmentation is the breakage of the particle due to thermal stresses and internal overpressure during thermal decomposition, while attrition is considered to involve abrasion due to collision as particles rub against each other or against the furnace and cyclone walls (Li, Ke et al. 2019). Both fragmentation and attrition result in the reduction of the particle size. The difference is that fragmentation results in the generation of both coarse and fine fragments while attrition is considered to generate fine particles. The reduction of size distribution would lead to the change of residence time of the limestone particles, and eventually the conversion ratio as well as the desulfurization efficiency.

The previous study shows that the attrition of limestone in calcination stage is much higher than that in the sulfation stage(Scala, Salatino et al. 2000). Yao also found the attrition rate decreases dramatically when the sulfation reaction happens, and found the attrition rate increases while the particle size decreases (Yao, Zhang et al. 2010). F. Scala et al. attributes the formation of the $CaSO_4$ shell for the decreasing of attrition rate in sulfation stage (Scala, Montagnaro et al. 2008). J.M. Cordero and M. Alonso found the $CaSO_4$ shell with unreacted core in a calcium loop system (Cordero and Alonso 2015). However, the product layer is not discussed in detail in the previous studies. M. Obras-Loscertales et al. proposed a method to analyze the product layer of the limestone under sulfation reaction with shrinking core model and predicted the product layer thickness to be 18~40 μm for limestone with particle size of 200~630 μm (de las Obras-Loscertales, de Diego et al. 2013). However, the attrition is not discussed.

The present research is to investigate the product layer development of the limestone particle and its influence on the attrition rate change during sulfation reaction of limestone in a batch bubbling fluidized bed reactor. A scanning electron microscope (SEM) coupled with an energy dispersive X-ray(EDX) analyzer is used to measure the product layer thickness.

Experiment

The schematic of the atmospheric bubbling fluidized bed reactor is shown in Fig. 1. The main body of the reactor is made of quartz tube with 54mm ID and 950mm high. The air distributor made of sintered silica sand is 600 mm from the top of the quartz tube. Gas is preheated before being injected into the upper reaction part of the quartz tube. The lower part of the quartz tube below the air distributor is packed with glass bead to promote the preheating of the gas. The reactor is electrical heated, and the temperature is controlled at 850℃.

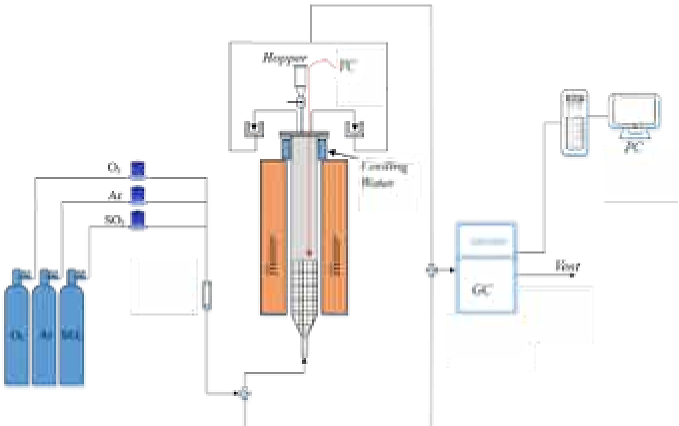

Fig. 1. Schematic of the bubbling fluidized bed reactor

100g of Silica sand sieved in the size rage of 250~350 μm with Sauter mean diameter d = 328μm and minimum fluidizing velocity U_{mf} = 0.025 m/s, terminal velocity U_t = 1.70 m/s is used as bed material. The Mohs hardness of silica sand is much higher than that of limestone and calcium sulfate, therefore the attrition of silica sand is negligible.

The superficial velocity of the fluidizing gas U_g is 0.3m/s at each condition. The silica sand is first fed into the reactor in Ar atmosphere and is heated up to 850℃. The temperature is then maintained at 850℃. The Ar gas is continuously injected into the reactor as fluidizing air for five minutes to elutriate the fines attached in the silica sand particles. Then, the Ar gas is cut off and 20g of limestone prepared in the hopper above the top of the reactor is fed into the reactor. Ar gas is injected with superficial velocity of 0.025m/s for 60~70 min for the limestone calcination till the CO_2 concentration of the flue gas drops under 0.5%. Then the mixed gas of Ar, SO_2 2000 ppm and O_2 5% is injected into the reactor for sulfation reaction.

The elutriated fines are collected via two removable filters of sintered copper alternately every five or ten min. The attrition rate R_s is defined as

$$R_s = -\frac{1}{m}\frac{dm}{dt} \tag{1}$$

where m is the mass of the particles at a given time and dm/dt is the mass variation rate due to attrition. The attrition rate constant is defined as

$$K_a = \frac{R_s}{(U_g - U_{mf})} d \tag{2}$$

The CO_2 and SO_2 concentration of the flue gas are analyzed by a GAM 200 mass spectrometer and recorded in a computer. The conversion ratio X of the limestone could be calculated according to

$$\frac{dX}{dt} = \frac{M_{CaCO_3} q}{m\lambda}(c_{in} - c_{out}) \tag{3}$$

where *dX/dt* is the conversion rate, M_{CaCO_3} is the molar weight of $CaCO_3$, *q* is the molar flow rate of the mixed gas, *m* is the mass of the limestone, *λ* is the mass fraction of $CaCO_3$ in the limestone, c_{in} and c_{out} are the inlet and outlet molar fraction of SO_2 respectively.

The limestone sample used as in situ desulfurization sorbent is supplied from the Samcheok plant. The mass fraction of $CaCO_3$, i.e. λ is 94.3% via XRF analysis. Batches of limestone are sieved into two size range, 200-400 μm, 400-600 μm, respectively. The pore size distribution for each size of limestone after calcination at 850℃ is measured with a mercury porosimeter. The physical parameters for each size of limestone are listed in Table 1, where S_0, L_0 and φ are the initial reaction surface of the pore system, the length of the pore system and the structure parameter, respectively. The structure parameter is defined as the following equation:

$$\varphi = \frac{4\pi L_0(1-\varepsilon)}{S_0^2} \tag{4}$$

where ε is the porosity of the particle.

Table 1. Physical characteristics for each size of limestone

	d, μm	*U_{mf}*, m/s	*S₀*, m²/m³	*L₀*, m/m³	ε	φ
200-400μm	320	0.024	$6.55×10^6$	$1.85×10^{13}$	0.301	3.73
400-600μm	596	0.032	$6.21×10^6$	$1.89×10^{13}$	0.309	4.29

Results

The conversion ratios for sulfation reaction are shown in Fig. 2. The sulfation reaction started with a high initial conversion rate. As the conversion ratio X of the limestone increased, the conversion rate decreased for each case. The sulfation reaction is considered to involve the formation of the calcium sulfate product layer as well as an increasing diffusion resistance of SO_2 gas against the product layer or even the pore blockage. Thus, the reaction is commonly considered to perform in the initial fast chemical kinetic-controlled regime and in the following diffusion-controlled regime. Within the initial 10 min, the conversion ratio for each case increased almost linearly, and similar initial conversion rate for each case was observed via the overlapped curves with each other. Following the initial stage, as the conversion ratio increased, the conversion rate decreased due to formation of calcium sulfate layer and the increasing diffusion resistance. The molar volume of the $CaCO_3$, CaO and $CaSO_4$ are 36.9 cm^3/mol, 16.9 cm^3/mol and 46.0 cm^3/mol, respectively (Anthony and Granatstein 2001). The pore of the particle would be plugged as the produce layer thickness increases due to the higher molar volume of $CaSO_4$, and the reaction surface became even smaller, which results in decreasing conversion rate. This stage of the reaction is the transition regime. After 50 min of the reaction, the conversion ratio increased very slowly, and the conversion rate was predominantly controlled by diffusion, which was known as diffusion-controlled regime (Mattisson and Lyngfelt 1998).

As shown in Fig. 3, as the sulfation reaction proceeded, the attrition rate constant showed a dramatical drop at the initial 10 min, corresponding to the chemical kinetic-controlled regime of the sulfation reaction. The attrition rate constant then continuously but very slowly decayed in the diffusion-controlled regime of the sulfation reaction. The size of the particles made remarkable difference on the attrition rate in the initial stage. The attrition rate constants of the particles with size of 200~400 μm were observed to be higher than those of the particles with size of 400~600 μm.

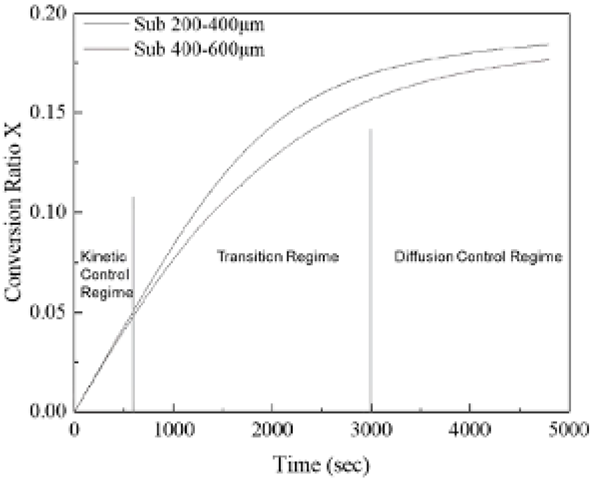

Fig. 2. Conversion ratio of sulfation reaction

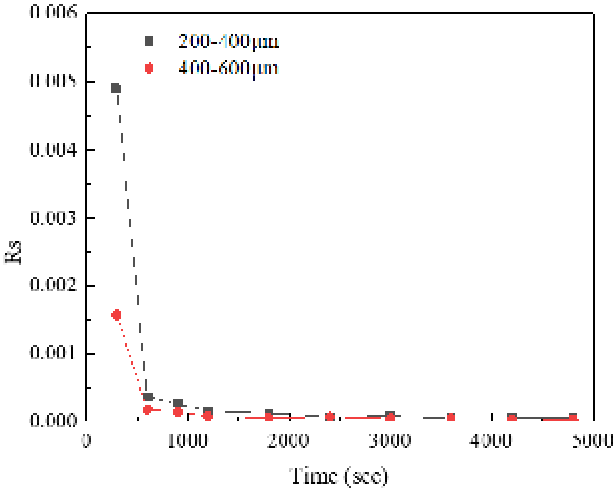

Fig. 3. Attrition rate constant for each case

SEM-EDX was conducted on the elutriated samples and the results are shown in Fig. 4. Since the sulfur was captured in the form of calcium sulfate, the EDX for sulfur element indicated the distribution of calcium sulfate, i.e. the product layer.

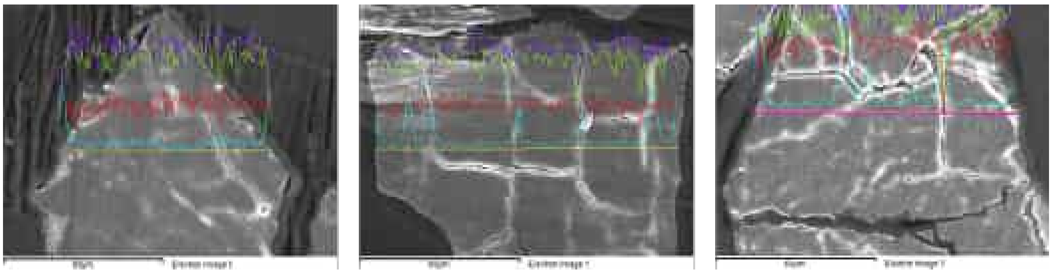

(a) (b) (c)

Fig. 4. SEM EDX results for 200-400μm at different sulfation time (a) 0~10 min (b) 10~50min (c) 50~80 min.

The line EDX result shown in Figure 4(a) showed that the sulfur distribution alone the line had two peaks on the both ends of the line, which indicated that product layer was distributed on the surface covering the particle with an unreacted core. The line EDX results for both cases in Figure 4(b) and Figure 4(b) showed multiple peaks on the particle surfaces and on the cracks. The uniform distribution of calcium sulfate reported by J.M. Cordero, M. Alonso in calcium looping condition (Cordero and Alonso 2015) could not be found in the present research. Anders Lyngfelt and Bo Leckner found the uniform distribution of calcium sulfate could not be obtained in the oxidizing condition even after 20 h operation, which showed similar phenomenon with the present research (Lyngfelt and Leckner 1999).

The product layer thickness was measured by SEM with EDX mapping. An example is shown in Fig. 5, with the element analysis results of sulfur for the product layer and the unreacted core zone.

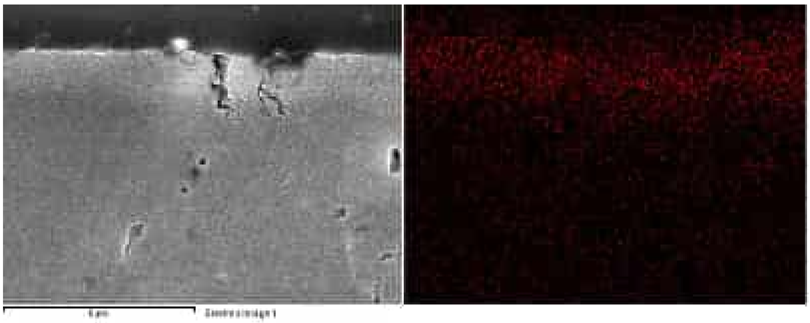

Fig. 5. SEM EDX analysis for product layer thickness

The particle collected in the chemical kinetic-controlled zone was found to be covered with $CaSO_4$ shell, however, the product layer was not uniformly distributed. The product layer shown in Fig. 6 shows that the particle surface was surrounded with product layer about 1 μm, and the crack was also covered with product. Porous structure could also be observed in the unreacted core zone, which indicated the delay of reaction due to pore blockage. This founding shows different results frome Barker and D. Alvarez et al., who proposed the product layer that resulting the regime change was in the range of 20~50 nm (Barker 1973, Alvarez and Abanades 2005).

Fig. 6. SEM analysis for subsequent 200~400 μm, 0~10 min

The product layer at the end of the sulfation reaction was found to be at the range of 1~2 μm, which was quite different from the predicted value proposed by M. Obras-Loscertales et al (de las Obras-Loscertales, de Diego et al. 2013).

Conclusion

The limestone used in a 550 MWe ultra-supercritical CFB plant was tested in a lab-scale bubbling fluidized bed reactor. The sulfation reaction could be divided as chemical kinetic-controlled regime, diffusion-controlled regime, and the transition regime between the two regimes. The product layer was developed fast in the kinetics-controlled regime and resulted in the formation of calcium sulfate shell in the initial 10 min of the sulfation reaction. However, the product layer was not uniformly distributed. The reacted surface and the unreacted core structure was found, and the product layer thickness was found to be above 1μm by measuring via SEM coupled with EDX mapping in the initial 10 min of the reaction. The product layer at the end of the reaction was found to be in the range of 1~2 μm, and the crack and were also found to be covered by product layer due to the line EDX analysis results.

Notation

c_{in}	inlet molar fraction of SO_2	R_s	attrition rate, min^{-1}
c_{out}	outlet molar fraction of SO_2	S_0	surface area of the pore system, m^2/m^3
d	diameter, μm	t	time, s
K_a	attrition rate constant	U_g	superficial gas velocity, m/s
L_0	total length of the pore system,m/m^3	U_{mf}	minimum fluidization gas velocity, m/s
m	mass, g	ε	porosity
M_{CaCO_3}	molar weight of CaCO3, g/mol	λ	purity of limestone
q	molar flow rate, mol/s	φ	structure parameter

References

Alvarez, D. and J. C. Abanades. Determination of the Critical Product Layer Thickness in the Reaction of CaO with CO2. Ind. Eng. Chem. Res. 2005. 44(15): 5608-5615.

Anthony, E. and D. Granatstein. Sulfation phenomena in fluidized bed combustion systems. Prog. Energ. Combust. 2001. 27(2): 215-236.

Barker, R. "The reversibility of the reaction CaCO3⇄ CaO+ CO2." J. Appl. Chem. Biotechn. 1973. 23(10): 733-742.

Cordero, J. and M. Alonso. Modelling of the kinetics of sulphation of CaO particles under CaL reactor conditions. Fuel, 2015. 150: 501-511.

de las Obras-Loscertales, M., L. F. de Diego, F. García-Labiano, A. Rufas, A. Abad, P. Gayán and J. Adánez. Modeling of Limestone Sulfation for Typical Oxy-Fuel Fluidized Bed Combustion Conditions. Energ. Fuel. 2013. 27(4): 2266-2274.

Li, D., X. Ke, H. Yang, S.-G. Ahn, J. Lyu, C.-H. Jeon and M. Zhang. The ash formation and attrition characteristics of an Indonesia lignite coal ash for a 550 MWe ultra supercritical CFB boiler. Chem. Eng. Res. Des. 2019. 147: 579-586.

Lyngfelt, A. and B. Leckner. Sulphur capture in circulating fluidized-bed boilers: can the efficiency be predicted? Chem. Eng. Sci. 1999. 54(22): 5573-5584.

Lyu, J., H. Yang, W. Ling, L. Nie, G. Yue, R. Li, Y. Chen and S. Wang. Development of a supercritical and an ultra-supercritical circulating fluidized bed boiler. Front. Energy. 2017. 1-6.

Mattisson, T. and A. Lyngfelt. A method of evaluating limestone reactivity with SO2 under fluidized bed combustion conditions. Can. J. Chem. Eng. 1998. 76(4): 762-770.

Scala, F., F. Montagnaro and P. Salatino. Sulphation of limestones in a fluidized bed combustor: the relationship between particle attrition and microstructure. Can. J. Chem. Eng. 2008. 86(3): 347-355.

Scala, F., P. Salatino, R. Boerefijn and M. Ghadiri. Attrition of sorbents during fluidized bed calcination and sulphation. Powder Technol. 2000. 107(1): 153-167.

Yao, X., H. Zhang, H. Yang, Q. Liu, J. Wang and G. Yue. An experimental study on the primary fragmentation and attrition of limestones in a fluidized bed. Fuel Process. Technol. 2010. 91(9): 1119-1124.

Yue, G., R. Cai, J. Lu and H. Zhang. From a CFB reactor to a CFB boiler – The review of R&D progress of CFB coal combustion technology in China. Powder Technol. 2017. 316: 18-28.

HYDRODYNAMIC CHARACTERIZATION OF 1.5 MW CHEMICAL LOOPING COMBUSTION COLD FLOW MODEL

Sina Tebianian[1]*, Stéphane Girardon[1], Benjamin Amblard[1], Stéphane Bertholin[1], Ann Cloupet[1], Mahdi Yazdanpanah[2], Aoling Zhang[3], Zhenshan Li[4] , Hu Chen[4] , Weicheng Li[5] , Xinglei Liu[5]

[1]IFP Energies nouvelles, Rond-point de l'échangeur de Solaize, BP 3, 69360 Solaize, France

[2]TOTAL TRTG, HARFLEUR, France

[3]TOTAL China, Beijing (China)

[4]Tsinghua University, Beijing (China)

[5]Dongfang Boiler Group Co. Ltd. and Clean Combustion and Flue Gas Purification Key Laboratory of Sichuan Province (China)

*Email: *sina.tebianian@ifpen.fr*

Abstract

Stable operation and viable design of Chemical Looping Combustion (CLC) process rely on various parameters including: stable and controlled solid circulation, hydrodynamic stability in both Fuel reactor (FR) and Air reactor (AR), heat exchange adaptability to the thermal power and oxygen carrier separation from unburnt solid fuel in the Carbon Stripper (CS) unit.
As a part of the H2020 CHEERS (Chinese European Emission Reducing Solutions) project, a cold-flow model of the future hot demonstration unit was built in order to study the hydrodynamics associated with different elements of the entire loop. The cold flow model was equipped with FR, AR and CS with dimensions that were relevant to demonstrate the technology hydrodynamics at pilot scale (equivalent of 1.5 MW_{th}). Stable and continuous solid circulation at different rates was achieved in the entire loop by using control L-valves and loop seals.
In this work, experiments were performed to evaluate the hydrodynamic features of different elements of the loop. The experimental results provide valuable data for model validation.

Introduction

The growing concern over global warming imposes strict objectives for reductions in greenhouse gas emissions. Fossil fuels represent the largest point source of CO_2 production accounting for about 40 % of total emissions as reported by Spigarelli and Kawatra, (2013). CO_2 capture and storage (CCS) is among the solutions to decrease the global greenhouse emissions and according to the IEA research report of 2013, it will contribute for 14% of the cumulative emission reductions by 2050. Processes based on post-combustion separation or oxycombustion have been demonstrated at large scale and represent mature technology. However, the resulting energy penalty of these techniques is high such as for the same net amount of energy produced, these processes will use up to 15 – 25% more fuel than a conventional power plant with no CO_2 capture as reported by Gauthier et al. (2017). Chemical looping combustion (CLC) represents a promising technology for CO_2 capture since it presents lower carbon avoidance cost and higher thermal efficiency compared to other techniques as given by Tang and You (2018).

H2020 CHEERS (Chinese European Emission Reducing Solutions) project is a collaboration among different European and Chinese partners for demonstration of CLC technology at TRL7. As part of technology demonstration at pilot scale, an equivalent of 1.5 MW_{th} cold-flow model was built and operated in order to study the hydrodynamic characteristics associated with different elements of the entire loop.

The unit was successfully commissioned and operated under different operating conditions. This paper presents part of the experimental results obtained for the main elements of the unit such as:

1. Fluidization behavior in the Fuel Reactor (FR) for different solid circulation rates at different superficial gas velocities;
2. Control of solid circulation in the entire loop by employing L-valves of different geometries;
3. Solid transport hydrodynamics in the Air reactor (AR) with different solid mass flux and superficial gas velocities.

Experimental

The main components of the cold flow model (Fig.1) are as follow :

- Air reactor represented by a 10 m high riser with a square cross section of 0.25 x 0.25 m;
- Dividing fluidized bed (DFB) where the solids transported in the riser and collected by the cyclone flow to be either recycled back to the AR either transferred to the FR;
- L-valves (0.15 m I.D.) for controlling the solid circulation rate between Fuel and Air reactors, and of 0.2 m I.D. for controlling the recycle ratio to the AR ;
- Fuel reactor represented by a fluidized bed column of a height of 2.5 m and a cross section of 0.6 x 0.6 m connected through a riser to an annular carbon stripper.

The entire loop was equipped with pressure transducers with an acquisition frequency of 1 Hz. The solid circulation was measured by closing the butterfly valve of the AR cyclone dipleg and recording the filling time.

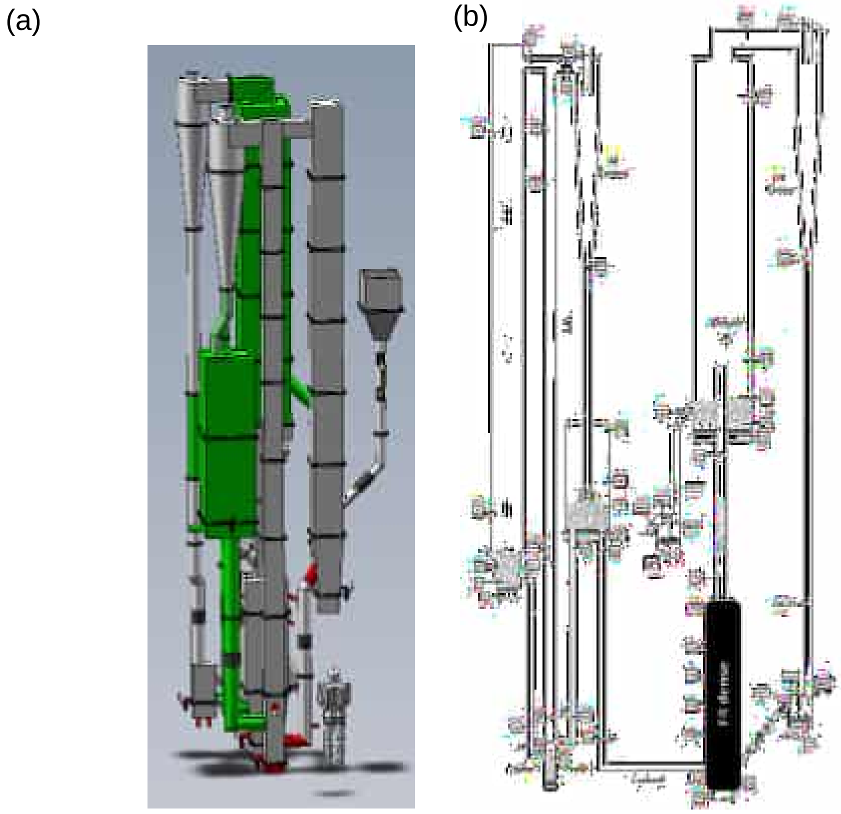

Fig. 1. (a) 3D representation of the cold flow model and (b) 2D scheme of the pressure measurement locations

Sand particles of d_{sauter} = 385 µm and a particle density (ρ_p) of 2922 kg/m^3 were employed as bed material. The AR was operated with superficial gas velocities (U_g) ranging between 5 and 10 m/s and FR was operated with U_g's between 0.7 to 1.5 m/s.

Results and Discussion

Air reactor and L-valves

Hydrodynamics of the AR was characterized by operating the closed loop consisting of AR – DFB connected by the AR cyclone and recycle L-valve. The solid mass flux was controlled by the aeration of the L-valve. For a given superficial gas velocity, the AR was operated with different solid flux in order to investigate the choking conditions specially at low U_g's.

Fig.2 presents an example of solid flux in the riser controlled by the recycle L-valve aeration when the dense fluidized bed height in the DFB was 0.5 m. The solid flow in the L-valve depends on the amount of gas that flows in the horizontal section which is a combination of the gas that flows due to the pressure balance and the injected gas, as explained by Yang and Knowlton (1993) and Yazdanpanah et al. (2012). The lower the U_g in the riser for a given solid mass flowrate, the higher the riser pressure drop (Fig. 2(b)) and therefore, the less the amount of gas flowing in the L-valve horizontal section.

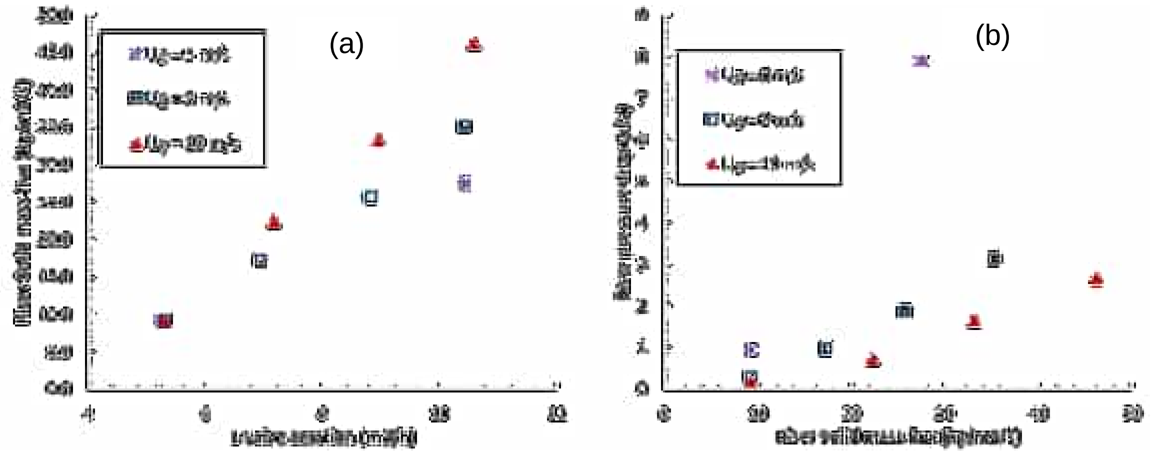

Fig. 2. (a) Solid circulation control by L-valve aeration; (b) riser pressure drop as a function of solid flux and superficial gas velocity

Under certain operating conditions, it could be of interest to operate the AR with low superficial gas velocity in order to increase the residence time of oxygen carrier, decrease the operating cost, etc. However, it is important to operate at a safe margin from choking conditions.

For a superficial gas velocity of 5 m/s, the solid flowrate was increased gradually by increasing the amount of L-valve aeration in order to determine the maximum solid flowrate transportable by the gas. As indicated in Fig.3, the riser pressure drop as a function of solid flux indicates that, for the employed superficial gas velocity, choking conditions may be approached with solid flux higher than 40 kg/(m^2 s) which was also visually observable during the operation.

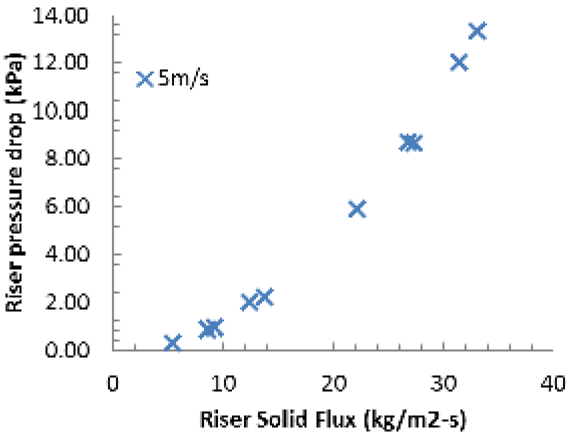

Fig. 3. Maximum transportable solid flow at U_g = 5m/s

Fuel Reactor

The entire loop was operated continuously with the L-valves connecting AR and FR sections controlling the solid circulation rate. Conversion of the feed in the fuel reactor is directly related to the residence time in the FR dictated by the dense and dilute volumes and respective solid velocities. It is, therefore, of interest to know how the fluidized bed level in the FR changes with the variation of solid circulation rate due to different operating conditions (ex. lower oxygen carrier oxidation state) or different thermal input. This was investigated by varying the solid circulation rate at a given superficial gas velocity in the FR and recording the variation of the dense bed level. Table 1 presents the relative change of FR bed level once the solid circulation rate (G_s) changes for a given superficial gas velocity. In order to better appreciate the influence of different parameters, the sensitivity of the FR bed level to the operating conditions is given in relative compared to a reference case at a superficial gas velocity of 1 m/s. Note that the fluidized bed level in the FR decreases by increasing the superficial gas velocity and decreasing the solid circulation rate. A more comprehensive experimental database is being produced and will be presented in a future work.

Tab. 1. FR bed level change as a function of superficial gas velocity and solid circulation rate

G_s (kg/s)	**FR U_g (m/s)**	**H_{FR} (m)**
A	1.0	B
0.8*A	1.0	B-0.2
2.2*A	1.0	B+0.6
0.6*A	1.5	B-1.1
2.2*A	1.5	B-0.1
0.5*A	0.7	B+0.5

Conclusion and future work

The cold flow model of an equivalent 1.5 MW_{th} CLC unit was designed and operated in order to study the hydrodynamic features of different elements under typical operating conditions. The control of the solid circulation rate by using L-valves was demonstrated and main features associated with AR and FR were studied. The features of the CS and solid mixing in the FR is being studied currently and will be provided in future works.

The experimental results are currently being utilized for a CFD and other models comparison.

Notation

ρ_p	particle density [kg/m^3]	d_{sauter}	Sauter mean diameter, [μm]

U_g	superficial gas velocity [m/s] I.D.	H_{FR}	bed level in the Fuel reactor [m]
G_s	solid circulation rate [kg/s]	I.D.	internal diameter [m]

References

Gauthier, T., M. Yazdanpanah, A. Forret, B. Amblard, A. Lambert, S. Bertholin. CLC, a promising concept with challenging development issues. Powder technology. 2017. 316, 3-17

International Energy Agency. Technology roadmap, Carbon capture and storage. Report 2013.https://www.iea.org/publications/freepublications/publication/TechnologyRoadmapCarbonCaptureandStorage.pdf

Spigarelli, B.P., S.K. Kawatra. Opportunities and challenges in carbon dioxide capture. Journal of CO2 Utilization. 2013. 1, 69-87

Tang, Y., F. You. Life cycle environmental and economic analysis of pulverized coal oxy-fuel combustion combining with calcium looping process or chemical looping air separation. Journal of cleaner production. 2018. 181, 271-292

Yang, W. C., T.M. Knowlton. L-valve equations. 1993. Powder Technology. *77* (1), 49-54.

Yazdanpanah, M. M., A. Forret, T. Gauthier, A. Delebarre. An experimental investigation of L-valve operation in an interconnected circulating fluidized bed system. 2012. Powder technology. 221, 236-244.

EVOLUTION AND FLOW OF VAPORS IN A FLUIDIZED BED

Hansen M. Silitonga[1], Cedric Briens[1]*, Franco Berruti[1], Francisco Sanchez Careaga[1], Jennifer McMillan[2]

[1] *Institute for Chemicals and Fuels from Alternative Resources, Western University, 22312 Wonderland Rd. North RR#3, Ilderton, ON, N0M 2A0, Canada*
[2] *Syncrude Canada Ltd, Edmonton Research Centre, 9421 17th Ave., Edmonton, AB, T6N 1H4, Canada*

*Email: *cbriens@uwo.ca*

Abstract – In the Fluid Coking™ process, heavy oil is atomized with steam and sprayed into a fluidized bed of hot coke particles. The jet-bed interaction tends to promote agglomerate formation that delay the vaporization of product vapors. Prolonged residence time of vapors also leads to undesired over-cracking of products to non-condensable gases. Previous studies have indicated that jet-bed interactions determine the initial liquid distribution and agglomerate formation and stability inside the bed. This study is therefore intended to develop a novel experimental method to provide information on the impact of nozzle characteristics and bed hydrodynamics on the evolution and flow of vapors in a fluidized bed. The experiments were conducted in a pilot scale fluidized bed with a rectangular cross-section. Atomized deionized water and Silica sand particles were used to simulate jet-bed interaction. An oxygen sensor was used to detect non-oxygen gases (i.e. water vapor). As atomized water was injected into the fluidized bed, the concentration of oxygen at the column outlet was recorded and analysed to obtain the vapor residence time distribution profile. Results showed an instant freeboard pressure jump when a pulse of gas tracer was injected at several axial locations between the column outlet and the bed bottom. Injection with a scaled down version of an industrial feed nozzle with a throat diameter of 1.41 mm indicated a fast vaporization at a Gas-to-Liquid Ratio of 1.25 %. When GLR was increased above 1.25 %, both vaporization time and vapor residence time increased slightly and stabilized. Varying nozzle tip penetration resulted in a slight increase for vaporization rate and residence time. Finally, the injection from a single larger nozzle scale had shown a faster vaporization than that from dual smaller nozzles.

Introduction

In Fluid Coking™ process, the coke particles provide heat for the reaction and vaporization of the heavy feed into smaller molecular weight and more valuable hydrocarbon vapors, which flow up through the bed, freeboard and cyclones (Gray, 1994). Several studies (Ariyapadi, 2004; Weber, 2009) have shown that agglomerate formation limits the heat transfer and vaporization. Prolonged residence time of vapors also leads to over-cracking of products to non-condensable gases while lower vapor residence time promotes coke formation and fouling of cyclones (Mallory et al., 2000). Portoghese (2007) had indicated that jet-bed interactions determine the initial liquid distribution and agglomerate formation. The vaporization rate was found to be determined by droplet size distribution of injected liquid on bed particles (Leclère et al., 2004).

Li et al. (2012) showed that the vaporization rate of injected liquid into the Fluid Coker has a significant impact on reactor hydrodynamics, which in turn affects the distribution of injected liquid on fluidized bed particles. The objective of this study is to develop a novel experimental model to elucidate the impact of spray nozzle characteristics and column hydrodynamics on the vaporization rate of injected liquid and the residence time distribution of the vapors.

Equipment and Method

Experiments were performed in a fluidized bed, shown in Fig. 1, with a rectangular cross-section of 1.2 m × 0.15 m and an expanded freeboard with a cross-section of 1.2 m × 0.47 m at 1.5 m from the gas distributor plate. A pressure transducer was installed at the top of the column to record the freeboard pressure $P_{freeboard}$ during the experiment. An oxygen probe was installed at the column outlet to record the concentration of oxygen in the gas coming out of the column: this oxygen probe had a fast response (less than 100 ms) and was sturdy enough to resist erosion by the fines suspended in the gas exiting the column.

To test the monitoring technique, 3 moles of N_2 pulse was injected to the column at room temperature at different axial positions (Δz_i) relative to the column outlet (Fig. 1a). In all experiments, the left hand side on Fig. 1a is called the west side. Sand was not in the bed and air was flowing from the windbox with a velocity of 0.3 m/s.

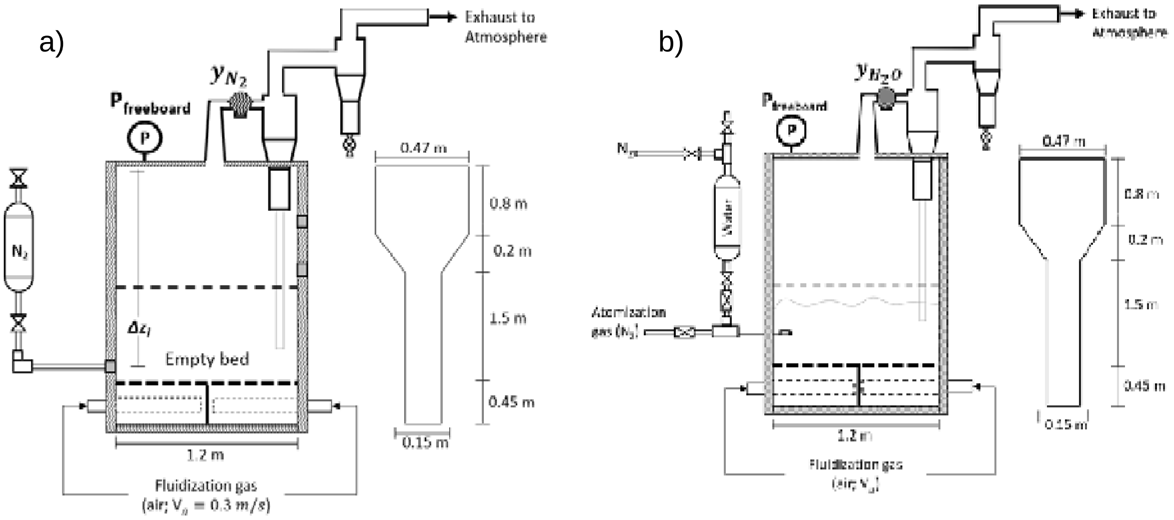

Fig. 1. Schematic of Fluid Coker model for: a) N_2 pulse injection and b) liquid injection.

The regular experiments used the same column with 150 kg of Silica sand (Sauter mean diameter of 190 μm and particle density of 2650 kg/m^3), which corresponded to a static bed height of 0.60 m. Gas atomized-water was injected into the fluidized bed from the west side through a scaled-down version of an industrial spray nozzle (Bennett et al., 2001). The schematic of the experimental setup is shown in Fig. 1b. During injection, the water flux through the nozzle tip was 22.5 g/mm^2·s. A water and Silica sand system were chosen because of the similarity of the viscosity of water at ambient temperature and heavy oil at injection temperature, and the wettability is similar to that of bitumen and coke (Prociw et al., 2018). The initial bed temperature, before injection, was 135 °C.

The impact of spray nozzle characteristics and column hydrodynamics

The studied spray nozzle characteristics in the experiments were the atomization Gas-to-Liquid ratio and the spray nozzle size. The flowrate of atomization gas was adjusted to achieve a Gas-to-Liquid mass ratio (GLR) in the range between 0.5 % and 2.5 %. The air mass flow rate was adjusted by regulating the gas pressure upstream of a calibrated flow control orifice. A set of experiments was performed to study the impact when the spray nozzle scale was switched to dual 1 mm nozzles. Dual injections were performed from both the West and East side of the bed. The impact of nozzle penetration into the bed was also studied.

The experiments to study the impact of nozzle tip penetration (X_{inj}) was performed for distances of 0.1, 0.2, 0.3 and 0.4 m from wall into the bed. The bed was usually operated at a fluidization velocity of 0.3 m/s.

Vaporization rate model and vapors residence time distribution

Equations were developed to determine both the instantaneous vaporization rate and the residence time distribution of the vapors from the recorded pressures in the freeboard and in the windboxes, and from the oxygen concentration in the column outlet (Fig. 2). The model equations are shown in Table 1. The first step was to obtain the concentration of water vapor in the column outlet from the oxygen sensor (Eq.1). The flowrate of gas exiting the column was obtained from the freeboard pressure transducer readings, using the ideal gas law and the observed linear relationship between flowrate through the cyclones and the voltage of the freeboard pressure transducer.

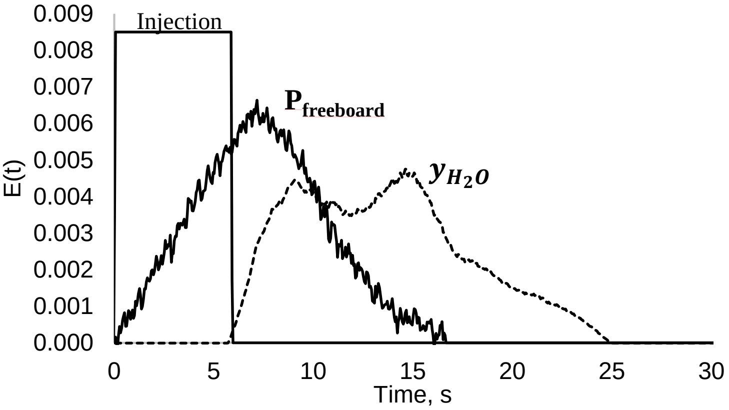

Fig. 2. Normalized results from the recorded freeboard pressure and water vapor concentration in column outlet (GLR=2 %; V_g= 0.3 m/s; F_L=22.5 g/mm^2·s; m_L= 0.2 kg).

Calibration of the pressure transducers in the freeboard and the two windboxes was necessary to provide the instantaneous flowrate of fluidization air from the two windboxes into the fluidized bed. A molar balance of all the flows into and out of the bed provided the instantaneous rate at which vapor was generated from the injected liquid within the bed.

Table 1. Model equations for vaporization rate of injected water and vapors residence time distribution.

Mole fraction of water vapor in column outlet at time i ($y_{H_2O,i}$)	$y_{H_2O,i} = 1 - (1+\lambda_{air})y_{O_2,i}$ $\lambda_{air} = \frac{1-y_{O_{2,air}}}{y_{O_{2,air}}} = \frac{1-0.20946}{0.20946} = 3.7742$	(1) (2)
Normalized fraction of injected water between i_{sz} and i_{ez} Molar flow rate through the column before injection ($F_{out,0}$) Molar flow rate out of the column at time i ($F_{out,i}$)	$\beta = \frac{N_{H_2O}}{\Delta t_{DAQ}\sum_{i=i_{sz}}^{i_{ez}}(V_{F_i}-V_{F_0})}$ $F_{out,0} = A \cdot V_g \cdot \frac{P_{atm}}{R(273.15\,K+T_{bed})}$ $F_{out,i} = F_{out,0} + \beta\left(V_{F_i} - V_{F_0}\right)$	(3) (4) (5)
Molar flow rate of water vapor in gas outflow ($F_{H_2O,out,i}$)	$F_{H_2O,out,i} = y_{H_2O}F_{out,i}$	(6)
Calibration of pressure transducers - Freeboard pressure - East side windbox - West side windbox	$P_{freeboard} = a_F + b_F V_F$ $P_{wb,east} = a_{east} + b_{east}V_{wb,east}$ $P_{wb,west} = a_{west} + b_{west}V_{wb,west}$	(7) (8) (9)
Molar flow rate of air from east and west windboxes	$F_{in,east,i} = F_{in,east,0} + \beta_{east}(V_{wb,east,i} - V_{wb,east,0})$ $F_{in,west,i} = F_{in,west,0} + \beta_{west}(V_{wb,west,i} - V_{wb,west,0})$	(10)

Molar flow rate of air through the gas distributor into the column ($F_{in,i}$) - Molar flow rate before liquid injection ($F_{in,0}$) - Windbox average voltage before the start of injection	$F_{in,i} = F_{in,0} + \beta_{east}\left(V_{wb,east,i} - V_{wb,east,0}\right) - \frac{b_F}{b_{east}}\left(V_{F_i} - V_{F_0}\right) + \beta_{west}\left(V_{wb,west,i} - V_{wb,west,0}\right) - \frac{b_F}{b_{west}}\left(V_{F_i} - V_{F_0}\right)$ $F_{in,0} = \frac{P_{atm}}{R(273.15\ K + T_{bed})} \frac{A}{2}\left(V_{g,east} + V_{g,west}\right)$ $V_{wb,east,0} = \frac{1}{i_{sz}} \sum_{i=1}^{i_{sz}} V_{wb,east,i}$ $V_{wb,west,0} = \frac{1}{i_{sz}} \sum_{i=1}^{i_{sz}} V_{wb,west,i}$	(11) (12) (13) (14)
Molar flow of vaporized liquid in the bed at time *i* ($F_{V,i}$) - The moles of gas accumulated	$F_{V,i} = F_{out,i} - F_{in,i} + n_{accu,i}$ $n_{accu,i} = \left(V - \frac{M_s}{\rho_p}\right)\left(\frac{1}{R(273.14\ K + T_{bed})}\right) b_F\left(V_{F,i} - V_{F,0}\right)$	(15) (16)

For this study, vaporization was characterized by the difference (Δt_{vap}) between the median time of the vapor generation in the bed, i.e. the time at which half of the liquid injected into the bed had vaporized, and the median time for liquid injection, i.e. the time at which half of the liquid had been injected. Similarly, the vapor residence time was characterized by the difference (Δt_{out}) between the median times for vapor flow through the column exit and for vapor generation in the bed. The median times were used instead of the mean times because they were found to be less sensitive to signal noise.

Results and Discussion

Fig. 3 presents the results when a nitrogen pulse was injected at 3 different axial distances Δz from column outlet. All curves represent integrated or cumulative normalized results (F(t)). The first series of curves (shown with solid lines) represent the cumulative volume of injected nitrogen: they are nearly identical. The second series of curves (shown with solid lines) represent the cumulative change in freeboard pressure: they are also nearly identical. The third series of curves (shown with dashed lines) represent the cumulative mole fraction of nitrogen in the column exit: they are greatly dependent on the distance of the pulse injection location from the column outlet. These results demonstrate that it will be possible to use the freeboard pressure transducer to detect instantaneously vaporization anywhere within the bed.

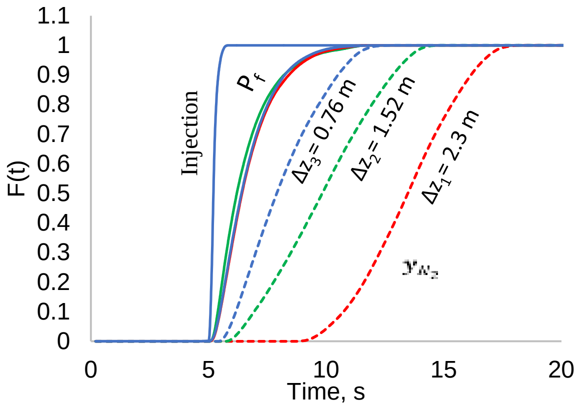

Fig. 3. Results of N_2 pulse injection at 3 axial positions (shown by different colours) from the column outlet; the injection and freeboard pressure (P_f) profiles are shown with solid lines and the N_2 concentration profile is shown with dashed lines.

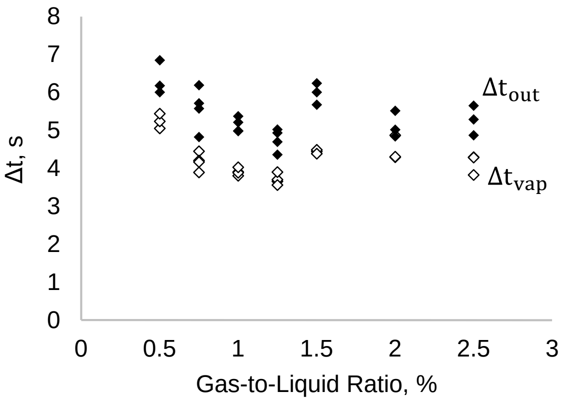

Fig. 4. The impacts of GLR on Δt_{vap} (hollow fill) and Δt_{out} (solid fill);
F_L= 22.5 g/mm^2·s; 1.41 mm nozzle; V_g = 0.3 m/s.

Fig. 4 shows that, as the atomization Gas-to-Liquid ratio (GLR) was increased, both vaporization and residence time intervals initially decreased until a GLR of 1.25 % was reached; when the GLR was increased past 1.25 %, both times increased slightly and stabilized. Portoghese (2007) obtained similar results for liquid-solid contact, although the transitional GLR was 1.5 % instead of 1.25 %, presumably because of a much lower liquid flux through the nozzle tip.

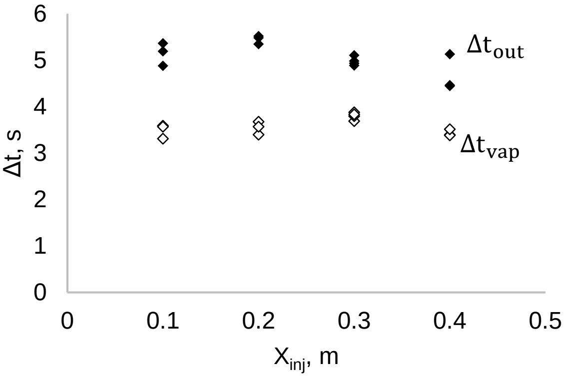

Fig. 5. The impacts of nozzle tip penetration on Δt_{vap} and Δt_{out}; X_{inj} is nozzle tip penetration depth from the wall ($X_{inj,\ wall}$ = 0) into the bed; 2 % GLR; F_L= 22.5 g/mm^2·s; 1.41 mm nozzle; V_g = 0.3 m/s.

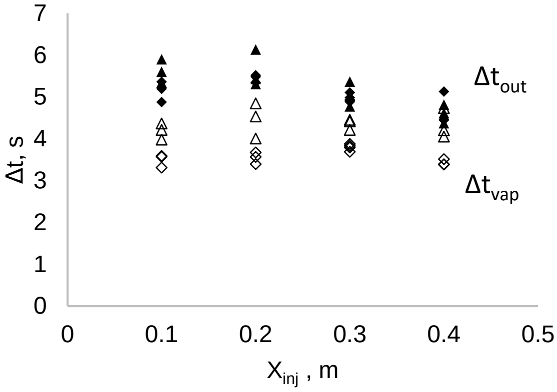

Fig. 6. The impact of injection nozzle scale: dual 1 mm nozzles (triangle) vs. single 1.41 mm nozzle (diamond); 2 % GLR; F_L = 22.5 g/mm^{2}s; m_L = 0.2 kg.

Fig. 4 also shows that the vapor residence time followed the same trends as the vaporization time; although the change in GLR had a negligible impact on column hydrodynamics, a slower vaporization indicated that more agglomerates were formed: these agglomerates would then sink to the bottom of the bed (Bhatti, 2017), generating vapors that spent more time rising through the bed.

Fig. 5 shows how the nozzle tip penetration affected the vaporization and vapor residence times when experiments were performed at a fluidization velocity of 0.3 m/s. The results show that when moving the nozzle tip from near the wall deeper into the bed, the vaporization time at first increased and then dropped when the penetration reached 40 cm. The correlation between local bed hydrodynamics and average free liquid after injection was previously investigated by (Mohagheghi Dar Ranji, 2015). It was shown that the initial liquid distribution on solid particles was a strong function of the bubble volume fraction near the tip of the spray nozzle.

Experiments were conducted with 2 non-interacting 1 mm nozzles operating with the same liquid flux and GLR as the 1.41 mm nozzle and injecting the same total amount of liquid. Fig. 6 compares the results obtained with both systems: dual 1 mm nozzles and a single 1.41 mm nozzle, for various nozzle penetrations. Liquid vaporized faster with the single 1.41 mm nozzle for all nozzle penetrations. These results agree with results obtained with a different method that measured the characteristics of the agglomerates formed when liquid was injected into the fluidized bed (Joness, 2019). On the other hand, although the vapor residence time varied with nozzle penetration, it did not seem affected by the nozzle size.

Conclusion

A novel experimental method successfully monitored the vaporization rate of liquid injected into a fluidized bed by measuring the freeboard pressure and using pressure variations to monitor the flows into and out of the fluidized bed column. The system used a fast response, sturdy oxygen detector to record the concentration of water vapor in the gas outflow and thus, by comparison with the vaporization rate, determined the residence time distribution of vapor in the column. Increasing the atomization Gas-to-Liquid Ratio had a non-monotonic impact on vaporization rate and vapor residence time. Varying nozzle tip penetration resulted in slight variations in vaporization rate and residence time. Finally, experiments showed that injecting the same flowrate of liquid with a large nozzle instead of two small nozzles accelerated vaporization while having a negligible impact on vapor residence time distribution.

Acknowledgments

We gratefully acknowledge scholarship by Indonesia Endowment Fund for Education and funding by the Natural Sciences and Engineering Research Council of Canada (NSERC) and Syncrude Canada Limited.

Notation

A	Bed cross sectional area, m^2	P_{atm}	Atmospheric pressure
a_F	Freeboard pressure calibration constant	R	Ideal gas law constant
a_{east}	East windbox pressure calibration constant	T_{bed}	Average bed temperature, ^oC
a_{west}	West windbox pressure calibration constant	V	Total column volume, m^3
b_F	Freeboard pressure calibration slope	V_g	Average superficial velocity, m/s
b_{east}	East windbox pressure calibration slope	V_{F_i}	Voltage from freeboard pressure transducer, VDC
b_{west}	West windbox pressure calibration slope	V_{F_0}	V_{F_i} for t = 0
F_L	Liquid flux of the injection, g/mm^2·s	$V_{wb,east,i}$	Voltage of pressure transducer in East windbox at time *i*, VDC
i_{ez}	$\frac{t_{end-zero}}{\Delta t}$	$V_{wb,west,i}$	Voltage of pressure transducer in West windbox at time *i*, VDC
$t_{end-zero}$	Chosen time after the end of injection, s	V_g	Average superficial gas velocity, m/s
i_{sz}	$\frac{t_{start-zero}}{\Delta t}$	$y_{O_2,i}$	Mole fraction of oxygen measured by oxygen probe in column outlet at i
$t_{start-zero}$	Chosen time before the start of injection, s	$y_{O_{2,air}}$	Mole fraction of oxygen in air
m_L	Total mass of injected liquid, kg	γ	The amount of gas phase in the column, mole
M_w	Molecular weight of water, 18×10^{-3} mol/kg	Δt	Difference of median time, s
M_s	Mass of bed particles, kg	Δt_{DAQ}	Data acquisition time step, s
N_{H_2O}	Total moles of injected water, mole	ρ_p	Particle density, kg/m^3

References

Ariyapadi S. 2004. Interaction between Horizontal Gas-Liquid Jets and Gas-Solid Fluidized Beds. PhD Thesis. The University of Western Ontario.

Bennett A., Base, T., Chan, E., Kennett, R., Emberley, D., Jonasson, K., & McCracken, T. 2001. Nozzle for Atomizing Liquid in Two Phase Flow, Canadian Patent CA2224615C.

Gray M. 1994. Upgrading of petroleum residues and heavy oils. New York: Marcel Dekker Inc.

Joness AM. 2019. The Effect of Scale on Spray Nozzle Performance. MESc Thesis. The University of Western Ontario.

Leclère K, Briens C, Gauthier T, Guigon P, Bergougnou M. 2004. Experimental measurement of droplet vaporization kinetics in a fluidized bed. 43:693–699.

Li T, Grace J, Bi X, Reid K, Wormsbecker M. 2012. Numerical investigation of FLUID COKING^{TM} units, Part II: Modelling of feed vaporisation. Can J Chem Eng. 90(2):457–471.

Mallory DG, Mehta SA, Moore RG, Richardson S. 2000. The role of the vapour phase in fluid coker cyclone fouling: Part 1. Coke yields. Can J Chem Eng. 78(2):330–336.

Mohagheghi Dar Ranji M. 2015. Impact of Local Bed Hydrodynamics on Jet-Bed Interaction. PhD Thesis. The University of Western Ontario

Owais M, Bhatti I. 2017. Study of Motion of Agglomerates Through a Fluidized Bed. MESc Thesis. The University of Western Ontario.

Portoghese F. 2007. Interactions between Gas-Liquid Jets and Gas-Solid Fluidized Beds. PhD Thesis. The University of Western Ontario.

Prociw N, Briens C, Berruti F, McMillan J. 2018. Effect of spray nozzle attachment geometry on rate of liquid released from agglomerates produced by gas-atomized liquid injection into a fluidized bed. Powder Technol. 325:280–288.

Weber SC. 2009. Agglomerate Stability in Fluidized Beds. PhD Thesis. The University of Western Ontario.

Spouting Regimes of Fine Particles in Fountain Confined Conical Spouted Beds

Mikel Tellabide*, Aitor Atxutegi, Idoia Estiati, Haritz Altzibar, Roberto Aguado, Martin Olazar

Department of Chemical Engineering, University of the Basque Country, P.O. Box 644, 48080 Bilbao, Spain. Tel: +34946015994; Fax: 946013500

*Email: *mikel.tellabide@ehu.eus*

Abstract

The hydrodynamics has been studied in conical spouted beds of fine particles equipped with a novel device called fountain confiner. Characteristic curves have been obtained for the different configurations in order to analyse the behaviour of the system and determine different spouting regimes. Moreover, an optical system fitted with a borescope has been tuned with the aim of tracking particles in the contactor.

Introduction

Nowadays, fluidized beds are commonly used in industrial operations when fixed beds are not suitable. Nevertheless, these contact methods perform poorly when particle size exceeds 1 mm. Given the versatility in the gas flow rate, spouted beds have been successfully applied in operations with coarse particles, those of irregular texture, wide size distribution and sticky ones, whose treatment is difficult using other gas-solid contact regimes (Olazar et al. 1993). Moreover, the recirculation of particles between the spout and annulus is one of the more relevant characteristics of spouted beds, which differs from fixed and fluidized beds.

Conical spouted beds have proven to perform well in many chemical and physical applications, especially in drying (Vieira et al. 2019) and coating (Chen and Kuo 2015). Nevertheless, many of these operations involve the treatment of fine particles and spouted bed have serious limitations in these situations. The gas expands through the whole bed in the form of a big bubble instead of ascending through a well-defined spout in the centre of the bed. This phenomenon is known as slugging (incipient, radial or axial) and is generally accepted as the main cause of instability in spouted beds.

Stable operation is only attained when the ratio between the gas inlet diameter and particle diameter, D_0/d_p, is smaller than 20-30 times the particle diameter (Mathur, K. B., Epstein 1974; Olazar, M. et al. 1992). Higher values of this ratio lead to slugging and highly unstable beds, with these phenomena occurring with either fine or coarse particles.

The usual solution to stabilise the bed is the insertion of any kind of a draft tube (Berghel and Renström 2014; Shuyan et al. 2010): conventional nonporous draft tube, porous draft tube or open-sided draft tube. Nonetheless, draft tubes modify the hydrodynamics and solid circulation flow rate of the system (Epstein and Grace 2011; Ishikura, Nagashima, and Ide 2003), changing the minimum spouting velocity, operating pressure drop, solid circulation patterns, gas distribution and particle cycle times. Moreover, these devices with fine particles lead to very high fountains, and therefore to severe elutriation.

In view of these problems, the use of a fountain confiner is the best solution to treat fine particle beds. This device is a cylindrical tube with the upper outlet closed, and has been successfully applied in gasification (Cortazar et al. 2018) and drying (Estiati et al. 2019). It is placed above the bed and collects the particles from the spout, avoiding their entrainment (Altzibar et al. 2017). Moreover, the use of this device allows increasing the upper limit of the residence time of the gas and improves gas-solid contact in the bed.

The main aim of this work is to study the hydrodynamics and performance of the fountain confined spouted bed made up of fine particles in two situations, i.e., without draft tube and with draft tubes. Runs have been carried out following an experimental design in order to allow a reliable data analysis.

Experimental

The pilot plant consists of a blower, flowmeter, pressure drop gauge, contactor, filter and cyclone. The blower has a power of 5.5 kW and supplies the air required for spouting the beds in the contactor. The gas flow rate is measured by means of a thermal mass flowmeter in the 0-600 Nm^3/h range. The blower supplies a constant flow rate, and the flow that enters in the contactor is controlled by acting on a motor valve that reroutes the remaining air to the outside, or changing the frequency of the blower motor when strict control is necessary. Pressure measurements are carried out by means of two pressure taps, which are connected to the contactor input and output. Moreover, a cyclone and a filter are connected in series in order to separate the solids dragged by the air. The cyclone separates the coarser particles from the air, whereas the filter traps the fine ones.

A conical contactor made of polymethyl methacrylate has been used. Fig. 1a shows the geometric factors of this contactor. The dimensions of the contactor are the following: column diameter, D_c, 0.36 m; contactor angle, γ, 36º; height of the conical section, H_c, 0.45 m; gas inlet diameter, D_0, 0.04 m; and base diameter, D_i, 0.068 m. The static bed height used is, H_0, 0.20 m.

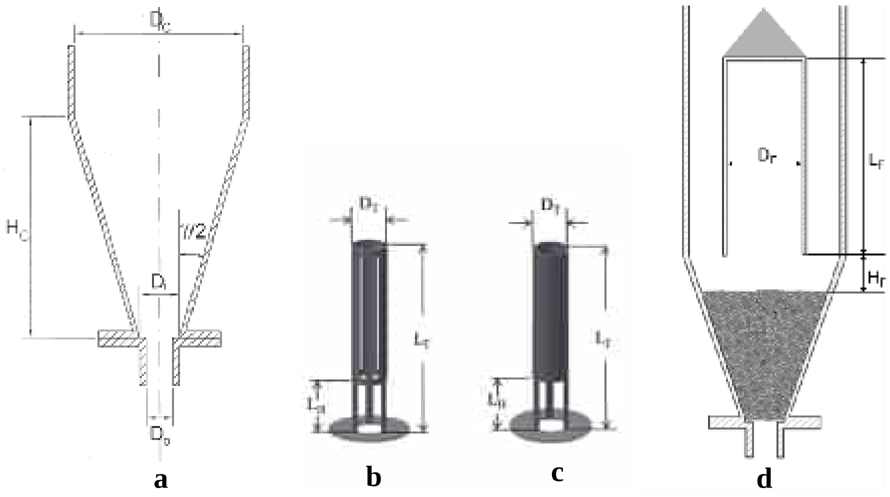

Fig. 1. Geometric factors of the conical contactor (a), open-sided draft tube (b), nonporous draft tube (c) and fountain confiner (d).

Two different types of draft tubes have been used in this study: open-sided and nonporous draft tubes. Figs. 1b and 1c show a scheme of both types of internal devices.

In the case of the nonporous draft tube, the main parameters governing hydrodynamics are the height of the entrainment zone (distance between the gas inlet nozzle and the lower end of the tube), L_H, 0.07 m; and the tube diameter, D_T, 0.04 m. The length of the tube is the same as the bed height, L_T, 0.20 m. On the other hand, the open-sided draft tube has part of its lateral surface area opened in order to allow solid cross-flow from the annulus into the spout and gas diversion from the spout into annulus along the whole length of the spout. Its main design parameters are aperture ratio, 57%; and tube diameter, D_T, 0.04 m. As in the case of the nonporous draft tube, its length is the same as the bed height, L_T, 0.20 m.

Moreover, in order to operate with fine particles, a novel device called fountain confiner has been used (Fig. 1d). It is a cylindrical tube made of polyethylene terephthalate (for allowing visual observation) with the upper end closed to avoid gas and solid leaving the contactor through this device and force them to describe a downward trajectory. The confiner forces both the fountain to adopt the shape of the confiner and the air to make a longer trajectory. Therefore, operation is possible at high values of the gas flow rate without loss of material in the bed and ensuring high solid circulation flow rates. Thus, it enhances the gas-solid contact. The diameter and length of the fountain confiner are, D_F, 0.20 m; and L_F, 0.50 m. Finally, the distance between the bed surface and the lower end of the confiner, H_F, is 0.06 m.

Furthermore, an optical system has been used to track particles inside the contactor. As shown in Fig. 2, the optical system is composed of a camera, borescope, camera displacement system and a light source. The camera is an *AOS S-PRI* model with a maximum recording resolution of 900x700 and a range of recording velocities of up to 16500 frames per second with reduced resolution. The borescope and the displacement device are described in a previous paper (Atxutegi et al. 2019).

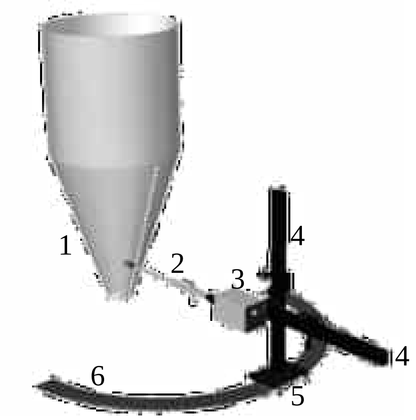

Fig. 2. Image recording system: (1) Contactor, (2) borescope, (3) camera, (4) straight sliders, (5) sliding platform, and (6) perimeter slider.

In the annular zone, particles tend to move in clusters and individual particle rotations are negligible, which means that the relative displacement of one particle from the other is minimum. Therefore, Farneback pyramidal algorithm (Farnebäck 2000) from OpenCV has been found to be especially suitable to average edge movements, assuming the lightening conditions are kept steady enough and that particle rotations are kept to a bare minimum. More details about image processing are described in a previous paper (Atxutegi et al. 2019).

The material used is building sand. The average size of the sand is 0.246 mm and its density 2387 kg/m^3.

Results and discussion

Characteristic curves of fountain confined conical spouted beds

Unstable regime is obtained operating with fine particles without draft tube due to the great value of the ratio between the gas inlet diameter and particle diameter. Nevertheless, the use of a fountain confiner makes possible the treatment of fine particles without any draft tube. Fig. 3 shows the characteristics curves (pressure drop vs. air velocity) for different configurations (without draft tube, open-sided draft tube and nonporous draft tube).

As shown in Fig. 3, different curves are obtained depending on the configuration used, but all of them have a similar shape up to the peak pressure drop. Thus, pressure drop increases almost linearly with air velocity to the peak value. In the case of no draft tube and open-sided draft tube, three different regimes are obtained. At high air velocities bubbles and slugging appear, and pressure drop increases as air velocity is increased. Thus, this regime has been termed “bubbling spouting”. As air velocity is decreased pressure drop decreases linearly until a point in which pressure drop levels off and a nice stable spouting is attained for no draft tube systems. Using open-sided draft tube, pressure drop remains constant for a range and then, increases steadily until it smoothly peaks. This range corresponds to stable spouting with a high solid circulation flow rate in the annulus, and therefore it has been termed “full spouting” regime. Finally, as air velocity is decreased pressure drop remains constant in systems without draft tube and decreases using open sided draft tube for a range of velocities until a slight decrease leads to the fountain collapse, and so to static bed. This point corresponds to the minimum spouting velocity. The range between the minimum spouting velocity and the full spouting velocity has been term “spouting regime”.

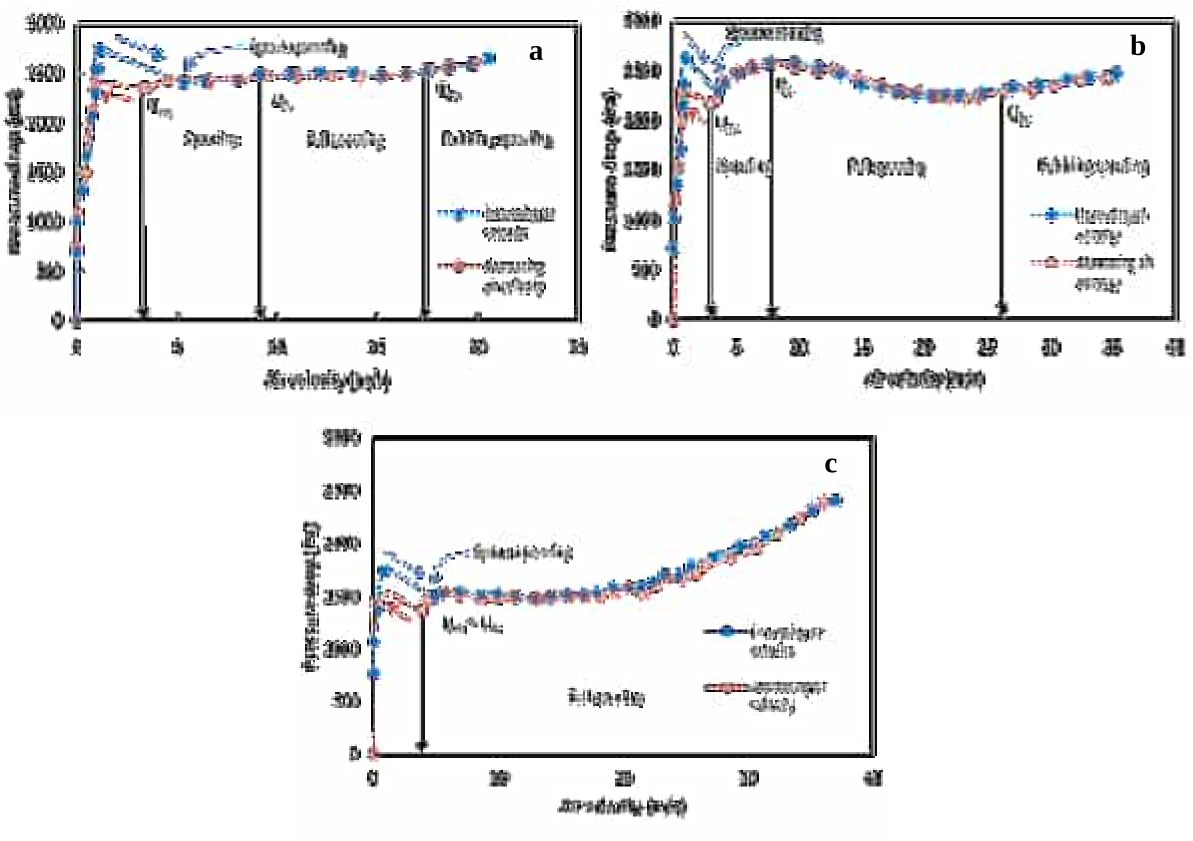

Fig. 3. Characteristic curves for the fountain confined conical spouted bed without draft tube (a), with open-sided draft tube (b) and with nonporous draft tube (c).

On the other hand, using nonporous draft tube (Fig. 3c) there is a stable spouting regime all the way from the minimum spouting velocity to very high velocities. Pressure drop remains constant for a range above the minimum spouting velocity, but subsequently increases according to a linear trend.

As shown in Fig. 3, great differences are observed in the characteristic curves depending on the configuration used. Thus, in the systems with no draft tube or open-sided draft tube, the spouting regime is delimited by the minimum velocities for spouting and full spouting. The full spouting regime ranges from the end of the spouting regime to the beginning or the bubbling spouting regime. Nevertheless, nonporous draft tube systems lead to only the full spouting regime, which is established once the minimum spouting velocity is overcome.

Particle velocity in the annulus

An optical system fitted by a borescope was used in order to measure particle velocity in the annulus. Fig. 4 shows the results obtained at minimum spouting velocity for the system studied.

As shown in Fig. 4, particles descending through the annular zone follow an oscillatory trend with time. In fact, particles are accelerated and decelerated all the time instead of descending with a constant acceleration along the whole annulus height. When no draft tube is used (Fig. 4a) or an open-sided draft tube is used (Fig. 4b), the ascending velocity may be even higher than the descending one in certain radial positions in the annulus. Nonetheless, when nonporous draft tube systems are used (Fig. 4c), although the trend is oscillatory, the particles are descending all the time. Moreover, there is a short stop of the particles and this is shown in all the different configurations. This means that the whole system is stopped during a short time in each velocity cycle. Thus, using fine particles the system operates at a given frequency depending on the configuration and air velocity. In our system, they are 6.87 Hz for both no draft tube and open sided draft tubes, and 6.49 Hz for nonporous draft tubes.

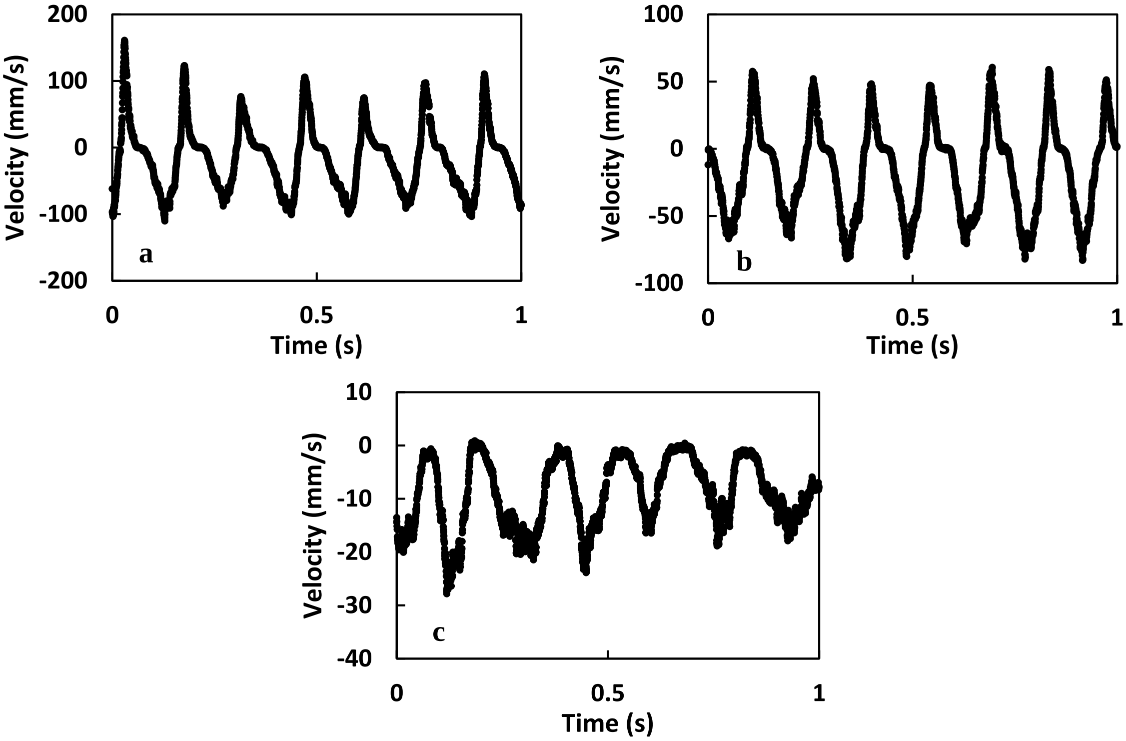

Fig. 4. Particle vertical velocity in the annulus for systems without draft tube (a), open-sided draft tube (b) and nonporous draft tube (c).

Furthermore, the highest particle velocities (160-(-110) mm/s) are obtained for systems without draft tube (Fig 4a), the lowest for those equipped with nonporous draft tubes (0-(-27) mm/s) and, finally, open-sided draft tubes (60-(-60) mm/s) lead to intermediate values. This is due to both the great gas percolation in the annulus and the high values of the minimum spouting velocity for systems without draft tube.

Conclusions

The fountain confiner device has proven to stabilize beds made up of fine particles without any draft tube. This device is an essential element for the scaling up of the spouted bed technology at industrial level.

New different regimes have been attained with fine particles when a fountain confiner is used. In the case of no draft tube and open-sided drat tube, three different regimes are obtained, with two being stable and one unstable. Nevertheless, nonporous draft tubes lead to only one stable regime.

Furthermore, particles show an oscillatory trend in the annulus, with velocities being negative (descending) and positive (ascending) when no draft tube or an open-sided draft tube are used. Nevertheless, using nonporous draft tubes, particles only show negative velocities, with their magnitude oscillating between zero to a given descending value.

Acknowledgment

This work has received funding from Spain’s Ministry of Economy and Competitiveness (CTQ2016-75535-R (AEI/FEDER, UE)) and the European Commission (HORIZON H2020-

MSCA RISE-2018. Contract No.: 823745). M. Tellabide thanks Spain’s Ministry of Education, Culture and Sport for his Ph.D. grant (FPU14/05814). A. Atxutegi is grateful for this Ph.D. grant from the University of the Basque Country UPV/EHU (PFI15-2017). I. Estiati thanks the University of the Basque Country for her postgraduate grant (ESPDOC18/14).

Notation

γ	Contactor angle, °
D_0	Gas inlet diameter, m
d_p	Average particle diameter, m
D_C	Column diameter, m
D_F	Diameter of the fountain confiner, m
D_i	Contactor base diameter, m
D_T	Draft tube diameter, m
H_0	Static bed height, m
H_C	Height of the conical section, m
H_F	Distance between the bed surface and the confiner, m
L_F	Height of fountain confiner, m
L_H	Height of the entrainment zone of the nonporous draft tube, m
L_T	Height of the draft tube, m

References

Altzibar, H., I Estiati, G Lopez, Juan F Saldarriaga, R Aguado, J Bilbao, M Olazar. 2017. “Fountain Confined Conical Spouted Beds.” *Powder Technology* 312:334–346.

Atxutegi, A., M Tellabide, G Lopez, R Aguado, J Bilbao, M Olazar. 2019. “Implementation of a Borescopic Technique in a Conical Spouted Bed for Tracking Spherical and Irregular Particles.” *Chemical Engineering Journal* 374 (February): 39–48. (10.1016/j.cej.2019.05.143).

Berghel, J., R Renström. 2014. “An Experimental Study on the Influence of Using a Draft Tube in a Continuous Spouted Bed Dryer.” *Drying Technology* 32(5):519–27.

Chen, WY, HP Kuo. 2015. “Surface Coating of Group B Iron Powders in a Spouted Bed.” *Procedia Engineering* 102:1144–49. (10.1016/j.proeng.2015.01.238).

Cortazar, M., G Lopez, J Alvarez, M Amutio, J Bilbao, M Olazar. 2018. “Advantages of Confining the Fountain in a Conical Spouted Bed Reactor for Biomass Steam Gasification.” 153:455–63.

Epstein, N., J Grace. 2011. *Spouted and Spout-Fluid Beds Fundamentals and Applications*. Cambridge.

Estiati, I., M Tellabide, JF Saldarriaga, H Altzibar, M Olazar. 2019. “Influence of the Fountain Confiner in a Conical Spouted Bed Dryer.” *Powder Technology* 356:193-199 (10.1016/j.powtec.2019.08.005).

Farnebäck, G. 2000. “Fast and Accurate Motion Estimation Using Orientation Tensors and Parametric Motion Models.” *Proceedings - International Conference on Pattern Recognition* 15(1):135–39.

Ishikura, T., N Hiroshi, I Mitsuharu. 2003. “Hydrodynamics of a Spouted Bed with a Porous Draft Tube Containing a Small Amount of Finer Particles.” *Powder Technology* 131(1):56–65.

Mathur, KB, and N. Epstein. 1974. *Spouteds Beds*. Academic.

Olazar, M., MJ San Jose, AT Aguayo, JM Arandes, J Bilbao. 1992. “Stable Operation Conditions for Gas Solid Contact Regimes in Conical Spouted Beds.” *Industrial & Engineering Chemistry Research* 31:1784–92.

Olazar, M., MJ San José, FJ Peñas, AT Aguayo, J Bilbao. 1993. “Stability and Hydrodynamics of Conical Spouted Beds with Binary Mixtures.” *Industrial and Engineering Chemistry Research* 32(11):2826–34.

Shuyan, W., H Zhenghua, S Dan, L Yikun, W Lixin, W Shuai. 2010. “Hydrodynamic Simulations of Gas-Solid Spouted Bed with a Draft Tube.” *Chemical Engineering Science* 65(4):1322–33. (10.1016/j.ces.2009.09.060).

Vieira, GNA., M Olazar, JT Freire, and FB Freire. 2019. “Real-Time Monitoring of Milk Powder Moisture Content during Drying in a Spouted Bed Dryer Using a Hybrid Neural Soft Sensor.” *Drying Technology* 37(9):1184–90. August 20, 2019.

EVALUATION OF THE CFD CODE OPENFOAM FOR THE EXTRAPOLATION OF CIRCULATING FLUIDIZED BED HYDRODYNAMIC WITH GROUP A PARTICLES

Benjamin Amblard[1*], Sina Tebianian[1], R.Cocco[2] Thierry Gauthier[1]

[1]*IFP Energies nouvelles, BP3, Solaize, 69360, France*
[2]*PSRI, 4201 West 36th Street, Building A, Chicago, IL, USA*

*Email: *benjamin.amblard@ifpen.fr*

Abstract

In this study, we evaluate the capability of using the open source CFD software OpenFoam for the simulation of fluidized beds with Geldart group A powders at different scales. For this purpose, two focused specific experiments are used as a reference:

- First a 20 cm turbulent fluidized bed at IFPEN, operating at a velocity of with two gas injection configurations (homogeneous and heterogeneous), where bed density and local volume fraction were carefully measured
- Then a 90 cm fluidized bed at Particulate Solid Research Incorporation (PSRI), operating at three fluidization velocity (30 cm/s, 60 cm/s, and 85 cm/s) where bed density and particle entrainment were measured.

In order to simulate the experiments, it is first necessary to adjust the gas-solid flow CFD model. Thus, a drag law was adjusted based on the comparison of the CFD results with the experimental data of the 20 cm fluidized bed. The extrapolation of this drag law at larger scale is then investigated by first using a coarser mesh for the 20 cm fluidized bed simulation. In a second step, the 90 cm fluidized bed is well simulated using the same mesh size than the coarser mesh of the 20 cm fluidized bed simulation. Therefore, this work highlights a methodology to evaluate the “scale-up ability” of CFD codes.

Introduction

The Research and Development for new multiphase flow technologies and processes in the field of energy still face challenging scale-ups. The main difficulty remains in the extrapolation of lab-scale physical phenomena to industrial applications. However, minimizing the risk of extrapolation is mandatory when developing such processes and technologies (Gauthier *et al.*, 2000). Extrapolation relates to first the understanding of physical phenomena at accessible scales through dedicated and focused experiments. In a second step, modeling is utilized to transpose observation from lab scale to an industrial perspective. This extrapolation process is particularly difficult for gas-solid flows encountered in circulating fluidized bed processes and technologies. In this field, physical phenomena and corresponding reactor technologies are complex.

In this context, CFD tools are increasingly used for the understanding, the development, and the extrapolation of processes and technologies (V. Ranade, 2001). However, concerning CFD for circulating fluidized beds, there is still a great effort on-going for understanding and modelling the fundamental physics of gas-particles and particles-particles interactions (Ozel *et al.*, 2013). We therefore, face a situation where CFD tools are essentials for extrapolation purposes (Amblard *et al.*, 2017), but their prediction capacities need to be evaluated for each configuration simulated in order to check the validity and put into perspectives the simulation results. It is therefore of great importance to better understand how to use CFD properly to assist extrapolation through relevant strategies of simulation.

When simulating circulating fluidized beds in a Eulerian/Eulerian frame, the drag and particle-particle interaction sub-grid models are the primary source of concern. These sub-grid models are usually adapted to fit experiments for a given configuration with specific operating conditions. Yet, it is important to evaluate how these models behave when they are used in simulations at a larger scale with larger mesh cell sizes. In this study, this issue is investigated considering physics and sub-grid models available in the open source CFD code OpenFoam (Engen, 2016), to simulate systems in a perspective of scale-up. For this purpose, experiments with Geldart Group A particles are used to evaluate the hydrodynamic prediction of the simulations. The CFD code response at different scales is studied investigating the effect of mesh size and operating conditions to evaluate the “scaling-up” abilities of the simulation tool.

Experimentation

20 cm fluidized bed

Fig.1 presents the 20 cm fluidized bed cold flow mock-up at IFPEN used for the experimentation (B.Amblard et al, to be published). It consists of a fluidized bed connected to a cyclone to return entrained particles back to the bed through a dipleg and an automatic L-Valve. Two air injections are available with first a porous plate at the bottom of the bed and second a jet injection located within the bed. The particles used for the experiments are (Amblard *et al.*, 2017) Geldart group A particles with a grain density of 1260 kg/m^3 and a mean diameter of 75 microns. The mass of particles is around 17 kg.

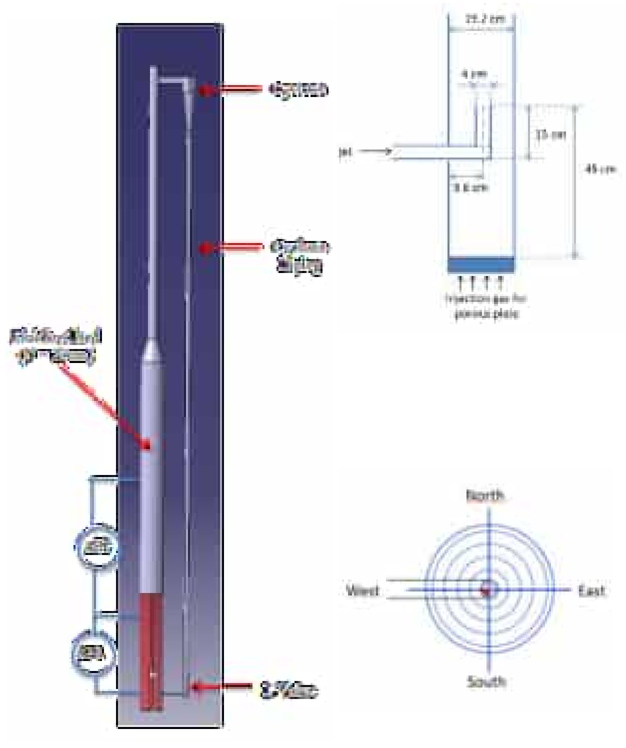

Fig. 1.: 20 cm fluidized bed cold flow mock-up

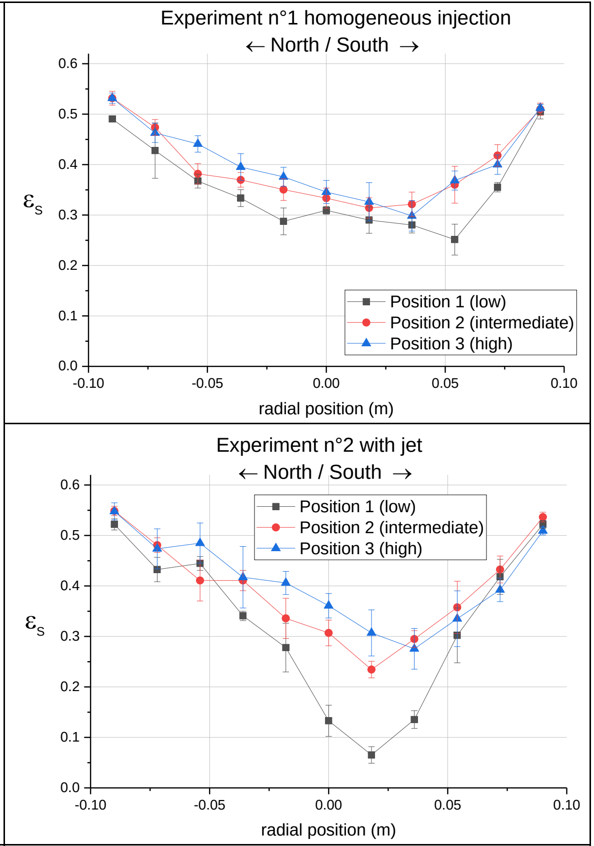

Fig. 2.: Local solid volume fraction profiles

The bed density and height are measured thanks to differential pressure probes as shown in Fig.1. Local solid volume fraction profiles are measured with optical probes into two directions (West/East and North/South) for three different elevations at respectively 50 cm, 55 cm and 60 cm from column bottom. These three elevations are named respectively “Position 1 (low)”, “Position 2 (intermediate)” and “Position 3 (high)”. Two different experiments are carried out at a superficial gas velocity of 0.7 m/s but with a different gas injection configuration. In experiment n°1, all the gas is injected through the bottom of the column. In experiment n°2, a small part if the gas is injected through the bottom and the rest through the jet located within the bed. The interest of injecting gas through the jet is to create a mal-distribution within the bed. It will serve as a good validation case for the CFD models.

Table 1 presents the two experiments operating conditions as well as the bed density measured with the differential pressure probes.

Table 1: Experiments operating conditions and bed density measured

Experiment	Air Bottom injection (Nm^3/hr):	Air Jet injection (Nm^3/hr):	Superficial gas velocity (m/s)	Bed density (kg/m^3)
n°1	66	0	0.7	504
n°2	16.5	49.5	0.7	631

One can see from Table 1 that in experiment n°2 with the gas injection through the jet, the bed density is higher. The result makes sense and is representative of a mal-distribution where part of the gas is flowing faster in the jet and by-passes the bed (Allan S. Issangya *et al.*, 2007).

Local solid volume fractions profiles were obtained from optical probe signals using a reconstruction method presented in (Schweitzer *et al.*, 2001). Fig. 2 presents the local solid volume fraction profiles for experiment n°1 and experiment n°2 in the North/South direction.

One can observe from Fig. 2 that with the homogeneous injection the solid volume fraction profiles obtained are elliptical and rather symmetrical with respect to the column axis. This result is similar to the one obtained by (Schweitzer et al., 2001). Then, one can also see from that the jet effect seems to dissipate at Position 3 where the profiles obtained are similar to the ones presented in Fig. 2 with the homogeneous injection.

90 cm fluidized bed

Fig. 3 presents the 90 cm fluidized bed cold flow mockup configuration at PSRI. Fluidizing gas is injected through an injector with nozzles located at the bottom of the column Particles entrained out of the bed are collected with a cyclone and are re-injected into the bed through a dipleg and an automated L-Valve. The solid used for the experiments are Geldart Group A particles with a grain density of 1490 kg/m^3 and a mean diameter of 75 microns. The total mass of particles is around 1800 kg. Three experiments are carried out for different gas superficial velocities of respectively 0.3 m/s, 0.6 m/s and 0.85 m/s. Density profiles are measured with differential pressure probes located on the side of the column, results are shown in Fig. 4.

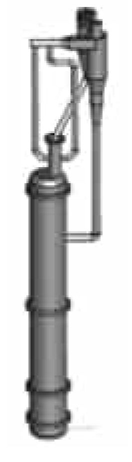

Fig. 3.: 90 cm fluidized bed

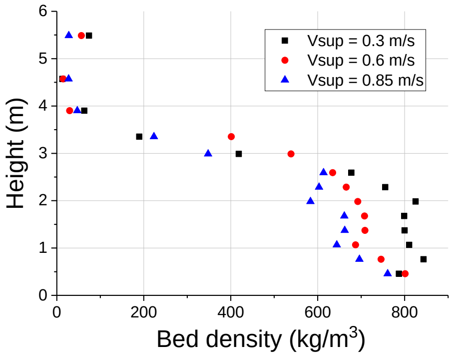

Fig. 4.: Bed density profiles

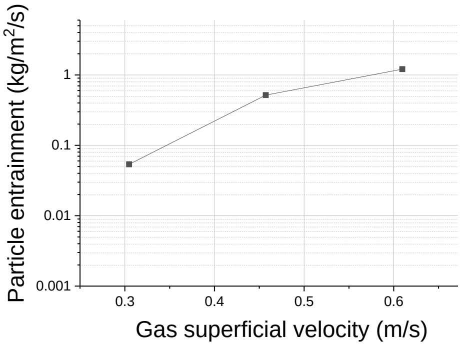

Fig. 5.: Particles entrainment versus superficial gas velocity

Particle entrainment flux is also measured by interrupting the L-Valve and measuring the accumulation of particles within the dipleg. Results are also shown in Fig. 5.

CFD simulations

CFD simulations were carried out with the Openfoam solver “twoPhaseEulerFoam” v1712. It consists of gas-particles solver where both phases are considered in an Eulerian continuous frame. Mass and momentum equations are therefore solved for both phases using the finite volume method. A k-ε turbulence model is considered for the gas phase while the kinetic theory with a granular temperature equation is applied to model the particle-particle interactions of the solid phase. For more details about the equations, readers are invited to read the following papers (Engen, 2016; Peltola, 2019). The gas-particle interaction is first modelled with the Gidaspow drag correlation (Gidaspow, 1994; Peltola, 2019): Simulations are run in a unsteady mode, results presented are averaged once the simulation is considered in a steady state (parameters of interested do not evolve with simulation time anymore). However, as shown below it was then necessary to adjust drag force.

20 cm column simulations

The mesh used has 500000 hexahedral cells with a size of 5 mm. The first simulation was run for experiment n°1 with homogeneous gas injection. No dense phase was predicted by the simulation with the Gidaspow drag correlation. This result is typical of Geldart Group A particles simulations in turbulent regime where drag is overestimated with the default Gidaspow drag law (Li *et al.*, 2009; Ozel *et al.*, 2013). In a second simulation, a drag law similar to the one developed by (Li *et al.*, 2009) was adjusted. The assumption is that cluster of particles are formed in the bed and equivalent cluster diameters are used at specific solid volume fraction to compute the drag force. In this study, the clustering approach shown in Table 2 was chosen after a parametric investigation carried out based on experiment n°1 results.

Table 2: Clustering approach from parametric investigation.

Solid Volume fraction	Equivalent diameter
0.62 to 0.08	500
0.08to 0.01	150 + multiplier 0.31
0.01 to 0	75

It is important to point out that with this approach the Gidaspow drag law is still used only the equivalent diameter is modified according to the solid volume fraction. Fig. 6 and Fig. 7 present the comparison between experiments and simulation for the solid volume fraction profiles. Table 3 presents the same comparison for the bed density.

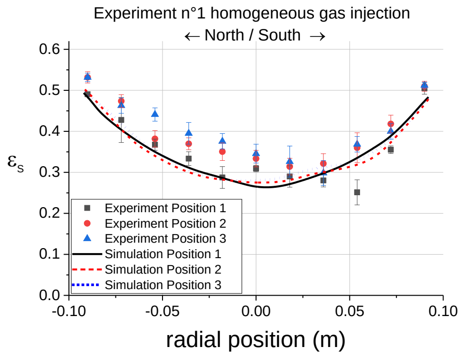

Fig. 6.: Comparison between experiment n°1 and simulation results

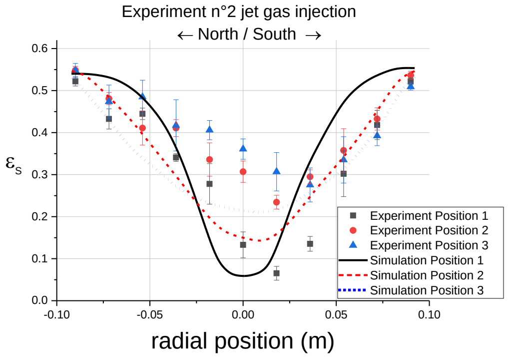

Fig. 7.: Comparison between experiment n°2 and simulation results

Table 3: Bed density comparison between experimentation and simulation.

	Experimentation	Simulation	Relative error (%)
Experiment n°1	504	482	4.4
Experiment n°2	631	666	5.5

One can see that the simulations catches the change of bed density between experiment n°1 and experiment n°2 with a relative error lower that 6% for both cases. Concerning the solid volume fraction profiles, the simulations also catches the evolution between both experiments. For experiment n°1, the simulation predicts quantitatively the different profiles. For experiment n°2, the simulation prediction is less quantitative but the trend with the jet attenuation is well captured.

At this point, simulations results were considered satisfactory. The second step was then to evaluate how this CFD model could be used for extrapolation. For this purpose, the same simulations were carried out with a coarser hexahedral mesh of 20000 cells with a size of about 2 cm. Results are presented in Fig. 8 and Fig. 9 for the solid volume fraction profiles and in Table 4 for the bed density.

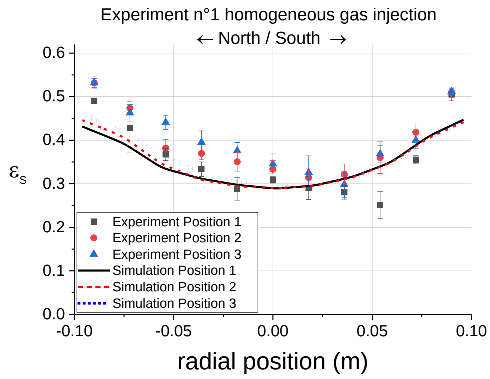

Fig. 8.: Comparison between experiment n°1 and simulation with coarse mesh results

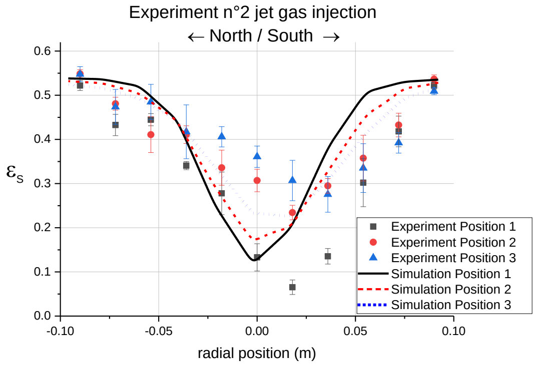

Fig. 9.: Comparison between experiment n°2 and simulation with coarse mesh results

Table 4: Bed density comparison between experimentation and simulation with coarse mesh.

	Experimentation	Simulation	Relative error (%)
Experiment n°1	504	510	1.1
Experiment n°2	631	668	5.9

One can see that with the coarser mesh of 20000 cells, the difference of density and solid volume fraction profile is still captured by the CFD model. Profiles predictions are less precise quantitatively compared with the simulation with a finer mesh, overall bed density is still well predicted. The CFD model was considered satisfactory for such a mesh cell size and it was then decided to apply the same model with a similar mesh size on the simulations of the 90 cm fluidized bed.

90 cm column simulations

Using the same model as before, the mesh cell size of 2 cm was used for this simulation for a total mesh cell number of 700000 cells. Results are presented in Fig. 10 and Fig. 11 with the comparison between experiments and simulation for the bed density profiles and the particles entrainment.

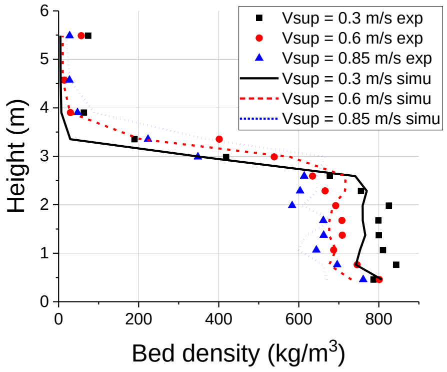

Fig. 10.: Bed density profiles comparison

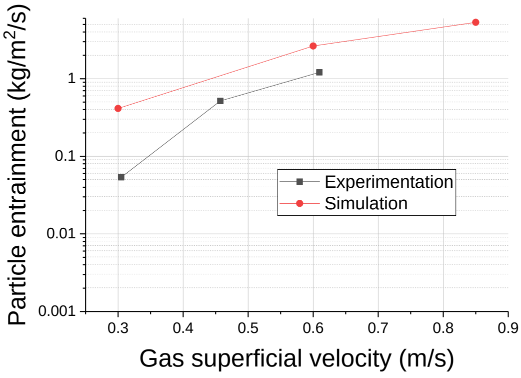

Fig. 11.: Particles entrainment comparison

One can see that the density profiles evolution between the different experiments is well captured by the CFD model. The overall bed density is well predicted with a relative error lower than 5%. Entrainment is over-predicted by the simulation but the trend versus the superficial gas velocity is well captured.

Conclusions and discussions

A method evaluating the “scale-up” ability prediction of the opensource CFD code Openfoam is presented. For this purpose, a drag law is first adjusted using a fluidized bed experiment at lab scale for a given simulation mesh cell size. The CFD model is then used with success for predicting different operating conditions at lab scale. A coarser mesh is then used on the same simulations to evaluate the cell size effect for extrapolation purposes. The results show satisfactory results with the coarse mesh. Finally, the CFD model is applied on a large scale fluidized bed with the same cell size than the lab scale simulation with coarse mesh. The results show good prediction of the bed density while the entrainment is over-estimated but the trend versus the gas superficial velocity is respected. It has to be pointed out that the same approach was applied to some other CFD codes that did not perform as well.

Different points can be discussed:

- First, the drag law adjusted in this work is rather simplistic and it is not claimed to be universal. The idea presented in this work is that when using CFD for extrapolation purposes where coarser mesh has to be used for computing limitations reasons, it is important to assess the effect of the coarse mesh through a relevant simulation strategy.
- Second, one can wonder about the prediction of other hydrodynamic parameters that have not been studied in this work such as the average particle velocities, the mixing time, the gas velocity, … Further model refinement is probably required to better capture these parameters. Similar methodologies than the one developed in this work are then required to investigate the ability of the CFD codes to predict these parameters at different scales, the difficulty being that experimental validations are challenging for such local physical parameters.

References

Allan S. Issangya, Ted Knowlton and S. B. Reddy Karri (2007), “Detection of Gas Bypassing due to Jet Streaming in Deep Fluidized Beds of Group A Particles”, *The 12th International Conference on Fluidization,* 2007.

Amblard, B., Singh, R., Gbordzoe, E. and Raynal, L. (2017), “CFD modeling of the coke combustion in an industrial FCC regenerator”, *Chemical Engineering Science*, Vol. 170, pp. 731–742.

Amblard, B. and M.Troiano, “Experimental characterization and CFD simulations of gas maldistribution relevant to fluidized beds of Group A particles”, submitted to powder technology journal in November 2019.

Engen, T. (2016), “CFD analysis of gas-particle flow in a scaled circulating fluidized bed”, *master thesis*, master thesis.

Gidaspow, D. (1994), *Multiphase flow and fluidization: Continuum and kinetic theory descriptions*, Academic Press, London.

Li, P., Lan, X., Xu, C., Wang, G., Lu, C. and Gao, J. (2009), “Drag models for simulating gas–solid flow in the turbulent fluidization of FCC particles”, *Particuology*, Vol. 7 No. 4, pp. 269–277.

Ozel, A., Fede, P. and Simonin, O. (2013), “Development of filtered Euler–Euler two-phase model for circulating fluidised bed. High resolution simulation, formulation and a priori analyses”, *International Journal of Multiphase Flow*, Vol. 55, pp. 43–63.

Peltola, J. (2019), “MSc Thesis Juho Peltola - Dynamics in a Circulating Fluidized Bed: Experimental and Numerical Study”.

Schweitzer, J.-M., Bayle, J. and Gauthier, T. (2001), “Local gas hold-up measurements in fluidized bed and slurry bubble column”, *Chemical Engineering Science*, Vol. 56 No. 3, pp. 1103–1110.

Gauthier, T., J.Bayle and P.Leroy (2000), “FCC: Fluidization Phenomena and Technologies”, *Oil & Gas Science and Technology – Rev. IFP,,* 2000.

Ranade, V. (2001), “Computational Flow Modeling for Chemical Reactor Engineering”, Volume 5.

THE DYNAMIC CHARACTERISTICS OF GAS SOLID FLOW IN CFB FULL-LOOP

Hao Kong, Man Zhang, Yi Zhang，Jiayi Wuang, Junfu Lyu, Hairui Yang*

Key Laboratory for Thermal Science and Power Engineering of Ministry of Education, Department of Thermal Engineering, Tsinghua University, Beijing 100084

*Email: *yhr@mail.tsinghua.edu.cn*

Abstract

Nowadays, the circulating fluidized bed (CFB) boiler has become one of the most widely used clean coal combustion technologies due to its wide fuel adaptability, high combustion efficiency and low emission control. At the same time, it has excellent load flexibility, which can adapt the peak regulation required by the power grid, especially with more and more renewable power connecting to the grid. So, it is necessary to study the dynamic characteristics of the CFB boiler, which depends on the mass and pressure balance between the furnace and external loop. In this paper, the dynamic test was carried out on the CFB cold test rig with a riser height of 10 m and a square section of $0.1\times0.1\text{m}^2$. In the experiment, the actual peak regulation condition was simulated by rapidly changing the fluidizing air velocity in the furnace and aerated air velocity in the loop seal, respectively. The solid circulating rate and bed pressure drop of each part as a function of time was obtained with an on-line measuring technique. Also, the factors affecting the time lag between the peak regulation conditions and mass balance reached were discussed.

Introduction

With the rapid economic development in recent years, China's total energy consumption is also constantly increasing. Although the proportion of raw coal in total energy consumption decreases, it can still reach about 60% of the total [1], which proves that coal will remain as the resource for China's energy consumption in near future. At same time, clean energy utilization such as wind energy and solar energy increases quickly in recent years, acting more role in the total power generation. However, such energy power is greatly affected by the environment and fluctuates. To encourage clean energy power to the power grid, it is necessary to peak the controllable coal power generation.

In comparison, circulating fluidized bed (CFB) boiler, one of the most widely used clean coal technologies due to its wide fuel adaptability, high combustion efficiency and low coast emission control, has the potential preference in peak regulation because of the excellent load flexibility.

While, CFB boiler still has limits to meet the fast speed of peak regulation. Because of the complicated structure and huge materials, there will be a certain time lag with peak requirement. Therefore, how to realize the rapid peaking of the CFB boiler becomes a key point. Besides, frequent CFB boiler peaking will change the flow state, pressure and redox atmosphere in the furnace, which will have a great impact on the combustion of CFB boilers [7]. So, it is necessary to study the dynamic characteristics of gas solid flow in CFB full-loop, especially the mass balance between the furnace and standpipe.

At present, most studies are focusing on control, combined with field practice and some debugging, to achieve rapid peak regulation and deep peak regulation of CFB[8-10]. Some numerical simulation works investigated the dynamic gas-solid flow characteristics in CFB full-loop [11-15]. Fewer studies focus on the characteristics of gas solid flow between the furnace and out loop during the dynamic process.

In this paper, the dynamic test was carried out in the CFB cold test rig with a riser height of 10 m and square section of 0.1×0.1m^2. In the experiment, the actual peak regulation condition was simulated by rapidly changing the fluidizing air velocity in furnace and looping air velocity in loop seal, respectively. The solid circulating rate and bed pressure drop of each part as a function of time were obtained with on-line measuring technique. Also, the factors affecting the time lag between the peak regulation conditions and mass balance were discussed.

Experiment Description

The circulating fluidized bed cold test rig is shown in Fig. 1. The riser section is more than 10m high. The two-stage cyclones have equivalent diameters of 160 mm and 200 mm. A hopper is provided above the loop seal return valve for storing the material, and the bed pressure is stabilized by enlarging inner diameter of the position.

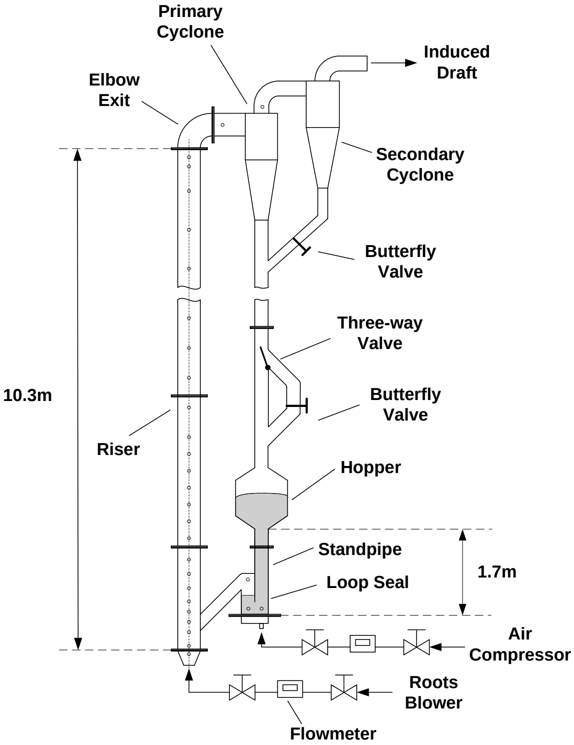

Fig.1. Schematic diagram of the experimental device

The primary air fan is a Roots blower. The aerated air uses compressed air to ensure a stable flow. Besides, the riser outlet is designed with a smooth elbow, which is a typical resistance component and can be used to calibrate the relationship between flow resistance and circulation flow rate.

In the experiment, the gas flow rates are measured with a target flowmeter, and the solid mass fraction is measured with optical fiber probe. Along the full loop, 53 pressure sensors are installed and output the standard signal of 4-20 mA. On-line measurement of flow, pressure and solid mass fraction is achieved.

In the actual CFB boiler peak regulation process, the boiler load is adjusted mainly by changing the fluidizing air velocity and feeding coal rate. Also, the aerated air will affect the mass balance between furnace and outer loop. Therefore, in this experiment, it is intended to analyse the effects of two air rates on the gas solid flow in CFB full-loop.

Firstly, the condition with fluidizing air velocity as U_{g1} and bed pressure at around 2kPa was realized and stabilized. And then recorded the pressure and flow data of the system for a period, and suddenly increased or decreased the fluidizing air velocity to U_{g2}. At last, after the system reached a new steady condition, the recording of the experimental data was ended. In the case of studying the effect of aerated air velocity on the flow, it only needs to keep the fluidizing air velocity constant and increase or decrease the aerated air velocity without changing the other steps. The recorded data in the experiment at one set of conditions is shown in the Fig. 2. Seen in Fig. 2, the air velocity will reach the new steady state within 20s, achieving the purpose of simulating the actual rapid peak regulation.

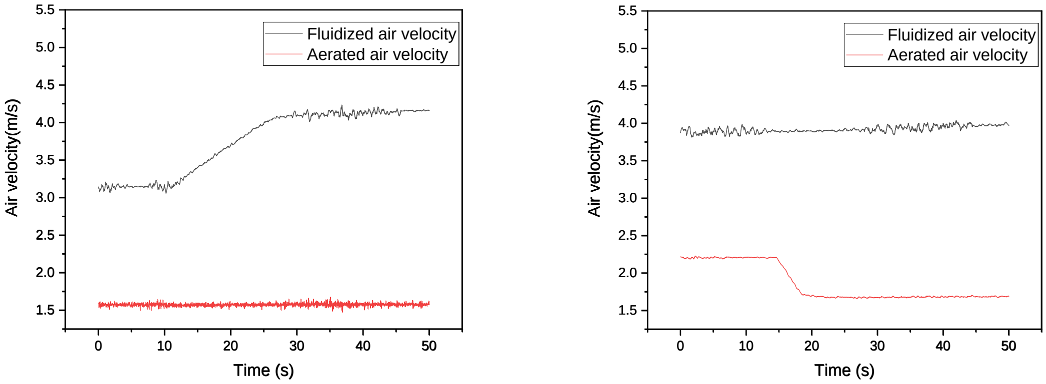

Fig.2 Air velocity changing. Changing fluidization air (left); changing aerated air velocity (right)

Result and Discussion

At each condition, the dynamic experiment was repeated twice to minimize error. As shown in Fig. 3, with increasing fluidizing air velocity quickly, bed pressure in riser will slowly drop with a large time lag and elbow resistance will rise first and then drop, while cyclone resistance will drop first and then rise.

When fluidizing air velocity increases, the material in the riser is blown out quickly and accumulates in the standpipe, so the bed pressure will continually drop until the new balance is reached. The resistance of the smooth elbow mainly depends on the solid mass fraction near the elbow[16]. The solid mass fraction or pressure drop gradient passing through the elbow will increase due to velocity increasing firstly and then decrease in a short time due to the total material in riser decreasing, as shown in Fig. 4 and 5.

For the phenomenon that the cyclone resistance first decreases and then increases, the reason may lie in the both influences of fluidizing velocity and solid concentration. At the beginning of velocity increasing, the solid mass fraction or the pressure drop gradient increases faster and then decreases faster to the value even smaller than initial one, as shown in Fig. 4 and 5. According the previous studies [16-20], at the same inlet velocity, the pressure resistance of cyclone has nonlinear relation with solid mass fraction and reaches the minimum value near the critical fraction. In present dynamic experiment, the lag between the changing of velocity and solid mass fraction may cause this tendency of cyclone resistance. At the new balance, the higher velocity will dominate the resistance of cyclone [16].

As shown in Figs. 4,5 and 6, both solid mass fraction and pressure difference first increase and then decrease, and there are different time lags at different heights. Increasing the fluidizing air velocity will reduce the height of the dense phase zone, it can also increase the solid mass fraction above 9m first and then decrease than the initial one as shown in Fig 6.

For the phenomenon that the time lag increases with height, the reason is that the upper flow state depends on the lower flow state, and the time scale at which the solid mass fraction reaches new balance is much larger than the time scale at which the air velocity changes.

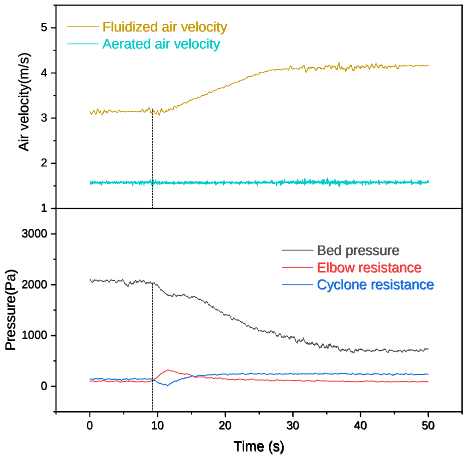

Fig. 3. Data under changing fluidizing air velocity condition

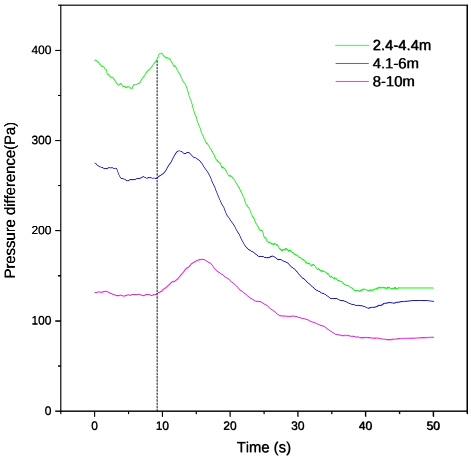

Fig.4. Pressure difference at different heights over time

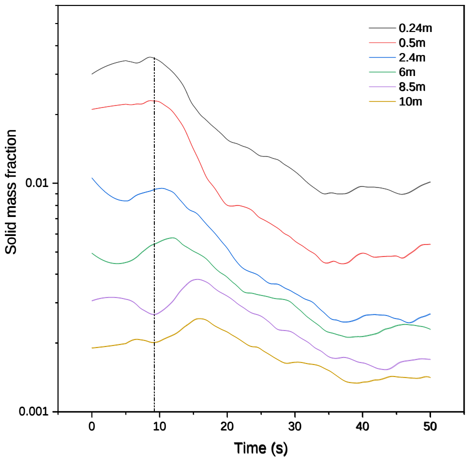

Fig. 5. Solid mass fraction at different heights over time

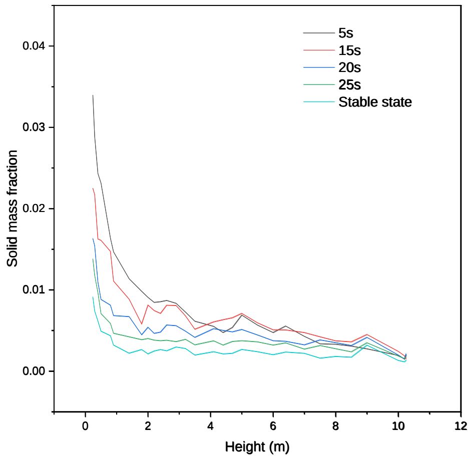

Fig. 6. Solid mass fraction changes with height at different times

As shown in Fig. 7, with increasing aerated air velocity quickly, fluidizing air velocity will drop slightly due to the pressure head of fan increases, bed pressure in riser will rise with a large time lag, while elbow resistance and cyclone resistance will only change slightly.

Different from the fluidizing air, the aerated air has little effect on elbow resistance and cyclone resistance. The reason is that under this condition, the solid capacity of the fluidizing air velocity is limited, while the dense zone height in riser increases with bed pressure increasing, so the pressure difference and solid mass fraction at the position above 8m increases slightly, as shown in Fig. 8 and 9. So under this condition, elbow resistance and cyclone resistance changes slightly, which will mainly be affected by slightly changing fluidizing air velocity.

As shown in Figs. 8 and 9, both pressure difference and solid mass fraction are positively correlated with aerated air velocity. And the same as changing the fluidizing air velocity, the changes of pressure difference and solid mass fraction are also accompanied by time lag. Increasing the aerated air velocity will also change the distrubition of solid mass fraction along the height and those between the riser and outer loop.

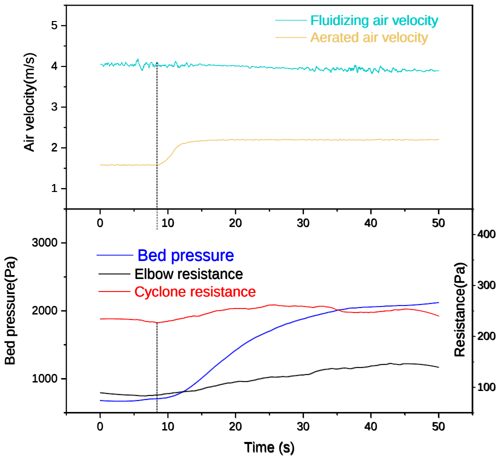

Fig. 7. Data under changing aerated air velocity condition

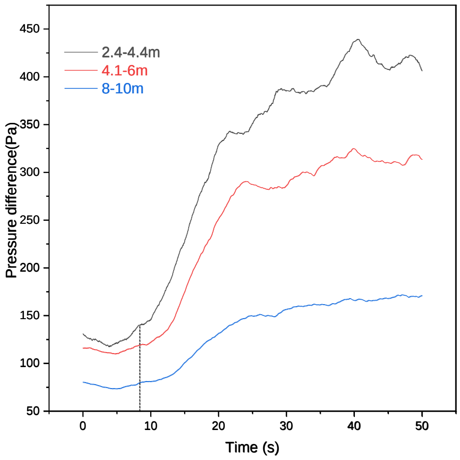

Fig. 8. Pressure difference at different heights over time

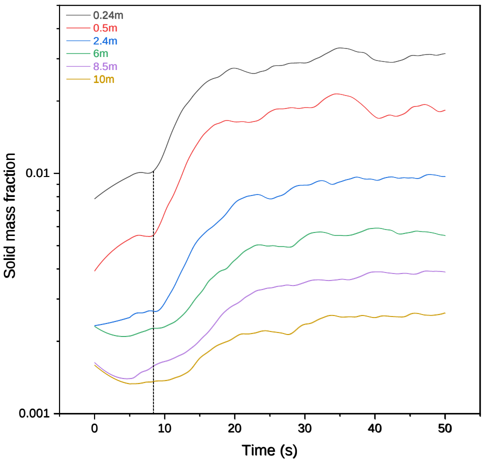

Fig. 9. Solid mass fraction at different heights over time

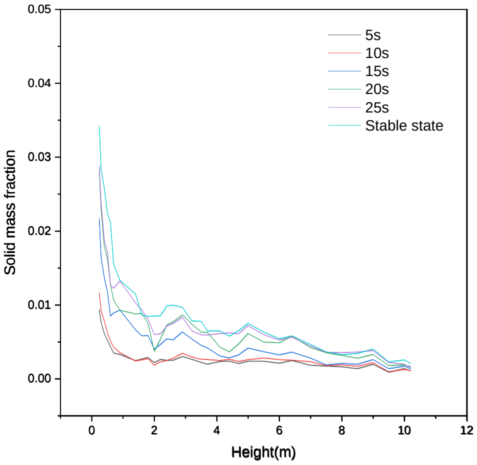

Fig. 10. Solid mass fraction changes with height at different times

Conclusion

In this paper, the dynamic test was carried out in the CFB cold test.The actual peak regulation condition was simulated by rapidly changing the fluidizing air velocity in furnace and looping air velocity in loop seal, respectively,the following conclusions are drawn :

1) Increasing the fluidizing air velocity will lower the bed pressure with time lag, it will also make resistance of the elbow first increase and then decrease, which is only affected by the solid mass fraction. And it will make cyclone resistance first decrease and then increase, which is affected by both the fluidizing air velocity and solid mass fraction.

2) Increasing the aerated air velocity causes the bed pressure to rise slowly, and has no significant effect on the elbow resistance and the cyclone resistance. The pressure difference and solid mass fraction in uper riser are positively correlated with aerated air velocity.

3) Because the time scale at which the solid mass fraction reaches new balance is larger than the time scale at which the air velocity changes, the parameter affected by the solid fraction changes with a time lag, which increases as the height increases.

Acknowledgment

This study was financially supported by the National Natural Science Foundation of China (U1810126).

References

[1]. China Statistical Yearbook 2018 [M]. National Bureau of Statistics, 2018.
[2]. Gu Yuchao, Yu Wenjia, Ma Xiaolei. Comparative study on the status quo and policy of coal washing at home and abroad[J].Coal Preparation Technology,2012(04):110-112+116.
[3]. Lyu Junfu, Zhang Jiansheng, Yue Guangxi. Operation and Maintenance of Circulating Fluidized Bed Boiler[J]. Beijing: China Water Resources and Hydropower Press, 2003.
[4]. Ke Xiwei, Cai Runxia, Yang Hairui, et al. NOx Formation and Ultra-low Emissions in Circulating Fluidized Bed Combustion[J]. Proceedings of the CSEE, 2018, 38(2): 390-396.
[5]. LI Bin, LI Jianfeng, LU Junfu, et al. Status of large scale circulating fluidized bed boiler operation in China [J]. Boiler Technology, 2012, 43(1): 22-28.
[6]. Cai Runxia，Lyu Junfu，Ling Wen，et al．Progress of supercritical and ultra-supercritical circulating fluidized bed boiler technology[J]．Electric Power，2016，49(12)：1-7
[7]. Yang Hairui，Yue Guangxi，Wang Yu，et al．Analysis of mass balance in a circulating fluidized bed boiler[J]．Journal of Engineering for Thermal Energy and Power，2005，20(3)：291-295．
[8]. Liu Jizhen, Hong Wei, Gao Mingming, Li Yuliang, Chen Feng. Study on the control strategy of rapid variable load operation of circulating fluidized bed unit[J].Proceedings of the CSEE,2017,37(14):4130-4137+4292.
[9]. Gao Mingming, Hong Wei, Zhang Bao, Liu Jizhen, Yue Guangxi, Yang Aidong, Chen Feng. Study on nonlinear control model of super (super) critical circulation fluidized bed unit[J]. Proceedings of the CSEE, 2018, 38(02):363 -372+666.
[10]. Yang Qiaofa. Research on Deep Peak Load Regulation of Circulating Fluidized Bed Unit[J].Shanxi Electric Power,2018(06):51-53.
[11]. Wang S , Luo K , Hu C , et al. Effect of superficial gas velocity on solid behaviors in a full-loop CFB[J]. Powder Technology, 2018, 333.
[12]. Wang S , Luo K , Hu C , et al. CFD-DEM study of the effect of ring baffles on system performance of a full-loop circulating fluidized bed[J]. Chem Eng Sci, 2018.
[13]. Li T , Dietiker J F , Shadle L . Comparison of full-loop and riser-only simulations for a pilot-scale circulating fluidized bed riser[J]. Chemical Engineering Science, 2014, 120:10-21.
[14]. Luo K , Wu F , Yang S , et al. High-fidelity simulation of the 3-D full-loop gas–solid flow characteristics in the circulating fluidized bed[J]. Chemical Engineering Science, 2015, 123:22-38.
[15]. Shan Lu, Zhang Wei, Zhang Yi, et al. Dynamic Model and Analysis of Gas-Solid Flow in Circulating Fluidized Bed[J]. Proceedings of the CSEE, 2017(S1):101-107.
[16]. Yang S , Yang H , Zhang H , et al. A transient method to study the pressure drop characteristics of the cyclone in a CFB system[J]. Powder Technology, 2009, 192(1):105-109.
[17]. C.J. Stairmand, Pressure drop in cyclone separators, Engineering 168 (1949) 409–412.
[18]. E. Kiegel, Effect of the dust loading on the throughput and pressure drop of cyclone collectors, Aufbereit.-Tech. 1 (1968) 1–8.
[19]. C.B. Shepherd, C.E. Lapple, Flow pattern and pressure drop in cyclone dust collectors, Ind. Eng. Chem. Res. 31 (1939) 972–984.
[20]. J.Y. Chen, M.G. Shi, A universal model to calculate cyclone pressure drop, Powder Technol. 171 (2007) 184–191.

A GENERALIZED FLUIDIZATION MAP FOR BUBBLING AND FAST FLUIDIZED BEDS BY AN ARTIFICIAL INTELLIGENCE APPROACH

Jaroslaw Krzywanski[1*], Marcin Sosnowski[1], Anna Zylka[1], Karolina Grabowska[1], Anna Kulakowska[1], Tomasz Czakiert[2], Kamil Idziak[2], Karol Sztekler[3], Marta Wesolowska[3], Wojciech Nowak[3]

[1]Jan Dlugosz University in Czestochowa, Faculty of Science and Technology
Armii Krajowej 13/15, 42-200 Czestochowa, Poland;
[2]Czestochowa University of Technology, Institute of Advanced Energy Technologies
Dabrowskiego 73, 42-200 Czestochowa, Poland;
[3]AGH University of Science and Technology, Faculty of Energy and Fuels
Mickiewicza 30, 30-059 Cracow, Poland;

*Email: *j.krzywanski@ujd.edu.pl*

Abstract

The paper introduces a fuzzy logic (FL) approach as one of the main artificial intelligence (AI) methods to plot a fluidization map for bubbling and fast fluidized beds. An innovative idea of fluidized bed application in adsorption chillers instead of the conventional fixed or packed bed, commonly used in typical adsorption cooling and desalination systems, is proposed in the paper. The first results of fluidization dynamics modeling are discussed. The created AI model correctly describes the fluidization dynamics and can be applied to study the fluidized adsorption beds. The FLFMap application developed in the study allows describing the behavior of adsorption beds of various sorption pairs and plots a generalized fluidization map for bubbling and fast fluidized beds.
To our best knowledge, it is the first work, where an AI approach is employed to plot flow regimes map for gas-solid/adsorbate(refrigerant)-adsorbent suspensions in adsorption cooling and desalination systems.

Introduction

Besides the high valued energy sources, e.g., electricity and fossil fuel-driven appliances, a wide range of low-grade sources of thermal energy, e.g., sewage water, underground resources, solar heat, low-grade waste heat, which can be used for both heating or cooling, according to Ammar et al. (2012), Krzywański et al. (2016), Stanek and Gazda (2014). However, low heat transfer coefficients between fixed or packed beds and the submerged surfaces are considered as primary reasons for low coefficients of performance (COP), regarded as the major disadvantages of conventional adsorption chillers. Various techniques have been developed and applied to enhance heat and mass transfer in adsorbent beds. Their effects on the performance of adsorption systems can be found, e.g., in Sur and Das (2016). There are also some works on the use of fluidization, e.g., Chen et al. (2015), Hamed, (2005), Rogala et al. (2017), Wang et al. (2012). However, none of them deals with operating conditions as well as with the adsorption bed configurations corresponding to the ones of multi-bed adsorption chillers. Since the complexity of such systems is still not sufficiently recognized, the study of the fluidized-bed adsorption cooling and desalination systems is a challenging task.

The paper introduces a fuzzy logic (FL) approach as one of the primary artificial intelligence (AI) methods to plot a fluidization map for bubbling and fast fluidized beds. The developed FLFMap model allows describing the behavior of adsorption beds in various adsorbent-adsorbate pairs configurations suitable for adsorption cooling and desalination systems. To our best knowledge, it is the first work with an AI method employed to plot flow regime map for adsorbate-adsorbent as gas-solid suspensions.

Methods

The behavior of solids during fluidization can be classified into for recognizable groups described by the difference of solid and gas density, and mean particle size, according to Bi and Grace (1995), Kunii and Levenspiel, (2013), Geldart (1973), Yang (2003), Blaszczuk, Nowak and Krzywanski (2017), Win et al. (1995); Krzywanski et al. (2017). As it was underlined by Kunii and Levenspiel, (1997), these two factors are also the critical parameters in describing the gas/solid contact regimes. To determine what contacting regime is involved, Kunii and Levenspiel (1997) also defined two dimensionless measures of particle size and gas velocity:

$$d = d_p \left[\frac{\rho_g(\rho_s - \rho_g)g}{\mu^2}\right]^{1/3} \tag{1}$$

$$u = u_0 \left[\frac{\rho_g^2}{\mu^2(\rho_s - \rho_g)g}\right]^{1/3} \tag{2}$$

The authors pointed out, that the use of these two measures allows preparing a graph showing the expected behavior of gas-solid systems.

An alternative method turns out to be a Fuzzy Logic approach. One of the main representatives of the artificial intelligence (AI) methods is the fuzzy logic (FL) approach. According to Ross (2005), Krzywanski et al. (2016, 2018), this approach allows developing knowledge-based systems for solving complex problems. The method is based on the use of fuzzy sets and linguistic variables to deal with imprecise, vague and uncertain information and to employ qualitative judgment to parameters quantitative in nature for describing the behavior of processes or objects. A fuzzy logic-based model consists of three parts: the fuzzy rule base, the inference engine, and the defuzzifier, which are responsible for three principal operations, i.e. fuzzification, inference, and defuzzification (Fig. 1).

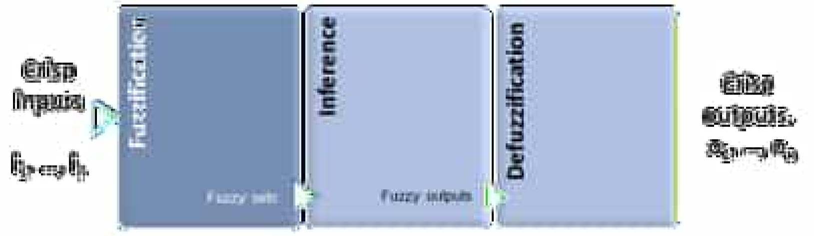

Fig. 1. An algorithm of the FL approach.

The entire development procedure of a model starts from covering the domain of all the inputs by the previously defined fuzzy sets. This operation allows defining a membership function values between 0 and 1 corresponding to a numeric value of an input, via the so-called fuzzification process. According to Ross (2005), the fuzzy sets can be then expressed by Zadeh's notation:

$$S = \{m_S(i_1)/i_1 + m_S(i_2)/i_2 + \ldots + m_S(i_n)/i_n\} \tag{3}$$

where, i_1, i_2, …i_n are input variables.

The IF-THEN fuzzy rule base allows the fuzzy outputs to be generated. A typical fuzzy rule with two inputs i_1 and i_2 and two outputs o_1 and o_2 can be written as follows:

IF i_1 *is* S_1 *and* i_2 *is* S_2 *THEN* o_1 *is* $f_1(i_1, i_2)$ *and* o_2 *is* $f_2(i_1, i_2)$ (4)

where $f_1(i_1, i_2)$ and $f_2(i_1, i_2)$ are polynomial functions of inputs i_1 and i_2.

Finally, during the defuzzification stage, crisp outputs are generated, corresponding to the previously produced fuzzy outputs.

An essential feature of the method is that it allows an empirical problem to be formalized using the experience rather than the strict knowledge of the process, and the theory is not essential here, which was also depicted in Krzywanski (2019), Sosnowski et al. (2019).

Results and discussion

The above-described methodology allows developing a Fuzzy Logic Fluidization Map (FLFMap), model. The FuzzyLite control application was employed during the study (http://www.fuzzylite.com). The dimensionless particle size stands for input and the dimensionless gas velocity constitutes an output. These input and output parameters are covered by two triangular and constant linguistic variables, respectively, with terms: low (L) and high (H) (Fig. 2). Since the range of particle size and gas velocity are different for bubbling (bfb) and fast (ffb) fluidized conditions, the FLFMap model consists of separate inputs d, corresponding to bubbling (d_bfb) and fast (d_ffb) fluidization regimes, respectively (Fig. 2a). Similar applies to the dimensionless gas velocities as output parameters for bubbling (bfb) and fast (ffb) fluidized conditions, corresponding to lower (uL) and the upper (uH) boundary of a fluidization regimes (Fig. 2b).

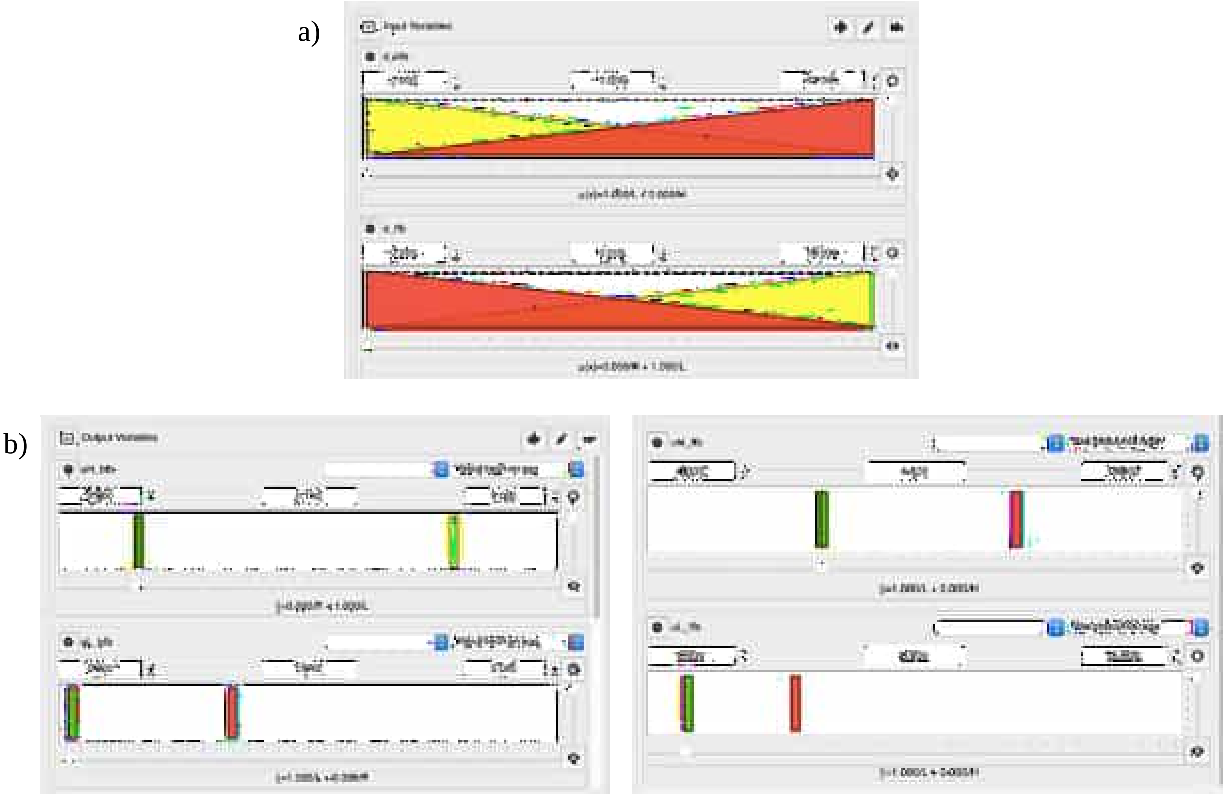

Fig. 2. Membership functions for input (a) and output (b) parameters (x-axes and y-axes correspond to parameter values from Kunii and Levenspiel, 1997).

The Takagi-Sugeno inference engine is used to determine the fuzzy output variable. The weighted average method is employed during the defuzzification stage to produce a crisp output value, as it is one of the most common and computationally efficient techniques, according to Ross (2005):

$$o = \sum m_s(\bar{o}) \, . \, \bar{o} / \sum m_s(\bar{o}), \tag{5}$$

where $\bar{o}$ is the centroid of each membership function.

Such established fuzzy sets allow a numeric value of a considered input parameter to be assigned to a value of a membership function (from the range between 0 and 1). The set of fuzzy rules is shown in Fig.3.

Fig.3. Fuzzy rule base for the FLFMap model.

The developed FLFMap model allows plotting fluidization map for bubbling and fast fluidized beds, given in Fig. 4. The application created within the paper can serve as a useful tool to define a flow regime map for gas-solid/sorbet-adsorbent suspensions. Since the FLFMap model is dedicated to adsorption and desalination systems, with a wide variety of adsorbent-adsorbate pairs, the model can be enriched by the additional functionalities. Additional inputs and outputs can be introduced, allowing to describe, e.g. specific operating conditions or properties of adsorbate, adsorbent, or other additives, e.g., metal powders or carbon nanotubes which added may improve thermal diffusivity of an adsorption bed. Since particles of some additives have an irregular shape, e.g., carbon nanotubes, their sphericity, should be correctly determined and applied to define the particle size and the dimensionless measure of particle diameter, which was underlined by Kunii and Levenspiel (1997). This undertaking can make the model more flexible and effective in the use and provides additional capabilities.

On the matter of fluidization dynamics, the FLFMap model allows mapping the areas of operating conditions in regions, where the real measurements are unavailable. Therefore, it can be used for optimization purposes to choose the optimal operating parameters concerning the thermal conductivity of the bed and the performance of the system. To our best knowledge, it is the first work, where an AI method was employed to plot flow regimes map for gas-solid/adsorbate(refrigerant)-adsorbent suspensions.

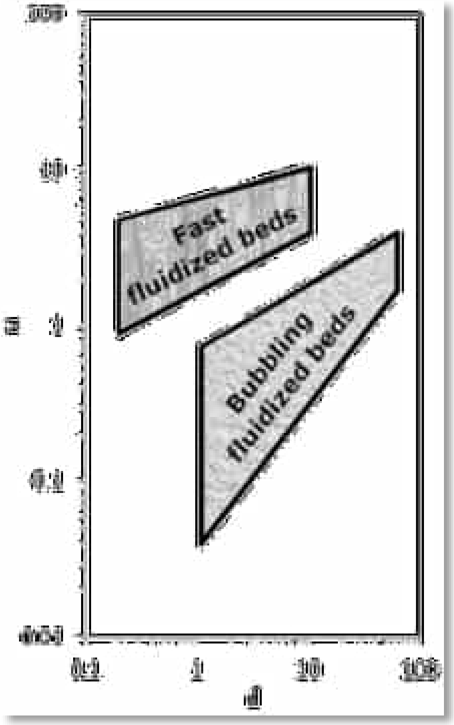

Fig.4. The fluidization map, generated by the FLFMap model.

Conclusions

The present work is the first one in the literature dealing with the use of the fuzzy logic approach for modeling bubbling and fast fluidized bed regimes map. The developed FLFMap model allows predicting the upper and the lower limit of the dimensionless fluidizing gas velocity, describing the area in flow regimes where the bubbling and fast fluidized bed conditions exist.

The FLFMap model constitutes an effective optimization tool, capable of predicting the operating parameters necessary to assure demanding fluidization conditions.

However, this new model needs further work providing new capabilities, allowing its practical utilization for modeling of cooling and desalination adsorption systems.

Acknowledgments

The scientific work was performed within the project No. 2018/29/B/ST8/00442, “Research on sorption process intensification methods in modified construction of adsorbent beds”, supported by the National Science Center, Poland. The support is gratefully acknowledged.

Notation

d	dimensionless measure of particle diameter
d_p	particle diameter, m
g	acceleration due to gravity, (= 9.81 m/s^2)
i	input
m	degree of membership
o	output
u	dimensionless gas velocity
u_0	superficial gas velocity, m/s

Greek letters

ρ	density, kg/m^3
μ	viscosity of gas, kg/m·s

Subscripts

bfb	bubbling fluidized bed
ffb	fast fluidized bed
g	gas phase
s	solid

Acronyms

AI	artificial intelligence
COP	coefficient of performance
S	fuzzy set
FL	fuzzy logic

References

Ammar, Y., Joyce, S., Norman, R., Wang, Y., Roskilly, A. P. Low grade thermal energy sources and uses from the process industry in the UK. Applied Energy, 2018. 89(1), 3–20.

Bi, H. T., Grace, J. R.Flow regime diagrams for gas-solid fluidization and upward transport. International Journal of Multiphase Flow, 1995. 21(6), 1229–1236

Blaszczuk, A., Nowak, W., Krzywanski, J. Effect of bed particle size on heat transfer between fluidized bed of group b particles and vertical rifled tubes. Powder Technol. 2017. 316, 111–122

Błaszczuk, A., Krzywański, J. A comparison of fuzzy logic and cluster renewal approaches for heat transfer modeling in a 1296 t/h CFB boiler with low level of flue gas recirculation. Archives of Thermodynamics. 2017. 38(1), 91–122

Chen, C.H., Schmid, G., Chan, C.-T., Chiang, Y.-C., Chen, S.-L. Application of silica gel fluidised bed for air-conditioning systems. Applied Thermal Engineering. 2015. 89

Geldart, D. Types of gas fluidization. Powder Technol. 1973.7(5), 285–292

Hamed, A. M. Experimental investigation on the adsorption/desorption processes using solid desiccant in an inclined-fluidized bed. Renewable Energy. 2005. 30(12), 1913–1921

Krzywanski, J., Wesolowska, M., Blaszczuk, A., Majchrzak, A., Komorowski, M., Nowak, W. The Non-Iterative Estimation of Bed-to-Wall Heat Transfer Coefficient in a CFBC by Fuzzy Logic Methods. Procedia Engineering. 2016. 157, 66–71

Krzywanski, J., Fan, H., Feng, Y., Shaikh, A. R., Fang, M., Wang, Q. Genetic algorithms and neural networks in optimization of sorbent enhanced H2 production in FB and CFB gasifiers. Energy Conversion and Management. 2018. 171, 1651–1661

Krzywanski, J., Wesolowska, M., Blaszczuk, A., Majchrzak, A., Komorowski, M., Nowak, W. Fuzzy logic and bed-to-wall heat transfer in a large-scale CFBC. International Journal of Numerical Methods for Heat and Fluid Flow. 2018. 28, 254-266

Krzywanski, J., Żyłka, A., Czakiert, T., Kulicki, K., Jankowska, S., Nowak, W. A 1.5D model of a complex geometry laboratory scale fuidized bed CLC equipment. Powder Technology, 2017. 316, 592–598

Krzywański, J., Szyc, M., Nowak, W., Kolenda, Z. Experience in modelling of a single-stage silica gel-water adsorption chiller. Technical Sciences. 2016. 19, 367-386.

Krzywanski J, Heat Transfer Performance in a Superheater of an Industrial CFBC Using Fuzzy Logic-Based Methods, Entropy 2019, 21 919

Kunii, D., Levenspiel, O. Fluidization Engineering. 2013. Elsevier.

Kunii, Daizo, Levenspiel, O. Circulating fluidized-bed reactors. Chemical Engineering Science. 1997. 52, 2471–2482

Rogala, Z., Kolasiński, P., Gnutek, Z. Modelling and experimental analyzes on air-fluidised silica gel-water adsorption and desorption. Applied Thermal Engineering. 2017. 127, 950–962

Ross, T. J. Fuzzy Logic with Engineering Applications. John Wiley & Sons. 2005.

Sosnowski M., Krzywanski J., Scurek R., A Fuzzy Logic Approach for the Reduction of Mesh-Induced Error in CFD Analysis: A Case Study of an Impinging Jet. Entropy. 2019. 21, 1047.

Stanek, W., Gazda, W. Exergo-ecological evaluation of adsorption chiller system. Energy, 2014. 76, 42–48

Sur, A., Das, R. K. Review of Technology Used to Improve Heat and Mass Transfer Characteristics of Adsorption Refrigeration System. International Journal of Air-Conditioning and Refrigeration. 2016. 24, 1630003

Wang, Q., Gao, X., Xu, J. Y., Maiga, A. S., Chen, G. M. Experimental investigation on a fluidized-bed adsorber/desorber for the adsorption refrigeration system. International Journal of Refrigeration. 2012. 35, 694–700

Win, K. K., Nowak, W., Matsuda, H., Hasatani, M., Bis, Z., Krzywanski, J., Gajewski, W. Transport Velocity of Coarse Particles in Multi-Solid Fluidized Bed. Journal of Chemical Engineering of Japan. 1995. 28, 535–540

Yang, W.-C. Handbook of Fluidization and Fluid-Particle Systems. CRC Press.2003.

HYDRODYNAMICS OF A COLD MODEL FLUIDIZED BED WITH MULTIPLE INCLINED DOWNWARD NOZZLES

Xudong Zhong, Bicai Zhu, Mengxi Liu*, Chunxi Lu

The State Key Laboratory of Heavy Oil Processing, Faculty of Chemical Engineering and Environment, China University of Petroleum-Beijing, Changping, Beijing, 102249, People’s Republic of China.

*Email: *mengxiliu@sina.com*

Abstract

A cold model fluidized bed was designed for the fluid coking operation, aiming to improve poor distribution of liquid feed, and eliminate the formation of liquid-rich agglomerates of coke particles in the reaction section. The nozzles were mounted at 30 degrees obliquely downward. Based on Kutta-Joukowski Lift Theorem, the obliquely downward jets from the nozzles force coke particles moving to the center of the fluidized bed. It increases the residence time of the coke particles, improves contact between coke particles and fresh raw material and facilitates the long-term operation of the device.

Local solid holdup distribution was measured using a regular optical fiber probe. Signals associated with the mesoscale structure such as particle agglomerates were registered by a specially designed optical fiber probe which has a large distance between the two tips. The signals were decoupled based on the moment consistency principle and the thresholds were determined to identify bubbles and agglomerates, respectively. The average residence time was defined to characterize the particle renewal rate in the vicinity of the jets.

Introduction

Delayed coking is an important heavy oil processing technology. In recent years, as the environmental emission standards have become tightened, burning the coke rich in heavy metal and sulfur is strictly prohibited, which directly threatens the survival of delayed coking. As an alternative process, flexi-coking process converts coke into low calorific value syngas, and removes pollutants efficiently, offering great economic and environmental benefits, and showing great application potential can be found in Zhang et al. (2013).

Due to poor contact between the hot coke particles and the liquid crude oil feed, liquid-rich agglomerates form continually in the coker of the flexi-coking process which can even cause bogging, resulting in low product yields, poor product selectivity and even unplanned shutdown can be found in Cedric et al. (2017). Gray et al. (2002) revealed different mechanisms of forming a coke layer on hot coke particles with a boundary thickness of 70 μm. When the particle size was less than 70 μm, the coke layer formed mainly by granulation mechanism and facilitated the aggregation of larger particles. While for particles or particle aggregates larger than 70 μm, they grew continuously through the coating process. McDougall (2005) observed that the existence of liquid bridge among particles will greatly increase the survival probability of the agglomerates. Darabi et al. (2010) found that agglomeration occurs easier at high coking temperatures than low coking temperatures, and the larger coke agglomerates may contain hundreds of initial coke particles. Weber et al. (2011) studied the effect of fluidization quality on the stability of agglomerates, but they did not consider the distribution and frequency of particle agglomerates in different locations of the fluidized bed. A reactor with inclined downward nozzles is proposed in this study to address the feeding problem in the fluid coker.

Experiments

Experimental Setup

Figure 1 shows the schematic diagram of the cold model experimental apparatus. The fluidized bed was 0.476 m in inner diameter and 1.5 m in height. The freeboard had an inner diameter of 0.77 m and a height of 6 m. Four nozzles were mounted at 30 degrees obliquely downward and with an inner diameter of 0.02 m. The four nozzles were arranged in two cross-section with an interval of 0.57 m and the lower nozzles were mounted 0.22 m above the distributor.

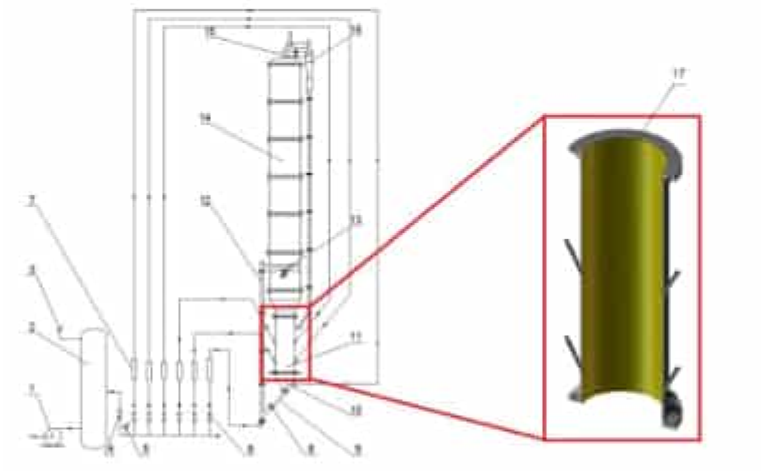

Fig. 1. Schematic diagram of experimental setup. (1-Air Blower. 2-Pressure Buffer Tank. 3-Pressure Gauge on Buffer Tank. 4-Pressure Control Valve. 5-Pressure Gauge on Pipeline. 6-Stop Valves. 7-Air Rotor Flowmeters. 8-Butterfly valve. 9-Particle Returning Pipe. 10-Air Distributor. 11-Dense Phase Zone of Fluid Coker. 12-Riser Vessel. 13-Feeding Distributor. 14-Freeboard of Fluid Coker. 15-Primary Cyclone Separator.16-Secondary Cyclone Separator. 17- Novel Fluid Coker with 30° Downward Nozzles.)

Operating Conditions

Table 1 gives typical operating conditions of the cold model apparatus. The dense phase fluidized bed was operated as a bubbling bed with a superficial gas velocity of 0.2 m/s. Large amount of air was introduced into the bed by four nozzles. The jet velocities varied between 14.16 m/s and 56.64 m/s, leading to a superficial gas velocity between 0.3 m/s to 0.6 m/s in the dense fluidized bed above the nozzles.

Because the black coke particles absorb most light from the optical fiber tips, the registered optical fiber signals are weak and may not represent hydrodynamics precisely. Therefore, the FCC catalyst was selected as the substitute particle of the fluid coke particles for investigation.

Table 1. Feed nozzle jet velocity.

Superficial gas velocity, u_g (m.s^{-1})	Jet velocity, u_o (m.s^{-1})
0.2	0
0.3	14.16
0.4	28.32
0.5	42.48
0.6	56.64

Table 2 gives physical properties of the fluid coke and FCC catalyst, and Figure 2 compares the size distribution of the two particles. The fluid coke particles come from a commercial syncrude units.

Table 2. Properties of the FCC catalyst and fluid coke

Properties	FCC catalyst	Fluid coke
Particle density (kg.m^{-3})	1423	1638
Mean Particle size (μm)	75	155
Particle size range (μm)	10~300	30~340
Solid holdup at the minimum fluidization	0.51	0.54

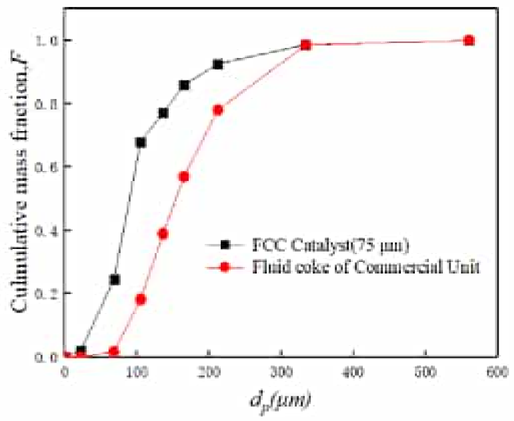

Fig. 2. The particle size distribution (PSD) of the fluid coke and FCC catalyst.

Experimental Method

Hydrodynamics of the fluid coker was registered by a PV-6D particle velocity analyzer (Institute of Process Engineering, Chinese Academy of Sciences) connected with an optical fiber probe. The vertical distance between the two tips of the probe is 3.95 mm (Figure 3).

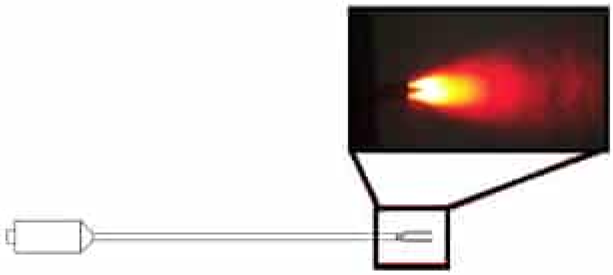

Fig. 3. Schematic diagram of optical fiber probe.

The sampling rate is 20 kHz, and the total sampling time is 196.68 s. The relationship between the output signals and the local solid holdup was fitted with an error of <5%. Considering the difference of the two fiber probe channels, the two channels are calibrated separately.

$$\varepsilon_S=0.023e^{0.731V}[\text{Channel1}] \qquad (1)$$

$$\varepsilon_S=0.025e^{0.706V}[\text{Channal2}] \qquad (2)$$

Identification of Particle Agglomerates

In flexi-coking process, liquid-rich agglomerates and bogging are two operational problems with the causal relationship. The existence of agglomerates is a prerequisite, and then the bogging may happen when agglomerates encounter the feed spray. Therefore, the characteristics of the agglomerates in fluid coker are very important.

Bi et al. (2001) proposed a two-phase structural model to analyze local voidage fluctuation signals. Zhu et al. (2013) proposed a moment consistency data processing method to identify flow structures and transition regime in gas-solid fluidized bed. Liu et al. (2014) proposed that, in the probability density distribution of the solid holdup, the component having a solid holdup higher than the solid holdup in minimum fluidization, represent agglomerates. In this paper, the solid holdup at the minimum fluidization was 0.51, determined by the plot of pressure drop versus air flow rate. Based on the structural model and criteria for identifying agglomerates, Niu et al. (2019) proposed an algorithm to identify the bubbles and agglomerates in gas-solid two-phase flow by using statistical moment consistent principle. In this paper, this algorithm is adopted, and the statistical moment formulas are shown as Eqs. (3) - (5).

$$f_d=\frac{1}{2}(1-S\sqrt{\frac{1}{4+S^2}}) \tag{3}$$

$$\varepsilon_{sd}=\varepsilon_s+\frac{\sigma}{2}\left[\sqrt{4+S^2}+S\right] \tag{4}$$

$$\varepsilon_{sb}=\varepsilon_s-\frac{\sigma}{2}\left[\sqrt{4+S^2}-S\right] \tag{5}$$

Eq. (6) gives a root-mean residence time that is defined by Chen (2003) in the research of multiphase heat transfer. In this paper, the mean residence time of particle agglomerates in the feeding region was calculated by Eq. (6) to characterize the survival time of agglomerates in liquid-rich environment.

$$\tau_{pa}=\left[\frac{\sum_{i=1}^{n}\tau_{pa,i}}{\sum_{i=1}^{n}\sqrt{\tau_{pa,i}}}\right]^2 \tag{6}$$

Experimental Results

Solid Holdup under the Influence of Jet

Figure 4 shows the influence of jets on the solid holdup distribution. When jets are not introduced into the bed, the superficial gas velocity is 0.2 m/s. Solid holdup seems low at the center and high near the wall, which is a typical bubbling fluidized bed characteristic. When the downward jets are introduced, solid holdup increases to 0.4 in the center and significantly decreases in the vicinity of the wall.

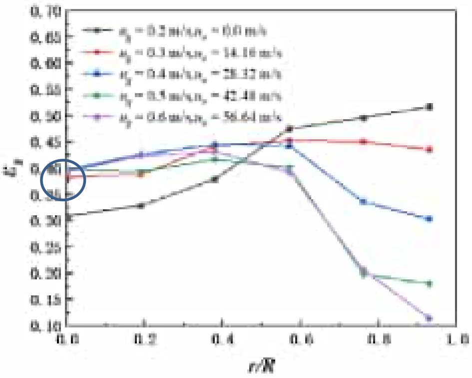

Fig. 4. The solid holdup at the feeding region (*h/H* = 0.11).

The increase in solid holdup of the central region is induced by a transverse force called the Kutta-Joukowski lift force, which promotes particles move to the center when the jet is introduced into the fluidized bed. When a 2D steady irrotational flow pasts a closed body, the lift $F_{K\text{-}J}$ on per unit span of the body can be given by Eq. (7).

$$F_{K\text{-}J}=\rho\Gamma U_\infty \tag{7}$$

where Γ is the velocity circulation around the body. Meanwhile, the flow be uniform with a velocity U_∞ and a density ρ. Fan et al. (2009) employed this theory to explain the effect of jets in a gas-solid riser. In this paper, the lift force on particles formed by the inclined downward jet is directed towards the center of the bed, and thus increases solid holdup in the central region.

Volume Fraction of the Mesoscale Flow Structures

Figure 5 shows the volume fraction of dense phase and dilute phase. Before the jets are introduced into the bed, more bubbles appear in the central region of the fluidized bed and no bubbles are observed in the vicinity of the wall, leading to a decrease in the volume fraction of dilute phase along the radial direction. When the downward jets are introduced, it can be observed that in the center the dense volume fraction increases and the dilute phase volume fraction decreases. Figure 5 (a) shows that more bubbles tend to rise near the wall rather than rising at the center with the introduction of jets, leading to a solid holdup increase in the central region. Figure 5 (b) shows that the volume fraction of the dense phase increases in the center because the Kutta-Joukowski lift force prompts particles to move to the central region, leading to a solid holdup increase in the center. From the perspective of mesoscale flow structure, the effect of jets being introduced into the fluidized bed can be clearly observed. The introduction of jets will cause the particle agglomerates near the side wall to be impacted and easily broken, then the number of particle agglomerates is greatly reduced. On the contrary, due to the decrease of bubbles in the center of the fluidized bed, the broken probability of particle agglomerates is low, resulting in a significant increase in the number of particle agglomerates.

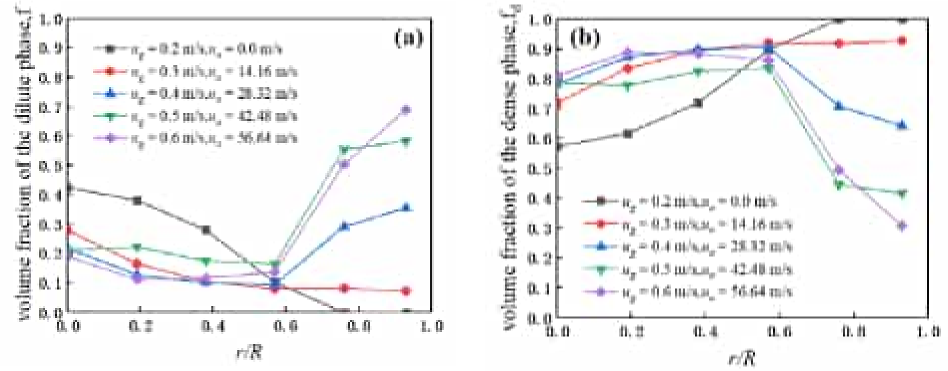

Fig. 5. The volume fraction of mesoscale flow structure (*h/H* =0.11).

Residence Time of Particle Agglomerates

Figure 6 indicates the variation in the residence time of particle agglomerates with superficial gas velocity. Before the jets are introduced into the bed, the residence time of particle agglomerates is very high, especially near the wall of the fluidized bed. With the introduction of jets, the residence time of particle agglomerates decreases significantly. As the jet velocity increases, the residence time of particle agglomerates near the wall decreases obviously, but the influence on the center position seems not significant.

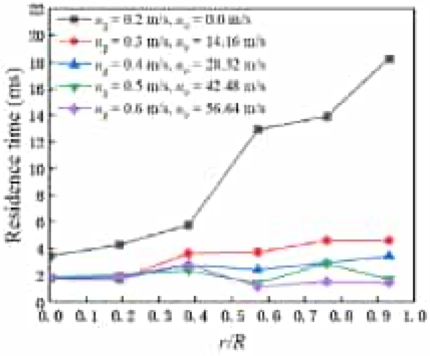

Fig. 6. Residence time of particle agglomerates in the feeding region (*h/H*=0.11).

Conclusions

In this paper, a fluid coker with a downward 30 degrees nozzle is proposed, and the influence of downward jet on the solid holdup distribution is measured by a novel optical fiber probe. The mesoscale flow structure in the apparatus is analyzed based on theorem of statistical moment consistency for solid holdup signals. The following conclusions are mainly obtained: (1) The Kuta-Jukovsky lift force pushes the particles to move to the center of the bed, promoting the particles to escape from feeding region after contact with the fresh raw material and reducing the possibility of agglomeration survival and the risk of bogging; (2) The bubbles prefer to rise near the wall because the presence of jets improves fluidization in the feeding region. The residence time of particle agglomerates prominently decreases in the feeding region of the fluid coker, which makes particle agglomerates renew faster.

Notation

F particle cumulative fraction

ρ_p particle density, kg·m^{-3}

$\overline{d_p}$ mean particle diameter, m

PSD particle size distribution

d_o inner diameter of nozzle, m

u_o feed nozzle jet velocity, m.s^{-1}

u_g superficial gas velocity at dense phase bed surface, m·s^{-1}

ε_s local solid holdup

τ resistance time, ms

ε_{sb} time-average solid holdup of the bubble phase

ε_{sd} time-average solid holdup of the emulsion phase

f_d volume fraction of the dense phase

f volume fraction of the dilute phase

σ standard deviation of solids holdup

S skewness of solids holdup

$F_{K\text{-}J}$ Kutta-Jou-kowski lift force, N·m^{-1}

ρ density of uniform flow, kg·m^{-3}

U_∞ velocity of uniform flow, m·s^{-1}

Γ velocity circulation around the body, m^2·s^{-1}

h Height of optical fiber measuring point, m

H Height of dense bed, 1.5m

r radial position of measurement points, m

R radius of the reactor, m

References

Bi, Hsiaotao T. and Su, Peng-Cheng. Local phase holdups in gas - solids fluidization and transport. AIChE J. 2001. 47(9), 2025-2031.

Briens, Cedric, Hamidi, Majid, Berruti, Franco, McMillan, Jennifer. Development and study of measurement methods for bogging in a fluidized bed. Powder Technology. 2017.316, 92–100.

Chen, John C. Surface Contact—Its Significance for Multiphase Heat Transfer: Diverse Examples. Journal of Heat Transfer. 2003. 125(4), 549-566.

Darabi, Pirooz, Pougatch, Konstantin, Salcudean, Martha and Grecov, Dana. Agglomeration of Bitumen-Coated Coke Particles in Fluid Cokers. International Journal of Chemical Reactor Engineering. 2010. A122, 1-12.

Fan, Yiping, E, Chenglin, Shi, Mingxian, Xu, Chunming, Gao, Jinsen, Lu, Chunxi. AIChE J. 2009. 56(4),858-868.

Gray, Murray R. Fundamentals of Bitumen Coking Processes Analogous to Granulations: A Critical Review. The Canadian Journal of Chemical Engineering, 2002. 80,393-401.

Liu, Mengxi, Shen, Zhiyuan, Yang, Lijun, and Lu, Chunxi. Micro-scale Two-Phase Flow Structure in a Modified Gas−Solid Fluidized Bed. Ind. Eng. Chem. Res. 2014. 53, 13475-13487.

McDougall, S., Saberian, M., Briens, C., Berruti, F., Chan, E. Effect of liquid properties on the agglomerating tendency of a wet gas–solid fluidized bed. Powder Technology. 2005.149,61-67.

Niu, Li, Huang, Yahang, Chu, Zhimin, Cai, Min, Liu, Mengxi. Identification of Mesoscale Flow in a Bubbling and Turbulent Gas–Solid Fluidized Bed. Ind. Eng. Chem. Res. 2019. 58(19), 8456-8471.

Weber, Sarah, Briens, Cedric, Berruti, Franco, Chan, Edward, Gray, Murray. Stability of agglomerates made from fluid coke at ambient temperature. Powder Technology. 2011.209,53-64.

Zhang, Chongwei, Wang, Xiaomei, Tian, Hui, Li Xiaona. Introduction and comparison of flexi coking and delayed coking. Sino-Global Energy. 2013,18(2),68-72.

Zhu, Jesse; Qi, Maozhan; Barghi, Shahzad. Identification of the flow structures and regime transition in gas-solid fluidized beds through moment. AIChE J. 2013.59(5),1479-1490.

EFFECT OF VAN DER WAALS FORCE ON FLUIDIZATION OF FINE PARTICLES

Youssef Badran[1,2,*], **Renaud Ansart**[1], **Jamal Chaouki**[2], **Olivier Simonin**[3]

[1]*Laboratoire de Génie Chimique, Université de Toulouse, CNRS, Toulouse, France*
[2]*Department of Chemical Engineering, Polytechnique Montreal, Montreal, Canada*
[3]*Institut de Mécanique des Fluides de Toulouse, Université de Toulouse, CNRS, Toulouse, France*

*Email: *youssef.badran@toulouse-inp.fr*

Abstract

The performance of a gas-solid fluidized bed can be influenced by interparticle forces due to their effect on the bed hydrodynamics. These forces contribute to some observed phenomena in fluidization such as the overshoot in the bed pressure drop at the minimum fluidization velocity during the transition from fixed to fluidized bed state. In this work, two adhesive particle pressure closures are used in two-fluid model simulations to account for the effect of interparticle van der Waals force in order to predict the pressure overshoot. The first adhesive pressure model derived in the framework of the kinetic theory of rapid granular flows failed to produce the overshoot due to the dominant effect of multiple and long duration contacts in the fixed-bed flow. Another closure based on the coordination number is proposed, which gives an adhesive contribution much larger than the one of the kinetic theory model and is able to create the pressure drop overshoot.

Introduction

The overshoot of total bed pressure drop around the minimum fluidization velocity is a typically observed phenomenon for fine particles belonging to the group A of Geldart's classification (Soleimani et al. 2020). This observation is due to the dominant role of the interparticle forces over the hydrodynamic forces in fixed beds of these solids. At dry ambient conditions, the dominant interaction force between fine particles is the van der Waals attractive force (Visser 1989). Eulerian-Eulerian models that account for the effect of interparticle van der Waals force are rare in the literature. Parmentier (2010) worked on the implementation of Van der Waals force in the two-fluid model using the BBGKY hierarchy. In the frame of the kinetic theory of granular flows, an adhesive pressure was added to the solid pressure to take into account the van der Waals attractive interaction. The numerical data of discrete element simulations can be used to extend the kinetic theory that is based on the assumptions of binary collision and molecular chaos from modest to very dense gas-solid flows (Chialvo et al. 2012).

In our study, we account for the short-range van der Waals force through a gradient of adhesive particle pressure in the solid phase momentum equation under the Eulerian-Eulerian framework. We propose two adhesive pressure models, a kinetic-theory-based model and a coordination-number-based one, and we check their ability to produce an overshoot in the bed pressure drop of Geldart group A particles.

Prediction of Pressure Drop Overshoot

Bed pressure drop and voidage profiles as a function of superficial gas velocity of 156 and 67 micron glass beads (Geldart B and A particles, respectively) measured by Soleimani et al. (2020) are presented in Fig. 1. As we can see, there is no overshoot in the increasing velocity pass pressure drop profile of the Geldart B particles as the corresponding fixed-bed and minimum fluidization voidages are practically identical. However, a discernible pressure drop overshoot is observed at the minimum fluidization velocity in the fluidization branch of the experiment with Geldart A particles, which corresponds to the difference between ε_0 and ε_{mf}.

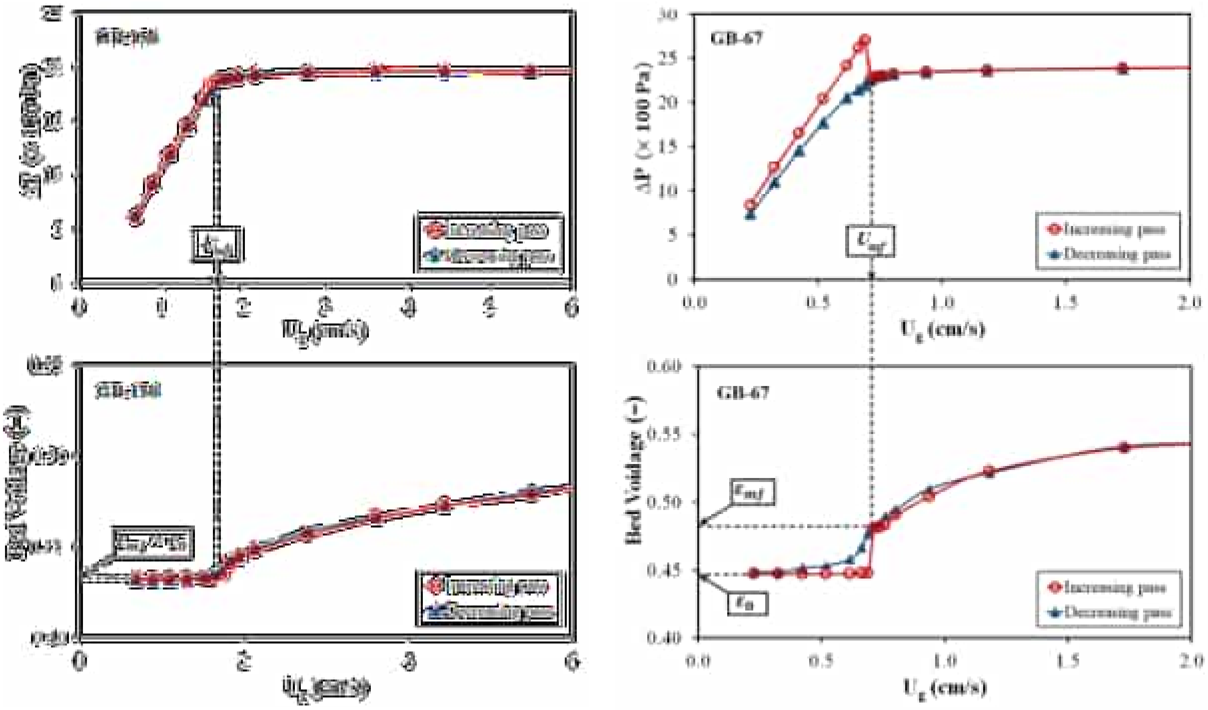

Fig. 1. Bed pressure drop and corresponding voidage profiles of particles with typical behaviors of Geldart group B (GB-156) and A (GB-67) measured by Soleimani et al. (2020). 'U_{mf}' represents minimum fluidization velocity, 'ε_0' bed voidage at fixed bed state (loose bulk voidage) and 'ε_{mf}' bed voidage at minimum fluidization.

In our work, we carry out Eulerian-Eulerian simulations using the NEPTUNE_CFD code. Transport equations and models implemented in this code can be found in Ansart et al. (2017). In the two-fluid model, the solid stress is composed of kinetic, collisional, and frictional contributions. The kinetic and collisional stresses are based on the kinetic theory of granular flow. The former is dominant in dilute flows while the latter in moderately dense flows. The friction stress of particles is used to account for the interaction of individual particles with multiple neighbors through sustained contact at high solid volume fractions. The solid pressure represents the solid phase normal forces caused by particle-particle interactions. For the frictional pressure of particles, the following semi-empirical model (Johnson et al. 1990) is used:

$$P_p^f = Fr\frac{\left(\alpha_p - \alpha_{p,min}\right)^n}{\left(\alpha_{p,max} - \alpha_p\right)^m} \qquad \alpha_p > \alpha_{p,min} \tag{1}$$

where Fr, n and m are constants and $\alpha_{p,min}$ and $\alpha_{p,max}$ are the threshold solid volume fraction for friction and the close-packing solid volume fraction, respectively. In this study, a negative adhesive pressure is added to the solid pressure for all values of α_p in order to take into consideration the van der Waals interaction among the particles. The added negative term has the effect of decreasing the repulsion between particles. In what follows, we propose two adhesive pressure models and test their ability to create a bed pressure drop overshoot.

Kinetic-theory-based adhesive pressure model

The kinetic theory approach is based on the analogy between the random motion of particles in rapid granular flow and the thermal motion of molecules in gas. The derivation of the adhesive pressure model using the kinetic theory of granular flow is based upon the work of Parmentier (2010). The van der Waals force can be introduced in the Boltzmann-Liouville equation using the BBGKY hierarchy:

$$\frac{\partial f_p}{\partial t} + \frac{\partial}{\partial x_i}\left(c_{p,i} f_p\right) + \frac{\partial}{\partial c_{p,i}}\left(\langle\frac{F_{p,i}}{m_p} \mid \boldsymbol{x_p} = \boldsymbol{x}, \boldsymbol{u_p} = \boldsymbol{c_p}\rangle f_p\right) = \left(\frac{\partial f_p}{\partial t}\right)_{coll} + \left(\frac{\partial f_p}{\partial t}\right)_{ad} \tag{2}$$

with (He and Doolen 2002)

$$\left(\frac{\partial f_p}{\partial t}\right)_{ad} = \iint \frac{\partial f_p^{(2)}}{\partial c_{p,i}} \frac{\partial}{\partial x_i}\left(\frac{V(\|\boldsymbol{x}^* - \boldsymbol{x}\|)}{m_p}\right) d\boldsymbol{c}_{\boldsymbol{p}}^* d\boldsymbol{x}^* \tag{3}$$

The two terms on the right-hand side of Eq. (2) represent the rate of change in the probability density function due to particle-particle collision and van der Waals adhesive interaction, respectively. $f_p^{(2)}(\boldsymbol{c}_{\boldsymbol{p}}, \boldsymbol{x}, \boldsymbol{c}_{\boldsymbol{p}}^*, \boldsymbol{x}^*, t)$ is the two-particle probability density function and $V(\|\boldsymbol{x}^* - \boldsymbol{x}\|)$ is the interaction potential between two particles leading to the adhesive force. The Van der Waals interaction potential between two spheres proposed by Elimelech et al. (1998) is used:

$$V(\|\boldsymbol{x}^* - \boldsymbol{x}\|) = -\frac{A}{24}\left[\frac{2}{2u + u^2} + \frac{2}{(1 + u)^2} + 4\ln\left(\frac{2u + u^2}{[1 + u]^2}\right)\right] \tag{4}$$

with $u = \|\boldsymbol{x}^* - \boldsymbol{x}\|/d_p - 1$ is the dimensionless distance between the two particle surfaces. A is the Hamaker constant which depends on the composition of the particles and of the interstitial gas. The force associated with this interaction potential is written:

$$F_{p^* \to p}^{ad} = \frac{A}{6d_p} \frac{1}{(2u + u^2)^2} \frac{1}{(1 + u)^3} \frac{\boldsymbol{x}^* - \boldsymbol{x}}{\|\boldsymbol{x}^* - \boldsymbol{x}\|} \tag{5}$$

$F_{p^* \to p}^{ad}$ represents the adhesive force exerted by particle p^* with center at $\boldsymbol{x}^*$ on particle p with center at $\boldsymbol{x}$. For distance between the surfaces of two particles smaller than a typical interatomic distance S_0, Eqs. (4) and (5) are no longer valid and the Van der Waals force is set to a constant and maximal value in order to represent the physical repulsive nature and avoid the singular attractive force when the surface separation distance is equal to zero. Assuming uncorrelated colliding particle velocities (Enskog approximation for dense flows), a momentum equation of the solid phase containing a gradient of adhesive particle pressure can be derived from Eq. (2). The negative adhesive pressure resulting from the attraction between particles is written as (Parmentier 2010):

$$P_p^a \approx -A\frac{n_p}{\alpha_p}\ln\left(\frac{d_p}{S_0}\right)\int_0^{\alpha_p} \alpha_p\left(g_0 + \alpha_p\frac{\partial g_0}{\partial \alpha_p}\right) d\alpha_p \tag{6}$$

The radial distribution function, g_0, which can be seen as a measure for the probability of interparticle contact, is written (Lun and Savage 1986):

$$g_0 = \left(1 - \frac{\alpha_p}{\alpha_{p,max}}\right)^{-2.5\alpha_{p,max}} \tag{7}$$

Using Eq. (6), the adhesive pressure is expressed as:

$$P_p^a = -\frac{B}{d_p^3} 2\alpha_{p,max}^2 \left[\frac{25}{6} + \left(-\frac{3}{2}\frac{\alpha_p^2}{\alpha_{p,max}^2} + \frac{20}{3}\frac{\alpha_p}{\alpha_{p,max}} - \frac{25}{6}\right) g_0\right] \tag{8}$$

with

$$B = A\frac{3}{\pi}\ln\left(\frac{d_p}{S_0}\right) \tag{9}$$

Quasi-two-dimensional simulations of Geldart A particles having a diameter of $100\ \mu m$ and a density of $1440\ kg/m^3$ were conducted. In these simulations, the particles are fluidized with a gas having density of $1.205\ kg/m^3$ and viscosity of $1.8 \times 10^{-5}\ Pa.s$ in a cuboid bed with thickness of $4d_p$, width of $60d_p$ and height of $200d_p$. The geometry is meshed using square cells having a size of $2d_p$. The bed is initially filled with the solids up to a height of $36d_p$ with a uniform solid volume fraction of 0.6. The frictional pressure model is activated above $\alpha_{p,min}$ equals to 0.58. Substituting $2.1 \times 10^{-21}\ J$ for A and $1\ nm$ for S_0 in Eq. (9) gives B equals to $2.3 \times 10^{-20}\ J$. The curves of the normalized bed pressure drop and average gas volume fraction in the bed as a function of the superficial gas velocity during fluidization and defluidization cycles with different B values are shown in Fig. 2. The normalized bed pressure drop is defined as the ratio of the pressure drop across the whole bed to the pressure drop equivalent to the weight of particles ($m_b g/S_b$), where m_b denotes the mass of the particles bed and S_b the cross-sectional area of the bed. As seen in Fig. 2, producing a pressure overshoot requires multiplying B by 10^6 and the hysteretic behavior between the increasing and decreasing velocity pass curves is not predicted. The curves of the bed voidage presented in Fig. 2 show the decrease in the gas fraction for $B = 2.3 \times 10^{-14}\,J$ because of the relatively high adhesion effect.

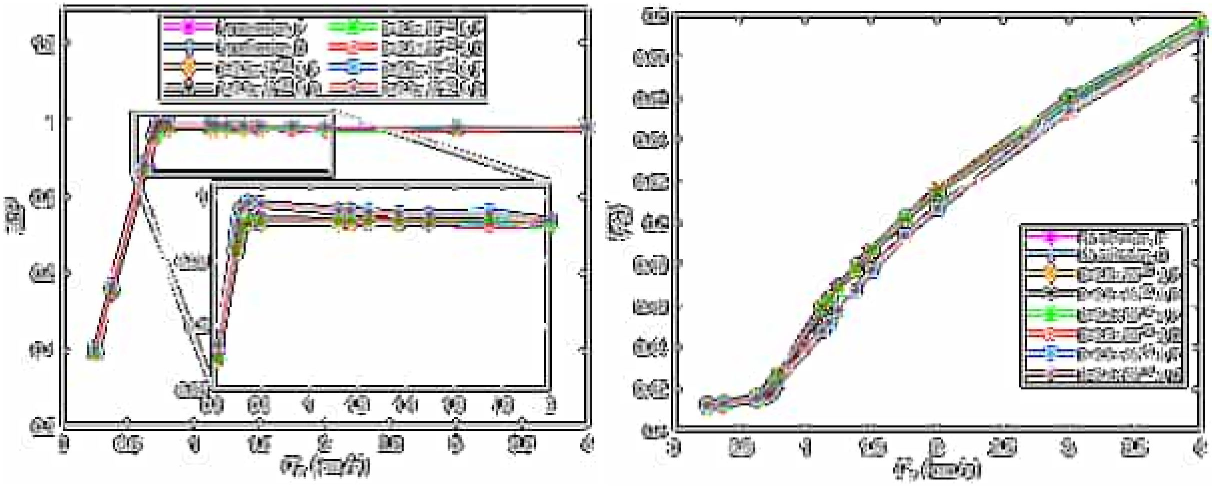

Fig. 2. Normalized time-averaged overall bed pressure drop and time-spatial averaged gas volume fraction in the bed during fluidization and defluidization cycles with different B values. ‘F’ represents fluidization branch and ‘D’ defluidization branch in this and Fig. 3.

Therefore, the adhesive contribution introduced by the kinetic theory model is not sufficient to generate an overshoot in the bed pressure drop. This might be attributed to the binary and instantaneous collisions assumption used in the kinetic theory because fixed-bed flows are dominated by the effect of multiple and long duration contacts. In addition, the pressure-drop hysteresis is not predicted because the history effect is not taken into account. The adhesive pressure is function of α_p only (symmetric closure). In the next section, we propose an approach suitable for quasi-static flows based on the coordination number.

Coordination-number-based adhesive pressure model

In what follows we derive an adhesive pressure model by assuming that the dominant van der Waals interaction is between particles in long time contact characterized by coordination number. The coordination number is defined as the mean number of particles in contact with a given particle, which can be expressed as:

$$CN = 2\frac{n_c}{n_p} \tag{10}$$

where n_c is the average number of contacts per unit volume and n_p is the number of particles per unit volume. The factor 2 is present since each contact is shared by two particles.

Goldenberg et al. (2006) proposed an expression for the stress tensor in quasi-static granular matter (without the kinetic contribution). According to them, the interparticle stress tensor component due to adhesive force may be computed as:

$$\sigma_{ij}^{ad} = -\frac{1}{V}\sum_{c\in V} f_i^c b_j^c \tag{11}$$

where the sum is over all the contact points c in volume V. f_i^c represents the interaction force between two particles in contact at c and b_j^c represents the vector joining the centers of these two particles if both centers are included in V, or only the part in V if one of the centers is apart from the volume V.

Using Eq. (5), the adhesive contact force is written:

$$F^c_{p^*\to p} = \frac{A}{6d_p}\frac{1}{(2u_0+u_0^2)^2}\frac{1}{(1+u_0)^3}\boldsymbol{k}^* \approx \frac{A}{6d_p}\frac{1}{4u_0^2}\boldsymbol{k}^* \tag{12}$$

with $u_0 = S_0/d_p$ is a minimum dimensionless separation distance between two particle surfaces and $\boldsymbol{k}^* = (\boldsymbol{x}^* - \boldsymbol{x})/\|\boldsymbol{x}^* - \boldsymbol{x}\|$ is a unit vector along the line of centers of two interacting particles. Then, the adhesive stress in a homogeneous system can be written as:

$$\sigma^{ad}_{ij} = \frac{1}{V}\sum_{c\in V}\frac{A}{24u_0^2}k_i^* k_j^* \tag{13}$$

The isotropic component of the adhesive stress is the adhesive pressure:

$$P_p^a = -\frac{\sigma^{ad}_{ii}}{3} = -\frac{n_c}{3}\frac{Ad_p^2}{24S_0^2} \tag{14}$$

Using relation (10), the adhesive pressure can be expressed as:

$$P_p^a = -\frac{\alpha_p}{\pi d_p^2}CN\frac{Ad_p}{24S_0^2} \tag{15}$$

We performed simulations of the 100 micron particles using $A = 2.1 \times 10^{-21}\,J$ and $S_0 = 1\,nm$ to check the ability of the model presented in Eq. (15) to create the pressure drop overshoot. We used a constant coordination number of 4.77 corresponding to a fixed bed state and correlations between the coordination number and the solid volume fraction proposed by Hou et al. (2012) based on their CFD-DEM simulation results:

$$CN = 2 + 3.25\alpha_p^{0.4} \qquad \text{for expanded beds} \tag{16}$$

$$CN = 4.87 \times 10^{-5}\frac{1-(1-\alpha_p)^{2.8}}{(1-\alpha_p)^{11.6}} \qquad \text{for fluidized beds} \tag{17}$$

The profiles of the normalized bed pressure drop and the average gas volume fraction in the bed are shown in Fig. 3. As we can see, an overshoot is predicted using the constant fixed-bed coordination number and the expanded-bed correlation, while no overshoot is generated using the fluidized-bed correlation. Thus, the coordination-number-based model gives an adhesive contribution large enough to produce an overshoot in the bed pressure drop.

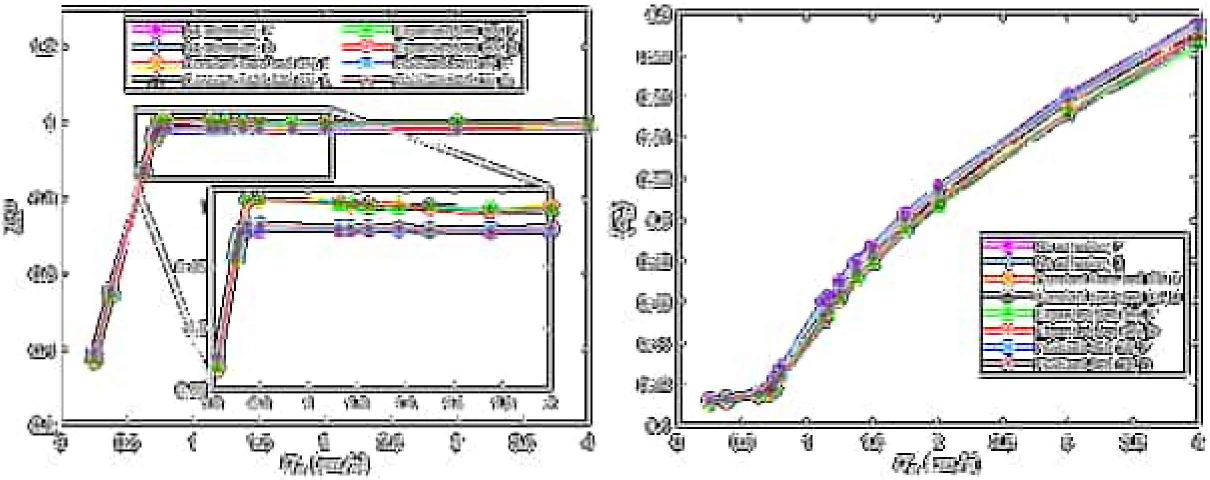

Fig. 3. Normalized time-averaged overall bed pressure drop and time-spatial averaged gas volume fraction in the bed during fluidization and defluidization cycles without and with adhesion effect using the coordination-number-based model.

The experimental bed voidage profile of Geldart A particles presented in Fig. 1 shows that at superficial gas velocities lower than U_{mf} in the increasing velocity pass, the bed is at a constant voidage ε_0. When the gas velocity reaches U_{mf}, the forces exerted by the gas on the particles overcome the interparticle forces and the weight of particles leading to destruction of the contact network and sudden jump in the bed voidage from ε_0 to ε_{mf}. However, in the decreasing pass, the bed voidage gradually decreases from ε_{mf} to ε_0 with the decrease in the gas velocity from U_{mf} to zero. Fig. 3 shows a decrease in the bed voidage due to adhesion, but the hysteretic behavior between the fluidization and defluidization cycle curves observed in the experiments is not predicted. In order to get this behavior, the role of interparticle forces should be dominant over that of hydrodynamic forces in the fixed bed state (the values of the different model parameters) and the contact network formation and destruction should be considered (the coordination number evolution).

Conclusion

This work presents two adhesive pressure models accounting for the van der Waals interaction among particles. The kinetic theory model, which is suitable for rapid granular flows, is not appropriate for quasi-static flows because it does not account for the long term and multi particle-particle contacts. This model gives an adhesion effect not strong enough to create the bed pressure drop overshoot. The other model expressed in terms of the mean number of contacts per particle accounts for the multiple and sustained contacts. It gives an adhesive contribution much larger than the one of the kinetic theory model and is able to produce the overshoot in the bed pressure drop. Currently, we are working on a quantitative comparison with experiments by testing the effect of different model parameters. The next step is to propose a transport equation for the coordination number able to account for the history effect and the transition between the different flow regimes (fixed, expanded and fluidized bed states) in order to predict the pressure-drop hysteresis.

References

Ansart, R., Garcia-Triñanes, P., Boissière, B., Benoit, H., Seville, J. P., and Simonin, O. *Dense gas-particle suspension upward flow used as heat transfer fluid in solar receiver: Pept experiments and 3d numerical simulations.* Powder Technology 307, 25–36. 2017.

Chialvo, S., Sun, J., and Sundaresan, S. *Bridging the rheology of granular flows in three regimes.* Physical review E 85 (2), 021305. 2012.

Elimelech, M., Jia, X., Gregory, J., and Williams, R. *Particle deposition and aggregation: Measurement, modelling and simulation woburn.* Massachusetts Butterworth-Heinemann 440. 1998.

Goldenberg, C., Atman, A. P., Claudin, P., Combe, G., and Goldhirsch, I. *Scale separation in granular packings: stress plateaus and fluctuations.* Physical review letters 96 (16), 168001. 2006.

He, X. and Doolen, G. D. *Thermodynamic foundations of kinetic theory and lattice boltzmann models for multiphase flows.* Journal of Statistical Physics 107 (1-2), 309–328. 2002.

Hou, Q., Zhou, Z., and Yu, A. *Micromechanical modeling and analysis of different flow regimes in gas fluidization.* Chemical engineering science 84, 449–468. 2012.

Johnson, P. C., Nott, P., and Jackson, R. *Frictional–collisional equations of motion for particulate flows and their application to chutes.* Journal of fluid mechanics 210, 501–535. 1990.

Lun, C. and Savage, S. *The effects of an impact velocity dependent coefficient of restitution on stresses developed by sheared granular materials.* Acta Mechanica 63 (1-4), 15–44. 1986.

Parmentier, J.-F. *Extension du formalisme Euler/Euler pour la simulation des lits fluidises de particules du groupe A dans la classification de Geldart.* PhD thesis, Institut National Polytechnique de Toulouse. 2010.

Soleimani, I., Elahipanah, N., Shabanian, J., and Chaouki, J. *In-situ quantification of the magnitude of interparticle forces and its temperature variation in a gas-solid fluidized bed.* Chemical Engineering Science, page 116349. 2020.

Visser, J. *Van der Waals and other cohesive forces affecting powder fluidization.* Powder Technology 58 (1), 1–10. 1989.

STUDY ON THE DYNAMIC CHARACTERISTIC OF THE CIRCULATING FLUIDIZED BED WHOLE LOOP AT VARIABLE LOAD

Boyu Deng[1], **Man Zhang**[1], **Yi Zhang**[1], **Junfu Lyu**[1], **Hairui Yang**[1*], **Mingming Gao**[2*]

[1]Key Laboratory for Thermal Science and Power Engineering of Ministry of Education, Department of Energy and Power Engineering, Tsinghua University, Beijing, 100084, China
[2]The State Key Laboratory of Alternate Electric Power System with Renewable Energy Sources, North China Electric Power University, Beijing, 102206, China

*Email: *yhr@mail.tsinghua.edu.cn, mingminggaoncepu@163.com*

Abstract

With more and more renewable energy power plants connecting to the power grid in China, to ensure the power quality and the security of the power grid, all thermal power units connected to the power grid are required to participate in the depth peak regulation, which proposes a high standard for the tracing performances to the load demand of all units. However, currently, the maximum load change rate of many circulating fluidized bed (CFB) units cannot satisfy the assessment criteria laid down by the power grid. To increase the ability of CFB units in load change and meet the ultra-low emission standard of China, it is necessary to first pay attention to the characteristic of the gas-solid flow in the CFB whole loop at variable load, which lays the foundation of other physical processes, to optimize the design and operation of CFB units. Aiming to develop a deeper understanding of the gas-solid flow in the CFB whole loop at variable load, a visual cold CFB test rig was built, which has a height of 10.3 m and a square section area of 0.1×0.1 m^2. CFD models based on the test rig were also set up using CPFD Software Barracuda and were verified with experiments conducted on the same test rig at fixed and variable loads. The dynamic characteristic of the mass and pressure balance among the whole loop during the load changing process were studied by decreasing the fluidizing velocity in the riser. Results showed that the total particle mass in the standpipe decreased gradually whereas the pressure drop in the riser increased accordingly during the load reduction process.

Introduction

Due to its outstanding advantages in combustion efficiency (can be found in Yue et al. (2016)), fuel flexibility (can be found in Cai et al. (2018)) and emission control, circulating fluidized bed (CFB) boiler combustion technology has become the best option for large-scale utilization of low calorific value fuels in China. Therefore, CFB combustion technology has developed rapidly in China, with more than 350 units of 100MW class and above, which makes China the world's largest CFB technology application market. However, with the rapid development of renewable energy power generation, more and more renewable energy power plants are connected to the power grid in China. In order to ensure the power quality and the security of the power grid, all thermal power plants connected to the power grid are required to adopt automatic generation control (AGC) mode to participate in the depth peak regulation, compensating for the inherent intermittency of renewable energy power generation. In this mode, owing to the complexity of the power grid, the load command of each unit is in a state of frequent change, which proposes a high standard for the tracing performances to the load demand of all units.

On the contrary, owing to the huge hydrodynamic and thermal inertia of the bed materials in CFB boilers, the maximum load change rate of many CFB units is still below 2%/min currently, which cannot satisfy the assessment criteria laid down by the power grid. To increase the ability of CFB units in load change and meet the ultra-low emission standard of China, it is necessary to first pay attention to the characteristic of gas-solid flow in the CFB whole loop at variable load, which lays the foundation of other physical processes in CFB boilers. This is because the hydrodynamic characteristics such as solid concentration determine the distribution of combustion profile and the heat transfer coefficient, and thus have a profound impact on the combustion and heat transfer processes (can be found in Lu et al. (2002) and Yang et al. (2009)). Besides, under variable load conditions, bed materials will be distributed dynamically between the furnace and the external loop consisted of a cyclone, standpipe, and loop seal based on the mass and pressure balance of the CFB whole loop. And the mass distribution of bed materials also has a great influence on the combustion and heat transfer processes. Therefore, under such circumstances, it is highly essential to conduct experimental and simulation studies on the hydrodynamic characteristic of the CFB whole loop under variable load conditions.

So far, the common numerical models proposed for the simulation of the two-phase flow in CFB boilers can be mainly distinguished into two categories: the Eulerian-Eulerian (EE) models and the Eulerian-Lagrangian (EL) models. The EE models treat the solid phase as pseudo continuum and use generalized Navier–Stokes equations for modeling both solid and fluid phases (can be found in Wang et al. (2014)). Nevertheless, it is difficult for the EE models to consider the variations of particle properties, such as the particle size distribution (PSD), density diversification and sphericity. On the other hand, the EL models treat particles as separate, solid points and use Newtonian equations of motion to model their behaviors. Among all EL models, the computational particle fluid dynamics (CFPD) method has gained popularity in recent years as a result of its distinct advantages in the description of particle properties and the requirement of computing resources. The CPFD method treats the fluid as a continuum and the particles as Lagrangian computational particles with specific size and density distributions (can be found in Wang et al. (2014)). The fluid is modeled by large-eddy simulation (LES) while the particle motion is solved by the multiphase-particle-in-cell (MP-PIC) numerical method. Many studies have been conducted on the gas-solid flow in the CFB whole loop using this method, however, few have been conducted on the hydrodynamic characteristic of the CFB whole loop at variable load.

Aiming to solve practical engineering problems and develop a deeper understanding of the gas-solid flow in the CFB whole loop at variable load, a visual cold CFB test rig was built. CFD models based on the test rig were also set up using CPFD Software Barracuda and were verified with experiments conducted on the same test rig at fixed and variable loads. The dynamic characteristic of the mass and pressure balance among the whole loop during the load changing process were studied with the help of this model by decreasing the fluidizing velocity in the riser.

Experimental Setup

The experiments in this study were conducted in a cold CFB test rig, as schematically shown in Fig. 1. The test rig is mainly composed of a riser, an air distributor in the bottom of the riser, a cyclone, a loop seal and a standpipe between the cyclone and the loop seal. The riser has a height of 10.3 m and a square section area of 0.1×0.1 m^2. The cyclone has a diameter of 0.16 m and high separation efficiency. The loop seal has an equivalent diameter of 0.06 m and the standpipe has a height of 9.5 m. A series of pressure points are arranged along the circulation loop to get the pressure distribution in the test rig. The aeration air to the loop seal is only supplied to the right part of the chamber. The bed materials used in the experiments are quartz sand, whose physical properties are shown in Table 1. More detailed information on the test rig can be found in another paper submitted by Hao Kong for CFB13 conference.

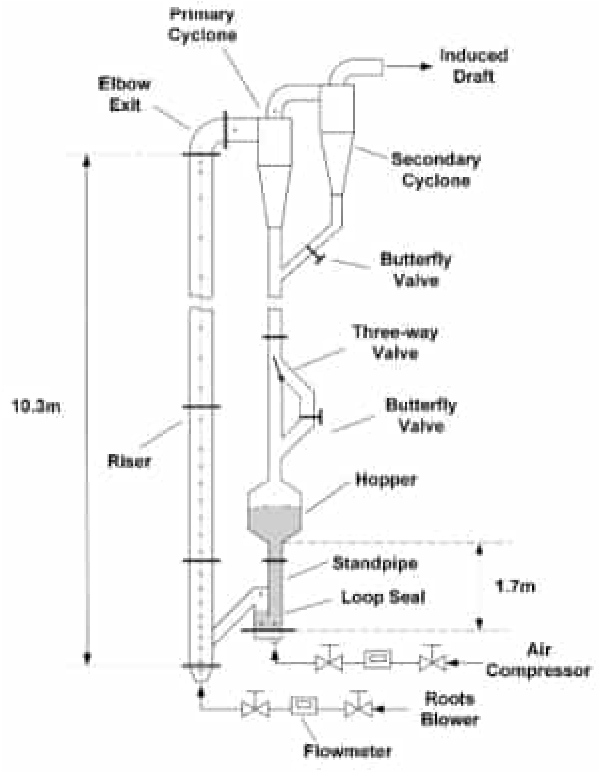

Fig. 1. Schematic of the CFB test rig.

Fig. 2. Schematic of the simulated CFB model.

Table 1. Physical properties of the bed materials.

Variable	Content	Unit
Real density, ρ_p	2650	kg·m^{-3}
Close pack volume fraction, θ_{cp}	0.58	/
Minimum fluidized velocity, u_{mf}	1.1	cm·s^{-1}
Size range, d	5-355	μm
Volume weighted mean diameter, d_{43}	130	μm
Surface weighted mean diameter, d_{32}	92	μm

Model Description and Validation

Model description

The CPFD numerical methods incorporated in Barracuda were used to solve the gas-solid flow in the test rig, and a self-adapting time step was utilized to speed up the calculation. The detailed gas-solid flow models used in the CPFD method are shown below.

(1) Continuity equation for fluid

$$\frac{\partial}{\partial t}(\theta_f \rho_f) + \nabla \cdot (\theta_f \rho_f \vec{u}_f) = 0 \tag{1}$$

(2) Momentum equation for fluid

$$\frac{\partial}{\partial t}(\theta_f \rho_f \vec{u}_f) + \nabla \cdot (\theta_f \rho_f \vec{u}_f \vec{u}_f) = -\nabla p - \vec{F} + \theta_f \rho_f \vec{g} + \nabla \cdot \rho_f \tau_f \tag{2}$$

(3) Momentum equation for particle

$$\frac{d\overrightarrow{u_p}}{dt} = D_p(\overrightarrow{u_f} + \overrightarrow{u_p}) - \frac{1}{\rho_p}\nabla p + \vec{g} - \frac{1}{\theta_p \rho_p}\nabla \tau_p \tag{3}$$

(4) Implicit numerical integration of the momentum equation for particle

$$\vec{u}_p^{\,n+1} = \frac{\vec{u}_p^{\,n} + \Delta t\left[D_p \vec{u}_{f,p}^{\,n+1} - \frac{1}{\rho_p}\nabla p_p^{n+1} - \frac{1}{\theta_p \rho_p}\nabla \tau_p^{n+1} + \vec{g}\right]}{1 + \Delta t D_p} \tag{4}$$

$$\vec{x}_p^{\,n+1} = \vec{x}_p^{\,n} + \Delta t \vec{u}_p^{\,n+1} \tag{5}$$

(5) Particle stress

$$\tau_p = \frac{p_s \theta_p^{\beta}}{\max\left[(\theta_{CP} - \theta_p), \varepsilon(1-\theta_p)\right]} \tag{6}$$

Initial and boundary conditions

Slight differences had been made to the geometric structure of the simulated CFB model to accelerate the simulation. As shown in Fig. 2, the secondary cyclone and three-way valve in the CFB test rig were not included in the simulated model, for the butterfly valves on top and bottom of the three-way valve and the three-way itself were closed during the experiments, causing the secondary cyclone and three-way valve to have little impact on the pressure distribution along the whole loop. Besides, the frequency of the induced fan was carefully controlled to keep the pressure of the outlet of the primary cyclone remain atmospheric pressure during the experiments.

As for the operating parameters, they were set strictly according to the experiments. The total particle mass (M_p) was set as 27 kg and particles were initialized in both the riser and the loop seal. Real PSD was used. Besides, the bottom plane of the riser and the bottom plane of the loop seal were set as flow boundary conditions. The fluidized air velocity (U_r) and the aeration (Q_l) were set as 4.15 m·s^{-1} and 1.58 m^3·h^{-1}. The top plane of the cyclone was set as pressure boundary condition, where the pressure was set as 101.325 KPa and particles were allowed to flow out. Wen-Yu/Ergun model was used to calculate the drag force on particles.

Sensitivity analysis and model validation

The accuracy of the simulation is largely dependent on the resolution of the mesh size and the number of computational particles, thus the mesh independence test should be made before carrying out the further simulation. The calculation domain was divided into 317145, 441663, and 633245 cells and the pressure drop in the riser was used to check the influence of mesh size, as shown in Table 2.

Table 2. Comparison of the time-averaged pressure drop in the riser under different mesh size.

Coarse size (Pa)	Medium size (Pa)	Fine size (Pa)	Experiment (Pa)
772	820	835	760

It can be seen that the mesh size has a clear effect on the pressure drop in the riser. When the coarse-size mesh was used, the pressure drop in the riser had an obvious deviation to the results obtained from the cases of finer mesh. When the medium-size mesh and the fine-size mesh were used, similar results were obtained, and they were both in good agreement with the experiment result. To make a balance between the simulation accuracy and computational cost, the medium-size mesh was preferred in this work, which can get a relatively satisfactory result on one hand and shows a tolerable computational speed on the other.

Results and Discussion

Given space limitations, this paper only discussed the dynamic characteristic of the CFB whole loop under load reduction condition, and the load reduction process was simulated by decreasing the fluidized air velocity (U_r) in the riser (after applying a 40th-order one-dimensional median filter), as shown in Fig. 3.

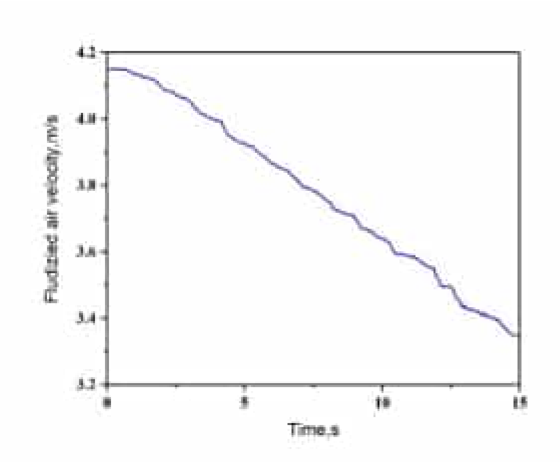

Fig. 3. Fluidized air velocity-time curve.

Aiming to obtain the dynamic characteristic of the mass and pressure balance among the whole loop during the load reduction process, particular attention should be paid to the total particle mass in the standpipe and the pressure drop in the riser, and their evolution with time under such conditions are shown in Fig. 4 and Fig. 5 (after applying a 40th-order one-dimensional median filter), respectively.

It can be seen that the particle mass in the standpipe decreased gradually whereas the pressure drop in the riser increased accordingly during the load reduction process. And this phenomenon can be explained by the following mechanism. Once the fluidized air velocity descends, the flow rate of the particles exiting the riser will decrease correspondingly. On the contrary, the flow rate of the returning particles will almost remain the same at the moment, resulting in the increase of the particle mass (solid concentration) in the riser, which leads to fewer particles in the standpipe and higher pressure drop in the riser.

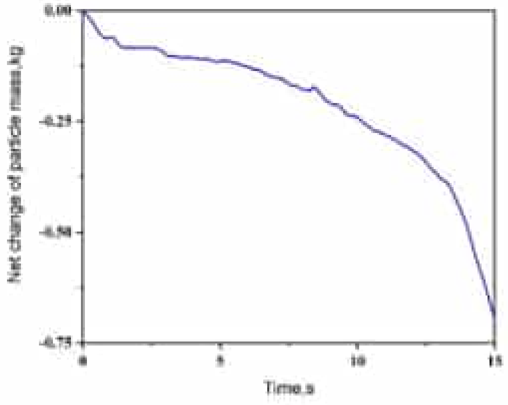

Fig. 4. Net change of particle mass-time curve.

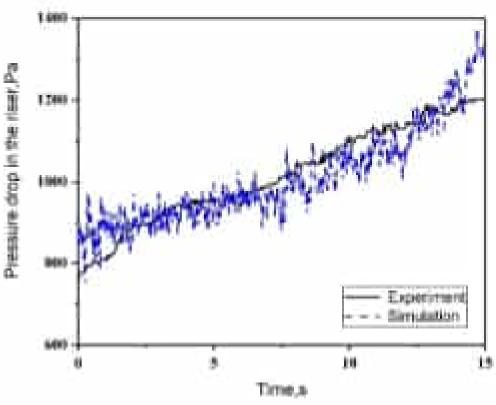

Fig. 5. Pressure drop in the riser-time curve.

Conclusion

The CPFD method was applied in the simulation of a circulating fluidized bed whole loop at variable load in this paper, and the dynamic characteristic of the mass and pressure balance among the whole loop during the load changing process were investigated by decreasing the fluidizing velocity in the riser. The simulation results were compared with the experimental data conducted in the same CFB test rig, and the accuracy of applying this method to the CFB whole loop modeling was verified.

The results showed that the mass and pressure distribution in the CFB whole loop would change over time during the load changing process. Particularly, for the load reduction condition, the total particle mass in the standpipe decreased gradually whereas the pressure drop in the riser increased accordingly until the equilibrium state was reached.

Acknowledgement

This study was financial supported by C9 League Science and Technology Cooperation Project(201903D421009) and Heilongjiang Key Science and Technology project(CG18A002).

Notation

u_f	fluid velocity, m·s^{-1}	θ_f	fluid volume fraction
ρ_f	fluid density, kg·m^{-3}	p	fluid pressure, Pa
τ_f	fluid stress tensor, m^{2}·s^{2}	F	interphase momentum transfer, N·m^{-3}
D_p	drag function, s^{-1}	u_f	particle velocity, m·s^{-1}
ρ_p	particle density, kg· m^{-3}	τ_p	particle normal stress, Pa
θ_{cp}	particle close pack volume fraction		

References

Cai R., Zhang H., Zhang M., et al. Development and application of the design principle of fluidization state specification in CFB coal combustion. Fuel Processing Technology. 2018. 174, 41-52

Lu J., Zhang J., Yue G., et al. Method of calculation of heat transfer coefficient of the heater in a circulating fluidized bed furnace. Heat Transfer-Asian Research. 2002. 31(7), 540-550

Wang Q., Yang H., Wang P., et al. Application of CPFD method in the simulation of a circulating fluidized bed with a loop seal, part I-Determination of modeling parameters. Power Technology. 2014. 253, 814-821

Yang H., Hai Z., Shi Y., et al. Effect of bed pressure drop on performance of a CFB boiler. Energy & Fuels. 2009. 23(6), 2886-2890

Yue G., Lyu J., Xu P. The up-to-date development and future of circulating fluidized bed combustion technology. Electric Power. 2016.01

EFFECT OF SOLIDS INLET AND OUTLET ON HYDRODYNAMICS OF BUBBLING FLUIDIZED BEDS WITH MACRO SOLIDS CIRCULATION

Yongmin Zhang[1*], Yongshi Liang[1], Meng Wang[1], Xiaotao Bi[2]

[1] *State Key Laboratory of Heavy Oil Processing, China University of Petroleum, Beijing, 102249, P. R. China*
[2] *Department of Chemical and Biological Engineering, University of British Columbia, 2360 East Mall, Vancouver, Canada V6T 1Z3*

*Email: *zym0876@gmail.com*

Abstract

The effect of macro solids flux on the hydrodynamics of bubbling fluidized beds of Group A particles was studied experimentally. Both radial and circumferential homogeneities were found to be improved in our beds of FCC particles, which is in contrast to the finding in Issangya et al. (2010) who found that increasing the solids flux worsens fluidization quality in their deep fluidized beds of similar FCC particles. Later, our CPFD simulations proved the validation of both findings and found the root cause of these two contradict findings is due to the different geometric configurations of the solids inlets in the two beds. In our bed, solids were fed in a more uniform way with higher lateral velocity component, which helps improve the fluidization quality, while the decentering feeding of solids into the bed by Issangya et al. (2010) aggregates the non-uniform flow distribution in bed and thus results into reduced fluidization quality.

Introduction

Dense fluidized bed reactors operated in bubbling or turbulent flow regimes are widely used in various industrial applications. Some are often operated with macro solids circulation, e.g. the regenerator and stripper of fluid catalytic cracking (FCC) units and the reactor and regenerator of methanol to olefin (MTO) units. The macro solids circulation fluxes in some fluidized beds are very high. For example, an FCC stripper is a typical bubbling fluidized bed operating with a solids circulation flux in 50~100 kg/(m^2.s).

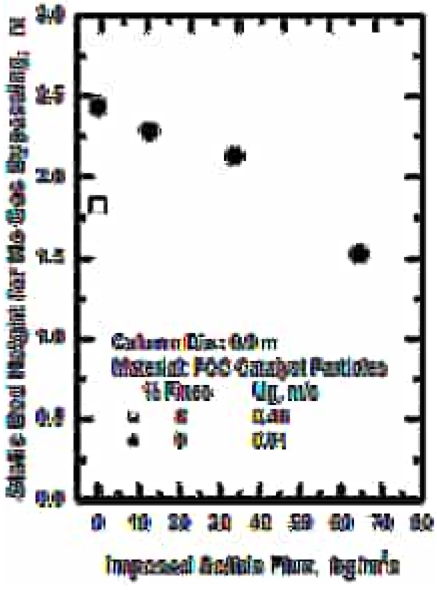

Fig. 1. Critical bed heights under different solids fluxes (Issangya et al., 2010)

In a dense fluidized bed with fine Group A particles, Wells (2001) found a special flow phenomenon, which they called “gas streaming” or “jet streaming”, in these beds if the bed height exceeds a critical value. This gas bypassing or channeling decreases the gas-solids contact efficiency and therefore the reactor performance. During gas streaming, pressure fluctuations will be higher and differ at the different circumferential measurement points. Wells (2001) attributed gas streaming to the compression of gas in emulation and the formation of local defluidized zone due to the high bed pressure drop.

When investigating the effect of macro solids flux on gas streaming in their deep bed, Issangya et al. (2010) found that increasing solids flux worsened bed fluidization quality as indicated by the higher magnitudes of pressure fluctuation and the smaller critical bed height for gas streaming under higher macro solids fluxes (Fig. 1) found in their experiment. They concluded that imposing a solids flux increases the potential for gas streaming.

Recently, we found a contrast phenomenon on the effect of macro solids flux in our cold fluidized bed model for studying FCC catalyst strippers. Later, we simulated the two fluidized beds with the Eular-Lagrangian CPFD model, trying to explain the different inner mechanisms of the two different findings. The aim of this paper is to describe how our experimental results are different from previous findings and explain the reasons to the differences.

Experimental setup and CPFD simulation

The experimental unit is shown in Fig. 2. The stripper section (7) is denoted by a red dashed box. The inner diameter of the stripper was 376 mm and its height was 2.1 m. Compressed air was used as fluidizing gas. An electrically controlled rotary valve was installed at the bottom of the stripper, by which solids circulating flux can be controlled accurately by changing the rotation speed of the connected motor via a frequency convertor. A ring distributor was used for gas distribution. A vortex quick separator and a cyclone in series captured the solids entrained in the gas stream. Fluidized particles were equilibrium FCC catalyst with a particle density of 1480 kg/m^3 and a Sauter mean diameter of 79 μm.

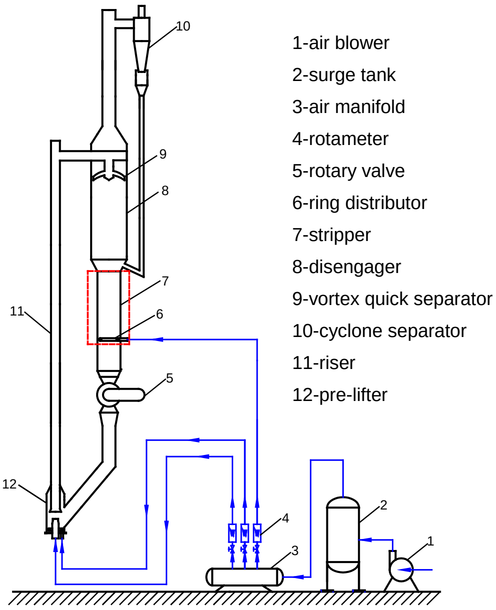

Fig. 2 Schematic of the experimental setup

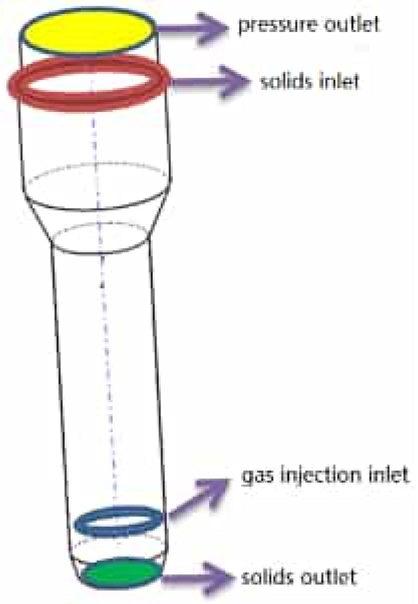

Fig. 3. Simulation geometry and boundary conditions

A four-channel fiber optical densitometry developed by the Institute of Process Engineering, Chinese Academy of Sciences was used to measure the local solids holdup. It could connect four probes to measure four solid holdups at a given radial distance from four differential circumferential positions synchronously. In this study, this method was used to measure the solids holdup at a same radial position from four evenly distributed circumferential angles. Therefore, both radial and circumferential profiles of solids holdup could be evaluated.

To simulate the hydrodynamics in the stripper section, the CPFD model based on the commercial platform Barracuda was used. The simulated geometry is shown in Fig. 3, where only the stripper section and a part of disengager are simulated. In the experiment, there were 24 holes on the ring distributor. To simulate this effect, a gas injection inlet is employed, which consists of 24 virtual nozzles facing downwards and inclined 45° outwards as in the experiment. A pressure outlet of 101 kPa was applied at the top of the stripper where both gas and solids are allowed to exit. Solids is fed into the bed from an annular boundary at the top of the stripper whose flow rate is controlled automatically to be equal to the sum of that entrained out from the gas outlet plus that leaving through the bottom solids outlet. As predominant solids enter into the bed from the four arms of the vortex quick separator, a lateral tangential velocity component is added based on the gas ejection velocity of the separator.

During the simulations, the properties of gas and solids (density and particle size distribution) as well as operating conditions were all kept the same as in the experiment. Sixty seconds were simulated for all cases in this study, which was long enough to capture the heterogeneous gas-solids flow in the bed. It took less than 10 s for the bed to reach a steady fluidization state. Therefore, the first 10 s of the simulated results were removed from the averaged simulation results to eliminate the influence during starting up of the bed. The mathematical equations and other setting of the CPFD model can refer a previous paper on a disc-donut stripper installed in the same stripping column by our team (Liang et al, 2015).

Results and Discussion

Figure 4 shows the measured radial profiles of solids holdup under a typical superficial gas velocity. The three subfigures correspond to the conditions under three different solids fluxes. Here, solids flux is calculated based on the cross sectional area of the stripper column. Except for the central point, there are four solids holdups at a radial position measured synchronously from four evenly distributed circumferential angles by the optical fiber probes.

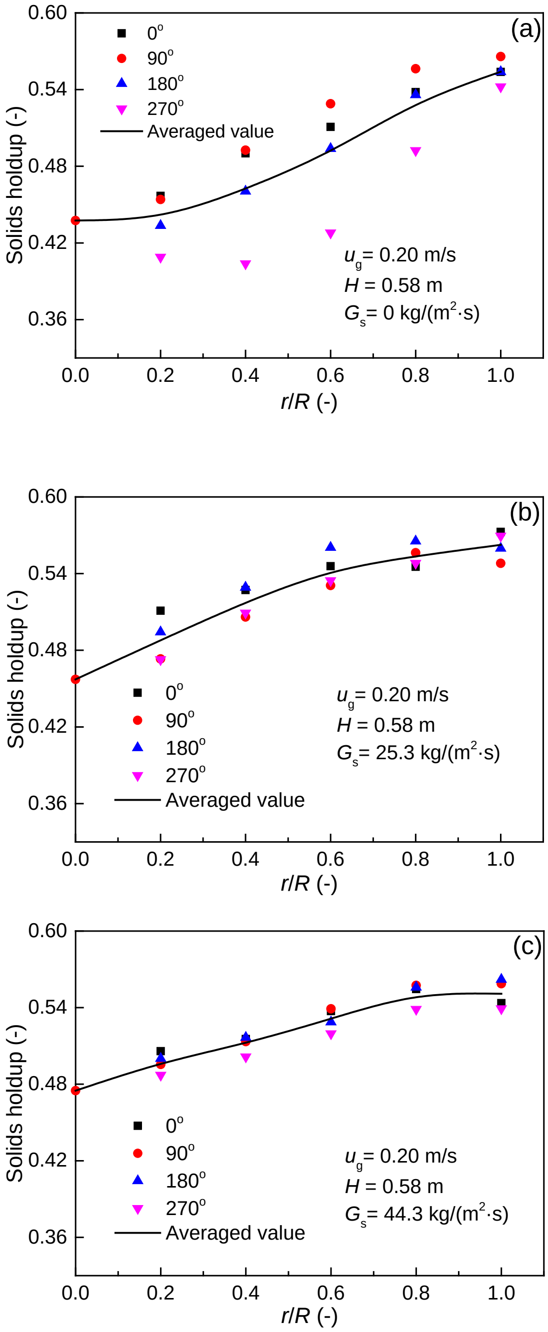

Fig. 4. The measured radial profiles of solids holdup under different solids fluxes

When there is no solids circulation, i.e. under G_s= 0 kg/(m^2.s), it can be seen from Fig. 4(a) that there exists serious circumferential flow heterogeneity among radial positions. Especially at r/R=0.4~0.6, scattering of the four measured solids holdups is the strongest. Gas seems to rise up preferentially at θ=270°, as the measured solids holdups are all minimum there. When the probe approaches to the column wall, the difference among the four solids holdups is much smaller than those in the other radial positions. Along the radial direction, the average solids holdup increases as the probe tips approach to the column wall.

When solids start to circulate through the stripper column, circumferential flow heterogeneity also exists in all radial positions. The measured average solids holdup still follows a similar trend along the radial direction. However, it can be clearly observed in Figs. 4(b) and 4(c) that circumferential scattering of solids holdups at most radial positions weakens with increasing solids fluxes.

To quantify the strength of circumferential and radial flow heterogeneities, we defined two indices. One is the circumferential heterogeneity index σ_θ which is the standard deviation of the four measured solids holdups at a given radial position. The other is the radial heterogeneity index σ_r which is the standard deviation of the six measured average solids holdups. The results of the two heterogeneity indices are plotted in Fig. 5(a) and Fig. 5(b), respectively. In general, σ_θ decreases with increasing solids flux, especially at r/R=0.4~0.6. Moreover, σ_r also decreases with increasing solids flux.

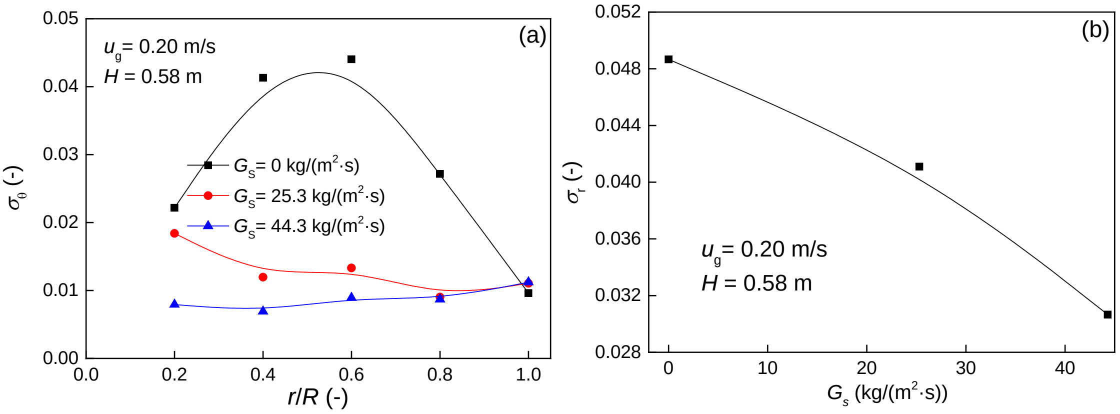

Fig. 5. Effect of solids flux on circumferential and radial heterogeneity indices

The reduction of both σ_θ and σ_r demonstrates clearly the improvement in bed homogeneity and bed fluidization quality. The finding shown in Figs. 4 and 5 are not only a single example. Almost all experimental results show a similar trend on the effect of macro solids flux. This trend clearly contrasts to that found by Issangya et al. (2010).

We carried out a series of CPFD simulations based on the experiments. Figure 6 shows the simulated contours of solids holdup at a same superficial gas velocity to that in Fig. 4. Simulations under three solids fluxes were conducted. It is seen that the distribution of solids holdup in the stripper section are axially symmetric, but more and more uniform with increasing solids flux. The results are agreeable with the experimental finding (Figs. 4 and 5). The agreement also validates the feasibility of CPFD model in predicting basic hydrodynamic features in these fluidized beds.

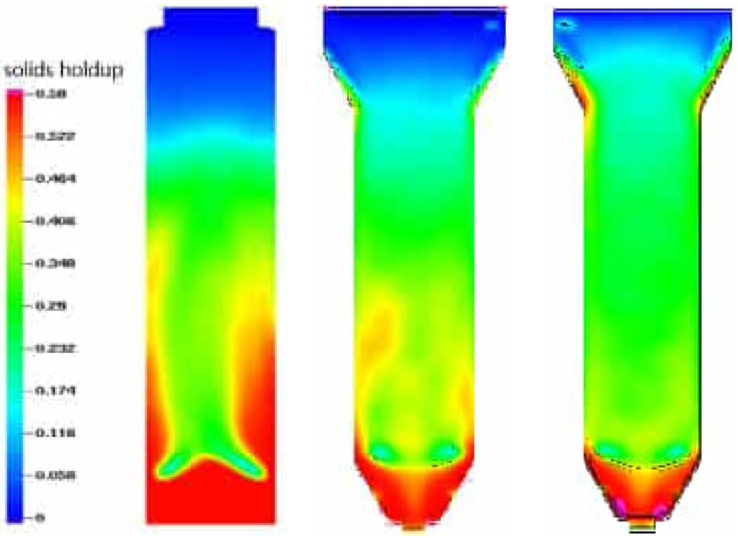

G_s=0 kg/(m^2.s) G_s=25 kg/(m^2.s) G_s=61 kg/(m^2.s)

Fig. 6. Simulated contours of solids holdup at different solids fluxes (u_g=0.2 m/s)

To explain the two contrasting findings by Issangya et al. (2010) and us, we compared carefully the differences in the operating conditions, particle properties, and bed geometry etc. Finally, we found that the configuration of solids inlet should be preferentially suspected. As both groups used FCC particles in the experiment, other small differences, e,g. bed dimension, static bed height are, by our experiences in fluidization, impossible to result into such contrasting changes in bed hydrodynamics. In our experiment, a predominant fraction of particles were collected by the vortex quick separator in the top of the disengager. The geometry and figure of the vortex quick separator are shown in Fig. 7. As a result, solids entered into the bottom stripper bed near the circumference of the stripper column. Moreover, the distribution of solids feeding into the stripper section were axially symmetric. Although there is some distance between the vortex injection arm and the bed surface, high solids speeds could be maintained by our observation via the transparent stripper column wall in experiment. For simplification, we used the same tangential velocity components to that of the gas ejection velocity in our simulations.

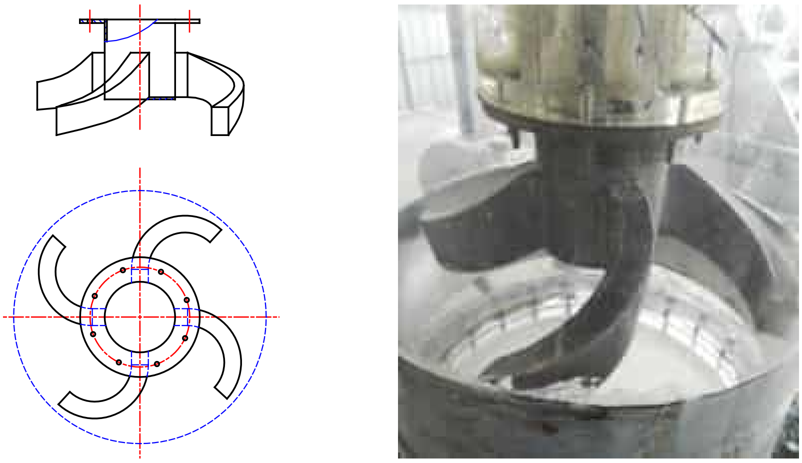

Fig. 7. Geometry of the vortex quick separator

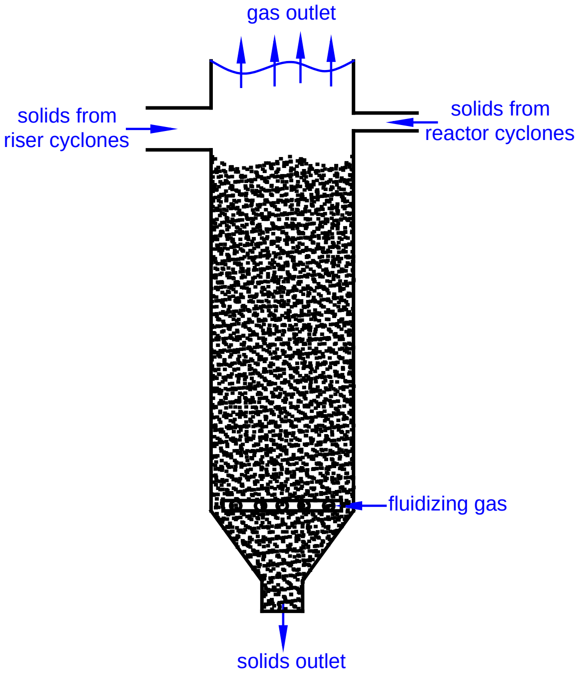

Fig. 8. Schematic solids inlet geometry of the fluidized bed of Issangya et al (2010)

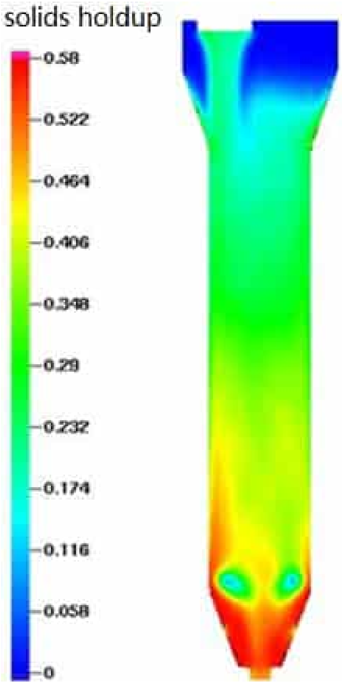

Fig. 9. Simulation result of a similar unit to that of Issangya et al (2010) with solids flux

Based on the description of their experimental unit, a schematic drawing of the solids inlet geometry of the fluidized bed of Issangya et al. (2010) is shown in Fig. 8. Most solids entering into the dense bubbling bed was from the dipleg of the two-stage riser cyclones. Only a small part of solids was from the dipleg of the two-stage reactor cyclones. Compared to our solids inlet geometry, solids feeding in Issangya et al. (2010) was from a single inlet near the column wall. This is clearly neither axially symmetric nor even compared to ours. The configurations of the solids outlets were almost the same, i.e. located in the column center.

As the detailed information on the dimensions of the bed of Issangya et al. (2010) is not available, we simulated a similar decentered solids feeding based on the simulated geometry of our simulation. The contour of solids holdup at a high solids flux is shown in Fig. 9. Compared to Fig. 6(a) where there is no macro solids circulation, the distribution of solids holdup in Fig. 9 is clearly not symmetrical. There is an area with higher solids holdup just beneath the location of solids inlet tube. This is generally agreeable with the worsening of the fluidization quality found by Issangya et al. (2010) under increased solids fluxes.

These simulations proved that both experimental findings on the effect of macro solids flux were real and right. It is the symmetrical solids inlets near the column wall and the central outlet of solids that leads to the improved fluidization quality under increased solids fluxes in our bed. The high lateral tangential solids velocity component also helped to break up bubbles and improve fluidization quality. The solids distribution uniformity in Issangya et al. (2010) was not expected to be good due to the decentered solids inlet. That is why a contrasting effect was observed. This indicates the importance to maintain uniform solids feeding when designing an industrial fluidized bed reactor with high macro solids circulation rates. To maintain good fluidization, we also suggest introducing high lateral velocity components for feeding solids into the bed.

Conclusion

1. In a deep-bed FCC stripper cold model, different effects of macro solids flux was found, which is in contrast to the previous finding by Issangya et al. (2010). The special solids inlet geometry and the induced strong lateral solids movement played an important role.
2. The CPFD simulations successfully predicted agreeable effects of the macro solids flux measured in both our unit and that of Issangya et al. (2010).
3. In industrial FCC reactors with high macro solids circulation rate, uniform multiple solids entries and means to create stronger lateral solids movements, e.g.by baffles or special separation device like in this study, are suggested to achieve better fluidization quality and improved reactor performance.

Notation

G_s	solids flux, kg/(m^2.s)
H	height above the distributor, m
r	radial position, m
R	radius of the stripper column, m
u_g	superficial gas velocity, m/s
σ_r	radial heterogeneity index, -
σ_θ	circumferential heterogeneity index, -
θ	circumferential angle, degree

References

Issangya AS, Karri SBR, Knowlton T. Effects of imposed solids flux and pressure on gas bypassing in deep fluidized beds of Group A materials. Proceeding of the 13th International Conference on Fluidization - New Paradigm in Fluidization Engineering. 2010, Gyeongju, Korea, pp.105-112.

Liang Y, Zhang Y, Lu C. CPFD simulation on wear mechanisms in disc-donut FCC strippers. Powder Technol., 2015, 279: 269-281.

Wells, JW. Streaming flow in large scale fluidization. Proceeding of AIChE Annual Meeting, Particle Technology Forum. 2001, Reno, Nevada, USA.

BINARY MIXING AND SEGREGATION OF BIOMASS AND SILICA SAND IN A FLUIDIZED BED

Tolu Emiola-Sadiq[1], Jiachen Wang[1], Lifeng Zhang[1*] and Ajay Dalai[1]

[1]Department of Chemical and Biological Engineering, University of Saskatchewan,
57 Campus Drive, S7N 5A9, Canada.

*Email : *lifeng.zhang@usask.ca*

Abstract

Binary mixing and segregation of biomass materials in a fluidized bed was experimentally investigated. Two different biomass materials were studied: willow sawdust and pelletized soy hull materials. Biomass loading investigated ranged from 5% to 30% by weight. The extent of mixing for each of the biomass composition was investigated using Lacey's mixing index based on the standard deviations of the sample at different axial positions in the bed. The experiments revealed the differences in the extent of particle distribution for pelletized biomass materials vs non-densified materials because of differences in particle size, density and importantly, the particle shape of the materials utilized. The results showed an increase in the extent of mixing as the fluidizing velocity increased for both pellet materials while the mixing index for sawdust decreased beyond a loading of 20%. With an increase in biomass loading, an increase in mixing index was found for the densified biomass material. A similar trend was observed for sawdust at the lower loading level. However, for the sawdust, the mixing index started to decrease at higher loading level beyond 20%. The results greatly contributed to the understanding of the hydrodynamics of binary and multicomponent mixtures involving biomass materials, especially, pelletized materials in fluidized beds.

Introduction

Thermochemical conversion of biomass to energy is usually carried out in fluidized bed reactors due to their excellent heat transfer, mass transfer and particle mixing between the bed materials (Kunii and Levenspiel 1991). The different physical characteristics of the components of binary mixtures make perfect mixing a challenge during fluidization. The lighter or smaller materials (flotsam) are more likely to agglomerate at the top part of the bed, while the heavier or larger materials (jetsam) tend to aggregate at the bottom of the bed (Rowe and Nienow 1976).

Several studies have been conducted on binary mixtures in fluidized bed columns (Peng et al. 2013; Huilin et al. 2007). Busciglio, Vella and Micale, (2012) utilized the digital imaging technique in quantifying and analyzing the mixing behavior of different binary material types in fluidized beds. Fotovat *et al.* (2015) conducted experiments on binary mixtures of large biomass particles in sand using the radioactive particle tracking technique. Bai *et al.* (2013) studied the mixing and segregation behavior with mixtures of ground walnut shell particles and glass beads in a fluidized bed using X-ray computed tomography measurements and digital image analysis. Sutar and Das (2012) investigated mixing patterns of glass beads in dolomite using the frozen bed method and computer simulation.

Many of the cited literature have studied mixing and segregation patterns of synthetic particles with only a few focusing on biomass materials. It is therefore hypothesized that the mixing and segregation pattern for biomass with different shapes, size and density would differ based on these aforementioned physical properties. The axial distribution pattern of the materials along the height of the reactor is therefore an important aspect to study as the amount of volatiles given off depends on the portion of the bed with the highest biomass distribution. While many previous studies have made use of synthetic materials like glass beads, woody biomass residues in form of particles; this study makes use of densified agricultural biomass residues in the form of pellets and compares the mixing behavior with non-densified biomass particles.

Experimental

The setup of the experiment consists of a cylindrical Plexiglas column of diameter 0.14m and a height of 0.78m. A rotary blower was used to supply fluidizing gas for the bed. Pressure transducers and a U-tube manometer were used to measure the pressure drop across the bed.

The biomass materials used for the experiment were soy hull pellets and willow sawdust. Silica sand served as the inert bed particles to foster fluidization of the biomass materials. The soy hull pellets have a cylindrical shape (D=5mm, L=10mm) and a bulk density of 731kg/m^3. The sawdust and silica sand have average particle sizes of 1120µm and 329µm, respectively. The bulk densities for sawdust and silica sand are 210kg/m^3 and 1510kg/m^3, respectively.

The frozen bed method was used to analyze the extent of mixing and segregation of the binary mixture. The biomass and sand were placed in alternate segments along the vertical axis of the bed. The final fluidization velocity (U_{ff}) also often called the complete fluidization velocity (Geldart, 1986) of the binary mixture was determined using the standard method of pressure drop against superficial velocity. A bed height to diameter ratio of 1.5 and fluidization time of 30 minutes were found sufficient for the experiment based on initial experimental runs conducted as well as existing literature. The range of fluidization velocity used was between U_{ff} and 4U_{ff}. Multiple runs were carried out for each experiment to ascertain reproducibility of the result with a maximum deviation of 6% recorded for all the runs. The fluidized bed material was extracted via suction from the bed in ten equal sections along the vertical axis of the bed. The samples taken from the bed were then sieved to separate the biomass from the silica sand.

Results and Discussion

Soyhull Pellets Axial Distribution

Six different loadings, 5 wt.% - 30 wt.% (with an increment of 5%) of soy hull pellets in silica sand were investigated. The axial distribution of the soy hull pellet and silica sand binary mixtures at different fluidizing velocities are shown in Fig.1. The dotted vertical lines on these figures correspond to mass percentage of biomass materials at perfect mixing for each biomass loading.

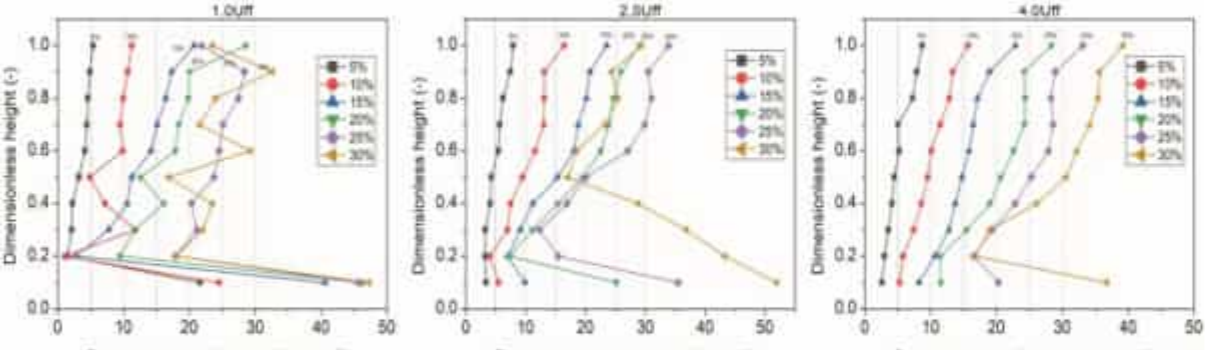

(a.) (b.) (c.)

Fig 1. Axial distribution of soy hull pellets in silica sand of different biomass composition and fluidization velocities at (a) 1.0 U_{ff}; (b) 2.5U_{ff}; and (c) 4.0U_{ff}

The higher density of the silica sand as compared to soy hull pellets prompted the movement of the denser silica sand to the bottom of the fluidized bed. The axial distribution profile for six loadings (5 wt.%-30 wt.%) of the soy hull pellets at 1.0U_{ff} is shown in Fig 1a. The distribution shows a heavily segregated bed for all six biomass loadings, most obvious at a dimensionless height of 0.1. The dimensionless or normalized height scale used corresponds to a zero value at the distributor position and a maximum unit value of 1 at the top of the bed material. As seen in the figure, for a biomass loading of 5 wt.% soy hull pellets in sand, there is about 20% of soy hull pellets at the base of the bed of dimensionless height 0.1. This heavily segregated pattern is also noticeable for the remaining biomass loading where a higher percentage weight of biomass is observed compared to the initial loading of the binary mixture. For example at 15 wt.% soy hull pellet loading, there is as much as 40% of the pellets at the 0.1 height position. Bai et al. (2013) reported a similar observation of increased segregation with increasing biomass loading. The top section of the bed shows a uniform random distribution, however higher loadings, 25 wt.% - 30 wt.%, of the soy hull pellets showed a less uniform pattern. The observed distribution at the low 1.0U_{ff} shows the extent of the effects of the gravity forces on the pelletized soy hull, which are much higher than the buoyant and drag forces.

The axial distribution profile for the six loadings of soy hull pellets at 2.5U_{ff} is shown in Fig 1b. It can be observed that an increase in the fluidization velocity from 1.0 U_{ff} to 2.5 U_{ff} had a remarkable effect on the soy hull pellet distribution especially for the 5 wt.% -15 wt.% initial loadings. At the 0.1 dimensionless height, the degree of segregation for the 5 wt.% and10 wt.% initial loading changed from about 22% and 25% at 1.0 U_{ff} to 4% and 6% respectively. Soy hull pellet loadings of 20 wt.% - 30 wt.% had little or no marked difference in terms of segregation especially at the bottom of the bed since the effect of the gravity forces are still well pronounced. As the fluidization velocity of the gas increased, more of the biomass materials moved to the upper section of the bed and the upward movement becomes less pronounced as the biomass loading increases. This shows why all loadings of the soy hull pellets have a little more composition by weight at the upper section of the bed (dimensionless height 0.7-1) than their respective initial loadings. This increased upward motion of biomass material as fluidization velocity increased was also observed by Zhang, Jin, and Zhong (2009).

At 4.0 U_{ff} it can be observed that the segregation at the bottom of the bed has decreased significantly for the soy hull pellet – sand binary mixture as compared to when the fluidization velocity was 2.5 U_{ff}. For a dimensionless height of 0.1, the 30 wt.% initial loading decreased from about 51% at 2.5U_{ff} to 37% at 4.0 U_{ff}. Although the 4.0 U_{ff} was not adequate to reduce the weight percent of the biomass to its initial loading of exactly 30 wt.%, there is a remarkable reduction in segregation.

Sawdust Axial Distribution

The percentage loading for the sawdust in silica sand binary mixture ranged from 5 wt.% - 20wt.%. The sawdust loading did not reach 30 wt.% composition unlike the soy hull pellets because severe channeling was observed within the bed at loadings beyond 20 wt.%. The relatively low density of the sawdust material required more volume to fill an equivalent mass as the soy hull pellets. The low density consequently meant that a relatively low mass of the sawdust would fill a larger volume within the bed than the pelletized soy hull materials. Thus, a 10% mass fraction of sawdust in silica sand would correspond to approximately 58% volume fraction of the same sawdust in silica sand binary mixture. The shape and morphology of the sawdust particles caused agglomeration with the silica sand in the bed especially at higher loadings of the sawdust i.e. beyond 15 wt.%. The higher volume and needle-like shape of the sawdust reduced the ease of fluidization. Therefore, as the loading of the sawdust particles increased in the binary mixture, the accompanying increase in the difficulty of fluidization resulted in an increase in the final/complete fluidization velocity. A similar observation of increased fluidization velocity was reported by Rao and Bheemarasetti (2001) for sawdust – sand binary mixtures .Fig 2 shows the axial distribution profile in weight percent of four different loadings (5 wt.% - 20wt.%) of sawdust inn silica sand along the height of the fluidized bed used for the experiment.

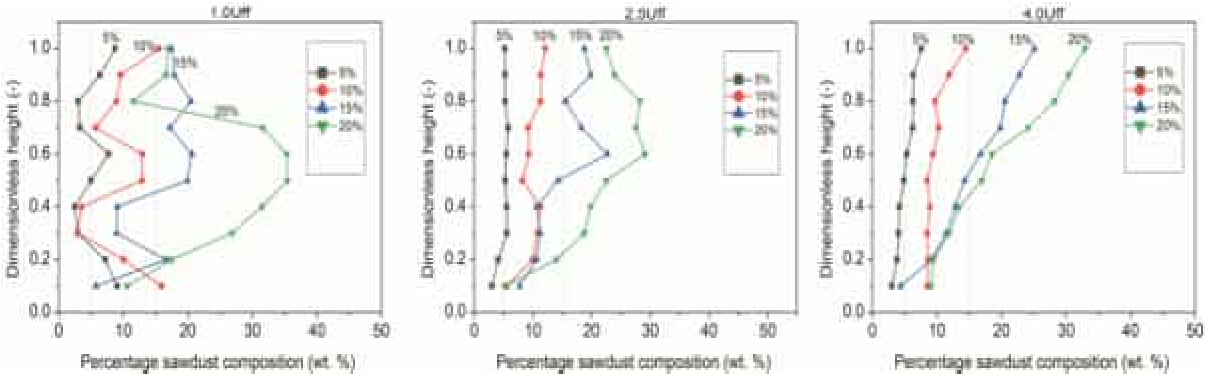

(b.) (b.) (c.)

Fig 2. Axial distribution of sawdust in silica sand of different biomass composition and fluidization velocities at (a) 1.0 U_{ff}; (b) 2.5U_{ff}; and (c) 4.0U_{ff}

The axial distribution profile for four loadings (5 wt.% - 20 wt.%) of sawdust-silica sand binary mixtures at 1.0 U_{ff} are shown in Fig 2a. All four binary mixtures exhibit some level of segregation along the bed. The degree of segregation of the sawdust in silica sand mixture is directly proportional to the weight percent of the sawdust loading. The segregation observed at this low velocity mainly due to the shape and density of the sawdust particles. Particles with low density and large diameter tend to exhibit a low mixing ability whenever they are in a binary mixture with more dense smaller particles. This limited mixing propensity was also reported in findings by Wirsum et al. (2001). As stated earlier, the higher loading biomass (20 wt.%) exhibited the highest segregation pattern since the high-volume content of sawdust in the bed hindered proper fluidization.

At a fluidization velocity of 2.5U_{ff}, it can be observed that the distribution of the sawdust in silica sand binary mixture is more uniform compared to the distribution at 1.0U_{ff}. The 5 wt.% sawdust loading shows an almost perfect distribution by weight percent along the axial direction of the fluidized bed as all the data points almost coincide with the perfect mixing black dotted line. The 15 wt.% and 20 wt.% sawdust loading have the lower half of the bed (0.1-0.5 dimensionless height) with less weight percent of sawdust because the fluidizing velocity at 2.5U_{ff} is sufficient to suspend the low-density sawdust particles in the mixture beyond the bed midsection. An increase in the fluidization velocity beyond 2.5U_{ff} should therefore move the particles beyond the bed midsection.

At a fluidization velocity of 4U_{ff} there is no significant change in the 5 wt.% sawdust loading when compared to the 2.5U_{ff}. There exists a slight difference in the distribution pattern for the 10 wt.% sawdust loading with the distribution getting more uniform along the lower half section of the bed. The most significant changes were observed for the 15% and 20% sawdust loadings where the distribution shows a linear profile along the bed height. The sawdust content at each section of the bed steadily increased from bottom to the top of the bed which can be explained by the buoyant and drag forces superseding the gravity forces due to the low density of sawdust.

Mixing Index

Lacey mixing index (Lacey 1954) was used to quantify the extent of mixing based on the variance between the biomass composition at total segregation and at a perfectly mixed scenario. The mixing index (M) is given by Eqs. 1 and 2

$$M = \frac{\sigma_0^2 - \sigma^2}{\sigma_0^2 - \sigma_r^2} \tag{1}$$

$$\sigma = \sqrt{\frac{1}{n-1} \sum_{i=1}^{n} (\, x_i - \overline{x}\,)^2} \tag{2}$$

Where, σ_0^2 is the variance of the biomass material concentration at complete segregation, σ^2 is the concentration variance at the actual mixed state, σ_r^2 is the variance of the random mixture at an almost perfectly mixed condition, x_i is the composition of biomass in the biomass-sand mixture, $\bar{x}$ is the average mass concentration of the biomass and n is the total sample number. Thus, a perfect mixture would have a value of M=1 and a totally segregated mixture a mixing index M=0. A perfect mixture would occur when the biomass concentration at any point along the bed axial direction equals the initial loading of the binary mixture. Fig 3 show the mixing indices for soy hull pellets and sawdust binary mixtures in silica sand at different loadings and gas velocities.

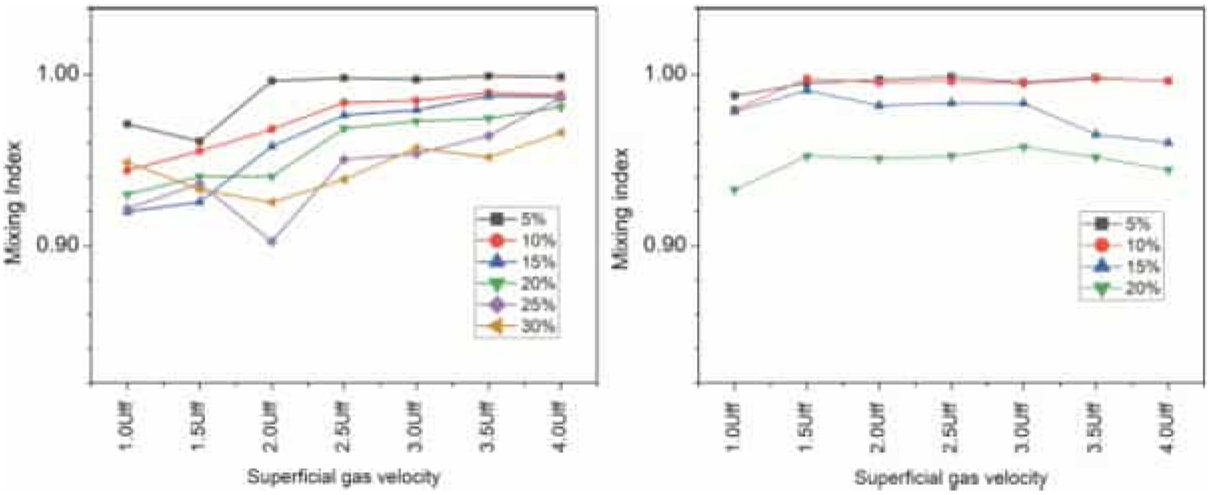

(a.) (b.)

Fig 3. Mixing index for different percentage composition and gas velocities for (a) soy hull pellets (b) sawdust particles

The mixing index for soy hull pellets in silica sand is illustrated in Fig. 3a. Generally, the mixing index increased as the superficial gas velocity increased as a result of the increased convective mixing caused by bubble motion in the bed. From the figure, it can be seen that further mixing at a fluidization velocity beyond $3.0U_{ff}$ had no significant effect on the mixing index value for the 5 wt.% - 20 wt.% loadings of the soy hull pellets in silica sand. This observation was also documented in mixing index results presented by Peng et al. (2013). Another noticeable trend observed is the decline in the values of mixing index as the percentage weight loadings of the soy hull pellets increased. This is attributed to the increase in particle segregation as the biomass loadings increased. At a gas velocity of $2.5U_{ff}$, the 5 wt.% soy hull pellets in silica sand binary mixture has a higher mixing index at about 0.98 compared to the 30% mixture which has a mixing index of 0.93.

For the sawdust - silica sand binary mixture, there is also a decrease in the mixing index with increasing biomass loading. This can be seen in Fig 3b. The low density of the sawdust makes a weight loading of 20% equivalent to 72% volume percent of the sawdust in silica sand binary mixture. A similar observation was noted by Clarke, Pugsley, and Hill (2005) where fluidization did not occur beyond a sawdust loading of 75% volume in the binary mixture. Similar to the pelletized soy hulls, there was an increase in values of mixing index as the fluidization velocity increased for the sawdust-silica sand binary mixture. The mixing index reached a peak and became almost constant at the $2.5U_{ff}$ fluidization velocity as the effect of increasing the fluidization velocity beyond this had negligible effects on the 5 wt.% and 10 wt.% sawdust loadings. Beyond $3.0U_{ff}$ the mixing index value dropped as some of the sawdust particles elutriated from the bed as a result of the low-density sawdust particles present in the bulk volume in the upper region of the bed.

Conclusion

The mixing behavior of two different biomass materials in binary mixtures with silica sand was investigated in a cylindrical fluidized bed. One of the biomass materials was pelletized while the other was in the powdered form. The mixing pattern along the axial axis of the bed was investigated by analyzing the distribution profile by weight percent of the biomass binary mixtures within the bed at different fluidization velocities. The mixing index for the biomass materials was used to quantify the extent of the mixing of the biomass with silica sand. An increase in the fluidization gas velocity increased the biomass content towards the top of the bed. The smaller biomass particles showed a higher mixing index value compared to the pelletized biomass, but the particle fluidization was limited to 20 wt.% particle loading while the pelletized biomass fluidized at up to 30 wt.% loading of the pellets in the silica sand. Increase in the biomass loading showed a decrease in the mixing index. Increasing the fluidization velocity led to an increase in the mixing index for the two biomass types.

References

Bai, Wei, Norman K. G. Keller, Theodore J. Heindel, and Rodney O. Fox. 2013. “Numerical Study of Mixing and Segregation in a Biomass Fluidized Bed.” *Powder Technology* 237:355–66.

Busciglio, A., G. Vella, and G. Micale. 2012. “On the Bubbling Dynamics of Binary Mixtures of Powders in 2D Gas-Solid Fluidized Beds.” *Powder Technology* 231:21–34.

Clarke, K. L., T. Pugsley, and G. A. Hill. 2005. “Fluidization of Moist Sawdust in Binary Particle Systems in a Gas-Solid Fluidized Bed.” *Chemical Engineering Science* 60(24):6909–18.

Fotovat, Farzam, Renaud Ansart, Mehrdji Hemati, Olivier Simonin, and Jamal Chaouki. 2015. “Sand-Assisted Fluidization of Large Cylindrical and Spherical Biomass Particles: Experiments and Simulation.” *Chemical Engineering Science* 126:543–59.

Geldart, D. 1986."Gas Fluidization Technology", D.Geldart (ed.) pg.26, John Wiley & Sons, New York.

Huilin, Lu, Zhao Yunhua, Jianmin Ding, Dimitri Gidaspow, and Li Wei. 2007. “Investigation of Mixing/Segregation of Mixture Particles in Gas-Solid Fluidized Beds.” *Chemical Engineering Science* 62(1–2):301–17.

Kunii, Daizo. and Octave Levenspiel. 1991. *Fluidization Engineering*. 2nd ed. Stoneham MA: Butterworth-Heinemann.

Lacey, P. M. C. 1954. “Developments in the Theory of Particle Mixing.” *Journal of Applied Chemistry* 4:257–68.

Peng, Zhengbiao, Elham Doroodchi, Yusif Alghamdi, and Behdad Moghtaderi. 2013. “Mixing and Segregation of Solid Mixtures in Bubbling Fluidized Beds under Conditions Pertinent to the Fuel Reactor of a Chemical Looping System.” *Powder Technology* 235:823–37.

Rao, T. R. and J. V. R. Bheemarasetti. 2001. “Minimum Fluidization Velocities of Mixtures of Biomass and Sands.” *Energy* 26(6):633–44.

Rowe, P. N. and A. W. Nienow. 1976. “Particle Mixing and Segregation in Gas Fluidised Beds: A Review.” *Powder Technology* 15(2):141–47.

Sutar, Harekrushna and Chandan Kumar Das. 2012. “Mixing and Segregation Characteristics of Binary Granular Material in Tapered Fluidized Bed: A CFD Study.” *Engineering* 04(04):215–27.

Wirsum, Manfred, Franz Fett, Natalia Iwanowa,Genadij Lukjanow. 2001. “Particle Mixing in Bubbling Fluidized Beds of Binary Particle Systems.” *Powder Tech.* 120(1–2):63–69.

Zhang, Yong, Baosheng Jin, and Wenqi Zhong. 2009. “Experimental Investigation on Mixing and Segregation Behavior of Biomass Particle in Fluidized Bed.” *Chemical Engineering and Processing: Process Intensification* 48(3):745–54.

THE GAS-SOLID SUSPENSION DRAG ON LARGE PARTICLES IN THE TRANSPORT ZONE OF A CIRCULATING FLUIDIZED BED

Anna Köhler*, Jesper Aronsson, David Pallarès, and Filip Johnsson

Dept. of Space, Earth and Environment, Chalmers University of Technology,
SE-412 96 Gothenburg
**E-mail: anna.koehler@chalmers.se*

Abstract

The effective drag of the gas-solid suspension on large particles representing fuel particles in fluidized beds, has a crucial effect on the mixing of the fuel particles. The suspension drag is therefore an important parameter in CFB reactor modeling, but little is known on its magnitude. This paper presents a method to experimentally determine the suspension drag by measuring the terminal velocity of large particles in the transport zone of a fluidized bed, which is compared with the terminal velocity in the absence of bed material. The drag coefficient of the particles suspended in the gas-solids flow and Reynolds numbers of the fluid flow are presented and compared to the standard drag curve of a single spherical particle. Finally, the effective viscosity of the gas-solid suspension is determined.

Introduction

The increased awareness of the environmental impact of CO_2 emissions on global warming has risen the interest for thermochemical conversion of renewable fuels such as biomass. A commonly applied technology for biomass conversion is fluidized beds (FB), as they have a high fuel flexibility and can handle low-rank and heterogeneous fuels. This is important since there is an interest to burn biomass residues rather than refined biomass fuels. For FB processes the mixing of fuel particles in the bed is a fundamental aspect which determines the location of chemical reactions and thereby temperature distributions as well as emissions. With biomass fuels rich in volatile compounds, uneven combustion may occur such as in the form of volatiles-rich zones near the fuel inlet, as a result of poor mixing which may also cause oxygen-rich streams with temperature peaks fostering higher emissions. Areas of low oxygen concentrations in the bottom of the reactor may result in a shift of carbon burn-out to the reactor outlet and cyclone, where heat transfer is insufficient.

When studying the forces acting on a fuel particle in a fluidized bed the drag from the surrounding gas-solids suspension is the main contributors to mixing. This makes the understanding of drag crucial for the realization of reactor models which are used for design and operational purposes as shown by Nikku *et al.* (2016). To keep complexity and computational time low models usually focus on dispersed and spherical particles as the drag coefficients of these particles are well-known, e.g. Yin *et al.* (2004). Correlations for single particles with common shapes such as spheres, cylinders and discs, in multiphase flow systems can be found in e.g. Crowe *et al.* (2011). However, as mentioned by Nikku *et al.* (2014) the drag force of multiple irregular particles is not very well understood, which is why they study an average behavior of the fuel experimentally without identifying single particles instead. Further, the apparent fluid properties of multiphase flow systems like fluidized beds are hard to access. While the density of the gas-solid suspension can be determined from pressure measurements, common methods to measure the viscosity, a parameter to which the drag is often correlated to as it describes the fluids resistance to flow, can usually not be applied to fluidized beds.

This work aims at studying how the drag from the surrounding gas-solids suspension act on large particles, i.e. such as representing fuel particles. We focus on the transport zone of a circulating fluidized bed, i.e. the freeboard above the dense bed and its splash zone which builds up a solids flow when the gas velocity exceeds the transport velocity of the bed solids. We do this by experimentally obtaining the effective terminal velocity by which the gas-solids suspension is able to lift the different mass fractions of a particle sample, i.e. determining a distribution of the effective terminal velocity of the particles. From the terminal velocity the drag of the gas-solids suspension on the large particles can be calculated, which is compared to the drag in absence of bulk solids. Finally, the effective viscosity of the gas-solid suspension is obtained with different common drag curves.

Theory

The drag force on a single particle immersed in a fluid is described as

$$F_D = \frac{1}{2}\rho_f A_p C_D \left(u_f - u_p\right)^2 \quad (1)$$

where ρ_f is the fluid density, A_p is the particle projected area, C_D is the drag coefficient and u_f and u_p are the fluid and particle velocity, respectively. A common way to measure the drag force on particles in a fluid is through the terminal velocity, in other words when gravitational forces, buoyancy and drag force are in balance and the particle's acceleration is zero, as in Eq. (2):

$$F_D = F_G - F_B = \left(\rho_p - \rho_f\right) g V \quad (2)$$

where g is the gravitational acceleration and V_p is the particle volume. By combining Eqs. (1) and (2) the terminal velocity of a spherical particle can be obtained as

$$u_t = \left[\frac{4 d_p\,(\rho_p - \rho_f)\,g}{3\rho_f\,C_D}\right]^{0.5} \quad (3)$$

where d_p is the particle diameter and ρ_p is the density of the single particle. The drag coefficient can be expressed through semi-empirical expressions as a function of the particle Reynolds number. While for low *Re*-numbers (*Re*<0.5) the Stokes flow expression $C_D = Re/24$ applies (Stokes, 1850), in the transition regime (0.5>*Re*>1000), the following expression by Schiller and Naumann (1933) is typically used:

$$C_D = \frac{24}{Re}\left(1 + 0.15 Re^{0.687}\right) \quad (4)$$

Results from Eq. (4) are compared to an expression, which was derived from experiments in a liquid-solid FB by Wen and Yu (1966) and which was proposed by Palchonok et al. (1997) to suit the transport zone of gas-solid FBs:

$$C_D = \left(\frac{24}{Re} + 0.44\right)\varepsilon^{-4.75} \quad (5)$$

where the particle Reynolds number is defined as

$$Re_p = \frac{\rho_f u_f d_p}{\mu_f} \quad (6)$$

with μ_f being the viscosity of the fluid.

Methodology

The effective terminal velocity, i.e. the velocity by which the fluid (here air or a gas-solids suspension) is elutriating different mass fractions of a reference sample of large particles, is studied experimentally in two different units, one unit for the air experiments and one for the particle suspension measurements.

The reference sample of large particles used in the experiments consists of expanded clay aggregates (ECA) with a size range of 7 to 19 mm. A sample consists of about 75 particles. As can be seen in Fig. 1b the particles are relatively round with a measured average sphericity of 0.82. Their effective terminal velocity was investigated in batch tests with a low concentration of large particles in relation to bed material (<5%), representative for the transport zone of large-scale CFB boilers.

Experiments with air as the fluid are conducted in a 0.074 m i.d. riser with a height of 1 m. The riser is open toward the atmosphere and the particles elutriated are collected in a container. The controlled air flow is provided by a fan. The gas temperature is measured at the bottom of the riser, i.e. velocity, density and viscosity are corrected accordingly. The gas velocity is raised in small steps (0.2 m/s), elutriating the fraction of large particles with a terminal velocity lower than the fluid velocity. For each elutriated fraction the dimensions of the particles are measured and the mean diameter is calculated accounting for the mean sphericity as suggested by Sneed and Folk (1958). This corrected mean diameter is used to calculate the average drag coefficient of each fraction from Eq. (3). The Reynolds number is obtained through Eq. (6) using the fluid properties of air.

The experiments with the gas-solids suspension are carried out in a circulating fluidized bed with a 0.19 m i.d. riser with a height of 1.8 m and a solids recirculation system consisting of series-coupled cyclone, bubbling bed and loop seal (Fig. 1a). The unit is built in acryl glass and operated with pressurized air at ambient temperature. Sand with an average solids size of 150 µm, solid density of 2600 kg/m^3 and average sphericity of 0.85 was used as bed material. With these properties, the bed material has a mean terminal velocity of $u_{t,s}$=0.96±0.02 m/s according to the expressions by Haider and Levenspiel (1989). Values of the solids concentration at the top of the riser are derived from measurements in two pressure taps located below the exit of the riser. The elutriated ECA particles are separated from the bulk solids by means of size through a mesh (5 mm sieve size) placed above the bubbling bed in the solids recirculation system. At the fluidization velocities for which ECA particles are entrained, the riser operates at fast fluidization conditions, while a bubbling dense bed is kept at the bottom region.

In order to measure the effective terminal velocity of the ECA particles, a batch is placed in the riser and the fluidization velocity is gradually increased. The unit is operated at a certain fluidization velocity until the elutriation of ECA particles is visually observed to deplete in order to make sure all particles with an effective terminal velocity below the fluidization velocity are elutriated. After this, the elutriated ECA particles are manually removed from the sieving mesh and weighted and measured before the test proceeds with a further increase in fluidization velocity.

Fig. 1: (A) Experimental setup for elutriation measurements with gas-solids emulsion. (B) Sample of expanded clay particles used as large particles.

Thus, applying experimental values of the terminal velocity and solids concentration, the drag coefficient from the gas-solids suspension on a fraction of large particles of known size and shape can be calculated through Eq.(3). Having this, the Reynolds number of the flow can be calculated from Eqs. (4) or (5) and with Eq. (6) the corresponding effective viscosity of the gas-solids suspension in the transport zone is obtained.

Results

Fig. 2 plots the cumulative elutriated mass fractions of the large particles (ECA sample) obtained from the experiments with air and in the 0.19 m i.d. fluidized bed. As seen in Fig. 2, with the presence of bed material the sample is elutriated at much lower gas velocities and with a narrow velocity range of 1.53 to 1.76 m/s. To lift the same sample with solely air a velocity range of 9.0 to 11.9 m/s was needed. This distinct influence of the presence of the gas-solids suspension on the elutriation velocity of large particles suggests – as expected – the bed solids to be the dominant phase in the momentum exchange with the large ECA particles. Therefore, when calculating the drag coefficient for the large particles in the gas-solids suspension through Eq.(3) the velocity at which the bed solids flow upwards (assumed to be $u_g - u_{t,s}$), is used and the effect of the gas velocity is assumed to be neglectable.

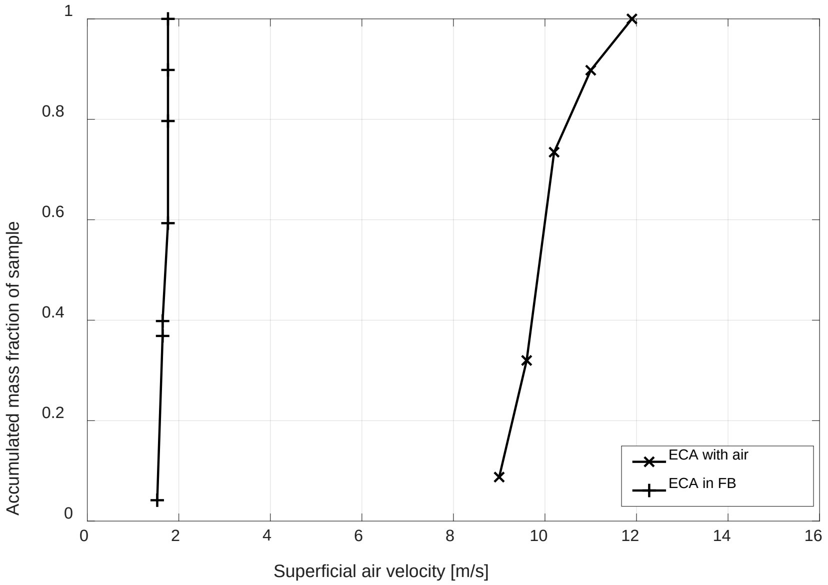

Fig. 2: Accumulated mass fraction of large particles (ECA) for elutriation experiments with air and in a fluidized bed with air and sand (exit solids concentrations from 4.9 to 9.1 kg/m^3).

Fig. 3 plots the standard drag curve of a single spherical particle with the expression by Schiller and Naumann (1933) and $C_D = 0.44$ for the turbulent regime (solid line) as well as the measured values for the ECA particles in air (○ symbols). As can be seen, the approximation of the ECA particles being spherical is supported by the measurement points located close to the standard drag curve for a single spherical particle in a turbulent flow regime.

Fig. 3 also shows the data points derived from experiments in the circulating fluidized bed. For these, when calculating the Reynolds numbers with Eq. (4) (□) from the measured drag coefficients, the data points end up on the drag curve of a single spherical particle for Reynolds numbers corresponding to a transition flow regime (Re ranging from 1.36 to 2.64). The measurement points calculated with Reynolds numbers from Eq. (5) (◊) are located slightly below the drag curve of a single spherical particle within the same flow regime.

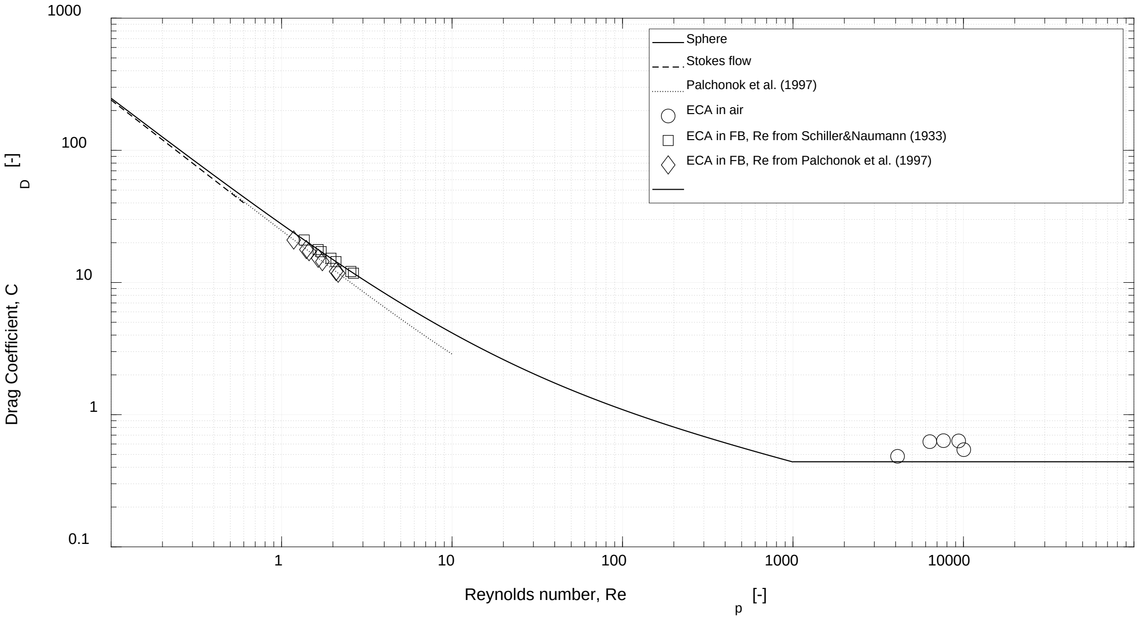

Fig. 3: Drag coefficient vs. Reynolds number. Elutriation experiments with solely air (○) show the suitability of assuming particles as spherical. In a gas-solids suspension the large particles experience much lower Reynolds numbers (□, ◊).

Fig. 4 shows the effective viscosities of the gas-solids suspension of the fluidized bed, resulting from the different Reynolds numbers obtained from each sample data point plotted in Fig. 3. The air viscosity is potted (▽) for comparison. Calculating Re from the Schiller and Naumanns (1933) correlation (Eq 4) for a flow in the transition flow regime (S&N, □) results in an effective viscosity of 0.025±0.008 Pa·s while the drag correlation from Palchonok *et al.* (1997) results in an effective viscosity value of 0.029±0.009 Pa·s. These values of the effective viscosity in the transport region of the fluidized bed riser (with solids concentrations from 4.9 to 9.1 kg/m^3) are in the orders of 10^3 and 10^2 times larger than the viscosities of air and water, respectively, and similar to those of sulfuric acid and sucrose solutions of about 50%.

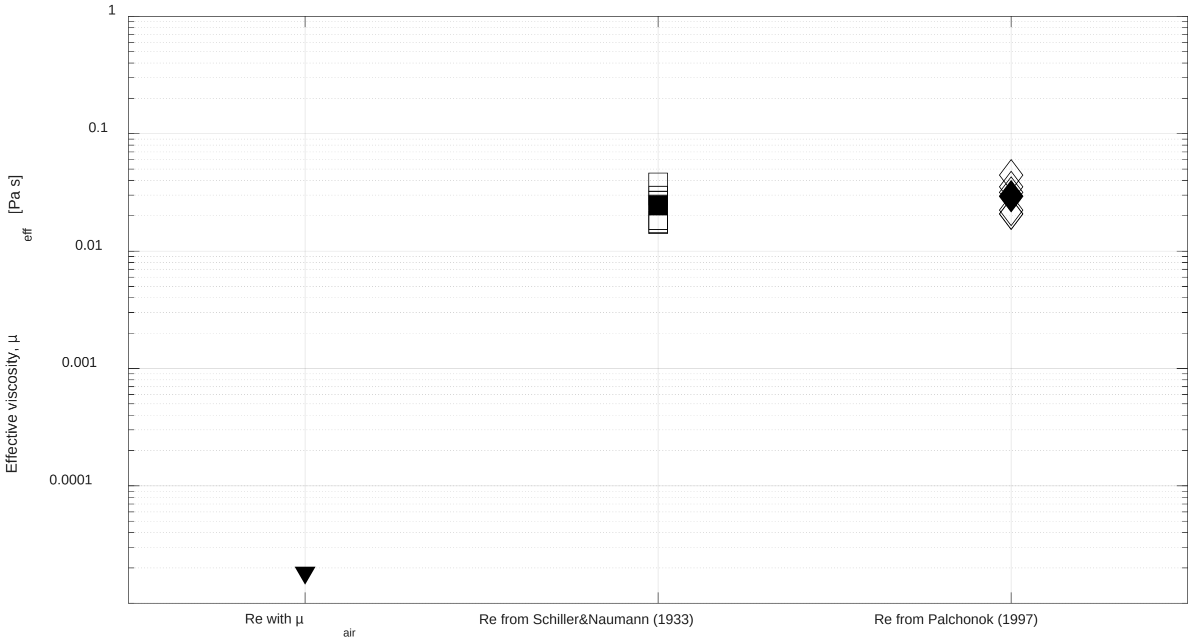

Fig. 4: Effective viscosity of the transport region of the fluidized bed from elutriation experiments. The mean value is plotted with a filled symbol.

Conclusions

This work present a method to measure the effective terminal velocity of large particles in the transport zone of a fluidized bed and compares the results with measurements of the terminal velocity of the particles in air in absence of bed material. It is found that the presence of bed material lowers the terminal velocity significanty. In the gas-solid emulsion the drag is much higher and Reynolds numbers indicate that the conditions investigated are in a transition flow regime. A effective viscosity of the gas-solid emulsion of about 0.025 Pa s was obtained with the measurements, which covered solids concentrations from 4.9 to 9.1 kg/m^3.

Notation

Roman Letters		Indices	
A	Area, m^2	B	Buoyancy
C_D	Drag coefficient, -	D	Drag
d	Diameter, m	eff	effective
F	Force, N	f	fluid
g	Gravitational constant, m/s^2	G	Gravitation
u	Velocity, m/s	g	gas
V	Volume, m^3	p	particle
Greek letters		s	solid
ε	voidage, -	t	terminal
μ	Viscosity, Pa s		
ρ	Density, kg/m^3		

References

Crowe, C. T., et al., *Multiphase Flows with Droplets and Particles*. Second Edi2011

Haider, A., and Levenspiel, O., Drag coefficient and terminal velocity of spherical and nonspherical particles.Powder Technology. 1989. 58(1). pp. 63–70

Nikku, M., et al., Characterization method of average gas–solid drag for regular and irregular particle groups.Powder Technology. 2014. 253. pp. 284–294

Nikku, M., et al., Three-dimensional modeling of biomass fuel flow in a circulating fluidized bed furnace with an experimentally derived momentum exchange model.Chemical Engineering Research and Design. 2016. 115. pp. 77–90

Palchonok, G. I., et al., Impact of heat and mass transfer on combustion of a fuel particle in CFB boilers.in1997

Schiller, L., and Naumann, A., Über die grundlegenden Berechnungen bei der Schwerkraftaufbereitung.Verein Deutscher Ingenieure. 1933. 44. pp. 318–320

Sneed, E. D., and Folk, R. L., Pebbles in the Lower Colorado River, Texas a Study in Particle Morphogenesis.The Journal of Geology. 1958. 66(2). pp. 114–150

Wen, C. Y., and Yu, Y. H., A generalized method for predicting the minimum fluidization velocity.AIChE Journal. 1966. 12(3). pp. 610–612

Yin, C., et al., Use of numerical modeling in design for co-firing biomass in wall-fired burners.Chemical Engineering Science. 2004. 59(16). pp. 3281–3292

A REVIEW OF PERFORMANCE CHARACTERISTICS OF FLUIDIZED BED STRIPPER INTERNALS

A. S. Issangya*, R. A. Cocco, S. B. Reddy Karri, T. Knowlton and B. Freireich

Particulate Solid Research, Inc., 4201 W. 36th Street, Building A, Chicago, IL 60632 USA

*Email: *allan.issangya@psri.org*

Abstract

Fluidized bed strippers play a major role in fluid catalytic cracking (FCC) and fluid coking operations. FCC strippers use steam to strip out the entrained and adsorbed hydrocarbon vapors from the catalyst collected by the FCC reactor cyclones. Failure to remove these vapors results in a loss of a valuable product and undesired high temperatures in the regenerator. In a fluid coker stripper, steam is used to remove entrained and adsorbed hydrocarbons from the coke particles descending from the fluid coker reactor, thus minimizing carry-under of valuable hydrocarbon product. Disk and donut trays, horizontal sheds, and structured packings are the most widely used types of stripper internals. Grating trays are also used but to a much lesser extent. This paper reviews the literature on fluidized bed strippers. Most studies are from industry and have dealt with stripping efficiencies, stripper flooding and benchmarking of different types of stripper internals. Overall, FCC strippers, in particular disk and donut strippers, have received the most attention, due to their wide industrial usage.

INTRODUCTION

Fluidized bed strippers are fluidized beds with an imposed solids circulation where an up-flowing gas strips out a gaseous product entrained in the down-flowing solids stream. Fluidized bed strippers are widely used (Kunii and Levenspiel, 1991) in fluid catalytic cracking (FCC) and fluid coking processes. The fluid catalytic cracking process breaks down heavy fuel oil or petroleum residue feedstock into lower molecular weight products. The FCC fluidized bed stripper recovers product hydrocarbon vapors entrained by catalyst particles after exiting the riser reactor, and before the catalyst is reactivated in the regenerator. FCC units with internal riser reactors have annular strippers while other configurations can have either internal or external, side cylindrical strippers (King, 1993; Senior et al., 1998). Typical operating parameters of commercial FCC strippers are shown in Table 1.

In the fluid coking process, heavy petroleum feeds, such as non-distillable residues, oil sands bitumen, etc. are converted into lighter products by thermal decomposition in a tapered fluidized bed containing hot coke particles. The cracking reactions deposit a thin layer of coke on the bed coke particles. The fluid coker has a cylindrical stripping section at the bottom where steam is used to strip the interstitial hydrocarbons from the descending coke particles before they are transferred to the burner to be reheated and returned to the fluid coker. Fluid cokers operate in the turbulent fluidization regime at temperatures of about 500 to 600ºC with 150 – 200 micron diameter coke particles (Bi et al, 2005).

In open fluidized beds, bubbles rise, interact, coalesce and tend to move laterally toward the center. Bubbles in jet streams that bypass significant portions of the bed (Knowlton, 2001; Wells, 2001; Issangya et al., 2006) can also form in open beds. Installing baffles in strippers disrupts these patterns and redistributes the gas which improves the emulsion phase/bubble gas interchange. Disk and donut trays, horizontal sheds and structured packings (Fig. 1) are the most widely used stripper internals. Grating trays have only limited applications. Disk and donut baffles typically slope down at 45° which enables solids particles to move off one tray down to the next in the stripping vessel. The projected open area in disk and donut strippers is about 50%. Direct vertical paths in the stripper are avoided which forces the solids particles

Table 1. Typical operating parameters of FCC strippers (King, D., 1993; Senior et al., 1998)

Parameter	Nominal Minimum	Conventional Operating Range	Nominal Maximum
Stripping steam flowrate (kg steam/1000 kg catalyst)	1	2 - 4	5
Superficial steam velocity (m/s)	0.12	0.15 – 0.30	0.76
Superficial catalyst flux (kg/s-m^2)	35	40 - 75	110
Superficial catalyst velocity (m/s)	0.03		0.12
Solids flux through the smallest flow area (kg/s-m^2)	60		250
Mean catalyst residence time (s)	50	60 - 120	150
Stripper temperature (°C)	495		565
Stripper height-to-diameter ratio	1		
Stripper diameter, m		5 - 6	
Stripper height, m		6 - 9	
Bed density, kg/m^3		640 - 720	
Regime exhibited		Bubbling &Turbulent	

to cascade from side to side as they move down the stripper and interact with the rising stripping gas bubbles. Disk and donut baffles often have skirts welded on their trailing edge and vent holes, typically located near the lower edge, as well as flux tubes (Johnson and Senior, 1996).

Horizontal sheds come as inverted-V channels (chevrons), or inverted-V channels with vertical lips on each side (tents). The included angle is typically 45º. Direct vertical paths are also avoided. Sheds can have vent holes and sheds are arranged in parallel or cross-hatched layers. Structured packings are formed with slanted metal plates arranged in ways that force the solids to take complicated paths through the column, thereby creating a large surface area for contact with the stripping gas. The plates slant angle is typically between 30° to 60°. Grating baffles are cut from steel grates. Stripper grating trays have a portion cut off at one end to allow for a downcomer opening. They can also have blocked-off section(s) to promote cross-flow, gas-solid contacting.

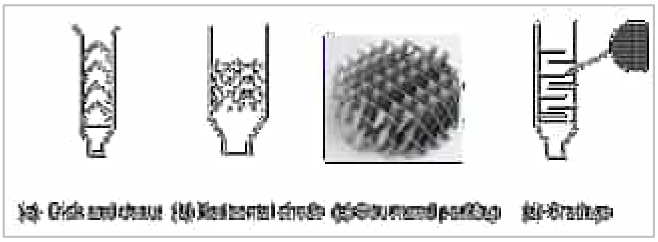

Fig. 1. Schematics of types of fluidized bed stripper internals

STRIPPER PERFORMANCE STUDIES

Most studies (Table 2) originate from the FCC industry with the focus being on stripping efficiency and flooding characteristics and, benchmarking of different types of internals. Disk and donut strippers have been studied the most, due to their wider use. Stripping efficiency is determined from gas tracer concentration measurements. Helium, with its ease of detection in an air mixture, has been utilized the most as a tracer gas. However, Helium's relatively low density and inability to adsorb on FCC catalyst particles are shortcomings as a gas tracer that need to be addressed.

Rivault et al. (1996) found that stripping efficiencies in an annular semicircular disk and donut stripper were greater than 98% for solids fluxes, G_s, as high as 108 kg/s.m^2 and air superficial velocities, U_g, of up to 0.4 m/s. Stripping efficiency decreased with increasing solids flux, due to decreased solids residence time and increased with increasing superficial gas velocity at a fixed solids flux because more gas bubbles were now interacting with the emulsion phase. Radial bubble frequency profiles were roughly the same at different heights in the stripper as bubble properties readjusted when they rose through a pair of disk and donut trays. The flow mechanism in disk and donut fluidized bed strippers was suggested to consist of the solid phase flowing down from one baffle to the next by sliding down on the top sides of the baffles and the gas bubbles flowing up to the inclined tray and creating a dilute space (void) underneath the tray. Bubbles then escaped the baffles by flowing under the skirts and then moved upwards and laterally to the next upper tray. The highest gas interchange occurred where the bubble and the emulsion phases were forced to cross one another.

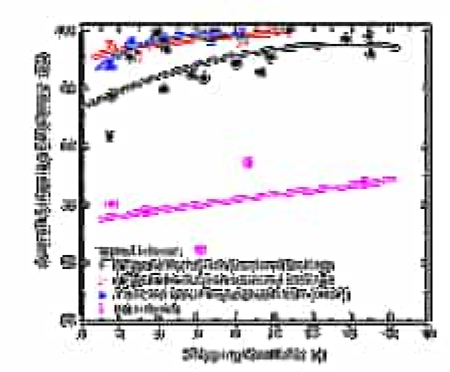

Fig. 2. Stripping efficiencies of disk and donut trays and structured packings strippers (Rall and Pell, 1999)

Rall and Pell (1999) found from their study (Fig. 2) that disk and donut trays had about the same stripping efficiency as that of the best performing structured packing. Without baffles in the stripper the stripping efficiency was significantly lower. The bed height above the baffled section had a significant effect on the operation of the stripper. It had to be limited to about 0.15 to 0.3 m and, when operating with no internals to about 1.22 m otherwise the stripper unit experienced excessive vibrations and an overall system instability. Small bubbles coalescing into large bubbles then rising rapidly and unpredictably through the catalyst bed was described as the reason for the operational problems. Bolthrunis, et al. (2010) made similar observations in an unbaffled fluidized bed reactor which ceased when grating baffles were installed in the unit. Karri et al. (2004) and Issangya et al. (2007) suggested that gas bypassing can occur in unbaffled fluidized beds and was probably the reason for the operational problems noted above.

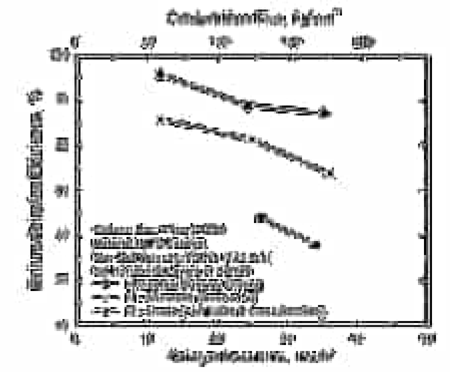

Fig. 3. Stripping efficiency vs solids flux for three types of baffles (Beech et al., 2007)

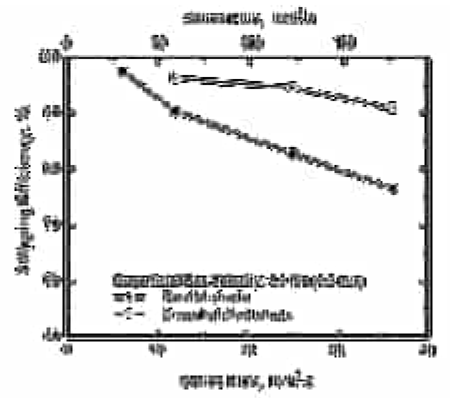

Fig. 4. Stripping efficiency vs solids flux for parallel and cross-hatched sheds strippers (Cunningham et al. (2010)

Couch et al. (2003) discusses UOP LLC tests of 15 different types of stripper internals in two large-scale test units for solids fluxes of up to 191 kg/s-m^2. Koebel et al. (2004) found that the stripping efficiency of disk and donut trays was lower than grating trays that had skirts at the edge of the downcomers and that the stripping efficiency of the grating trays increased with increasing solids flux. Both results were unexpected. Relatively high grating trays stripping efficiencies approaching structured packings values were also reported by Hedrick et al. (2005). Beech et al (2007) studied cross-hatched horizontal sheds and steel gratings in a 1-m-diameter unit with MTO catalyst. The sheds with vertical lips and vent holes had the highest stripping efficiency (Fig. 3) followed by the simple chevrons and the grating baffles. The height of the gas distributor above the standpipe inlet affected solids circulation and needed to be sufficiently short to ensure that the solids remained fluidized at the standpipe entrance. Cuningham et al. (2010) measured the stripping efficiencies of cross hatched sheds and parallel sheds in a 0.9-m-diameter fluidized bed stripper with five risers circulating the solids (Fig. 4). For both internals, the stripping efficiency increased with increasing gas velocity and decreased with increasing solids flux. The cross-hatched sheds gave significantly better stripping than the parallel sheds at all operating conditions.

Flooding (Senior et al, 1998) is a major problem in commercial FCC strippers. Flooding occurs when the solids flow out of the stripper is higher than the solids flow into the stripper baffles.

This results in the catalyst cascading rapidly over the baffles. Senior et al (1998) found that most of the injected fluidizing steam was entrained down the standpipe into the regenerator during flooding. They suggested that in pilot-scale strippers, transition to flooding is relatively abrupt but in large-diameter commercial strippers the transition is more gradual, and the unit generally continues to circulate catalyst smoothly with no control problems.

In this study, tests were conducted with gratings and disk and donut internals (Fig. 5) in a 0.6-m-diameter, 7.6 m tall steel fluidized bed unit with FCC catalyst particles. The unit had a 0.25-m-diameter, 3.4 m long vertical standpipe feeding a 0.3-m-diameter, 15 m tall riser that conveyed the solids via cyclones back into the stripper.

The bed density in the stripping zone of the disk and donut stripper (Fig. 6) decreased linearly with increasing solids flux until a solids flux was reached at which it dropped precipitously. This solids flux was taken as the flooding point for the given gas velocity. The stripper flooded when the solids flux exceeded about 45, 60 and 65 kg/s.m^2 at U_g = 0.15, 0.3 and 0.46 m/s, respectively. It was proposed that the stripper density drop at flooding was due to one of two scenarios. In one scenario, a bubble would stagnate in the bed and other rising bubbles would feed into this stagnated gas void causing it to grow in size. As the stagnation void size increased, the bed density would drop sharply. In the second scenario, a bubble would become momentarily trapped under the cone or donut. Other rising bubbles would feed into this trapped bubble and cause it to enlarge. When many such voids escaped from under the physical barriers of the baffles, they could occupy large enough volumes to lower the stripper density.

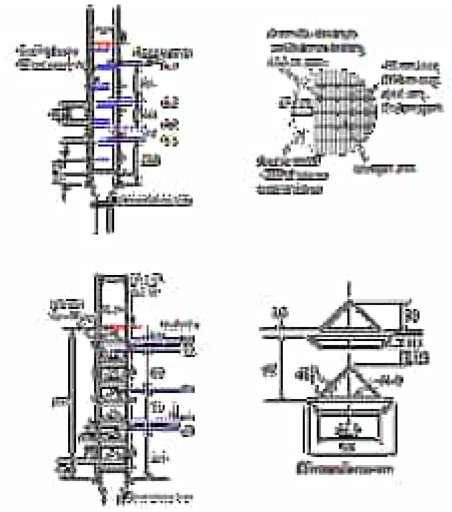

Fig. 5. Grating and disk and donut stripper columns and baffles dimensions (this study).

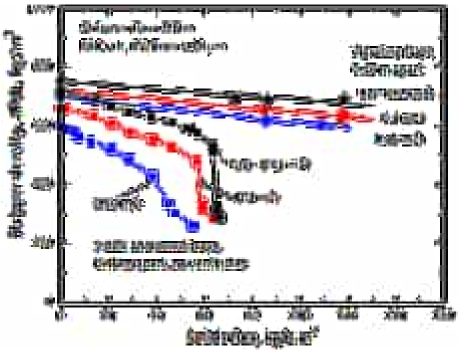

Fig. 6. Stripper density vs. solids flux for disk and donut trays and grating trays (this study).

With the high solids flux at flooding and a significant number of bubbles stagnating or slowed down in the baffled zone, it became difficult for bubbles to rise up against the solids downflow in the annular space between the disk and the donut baffles. And, at the bottom, bubbles started to be entrained downwards into the standpipe, which reduced the exiting solids flowrate. For a period of time, the solids flowrate down the standpipe become less than that of the incoming solids causing solids to start accumulating at the top of the bed and, with time, back up into the cyclones diplegs and eventually escaping into the exhaust air system. The grating trays stripper density decreased gradually and linearly with increasing solids flux without any sharp drop. No flooding was encountered with these trays. The reason that the grating trays did not flood easily was because the open area of the trays is about 85% while that of the disk and donut (D&D) baffles is about 50%. Therefore, the actual flux through the opening is greater for the D&D baffles compared to the trays. This makes it easier in the gratings stripper for the gas to flow upward against the lower solid flux.

Johnson and Senior (1996) found from Helium stripping tests (Fig. 6) that up to solids fluxes of about Gs 150 kg/s.m^2, there was little influence of adding flux tubes to disk and donut trays. At higher solids fluxes, however, the stripping effectiveness of the conventional baffles decreased sharply because of flooding. No flooding occurred for the flux tube baffles up to the highest flux tested of 235 kg/s.m^2. Similar findings were later reported by Senior et al. (1998) and Miller et al. (2000).

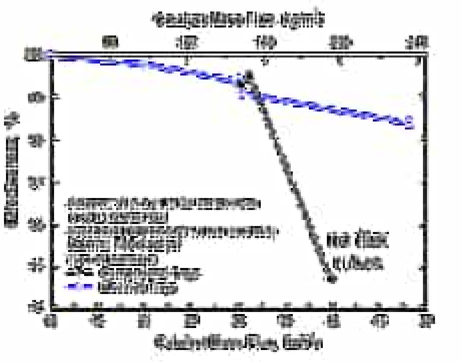

Fig.6 Stripping effectiveness vs. solids flux for disk and donut trays with and without flux tubes (Johnsohn and Senior, 1996)

Chen et al (2005) measured helium underflow as a function of solids flux and compared the performances of conventional disk and donut, disk and donut with flux tubes and a proprietary PentaFlow™ baffle developed to replace conventional structured packings. Helium carry-under increased with increased solids flux for all three types of internals. The disk and donut internals flooded at a relatively low catalyst flux, followed by the disk and donut trays with flux tubes. The PentaFlow™ baffles stripper did not flood for all solid fluxes tested.

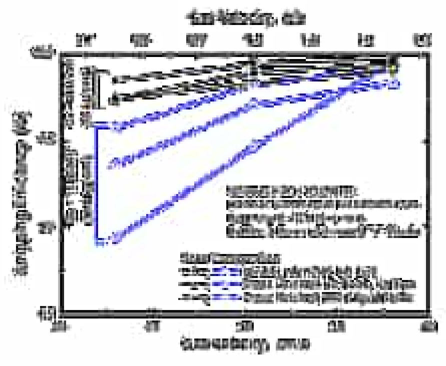

Fig. 7. Stripping efficiency vs gas velocity for a sheds flexicoke stripper (Davuluri et al., 2011).

Fluid coker stripper studies are far fewer compared to FCC stripper studies. The bulk of fluid coker studies are those conducted at UBC (Knapper, et al., 2002; Bi et al. ,2004; Bi et al., 2005; Rose et al., 2005 and Cui et al., 2006a,b) and by Davuluri et al. (2011). Baffles in fluid coker strippers are prone to fouling which can lead to early flooding and reduced unit reliability. Bi et al (2004) used inverted-V sheds of various included angles with styrofoam slabs glued onto the sheds to simulate fouling in a 0.61 ft semicircular fluidized bed stripper. Flooding occurred at different solids fluxes depending on the superficial gas velocity, separation distance between sheds in a row, shed angle (shed cross-sectional shape, steep or shallow), and stripper percent open area. A semi-empirical model for predicting flooding in fluidized bed strippers with shed internals was proposed from the study. Davuluri et al. (2011) found that (Fig. 7) the stripping efficiency of cross-hatched sheds with lips and holes was better than that of cross-hatched sheds without lips and holes which, in turn, performed better than plain, parallel sheds. The higher stripping efficiency of the sheds with lips and holes was said to be due to the tortuous path provided for the solids that allowed the gas to redistribute itself as it ascended the stripper leading to improved stripping by avoiding bypassing.

The onset of flooding in commercial and large scale fluidized bed strippers (Senior, et al., 1998) can be detected from a marked difference between the rates of steam injected into the stripper and of water condensed from the downstream hydrocarbon products, higher carry-under of hydrocarbons, detection at stripper exit of a dramatic increase in the tracer injected above the stripper, and a high voidage region detected e.g. by gamma densitometry developing inside the stripper. Wilcox, J.R. (2011) proposed methods to diagnose problems encountered in FCC stripper operation.

CONCLUSION

Disks and donuts, sheds and structured packings are the most widely used stripper internals. Stripping efficiency decreases with increasing solids circulation flux at a fixed gas velocity and it increases with gas velocity at a given solids flux. Flooding is more prevalent in disk and donut strippers. Stripping efficiency and stripper bed density decrease significantly if flooding occurs. Flooding in small units is relatively abrupt, but it is more gradual in large or commercial strippers. Methods to improve stripping efficiency and/or increase the operating solids flux include having skirts, flux tubes and vent holes on disk and donut baffles and, lips and vent holes on sheds and arranging sheds in cross-hatched layers. Downcomer openings are needed in grating baffles and, adding non-grated sections can promote crossflow contacting.

Table 2. Hydrodynamics and Stripping Efficiency Studies on Fluidized Bed Strippers

Reference	D (m), H (m)	Internal	Material	Ug (m/s)	Gs (kg/s.m^2)
Rivault et al. (1995)	Di = 0.2, Do = 0.5, H = 1.35	D&D	FCC	0.1, 0.18, 0.33, 0.4	28, 58, 108
Johnson&Senior(1996)	0.28 x 0.53, H = 12.2	D&D	FCC	0.43	49 - 196
Johnson&Senior(1996)	Di = 2.34, Do = 3.5, H = 12.2	D&D, D&D w/ FT	FCC	0.43	49 - 196
Rall and Pall (1999)	D = 0.61, H = 2.0	SP, D&D	FCC	up to 0.53	64
Rall&DeMulder (2000)	D = 0.6, H = 1.9	SP, D&D	FCC	-	147
Miller et al. (2000), Senior et al. (2001)	-	D&D	FCC	-	-
Padyen et al. (2001)	D = 0.29, semicircular	D&D	FCC	0.01 - 0.15	3 - 18
Hedrick (2002)	19° pie, Area = 0.186 m^2, H = 6	D&D	FCC	Equiv. to S = 1 - 3	40 - 190
McKeen&Pugsley (2003)	0.15 x 0.15	D&D	FCC	0.1 - 0.3	28 - 90
Bi et al (2004)	D = 0.61 semicirc., H = 0.921	Sheds	FCC	0.12, 0.25, 0.37	0 - 80
Koebel et al. (2004)	19° wedge, A=0.186 m^2, H = 3.6	GT w/skirts	FCC	Equiv. to S = 1	40 - 150
Koebel et al. (2004)	D = 0.6, H = 2.5 bed	GT, D&D	FCC	Equiv. to S = 1	40 - 150
Bi et al (2005)	D = 0.61 semicirc., H = 0.921	Sheds	FCC	0.17, 0.24, 0.36	17 - 65
Rose, et al. (2005)	D = 0.61 semicirc, H = 0.921	Sheds	FCC	0.24	46 - 75
Hedrick et al. (2005)	D = 0.6, H = 2.2 to 2.3	SP	FCC	Ug* = 0.8 – 3.2	41, 82,122
Chen (2005, 2007)	D = 0.3	D&D, PFP	FCC	-	> 160
Cui, et al. (2006)	D = 0.61 semicircular, H = 0.921	Sheds	FCC	-	46 - 75
Cui, et a. (2006)	D = 0.61, H = 0.921	Sheds	FCC	0.24	46
Beech et al. (2007)	D = 1.0	Sheds, GT	MTO	0.15	49 - 176
Wiens et al. (2010)	D = 0.29, H = 1.2	D&D	FCC	0.1, 0.2, 0.3	43, 60, 74
Cuningham et al. (2010)	D = 0.9	Sheds	FCC	0.09, 0.15, 0.3	29, 59, 122, 176
Davuluri, et al. (2011)	D = 0.91, H = 3	Sheds	Flexicoke	0.23 to 0.38	44, 73
This study	D = 0.6, H = 6	D&D; GT	FCC	0.15, 0.3, 0.46	0 – 69; 0 - 122

D&D = Disk & donut, GT = Grating, SP = Structured packing, PFP = PentaFlow^{TM} packing, S = kg steam per 1000 kg catalyst

REFERENCES

Beech, J. H., R. E. Walter, A. K. Sharma and J. S. Smith, US Patent Pub. No. US 2007/0232843 A1, Oct. 4, 2007

Bi, H., H. Cui, J. Grace, A. Kern, C. Lim, D. Rusnell, X. Song and C. McKnights (2004), Ind. Eng. Chem. Res., 2004, 43, 5611–5619

Bi, H., J. Grace, C. Lim, D. Rusnell, D. Bulbuc and C. McKnight, Can. J. Chem. Eng., 2005, 83, 161–168

Bolthrunis, C. O., M. Hagan and W. A. Mukaddam, in Fluidization XIII, S. D. Kim, Y. Kang, J. K. Lee and Y. C. Seo, eds., Engineering Conferences International, New York, 2010, 329 - 336

Chen, Y.-M., R. Samson, D. Brostein, and H. Dries, Paper AM-05-25 presented at NPRA Annual Meeting, March 13 – 15, 2005, San Francisco, CA

Couch, K.A., K.D. Seibert and P. van Opdorp, Paper AM-04-45 presented at NPRA Annual Meeting, San Antonio, TX, March 23-25, 2003

Cui,H., J. Grace, C. McKnight, T. Zhang, I. Rose, X. Bi, J. Lim and D. Burgardt, Chem. Eng. J., 2006a, 125, 1–8

Cui, H., M. Strabel, D. Rusnell, H. Bi, K. Mansaray, J. Grace, C. Lim, C. McKnight and D. Bulbuc, Chem. Eng. Sci., 2006b, 61, 388–396

Cunningham, B. A., C. G. Smalley, R. C. Senior, J. S. Famolaro, R. P. Davuluri, D. L. Johnson, J. H. Beech, and J. S. Smith, US Patent No. US7,744,746 B2, Jan. 29, 2010

Davuluri, R. P., J. R. Bielenberg, C. R. Sutton and B. A. Raich, US Patent Application, Pub No. 2011/0114468 A1, May 19, 2011

Hendrick, B. W., US Patent Application, Pub. No. US 2002/0008052 A1, Jan. 24, 2002

Hedrick, B. W., X. Zhanping, P. Palmas, M. J. Kowalczyk, M. J. Westby, W. Gu, J. M. Houdek and D. R. Monkelbaan, US Patent Pub. No. US 2005/0205467 A1, Sep. 22, 2005

Issangya A. S., T. M. Knowlton and S. B. Reddy Karri, in Fluidization XII, X. Bi, F. Berruti and T. Pugsley, eds., 2007, 775 - 782

Johnson, D. L. and R. C. Senior, US Patent No. 5,531,884, Jul. 2, 1996

Johnson, D. L. and R.C. Senior, International Patent Application No. PCT/US95/09335, Jul. 25, 1995

Karri Reddy, S. B., A. Issangya and T. M. Knowlton, in Fluidization XI, Sorento, Italy, U. Arena, R. Chirone, M. Miccio and P. Salatino, eds., 2004, 515 – 521King, D., in Fluidization VII, O. E. Porter and D. J. Nicklin, Engineering Foundation, New York, 1992, 15 – 26

Knapper, B, F. Berruti, J. R. Grace, H. T. Bi, and C. J. Lim, in Circulating Fluidized Bed Technology VII, J. Grace, J. Zhu and H. de Lasa, eds., C.S.Ch.E., Ottawa ON, 2002, 263 - 270

Knowlton, T. M., Video shown at Fluidization X, Beijing, China, 2001

Koebel, J. P., B. W. Hedrick and K. Puppala, US Patent No. 6,680,030 B2, Jan. 20, 2004

Kunii D. and O. Levenspiel, Fluidization Engineering, 2nd Ed., Butterworth-Heinemann, Boston, 1991, 39 – 40

McKeen, T., T. Pugsley, Powder Technol., 2003, 129, 139–152

McKeen,T. and T. Pugsley, Int. J. Chem. Reactor Eng., Vol. 1, Article A18, 2003

Miller, R. B., Y. L. Yang, E. Gbordzoe, D. L. Johnson, and T. A. Mallo, NPRA Annual Meeting, AM-00-08, San Antonio, Texas, 2000

Padyen, S., T. M. Knowlton, and H. Arastoopour, in Fluidization X, M. Kwauk, J. Li, W. C. Yang, eds., Engineering Foundation, New York, 2001, 581 – 588.

Rall, R. R. and B. DeMulder, Paper presented at the 12th Refining Seminar, San Francisco, CA, October 10, 2000

Rall, R. R and M. Pell, Paper presented at the 6th. Int. Conf. on Circulating Fluidized Beds, Wurzburg, Germany, 1999

Rivault, P., C, Nguyen, C. Laguerie, J. R. Bernard, and E. Aquitaine, in Fluidization VIII, Large, J.-F., Laguerie, C., eds., Engineering Foundation, New York, 1995, 725 - 732.

Rose, I. H. Cui, T. Zhang, C. McKnight, J. Grace, X. Bi, and J. Lim, Powder Technol., 2005, 158, 124–132.

Senior, R. C., C. G. Smalley and T. P. Holtan, US Patent No. 5,910,240, Jun. 8, 1999

Senior, R. C., C. G. Smalley, and E. Gbordzoe, in Fluidization IX, L.-S. Fan and T. M. Knowlton, eds., Engineering Foundation, New York, 1998, 725-32.

Wiens, J. S., PhD Thesis, University of Saskatchewan, Canada, 2010

Wilcox, J. R., in “Advances in Fluid Catalytic Cracking”, 2010, 101 – 118.

FLUID-DRIVEN JAMMING IN FLUIDIZED BEDS

John R. Grace[1]* and Richard J. Kerekes[1]

[1] *Department of Chemical and Biological Engineering, University of British Columbia, 2360 East Mall, Vancouver, Canada V6T 1Z3*.

*E-mail: *jgrace@chbe.ubc.ca*

Abstract

Preventing jamming, the unwanted local blockage of multi-phase flows by particles as they try to pass through a constriction, is important in many fluidized bed processes. Flow-driven jamming depends on a number of key particle properties, as well as the operating conditions and the size and geometry of the constriction. Some guidelines for avoiding jamming are provided in this paper. There is a major need for further studies.

Introduction to Jamming

The accumulation of particulate matter in confined flows, causing blockages, is called "jamming". This can occur in various settings such as gravity-fed hoppers and fluid-driven blockage in flow constrictions. Jamming can result in equipment failure, sometimes catastrophic. Accordingly, it is of interest in feeding and operating fluidized beds[1] and other dense two-phase process flows. However, the causes and prevention of jamming have received little attention. The objectives of this study are to highlight key factors affecting jamming, to propose some measures that can be helpful in preventing or alleviating jamming, and to stimulate further study of the subject.

The ability of particles to circulate freely is important in both gas- and liquid-fluidized beds. For example, as shown by Molerus and Wirth (1997), favourable bed-to-surface heat transfer relies on the ability of particles to reach heat-exchange surfaces and then return quickly to the bulk. Temperature uniformity, an important advantage of fluidization for many processes, relies on mixing and transport of particles. Internal circulation of particles and reduced spread in particle residence times are important in achieving efficient drying and gas-solid reactions. Immobilization of regions of particulate beds reduces the efficiency of the contactor. Blockages and jamming impede particle and fluid circulation and are therefore harmful for many applications.

Jamming and blockage occur in fluidized beds when particles are unable to flow through passages intended to allow free communication. This may occur when large particles bridge openings, e.g. after a few oversize particles span thin openings, or in ramped openings when smaller particles become wedged and ultimately lodged, blocking further particle flow through the opening. Feeding of biomass particles from hoppers, important for reduction of carbon emissions from thermal processing of fuels, requires smooth continuous feeding, but may experience severe interruptions due to gravity-driven jamming of irregular particles (Dai et al., 2012). Baffles of various geometries are provided in some applications to divert and promote solids flow (Zhang, 2020). Jamming may also occur when heat transfer tubes are too tightly packed, so that particles become immobilized, reducing circulation through tube bundles (Lese and Kermode, 1972). It can also occur on the surface of finned heat exchange surfaces if particles lodge in the thin gaps between fins, causing the surface to become insulated by stagnant particles, rather than experiencing augmented heat transfer due to increased surface area (Priebe and Genetti, 1973). Jamming may also reduce mass transfer, e.g. in fluidized bed membrane reactors (Adris and Grace, 1997; Grace et al., 2005), where congested internals are needed to maximize the permeation and generation of product hydrogen. In

---

[1] Note that the word "jamming" has also been associated with fluidization in the freezing of voidage at a given value (Valverde and Castellanos, 2007) and study of glass transitions of hard spheres (e.g. Daniels et al., 2012).

addition, various operations, such as chemical looping, coking and catalytic cracking, involve transfer of solids between adjacent reactors or compartments, requiring uninterrupted particle flow through constrictions.

Experimental Studies of Fluid-Driven Jamming in Rectangular Channels

This paper focuses on practical aspects of fluid-driven jamming, in particular its avoidance. Although gravity-driven jamming of granular materials in hoppers has received some attention, there are few publications of direct relevance to flow-driven blockages in fluidized beds. We consider experimental and simulation studies related to particle flow through narrow constrictions.

Grace and Harrison (1968) performed experiments in which they lowered a ruler from above with its flat faces parallel to, and a small distance away from, a transparent wall of a column in which sand or glass beads of uniform size were being fluidized by air. If the gap thickness was reduced to 10-20 particle diameters, jamming occurred as particles tried to enter the gap from below. Instead, gas and particles entered from the edges of the ruler, short-circuiting at high velocity and low loading along the gap, while channelling to the bed surface. Jamming occurred if the ratio of gap-width-to-particle-diameter, henceforth referred to as *B* = Blockage number, was too small. Jamming could also be observed when multiple vertical rods were too tightly packed together. Bearing in mind that most practical fluidized beds have wide distributions of particle size and shape, the authors suggested that vertical parallel surfaces should not be closer than approximately 30 mean particle diameters of each other to prevent jamming and channelling.

Dai and Grace (2010) examined fluid-driven jamming in rectangular and ramped constrictions, as illustrated in Fig 1. The conveying fluid was water, and the approaching suspension was dilute, ~2% by volume. The particles were plastic and rubber spheres, discs, cylinders and cuboids, with aspect ratios up to 8.3, dimensions 2 to 50 mm and densities 860-2100 kg/m^3. Blockage was classified by an Index ranging from 0 to 1, with 0 for no blockage, 0.5 for unstable blockages which break up without operator intervention, and 1 for stable blockages. Some of their findings are shown in Fig 2. Blockage (jamming) was found to be a function of several factors – particle size, shape, volumetric concentration, density and compressibility, ramping angle and Reynolds number. Complex flow behaviour occurred as conveyed particles approached the constrictions.

Fig. 1. Jamming in rectangular and ramped constrictions (Dai and Grace, 2010).

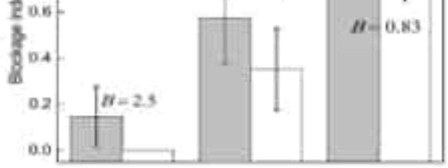

Fig. 2. Dai and Grace (2010) findings illustrating effects of Blockage number (*B*), constriction geometry and Reynolds number for silicon rubber cuboids. Constrictions: rectangular, *Re* = 38,100 for white areas; ramped, *Re* = 29,700 for shaded areas.

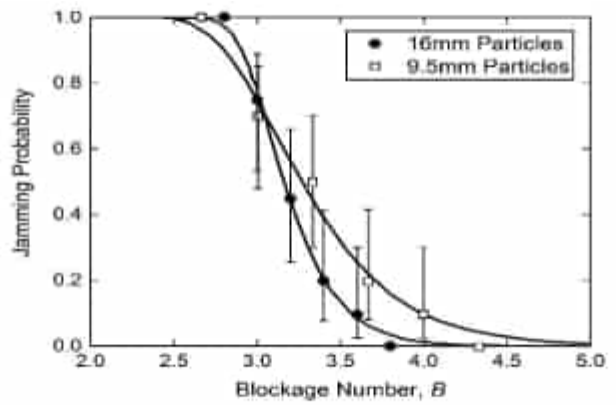

Fig. 3. Experimental findings of Guariguita et al (2012) for jamming of flat discs of thickness 2 mm and different diameters.

A useful, but limited, picture of fluid-driven jamming in constrictions was presented by Guariguata et al (2012), who described jamming as governed by two factors. First, the particulate flow rate must exceed the maximum flow capacity of the constriction, estimated from the Beverloo et al. (1961) equation for gravity-driven flows. When this capacity is exceeded, particle accumulation leads to a dense flow during which particles may continue to pass through the constriction, but whether or not passage occurs is governed by stochastic factors. Both the maximum flow from the Beverloo equation and the probabilistic passage of dense flow depend strongly on *B*, the ratio of the lesser of the constriction height or width to the maximum dimension of the particles. This is shown by an example of the experimental findings in Fig. 3, conducted by releasing 400 to 1200 particles into the upstream flow. Jamming probability is seen to decrease with increasing *B.*

Of particular interest are conditions for which blockage does not occur. For discs smaller than the opening size (B>1), Fig. 3 shows no blockage for $B \geq 5$. For cuboids, Dai and Grace found that blockage did not occur for $B \geq 3$. For asymmetric particles with largest principal dimension > minimum constriction dimension ($B<1$), the situation is complex. To pass through the constriction, particles must bend or re-orient and have their minimum principal dimension < opening width. Stiffness, particle orientation, constriction shape and Reynolds number all then play key roles in determining whether or not particles can pass freely. Decreasing *Re* was then found to decrease blockage for both rectangular and ramped constrictions. In some cases, with other conditions held constant, rectangular constrictions blocked completely, while ramped ones gave no blockage.

Related Findings from Pulp Fibres

Jamming in narrow channels also occurs in paper-making. Pulp is mechanically treated in refiners, consisting of parallel rotating discs, with radial bars on their surfaces and pulp flowing in channels. Fibres occasionally jam in the narrow channels. Having sufficient *B,* defined in this case as the ratio of channel width between bars to the average fibre length, is essential to avoid jamming. However, some unique factors must be taken into account. Pulp fibres have large aspect ratios, ~70, and suspensions are concentrated, ~4% by volume, resulting in flocs of high mechanical strength caused by bending forces within the flocs (Kerekes, 2006). These forces may also press on channel walls, potentially causing jamming. Given that floc dimensions are typically twice the length of individual fibres, the minimum distance between bars is commonly set so that $B \geq 2.$ This is less than the values discussed above for constrictions in fluidized beds, but pulp fibres have low bending stiffness, of order $10^{-11}\,N.m^2$ (Kerekes and Tan Doo, 1985), enabling them to bend significantly, without exerting excessive force on the channel wall, and thereby pass through channels without causing blockage that would render the refiner ineffective.

Coupled CFD-DEM Simulations

Several more recent studies (Mondal et al., 2016; Sun et al., 2019; Xu et al. 2020) have modelled suspension flow through constrictions based on coupled CFD-DEM, i.e. combining computational fluid dynamics for the fluid (numerically solving the Navier-Stokes equations) and the discrete element method to predict the three-dimensional trajectories and fluid-driven jamming of mono- and poly-dispersed particles. All three of these papers only considered spherical particles, limiting the usefulness of this approach, since irregular and extreme particle shapes are more common in practice and more likely to cause jamming. Nevertheless, some valuable findings have been reported, and good agreement is claimed between CFD-DEM predictions and experimental jamming data reported by Lafond et al. (2013) for bi- and tri-dispersed suspensions.

Jamming is predicted by these models to increase as the volumetric concentration of particles in the suspension increases and as the mass flow rate of particles through the orifice increases. As the orifice size increases, the discharge capacity increases, whereas the probability of jamming decreases. For particles of different sizes, the probability of jamming is predicted to increase with increasing fluid velocity, while the shape of the packed jamming dome is also affected. At higher particle stiffness (investigated by adjusting the Young's modulus), particles are predicted to bridge more quickly. Increasing the ratio of particle density to fluid density is predicted to increase the probability of jamming. It is also predicted that varying the ramping angle of the constriction can increase or decrease jamming, depending on the range of angles covered.

Except for entrainment, where the lower end of particle size distributions needs to be considered, the design of fluidized bed reactors typically considers a single mean particle diameter when specifying a wide range of fluidized bed properties and performance parameters. Jamming is different in that it is critically dependant on the upper end of the particle size distribution. The CFD-DEM approach again shows clearly that it is the largest particles, not those of average size, which are important in determining whether or not jamming will occur. Note that a single over-sized particle could initiate blockage. It is prudent therefore to base B on either (a) the screen size through which all the particles have passed before being fed to a reactor, or (b) d_{p90}, the diameter corresponding to 90% by mass cumulatively smaller than that diameter. For given operating conditions and constriction geometry, jamming occurs more quickly with increasing d_{p90} and with increasing range of particle sizes at the upper end of the distribution. Unstable arch-like structures (bridges) are predicted to form at the orifice through which particles are passing. Particles may then accumulate upstream of the unstable bridges, leading to breakage of the bridges and self-avalanche phenomena.

Particle and Constriction Properties Affecting Jamming

Observations of multiphase flows, a limited number of experimental measurements, CFD-DEM predictions and common sense suggest that a number of particle and constriction properties, in addition to operating conditions, play significant roles in determining the extent of jamming. Relevant properties are listed in Table 1, with brief summary comments on their importance and indications of the direction of the effect. Note that several of these properties, such as compressibility, particle shape and the extreme top end of the particle size distribution, are rarely determined or reported carefully by those who design and describe fluidized bed equipment and processes, in spite of their importance with respect to jamming.

While the exact relative importance of the properties and operating conditions listed in Table 1 is unknown, and no doubt varies from case to case, items near the top of the list appear to be the most important factors, with lesser importance towards the bottom. Experimental work is required to investigate the influence of each of the factors in Table 1.

Table 1. Properties and variables that affect flow-driven jamming in constrictions.

Property/Variable	Effect
Maximum particle dimension	Larger particles are more likely to jam.
Constriction width	Narrower and smaller constrictions are more likely to jam.
Particle shape	More angular and extreme shapes are more likely to jam.
Particle size distribution	Wide distribution, especially very large particles, more likely jam.
Particle stiffness	Stiffer particles are more likely to jam.
Particle roughness	Rougher particles with more friction are more likely to jam.
Particle concentration	Higher solids concentration (lower voidage) more likely to jam.
Particle compressibility	Greater compressibility gives greater probability of jamming.
Inter-particle attractive forces	Greater forces promote closer packing and hence jamming.
Fluid velocity	Surprisingly little influence in the limited data available.
Gas and particle density	Unknown; most studies had liquid, but gas-fluidization is critical.
Gas or liquid viscosity	Unknown; unlikely to be a major factor.
Constriction X-sect. shape	Slits and corners likely promote jamming.
Ramping of approach	May promote or reduce jamming.
Surface moisture	By contributing to inter-particle forces, likely promotes jamming.
Vibrations and pulsations	May promote or help break up jamming.
Duration of operation	Longer operation increases probability of jamming.

Other Cases and Causes of Jamming

The jamming discussed in this paper has been limited to a few well-defined particles and flows. However, in many applications the size, shapes and other properties of suspended particles are not well defined. Nor are flows in which jamming takes place limited to constrictions and channels. For example, in circulating fluidized beds, placement of louver partitions or vertical surfaces close to one another may cause jamming in the gaps between them (Zhang, 2020). In addition, jamming establishes the minimum diameter of tubes or vessels without constrictions used to contain fluidized beds of given particles (Cunez and Franklin, 2020).

Conclusions and Some Recommendations on Preventing Jamming

Given the complexity of jamming phenomena, it is not currently possible to give definitive criteria to avoid jamming. Nevertheless, based on the experimental data and numerical predictions summarized above, some guidance is possible:

1. For well-defined particles and constrictions, previous work suggests that when constriction opening sizes are larger than the maximum particle size in the range $B \geq 5$, jamming is unlikely.

2. B should be based on the diameter of the largest particles present or on d_{p90}.

3. For suspensions of highly asymmetric, flexible fibrous material flowing in three-sided channels, jamming is unlikely when $B \geq 2$.

These recommendations are based on limited evidence. Accordingly, our major recommendation is that further research be undertaken on jamming, with the aim of developing rational operational criteria and measures to prevent jamming, thereby reducing process interruptions and safety hazards. In particular, further investigation is needed to delineate the effects of all variables in Table 1 on their influence with respect to jamming.

Notation

B Blockage number = constriction width/maximum particle dimension, -

d_{pi} Particle diameter corresponding to i percentage by mass being smaller, m

Re Reynolds number based on constriction opening dimension, fluid velocity through constriction, fluid density and fluid viscosity, -

References

Adris, A.E.M., Grace, J.R., Characteristics of fluidized-bed membrane reactors: scale-up and practical issues, Ind. Eng. Chem. Res., 1997, 36, 4549-4556.

Beverloo, W.A., Leniger, H.A., Van de Velde, J., The flow of granular materials through orifices, Chem. Eng. Sci., 1961, 15, 260-269.

Cunez, F..D., Franklin, E.M., Crystallization and jamming in narrow fluidized beds, Phys. Fluids, 2020, 32, 083303.

Dai, J., Cui, H.P., Grace, J.R., Biomass feeding for thermochemical reactors, Progr. Energy & Combustion Sci., 2012, 38, 716-736.

Dai, J. and Grace, J.R. Blockage of constrictions by particles in fluid-solid transport Int.J.Multiph. Flow, 2010, 36, 78-87.

Daniels, L.J., Haxton, T.K., Xu, N., Liu, A.J., Durian, D.J., Temperature-pressure scaling for air-fluidized grains near jamming, Phys. Review, 2012, 108, 138001.

Grace, J.R., Elnashaie, S.S.E.H., Lim, C.J., Hydrogen production in fluidized beds with *in situ* membranes, Int. J. Chem. Reactor Engng., 2005, 3, A41.

Grace, J.R, Harrison D. The effect of internal baffles in fluidized beds: a guide to design, Institution of Chemical Engineers Symp. Series, 1968, No 27, pp 93-100.

Guariguata, A., Pascall, M.A., Gilmer, M.W., Sum, A.K., Sloan, E.D., Koh, C., Wu, D.T., Jamming of particles in a two-dimensional fluid driven flow, Phys. Review, 2012, E86, 061311.

Kerekes, R.J., Tam Doo, P.A. Wet fibre flexibility of some major softwood species pulped by various processes, J. Pulp Paper Sci., 1985, 11(2), pp J60-J61.

Kerekes, R.J. Rheology of fibre suspensions in papermaking: an overview of recent research, Nordic Pulp and Paper Res. J, 2006, 25(5), 598-612.

Lafond, P.J., Gilmer, M.W., Koh, C.A., Sloan, E.D., Wu, D.T., Sun, A.K., Orifice jamming of fluid-driven granular flow, Phys. Review E., 2013, 87 (4), 042204.

Lese, H.K., Kermode, R.A., Heat transfer from a horizontal tube to a fluidized bed in the presence of unheated tubes, Can.J.Chem.Eng., 1972, 50, 44-48.

Molerus, O., Wirth, K.E. Heat Transfer in Fluidized Beds, Chapman & Hall, London, 1997.

Mondal, S., Wu, C-H, Sharma, M.M., Coupled CFD-DEM simulation of hydrodynamic bridging at constrictions, Int. J. Multiph. Flow, 2016, 84, 245-263.

Priebe, S.J., Genetti, W.E., Heat transfer from a horizontal bundle of extended surface tubes to an air fluidized bed, AIChE Symp. Ser., 1973, 73(161), 38-43.

Sun, H.L., Xu, S.L., Pan, X.D., Li, S., Geng, X.Y., Cai, Y.Q., Investigating the jamming of particles in a three-dimensional fluid-driven flow via coupled CFD-DEM simulations, Int. J. Multiph. Flow, 2019, 114, 140-153.

Valverde, J.M., Castellanos, A., Fluidization, bubbling and jamming of nanoparticle agglomerates, Chem. Eng. Sci., 2007, 62, 6947-6956.

Xu, S.L., Sun, H.L., Cai, Y.Q., Geng, X.Y., Studying the orifice jamming of a polydispersed particle system via coupled CFD-DEM simulations, Powder Technol., 2020, 368, 308-322.

Zhang, Y.M., Baffles and aids to fluidization, Chapter 18 in Essentials of Fluidized Bed Technology, ed. J.R. Grace, X.T. Bi, N. Ellis, Wiley, New York, 2020.

NUMERICAL INVESTIGATION OF FLOW FIELDS IN A NOVEL METHANOL-TO-OLEFINS REACTOR

Chunhua Zhang[1,2], Bona Lu[2,3]*, Fenfen Wang[1], Wei Wang[2,3], Mengxi Liu[1], Chunxi Lu[1]*

[1]State Key Laboratory of Heavy Oil Processing, China University of Petroleum, Beijing, 102249, PR China
[2]State Key Laboratory of Multiphase Complex Systems, Institute of Process Engineering, Chinese Academy of Sciences, Beijing, 100190, PR China
[3]University of Chinese Academy of Sciences, Beijing, 100049, China

*Email: *bnlu@ipe.ac.cn; lcxing@cup.edu.cn*

Abstract

A novel MTO reactor consisting of two primary reaction regions is numerically investigated using a combination of multi-fluid model and mesoscale drags. The model validation is firstly conducted through the comparison of simulation results and the experimental data in axial/radial profiles of solids hold-up and the external solids flux. Further numerical experiments find that compared to the traditional reactor, an internal circulating flow structure and multiple reaction zones are formed in the novel reactor, which is expected to be favorable for improving MTO reactions.

Introduction

The process of methanol-to-olefins (MTO) enables economical production of ethylene and propylene from coal or natural gas as pointed by Amghizar et. al (2017). It hence greatly reduces the dependence on petroleum resources, and has attracted much attention in recent years, especially in China. As reported by Tian et. al (2015), the selectivity to light olefins in current industrial MTO technologies is about 80%, much lower than the ideal level obtained in experiments on a lab-scale reactor. Actually, the present design of MTO reactor is based on the relative concepts of modern fluid catalytic cracking (FCC) as presented by Liu et.al (2015), ignoring the distinctive characteristics of both reaction processes. The MTO reaction shows several typical features, e.g. existence of an induction period at initial stage, high selectivity of catalyst to ethylene with certain coke deposition, autocatalysis phenomenon. Consequently, a suitable reactor is desired to possess following features: (1) high-efficient mass and heat transfer; (2) controllable solid residence time to achieve an optimum distribution of coke content; (3) slight back-mixing and short gas-solid contact time to inhibit the generation of high hydrocarbon; (4) a pre-coking process of catalyst is preferred to avoid the fresh catalysts firstly contact with methanol, thus the induction period could not be produced.

Previous studies have shown that gas-solid internal circulating fluidized bed reactor (ICFB), has great advantages in forming structured flow fields and improving heat/mass transfer over traditional free bed reactor as introduced by Meng (2018), Yan (2018) and Liu (2013). Therefore, it is considered as a potential reactor to optimize the coordination between the MTO reactions and flow hydrodynamics. In this study, this novel reactor with two primary reaction regions by introducing a draft tube in the bottom center is investigated for MTO process, and three-dimensional (3D) simulations using a combination of two-fluid model (TFM) and EMMS-based mesoscale drags are carried out to find out the favorable flow features.

Model and simulation settings

The schematic diagram of the novel pilot-scale experimental setup is presented in Fig.1. The experiment system consists of a fluidized bed reactor, a riser section and two-stage cyclone separators and diplegs. The transparent Plexiglas column facilitated the observation of gas-solid flow behavior, except that the gas distributors, the draft tube and cyclone separators are made of steel. The total height of the fluidized bed reactor is 3.3 m and the diameter of its column part is 0.38 m. Above the fluidized bed is the riser section with the I.D. of 0.12 m and the height of 5 m. A draft tube is introduced to the fluidized bed and divides the primary reaction zone along the lateral direction into two regions, i.e. the draft region which is 0.3 m in I.D. and 0.8 m in height, and the annulus region which surrounds the draft tube. Above the primary reaction zone is the disengagement region with 2.2 m in height and 0.38 m in I.D. Below the primary reaction zone is the distributor region where installed two different distributors respectively for the gas distribution for the draft tube and annulus region. The perforated plate distributor is selected to supply the gas for the draft tube where 35 orifices with the diameter of 10 mm are arranged in the plate and the total opening ratio is about 3.9%. The ring pipe distributor is used to provide the gas for annulus region where 18 downward orifices with 6 mm in diameter are uniformly distributed along the pipe and opening ratio is about 1.9%. This study aims to study the novel fluidized bed reactor for MTO process shown in the central part of Fig.1. The total height of this reactor is 4.5 m. The Gambit®2.4 is used to generate the three-dimensional (3-D) geometry and corresponding meshes. There are 447639 meshes in total and its average size is 149.5 times the single particle diameter. The hexahedral meshes are employed for regions above the distributors while the tetrahedral ones are used for distributor region and other regions with complex geometry.

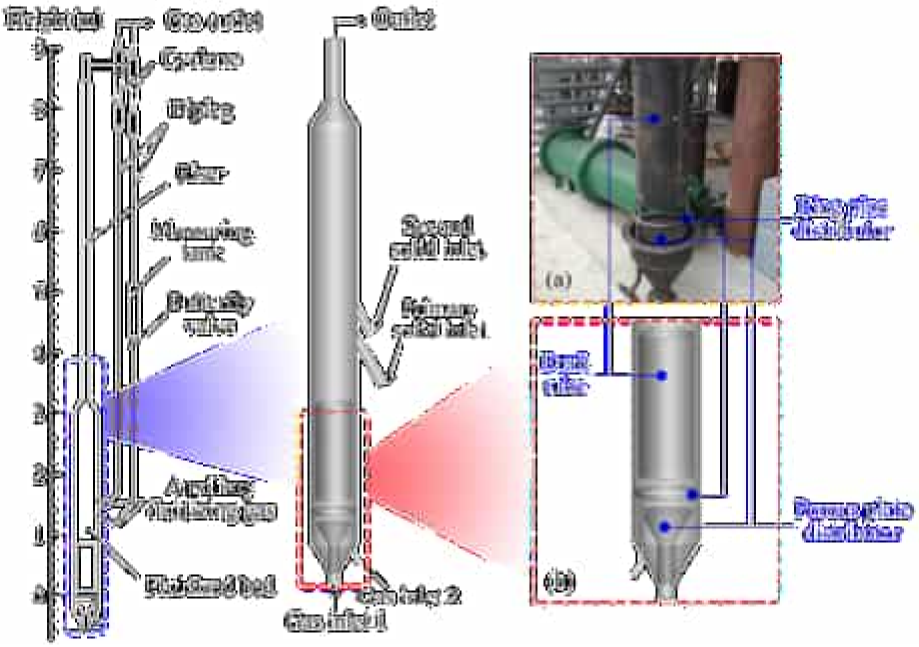

Fig. 1. Geometry of the novel MTO reactor.

The multiphase continuum model was employed and resolved using the Ansys®Fluent 15.0. As the heterogeneous structures have significant impact on the drag force, the EMMS (Energy Minimization Multi-Scale)-based drags which considers the effect of heterogeneous structures are used and the formulation of this structure-dependent drag is written by

$$\beta_\mathrm{E} = \frac{3}{4} C_\mathrm{d} \frac{\varepsilon_\mathrm{s}\varepsilon_\mathrm{g}\rho_\mathrm{g}|u_\mathrm{g}-u_\mathrm{s}|}{d_\mathrm{p}} \varepsilon_\mathrm{g}^{-2.65} H_\mathrm{d} \tag{1}$$

Where C_d refers to the standard drag coefficient for a single particle, and H_d is defined as the ratio of structure-dependent drag coefficient β_E to the drag coefficient obtained from the nearly homogeneous fluidization β_0, such as the Wen & Yu correlation. As the draft and annulus reaction zones are operated in different fluidization state, the EMMS-bubbling drag model proposed by Hong et al. (2013) and suited for dense fluidization, is employed for the annulus reaction zone and the EMMS-matrix drag model proposed by Lu et al. (2009) which is applicable to higher-velocity fluidization such as fast fluidization, is used for draft tube region.

Simulations are first performed for 40 seconds after which the solid mass flux at the top exit reaches a quasi-steady-state condition. And then time-averaged statistics is started for another period of 10 s. More simulation settings are listed in Table 1.

Table 1 Simulation settings

Pressure-velocity coupling	Phase coupled SIMPLE
Gradient discretization	Least squares cell based
Transient formulation	First-order implicit
Momentum discretization	Second-order upwind
Volume fraction discretization	Quick
Granular temperature	Algebraic
Granular viscosity	Gidaspow
Granular bulk viscosity	Lun et al
Frictional viscosity	Schaeffer
Frictional pressure	Based-ktgf
Angel of internal friction	30
Solid Pressure	Lun et al
Radial distribution	Lun et al
Restitution coefficient	0.9
Frictional packing limit	0.61

Results and discussion

The model validation is firstly conducted by examining the agreement of simulation results and the experimental data. As a comparison, the simulation using the homogeneous drag model such as Gidaspow model is also performed. Fig.2 presents the snapshots of solids concentration and the radial profiles of solids concentration at different heights using two different drag models. It can be seen that the radial profiles of solids concentration predicted by using EMMS-based drag model show better agreement with the experiment than those predicted by the other simulation. From the instantaneous distribution of solids concentration, we can see that the simulation using EMMS drags capture the dense fluidization state in the annulus region and the fast fluidization in the draft tube which is consistent with the experiment, whereas the other simulation fails to predict the above phenomena. In addition, the simulation using the EMMS drag also well predicts the solid flux at outlet, being about 90.4kg/(m2·s), 8.5% less than the experiment.

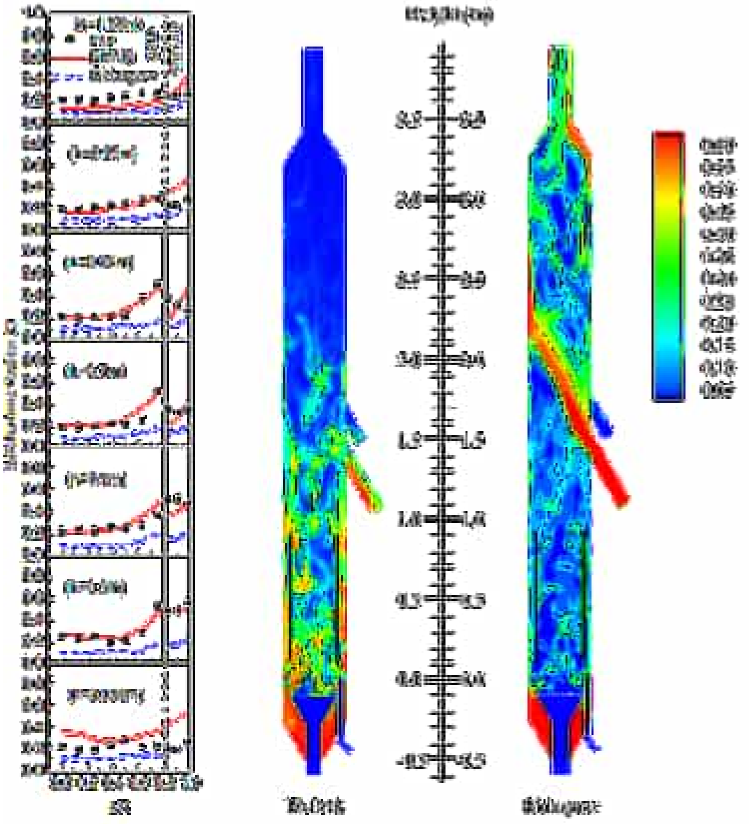

Fig. 2. Solids volume distribution using EMMS-based drag model and Gidaspow model.

Fig. 3. Comparison of distribution of instantaneous solids concentration in the novel MTO reactor and the traditional reactor.

Fig.3 shows the distribution of solids concentration in the entire novel reactor and traditional reactor, respectively. It can be found that an orderly plug flow occurs in the draft region, thus greatly reduces the backmixing compared to the traditional reactor. As the experiment on a microscale fluidized bed reactor by Ye et. al (2015) showed that the decrease in the gas-solid contact time from 3.05 s to 0.61 s could improve the selectivity to light olefins by 5.7%. The formation of fast plug flow in draft region which shortens the gas-solid contact time to less than 0.5 s is expected to help produce more olefins.

Fig. 4. The time-averaged streamlines of solids flow for the novel MTO reactor and the traditional reactor.

Besides, as shown in Fig.4, we can see that a steady internal circulation of particles from the draft region to annulus is formed. As above-mentioned, the modification of a certain coke content on the solid catalysts is favorable to the selectivity of ethylene. This internal circulation could be utilized to control the coke content through changing the residence time of solids by varying operating conditions for the draft tube and the annulus region, thus a much narrow distribution of coke content could be achieved.

Last but not the least, more significant flow features should also be noted, for example, a pre-coking behavior for catalyst could be taken into consideration in this novel reactor, due to the existence of two primary reaction zones with different specified gas inlets. According to hydrocarbon pool mechanism, the induction period after which the hydrocarbon pool species are generated, should be shorten or avoided to spark the methanol conversion very rapidly. In the conventional reactor design, e.g. DMTO reactor, although the fresh catalysts are introduced to the position above the dense phase, the rapid contact between fresh catalysts and methanol cannot be fully avoided due to the serious backmixing in the turbulent fluidization. If using this novel reactor, most methanol enters the draft tube and reacts with the catalysts with certain coke content. Then a percentage of gaseous products will enter the annulus region where the hydrocarbon products contact with the fresh catalysts and help accelerate the reactions under the act of autocatalysis. The related simulations coupling with reaction kinetics are undergoing.

Conclusion

A novel MTO reactor which contains two primary reaction regions is numerically investigated by using a combination of two-fluid model and EMMS-based drags and is expected to be favorable for the MTO reactions. The model validation is firstly conducted and finds that the predicted radial/axial profiles of solid volume fraction show good agreement with experimental data. The further numerical experiments find that compared with the traditional reactor, the backmixing is greatly reduced in the draft region due to the formation of a nearly plug flow. And some of solids out of the draft region enter into the annulus, forming a steady internal circulation. This flow features make the most gas products quickly leave the primary reaction zone, thus avoiding the over-conversion of light olefins to high hydrocarbon. The multiple reaction zones can be also used to regulate the distribution of coke content. Further numerical experiments considering chemical kinetics are expected to probe more details in reaction performance.

Notation

H_d	heterogeneity index	β_E	drag coefficient with structure, $\mathrm{kg \cdot m^{-3} \cdot s^{-1}}$
C_d	effective drag coefficient for a particle		

References

Amghizar I, Vandewalle LA, Van Geem KM, Marin GB. New Trends in Olefin Production. Engineering-Prc. 2017. 3(2):171-8.

Tian P, Wei Y, Ye M, Liu Z. Methanol to Olefins (MTO): From Fundamentals to Commercialization. ACS Catal. 2015. 5(3):1922-38.

Liu Z. Methanol to Olefins. Science Press. 2015. Beijing.

Yan C, Lu C, Fan Y, Cao R, Liu Y. Experiments and simulations of gas-solid flow in an airlift loop reactor. Particuology. 2011. 9(2):130-8.

Meng Z, Liu M, Xie J, Wang W, Lu C. Comparative study on the hydrodynamics and mixing characteristics of a new-type particle mixer. Powder Technol. 2018. 332:90-105.

Liu M, Lu C, Shi M. Advances in gas-solids airlift loop reactor. CIESC Journal. 2012(01):116-23.

Lu B, Wang W, Li J. Searching for a mesh-independent sub-grid model for CFD simulation of gas-solid riser flows. Chem Eng Sci. 2009;64(15):3437-47.

Hong K, Shi Z, Wang W, Li J. A structure-dependent multi-fluid model (SFM) for heterogeneous gas-solid flow. Chem Eng Sci. 2013; 99:191-202.

Ye M, Li H, Zhao Y, Zhang T, Liu Z. Chapter Five - MTO Processes Development: The Key of Mesoscale Studies. In: Marin GB, Li J, eds. *Advances in Chemical Engineering*: Academic Press. 2015:279-335.

CONSIDERATIONS FOR PRACTICAL INDUSTRIAL CFD SIMULATIONS OF FLUIDIZED SYSTEMS

Sam Clark[1*], Peter Blaser[1], Ray Cocco[2]

[1]CPFD Software, 1255 Enclave Parkway, Suite E, Houston, TX 77077, USA
[2]Particulate Solids Research, Inc., 4201 West 36th Street, Chicago, IL 60632, USA

*Email: *sam.clark@cpfd-software.com*

Abstract

Computational Fluid Dynamics (CFD) is based on both fundamentals and empirical models. The fundamental principles, such as conservation of mass, momentum, and energy, are known. Empirical models, on the other hand, have more limited scopes of applicability, and thus are less understood. CFD for fluidized systems, such as fluidized beds or circulating systems, has additional inherent complexity, compared with pure fluid flows. Results can be highly dependent upon empirical models related to fluid-particle, or particle-particle interaction terms, which take the form of drag, collisional, stress, granular temperature, or similar models. The development and validation of these models, which is often undertaken at small test scales, is a topic of significant, current research. Many industrial systems utilizing fluidization, on the other hand, are constructed and operated at scales which may be orders of magnitude larger than the lab-scale or pilot-scale units upon which they are based. Industrial processes such as Fluidized Catalytic Cracking (FCC), polyolefins production, gasification, pyrolysis, or cement manufacture, to name a few, often involve characteristic length scales that can be up to ten meters or greater. This paper and presentation examine the relationship between empirical model development and practical CFD simulations of industrial systems.

Introduction

Industrial fluidization systems are at the heart of many chemical, petrochemical, and power generation processes but can be challenging to design, scale, and operate well. In recent years Computational Fluid Dynamics (CFD) models have been extended to include both particulate and fluid phases. These CFD models are based on both fundamentals and empirical models. The fundamental principles, such as conservation of mass, momentum, and energy, are known. Empirical models, on the other hand, have more limited scopes of applicability, and thus are less understood. CFD for fluidized systems, such as fluidized beds or circulating systems, has additional inherent complexity, compared with pure fluid flows. For some phenomena, results can be highly dependent upon empirical models related to fluid-particle, or particle-particle interaction terms, which take the form of drag, collisional, stress, granular temperature, or similar models.

This paper examines three case studies in which thoughtful calibration of empirical models was used to extend the validity of the overall CFD results. Practical advice is given for simulations of industrial systems.

Using U_{mf} Data to Calibrate Close-Pack Volume Fraction

In 2010, Particulate Solid Research, Inc. (PSRI) and the National Energy Technology Laboratory (NETL) released Challenge Problem III for CFD model validation. The challenge problem included two distinct systems: a circulating fluidized bed (CFB) riser experiment constructed and operated by NETL, as described by Panday et al. (2014); and a bubbling fluidized bed (BFB) constructed and operated by PSRI. For the BFB system, PSRI provided many important pieces of information about the system, including physical dimensions, static bed height, superficial gas velocity, and particle size distribution (PSD). Additionally, minimum fluidization velocity (U_{mf}) test data was provided for the particles used in the BFB, along with detailed information about the geometry and pressure tap locations in the U_{mf} experimental unit.

However, neither the close-pack volume fraction nor the apparent bulk density of the particles, from which the close-pack volume fraction could be calculated, was provided. The close-pack particle volume fraction is an important parameter in fluid-particle CFD models[1]. The particle normal stress tensor model from Snider et al. (2011), for example, ensures that particles do not exceed the physical close-pack limit observed experimentally.

The pressure drop in a U_{mf} experiment can be described by the Ergun (1952) equation. When the fluid velocity is below U_{mf}, the linear term becomes dominant, and the quadratic term is negligible. Below the minimum fluidization velocity, particle volume fraction stays constant at the close-pack value. Given experimental U_{mf} data, it is therefore possible to determine the particle close-pack volume fraction needed by a CFD model so that the measured pressure drop is reproduced. If the particles in the system are monosize, the linear term in the Ergun equation can be solved directly for volume fraction at a given fluid velocity and the corresponding measured pressure drop. However, in the PSRI BFB system, as with the most industrial fluidized bed systems, the particles have a PSD. Because the CFD model was able to account for the effects of PSD, we chose to run a series of U_{mf} simulations with different values of assumed close-pack volume fraction in order to identify the value giving the closest agreement with the initial slope of the experimental U_{mf} curves as shown in Fig. 1.

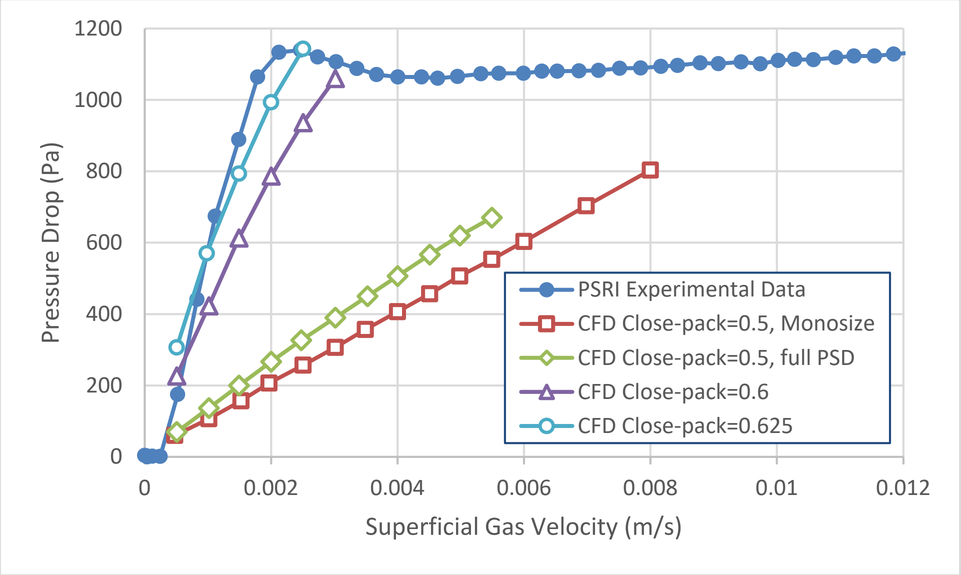

Fig. 1. Experimental U_{mf} data compared with CFD simulations using different close-pack particle volume fraction values.

Based on simulations of the U_{mf} system, we were able to identify that an appropriate value for the close-pack particle volume fraction was 0.625. Fig. 2 shows the predicted pressure profiles from two CFD simulations compared with PSRI's experimentally measured pressure profile for "Case 3" of the large-scale BFB system. The only difference between the two simulations was the close-pack particle volume fraction specified. Using a close-pack particle volume fraction of 0.5 resulted in an under-prediction of the apparent bed density in the dense bed region. By contrast, using a close-pack particle volume fraction of 0.625 raised the apparent bed density predicted by the CFD model in the dense bed region, giving much closer agreement to the experimentally measured data.

---

[1] All CFD results in this paper were created using Barracuda Virtual Reactor®.

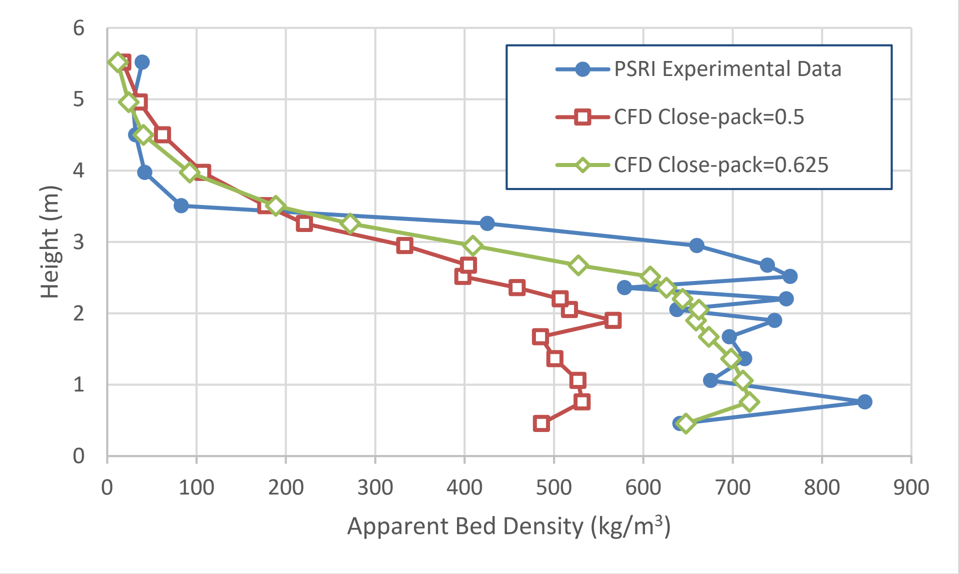

Fig. 2. Experimental apparent bed density data compared with CFD simulations using different close-pack particle volume fraction values.

Using Pressure Data to Calibrate Fluid-Particle Drag Models

Industrial fluid catalytic cracking units (FCCUs) employ fluidized bed strippers to recover hydrocarbons carried along with downward flowing spent catalyst particles from the reactor, preventing these valuable hydrocarbons from entering and combusting in the regenerator. Issangya et al. (2017) presented pressure profile results from a large-scale experiment performed by PSRI. Clark et al. (2017) presented CFD simulation results of this experimental system. The primary metric for the performance of the simulations was how well they predicted the stripper bed density as a function of gas velocity (U_g) and solids flux. Fig. 3 shows the experimentally measured data from PSRI as filled circles.

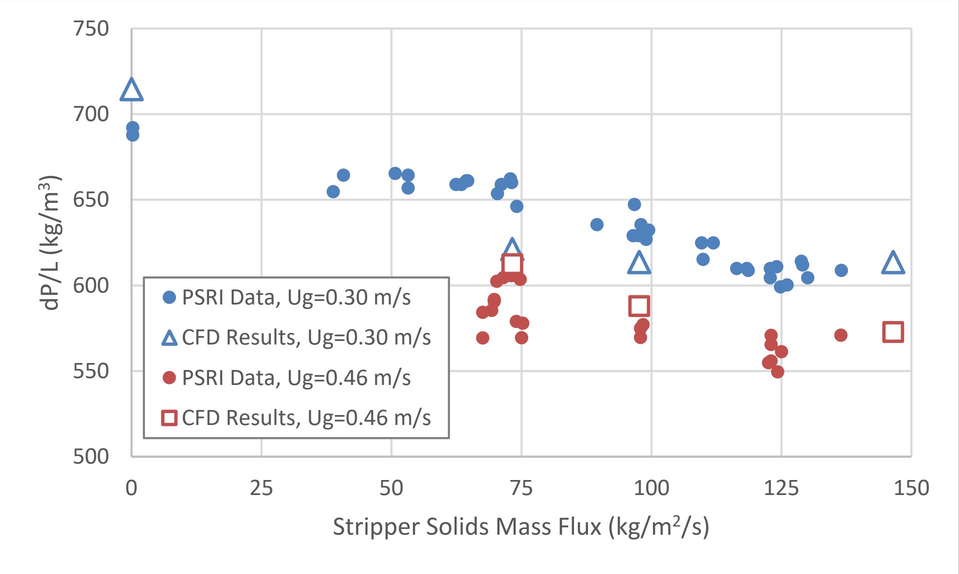

Fig. 3. Comparison of experimental data with CFD simulation results for apparent bed density

As the CFD simulation work began, the initial predictions of apparent bed density were consistently lower than the experimentally measured values. The drag model chosen for this study was a blend of the Ergun (1952) and Wen and Yu (1966) drag models, similar to the well-known blend by Gidaspow (1994). This type of blended drag model is often the first choice for simulations of fluidized bed systems because it captures different phenomena at dense loadings (for which the Ergun drag model is generally valid) and dilute loadings (where the Wen and Yu drag approaches the Shiller-Nauman correlation in the single-particle limit).

However, for simulations of Geldart Group A particles, such as the FCC catalyst used in this system, it has been observed that the Wen and Yu drag model tends to under-predict apparent bed density and over-predict particle entrainment rate from fluidized-bed systems. The authors' current best understanding of why this might happen is that CFD code implementations of drag models typically assume particles are uniformly distributed within a computational cell, and that each particle within the cell encounters the same fluid velocity. While this is generally true for homogeneously fluidized systems, as observed in liquid-solid settling experiments, such behavior does not adequately describe bubbling fluidized systems, where small-scale grouping or clustering behavior is observed.

This phenomenon of particle clustering has been a topic of significant research over the past decade, with multiple additional models proposed in an attempt to capture the missing physics. Such models, based on stable cluster size or energy minimization principles, are beyond the scope of this paper. Nonetheless, we know that some attenuation of the drag force often needs to be imposed on the Wen and Yu portion of the blended drag model so that the apparent bed density predicted by CFD models can be increased to realistic levels.

The strategy used for adjusting the drag in this study was to apply a constant multiplier, M, to the Wen and Yu portion of the blended drag model. The multiplier was also applied within the blending function to maintain a smooth transition from the Ergun drag model at higher particle volume fractions and the Wen and Yu drag model at lower particle volume fractions. To calibrate the value of M, a base case was chosen. All calibration test runs were performed on this single case, and a value of M=0.7 was found to give good agreement with the experimental data. This value was then applied consistently to all other simulations, with no further modifications to the drag model.

Fig. 3 shows the CFD simulation results compared with PSRI's experimental data. The apparent bed densities predicted by the CFD simulations captured the trends in the experimental data, and were quantitatively within the scatter of the experimental results.

Using Deaeration Data to Calibrate Particle Stress Models

An industrial example of using small-scale test data to inform empirical models used in simulations of a large-scale system was given by Loezos and Tomsula (2019). A U.S. Gulf Coast refiner was experiencing erratic stripper/standpipe catalyst circulation. Over-aeration of the standpipe was required in order to achieve stable operation of the stripper, which resulted in a low pressure build in the standpipe. A unique aspect of the operation in this unit was that the FCC equilibrium catalyst (Ecat) PSD was coarse compared with typical PSDs seen in most FCCUs.

Deaeration experiments, similar to those described by Loezos et al. (2002), were performed to measure the expansion and deaeration characteristics of Ecat with both typical and coarse PSDs. Fig. 4 shows the experimental results for bed pressure drop and bed expansion versus superficial gas velocity. The difference in fines content between the typical and coarse Ecat particles had minimal effect on the U_{mf} curve. However, it had a significant effect on the bed expansion above minimum fluidization. The sample of typical Ecat showed much greater bed expansion than the sample of coarse Ecat.

Measurements from the deaeration experiments were used to adjust the particle stress and drag models in CFD simulations of the industrial-scale stripper system, and significant differences in the particle flow behavior for the two PSDs were predicted. Fig. 5 shows particle concentration results from the CFD models at a representative instant in time. Red color indicates high particle volume fraction, and blue color represents low particle volume fraction.

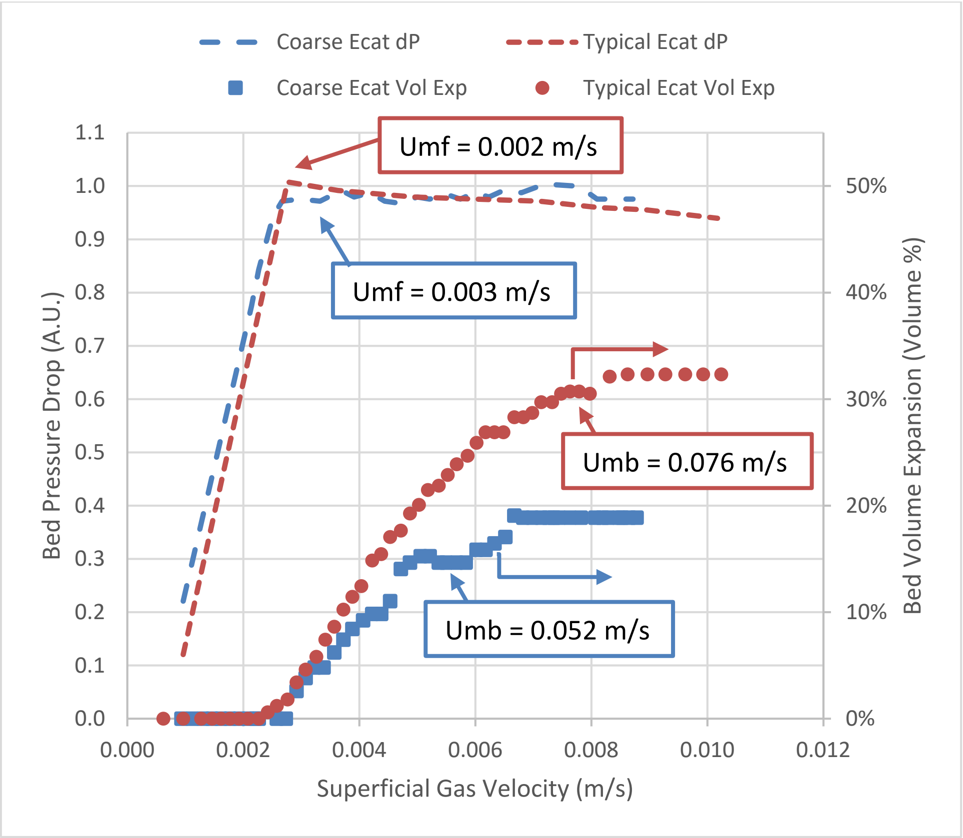

Fig. 4. Experimental data for bed pressure drop and bed volume expansion

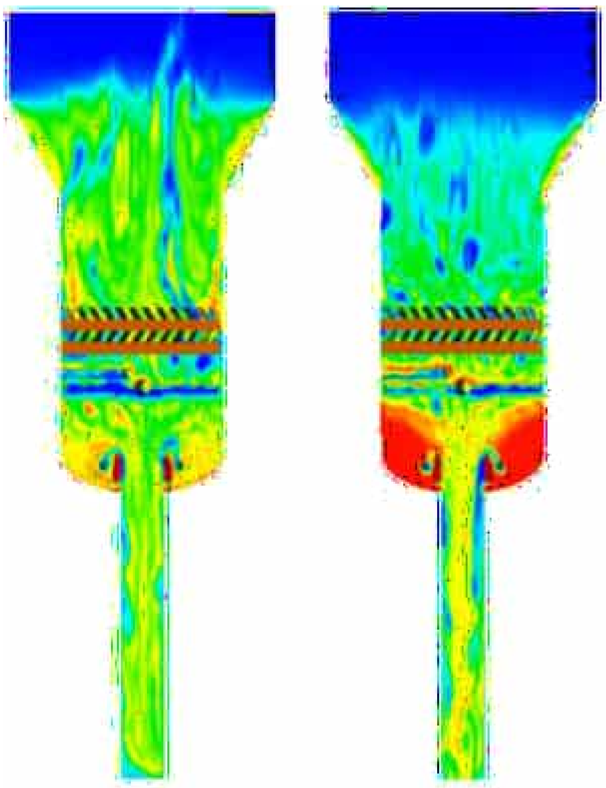

(a) Typical Ecat
(b) Coarse Ecat

Fig. 5. CFD Simulation results comparing particle flow of typical PSD Ecat and coarse PSD Ecat

The longer deaeration time for typical PSD Ecat allows for smoother flow through the stripper and into the standpipe. In the coarse Ecat simulation, a large defluidized catalyst zone forms in the elliptical head, extending almost all the way up to the main stripping steam ring. The fluffing steam ring cannot effectively penetrate into the defluidized zone. Additional fluffing steam, intended to fluidize the bottom of the stripper better, only acts to dilute the catalyst in the standpipe, resulting in low pressure build.

Conclusions

CFD results are partly based on empirical models, and the applicability of the output improves with model calibration. Calibration against smaller-scale test data has been shown to increase the validity of simulations and should be undertaken whenever practical. Additional calibration against operational data from the full-scale operating unit is recommended when possible. Model calibration should be targeted to the empirical models which directly relate to the phenomena of interest. Well-chosen calibration tests should be used to address specific models, preferably in isolation if practical.

CFD practitioners are encouraged to determine a reasonable set of model parameters for a system, and to avoid the temptation to tune model settings for each simulation. Models using empirical parameters which capture trends over a range of input conditions are more useful than those which require re-calibration for each case.

References

Clark, S., Issangya, A., Cocco, R., Blaser, P. Numerical Simulations of PSRI Cold-Flow FCC Stripper Experiment with Subway Grating Baffles. AIChE Annual Meeting 2017, Session 751g. https://www.aiche.org/conferences/aiche-annual-meeting/2017/proceeding/paper/751g-numerical-simulations-psri-cold-flow-fcc-stripper-experiment-subway-grating-baffles

Ergun, S. Fluid Flow through Packed Columns. Chemical Engineering Progress 1952 (48), 89-94.

Gidaspow, D. Multiphase Flow and Fluidization. Continuum and Kinetic Theory Description. Academic Press, Boston, 1994.

Issangya, A., Karri, S. B. R., Knowlton, T. M., Cocco, R., Freireich, B. Bed Density in a Grating Internals Fluidized Bed Stripper. AIChE Annual Meeting 2017, Session 223f. https://www.aiche.org/conferences/aiche-annual-meeting/2017/proceeding/paper/223f-bed-density-grating-internals-fluidized-bed-stripper

Loezos, P. N., Costamagna, P., Sundaresan, S. The Role of Contact Stresses and Wall Friction on Fluidization. Chemical Engineering Science 2002, 57 (24), 5123–5141. https://doi.org/10.1016/S0009-2509(02)00421-9.

Loezos, P. N., Tomsula, B. FCCU Spent Catalyst Standpipe Troubleshooting Case Study. 2019 Barracuda Virtual Reactor Users Conference, Chicago, IL.

NETL Challenge Problem III (2010): NETL’s Circulating Fluidized Bed (CFB) and PSRI’s Bubbling Fluid Bed (BFB). https://mfix.netl.doe.gov/experimentation/challenge-problems/challenge-problem-iii-2010/

Panday, R., Shadle, L. J., Shahnam, M., Cocco, R., Issangya, A., Spenik, J. S., Ludlow, J. C., Gopalan, B., Shaffer, F., Syamlal, M., Guenther, C., Karri, S. B. R., Knowlton, T. Challenge problem: 1. Model validation of circulating fluidized beds. Powder Technology 2014, 258, 370-391. https://doi.org/10.1016/j.powtec.2014.02.010

Snider, D. M., Clark, S. M., O’Rourke, P. J. Eulerian–Lagrangian Method for Three-Dimensional Thermal Reacting Flow with Application to Coal Gasifiers. Chemical Engineering Science 2011, 66 (6), 1285–1295. https://doi.org/10.1016/j.ces.2010.12.042

Wen, C.Y., Yu, Y.H. Mechanics of fluidization. Chemical Engineering Progress Symposium, 1966, 100-111.

CFD-DEM INVESTIGATION OF WALL SHEETING IN GAS-SOLID FLUIDIZED BED CONSIDERING ELECTROSTATIC EFFECTS

Saman Kazemi[1], Shahab Golshan[1, 2], Reza Zarghami[1], Navid Mostoufi[1*], and Jamal Chaouki[2]

[1]Multiphase Systems Research Lab, School of Chemical Engineering, University of Tehran, P.O. Box 11155/4563, Tehran, Iran
[2]Department of Chemical Engineering, Polytechnique Montreal, P.O. Box 6079, Station Centre-Ville, Montreal, Quebec, Canada

*Email: *mostoufi@ut.ac.ir*

Abstract

The aim of this work is to model the two-dimensional wall sheeting phenomenon in fluidized beds with CFD-DEM. Formation of electrostatic charges due to consecutive contacts of solid particles with each other and with wall, and adhesion of the particles on the wall were investigated. Initial charges were considered for particles and the wall was examined in conductive and nonconductive cases. It was observed that positive and negative particles exist in both bulk and wall area, and adhesive particles from a layer on the wall. Also, it was observed that aggregation of the bulk agglomerates form the wall layer and the particles do not aggregate on the wall individually. Residence time of the particles increases near the wall in the presence of electrostatic charges. It was observed that formation of net charges in bed, when there is no elutriation, is the result of contact between particles and wall. Although bed particles produce electrostatic charge in contact with each other, they are not effective in net charge of the bed. At the end, wall sheeting on a conductive wall was investigated and it was found that being insulated or grounded has no significant effect on number and residence time of particles near the wall.

Introduction

Gas-solid fluidization is a process in which granular materials behave like a fluid and suspend in the gas. This process has various applications in industry due to its great interphase heat and mass transfer characteristics. Production of the electrostatic charges arising from consecutive contacts between solid particles with each other or particles with wall is one of the problems in the gas-solid beds. Presence of electrostatic charge leads to significant operational challenges like: aggregation of the particles on the fluidization bed wall, aggregation and agglomeration of particles, production of high voltage electric fields, electrostatic discharge, which may lead to destruction of the process equipment. The aim of this article is to investigate aggregation of the particles due to electrostatic charges on the gas-solid fluidized bed wall. Aggregation of particles on the bed wall forms a layer of positive and negative particles. If aggregation continues, the layer becomes thicker and separated from the bed wall, falls on the distributer plate and may block it. Modeling of these phenomena in a two-dimensional fluidized bed using CFD-DEM[1] is accomplished in this article. An extended CFD-DEM model was used to calculate electrostatic forces. Many experimental investigations have been carried out in this field. Production of electrostatic charge happens by particle-particle and particle-wall contacts. Particle-wall contact produces a net charge in the bed while particle-particle contact does not produce a net charge if elutriation does not exist (although produces positive and negative particles). Aggregated particles on the wall have a layer structure, consisting of a group of positive and negative particles (Song and Mehrani, 2017; Salama et al., 2013). Effect of a grounded conductive bed was investigated and observed that it has no significant effect on electrostatic charge decrease and aggregation of the particles

---

[1] Computational Fluid Dynamics-Discrete Element Method

on the wall (Sowinski et al., 2011). Increasing the pressure results in higher bubble rise velocity and reduction of size of bubbles. Therefore, mixing of particles improves in the bulk and thus increases electrostatic charge production and aggregation of particles on the wall (Salama et al., 2013; Song et al., 2013). Effect of gas velocity and flow regime have been examined. Increasing the gas velocity and transition of the flow regime from bubbling to turbulent increases the aggregation of the particles on the wall because of increased contacts between particles and bed wall (Song et al., 2013). Particle size effect was investigated and it was observed that smaller particles in resin (with a wide size distribution) have a great effect on aggregation of the particles on the wall due to their large charge/mass ratio (Sowinski et al., 2012; Tian and Mehrani, 2015). Modeling of these phenomena have not been accomplished yet. However, a few related investigations have been described, briefly. It was observed that wall and particles work functions affect the particles behavior during fluidization. When two particles with different work functions are used, fluidization quality decreases due to contact electrification and electrostatic interaction of particles. In such a case, particles cannot become fluidized at low velocities because of the presence of agglomerates. Higher gas velocities will break agglomerates (Pei et al., 2016). Investigating the effect of electrostatic charge on bubbles size showed that in the case of single type charge, bubbles are smaller than the case of neutral and charged with opposite polarity particles (Hassani et al., 2013). Since the work function was different between particles and wall, their charges were opposite and particles were attracted to the wall. By increasing the particles diameter, their charges and repulsive electrostatic force increases and bubbles size decreases subsequently (Hadisarabi et al., 2019).

Modeling

Extended CFD-DEM model was used for modeling of wall sheeting phenomenon, which considers transfer and separation of the charge between particles and the wall. CFD-DEM can describe solid particles and gas flow motion in the fluidized bed. Transfer and separation of the charge between particles and the wall were investigated using the condenser model.

Solid Phase

Particles in multiphase flow can interact with each other or with the wall through contact forces in either direct contact or long range forces (such as van der Waals, electrostatic, etc.). Effective forces on particles are calculated separately in this method. Soft sphere model was utilized to model the motion and contact of the particles. In the soft sphere method, particles can overlap with each other and the force and the torque resulted by the contact are calculated based on their overlap (Norouzi et al., 2016). In this approach, it is possible to consider multiple contacts between particles since the contact time is not nil. This method can be used for dense and dilute flows. Newton's second law was utilized to calculate translational and rotational velocities and the position of particle *i* with mass m_i and volume V_i:

$$m_i \frac{d\vec{v}_i}{dt} = m_i \frac{d^2\vec{r}_i}{dt^2} = -V_i \nabla p + m_i \vec{g} + \vec{F}_{d,i} + \vec{F}_{c.i} + \vec{F}_{e.i} \tag{1}$$

$$I_i \frac{d\vec{\omega}_i}{dt} = \vec{T}_i \tag{2}$$

Here, $\vec{v}_i$, $\vec{\omega}_i$ and I_i are the translational velocity, the rotational velocity and the moment of inertia, respectively. The terms of the right hand side of Eq. (1) are far field pressure gradient force, gravity force, fluid drag force, contact force and electrostatic forces, respectively. $\vec{T}_i$ is the torque which is the summation of the tangential and rolling resistant torques.

Gas Phase

Gas motion is described by continuity and Navier-Stokes equations:

$$\frac{\partial}{\partial t}(\varepsilon_g \rho_g) + \nabla.(\varepsilon_g \rho_g \vec{u}_g) = 0 \tag{3}$$

$$\frac{\partial}{\partial t}(\varepsilon_g \rho_g \vec{u}_g) + \nabla.(\varepsilon_g \rho_g \vec{u}_g \vec{u}_g) = -\varepsilon_g \nabla P_g - \nabla \cdot (\varepsilon_g \tau_g) - \vec{S}_p + \varepsilon_g \rho_g \vec{g} \tag{4}$$

where ρ_g, P_g, $\vec{u}_g$ and τ_g are the gas density, the gas pressure, the average local gas velocity and the gas stress tensor, respectively. ε_g and $\vec{S}_p$ are the computational cell voidage and the volumetric exchange rate of momentum between the phases, defined as:

$$\vec{S}_p = \frac{1}{V_{cell}} \sum_{i=0}^{N_p} \vec{F}_{d,i} dV \tag{5}$$

$$\varepsilon_g = 1 - \frac{1}{V_{cell}} \sum_{\forall i \in cell} \varphi_{cell}^i V_p^i \tag{6}$$

In which V_{cell} and φ_{cell}^i are the volume of fluid cell and the fraction of particle i inside the intended fluid cell.

Condenser Model

The condenser model is a simple useful model for explanation and investigation of the transfer and separation of the charge. The area between particles or particle and wall is considered as a capacitor in this model. Contact time of a particle with other particles or with the wall is short, but enough for charge transfer. Transferred and separated charges due to particle-particle or particle-wall contact is calculated from (Hadisarabi et al., 2019):

$$\Delta q = k \, S \, \Delta V \tag{7}$$

where *k*, *S* and Δ*V* are the charge transfer constant, the contact area and the total potential difference, respectively. It is noticeable that because of usage of the soft-sphere method, each contact takes place in multiple time steps. To make charging of the particles and wall quicker, the maximum particle-particle and particle-wall contact area is considered as the contact area of the collision. In the case of collision between a particle (*i*) and the wall (*w*), the following is used to calculate the total potential difference:

$$\Delta V = W_w - W_i - \frac{z}{\varepsilon_0} \left(\frac{q_i}{4\pi R_i^2} - \frac{\sigma_w}{2}\right) \tag{8}$$

where W_w and W_i are the electric work functions of the wall and the particle (i). After contact, wall and particle charges become $q_w - \Delta q$ and $q_i + \Delta q$, respectively. In case of contact between particle (*i*) and particle (*j*), the following equation is used for calculating total potential difference:

$$\Delta V = W_i - W_j - \frac{z}{4\pi\varepsilon_0} \left(\frac{q_j}{R_j^2} - \frac{q_i}{R_i^2}\right) \tag{9}$$

where W_i and W_j are the electric work functions of particle (*i*) and particle (*j*), respectively. After the contact, charges of particles (i) and (j) become $q_i - \Delta q$ and $q_j + \Delta q$, respectively.

Results and Discussion

Modeling was accomplished in a two-dimensional fluidized bed with 5 cm width, 25 cm length and 1 cm thickness. Bed wall was assumed for two cases of conductive and nonconductive. Fluidized particles were polyethylene (density 900 kg/m^3, diameter 400 µm, work function 6.04 eV) and polycarbonate (density 1200 kg/m^3, diameter 600 µm, work function 3.85 eV). The number of both particles were 20000. Wall work function was considered to be 4.5 eV and the initial charge of the fluidized particles was equal to 25% of the maximum charge calculated from the Gauss law (Hendrickson, 2006):

$$|q|_{max} = 2/64 \times 10^{-5} \left(\pi d_p^2\right)\left(\frac{3\varepsilon_r}{2 + \varepsilon_r}\right) \tag{10}$$

The initial charge for polyethylene and polycarbonate (after considering the 25% limit) were $-5/3 \times 10^{-12}$ and $1/25 \times 10^{-11}$, respectively. Fluid characteristics, geometric characteristics of the bed and other needed data for modeling are given in Table 1.

Table 1. Fluid characteristics, geometric characteristics of the bed and other needed data for Modeling

Fluid density	1.25 kg/m^3	Fluid viscosity	0.000018 kg/m.s
Time step of fluid	20 µs	Time step of particles	2 µs
Particle cell size	0.001 m	Fluid cell size	0.003 m
charge transfer constant	0.0003 C/m^2.V	Critical gap (z)	260 nm
Spring coefficient	800 N/m	Coefficient of restitution	0.9
Rolling resistance coefficient	0.3		

Nonconductive Wall

The model was implemented in three cases: a) charged particles and charged wall ($10^{-11}\ C$), b) charged particles and neutral wall, and c) without production of electrostatic charge. Fluidization velocity was considered as 1.5 m/s for all cases. Fig. 1 shows the layer structure of particles on the charged wall. Also, focusing on the particles near the wall, aggregation of the particles on the bed wall is shown and it is observed that a layer of the bed particles forms from aggregation of agglomerates on the wall. In other words, particles do not aggregate on the wall individually. In most cases, when wall-aggregated particles become heavy enough, they move down. But in some cases, they separate from the wall before touching the bottom of the bed. It can be seen that particles in both bulk of the bed and at the wall, consist of a group of positive and negative particles. Wall particles have a layered structure and it can be said that the layer is made up of a group of positive and negative particles. Presence of the layered structure in adhesive particles to the wall has been reported by Sowinski et al. (2010). Fig. 2 shows the residence time of particles near the left and right walls. Residence time and number of particles near the wall in a specific height range in both cases (a) and (b) is more than case (c). Average residence time in case (b) is more than in case (a) which may be due to presence of repulsive electrostatic force between large particles and positive charged wall (in case (a)), because of their same charge.

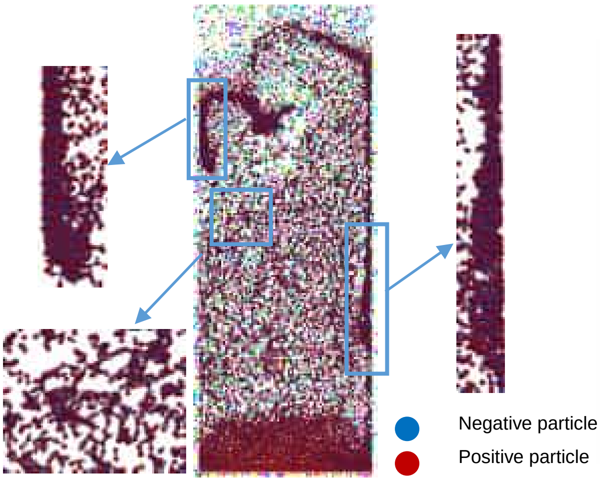

Fig. 1. Layer structure of particles on the charged nonconductive wall

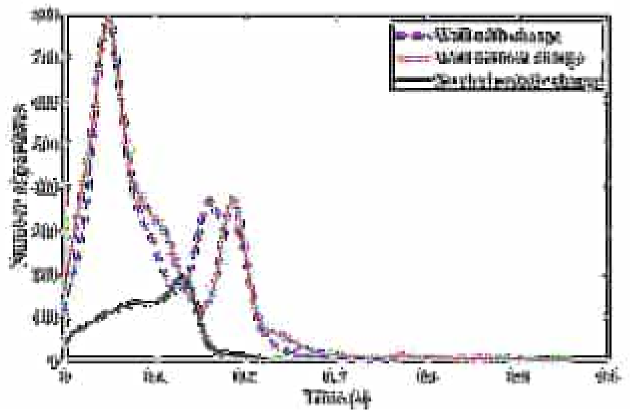

Fig. 2. Residence time of particles near the nonconductive wall

Fig. 3 shows the net charge of bed (summation of positive and negative charges of particles) against time for cases (a) and (b). It can be seen in this figure that the net charge of bed increases in both cases. In other words, the net charge becomes more positive with time. As shown in Fig. 3, net charge of particles in case (a) is more positive than case (b) which is due to presence of initial positive charge on the bed wall. Fig. 4 shows summation of charge density of surface of both left and right walls with time. Since the net charge of the particles is positive, the total wall surface density decreases and becomes more negative, because of charge conservation and inexistence of elutriation. This situation was observed in both cases (a) and (b).

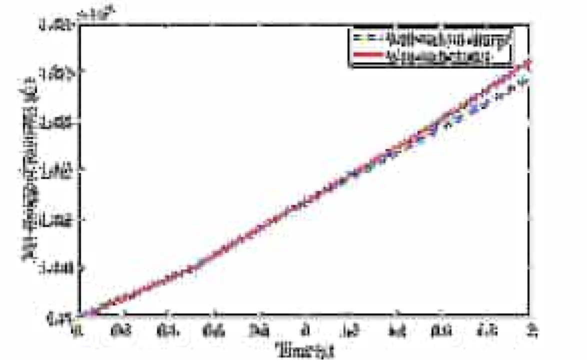

Fig. 3. Net charge of particles

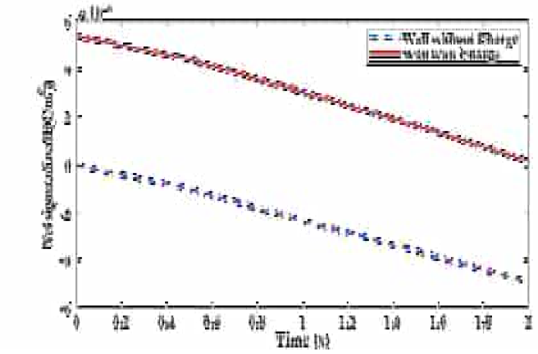

Fig. 4. Summation of charge surface density of both left and right walls

Conductive Wall

The main difference of a conductive and a nonconductive wall is in the presence of an attracting force from the wall for neighboring particles, which is referred to as the image force. In the conductive wall, two cases were investigated: isolated wall without initial charge and grounded wall. In the latter, since the charge does not accumulate on the wall, the vital force which plays the main role in particles adhesion is the image force. In this situation, electrostatic force is the main force for adhesion of the particles to the wall in the next layers. Fig. 5 shows the wall sheeting process on a grounded conductive wall. All modelling conditions in this case is similar to the nonconductive wall. The fluidization velocity for both types of isolated and grounded walls was considered as 1.5 m/s. Fig. 5 shows the bed structure for grounded conductive wall at 0.2, 0.24, 0.28 seconds. It is shown in this figure that how the wall layer is formed and how it moves on the wall.

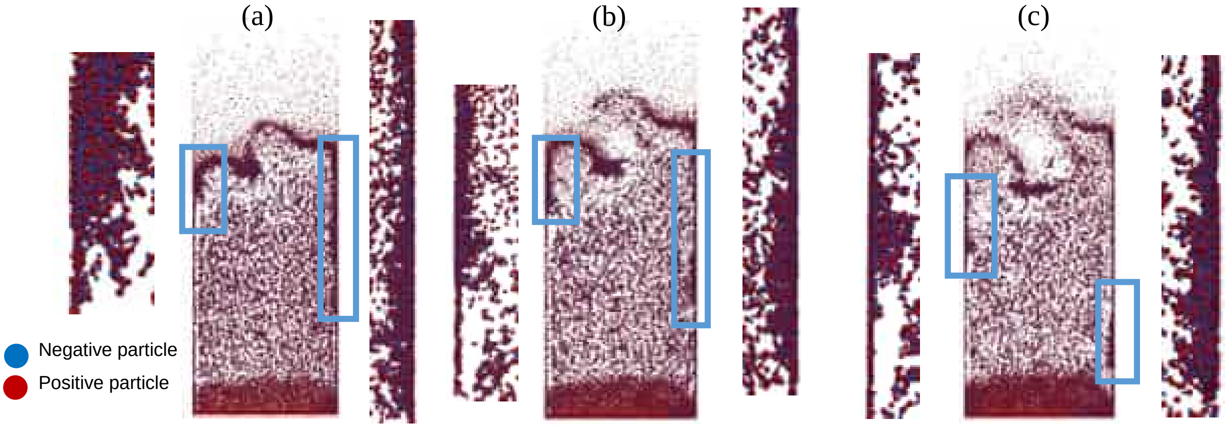

Fig. 5. Bed structure for grounded conductive wall in a) 0.2 s, b) 0.24 s, c) 0.28 s

Fig. 6 shows the residence time distribution of the particles near left and right walls in cases of isolated conductive wall and grounded conductive wall. Residence time and number of particles near the wall are approximately equal in both cases. This trend was reported experimentally by Sowinski et al. (2011). They believed that the connection of a conductive bed to the ground may not affect the aggregation of particles on the wall significantly.

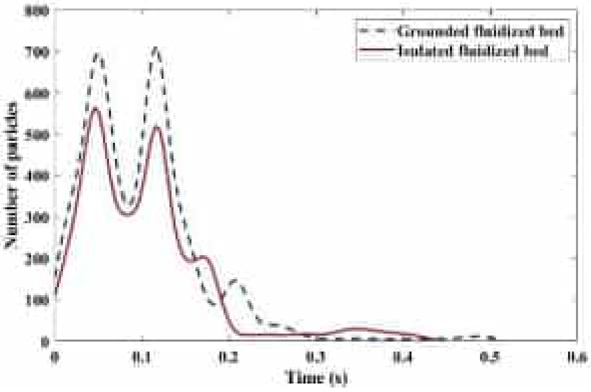

Fig. 6. Residence time of particles near the wall of the conductive bed

Conclusions

The aim of this article was to investigate the process of wall sheeting and formation of wall layer due to electrostatic forces. To fulfilling of this goal, a two-dimensional fluidized bed was modeled by the CFD-DEM technique and the condenser model for transfer and separation of charge. Negative and positive particles were present in both bulk and wall area and adhesive particles to the wall had a layered structure. Aggregation of the bulk agglomerates form the wall layer and individual particles do not aggregate on the wall. Aggregated particles on the wall move mostly downward, but in some cases, it was observed that they separate from the wall before reaching the bottom of the bed. Residence time and number of particles near the wall in the charged particles simulation were more than when the charge does not exist in the bed. Also, it was observed that contacts between particles and the wall cause generation of the net charge in the bed. Wall sheeting on a conductive wall was investigated and it was found that the bed being insulated or grounded has no significant effect on number and residence time of the particles near the wall.

Notation

d_p	Particle diameter (m)	z	Critical gap (m)
$\vec{g}$	Gravitational acceleration (m.s^{-2})	σ_w	Surface charge density (C/m^2)
q_i	Charge of particle i (C)	ε_0	Absolute permittivity of gas(C^2/N.m^2)
$\vec{r}_i$	Position vector of particle i (m)	ε_r	Relative permittivity
R_i	Radius of particle i (m)	$\vec{\omega}_i$	Angular velocity of particle i (s^{-1})

References

Hadisarabi, M, R Sotudeh Gharebagh, R Zarghami, N Mostoufi. Computational modeling of the electrostatic charge build-up in fluidized beds. Journal of Electrostatics. 2019. 97, 108-120

Hassani, MA, R Zarghami, HR Norouzi, N Mostoufi. Numerical investigation of effect of electrostatic forces on the hydrodynamics of gas–solid fluidized beds. Powder Technology. 2013. 246, 16-25

Hendrickson, G. Electrostatics and gas phase fluidized bed polymerization reactor wall sheeting. Chemical Engineering Science 2006. 61, 1041-1064

Norouzi, HR, R Zarghami, R Sotudeh-Gharebagh, N Mostoufi. Coupled CFD-DEM modeling: formulation, implementation and application to multiphase flows, John Wiley & Sons, 2016

Pei, C, C-Y Wu, M Adams. DEM-CFD analysis of contact electrification and electrostatic interactions during fluidization. Powder Technology. 2016. 304, 208-217.

Salama, F, D Song, P Mehrani. Characterizing electrostatic charges in high-pressure gas-solid fluidized beds: experimental design and preliminary results. in: JAM Kuipers, RF Mudde, JR van Ommen, NG Deen (Eds.), Fluidization XIV, ECI, New York. 2013.

Salama, F, A Sowinski, K Atieh, P Mehrani. Investigation of electrostatic charge distribution within the reactor wall fouling and bulk regions of a gas–solid fluidized bed. Journal of Electrostatics. 2013. 71, 21-27.

Song, D, F Salama, P Mehrani. Study of Electrostatic Charging in Gas-Solid Fluidized Bed Polyethylene Reactors. ESA Annual Meeting on Electrostatics. 2013.

Song, D, P Mehrani. Mechanism of particle build-up on gas-solid fluidization column wall due to electrostatic charge generation. Powder Technology. 2017. 316, 166-170.

Sowinski, A, A Mayne, B Javed, P Mehrani. Comparison of the effect of grounding the column wall in gas-solid fluidized beds on electrostatic charge generation. in: Journal of Physics: Conference Series, 012068. IOP Publishing. 2011.

Sowinski, A, A Mayne, P Mehrani. Effect of fluidizing particle size on electrostatic charge generation and reactor wall fouling in gas–solid fluidized beds. Chemical Engineering Science. 2012. 71, 552-563.

Sowinski, A, L Miller, P Mehrani. Investigation of electrostatic charge distribution in gas–solid fluidized beds. Chemical Engineering Science. 2010. 65, 2771-2781.

Tian, Y, P Mehrani. Effect of particle size in fluidization of polyethylene particle mixtures on the extent of bed electrification and wall coating. Journal of Electrostatics. 2015. 76, 138-144.

EFFECT OF WALL BOUNDARY CONDITIONS ON 3D HYDRODYNAMIC NUMERICAL SIMULATION OF A CLC UNIT WITH DUAL CIRCULATING FLUIDIZED-BED REACTORS

Liyan Sun[1], Enrica Masi[1*], Olivier Simonin[1],
Øyvind Langørgen[2], Inge Saanum[2], Nils Erland L. Haugen[2]

[1]*Institut de Mécanique des Fluides de Toulouse* (*IMFT*)*, Université de Toulouse, CNRS, Toulouse, France*
[2]*Department of Thermal Energy, SINTEF Energy Research, Trondheim, Norway*

*Email: *enrica.masi@imft.fr*

Abstract

3D unsteady numerical simulations of a chemical looping combustion (CLC) unit constructed at SINTEF Energy Research (Trondheim, Norway) are performed with the goal to investigate the effect of the particle-wall boundary conditions on the CLC flow behavior. Simulations are carried out using NEPTUNE_CFD, a simulation tool based on a two-fluid modelling approach. Three types of boundary conditions are used for the solid phase: free-slip, no-slip and friction conditions. Comparison between predictions shows that the dominant frictional effect on the particle phase velocity is due to the long-time frictional contact of the particles with the wall. Results show that different boundary conditions may have an effect on the pressure distribution because of the modification of the flow behavior inside the reactors. Noteworthy is the effect that such a modification entails on the different parts of the system because of their coupling.

Introduction

Chemical looping combustion (CLC) allows to control CO_2 emissions by CO_2 separation from the combustion products with a very low energy penalty (Lyngfelt et al. 2011). It is now a well-established technology, intended for use on an industrial scale. New processes based on this technology are being developed and they need as much information as possible to design units that ensure efficiency along with low costs. In this regard, the three-dimensional (3D) numerical simulations may help in both the development and scale-up stages, especially when understanding the instantaneous and local behavior of the flow is crucial for optimizing some parts of the CLC system. In present work, a multiphase computational-fluid-dynamics (CFD) strategy is used to investigate the flow behavior of an existing CLC pilot constructed at SINTEF Energy Research (Trondheim, Norway). Such a strategy uses a two-fluid model approach which is well known to allow numerical simulations at larger scales. This approach relies on the modeling of the particulate flows inside the flow as well as at the wall. The present study aims at investigating the effect of the particle-wall boundary conditions (BC) on the CLC predictions. Three different BC are tested: free-slip, no-slip and friction conditions, with a given set of particle/wall interaction parameters. Results are mainly analyzed on the basis of the time-averaged relative pressure predictions comparing with experimental measurements.

Mathematical Models

The two-fluid model implemented in NEPTUNE_CFD has been used to predict the local and instantaneous behavior of both the gas and solid phases under isothermal conditions. Details about the whole modeling may be found in previous works (see, for example, Hamidouche et al. 2019). The present study is focusing on the effect of particle-wall BC on the hydrodynamic of the dual circulating fluidized bed reactor systems. The wall BC for the particle phase consist in the modelling of the mean particle tangential momentum and random kinetic energy fluxes at the wall, namely at a particle center distance $d_p/2$, where d_p is the particle diameter. Particle-wall BC may be written in the very general form as

$$\left(\mu_p \frac{\partial U_{p,\tau}}{\partial n}\right)_{wall} = \Sigma_{w,\tau n} \tag{1}$$

$$\left(\lambda_p \frac{\partial q_p^2}{\partial n}\right)_{wall} = \phi_w \tag{2}$$

where $\Sigma_{w,\tau n}$ and ϕ_w represent, respectively, the mean particle tangential momentum and random kinetic energy fluxes transferred by the particle assembly to the wall. The unit vector normal to the wall, $\mathbf{n}$, is directed towards the flow, and the unit vector tangent to the wall, $\boldsymbol{\tau}$**,** is given as colinear to the projection of the particle velocity on the wall. Accordingly, the tangential particle velocity component is written as $U_{p,\tau}=\left|\mathbf{U}_p-\left(\mathbf{U_p}.\mathbf{n}\right)\mathbf{n}\right|$. In Eqs. (1) and (2), μ_p and λ_p are the particle dynamic viscosity and random kinetic energy diffusivity which account for the transport within the particle assembly due to kinetic, collisional and frictional effects.

$\Sigma_{w,\tau n}$ and ϕ_w depend on how the discrete particles interact with the wall and, in particular, may be a function of the elastic normal and tangential restitution coefficients, of the friction coefficient, as well as of the wall roughness. In the simplest case, the BC may be derived by assuming pure elastic frictionless bouncing of the particles on a flat wall and are written as

$$\left(\mu_p \frac{\partial U_{p,\tau}}{\partial n}\right)_{wall} = 0 \tag{3}$$

$$\left(\lambda_p \frac{\partial q_p^2}{\partial n}\right)_{wall} = 0 \tag{4}$$

These boundary conditions are referred to as free-slip BC in this work.

In practical flow configurations, $\Sigma_{w,\tau n}$ takes positive value and increases with the particle-wall friction and wall roughness effect. However, according to Fede et al. (2016), the flux transferred by the particles towards the wall is limited by the transport effect within the particle assembly, accounted for by using the viscosity assumption, and such a maximum value is obtained for a zero particle tangential velocity condition at the wall. Therefore, the corresponding BC are

$$\left(U_{p,\tau}\right)_{wall} = 0 \tag{5}$$

$$\left(\lambda_p \frac{\partial q_p^2}{\partial n}\right)_{wall} = 0 \tag{6}$$

These BC are referred to as no-slip BC in this study.

Finally, as pointed out by Johnson and Jackson (1987), $\Sigma_{w,\tau n}$ may be written as the sum of a collisional and frictional contributions: $\Sigma_{w,\tau n} = \Sigma_{w,\tau n}^{col} + \Sigma_{w,\tau n}^{fr}$. The first contribution corresponds to the frictional effect due to the short particle contacts with the wall occurring when particles are in a wide space and bounce off the wall. The second contribution corresponds to the effect of particle contacts with the wall sustained for long times, which may occur when particles are very close to each other and slide together along the wall.

In the case of Coulomb's law for full sliding collisions on a flat surface with a friction coefficient μ_w^{col} , $\Sigma_{w,\tau n}^{col}$ may be written as (Sakiz and Simonin, 1999):

$$\Sigma_{w,\tau n}^{col} = \mu_w^{col}\left(\alpha_p\, \rho_p \frac{2}{3}\, q_p^2\right)_{wall} \tag{7}$$

$\Sigma_{w,\tau n}^{fr}$ may then be written as the product of a Coulomb friction coefficient, μ_w^{fr}, and the wall-normal component of the particle-wall frictional stresses, $\Sigma_{w,nn}^{col}$. In practice, $\Sigma_{w,nn}^{col}$ is assumed to be nearly identical to the inter-particle frictional pressure $P_p^{fr}\left(\alpha_p\right)$ given as an empirical function of the particle volume fraction $\alpha_p\big|_{wall}$ computed at particle center distance $d_p/2$ from the wall (Johnson and Jackson, 1987 ; Srivastava and Sundaresan, 2003). Finally, the particle-wall BC accounting for friction are written as

$$\left(\mu_p \frac{\partial U_{p,\tau}}{\partial n}\right)_{wall} = \mu_w^{col}\left(\alpha_p\, \rho_p \frac{2}{3}\, q_p^2\right)_{wall} + \mu_w^{fr} P_p^{fr}\left(\alpha_p\big|_{wall}\right) \tag{8}$$

$$\left(\lambda_p \frac{\partial q_p^2}{\partial n}\right)_{wall} = 0, \tag{9}$$

where the two Coulomb coefficients are depending on the particle and wall properties.

We may point out that the second term on the right-hand side of Eq. (8) is the dominant contribution in the dense regions of the system. In contrast, the frictional pressure is taken equal to zero for particle volume fraction less than $\alpha_{p,min} = 0.55$ and the only remaining contribution to particle friction at the wall is the collisional contribution which is proportional to the particle volume fraction α_p and to the random kinetic energy q_p^2.

Experimental System and Simulation Setup

The CLC system reproduced by the unsteady 3D numerical simulation is a 150 kW_{th} pilot operating at SINTEF Energy Research (Trondheim, Norway). A schematic diagram of the unit is given in Fig. 1. It is composed of two reactors, the air reactor (AR) and the fuel reactor (FR), each connected with its own cyclone and loop seal, and a lifter allowing the particles to flow from FR to AR according to the CLC design. AR dimensions are 23 cm in diameter and 6 m in height, and FR dimensions are 15.4 cm in diameter and 6.7 m in height (including lifter). In the experiments, the oxygen carrier is ilmenite from Titania A/S in Norway. Particle mean diameter (D_{50}) and bulk density are 90 μm and 2600 kg/m^3, respectively. In the numerical simulations, spherical particles with same mean properties are used, and a total mass inventory of 125.9 kg, estimated by the experiments, is imposed. Gas properties are computed at the temperature of 1273 K, which represents a mean temperature value of the CLC system at such operating point. Mass flow rates are chosen according to the experimental conditions, with the exception of the FR inlet, which is supplemented by the amount of volatiles released by the biomass during the pyrolysis, estimated by the proximate analysis. Mass flow rates are given in Table 1. Pressure boundary conditions at the two cyclone outlets are estimated from the experiments.

Table 1. Gas inlet flow rates.

Item	Value (kg/h)	Item	Value (kg/h)
Primary gas of AR	146.67	AR loop seal, inlet leg	2.23
Secondary gas of AR, G1	17.04	AR loop seal, outlet leg	3.21
Secondary gas of AR, G2	29.16	FR loop seal, inlet leg	2.15
Inlet of FR	27.82	FR loop seal, outlet leg	1.73
Inlet of Lifter	2.27		

Table 2. Parameters for particle-wall boundary conditions.

		μ_w^{col}	μ_w^{fr}
Case 1	No-slip BC	--	--
Case 2	Free slip BC	(0.0)	(0.0)
Case 3	Friction BC	0.5	0.5
Case 4	Friction BC	0.5	0.0

Numerical simulations are performed using NEPTUNE_CFD, which is a multiphase CFD code based on a cell-center type finite volume method and a first order temporal scheme (Neau et al., 2020). The CLC geometry is modeled by a mesh of about 0.76 million cells. Simulations are performed using 144 cores (4 nodes) corresponding to a mean computational cost of about 278 hours per second of physical time. A multiphase version of the k-ε model is used to predict the gas turbulence accounting for the effect of the particulate phase on the fluid flow. This model is coupled with an uncorrelated collision model for the particle random kinetic energy prediction. More details can be found in Hamidouche et al. (2019). In order to study the effects of the particle-wall BC, different BC are used. Table 2 gives the corresponding parameters for each test case.

Results and Discussion

Fig. 1 (first on the left) shows the distribution of the time-averaged relative pressure in the CLC system for Case 3, as an example. In the numerical simulation, pressure is taken at the center of the reactors (but it was found radially uniform inside). In the experiments, pressure was measured by transmitters (Fuji Electric, model FKCW33V5AKCYYAU, 0 – 320 mbar, 4 – 20 mA signal), mounted together on a skid / panel with 10 or 12 mm pipes to their respective pressure measurement points. They are differential pressure transmitters, but the reference pressure is to the atmosphere (the low-pressure entrance of the transmitter is open to the atmosphere) (Bischi et al. (2013)). The pressure is minimum at the top of the reactors and maximum at the bottom of the lifter, as expected. The pressure is much larger in the bottom part of the FR than in the bottom part of the AR, corresponding to a much larger solid inventory, about three times larger for Case 3 (using frictional BC as shown by Table 1). The distribution of the instantaneous solid volume fraction predicted by using frictional BC is shown by Fig. 1 (second on the left). The corresponding time animations show that in the AR, operating in a circulating regime, solids are transported by the fluidization gas to be separated by the cyclone. Then, these particles are sent to the FR through a loop seal. In the FR, solids are transported downward and injected in the AR through the Lifter, but some particles are also transported upward towards the cyclone, to be separated and reinjected in the AR through the loop seal. Results show that the solid volume fraction is higher in the FR than in the AR due to the different fluidization gas velocity, but the solid mass flow rate transported in FR to the cyclone represents only a small part of the total solid circulation rate (about 10%).

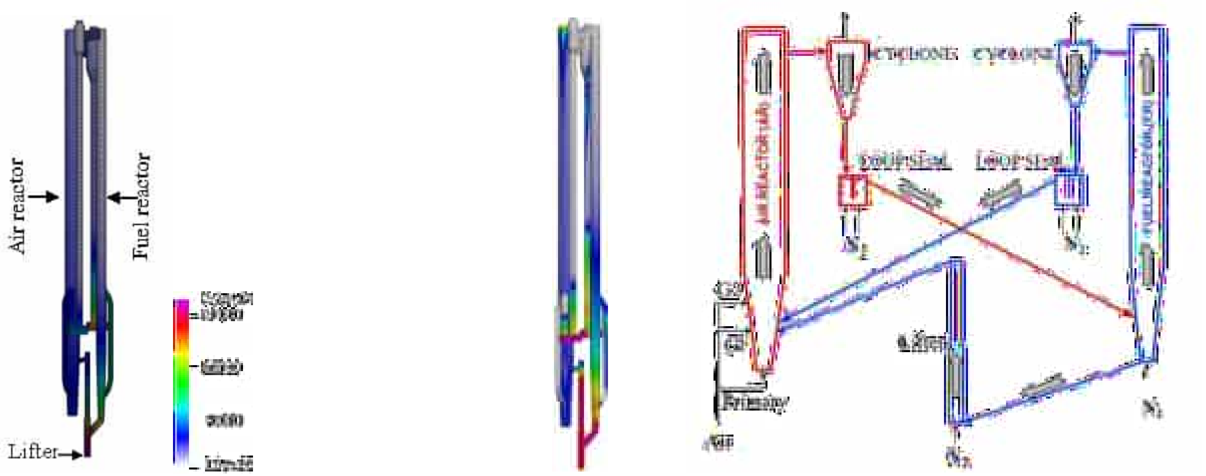

Fig. 1. From the left to the right: time-averaged relative pressure, instantaneous solid volume fraction, time-averaged solid volume fraction, for frictional wall BC (Case 3), schematic diagram of the CLC.

Fig. 2 shows the vertical profiles of time-averaged relative pressure predicted by using different BC. Results are globally in a good agreement with experimental data. However, significant differences in the mean pressure predictions may be observed between simulation results according to the wall BC used for the particle phase velocity. Fig. 2 (left) shows a comparison of the different boundary conditions in the AR. The figure shows a more rapid development of the linear pressure profile and less accumulation of solid in the bottom part of the reactor for no-slip than for free-slip BC. Fig. 2 shows that the pressure profiles obtained with partial friction BC corresponding to Case 4 (μ_w^{col} = 0.5, μ_w^{fr} = 0) are nearly identical to the free-slip BC predictions, meaning that the BC representing only the short-time frictional collision with a flat wall has a negligible effect on the flow behavior, as also shown in dense fluidized bed configuration by Fede et al. (2016). In contrast, Fig. 2 shows that the full friction BC (μ_w^{col} = 0.5, μ_w^{fr} = 0.5) has an effective effect on the mean pressure profiles but it is more difficult to analyze. As a matter of fact, according to the values of the solid volume fraction predicted in the AR along the wall ($\alpha_p < 0.2$), the long-time friction BC contribution represented by μ_w^{fr} = 0.5 should not have any influence in this part of the system. Indeed, Fig. 2 (left) shows that the corresponding pressure profile in AR has a very similar shape than the pressure profile obtained in the free-slip case in terms of the height of the acceleration region and the extension of the linear pressure profile region, but the total mass and flow rate in the AR are smaller than in the free-slip case (see Fig. 4 and 5). So we may expect that the differences observed between the predictions of Case 3 (full friction) and those of Case 2 (free-slip) and Case 4 (partial friction) are mainly due to the effect of the long-time friction effect in the Lifter and in the FR, but also in the connecting pipes, which leads to modify the coupling conditions with the AR in the bottom region and to reduce the global circulation rate.

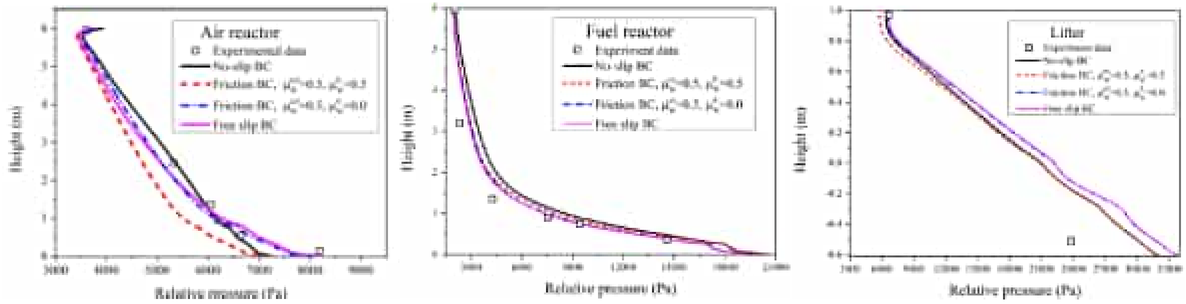

Fig. 2. Vertical profiles of time-averaged relative pressure. AR: left; FR: center; Lifter: right.

Radial profiles of time-averaged vertical solid velocity in AR and FR are displayed in Fig. 3 at a height far from connections. Particles flow up in the center and flow down near the wall. Negative velocities are detected in both the AR and FR in the region near the wall. As shown by the figure, in the AR, the time-averaged vertical velocities predicted using frictional BC are close to the one of simulation using free-slip BC, in the center. However, the asymmetry at the wall leads to conclude that these results are not statistically converged. In the FR, such differences are smaller.

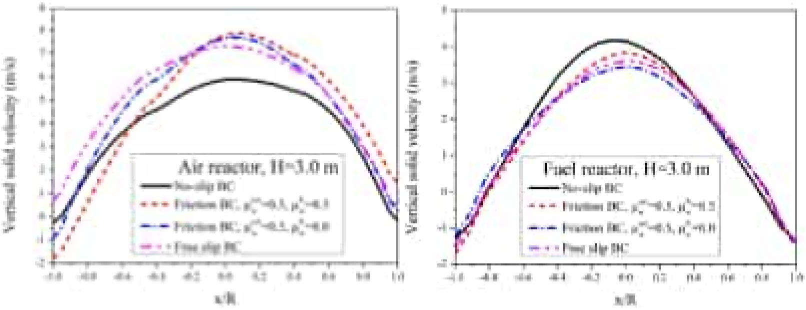

Fig. 3. Time-averaged vertical solid velocity. AR: left; FR: right.

The simulated flow rates of solids leaving the reactors from the top, based on different BC, are shown in Fig. 4. A substantial amount of solids leave the AR from the top, because it operates as a circulating fluidized bed. For the FR, most particles leave from bottom and enter the AR through the Lifter. The mass distributions in the different parts of the CLC, obtained using different BC, are shown in Fig. 5. The solid mass obtained in the FR based on free-slip and partial frictional BC (μ_w^{fr} = 0) are very similar. While, the mass based on a full frictional model (μ_w^{fr} = 0.5) is similar to that obtained with no-slip BC. In the Lifter and in the AR, the mass inventory is decreasing with the increase of the frictional effect, from free-slip to no-slip BC, and this effect is depending on the amount of solid inventory in the connecting parts of the system (cyclones, loop seals, pipes).

Conclusions

3D unsteady numerical simulations of a CLC system were carried out using the NEPTUNE_CFD multiphase code based on a two-fluid model approach. Several BC modeling assumptions were tested on a dual fluidized bed configuration corresponding to a pilot operating at SINTEF, Trondheim, Norway. The predicted time-averaged vertical pressure profiles were analyzed and compared with the experimental measurements. Radial profiles of the time-averaged solid vertical velocity, as well as the solid mass distribution and flow rate were also shown for various BC models. The analysis pointed out the dominant particle-wall frictional effect of the long-time contacts in the Lifter and in the FR and the negligible particle-wall frictional effect of short-time collisions in the AR. The friction model is particularly suitable for prediction of systems with complex structures and different flow regimes. Further study should be carried out to analyze the effect of the wall roughness or irregular particle shape which may increase the particle-wall friction particularly in the dilute configuration of the AR.

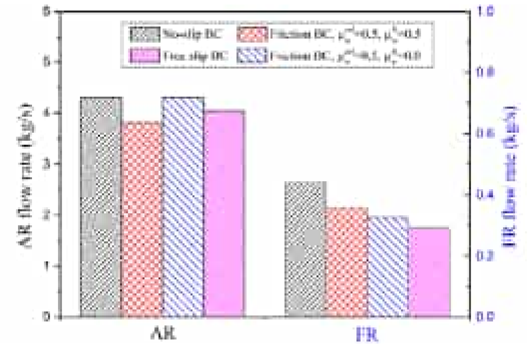

Fig. 4. Time-averaged solid mass flow rates at the top of the AR and FR.

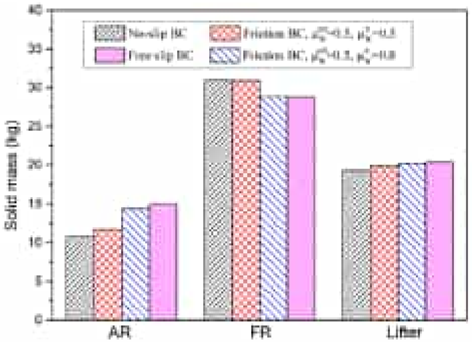

Fig. 5. Time-averaged distribution of solids in the different parts of the CLC.

References

Bischi, A., Langørgen, Ø., Bolland, O. Double loop circulating fluidized bed reactor system for two reaction processes, based on pneumatically controlled divided loop-seals and bottom extraction/lift. Powder Technol. 2013. 246, 51-62.

Fede, P., Simonin, O., Ingram, A. 3D numerical simulation of a lab-scale pressurized dense fluidized bed focussing on the effect of the particle-particle restitution coefficient and particle–wall boundary conditions. Chem. Eng. Sci. 2016. 142, 215-235.

Hamidouche, Z., Masi, E., Fede, P., Simonin, O., Mayer, K., Penthor, S. Unsteady three-dimensional theoretical model and numerical simulation of a 120-kW chemical looping combustion pilot plant. Chem. Eng. Sci. 2019. 193, 102-119.

Johnson, P. C., Jackson, R. Frictional-collisional constitutive relations for granular materials, with application to plane shearing. J. Fluid Mech. 1987. 176, 67–93.

Lyngfelt, A., Leckner, B., Mattisson, T. A fluidized-bed combustion process with inherent CO2 separation; application of chemical-looping combustion. Chem. Eng. Sci. 2001. 56, 3101–3113.

Neau, H., Pigou, M., Fede, P., Ansart, R., Baudry, C., Mérigoux, N., Laviéville, J., Fournier, Y., Renon, N., Simonin, O. Massively parallel numerical simulation using up to 36,000 CPU cores of an industrial-scale polydispersed reactive pressurized fluidized bed with a mesh of one billion cells. Powder Technol. 2020. 366, 906–924.

Sakiz, M., Simonin, O. Development and validation of continuum particle wall boundary conditions using Lagrangian simulation of a vertical gas/solid channel flow. Proc. 8th Int. Symp. on Gas-Particle Flows, ASME Fluids Engineering Division Summer Meeting. 1999.

Srivastava, A., Sundaresan, S. Analysis of a frictional-kinetic model for gas-particle flow. Powder Technol. 2003. 129, 72–85.

RESID FLUID CATALYTIC CRACKING (RFCC) UNIT MODEL DEVELOPMENT FOR A DUAL-RISER 2-STAGE REGENERATOR CONFIGURATION

Mohammad Abdur Rakib[1*], Biswanath Saha[1], Mohamed Al Musharfy[1], Steve Dziuk[2] and Dhanasekar Periasamy[2]

[1]ADNOC Refining Research Centre, Abu Dhabi National Oil Company (ADNOC) Refining, PO Box 3593, Abu Dhabi, UAE
[2]AspenTech Inc., 2500 Citywest Blvd Ste 1600, Houston, TX 77042, USA

*Email: *mrakib@adnoc.ae*

Abstract

Recently coming into service in many modern refineries, highly flexible fluid catalytic cracking (FCC) units, capable of processing a wide range of feeds from atmospheric residue to light naphtha at various process conditions, have become the key candidates in bridging the gap between the supply and demand of propylene, and thus in securing efficient refinery-petrochemical integration.

In this endeavour, the existing Catalytic Cracker model in Aspen HYSYS was upgraded to take in atmospheric residue as the feed, and accurately predict the yields on propylene produced by this unique dual riser, 2-stage regenerator configuration. The existing 2-riser, 1-regenerator model in HYSYS has been upgraded to a 2-riser, 2-regenerator 2R2R configuration to match ADNOC Refining unit configuration by appropriately capturing the detailed geometry of each riser, and injection locations for fresh feed as well as the recycle streams.

The existing reaction kinetics of the Aspen HYSYS Catalytic Cracker model comprising of a 21 lump model involved cracking heavy feeds to make naphtha boiling range material, which further cracked down to light gases including propylene; the latter step involving correlation-based distributions of the light gas components. In the upgraded version of this kinetics, additional cracking pathways were included to derive these lighter components especially the individual C3 and C4 components directly from the first principle kinetic equations, thereby improving the accuracy of their predictions.

In this work, model improvements, along with the model validation results (by performing prediction accuracy analysis (within +/- 3% accuracy) and sensitivity studies on the model for various practical variations in RFCC operation) will be presented.

Introduction

Fluid catalytic cracking (FCC) is a major conversion process in modern refineries, and a major contributor to the commercial gasoline market. Of late, many FCC/RFCC (Resid Fluid Catalytic Cracking) units are designed to achieve higher propylene yield either to meet the propylene demand or to feed the downstream petrochemical complex. This capability of upgrading low value petroleum fractions into high value propylene and commercial gasoline makes FCC unit the most profitable unit in most of the refinery configurations. Since the RFCC unit is the heart of the refinery, optimization of the operating conditions to maximize the production of valuable products can generate significant additional revenue for the refinery.

In the FCC process, low value, high molecular weight hydrocarbons like resids and vacuum gas oils from atmospheric and vacuum columns respectively are converted into valuable products, thereby improving refinery profit margins. The main products are usually LPG and gasoline, and depending on market requirements, the process can be optimized to maximize these or any other desired product. Coke, a by-product from cracking reactions temporarily deactivates the catalyst; however, this has been converted to an advantage by burning it off during regeneration step, thereby also providing the heat requirement to the otherwise endothermic process.

For the RFCC unit considered for this work, Atmospheric Residue (AR) is fed to the main riser of the RFCC unit. Products from the riser are separated in a main fractionator, and naphtha is recycled back to the unit as feed to the secondary riser, where it is further cracked to enhance the overall yield of propylene. Since the process generates coke, catalyst regeneration by coke combustion is conducted in a 2-stage regenerator to minimize any hydrothermal deactivation of the catalyst in the regenerator. Figure 1 represents a schematic of the RFCC unit considered for modeling.

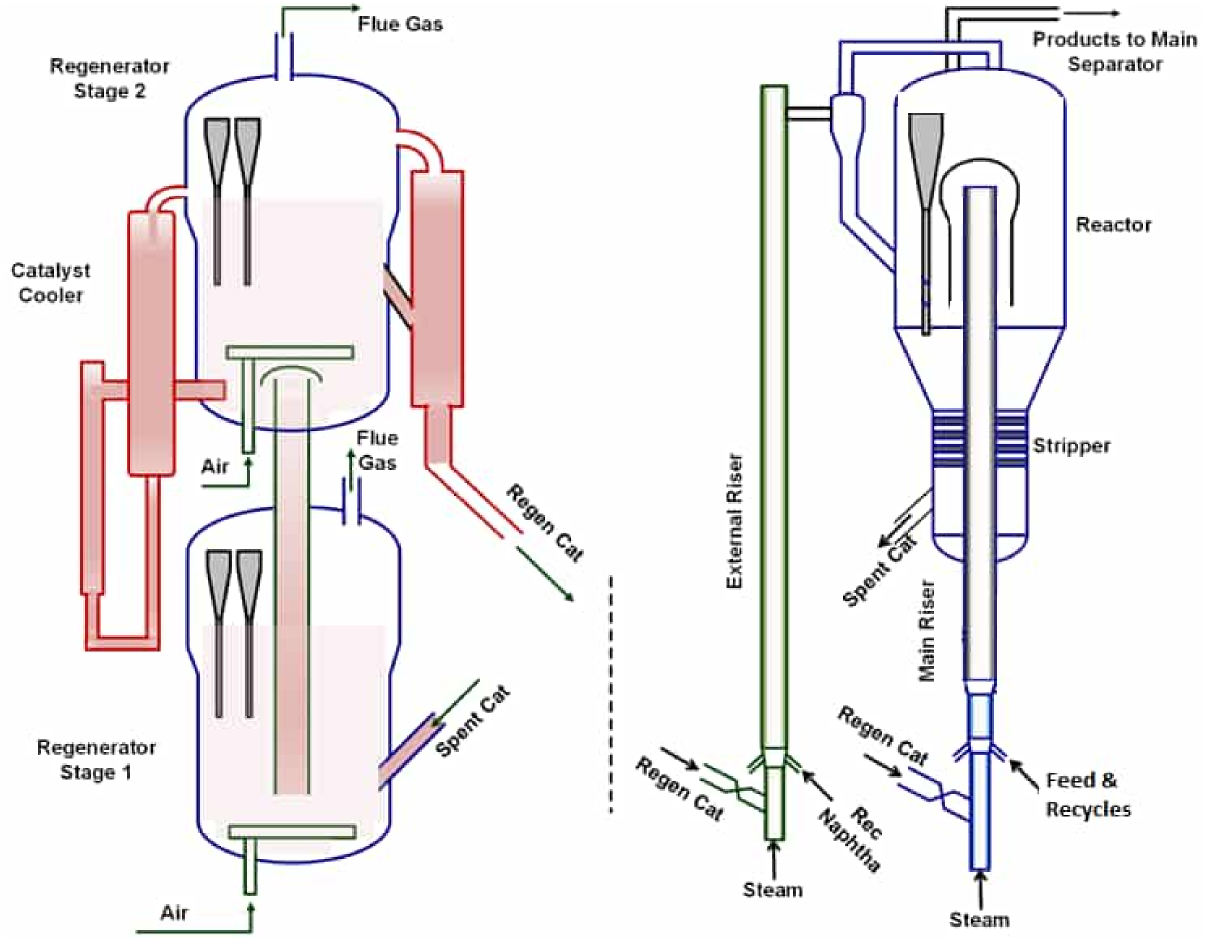

Fig.1. Schematic of a dual riser 2 stage regenerator RFCC configuration.

One of the biggest advantages of RFCC units is its flexibility. It can process feeds with varying qualities and can switch operating modes (Max propylene, Max gasoline, Max distillate) very easily and in a short time span. RFCC being the unit with many upstream and downstream process units, demand such flexibility to absorb the disturbances on either side as well as product demand. It might also encounter change in the feedstock quality depending on the properties of crude introduced to the Crude Distillation Unit, especially when the refiner would like to introduce opportunity feedstock to enhance refining margins. Changes in the unit throughput can significantly impact the hydrodynamics especially in the RFCC riser sections, whereas, changes in the feedstock quality can impact the product yields, as well as the heat load on the regenerators, especially on the catalyst cooler in the 2nd stage regenerator, depending on the feed Conradson Carbon Residue (CCR), and its contribution to the coke yield in the process.

Complex inter-dependent operating parameters of a key profit-driving unit like the RFCC unit necessitates availability of robust predictive models, developed from first principles for the two risers and the two regenerators, and effectively integrating them. Arbel et al. (1995), Fernandes et al. (2008), and Gupta et al. (2001) are among the key works on first principles model development for a commercial FCC process. Accurate prediction of the performance of the commercial Resid Fluid Catalytic Cracking (RFCC) unit is required to enable the process engineers with guiding principles during their daily operation, which consists of several operating conditions, and to establish an optimum operation widow to maximize refinery profits, as well as to adapt to changing requirements to visualize the impacts on product yields and properties as well as determine any associated potential equipment limitations. Most importantly, a robust and accurate unit process model is utilized in refining companies to generate Base & Delta vectors, collectively called as LP vectors for their operations and production planning model (e.g. in PIMS software of AspenTech) utilized for optimizing refinery operations for maximizing profit margins.

In this endeavour, the following modifications were done on the existing Catalytic Cracker model in Aspen HYSYS:

1. Underlying flowsheet of FCC was changed to include 2R-2R (2-riser 2-regenerator) configuration with the recycle options that match ADNOC RFCC configuration.
2. Underlying reaction network and kinetics upgraded to introduce higher resolution on the C3 and C4 components to accurately predict the yields on these components.
3. Estimation of kinetic parameters for the new reaction mechanisms using ADNOC RFCC data.

Table 1. Typical range of plant operating data utilized to calibrate and validated the Model.

Quantity	Value
Fresh ATB Feed [tonne/h]	780 - 850
Total feed to External riser [tonne/h]	100 - 150
Specific gravity of Main riser feed [60 °F/ 60 °F]	0.923 – 0.924
Main Riser ROT (Riser Outlet Temperature [°C]	545 - 550
Feed Temp [°C]	250 - 290
Fresh Make Up Rate [tonne/h]	1.2 – 1.5
Equilibrium Catalyst MAT [%]	68 - 70
Regenerator 2 Dense Bed Temperature [°C]	720 - 730
Reactor Pressure [bar g]	1.7 – 1.8

Typical range of operating data are provided in Table 1. Exact details have not been included in this table for proprietary and confidentiality reasons.

Modeling Approaches

Reactor Hydrodynamics: The reactor-regenerator system in a fluid catalytic cracking system witnesses various fluidization regimes, viz, fast fluidization regimes in the risers, whereas the regenerators operate in the turbulent fluidization regime. The lift riser transporting partially regenerated catalyst from the first stage regenerator to the second stage regenerator operates in the fast fluidization regime. Standard model equations are used in the catalytic cracker model to capture the reactor-regenerator hydrodynamics.

Reaction Chemistry: Catalytic cracking involves a very complex reaction mechanism with thousands of elementary step reactions involving thousands of individual components. Furthermore, the cracking feedstock is also mixture of thousands of components and traditional reactor models till now had been utilizing a simplified chemistry using lumped kinetic models. Fundamentally, increasing the number of lumps enhances the accuracy of the model, provided there are enough measurements and analysis available to support the increased resolution of the model. Most of the discrete lumping approaches found in literature are based on lumps defined purely according to boiling point (yield lumps) as the simplest approach. Alternative approaches also consider some molecular characteristics of the lumps, such as paraffins, aromatics or S-compounds (chemical lumps). Kinetic models with chemical lumps have the potential to be more predictive over wider ranges of feedstock compositions and operating conditions. However, they also require measurements of the corresponding chemical structure for the feedstock and products.

The current catalytic cracker model in Aspen HYSYS involves a 21-lump model that represents the chemicals involved in the cracking mechanisms. This 21-lump model is defined by a grouping of chemicals by molecular type and size (or boiling point). They are the reactants and the products in the cracking chemistry for the model. These lumps are created from the feed distillations and feed properties (e.g., gravities, viscosity, refractive index, etc.). These lumps have an aromatic, naphthenic or paraffinic character as they participate in the cracking reaction paths. The reactions themselves are all based on well-understood first order kinetics that occur in the vapor phase. The reaction kinetic expressions are integrated along the length of the riser and are dependent on the catalyst properties like bulk density, coke on catalyst, MAT activity, and basic nitrogen etc. The catalyst bulk density and coke on catalyst are also integrated along the riser length and are themselves a function of pressure drop, coke make, and molar expansion. Different cracking reaction kinetics are used for these chemical types. The cracking paths are mainly divided into four classes of reactions representing paraffins, naphthenics, aromatic ring carbons and paraffinic carbon structures attached to aromatic rings. There is a set of reactions for conversion of the 950+ °F, resid type material, to heavy material in the 650 to 950 °F range. A second set of reactions covers the conversion of heavy material to light material (221 to 343 °C). Finally, the cracking paths go to a G lump that represents the naphtha production. The C lump product (light gaseous ends) in the reactions is decomposed to the light gases (butanes, butenes, propane, propene, and methane) by correlation. In the ADNOC RFCC reactor, the main riser involves cracking of higher boiling range material to naphtha and lighter components, whereas the secondary external riser causes high severity cracking of naphtha boiling range material to propylene and the other lighter components. In order to capture these details, especially the accuracy of C3 and C4 components, in the upgraded catalytic cracking chemistry additional kinetic pathways have been included to add cracking paths to propylene and other chemicals currently derived from the C lump.

Solution Algorithms/Strategy: The catalytic cracker model in Aspen HYSYS is solved using an equation-oriented platform. Specifically, the model equations of the two risers have been set up in Aspen Custom Modeler (ACM). As such, the default initial guesses of the variables, most importantly the kinetic parameters have been set to very good values by an initial calibration of the model with multiple sets of plant operating data. Henceforth, the model robustness has been found to be quite excellent for further continuous tuning with any new sets of plant operating data as is usually required. Furthermore, the structure of the ACM riser model is generalized so that for the end user, it is not necessary to modify the ACM code to add cracking chemistry for the G or naphtha lump. These modifications can be done using a scripting language in the open object modeling framework that enables connection and integration of the various modules within the HYSYS Petroleum Refining system to build the FCC model from individual modelling components (e.g., risers, regenerators, reactor, etc.). These scripts provide the ability to change cracking mechanisms and feed these mechanisms to the ACM module.

Results and Discussions

The catalytic cracker model in Aspen HYSYS generates individual sets of calibrated parameters for each set of operating data. An average of the calibrated parameters had been used to cross-predict each set of operating data which was used for the model calibration. Excellent cross-prediction were achieved within a band of +/-3% of the key performance indicators of the unit. Sensitivity analysis was performed to gauge the model response for changes in the major operating parameters, feed qualities e.g. density, feed CCR (Conradson Carbon Residue) and feed rates and qualities using HYSYS standard case study feature. The following section summarizes the case study results.

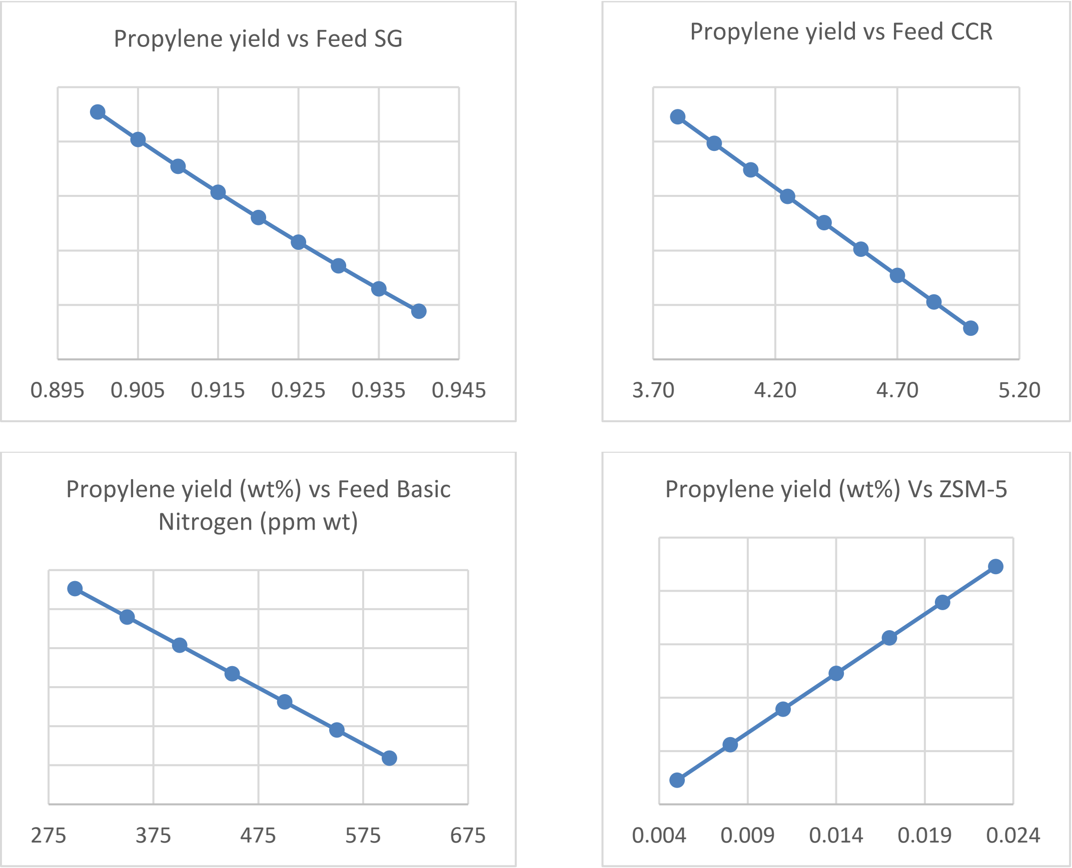

Fig.2. Representative key product yields for variations of key feed properties and catalyst additive.

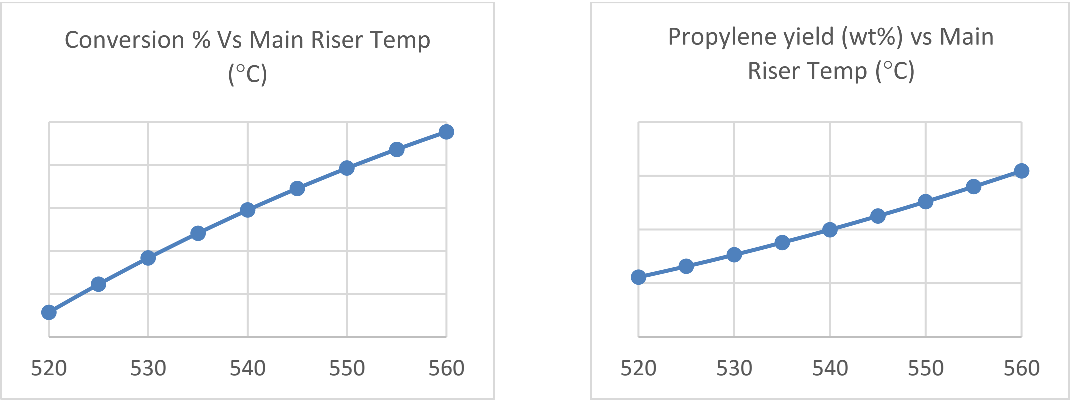

Fig.3. Representative key performance indicators for variations of main riser outlet temperature.

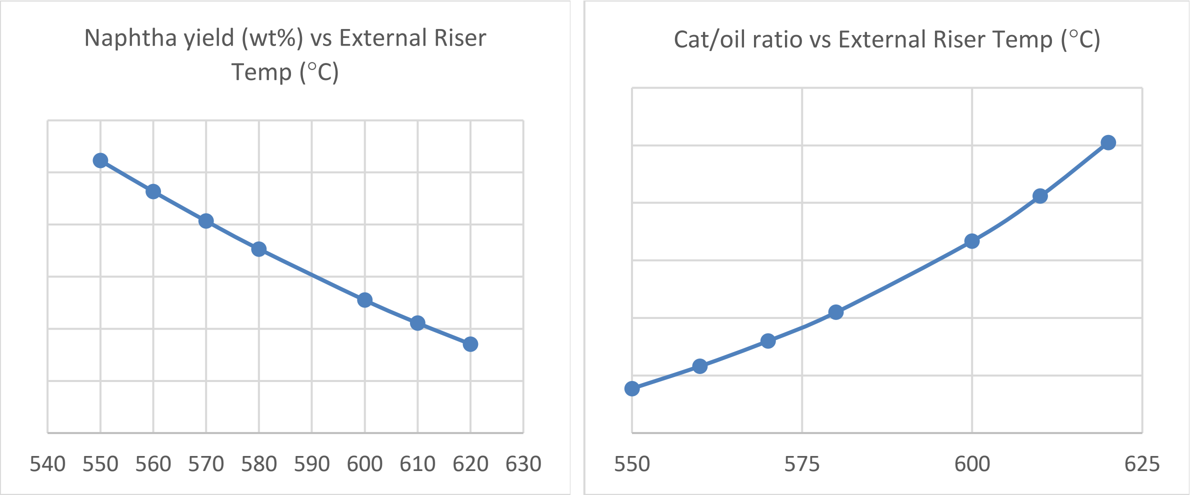

Fig.4. Representative key performance indicators for variations of external riser outlet temperature.

Conclusions

The general version of the catalytic cracker model of Aspen HYSYS could address only a three-equipment combination of reactor and regenerator systems, and hence was not adequate to model a dual riser 2 stage regenerator configuration. Further, the available reaction pathways had not been adequate to address the high accuracy required for prediction of C3 and C4 components in the products profile from the RFCC unit of ADNOC Refining. This work demonstrates the successful upgradation of this existing model in an equation-oriented environment to address these key requirements to accurately predict the performance of the unit. The model has been tested for performance prediction with variations of some key variations of feed quality, and operating conditions of the main riser and external riser.

References

Arbel, A., Huang, Z., Rinard, I. H., Shinnar, R. Dynamics and control of fluidized catalytic crackers. 1. Modelling of the current generator of FCC's. Industrial & Engineering Chemistry Research, 1995. 34, 1228-1243.

Fernandes,J.L., Pinheiro, C.I.C, Oliveira, N.M.C., Inverno J., and Ribeiro, F.R., Model Development and Validation of an Industrial UOP Fluid Catalytic Cracking Unit with a High-Efficiency Regenerator, Ind. Eng. Chem. Res. 2008, 47, 850-866.

Gupta, A., and Subba Rao, D., Model for the performance of a fluid catalytic cracking (FCC) riser reactor: effect of feed atomization, Chemical Engineering Science 56 (2001) 4489–4503.

THREE-DIMENSIONAL FULL-LOOP SIMULATION OF COLD GAS-SOLID FLOW IN A PILOT-SCALE DUAL-FLUIDIZED BED SYSTEM

Frederik Zafiryadis[1], Yashasvi Laxminarayan[1], Anker Degn Jensen[1], Elisabeth Akoh Hove[2], Morten Boberg Larsen[2], Hao Wu[1*]

[1]Technical University of Denmark, Department of Chemical and Biochemical Engineering, Søltofts Plads 229, 2800 Kgs. Lyngby, Denmark
[2]Haldor Topsøe, Haldor Topsøes Allé 1, 2800 Kgs. Lyngby, Denmark

*Email: *haw@kt.dtu.dk.dk*

Abstract

A cold-flow model of a dual-fluidized bed (DFB) system was simulated using the commercial computational particle fluid dynamics (CPFD) code Barracuda VR ®. The DFB system comprises of a reactor and a regenerator bubbling bed, each connected to a fast fluidized bed with bed material circulating between them. Three-dimensional, transient, segregated full-loop simulations were performed to study the hydrodynamics of the system at varying material recirculation rates and reactor riser superficial gas velocities. Numerically estimated pressures and particle distributions were compared with experimental results. Overall trends in these quantities were well predicted by the model. Further work is required to improve the performance of the simulations for accurate predictions across a span of operating conditions.

Introduction

Over the last few decades, computational fluid dynamics (CFD) has been used for evaluating, designing, and scaling-up circulating fluidized bed (CFB) reactors, such as fluid catalytic cracking (FCC) units (Kraft, 2018). However, most numerical studies of CFB systems have been limited to the reactor riser. The Eulerian-Eulerian two-fluid model (TFM) has been widely adopted for simulating FCC riser systems of Geldart Group A particles (Shah et al. 2016), for which immense efforts by e.g. Jiradilok et al. (2006), Lu et al. (2011), and Wang and Li (2007) have been dedicated to develop and scrutinize drag models for properly capturing the hydrodynamics of the riser-only section. However, Li et al. (2014) and Wang et al. (2019) have shown that the lower part of the riser is highly influenced by the inlet conditions of the particles and fluidizing gas, especially at high solids circulation rates.

In light of such revelations, full-loop CFB simulations have emerged over the past decade (Tu et al. 2018), obviating the need for experimental determination of inlet and boundary conditions within the system. Again, the TFM model has been the most widely adopted simulation approach for small- and medium-scale systems (Zhang et al. (2008), Lu et al. (2013), and Luo et al. (2019)). In recent years, the computational particle fluid dynamics (CPFD) model in terms of a hybrid Eulerian-Lagrangian multiphase particle-in-cell (MP-PIC) method, proposed by Andrews and O'Rourke (1996) and further developed by Snider (2001), has gained increased attention due to its ability to model large-scale systems with polydisperse particles at acceptable computational costs (Pannala et al., 2011). Several hydrodynamic studies of cold gas-solid flows in CFB risers, by e.g. Rodrigues et al. (2015) and Xie et al. (2018), have been performed using the MP-PIC method. However, only a few full-loop cold-flow CFB simulations using the MP-PIC method are reported in the literature. Thapa et al. (2016) performed a hydrodynamic study on a lab-scale CFB system and used the model to evaluate the effect of primary and secondary air feed positions. Tu and Wang (2018) performed a simulation of a large-scale CFB with six cyclones, where the predicted system pressures were in good agreement with measurements. Additionally, Kraft et al. (2018) used a CPFD model to study a cold-flow, pilot-scale, dual-fluidized bed (DFB) system for biomass gasification. They were able to achieve results of accuracies within 20% of experimental data, similar to the work of Wang et al. (2014), although adopting a different interphase drag law.

The accuracy of the simulations is highly case sensitive, and only limited work has been conducted on modeling cold-flow DFB systems using CPFD. To close this gap in literature, this study adopts the MP-PIC method for conducting full-loop simulations of a cold-flow, pilot-scale DFB system, with the aim of capturing and describing its hydrodynamics in terms of pressure and particle distributions.

Experiments

Experiments were performed on a cold-flow DFB at the Technical University of Denmark. The cold-flow DFB consists of a reactor and a regenerator loop. Each loop is comprised of a riser, primary and secondary cyclones, a bubbling bed, and a transfer line for connecting the two loops. Furthermore, a gas stripper is located below the regenerator bubbling bed. The main part of the reactor riser has a height of 3960 mm and a diameter of 60 mm. The reactor and regenerator bubbling beds have diameters of 450 mm and 600 mm, respectively. A schematic diagram of the system is shown in Fig. 1a, along with the location of the pressure acquisition points at which differential pressure transducers are used to measure the pressure drops over the system.

Fluidizing gas is added at several locations, as is indicated on Fig. 1a. Spargers are used to fluidize the bubbling beds, the stripper, and the bottom part of the reactor riser (conditioning zone). Lift gas, simulating vapor-phase products and steam, is injected into the reactor riser through a 30° angled pipe to dilute the particle-laden flow. Simultaneously, lift gas, simulating hot flue gas, is injected into the regenerator riser. The fluidizing gas exists the system through the cyclones. Contrary, solids are recirculated throughout the system; up through the reactor riser and into the primary and secondary reactor cyclones, before entering the reactor bubbling bed, where solids are transferred to the regenerator loop, operating in a similar manner. Geldart B particles with a true density of 2590 kg/m^3 and a bulk density of 1650 kg/m^3 are used as bed material. The particle size distribution is shown in Fig. 1b, ranging from 35 µm to 240 µm with a Sauter mean diameter of d_{32} = 89 µm.

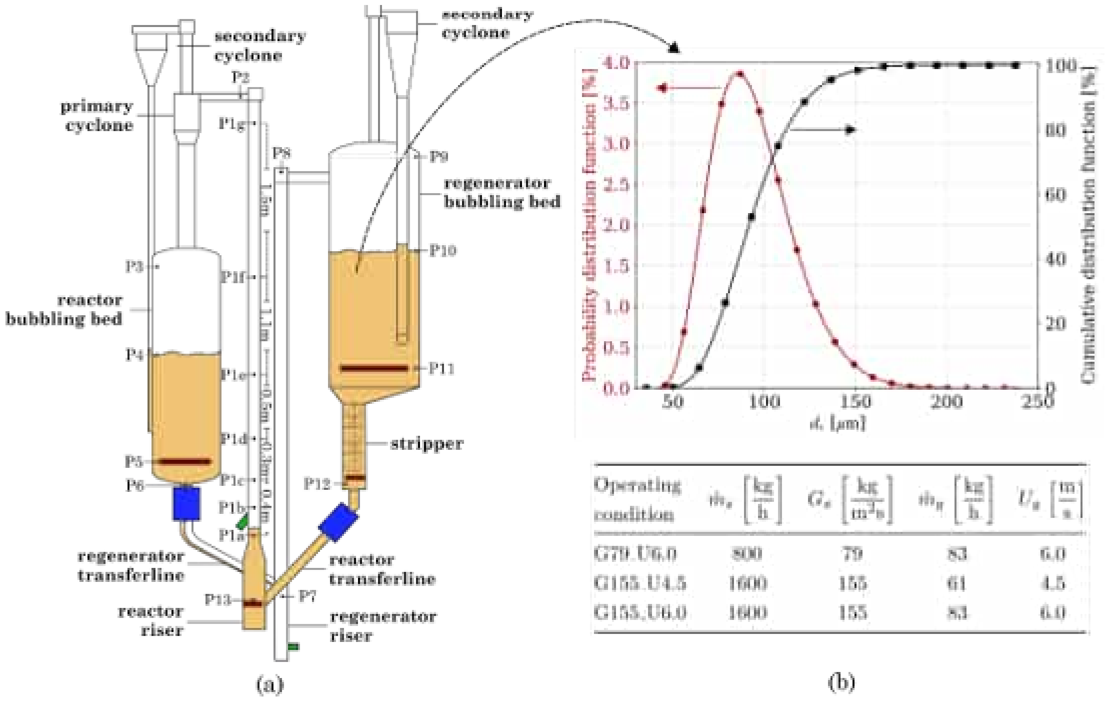

Operating condition	$\dot{m}_s$ $\left[\frac{kg}{h}\right]$	G_s $\left[\frac{kg}{m^2 s}\right]$	$\dot{m}_g$ $\left[\frac{kg}{h}\right]$	U_g $\left[\frac{m}{s}\right]$
G79_U6.0	800	79	83	6.0
G155_U4.5	1600	155	61	4.5
G155_U6.0	1600	155	83	6.0

Fig. 1 (a) schematic of cold-flow pilot-scale DFB system. Location of pressure tapping points are indicated by P's. Green: lift gas injections. Red: spargers. Yellow: solids phase dense regions. Blue: locations of pinch valves. (b) particle size distribution with system operating conditions based on reactor riser flows and dimension.

Experiments are conducted at three different operating conditions (see Fig. 1b), in which the solids circulation rate and the flow rate of the lift gas added to the reactor riser are varied. Two pinch valves, located at each of the transfer lines, are used to control the solids circulation rate. Differential pressure measurements are conducted at steady state conditions over a period of least 90 s for each operating condition.

Simulations

The gas-solid flow in the pilot-scale DFB is solved numerically using the CPFD implementation in Barracuda Virtual Reactor ® 17.4.0. The continuous gas phase equations are solved in an Eulerian reference frame, while dispersed particles are grouped together in parcels for easy tracking using the Lagrangian MP-PIC scheme. The kernel of the CPFD method lies in the treatment of the particulate phase, which is governed by the Liouville particle distribution function to solve for solids velocity, volume fraction, density as well as the interphase momentum force. The governing equation for the solids movement is defined according to Snider (2001) for an incompressible particulate phase (denoted by subscript *s*)

$$\frac{\partial \mathbf{u}_{\mathrm{s}}}{\partial \mathrm{t}} = \mathrm{D}_{\mathrm{s}}\left(\mathbf{u}_{\mathrm{g}}\text{-}\mathbf{u}_{\mathrm{s}}\right) - \frac{1}{\rho_{\mathrm{s}}}\nabla \mathrm{p} + \mathbf{g} - \frac{1}{\varepsilon_{\mathrm{s}}\rho_{\mathrm{s}}}\nabla\tau_{\mathrm{s}}, \tag{1}$$

in which D_s the interphase drag coefficient. In this study, a combined Wen-Yu/Ergun drag coefficient, similar to that of Kraft et al. (2018), is adopted with a Sauter mean diameter correction inspired by the work of Beetstra et al. (2007). The last term of (1) entails the gradient of an interparticle normal stress. The CPFD method assumes that particles are constantly colliding with a random set of particles. Hence, this approach considers the solids phase as a continuum exerting a normal stress on itself, defined as

$$\tau_{\mathrm{s}}(\varepsilon_{\mathrm{s}}) = \frac{\mathrm{P}_{\mathrm{s}}{\varepsilon_{\mathrm{s}}}^{\beta}}{\max\left(\varepsilon_{\mathrm{cp}} - \varepsilon_{\mathrm{s}}, \alpha(1\text{-}\varepsilon_{\mathrm{s}})\right)} \tag{2}$$

with the values of the constant P_s, the close-pack volume fraction $\varepsilon_{\mathrm{cp}}$, and the coefficients α and β set according to the recommendations of Snider (2001).

For performing a CPFD simulation of the full-loop system, the geometry of the setup, as well as initial and boundary conditions, simulating the experimental conditions, are used. The discretized fluid domain with applied boundary conditions are depicted in Fig. 2a-b. For simplicity reasons, secondary cyclones are neglected, and exiting solids are recirculated directly to the bubbling beds. Thin solid surfaces (baffles), impermeable to solids and fluid flow, are used to simulate the presence of vortex finders in the primary cyclones and the internals of the stripper. Spargers are modeled using fluid (either air or nitrogen) point sources at the locations of the sparger holes. The fluidizing gas leaves the system through the outlets at specified pressures. Consequently, pressures monitored in the vicinity of gas outlets (i.e. P2 and P9 of Fig.1 a) are largely governed by the imposed Dirichlet pressure boundary conditions. The cold-flow system is considered isothermal with a temperature of 300 K.

Only excerpts of the transfer lines are included in the simulation. Boundary condition (BC) connectors (red, dashed arrows in Fig. 2) are implemented instead of the main portions of the transfer lines and the pinch valves. The BC connectors allow for specifying the solids flow rate of the system to match that of the experimental conditions. Using this method, it is assumed that the flow of solids and gas is uniformly distributed across the inlets to the transfer lines, resulting in a segregated or pseudo full-loop simulation setup.

A Cartesian, staggered grid arrangement with 464,000 cells is used to discretize the fluid domain. Cell lengths vary from $108d_{32}$ in finely resolved areas (reactor riser and conditioning zone) to $155d_{32}$, with an average value of $140d_{32}$ for the entire domain. A grid sensitivity study was conducted for cell counts of 290,000, 464,000, and 635,000, with the latter two resulting little or no difference in the predicted pressure distribution of the loop. The system is initialized with 795 kg of bed inventory, of which most is contained in the bubbling beds, as indicated on

Fig. 2b. A complete overview of the simulation parameters, including simulation time, time averaging period, and numerical time step, can be found in the table of Fig. 2.

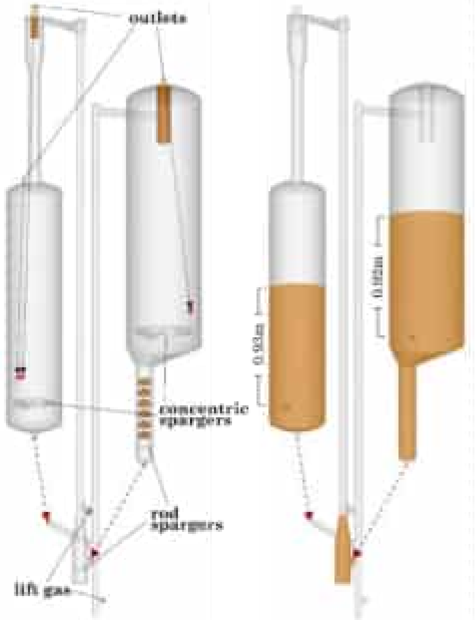

(a) (b)

Parameters	Units	Values
Wall normal retention coefficient	-	0.3
Wall tangential retention coefficient	-	0.99
Diffuse bounce	-	5
Close-pack volume fraction, ε_{cp}	-	0.637
Pressure constant, P_s	Pa	10
Exponent, β	-	3
Constant, α	-	10^{-8}
Cell count	-	4.6×10^5
Bed inventory	kg	795
Parcel count, N_p	-	6.5×10^6
Physical particles per parcel, n_p	-	1.5×10^5
Time step	s	2.0×10^{-4}
Simulation time	s	30
Time averaging period	s	15

Fig. 2. (a) boundary conditions and (b) initial bed inventory. Simulations parameters are included in the table.

Results and Discussion

Results of the CFPD simulations of the cold-flow system are depicted in Fig. 3 and 4. Fig. 3a displays the instantaneous distribution of particles in the system after 30 seconds of simulation for the case of G155_U6.0. Parcels are colored by cell solids volume fraction, indicating a high degree of packing in the bubbling beds, stripper, and reactor riser conditioning zone. Dilute fast fluidization regimes are observed in the two risers, while bubble coalescence and splashing at the freeboard is found in the two bubbling beds.

The gauge pressure distribution in the system is plotted as function of height in Fig. 3b. Numerical pressures are obtained from time averaged values over the vessel cross-section at the probe locations of Fig. 1a. The standard error of the time-space-averaged absolute pressures throughout the system varies from below 0.01% to 2.7%. Overall, a good agreement is found between simulation and experiment, in the upper parts of the system and in the reactor loop. Deviations are observed at the bottom of the two reactors (P7 and P13) and at the bottom of the stripper (P12). The former is most likely due to the use of BC connectors affecting the inflow conditions to the riser conditioning zones, while the latter is presumably related to modeling of the stripper internals using surface baffles.

Simulated apparent bed densities of the reactor bubbling bed (1439 kg/m^3), regenerator bubbling bed (1444 kg/m^3), and reactor riser (182 kg/m^3) are in agreement with experimental findings of 1434 kg/m^3, 1447 kg/m^3, and 183 kg/m^3 for the bubbling beds and the reactor riser, respectively. The apparent density across the regenerator riser is underestimated, resulting in the slope discrepancy between experiments and simulations from pressure point P7 to P8.

A comparison of simulated and measured gauge pressures in the cold-flow system for all conducted simulations is shown in Fig. 4a. The two dashed lines mark deviations of ±25% from complete agreement between numerical predictions and measurements. Despite some outliers, the deviation is within ±25%, suggesting that the current simulation approach can be used to predict behavioral trends at different operating conditions. Fig. 4b compares the predicted and measured gauge pressure profiles across the height of the reactor. Profiles are normalized with respect to the pressure at the top of the riser (P1g) to allow for direct comparisons of the pressure profiles. The model consistently overpredicts the pressure drop in the acceleration zone, leading to an underprediction of pressure throughout the entire riser height, as also concluded by Rodrigues et al. (2015) and Kraft et al. (2018). Nonetheless, the overall pressure drop is estimated within an error of only 3-10%.

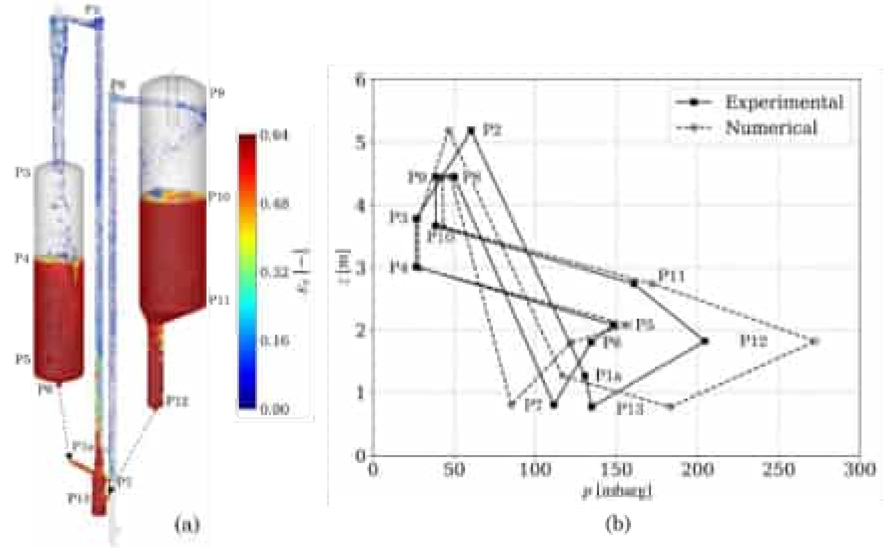

(a) (b)

Fig. 3. Simulation results for G155_U6.0. (a) instantaneous particle volume fractions in the cold flow model at t=30 s. (b) comparison of experimental and computational average pressure distributions.

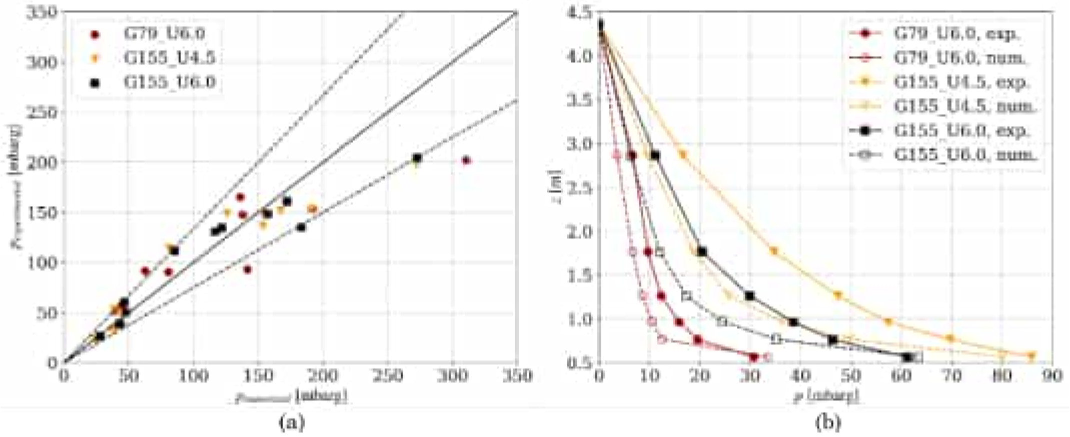

(a) (b)

Fig. 4. (a) Simulated and experimental pressures in the cold flow model. The dashed lines represent a deviation of ±25%. (b) comparison of experimental and numerical pressure profiles across the height of the reactor riser (P1a-P1g of Fig. 1a).

Conclusions

Segregated full-loop simulations of the cold gas-solid flow in a pilot-scale dual fluidized bed system have been conducted using the Eulerian-Lagrangian MP-PIC formulation implemented in Barracuda VR ®. Acceptable agreement with deviations below ±25% is found when comparing experimental and numerical pressures throughout the system, demonstrating the ability of the presented model to capture behavioral trends at varying operating conditions.

Prior to extending the simulation to include transfer lines and pinch valves, additional work is required to improve the model accuracy by including submodels for collisional transfer of momentum and by comparing numerical predictions with measurements of solids holdup and velocity for further validation and identification of inconsistencies with numerical predictions.

Acknowledgement

The project is funded by the Innovation Fund Denmark (Project 7045-00009A) and carried out in collaboration between Haldor Topsøe A/S and the Technical University of Denmark, Department of Chemical and Biochemical Engineering.

Notation

d_{32}	Sauter mean diameter, m	U_g	superficial gas speed, m/s
$\mathbf{F}$	rate of momentum exchange, kg/m^2-s^2	$\mathbf{u}_g$	gas velocity, m/s
$\mathbf{g}$	gravitational acceleration, m/s^2	$\mathbf{u}_s$	solids velocity, m/s
G_s	solids mass flux, kg/m^2-s	α	constant in (2), -
$\dot{m}_g$	solids mass flow rate, kg/s	β	exponent in (2), -
$\dot{m}_s$	solids mass flow rate, kg/s	ε_{cp}	close-pack volume fraction, -
n_p	physical particles per parcel, -	ε_g	gas phase volume fraction, -
N_p	parcel count, -	ε_s	solids phase volume fraction, -
p	pressure, Pa or mbar	ρ_s	solids density, kg/m^3
P_s	pressure constant in (2), Pa	τ_s	interparticle stress, Pa
t	time, s		

References

Andrews, MJ and PJ O'Rourke. The multiphase particle-in-cell (MP-PIC) method for dense particulate flows. International Journal of Multiphase flow. 1996. 22(2), 379-402.

Beetstra, R, MA van der Hoef, JAM Kuipers. Drag force of intermediate Reynolds number flow past mono- and bidisperse arrays of spheres. American Institute of Chemical Engineers. 2007. 53(2), 489-501.

Jiradilok, V, D Gidaspow, S Damronglerd, WJ Koves, R Mosto. Kinetic theory based CFD simulation of turbulent fluidization of FCC in a riser. Chemical Engineering Science. 2006. 61(17), 5544-5559.

Kraft, S, F Kirnbauer, H Hofbauer. Influence of drag laws on pressure and bed material recirculation rate in a cold flow model of an 8 MW dual fluidized bed system by means of CPFD. Particuology. 2018. 36, 70-81.

Li, T, JF Dietiker, L Shadle. Comparison of full-loop and riser-only simulations for a pilot-scale circulating fluidized bed riser. Chemical Engineering Science. 2014. 120, 10-21.

Lu, B, W Wang, J Li. Eulerian simulation of gas-solid flows with particles of Geldart groups A, B and D using EMMS-based meso-scale model. Chemical Engineering Science. 2011. 66(20), 4624-4635.

Pannala, S, M Syamlal, TJ O'Brien. Computational gas-solids flows and reacting systems: theory, methods and practice. IGI Global. 2011.

Rodrigues, SS, A Forret, F Montjovet, M Lance, T Gauthier. CFD modeling of riser with Group B particles. Powder Technology. 2015. 283,519-529.

Shah, MT, RP Utikar, VK Pareek, Evans, GM, JB Joshi. Computational fluid dynamic modeling of FCC riser: a review. Chemical Engineering Research and Design. 2016. 111, 403-448.

Snider DM. An incompressible three-dimensional multiphase particle-in-cell model for dense particle flows. Journal of Computational Physics. 2001. 170(2), 523-549

Thapa RK, A Frohner, G Tondl, C Pfeifer, BM Halvorsen. Circulating fluidized bed combustion reactor: computational particle fluid dynamics model validation and gas feed position optimization. Computers and Chemical Engineering. 2016. 92, 180-188.

Tu, Q and H Wang. CPFD study of a full-loop three-dimensional pilot-scale circulating fluidized bed based on EMMS drag model. Powder Technology. 2018. 323, 534-547.

Wang, W, J Li. Simulation of gas-solid two-phase flow by a multi-scale CFD approach of the EMMS model to the sub-grid level. Chemical Engineering Science. 2007. 62, 208-231.

Wang, Q, H Yang, P Wang, J Lu, Q Liu, H Zhang, L Wei, M Zhang. Application of CPFD method in the simulation of a circulating fluidized bed with a loop seal, part I – determination of modeling parameters. Powder Technology. 2014. 253, 814-821.

Wang, M, Y Wu, X Shi, X Lan, C Wang, J Gao. Comparison of riser-simplified, riser-only, and full-loop simulations for a circulating fluidized bed. Processes. 2019. 7(5), 306.

Xie, J, W Zhong, A Yu. MP-PIC modeling of CFB risers with homogeneous and heterogeneous drag models. Advanced Powder Technology. 2018. 29(11), 2859-2871.

Zhang, N, B Lu, W Wang, J Li. Virtual experimentation through 3D full-loop simulation of a circulating fluidized bed. Particuology. 2008. 6(6), 529-539.

THE FILTERED APPROACH FOR NUMERICAL PREDICTION OF AN INDUSTRIAL-SCALE FCC REGENERATOR

Wenchao Yu[1], Pascal Fede[1*], Mahdi Yazdanpanah[2], Benjamin Amblard[3], Florian Euzenat[2] and Olivier Simonin[1]

[1] *Institut de Mécanique des Fluides de Toulouse (IMFT), Université de Toulouse, CNRS, Toulouse, 31400, France*
[2] *Total Research & Technology Gonfreville (TRTG), Harfleur, 76700, France*
[3] *IFP Energies nouvelles, BP3, Solaize, 69360, France*
*Email: *pascal.fede@imft.fr*

Abstract

In the present work, a CFD study of an industrial-scale FCC regenerator is investigated by means of numerical simulations based on an Eulerian n-fluid modelling approach. Due to the limitation on the computational resources, it is unaffordable to use a sufficiently fine grid for predicting the very small solid structures presented in the fluidized bed which are crucial for the hydrodynamics prediction. Hence, a SubGrid Scale (SGS) drag model based on the filtered approach is used here to take into account the effect of unresolved structures on the resolved flow. The numerical results obtained by using the SGS drag model are in good agreement with the experimental data carried out in a pilot-scale cold-flow fluidized bed unit (Yu et al., 2020). After the validation of the SGS drag model on the pilot-scale case, the simulations are now performed on an industrial-scale FCC regenerator in the presence of the coke combustion reactions.

Introduction

Fluid Catalytic Cracking (FCC) is one of the most important conversion processes used in refineries all over the world. The regeneration of spent catalyst deactivated by coke deposition is a key performance factor to the FCC process for both economic and environmental needs (Amblard et al., 2016). CFD simulations can be used as an useful tool for investigation and optimization of FCC regenerators to improve process performance. However, large scale simulation has some specific challenges mainly related to the computation limitation and validation of results. Even with HPC performances (Neau et al., 2013), the computational resources are limited leading to perform these kinds of simulations with grid insufficiently fine for predicting the very small solid structures present in a FCC regenerator. It has been shown (Igci and Sundaresan, 2011) that this would lead to a major overestimation of bed expansion and of entrainment flux related to the effect of unresolved structures on the resolved flow.

Several detailed reviews have been dedicated to the coarse-grid simulation of gas-solid flows in fluidized bed (van der Hoef et al., 2008; Wang et al., 2009; Schneiderbauer et al., 2013; Fullmer et al., 2017; Sundaresan et al., 2018). Various methods have been well summarized. The SubGrid Scale (SGS) drag models proposed by Parmentier et al., 2012 and Ozel et al., 2013 are ones of them which are based on the filtering of well-resolved Euler-Euler simulations. Especially, the SGS drag model of Ozel et al. (2013) which takes into account the local flow properties has been proven effective by validating our numerical simulations (Yu et al., 2020) with very detailed experimental results provided by Particulate Solid Research Inc (PSRI). Based on these validations, the simulations in the actual study are performed on an industrial-scale FCC regenerator. Results about the hydrodynamics are discussed here.

Numerical simulation

The unsteady three dimensional numerical simulations of the fluidized-bed reactor were performed using the Eulerian n-fluid modeling approach for poly-dispersed fluid-particle turbulent reactive flows implemented in NEPTUNE_CFD V4.0.1@Tlse version by IMFT (Institut de Mécanique des Fluides de Toulouse). NEPTUNE_CFD is a computational multiphase flow software developed in the framework of the NEPTUNE project, financially supported by CEA (Commissariat à l'Energie Atomique), EDF (Electricité de France), IRSN (Institut de Radioprotection et de Sûreté Nucléaire) and AREVA-NP. The approach is derived from a joint fluid-particle Probability Density Function equation allowing to derive transport equations for the mass, momentum and agitation of particle phases. In the proposed modeling approach, transport equations (mass, momentum and fluctuating kinetic energy) are solved for each phase and coupled together through interphase transfer terms. For more details about the modeling approach and NEPTUNE CFD, readers are invited to see reference papers (Simonin, 2000; Gobin et al., 2003; Neau et al., 2013; Fede et al., 2016; Hamidouche et al., 2018).

The SGS drag models developed by Parmentier et al., 2012 and Ozel et al., 2013 are used to take into account the effect of the unresolved solid structures that cannot be solved on a coarse grid. The idea is similar to the filter approach using in the Large Scale Simulation (LES) in single-phase turbulent flow. A filter is applied to the transport equations. We assume that the filtered drag term can be split into a resolved part and an unresolved part. The unresolved part needs to be modeled using the resolved particle relaxation time and resolved particle and gas velocities. More details can be found in Parmentier et al. (2012) and Ozel et al. (2013). The model of Ozel et al. (2013) is used in the actual study.

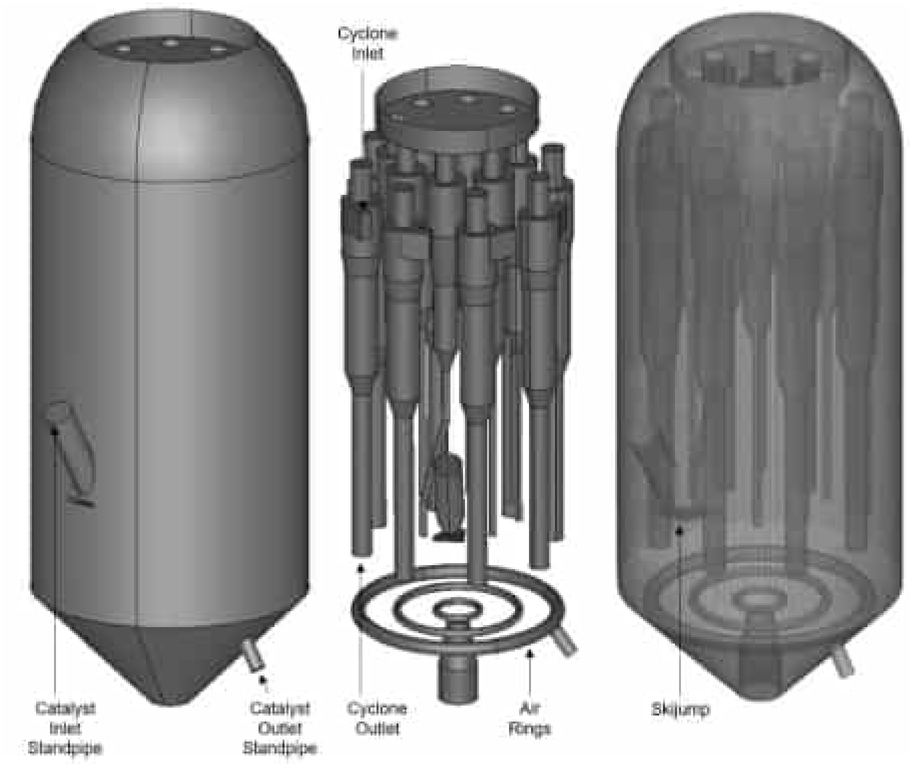

Fig. 1. Geometry and mesh

Fig. 1 shows the geometry and the mesh of the FCC regenerator. The main body of the regenerator has a height of $24\,m$ and a diameter of $9.15\,m$. The catalyst with the fresh deposition of the coke is fed into the regenerator through the large standpipe. After the combustion process, the regenerated catalyst falls from the small standpipe. Inside the regenerator, it contains several internal structures, the air distributor at the bed bottom consisted of three rings of different diameters, eight cyclone groups with each of them a main cyclone close to the wall and a secondary cyclone close to the bed center. We assume that the internal recirculation of particles can only pass through the main cyclones. The secondary cyclones would only be treated as an internal wall body. A slightly inclined slab (also called as "Skijump") is located just below the catalyst inlet standpipe to avoid the direct impact of the catalyst on the air rings. In order to respect the whole geometry and the complex internal structures, the mesh was generated by using the unstructured tetrahedral type cells. There are 1,963,565 cells with a typical length of the cell $0.15\,m$ for the mesh demonstrated here.

According to the operating condition, the fluidization velocity is set to 1 m/s based on the main body section, which corresponds to a gas mass flow rate $60.2\,kg/s$. The density and viscosity of air are $0.74\,kg/m^3$ and $4.2 \times 10^{-5}\,kg/m/s$, respectively. The particle diameter is $82.3\,\mu m$ with a density $1361\,kg/m^3$. The total mass of the catalyst inside the regenerator is around $310\,ton$. The catalyst is fed into the regenerator with a fixed mass flow rate $538.6\,kg/s$, a dynamically adjusted pressure gradient is set at the catalyst outlet standpipe to maintain the outflow fluctuated around this value. A free pressure condition is used at the cyclone outlet. A friction wall boundary condition is used for gas phase and a no-slip wall boundary condition is used for solid phase.

Due to the large solid to gas density ratio, the drag force is dominant for mean gas-particle interphase momentum transfer. To take into account the effect of large solid volume fraction, the drag law of Gobin et al. (2003) is selected here. For the gas phase we use $k-\epsilon$ model with additional terms that take into account the effect of particles on gas turbulence, and the turbulence viscosity is also modified by the presence of solid phase. Particle agitation is modeled by the approach of two transport equation $q_p^2 - q_{fp}$, one for particle agitation and another for gas-particle covariance. Collisions between particles are also taken into account and assumed uncorrelated and inelastic (particle-particle normal restitution coefficient is set to 0.9). The numerical simulations are performed during 70 seconds of physical time. Flow inside the regenerator is established around at $30\,s$. Then, the time-averaged statistics are computed from $30\,s$ to the end of simulations.

Results

The results of the simulations are presented here.

Fig. 2 shows the instantaneous solid volume fraction on a vertical plane cut through the catalyst inlet standpipe at 40 seconds with or without the presence of the SGS drag model. In Fig. 2 (center), in the absence of the SGS drag model, particles flew up to the top of the cyclone, an homogeneous particle distribution can be observed from the air distributor to the top of the cyclone, which is not credible with the actual operating condition. This result is due to the overestimation of drag force related to the coarse mesh we used here. It should be noted here, even a finer mesh (up to 16,811,882 cells) could not improve the result, which may suggest that we need to refine the mesh again till a mesh-independent result obtained, then the computational cost becomes unaffordable in that case. In order to avoid this situation, the SGS drag model of Ozel et al. (2013) is used here to represent the effect of the unresolved solid structures that cannot be solved on the coarse grid. In Fig. 2 (right), the effect of the SGS drag model is evident. A dense region is formed between the air distributor and catalyst inlet standpipe, less particles can fly to the top of the regenerator.

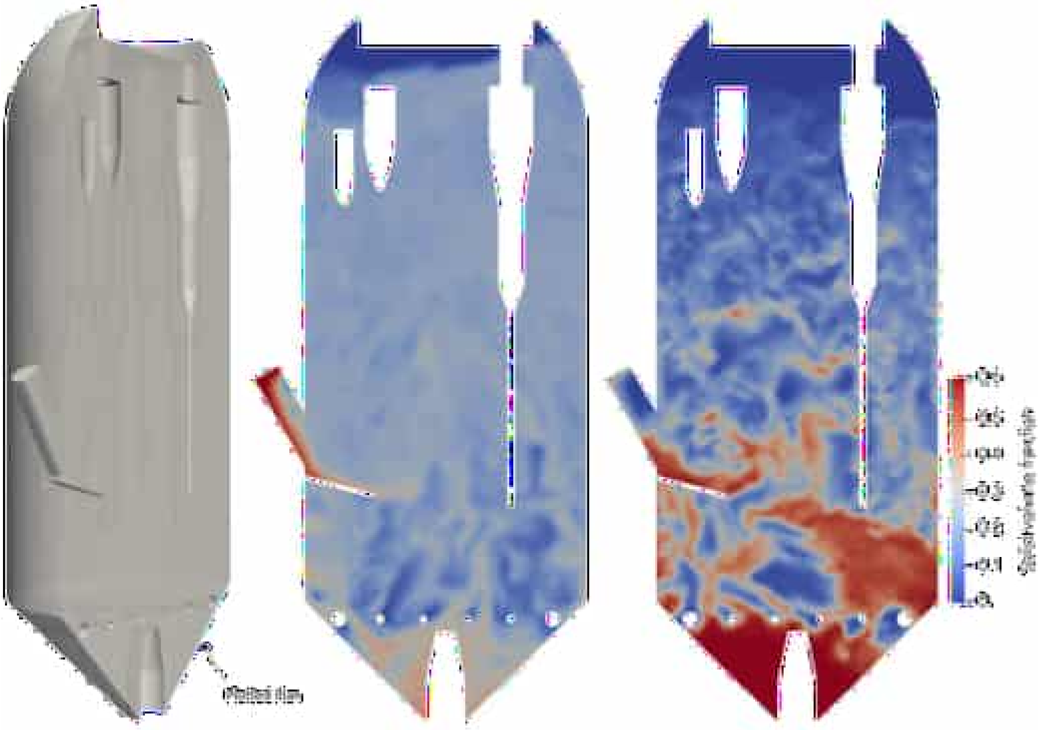

Fig. 2. Left: the plotted plan cut through the catalyst inlet standpipe. Solid volume fraction at 30 seconds, center: without the SGS drag model; right: with the SGS drag model.

A huge difference is observed in Fig. 3 for the recirculation through the cyclone between the cases with and without the SGS drag model. The time-averaged solid mass flow rate decreases from 4089 to 667.3 kg/s when the SGS drag model is activated. This confirms the previous observation in Fig. 2, less particles would fly to the top of the cyclone.

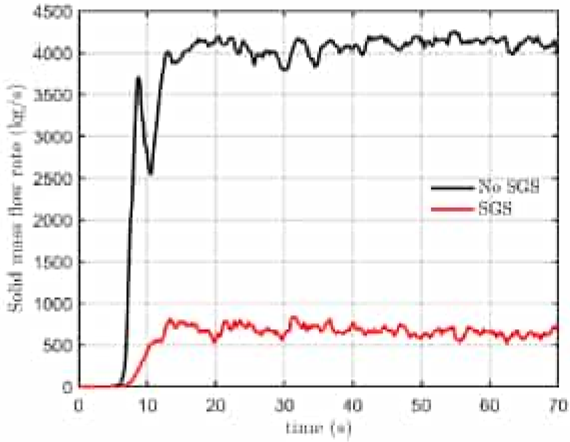

Fig. 3. Solid mass flow rate through one of the main cyclones.

The mean vertical bed density profiles are shown in Fig. 4 where the bed density is calculated based on the mean pressure drop (DP) over a distance (L) and divided by the gravity (g). The zero point of the height in this figure corresponds to the top of the air distributor. For the case without the SGS drag model, the bed density is basically unchanged along the regenerator height, as already observed qualitatively in Fig. 2 (center). When the SGS drag model is applied, a dense region is formed at the lower part of the regenerator and its bed density is well predicted compared to the experimental measurement.

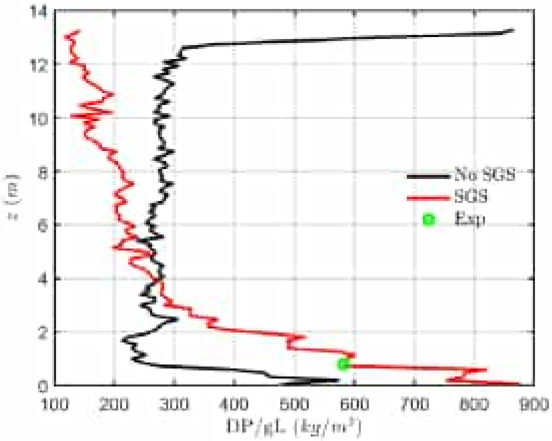

Fig. 4. Mean vertical bed density profile along the regenerator height.

Conclusion

A CFD study of an industrial-scale FCC regenerator is investigated by NEPTUNE_CFD which is based on an Eulerian n-fluid modeling approach. With the help of the SGS drag model, the hydrodynamics of gas-solid flows can be predicted in the realistic industrial configurations using a relative coarse grid, which provides the possibilities for the further studies about the mass and heat transfer problems during the coke combustion, with an affordable computational cost. Once all these mechanisms are taken into account and validated with the bed density and the catalyst recirculation rate measured in this configuration, the whole tool can be used to provide more information to control and to optimize the existing units, or to design the future units.

Acknowledgement

This work was performed using HPC resources from CALMIP (Grant 2019 – p0111) and from CINES Occigen under the allocation n°A0022B06012 and n°A0042B06012.

References

Amblard, B., Singh, R., Gbordzoe, E., Raynal, L. CFD modeling of the coke combustion in an industrial FCC regenerator. Chem. Eng. Sci. 2017. 170, 731-742

Fede, P., Simonin, O., Ingram, A. 3D numerical simulation of a lab-scale pressurized dense fluidized bed focussing on the effect of the particle-particle restitution coefficient and particle-wall boundary conditions. Chem. Eng. Sci. 2016. 142, 215-235

Fullmer, W.D., Hrenya, C.M. The clustering instability in rapid granular and gas-solid flows. Annual Review of Fluid Mechanics. 2017. 49(1), 485-510.

Gobin, A., Neau, H., Simonin, O., Llinas, J.R., Reiling, V., Sélo, J.L. Fluid dynamic numerical simulation of a gas phase polymerization reactor. International Journal for Numerical Methods in Fluids. 2003. 43, 1199-1220

Hamidouche, Z., Masi, E., Fede, P., Ansart, R., Neau, H., Hemati, M., Simonin, O. Numerical simulation of multiphase reactive flows. In Bridging scales in modelling and simulation of non-reacting and reacting flows. Alessandro Parente and Juray De Wilde, Academic Press, 1st edition. 2018. 52, Part I, pp 55-121.

Igci, Y., Sundaresan, S. Verification of filtered two-fluid models for gas-particle flows in risers. AIChE Journal. 2011. 57, 2691-2707

Neau, H., Fede, P., Laviéville, J., Simonin, O. High performance computing (HPC) for the fluidization of particle-laden reactive flows. 14th International Conference on Fluidization, Noordwijkerhout, The Netherlands. 2013. pp. 589-596

Ozel, A., Fede, P., Simonin, O. Development of filtered Euler-Euler two-phase model for circulating fluidised bed: High resolution simulation, formulation and a priori analyses. International Journal of Multiphase Flow. 2013. 55, 43-63

Parmentier, J.F., Simonin, O., Delsart, O. A functional subgrid drift velocity model for filtered drag prediction in dense fluidized bed. AIChE Journal. 2012. 58, 1084-1098

Schneiderbauer, S., Puttinger, S., Pirker, S. Comparative analysis of subgrid drag modifications for dense gas-particle flows in bubbling fluidized beds. AIChE Journal. 2013. 59, 4077-4099

Simonin, O. Statistical and continuum modelling of turbulent reactive particulate flows. Lecture Series 2000-06, von Karman Institute for Fluid Dynamics, Rhode Saint Genèse (Belgium).

Sundaresan, S., Ozel, A., Kolehmainen, J. Toward constitutive models for momentum, species, and energy transport in gas-particle flows. Annual Review of Chemical and Biomolecular Engineering. 2018. 9(1), 61-81.

van der Hoef, M.A., van Sint Annaland, M., Deen, N.G., Kuipers, J.A.M. Numerical simulation of dense gas-solid fluidized beds: a multiscale modeling strategy. Annual Review of Fluid Mech. 2008. 40, 47-70

Wang, J., van der Hoef, M. A., Kuipers, J. A. M. Why the two-fluid model fails to predict the bed expansion characteristics of Geldart A particles in gas-fluidized beds: A tentative answer. Chem. Eng. Sci. 2009. 64, 622-625

Yu, W., Fede, P., Yazdanpanah, M., Amblard, B., Euzenat, F., Simonin, O. Gas-solid fluidized bed simulations using the filtered approach: Validation against pilot-scale experiments. Chem. Eng. Sci. 2020. DOI: https://doi.org/10.1016/j.ces.2020.115472.

THE MP-PIC METHOD FOR CFD-SIMULATION OF BIOMASS GASIFICATION IN A LAB-SCALE FLUIDIZED BED

Timo Dymala[1*], Ernst-Ulrich Hartge[1], Tao Song[2], Laihong Shen[3], Stefan Heinrich[1]

[1]Hamburg University of Technology, Institute of Solids Process Engineering and Particle Technology, Denickestrasse 15, 21073 Hamburg, Germany
[2]School of Energy and Mechanical Engineering,
Nanjing Normal University, Nanjing 210023, China
[3]Key Laboratory of Energy Thermal Conversion and Control of Ministry of Education,
Southeast University, Nanjing 210096, China

**Email: timo.dymala@tuhh.de*

Abstract

Aim of the project “Multi-scale analysis and optimization of chemical looping gasification of biomass” of the Hamburg University of Technology (TUHH) with the Southeast University (SEU) is the detailed modeling and subsequent optimization of a Chemical Looping Gasification (CLG) process. For this purpose, the process is simulated using the multiphase particle-in-cell (MP-PIC) method, which allows a detailed simulation of even large-scale units with affordable computational efforts. This paper deals with the implementation and validation of the reaction model for the gasification reactions.

Introduction

Biomass as renewable energy source is gaining an increased interest as CO_2-neutral alternative compared to fossil fuels (Yu et al. 2011). A promising technology for the conversation of biomass is the fluidized bed gasification. The produced syngas may be utilized to generate heat and electricity or synthetic fuels (Kraft et al. 2017). A detailed description of the CLG principle is given in the work of Ge et al. (2016). The MP-PIC method in combination with a reduced reaction network will be used as approach for the model.

As a first step, the applicability of the MP-PIC method for the simulation of the fluid mechanics was investigated. The MP-PIC method results from a modification of the Euler-Lagrange approach, where the fluid is described by the Navier-Stokes equations on a Eulerian grid in combination with Lagrangian particles. To reduce the computational costs a defined number of particles with the same properties is represented by so-called parcels and the influence of collisions is modelled by a particle stress model. This facilitates the consideration of particle size distribution and shrinkage without the increase of computational requirements and increases the computational speed compared to the discrete particle model (DPM) (Loha et al. 2014).

As the next step, the gasification kinetics of biomass are modeled. Due to the large number of chemicals reactions in a gasification process the reaction network has to be simplified in order to reduce computational requirements. For the validation of this approach the work of Song et al. (2012) will be used.

The proprietary software Barracuda VR 17.3 by CPFD Software, LLC is used as implementation for the MP-PIC method.

Governing Equations

MP-PIC method

A detailed documentation of the MP-PIC method is presented in the work of Andrews and O'Rourke (1996) and Snider (2001). Further information regarding the implementation of the

MP-PIC method in the Barracuda framework is given in the user manual of Barracuda VR (CPFD Software, LLC 2018).

Reaction kinetics

The gasification of biomass in a fluidized bed can be subdivided in three main steps: The drying and pyrolysis of biomass, and the gasification of char. The drying of biomass occurs at relatively low temperatures which leads to the evaporation of the moisture content. During the pyrolysis the volatile matter of biomass is released and char is produced. The produced gas consists mainly of CO, CO_2, CH_4 and H_2. In addition to CH_4 further lower hydrocarbons as well as higher hydrocarbons (tar) are formed. Afterwards the char and tar react with steam which leads to a partly conversion of the char and decomposition of the tar into gaseous species (Song et al. 2012).

The drying and pyrolysis of biomass is modeled using Eq. (R1) with $\sum \nu_i = 1$. At this point it has to be noted that the formation of tar is neglected and CH_4 is the only hydrocarbon species considered in this work. All other lower hydrocarbons are subsumed as CH_4. This approach is used in literature and it is assumed that tar is completely converted to the non-condensable gas species CO, CO_2, CH_4 and H_2 (Gerber et al. 2010; Ku et al. 2015).

$$Biomass \rightarrow \nu_1 CO + \nu_2 H_2O + \nu_3 CO_2 + \nu_4 H_2 + \nu_5 CH_4 + \nu_6 char + \nu_7 ash \qquad \text{(R1)}$$

The volatile release and the drying of biomass are modeled using a single step first-order Arrhenius reaction (Chan et al. 1985; Bonnefoy et al. 1993). The equation for the release of moisture and volatiles is given in Eq. (1) with m_i as the mass of volatiles or moisture respectively.

$$\frac{dm_i}{dt} = -A_i \cdot exp\left(-\frac{E_i}{T}\right) \cdot m_i \qquad (1)$$

The drying kinetics for biomass were taken from Chan et al. (1985) with A_{moist} = $5.12 \cdot 10^6$ s^{-1} and E_{moist} = 10585 K, while the volatile release kinetics were taken from Bonnefoy et al. (1993) with A_{vol} = $5.0 \cdot 10^6$ s^{-1} and E_{vol} = 14433 K. According to Abani and Ghoniem (2013) the heat of devolatilization is negligible compared to the heat of reactions. Therefore, the heat of devolatilization is not considered in this work.

It has to be noted that in Barracuda VR the drying, volatile release and chemical reactions only affect the density of the particles but not the size, i.e. particle shrinkage is not yet considered in this work.

The composition of the released volatiles can be predicted using different models or calculated using experimental data. Since the prediction of the volatile composition is not accurate (Kraft et al. 2017) and experimental data for wood biomass is available, the volatile composition used in this work is based on pyrolysis experiments performed at the Southeast University, Nanjing.

Due to the complexity of the chemical reactions in a gasification process the reaction network is simplified. This approach is widely used by other researchers to ensure a feasible computational speed while maintaining reasonable accuracy. In this work the reaction network is described by a reduced set of equations proposed by Song et al. (2012). The heterogeneous reactions including the reaction rate constants are given in Eqs. (R2) and (R3), while the homogeneous gas phase reactions are given in Eqs. (R4) and (R5).

(R2)	Steam gasification	Syamlal and Bissett (1992)	Reaction rate in [mol m^{-3} s^{-1}]
	$C + H_2O \rightleftharpoons CO + H_2$ $r_{2f} = 1.272 \cdot m_C \cdot T \cdot exp\left(-\frac{22645K}{T}\right) \cdot [H_2O]$ $r_{2b} = 1.044 \cdot 10^{-4} \cdot m_C \cdot T^2 \cdot exp\left(-\frac{6319K}{T} - 17.29\right) \cdot [H_2] \cdot [CO]$		
(R3)	CO_2 gasification	Syamlal and Bissett (1992)	Reaction rate in [mol m^{-3} s^{-1}]
	$C + CO_2 \rightleftharpoons 2CO$ $r_{3f} = 1.272 \cdot m_C \cdot T \cdot exp\left(-\frac{22645K}{T}\right) \cdot [CO_2]$ $r_{3b} = 1.044 \cdot 10^{-4} \cdot m_C \cdot T^2 \cdot exp\left(-\frac{2363K}{T} - 20.92\right) \cdot [CO]^2$		
(R4)	Water-gas-shift	Gómez-Barea and Leckner (2010)	Reaction rate in [kmol m^{-3} s^{-1}]
	$CO + H_2O \rightleftharpoons CO_2 + H_2$ $r_{4f} = 2.78 \cdot 10^3 \cdot exp\left(-\frac{1515.5K}{T}\right) \cdot [CO] \cdot [H_2O]$ $r_{4b} = 9.59 \cdot 10^4 \cdot exp\left(-\frac{5606K}{T}\right) \cdot [H_2] \cdot [CO_2]$		
(R5)	Methane reforming	Jones and Lindstedt (1988)	Reaction rate in [kmol m^{-3} s^{-1}]
	$CH_4 + H_2O \rightarrow CO + 3H_2$ $r_5 = 3.0 \cdot 10^8 \cdot exp\left(-\frac{15155K}{T}\right) \cdot [H_2O] \cdot [CH_4]$		

Experimental setup and model settings

For the validation of the model the experimentally investigated spouted bed by Song et al. (2012) was simulated. For the implementation of the reaction kinetics no fitting of the literature data has been performed. The process parameters for the two simulated cases are given in Table 1. The operating temperature of the gasifier was varied, while the steam-to-biomass ratio (S/B-ratio) was kept constant at S/B = 1.2.

Table 1: Process parameters for the simulation.

Case	**S/B-ratio** [-]	**Steam flow rate** [kg h^{-1}]	**Biomass feed rate** [kg h^{-1}]	**Temperature** [°C]
A	1.2	3.6	3.0	820
B	1.2	3.6	3.0	920

Materials

Quartz sand with a sauter mean diameter of 350 µm and density of 2600 kg m^{-3} was used as bed material for heat and mass transfer. The total weight of the sand particles is 11 kg. Pine wood from the Jiangsu Province (China) was used for the experiments with a sauter mean diameter of 1.5 mm and density of 470 kg m^{-3} (Song et al. 2012). The proximate and ultimate analysis of the biomass are given by Song et al. (2012).

The volatile composition for the wood biomass was calculated based on pyrolysis experiments performed at 900 °C at Southeast University, Nanjing. The produced gas is composed of 57.76 wt.% CO, 24.06 wt.% CO_2, 16.25 wt.% CH_4 and 1.93 wt.% H_2.

Geometry and mesh

The spouted bed presented by Song et al. (2012) consists of a 40 x 230 x 1500 mm^3 rectangular bed and a 60° conical distributor at the bottom. In the experimental setup presented by Song et al. (2012) the conical distributor is connected to a tube with an inner diameter of 20 mm, while an orifice of equal area with a width of 7.85 mm was used for the simulated domain.

A grid of 57288 cells was chosen for an accurate representation of the gasifier. Typical dimensions for the mostly hexahedral cells are approximately 6 x 6 x 6 mm^3. The experimental set-up and the mesh of the simulated gasifier are shown in Fig. 1.

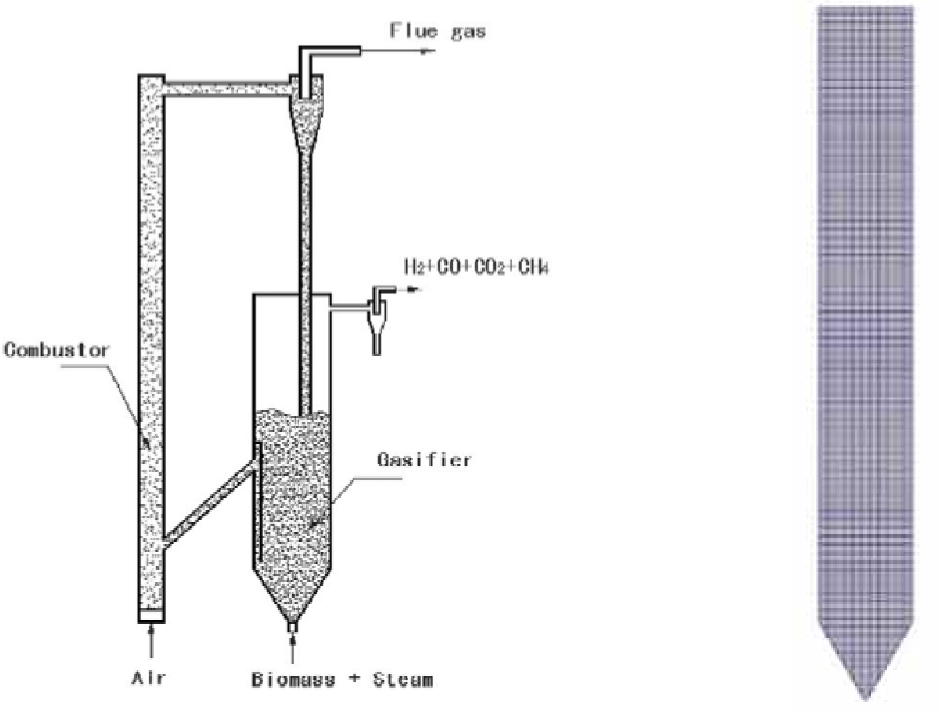

(a) (b)

Fig. 1: (a) Sketch of the experimental lab-scale plant (Song et al. 2012) (b) mesh of the simulated gasifier.

Steam and biomass are introduced at the bottom of the domain with the respective mass flows given in Table 1. The inlet temperature of the steam flow is equivalent to the operating temperature, while the initial temperature of the biomass particles is 300 K. The initial temperature of the sand particles and a constant temperature for the walls are set to the operating temperature, while the pressure at the reactor outlet is set to atmospheric pressure.

For the investigation of the gas production the simulation was performed for 40 seconds (real-time) while taking the last 20 seconds for the averaging. The simulation took 44 computational hours on a workstation with an Intel Core i7-7700K and a GeForce GTX 1070 graphics card.

Results

In Fig. 2 the concentrations of the product species at the reactor outlet of case A are plotted over the simulation time of 40 s. The S/B-ratio was set to 1.2 and the reactor temperature to 820 °C. After a short start-up time of around 5 s quasi-stationary conditions are observed.

For the validation of the model the comparison of the normalized averaged syngas species is shown in Fig. 3. The results are based on dry gas for comparison with experimental data presented by Song et al. (2012).

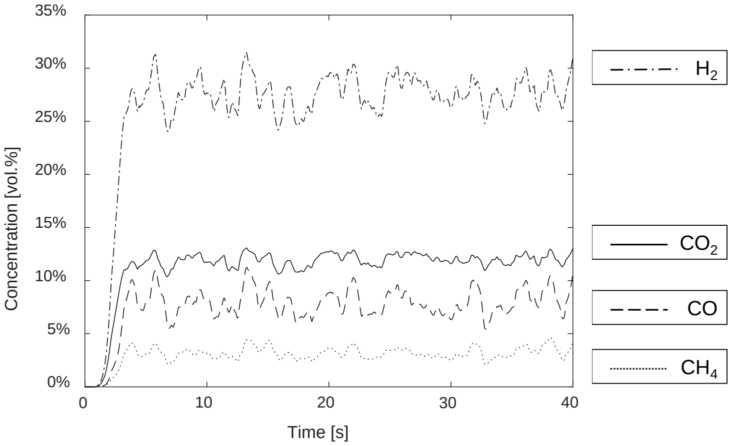

Fig. 2: Concentrations of the product gas species at the outlet of the reactor at T=820 °C with S/B=1.2.

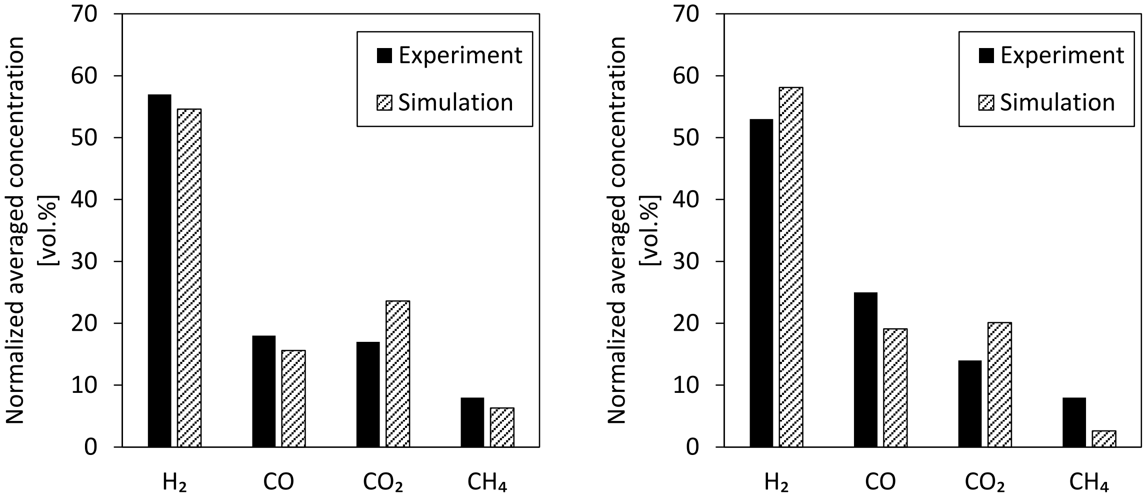

(a) Case A: S/B=1.2, T=820 °C

(b) Case B: S/B=1.2, T=920 °C

Fig. 3: Comparison of the normalized averaged syngas species between experimental data presented by Song et al. (2012) and simulation results.

For case A, the results show a good agreement especially for H_2, CO and CH_4. Only the concentration of CO_2 is overestimated while all other concentrations are slightly underestimated in the simulation.

With increasing temperature, the CO concentration increases, while the CO_2 concentration decreases. This behavior is also captured by the simulations. Contrary to the experiments the H_2 concentration increases with increasing temperature in the simulations and the decrease of the CH_4 concentration is overestimated. This is probably due to the methane reforming reaction (R5).

Deviations between experiment and simulation cannot be eliminated, considering the fact that the reaction network is reduced, the devolatilization is simplified and the formation of tar is neglected. Nevertheless, the simulation shows sufficient accuracy while being computationally affordable.

Conclusion and outlook

The simulations show satisfying results. Errors are probably due to the neglection of tar formation. Therefore, the formation and decomposition of tar will be considered in future work by the implementation of primary and secondary pyrolysis. Furthermore, the particle shrinkage shall be considered.

As the next step, the validated model will be used for the simulation of a CLG system to study the influence of various operation parameters like particle size, density and devolatilization behavior on the plant operation.

Notation

ν_i	Stoichiometric coefficient, -	t	Time, s
T	Temperature, K	m	Mass of the volatiles, kg
r	Reaction rate, *	E	Activation energy, K
A	Pre-exponential factor, s^{-1}		

*: differs

References

Abani, N.; Ghoniem, A. F. (2013): Large eddy simulations of coal gasification in an entrained flow gasifier. In *Fuel* 104, pp. 664–680.

Andrews, M. J.; O'Rourke, P. J. (1996): The multiphase particle-in-cell (MP-PIC) method for dense particulate flows. In *International Journal of Multiphase Flow* 22 (2), pp. 379–402.

Bonnefoy, F.; Gilot, P.; Prado, G. (1993): A three-dimensional model for the determination of kinetic data from the pyrolysis of beech wood. In *Journal of Analytical and Applied Pyrolysis* 25, pp. 387–394.

Chan, W.-C. R.; Kelbon, M.; Krieger, B. B. (1985): Modelling and experimental verification of physical and chemical processes during pyrolysis of a large biomass particle. In *Fuel* 64 (11), pp. 1505–1513.

CPFD Software, LLC (2018): Barracuda Virtual Reactor User Manual. Release 17.3.0.

Ge, H.; Guo, W.; Shen, L.; Song, T.; Xiao, J. (2016): Biomass gasification using chemical looping in a 25 kW th reactor with natural hematite as oxygen carrier. In *Chemical Engineering Journal* 286, pp. 174–183.

Gerber, S.; Behrendt, F.; Oevermann, M. (2010): An Eulerian modeling approach of wood gasification in a bubbling fluidized bed reactor using char as bed material. In *Fuel* 89 (10), pp. 2903–2917.

Gómez-Barea, A.; Leckner, B. (2010): Modeling of biomass gasification in fluidized bed. In *Progress in Energy and Combustion Science* 36 (4), pp. 444–509.

Jones, W. P.; Lindstedt, R. P. (1988): Global reaction schemes for hydrocarbon combustion. In *Combustion and Flame* 73 (3), pp. 233–249.

Kraft, S.; Kirnbauer, F.; Hofbauer, H. (2017): CPFD simulations of an industrial-sized dual fluidized bed steam gasification system of biomass with 8 MW fuel input. In *Applied Energy* 190, pp. 408–420.

Ku, X.; Li, T.; Løvås, T. (2015): CFD–DEM simulation of biomass gasification with steam in a fluidized bed reactor. In *Chemical Engineering Science* 122, pp. 270–283.

Loha, C.; Gu, S.; Wilde, J. de; Mahanta, P.; Chatterjee, P. K. (2014): Advances in mathematical modeling of fluidized bed gasification. In *Renewable and Sustainable Energy Reviews* 40, pp. 688–715.

Snider, D. M. (2001): An Incompressible Three-Dimensional Multiphase Particle-in-Cell Model for Dense Particle Flows. In *Journal of Computational Physics* 170 (2), pp. 523–549.

Song, T.; Wu, J.; Shen, L.; Xiao, J. (2012): Experimental investigation on hydrogen production from biomass gasification in interconnected fluidized beds. In *Biomass and Bioenergy* 36, pp. 258–267.

Syamlal, M.; Bissett, L. A. (1992): METC Gasifier Advanced Simulation (MGAS) Model. DOE/METC-92/4108. DE92 001111.

Yu, J.; Yao, C.; Zeng, X.; Geng, S.; Dong, L.; Wang, Y. et al. (2011): Biomass pyrolysis in a micro-fluidized bed reactor: Characterization and kinetics. In *Chemical Engineering Journal* 168 (2), pp. 839–847.

NUMERICAL INVESTIGATION OF FLOW AND REACTION PROCESSES IN A DUAL-CFB COAL GASIFIER USING THE QC-EMMS DRAG MODEL

Yang Liu[1], Pengju Huo[2], Xiaohong Li[2], Haiying Qi[1*]

[1]*Key Laboratory for Thermal Science & Power Engineering of Ministry of Education,*
Tsinghua University, Beijing, 100084, P.R. China
[2]*Hydrocarbon High-efficiency Utilization Technology Research Center, Shaanxi*
Yanchang Petroleum Co. Ltd, Xi'an, 710075, P.R. China

*Email: *hyqi@mail.tsinghua.edu.cn*

Abstract

The characteristics of gas-solid flow and reactions in an industrial dual circulating fluidized bed (CFB) coal gasifier were investigated by numerical simulation. The Eulerian-Eulerian approach with the heterogeneous drag model QC-EMMS was used to model the fluidization and gasification processes. The simulated pressure drops and volume-averaged temperatures agree with the experimental data well. The gas-solid flow patterns and the temperature distribution in the gasifier was revealed. The influences of loose gas flow rate on gasification performance were analyzed based on the simulation results. The above studies verified the capability of the QC-EMMS model to accurately describe the drag during complex reactive fluidization processes and also enrich the knowledge on flow and reaction mechanism in the large-scale CFB coal gasification process.

1 Introduction

To increase the coal capacity and syngas yield in the coal gasification process, a dual-CFB coal gasification technology has been developed as found in Liu et al. (2020). The basic idea is enhancing the gasification intensity through a gasifier composed of two circulating loops. The pilot-scale plant has been in field test but with some difficulties in operation due to the complex interactions among fluidization, heat and mass transfer, and reactions. Therefore, numerical simulation was expected to be carried out to investigate the characteristics of flow and reactions inside the plant and then support industrial applications.

The coal gasification in the CFB is a typical multi-scale process. The existence of a large number of meso-scale structures (particle clusters) has a great impact on the momentum exchange between gas and solid phases, leading to a large reduction in the gas-solid drag and then a heterogeneous fluidization state in the macro-scale reactor. Moreover, the drag reduction degree has complicated correlations with fluidization states as found in Qi (2017). Therefore, a heterogeneous drag model that can be generalized for wide flow conditions is needed to ensure the simulation accuracy.

Based on the theory of Energy Minimization in Multi-Scale (EMMS) proposed by Li (1987), the QC-EMMS drag model has been developed by Chen et al. (2016). The model reproduced the drag reduction consistent with the experimental results of O'Brien and Syamlal (1993) by introducing new cluster property models into EMMS equations. It has been verified by Chen et al. (2016) and Dai et al. (2015) that the QC-EMMS model has a universal ability to cover wide flow conditions with simulation errors<10%. However, the model still needs further tested in the simulation of reactive fluidization processes in the large CFB plant.

This study investigated the flow and reaction processes in a dual-CFB coal gasifier based on the Eulerian-Eulerian approach with the QC-EMMS drag model. The purpose of this study is to enrich the knowledge on flow and reaction mechanism during large-scale CFB coal gasification and also to provide supports for the optimization of industrial operations.

2 Plant Configuration

The simulated dual-CFB coal gasifier is composed of two circulating loops (Fig. 1) as reported in Liu et al. (2020). In cold-flow operations, nitrogen N_2 was used for fluidization gas, and the bed material was sand. During the gasification process, N_2 was replaced by gasification agents (the mixture of O_2 and steam), and coal was fed into the 1st loop riser. Loose gas (N_2) was injected at standpipes, L-valve, and loop seals of two loops.

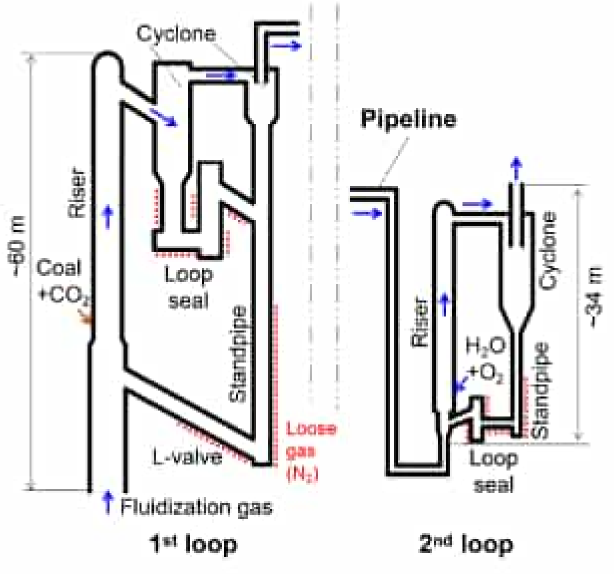

Fig. 1. Configuration of the dual-CFB coal gasifier.

3 Numerical Models

The Eulerian-Eulerian approach was used for simulation. The drag function, β, in momentum equations (Eq. (1)) was modified by a correction factor, H_D, (value less than 1) to consider the reduction on homogeneous drag function, β_0, caused by particle clusters (Eq. (2)).

$$\frac{\partial}{\partial t}\left(\rho_k u_{k,i}\right)+\frac{\partial}{\partial x_j}\left(\rho_k u_{k,i} u_{k,j}\right)=-\varepsilon_k\frac{\partial p_g}{\partial x_i}+\frac{\partial \tau_{k,ij}}{\partial x_j}+\beta\left(u_{s,i}-u_{g,i}\right)+\rho_k g_i \tag{1}$$

$$\beta = H_D \beta_0 \tag{2}$$

3.1 QC-EMMS Drag Model

This study used the QC-EMMS model to solve the H_D. The model introduced sub-models of cluster solid holdup, ε_{sc}, and size, d_{cl}, (Eqs. (3) and (4)) proposed by Chen et al. (2016) into the original EMMS equations. Then, the H_D can be calculated by solving the new equations.

$$\varepsilon_{sc}=\varepsilon_s+\Psi\frac{211.74\varepsilon_s^{\ 2}}{e^{\left(3.098\varepsilon_s+0.9398\right)^2}-2.42}\left(\varepsilon_{s,mf}-\varepsilon_s\right) \tag{3}$$

$$d_{cl}=\left[\Psi\frac{211.74\varepsilon_s^{\ 2}}{e^{\left(3.098\varepsilon_s+0.9398\right)^2}-2.42}\cdot\frac{\left(\dfrac{U_p}{1-\varepsilon_{\max}}-U_{mf}-\dfrac{\varepsilon_{mf}U_p}{1-\varepsilon_{mf}}\right)}{\left(N_{st}\cdot g\dfrac{\rho_p}{\rho_p-\rho_g}-U_{mf}-\dfrac{\varepsilon_{mf}U_p}{1-\varepsilon_{mf}}\right)}+1\right]d_p \tag{4}$$

In Eqs. (3) and (4), a heterogeneity factor, Ψ, (value from 0 to 1) was introduced to cover the whole heterogeneity range of cluster properties. Considering that the cluster properties are determined by macro-scale flow states in CFB, the relations between Ψ and CFB operation parameters were proposed by Liu and Qi (2018) as shown in Eq. (5). Therefore, the drag reduction degree under different operation conditions can be automatically calculated.

$$\Psi = a \cdot {\varepsilon_{s,bed}}^{0.4} \left(\varepsilon_{s,mf} - \varepsilon_{s,bed} \right)^{b} \left(1 - \frac{5}{4 + \exp\left(6400 \cdot \varepsilon_{s,bed}^{2} \right)} \right) \tag{5}$$

$$a = 3.005 Gs^{0.3847}, \qquad b = 0.9295 Gs^{0.2496}$$

3.2 Reaction Models

Chemical reactions included in the simulation are shown in Table 1. The reactions contain coal decomposition, homogeneous gas reactions, and gas-solid heterogeneous reactions. The detailed reaction kinetic parameters can be found in Liu et al. (2020) and Li et al. (2020).

Table 1. Chemical reaction equations

Type	Equations	
Decomposition	$Coal \rightarrow 4.75C + 0.78CH_4 + 0.4H_2 + 0.08CO_2 + 0.33CO + 0.1H_2O + 0.14Tar$	
Homogeneous	$CO + 0.5O_2 \rightarrow CO_2$	$CO + H_2O \leftrightarrow CO_2 + H_2$
	$H_2 + 0.5O_2 \rightarrow H_2O$	$CH_4 + 0.5O_2 \rightarrow CO + 2H_2$
	$CH_4 + H_2O \rightarrow CO + 3H_2$	$Tar + 2.99O_2 \rightarrow 6CO + 3.64H_2$
Heterogeneous	$C + O_2 \rightarrow CO_2$	$C + 0.5O_2 \rightarrow CO$
	$C + CO_2 \rightarrow 2CO$	$C + H_2O \rightarrow CO + H_2$
	$C + 2H_2 \rightarrow CH_4$	

3.3 Simulation Conditions

The numerical study contains cold-flow and gasification process simulations. The simulation under the cold-flow condition shown in Table 2 was firstly performed to investigate the gas-solid flow characteristics.

Table 2. Conditions for cold-flow process simulation

Loops	Superficial velocity, U_g (m/s)	Bed inventory, I_{bed} (t)	Loose gas flow rate, Q (m^3/h)
1st	1.7	2.12	650
2nd	1.85	1.65	86

Then, the simulation of the gasification process was carried out with the reaction model in Table 1. The conditions referred to the previous study by Liu et al. (2020) but with different loose gas (N_2) flow rates, Q, of the 1st loop as shown in Table 3. The time step of the iteration was set to 2 ms in all simulation cases.

Table 3. Conditions for gasification process simulation

Parameters	1st loop					2nd loop		
	O_2	Steam	Coal	CO_2	N_2	O_2	Steam	N_2
Flow rate (kg/h)	2002	1512	2900			326.5	326.5	
Inlet temperature (K)	423	423	323	323	383	423	423	383
Flow rate (m^3/h)				102.1	465/103			273

Initial inventory (kg)	1738	1076

4 Results & Discussion

4.1 Gas-Solid Flow Characteristics

The accuracy of the simulation was firstly verified. As shown in Fig. 2, the simulated axial pressure drops, Δp, in the risers of two loops agree with the experimental data well. The clear transitions of the pressure drop indicate the boundaries between the bottom-dense and upper-dilute phase regions. Due to the differences in geometry between risers of two loops, the Δp in two risers exhibit different profiles. The 2nd loop riser has a smaller total height, H, compared with the 1st loop riser, thus the Δp transition in the 2nd loop riser is closer to the riser top. In addition, the 2nd loop riser has a narrow section at the bottom, which makes the local gas velocity here very high as reported in the study by Liu et al. (2020). Therefore, the solid volume fraction and pressure drop are lower at the bottom of the 2nd loop riser.

As shown in Fig. 3, the particle distributions in the risers exhibit strong heterogeneity. The relative height of the dense phase region in the 1st loop riser is about 0.23, which is consistent with the axial Δp distribution in Fig. 2. The particles in the loop seal and standpipe of the 1st loop are apparently fluidized by loose gas with a high flow rate, Q, of 650 m^3/h (Table 2), while particles in the standpipe of the 2nd loop keep plastic flow state under low Q.

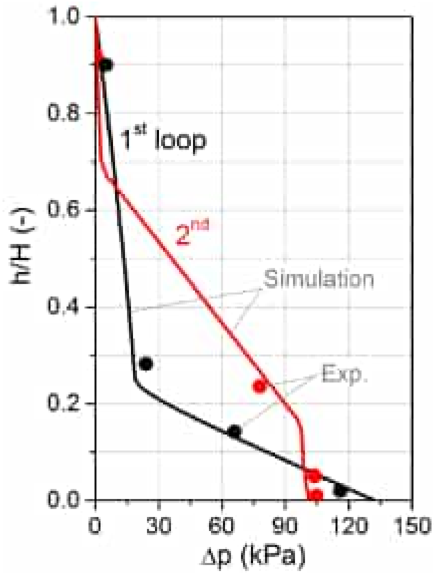

Fig. 2. Pressure drops in the risers.

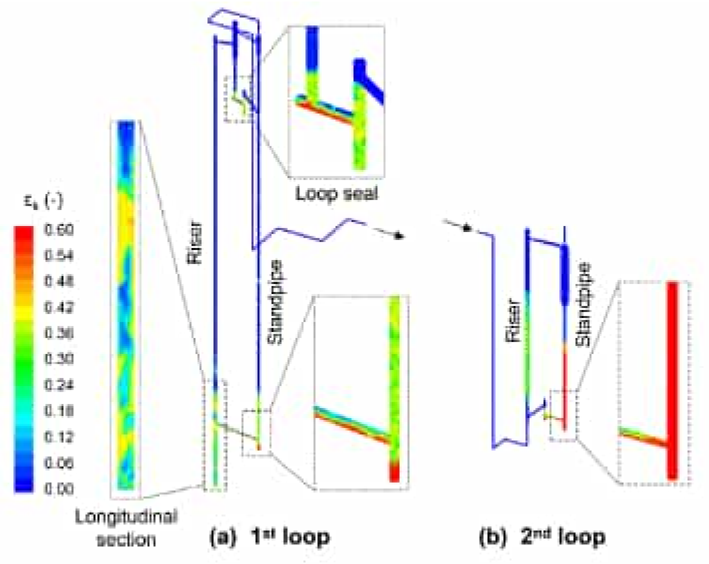

Fig. 3. Full-loop solid volume fraction distribution.

4.2 Gasification Characteristics

As shown in Fig. 4, the temperatures in two risers are relatively high with the volume-averaged temperatures over 1150 K because of the reaction heat from the oxidation of carbon particles. The local low-temperature areas occur near the loose gas inlets located on the loop seals and standpipes due to the injection of 383 K cold loose gas. The simulation results of volume-averaged temperatures agree with the experimental data.

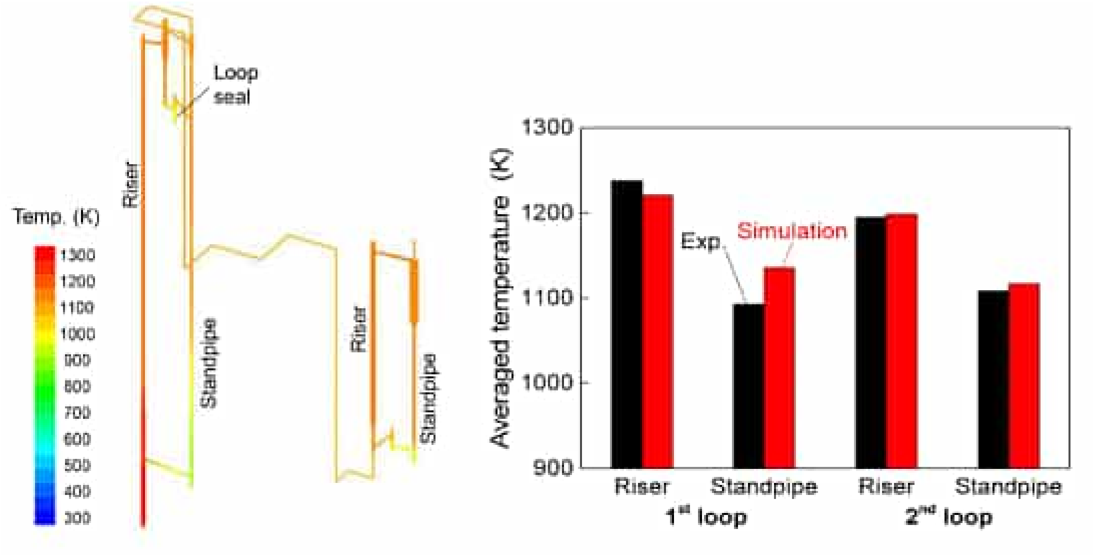

Fig. 4. Full-loop temperature distribution (Loose gas flow rate Q=465 m^3/h).

The influence of the loose gas (N_2) was also investigated together with the simulation results from a high loose gas flow rate case (Q=1196 m^3/h) as reported in Liu et al. (2020). It can be seen from Fig. 5 that the main components of the syngas at the gasifier outlets are CO and CO_2 formed during carbon oxidation, H_2 generated by the reaction between carbon particles and H_2O, and loose gas N_2. The other gas components not shown in Fig. 5 include small amounts of O_2 and CH_4. The not fully reacted carbon particles from the 1st loop could further react in the 2nd loop, resulting in the increase of molar fractions of H_2 and CO at the 2nd loop outlet. With the increase of the loose gas flow rate, Q, the molar fraction of N_2 in the syngas at the two outlets increases significantly. As shown in Fig. 5, the molar fraction of N_2 can increase by about 100% with the increasing Q from 103 m^3/h to 1196 m^3/h, while the molar fractions of other gas components such as CO, H_2, and CO_2 all decreases. However, such a large amount of N_2 will reduce the calorific value of the syngas and also increases the cost of subsequent separation of N_2 from syngas.

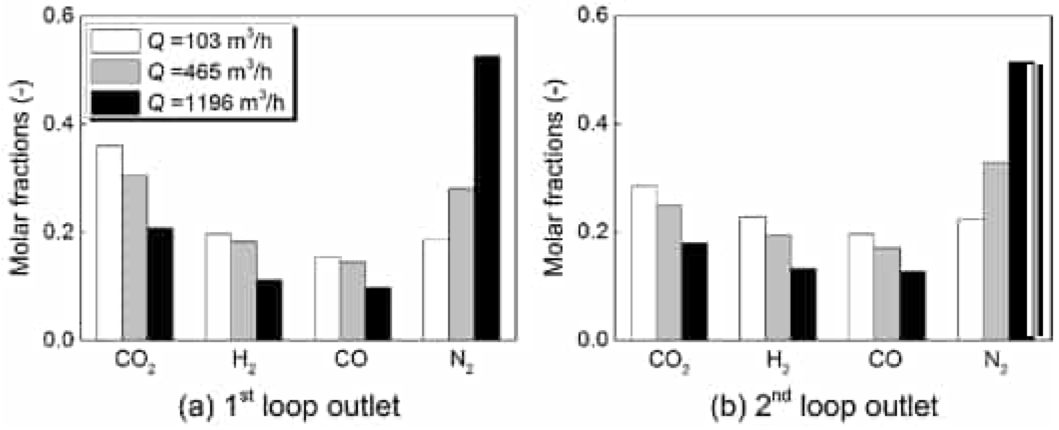

Fig. 5. Major syngas components for various loose gas flow rates.

With the increase of loose gas flow rate, Q, the molar fraction of N_2 in the whole reactor increases (Fig. 5). As an inert gas, N_2 does not participate in the gasification reactions, but reduces the molar concentrations of other reactive gases and then weakens the production rate of H_2 and CO. Table 4 shows that the effective syngas yield (the total flow rate of H_2 and CO), Y, at the gasifier outlets decreases by 5%~9% with the increasing Q, indicating that excessive inert loose gas will cause the reduction in coal gasification efficiency.

The loose gas also affects the bed temperature, T_{bed}. The gasification efficiency of carbon particles is improved after reducing the loose gas flow rate (Table 4). As the main gasification reactions (Boudouard reaction $C+CO_2 \rightarrow 2CO$ and water-gas reaction $C+H_2O \rightarrow CO+H_2$) are strong endothermic reactions, more heat generated from oxidation reactions is consumed with the decreasing Q and then the bed temperature decreases. However, Table 4 shows that the bed temperature, T_{bed}, only decreases slightly with the decreasing Q.

The decrease of the bed temperature will enhance the H_2 production rate of the water-gas shift reaction ($CO+H_2O \leftrightarrow CO_2+H_2$), resulting in the change of the molar ratio of H_2 to CO, H_2/CO, in the syngas. It can be seen from Table 4 that the H_2/CO of syngas at the two outlets has a linear relationship with Q. As Q decreases by 10%, the H_2/CO of the 1st and 2nd loop outlets could increase by about 0.051 and 0.033.

In summary, it is necessary to reduce the loose gas N_2 flow rate or use other reactive gases as loose gas in future operations to improve the syngas quality and the effective syngas yield.

Table 4. Performance parameters for various loose gas flow rates

Q (m^3/h)	1st loop			2nd loop		
	Y (kg/s)	T_{bed} (K)	H_2/CO (-)	Y (kg/s)	T_{bed} (K)	H_2/CO (-)
103	0.398	1219	1.28	0.581	1195	1.16
465	0.387	1221	1.26	0.555	1199	1.15
1196	0.380	1223	1.14	0.532	1205	1.07

5 Conclusion

(1) The characteristics of gas-solid flow and gasification reaction in a large dual-CFB plant were analyzed using the Eulerian-Eulerian approach. The simulation results are in agreement with the field test data.

(2) The study found that the loose gas flow rate has important influences on the performance parameters of the gasifier. With the increasing loose gas flow rate, the bed temperature increases while the effective syngas yield and H_2/CO ratio decrease.

(3) The accuracy and condition applicability of the QC-EMMS drag model has been further verified in this study.

Notation

d_{cl}	cluster size, μm
d_p	particle size, μm
g	gravitational acceleration, m/s^2
Gs	solid mass circulation rate, kg/m^{2}s
h	height of the riser, m
H	total height of the riser, m
H_D	drag correction factor, -
I_{bed}	bed inventory, kg
N_{st}	energy for suspending particles, J/kg
p	pressure, Pa
Q	loose gas flow rate, m^3/h
T_{bed}	bed temperature, K
u	local velocity, m/s
U_g	superficial velocity, m/s
U_{mf}	minimal fluidization velocity, m/s
U_p	superficial solid velocity, m/s
Y	effective syngas yield, kg/s
β	heterogeneous drag function, Ns/m^4
β_0	homogeneous drag function, Ns/m^4
Δp	pressure drop, kPa
ε_g	gas volume fraction, -
ε_{max}	maximum gas volume fraction, -
$\varepsilon_{s,mf}$	minimal fluidized solid volume fraction, -
ε_s	solid volume fraction, -
$\varepsilon_{s,bed}$	bed-averaged solid volume fraction, -
ε_{sc}	solid holdup of cluster, -
ρ	density, kg/m^3
τ	stress tensor, Pa
Ψ	heterogeneity factor, -

References

Chen, C., Dai, Q.T., Qi, H.Y. Improvement of EMMS Drag Model for Heterogeneous Gas-solid Flows based on Cluster Modeling. Chemical Engineering Science. 2016. 141, 8-16

Dai, Q.T., Chen, C., Qi, H.Y. A Generalized Drag Law for Heterogeneous Gas-Solid Flows in Fluidized Beds. Powder Technology. 2015. 283, 120-127

Li, J. Multi-Scale Modeling and Method of Energy Minimization for Particle-Fluid Two-Phase Flow, Doctor thesis, Institute of Chemical Metallurgy. 1987. Chinese Academy of Sciences, Beijing

Li, X.H., Huo, P.J., Liu, Y., Qi, H.Y. Numerical Study of Load Characteristics of a CFB Coal Gasifier by Using the Generalized Drag Model. Energy and Fuels. 2020. 34, 5084-5094

Liu, Y., Qi, H.Y. Study on Condition Adaptability of Fluidized Heterogeneous Drag Model, Proceedings of the Annual Meeting on Multiphase Flow, Chinese Society of Engineering Thermophysics, Beijing. 2018

Liu, Y., Huo, P.J., Li, X.H., Qi, H.Y. Numerical Study of Coal Gasification in a Dual-CFB Plant Based on the Generalized Drag Model QC-EMMS. Fuel Processing Technology. 2020. 203, 106363

O'Brien, T.J., Syamlal, M. Particle Cluster Effects in the Numerical Simulation of a Circulating Fluidized Bed, CFB-4, Somerset, USA. 1993. pp. 430-435

Qi, H.Y. Meso-Scale Structure, Drag Model and Eulerian Simulation of Fluidization Processes, CFB-12, Krakow, Poland. 2017

Acknowledgments

This study was supported by Shaanxi Yanchang Petroleum Co. Ltd. and the

Tsinghua-Huaneng Basic Energy Joint Research Institute (grant no. U20YYJC07).

PREDICTING PRODUCT PROPERTIES OF FLUIDIZED BED SPRAY GRANULATION USING CFD-DEM SIMULATIONS

Paul Kieckhefen[1*], Swantje Pietsch[1], Stefan Heinrich[1]

[1] Institute of Solids Process Engineering and Particle Technology, Denickestrasse 15, 21073 Hamburg, Germany

*Email: *paul.kieckhefen@tuhh.de*

Abstract

CFD-DEM is the most promising way of describing the micro- and meso-scale behavior of fluidized beds. In particular, the interaction of single particles with both flow and other particles, as well as liquid droplets can be resolved, while preserving their individual fate.

Fluidized bed spray granulation is the preferred way of generating functional, high value granular products. By injecting a solution or suspension onto a particle bed, the particles grow layer by layer. Here, the drying conditions have a major influence on the structure of the layers, due to the pre-concentration of droplets that cause changes in the viscosity and velocity of impinging droplets. This affects the spreading behavior of droplets on the surface, together with the crystallization occurring within the droplets themselves in the case of solutions, resulting in either porous or dense layers. As these phenomena are well accessible in CFD-DEM simulations, their combination can be a powerful tool in the design of granulators that produce tailor-made particles.

In this work, a compressible CFD-DEM solver, capable of modelling heat transfer, spray injection and evaporation, is presented and validated against experimental data. A simple concept for tracking the progress of the structure-determining processes taking place within the droplets and on the surface of the wetted particles is presented. Calibration granulation experiments from literature were recreated in simulations and used to correlate between resulting shell porosity and micro-scale event timescales.

Introduction

The process conditions of fluidized bed spray granulation have a strong influence on the properties of the resulting product, for example hardness, porosity, and roughness. These properties, in turn, affect the usability of the product for its intended application. A fertilizer, for example, must have a low porosity to slow its dissolution while detergent particles must dissolve quickly as to not leave residues in the fibers of clothing.

Rieck et al. (2015) and Hoffmann et al. (2015) have performed layering granulation experiments under variation of spray rate and air inlet temperature and analyzed the resulting layer porosities $\varepsilon_{\mathrm{sh}}$ using micro-tomography. These were then correlated with the corresponding macroscopic drying potential η:

$$\eta = \frac{Y_{\mathrm{wb}} - Y_{\mathrm{out}}}{Y_{\mathrm{wb}} - Y_{\mathrm{in}}}, \qquad (1)$$

where the wet-bulb saturation loading Y_{wb} is either calculated from the outlet gas temperature in the case of Rieck et al. or the inlet gas temperature in the work of Hoffmann et al. These correlations provide a linear manifold relationship $\varepsilon_{\mathrm{sh}} = \varepsilon_{\mathrm{sh}}(\eta)$ that data with a good fit. While this is enough for small lab-scale fluidized beds with perfect mixing and homogeneous aeration, this may differ on the industrial scale. In addition, the distribution of porosities is imperfectly captured by this linear model. Diez et al. (2018) extended this work by running continuous granulation experiments in a pilot-scale granulator with an external sieve-milling cycle and subsequent characterization of particle SEM images, surface roughness values, densities, compression strength, porosities and wetting behavior (contact angle). Fries et al. (2013,2014) correlated micro-scale phenomena like particle collision rates and velocities with the resulting product properties like breakage strength to tailor process conditions and granulator configuration to product requirements.

Numerical Model of Drying Solver in CFD-DEM

The CFDEMcoupling-PFM suite for unresolved CFD-DEM simulations that combines the DEM code LIGGGHTS and the CFD code OpenFOAM was used and its *cfdemSolverRhoPimpleChem* solver for compressible flows with species transport was extended to consider a discrete droplet phase, derived from the *sprayFoam* solver, that interacts with the particles using a droplet deposition scheme according to Kieckhefen et al. (2018). The details of the dynamics and heat transfer implementation, as well as heat transfer validation, can be found in Lichtenegger et al. (2017). The Lagrangian droplet phase was accelerated using Stokesian drag forces and modelled evaporation according to the correlation of Ranz & Marshall (1952).

Evaporation of the particles surface liquid was determined by calculating the mass transfer coefficient according to Gunn (1978), evaporation-active surface area and saturation temperature per particle, mapping their products $\beta A_{\mathrm{liq}} \rho_{\mathrm{g}} y^{*}_{\mathrm{H_2O}}(T_{\mathrm{g}})$ and $\beta A_{\mathrm{liq}} \rho_g$ as their sums over all particles to the Eulerian field to include a semi-implicit source term

$$\dot{M}_{\mathrm{evap}} = \rho_{\mathrm{g}}\, \beta A_{\mathrm{liq}} \big(y^{*}_{\mathrm{H_2O}}(T_{\mathrm{g}}) - y_{\mathrm{H_2O}}\big), \tag{2}$$

when solving for a new vapor fraction field $y_{\mathrm{H_2O}}$. After a new solution is found, the new vapor fractions are interpolated to the particles i and a sink term

$$\dot{M}_{\mathrm{evap},i} = \rho_{\mathrm{g}}\, \beta_i A_{\mathrm{liq,i}} \big(y^{*}_{\mathrm{H_2O}}(T_{\mathrm{g}}) - y_{\mathrm{H_2O},i}\big) \tag{3}$$

is used for integrating the material liquid balance. An additional explicit enthalpy sink is included on the particle side to consider the heat of evaporation. The area of the particle surface that is covered by liquid is calculated using the surface coverage model of Kariuki et al. (2013).

The simulation was coarse-grained using the approach of Bierwisch (2009). Thus, the resulting calculations were performed using the original particle size and then scaled to consider the number of particles represented in a parcel.

Solver Validation

For validation, fluidized bed experiments were run on a *Glatt GF3* granulator (bottom diameter of 200 mm) with distilled water injected through a *Schlick 970-S4* two-fluid nozzle in bottom spray configuration, as shown in the setup in Fig. 1 (a). 2.5 kg of silica glass particles with a mean diameter of 1000 µm were used at spray rates of up to 40 g/min, temperatures between 30°C and 90°C and gas flow rates equating to 2 to 4 times the minimum fluidization velocity at ambient conditions.

As one of the few true degrees of freedoms in fluidized bed drying that is both easily accessible and measurable, we chose the bed temperature as our validation criterion and recorded it using a Pt100 thermocouple element. Air temperature, fluidization air flow rate and spray rate were varied and yielded agreement within a 10% accuracy window, as can be seen in the parity plot in Fig. 1(b). As no wall heat transfer was considered and experimental temperatures are below the simulated ones, this is deemed to be the cause of the disparity. Further validation regarding the dynamic behavior was performed by introducing step changes, which yielded good agreement.

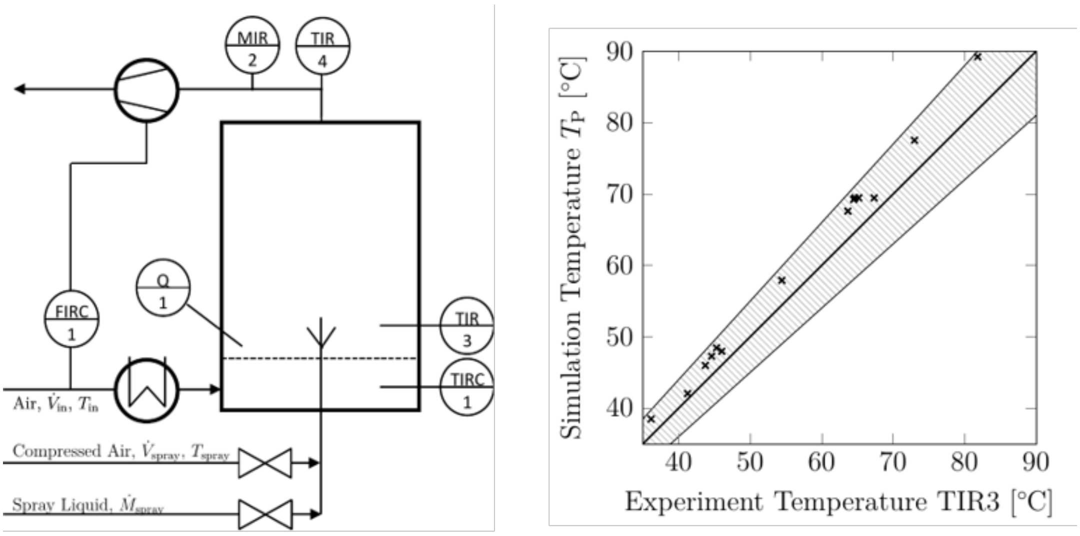

(a) (b)

Fig. 1. (a) Schematic of validation experiment plant layout. (b) Parity plot between simulation particle temperatures and experimental bed temperatures. The shaded area is a 10% margin.

Micro-Scale Phenomena and Event Tracking

The resulting surface structure of particles is dependent on three types of phenomena: first, the nucleation/crystallization processes and pre-concentration within the droplet (Hoffmann et al., 2015), as well as impact parameters (relative velocity), second, the spreading of droplets on the surface and dissolution/imbibition phenomena (Heine et al., 2013), and third, attrition, compaction and agglomeration due to particle-particle and particle-wall collisions (Fries et al., 2014). In this work, we consider the first two types.

The effect of in-droplet nucleation & crystallization for salts is explained by Hoffmann et al. (2015) in the following manner: if the drying potential is high, the rapid drying of droplets allows less time for nuclei to grow into larger crystals, resulting in smaller crystals and giving the process more of the character of a precipitation – leading to a smoother surface and dense layering. If the drying potential is low instead, the nuclei may grow into larger crystals that can pack less densely, resulting in a rougher surface and higher porosity of the resulting particles.

In a CFD-DEM simulation, this may be simply assessed by the concentration of the droplet at impact or be modelled by calculating the moments of the concentration of the droplets over time.

We furthermore hypothesize that the velocity at which the droplet impacts, and its concentration at impact, has an influence on its spreading behavior and thus the porosity. The resulting viscosity of the liquid layer is deemed to have an influence on the spreading as well. This and further surface phenomena like dissolution of the present surface and imbibition of the liquid into the particle (Heine et al., 2013) decrease both the surface roughness and overall porosity as time progresses.

Thus, the time until the liquid layer on the particle surface evaporates is a promising indicator for the porosity and roughness and, therefore, tracking this quantity was implemented in the CFD-DEM solver used in this study.

Tracking both impact parameters and particle evaporation times has the advantage of allowing for evaluation after the numerically costly simulation itself and providing more flexibility.

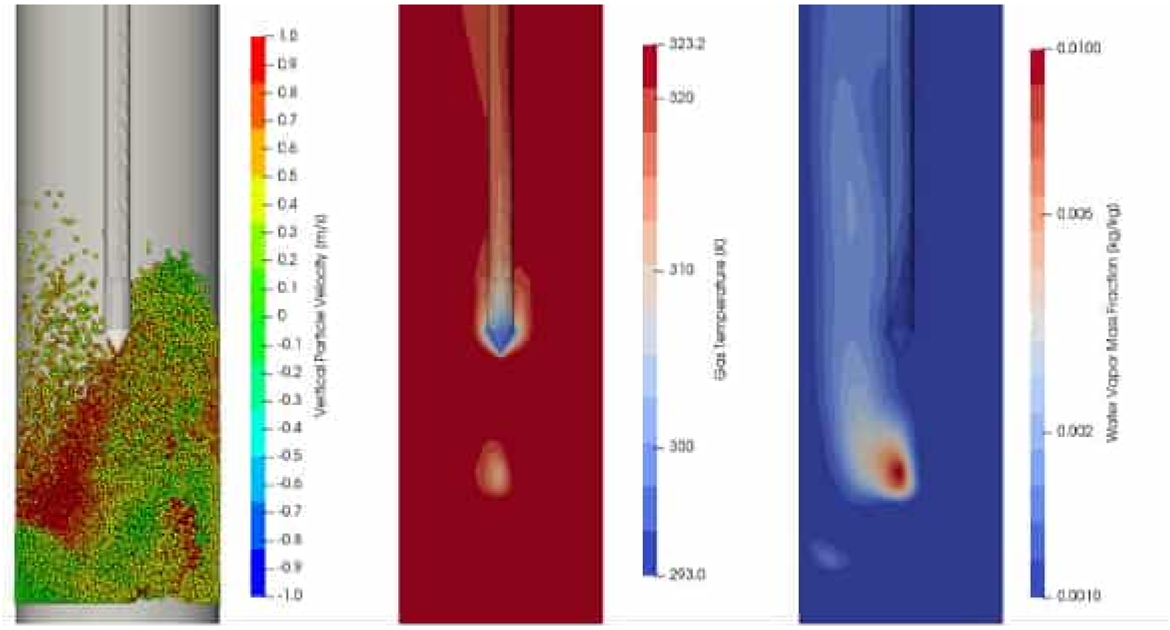

(a) (b) (c)

Fig. 2. Snapshot of a granulation simulation, cut through the midplane. (a) Particle positions and velocities, (b) Gas temperature distribution in apparatus midplane, (c) Water vapor mass fraction distribution in the apparatus midplane.

Application of the Method

For testing the method, cases E10, E11, E12 and E13 of Hoffmann (2016) were recreated in CFD-DEM simulations. The granulator in question was a modified Glatt granulator with a cylindrical base (diameter 150 mm), a top-spray two-fluid nozzle and air-preconditioning to a water vapor loading of 1 g/kg. In the experiments, 1 kg of sodium benzoate solution (30 wt-%) was injected onto 1 kg of glass particles (diameter 500 µm) at a fluidization air flow rate of 120 kg/h and a nozzle air flow rate of 1.68 kg/h. The fluidization air temperature and spray solution flowrate were varied from 50°C to 95°C and 500 g/h to 1000/1200 g/h. An overview of the cases is given in Tab. 1.

These conditions were chosen as boundary conditions in the simulations. Droplets were injected at a rate of 10^5 1/s. Particles were treated as parcels with a scaling factor of 4, resulting in less than 95 495 parcels that were time-integrated using a DEM time step of 8E-5 s. The modulus of elasticity was reduced to 1 MPa to allow for faster calculations. The mesh was created using a grid size of 8 mm and refinement to 4 mm in the proximity of the nozzle. This allowed timesteps of 8E-4 s. Diffusive smoothing of exchange fields was employed to generate realistic solids volume fractions and momentum sink/source terms.

The simulations yielded realistic particle flow and evaporation patterns (Fig. 2). The corresponding times required for drying the surface layer is shown in Fig. 3. (a), where we can observe much shorter cycles for case E12 at the highest spray rate with a maximum at 1 s, whereas the other cases have a maximum around 10 s. The distribution of solids fraction of droplets upon impact ranges into much higher values for this case as well. Therefore, we expect this case to yield a much smoother surface and lower porosity than the others, followed by case E10 and cases E11 and E13 to result in fairly similar surfaces due to the drying cycle time distribution being almost equal and the mean solids fraction in droplets upon impact being higher in case E10 than E11 and E13.

Table 1. Case overview, experimental porosities taken from (Hoffmann, 2016).

Case	Process Conditions			Exp. Data	Simulation Result
	Air Temperature [°C]	Spray Rate [g/h]	Drying Potential [-]	Porosity [%]	Mean Cycle Time [s]
E10	50	504	0.77	53.7 ± 2.3	16.0 ± 7.7
E11	50	967	0.56	63.8 ± 2.2	16.0 ± 7.7
E12	95	512	0.88	46.3 ± 0.7	10.7 ± 8.9
E13	95	1277	0.71	49.7 ± 1.7	16.5 ± 8.3

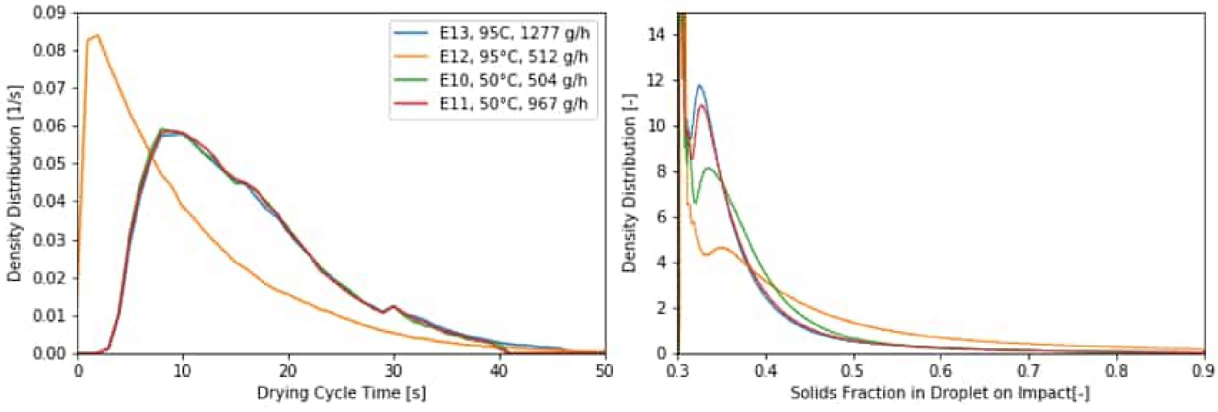

(a) (b)

Fig. 3. (a) Surface liquid layer drying time distribution. (b) Distribution of solids fraction in droplets upon impact on particles.

Outlook

The method presented here will be further refined to take into consideration single-particle drying cycles that combine the succession of impacts instead of mere separate population-distributions. The model will be validated by more sophisticated experiments that incorporate different solids concentrations to gain more insight into the role of crystallization kinetics. A way to thoroughly calibrate the model to quantitatively predict porosities and roughness, as well as other target quantities, will be devised.

To test the usefulness and predictiveness of the approach, a pilot-scale experiment will be designed using simulations and subsequently performed to see if the predicted target quantities are obtained.

Notation

η	drying potential, -	β	mass transfer coefficient, m^3/m^{2}s
Y_{wb}	wet-bulb vapor loading, kg$_{\mathrm{H2O}}$/kg$_{\mathrm{dryair}}$	$y^*_{\mathrm{H_2O}}$	wet bulb water vapor fraction, -
Y_{in}	inlet vapor loading, kg$_{\mathrm{H2O}}$/kg$_{\mathrm{dryair}}$	i	subscript indicating per-particle property
Y_{out}	outlet vapor loading, kg$_{\mathrm{H2O}}$/kg$_{\mathrm{dryair}}$	$y_{\mathrm{H_2O}}$	water vapor fraction, -
t	time, s	ρ_{g}	gas phase density, kg/m^3
$\dot{M}_{\mathrm{evap}}$	evaporation rate, kg/s	A_{liq}	liquid surface area, m^2

References

Bierwisch, C., Kraft, T., Riedel, H., & Moseler, M.. Three-dimensional discrete element models for the granular statics and dynamics of powders in cavity filling. Journal of the Mechanics and Physics of Solids. 2019 57(1), 10–31.

Fries, L., Antonyuk, S., Heinrich, S., Dopfer, D., & Palzer, S.). Collision dynamics in fluidised bed granulators: A DEM-CFD study. Chemical Engineering Science. 2013. 86, 108–123.

Fries, L., Antonyuk, S., Heinrich, S., Niederreiter, G., & Palzer, S. Product design based on discrete particle modeling of a fluidized bed granulator. Particuology. 2014. 12, 13–24.

Gunn, D. J. Transfer of heat or mass to particles in fixed and fluidised beds. International Journal of Heat and Mass Transfer. 1987. 21(4), 467–476.

Heine, M., Antonyuk, S., Heinrich, S., Dopfer, D., & Palzer, S. Droplet deposition on amorphous particles in a fluidized bed spray agglomeration process. Presented at the 5th International Granulation Workshop, Lausanne. 2013

Hoffmann, T. Experimentelle Untersuchungen des Einflusses von verschiedenen Prozessparametern auf das Partikelwachstum bei der Wirbelschicht-Sprühgranulation, PhD thesis, University of Magdeburg, Magdeburg. 2016.

Hoffmann, T., Rieck, C., Bück, A., Peglow, M., & Tsotsas, E. Influence of Granule Porosity during Fluidized Bed Spray Granulation. Procedia Engineering. 2016. 102, 458–467.

Kariuki, W. I. J., Freireich, B., Smith, R. M., Rhodes, M., & Hapgood, K. P. Distribution nucleation: Quantifying liquid distribution on the particle surface using the dimensionless particle coating number. Chemical Engineering Science. 2013. 92, 134–145.

Kieckhefen, P., Lichtenegger, T., Pietsch, S., Pirker, S., & Heinrich, S. Simulation of spray coating in a spouted bed using recurrence CFD. 2019. Particuology.

Lichtenegger, T., Peters, E. A. J. F., Kuipers, J. A. M., & Pirker, S. A recurrence CFD study of heat transfer in a fluidized bed. Chemical Engineering Science. 2017. 172, 310–322.

Ranz, W. E., & Marshall, W. R. Evaporation from Drops, Part I. Chemical Engineering Progress. 1952. 48(3), 141–146.

Rieck, C., Hoffmann, T., Bück, A., Peglow, M., & Tsotsas, E. Influence of drying conditions on layer porosity in fluidized bed spray granulation. Powder Technology. 2015. 272, 120–131.

CPFD SIMULATION AND EQUIPMENT DESIGN OF A NOVEL FLUIDEIZED BED DESULFURIZATION WASTERWATER DRYER

Xiandong Liu, Man Zhang, Runxia Cai, Xuan Yao, Junfu Lyu, Hairui Yang*

*Key Laboratory for Thermal Science and Power Engineering of Ministry of Education,
State Key Laboratory of Power Systems, Department of Energy and Power Engineering,
Tsinghua University, Beijing 100084, China*

*Email: *yhr@mail.tsinghua.edu.cn*

Abstract

The limestone/gypsum flue gas desulfurization (FGD) as a high SO_2 removing efficiency desulfurization technology attracts much interests, while the wastewater produced in desulfurization process is a severe problem to solve. Traditional method using chemical precipitation, ion exchange, activated carbon adsorption cannot fulfill the zero-emission regulation on wastewater in China. Bypass evaporation tower zero-liquid discharge (ZLD) technology has been developing rapidly because of its simple pretreatment, high reliability and low operation and equipment cost. In this paper, a novel desulfurization wastewater dryer using Wurster fluidized bed was put forward. Numerical simulation based on Computational Particle Fluid Dynamics (CPFD) was applied to verify its flow state and wastewater evaporation efficiency. The results indicates that Wurster fluidized bed flow state can be approached through reasonable structure with cone section in the bottom and appropriate aeration strategy. Meanwhile, compared with the amount of wastewater vapor, the mass of droplet leakage is little, which indicates great evaporation efficiency. With simulation results, a design for industrial desulfurization wastewater dryer was put forward.

Introduction

As the development of Chinese industry, the excessive SO2 emission has caused severe environment problems including acid rain and smog. Therefore, government published stricter flue gas treatment criterion, making power plants under more pressure of SO2 reduction [1].

Presently, wet limestone-gypsum flue gas desulfurization (WFGD) technology is widely used in Chinese coal fired power plant. WFGD is a mature desulfurization technology with high efficiency and wide availability, which can adapt to various kinds of coal and has low operation cost [2]. During the continuous WFGD process, the slurry will gradually enrich the heavy metal element and chloride ions derived from flue gas and dissolved limestone [3]. It's necessary to discharge a certain amount of wastewater to control the concentration of chloride ions in the circulating slurry for the sake of protecting desulfurization equipment from corrosion. The character of low pH and large amounts of nitrite, chloride ions, suspended solids, heavy metals, etc. makes it indispensable to deal with desulfurization wastewater before emission [4].

Meanwhile, regarding wastewater treatment, traditional wastewater evaporation technology using chemical precipitation, ion exchange, activated carbon adsorption cannot fulfill government zero-emission requirement. Therefore，zero-liquid discharge (ZLD) technology has attracted most interest for coal fired power plants since no water is discharged from system and it eliminates the risk of water pollution [5].

Traditional ZLD methods includes pre-treatment, pre-concentration and solidification. The evaporation & crystallization as a traditional solidification process has mature technology and reliable operation, while high operation and equipment cost constrains its further development [6]. Nowadays, thermal desalination dryer that is suitable for desulfurization wastewater and can fulfill zero-emission regulation has been developing rapidly, which can be divided into main flue gas evaporation and bypass evaporation tower technology. The former one is to inject wastewater after atomization into main flue between air pre-heater and dust filter, whose problems are flue blocking, dust deposition and low efficiency at low load condition [7].

Different from main flue gas evaporation technology, bypass evaporation tower dryer is to inject atomized wastewater droplets into evaporation tower and dry it with heat air such as heat flue gas or the second air. Bypass evaporation tower technology has been attracting wide interest because of its advantages of low equipment and operation cost, no blocking and corrosion in flue and reliable operation.

The key of bypass evaporation technology is to design appropriate structure to increase evaporation efficiency and convenience to collect salts. Many scholars have done many researches on exploration of efficient structure: Ma et al. [8] put forward a new type of bypass evaporation tower technology which rotates flue gas using 24 deflectors to enhance gas-liquid contact and investigate the effect of structure parameter. However, it has difficulties of even flue gas distribution, high equipment investment and short droplet residence time. Li et al. [9] used CPFD method to establish evaporation and mass transfer processes in evaporation tower and investigate flow state and slurry droplet evaporation process. But the parallel flow of flue gas and droplets in rotating atomization tower cannot provide sufficient heat transfer.

Facing the existing shortcomings of bypass evaporation technologies, a novel bypass evaporation tower is put forward using Wurster fluidized bed to enhance heat transfer between heating air and wastewater. Wurster fluidized bed is widely employed in coating of pellets and tablets, drying and granulation processes [10], [11], [12]. The character of high heat and mass transfer efficiency between droplets and particles for Wurster fluidized bed perfectly fulfils the requirement of wastewater evaporation. In the novel evaporation tower technology, inert particles are set in the bottom of evaporation tower and fluidized by heating air as the form of Wurster fluidized bed. Droplets are absorbed on the surface of inert particles when droplet-particle collision occurs and carried into inner circulation of Wurster fluidized bed to increase residence time. Also, the strong mixing of gas-solid increases heat transfer efficiency [13]. The handle of salinities left is a difficulty for other desulfurization process, while it’s easy to remove them in the fluidized bed because violent particle collisions will grind off absorbed salinities and heating air can carry out them to dust filter to collect.

In this paper, computational particle fluid dynamics (CPFD) was applied to investigate inner gas-solid-liquid flow field in evaporation tower and heat state experiment was carried to verify evaporation effect. Based on simulation results, an industrial equipment designed for CFB desulfurization wastewater was put forward.

CPFD Model

In this research, numerical simulation is based on Barracuda Virtual Reactor solver using CPFD method. CPFD is a kind of Eulerian–Lagrangian approach for fluid and particles. In the particle tracking, the Multiphase Particle-In-Cell (MP-PIC) algorithm is applied, which is suitable for dense phase particle flow. Turbulence model of Barracuda is large eddy method. The Eulerian and Largrangian equations used in CPFD model are summarized in Table. 1.

Table 1 Eulerian and Largrangian equations used in simulation

Eulerian equations for fluid

Continuum equation

$$\frac{\partial(\varepsilon_{\mathrm{g}}\rho_{\mathrm{g}})}{\partial t}+\nabla\cdot(\varepsilon_{\mathrm{g}}\rho_{\mathrm{g}}\mathbf{v}_{\mathrm{g}})=\delta\dot{m} \tag{1}$$

Momentum equation

$$\frac{\partial(\varepsilon_{\mathrm{g}}\rho_{\mathrm{g}}\mathbf{v}_{\mathrm{g}})}{\partial t}+\nabla\cdot(\varepsilon_{\mathrm{g}}\rho_{\mathrm{g}}\mathbf{v}_{\mathrm{g}}\mathbf{v}_{\mathrm{g}})=-\varepsilon_{\mathrm{g}}\nabla p+\nabla\cdot\boldsymbol{\tau}_{\mathrm{g}}+\varepsilon_{\mathrm{g}}\rho_{\mathrm{g}}\mathbf{g}-\mathbf{F} \tag{2}$$

Transport equation of specie i

$$\frac{\partial(\varepsilon_{\mathrm{g}}\rho_{\mathrm{g}}Y_{\mathrm{g},i})}{\partial t}+\nabla\cdot(\varepsilon_{\mathrm{g}}\rho_{\mathrm{g}}Y_{\mathrm{g},i}\mathbf{v}_{\mathrm{g}})=\nabla\cdot(\varepsilon_{\mathrm{g}}\rho_{\mathrm{g}}D\nabla Y_{\mathrm{g},i})+\delta\dot{m}_i \tag{3}$$

Energy equation

$$\frac{\partial(\varepsilon_{\mathrm{g}}\rho_{\mathrm{g}}h_{\mathrm{g}})}{\partial t}+\nabla\cdot(\varepsilon_{\mathrm{g}}\rho_{\mathrm{g}}h_{\mathrm{g}}\mathbf{v}_{\mathrm{g}})=\varepsilon_{\mathrm{g}}(\frac{\delta p}{\delta t}+\mathbf{v}_{\mathrm{g}}\cdot\nabla p)+\varphi+\dot{Q}-\nabla\cdot(\varepsilon_{\mathrm{g}}q)+S_h+\dot{q}_D \tag{4}$$

For solid phase, the distribution of particle is described by probability function $f(\mathbf{x},\mathbf{v}_{\mathrm{p}},\rho_{\mathrm{p}},V_{\mathrm{p}},t)$, where $\mathbf{x}$, $\mathbf{v}_{\mathrm{p}}$, ρ_{p}, V_{p} are particle spatial position, velocity, density and volume respectively, and t is current time. The transport equation for f is:

$$\frac{\partial f}{\partial t}+\nabla_{\mathbf{x}}\cdot(\mathbf{v}_{\mathrm{p}}f)+\nabla_{\mathbf{v}_{\mathrm{p}}}\cdot(\mathbf{A}f)=\frac{f_{\mathrm{D}}-f}{\tau_{\mathrm{D}}} \tag{5}$$

where $\mathbf{A}$ is the particle acceleration; f_{D} is the PDF for the local mass-averaged particle velocity and τ_{D} is the collision damping time.

$$\mathbf{A}=\frac{\mathrm{d}\mathbf{v}_{\mathrm{p}}}{\mathrm{dt}}=D_{\mathrm{p}}(\mathbf{v}_{\mathrm{g}}-\mathbf{v}_{\mathrm{p}})-\frac{1}{\rho_{\mathrm{p}}}\nabla p+\mathbf{g}-\frac{1}{\varepsilon_{\mathrm{p}}\rho_{\mathrm{p}}}\nabla\cdot\boldsymbol{\tau}_{\mathrm{p}} \tag{6}$$

where D_{p} is calculated by Wen-Yu model [14] and $\boldsymbol{\tau}_{\mathrm{p}}$ represents particle normal stress and can be calculated by:

$$\boldsymbol{\tau}_{\mathrm{p}}=\frac{p_{\mathrm{s}}\varepsilon_{\mathrm{p}}^{\beta}}{\max[(\varepsilon_{\mathrm{cp}}-\varepsilon_{\mathrm{p}}),\zeta(1-\varepsilon_{\mathrm{p}})]} \tag{8}$$

where p_{s} depends on material parameter, $\beta=2\sim5$ is a recommend parameter in the model, $\varepsilon_{\mathrm{cp}}$ is the particle packing limit and ζ is a small number to eliminate singularity.

So the particle volume fraction can be calculated by

$$\varepsilon_{\mathrm{p}}=-\iiint fV_{\mathrm{p}}dV_{\mathrm{p}}d\rho_{\mathrm{p}}dv_{\mathrm{p}} \tag{9}$$

Besides, droplet evaporation is represented by chemical reaction and reaction rate is:

$$r_{\mathrm{evaporation}}=\frac{-0.9093T_{\mathrm{p}}^{0.5}\exp(-4822.21/T_{\mathrm{p}})\frac{A_{\mathrm{p}}}{d_{\mathrm{p}}}+1.8215\times10^{-10}T_{\mathrm{p}}^{1.5}\frac{A_{\mathrm{p}}}{d_{\mathrm{p}}}C_{\mathrm{H_2O,bulk}}}{1+9909.6T_{\mathrm{p}}^{-1.5}\exp(-4822.21/T_{\mathrm{p}})\frac{A_{\mathrm{p}}}{m_{\mathrm{p}}d_{\mathrm{p}}}} \tag{10}$$

Simulation Setup

Fig. 1 shows the schematic diagram of simulation object, which is 1:1 to industrial design and all the simulation setup corresponds with practical condition. The simulation object consists of a cone section and a cylinder section. The former one makes spouted particles easier to come back to bottom of tower and the cylinder section is to give droplets enough time to evaporate. The diameter of the bottom and top circle surface is 1 m and 1.35 m respectively and the height of cone section and cylinder section is 1 m and 3 m. Three nozzles were evenly distributed in the circumferential direction with the distributed height of 0.6 m and insert depth of 0.3 m. Slit nozzle is selected and 6 slits are evenly located in the direction of length.

Meanwhile, there is an inclination of 15 degrees to make wastewater injected into center of tower. Initially, inert particles lay on the bottom of tower with accumulation height of 0.24 m.

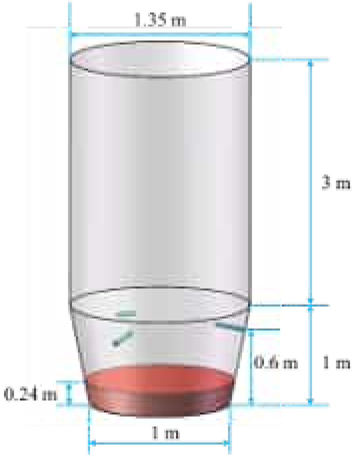

Fig. 1 3D schematic diagram of simulation object

The boundary condition of top surface is pressure boundary condition with atmosphere pressure and wastewater droplets are set as injection boundary condition with the flow rate of 0.104 kg/s and the injection velocity of 5 m/s. Inlet and outlet temperature of heating air is 240 ^{o}C and 160 ^{o}C respectively, so the amount of aeration is 1×10^4 Nm^3/h and average air velocity is 6 m/s which are calculated by heat balance. In practical equipment, heating air is supplied into evaporation tower through air distributor, thus the boundary condition of bottom surface is chosen as injection conditions with 9400 injection hole. In order to constitute particle inner circulation, the central area with 0.3 m diameter in the bottom surface is set as larger air supplement per area. The time step is set as 1×10^{-4} s and total simulation time is 10 s. The mesh number is set as 2×10^5.

Droplet evaporation is realized by chemical reaction, in which evaporation rate can be presented by the formulation proposed by Chen et al. [15] (as shown in eq. 9). Droplet absorption is also presented by chemical reaction. When there is a collision between inert particle and droplet, the reaction happens and water transfer from droplet to particle. The absorbed water still evaporates on the particle surface following the relationship of eq. 9.

Results and Discussion

3.1 Gas-solid-droplet Flow Field in Evaporation Tower

Initially, gas-solid flow field is considered and droplet evaporation and absorption are ignored. Fig 2 shows flow state at longitudinal section in different moment and droplet is injected into evaporation tower at 0.5 s moment.

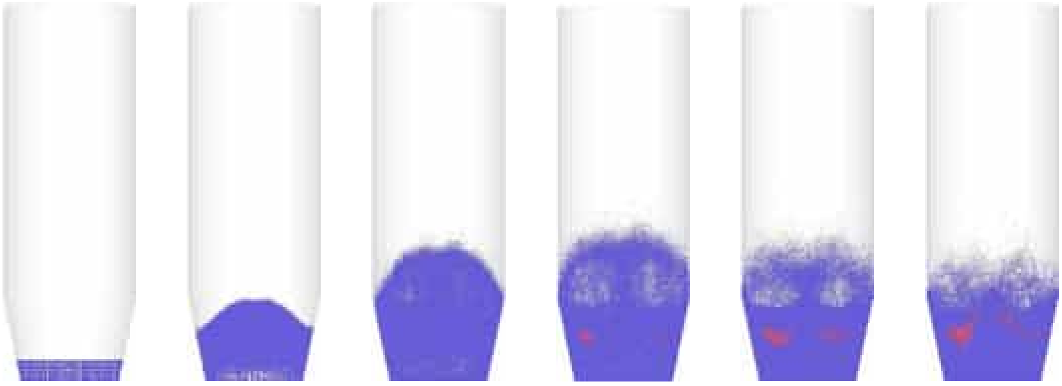

t = 0s t = 0.2s t = 0.4s t = 0.6s t = 0.7s t = 0.8s

Fig 2. Gas-solid flow field in first one second

The figure shows that the aeration strategy that supply central part higher wind supply ratio constitutes Wurster fluidized bed flow structure, in which central part of fluidized inert particles has higher injection height and then scatters around and slide down to the bottom along the side wall. The insert depth of nozzles is lower than the depth of slide down part, so that injected droplets are surrounded by particles and further carried down to the bottom joining particle inner circulation, which increases droplets residence time.

3.2 Wastewater Evaporation Flow Field

Droplet evaporation and absorption in the form of chemical reactions are added in this part. Considering that the amount of droplet injection and evaporation discharge are less compared with the amount of inert particles and aeration supply, the influence of droplet on the solids and gas flow field is negligible. The key to evaluate the evaporation tower is droplet evaporation efficiency, which can be depicted by the ratio of the mass of wastewater evaporation and total wastewater injection. The amount of escaped droplet should be decreased to keep high evaporation efficiency. Fig.3 indicates the outlet mass of droplet and water vapor in 10 seconds. The reason why the amount of outlet water vapor is nearly zero at first one second is because it need time for droplets to evaporate and for vapor to escape evaporation tower. That the increase of vapor outlet mass is nearly linear represents stable evaporation rate of wastewater. The line of droplet outlet mass has a much lower growth rate, which reveals droplet leakage is little compared with evaporation mass.

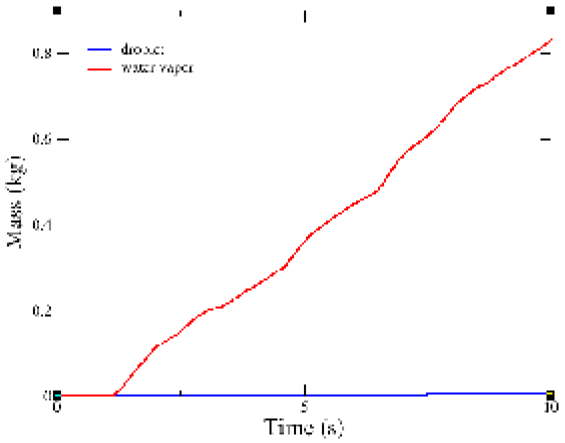

Fig.3 the mass of outlet droplet and water vapor

Industrial Equipment Design

Industrial desulfurization wastewater dryer equipment using structure described above will be established in the end of this year. CPFD simulation results is used as a reference and to optimize structure parameters.

Conclusions

In this paper, a novel evaporation tower structure dealing with desulfurization wastewater using Wurster fluidized bed was put forward. Inert particles cycling in the tower can absorb injected wastewater droplets to increase its residence time and strong gas-solid mixing in Wurster fluidized bed can enhance heat transfer between heating air and absorbed wastewater. After wastewater finishes evaporating, salinities stay on the particle surface which will be grinded off by particle collisions and carried out by heating air.

CPFD simulation was used to investigate flow state and evaporation efficiency of the novel evaporation tower. The gas-solid flow field was researched firstly and the simulation results showed the constitution of Wurster fluidized bed inner circulation, which is beneficial to increase droplet residence time. The evaporation efficiency defined by the ratio of vapor mass outlet and total wastewater injection mass was approaching 100%, which indicates great wastewater handling effect.

Based on knowledge about flow state in evaporation tower derived from CPFD simulation, a design scheme was put forward used in desulfurization wastewater treatment process of industrial circulating fluidized bed. The design was finished and industrial equipment would build up later.

Acknowledgements

This study was financial supported by C9 League Science and Technology Cooperation Project (201903D421009) and Heilongjiang Key Science and Technology project (CG18A002).

References

[1] Jr-Tsung Huang. Sulfur dioxide (SO2) emissions and government spending on environmental protection in China - Evidence from spatial econometric analysis. Journal of Cleaner Production. 2018, 175, 431-441

[2] Jie Zhu, Shi-chao Ye, Jie Bai, et al. A concise algorithm for calculating absorption height in spray tower for wet limestone–gypsum flue gas desulfurization. Fuel Processing Technology. 2019, 129, 15-23

[3] Hamed Azizi Namaghi, Mahdi Pourafshari Chenar, Ali Haghighi Asl, et al. Ultra-desulfurization of sulfur recovery unit wastewater using thin film nanocomposite membrane. Separation and Purification Technology. 2019, 221, 211-225.

[4] Zhengxing Liang, Li Zhang, Zhongqing Yang, et al. The effect of solid particles on the evaporation and crystallization processes of the desulfurization wastewater droplet. Applied Thermal Engineering. 2018, 134, 141-151

[5] Xian Zhang, Chunsong Ye, Kewu Pi, et al. Sustainable treatment of desulfurization wastewater by ion exchange and bipolar membrane electrodialysis hybrid technology. Separation and Purification Technology. 2019, 211, 330-339

[6] Muhammad Yaqub, Wontae Lee. Zero-liquid discharge (ZLD) technology for resource recovery from wastewater: A review. Science of The Total Environment. 2019, 681, 551-563

[7] Ma Shuangchen, Chai Jin, Chen Gongda, et al. Research on desulfurization wastewater evaporation: Present and future perspectives. Renewable and Sustainable Energy Reviews. 2016, 58, 1143-1151.

[8] Ma, SC, Chai J, Wu K, et al. Experimental research on bypass evaporation tower technology for zero liquid discharge of desulfurization wastewater. Environmental Technology. 2019, 40, 2715-2725.

[9] Chunxi Li, Zhennan Jia, Xuemin Ye, et al. Simulation on deacidification performance of waste incinerator flue gas by rotating spray drying. Energy. 2018, 152, 652-665.

[10] H. Q. Che, M. Wu, J. M. Ye. Monitoring a lab-scale wurster type fluidized bed process by electrical capacitance tomography. Flow Measurement and Instrumentation. 2018, 62, 223-234.

[11] Rui Correia, Bruna Barbon Paulo, Ana Silvia Prata. Fluid dynamics performance of phase change material particles in a Wurster spout–fluid bed. Particuology. 2019, 42, 163-175.

[12] Cheuk-Yui Leung, Andrea N. Trementozzi, Yiqing Lin. Enteric coating of micron-size drug particles through a Würster fluid-bed process. Powder Technology. 2017, 317, 247-252.

[13] Liang Li, Johan Remmelgas, Berend G. M. van Wachem. Residence time distributions of different size particles in the spray zone of a Wurster fluid bed studied using DEM-CFD. Powder Technology. 2015, 280, 124-134.

[14] Qinggong Wang, Hairui Yang, Peining Wang, et al. Application of CPFD method in the simulation of a circulating fluidized bed with a loop seal, part I—Determination of modeling parameters. Powder Technology, 2014, 253: 814-821.

[15] G.Q. Chen, J.H. Gao, Z.R. Gong. Numerical simulation and experimental study on evaporation characteristics in multi-spouted bed. J Environ Eng. 2019, 06, 79-84. (in Chinese)

DEVELOPMENT AND VALIDATION OF A STEADY FLOWSHEET MODEL FOR A SUPERCRITICAL CIRCULATING FLUIDIZED BED BOILER

Shahong Zhu, Man Zhang, Hairui Yang*, Junfu Lyu

Tsinghua University, Department of Energy and Power Engineering, Key Laboratory for Thermal Science and Power Engineering of Ministry Education, State Key Laboratory of Power Systems, Beijing, 100084, China

* Email: yhr@mail.tsinghua.edu.cn

ABSTRACT

The circulating fluidized bed (CFB) boiler unit is highly recommended in peak shaving for its wide load regulating range compared with the pulverized coal (PC) boiler unit. Therefore, the dynamic model of the CFB boiler has become a hot research topic in recent years. In this paper, a steady state model of a supercritical CFB boiler was developed in the Aspen Plus based on the sequential modular approach to lay foundation to the future dynamic model. It should be noted that in the CFB boiler, the hydrodynamic parameters changed with the operation parameters and in turn influenced the heat transfer coefficient between the furnace and the working substance.Thus, the dynamic overall heat transfer coefficient of the water wall, was further defined by a Fortran subroutine. This model was then validated by a 350 MWe supercritical CFB boiler and was proved of reliable accuracy. Based on this model, the influences of the basic input parameters were analyzed.

Key words: Aspen, supercritical CFB boiler, flowsheet model, heat transfer coefficient

1. Introduction

With the rising of renewable energy system, the traditional power system is required to operate in lower load but obtain higher operational flexibility to balance the electrical supplies and demands due to the intermittent and cyclical features of renewable energy system. The circulating fluidized bed (CFB) boiler unit is highly recommended in peak shaving for its wide load regulating range compared with the pulverized coal (PC) boiler unit. Thereinto, the dynamic characteristic of the CFB boiler unit has become a hot research topic in recent years. The dynamic model of PC boiler unit is quite mature while the dynamic model of CFB boiler unit remains to be controversial since the dynamic flowsheet model of CFB boiler is more complex due to the fluidization characteristics. Similarly, in a CFB boiler, the characteristics depend on the other components largely as well since the temperature of the primary air, secondary air and feed water is determined by the flue gas in the tail flue.

Aspen Plus is widely accepted in the steady state flowsheet simulation due to its user-friendly interfaces, complete built-in physical property parameters database and wide flexibility to user defined models integrated with Fortran. Moreover, based on the steady state model, a dynamic model can be built in Aspen dynamics. However, the literature of CFB boiler flowsheet simulation is quite limited. PC power plants flowsheet models are more widely developed and can provide references to the model of the CFB boiler. It can be found in Parikshit Sarda (2018), R. Sotudeh-GHarebaagh (1995) and Alobaid (2014). The main differences between the CFB boiler and the PC boiler are the flow regime and the large amount of bed materials. Moreover, in the dynamic model, the hydrodynamic parameters changed with the operation parameters and in turn influenced the heat transfer coefficient between the furnace and the working substance. Thus, considering the future dynamic model, the overall heat transfer coefficient of the water wall cannot be assumed as a constant parameter in this steady model as most researchers used to do. Above all, this paper developed a steady flowsheet model of a 350 MWe CFB boiler which laid foundation of the further dynamic model. Based on this model, the influences of the basic input parameters were analyzed.

2. CFB Boiler Configuration

The structure of the 350 Mwe Supercritical CFB boiler is shown in Fig.1.

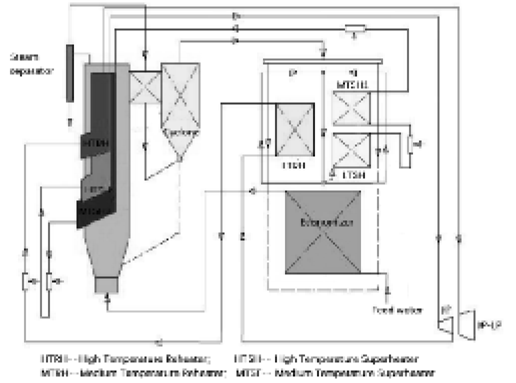

Figure 1 Structral diagram of the 350 MWe CFB boiler

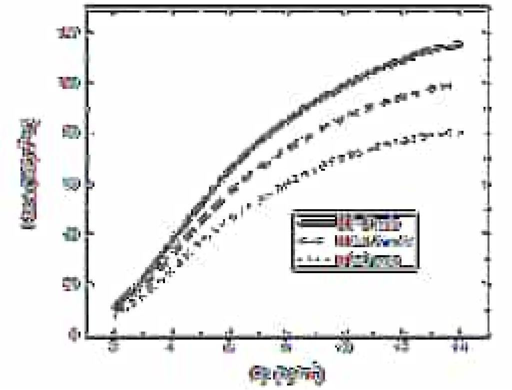

Figure 2 Relations between H_{con}^{ext} and C_p

The proximate analysis and ultimate analysis of coal used are listed in Tab.1.

Table 1 Proximate analysis and ultimate analysis of coal sample

	M_{ad}/%	V_{ad}/%	A_{ad}/%	FC_{ad}/%	C_{ad}/%	H_{ad}/%	O_{ad}/%	N_{ad}/%	S_{ad}/%
Coal	8.88	10.06	38.05	43.01	44.69	2.38	3.32	0.67	2.01

3. Model Description

To model the CFB boiler combustion using ASPEN Plus, the overall process must be divided into two sub-processes, the rapid pyrolysis process and the combustion of pyrolysis products process. Specially, before pyrolysis process, since the coal cannot be described by a molecular formula due to its structural complexity and composition diversity, it is recommended by Aspen Plus that the coal can be considered as a mixture composed of a series of stable elementary substances, such as carbon, hydrogen, oxygen, nitrogen, sulfur, and ash according to the ultimate analysis and proximate analysis. This decomposition process can be accomplished by a RSTOIC module integrated with Fortran subroutines to calculate the yield of each elementary substance. Then the pyrosis process can be accomplished by a RYIELD module. The major pyrolysis products of coal are gaseous volatile matters (CH_4, H_2, CO_2, CO, H_2O, and tar) and char. The yield of volatile matters can be calculated from Eq.(1)- Eq.(3), can be found in Gungor A (2008).

$$V_{yield} = VM - \alpha - \beta \tag{1}$$

$$\alpha = \exp(26.41 - 3.96 \ln T + 1.15VM) \tag{2}$$

$$\beta = 0.2(VM - 10.9) \tag{3}$$

The mass fraction w_i of each component in volatile matters from coal rapid pyrolysis can be calculated by Eq.(4)- Eq.(8)

$$w_{CH_4} = 0.201 - 0.469(VM/100) + 0.241(VM/100)^2 \tag{4}$$

$$w_{H_2} = 0.157 - 0.868(VM/100) + 1.388(VM/100)^2 \tag{5}$$

$$w_{CO_2} = 0.135 - 0.900(VM/100) + 1.906(VM/100)^2 \tag{6}$$

$$w_{H_2O} = 0.409 - 2.389(VM/100) + 4.554(VM/100)^2 \tag{7}$$

$$w_{Tar} = -0.325 + 7.279(VM/100) - 12.880(VM/100)^2 \tag{8}$$

Then, the combustion process of pyrolysis products can be modelled by the GIBBS module. The GIBBS module is a thermodynamic equilibrium reactor. Since the injection of secondary air in the CFB boiler roughly divides the boiler into a dense zone and a dilute zone, the combustion process in the furnace is simulated by two GIBBS modules.

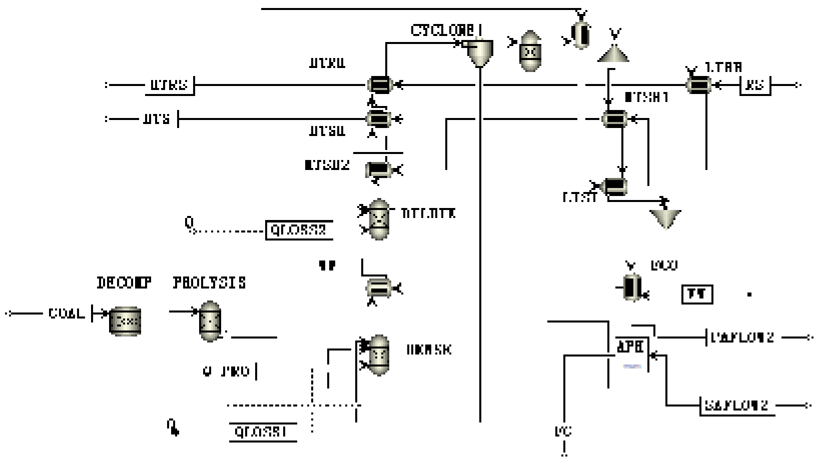

Figure 3 Aspen Plus flowsheet of a CFB boiler

After combustion, the high temperature flue gas flows through a series of heat exchangers (water wall, secondary medium temperature superheater, high temperature superheater and high temperature reheater). Then, a SEPARATOR module is used to model the cyclone. Considering the post combustion in the cyclone, a GIBBS module is applied. Finally, the flue gas reaches the tail flue and is further cooled by the tail heating surfaces (primary medium temperature superheater, low temperature reheater, low temperature superheater, economizer and air preheaters). Additionally, the data of heaters like their types and sizes are provided from the 350 MWe CFB boiler.

For the water side, the feed water successively passes through economizer, water wall, low temperature superheater, medium temperature superheater and high temperature superheater. The low temperature reheat steam successively passes through the low temperature reheater and high temperature reheater. The overall Aspen Plus flowsheet of the CFB boiler is depicted by Fig.3.

As for the user-defined overall heat transfer coefficient of the water wall, it is accomplished by embeding Fortran subroutine and can be calculated as follows.

$$\frac{1}{H_{bt}^{0}}=\frac{1}{H_{con}^{ext}+H_{rad}^{ext}}+\frac{1}{H_{\mathrm{int}}}+\frac{e}{\lambda} \tag{9}$$

Where H_{bt}^{0} is overall heat transfer coefficient of the water wall, H_{con}^{ext} is convective heat transfer coefficient, H_{rad}^{ext} is radiative heat transfer coefficient, H_{int} is inter water heat transfer coefficient, e is the thickness of water wall pipes, λ is its heat conductivity coefficient. $\frac{1}{H_{int}}$ can be neglected in supercritical cases. H_{con}^{ext} is the function of flue gas velocity u_f and suspended sediment concentration C_p. An industry design diagram can be applied to calculate H_{con}^{ext} as shown in Fig.2.

Since C_p used is the average suspended sediment concentration and can be calculated by Eq.(10). It can be found in Man Zhang (2005)

$$C_p=\int_{0.16}^{1} 14\frac{G_s}{u_f}\exp(-2.61\frac{h}{H})d(\frac{h}{H})=3.138\frac{G_s}{u_f} \tag{10}$$

H_{rad}^{ext} can be calculated by Eq.(11).

$$H_{rad}^{ext}=\varepsilon\sigma\frac{T_{bed}^{4}-T_{wall}^{4}}{T_{bed}-T_{wall}} \tag{11}$$

Where ε is the flame emissivity, σ is the Boltzmann constant, T_{bed} is the bed temperature and is simplified equal to the average temperature of flue gas, T_{wall} is the temperature of wall and is simplified equal to the average temperature of steam in the water wall.

The flame emissivity can be influenced by the composition of the flue gas and its detailed calculation method can be referred from Junfu Lyu's paper (2002) and will not be listed due to the limit of the paper pages.

4. Results and Discussions

This model is validated by the operation data of BMCR case. The calculation results are listed in Tab.2. As can be observed from the results, the error is far below 15% within the industrial measuring errors. Thus, this steady state model has high accuracy is proved of reliable accuracy.

Table 2 Validation of the Aspen Plus model

	Furnace exit gas temperature	Air preheater exit gas temperature	Superheated steam temperature	Reheated steam temperature
Model (K)	1179.15	418.15	845.15	839.15

Operation (K)	1160.15	408.15	844.15	841.15
Error	6.24%	7.41%	0.17%	-0.35%

Based on this steady state flowsheet model, the dynamic model can be further accomplished in Aspen Dynamics. In order to give some reasonable operation suggestions at this stage, the influences of air temperature, water temperature, flow rate of primary air and flow rate of secondary air are investigated.

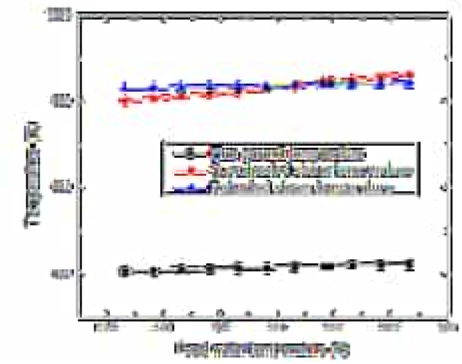

Figure 4 Influence of feed water temperature

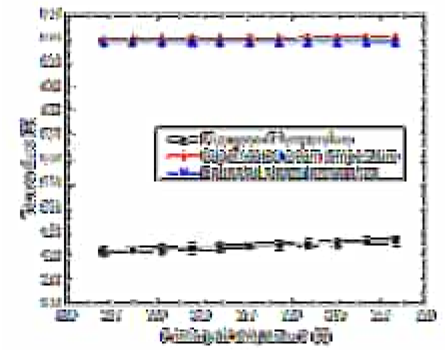

Figure 5 Influence of primary air temperature

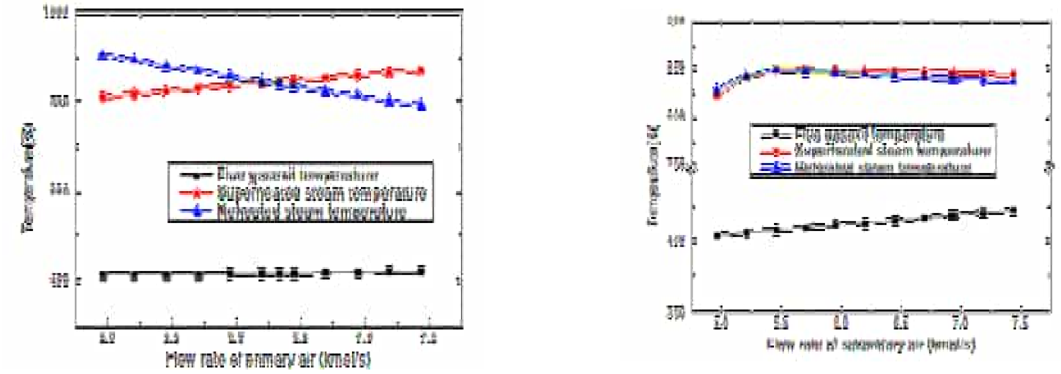

(a) Primary air flow rate

(b) Secondary air flow rate

Figure 6 Influence of primary air and secondary air flow rate

Fig.4 indicates that superheated steam temperature is more sensitive to the feed water temperature. The increase of feed water temperature leads to liner increase of flue gas exit temperature, superheated steam temperature and reheated steam temperature. The thermal economic benefit remains to be studied after combining the turbine system model which is under work. The primary air temperature has little influence to superheated steam temperature and reheated steam temperature as can be observed in Fig.5. Thus, the steam air heater is not suggested applied in this boiler from the aspect of thermal economy. Fig.6 shows that the superheated steam temperature increases with the increase with the primary air flow rate while reheated steam temperature decreases. It indicates that the superheated steam is more prone to be overheated thus its desuperheating method should be emphasized. The superheated steam temperature increases then decreases with the increase of secondary air flow rate, similar to the reheated steam temperature. The nonlinear results proved the complexity of the boiler system. Thus, when adjusting the coal-air ratio, the ratio of primary air flow rate and secondary air flow rate also has a considerable effect on the results.

5. Conclusions

The main work of this paper is building a steady state model of a supercritical CFB boiler considering the user defined heat transfer coefficient, which laid foundation to the future dynamic model. Based on the steady state model, basic influences of the input parameters are analyzed. The increase of feed water temperature leads to liner increase of superheated steam temperature and reheated steam temperature. The superheated steam temperature increases with the increase with the primary air flow rate while reheated steam temperature decreases. The superheated steam temperature increases then decreases with the increase of secondary air flow rate, similar to the reheated steam temperature.

When transferring into the dynamic model, future work should be focused on the detailed reaction kinetics and the gas-solid flow hydrodynamics coupled by the user defined Fortran subroutine to have more accuracy on the flue gas composition.

Acknowledgments

Financial supports of the National Natural Science Foundation of China (U1810126) are gratefully acknowledged.

Notation

V_{yield}	Yield of volatile matter during pyrolysis of coal, kg/(100 kg coal)	VM	Content of volatile matter in coal, kg/(100 kg coal)
H_{bt}^{0}	Overall heat transfer coefficient, W/(m^2·K)	H_{con}^{ext}	Convective heat transfer coefficient, W/(m^2·K)
e	Thickness of water wall pipes, m	λ	Heat conductivity coefficient, W/(m·K)
C_p	Suspended sediment concentration, kg/m^3	G_s	Mass flux of solid particles, kg/(s·m$^{2)}$
σ	Boltzmann constant, J/K	T	Absolute temperature, K
ε	Flame emissivity	u_f	Gas superficial velocity, m^3 /s
H_{rad}^{ext}	Radiative heat transfer coefficient, W/(m^2·K)	w_i	Mass fraction of component i in pyrolysis gas

References

Falah Alobaid, Karl Karner, Jörg Belz, et al. Numerical and experimental study of a heat recovery steam generator during start-up procedure. Energy, 2014,64,1057-1070.

Basu, P. Combustion of coal in circulating fluidized-bed boilers: a review. Chemical Engineering Science, 1999, 54 (22), 5547–5557.

Gungor, A., Eskin, N. Two-dimensional coal combustion modeling of CFB. International Journal of Thermal Sciences, 2008, 47 (2), 157–174.

Zhang Man, Bie Rushan. Heat Transfer Coefficient of Water Wall in Circulating Fluidized Bed Boiler. Boiler Manfacturing, 2005(02),32-33+58.

Lyu Junfu, Zhang Jiansheng, Yue Guangxi, et al. Heat transfer coefficient calculation method of heater in circulating fluidized bed furnace. Heat Transfer-Asian Research, 2002,31(7),540-550.

Parikshit Sarda, Elijah Hedrick, Katherine Reynolds, et al. Development of a Dynamic Model and Control System for Load-Following Studies of Supercritical Pulverized Coal Power Plants. Process, 2018, 6(11), 226.

STOCHASTIC SIMULATION OF SPRAY AGGLOMERATION PROCESS IN A CONTINUOUSLY OPERATED HORIZONTAL FLUIDIZED BED BY MONTE CARLO METHOD

Jiajie Du [1*], Kaicheng Chen[1], Andreas Bück [2], Evangelos Tsotsas[1]

[1]*Otto von Guericke University Magdeburg, Chair of Thermal Process Engineering, Institute of Process Engineering, Universitaetspl 2, Magdeburg, 39106, Germany*
[2]*Friedrich-Alexander University Erlangen-Nuremberg, Solids Processing Group, Institute of Particle Technology, Cauerstrasse 4, Erlangen, 91058, Germany*

*Email: *jiajie.du@ovgu.de*

Abstract

In this work, the usage of event-driven constant volume Monte Carlo (CVMC) method is extended from the batch operated process to a continuously operated process by continuously adding and removing particles from the simulation boxes. To control the particle residence time distribution, backflow cell model is coupled with the Monte Carlo model. The feed rate is varied, and the results from experiments and simulations are compared to verify the model.

Introduction

Size enlargement process is widely used in chemical, pharmaceutical and food industry to enhance the properties of powders such as size, flow behavior, rewettability and density (Ennis, 1996). In the agglomeration process, it is commonly done by dispersing liquid binders onto the powder bed and forming inter-particulate bonds. One of the most successfully applied equipment for this propose is the fluidized bed spray agglomerator. In such equipment, fluidized particles are wetted by spraying a liquid; agglomeration occurs when a wet particle collides with another particle forming initially a liquid bridge which then solidifies by drying. The process can be done batch-wise or in continuous mode. Compared to the batch-wise process, the continuous mode has the advantages of high throughput, low labor requirement and less downtime.

However, when we turn to the continuously operated agglomeration process, much less work has been done compared to the batch operated process. Schmidt et al. (2018) and Strenzke et al. (2018) studied the effect of different materials and different process parameters by using a cylindrical fluidized bed with a downpipe installed inside the bed which can discharge the products continuously during the process experimentally. To simulate the continuous process, only a PBE model developed by Golovin et al. (2018) which is strongly depends on the results of experiment is available. To extend the usage of Monte Carlo (MC) model is desired.

In this paper, the MC model developed by Terrazas-Velarde et al. (2009) which was used to simulate the batch operated fluidized bed agglomeration process is used as the fundamental. By coupling the backflow cell model with the MC model, the continuous feed and discharge of particles from the simulation box during simulation is enabled.

Theory and Computational Method

In this study, the Constant Volume Monte Carlo method (CVMC) is used due to its better performance for processes governed by coalescence which has been suggested by Zaho et al., (2007). Meanwhile, this method can ensure the trace of particle residence time in the simulation box. As the particles in the simulation box agglomerate, the number of particles decreases. Once the number of the particles in the simulation box is less than half of the initial, a copy of the population is made and introduced into the simulation box. By periodical particle number regulation, the number of particle number can be controlled. CVMC is an event-driven method where first an event is chosen to happen, and then the simulation runs in time according to the interval necessary for the event. Here, the event is defined as a pairwise collision between two randomly chosen groups of particles. In the collision, two colliding particles are assumed to agglomerate when the collision is in a wet region, as well as when the agglomeration condition is satisfied. The agglomeration condition is given by

$$St_{coal} < St_{coal}{}^{*} \tag{1}$$

Eq. (1) is the widely used Stokes criterion developed by Ennis et al. (1991) where St_{coal} is the Stokes number given by

$$St_{coal} = \frac{2M_p u_c}{3\pi\mu_l d_p{}^2} \tag{2}$$

and $St_{coal}{}^{*}$ is the critical Stokes number defined by

$$St_{coal}{}^{*} = \left(1 + \frac{1}{e}\right) ln\left(\frac{h}{h_a}\right) \tag{3}$$

The Stokes criterion describes the ability of a binder layer at height h and viscosity μ_l to dissipate the collision energy of two colliding particles of diameter d_p and weight M_p at a collision velocity u_c. In the case of collision between particles of unequal size, a combined weight and diameter are used in the calculation (shown in Eq. (4) and Eq. (5)).

$$M_p = \frac{2M_1M_2}{M_1 + M_2} \tag{4}$$

$$D_p = \frac{2d_1d_2}{d_1 + d_2} \tag{5}$$

Here, the collision velocity u_c in Eq. (2) is assumed as a normally distributed quantity with standard deviation u_c = 0.1 m/s and mean $0.5u_0$.

To calculate the length of time step, inter-particle collision rate must be calculated. Here, the collision frequency f_c is defined as the number of collisions undergone by a single particle per unit time. an empirical correlation proposed by Buffiere et al. (2000) is used as

$$f_c = F_{coll}\left[1 - \left(\frac{\emptyset_{fix}}{\emptyset_{exp}}\right)\right]\left(\frac{\emptyset_{fix}}{\emptyset_{exp}}\right)^2 u_0 \tag{6}$$

Where u_0 is the superficial fluidization velocity, and $\emptyset_{exp}$ and $\emptyset_{fix}$ give the solid volume fraction of the expanded and fixed bed, respectively. Then length of time step for each collision can be calculated as

$$t_{step} = \frac{1}{f_c} \tag{7}$$

To calculate the number of added droplets in each event, the droplet addition rate γ which stands for the number of droplets per particle per unit time is defined here as

$$\gamma = \frac{\dot{m}_l}{m_{bed}}\left(\frac{\rho_p}{\rho_l}\right)\left(\frac{d_p}{d_d}\right)^3 \tag{8}$$

With the number of particles within the simulation box N_p and the droplet addition rate γ, the droplet addition time t_{ad} is defined as follows:

$$t_{ad} = \frac{1}{\gamma\ N_p} \tag{9}$$

Depositing of droplets on the particle surfaces is a complex phenomenon. Here, the assumption that the equilibrium shape of droplets is attained immediately after the collision of the droplets and particles. Meric et al. (1998) developed the equation to calculate the contact angle θ

$$a = \left(\frac{3\ V_d}{\pi}\ \frac{sin^3\ \theta}{2 - 3\,cos\,\theta + cos^3\,\theta}\right)^{1/3} \tag{10}$$

and

$$h = a\ \frac{1 - cos\,\theta}{sin\,\theta} \tag{11}$$

where V_d is the initial volume of the sprayed droplet, *a* is the base radius of the spherical cap and *h* is the maximum height of the deposited binder layer.

In the real process, the droplet addition and drying occur simultaneously and need to be included in the model. Terrazas-Velarde et al. (2009) derived a model from suitable mass balances coupled with the geometrical relationships which give the equilibrium shape of the deposited droplet on the particle. The expression for the reduction of the binder layer as a function of the time can be calculated by

$$h = h_o - \frac{2}{3}\,\frac{\rho_g}{\rho_l}\,\frac{\tilde{M}_l}{\tilde{M}_g}\ \frac{\beta}{1 - cos\,\theta}\ \frac{P_v{}^*}{P}\left[\frac{1}{1 - cos\,\theta} - \frac{1}{3}\right]^{-1} t \tag{12}$$

To control the particle exchange rate between different process compartments, the backflow model developed by Roemer et al. (1967) is employed here. The relationship between the reflux factor and Bodenstein number (Bo) can be shown as follows

$$\sigma^2 = \frac{1 + 2R}{N_{geo}} - \frac{2R(1 + R)}{N_{geo}^2}\left[1 - \left(\frac{R}{1 + R}\right)^{N_{geo}}\right] \tag{13}$$

and

$$\sigma^2 = \frac{2}{Bo^2}\left[Bo - 1 + e^{-Bo}\right] \tag{14}$$

where N_{geo} is the geometrical number of tanks, and *R* is the reflux factor.

By coupling this model with the MC model, the flow behavior of particles between different simulation boxes which stand for different operation compartments can be calculated. As shown in Fig.1, $\dot{N}p$ is the number of newly feed particles per unit time which is calculated according to the mean particle residence time. The number of simulation boxes can be adjusted according to the configuration of the experiment plant.

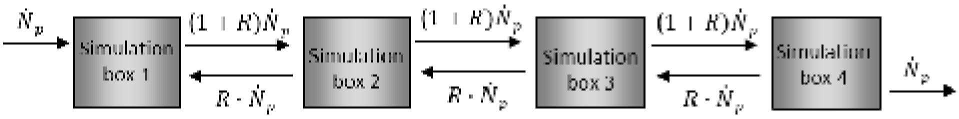

Fig.1. Status of particles flow between simulation boxes

The growth of particle size is a main indicator of agglomeration. However, the growth of particle size is indicated by the increase in number of per agglomerate. For better comparison, the relationship between number of primary particles per entity and agglomerate diameter is calculated by the equation newly derived by Singh et al. (2019) which are shown as follows.

$$D_{agg} = 1.291 \times D_p\left(\frac{N_{sp}}{k}\right)^{1/D_f} \tag{15}$$

with

$$k = 5.323 - 1.4802D_f \tag{16}$$

$$D_f = \left(0.0105 \times T_g\right) - (0.067 \times x_b) + 2.13 \tag{17}$$

where D_f is the fractal dimension, N_{sp} is the number of particles in single particle, and x_b is the binder mass fraction.

Experimental Study

In order to investigate the influence of feed rate and compare with the simulation results, two experiments varying the feed rate were carried out in a pilot horizontal fluidized bed (GF/Procell 20, Glatt GmbH) which is shown in Fig.2. Three two-fluid nozzles (type: model 940/3, Düsen-Schlick GmbH) are used to spray the binder in bed.

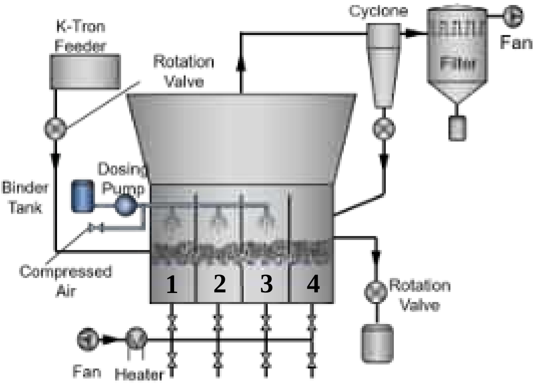

Fig.2. Scheme of horizontal fluidized bed plant

The particles used for the experiments were glass beads (Sigmund Lindner GmbH, Germany) with an average diameter of 200 µm. The binder used was hydroxy-propyl-methyl-cellulose (HPMC, trade name Pharmacoat 606, Shin-Etsus, Japan) water solution with mass fraction in 4 wt%. Outlet weir at the height of 135mm was used for both experiments.

Table 1 Experimental process parameters

Experiment	T_g [℃]	u_0 [m/s]	Spray rate [g/min]	Feed rate [g/min]
Exp.1	80	1	79	400
Exp.2	80	1	78	300

To start the experiment, the plant was heated up until the pre-set temperature has been reached. Afterwards, 5 kg of primary particles were fed in the bed simultaneously as the initial bed mass. At the same time, the inlet feeder and outlet rotary valve were started. When the particle flow rate at the outlet became equal to the feed rate and remained stable, the binder pump was turned on to start the spray. Samples were taken periodically from compartment 4, then analyzed offline by Camsizer. To measure the particle residence time distribution, tracers (the same glass beads coated with sodium benzoate) were injected into the bed via the filling tube after 80-90 minutes of the spray time. Then, the particle residence time distribution was measured by conductivity method and used in the simulation.

Results

In order to investigate the effect of particle feed rate, both experiments and simulations with different feed rates were carried out. Afterwards, the evolution of particle Sauter diameter of the samples taken in Compartment 4 is compared with the results from simulations. Meanwhile, the particle residence time distribution can be traced in the simulation and then compared with the experiment results.

Table 2 Summary of simulation parameters

Simulation	T_g [℃]	h_a *[mm]*	u_0 [m/s]	σ_{uc} [m/s]	Spray rate [g/min]	Mean residence time [s]	*Bo*	F_{Coll} *[1/m]*	θ [°]	d_d [µm]	*e*
Sim.1	80	0.01	1	0.1	79	1350	0.70	30	40	45	0.8
Sim.2	80	0.01	1	0.1	78	1740	0.45	30	40	45	0.8

The collision frequency pre-factor F_{Coll} is a parameter that can be adjusted to describe the collision behavior of a specific particle population. In this paper, the value is correlated with the result of a batch operated agglomeration experiment with similar parameters and keep constant in all simulations. Table 2 presents the main simulation parameters. The total particle number in the simulation boxes is 4000 (1000 each).

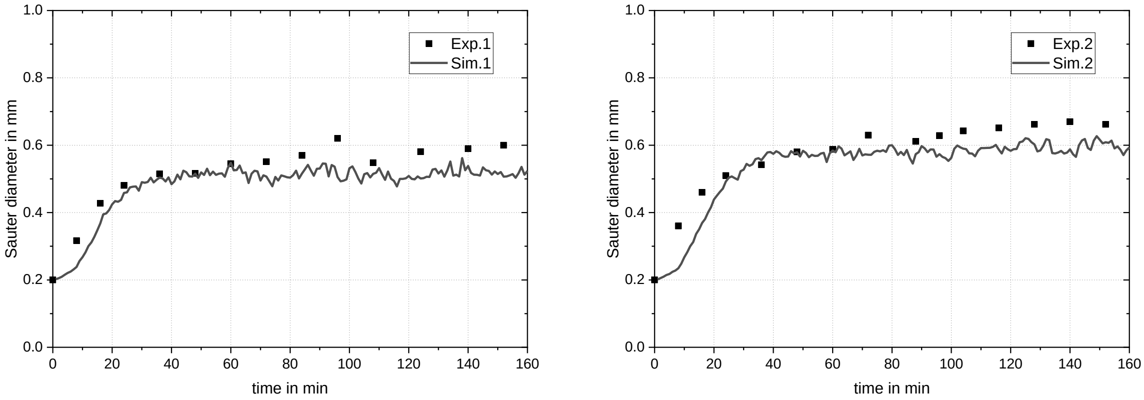

Fig.3. Comparison of the particle Sauter diameter from experiments and simulations (left: Exp.1 and Sim.1, right: Exp.2 and Sim.2)

Fig.3 shows the comparison of the results from experiments and simulations. In both experiments, we can see a fast growth of particle size in the first 20-30 minutes. Then, the growth rate decreases, and the particle size tends to be stable. Compare the result of Exp.1 and Exp.2, we can see the decrease in feed rate increases the particle size. It caused by the increase of mean particle residence time. Both the simulation results fit well with well the experiment results. The same tendency is seen in the simulation results. The model is able to predict the growth of particle size.

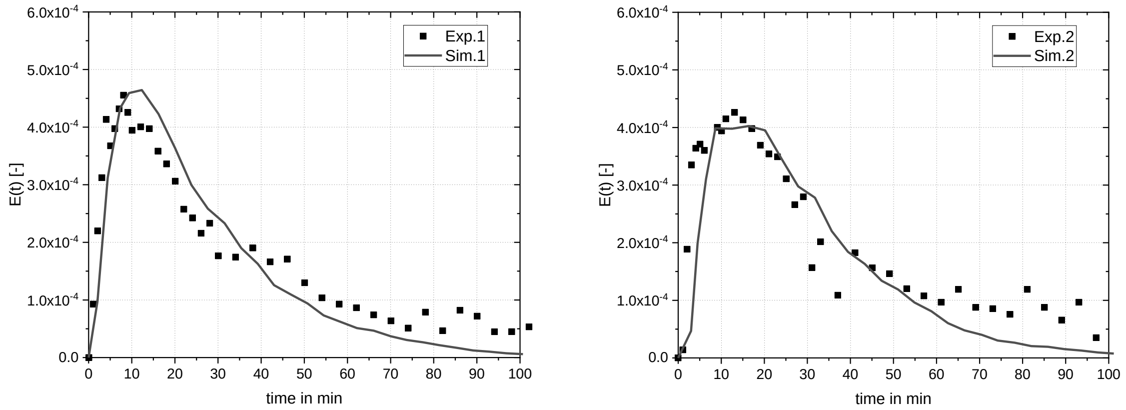

Fig.4. Comparison of the particle residence time distribution from experiments and simulations (left: Exp.1 and Sim.1, right: Exp.2 and Sim.2)

From Fig. 4, we can see by coupling the backflow model, the particle residence time distribution can be controlled which means the flow of the particles between different simulation boxes can also be controlled according to the data from experiments by this model.

Conclusions and Outlook

The usage previous MC model is extended to the continuously operated process by continuous adding and removing particles from simulation boxes. Future more, to control the flow of particles between different simulation boxes, the backflow model is coupled with the MC model. The results from simulation fit well with the results from experiments that decrease the particle feed rate will increase particle size. In future work, the change of bed mass and separation effect need to be included in the model.

Notation

a	base radius of spherical cap, m	d	diameter, m

D_f	fractal dimension, -
e	restitution coefficient, -
f_c	collision frequency, 1/s
F_{Coll}	collision frequency pre-factor, 1/m
h	binder layer thickness, m
h_a	height of particle surface asperities, m
k	prefactor, -
M	mass, kg
N	number, -
$\dot{N}p$	flow rate, -

P	pressure, Pa
P_v^*	saturation vapor pressure, Pa
St	Stokes number, -
t	time, s
T	temperature, °C
u_c	collision velocity, m/s
u_0	fluidization gas velocity, m/s
V	Volume, m^3
x_b	binder mass fraction, wt%

Greek letters

β	mass transfer coefficient, m/s
γ	droplet addition rate, 1/s
θ	contact angle, °
μ	viscosity, Pa s

σ_{uc}	standard deviation, collision velocity, m/s
ρ	density, kg/m^3
ϕ	solid volume fraction, -

Subscripts

b	binder
coal	coalescence
cr	critical
d	droplet
exp	expanded bed
fix	fixed bed
g	fluidization gas

sp	single particle
in	inlet
l	liquid
p	particle
0	initial
*	saturation
geo	geometry

References

Buffière, P., Moletta, R. Collision frequency and collisional particle pressure in three-phase fluidized beds. Chemical Engineering Science. 2000. 55(22), 5555–5563.

Ennis, B. J., Tardos, G., & Pfeffer, R. A microlevel-based characterization of granulation phenomena. Powder Technology. 1991. 65(1–3), 257–272

Ennis, B.J. Agglomeration and size enlargement. Session summary paper, Powder Technol. 1996. Vol. 88, 203-225

Golovin, I., Wegner, M., Strenzke, G., Tsotsas, E., Bück, A., Kienle, A., Palis, S. Influence of drying conditions on process properties and parameter identification for continuous fluidized bed spray agglomeration, Processes. 2019. September, 11–14

Meric, R.A., Erbil, H. Y. Evaporation of sessile drops on solid surfaces: Pseudospherical cap geometry, Langmuir. 1998. Vol. 14, 1915-1920

Roemer, M.H., Durbin, L.D. Transient Response and Moments Analysis of Backflow Cell Model for Flow Systems with Logitudinal Mixing. Industrial & Engineering Chemistry Fundamentals. 1967. Vol. 6, 120-129

Singh, A. K., Tsotsas, E. Stochastic model to simulate spray fluidized bed agglomeration: a morphological approach. Powder Technology. 2019. 355, 449–460

Schmidt, M. Process dynamics and structure formation in continuous spray fluidized bed process. PhD thesis, Otto von Guericke University Magdeburg, 2018

Strenzke, G., Golovin, I., Wegner, M., Palis, S., Bück, A., Kienle, A., Tsotsas, E. Influence of drying conditions on process properties and parameter identification for continuous fluidized bed spray agglomeration. In Proceedings of 21st International Drying Symposium, 2018. Valencia, Spain

Tan, H., Salman, A., and Hounslow, M. Kinetics of fluidised bed melt granulation, Part I: The effect of process variables. Chemical Engineering Science. 2006. 61(5), 1585-1601

Terrazas-Velarde, K., Peglow, M., Tsotsas, E. Stochastic simulation of agglomerate formation in fluidized bed spray drying: A micro-scale approach. Chemical Engineering Science. 2009. 64(11), 2631–2643

Zhao, H., Maisels, A., Matsoukas, T., & Zheng, C. Analysis of four Monte Carlo methods for the solution of population balances in dispersed systems. Powder Technology. 2007. 173(1), 38–50

ALGEBRAIC CLOSURE MODEL COUPLING THE PARTICLE CHARGE-VELOCITY COVARIANCE AND CHARGE VARIANCE IN GAS-SOLID FLOW WITH TRIBOLELECTRIC CHARGING

Carlos Montilla[1*], Renaud Ansart[1], Olivier Simonin[2]

[1]*Laboratoire de Génie Chimique, Université de Toulouse, CNRS, INPT, UPS, Toulouse. France*

[2]*Institut de Mécanique des Fluides de Toulouse, Université de Toulouse, CNRS, France*

*Email: *carlos.montillaestrella@toulouse-inp.fr*

Abstract

The triboelectric charging phenomenon is a well-known problem in many industrial configurations involving gas-solid flow systems. Although their effects have been experimentally studied for many years, the mathematical modeling of these configurations is still poorly understood. In the last years, some efforts have been made towards the development of an Euler-Euler model for gas-particle flows that takes into consideration the effect of the electrostatic force. However, a closure model is needed for the kinetic transport term. As a first approximation, all previous works have chosen to neglect the effect of the electric charge variance in their closure models. In this work, we present a closure model for the particle velocity-charge covariance that includes the effect of the charge variance. We use the kinetic theory of granular flows to derive the transport equations for both the particle velocity-charge covariance and the electric charge variance. Using some simplifying hypotheses, we obtain a linear system of equations that can be solved to obtain an algebraic closure model. Testing this model in a 1D system show that neglecting the electric charge variance can lead to an underestimation of the mean charge kinetic transport term. We also observe that the proposed model might lead to unphysical predictions and therefore it needs to be used very carefully.

Introduction

The generation of electrical charges can be undesirable for many industrial processes. There are safety hazards such as the risk of explosions due to a spark, wall sheeting, and the generation of an intense electric field. It is also known that the electrostatic force can have different effects on the dynamics of a gas-particle flow, such as: modification of the minimum fluidization velocity, the entrainment rate, and the heat transfer coefficient. (Hendrickson 2006; Miller & Logwinuk 1951).

Currently, some efforts have been made to add the electrostatic force to the existing Eulerian codes. Rokkam et al. (2010) developed a model in which the electrostatic effect is added as a body force in the solid momentum equation. Later, the same authors (Rokkam et al. 2013) tested this model in a fluidized bed reactor using ANSYS Fluent software. Their model was in good agreement with the experimental observations, especially concerning the radial segregation of the solid phase. In this approach, however, the electrical charge is an input parameter and remains fixed throughout the simulation. Recently, a more complex approach has been studied. This approach relies on the kinetic theory of rapid granular flow to derive a transport equation for the mean particle electric charge (Kolehmainen et al. 2018; Ray et al. 2019; Montilla et al. 2020). To fully close the transport equation for the mean particle electric charge, these works have chosen to neglect the effect of the charge variance on the transport of the electric charge due to the fluctuant particle velocity. In this work, we derive a closure model for the particle velocity-charge covariance accounting for the effect of the electric charge variance. We show that, under certain hypotheses, we can use the kinetic theory of rapid granular flow to derive a linear system of equations that can be solved to obtain an algebraic closure model for the particle velocity-charge covariance and the particle electric charge variance. We analyze the difference between this new model and the previous models already published in the literature.

Eulerian modeling of electrostatic phenomenon

Following an analogy with the statistical modeling of molecule velocity distribution in a gas, we can establish a Boltzmann like equation for the dispersed solid phase velocity distribution. From this equation, we can derive a transport equation for the average of any particle property $\phi(c_{p,i}, \xi_p)$ (Chapman & Cowling 1970):

$$\frac{\partial n_p\langle\phi\rangle}{\partial t}+\frac{\partial n_p\langle\phi c_{p,i}\rangle}{\partial x_i}-n_p\left\langle\frac{F_i}{m_p}\frac{\partial\phi}{\partial c_{p,i}}\right\rangle=\mathcal{C}(\phi) \tag{1}$$

Setting $\phi = \xi_p$ leads to the transport equation for the mean electric charge ($\langle\xi_p\rangle = Q_p$):

$$n_p\frac{\partial Q_p}{\partial t}+n_p\,U_{p,i}\frac{\partial Q_p}{\partial x_i}+\frac{\partial n_p\langle\xi'_{\mathrm{p}}c'_{p,i}\rangle}{\partial x_i}=\mathcal{C}(\xi_p) \tag{2}$$

The right-hand side of the equation accounts for the mean rate of change of the electric charge due to particle-particle collisions. Closure models for this term can be found in the literature (Kolehmainen et al. 2018; Montilla et al. 2020).

Closure model for the particle velocity-charge covariance

The other term that needs to be closed is the last term of the left-hand side of equation 2. This term accounts for the mean rate of transfer of electric charge due to particle fluctuant velocity. Previous works have chosen to derive an algebraic closure model neglecting the particle charge variance (Ray et. al. 2019; Montilla et. al. 2020). In order to account for the particle charge variance effect, let us write the transport equation for the particle velocity-charge covariance from equation 1 with $\phi = c_{p,i}\xi_p$, and by using the particle number density transport equation, the particle mean momentum transport equation, and the particle mean charge transport equation (equation 2). If we neglect the time derivative, the velocity gradient, the granular temperature gradient, and any third-order statistical moment, we obtain the following equation:

$$\begin{aligned}\left(\frac{1}{3}\cdot\frac{1+e_c}{\tau_c}+\frac{1}{\tau_p}+\frac{2}{5}\cdot\frac{3-e_c}{\tau_\xi}\right)\langle c'_{p,i}\xi'_{\mathrm{p}}\rangle-\frac{1}{m_p}\langle\xi'_{\mathrm{p}}\xi'_{\mathrm{p}}\rangle E_i\\=-\left(1+0.542e_c\frac{D_p^{coll}}{d_p\sqrt{\Theta_p}}\right)\Theta_p\frac{\partial Q_p}{\partial x_i}+0.542e_c\frac{\sqrt{\Theta_p}}{d_p}\sigma_p^{coll}\,E_i\end{aligned} \tag{3}$$

Here the collision term $\mathcal{C}(c_{p,i}\xi_p)$ was calculated by taking into account the particle velocity-charge correlation using a linear model (Montilla et al. 2020).

To close the variance term ($\langle\xi'_{\mathrm{p}}\xi'_{\mathrm{p}}\rangle$) in equation 3, we follow the same procedure as above. Indeed, from equation 1 written for $\phi = \xi_p\xi_p$ and using the particle number density equation and equation 2, we obtain the transport equation for the particle electric charge variance. Neglecting any cross product between Q_p and E_i (or their gradients), the velocity gradient, the granular temperature gradient, and the temporal derivative, we obtain the following expression:

$$\left(2n_p\frac{\partial Q_p}{\partial x_i}+8\frac{\sigma_p^{coll}}{\sqrt{\Theta_p}\,d_p}E_i-71.13\frac{\sigma_p^{coll}D_p^{coll}\tau_c}{\sqrt{\Theta_p}\,d_p^3}E_i\right)\langle c'_{p,i}\xi'_p\rangle + \left(\frac{1}{\tau_\xi}-\frac{21.29\,\left(D_p^{coll}\right)^2\tau_c}{d_p^4}\right)n_p\langle\xi'_p\xi_p{}'\rangle = 14.20\frac{\left(\sigma_p^{coll}\right)^2\tau_c}{n_p d_p^2}E_iE_i \tag{4}$$

Equations 3 and 4 form a linear system of equation whose unknowns are $\langle c'_{p,i}\xi'_{\mathrm{p}}\rangle$ and $\langle \xi'_{\mathrm{p}}\xi'_{\mathrm{p}}\rangle$. For the sake of simplicity, we can write this as the following linear system of equations:

$$\begin{cases} A\langle c'_{p,i}\xi'_p\rangle + B_i\langle\xi'_p\xi_p{}'\rangle = C_i \\ D_i\langle c'_{p,i}\xi'_p\rangle + F\langle\xi'_p\xi_p{}'\rangle = G \end{cases} \tag{5}$$

This system can be solved to obtain an algebraic model for that particle velocity-charge covariance that takes into account the effect of the particle variance:

$$\langle c'_{p,i}\xi'_{\mathrm{p}}\rangle = \frac{C_i\left(AF-D_jB_j\right)-B_i\left(G-D_mC_m\right)}{A\,\left(AF-D_kB_k\right)} \tag{6}$$

$$\langle \xi'_{\mathrm{p}}\xi'_{\mathrm{p}}\rangle = \frac{G-D_iC_i}{AF-D_jB_j} \tag{7}$$

These equations form an algebraic closure model for both the particle velocity-charge covariance and the electric charge variance. They can now be used in equation 2 to have a fully closed mean electric charge transport equation. We draw special attention to the variance algebraic model (equation 7). Although we were able to successfully obtain a closure model for this term, we can see, that under certain conditions, the model could lead to unphysical results such as a negative variance.

Numerical Tests

We tested our model in a periodic 1D dimensional domain of length L with a constant solid volume fraction, constant granular temperature, and zero mean velocity for the particles. Under these conditions, we can prove that our equations can be expressed as a function of 7 independent dimensionless parameters:

$$\frac{L}{d_p} \qquad \tau_c^* = \tau_c\frac{\sqrt{\Theta_p}}{L} \qquad \tau_p^* = \tau_p\frac{\sqrt{\Theta_p}}{L} \qquad \tau_\sigma^* = \tau_\sigma\frac{\sqrt{\Theta_p}}{L}$$

$$Pe = \frac{D_p^{coll}}{L\sqrt{\Theta_p}} \qquad e_c \qquad \frac{u_e}{u_k} = \frac{E_{ref}^2\varepsilon}{n_p m_p\Theta_p}$$

They represent: aspect ratio between the domain and the particle size, the dimensionless particle collision time, the dimensionless particle relaxation time, the dimensionless triboconductivity time, the electric Peclet number, the collisional restitution coefficient, and the ratio between the electric energy and the fluctuant kinetic energy. The reference electric field is given by:

$$E_{ref} = \frac{n_p Q_p^{ref} L}{\varepsilon} \tag{5}$$

The reference electric charge is defined as the maximum value of the electric charge at $t = 0$. Also, the reference velocity is given by $\sqrt{\Theta_p}$ the reference length by L and the reference time by $L/\sqrt{\Theta_p}$

For the sake of brevity, we studied the case where the triboconductivity and the fluid drag force are neglected ($\tau_p^* = \infty$; $\tau_\sigma^* = \infty$). The other parameters were set as follow: $\tau_c^* = 1 \times 10^{-4}$, $L/d_p = 192$, $Pe = 100{,}000$ and $u_e/u_k = 30$. The initial condition for the electric charge is a sinus function. We can now fully solve equation 2 using the algebraic model proposed in this work (equations 6 and 7). This equation is solved using an adaptative Runge-Kutta Felhberg 7(8) (Felhberg E. 1968) and the spatial derivatives were treated using an 8th order central finite difference scheme.

In figure 1, we show a grid view at the initial condition and at a later time of the dimensionless electric charge, electric field, particle velocity-charge covariance, and the charge variance for the model presented in this work and the model where the charge variance is neglected. From the initial condition, we remark that not considering the charge variance leads to an underestimation of the magnitude of charge-velocity covariance. This underestimation is more pronounced in the regions where the electric field is stronger. When we let the system evolve, we see that globally the electric charge will tend towards the equilibrium in both models. However, including the charge variance in the analysis speeds up this process. Indeed, the charge variance term will increase the magnitude of the charge-velocity covariance in some parts. This will enhance the transport of electric charge due to the random motion of particles.

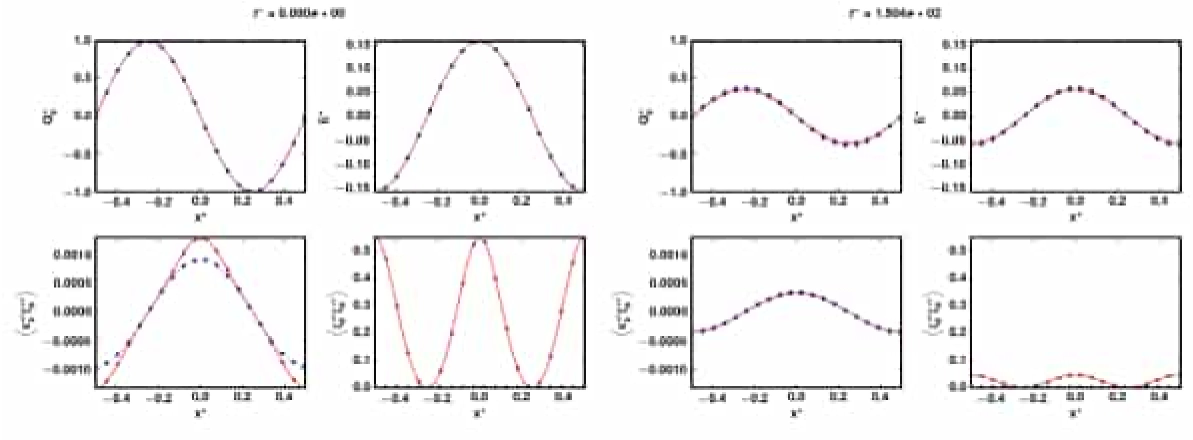

Fig. 1. Comparison between the model results given by the algebraic model presented in this work (solid red line with circle markers) and the algebraic model neglecting the electric charge variance (dotted blue line with square markers). The initial condition is shown at the left and the results at $t^* \approx 150$ is shown at the right.

As we stated before, the algebraic model can become unphysical under some conditions. For example, figure 2 shows the initial charge variance when $u_e/u_k = 300$ (all other parameters remained unchanged). We notice that there are some singular points in the results produced by the algebraic model, and we can even have negative values for the charge variance. This is not physical, and it reveals the limits of this model. We also observed that this model was difficult to solve numerically as the electric charge increased. Even when we were below the unphysical region. All of this can be arguments against the use of this algebraic model for configurations with a high electrical energy. More accurate approaches need to be used in that case, such as fully solving the electric charge variance transport equation.

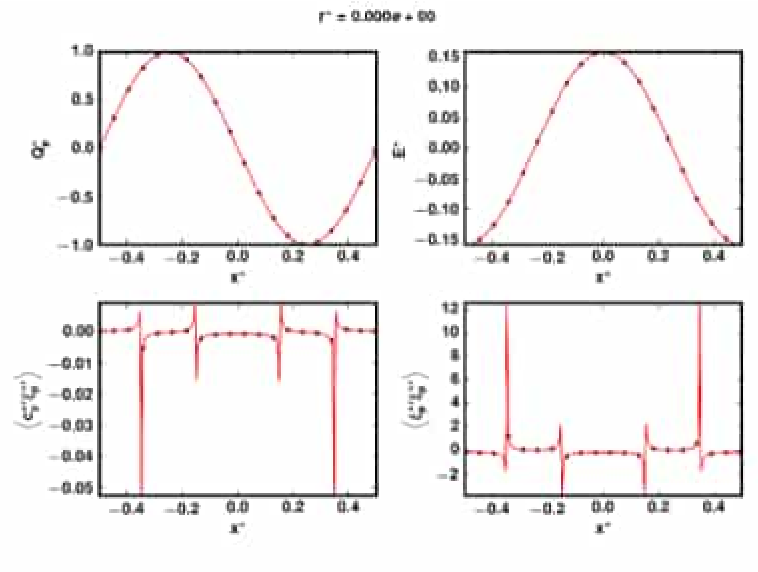

Fig. 2. Initial condition produced by the proposed algebraic model when : $\tau_c^* = 1 \times 10^{-4}$; $L/d_p = 192$; $Pe = 100{,}000$; $u_e/u_k = 300$; $\tau_p^* = \infty$; and $\tau_\sigma^* = \infty$

Conclusion

In this work, we have shown that we can derive an algebraic closure model for the particle velocity-charge covariance that takes into account the particle electric charge variance. Using the kinetic theory of rapid granular flow, we derived the transport equation for both the particle velocity-charge covariance and the electric charge variance. Then after some simplifying hypotheses, we obtained a linear system of equations that can be solved for both physical quantities. To study the behavior of this new algebraic model, we solved the equations in a 1D configuration. Our results showed that including the electric charge variance in the analysis leads to an increase in the charge-velocity correlation in the zones where the electric field is strong. This, in turn, will amplify the effect of the transport of electric charge due to the random motion of particles. Although this approach allowed us to fully close the mean charge transport equation, the model presented here could potentially yield unphysical results such as a negative electric charge variance. This means that the hypotheses taken in this approach are too restrictive to be physically meaningful. This shows the limits of the algebraic model as closure for the mean electric charge transport equation. To avoid these problems a more complete approach should be studied, like directly solving the transport equations for the electric charge variance and charge-velocity covariance. However, this model could still be useful to study the effect of the charge variance when the ratio between the electric and kinetic energy is not very large.

Notation

n_p	number of particles per unit of volume	Θ_p	particle granular temperature
U_p	mean velocity of particles	d_p	particle diameter
c_p	particle velocity in the phase space	e_c	restitution coefficient
c'_p	particle velocity fluctuation in the phase space	τ_c	particle-particle collision time
Q_p	mean particle electric charge	τ_p	particle relaxation time

ξ_p	particle electric charge in the phase space	τ_ξ	electric charge covariance relaxation time
ξ_p'	particle electric charge fluctuation in the phase space	σ	triboconductivity coefficient
E	electric field	D_p	dispersion coefficient
m_p	particle mass	F	external force
ε	medium permittivity		

Reference

Chapman, S. & Cowling, T. G. *The mathematical theory of non-uniform gases.* 3rd edition. 1970.

Fehlberg, E. *Classical Fifth-, Sixth-, Seventh-, and Eighth-Order Runge-Kutta Formulas*. Technical Report TR R-287, NASA Johnson Space Center, Houston. 1968

Hendrickson, Gregory. *Electrostatics and gas phase fluidized bed polymerization reactor wall sheeting.* Chemical Engineering Science 61 (4), 1041–1064. 2006.

Kolehmainen, Jari, Ozel, Ali & Sundaresan, Sankaran Eulerian. *Modelling of gas–solid flows with triboelectric charging.* Journal of Fluid Mechanics 848, 340–369. 2018.

Miller, Clark O. & Logwinuk, A. K. *Fluidization Studies of Solid Particles. Industrial & Engineering Chemistry* 43 (5), 1220–1226. 1951.

Montilla C., Ansart R., Simonin O. *Modeling of the mean electric charge transport equation in a mono–dispersed gas–particle flow*. Journal of Fluid mechanics. 2020.

Ray, M., Chowdhury, F., Sowinski, A., Mehrani, P. & Passalacqua, A. *An Euler-Euler model for mono-dispersed gas-particle flows incorporating electrostatic charging due to particle-wall and particle-particle collisions.* Chemical Engineering Science 197, 327–344. 2019.

Rokkam, Ram G., Fox, Rodney O. & Muhle, Michael E. *Computational fluid dynamics and electrostatic modeling of polymerization fluidized-bed reactors*. Powder Technology 203 (2), 109–124. 2010.

Rokkam, R. G., Sowinski, A., Fox, R. O., Mehrani, P. & Muhle, M. E. *Computational and experimental study of electrostatics in gas-solid polymerization fluidized beds*. Chemical Engineering Science 92, 146–156. 2013.

MICROKINETIC MODELING OF CATALYTIC REACTIONS IN MILLION PARTICLES BUBBLING BEDS

Riccardo Uglietti[1], Daniele Micale[1], Mauro Bracconi[1], Matteo Maestri[1*]

[1]*Politecnico di Milano, Laboratory of Catalysis and Catalytic Processes, Dipartimento di Energia, via La Masa 34, 20156 Milano, Italy.*

*e-mail: *matteo.maestri@polimi.it*

Abstract

In this work, we apply two speed-up techniques, Particle Agglomeration (PA) and In Situ Adaptive Tabulation (ISAT) to reduce the computational cost of the reactive CFD-DEM simulation of catalytic fluidized beds in case a microkinetic description of the chemistry is adopted. To do so, the PA has been optimized to handle high number of species problems. The optimized PA technique has been assessed in a small test reactor in the order of 10^4 particles in case of a methanation microkinetic model. Then, the optimized PA and ISAT have been compared, and the PA resulted to be the best performing one in case of the adopted microkinetic model. Finally, a methanation lab scale reactor, consisting of 1.2 million particles, has been simulated. An 18-fold speed-up has been obtained, enabling the reduction of the chemistry weight from 90% to 30% of the simulation computational time. At this particle number and level of detail of the chemistry description, the work paves the way towards the fundamental investigation of reactive fluidized systems of technical relevance.

Introduction

Reactive CFD-DEM simulations can offer a deep understanding of lab scale catalytic fluidized systems, which can be combined with experimental investigations to optimize the design procedure of these units. However, the first-principle driven description of the chemistry in each particle tracked in the system is usually not performed due to the required computational cost. Indeed, even lab scale fluidized beds are composed of 10^5 -10^6 particles which are all active in case of catalytic processes. As a consequence, the reactive CFD-DEM modeling is applied on diluted beds where only few thousands of particles are reactive (Zhuang Y., 2015 and Yang S., 2019). Moreover, the computation of a rate equation kinetics is usually performed on a computational cell and not on a particle basis (Snider D.M., 2011) to furtherly reduce the simulation time. In this work, the reactive CFD-DEM modeling is applied to a million particle methanation fluidized bed (experimentally investigated by Li J. and Yang B., 2019). Moreover, a microkinetic model composed of 14 site species and 52 reactions (Delgado K.H., 2014) has been used. The computational cost introduced by the microkinetic model has been relevantly reduced by applying the speed-up algorithm selection strategy proposed in our previous work in case of rate equation kinetics (Uglietti R. et al., 2020). According to this strategy two speed-up algorithms must be tested in a small bed, representative of the million particle one, to determine the best performing algorithm for the case under investigation: operator-splitting (OS) & In Situ Adaptive Tabulation (ISAT, Pope S.B., 1997) and coupled & Particle Agglomeration (PA). The first algorithm provides higher simulation speed-up factors. However, the required decoupled solution of gas-particle transport and reaction phenomena in each particle necessitates a maximum simulation time step lower than the characteristic time of the fastest phenomenon in the system. In case the maximum time step becomes limiting with respect to the maximum time step allowed in case of no speed-up, the coupled & PA can be used. Indeed, it allows for the same time step adopted in case of no simulation speed-up, since transport and reaction are solved coupled in each particle. In this view, the PA speed-up technique has been optimized to efficiently manage high dimensionality problems, i.e. for microkinetic modeling cases. Then, the accuracy of the optimized coupled & PA has been compared with the one of OS & ISAT, revealing the first one as the best performing algorithm for the methanation process under investigation. Finally, the reactive CFD-DEM microkinetic simulation of the target million particle reactor has been performed with the optimized coupled & PA algorithm. A relevant 18-fold speed-up has been obtained, paving the way for the application of CFD-DEM to the fundamental investigation of lab scale fluidized bed reactors.

Speed-Up Algorithms

The OS & ISAT and coupled & PA algorithms have been implemented to speed-up the solution of the ODE system representing the species and energy balances in each tracked catalytic particle within the reactive CFD-DEM framework proposed in our previous work (Uglietti R. et al., 2018). OS & ISAT is based on the sequential solution of gas-particle transport and catalytic reactions within a time step, for each particle in the system. This enables the application of ISAT which reduces the computational time of the solution of catalytic reactions. In case a particle must be solved, ISAT aims to retrieve the results from similar particles integrated in previous time steps and stored in his table. If this procedure fails, it solves the particle and updates the table. Instead, the PA technique, derived from Cell Agglomeration (CA, Rebughini S. et al., 2017), speeds up the ODE system describing transport and reaction coupled by agglomerating similar particles in the bed into computational parcels at each time step.

Optimization of Particle Agglomeration algorithm

According to PA, the agglomeration is performed with an index (i_{PA}), computed runtime and particle-wise according to Eq.(1), which is updated with respect to CA index formula (Eq.(2)):

$$i_{PA} = \sum_{i=1}^{NV} i \cdot ln\left(NV \cdot \left\lfloor \frac{\phi_i}{tol_{PA}} \right\rfloor\right) \tag{1}$$

$$i_{CA} = \sum_{i=1}^{NV} \phi_i \left(\frac{1}{tol_{CA}}\right)^i \tag{2}$$

where the logarithm has been introduced in Eq.(1) as hash function to prevent the numerical overflow of the index due to the high number of species. Two main parameters govern the accuracy of the agglomeration: the PA tolerance tol_{PA} and the variables accounted for the assessment of particle similarities (i.e. composition and temperature of both the particle and the gas around it, and Reynolds Number of the gas). The PA tolerance plays a key role in the accuracy provided by the technique. Indeed, the decrement of the tolerance value causes the decrement of the number of particles per computational parcel, leading to higher accuracy but lower speed-up. Preliminary numerical tests are required for each studied kinetics to find the optimal tolerance, since it cannot be directly derived from transport and chemical properties of the system. The i-*th* variable has been normalized with a logarithmic scale instead of the linear scale usually employed in case of CA:

$$\phi_i = \frac{\ln(y_i) - \ln(y_{i,min})}{\ln(y_{i,\max}) - \ln(y_{i,\min})} \tag{3}$$

In particular, the logarithmic scale improves the PA accuracy in case of uneven distribution of the species in the composition space, e.g. during the initial dynamics of the fluidized reactor. By doing so, the classification of PA is refined close to the low species mass fractions enabling the PA to discriminate sharp composition gradients. Once the same index is found in two or more particles, they are grouped into a computational parcel, whose properties are the arithmetic average of the properties of the grouped particles. The results of the ODE solutions of the parcels are mapped back to each particle, accordingly to CA (Rebughini S. et al., 2017).

Computational Domains and Operating Conditions

The lab scale million particle bubbling bed reactor (1.5 cm of diameter and 1.2 cm high) experimentally investigated by Li J. and Yang B. (2019) has been selected as target reactor for the application of the speed-up algorithms in case of microkinetic modeling. The geometrical and mechanical properties of the particles are reported in Table 1. The test reactor has been chosen fluid dynamically and chemically similar to the target reactor. To do so, the similarity criteria presented in our previous work (Uglietti R. et al., 2020) and based on the comparison of the fluidization ratio ζ and the GHSV of test and target reactor, have been adopted. Based on these indications, the pseudo-2D parallelepiped reactor tested in our previous work (Uglietti R. et al., 2018) has been selected. Its dimensions have been adapted (i.e. 6 mm width, 3 cm height and 500 µm depth) to fill the reactor vessel with the same number of particles resulted to be computationally affordable in the previous study, i.e. 10^4. The inlet superficial velocity has been selected equal to 0.152 m/s, obtaining a maximum ratio of 2 for both the ζ and GHSV computed in the two reactors. The reactor has been investigated in case of the methanation process, whose operating conditions are reported in Table 2.

Table 1 Geometrical and mechanical characteristics used in the target reactor simulation.

Particle Properties					
Diameter [µm]	125	**Density [kg m^{-3}]**	1684	**Number [-]**	$1.2 \cdot 10^6$
Young Modulus [Pa]	10^6	**Restitution Coefficient [-]**	0.8	**Friction Factor [-]**	0.3

Table 2 Operating conditions of the methanation process.

Methanation			
Pressure [bar]	1.01325	**Temperature [K]**	673.15
Composition [v/v] – CO / H_2 / Ar	0.2 / 0.6 / 0.2	**Inlet Velocity [m/s]**	0.162

Results and Discussion

The accuracy and speed-up obtained with the optimized coupled & PA has been first tested and compared with OS & ISAT in the small test reactor of 10^4 particles. This step allowed to assess the accuracy provided by the new implemented index formula (Eq.(1)) and the logarithmic normalization formula in case of high number of species, enabling the comparison between the two speed-up algorithms. Finally, the computational gain achieved in case of microkinetic modeling of million particle reactors is discussed.

Assessment of coupled & PA formula and comparison with OS & ISAT in the test reactor

The average composition of the bed <ω> at each time step *k* has been selected as well-describing the reactor performances as a function of the simulation time:

$$< \boldsymbol{\omega} >_k = \frac{\sum_{p=1}^{NP} \boldsymbol{\omega}_{p,k}}{NP} \tag{4}$$

The averaged mean global error ε (Bracconi M. et al, 2017) has been computed for each time step of the simulation and the temporally averaged mean global error $\underline{\varepsilon}$ (Eq.(5)) has been computed as indicator of the accuracy provided by OS & ISAT or coupled & PA.

$$\underline{\varepsilon} = \sum_{k=1}^{NT} \varepsilon_k / NT = \left(\sum_{k=1}^{NT} \sum_{p=1}^{NP} \left\| Y_{p,k} - Y_{p,k}^{no\ speed-up} \right\| \right) / (NP \cdot NT) \tag{5}$$

Moreover, the speed-up of the solution of the chemistry and transport phenomena in the particles, has been computed with the chemical speed-up factor (SP_c), defined in Eq.(6).

$$SP_C = \boldsymbol{\tau}_k^{\boldsymbol{no\ speed-up}} / \boldsymbol{\tau}_k^{\boldsymbol{speed-up}} \tag{6}$$

Three coupled & PA tolerances, i.e. 0.2, 0.1, 0.05, have been investigated by means of the new implemented index (Eq.(1)) and logarithmic normalization formulas. The tolerance equal to 0.1 (average error $\underline{\varepsilon}$ of 0.43% and 1.28% for species mass and site fractions) has been identified as the optimal one. Indeed, negligible improvements of accuracy have been obtained by reducing the tolerance to 0.05 ($\underline{\varepsilon}$ of 0.37% and 1.31%). Once performed the tolerance analysis, we assessed the accuracy and the speed-up provided by PA modifications in case of microkinetic modeling and the optimal tolerance. Fig. 1 reports the average composition of the bed in terms of the main species mass (Fig.1a) and site (Fig.1b) fractions in case of the PA without the new formulas, with the new index formula and with both the new index and normalization formulas. In the first case, PA is not able to properly agglomerate the similar particles with the traditional CA formula (error > 15% for methane and hydrogen). In fact, the index computed according to CA resulted in the order of 10^{23} with respect to $8 \cdot 10^{2}$ obtained with the new index formula. This situation leads to the reduction of machine precision in case of the traditional CA formula, causing erroneous agglomerations.

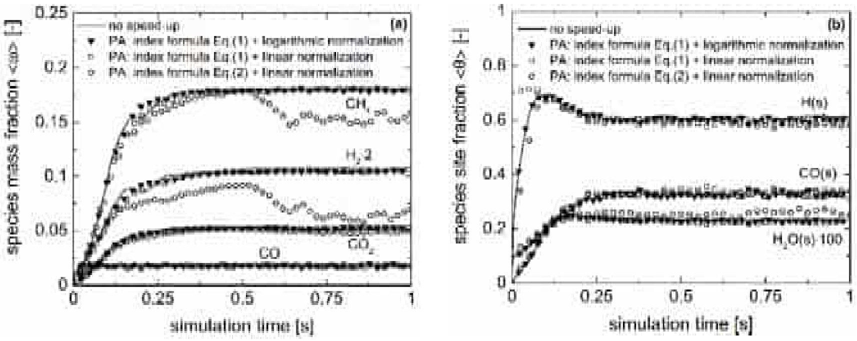

Fig. 1 Comparison of the temporal trend of average main species mass (a) and site (b) fractions predicted with PA technique applied with the index formula in Eq. (2) and linear normalization (open circle), with the index formula in Eq.(1) and linear normalization (open squares) and with the index formula in Eq.(1) and logarithmic normalization (solid triangles).

Once implemented the new index formula, these errors are avoided but an accuracy issue is still present for the coverage dynamics during the first 0.15s, i.e. during the transport of the reactants in the reactor mostly full of inert. In such situation, the particles reached by reactant diffusion are agglomerated with the particles full of inert. This reflects into a faster dynamic of the average adsorbed hydrogen site fraction in the bed. In this context, the logarithmic normalization formula emphasizes the composition differences in the low concentration range to avoid the erroneous particle agglomeration. Additionally, the logarithmic formula minimally impacted the speed-up provided by coupled & PA which was equal to 6.4 and 7 with and without the new normalization. Then, we assessed the accuracy and speed-up of the OS & ISAT by investigating three tolerances equal to 10^{-3},$5 \cdot 10^{-4}$ and 10^{-4}. The ISAT tolerance of $5 \cdot 10^{-4}$ ($\underline{\varepsilon}$ of 1.40% and 1.47% for species mass and site fractions) is discussed, since negligible improvements of accuracy have been obtained by furtherly decreasing the tolerance.

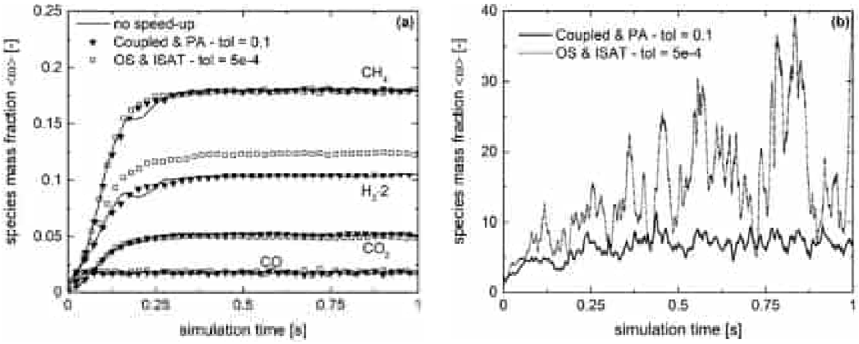

Fig. 2 Comparison of coupled & PA and OS & ISAT: (a) temporal trend of average bed composition predicted applying or not the speed-up algorithms, (b) provided speed-up of the chemistry.

Fig. 2a shows the average composition of the bed as a function of time for the main species involved in the process in case of the two algorithms and no speed-up applied. A temporally averaged error $\underline{\varepsilon}$ equal to 0.43% and 1.28% is obtained for species mass fractions and site fractions in case of coupled & PA. Instead, OS & ISAT leads to a relative error, with respect to hydrogen, higher than 15%, for all the tolerances investigated, proving that the maximum time step allowed by OS & ISAT algorithm is lower than the converged time step for the simulation without speed-up. In particular, the error on hydrogen has been ascribed to the wrong description of hydrogen gas-particle transport decoupled from reaction (Uglietti R. et al., 2020), since the converged time step in case of no speed-up, i.e. 5 μs, is higher than the characteristic time of hydrogen transport, i.e. 3.84 μs. Fig. 2b shows the chemical speed-up factor obtained in case of coupled & PA and OS & ISAT. Despite the 2.2 times higher speed-up offered by OS & ISAT with respect to the 6.4 obtained with coupled & PA, the latter has been chosen as the best performing strategy. In fact, the coupled & PA algorithm confirmed to be not affected by the numerical issues related to OS & ISAT, due to its application to the coupled solution of transport and reaction phenomena. However, it also worth noticing that in absence of the OS & ISAT time step limitations an improvement of the speed-up could be achieved, highlighting the importance of the preliminary numerical tests.

Simulation of the target reactor by means of methanation microkinetic model

We applied the coupled & PA tuned in the test reactor to the simulation of the million particles reactor experimentally investigated by Li J. and Yang B. (2019) by means of the methanation microkinetic model. The operating conditions reported in Table 2 has been adopted. Fig. 3 shows the chemical speed-up factor provided by the coupled & PA algorithm as a function of the simulation time which has been chosen equal to 0.8s, corresponding to 3 residence times in order to have an insight of the computational gain among the whole evolution of the process. A reactive CFD-DEM simulation without speed-up was not performed for the whole simulation time, due to the unsustainable cost of the microkinetic modeling of the chemistry. Thus, the speed-up factors have been computed according to the following strategy. At each selected time, the results obtained by means of the simulation performed with speed-up has been considered the initial conditions for the solution of two time steps by means of the reactive CFD-DEM framework without speed-up. Then, the chemical speed-up factor (Eq.(6)) has been computed considering the computational cost required to perform the second time step with and without speed-up. An 18-fold chemical speed-up has been evaluated, corresponding to a reduction of the chemistry cost from 90% to 30% of the total CPU time.

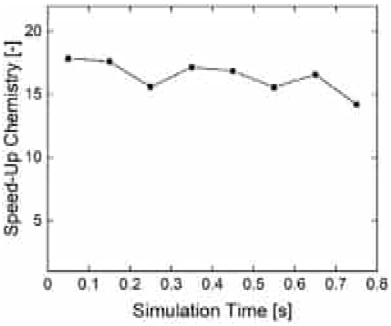

Fig. 3 Target reactor simulation: temporal trend of the obtained chemistry speed-up.

Conclusions

Two speed-up algorithms have been investigated to reduce the computational cost related to the detailed description of the chemistry: coupled & PA and OS & ISAT. First, the accuracy and computational gain of the optimized coupled & PA algorithm, specifically optimized for high dimensionality problems, has been assessed in a small test reactor of 10^4 particles. Then, the performances of the coupled & PA and OS & ISAT has been compared. The OS & ISAT provided a 2.2 times higher speed-up of the chemistry with respect to the one achieved with coupled & PA, i.e. 6.4. Nevertheless, a higher accuracy has been obtained by means of coupled & PA. Therefore, it has been selected for the microkinetic simulation of methanation process in a 1.2 million particle lab scale reactor. A relevant 18-fold speed-up of the chemistry has been obtained, reducing its cost until 0.44 times the cost of the particle tracking. The accuracy and computational gain obtained in this work push the frontier of the fundamental investigation of fluidized bed reactors to the usage of CFD-DEM data to improve Euler-Euler models, paving the way towards the simulation of fluidized systems of technical relevance.

Acknowledgements

The project leading to this work has received funding from the European Research Council (ERC) under the European Union's Horizon 2020 research and innovation programme (Project SHAPE - grant agreement No. 677423). Computational time at CINECA, Bologna (Italy) is gratefully acknowledged.

Notation

Roman Letters

GHSV [1/h]	Gas Hourly Space Velocity
i_{PA} [-]	Index of Particle Agglomeration
NP [-]	Number of Particles
NT [-]	Number of Time Steps
NV [-]	Number of Variables
SP_c [-]	Chemical Speed-Up Factor
tol_{PA} [-]	User Defined Tolerance for Particle Agglomeration
Y [-]	Vector of Species Mass Fractions or Species Site Fractions

Greek Letters

ε [-]	Mean Global Error Time Averaged
$\underline{\varepsilon}$ [-]	Mean Global Error
ζ [-]	Fluidization Ratio defined as the Inlet Velocity divided by the Minimum Fluidization one
τ [s]	Time Spent to Solve the Species Balances within a Time Step
ϕ [-]	Normalized Variable (mass fractions, site fractions, Reynolds Number)
$\langle\omega\rangle$ [-]	Average Species Mass Fraction Vector in the Fluidized Bed

References

Bracconi, M., M Maestri, A Cuoci. In situ adaptive tabulation for the CFD simulation of heterogeneous reactors based on operator - splitting algorithm. AIChE J. 2017. 63, 95-104

Delgado, K.H., Surface Reaction Kinetics for Oxidation and Reforming of H2, CO, and CH4 over Nickel-based Catalysts. Ph.D. Thesis. 2014. Karlsruher Institut für Technologie

Li, J., B Yang. Bubbling fluidized bed methanation study with resolving the mesoscale structure effects. AIChE J. 2019. 65, 1-15

Pope, S.B. Computationally efficient implementation of combustion chemistry using in situ adaptive tabulation. Combust. Theory Model. 1997. 1, 41-63

Rebughini, S., A Cuoci, AG Dixon, M Maestri. Cell agglomeration algorithm for coupling microkinetic modeling and steady-state CFD simulations of catalytic reactors. Comput. Chem. Eng. 2017. 97, 175-182

Snider, D.M., SM Clark, PJ O'Rourke. Eulerian–Lagrangian method for three-dimensional thermal reacting flow with application to coal gasifiers. Chem. Eng. Sci. 2011. 66, 1285-1295

Uglietti, R., M Bracconi, M Maestri. Coupling CFD–DEM and microkinetic modeling of surface chemistry for the simulation of catalytic fluidized systems. React. Chem. Eng. 2018. 3, 527-539

Uglietti, R., M Bracconi, M Maestri. Development and assessment of speed-up algorithms for the reactive CFD-DEM simulation of fluidized bed reactors. React. Chem. Eng. 2020, DOI: 10.1039/C9RE00440H.

Yang, S., H Wang, Y Wei, J Hu, JW Chew. Particle-scale modeling of biomass gasification in the three-dimensional bubbling fluidized bed. Energy Convers. Manag. 2019. 196, 1–17

Zhuang, Y., X Chen, D Liu, C Bu, CFD–DEM Modeling of O2/CO2 Char Combustion in a Fluidized Bed. Clean Coal Technology and Sustainable Development, Springer, 2015.

COARSE-GRAIN DEM-CFD MODELLING OF CYCLONE FLOW

Erasmo S. Napolitano[1], **Alberto Di Renzo**[1]*, **Francesco P. Di Maio**[1]

[1]*Università della Calabria, Via P. Bucci, Cubo 45a, 87036 Rende (CS), Italy*
*Email: *alberto.direnzo@unical.it, erasmo.napolitano@unical.it*

Abstract

Design, scale-up and operation of cyclones for circulating fluidized beds are still mostly based on simplified models and experience. Due to their prohibitive computational cost for medium- to large-scale systems, pure DEM-CFD models cannot be used to study the cyclone two-phase flow. In the recent years, methods based on lumping smaller particles into parcels or grains have been proposed to reduce the number of elements and increase the time-step. However, much remains to be understood and characterized. In the present work, coarse-grain DEM-CFD methods to simulate the two-phase flow in gas-solid cyclones at different gas and solid loadings are investigated. In particular, the focus is on the effect that the coarse graining strategy and degree exert on the replicability of the results as compared to pure DEM-CFD simulations. Taking a Stairmand high- efficiency cyclone design, it is shown that the macroscopic quantities characterizing the cyclone performances are generally maintained after an increase of the number of particles per grain (NPG) up to 64. However, some of the detailed features of the solids flow (e.g. strand formation) appear heavily affected by the coarse graining degree, already at NPG = 8 and 27.

Introduction

Gas-solids separation occurring in cyclones is a key operational element of circulating fluidized bed systems. The complex two-phase flow inside a cyclone determines its performance in terms of gas pressure drop and separation efficiency. Theories proposed are based on established but simplified models of the gas and particle flow inside the device (see e.g. Muschelknautz and Greif, 1997). On the other hand, numerical simulations have been mostly aimed at improving single-phase flow (see e.g. Gronald and Derksen, 2011), in which the presence of the particles, even close to the walls, was neglected. Lagrangian particle tracking (i.e. without particle-particle interaction) has been utilized in combination with CFD (Wan et al., 2008). Some authors attempted the use of Euler-Lagrange methods using commercial codes (Kozołub et al., 2017) showing a dramatic influence of the particles on the gas flow under high-loading conditions; others adopted the DEM-CFD approach with full four-way coupling for dense medium hydrocyclones (Chu et al., 2009). The latter ones also evaluated the use of coarse-grain DEM-CFD model in dense medium cyclone simulations (Chu et al., 2015), concluding that the approach could be used usefully at least qualitatively, if not quantitatively. However, the trade-off between accuracy and computer speed-up due to the coarse-graining procedure in DEM-CFD simulations of the cyclone flow remains essentially to be explored. In the present contribution a DEM-CFD model of a cyclone is investigated at different levels of coarse graining of the solid phase, with the aim to investigate both macroscopic indicators of the cyclone performance and the local dynamics of the two-phase flow. In the absence of sufficient detail of experimental data, the base-case is assumed to be the pure CFD-DEM case.

Coarse-grain DEM-CFD numerical model

The simulations presented below are based on a modelling approach combining the Discrete Element Method for the solid phase and a local average CFD approach for the fluid phase. The basic equations governing the motion of the particles and of the fluid are those implemented in the code MFIX-DEM (Garg et al., 2012) with the use of the Cartesian grid cut-cell method (Dietiker et al, 2013) to adapt the domain to the cyclone geometry. In-house developed code extensions have been added, including a coarse-grain methodology similar to the one proposed by Bierwisch et al. (2009), a modification to ensure prescribed constant solids mass inflow with coarser particles, a drag model implementing Di Felice's formula (see below) and other minor numerical optimizations. The key elements of the model are summarized below.

Contact forces between the particles were considered using the Hertzian non-linear elastic-frictional model with dissipation based on a constant coefficient of restitution. Di Felice's formula for the drag force on a particle is as follows:

$$F_d = F_{d0}\varepsilon^{-\chi} \tag{1}$$

$$\chi = 3.7 - 0.65 \cdot e^{-0.5[1.5-\log_{10} Re_p]} \tag{2}$$

where $F_{d0} = \frac{\pi}{4} d^2 C_d 0.5 \rho_f \varepsilon^2 |u - v|(u - v)$ is the drag force on isolated particles, where d is the particle diameter, ε the gas volume fraction, ρ_f the fluid density, $C_d = \left(0.63 + \frac{4.8}{\sqrt{Re_p}}\right)^2$, $Re_p = \frac{\rho_f d \varepsilon |u-v|}{\mu_f}$ and u is the average fluid velocity. The pressure gradient force is $F_b = V_p \nabla p$ where V_p is the particle volume and ∇p is the gradient of the average pressure.

The combination of the locally averaged equations of continuity and momentum balance with a source term balancing the drag force and pressure gradient force on the particles ensures two-way coupling, which added to the particle-particle interactions determines a four-way coupled model. Compared to other approaches, it is worth to note that in the present model no turbulence model is accounted for, also in consideration of the presence of the particles (particularly at the walls) and the relatively coarse grid required by the DEM, possibly leading to inaccuracy in the prediction of the gas flow details. On the other hand, the particle dynamics includes particle-particle collision dissipation, particle rotation and sliding also with the walls, and the solids flow is fully coupled to the gas-flow. It is not clear, however, to what extent the coarse graining procedure can deteriorate the value of such advantages.

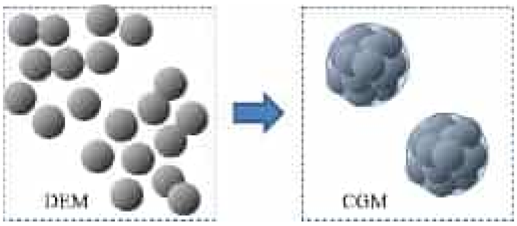

Fig. 1 - Concept of the coarse-grain DEM model: original particles (left), representative grains (right).

The coarse grain concept is illustrated in Figure 1. In practice, the total volume of the grain is equal to the sum of volume of the real particles. Density is also the same as the real particles, so the total mass is also preserved. The inertial mass used in collisions is the grain's, not the particle's. The radius of the grain can thus be determined by that of the original particles and the number of particles embodied into the grain. If NPG is the number of particles-per-grain, the equivalence leads to

$$V_g = NPG \cdot V_p \tag{3}$$

$$V_g = NPG \cdot V_p \tag{4}$$

The drag and buoyancy forces become, respectively

$$F_{d,g} = NPG \cdot F_{d,p} \tag{5}$$

$$F_{b,g} = NPG \cdot F_{b,p} = V_g \nabla p \tag{6}$$

To determine a priori the collision properties of the grain is still an open problem. In this study, the material properties of a grain particle were assumed to be the same as those of real particles it represents, including spring stiffness and the friction and damping coefficients.

Simulated System

Geometry

Starting from a high-efficiency Stairmand scheme of cyclone separator (Fig. 2), a 9-cm barrel diameter cyclone is simulated in the present work.

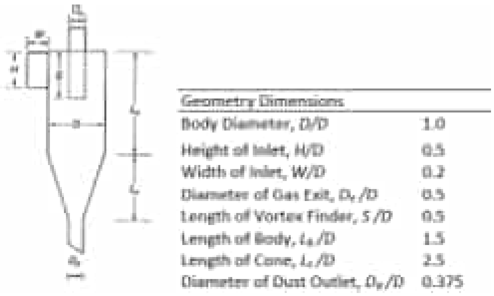

Geometry Dimensions	
Body Diameter, D/D	1.0
Height of Inlet, H/D	0.5
Width of Inlet, W/D	0.2
Diameter of Gas Exit, D_e/D	0.5
Length of Vortex Finder, S/D	0.5
Length of Body, L_b/D	1.5
Length of Cone, L_c/D	2.5
Diameter of Dust Outlet, D_d/D	0.375

Fig. 2 - Stairmand configuration with geometrical dimension ratios.

Additional data are: the length of the vortex finder outside the cyclone set to 3.5·D_e; the length of the inlet duct before entrance set to 3·H, the length of the solids outlet pipe set to 4·D_d.

Boundary conditions (BCs)

The gas enters inside the cyclone separator with a fixed and uniform velocity u_{in}. Constant atmospheric pressure BC is set at the top gas outlet. Pressure BC is also adopted at the bottom exit, at a value of 50 Pa above the reference (top outlet) pressure. This is preferred to setting some condition on the fluid velocity (e.g. no normal flow), because, compared to typical dust collectors in which the gas flow is prevented, in CFBs the gas flow is “free” to swirl while being (limitedly) dragged down or even flow up the downpipe. The particles enter via a random position generator with the same velocity as the gas. No-slip wall condition is adopted to all cyclone walls.

Simulation set-up

To examine the effect of the coarse grain degree in the cyclone separator, the same simulation set-up has been utilized with NPG ranging from 1 (DEM) to 64, as reported in Tab. 1. It is interesting to note how the number of elements (particles or grains) to simulate changes very significantly; also, the time step increases with NPG. Both aspects provide an impressive speed up of the simulation increasing NPG already at a value of 8 or 27. Since the process stabilizes quickly, 1 second of simulated time was sufficient to achieve steady-state conditions.

Tab. 1 - Summary table of the variables and parameters used.

Particle properties	$D =$ 500 mm, $\rho =$ 2500 kg m-3			
Contact model	Hertz, $E =$ 5·107 Pa, $e_n =$ 0.9			
Solids loading (%vol)	0.1%, 0.2%, 0.5%			
Inlet velocities	10, 14, 20 m/s			
Particle or grain size, d [mm]	500	1000	1500	2000
Particles per grain, NPG [-]	1 (DEM)	8	27	64
Grain-to-particle size ratio	**1**	**2**	**3**	**4**
Holdup in number of grains, [-]	136k–717k	11k–94k	6k–25k	2.8k–10.6k
Solid-phase time-step, Dts [10-6 s]	0.6	1.9	3.1	4.1
Fluid-phase (typical) time-step	5·10-4 s			

Results and Discussion

Hydrodynamics and gas flow

In all the simulations, the gas motion shows the expected externally downward spiral flow that, in the proximity of the bottom of the cyclone cone, reverts direction, rising into the inner vortex.

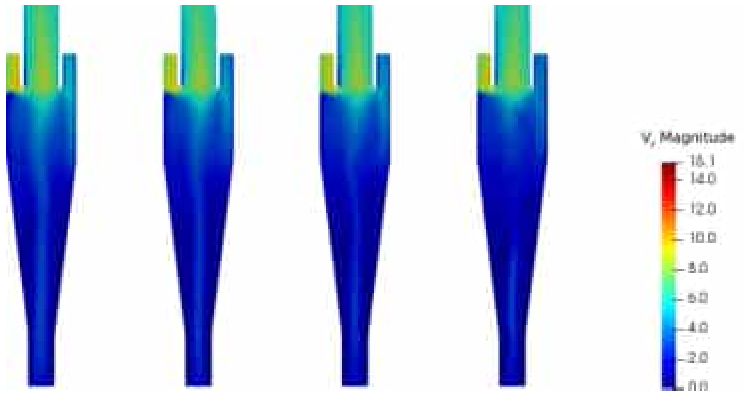

Fig. 3 - Comparison of the velocity magnitude at u_{in} = 10 m/s and ε_s = 0.2%. NPG is 1, 8, 27, 64 in the colormap figures from left to right, respectively.

In Fig. 3 the magnitude of the velocity field at ε_s = 0.2% and u_{in} = 10 m/s is plotted along a median vertical cut-plane. It turns out that the influence of the coarse graining degree does not manifest appreciably.

Two important macroscopic indicators of the gas flow in the cyclone have been considered: the overall pressure drop and the length of the inner vortex cone. The latter is evaluated by considering the lower tip of the iso-surface characterized by zero axial velocity. This surface originates from the edge of the vortex finder and develops down, first cylindrically and further down conically, eventually forming the vortex “tip”. Such a vortex “length” measure is divided by the barrel diameter to yield the dimensionless variable indicated hereinafter as L_v. The dependence of the two variables on solids loading, gas velocity and NPG is plotted in Fig. 4.

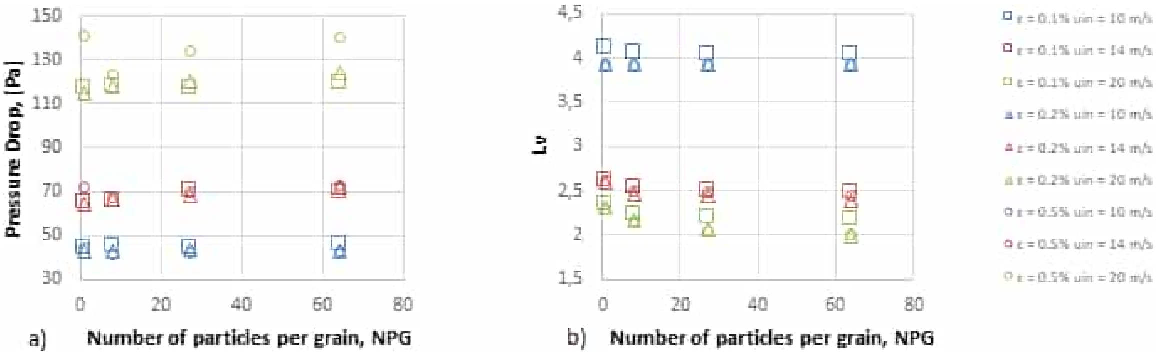

Fig. 4 - Pressure drop (a) and vortex “length” L_v (see text) (b) vs. NPG for various gas velocity u_{in} and solids volume loading ε_s.

As expected, the pressure drops exhibits a dependence on the inlet velocity; the solids loading manifest an effect on the pressure drop only at the highest loading and gas velocity. The coarse graining degree, represented by the NPG, does not cause any appreciable change, as nearly all the differences with respect to the value at NPG = 1 (DEM) are within 10%. In Fig.4.b the vortex length exhibits variations primarily with the inlet velocity, while solids loading and NPG show no significant influence. Variations with the coarse graining degree are limited within 15%. It shall be pointed out that at the lowest velocity (10 m/s) the vortex shape was not always well defined, often reaching the bottom of the domain.

Solid flow and efficiency

In all the conditions considered, the particle flow showed the expected separation behaviour, i.e. particles descended while sliding/rolling along the cyclone walls; a very small fraction of the particle was entrained by the gas, giving rise to a measurable loss of efficiency. At high number of particles, solids helicoidal “strands” formed along the cyclone walls. Fig. 5 shows the particle positions and velocities at u_{in} = 20 m/s and ε_s = 0.1, 0.2, 0.5%.

The view of the particle instantaneous locations offers the possibility to identify the role of the coarse graining procedure more clearly. Indeed, despite the ratio of the grain to particle size changes to 2, 3 and 4 for NPG = 8, 27 and 64, respectively, the description of the solids flow clearly loses details. In some case, like the ε_s = 0.5% condition, the strands sharpness of DEM decays already at NPG = 8, and they disappear at NPG = 27 or 64. It shall be noted that moving from NPG = 1 to 8, the overall number of grains drops from 717k to 94k, falling further to 25k at NPG = 27. This may be partly responsible for the different microdynamics observed.

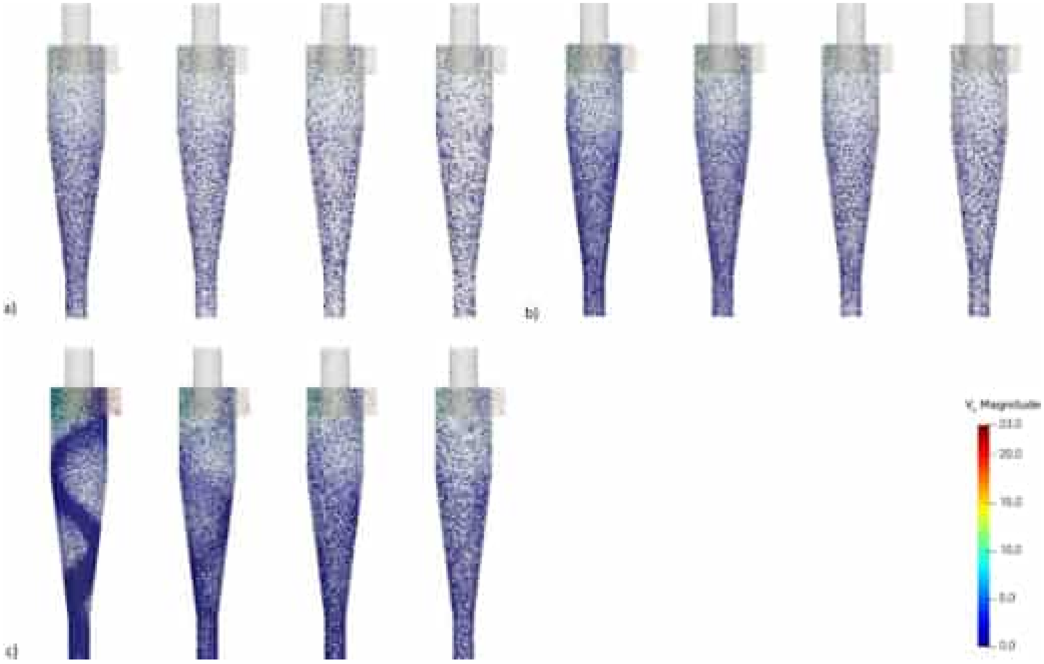

Fig. 5 - Solid flow at time = 1 s, u_{in} = 20 m/s and ε_s = 0.1% (a), ε_s = 0.2% (b) and ε_s = 0.5% (c). For every ε_s, NPG takes the values 1, 8, 27 and 64, from left to right.

To investigate whether the difference in the solids flow manifested also into macroscopically relevant properties like the separation efficiency, the ratio of solids flowrate out of the bottom outlet to the corresponding inflow was calculated as average across the last 0.3 s of simulation. The results are shown in Fig. 6 for all examined conditions. It can be observed that the increase of the NPG value exerts a marginal effect on the overall efficiency, where most of the variations can be attributed to the scatter due to the occasional passage of particles (or grains).

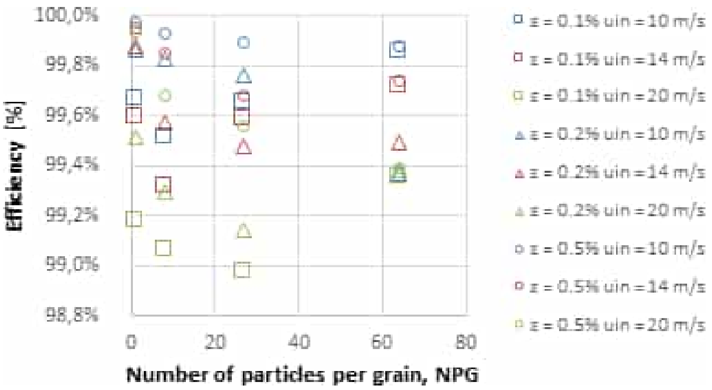

Fig. 6 - Efficiency at different NPG, u_{in} and ε_s

Conclusions

Large-scale cyclones or the treatment of very fine particles are prohibitive for reasonable DEM-CFD models due to the excessive number of particles and the small time-step. Simulation exercises were conducted on a small scale Stairmand cyclone, in order to be able to compare conventional DEM-CFD with its coarse grain approximation at different levels. The comparison showed that the scaling of properties in the coarse graining method is sufficient to guarantee the conservation of the macroscopic variables - with respect to the pure DEM – at least up to NPG = 27 (grain to particle size ratio = 3). For example, quantities such as the pressure drop, the length of the internal vortex and the separation efficiency are affected marginally by the coarse graining, even at NPG = 64. However, when looking at the local solids flow field, severe qualitative discrepancies appeared already at NPG = 27, even at NPG = 8. Therefore, the computational savings granted by the coarse graining procedure should be carefully assessed against the possible inaccuracies that it introduces when the number of grains decreases below an acceptable threshold. Unfortunately, this value appears to be problem dependent, and more thorough investigations are necessary to quantify it. It is expected that an improved treatment of the wall-grain interaction can positively impact the simulation, for example taking rolling friction into effect. However, scaling of such mechanism within coarse-graining is not established yet and it is currently under development also in our group.

Notation

ρ	density, kg/m^3	F_d	drag force, N
d	particle diameter, m	F_b	pressure gradient (buoyant) force, N
χ	exponent in Di Felice’s drag law, -	u_{in}	inlet velocity, m/s
C_d	drag coefficient, -	ε_s	inlet solids fraction, -
v	particle velocity, m/s	NPG	degree of coarse graining
V_p	particle volume, m^3	L_v	length of inner vortex to cyclone diameter ratio, -
p	pressure, Pa		

References

Bierwisch, C., T Kraft, H Riedel, M Moseler. Three-dimensional discrete element models for the granular statics and dynamics of powders in cavity filling. J Mech Phys Solids. 2009. 57(1), 10-31

Chu, K.W., B Wang, AB Yu, A Vince, GD Barnett, PJ Barnett. CFD–DEM study of the effect of particle density distribution on the multiphase flow and performance of dense medium cyclone. Miner Eng. 2009. 22(11), 893-909

Chu, K., J Chen, AB Yu. Applicability of a coarse-grained CFD–DEM model on dense medium cyclone. Miner Eng. 2015. 90, 43-54

Dietiker, J.-F. T Li, R Garg, M Shahnam. Cartesian grid simulations of gas–solids flow systems with complex geometry. Powder Technol. 2013. 235, 696-705

Garg, R., T Li, S Pannala. Documentation of Open-Source MFIX–DEM Software for Gas-Solids Flows. 2012. From URL: https://mfix.netl.doe.gov/documentation/dem_doc_2012-1.pdf

Gronald, G., JJ Derksen. Simulating turbulent swirling flow in a gas cyclone: A comparison of various modeling approaches. Powder Technol. 2011. 205(1-3), 160-171

Kozołub, P., A Klimanek, RA Białecki, WP Adamczyk. Numerical simulation of a dense solid particle flow inside a cyclone separator using the hybrid Euler–Lagrange approach. Particuology. 2017. 31, 170-180

Muschelknautz, E., V Greif. Cyclones and other gas-solids separators. In: JR Grace, TM Knowlton, AA Avidan (Eds). Circulating Fluidized Beds. Blackie Academics and Professional. 1997. pp. 181-213.

Wan, G., G Sun, X Xue, M Shi. Solids concentration simulation of different size particles in a cyclone separator. Powder Technol. 2008. 183(1), 94-104

ROOT CAUSE ANALYSIS OF AFTERBURN IN RFCC REGENERATOR USING COMPUTATIONAL FLUID DYNAMICS

Mohammad Abdur Rakib[1*], Tommy Firmansyah[1], Syed Basheer[1], Mohamed Al Musharfy[1] and Sam Clark[2]

[1]ADNOC Refining Research Centre, Abu Dhabi National Oil Company (ADNOC) Refining, PO Box 3593, Abu Dhabi, UAE
[2]CPFD LLC, 10899 Montgomery Blvd. NE Suite A, Albuquerque, NM 87111, USA

*Email: *mrakib@adnoc.ae*

Abstract

The regenerator is typically the largest vessel of the Residue Fluid Catalytic Cracking (RFCC) unit, usually operated in the turbulent fluidization regime. In a typical RFCC unit, catalyst regeneration is conducted in a 2-stage regenerator to minimize hydrothermal deactivation of catalyst, due to high Conradson Carbon Residue (CCR) content of the feed. One of problems faced in this regenerator is afterburn or post combustion in the dilute bed region, resulting in high temperatures in the overhead line of the regenerator.

The present study concerns with observed thermal asymmetry and afterburn in a commercial RFCC regenerator, which resulted in reduced RFCC unit severity. Detailed Computational Fluid Dynamics (CFD) model of RFCC regenerator was developed to study the temperature distribution across the dense and dilute phase of the regenerator. This also included the spatial distribution of partly-regenerated catalyst entering the 2nd Stage Regenerator from the 1st Stage Regenerator, and any mal-distribution of air and catalyst in the regenerator.

Uniformity of gas flow is always important for good performance of regenerators, and low uniformity in the dense bed of regenerators is usually associated with afterburn and high levels of NOx emissions. CFD simulation revealed strong bias of higher flow near the axis and the outer wall of the regenerator with very little radial/ lateral velocity components, leading to inefficient mixing of gas and catalyst in the bed, and radial temperature gradient and maldistributions of O2 and CO concentration. The O2-rich air was found streaming near the outer walls and the centre of the dense bed region, and the CO-rich combustion product gases from the dense bed further mixes in the dilute bed region proceeding to complete combustion, leading to further temperature spikes.

Additionally, the distribution of partially regenerated catalyst was revealed to be not optimal. Most of the partially regenerated catalyst goes directly upward from the catalyst distributor without significant lateral distribution, further aggravating the problem.

Introduction

Good temperature distribution across the dense bed of the RFCC regenerator is important to maintain catalyst regeneration and recovering the catalyst activity. One of major problems faced in the regenerator is afterburning or post combustion problem with the presence of abnormally high temperatures in the overhead line of the regenerator. This paper presents root cause analysis (RCA) study of afterburn in an industrial RFCC regenerator.

A computational model was constructed, executed, and analyzed using a commercial Computational Fluid Dynamics (CFD) software specialized in highly densed particulate system called Barracuda Virtual Reactor (VR).

The primary focus of the analysis was mixing of air and partially-regenerated catalyst in the 2nd stage regenerator dense phase and afterburn in the dilute phase.

Modeling Approaches

Barracuda VR is based on Lagrangian-Eulerian approach called Multiphase Particle-in-Cell (MP-PiC), which was first introduced by Snider (2001, 2007) and O'Rourke et. al (2009). The gas phase is represented as continuum Eulerian whereas the solid particles phase is represented by Lagrangian discrete particles with strong coupling between both phases. It solves the transient fluid and particle mass, momentum and energy equations in three dimensions. Particles-particles interaction is modeled with collision stress, based on lumping particles in numerical parcels.

A 3D solid model of the RFCC 2nd stage regenerator was created, as shown in the left of Figure 1. All major components were explicitly modelled including cyclones and diplegs, outlets to withdrawal wells, catalyst cooler withdrawal, air rings, spent catalyst distributor, and catalyst cooler return. The computational mesh comprises 870K cartesian cells, as shown in the right of Figure 1.

Figure 1. Geometry and Computational Mesh of RFCC 2nd Stage Regenerator.

Air is introduced through the lift line, catalyst cooler distributor, air ring distributors, and vents above the withdrawal wells and catalyst cooler withdrawal. Particles were initialized in the system following the catalyst bed inventory at the actual operation.

The model assumes that all hydrogen has been burned off the particles in the 1st stage regenerator and that only carbon remains in the coke that enters the 2nd stage regenerator. Therefore, the initial particle bed only had carbon components in the coke, with 0.02% coke on catalyst. The catalyst and gas flow from the 1st stage regenerator lift line was introduced through 8 flow boundary conditions at the mushroom distributor window locations.

The fluid flow into the system is assumed to be 100% air with a relative humidity of 50%. Particles exited the regenerator through a particle exit flow boundary condition on the catalyst cooler withdrawal well and returned via the cooled catalyst distributor flow boundary condition.

There are two air distributor rings; an inner and an outer air ring. The inner air ring is at a lower elevation than the outher air ring. This was represented by injection boundary condition at the location of each nozzle.

The regenerator has an outer ring of 17 sets of cyclones and an inner ring of 3 sets of cyclones. Each set comprises a first and second stage cyclone. The model assumes 100% efficiency of the cyclones, so all particles exiting the pressure boundary conditions were returned to the first and second stage dipleg flow boundary conditions.

Chemical reactions were modelled with a simplified set of chemical equations. The chemistry was taken from Arbel et. al. (1995) whilst the coke combustion kinetics set was based primarily on the work of Weisz (1966) and Weisz and Goodwin (1966).

Results and Discussions

Figure 2 shows time averaged of different resulting variables along the middle vertical cross-sectional plane. It provides a good overview of flow pattern and overall behavior of particles solid concentration, gas temperature, along with O_2, CO_2 and CO concentration.

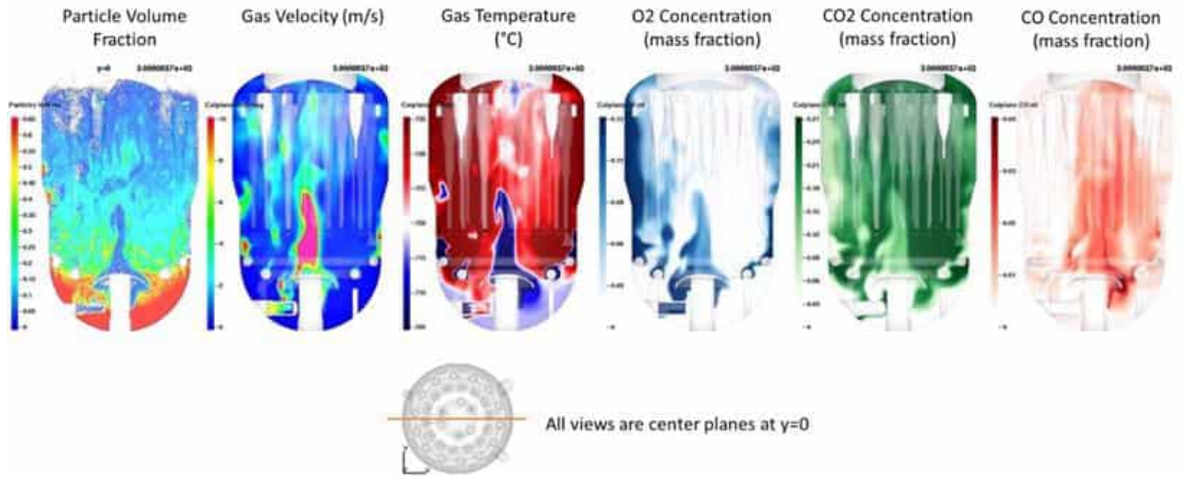

Figure 2. Resulting Variables.

A clear distinct feature of the flow pattern appears at the core and near the outer wall of the 2nd Stage Regenerator. This is highlighted in the high gas velocity regime downstream of the central mushroom distributor and the outer air ring, as shown in the second picture from the left in Figure 2.

As a result of this strong flow regime, most of the solids particles drawn to this region are immediately swept upwardly. Figure 3 shows the impact of the high gas velocity to the solids particle concentration.

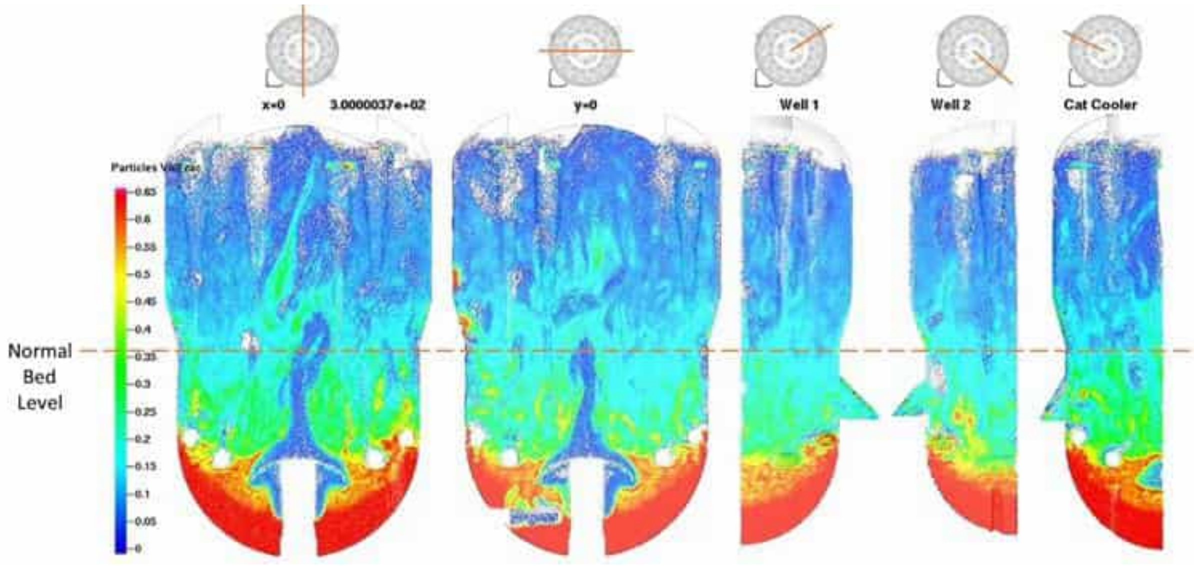

Figure 3. Resulting Solids Particle Concentration.

Movement of catalyst particles are mostly influenced by gas flow stemming from the partially burnt catalyst distributor, i.e. mushroom distributor with underneath lateral window slots, catalyst cooler return distributor and air ring distributors. As the gas flow tends to push axially with no significant radial or lateral component, it thus leads to major stagnant region of catalyst particles at the base of the 2nd Stage Regenerator, as depicted clearly in Figure 3. The stagnation of catalyst could also be due to the inability of Barracuda to model particle-wall stresses correctly resulting in catalyst packing at the wall. The high density zones at the bottom could be caused by the above two factors. Which factor dominates was not the subject of this investigation. Furthermore, the solid volume fraction profile is not uniform above the mushrooom and air ring distributors, showing inefficient mixing of gas and catalyst in the bed.

The non-uniformity of gas flow pattern has also led to mal-distribution of O_2 and CO and temperature gradient across the 2nd Stage Regenerator, as shown in Figure 4. O_2 breakthrough in the dense bed region is clearly visible at the core and near the outer wall following strong axial gas flow from the mushroom distributor and the outer ring distributor, respectively. On the other hand, the CO concentration tends to present more significantly at the core region going into the inner cyclones. This CO imbalance may potentially lead to afterburn problem in the dilute phase as well as the flue gas line when localized combustion of CO with O2 occurs and causes temperature spikes.

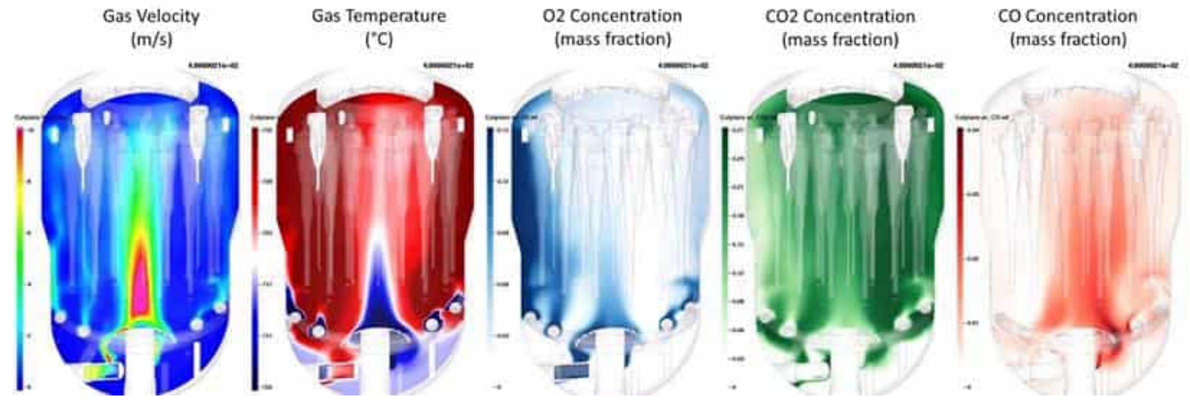

Figure 4. Time Averaged Axial Distribution.

Gas temperature distribution in Figure 4 shows similar pattern to that of velocity, with relatively cool temperature near the air grid distributors (mushroom and air rings). The gas quickly heats to the regenerator operating temperature in the dilute phase where the catalyst density is low.

Figure 5 shows the distribution of partiallly regenerated catalyst from the 1st Stage Regenerator after entering through the mushroom distributor. The color represents the particles residence time with the upper scale (red) showing the residence time of 10 seconds and above. The high gas axial velocity obviously pushes the partly regenerated particles immediately upward as soon as it enters the lateral window slots in the lift line and passes through the mushroom distributor. This again illustrates that the distribution of spent catalyst in the dense bed is poor due to very little lateral mixing of catalyst into the dense bed.

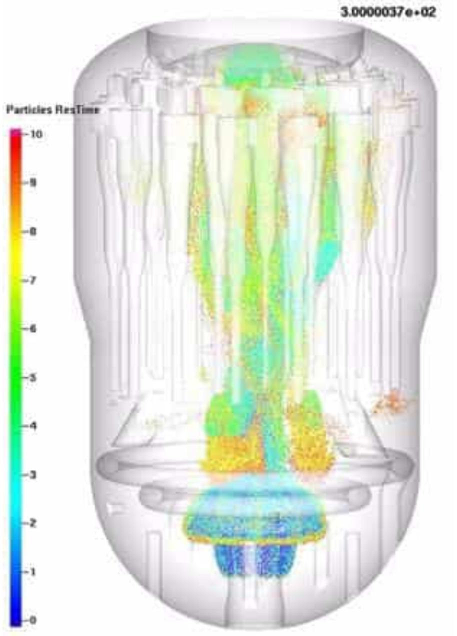

Figure 5. Particles Residence Time of Partially Regenerated Catalyst.

Conclusions

The simulation results revealed strong bias of flow at the core and the outer wall of the 2nd Stage Regenerator with very little radial/ lateral velocity components. This in turn led to inefficient mixing of gas and catalyst in the bed, temperature gradient and maldistribution of O2 and CO concentration. Afterburn and thus temperature spike along the dilute phase and flue gas line is likely due to O2-rich air which streams near the outer walls contacting CO-rich combustion gases near the center.

References

Arbel, A., Huang, Z., Rinard, I. H., Shinnar, R. Dynamics and control of fluidized catalytic crackers. 1. Modelling of the current generator of FCC's. Industrial & Engineering Chemistry Research, 1995. 34, 1228-1243.
O'Rourke, P. J., Zhao, P., Snider, D. M. A model for collisional exchange in gas/liquid/solids fluidized beds, Chemical Engineering Science, 2009. 64, 1784-1799.
Snider, D. M. An incompressible three-dimensional multiphase particle-in-cell model for dense particle flows, Journal of Computational Physics. 2001. 170, 523-549.
Snider, D. M. Three fundamental granular flow experiments and CPFD predictions, Powder Technology. 2007. 176, 36-46.
Weisz, P. Combustion of carbonaceous deposits within porous catalyst particles. III. The CO_2/CO product ratio. Journal of Catalysis. 1966. 6, 425-430.
Weisz, P., Goodwin, R. Combustion of carbonaceeous deposits within porous catalyst particles. II. Intrinsic burning rate. Journal of Catalysis. 1966. 6, 227-236.

STOCHASTIC SIMULATION OF SPRAY FLUIDIZED BED AGGLOMERATION BY MODELING THE MORPHOLOGY

Abhinandan Kumar Singh*, **Evangelos Tsotsas**

Thermal Process Engineering, Otto von Guericke University, Universitätsplatz 2, 39106, Magdeburg, Germany

*Email: *abhinandan.singh@ovgu.de*

Abstract

Spray fluidized bed (SFB) agglomeration is a widely used size enlargement process in the food, pharmaceutical and chemical industries. The microscopic features of the respective agglomerates (like porosity, fractal dimension, prefactor, coordination number) influence their macroscopic properties (like density, strength, flowability). In order to understand the characteristics of a product, morphological descriptors of the formed agglomerates are imperative. In previous studies, a characteristic sphere with constant porosity (= 0.6) was used to predict the kinetics of the SFB agglomeration in a stochastic and discrete constant volume Monte Carlo (CVMC) model. However, the morphology of the emerging agglomerates was not captured. In the present study, a cross-correlation between the various morphological descriptors is implemented in the CVMC model to capture the morphological change. In addition, an aggregation model is incorporated instead of a simplistic approach to reconstruct the SFB agglomerates externally. Using a novel approach, agglomerates with different fractal properties are generated using a particle cluster algorithm by tuning the fractal dimension at a given prefactor (= 1). Consequently, the morphological descriptors of different agglomerates formed at varying input parameters (inlet fluidized gas temperature and binder content) are compared with experimental results.

1. INTRODUCTION

Agglomeration processes are widely used to modify the physical properties of powders such as size, shape, porosity to generate products with specific desired characteristics such as solubility, mechanical strength, or flowability. One of the most effective agglomeration processes is spray fluidized bed (SFB) agglomeration. The basic principle of this process is quite simple: a liquid binder (HPMC) is dispersed onto a bed of solid particles. Particle collisions promote the formation of liquid bridges among particles or agglomerates. The liquid evaporates in the fluidization gas forming solid bridges and “blackberry-like” agglomerates. Once the agglomerates reach a desired size, they are discharged from the fluidized bed.

Agglomerate formation is considered as a complex network of discrete micro-mechanisms among particles, agglomerates, and binder droplets, which occur in series and in parallel. Such micro-mechanisms are particle wetting, deposited droplet drying, collisions, liquid bridge formation and agglomerate breakage. Terrazas et al. (2009) introduced a discrete CVMC model by implementing most of these micro-mechanisms to enhance the understanding of SFB agglomeration. This model has a stochastic approach based on the use of random numbers and probability statistics. The connection between CVMC and the particulate system is provided by the event-driven nature of the method. An “event” is defined as a collision between particles in the fluidized bed. In the present study, these micro-mechanisms except the breakage are separately modeled and implemented into a comprehensive model (CVMC). Formed agglomerates are reconstructed using off-lattice particle-cluster (PC) algorithm tuned with its fractal property (fractal dimension and prefactor). A novel approach is incorporated to reconstruct the agglomerates of varied fractal properties using a single algorithm by tuning the fractal dimension at particular prefactor (which is taken as one in this study).

2. COMPUTATIONAL METHOD

In the present modeling scheme as shown in Fig. 1, the CVMC model is incorporated with an aggregation model.

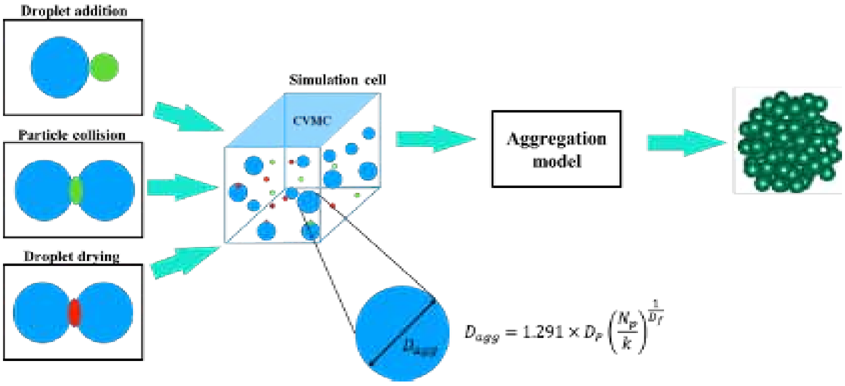

Fig. 1: Modeling scheme for spray fluidized bed agglomeration.

In the CVMC model, a binder is continuously added to the particles. The relationship between the real process and model is established by the concentration of droplets per unit time and particle inside the simulation box. The number of droplets added per unit time and particle in the real process, which depends on the liquid flow rate and the droplet diameter, is

$$\gamma = \frac{\dot{M}_l}{M_{bed}}\left(\frac{\rho_p}{\rho_l}\right)\left(\frac{D_p}{D_d}\right)^3. \tag{1}$$

Particle collision

Interparticle collisions play a crucial role in the numerical calculation carried out in this study; their discrete nature allows us to calculate the length of the time step during the simulation and thus to correlate real with computational time. In this study, the experimental correlation proposed by Buffière and Moletta (2000), is used to estimate the frequency of collisions within the fluidized bed

$$f_{coll} = F_{coll}\left(1 - \frac{\emptyset_{exp}}{\emptyset_{fix}}\right)\left(\frac{\emptyset_{exp}}{\emptyset_{fix}}\right)^2 u_0, \tag{2}$$

where u_o is the fluidization velocity, $\emptyset_{exp}$ and $\emptyset_{fix}$ are the solid volume fractions of the expanded bed and the fixed bed, respectively, and $F_{coll}(= 10)$ is the collision frequency prefactor. Solid volume fraction of the fixed bed is assumed 0.61. This correlation describes the behavior of the number of collisions that a particle experiences per unit time as the fluidized bed moves from the elutriation to the packed bed limit.

In order to advance the simulation in real-time, a number of events are set at the beginning of the simulation. As the events occur one after the other, the frequency of collisions for each event is calculated and the length of the time step for each collision is set to

$$t_{step} = \frac{1}{f_{coll}}. \tag{3}$$

Droplet drying

A liquid droplet deposited on a particle will take the shape of a spherical cap with a base radius a and height h_0 (Clarke et al. 2002),

$$a = \left(\frac{3V_d}{\pi}\frac{\sin^3\theta}{2-\cos\theta+\cos^3\theta}\right)^{1/3}, \tag{4}$$

$$h_0 = a\left(\frac{\sin\theta}{1+\cos\theta}\right). \tag{5}$$

A value of $\theta = 40°$ applies here for a binder deposited on the non-porous glass beads used as primary particles. Once the droplet has been deposited on the particle, it evaporates and eventually solidifies. Droplet drying is described by reduction of droplet height with time as

$$h_{dry} = h_0 - \frac{2}{3}\frac{\rho_g}{\rho_w}\frac{\tilde{M}_l}{\tilde{M}_g}\frac{\beta}{1-\cos\theta}\left(\frac{P_v^*}{P} - \tilde{y}_g\right)\left[\frac{1}{1-\cos\theta} - \frac{1}{3}\right]^{-1} t, \tag{6}$$

where β is the mass transfer coefficient, P_v^* and P are the saturation vapor pressure and the system pressure respectively. The molar fraction of water in the gas phase

$$\tilde{y}_g = \frac{Y_g}{Y_g - (\tilde{M}_w/\tilde{M}_g)}, \tag{7}$$

is obtained from gas moisture content Y_g by assuming that the fluidized bed is perfectly mixed and the amount of evaporating water is at any time equal to the amount of water sprayed.

Particle coalescence

Particles or agglomerates will coalesce if their initial kinetic energy is small enough to overcome the viscous lubrication resistance in the liquid layer. The critical conditions for the dissipation of kinetic energy by a viscous layer of a given thickness were first derived by Adetayo and Ennis (1997) in the form of a Stokes number

$$St_{coal} = \frac{2M_{agg}u_c}{3\pi\mu_l {D_{agg}}^2}\,. \tag{8}$$

Coalescence between two colliding particles (agglomerates) happens when the Stokes number is smaller than the critical Stokes number

$$St_{coal}^* = \left(1 + \frac{1}{e}\right)\ln\left(\frac{h}{h_a}\right). \tag{9}$$

In the case of collision between particles of unequal size, a combined mass and diameter are used:

$$M_{agg} = \frac{2M_{agg1}M_{agg2}}{M_{agg1} + M_{agg2}}, \tag{10}$$

$$D_{agg} = \frac{2D_{agg1}D_{agg2}}{D_{agg1} + D_{agg2}}\,. \tag{11}$$

The Stokes model depends strongly on the particle collision velocity. In this study, the collision velocity of the pair of particles is randomly chosen by assuming a normally distributed function around a mean value equal to $0.5u_0$.

Agglomerate diameter

For simplification, in CVMC model each formed agglomerate is considered as a sphere with a characteristic diameter

$$D_{agg} = \left[\frac{N_p {D_p}^3}{1 - \varepsilon_{agg}}\right]^{1/3}. \tag{12}$$

Assuming the primary particles as monodisperse, porosity of an agglomerate as developed by Singh and Tsotsas (2019) can be expressed as

$$\varepsilon_{agg} = 1 - 0.465 N_p \left(\frac{k}{N_p}\right)^{3/\mathrm{D_f}}\,. \tag{13}$$

Inserting the porosity expression (Eq. (13)) in Eq. (12), we finally get

$$D_{agg} = 1.291 \times D_P \left(\frac{N_p}{k}\right)^{1/\mathrm{D_f}}. \tag{14}$$

Agglomerate structure

SFB agglomerates formed using the CVMC model are restructured using an aggregation model. In the present aggregation model, we use the sequential algorithm (SA) proposed by Filippov et al. (2000). This is off-lattice particle-cluster (PC) model and the input parameters are the number and radius of primary particles (N_p & R_p) and the fractal property (D_f & k) of an agglomerate. The only limitation of SA is that prefactors, $k > 1.66$ are not possible. This limitation is overcome by tuning D_f with respect to the porosity correlation obtained in Eq. (13) and can be found in Singh and Tsotsas (2020). Keeping the porosity (ε_{agg}) and the number of primary particles (N_p) same, we change the fractal dimension by limiting the prefactor ($= 1$)

$$\varepsilon_{agg} = 1 - 0.465 N_p \left(\frac{1}{N_p}\right)^{3/D_{f\,tuned}}, \tag{15}$$

and the correlation for tuned fractal dimension at specific prefactor ($= 1$) is

$$D_{f\,tuned} = D_f \left(\frac{\log N_p}{\log \frac{N_p}{k}}\right). \tag{16}$$

If we use the power-law relationship (which correlates the number of primary particles of the agglomerates, N_p, with their radii of gyration, R_g),

$$N_p = k \left(\frac{R_g}{R_p}\right)^{D_f}, \tag{17}$$

to compute the change in the fractal property using the same radius of gyration, we end up with the same correlation as in Eq. (16). This can also be explained in Fig. 2 with the concept of straight lines formed on the log scale for the power-law relationship (Eq. (17)),

$$\log N_p = D_f \log \left(\frac{R_g}{R_p}\right) + \log k. \tag{18}$$

By tuning the fractal dimension with prefactor one, the formed agglomerates are almost the same. Therefore, by tuning the fractal dimension with prefactor one we can overcome the limitation of SA and construct all the agglomerates. However, there is a limitation as depicted in Fig. 2.

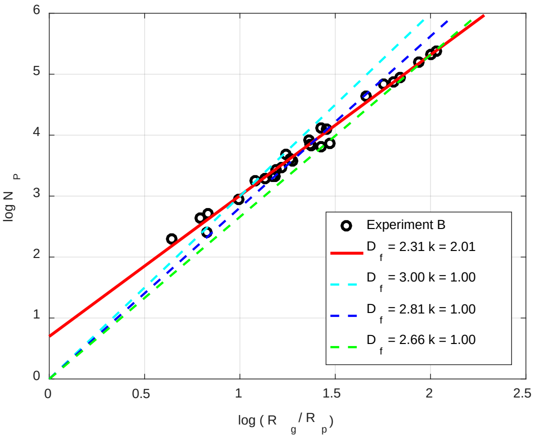

Fig. 2. Logarithmic plots of power-law from the origin (dashed lines) with same prefactor (= 1) and different slopes ($D_f = 3.00, 2.81, 2.66$) leading to a desired plot (solid line) with prefactor ($k = 2.01$) and fractal dimension ($D_f = 2.31$).

As the slope increases the fractal dimension also increases, but $D_f > 3$ is physically not feasible. The slopes of the dashed lines (in Fig. 2) can only be increased until 71.5°. This limits the formation of aggregates with primary particles less than

$$N_{p,lim} = k^{\left(\frac{3}{3-D_f}\right)}. \tag{19}$$

This limitation is overcome by constructing the aggregates until $N_{p,lim}$ at $D_f = 3$ and $k = 1$. The idea behind using this particular value of D_f and k is the compactness of smaller agglomerates in SFB agglomerator. Consequently, we are able to construct the agglomerates using the novel approach of tuned fractal dimension into SA. Further, we use this algorithm as tunable sequential aggregation (TSA) model for generating all the agglomerates.

3. RESULTS AND DISCUSSION

Morphological descriptors (D_f, k, average ε_{agg}, MCN) obtained for the different experiments by Dadkhah and Tsotsas (2014) especially for Exp. A to Exp. E with glass beads as the primary particles, are presented in Table 1. Experiments B, A, and C represent the increasing inlet fluidized gas temperature of 30℃, 60℃ and 90℃. Similarly, experiments A, D and E represent increasing binder (HPMC) concentration of 2 wt. %, 6 wt. % and 10 wt. %. Agglomerates with the same number of primary particles as examined by Dadkhah et al. (2014) are aggregated using the TSA model and the morphological descriptors obtained are averaged over five realizations. D_f and k of the synthetic agglomerates using TSA model are calculated using the power law relationship (Eq. (18)) for the entire sample, similar to Dadkhah et al. (2014) evaluation method. Average $\varepsilon_{\mathrm{agg}}$ and average MCN are the mean porosity and average MCN of all the agglomerates in a batch (experimental trial).

Table 1. Experimental and simulation results for each trial.

	A	B	C	D	E
Temperature [℃]	60	30	90	60	60
Binder [wt. %]	2	2	2	6	10
Experimental results for each trial as in Dadkhah and Tsotsas (2014)					
D_f [-]	2.45	2.31	2.94	2.24	2.09
k [-]	1.76	2.01	0.98	1.96	2.24
Average $\varepsilon_{\mathrm{agg}}$ [-]	0.57	0.62	0.53	0.58	0.63
Average MCN	3.32	3.10	4.02	2.92	2.87
TSA model results for each trial (averaged over 5 realizations)					
D_f [-]	2.37	2.24	2.72	2.17	2.05
k [-]	2.12	2.37	1.48	2.32	2.53
Average $\varepsilon_{\mathrm{agg}}$ [-]	0.54	0.59	0.53	0.55	0.64
Average MCN	3.61	3.52	3.90	3.31	3.09

Morphological descriptors obtained from the TSA model are in strong agreement with the experimental values as seen in Table 1. Overall simulations are carried out with the same parameters as in Singh and Tsotsas (2019) and results obtained (denoted by new model in Fig. 3) are quantitatively in agreement with them. With an increase of inlet gas temperature, the agglomerates become compact because the fractal dimension increases and the size (diameter) decreases (as shown in Fig. 3). Contrarily, as the mass fraction of the binder increases, the fractal dimension of the agglomerates decreases. Consequently, the agglomerates become branched and porous and their size (diameter) increases (Fig. 3).

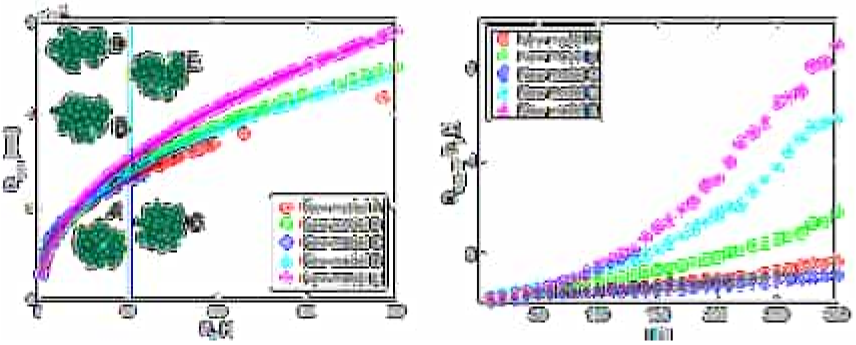

Fig. 3. CVMC simulation for different experiments by incorporating the TSA model.

4. CONCLUSION

A stochastic model to simulate the SFB agglomeration process was developed by incorporating the aggregation model to mimic the agglomerates formed rather than using a characteristic sphere. The tunable off-lattice PC aggregation model proposed by Filippov et al. was used for reconstructing the SFB agglomerates. This model could not construct all SFB agglomerates because it had the prefactor limitation (more than 1.66 not possible). A novel approach of tuning the fractal dimension with a given prefactor $(= 1)$ has been introduced to overcome the limitation of prefactor. This CVMC model incorporated with the TSA model can predict the kinetics as well as the morphological descriptors of the agglomerates formed at different operating conditions (inlet fluidized gas temperature and binder content) of SFB agglomeration. The model would become more accurate if we could model the breakage of the agglomerates, which is a future goal.

Notation

a	base radius, m
A	area, m^2
D	diameter, m
D_f	fractal dimension
e	restitution coefficient
f_{coll}	collision frequency, 1/s
F_{coll}	collision frequency prefactor, 1/m
g	gravity, m^2/s
h	binder layer thickness, m
h_a	height of particle surface asperities, m
k	prefactor
M	mass, kg
$\dot{M}$	mass flow rate, kg/s
$\widetilde{M}$	molecular weight, kg/kmol
N	number of particles
P	pressure, Pa
P_v^*	saturation vapor pressure, Pa
R_a	radius of an aggregate, m
R_g	radius of gyration, m
	Stokes coalescence number
	Stokes coalescence critical number
t	time, s
T	temperature, ℃
u_c	collision velocity, m/s
u_0	fluidization gas velocity, m/s
V	volume, m^3
x	mass fraction
$\tilde{y}_g$	molar fraction in the gas phase
Y	moisture content, kg/kg

Greek letters

β	mass transfer coefficient, m/s
γ	droplet addition rate, 1/s
ε	porosity
θ	contact angle, deg
μ	viscosity, Pa s
ρ	density of the particle, kg/m^3
$\emptyset$	solid volume fraction

Subscripts

agg	agglomerate
b	binder
d	droplet
dry	drying
g	fluidization gas
in	inlet
l	liquid, binder
p	primary particle
w	water
0	initial

References

Adetayo, A. A., B. J. Ennis. Unifying Approach to Modeling Granule Coalescence Mechanisms. AIChE Journal. 1997. 43(4), 927-934.

Buffière, P., René Moletta. Collision Frequency and Collisional Particle Pressure in Three-Phase Fluidized Beds. Chemical Engineering Sci. 2000. 55 (22), 5555–63.

Clarke, A., T. D. Blake, K. Carruthers, and A. Woodward. Spreading and Imbibition of Liquid Droplets on Porous Surfaces. Langmuir. 2002. 18(8), 2980-2984.

Dadkhah, M., E. Tsotsas. Influence of Process Variables on Internal Particle Structure in Spray Fluidized Bed Agglomeration. Powder Technol. 2014. 258, 165–73.

Filippov, A. V., M. Zurita, D. E. Rosner. Fractal-like Aggregates: Relation between Morphology and Physical Properties. Journal of Colloid and Interface Sci. 2000. 229(1), 261-273.

Singh, A. K., E. Tsotsas. Stochastic Model to Simulate Spray Fluidized Bed Agglomeration: A Morphological Approach. Powder Technol. 2019. 355, 449–60.

Singh, A. K., E. Tsotsas. A tunable aggregation model incorporated in Monte Carlo simulations of spray fluidized bed agglomeration. Powder Technol. 2020. 364, 417–28.

Terrazas-Velarde, K., M. Peglow, E. Tsotsas. Stochastic Simulation of Agglomerate Formation in Fluidized Bed Spray Drying: A Micro-Scale Approach. Chemical Engineering Sci. 2009. 64 (11), 2631–43.

WALL TEMPERATURE CALCULATION AND SAFETY ANALYSIS FOR THE WATER WALL OF 660 MW ULTRA-SUPERCRITICAL CIRCULATING FLUIDIZED BED BOILER

Dong Yang*, Ziyu Liang, Le Dong, Xihong Zhou, Juan Li

State Key Laboratory of Multiphase Flow in Power Engineering, Xi'an Jiaotong University, Xi'an 710049, Shaanxi, China

* Email: *dyang@mail.xjtu.edu.cn*

Abstract

Temperature safety analysis was conducted on the smooth tube of the supercritical circulating fluidized bed boiler through experiments, numerical simulation, and hydrodynamic calculation. The numerical simulation results of the inner wall temperature were compared with the results of the experiments and hydrodynamic calculation. Experimental results showed that heat transfer enhancement occurred near a pseudocritical point. Non-uniform circumferential heating weakened the buoyancy effect, which could effectively delay or prevent the occurrence of heat transfer deterioration, and the circumferential distribution of the wall temperature and heat flux was parabolic. The simulated results of the inner wall temperature were in satisfactory agreement with the experimental results. Furthermore, the inner wall temperature values of the hydrodynamic calculation were lower than the experimental values. These findings indicated that the temperature experimental results obtained by non-uniform circumferential heating were conservative.

Introduction

The circulating fluidized bed (CFB) boiler is extensively adaptable to coal and can decrease the density of emitted nitrogen oxides (NO_x) and sulfides to reduce combustion temperature. Therefore, the CFB boiler is a clear and effective coal combustion technology with high combustion efficiency. Moreover, the efficiency of the Rankine cycle is enhanced as CFB parameters improve. Supercritical CFB technology presents a remarkable advantage for economic development and environment protection. Therefore, it is necessary to analyze the safety of CFB boiler wall temperature. Dong et al. (2019) established the mathematical model of thermal-hydraulic calculation and calculated the thermal-hydraulic characteristics of 660 MW high-efficiency ultra-supercritical CFB boiler developed by China at four loads with this model. The results show that the metal temperature of the water wall at four loads are both permissible. The water wall will not flow instability and the operation of the boiler is safe.

Heat transfer deterioration (HTD) increases tube wall temperatures, thereby threatening the safe operation of a ultra-supercritical CFB boiler. Therefore, research has been conducted on ways to maintain wall temperatures within a safe range to avoid HTD. Ackerman (1970) claimed that pseudo film boiling leads to HTD. Jackson et al. (1989) further explained this phenomenon by claiming that buoyancy causes convective heat transfer change, from variable property forced convection to mixed convection. Shen et al. (2017) used an SST (shear stress transport) model to predict HTD under uniform heating conditions and identified the buoyancy effect as the main reason for abnormal heat transfer.

Ishikawa et al. (1982) utilized a heating rod to heat the smooth tube on one side. The experimental results showed that the wall temperature and heat transfer coefficient (HTC) are unevenly distributed in a circumferential direction, and the peak values appear at the midpoint of the heated side ($\varphi = 45°$). The heat transfer of ultra-supercritical water in a vertical upward tube under non-uniform heating has been investigated numerically (Qu et al, 2018). Studying the non-uniform heating of a vertical upward tube, which approximates an actual situation, and comparing it with uniform heating are necessary owing to conflicting conclusions from previous studies on the heat transfer of ultra-supercritical water in one-side heated tubes.

In the present study, the inner wall temperature of a supercritical CFB boiler is analyzed and calculated through experiments, numerical simulation, and hydrodynamic calculation to conduct a safety analysis.

Experimental Apparatus and Numerical Simulation

This experiment was conducted on a high-pressure steam water test loop, and the system structure is shown in Fig. 1 and Fig. 2.

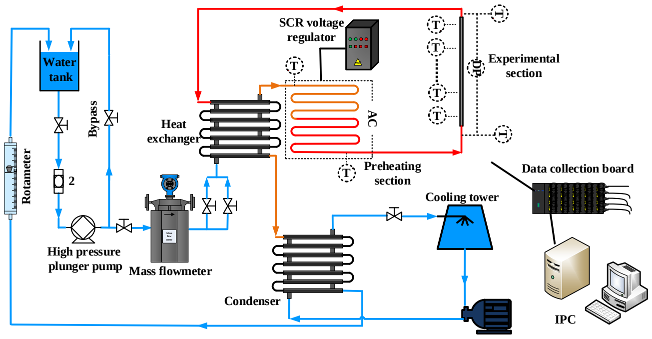

Fig. 1. Experimental system and apparatus.

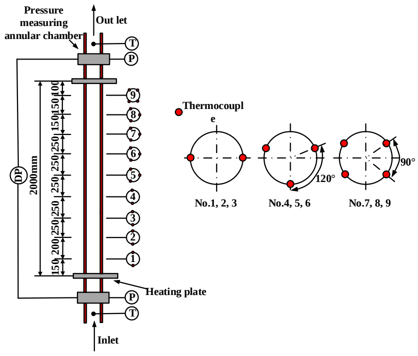

Fig. 2. Structure of experimental section.

The test system consisted of a deionized water tank, a high-pressure plunger pump, a mass flowmeter, a flow control valve, a regenerator, an experimental section, a cooling pump, and a cooling water tank. The smooth tube was connected to an alternating current with a large current and small voltage, and heat was generated by resistance. During the experiment, deionized water was driven from the water tank by the high-pressure plunger pump through the mass flow meter. Next, the water diverged into two paths. In one path, the water went through the bypass then back into the deionized water tank, which regulated flow and pressure. In the other path, the water entered the preheating section. The working temperature condition can reach the set working condition parameters by adjusting the heating power of the preheating section. The water was heated in the test section, and the hot water that entered the heat exchanger was finally chilled to below 70 °C in the condenser. Subsequently, the supercritical water returned to the cooling water tank, and the next cycle commenced. The outer wall temperature of the smooth tube was measured by the thermocouple. Meanwhile, the inner wall temperature was calculated on the basis of the heat transfer calculation. The temperatures of the inlet and outlet of the test section were measured by the armored thermocouple. Pressure and pressure drop were measured by the pressure and differential pressure transmitter, respectively.

The CFD software ANSYS Fluent with the SST *k-ω* turbulent model and the SIMPLEC algorithm were used for the calculation. The computational physical model is shown in Fig. 3. The smooth tube was Φ30 mm×5.5, with a length of 2 m, and made from 12CrMoVG material. An adiabatic section was included before the heated section to ensure the entrance of fully developed turbulence. The inlet of the adiabatic section was set as the constant velocity inlet, while the outlet was set as the pressure outlet. A no slip condition was set for the tube interface. The heat flux at the outer wall of the uniform heating tube was constant. Meanwhile, one side of the outer wall surface of the non-uniform heating tube was subjected to uniform heat flux, while the other side was set under an adiabatic condition. The circumferential angle (φ) was defined as 0° at the middle of the heated side. The structured computational mesh is shown in Fig. 4. The number of meshes used in the numerical simulation was 520×10^4 after the independence of the meshes was verified.

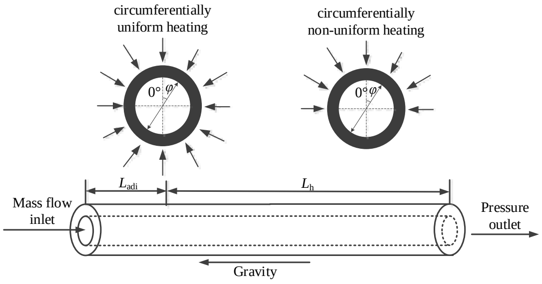

Fig. 3. Geometrical and boundary conditions.

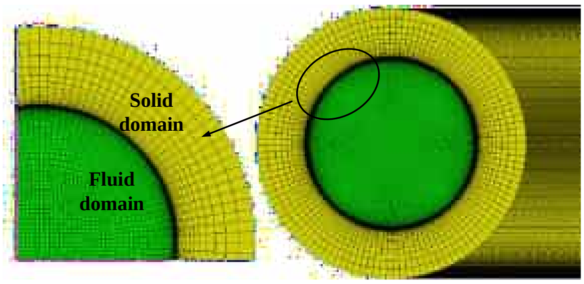

Fig. 4. Computational meshes adopted in simulation.

Uniform and non-uniform heating under the same parameters are simulated (Fig. 5 [a]) according to the HTD condition in the experiment of Ackerman (1970). In contrast to uniform heating, no HTD occurs in the smooth tube under non-uniform heating, and the maximum value of the inner wall temperature changes evenly with the bulk fluid temperature. HTD occurs when the maximum heat flux increases to 420 $\mathrm{kW{\cdot}m^{-2}}$ under non-uniform heating. Moreover, HTD occurs early because the local heat flux is higher in non-uniform heating compared with uniform heating.

Upward and downward flows result under the same heating conditions shown in Fig.5 (b). HTD occurs in the upward flow under uniform heating but is not observed in the downward flow. This phenomenon indicates that the buoyancy effect can lead to HTD. Buoyancy under two heating conditions is the main cause of HTD. Buoyancy increases axial velocity near the inner wall, decreases the radial velocity gradient, weakens turbulence intensity, and ultimately leads to the HTD of the upward flow.

Fig. 6 presents the simulation results of the distribution of the inner wall temperature and heat flux along the circumferential direction under non-uniform heating. The distribution of the inner wall temperature is parabolic under non-uniform heating, and the inner wall temperature is highest at the midpoint of the heated side (φ = 0°). Meanwhile, the inner wall temperature is lowest at the midpoint of the adiabatic side (φ= 180°). The temperature of inner wall shows a monotonous upward trend from the midpoint of the adiabatic side to the midpoint of the heated side. The distribution of heat flux in non-uniform heating is similar to that of the circumferential inner wall temperature. Maximum and minimum heat fluxes appear at the midpoints of the heated and adiabatic sides, respectively.

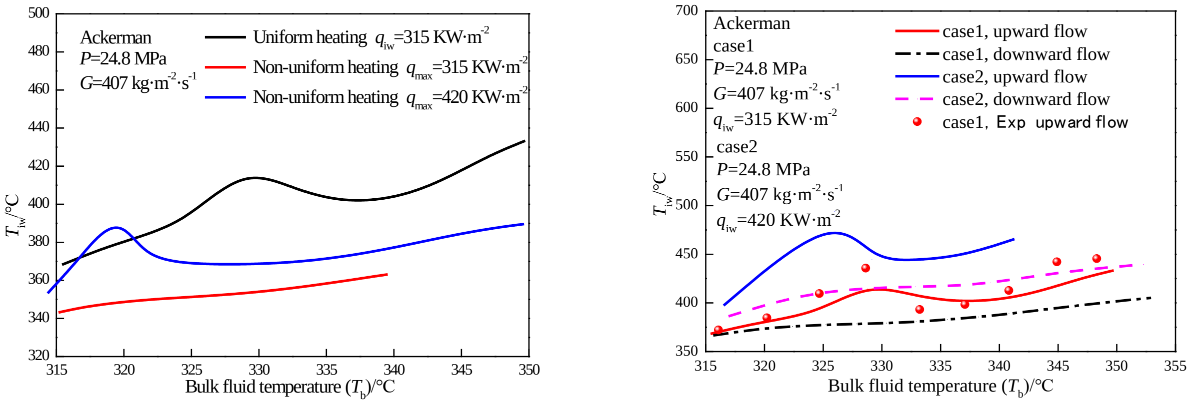

(a) uniform and non-uniform heating

(b) upward flow and downward flow

Fig. 5. Inner wall temperature distribution.

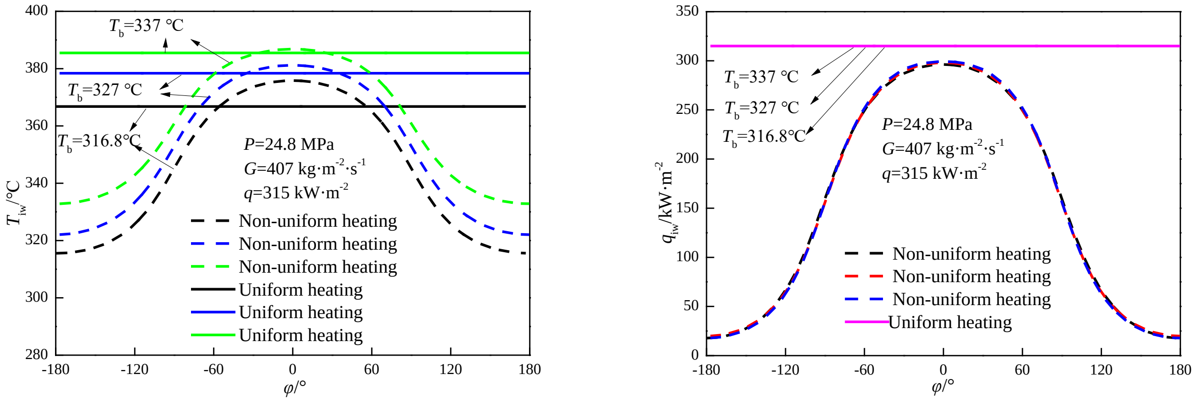

Fig. 6. Circumferential distribution of the inner wall temperature and heat flux of non-uniform heating.

Experimental Results

Fig. 7 shows the effects of mass flux, heat flux, and pressure on the inner wall temperature and on the HTC of the smooth tube. As shown in Fig. 7, the inner wall temperature sharply rises when the enthalpy increases, and then slowly and sharply increases once again when enthalpy exceeds 2400 kJ·kg^{-1}. The inner wall temperature decreases and the HTC increases with the rise of mass flux. The result shows that heat transfer is remarkably affected by mass flux. Thus, the HTC reaches an extreme value in the pseudocritical enthalpy region. The result indicates that heat transfer is enhanced when enthalpy reaches the pseudocritical region. However, the heat transfer enhancement disappears when enthalpy is outside the region.

The HTC in the pseudocritical enthalpy point decreases when heat flux increases. Moreover, the difference in the HTC between 90 and 250 kW·m^{-2} becomes 1.81 kW·m^{-2}·K^{-1} when enthalpy reaches 1600 kJ·kg^{-1}. The difference in the HTC becomes 10.02 kW·m^{-2}·K^{-1} when enthalpy reaches 2200 kJ·kg^{-1}. Thus, an increase in heat flux can decrease heat transfer performance. The HTCs are 11.13 kW·m^{-2}·K^{-1} and 9.09 kW·m^{-2}·K^{-1} as pressure values become 23 MPa and 25 MPa, respectively, when enthalpy reaches 2400 kJ·kg^{-1}. The curves of the inner wall temperature become flat, and the heat transfer curves rapidly increase when the bulk fluid enthalpy nears the pseudocritical point. The inner wall temperature increases and the HTC decreases as pressure rises. The experimental resluts show that the inner wall temperature on the water wall of a 660 MW ultra-supercritical CFB boiler are safe under ultra-supercritical parameters with uniform heating.

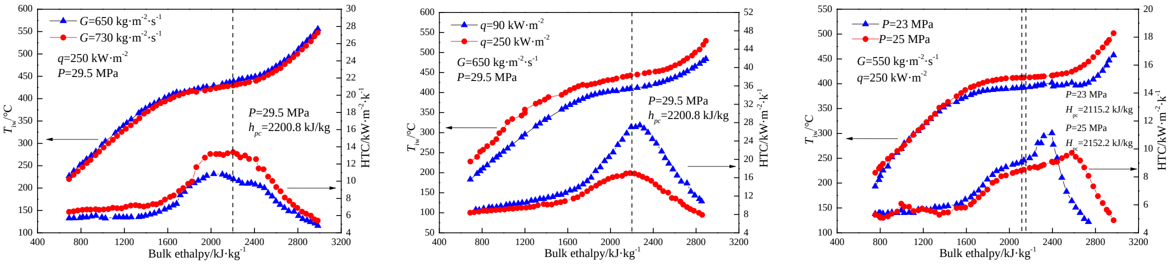

Fig. 7. Effect of mass flux, heat flux and pressure on the inner wall temperature and HTC.

The design scheme of the 660 MW high-efficiency ultra-supercritical CFB boiler, which is independently developed by China, is used, and four representative points, namely, A, B, C, and D, along the height direction (17.06 m, 32.01 m, 50.2 m, and 59.4 m, respectively) are selected for the wall temperature safety analysis. The numerical simulation model and method are the same as those described previously, but the size of the smooth tube is changed to Φ31.8×7 mm. The experimental results are obtained via the experimental platform of the State Key Laboratory of Multiphase Flow in Power Engineering at Xi'an Jiaotong University under the CFB boiler design and operation conditions. The hydrodynamic calculation results are obtained by a self-developed calculation software, which has been recognized by the industry in the calculation of boiler flow distribution and safety analysis in the project (Dong et al, 2019). The boundary conditions for positions of A, B, C, and D are selected from the actual operating parameters of the ultra-supercritical CFB boiler under BMCR load operation conditions, and the comparison results of the inner wall temperature numerical simulation, experiments, and hydrodynamic calculation are shown in Table 1. The subscript iw represents inner wall.

Table 1. The inner wall temperature results obtained from different methods.

Temperatures	units	experiments	hydrodynamic calculation	uniform heating	non-uniform heating
TA_{iw}	℃	388.7	379.0	384.8	366.8
TB_{iw}	℃	420.1	414.2	418.3	401.8
TC_{iw}	℃	434.1	425.5	436.2	418.4
TD_{iw}	℃	441.4	431.3	444.1	425.1

The simulated results of the inner wall temperature at points A, B, C, and D are in satisfactory agreement with the experimental results. However, the inner wall temperature results of the hydrodynamic calculation are lower than the experimental results. The numerical simulation results show that the inner wall temperature of non-uniform heating are always lower than that of uniform heating. These findings indicate that the experimental results obtained by circumferential uniform heating are conservative. The results of the experiments, hydrodynamic calculation, and numerical simulation show that the wall temperature of the 660

MW high-efficiency ultra-supercritical CFB boiler can be guaranteed within the allowable range of materials without film boiling and overheating under BMCR load operation conditions. In addition, the tube material used for boiler water wall can bear the maximum temperature of 550℃. Thus, the temperature of the water wall is safe.

Conclusion

(1) Non-uniform heating and downward flow can weakens the buoyancy effect so that can effectively delay or avoid the occurrence of heat transfer deterioration of ultra-supercritical fluid, that is, its critical heat flux is higher. The inner wall temperature and heat flux of the smooth tube under non-uniform heating are both distributed parabolically along the circumferential direction.

(2) The experimental results show that the inner wall temperature gradually increased with the increase of enthalpy in the pseudo-enthalpy region and sharply increased with the increase of enthalpy in the low-enthalpy region. The phenomenon indicated that heat transfer enhancement occurs near a pseudo-critical point.

(3) The simulated results of the inner wall temperature at Points A, B, C and D are close to the experimental results. The inner wall temperature results of hydrodynamic calculation are lower than the experimental results. That indicated the experimental results obtained by using circumferentially uniform heating are conservative.

Acknowledgment

This work is financially supported by the National Key Research & Development Program of China (No. 2016YFB0600201).

References

Ackerman, JW (1970). Pseudo-boiling heat transfer to supercritical pressure water in smooth and ribbed tubes. Journal of Heat Transfer, 92 (3):490.

Dong L., YF Xin, J Li, D Yang et al (2019). Computational analysis on thermal-hydraulic characteristics and flow Instability of a 660 MWe ultra-supercritical circulating fluidized bed boiler. Proceedings of The Chinese Society for Electrical Engineering (under review).

Ishikawa H., S Suhara, T Abe et al (1982). Forced convection heat transfer to supercritical water from semi-circumferential heated surface in vertical tubes. Transactions of the Japan Society of Mechanical Engineers Series B, 48 (430): 1093-1102.

Jackson JD, MA Cotton, BP Axcell (1989). Studies of mixed convection in vertical tubes. International Journal of Heat & Fluid Flow, 10 (1):2-15.

Qu MF, D Yang, ZY Liang et al (2018). Experimental and numerical investigation on heat transfer of ultra-supercritical water in vertical upward tube under uniform and non-uniform heating. International Journal of Heat and Mass Transfer, 127:769-783.

Shen Z., D Yang, SY Wang et al (2017). Experimental and numerical analysis of heat transfer to water at supercritical pressures. International Journal of Heat and Mass Transfer 108:1676-1688.

A NOVEL POPULATION BALANCE-BASED MODEL FOR BUBBLING FLUIDIZED BED REACTOR

Robert J. Macías[1], Juan C. Maya[1] and Farid Chejne*[1]

[1]*Universidad Nacional de Colombia, Facultad de Minas, Car. 80 No. 65-223, Antioquia, Colombia*

*Email: *fchejne@unal.edu.co*

Abstract

In this paper, a novel population balance-based model for a bubbling fluidized bed reactor is proposed. This model takes into account two continuum phases: bubble and emulsion. The bubble size distribution was modeled using a population balance inside the reactor, in which it was considered the motion in both axial and radial directions. This sub-model involves a new mathematical form for the aggregation frequency, which allows predicting the migration of bubbles located close to the reactor wall towards the reactor center. Besides, the reacting particles inside the emulsion phase were considered as a Lagrangian phase that exchange mass with both emulsion and bubble phases within the bed. For each particle, the variation on the pore size distribution was also considered. The coupling of the three models (two-phase theory, bubble size distribution model and pore size distribution model) allowed predicting accurately the experimental data on the charcoal gasification in a lab-scale bubbling fluidized bed reactor. Finally, it is concluded that the aggregation frequency can be used as scaling up the parameter, which may be an important tool for the design and scaling bubbling fluidized bed reactor.

Introduction

Due to the heterogeneous nature of the fluidized beds and the strong interaction between hydrodynamics, chemical kinetics, and heat and mass transfer phenomena, it has been necessary to use empirical correlations (Horio, Nonaka, Sawa, & Muchi, 1986) to predict variables such as profiles of temperature and concentration, char conversion, specific surface area, porosity, and bubble size distribution profile. However, these expressions do not consider the interaction between different phenomena and are only valid for given reactor scales. In addition, the bubbling regime, which is given by the characteristic bubbles interactions inside the bed, is not considered by most of these equations.

In a more detailed approach, several authors have explored the model of fluidized beds using population balances (Ahmadzadeh, Arastoopour, Teymour, & Strumendo, 2008; Bhole, Joshi, & Ramkrishna, 2007; Muralidhar, Gustafson, & Ramkrishna, 1987; Solsvik & Jakobsen, 2014; Sweet, Gustafson, & Ramkrishna, 1987). Models such as those proposed by Ramkrishna contemplate the growth, the coalescence and the rise of the bubbles within the bed. However, this model takes into account only the coalescence between bubbles belonging to the bin. However, it has been demonstrated that when bubbles coalesce, they move towards the center of the reactor, as was observed by several authors (Argyriou, List, & Shinnar, 1971; Muralidhar et al., 1987; Shah, Ramkrishna, & Borwanker, 1977; Sweet et al., 1987). Therefore, this paper aims to develop a model for bubbling fluidized beds that consider the migration of bubbles to the reactor center because of coalescence. For this purpose, a novel mathematical form for the aggregation frequency is presented and modified death and birth terms in the population balance equation are used. The model is solved by using the so-called Method of Moments (MOM) and some simulations are shown.

Mathematical Model

As mentioned above, a mathematical model to predict the behavior of the CO2 gasification process in a bubbling fluidized bed reactor was developed. This model takes into account two continuum phases: bubbling phase and emulsion phase. Additionally, the particles inside the emulsion were considered as a Lagrangian phase that reacts producing a variation on the pore size distribution. These reacting particles transfer mass to both emulsion and bubble phases along the bed. The Eq. (1) show the expression used for the specific surface area, which considers the effect of the pore overlapping:

$$S = S_e\left(1 - \varepsilon_p\right) \tag{1}$$

Furthermore, a model for both the growth and coalescence of bubbles based on a novel form for the aggregation frequency was proposed. This model assumes that the coalescence probability of a given bubble depends on the number of bubbles that surrounds it and that bubbles migrate toward the center of the rector when coalescence takes place (Darton, LaNauze, Davidson, & Harrison, 1977), as shown in Fig. 1.

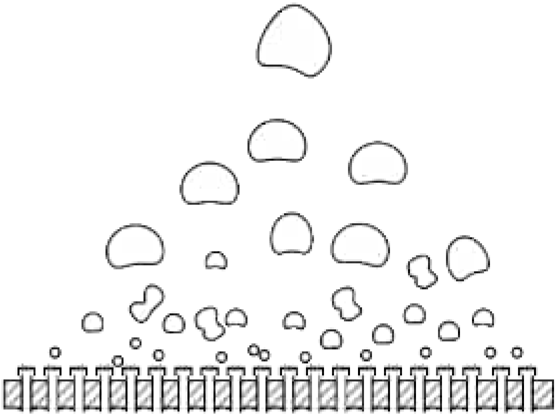

Fig. 1. Scheme designed for showing the bubble coalescence.

For each phase, the model takes into account both the mass and energy transfer, which allowed predicting the evolution of both the concentration and temperature profiles over time.

The balance equations are based on the generic fluidized bed model proposed by Grace and Abba (Abba, Grace, Bi, & Thompson, 2003) that takes into account different fluidization regimes such as bubbling fluidized bed, dispersed flow at low speeds, and core-annular flow at high velocities. The mass balance for both emulsion and bubble phases includes terms for accumulation, convection, axial dispersion, interphase mass transfer, and chemical reaction. The equations for the emulsion phase and bubble phase given by Eqs. (2) and (3), respectively

$$\frac{\partial \mathbb{C}_{i,e}}{\partial t} = -u_g \frac{\partial\, \mathbb{C}_{i,e}}{\partial z} - k_{E-B} a \left(\frac{\mathbb{C}_{i,b}(1-\epsilon_b)(\epsilon_{mf})}{\epsilon_b} - \mathbb{C}_{i,e} \right) + \frac{D_{g,e}}{\epsilon_{mf}} \frac{\partial}{\partial r}\left(r \frac{\partial \mathbb{C}_{i,e}}{\partial r} \right) + \sum_j \dddot{\Gamma}_j \alpha_{i,j} + \dot{N}'''_{p-e,i} \tag{2}$$

$$\frac{\partial(\mathbb{C}_{b,i})}{\partial t} = -u_b \frac{\partial(\mathbb{C}_{bi})}{\partial z} + D_{g,b} \frac{\partial}{\partial r}\left(r \frac{\partial \mathbb{C}_{i,b}}{\partial r} \right) + k_{E-B} a \left(\mathbb{C}_{b,i} - \frac{\mathbb{C}_{e,i}\epsilon_b}{(1-\epsilon_b)\epsilon_{mf}} \right) + \sum_j \dddot{\Gamma}_j \alpha_{i,j} \tag{3}$$

where $\mathbb{C} = (C_{ei}(1-\epsilon_b)(\epsilon_{mf}))$. The energy balance equation for emulsion phase and bubble phase are given by Eqs. (4) and (5), respectively

$$\frac{\partial T_e}{\partial t} = -u_g \frac{\partial\, T_e}{\partial z} + \frac{h_{be}}{\rho_e C p_e} a(T_b - T_e) + D_{Tg,e} \frac{\partial}{\partial r}\left(r \frac{\partial T_e}{\partial r} \right) + \sum_j \dddot{\Gamma}_j \, \Delta H_j + \dot{N}'''_{p-e,i} * h_i \tag{4}$$

$$\frac{\partial T_{i,b}}{\partial t} = -u_b \frac{\partial\, T_b}{\partial z} + \frac{h_{be}}{\rho_b C p_b} a(T_e - T_b) + D_{Tg,b} \frac{\partial}{\partial r}\left(r \frac{\partial T_b}{\partial r}\right) + \sum_j \dddot{\Gamma}_j\, \Delta H_j \tag{5}$$

Population Balance of Bubble Distribution

As mentioned above, in the model proposed in this work, a population balance for the bubbles within the bed was developed. This model explains the dynamic evolution of bubble size distribution as a function of process operating conditions. This model was solved through a variation of the Extended Method Of Moments (EMOM) proposed by (Maya & Chejne, 2016). By multiplying Eq. (6) by ${r_b}^n$ and integrating from 0 to ∞ we obtain

$$\frac{-\partial(M_n u_b)}{\partial z} + n\int_0^\infty {r_b}^{n-1} \frac{dr_b}{dt} f_b dr_b + \int_0^\infty {r_b}^n (B - D)\, dr_b = \frac{\partial(M_{n,i})}{\partial t} \tag{6}$$

where $M_{n,i}$ is the moment n of the bin i. M_0 is proportional to the density number (number of bubbles per unit of volume), M_1 is the sum of all radius of bubbles (m of bubbles per unit of volume), M_2 is proportional to the surface area of bubbles (m2 of bubbles per unit of volume), M_3 is proportional to the porosity inside the bed (m3 of bubble per unit of volume of reactor).

Aggregation Frequency

In this work, two ways for the coalescence of the bubbles are considered: the first one is defined as intra-element coalescence; i.e., the coalescence between bubbles belonging to the same differential element, and the second one is defined as inter-bin coalescence, which occurs between bubbles belonging to adjacent differential elements. The aggregation frequency for intra-bin coalescence is assumed to be proportional zero moment of the given differential element, whereas the aggregation frequency for inter-element is considered as proportional to the sum of the zero moments of the surrounding differential elements. After some mathematical manipulations, the Eq. (6) takes the form, Eq. (7)

$$\begin{aligned}\frac{\partial M_{n,i}}{\partial t} = -\vec{v}_i \frac{\partial M_{n,i}}{\partial x} - \frac{a_{g0} M_0}{2} \sum_{i=0}^{n} \binom{n}{i} M_{n-i} M_i - a_{g0} M_0 (M_0 M_n) \\ + \left[a_{g0}\left(M_{0,i-2} + M_{0,i}\right) M_{0,i-1} M_{n,i-1}\right] - \left[a_{g0}\left(M_{0,i-1} + M_{0,i+1}\right) M_{0,i} M_{n,i}\right]\end{aligned} \tag{7}$$

where a_{g0} is a constant that must be fitted from experimental data.

Result and Discussions

In this section, predictions of the model herein proposed are analyzed. A fluidized bed reactor at 850 °C in steady-state was modeled with particles of char of 1 mm in diameter inside the bed. The fluidized bed reactor has a radius of 0.4 m and a bed height of 0.6 m.

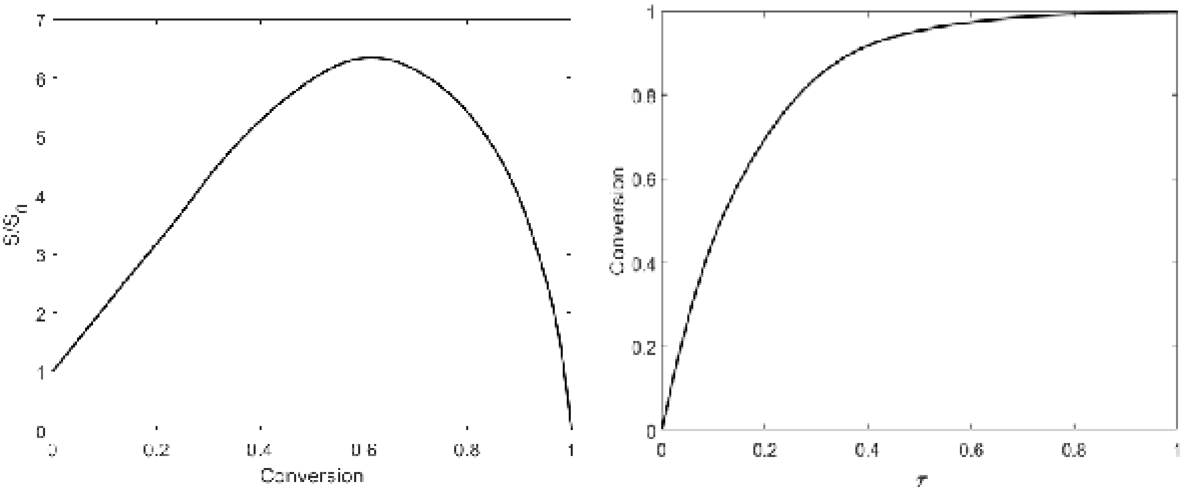

(a) (b)

Fig. 2. (a) Evolution of specific surface area over conversion and (b) Evolution of conversion

Fig. 2(a) shows the evolution of specific surface area over conversion. In this figure, it is seen that there is a maximum specific surface, which can be explained from the fact that, at initial stages of gasification, the reaction produces that pore grows, involving an increase on the specific surface area of the reacting particle. However, as the gasification takes place the pores begin to overlap with adjacent pores. Thus, there is a moment when the effect of pore overlapping is so strong that the specific surface area begins to decrease. In Fig. 2(b), it is shown the evolution of conversion over dimensionless τ, which is given by Eq. (8)

$$\tau = \frac{t}{\tau_c} \tag{8}$$

where τ_c is the time at which the complete conversion is obtained. From Fig. 2 (a) and (b), it is observed that the conversion at which the maximum specific surface area (X=0.61) is obtained corresponds just to the 15.5% of the time required for completing the reaction. Therefore, if a char with high specific surface area (for instance, activated coal) want to be obtained, long times of reaction must be avoided. Therefore you must stop the reaction at the 15.5% of total time.

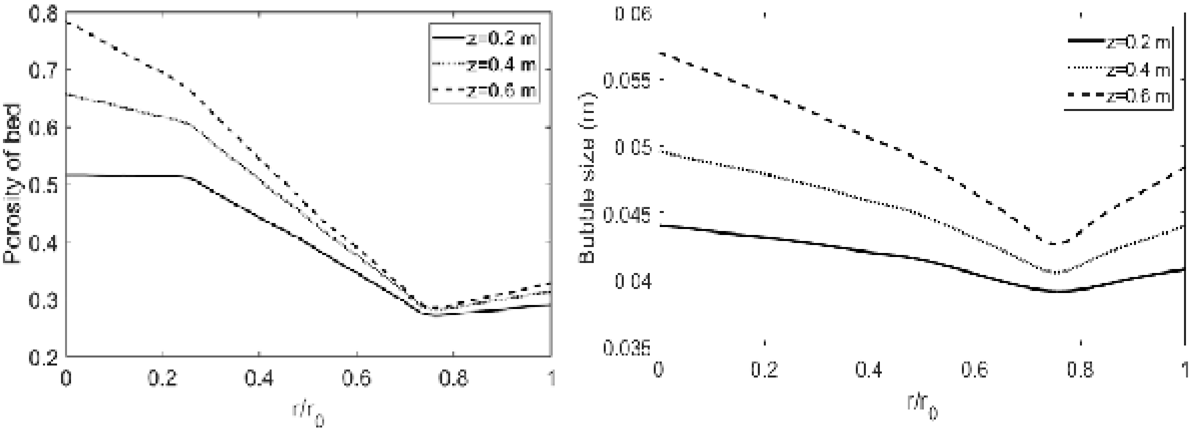

(a) (b)

Fig. 3. (a) Porosity distribution (M$_3$) and (b) Average radius of bubbles

Fig. 3(a) shows the porosity profile at different bed heights Z. In this figure, it is observed that the porosity in the reactor center is larger than that at reactor walls, which can be explained from the fact that bubbles located close to the reactor walls migrate towards the reactor center as coalescence takes place. Furthermore, it can be seen that as the bed height increases, the porosity in the reactor increases as well. This behavior is due to a larger bed height implies a larger time for bubbles coalescence; i.e., for larger bed heights the bubbles have had more time to migrate from the reactor walls to the reactor center because of coalescence. In the Fig. 3(b), the profile of the average radius of bubbles is shown. It is noted that the average radius of bubbles increases as the bed height increases, which again is due to larger bed heights are associated to larger times for the bubbles close to reactor walls move to the center due to the coalescence phenomenon. The above predictions are in agreement with experimental observations showing the phenomenon of bubbles migration from the walls to the reactor center (Kobayashi, Yamazaki, & Mori, 2000; Muralidhar et al., 1987; Sweet et al., 1987; Wang, Lu, & Xi, 2019). Finally, it must be said that this phenomenon cannot be modeled so far and is the main scientific contribution of this work.

Concluding Remarks

In this work, it is proposed a novel population balance-based model that considers the effect of bubbles coalescence on the evolution of the bubble size distribution. Mass and energy balances are considered by means of the so-called two-phase theory. A new mathematical form for the aggregation frequency is proposed, which allows simulating the phenomenon of bubble migration from the reactor wall towards the center; which is the main contribution of this paper. The latter can be used to design new reactors as new strategy that will take into account hydrodynamics, chemistry and energy transference effects as in a phenomena combined way.

Notation

a_{g0}	constant defined in Eq. (7), m^6/s
a	surface area of bubbles per unit volume, m^2/m^3
B	birth term in the population balance equation
$\mathbb{C}_{i,e}$	concentration species i in emulsion phase, mol/m^3 reactor
$\mathbb{C}_{i,b}$	concentration of species i in bubble phase, mol/m^3 reactor
Cp_e	average specific heat of the emulsion phase, (J/kg-K)
Cp_b	average specific heat of the bubble phase, (J/kg-K)
D	death term in the population balace equation
$D_{g,i}$	gaseous dispersion coefficients, axially and radially for emulsion and bubble phase (i=e and i=b), m^2/s
$D_{Tg,e}$	heat diffusivity of gas i in the emulsion phase, (m^2/s)
$D_{Tg,b}$	heat diffusivity of gas i in the bubble phase, (m^2/s)
f_b	density distribution function of bubble radius, number of bubbles/m^3 reactor- m of bubble radius
h_i	specific enthalphy of the gas I, J/mol
h_{be}	heat transfer coefficient between bubble and emulsion phases, W/m^2-K
k_{E-B}	mass transfer coefficient between emulsion and bubble phases, m/s
L	length, m
l	average pore length, m
M_n	moment n-th (n=0,1,2,3…), m^n/m^3 of reactor
$M_{n,i}$	n-th moment of the bin i, m^n/m^3 of reactor
$\dot{N}'''_{p-e,i}$	flow of the gas i from the particle per unit volume, mol/m^3-s
r	radial coordinate within the reactor, m
r_b	bubble radius, m
$\mathrm{r_p}$	pore raidus, m
S	specific surface area of particle, m^2/m^3
S_e	specific surface area of the extended pore system, m^2/m^3
S_0	specific surface area at the beginning of reaction, m^2/m^3
T	temperature, K
u_b	bubble velocity, m/s
u_g	gas velocity, m/s
X	Conversion
$\alpha_{i,j}$	stoichiometric coefficient of the gas i in the reaction j
$\ddot{r}_j$	j-th volumetric reaction rate, $kmol/m^3$-s
ΔH_j	Heat of reaction of reaction j, J/mol
ρ_b	Density of the bubble phase, kg/m^3
ρ_e	Density of the emulsion phase, kg/m^3
ϵ_{mf}	volume fraction of bubbles for the minimum fluidization velocity, m^3 of bubbles/m^3 of reactor
ϵ_b	volume fraction of bubbles within reactor, m^3 of bubbles/m^3 of reactor
ε_p	porosity of particle, m^3 of pore/ m^3 of particle

References

Abba, I. A., Grace, J. R., Bi, H. T., & Thompson, M. L. (2003). Spanning the flow regimes: Generic fluidized-bed reactor model. *AIChE Journal*, *49*(7), 1838–1848. https://doi.org/10.1002/aic.690490720

Ahmadzadeh, A., Arastoopour, H., Teymour, F., & Strumendo, M. (2008). Population balance equations' application in rotating fluidized bed polymerization reactor. *Chemical Engineering Research and Design*, *86*(4), 329–343. https://doi.org/10.1016/j.cherd.2008.02.004

Argyriou, D. T., List, H. L., & Shinnar, R. (1971). Bubble growth by coalescence in gas fluidized beds. *AIChE Journal*, *17*(1), 122–130. https://doi.org/10.1002/aic.690170126

Bhole, M. R., Joshi, J. B., & Ramkrishna, D. (2007). Population balance modeling for bubble columns operating in the homogeneous regime. *AIChE Journal*, *53*(3), 579–588. https://doi.org/10.1002/aic.11099

Darton, R., LaNauze, R., Davidson, J., & Harrison, D. (1977). Bubble growth due to coalescence in fluidised beds. *Transcripts of the Institute of Chemical Engineering*, *55*(October 1977), 274–280. Retrieved from http://ci.nii.ac.jp/naid/80014839677/

Horio, M., Nonaka, A., Sawa, Y., & Muchi, I. (1986). A new similarity rule for fluidized bed scale-up. *AIChE Journal*, *32*(9), 1466–1482. https://doi.org/10.1002/aic.690320908

Kobayashi, N., Yamazaki, R., & Mori, S. (2000). A study on the behavior of bubbles and solids in bubbling fluidized beds. *Powder Technology*, *113*(3), 327–344. https://doi.org/10.1016/S0032-5910(00)00315-6

Maya, J. C., & Chejne, F. (2016). Novel model for non catalytic solid–gas reactions with structural changes by chemical reaction and sintering. *Chemical Engineering Science*, *142*, 258–268. https://doi.org/10.1016/j.ces.2015.11.036

Muralidhar, R., Gustafson, S., & Ramkrishna, D. (1987). Population balance modelling of bubbling fluidized beds. II. Axially dispersed dense phase. *Sadhana*, *10*(1–2), 69–86. https://doi.org/10.1007/BF02816198

Shah, B. H., Ramkrishna, D., & Borwanker, J. D. (1977). Simulation of bubble populations in a gas fluidized bed. *Chemical Engineering Science*, *32*(12), 1419–1425. https://doi.org/10.1016/0009-2509(77)80238-8

Solsvik, J., & Jakobsen, H. A. (2014). Bubble Coalescence Modeling in the Population Balance Framework. *Journal of Dispersion Science and Technology*, *35*(11), 1626–1642. https://doi.org/10.1080/01932691.2013.866902

Sweet, I. R., Gustafson, S. S., & Ramkrishna, D. (1987). Population balance modelling of bubbling fluidized bed reactors—I. well-stirred dense phase. *Chemical Engineering Science*, *42*(2), 341–351. https://doi.org/10.1016/0009-2509(87)85064-9

Wang, H., Lu, Y., & Xi, K. (2019). Bubble behavior in gas–solid bubbling fluidized beds based on EMMS model: Comparison of 2D, Q2D, and 3D simulations. *Chemical Engineering Research and Design*, *149*, 65–80. https://doi.org/10.1016/j.cherd.2019.06.009

IMPACT OF LOCAL FLUIDIZED BED HYDRODYNAMICS ON THE DISTRIBUTION OF LIQUID SPRAYED INTO THE BED

Yuan Li[1], Francisco Sanchez Careaga[1], Cedric Briens[1]*, Franco Berruti[1], Jennifer McMillan[2]

[1]Institute for Chemicals and Fuels from Alternative Resources, Western University, 22312 Wonderland Rd., Ilderton, ON, Canada, N0M 2A0

[2]Edmonton Research Centre, Syncrude Canada Ltd, 9421 17th Ave, Edmonton, AB, Canada T6N 1H4

**Email: cbriens@uwo.ca*

Abstract – During the industrial Fluid Coking™ process, a portion of valuable liquid is trapped in undesirable agglomerates, which contribute to fouling in the stripper section. To solve this major operating issue, the objective of this research is to reduce agglomeration by modifying local bed hydrodynamics, such as changing the gas distributor, and adding internals, for example, baffles. Several lateral injection locations were tested until the jet tip hit bed wall. Various injection locations, above the baffle, below the baffle, and in the baffle pocket were compared. Different baffle geometries, such as an asymmetrical baffle with/out a flux-tube and a symmetrical baffle were investigated. By changing the gas distributor, the liquid trapped in agglomerates reduced by 20 %, while adding an asymmetrical baffle without a flux-tube further decreased it by 8 %.

Introduction

The Fluid Coking™ technology upgrades 15-20 % of the heavy oil from the oilsands to more valuable liquid products. In a Fluid Coker, bitumen (350 ℃) atomized with steam is sprayed into a fluidized bed filled with hot coke particles (500 - 550℃), where it is thermally cracked into liquid products (condensable vapors), gas products (non-condensable), and coke (Fig. 1). However, some of the injected bitumen is trapped in wet agglomerates formed with coke particles. While most of the agglomerates are broken up in the Coker, some carry unvaporized liquid down to the stripper section, resulting in fouling that can lead to premature shutdown. Therefore, it is essential to reduce the agglomerates formation. Modeling (House et al., 2004; House, 2007; Ali et al., 2010) and experiments (Kumar et al., 2015; Stanlick et al., 2017) show that improving the initial contact between bitumen and hot coke particles can reduce agglomerate formation. Agglomerate formation can be reduced by adjusting the gas distribution (Li et al., 2016) or introducing a baffle just below the spray nozzle (Jahanmiri, 2017). Fig. 2 shows a commercial baffle.

The main objective of this paper is to determine the best nozzle location to reduce agglomerate formation with various gas distributors and baffles, considering that in an industrial unit, it is unrealistic to penetrate the spray nozzle too far from the bed wall. An additional objective is to develop the best baffle geometry.

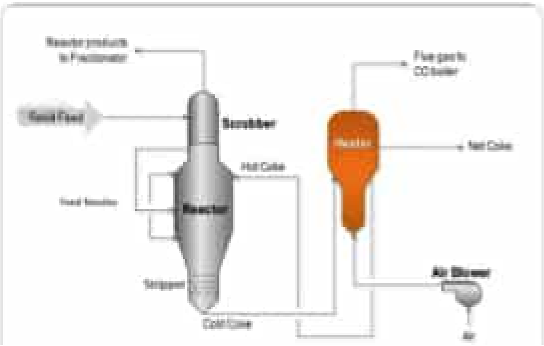

Fig. 1. Simplified Fluid Coking™ Scheme ExxonMobil (Adapted from Exxon Mobil website)

Fig. 2. Commercial baffle (Adapted from Exxon Mobil) (Kamienski, 2013)

Materials, Equipment and Methods

All the experiments used 108 kg of silica sand (Group B powder) with a Sauter mean diameter of 190 µm and an apparent particle density of 2650 kg/m3. The bed height was approximately 1.65 m. Dry compressed air, with a relative humidity lower than 5 % at room temperature, was used as the fluidization gas. The minimum fluidization gas velocity of the solids was 0.033 m/s and 0.027 m/s at 30 ℃ and 130 ℃, respectively.

A safe and convenient system developed by Reyes (2015) was used in this work to simulate agglomerate formation and breakup in a Fluid Coking process. The solution was made of 92 wt% water, 6 wt% Gum Arabic powder, and 2 wt% blue dye. The pH of the Gum Arabic solution was adjusted to 3 with HCl to match the viscosity of the preheated bitumen in Fluid Cokers, which is approximately 3 cP (Aminu et al., 2004). The amount of injection is 200 g to avoid bogging (Briens et al., 2017; Li et al., 2019b).

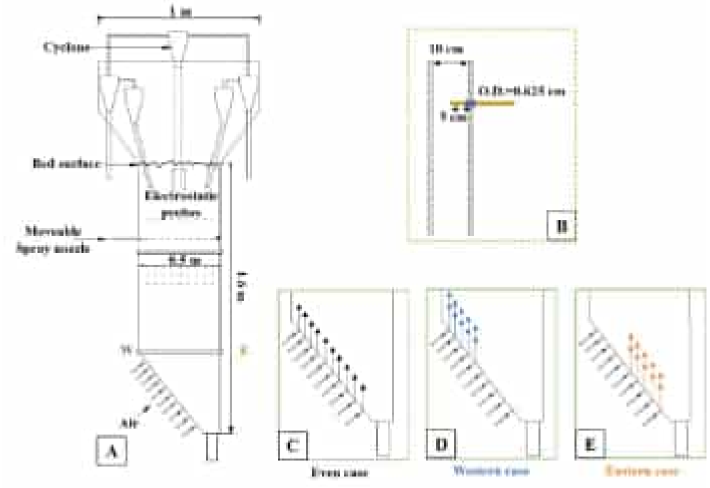

Fig. 3. Schematic diagram of A. High gas velocity bed, B. Side view of an electrostatic probe, C. Even gas distributor configuration, D. Western gas distributor configuration, E. Eastern gas distributor configuration,

Fig. 3A shows the schematic diagram of the fluidized bed used in this study. The bed had a rectangular cross-section of 0.5 m x 0.1 m x 1.15 m. Cyclones recovered entrained solids and allowed operation at a superficial fluidization gas velocity of 1 m/s. The liquid was mixed with atomization gas and injected through a scaled-down version of an industrial spray nozzle (Base et al., 1999). The outlet diameter of the spray nozzle was 1 mm, the gas to liquid mass ratio (GLR) was 2 %, and the liquid flowrate was 17.5 g/s (Joness, 2019).

The experimental setup was also equipped with 5 rows of electrostatic probes installed near the spray level to characterize the bubble flow (Fig. 3A). Fig. 3B shows that the probes penetration was half of the bed width. Each probe was made of a 0.635 cm diameter stainless steel rod, and its current to the electrical ground was recorded at a frequency of 1000 Hz.

As shown in Fig. 3A, the bottom of the bed tapered down with a 45 ° angle to drain the bed solids easily. The distributor consisted of 20 tuyeres, each with three, 3 mm holes, and with individual flow control to modify the gas distribution. By opening 10 tuyeres, the gas could be distributed uniformly across the distributor (even configuration) (Fig. 3C), concentrated towards the western wall (Fig. 3D), or the eastern wall (Fig. 3E).

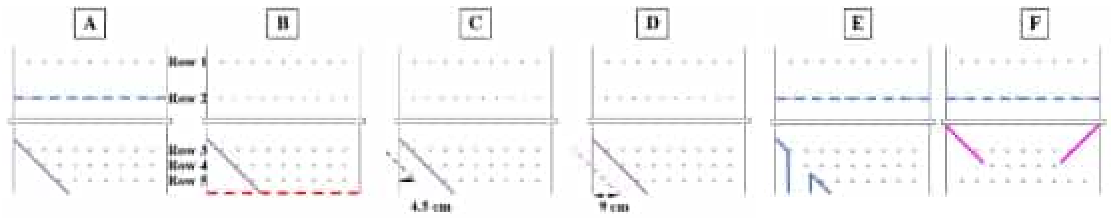

Fig. 4. Schematic diagram of location of A. Baffle type A.1, injection from above, B. Baffle type A.1, injection from below, C. Baffle type A.1, injection from baffle pocket 4.5 cm from bed wall, D. Baffle type A.1, injection from baffle pocket 9 cm from bed wall, E. Baffle type A.2, injection from above, F. Baffle type S.1, injection from above

Fig. 4 shows a baffle with a standard geometry (Type A.1) consisting of a single open-ended right triangle shape with an internal angle of 45° having the same width as the bed (0.18 m x 0.1 m x 0.18 m). Four injection levels were studied: 25 cm above the bottom edge of the baffle (Figure 4A), just below the bottom edge of the baffle (Figure 4B), half-way into the baffle pocket (Figure 4C) and to the bottom of the baffle pocket (Figure 4D). In position (Figure 4A) and (Figure 4B), the spray nozzle lateral injection location (x_{inj}) was 5, 10, 15, 18, 20 or 25 cm away from the western bed wall. The gas-liquid spray jet penetration is 23 cm (Li et al., 2019a; Li et al., 2020). Therefore, the injection locations are between 0 and 25 cm to avoid the spray jet hitting the opposing bed wall.

With the standard spray level above the baffle, 3 baffle geometries were compared in this paper, which were classified into an asymmetrical (Type A) and a symmetrical (Type S) baffle. Type A.1 (Fig. 4A) was the standard geometry. Type A. 2 (Fig. 4E) was modified with a cylindrical flux-tube at the baffle centre to simulate the frusto-conical industrial baffle (Fig. 2). Type S.1 (Fig. 4F) was the symmetrical baffle consisting of two smaller open-ended right triangle shapes with an internal angle of 45° (0.125 m x 0.1 m x 0.125 m) on opposite sides of the bed to simulate, in the 2D laboratory column, the industrial baffle, which blocks 50 % of the cross-sectional area of the bed.

When there is no liquid injection, the normalized local gas bubble volumetric flux ($q_{bi}/\overline{q_b}$) is obtained from the electrostatic probes signal, using a method described elsewhere (Li et al., 2019a), which was verified with radiation transmission. The whole procedure was controlled automatically with a computer and solenoid valves to ensure consistency. In each experiment, the bed was pre-heated to 130 ℃. The bed was fluidized at 1 m/s, followed by the injection of 200 g of Gum Arabic solution in 11.4 s. After cooling overnight, the whole bed was then drained, and the agglomerates were recovered by sieving. Agglomerates from each size cut were analyzed to determine the initial water trapped in these agglomerates, as described in (Reyes, 2015; Li et al., 2016; Jahanmiri, 2017).

Because the Gum Arabic method is time-consuming, a quick estimation method was developed using electrostatic probes by injecting DI water instead, which gives a average free moisture content in the bed after injection. The detailed procedure can be found in (Li et al., 2019a). Fig. 5 was obtained from an electrostatic probe after injection. The accumulative absolute value stopped increasing at 400 s, which was set as 100 %. Therefore, at any time t, the correspond normalized cumulative value y(t) (Fig.5) can be described with Eq. 2:

$$y(t) = \frac{\int_0^t |V|\,dt}{\int_0^{400} |V|\,dt} \tag{2}$$

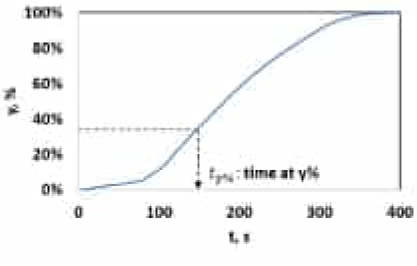

Fig. 5. Electrostatic probe signal: Normalized cumulative value

With multilinear regression, a good correlation ($R^2 = 0.9662$) between Gum Arabic and the electrostatic probe results was obtained:

$$\frac{initial\ water\ trapped}{water\ injected} = 0.024 + 0.0043 \times t_{35\%,\,row4} - 0.0056 \times t_{55\%.\,row1} + 0.0026 \times t_{95\%,\,row5} \qquad (2)$$

where $t_{35\%,\,row4}$ means the time from row 4 at y = 35 % (as shown in Fig. 5C). In the correlation, rows 4 and 5 make a positive contribution as large agglomerates tend to sink (Bhatti et al., 2019), then break up and release moisture near the bottom of the bed: a longer time for these rows indicates that the agglomerates do not break up quickly. Row 1 makes a negative contribution to Eq. (2) as moisture that is near row 1 is from wet particles and small agglomerates that do not sink; this moisture does not evaporate quickly since, at 30 °C, the air reaching row 1 is nearly saturated with water vapor. Figure 6 shows the good correlation between Gum Arabic and electrostatic probe results. The error bars in Figure 6 shows the spread between maximum and minimum measured values, which is minor comparing to the variations caused by baffle(s) or gas distributor modifications.

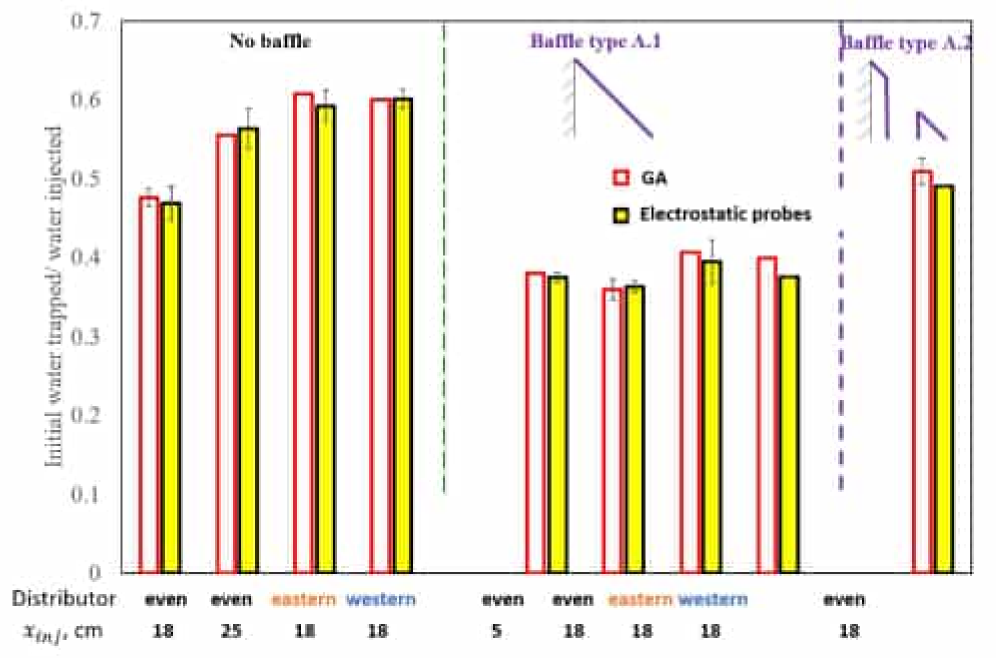

Fig. 6. Comparison of Gum Arabic and electrostatic probe estimation method results

Results and Discussion

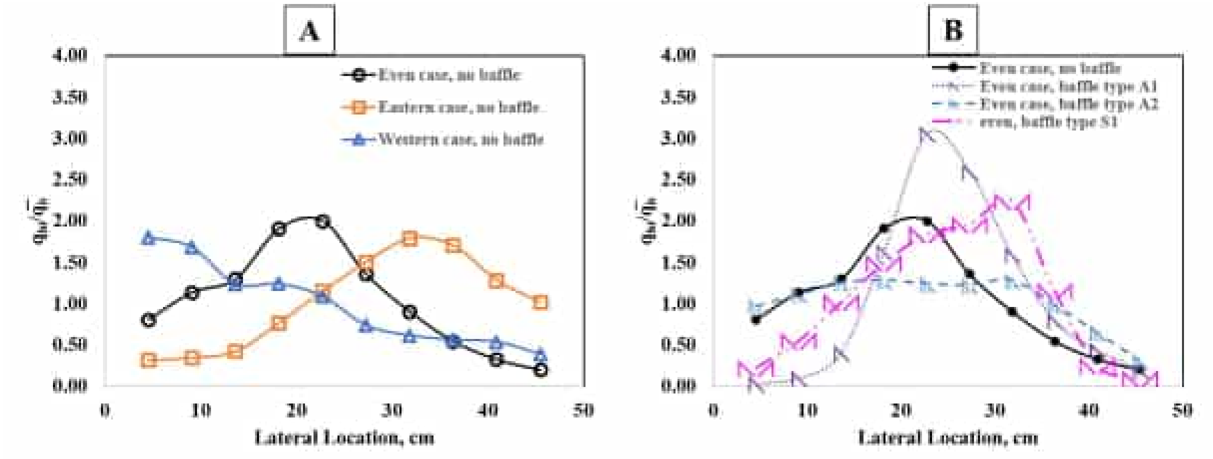

Figure 7 A. Impact of gas distributor configuration on gas distribution at spray level ($v_g = 1\ m/s$, 30 ℃), B Impact of baffle geometry on gas distribution at spray level ($v_g = 1\ m/s$, even case, 30 ℃)

Figure 7A shows the gas distribution at spray level modified by changing the gas distributor configuration without a baffle. By adjusting the gas distributor configuration, we were able to obtain 3 extreme cases which concentrate gas bubbles to the eastern, western or central regions. Figure 7B shows, with the even gas distributor configuration, which concentrates bubbles to the central region, the impact of various baffle geometries on gas distribution at spray level. It shows that baffle type A1 concentrated the bubbles more effectively.

Figure 8 shows that, without a baffle, adjusting the gas distributor can change the zone where the nozzle tip can be located for best performance, with the smallest amount of water trapped in agglomerates. For example, the optimal nozzle location can be moved near the bed wall ($x_{inj} = 10\ cm$) with the western distributor configuration.

Figure 9 shows that the Type A.1 baffle (standard baffle), with the even distributor configuration, can further decrease the amount of water trapped within agglomerates by 8 % when injecting above the baffle with the nozzle tip 5 cm from the wall. Larger reductions in water trapped can be obtained with the nozzle tip above the baffle and 25 cm from the wall.

Figure 10 shows that when the nozzle tip is located above the baffle injection level, with the even distributor configuration, the Type A.2 baffle with a flux-tube cannot match the best results obtained with the standard baffle; it cannot even match the best results obtained without a baffle. The presence of the flux tube prevents the effective concentration and diversion of gas bubbles that is achieved with the type A.1 baffle.

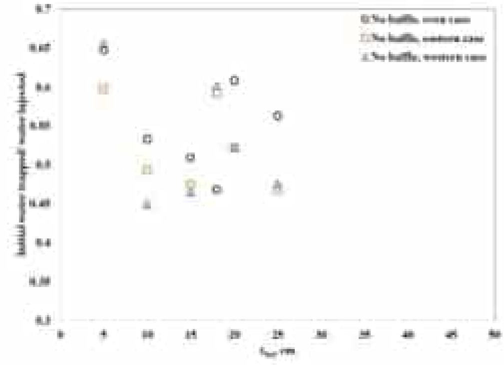

Fig. 8. Initial water trapped with 3 gas distributors and no baffle

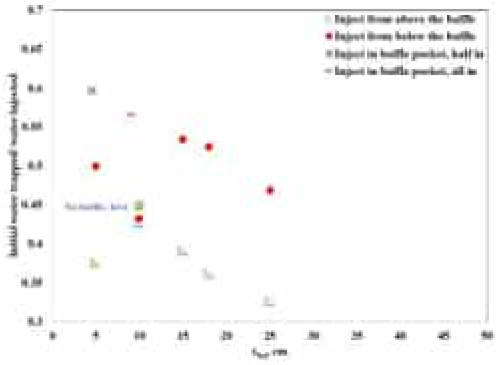

Fig. 9. Results with type A.1 baffle and even gas distributor

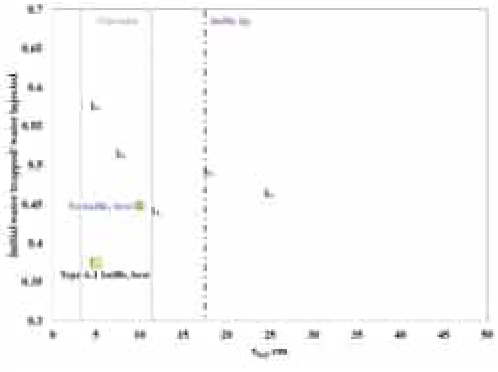

Fig. 10. Comparison of Type A.2 baffle with best case from with/out Type A.1

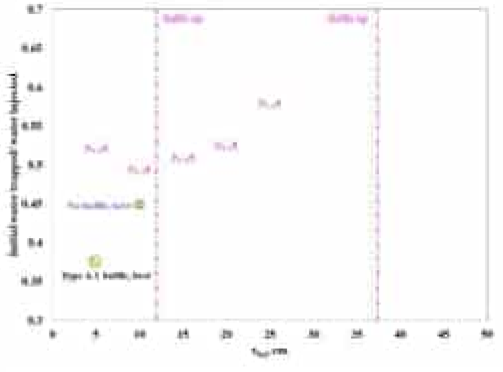

Fig. 11. Comparison of Type S.1 baffle with best case from with/out Type A.1

Figure 11 shows that when the nozzle tip is located above the baffle injection level, with the even distributor configuration, the Type S.1 baffle (symmetrical standard baffle) cannot match the best results obtained with the standard asymmetrical baffle. Although, when combined, the two halves of the symmetrical baffle block more of the cross-sectional area of the bed, each half is smaller and locally, does not divert as much of the bubbles as the asymmetrical baffle.

Conclusion

The gas distribution at spray level can be redistributed by adjusting gas distributor configurations and adding baffle(s). The gas distribution has a significant impact on the initial liquid distribution in bed. Without a baffle, by modifying gas distributor configuration, the fraction of the injected liquid that is trapped in agglomerates was reduced by 20 %. By adding an asymmetrical baffle without a flux-tube, trapped liquid fraction was reduced by a further 8 %.

Notation

q_{bi}	local bubble volumetric flux, $kg/(s.m^2)$
$\overline{q_b}$	average cross-sectional volumetric flux, $kg/(s.m^2)$
V_g	superficial gas velocity, m/s
U_{mf}	minimum fluidization gas velocity, m/s
$t_{y_{\%}}$	time at probability y, s
x_{inj}	Lateral injection location from western side bed wall, cm
V	Voltage from electrostatic probe, VDC

References

Ali M, Courtney M, Boddez L, Gray M. 2010. Coke yield and heat transfer in reaction of liquid-solid agglomerates of Athabasca vacuum residue. Can J Chem Eng. doi:10.1002/cjce.20242.

Aminu MO, Elliott JAW, McCaffrey WC, Gray MR. 2004. Fluid Properties at Coking Process Conditions. Ind Eng Chem Res. doi:10.1021/ie030550g.

Base TE, Chan EW, Kennett RD, Emberley DA. 1999. NOZZLE FOR ATOMIZING LIQUID IN TWO PHASE FLOW. :15.

Bhatti O, Briens C, Berruti F, Sanchez Careaga FJ, McMillan J. 2019. Behaviour of Agglomerates formed by Liquid Injection in Fluidized Beds. CFB-13 Conf Pap.

Briens C, Hamidi M, Berruti F, McMillan J. 2017. Development and study of measurement methods for bogging in a fluidized bed. Powder Technol. doi:10.1016/j.powtec.2017.01.075.

House P. 2007. Interaction of Gas-Liquid Jets with Gas-Solid Fluidized Beds: Effect on Liquid-Solid Contact and Impact on Fluid Coker Operation.

House PK, Saberian M, Briens CL, Berruti F, Chan E. 2004. Injection of a Liquid Spray into a Fluidized Bed: Particle−Liquid Mixing and Impact on Fluid Coker Yields. Ind Eng Chem Res. 43(18):5663–5669. doi:10.1021/ie034237q.

Jahanmiri M. 2017. Use of a baffle to enhance the distribution of a liquid sprayed into a gas-solid fluidized bed. Master's diss.

Joness A. 2019. The effect of scale on spray nozzle performance. Western University.

Kamienski P. 2013. FLEXICOKING ™ Resid Upgrading Technology • Coking is the Most Widely Used Resid Conversion.

Kumar D, Müller C, Pfeifer P, Wiens J, McMillan J, Wormsbecker M, McKnight C, Gray MR. 2015. Role of Liquid Concentration in Coke Yield from Model Vacuum Residue-Coke Agglomerates. Ind Eng Chem Res. doi:10.1021/acs.iecr.5b00806.

Li B, Careaga FS, Briens C, Berruti F. 2016. Effect of local hydrodynamics on the distribution of liquid sprayed into a Fluidized Bed. Fluid XV.

Li Y, Briens C, Berruti F, J. Sanchez Careaga F, McMillan J. 2020. Impact of Fluidized Bed Hydrodynamics on the Distribution of Liquid Sprayed into the Bed. Western University (Unpublished).

Li Y, Jahanmiri M, Briens C, Berruti F, J. Sanchez Careaga F, McMillan J. 2019a. Applications of Electrostatic Probes in Fluidized Beds. AICHE conference: Fluidization XVI. p. 23.

Li Y, Jahanmiri M, Briens C, Berruti F, J. Sanchez Careaga F, McMillan J. 2019b. Applications of Electrostatic Probes in Fluidized Beds. Unpublished.

Reyes LAP. 2015. Effect of Temperature and Successive Sprays on Liquid Distribution in Fluidized Beds.

Stanlick C, Berruti F, Briens C. 2017. Effect of mixing and vapor residence time on thermal cracking of bitumen in a Mechanically Fluidized Reactor. Fuel. doi:10.1016/j.fuel.2017.03.025.

ANALYSIS OF DRYING PARAMETER EFFECTS ON POROSITY EVOLUTION DURING SUCCESSIVE LAYER BUILD-UP FROM DRIED DEPOSITED DROPLETS

Manuel Janocha[*], **Evangelos Tsotsas**

Thermal Process Engineering, Otto von Guericke University
Universitaetsplatz 2, 39106 Magdeburg, Germany

*Email: *manuel.janocha@ovgu.de*

Abstract

An experimental series that replicates successive layer built-up from drying droplets is presented. In a droplet-by-droplet manner, sessile droplets are successively applied onto a glass substrate and dried under various conditions up to technical. Hereby, a simplified coating layer is incrementally created and examined via white light interferometry. The evolution of porosity during the addition of more droplets onto already existing deposits is investigated as well as the influence of convective drying parameters. Through this method, the effects of different parameters on layer porosity can be isolated and the coating process can continuously be monitored, which is not possible within a fluidized bed. The evaluated indices and obtained correlations are subsequently used to make statements about the more complex built-up process during fluidized bed coating. The overall goal of this project is to help to specifically influence the porosity of coating layers produced in fluidized beds.

Introduction

The application of solid containing droplets on a substrate followed by convective drying and deposit formation is a widespread process both in nature and technical applications. This consecutive microprocess of droplet-by-droplet drying, accompanied by the incremental formation of a coating layer from the droplets' individual deposition structures, is utilized by many industrial practices, for example inkjet printing or fluidized bed coating. However, despite it being a fundamentally important part, the exact evolution of a layer as well as its characterizing parameters during built-up, is not completely explored.

Deegan et al. (1997) were the first to describe the formation of ring structures during sessile droplet drying. This deposition of such a coffee-ring is founded in the pinning of the contact line on partially wetting substrates, as well as the resulting non-uniform evaporation flux along the surface. This combination of effects in turn causes internal flows that are directed towards the droplet edge. Alongside these flows, contained solids are transported towards the droplet-substrate contact line, resulting in enhanced accumulation along the edge and decreased deposit formation in the center. Deegan et al. (2000) further specified this phenomenon and also presented an analytical equation for the evaporation flux along the surface of sessile droplets in dependence of the formed contact angle. Potential problems for coating layers were discussed by Yunker et al. (2011), while Brutin et al. (2011) pointed out different possibilities.

The directed manipulation of such coffee-ring structures was discussed among others by Hu and Larson (2006). Namely methods like substrate heating or the addition of other substances have gotten much attention in the past (Mampallil and Eral, 2018). Sondej et al. (2018) studied the influence of drying conditions on the deposits of single sessile droplets with focus on morphology and porosity. They also presented a comparison between deposits of applied single sessile droplets and completed fluidized bed coating layers. Latter were further researched among others by Hampel et al. (2013) and Rieck et al. (2015).

Although the process of subsequent sessile droplet drying and deposit formation is important for the resulting coating layer, the great amount of concurrent effects during fluidized bed coating complicates the search for exact scientific correlations and the segregated observation of parameter influences. In addition to that, fluidized bed design prevents continuous observing of one particle, which in turn prevents the monitoring of successive layer build-up.

In this study, studies of incrementally resulting structures from subsequently deposited sessile droplets dried under various conditions were executed to isolate this core phenomenon. Through this method, the transition from single deposit to simplified layer can be monitored and is expected to contribute to the understanding of the more complex processes during fluidized bed coating.

Since coating and layering processes within a fluidized bed showed a strong dependence on drying conditions in the past (Hoffmann et al., 2015), the influence of different convective conditions during this layer built-up is analyzed as well. Hereby, focus is laid on layer porosity. The resulting correlations can be used as indicators for coating in a fluidized bed.

Experimental Setup

To study the deposit formation processes that occur during drying of sessile suspension or solution droplets, an experimental setup was constructed, in which the application of such droplets as well as the convective drying conditions can be controlled accurately. A cuboid drying chamber with a length of 100mm and a 20x20mm cross-section is used to set the drying environment. The chamber's sides and ceiling, as well as the bottom plate on which the sample is applied, are made of glass. This enables the usage of cameras to monitor the sample during the drying process.

A precise air supply is connected to the chamber, enabling the application of specific convective drying conditions, such as airflow velocity, temperature or humidity. The chamber itself is not heated or insulated. Therefore, any energy transferred to the drying droplet originates from the previously heated air flow. To ensure a uniform flow profile at the chamber's entry, two flow rectifiers made from porous sinter metals are inserted in front of and after the droplet application area. The experimental setup for droplet application and convective drying is schematically shown in Fig. 1.

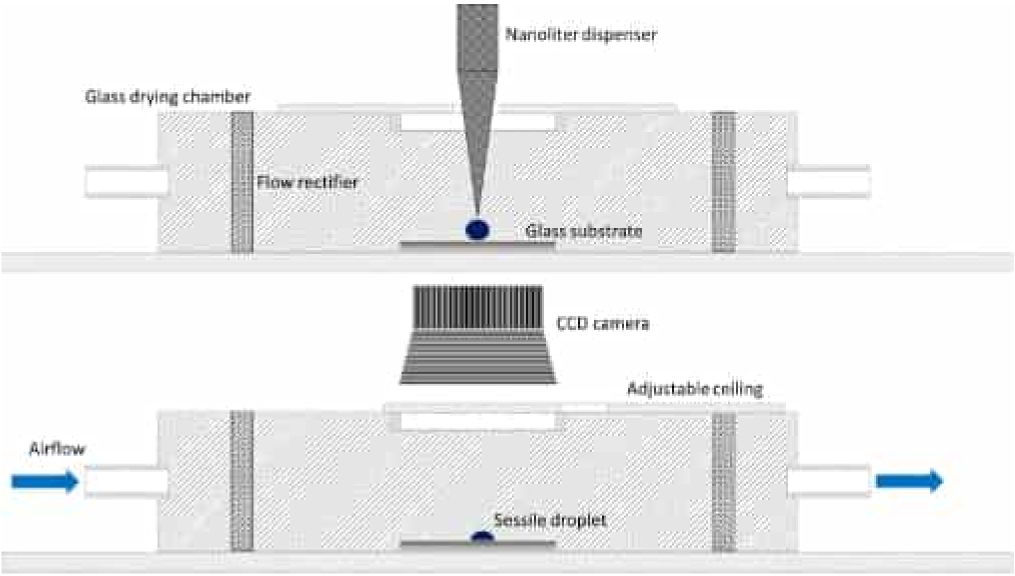

Fig. 1. Schematic of the experimental setup.

The droplets are applied via a nanoliter dispenser. This dispenser is inserted through the ceiling of the drying chamber. After successful application of a droplet, the dispensing pipette is removed, the chamber's ceiling closed and the drying airflow applied. After the droplet has dried completely and the deposit has formed, another droplet is consecutively applied on the existing deposition structure and is dried under the same conditions. Thereby, the incremental formation of small coating layers is experimentally replicated in a droplet-by-droplet manner.

Materials and Methods

After each individual deposition, or in other words, after the drying of each droplet, the surface of the entire structure is analyzed by means of white light interferometry (WLI). Hereby, the surface is incrementally scanned and a specific height is obtained for every pixel, creating a three-dimensional height profile of the structure. Fig. 2 shows the schematic of such a scan and an exemplary profile of a coffee-ring structure.

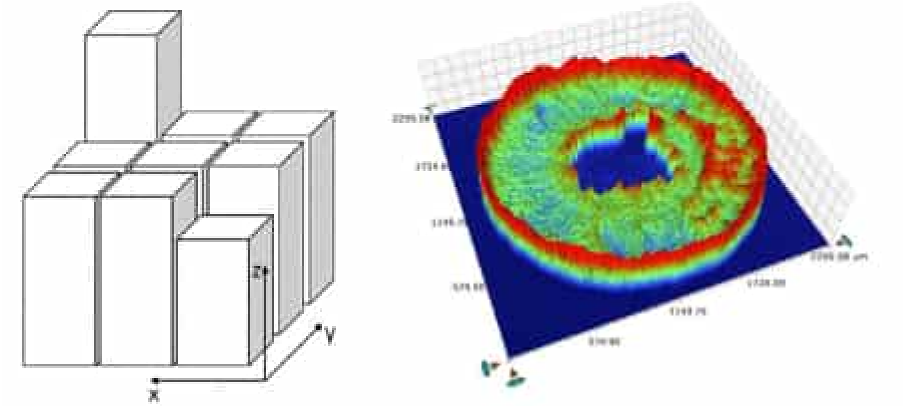

Fig. 2. Schematic of a WLI scan (left) and exemplary profile of a sodium benzoate deposit (right).

Apart from the deposit morphology, the total volume V_t of the gradually forming layer can thereby be calculated through surface integration of the corresponding height data of each pixel *j*:

$$V_t = \sum_j (X_j, Y_j, Z_j)\ . \tag{1}$$

Since the theoretical solid volume V_s is known through size and solid content of the applied droplets, the porosity ε can be obtained by:

$$\varepsilon = 1 - \frac{V_s}{V_t}\ . \tag{2}$$

With this procedure, the evolution of porosity and morphology within a layer, id est over the course of multiple samples, can be obtained.

In the experimental study presented herein, a water-based sodium benzoate solution was dried at different airflow velocities U and temperatures T. Up to three layers were applied on top of each other. Solid content c_s and droplet volume V_{drop} were also varied. Table 1 summarizes the tested convective parameters and droplet constitutions.

Table 1. Summary of experimental parameters.

parameter	value	unit
U	$0.1 - 1.5$	m/s
T	$21 - 75$	$°C$
V_{drop}	$0.1 - 1$	μl
c_s	$5 - 30$	$M\%$

Results

The evolution of porosity over the course of three sodium benzoate layers can be seen in Fig. 3 for a concentration of 5 M% and 30 M%, respectively.

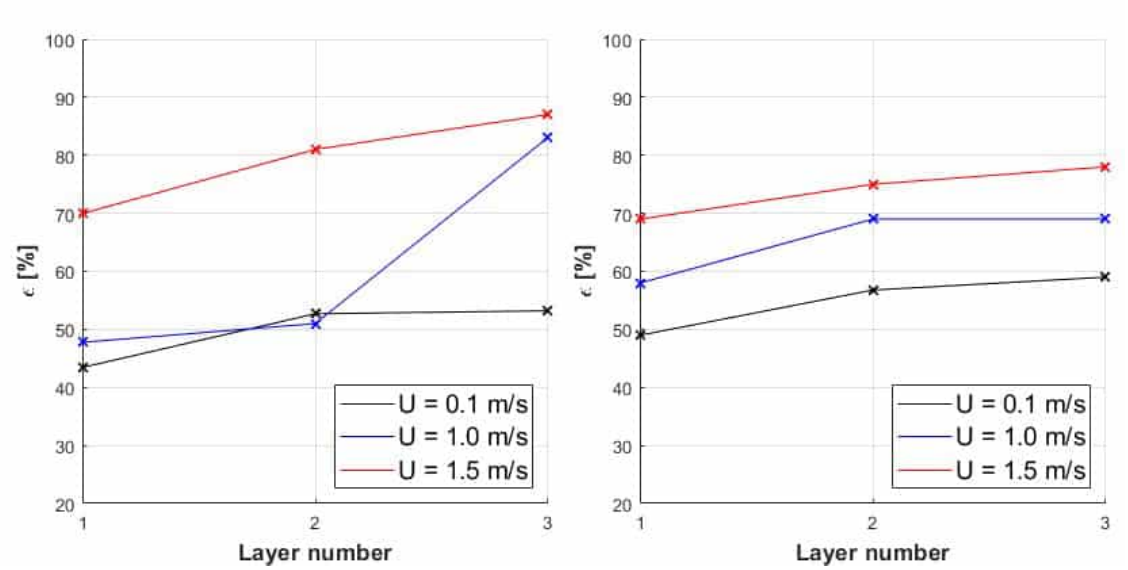

Fig. 3. Porosity development during layer built-up at different flow velocities for $T = 21\,°C$, $V_{drop} = 1\ \mu l$, $c_s = 5\ M\%$ (left) and $c_s = 30\ M\%$ (right).

The first trend that can be spotted is an increase in overall porosity of the structure with the addition of more layers. This increase was observed in all experimental series in this study. The first layer of solid residues forms coffee-ring deposits on the smooth glass substrate, as was reported for example by Deegan (2000) or Sondej et al. (2018). If droplets are not placed on such a smooth substrate but on a porous layer formed by ring structures of previous drops, further mechanisms take effect. Experiments showed that the droplets of the second and third layer are either sliding down the outer rim of an already existing coffee-ring, resulting in a placement between the deposits of the previous layer, or, the droplets are sucked in by the center of an existing ring, resulting in a placement on top of it with partial filling of the porous structure. The first case results in the formation of another ring, stretching between the already existing ones and therefore spanning the gap. Hereby, the now uneven morphology of the deposition plane and the slope on the sides of the drying area cause an increased inclusion of cavities. In the second case the droplet's residue expands the inner rim of a previous ring. During this process it spans or partially closes the center basin. This in turn results in increased inclusion of voids. Thus, both cases result in an increase of overall layer porosity, explained by the intensified tendency to form cavities. However, the amount of porosity increase strongly depends on morphology of the previous layer as well as final positioning of the droplet on it and therefore tends to fluctuate. As can be seen in the for $c_s = 5\ M\%$ and $U = 1.5\ m/s$, there can be a significant rise in porosity, if the applied layer is enclosing a basin or cavity of the existing structure.

In Fig. 3 it can further be seen that an increase in drying airflow velocity results in a general increase of porosity over all layers. This phenomenon can be explained by the faster drying rate, which is equivalent to less time for structural organization of the solutes and in turn results in increased formation of both large cavities of the entire coffee-ring and small cavities in the confining crystal structure.

Comparing the porosity of the first layer of the 5 M% solution to the corresponding 30 M% values, one can also observe an increasing trend for higher solid concentration. This effect is reasoned in faster crust formation and the in turn resulting steeper slope and increased height of the deposits (Handscomp et al., 2009).

Fig. 4 shows the development of porosity with layer addition at different drying gas flow temperatures with a constant velocity of 1.5 m/s. Herein again, the clearest visible correlation is the increase of overall porosity during the built-up process. Regarding the influence of drying gas inlet temperature, no clear trend can be made out. This also results in the fact that in some cases the highest porosities are obtained for low and sometimes for high temperatures. This suggests a weaker influence of temperature on porosity, compared to substrate condition or velocity.

An overall comparison of porosity of 1 µl droplets to 100 nl droplets dried under same conditions yields relatively similar values for both volumes. This means that both droplet sizes tested in this study behave alike during the drying process and therefore result in relatively similar deposition structures. This can be explained by the fact that the capillary number as well as the Bond number are very small at this scale. Therefore, gravity and drag forces have little to no influence and are negligible compared to adhesion forces between the initial substrate or already existing deposits (Lubarda and Talke, 2011). In turn, droplet shape and positioning on the substrate or previous layer stay the same and result in the same effects as described above.

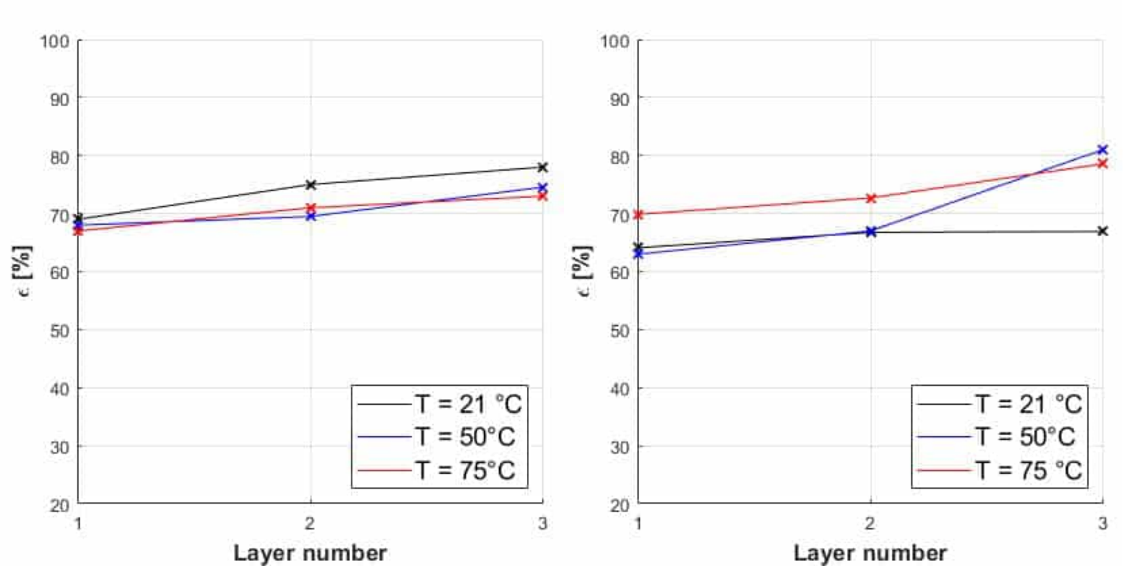

Fig. 4. Porosity development during layer built-up for different temperatures at $U = 1.5\ m/s$, $c_s = 30\ M\%$, $V_{drop} = 1\ \mu l$ (left) and $V_{drop} = 100\ nl$ (right).

Conclusions

In the course of this project, the layer structure resulting from dried deposited sodium benzoate solution droplets in the micro- and nanoliter range was analyzed with regard to porosity.

The droplet position during drying and the corresponding substrate condition each droplet is deposited on showed the strongest influence on porosity. With each addition of a new deposition structure, more cavities are enclosed within the layer. This results in a consistent increase of porosity with each step in the built-up process. Since the application of smaller droplets resulted in similar porosities, the application of less droplets with higher volume is recommended to create a less porous coating layer with the same amount of material. Consequently, the operation with smaller droplets during sessile droplet deposition as well as during spray on in fluidized bed is expected to result in more porous layers.

Layer porosity is also increased at higher gas velocities and with higher solid content in the coating solution. The same principles are expected to be valid within a fluidized bed. An increase of porosity alongside an increase of temperature, as reported by Rieck et al. (2015), could not be identified during the present experimental series.

It shall be noted that a direct comparison of coating layer porosity between fluidized bed and deposited droplets is still difficult and since there are additional effects taking place within a fluidized bed, an exact match of porosity values is not to be expected. Rather, the correlations presented herein are first means and guidelines that are expect to contribute to the overall understanding of coating processes in a fluidized bed and in turn lead to a more purposeful design of coating layers.

Notation

T	temperature, °C	ε	porosity, -
U	velocity, m/s		
V	volume, µl		

Subscripts

drop	droplet	t	total
s	solid		

Acknowledgements

The authors gratefully acknowledge the financial support for this study and the entire project by the German Research Foundation (DFG – Project I.D. TS28/11-1).

References

Brutin, D., Sobac, B., Loquet, B., Sampol, J. Pattern formation in drying drops of blood. J. Fluid Mechanics. 2011. 667, 85-95.

Deegan, R. D., Bakajin, O., Dupont T. F., Huber, G., Nagel, S. R., Witten, T. A. Capillary flow as the cause of ring stains from dried liquid drops. Nature. 1997. 389, 827-828.

Deegan, R. D., Pattern formation in drying drops. Physical Review E. 2000. 61, 475-485.

Deegan, R. D., Bakajin, O., Dupont T. F., Huber, G., Nagel, S. R., Witten, T. A. Contact line deposits in an evaporating drop. Physical review E: Statistical Physics, Plasmas, Fluids, and Related Interdisciplinary Topics. 2000. 62, 756-765.

Hampel, N., Bück, A., Peglow, M., Tsotsas, E. Continuous pellet coating in a Wurster fluidized bed process. Chemical Engineering Science. 2013. 86, 87-98.

Handscomp, C., Kraft, M., Bayly, A. A new model for the drying of droplets containing suspended solids. Chemical Engineering Science. 2009. 64, 628-637.

Hoffmann, T., Rieck, C., Schmidt, M., Bück, A., Peglow, M., Tsotsas, E. Prediction of shell porosities in continuous fluidized bed spray layering. Drying Technology. 2015. 33, 1662-1670.

Hu, H., Larson, R. G. Marangoni effect reverses coffee-ring depositions. J. Phys. Chem. B. 2006. 110, 7090-7094.

Lubarda, V. A., Talke, K. A. Analysis of the equilibrium droplet shape based on an ellipsoidal droplet model. ACS Journal of Surfaces and Colloids. 2011. 27, 10705-10713.

Mampallil, D., Eral, H. B. A review on suppression and utilization of the coffee-ring effect. Adv. Colloid Interface Science. 2018. 252, 38-54.

Rieck, C., Hoffmann, T., Bück, A., Peglow, M., Tsotsas, E. Influence of drying conditions on layer porosity in fluidized bed spray granulation. Powder Technology. 2015. 272, 120-131.

Sondej, F., Peglow, M., Bück, A., Tsotsas, E. Experimental investigation of the morphology of salt deposits from drying sessile droplets by white-light interferometry. AIChE Journal. 2018. 64, 2002-2016.

Yunker, P. J., Still, T., Lohr, M. A., Yodh, A. G. Suppression of the coffee-ring effect by shape-dependent capillary interactions. Nature 2011. 476, 308-311.

BEHAVIOUR OF AGGLOMERATES FORMED BY LIQUID INJECTION IN FLUIDIZED BEDS

Cedric Briens[1]*, Muhammad Owais Iqbal Bhatti[1], Francisco J. Sanchez[1], Franco Berruti[1], Jennifer McMillan[2]

[1]*ICFAR, Western University, London, Canada*
[2]*Edmonton Research Centre, Syncrude Canada, Edmonton, Canada*

*Email: cbriens@uwo.ca

Abstract

Formation of agglomerates in Fluid CokersTM can cause operating problems, such as excessive stripper shed fouling, which can lead to premature unit shut down. Better understanding of how agglomerates move through a fluidized bed can help improve the design and operation of Fluid Cokers and minimize the risk of agglomerates reaching regions where they cause problems. A Gum Arabic solution was injected into a two-dimensional (2D) fluidized bed under conditions that simulate agglomerate formation in Fluid Cokers, and the mass and density of recovered agglomerates were measured. A new 2D Radioactive Particle Tracking (RPT) method was developed to track the motion of model agglomerates. The fluidized bed had a steel wall, resulting in significant and non-uniform radiation absorption. The 2D RPT system was calibrated by placing the source at 290 locations in the bed, for each fluidization velocity. Since bubble flow patterns greatly affect agglomerate motion and segregation, a tribo-electric method was used to determine bubble flow distribution in the fluidized bed.

The RPT and liquid injection methods gave similar vertical distributions of agglomerates. The lateral distributions of agglomerates were slightly different, likely because escaping bubbles induced additional mixing during slumping of the bed, in liquid injection experiments. As expected, increasing the fluidization velocity reduced segregation, and larger and denser agglomerates were more likely to segregate. There was a strong correlation between the bubbles and agglomerates flow patterns: establishing a core-annular flow pattern by injecting more fluidization gas in one side of the bed greatly enhanced agglomerate segregation.

Introduction

Fluid Coking^{TM} and its Flexicoking^{TM} variant are processes that thermally crack heavy residual oils into lighter, more valuable oils. In the Coker, heavy oil is injected into a dense, downflowing fluidized bed of coke particles, which provide the heat required for thermal cracking of the feedstock and evaporation of the products. A major issue with Cokers is the formation of wet agglomerates when oil is sprayed into the fluidized bed (House et al. 2004). Some of these agglomerates reach the stripper before their liquid has fully reacted and evaporated, resulting in fouling of the stripper sheds (Sanchez and Granovskiy 2013). The flow patterns of large particles or agglomerates are important in other industrial processes, such as combustion, gasification or pyrolysis of large biomass particles in a fluidized bed of sand particles (Thy et al. 2010). Agglomerate formation due to hot spots is also an issue in polyolefin fluidized beds (Hulet et al. 2008). Finally, agglomeration is an important process for fertilizer, food and pharmaceutical industries, in which it is used to stabilize solids mixtures (Rajniak et al. 2007).

The objectives of this study are, first, to determine the size and density of the agglomerates that are formed when liquid is sprayed into a fluidized bed; second, to study the flow patterns of typical agglomerates; and, third, to determine how these flow patterns are related to the distribution of gas bubbles.

Review of Literature on Relevant Experimental Methods

Three main experimental methods are required for this study. First, the spraying of heavy oil in Cokers must be simulated at moderate temperature, using a safe model system that allows for the quick and accurate characterization of agglomerate properties. Second, agglomerates must be tracked in a fluidized bed to determine their flow patterns. Third, because agglomerate motion is induced by gas bubbles, the flow patterns of the gas bubbles must be measured.

The Gum Arabic model generate agglomerates that matches the agglomerates obtained in a pilot plant Fluid Coker (Reyes 2015). An advantage of this model is that it uses water as the solvent: water wets sand well, as bitumen wets coke in Cokers (Mohagheghi Dar Ranji 2014).

The simplest method to track agglomerates in a fluidized bed vacuums solids samples from the bed, and screens out the agglomerates. For larger agglomerates, the bed is usually slumped by shutting off the fluidization gas before solids are removed (Cluet et al. 2015; Coletto et al. 2017). This method is time-consuming and, while it provides their local concentration, does not provide direct information on the flow patterns of agglomerates.

Radioactive Particle Tracking (RPT) is a non-intrusive method that tracks a radioactive source embedded within a particle with the same size and density as a typical agglomerate. Several detectors are located just outside the column. Since the radiation intensity measured by a detector is a function of its distance from the source, the source position can be calculated from the radiation intensity, expressed as counts, reported by each detector. Two main calculation methods are used to determine the source position from the detector counts: standard Computer Aided Radioactive Particle Tracking (CARPT) and Monte Carlo Rendition.

The standard CARPT method first calibrates each detector so that its distance from the source can be accurately determined from its measured counts. The CARPT method is easy to implement and provides a solution quickly. Many researchers have applied this method (Sanchez Careaga et al. 2018). Its disadvantages are that it needs an extensive calibration. Monte Carlo Rendition eliminates the need for extensive in-situ calibration, but increases the computer processing time (Larachi et al. 1995). It is the method of choice when seeking accurate determination of a small number of tracer positions (Xu et al. 2019). The major issue with this method is the computational time, which ranges from 2.6 s to 17 s to determine a single source position when using a personal computer (Yadav et al. 2017). In a system where agglomerates can move at several m/s but move seemingly randomly, a one-hour period would require 100 hours of computation with Monte Carlo Rendition, which is prohibitive.

Various methodologies have been developed to visualize or quantify the bubble flow distribution. Some of the methodologies include X-ray image analysis, X-ray tomography or optical probes (Dubrawski et al. 2013). X-ray methods are costly and optical probes cannot withstand the stresses encountered in high velocity dense beds. A novel triboelectric method uses sturdy probes to quantify the gas bubbles distribution (Jahanmiri 2017). The triboelectric probes generate electric current when solids in the wake of the bubbles interact with the metal probe. This current can be analyzed to provide the local gas bubble flux (Jahanmiri 2017).

Equipment and Experimental Procedures

The equipment was 2.3 m high with a cross section of 1.2 m by 0.15 m. It had an expansion zone section of 1.2 m by 0.47 m starting at a height of 1.5 m from the gas distributor (Figure 1). Fluidization gas was provided with two independent gas distributors that each supplied half of the bed width (Bhatti 2017). Two cyclones in series recovered entrained bed solids. Silica sand with a Sauter mean diameter of 190 µm and a particle density of 2650 kg/m^3 was used as fluidized solids. For all experiments, 150 kg of silica sand was used, corresponding to a defluidized bed height of about 0.54 m. The minimum fluidization velocity for these group B particles is about 0.04 m/s. The liquid binder solution was injected at a constant flowrate from a blow tank, pressurized with nitrogen, into the fluidized bed. The solution consisted of 5 wt% gum arabic and 2 wt% blue dye, and hydrochloric acid to adjust the pH to 3 (Reyes 2015). A spray nozzle, with an exit diameter of 2.7 mm, used nitrogen gas to atomize the liquid into

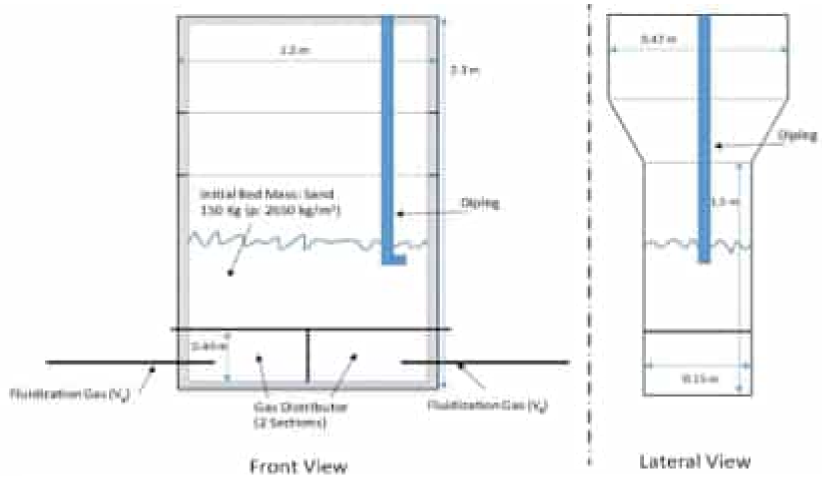

Fig. 1. Experimental setup.

small droplets directly into the fluidized bed (Reyes 2015). The ratio of atomization gas flowrate to liquid flowrate was 2 wt%, and the liquid flowrate was 30 g/s. Triboprobes at 36 locations were used to determine the lateral distribution of the gas bubbles.

For liquid injection experiments, the bed was fluidized and preheated to 120 ℃. Liquid was injected for 10 s. The bed was kept fluidized for a set duration after the liquid injection had been completed. Fluidization gas was then shut off to slump the bed so that the agglomerates stopped moving. After cooling, a vacuum cleaner was used to extract the bed solids layer by layer. The collected solids were sieved to recover agglomerates in size cuts, and measure their mass and density (Bhatti 2017).

Radioactive Particle Tracking (RPT) was used to measure agglomerate flow patterns. The radioactive source was Scandium-46 isotope. This study used 12 scintillation detectors distributed over the front of the bed wall. Monte Carlo Rendition is unsuitable for this study because of its prohibitive computation time. The standard CARPT method is unsuitable for two reasons. First, it could not provide reliable solutions for the 2D geometry used in this study. Second, the column had a steel wall, resulting in significant radiation absorption that was not uniform because of flanges, pressure taps and a dipleg. Therefore, it was decided to use multilinear regression to develop equations for the source coordinates from the data obtained by thorough calibration of the 2D RPT system. To map the complete bed, the source was placed at 290 locations within the bed and average normalized counts were calculated for each detector for each location. This data was then used to develop an empirical equation for each coordinate as a function of gas velocity and normalized counts measured by 12 detectors. Model agglomerates were manufactured with the radioactive source inside a Nylon ball and tungsten powder to adjust their mass. Two model agglomerates were prepared, with a diameter of either 5500 µm or 12500 µm. The final density of both model agglomerates was 1450 kg/m^3, corresponding to the density of agglomerates formed when injecting liquid.

Results and Discussion

Since the results indicated that most of the segregation occurred in the bottom and top layers, the results were summarized with two new dimensionless Indices of Segregation. The Index of Segregation for Bottom Layer (ISB) is the ratio of concentration of agglomerates in the bottom later to the average concentration of the agglomerates in middle layers. The Index of Segregation for Top Layer (IST), which is the ratio of concentration of agglomerates in the top later to the average concentration of the agglomerates in middle layers. A value higher than 1 identifies a higher concentration in the layer than in the middle section of the bed. A higher value of the index signifies a more pronounced segregation. Figure 2a shows the index of segregation for the bottom layer at the 0.60 m/s gas velocity. At high velocity, the agglomerates larger than 9500 µm segregated, but not as significantly as at lower velocities

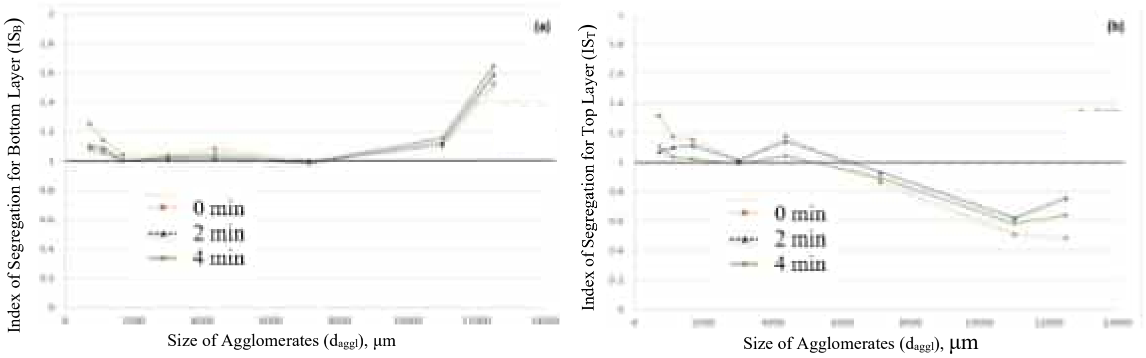

Fig. 2. Index of Segregation vs. size of agglomerates at 0.60 m/s fluidization gas velocity: (a) bottom layer; (b) top layer.

(Bhatti 2017). There was no significant segregation in the bottom layer for other agglomerates. Figure 2b shows that the proportion of agglomerates larger than 9500 µm was lower in the top layer than in the rest of the bed. However, the proportion of mid-size agglomerates (i.e. smaller than 3000 µm) was slightly higher in the top layer than in the rest of the bed.

Figure 3 summarizes the RPT results obtained for the large, 12500 µm model agglomerate. Each dot corresponds to a recorded location for the agglomerate, while the solid line shows the bubble flow distribution on the secondary y-axis. The agglomerate concentration was highest near the distributor, where it would wait to be picked by a gas bubbles. The concentration was lowest in the central region of the bed, where it would travel quickly in the wake of rising bubbles. There was a significant concentration near the bed wall, where the agglomerates carried by the gas bubbles to the bed surface would travel back to the bottom of the bed through the emulsion.

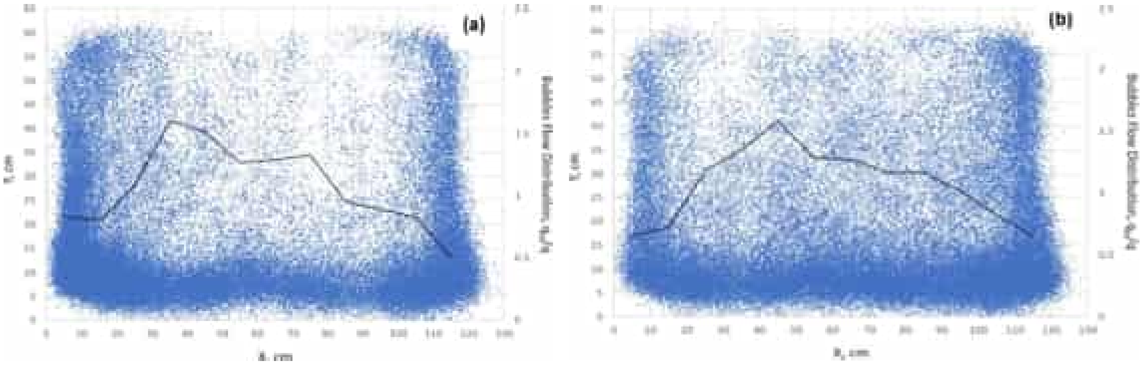

Fig. 3. Tracer locations (dots) and gas bubble flow distribution (line) for large agglomerate at room temperature: (a) V_g = 0.35 m/s; (b) V_g = 0.6 m/s.

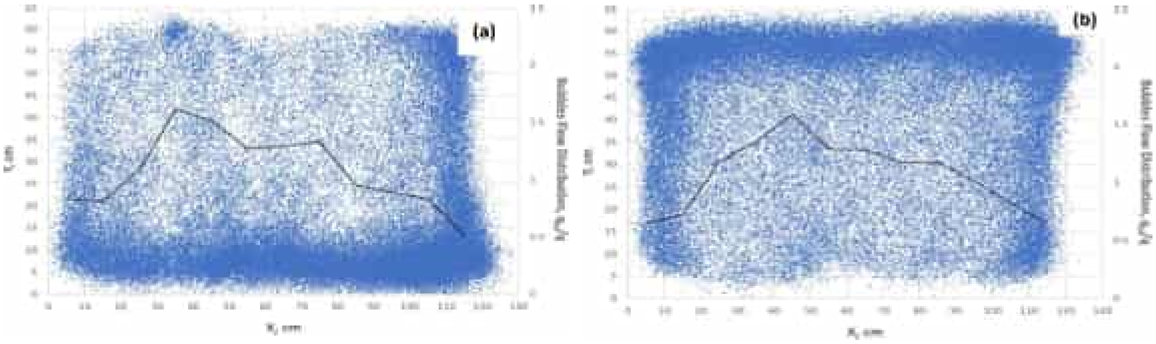

Fig. 4. Tracer locations (dots) and gas bubble flow distribution (line) for small agglomerate at room temperature: (a) V_g = 0.35 m/s; (b) V_g = 0.6 m/s.

Figure 4 shows the results obtained for the small, 5500 µm model agglomerate. At a fluidization velocity of 0.35 m/s, the small agglomerate spent more time in the lower bed regions (Figure 4a), thus behaving similarly to the large agglomerate (Figure 3a). However, at the higher fluidization velocity of 0.6 m/s, the two agglomerates behaved completely differently: while the large agglomerate spent more time in the lower bed regions (Figures 3b), the small agglomerate spent more time near the bed surface (Figure 4b). Similar results were obtained at a bed temperature of 120 °C.

Figure 5 shows the impact of uneven gas distribution. The large agglomerate spent more time in the region with low bubble flow and less time in the region with high bubble flow. The results obtained with a high bubble flow on the left hand size (Figure 5a) and with a high bubble flow on the right hand side (Figure 5b) were not exactly symmetrical because of the impact of the cyclone dipleg (Figure 1). Similar behavior was observed for the small agglomerate. Both liquid injection experiments and Radioactive Particle Tracking (RPT) showed that agglomerates segregated in the region of low bubble flow near the bottom of the bed for all cases; but concentration gradients and, hence, segregation were greatly enhanced by the split gas velocity. While agglomerates were distributed evenly between both halves of the bed for an even gas distribution, with an uneven gas distribution, a higher proportion of all agglomerates were present in the lower velocity side.

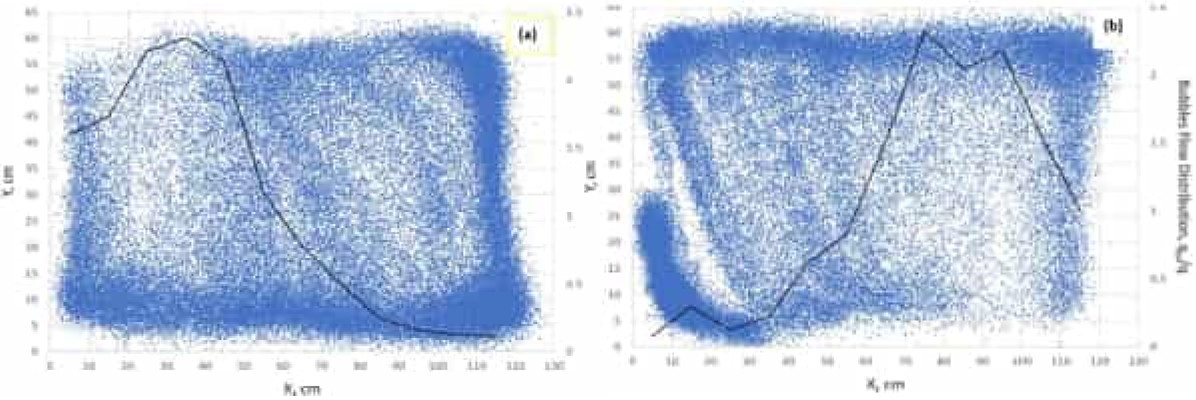

Fig. 5. Tracer locations (dots) and gas bubble flow distribution (line) for small agglomerate at room temperature: (a) V_g = 0.35 m/s; (b) V_g = 0.6 m/s.

Conclusions

A new Radioactive Particle Tracking (RPT) method was successfully developed to track the motion of model agglomerates in a 2D fluidized bed. It used a thorough calibration and obtained the agglomerate coordinates from a simple linear combination of the detector counts.

The Radioactive Particle Tracking (RPT) and liquid injection methods gave similar vertical distributions of agglomerates. The lateral distributions of agglomerates were slightly different, likely because escaping bubbles induced additional mixing during slumping of the bed, in liquid injection experiments.

As expected, increasing the fluidization velocity reduced segregation, and larger and denser agglomerates were more likely to segregate. At high fluidization velocities, agglomerates could also concentrate near the bed surface.

There was a strong correlation between the bubbles and agglomerates flow patterns: establishing a core-annular flow pattern by injecting more fluidization gas in one side of the bed greatly enhanced agglomerate segregation.

Acknowledgments

The authors gratefully acknowledge funding from the NSERC/Syncrude/ExxonMobil Industrial Research Chair in Fluid Coking Technologies.

References

Bhatti MOI. 2017. Study of motion of agglomerates through a fluidized bed. MESc thesis, Western University.

Cluet B, Mauviel G, Rogaume Y, Authier O, Delebarre A. 2015. Segregation of wood particles in a bubbling fluidized bed. Fuel Processing Technology. 133:80-88.

Coletto MM, Marchisio DL, Barresi AA. 2017. Mixing and segregation of wheat bran and vegetable pieces binary mixtures in fluidized and fluid-spout beds for atmospheric freeze-drying. Drying Technology. 35(9):1059-1074.

Dubrawski K, Tebianian S, Bi HT, Chaouki J, Ellis N, Gerspacher R, Jafari R, Kantzas A, Lim C, Patience GS et al. 2013. Traveling column for comparison of invasive and non-invasive fluidization voidage measurement techniques. Powder Technology. 235:203-220.

House P, Saberian M, Briens C, Berruti F, Chan E. 2004. Injection of a liquid spray into a fluidized bed: Particle-liquid mixing and impact on fluid coker yields. Industrial and Engineering Chemistry Research. 43(18):5663-5669.

Hulet C, Llinas JR, Selo JL, Briens C, Thomas S, Mouillet A. 2008. Multivariate analysis of process signals for early detection of agglomeration in a gas phase fluidized bed for polyethylene. Chemical Engineering and Processing. 47(8):1224-1233.

Jahanmiri M. 2017. Use of a baffle to enhance distribution of a liquid sprayed into a gas-solid fluidized bed [MESc]. MESc thesis, Western University.

Larachi F, Chaouki J, Kennedy G. 1995. 3-d mapping of solids flow-fields in multiphase reactors with rpt. AIChE Journal. 41(2):439-443.

Mohagheghi Dar Ranji M. 2014. Impact of local bed hydrodynamics on jet-bed interaction [PhD]. PhD thesis, Western University.

Rajniak P, Mancinelli C, Chern RT, Stepanek F, Farber L, Hill BT. 2007. Experimental study of wet granulation in fluidized bed: Impact of the binder properties on the granule morphology. Int J Pharm. 334(1-2):92-102.

Reyes LAP. 2015. Effect of temperature and successive sprays on liquid distribution in fluidized beds [MESc]. [Western University]: MESc thesis, Western University.

Sanchez Careaga FJ, Briens C, Berruti F, McMillan J, Gray M. 2018. Agglomerate behavior in a recirculating fluidized bed with sheds: Effect of bed properties. Powder Technology. 325:31-41.

Sanchez FJ, Granovskiy M. 2013. Application of radioactive particle tracking to indicate shed fouling in the stripper section of a fluid coker. Canadian Journal of Chemical Engineering. 91(6):1175-1182.

Thy P, Jenkins B, Williams R, Lesher C, Bakker R. 2010. Bed agglomeration in fluidized combustor fueled by wood and rice straw blends. Fuel Processing Technology. 91(11):1464-1485.

Xu Y, Li T, Lu L, Tebianian S, Chaouki J, Leadbeater TW, Jafari R, Parker DJ, Seville J, Ellis N et al. 2019. Numerical and experimental comparison of tracer particle and averaging techniques for particle velocities in a fluidized bed. Chemical Engineering Science. 195:356-366.

Yadav A, Ramteke M, Pant HJ, Roy S. 2017. Monte carlo real coded genetic algorithm (mc-rga) for radioactive particle tracking (rpt) experimentation. AIChE Journal. 63(7):2850-2863.

SPRAYING SLURRIES: IMPACT OF SLURRY PROPERTIES ON SPRAY CHARACTERISTICS AND AGGLOMERATE FORMATION IN FLUIDIZED BEDS

Cedric Briens[1]*, Josh Idowu[1], Francisco J. Sanchez[1], Dominic Pjontek[1], Jennifer McMillan[2]

[1]*ICFAR, Western University, London, Canada*
[2]*Edmonton Research Centre, Syncrude Canada, Edmonton, Canada*

*Email: cbriens@uwo.ca

Abstract

Fluid Coking™ is a process that upgrades heavy oil. In a Fluid Coker, heavy oil is sprayed into a fluidized bed of hot coker particles, where it undergoes thermal cracking. The formation of wet agglomerates slows thermal cracking and leads to operating problems. The product vapours exiting the coker are scrubbed to condense the heavier components, which are recycled to the coker. The recycle stream contains unwanted suspended fines that could affect the interaction between the liquid feed and the bed particles, and the resulting agglomerate formation.

The impacts of suspended solids on spray stability and angle were measured in open air, by analysing spray videos. The impacts on agglomerate stability and liquid distribution were studied in a fluidized bed of sand at 130 °C by spraying a gum arabic solution that was formulated to simulate oil-coke agglomerate formation in Fluid Cokers. The properties of the fine particles added to the gum arabic solution were varied to understand the effect of the suspended solids on agglomerates. In open air, the presence of suspended solids had a negligible impact on spray behaviour. Within the fluidized bed, changing the concentration of suspended solids affected agglomerate stability and liquid distribution. Different mechanisms were considered to explain the change in agglomeration behaviour when particles were added to the spray: increased viscosity, spray characteristics, drying kinetics and the solids filler effect. A dedicated experimental plan was designed to test each hypothesis. The only significant impact of the suspended solids results from a filler effect within the agglomerates: the fines strengthen the agglomerates, which become more resistant to breakage in the fluidized bed. This only occurs, however, when the suspended solids are wettable by the liquid: non-wettable suspended solids, instead, weaken agglomerates.

Introduction

Fluid Coking™ and its Flexicoking™ variant are processes that thermally crack heavy residual oils into lighter oils (Gray 2015). Figure 1 shows a diagram of the Fluid Coking process. The reactor unit consists of three main sections: the scrubber, the reactor and the burner. The feed stream is split and fed into both the scrubber and the reactor. Injection of the liquid feed is performed with spray nozzles that use atomization steam (Base et al. 1999). In the reactor, the residual oil is thermally cracked to produce coke and product vapors at about 550 °C (Gray 2015). The residual oil introduced into the scrubber contacts the product vapors: the lighter feed components vaporize and the heavier components in the product vapors condense (Jankovic 2005). Fine solid particles escaping from the reactor cyclones with the product vapors are captured by the liquid (Jankovic 2005).

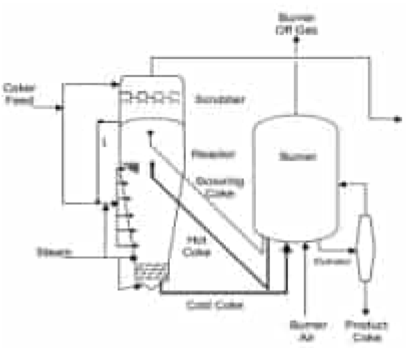

Fig.1. Fluid Coker process.
(adapted from Gray, 2015)

Stream 1 in Figure 1 is the recycle stream that contains suspended fines. Industrial experience suggests that the fines have a diameter of about 10 μm and that their concentration may reach 20 wt.% during process upsets. The reactor vessel also has a stripping section, at the bottom, where the coke flowing from the reaction zone is stripped using steam to remove hydrocarbon vapors. Wet agglomerates that reach the stripper contribute to fouling of the stripper internals, which may cause premature shutdowns (Sanchez and Granovskiy 2013).

Although this study is focused on the Fluid Coking process, there are other industrial processes where liquid with suspended solids is injected into a fluidized bed. In the food and pharmaceutical industries, agglomeration is used to stabilize solid mixtures, prevent dust explosions, and improve product properties such as flowability (Dhanalakshmi et al. 2011).

The objective of this study is to study the impact of suspended fines in a liquid first, on the characteristics of the spray formed when the liquid is atomized with gas in open air and second, on agglomeration formation and breakup when the liquid is sprayed into a fluidized bed.

Literature Review

The most important spray characteristics, when liquid is injected in a fluidized bed, are geometry and stability. The most important spray geometry characteristics are the spray expansion angle and the spray length. The expansion angle of a spray in the fluidized bed is about half its value in open air (Dawe et al. 2008; Newton et al. 2001) but is related, i.e. a change in spray angle in open air is associated to a change in a fluidized bed (Dawe et al. 2008). The spray jet penetration in a fluidized bed, on the other hand, should be measured directly in a fluidized bed (McMillan 2007). Experiments have shown the spray angle affects the liquid distribution performance in a fluidized bed (Prociw et al. 2018).

The spray stability, which characterizes spray pulsations, affects nozzle performance (Ariyapadi et al. 2005). Spray stability can be quantified by measuring pressure fluctuations upstream of the nozzle tip (Maldonado et al. 2008). Computerized analysis of fast videos of sprays in open air can also be used to quantify spray stability (Joness 2019). The time-averaged spray expansion angle can also be obtained in open air from videos (Joness 2019).

The spray jet penetration in a fluidized bed can be measured with either thermocouples or triboprobes. With thermocouples, liquid that is much colder than the bed is injected into the bed: if a thermocouple is within the spray jet cavity, it registers a lower temperature than the bed temperature (McMillan 2007). With triboprobes, the current generated by particle friction on the probe surface is much lower within the jet cavity (Dawe et al. 2008; Li et al. 2019).

Spraying a Gum Arabic solution in a fluidized bed of sand particles at 130 °C gave similar agglomerate formation as when bitumen was sprayed in bed of coke particles at 530 °C (Reyes 2015). The wet agglomerates issuing from the spray jet cavity are transported through the fluidized bed where most of them break up due to the shear forces induced by the gas bubbles (Weber 2009). A study of agglomerate breakup in fluidized beds showed that wet agglomerates were more stable when they included particles from a wide range of particle sizes (Weber 2009). Particle properties such as size, shape, porosity and abrasiveness significantly affected agglomerate breakup (Weber 2009). The wettability of the injected agglomerates also appeared to affect the breakage rate of the agglomerates (Weber 2009).

Equipment and Experimental Procedures

Table 1 shows the different suspended solids and their particle properties. Figure 2 includes a schematic diagram of the spraying system. The slurry mixture is mixed in a pressurized mixing tank using a compressed air motor and impeller. The flowrate of slurry is set with the mixing tank pressure. The slurry flowing from the mixing tank is mixed with atomization gas at the pre-

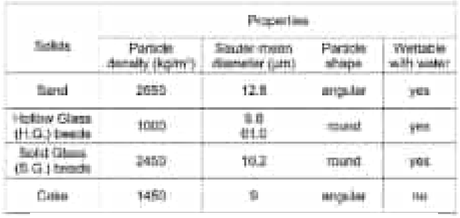

Solids	Properties			
	Particle density (kg/m³)	Sauter mean diameter (μm)	Particle shape	Wettable with water
Sand	2650	12.8	angular	yes
Hollow Glass (H.G.) beads	1000	8.8 61.0	round	yes
Solid Glass (S.G.) beads	2450	10.2	round	yes
Coke	1450	9	angular	no

Table 1. Slurry solids.

mixer and flows to the spray nozzle (Base et al. 1999). Preliminary tests confirmed that this system could deliver a well-mixed slurry (Idowu 2018).

To determine the spray characteristics, videos of sprays issuing into open air were taken at 420 frames per second in a chamber with controlled and optimized lighting (Idowu 2018). The videos were then analyzed using Matlab, adapting methods developed by other researchers (Joness 2019). Two basic measurements were selected to compare sprays: the spray geometry was characterized with the average spray angle and its stability.

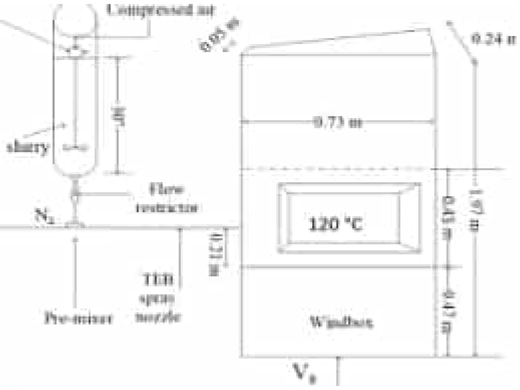

Fig. 2. Experimental setup.

The spray stability was obtained from the spray video, using a method developed and validated by Joness (2019). For each video frame, the spray area was identified from the change in colour between spray and background. The average pixel intensity was then calculated for the spray area. The coefficient of variation of this average pixel intensity was then determined from all the frames. The coefficient of variation of the premixer pressure was measured in both cases and found to be the same, as expected, when spraying in open air or in a fluidized bed (Idowu 2018).

Figure 2 shows the experimental set-up for the fluidized bed experiments. The bed, which had an approximate height of 0.45 m, contained 45 kg of silica sand with a Sauter-mean diameter of 190 µm and a particle density of 2650 kg/m^3. An induction heater was attached to the outside wall to heat the bed to 135 °C by heating the wall through the outer insulation. As a result, the heating system did not interfere with the fluidization process. The spray injections were carried out with a nozzle with a 1 mm throat diameter at 2 wt.% GLR (atomization Gas-to-Liquid Ratio). The spray nozzle was located 0.21 m above the windbox.

The agglomerate formation and breakup was characterized with the Gum Arabic model (Reyes 2015). The injected slurry consisted of slurry particles and Gum Arabic solution. The solution was a mixture of 92 wt.% water, 6 wt.% Gum Arabic powder and 2 wt.% blue dye. total mass of injected mixture was 200 g of slurry for all runs with an atomization gas flux of 0.463 g/s/mm^2 which corresponded to a GLR of 2 wt.% for 0 wt.% of solids. The fluidization velocity before and during injection was set at V_{gi} depending on the experiment. After the injection, the velocity was changed to a value V_{gd}. Using a value of about 0 m/s for V_{gd} (actually a value well below the minimum fluidization velocity) eliminated any agglomerate breakup subsequent to injection. The method developed by Li et al. (2019) was adapted to measure the jet penetration in the fluidized bed.

Results and Discussion

For all the tested solids (Table 1) and atomization gas flowrates, the liquid flowrate steadily decreased as the slurry concentration was increased but that the slurry volumetric flowrate was nearly independent of the slurry concentration (Idowu 2018). The average spray angle was not significantly affected by the slurry concentration. Similarly, the spray stability, whether obtained from the videos or the premixer pressure fluctuations, was not significantly affected by the slurry concentration (Idowu 2018). In the fluidized bed, the jet penetration was not affected by the presence of 20 wt.% fine sand in the injected liquid (Idowu 2018).

Figure 3 shows the cumulative plot of the fraction of injected liquid that was trapped within the agglomerates against size cuts of the agglomerates at different solids concentrations in the slurry (0, 10 and 20 wt.%). There was a small impact when going from 0 to 10 wt.%, but a more significant impact can be seen at 20 wt.% sand. The increase occurs over the entire range of agglomerate particle sizes. Increasing the solids concentration from 0 to 20 wt.% resulted in a 44 % increase in the fraction of injected liquid that was trapped.

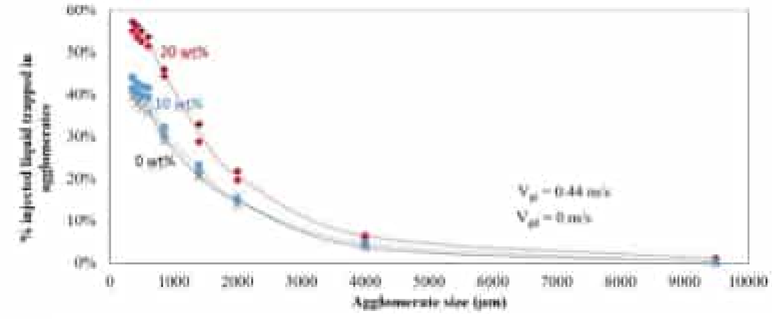

Fig. 3. Impact of sand concentration in the injected slurry on the fraction of injected liquid trapped within agglomerates of size larger than the specified size.

Figure 4 shows that increasing the gas velocity during drying significantly reduced the liquid trapped within agglomerates: there was significant agglomerate breakup during drying. Breakup was much smaller with a 20 wt.% sand slurry, indicating that the agglomerates were stronger when formed with a sand slurry instead of pure liquid.

The observed impact of suspended fines on agglomeration and breakup could be attributed to various mechanisms, such as changes in spray properties, effective viscosity, drying kinetics, or a filler effect on agglomerate stability.

The fines could affect the spray. Experiments showed no impact of fines on spray angle or stability. This was confirmed by fluidized bed experiments that showed no impact on jet penetration or stability.

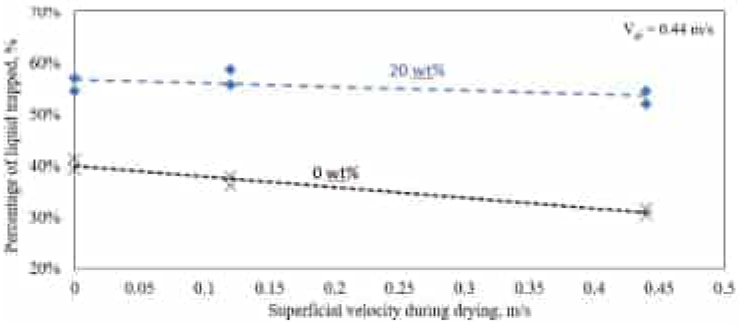

Fig. 4. Impact of gas velocity during drying n the fraction of injected liquid trapped within agglomerates.

The presence of suspended fines in a liquid increase its viscosity, and the increase is roughly proportional to the volumetric fraction of the slurry that is occupied by suspended particles (Thomas 1965). Increasing the liquid viscosity increases the stability of the agglomerates by making the liquid bridges linking the agglomerate particles stronger, especially under the high strain conditions expected in fluidized beds (Iveson et al. 2002), and this effect has been confirmed when spraying Gum Arabic solutions in fluidized beds (Reyes 2015). The increase in effective viscosity could thus, explain the results obtained with sand slurries. To confirm this mechanism, experiments were conducted with two types of glass beads, solid and hollow, which had the same size, the same shape and the same wettability and only differed in density (Table 1). A slurry of 20 wt.% solid glass beads contains a smaller volumetric fraction of fines than a 20 wt.% slurry of hollow glass beads and has, thus, a smaller effective viscosity. One would thus have expected the solid beads to reduce agglomeration, when compared to hollow glass beads; the results in Table 2 show that the opposite happened: increasing the fines density from 1000 to 2450 kg/m^3 had a detrimental impact, increasing the mass of agglomerates and the mass of liquid initially trapped in agglomerates. The increase in effective viscosity caused by the addition of suspended solids cannot therefore explain the results obtained with experimental observations.

Change in particle properties of injected solids	Percentage change in:			
	total liquid trapped	total mass of macro-agglomerates	Average L/S ratio	Sauter-mean diameter of agglomerates
Density: 1000 to 2450 kg/m^3	34	5	57	4
Size: 9.8 to 61 µm	4	-19	25	- 5
round to angular particles	12	3	6	- 1
Wettable to non-wettable	- 46	- 23	- 41	- 11

Table 2. Summary of impact from different particle properties.

The presence of fines affects the thermal conductivity of the wet agglomerates, and the amount of heat required to evaporate liquid from agglomerates, expressed per a unit volume of wet agglomerate material. When agglomerates are formed, the suspended fines in the slurry displace from the wet agglomerates a volume of liquid equal to their volume. To confirm this mechanism, experiments were conducted with two types of glass beads, solid and hollow, which had the same size, the same shape and the same wettability and only differed in density and thermal conductivity (Table 1). Increasing the fines particle density should be beneficial by slowing the drying by resulting in smaller displacement of liquid. The first line of Table 2 shows that, on the contrary, increasing the fines density from 1000 to 2450 kg/m^3 had a detrimental impact, increasing the mass of agglomerates and the mass of liquid initially trapped in agglomerates. The impact of suspended fines on drying kinetics cannot therefore explain the experimental observations.

In the polymer and construction industry, the use of fillers is useful in making stronger composites and concrete (Ahmad et al. 2008a; Bu et al. 2017; Tripathi and Dey 2019). This would explain the results obtained with fine sand, which would strengthen agglomerates by acting as a filler. To test the hypothesis that suspended fines resulted in the formation of stronger agglomerates, different types of suspended solids were tested to see if the observed effects corresponded to the effects reported for filler properties in the literature.

Increasing the filler particle size reduces tensile strength and durability of composites (Fu et al. 2008; Sanya et al. 2019). Table 2 shows that increasing the hollow glass beads particle size from 9.8 to 61 µm reduced agglomeration, which is consistent with the filler effect.

In composites, non-spherical filler particles generally give stronger composites than spherical particles (Ahmad et al. 2008b; Eichner et al. 2018). Table 2 shows that replacing, as suspended fines, the round glass beads with angular sand particles (Table 1) increased agglomeration, which is consistent with the filler effect.

In composites, wettability between the filler and the polymer is desired as it increases the composite strength (Gwon et al. 2010; Yatigala et al. 2018). Table 2 shows that replacing, as suspended fines, wettable sand particles with non-wettable coke particles (Table 1) greatly decreased agglomeration, which is consistent with the filler effect. With coke particles, agglomeration was actually decreased below the agglomeration level for the pure liquid case.

Conclusions

Introducing up to 20 wt.% of suspended fines to liquid spray with a gas-atomized nozzle does not markedly change the spray geometry, its stability or its penetration into a fluidized bed.

Suspended fines, when wettable, greatly increase wet agglomerate stability in the fluidized bed. The main mechanism is a filler effect, similar to the effect of fillers in concrete and polymer composites: the fines strengthen the wet agglomerates produced when the sprayed liquid interacts with the fluidized bed particles. Agglomerates are, thus, more likely to survive the shear forces in the fluidized bed. An exception occurs when the suspended fines are not wettable. Such fines weaken the agglomerates.

Acknowledgments

The authors gratefully acknowledge funding from the NSERC/Syncrude/ExxonMobil Industrial Research Chair in Fluid Coking Technologies.

References

Ahmad FN, Jaafar M, Palaniandy S, Azizli KAM. 2008a. Effect of particle shape of silica mineral on the properties of epoxy composites. Composites Science and Technology. 68(2):346-353.

Ahmad FN, Jaafar M, Palaniandy S, Azizli KAM. 2008b. Effect of particle shape of silica mineral on the properties of epoxy composites. Composites Science and Technology. 68(2):346-353.

Ariyapadi S, Berruti F, Briens C, Knapper B, Skwarok R, Chan E. 2005. Stability of horizontal gas-liquid sprays in open-air and in a gas-solid fluidized bed. Powder Technology. 155(3):161-174.

Base T, Chan E, Kennett R, Emberley D, inventors; Canadian Oil Sands, assignee. 1999. Nozzle for atomizing liquid in two phase flow. US 6,003,789 patent 6003789.

Bu J, Tian Z, Zheng S, Tang Z. 2017. Effect of sand content on strength and pore structure of cement mortar. Journal Wuhan University of Technology, Materials Science Edition. 32(2):382-390.

Dawe M, Briens C, Berruti F. 2008. Study of horizontal sonic gas jets in gas–solid fluidized beds. The Canadian Journal of Chemical Engineering. 86(3):506-513.

Dhanalakshmi K, Ghosal S, Bhattacharya S. 2011. Agglomeration of food powder and applications. Critical Reviews in Food Science and Nutrition. 51(5):432-441.

Eichner E, Heinrich S, Schneider GA. 2018. Influence of particle shape and size on mechanical properties in copper-polymer composites. Powder Technology. 339:39-45.

Fu SY, Feng XQ, Lauke B, Mai YW. 2008. Effects of particle size, particle/matrix interface adhesion and particle loading on mechanical properties of particulate-polymer composites. Composites Part B: Engineering. 39(6):933-961.

Gray MR. 2015. Upgrading oilsands bitumen and heavy oil. University of Alberta.

Gwon JG, Lee SY, Chun SJ, Doh GH, Kim JH. 2010. Effects of chemical treatments of hybrid fillers on the physical and thermal properties of wood plastic composites. Composites Part A: Applied Science and Manufacturing. 41(10):1491-1497.

Idowu J. 2018. Spraying slurries: Impact of slurry properties on spray characteristics and agglomerate formation in fluidized beds. Western University.

Iveson SM, Beathe JA, Page NW. 2002. The dynamic strength of partially saturated powder compacts: The effect of liquid properties. Powder Technology. 127(2):149-161.

Jankovic J. 2005. Simulation of the scrubber section of a fluid coker. University of British Columbia.

Joness A. 2019. The effect of scale on spray nozzle performance Western University.

Li Y, Briens C, Berruti F, Careaga FJS, Jahanmiri M, McMillan J. 2019. Applications of tribo-electric probes in fluidized beds. Lateral. 10(10):30.

Maldonado S, Fleck B, Heidrick T, Amirfazli A, Chan EW, Knapper B. 2008. Development of an experimental method to evaluate the stability of gas-liquid sprays. Atomization and Sprays. 18(8):699-722.

McMillan J. 2007. Characterization of the interactions between high velocity jets and fluidized particles. PhD thesis Western University.

Newton D, Fiorentino M, Smith G. 2001. The application of x-ray imaging to the developments of fluidized bed processes. Powder technology. 120(1):70-75.

Prociw N, Briens C, Berruti F, McMillan J. 2018. Effect of spray nozzle attachment geometry on rate of liquid released from agglomerates produced by gas-atomized liquid injection into a fluidized bed. Powder Technology. 325:280-288.

Reyes LAP. 2015. Effect of temperature and successive sprays on liquid distribution in fluidized beds [MESc]. [Western University]: MESc thesis, Western University.

Sanchez FJ, Granovskiy M. 2013. Application of radioactive particle tracking to indicate shed fouling in the stripper section of a fluid coker. Canadian Journal of Chemical Engineering. 91(6):1175-1182.

Sanya OT, Oji B, Owoeye SS, Egbochie EJ. 2019. Influence of particle size and particle loading on mechanical properties of silicon carbide–reinforced epoxy composites. International Journal of Advanced Manufacturing Technology. 103(9-12):4787-4794.

Thomas DG. 1965. Transport characteristics of suspension: Viii. A note on the viscosity of newtonian suspensions of uniform spherical particles. Journal of Colloid Science. 20(3):267-277.

Tripathi D, Dey TK. 2019. Effect of particle size distribution on thermo-mechanical properties of nio filled ldpe composites. Bulletin of Materials Science. 42(4).

Weber SC. 2009. Agglomerate stability in fluidized beds [Doctoral Thesis]. Western University.

Yatigala NS, Bajwa DS, Bajwa SG. 2018. Compatibilization improves physico-mechanical properties of biodegradable biobased polymer composites. Composites Part A: Applied Science and Manufacturing. 107:315-325.

INFLUENCE OF PROCESS PARAMETERS ON THE GRANULE MORPHOLOGY DURING FLUIDIZED BED SPRAY GRANULATION

Swantje Pietsch[1*], Paul Kieckhefen[1], Maike Orth[1], Stefan Heinrich[1]

[1] *Institute of Solids Process Engineering and Particle Technology, Hamburg University of Technology, Denickestraße 15, 21073 Hamburg, Germany*

*Email: *swantje.pietsch@tuhh.de*

Abstract

Fluidized bed spray granulation has been applied for more than 60 years in various industries, as chemical, pharmaceutical and food industry and allows the production of tailor-made particles with defined product properties. Nevertheless, the connection between the process parameters and the later granule morphology and product properties is still challenging and not yet fully understood. In this study, spray granulation experiments were performed in a lab-scale fluidized bed (GF 3, Glatt GmbH, Germany) with various process parameters to determine the influence on the granule morphology and the surface roughness. Non-porous Cellets® 500 particles were sprayed with a sodium benzoate solution in bottom-spray configuration with a two-fluid nozzle. By applying a design of experiment approach, meaningful experiments with varying gas volume flow rate, fluidization gas temperature, spray rate and pressure of the nozzle air were performed. The influence of the temperature of the atomization air in the two-fluid nozzle is shown to have a major impact on the resulting surface structure.

Introduction

Fluidized bed spray granulation is one of the main unit operations in the field of solids process engineering and for example applied for the production of pharmaceuticals, fertilizers or detergents (Mörl et al. 2007). In a fluidized bed the particles are entrained by the upward flow of the fluidization gas resulting in a bed expansion coming along with a high heat, mass and momentum transfer. During granulation, an atomizable liquid (e.g. suspension, solution, emulsion or melt) is injected onto the fluidized solid granules resulting in a layered growth of the initial particles. The granulation process integrates several processes on micro-scale, e.g. heat and mass transfer with resulting evaporation, drying and wetting as well as granule growth, which then define the product structure characteristics on the macro-scale. The final product structure defines on one hand the particle size and its distribution and on the other hand the granule morphology including surface roughness and layer porosity. The particle morphology then later determines the product quality and its handling, e.g. the flow properties or the dispersibility of the powder.

The surface structure of particles produced in a fluidized bed process is defined by different process parameters, e.g. the fluidization gas flow rate, the gas temperature and the nozzle pressure applied for atomization of the liquid. As the different process parameters define the size of the injected droplets as well as the drying potential, they have a major influence on the surface roughness and the layer porosity. To collect the different influencing process conditions into one parameter, the dimensionless drying potential η has been established in literature. It is defined as the quotient of the still vaporizable amount of water in the air after passing the process chamber and the maximum vaporizable amount at the inlet:

$$\eta = \frac{Y_{wb} - Y_{out}}{Y_{wb} - Y_{in}} \tag{1}$$

with Y_{wb}[kg/kg$_{\text{dry air}}$] the wet bulb humidity of air, Y_{out}[kg/kg$_{\text{dry air}}$] the humidity at the outlet of the apparatus and Y_{in}[kg/kg$_{\text{dry air}}$] the humidity of the air at the inlet. The wet bulb humidity equals the maximum amount of liquid that can be evaporated at a certain initial temperature T_{in} and initial humidity Y_{in}[kg/kg$_{\text{dry air}}$]. It is calculated via the saturation pressure p_{sat} at the wet bulb temperature T_{wb}. The saturation pressure is calculated with the Antoine equation and the temperature-dependent parameters of A, B and C given in Stull (1947):

$$Y_{wb} = \frac{0.622}{\frac{p}{p_{sat}(T_{wb})} - 1}, \tag{2}$$

$$p_{sat} = 10^5 Pa \cdot 10^{4.6543 - \frac{1435.264}{T - 64.848}}. \tag{3}$$

To eliminate the effort of iterating material and enthalpy balances, a 2D polynomial was fitted to the wet bulb temperatures with the following equation:

$$\mathrm{T_{wb}} = \alpha_0 + \alpha_{01}\mathrm{T} + \alpha_{10}\mathrm{Y} + \alpha_{11}\mathrm{YT} + \alpha_{21}\mathrm{Y}^2\mathrm{T} + \alpha_{12}\mathrm{YT}^2 + \alpha_{22}\mathrm{Y}^2\mathrm{T}^2 + \alpha_{20}^2\mathrm{Y}^2 + \alpha_{02}\mathrm{T}^2, \tag{4}$$

with α_0=-31.7, α_{01}=1.67, α_{10}=12,000, α_{11}-=61.4, α_{21}=797, α_{12}=0.0826, α_{22}=-1.09, α_{20}=-150,000 and α_{02}=-0.00209, resulting in an error of less than 0.2 K for the temperature range of 10 - 90°C and initial moisture contents of 1-40 g/kg$_{\text{dry air}}$. The fit was done for the wet bulb temperature as the 2D polynomial is a better fit for this than for the wet bulb humidity. This can be calculated by inserting $\mathrm{T_{wb}}$ into eq. (2).

Rieck et al. (2015) investigated the influence of the dimensionless drying potential on the layer porosity during coating of non-porous glass particles and porous alumina particles with sodium benzoate. Particle size analysis, micro-CT measurements and scanning electron microscope images were used for the characterization of the layer porosity. The authors determined a linear correlation between the drying potential and the layer porosity for each particle system. A similar study with the same material was performed by Hoffmann et al. (2015). The authors also obtained linear correlations for the two material systems, even though different parameters were postulated than in the study of Rieck et al (2015). The porosities were determined by micro-CT analysis. The differences obtained for different drying potential values were explained by the crystallization process of the sodium benzoate.

Material and methods

All experiments were conducted in the laboratory system ProCell 5 (Glatt GmbH, Germany) with the fluidized bed insert GF 3. The apparatus is operated at under-pressure and fluidized by air. A two-fluid nozzle of type 970-S4 (Schlick, Germany) with an opening diameter of 1.2 mm was installed in bottom-spray configuration.

As core material, nearly monosized microcrystalline cellulose particles (Cellets® 500, Harke Pharma GmbH, Germany) with a mean particle diameter ($d_{p50,3}$) of 639 µm and a particle density ρ_p of 1515 kg/m³ were used. Experiments were performed with 2 kg particles. Sodium benzoate was used as spraying solution. Sodium benzoate is a white, crystalline and odorless solid, which is mainly used as food additive (also known as E211) due to its preservative effects. Spraying solutions were produced by dissolving 30 wt.-% in demineralized water. In each experiment 1 kg of the solution was sprayed onto the bed of Cellets® 500 particles. The following process parameters were varied during the experiments to study their influence on the surface roughness and particle morphology: superficial gas velocity, gas inlet temperature, nozzle pressure, spray rate and temperature of the nozzle air. For each parameter three different values were chosen. The limits of these values were determined in preliminary experiments as those parameters, at which agglomeration phenomena became the dominant mechanism, which should be avoided in this study. As the testing of each and every parameter combination would have resulted in 243 experiments, a design of experiments approach was used to identify meaningful experiments. By applying the central composited response surface design in software Minitab 18 with the lower and upper boundary and the mean value of each parameter, 32 experiments were identified. The different values are listed in Table 1.

At the end of each experiment, the particle size distribution was measured with the CamSizer XT (Retsch Technology, Germany), in which the distribution is calculated from images of the projection areas of the particles. The surface morphology of the produced particles was analyzed with the confocal 3D laser scanning confocal microscope VK-X160K (Keyence GmbH, Germany). The microscope allows 3D measurement on objects with complex geometries with a high resolution and low noise. Four different optical lenses were used allowing magnifications of 10x, 20x, 50x and 100x. With the microscope characteristic roughness values, in particular the arithmetical mean deviation of the surface (Sa), can be determined.

Table 1: Different values of the varied process parameters used for the conducted 32 experiments.

Values no.	Spray rate [g/min]	$\dot{V}_{gas}$ [m^3/h]	Temp. of fluidization gas [°C]	Nozzle pressure [bar]	Temp. of nozzle air [°C]
1	10	80	50	0,5	20
2	20	105	85	1,75	70
3	30	130	120	3,0	120

Results and discussion

Figure 1 shows an overview of the measured surface roughness values at the end of the experiments in dependence on the drying potential. Surface roughness was measured from three particles each at two different positions and from these six values the mean value and the 95% confidence interval have been calculated. Even though variations can be seen for particles having a similar drying potential, a trend is detectable: The higher the drying potential, the smaller is the surface roughness. In contrast to the results published by Hoffmann et al. (2015) and Rieck et al. (2015) no linear dependence of the surface roughness on the drying potential is detectable. Instead, the surface roughness is almost constant in the range between values of 0.6 and 0.82, which is also confirmed by the overlapping confidence intervals indicating that the difference between the surface roughness values of those experiments is not statistically significant. For potentials between 0.3 and 0.6 a small increase of the surface roughness with decreasing drying potential is detectable and the most significant change can be determined for small drying potentials (< 0.3) with the highest Sa values. In addition, it can be seen from Figure 1 that the confidence interval is tendentially larger at higher roughness values. Similar results have also been observed in the study of Diez et al. (2018), who investigated the influence of the drying conditions on the product properties of sodium benzoate particles during continuous fluidized bed spray granulation.

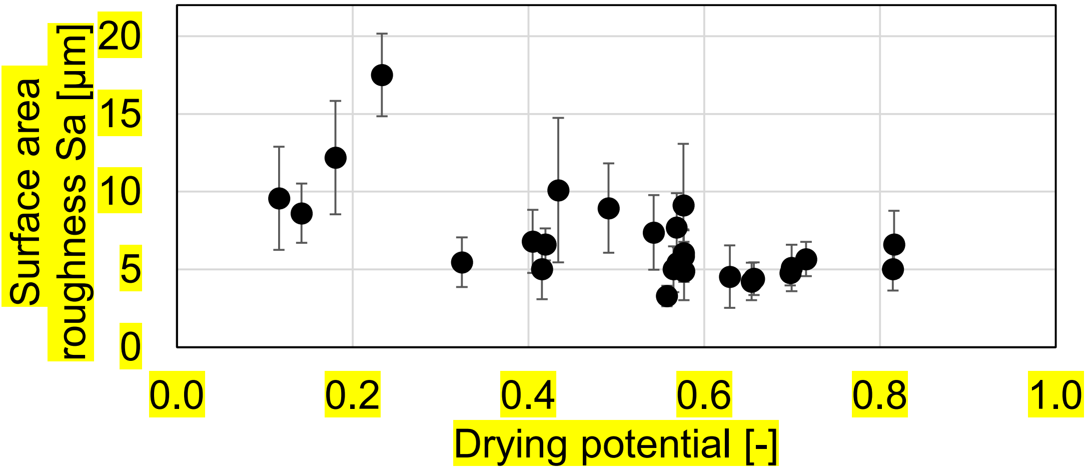

Figure 1: Mean surface area roughness (Sa values) of the final particles; initial roughness of the untreated Cellets 500 particles Sa$_0$ = 3.08.

The smaller surface roughness with increasing drying potential is explained by the crystallization process of sodium benzoate. With a higher drying potential, the water evaporates faster from the droplets, resulting in a faster nucleation of crystals. As the residual water in the droplets is still evaporating quickly, the growth of the crystals is inhibited resulting in a dense and compact layer consisting of small, homogenous salt crystals. In case of a lower drying potential, the evaporation is slower, which allows the formed salt nuclei to grow during the evaporating process resulting in larger crystals, which then result in a more porous and rougher layer.

In Figure 2 the mean particle diameters ($d_{p50,3}$) are shown in dependence on the drying potential. Particle size analysis was performed from a representative sample size of each experiment.

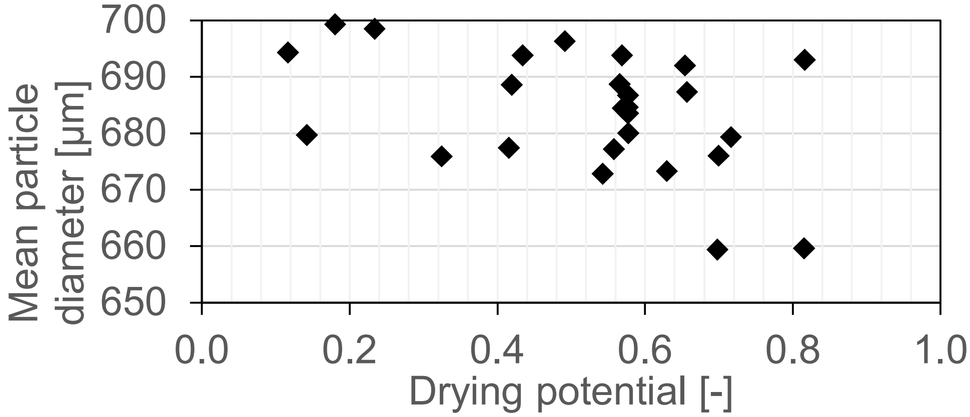

Figure 2: Mean particle diameters ($d_{p50,3}$) of the final particles; initial particle size; $d_{p50,3;0}$= 639 µm.

It can be seen that the particle diameter is smaller the higher the drying potential is. An increased particle size with decreased drying potential was also observed in the experiments by Rieck et al. (2015) and Hoffmann et al. (2015). The size of the particles is not only influenced by the structure of the sodium benzoate layer but also by other effects, as overspray or abrasion. Nevertheless, in none of the performed experiments a high dust formation or the production of a solid layer on the apparatus' walls was determined indicating that these phenomena are not that relevant in this study. As the same mass of coating solution was injected in all experiments, the deviations in final particle size indicate differences in the outer layer structure, which is confirmed by the increased surface roughness with lower drying potential. Images are taken with the confocal 3D laser scanning confocal microscope, as shown in Figure 3 for particles produced in experiments with different drying potentials. Wetter process conditions clearly result in a more inhomogeneous and rougher surface, which is caused by larger crystals. This rough structure comes along with an increased porosity, which then causes a larger layer thickness and thus particle size.

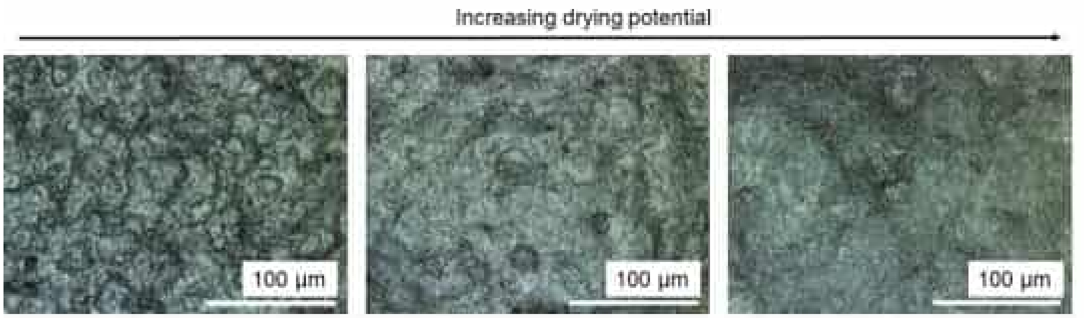

Figure 3: Images from surface characterization with the confocal 3D laser scanning confocal microscope VK-X160K: a) drying potential of 0.14, b) drying potential of 0.66 and c) drying potential of 0.82.

From both the quantitative comparison given in Figure 1 and the qualitative depiction given in Figure 3 it can be seen that the highest variations occur in case of wetter process conditions. For high drying potentials, the deviations are small indicating that starting at a drying potential of about 0.58 the drying rate is fast enough to inhibit further crystal growth. A further increase of the drying rate does not change the resulting surface morphology of the final granules. The investigation of lower drying potentials than 0.12 was not possible as agglomeration occurred during the corresponding preliminary experiments.

The influence of the temperature of the nozzle air has so far not been investigated in detail in literature. In this study, three different temperatures have been investigated as shown in Table 1. The temperature of the nozzle air is not considered in the calculation of the drying potential. The inlet temperature of the fluidization gas has been used for calculating the wet bulb temperature without considering the effect of mixing with the nozzle air as this volume flow rate is low in comparison to the fluidization gas. Nevertheless, the temperature of the nozzle air was observed to have a significant impact on the morphology.

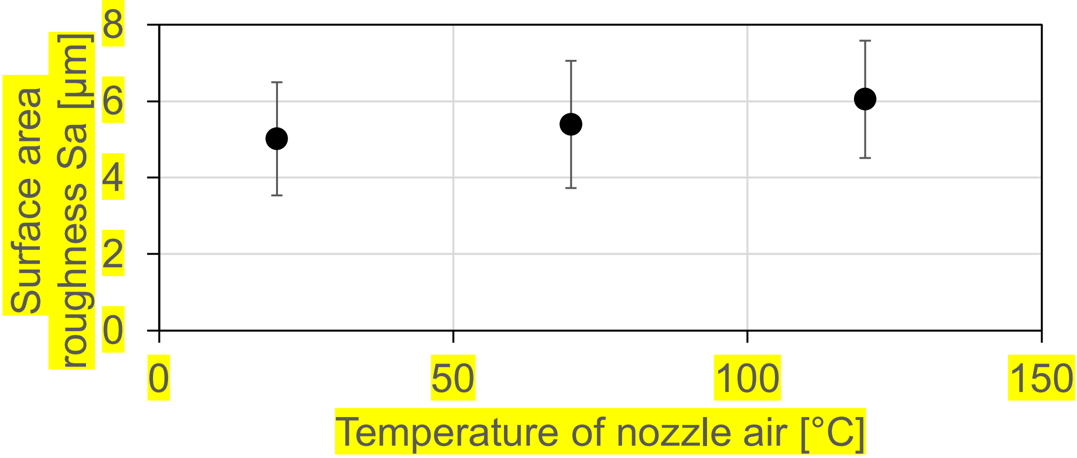

Figure 4: Influence of the temperature of the gas injected into the two-fluid nozzle on the surface roughness of the final particles.

The quantitative variations are small under consideration of the large and overlapping confidence intervals (95%) but a slight increase of the surface roughness with increasing temperature of the nozzle air can be determined. Nevertheless, when having a look onto the images obtained from laser scanning microscope (Figure 5), qualitative differences can be determined: The higher the temperature of the nozzle air, the more irregular is the surface area even though the mean roughness values are almost the same.

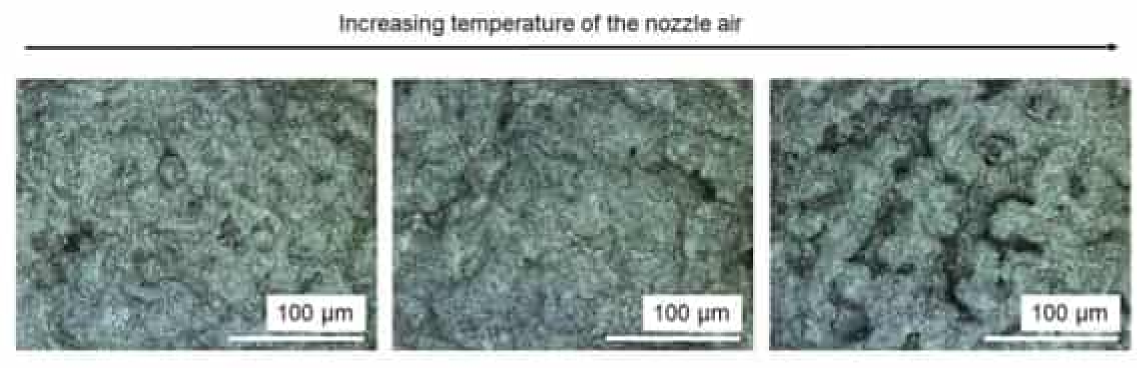

Figure 5: Change of surface roughness with increasing temperature of the air of the two-fluid nozzle.

An increased temperature of the nozzle air results in high temperatures in the area of the nozzle. The resulting local high drying potential allows the sodium benzoate droplets to solidify faster in the nozzle zone. This can cause two special phenomena: On the one hand spray-drying of droplets can occur if they solidify before hitting a particle or on the other hand droplets hitting particles can solidify so fast that a spreading is inhibited resulting in a rough surface. As no distinct dust formation was observed during the experiments, the spray-drying of droplets can be neglected. Nevertheless, during the experiments with the high temperature of the supplied gas for the two-fluid nozzle an increased agglomeration rate was observed, indicating that liquid bridges between colliding particles solidify faster due to the increased temperature in the nozzle area, which then inhibits the rebound of the particles and results in agglomerate formation. Alternatively, the higher viscosity of partially evaporated droplet impacting the surface might encourage sticking rather than rebound.

Conclusions

In this study the influence of five different process parameters during the spray granulation of microcrystalline particles with a sodium benzoate solution in a lab-scale fluidized bed was investigated. It was found that the surface roughness of the product particles is decreasing with increasing drying potential, which is caused by the inhibition of the crystal growth due to faster water evaporation. In addition, the temperature of the nozzle air was found to have an impact on the surface morphology, which could not be detected quantitatively due to the averaging but was found during qualitative analysis.

Notation

d_p	particle diameter, µm	$\dot{V}$	gas volume flow rate, m³/h
p	pressure, Pa	Y_{in}	humidity at inlet, $kg/kg_{dry\ air}$
p_{sat}	saturation pressure, Pa	Y_{out}	humidity at outlet, $kg/kg_{dry\ air}$
Sa	arithmetic mean deviation of surface roughness	Y_{wb}	wet bulb, $kg/kg_{dry\ air}$
		α	fitting parameter, -
T	temperature, K	η	dimensionless drying potential, -
T_{wb}	wet bulb temperature, K	ρ_p	particle density, kg/m³

References

E. Diez; K. Meyer; A. Bück; E. Tsotsas; S. Heinrich (2018): Influence of process conditions on the product properties in a continuous fluidized bed spray granulation process. In Chemical Engineering Research and Design 139, pp. 104–115.

Hoffmann, Torsten; Rieck, Christian; Bück, Andreas; Peglow, Mirko; Tsotsas, Evangelos (2015): Influence of Granule Porosity during Fluidized Bed Spray Granulation. In Procedia Engineering 102, pp. 458–467.

Mörl, Lothar; Heinrich, Stefan; Peglow, Mirko (2007): Chapter 2 Fluidized bed spray granulation. In A.D. Salman, M.J. Hounslow, J.P.K. Seville (Eds.): Granulation, vol. 11: Elsevier Science B.V (Handbook of Powder Technology), pp. 21–188.

Rieck, C.; Hoffmann, T.; Bück, A.; Peglow, M.; Tsotsas, E. (2015): Influence of drying conditions on layer porosity in fluidized bed spray granulation. In Powder Technology 272, pp. 120–131.

Stull, Daniel R. (1947): Vapor pressure of pure substances. organic and inorganic compounds. In Industrial & Engineering Chemistry 39 (4), pp. 517–540.

MAXIMIZING HEAT TRANSFER FOR ENERGY STORAGE APPLICATION – DESIGN OF A CONTINUOUS FLUIDIZED BED COLD MODEL

Elija Talebi[1*], Manuel Würth[1], Lukas Winklbauer[1], Stephan Gleis[1], Annelies Vandersickel[1], Hartmut Spliethoff[1]

[1]*Chair of Energy Systems, Technical University of Munich, Boltzmannstr. 15, 85748 Garching, Germany*
*Email: *elija.talebi@tum.de*

Abstract

The current research on energy storage systems at the Chair of Energy Systems focusses on the development of a large-scale concept for a continuous fluidized bed reactor. Heat transfer between the fluidized bed and immersed heat exchangers has been previously determined to be the predominant factor for the storage power. An important objective of the current research is to maximize the heat transfer by (1) characterizing the heat transfer coefficient and (2) maximizing the available heat exchanger area in a continuously operating fluidized bed reactor. Therefore a cold fluidized bed model is currently being commissioned to evaluate different heat exchanger geometries and their influence on the degree of fluidization and consequently on the heat transfer coefficient. The main focus herein is to evaluate entire tube bundles. The fluidized bed cold model has a bed volume of 80 L, divided into 4 sections separated by baffles to optimize the residence time. $Ca(OH)_2$-particles with a diameter of 250 to 400 µm are fluidized using dry air with temperatures up to 50 °C. The design of the cold model is modular, allowing for the investigation of different heat exchanger configurations. The measurement of the heat transfer coefficient is conducted with several overall-perimeter heat transfer probes at various positions in the tube bundles. The heat exchangers are tube bundles immersed either horizontally or vertically in the fluidized bed. Aspects of interest are upsides of staggered or aligned configurations, the influence of the clearing distance between the tubes, tube diameters and potentially occurring particle deposition on the tubes. Initial experiments in the fluidized bed cold model focus on (1) characterization of the overall heat transfer coefficient of the entire tube bundle and (2) optimization of the heat exchanger area while maintaining a sufficient degree of fluidization. The long-term goal is to establish correlations for reactor scale-up.

Introduction

In recent years, the increasing share of volatile renewable energy sources in today's energy markets has led to a growing demand for energy storage systems to provide the necessary flexibility (Buttler et al. 2015). Besides the development of large-scale electrical energy storage systems, research has also focused on the storage of heat in either sensible, latent or thermochemical heat storage (TCES) systems (Gibb et al. 2018). The latter has gained attention in current research due to generally high energy densities of the materials and theoretically unlimited storage times (Pardo et al. 2014). The calcium oxide hydration/dehydration is proposed as a promising reaction couple for the storage of thermochemical heat in industrial heat and power plant applications. The discharging/charging reaction given in eq. (1) is exploited at temperatures of 400-600 °C. For this storage system, the Chair of Energy Systems is developing a fluidized bed reactor (Würth 2018).

$$CaO_{(s)} + H_2O_{(g)} \rightleftharpoons Ca(OH)_{2(s)} + \Delta H_R \tag{1}$$

Calcium oxide as well as hydroxide are abundant, cheap and non-toxic. During the discharging step, calcium oxide is combined with steam, resulting in a rapid and highly exothermic reaction.

For the charging step, heating the hydroxide leads to the reverse reaction - the decomposition into calcium oxide and steam. After separation of the particles from excess steam and particle cooling, the charged as well as the discharged material can be stored in dry atmosphere for theoretically unlimited time at ambient conditions. Angerer et al. (2018) indicate that a TCES system based on the $CaO/Ca(OH)_2$ reaction couple can only be economically viable if the reactor is operated continuously. This allows a decoupling of storage capacity and power, which has a strong influence on the reactor size.

The use of a fluidized bed reactor is favorable due to its features of relatively simple transport of solid particles and typically high heat and mass transfer rates. However, reactor modelling – combined with preliminary experimental investigations of the material in a batch fluidized bed reactor as well as a fluidization test rig containing a heat flux probe – has shown that the heat transfer between the fluidized bed and reactor internals, i.e. tube bundles, predominantly defines the storage power (Angerer et al. 2018; Becker et al. 2018).

State of Research

Heat transfer in fluidized beds has been extensively studied over the last decades. Research can be distinguished into experiments with either single tubes immersed in fluidized beds (Chandran et al. 1980; Di Natale et al. 2010; Grewal und Saxena 1980; Ostermeier et al. 2018) or entire tube bundles with various configurations (Chandran et al. 1980; Kim et al. 2003; Zabrodsky et al. 1981). In general, no globally applicable correlation for the heat transfer coefficient can be proposed, since the heat transfer from a fluidized bed to immersed tubes or tube bundles is strongly dependent on various parameters such as the solid material, particle size, tube bundle configuration and general vessel geometry. For single horizontal immersed tubes, general statements could be derived. Higher values of the heat transfer coefficient have been observed at the sides of the tube than at the bottom and top positions of the tube. The maximum values for the heat transfer coefficient seem to shift to the top position for higher superficial gas velocities as this increases the turbulent behavior of the bed and leads to a more uniform distribution of the coefficient around the tube (Chandran et al. 1980; Olsson et al. 1995; Ostermeier et al. 2017).

Contrary to the findings for single tubes, the results for immersed horizontal tube bundles differ a lot more. Ostermeier et al. (2017) and Zabrodsky et al. (1981) have compared in-line and staggered tube bundle configurations. Zabrodsky et al. (1981) reported the effect of solids bridging between tubes in in-line bundles for intermediate superficial gas velocities, which led to a decrease of the heat transfer coefficient. Following Davidson (1985), the staggered configuration is considered to be favorable for the application in fluidized beds. Ostermeier et al. (2017) investigated tube bundle configurations with a previously verified simulation and found no significant difference for the overall heat flux of the in-line and the staggered configuration. The results of Chandran et al. (1980) and Ostermeier et al. (2017) both show that the heat transfer coefficients for tubes inside a bundle differ, depending on their position.

Olsson et al. (1995) and Kim et al. (2003) studied the effects of an immersed tube bundle on the hydrodynamic behavior of a fluidized bed. Olsson et al. (1995) studied the bubble characteristics with in-line as well as two different staggered tube bundle configurations. The results showed that immersed bundles strongly influence the bubble behavior in fluidized beds and may lead to a more turbulent behavior. Kim et al. (2003) correlated the bubble characteristics with the local heat transfer coefficients around a single tube in a tube bundle. The results are in good agreement with the previous findings for single tubes as the highest coefficients were observed at the sides of the tubes.

Becker (2021) studied the fluidizability and practical applicability of various $CaO/Ca(OH)_2$ particle sizes in a cold fluidized bed test rig as well as in a lab scale fluidized bed reactor. The results indicate a decrease in mechanical stability of the particles with increasing storage cycles, ultimately leading to particle-break up and decreasing particle sizes. Preliminary investigation of the heat transfer coefficient between a single tube and $Ca(OH)_2$ with a heat transfer probe has shown that the prediction of α_{max} with the widely applied correlation eq. (2)

by Zabrodsky (Zabrodsky et al. 1976) is satisfactory (Becker 2021). In eq. (2), ρ_p, k_g and d_s denote the particle density, the thermal conductivity of the fluid and the Sauter mean diameter, respectively.

$$\alpha_{max} = 35.8 \cdot \rho_p^{0.2} \cdot k_g^{0.6} \cdot d_s^{-0.36} \tag{2}$$

Application of eq. (2) to the data on particles obtained from TCES cycles (Becker 2021) yields the predicted maximum heat transfer coefficients depending on the number of storage cycles in tab. (1). CaO is used as initial material and an entire storage cycle is composed of a hydration with a subsequent dehydration. Hence the notation X.5 and X.0 for $Ca(OH)_2$ and CaO, respectively. A fluidized bed reactor has been used for all storage cycles, however, the setup for the first material in tab. (1) (Cycles 0.5 (I)) is different, resulting in a higher content of fines which ultimately increases α_{max}. The respective material was fluidized with nitrogen at $25\ °C$ at ambient pressure in the fluidized bed test rig, resulting in elutriation and thus the α_{max} calculated for cycle 0.5 (II). As Becker (2021) shows, the fluidized bed has most likely partly or entirely collapsed for the material with 20.5 storage cycles as it has reached Geldart C properties and is strongly cohesive. Eq. (2) is therefore technically not suitable to predict α_{max} as it is most likely to be an overprediction if fluidization is present at all.

Table 1. Max. heat transfer coefficients calculated for data reported by Becker (2021). FBR – fluidized bed reactor, TR – test rig.

Material	Setup	Cycles	d_s in μm	α_{max} in $Wm^{-2}K^{-1}$
$Ca(OH)_2$	FBR	0.5 (I)	263.4	364.3
$Ca(OH)_2$	FBR+TR	0.5 (II)	392.7	311.3
$Ca(OH)_2$	FBR	0.5	385.0	314.3
CaO	FBR	1.0	379.4	306.2
$Ca(OH)_2$	FBR	5.5	381.4	316.8
$Ca(OH)_2$	FBR	10.5	307.5	341.6
$Ca(OH)_2$	FBR	20.5	21.3	893.9

So far, little research has been done on the characterization of heat transfer coefficients between TCES material and immersed heat exchanger surfaces. Due to the occurrence of particle breakage and the resulting increase of the heat transfer coefficient, a dependency of α_{max} on the number of storage cycles is apparent. Considering a significant difference of reaction temperature between hydration and dehydration reaction, it becomes apparent that a TCES reactor has to cover a wide range of appearing heat transfer rates and conditions. Especially if heat transfer is limiting the storage performance, this poses a challenge to reactor design and operation. Until steady storage material is available, however, it is crucial to investigate heat transfer coefficients in a small-scale geometry for a range of possible particle sizes and distributions. Research at the TUM therefore focusses on (1) the detailed characterization of the heat transfer coefficient for cycled storage material as well as (2) the optimization of the active heat transfer surface with respect to (de-)fluidization effects.

Design of the Experimental Setup

The experimental setup consists of a fluidized bed vessel with a rectangular base (shown in fig. 1). The design resembles that of a multi-cell bubbling fluidized bed, which is commonly used in fluidized bed driers. It can be operated in batch as well as continuous mode. The bed is 0.2 m wide and 1.0 m long. The vessel is designed to hold a fluidized bed with up to 0.4 m height. The fluidized bed consists of 4 distinctive sections in longitudinal direction. Each section has a length of 0.25 m. The sections are separated by baffles with the purpose of guiding the flow in continuous operation and optimizing the solids residence time distribution. The vessel walls have acrylic glass windows, which can hold horizontally immersed tube

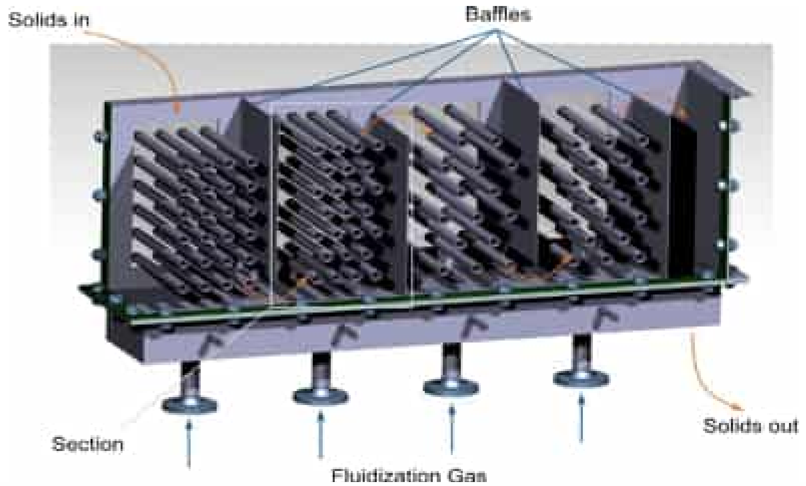

Fig. 1. CAD-model of the fluidized bed vessel with tube bundles (freeboard and filter section not shown).

bundles or provide the possibility of visual observation. The gas distributor is a tuyere nozzle type designed by SCHWING Technologies GmbH. Each section is equipped with a separate wind box with the purpose of being able to control the gas flow and thus the bed height for each section separately. This option allows to impose a pressure difference between solid inlet and outlet over the entirety of the fluidized bed. As a result, an additional flow control mechanism is created. In batch operation mode, each section can be considered as a separate fluidized bed, allowing for the investigation of 4 different tube bundle configurations at once or have one free as a “reference” state.

For the solids used in the test rig, calcium hydroxide from low temperature calcination and subsequent hydration of calcium carbonate with three different particle size fractions is available. The fractions are 100-250 µm, 250-400 µm and 400-800 µm. The smallest particle size fraction is expected to achieve the highest heat transfer, but for initial experiments, the particle size fraction of 250-400 µm will be used since it is easier to obtain high quality fluidization. The particles are fluidized by dry air heated up to 50 °C. To ensure steady-state operation, the heating control relies on individual temperature measurements located in each wind box.

For the first 4 tube bundle configurations, 2 are used to recreate the conditions described by Ostermeier et al. (2017). Contrary to those, stainless steel pipes with an outer pipe diameter d_R of 21.3 mm are used. The ratio of the horizontal as well as the vertical pitch and the tube diameter, h_h/d_R and h_v/d_R, were kept equal to those of Ostermeier et al. (2017) for the in-line as well as the staggered configuration. The remaining 2 bundles are chosen based on the recommendations from Davidson (1985) which were also used as basis for Kim et al. (2003). The equilateral staggered configuration is commonly used for all types of tube bundles in industrial applications. As the second of those two configurations, the Rivesville layout is chosen as a high surface tube bundle. The resulting horizontal and vertical tube pitches for all bundles are given in tab. 2.

Above the fluidized bed, the vessel holds a freeboard region with ports for temperature as well as pressure measurements, vertical tube bundle mounts and supply ports, solids feed and extraction ports. A filter system is mounted in the top section of the freeboard. The test rig is provided with a blow back filter system, so that continuous operation is possible without any pressure effects from filter blocking due to particle attrition.

Measurement of local heat transfer coefficients between the fluidized bed and immersed single tubes within a bundle are carried out with power adjustable overall-perimeter heat transfer probes, shown in fig. 2. The design is adapted from Ostermeier et al. (2018) and Di Natale et al. (2010). The instantaneous local heat transfer coefficient is calculated from eq. (3) with S_{HP}

being the contact surface of the copper cylinder to the fluidized bed. Temperatures are measured by high precision resistance thermometers (Pt100).

Table 2. Tube diameter and pitch of the tube bundles.

	d_R in mm	h_h in mm	h_v in mm
(Ostermeier et al. 2017) in-line	21.3	42.6	53.3
(Ostermeier et al. 2017) staggered	21.3	37.9	47.3
(Davidson 1985) equilateral	21.3	63.9	55.3
(Davidson 1985) Rivesville	21.3	63.9	42.6

$$\alpha = \frac{U_{HC} I_{HC}}{S_{HP} \cdot (T_{HP} - T_{FB})} \tag{3}$$

The outer diameter of the heat transfer probe equals the tubes diameter of 21.3 mm to allow for measurements at every position in the tube bundle. During operation, three probes are used simultaneously in each bundle at different positions.

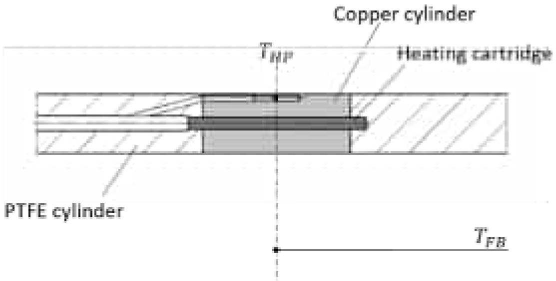

Fig. 2. Schematic illustration of the heat transfer probe design used in the continuous fluidized bed test rig.

Outlook

Within the next months, the commissioning of the test rig will be completed. First investigations will be in batch mode to compare first tube bundle configurations and validate the predicted heat transfer coefficients presented in tab. 1 for cycled storage materials. With the results obtained from these preliminary experiments, the existing heat transfer models will be validated and used for optimization of tube diameter and pitch. The next step is to investigate the optimized bundles in batch as well as continuous operation. In further steps, process parameters have to be optimized for maximum heat transfer. The main focus is to derive correlations for future scale-up of the process to a large-scale thermochemical energy storage system.

Acknowledgement

This research is part of the project “Thermochemische Energiespeicher im Wirbelschichtverfahren für Industrieanwendungen und Stromerzeugung” and is funded by the German Federal Ministry of Economic Affairs and Energy (BMWi) under the funding code 03ET1599A.

Notation

α	heat transfer coefficient, W/m^2K	d_s	Sauter mean diameter, μm
d_R	tube diameter, mm	h_h	horizontal pitch, mm

h_v	vertical pitch, mm
I_{HC}	heating cartridge current, A
k_g	thermal conductivity of fluid, W/mK
ρ_p	particle density, kg/m^3
S_{HP}	heat transfer probe surface, m^2
T_{HP}	heat transfer probe temperature, $°C$
T_{FB}	fluidized bed temperature, $°C$
U_{HC}	heating cartridge voltage, V

References

Angerer, M.; Becker, M.; Härzschel, S.; Kröper, K.; Gleis, S.; Vandersickel, A.; Spliethoff, H. Design of a MW-scale thermo-chemical energy storage reactor. Energy Reports 4. 2018. 507–519.

Becker, M.. 2021. Thermochemische Energiespeicherung mit Calcium-Oxid und -Hydroxid: Entwicklung eines Reaktorkonzeptes. Dissertation. Technische Universität München, München. Fakultät für Maschinenwesen. - IN PRINT

Becker, M.; Würth, M.; Angerer, M.; Härzschel, S.; Gleis, S.; Vandersickel, A.; Spliethoff, H. Thermochemical Energy Storage with CaO/Ca(OH)2. Development of a Continuous Fluidized Bed Reactor. IRES. Düsseldorf. 2018.

Buttler, A.; Hentschel, J.; Kahlert, S.; Angerer, M. Statusbericht Flexibilitätsbedarf im Stromsektor. 2015. TUM; Lehrstuhl für Energiesysteme.

Chandran, R.; Chen, J. C.; Staub, F. W. Local Heat Transfer Coefficients around Horizontal Tubes in Fluidized Beds. Journal of Heat Transfer 102 (1). 1980. 152–157.

Davidson, John Frank. Fluidization. 2. ed. Acad. Press. London. 1985.

Di Natale, F.; Bareschino, P.; Nigro, R. Heat transfer and void fraction profiles around a horizontal cylinder immersed in a bubbling fluidised bed. International Journal of Heat and Mass Transfer 53 (17-18). 2010. 3525–3532.

Gibb, D.; Seitz, A.; Johnson, M.; Romani, J.; Gasia, J.; Cabeza, L.; Gurtner, R. Applications of Thermal Energy Storage in the Energy Transition - Benchmarks and Developments. German Aerospace Center (DLR). 2018. IEA-ECES.

Grewal, N. S.; Saxena, S. C. Heat transfer between a horizontal tube and a gas-solid fluidized bed. International Journal of Heat and Mass Transfer 23 (11). 1980. 1505–1519.

Kim, S. W.; Ahn, J. Y.; Kim, S. D.; Hyun Lee, D. Heat transfer and bubble characteristics in a fluidized bed with immersed horizontal tube bundle. International Journal of Heat and Mass Transfer 46 (3). 2003. 399–409.

Olsson, S. E.; Wiman, J.; Almstedt, A. E. Hydrodynamics of a pressurized fluidized bed with horizontal tubes: Influence of pressure, fluidization velocity and tube-bank geometry. Chemical Engineering Science 50 (4). 1995. 581–592.

Ostermeier, P.; Dawo, F.; Vandersickel, A.; Gleis, S.; Spliethoff, H. Numerical calculation of wall-to-bed heat transfer coefficients in Geldart B bubbling fluidized beds with immersed horizontal tubes. Powder Technology 333. 2018. 193–208.

Ostermeier, P.; Vandersickel, A.; Gleis, S.; Spliethoff, H. Wärmeübergang in Gas-Feststoff Wirbelschichten: Simulation, Validierung, Anwendung. CADFEM ANSYS SIMULATION CONFERENCE. 2017.

Pardo, P.; Anxionnaz-Minvielle, Z.; Rougé, S.; Cognet, P.; Cabassud, M. Ca(OH) 2 /CaO reversible reaction in a fluidized bed reactor for thermochemical heat storage. Solar Energy 107. 2014. 605–616.

Würth, M. Development of a Continuous Fluidized Bed Reactor for Thermochemical Energy Storage Application. 2018 Clearwater Clean Energy Conference.

Zabrodsky, S. S.; Antonishin, N. V.; Parnas, A. L. On fluidized bed-to-surface heat transfer. Can. J. Chem. Eng. 54 (1-2). 1976. 52–58.

Zabrodsky, S. S.; Epanov, Y.G.; Galershtein, D. M.; Saxena, S. C.; Kolar, A. K. Heat transfer in a large-particle fluidized bed with immersed in-line and staggered bundles of horizontal smooth tubes. International Journal of Heat and Mass Transfer 24 (4). 1981. 571–579.

GAS-SOLID CONVECTION HEAT TRANSFER OF PARTICLE FROM MOVING-BED DURING HEAT RECOVERY FROM CENTRIFUGAL GRANULATION OF FURNACE SLAG

Zhiqiang Wu[1*], Chen Ma[1], Zhaoyu Xiao[2], Meiquan Li[2], Jun Zhao[2], Liwei Ma[2] and Shuzhong Wang [2]

[1] Shaanxi Key Laboratory of Energy Chemical Process Intensification, School of Chemical Engineering and Technology, Xi'an Jiaotong University, Xi'an, Shaanxi, 710049, P.R. China

[2] Key Laboratory of Thermo-Fluid Science & Engineering, Ministry of Education, School of Energy and Power Engineering, Xi'an Jiaotong University, Xi'an, Shaanxi Province 710049, P.R. China

*Email: *zhiqiang-wu@xjtu.edu.cn*

Abstract

In this paper, the gas-solid heat transfer characteristics of high-temperature slag particle in the moving-bed were studied. The cooling behavior of slag particle in the gas-solid heat transfer process in the moving bed was investigated. The key factor, such as the influence of initial temperature of the particle and airflow rate on the temperature distribution and gas-solid convection in the bed was obtained. When the particle inlet temperature raised from 166 °C to 335 °C, the average cooling rate of the particle increases from 0.6 $°C \cdot s^{-1}$ to 1.4 $°C \cdot s^{-1}$.When the air inlet velocity increased from 0.4 $m \cdot s^{-1}$ to 0.7 $m \cdot s^{-1}$, the average temperature of the layer decreased from 190.8 °C to 147.4 °C, and the average convective heat transfer coefficient of the layer increased from 40.46 $W \cdot m^{-2} \cdot K^{-1}$ to 70.81 $W \cdot m^{-2} \cdot K^{-1}$. The increasing of the inlet air velocity did not significantly enhance the heat transfer, but greatly increased the system energy consumption.

Introduction

Metallurgical industry is an important industrial raw material production department, which provides various metal materials for the national economy(Chen et al., 2017). At the same time, the metallurgical industry is also a high-carbon energy-intensive industry, which consumes large amounts of energy. China's metallurgical industry consumed about 868 million tons of standard coal in 2014, accounting for 20.40% of the total annual energy consumption(Sun & Zhang, 2016). The metallurgical industry has also shifted its reform focus to reducing consumption, reducing costs, increasing varieties, and increasing production. In terms of quality and environmental protection, efficient treatment of high-temperature slag and efficient recovery and utilization of waste heat are an essential energy issue(Wu et al., 2019a; Wu et al., 2019c; Zhang et al., 2013). Compared with the traditional water quenching method, the dry treatment method not only saves many water resources but also recovers the heat contained in the blast furnace slag, as shown in Fig. 1(Wu et al., 2019b).

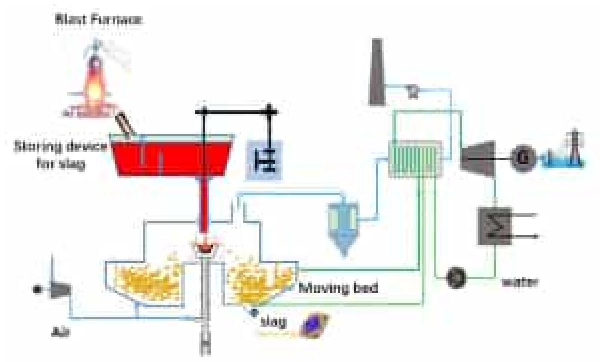

Fig. 1. Flow chart of dry centrifugal granulation and waste heat recovery and utilization system.

Table 1 and Table *2* illustrate the water quenching method and dry method for the treatment of furnace slag(Lin et al., 2016; Wang et al., 2016). Different forms of heat exchange devices were applied to recover the residual heat from the granulated particle, such as fixed bed, fluidized bed, and moving bed. The challenges of using a fixed bed to recover waste heat from slag particle were as follows: 1) continuous discharge of slag particle could not be achieved, 2) only be used as a replacement solution for laboratory-scale moving bed, 3) could not be combined with centrifugal granulation module. Using a fluidized bed to recover the residual heat of the slag could achieve rapid cooling of the particle and prevention of remelting of the semi-molten slag particle. However, it still faced the challenges as follows: 1) good sphericity of slag particle via centrifugal granulation resulting in high critical fluidization velocity and excessive power consumption of fan, 2) high dust content of the hot air would increase the dust removal cost, 3) particle blending was severe, and the hot air temperature was low.

Table 1. Comparison of technical indicators of water quenching method

Processing method	Power consumption (k·Wh/t)	Water consumption (Slag/Water)	Slag moisture content%	Area covered	Investment	Application Situation
INBA	5	1:(6-8)	15	Medium	Maximum	Many
TYNA	2.5	1:8	8-10	Medium	Large	Large
RASA	15~16	1:(10-15)	15-20	Large	Large	Few

Table 2. Comparison of technical indicators of dry method

Processing method	Processing capacity (t/h)	Shape and particle size (mm)	Cooling rate	Heat transfer medium	Vitrification rate and its application	Heat recovery rate (%)
Drum granulation	/	Slices, 2-3 mm thick	Quench	Organic liquid	95,cement	40
Mechanical agitation	30	About 20	Slow cooling	Water	Concrete aggregate	43
Air quenching	100	95%<5	Quench	Air	>95,cement	63
Dry centrifugal granulation	6	Average 2	Quench	Water and air	>95,cement	75

Compared with fixed bed and fluidized bed, using moving-bed to recover the waste heat have some advantages. It could effectively avoid the problem of slag particle mixing. Countercurrent heat exchange between slag and air could significantly improve the heat recovery efficiency and the thermal energy quality of the hot air; It also could effectively solve the uneven cooling of the particle and the power consumption of the fan.

In this paper, according to the unsteady gas-solid heat transfer characteristics of high-temperature slag particle, the cooling behavior of particle during heat transfer was studied by constructing experimental equipment, and the gas-solid heat transfer mechanism was revealed. The effects of air velocity, the initial temperature of the slag particle on the gas-solid convection heat transfer coefficient, and slag particle cooling rate were obtained.

Experimental

Fig. 1. Shows the schematic diagram of the moving bed heat exchanger, including slag particle heating device, the heat exchanger of moving bed, and discharge device. Particle with diameters of 2-4mm and a density of 2700 kg/m^3 were heated to about 335 °C. Detailed information about the experimental procedure was described in previous research (Ma, 2019).

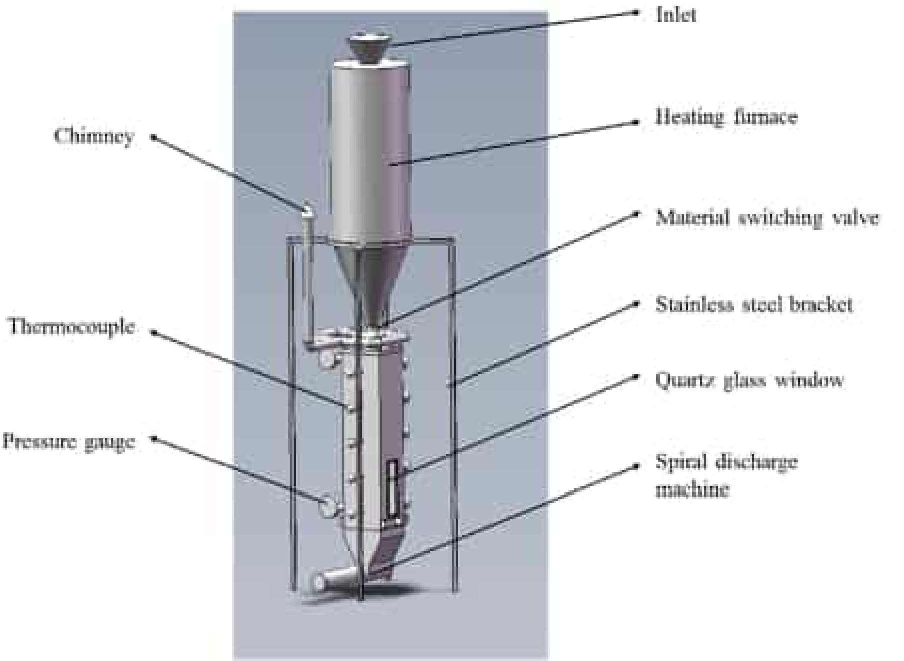

Fig. 2. Schematic diagram of the experimental equipment.

Results and Discussion

Influence of initial temperature of the particle

It can be seen from Fig. 3 that at the same layer height, as the inlet temperature of the particle increases, the temperature of the particle decreases. When the inlet temperature of the particle was 335 °C, the maximum temperature drop rate of the particle was 1.74 °C·s^{-1}; when the inlet temperature of the particle was 256 °C, the maximum temperature drop rate of the particle was 1.49 °C·s^{-1}; When the inlet temperature of the particle is 194 °C, the maximum temperature drop rate of the particle is 1.18 °C·s^{-1}. At the same initial temperature of the particle, the cooling rate of the particle decreased with increasing of the layer, and the cooling rate of particle increased more slowly. At the same level of the material, as the inlet temperature of the particle increased, the temperature of the out air increased, and the inlet parameters of the air do not change, resulting in an increase in the temperature difference between the particle and the air, eventually leading to the change of the particle in unit time. The increase in heat was manifested by an increase in the rate of the temperature drop of the particle. Fig. 3 (b) illustrates that the outlet temperature of the air increased with the height of bed.

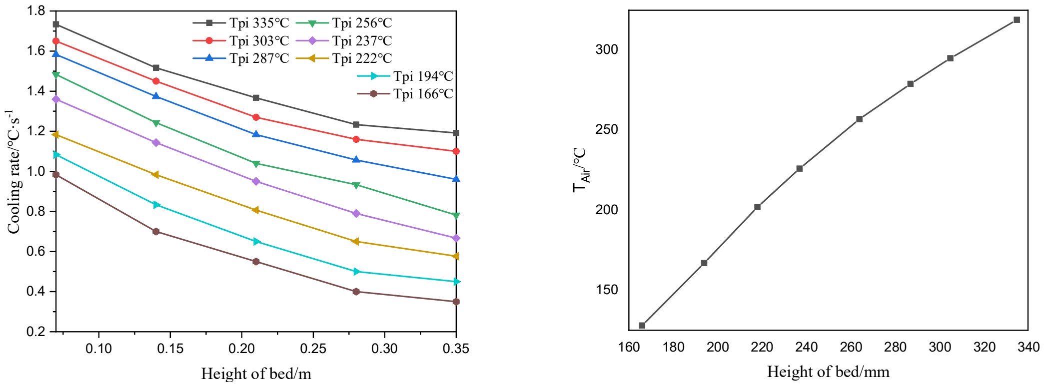

(a) The cooling rate of the particle in the bed

(b) The outlet temperature of the air

Fig. 3. Influence of initial temperature of particle.

Influence of airflow rate

Fig. 4 shows that as the inlet airflow rate in the moving bed increased, the average cooling rate of the particle increased, and the particle cooling rate also increased at the same layer height. At the same air flow rate, the cooling rate of the particle decreased with the increasing of the layer height. In the low-temperature section, under different air flow rate conditions, the cooling rate of the particle became closer. In addition to the gas-solid convection heat transfer coefficient, the particle cooling rate was closely related to the temperature difference. As the height of the layer increased, the heat exchange between the particle and the air was more sufficient, and the temperature difference between the air and the particle was gradually reduced.

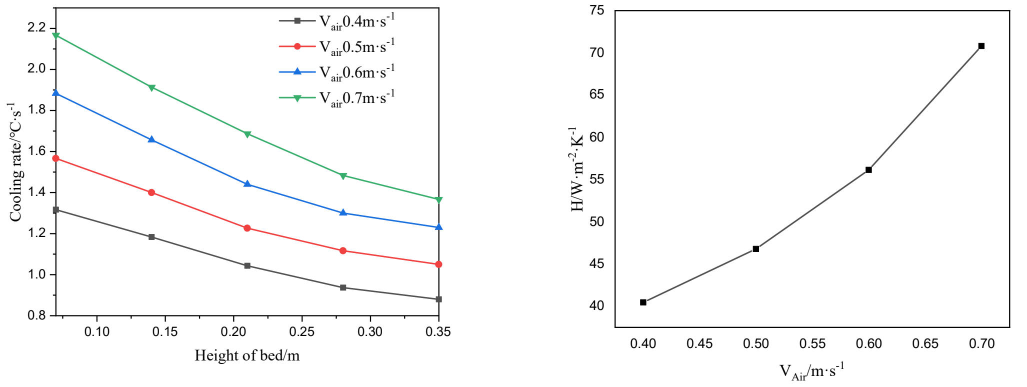

(a) The cooling rate of particle in the bed

(b) Convective heat transfer coefficient

Fig. 4. Influence of the airflow rate.

Conclusion

The air inlet velocity increased from 0.4 m·s^{-1} to 0.7 m·s^{-1}, the average temperature of the layer decreased from 190.8 °C to 147.4 °C, and the average convective heat transfer coefficient of the layer was increased from 40.46 W·m^{-2}·K^{-1} to 70.81 W·m^{-2}·K^{-1}. The increase in the inlet air velocity of the air did not significantly enhance the heat transfer, but greatly increased the system energy consumption. It was conceivable to provide a buried pipe in the upper part of the hood, and the integrated pipe inlet and outlet water are integrated with the membrane water wall of the moving bed to realize efficient waste heat recovery under low system energy consumption. This paper is helpful in understanding the gas-solid heat transfer mechanism of the particle group in the moving bed and provides a basis for the subsequent development of large-scale equipment and optimization of operating parameters.

Acknowledgment

This work was supported by the National Key R&D Program of China (Grant No: 2017YFB0603603).

References

Chen, L.G., Shen, X., Xia, S.J., Sun, F.R. 2017. Thermodynamic analyses for recovering residual heat of high-temperature basic oxygen gas (BOG) by the methane reforming with carbon dioxide reaction. *Energy*, **118**, 906-913.

Lin, B., Wang, H., Zhu, X., Liao, Q., Ding, B. 2016. Crystallization properties of molten blast furnace slag at different cooling rates. *Applied Thermal Engineering*, **96**, 432-440.

Ma, L. 2019. Study on High Efficiency Heat Transfer Technology of Slag Particle in Moving Bed. in: *Xi'an Jiaotong University*, Vol. Master, Xi'an Jiaotong University. Xi'an.

Sun, Y.Q., Zhang, Z.T. 2016. Heat Recovery from High Temperature Slags: Chemical Methods. *Energy Technology 2016: Carbon Dioxide Management and Other Technologies*, 41-48.

Wang, H., Wu, J.J., Zhu, X., Liao, Q., Zhao, L. 2016. Energy-environment-economy evaluations of commercial scale systems for blast furnace slag treatment: Dry slag granulation vs. water quenching. *Applied Energy*, **171**, 314-324.

Wu, Z., Li, Y., Zhao, J., Ma, L., Zhang, X., Meng, H., Xu, D. 2019a. Thermal effect and kinetic analysis on co-pyrolysis of furnace slag with cellulose from biomass. *Energy Procedia*, **158**, 440-445.

Wu, Z., Ma, C., Xiao, Z., Li, M., Ma, L., Zhang, X., Zhao, J., Wang, S. 2019b. Heat transfer characteristics of moving bed during energy saving from dry centrifugal granulation of furnace slag. in: *1st International Symposium on Thermal-Fluid Dynamics (ISTFD 2019)*. Xi'an, China,.

Wu, Z., Ma, C., Zhang, B., Zhao, J., Xiao, Z., Li, M., Meng, H., Xu, D., Wang, S. 2019c. Energy Recovery of Furnace Slag from Steel Industrial and Thermochemical Conversion of Lignocellulosic Biomass: Thermal Behavior and Kinetic Analysis on Cellulose under Fast Pyrolysis Conditions. *Energy & Fuels*.

Zhang, H., Wang, H., Zhu, X., Qiu, Y.J., Li, K., Chen, R., Liao, Q. 2013. A review of waste heat recovery technologies towards molten slag in steel industry. *Applied Energy*, **112**, 956-966.

SAFETY EVALUATION OF THE IMMERSED TUBE IN AN EXTERNAL HEAT EXCHANGER OF A CIRCULATING FLUIDIZED BED BOILER IN CASE OF ELECTRICITY SUPPLY FAILURE

Ling Jiang, Yuge Yao, Boyu Deng, Hairui Yang, Junfu Lyu, Man Zhang*
Key Laboratory for Thermal Science and Power Engineering of Ministry of Education,
Department of Energy and Power Engineering, Tsinghua University, Beijing 100084, China

*Email: *zhangman@tsinghua.edu.cn*

Abstract

External heat exchanger (EHE) is one of the key components of a circulating fluidized bed (CFB) boiler. Generally, the superheater and reheater tubes are arranged in the EHE for the excellent performance of the CFB boiler. In case of the electricity supply failure occurs, the fluidized air of the EHE shuts down quickly causing defluidization of the high temperature bed material in the EHE so that the tubes are immersed and the heat transfer from the bed particle is very strong. Meanwhile the steam flow rate is reduced which weakens the heating tubes cooling. The safety of the immersed tube is a concern problem.

In this paper, the safety of the immersed tube in an EHE of a CFB boiler in case of electricity supply failure is investigated. Firstly, the thermal conductivity of the bed material in the EHE is measured by transient hot wire method. It is found that it is the function of temperature as well as its chemical composition. Then the heat transfer of the tube from the bed is modeled and simulated by the ANSYS, from which the tube temperature is predicted. Finally, the safety of the immersed tube in an external heat exchanger of a 660MW ultra supercritical CFB boiler was evaluated.

Introduction

When an unexpected power failure occurs, all fans and pumps will stop running without power. The circulating bed material in the CFB boiler gradually loses fluidization and accumulates at the bottom of the furnace and the EHE. The heat exchange tubes in the EHE will be buried by the high temperature circulating materials, and a large amount of heat will be transferred to the heat exchange tubes. At the same time, since the supercritical CFB boilers do not have a drum, the natural circulation loop cannot be formed. So, the steam-water system also stops the circulation when the water pump stops. It is difficult to provide a continuous and stable cooling effect to the pipeline. In such situation, the pipe is gradually heated up under the heating of the high-temperature bed material, and if it exceeds the limit of the safe temperature, the pipe bursting accident is likely to occur. To investigate the safety of the buried pipe in the situation above, simulating the temperature of the pipe wall is necessary.

Since the circulating bed material remains stationary around the pipe, the heat will be transferred in the form of heat conduction, and the thermal conductivity of the material is the necessary parameter for numerical simulation. Although the formers have also measured the thermal conductivity of coal ash, due to the variety of coal ash, the available data is very few. In this paper, the thermal conductivity of the sieved coal ash was measured by the transient hot wire method and found to be a function of temperature, composition and particle size.

After obtaining the thermal conductivity of the circulating material, this paper numerically simulates a single heat exchange tube and plot the wall temperature curve.

Experimental

Measurement

Transient hot wire method, which was first proposed by Stalhane B et al.(1931), is used to measure thermal conductivity. When a constant current is applied to a single wire, the heat is generated by wire because of the Joule effect, and the heat is taken away by the surrounding sample to be tested. The process of the surface temperature changing of the hot wire can be described by Eq.(1)

$$\Delta T = \frac{q}{4\pi\lambda}\ln \mathrm{t} + \frac{q}{4\pi\lambda}\ln\left(\frac{4a}{r_0^2 C}\right) \tag{1}$$

Where C is a constant.

Differentiating the formula above:

$$\lambda = \frac{q}{4\pi}\frac{d(\ln t)}{d(\Delta T)} \tag{2}$$

The resistance and temperature of the wire per meter are in a linear function. At this time, the voltage value at both ends of the heating section of the wire is measured to calculate the temperature of the wire. The final equation is as follows:

$$\lambda = \frac{I^2 U R_0 \alpha}{4\pi l}\frac{d(\ln t)}{dU} \tag{3}$$

Eq.(3) shows that the thermal conductivity of the material can be obtained by measuring the voltage value across the wire as a function of time with a constant current through the wire.

In the experiment, the hot wire was inserted into the ash sample to be tested, and two solder joints were used to connect to the voltmeter.

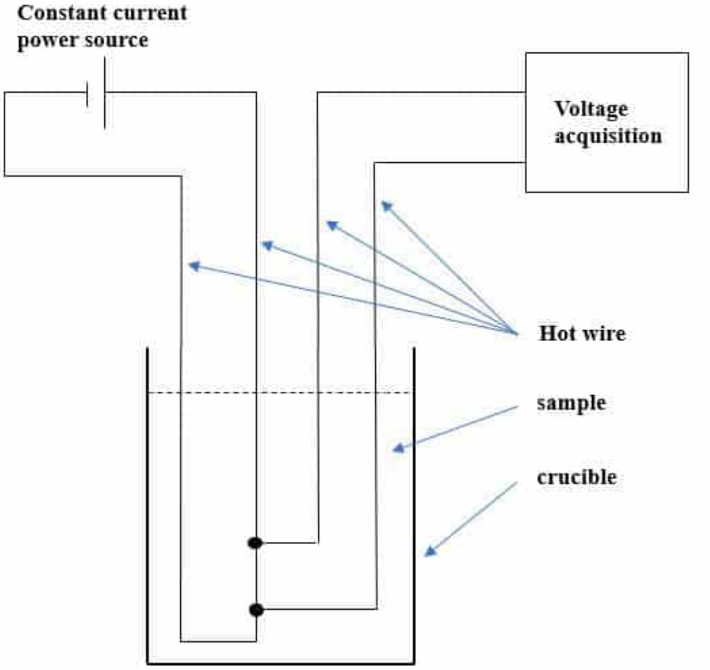

Fig.1. Measurement system of transient hot-wire method.

In Fig.1, Pt-6%Rh is used for the energization section of the hot wire, and Pt wire is used for connecting the voltage measurement according to Venart et al. (1980). The hot wire has a diameter of 0.5 mm. The voltage measuring section is 12 mm long.

In the experiment, the ash sample to be tested is placed in a crucible, which is placed in an electromagnetic heating furnace. The temperature is controlled in the furnace by program. Since the temperature of the circulating ash in the EHE generally does not exceed 880 °C and the heat exchange pipe is safe at 500 °C, so the temperature range of this experiment is 500-900 °C, setting the measurement point every 100 °C.

During measurement, the sampling frequency is 10 Hz in the voltage acquisition system, the constant current power supply output is set to 2 A. The voltage changing with time after power on is recorded online. 5-10 tests per measurement point are repeated to reduce random errors.

Results

Firstly, the thermal conductivities of coal ash from lignite (Indonesian) and coal slime (Changbin) are measured, as shown in Fig.2.

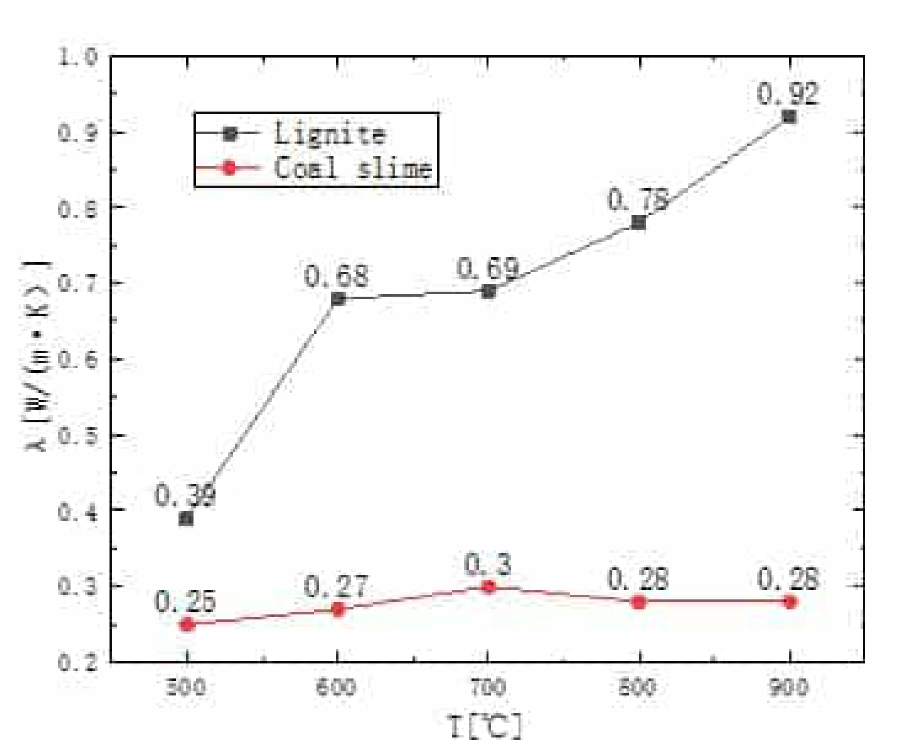

Fig.2. Thermal conductivity of coal ash from lignite (Indonesian) and coal slime (Changbin)

The thermal conductivity of lignite coal ash is between 0.4 and 0.9 W/(m • K), and that of slime coal ash is between 0.2 and 0.3 W/(m • K). The order of magnitude is the same as that of Zhao(2012).The thermal conductivity increases with increasing temperature because the pore of coal ash gradually collapses with the increase of temperature according to Rezaei et al.(2000).

Next, the coal ash of bituminous coal (Pingshuo) was further sieved and the thermal conductivity was measured.

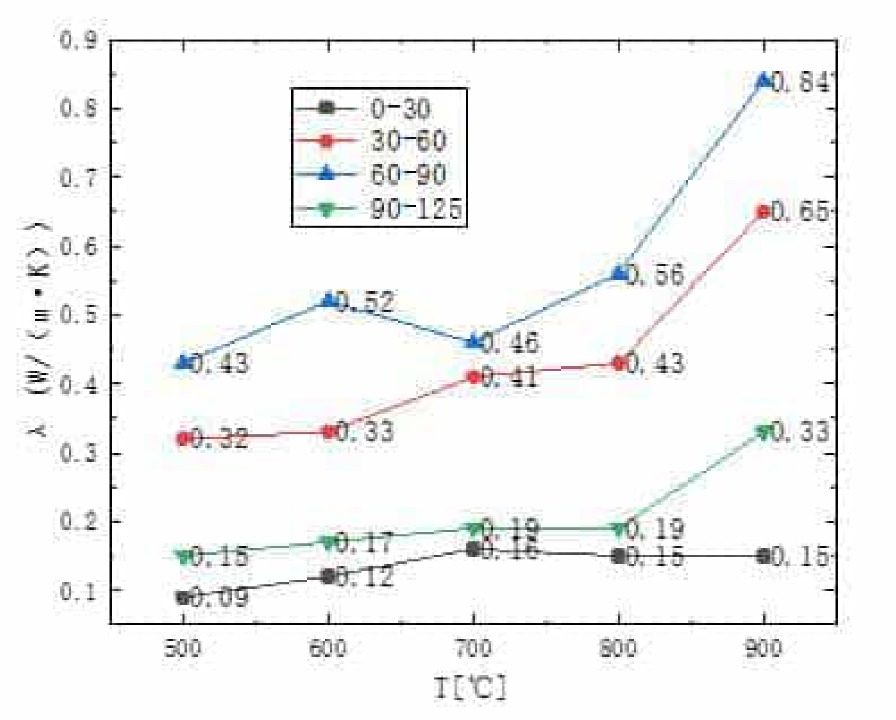

Fig.3. Thermal conductivity of lignite coal ash in different particle size.

As shown in Fig.3, the thermal conductivity of bituminous coal ash is also between 0.1 and 0.8 W/(m • K), which is not much different from other coal samples. From the aspect of particle size, the thermal conductivity increases with the increase of the particle size, but falls back at the particle size of 90-125 μm.

Numerical Simulation

In this paper, the heat transfer process of one single pipe after power loss is simulated. In an EHE, the pipes are arranged in a tube bundle. Take a pipe with an outer diameter of 51mm and a wall thickness of 3mm for simulation. The lateral spacing of the pipe rows is 4 times the pipe diameter and the longitudinal spacing is 2 times the pipe diameter. Due to the symmetry, a quarter of a calculation unit is taken for simulation calculation, and an adiabatic boundary is set around. The quarter circle in the lower left corner of the illustration is water vapor, the quarter ring is the pipe, and the upper right corner is the circulating ash.

Fig.4. The simulating object(2D)

Assumptions:

a) The tube bundles are perfectly symmetrical, so one quarter is used as the simulation object.

b) After the power is lost, the water vapor in the pipe stops flowing immediately and maintains constant pressure.

c) The material fills all the gaps between the pipes and has the same packing density.

d) In Fig.4, except for the heat exchange on the inner and outer walls of the pipe, the remaining surfaces are adiabatic boundaries.

e) Ignore the contact thermal resistance between the circulating ash and the outer wall of the pipe.

f) The entire physical model only considers heat conduction, regardless of convection and radiation.

g) The heat transfer of the simulated object at the initial time is steady.

h) Linear interpolation of thermal conductivity of circulating ash.

i) Measured values of bituminous coal ash at 90-125 um are taken as thermal conductivity of ash in simulation calculation.

Setting

Take the high-temperature section of high-temperature reheater EHE of 660MW ultra supercritical CFB boiler as an example according to Nie et al. (2018) and Sun et al. (2014). The initial temperature of the circulating ash is set 850 ° C, the working fluid in the tube is the initial temperature of 623 °C, 4 MPa of reheated steam. Combined with the above models and assumptions, the simulation calculations were performed using the Transient Thermal module of Ansys WorkBench.

Results and discussion:

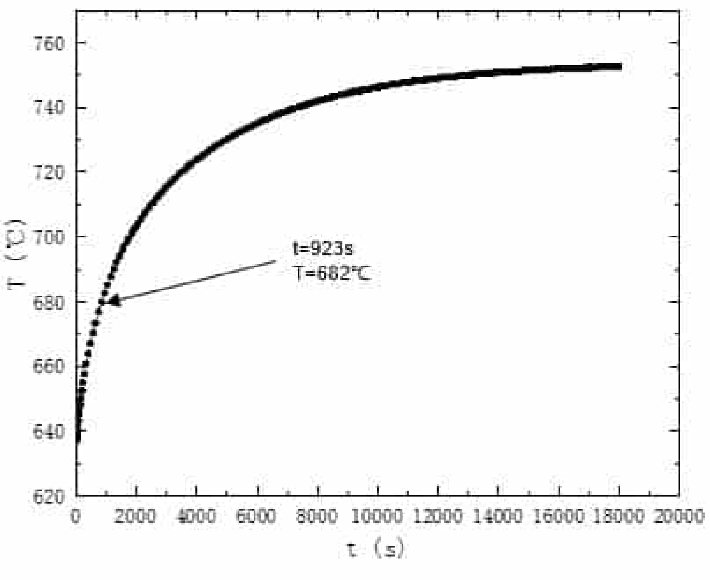

Fig.5. Wall temperature of heat exchange tube

Fig.5 shows the temperature of the outer wall of the above-mentioned pipe change with time after power failure. The allowable temperature of the alloy steel material in the ASME standard in the above conditions is 680 °C. As shown in the Fig.5, without considering the damage of the pipeline, the whole model finally reached the thermal steady state, the overall temperature was 752 °C, and the temperature of the outer wall of the tube rose to 680 °C at around 900 s. It can be seen from the results that the heat exchange pipeline has a danger of bursting in the case of power loss, but there is a certain time margin from the moment of power loss to the occurrence of danger. If the circulation of the cooling medium can be restored in time, take away the heat, the safety of the buried pipe will be much better.

Conclusion

In this paper, the thermal conductivities of several kinds of coal ash are measured by the transient hot wire method. The order of magnitude analysis and its variation with temperature show that it has certain reliability. The measured values are also used for numerical simulation, and the wall temperature curve of EHE high temperature reheater in 660MW Ultra Critical CFB boiler is simulated and calculated after power loss. The results show that the wall temperature is still in the safe range for a short period of time after power loss. The simulation results are of great significance to the safe operation of ultra-supercritical CFB boilers.

Notation

a	thermal diffusion coefficient, m^2/s
I	Current, A
l	length, m
q	heat generated by wire per unit length per unit time, W/m
r_0	radius of hot wire, m
R_0	Resistance of Metals at 0 °C，Ω
t	time, s
T	temperature, °C
U	voltage, V
α	Temperature coefficient of resistivity
λ	thermal conductivity, W/(m • K)

Acknowledgement

This work was supported by the National Key R&D Program of China (2016YFB0600201).

References

Nie L, Gong L. Study on wall temperature deviation characteristics of external heat exchanger In ultra supercritical circulating fluidized bed boiler. Journal of Engineering for Thermal Energy and Power 2019.34(06):85-90

Rezaei H.R et al. Thermal conductivity of coal ash and slags and models used .Fuel2000,(79);1697-1710

Stalhane B, Pyk S. Ny Metod för Bestämning av Värmelednings-Koefficienter. Teknisk Tidskrift 1931.61:389–393

Sun X et al. Tube wall temperature characteristic of external heat exchanger in 600MW supercritical CFB boiler. Electric Power Construction 2014.35(04)6-9

Venart J E S, Prasad R C. Thermal conductivity of water and oleum.Journal of Chemical and Engineering Data,1980,25(3);196-198

Zhao W. Experimental study on the influence of reactions on coal ash thermal conductivity 2012 U.D.C:621.18

SYNCHROTRON-BASED X-RAY IN-SITU IMAGING TECHNIQUES FOR ADVANCING THE UNDERSTANDING OF PHARMACEUTICAL GRANULATION

Chen Li[1]**, Ning Zhu**[1,2]**, Heather N. Emady**[3]**, Lifeng Zhang**[1*]

[1] Department of Chemical and Biological Engineering, University of Saskatchewan, 57 Campus Dr, Saskatoon, SK S7N 5A9
[2] Canadian Light Source Inc., Saskatoon, Canada
[3] School for Engineering of Matter, Transport and Energy, Arizona State University, AZ, USA
*Email: *lifeng.zhang@usask.ca*

Abstract

Wet granulation of powders is a key unit operation in the pharmaceutical industry. Due to the complexity of the granulation process taking place in a short time, observing and measuring the granulation process is challenging with conventional experimental methods. In this study, synchrotron-based X-ray imaging techniques were, for the first time, employed to capture the dynamic granulation process with a single drop impacting method in pharmaceutical powder beds. Five common pharmaceutical excipients, two active pharmaceutical ingredients (APIs) and their mixtures were used as the powder beds. The dynamic interaction between the liquid binder and solid powders were observed from high resolution X-ray images captured. Results show that pharmaceutical powder properties, including particle size and hydrophilicity, show significant influence on the dynamic granulation process and the final granular product.

Introduction

Wet granulation is an important unit operation in chemical and pharmaceutical industries. During the wet granulation process, wetting and nucleation, consolidation and growth, and breakage and attrition are the main processes that occur to produce granules. Liquid droplets wet fine powders to form granules in wet granulation. The wetting and nucleation process usually finish within a few seconds. Key factors influencing granule formation are drop penetration time, dimensionless spray flux, Bond number, and Stokes deformation number (Iveson et al., 2001). Recent research efforts have been placed on the wetting and nucleation regime of single droplet granulation, which can enhance the control of preferred granule properties (Hapgood et al., 2002). Granule properties such as granule size and size distribution have attracted the most attention. However, other important parameters, including granule shape and internal structure, are rarely investigated since these parameters are difficult to measure. Despite the success of visualization of the final granule product, understanding the granulation mechanisms and observing the dynamic granulation process are still challenging (Davis, 2015). The objective of this study was to employ synchrotron-based X-ray radiographic imaging techniques to understand the dynamics of the granulation processes of pharmaceutical powders.

Material and method

Materials

Microcrystalline Cellulose (MCC), Croscarmellose Sodium (CCS), Lactose Monohydrate (LMH), Acetaminophen (APAP) and Ibuprofen (IBU), and their mixture were used in the granulation experiment. The characterization of the powder materials, including median particle size, surface mean diameter, contact angle with water, particle skeletal density, and modified particle Bond number, used in this study is presented in Table 1. Deionized water was used as liquid binder. The surface tension of deionized water is 72.0 mN/m (Xi Yuan and Rosen, 1988) and the viscosity is 0.89 mPa·s (Wang et al., 2011). The contact angle of the pharmaceutical powders with water was measured with the Washburn capillary rise (WCR) method (Oka et al., 2015).

Single drop granulation setup

Single drop granulation experiments were conducted to investigate liquid drop impact with powder beds consisting of pharmaceutical ingredients. The powder bed was levelled with a metal panel to ensure a smooth surface. The setup is shown in Fig. 1. A micropipette, filled with deionized water as the liquid binder, was held 2.5 cm above the powders. The resulting impact velocity of the droplet was about 0.7 m/s. The powders were placed in a small cylindrical vessel with an inner diameter of 1 cm and a height of 3 cm. A syringe pump was used to control the release of liquid droplets. In this work, droplets with a volume of 15 μL were investigated.

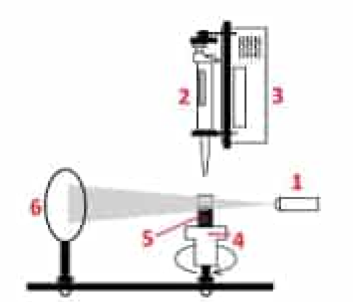

Fig. 1. Single drop experimental setup: 1) beam source, 2) micropipette, 3) syringe pump, 4) high precision motorized rotation stage, 5) sample vessel, and 6) beam camera.

Granule morphology and internal structure

An example of granule shape measurements is illustrated in Fig. 2. The droplet height above the powders surface (h_d) can be used to determine the penetration time. The penetration time in this study is defined as the time taken for a droplet from contacting the powders to the point that h_d stops changing for 1 s. For the dynamic granulation process (see Fig. 2a), d_d is the diameter of the droplet, h_g is the height of granule under the bed surface, and d_g is the diameter of the granule. For the final granules, the projected area equivalent diameter (D_a), projected area maximum diameter (D_{max}), projected area minimum diameter (D_{min}) and projected area equivalent height (H_g) were used to describe the granule size. The yellow outline in Fig. 2b shows the projected area of the granule, which can be obtained by binarization processing in ImageJ, and then the projected area equivalent diameter (D_a) can be calculated based on this projected area. The horizontal aspect ratio ($HAR=D_{max}/D_{min}$) and vertical aspect ratio ($VAR=D_a/H_g$) were employed to characterize the shape (Emady et al., 2011).

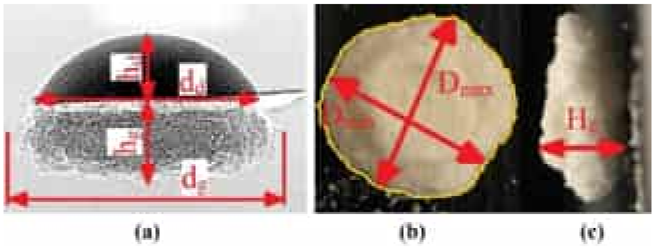

Fig. 2. Illustration of granule morphology measurements: (a) a representative X-ray image captured from the dynamic granulation process, (b) top view and (c) side view of the resultant granule.

Results and discussion

Physical Properties and Contact Angles of Pharmaceutical Powders

The results of characterization of physical properties and contact angles of excipients and APIs used in this work are presented in Table 1. IBU has the largest particle size (195 μm), and CCS has the smallest particle size (41 μm) among the powders used in this research. Wettability is an important property to measure the interaction between powder and liquid during granulation and is quantified via the contact angle. The contact angles of all the powders are smaller than 90°, which means they are all hydrophilic.

Table 1. Physical Properties and Contact Angles of Pharmaceutical Powders

Component	**Abbreviation**	**Median particle size, d_{50} (μm)**	**Contact angle, θ (°)**	**Particle skeletal density, ρ_p (g/cm^3)**	**Particle bulk density, ρ_{bed} (g/cm^3)**	**Surface mean diameter, d_s (μm)**	***Modified Bond number* Bo_g^***
Microcrystalline Cellulose	MCC	128	49.6±0.2	1.61	0.358	164.0	493.8
Lactose Monohydrate	LMH	70	79.6±6.6	1.52	0.558	96.9	252.8
Croscarmellose Sodium	CCS	41	84.9±0.6	1.62	0.542	71.4	236.1
Acetaminophen	APAP	96	82.9±3.1	1.72	0.566	167.8	56.8
Ibuprofen	IBU	195	83.8±2.1	1.38	0.608	278.4	16.8

Final granule size and morphology

For three excipients (LMH, CCS, and MCC), two APIs (APAP and IBU), and their mixtures, images of the final granules and their corresponding shape parameters are presented in Fig. 3 and Table 2, respectively. In Fig. 3o, it is observed that there is a spherical core on the top of the granule. This may be related to the IBU powders' natural tendency to be cohesive and form agglomerates.


(a) APAP 20%
(b) APAP 15%
(c) APAP 10%
(d) APAP 5%
(e) APAP 0%
(f) IBU 20%
(g) IBU 15%
(h) IBU 10%
(i) IBU 5%
(j) IBU 0%
(k) LMH
(l) CCS
(m) MCC
(n) APAP only
(o) IBU only

Fig. 3. Final granules produced using single drop granulation method

Granule internal structure

X-ray computed tomography (CT) was used to study the internal structure of the 20% APAP granule, and the results are shown in Fig.s 4a-g. The images of each slice were binarized using ImageJ to calculate the porosity. The porosity of each slice is shown in Fig. 4 as well. The reconstructed image from the CT scan and the locations of the slices for porosity studies are shown in Fig. 4h. The granule was not removed from the powder bed during the CT scan to prevent potential destruction of the sample. From the top view (Fig. 4b) and the side view of the granule (Fig. 4h), there is a gap region which separates the granule and the rest of the powder bed. Three regions can be found in Fig. 4h, including the gap region, the top region and the bottom region, based on the internal structure differences. The gap region has the highest porosity, and the top region has higher porosity than the bottom region, which is consistent with the trend in Fig.s 4a-g.

In Fig. 4d, two regions with different porosities can be observed. Similar results were reported by Gao et al. (2018). This may due to the natural tendency for the finer powders to be cohesive and form agglomerates. This property also results in the gap regions in Fig.s 4b-c and the high porosity region in Fig. 4d. In general, the porosity of the granule top region (Fig.s 4a-c) is higher than that of the bottom (Fig.s 4d-g). Fig.s 4e-g show a similar porosity distribution. After the initial droplet distortion stage, the main driving force of the water movement in the powder bed is the capillary force, which results in a relatively even porosity distribution in the bottom part of the resultant granule. The porosity of Fig. 4f is slightly higher than that of Fig. 4e and Fig. 4g. As shown in Fig. 3a and Fig. 4b, there is a crown embedded on the top of the granule. This crown structure results in the gap region and the noncontinuity of the porosity.

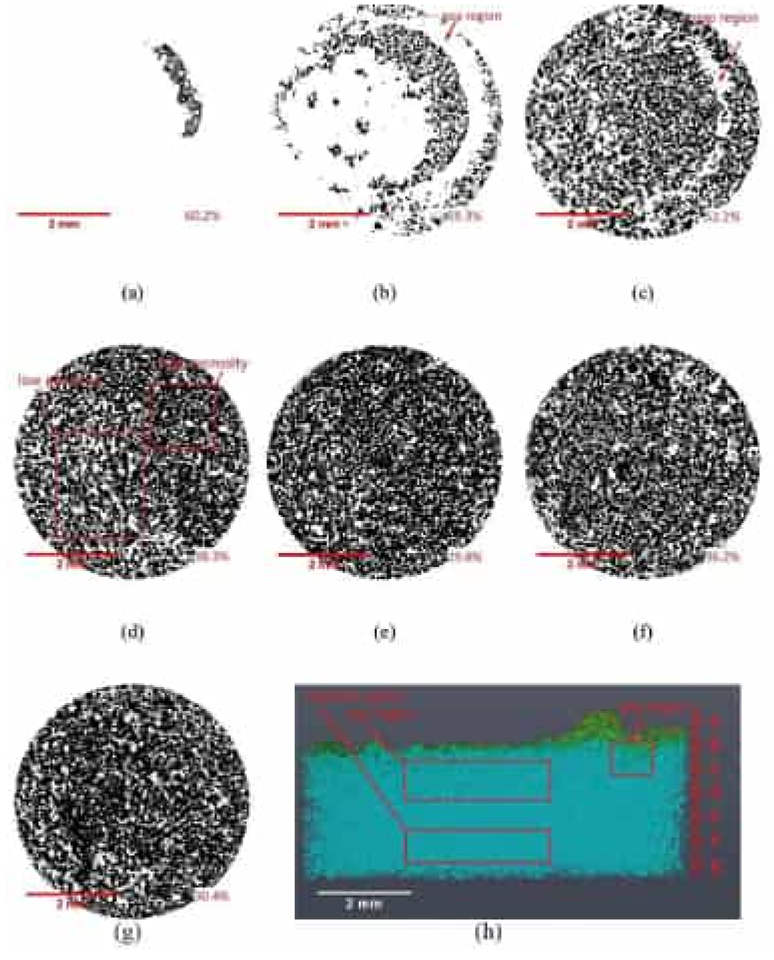

(a) (b) (c)

(d) (e) (f)

(g) (h)

Fig. 4. Internal morphology results of the 20 % APAP granule: (a)-(g) slices of the granule, and (h) side view of the resultant granule.

Wetting and nucleation process of LMH powders

The dynamic wetting and nucleation process of LMH powders is shown in Fig. 5. The image starts from the droplet moved into in the field of view (FOV). The time of the images is shown beneath the individual images in Fig. 5. This granulation process follows the spreading granule formation mechanism (Emady et al., 2011). It includes three phases: impaction, spreading and penetration.

Table 2 Size and Shape Parameters of Final Granule

Component	D_{max}, (mm)	D_{min}, (mm)	H_g, (mm)	D_a, (mm)	HAR	VAR
APAP 20%	7.23±0.21	6.09±0.03	3.47±0.07	6.82±0.06	1.19	1.97
APAP 15%	6.85±0.13	6.23±0.24	3.94±0.12	6.42±0.03	1.10	1.63
APAP 10%	7.32±0.14	6.12±0.05	3.10±0.02	6.74±0.10	1.15	2.17
APAP 5%	8.19±0.09	6.21±0.05	3.26±0.11	7.38±0.03	1.32	2.27
APAP 0%	8.22±0.18	6.21±0.07	2.24±0.12	7.42±0.07	1.34	3.31
IBU 20%	7.04±0.21	6.24±0.11	3.57±0.09	6.55±0.08	1.13	1.83
IBU 15%	6.35±0.20	5.64±0.21	3.11±0.11	5.99±0.04	1.13	1.93
IBU 10%	5.59±0.07	4.90±0.10	3.08±0.02	5.24±0.11	1.14	1.70
IBU 5%	6.54±0.16	5.47±0.17	3.18±0.07	6.02±0.05	1.20	1.89
IBU 0%	6.40±0.08	5.65±0.09	3.06±0.07	6.01±0.10	1.13	1.96
LMH	N/A	N/A	N/A	N/A	N/A	N/A
CCS	2.41±0.13	2.18±0.18	1.88±0.14	2.21±0.07	1.11	1.17
MCC	4.80±0.08	3.25±0.15	1.67±0.06	3.97±0.05	1.48	2.38
APAP	7.08±0.09	6.43±0.04	4.97±0.17	6.74±0.06	1.10	1.36
IBU	9.89±0.16	8.64±0.11	7.69±0.03	9.30±0.08	1.14	1.21

When the liquid droplet impacts the powders, the droplet rebounds and distorts within 50 ms (see Fig.s 5a and 5b). Afterward, LMH powders attach to the external surface of the liquid droplet and move upward (see Fig.s 5c and 5d). Two layers are observed from the granule beneath the powder bed at 125 ms, as shown in Fig. 5d. The inner layer with a darker color is the core of the granule and the outer layer represents the water-penetrating layer. The water-penetrating layer has a lower moisture content and was formed during penetration and spreading stages. The inner layer has a higher moisture content than the outer layer. High moisture can form more liquid films and enhance adhesion forces between the powders in granules. The strength of the granule increases with an increase in moisture content when the moisture content is lower than 20% (Verkoeijen et al., 2002). The internal structure of the granule core usually has higher strength than the water-penetrating layer (Aulton and Taylor, 2013).

The LMH granule size is shown in Fig. 6. The droplet diameter, d_d, increases when the kinetic energy releases. The distortion process lasts approximately 200 ms after the droplet contacts the powder bed surface. When d_d reaches its maximum, the gravity and capillary forces drive the growth of the granule beneath the bed surface from 200 ms to 1 s. In the meantime, the droplet above the bed surface diminishes gradually. After 1 s, the spreading process becomes almost stationary, as illustrated in Fig. 6. Because the spreading water exceeds the FOV of the camera, the granule size was not measured after 0.9 s.

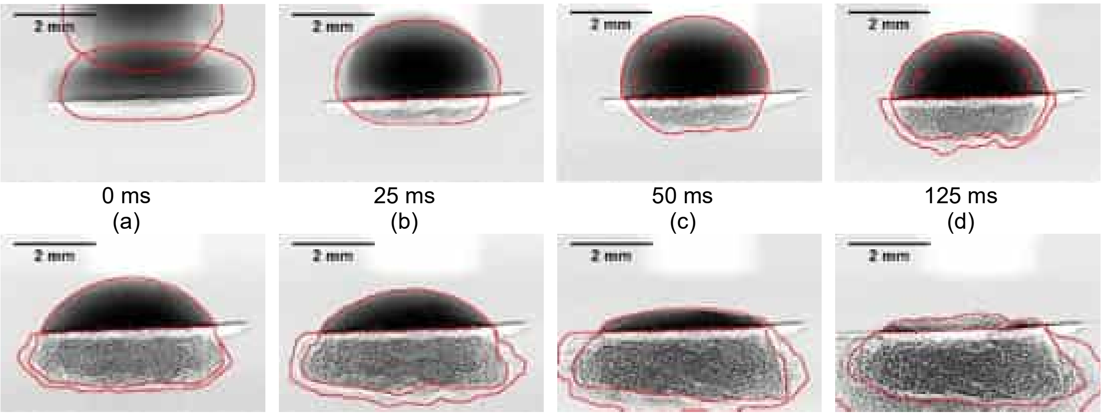

0 ms (a) 25 ms (b) 50 ms (c) 125 ms (d)

250 ms (e) 375 ms (f) 550 ms (g) 1.7 s (h)

Fig. 5. Time sequence X-ray images of dynamic wetting and nucleation process of LMH powders.

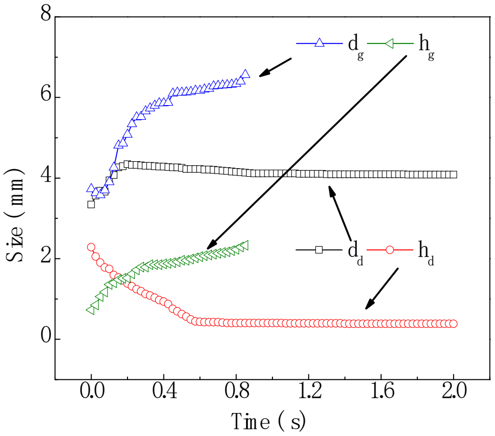

Fig. 6. Size of the LMH granule size.

Conclusions

In this work, the dynamic wetting and nucleation process for pharmaceutical powders was experimentally investigated for the first time through synchrotron-based X-ray imaging techniques. The following conclusions can be drawn from the experimental results:

The particle properties including size, and hydrophilicity show significant influences on the granulation process and final granules. The spreading granulation mechanism occurs with LMH.

The porosity of the granule decreases from the top part to the bottom part of the granule. Three regions can be found in the granule, including the gap region, the top region and the bottom region, based on the internal structure differences.

References

Aulton, ME., Taylor, KM., 2013. Aulton's pharmaceutics: the design and manufacture of medicines. Elsevier Health Sciences.

Davis, NB., 2015. Granulation of ultra-fine powders: Examination of granule microstructure, consolidation behavior, and powder feeding. Open Access Dissertations. 1108.

Emady, HN., Kayrak-Talay, D., Schwerin, WC., Litster, JD., 2011. Granule formation mechanisms and morphology from single drop impact on powder beds. Powder Technology 212, 69-79.

Hapgood, KP., Litster, JD., Biggs, SR., Howes, T., 2002. Drop Penetration into Porous Powder Beds. Journal of Colloid and Interface Science 253, 353-366.

Iveson, SM., Litster, JD., Hapgood, K., Ennis, BJ., 2001. Nucleation, growth and breakage phenomena in agitated wet granulation processes: a review. Powder Technology 117, 3-39.

Oka, S., Emady, H., Kašpar, O., Tokárová, V., Muzzio, F., Štěpánek, F., Ramachandran, R., 2015. The effects of improper mixing and preferential wetting of active and excipient ingredients on content uniformity in high shear wet granulation. Powder technology 278, 266-277.

Verkoeijen, D., Meesters, GMH., Vercoulen, PHW., Scarlett, B., 2002. Determining granule strength as a function of moisture content. Powder Technology 124, 195-200.

Wang, S., Huang, X., Yang, C., 2011. Mixing enhancement for high viscous fluids in a microfluidic chamber. Lab on a Chip 11, 2081-2087.

Xi Yuan, H., Rosen, MJ., 1988. Dynamic surface tension of aqueous surfactant solutions: I. Basic paremeters. Journal of Colloid and Interface Science 124, 652-659.

COMBINED MEASUREMENT TECHNIQUES FOR FAST DETECTION OF ALKALI RELEASE IN FLUIDIZED BED COMBUSTION

Tomas Leffler[1*], Fredrik Lind[2], Jesper Liske[3] and Pavleta Knutsson[1]

[1]Department of Chemistry and Chemical Engineering, Chalmers University of Technology, SE-41296 Gothenburg, Sweden

[2]Department of Space, Earth and Environment, Chalmers University of Technology, SE-41296 Gothenburg, Sweden

[3]Department of Chemistry and Chemical Engineering, Environmental Inorganic Chemistry, High Temperature Corrosion Centre, Chalmers University of Technology, SE-41296 Gothenburg, Sweden

*Email: letomas@chalmers.se

Abstract

This study presents an approach combining three alkali-measuring techniques to quantitatively measure the released alkali compounds during the thermal conversion of biomass and Municipal Solid Waste (MSW) in fluidized bed reactors. The method includes measurements of alkali-containing species in the gas phase, as aerosols, or taken up by the bed material. Two techniques are used for online alkali detection in the flue gas: An *In-situ* Alkali Chloride Monitor (IACM), and a Surface Ionisation Detector (SID). The third technique is an Electronic Tongue (ET) used for the post-analysis of alkali content in the bed material. These three techniques form a method used to determine the alkali present in gaseous state (IACM), as aerosols (SID), and in the bed material (ET). The use of these techniques can enable the determination of optimal intervals to regenerate the bed material and to avoid bed agglomeration, slagging and fouling, as well as high-temperature corrosion.

Introduction

Thermal conversion of fossil fuel has a substantial impact on climate and the environment. Different types of biomass such as herbaceous material (straw and grass), agricultural by-products (e.g. almond pits, shells and hulls), forest residues with a base of wood chips and bark, as well as MSW can replace parts of the used fossil fuels.

The ash content in biomass fuels ranges from one to a few weight percentages for wood and herbaceous fuels, respectively. The main ash components for biomass-derived fuels are: Ca, Si, K, Na, S, Cl, Al, Fe, P, Mg and Mn (Bostrom*, et al.*, 2012). In MSW the ash components also include Pb and Zn. The following chemical elements: K; Ca; Si; S and Cl are the most reactive ash-forming compounds according to Marinkovic et al. (Marinkovic, 2016). The implication of potassium and chlorine release during combustion of biomass fuels downstream the combustor has been surveyed by Johansen et al. (Johansen*, et al.*, 2011). According to Zevenhoven et al., these ash-forming components from the fuel can take three different interaction pathways with the bed particles: transportation on bed particles, undergoing chemical reactions with the bed particles, or a combination of transportation and chemical reactions (Zevenhoven-Onderwater*, et al.*, 2006).

These interactions can lead to increased costs for unplanned boiler stops and maintenance; e.g., interaction of ash-forming components with the bed material can cause bed agglomeration. The released ash components can also result in deposits on heat exchanger surfaces, which can result in operational stops due to surface cleaning and/or corrosion.

Fluidized bed (FB) combustion is a mature technique for thermal conversion of heterogeneous fuels such as biomass and MSW. The FB combustion process has been further developed into a concept known as Oxygen Carrier Aided Combustion (OCAC)

(Thunman*, et al.*, 2013). OCAC aims to improve the homogeneous distribution of oxygen and heat throughout the reactor during combustion. Another technique that is using the fluidized bed combustion process is Chemical Looping Combustion (CLC) (Lyngfelt*, et al.*, 2001). CLC enables the separation of carbon dioxide (CO_2) and its subsequent capture and storage (CCS). The common feature among these combustion techniques is the use of oxygen carriers as bed materials, which are more expensive and more surface sensitive than the conventionally used silica sand. The higher cost of bed material requires even better understanding of the ash-component interactions in the fluidized bed material.

Substantial research has been aimed at understanding both the mechanism and the ability to predict bed agglomeration in FB boilers (Ohman*, et al.*, 2000) combusting a complex mix of biomass fuels rich in alkali and chlorine-containing compounds in a fluidized bed of sand. This type of research has now moved forward to include even different bed materials used in gasification, CLC and OCAC; in particular, research on activity and ageing of different oxygen carriers and ash interactions with the selected bed materials (Gyllén, 2019; Marinkovic, 2016).

Online measurement of alkalis and their state are of great importance when predicting and avoiding unplanned plant stops. An extensive review by Monkhouse presents the status up to 2011 for online detection techniques of alkali metals in the flue gas, such as Excimer Laser-Induced Fluorescence (ELIF) and Surface Ionization (SI) (Monkhouse, 2011). Sorvajärvi (Sorvajärvi*, et al.*, 2014) developed a laser system that includes three lasers for the detection of atomic potassium (K), potassium hydroxide (KOH) and potassium chloride (KCl).

Most of the techniques described in the literature focuses on the measurement of alkali components in gaseous or aerosol state as a result of the fuel decomposition. However, to the knowledge of the authors, there is no online method or instrument that focuses on the uptake and release of alkali by the bed material.

This paper introduces a new approach to detect the alkali released in the gas phase and as aerosols during the thermal conversion of biomass and MSW fuels in a fluidized bed system, as well as to monitor the alkali uptake and release by the bed material. This new approach is based on three different measurement techniques: (1) optical gas-phase measurements of KCl and KOH with the *In-situ* Alkali Chloride Monitor (IACM) instrument; (2) aerosol measurements of KCl with the SID instrument; and (3) water-soluble compounds released from bed material dissolved in water at room temperature detected with the ET instrument. The idea of this new approach is to combine the selected measurement techniques to obtain an indication of alkali speciation and alkali distribution in the boiler that would allow to prevent slagging, fouling and high-temperature corrosion as well as to determine when the bed material has been saturated with alkali and/or risks agglomeration. Avoiding the above-mentioned ash-related problems would result in improved availability of the boiler as well as in decreased maintenance costs arising out of alkali-related problems.

Theory and Methods

Ash components take different pathways during thermal conversion, as shown in Fig. 1, where the pathways are numbered from 1 to 5. *The first pathway* of the ash-forming elements occurs where the components leave the boiler through the bottom ash without any interaction with the bed material. *The second pathway*, which is also the most common one, takes place where the ash-forming components interact with the bed material in three different ways: (1) by deposition and forming of a physical ash layer around the bed particles; (2) through chemical interaction of the ash-forming elements with the bed particles and the resulting build-up of an ash layer with a composition different than that of the ash components; and (3) through a combination of (1) and (2). The interaction between the ash components and bed material can result in the formation of sticky ash compounds that subsequently can lead to bed particles aggregation and cause bed agglomeration. Bed material agglomeration can be avoided if the bed material is regenerated at certain intervals.

The third pathway for ash components occurs when the ash-forming elements leave the fluidized bed as aerosols and gas-phase components and their interaction with furnace walls causes slagging and high-temperature corrosion. Corrosion and slagging, as well as bed agglomeration, can be further reduced through the use of different additives added to the furnace or to the fuel. *The fourth pathway* for the ash components occurs when the ash-forming elements in the gas phase condense on heat-transfer surfaces or aerosols that impact on these surfaces, which causes high-temperature corrosion and fouling. A suitable additive in combination with soot blowing can reduce these problems. *The fifth pathway* takes place where the ash-forming elements in the gas phase and as aerosol are collected in an electrical precipitator or a baghouse filter and subsequently leave the flue-gas cleaning system as fly ash.

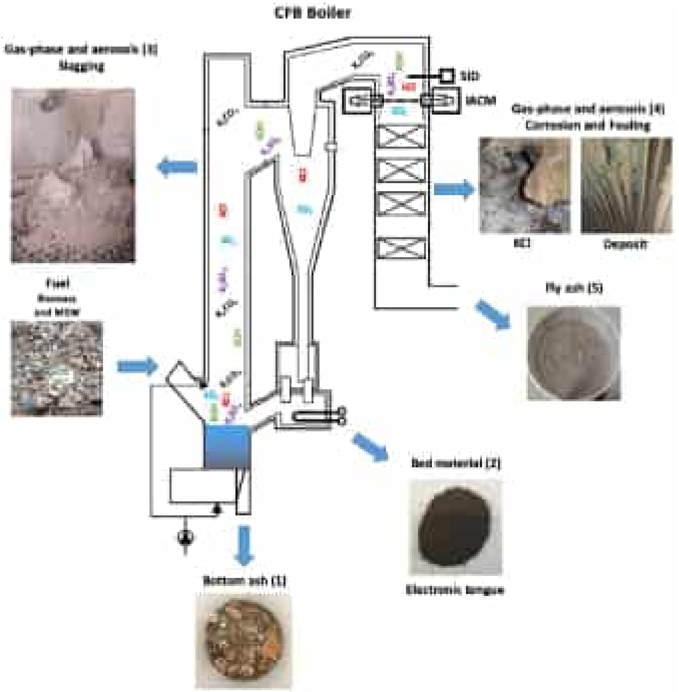

Fig. 1. Schematic presentation of the five different pathways that the ash-forming elements take.

In the present study, ash compounds that contain potassium (K), such as potassium chloride (KCl), potassium hydroxide (KOH), potassium sulphate (K_2SO_4) and potassium carbonate (K_2CO_3), are for simplicity denoted under the common category of alkali. In (1), the interaction of alkali with the bottom ash is not considered in the first approach. In (2), the interaction of alkali with the bed material is investigated by the ET, which is described below. In (3), the experiments do not consider alkali released as gas phase or as aerosols from the fuel that have not interacted with the bed material but are instead interacting with the furnace walls. In (4), alkali released in the gas phase and as aerosols, that have not interacted with the furnace walls, are measured with the IACM instrument and the SID instrument before they reach the heat exchangers in the convection path. The IACM instrument measures the sum of gas-phase alkali chlorides, while the SID instrument measures the sum of alkali chlorides as aerosols. These two measurement techniques are described below. In (5), the alkali compounds that leave the boiler with the fly ash are not considered in this experiment.

The IACM instrument is an optical measurement device that uses UV light and Differential Optical Absorption Spectroscopy (DOAS) to evaluate the concentration of gas-phase alkali and sulphur dioxide (SO_2) in the gas phase (Forsberg*, et al.*, 2009). The alkali concentration measured by the IACM instrument is in the ppm range. This instrument is preferably mounted upstream the first superheater in the temperature region of 650 – 1000 °C. Fig. 2

shows a principle schematic of the IACM instrument. This instrument is an integral part of the ChlorOut concept developed by Vattenfall AB, which aims to combat high-temperature corrosion.

The IACM instrument is used to measure the sum of gas-phase alkali chlorides (KCl and NaCl) and sulphur dioxide in the flue gas. In the present experiment the IACM instrument has been updated with a new spectrometer to enable simultaneous measurement KOH.

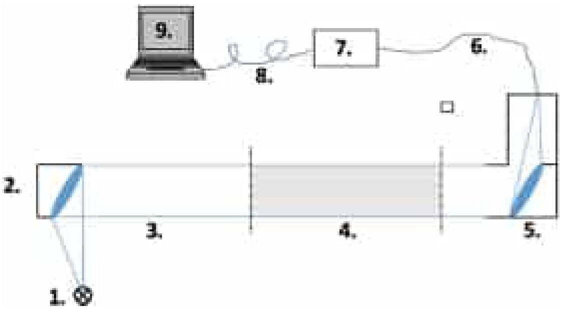

Fig. 2. Principle schematic of the IACM instrument: 1. Xenon light source; 2. parabolic mirror; 3. collimated light beam; 4. measurement volume; 5. parabolic mirror connected to an optical fibre; 6. optical fibre; 7. spectrometer; 8. USB cable; and 9. computer.

The surface ionization detector is based on absorption of alkali metal aerosols and desorption of ions of alkali metals from a hot platinum surface. The achieved ion current is a measure of the alkali concentration and the measuring range is in the ppb range (Davidsson, et al., 2002, Gall, 2018). Fig. 3 shows a picture (left) and a cross section of the SID instrument.

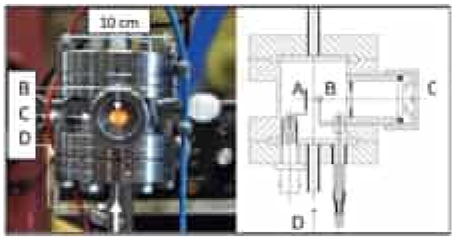

Fig. 3. A picture (left) and a cross section (right) of the SID instrument, where A is the ion collector, B is the Pt filament, C is a quartz window and D is the sample flow direction (Gall, 2018).

The SID instrument is used to measure the total sum of alkali metals (K and Na) as aerosols in the extracted flue gas. It measures the alkali aerosols in the flue gas, which can be ionized, and subsequently generates a current by means of alkali ions.

The electronic tongue is based on pulse voltammetry applied to a sensor array consisting of various catalytic metals (Winquist*, et al.*, 2002). The electronic tongue evaluates the measured signals with a multivariate data analysis software, SIRIUS. This software is provided by Pattern Recognition System A/S in Norway and is used for principal component analysis (PCA) of data. The electronic tongue was developed at Linköping University and is used to assess the quality of various fluids.

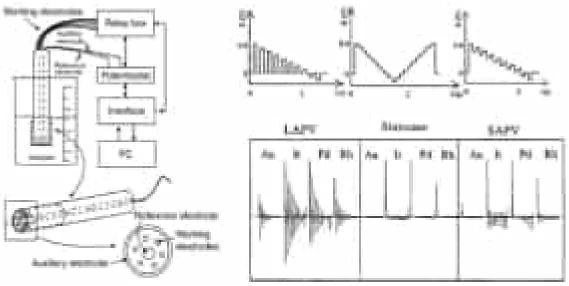

Fig. 4. The picture on the left shows a basic measurement set-up with the electronic tongue. The picture on the right shows different types of applicable signals (top) and their responses (bottom) (Winquist, et al., 2002).

An electronic tongue is used to measure the status of the bed materials and the tendency to bed agglomeration. Bed material is placed in a beaker with water at room temperature and is stirred well before the start of the measurement with electronic tongue.

Validation of Proposed Method

The present section describes the planned validation of the new approach to detect alkali uptake and release with the ET, gas-phase alkali with the IACM instrument, and alkali aerosols with the SID instrument. In this particular case, the alkali elements are represented by different potassium compounds in the following forms: gas-phase KCl and KOH (IACM), aerosols of KCl, where K can be ionized (SID), and a set of compounds leachable in water bound to the bed material (not necessary K (ET)).

The first step in the validation process is to generate a known concentration of alkali aerosols in the form of KCl that can be introduced into a small-scale laboratory FB reactor. Thereafter, the aim is to determine the amount of alkali aerosols in the flue gas that have passed thorough the bed material with the SID instrument. This simple experiment indicates how much of the introduced alkalis are still present in the flue gas after the passage through the FB reactor and through the bed material. The second step in the validation process is to examine the collected bed material with the ET to determine if the bed material composition has changed, compared to unexposed bed material. A third validation step would be to quantify the amount of alkali in the bed material with a total elemental analysis and complement it with a SEM/XRD analysis to reveal if and to what degree the alkali components have interacted with the bed material. By starting the validation process in a laboratory FB reactor, primary information and knowledge is obtained about the uptake and the release of alkali in the reactor as well as the degree of their interaction with the bed material and the FB reactor.

The second validation step aims at broadening the knowledge and understanding about the uptake and release of ash-forming elements by the bed material and the interaction with the bed material during thermal conversion of biomass. For this second validation step, a semi-industrial FB boiler could be used. Chalmers 12 MWth CFB-boiler has a suitable size, representing a semi-scale fluidized bed boiler, which may be operated for experimental purposes in contrast with a full-scale industrial fluidized bed boiler. It is suggested to only use biomass fuel containing alkali compounds of K to limit the complexity of the studied systems. The release of gas-phase KCl and KOH in the flue gas is detected with the help of the IACM instrument while the aerosols of K are detected by the SID instrument. In this case, if the concentration of KCl and KOH reaches ppm level it might be necessary to dilute the gas flow to the SID instrument to avoid a saturated signal. The bed material from the FB boiler during the experiment is continuously sampled and its status is evaluated by the ET and compared with a sample of pure bed material. A deposit probe could be used at different locations downstream the combustion chamber to collect deposits of alkali in the gas phase as well as alkali aerosols in the flue gas; e.g., condensed gas-phase KCl and KOH on the deposit probe. The amount of alkali in the bed material could be quantified by a total elemental analysis and complemented with a SEM-EDS and XRD analysis in order to reveal if the alkali has chemically interacted with the bed material.

Previous experience from an earlier validation process in a laboratory-scale FB reactor, which was further extended to include a semi-scale FB boiler, has given enough confidence in that the presented method can be validated in a full-scale industrial FB boiler. The inhomogeneity of the fuel could present a challenge in the validation process during thermal conversion of especially MSW fuel in a full-scale FB boiler. The alkali content in the fuel fed to the FB boiler varies a lot, which makes it harder to determine the uptake, release and interaction of ash-forming elements with the bed material.

Conclusion

This work presents a new method for mapping alkali compounds during the thermochemical conversion of solid fuel, in time and space, inside the a combustor. By combining IACM (alkali molecules in the flue gas), SID (alkali aerosols in the flue gas) and ET (alkali accumulated in the bed material), the goal is not only to quantify the total amount of alkali released from the fuel but also to describe where in the combustion process these alkali components end up.

Acknowledgements

Area of Advance Energy, Swedish Energy Agency/Biokraft (46450-1 Syrebärar stödd förbränning) are acknowledged for their financial support.

The authors thank ChlorOut AB for permitting them to use the IACM instrument.

Fredrik Winquist Linköping University in Sweden is acknowledged for the measurements with the electronic tongue.

References

Bostrom, D., et al., *Ash Transformation Chemistry during Combustion of Biomass.* Energy & Fuels, 2012. **26**(1): p. 85-93.

Davidsson, K.O., et al., *A surface ionization instrument for on-line measurements of alkali metal components in combustion: Instrument description and applications.* Energy & Fuels, 2002. **16**(6): p. 1369-1377.

Forsberg, C., et al., *Principle, calibration, and application of the in situ alkali chloride monitor.* Review of Scientific Instruments, 2009. **80**(2).

Gall, D., *Alkali metals and tar in biomass thermochemical conversion : development and application of online measurement techniques*. 2018.

Johansen, J.M., et al., *Release of K, Cl, and S during Pyrolysis and Combustion of High-Chlorine Biomass.* Energy & Fuels, 2011. **25**(11): p. 4961-4971.

Lyngfelt, A., et al., *A fluidized-bed combustion process with inherent CO2 separation; application of chemical-looping combustion.* Chemical Engineering Science, 2001. **56**(10): p. 3101-3113.

Marinkovic, J., *Choice of bed material : a critical parameter in the optimization of dual fluidized bed systems*. 2016.

Monkhouse, P., *On-line spectroscopic and spectrometric methods for the determination of metal species in industrial processes.* Progress in Energy and Combustion Science, 2011. **37**(2): p. 125-171.

Ohman, M., et al., *Bed agglomeration characteristics during fluidized bed combustion of biomass fuels.* Energy & Fuels, 2000. **14**(1): p. 169-178.

Sorvajärvi, T., et al., *In Situ Measurement Technique for Simultaneous Detection of K, KCl, and KOH Vapors Released during Combustion of Solid Biomass Fuel in a Single Particle Reactor.* Applied Spectroscopy, 2014. **68**(2): p. 179-184.

Thunman, H., et al., *Using an oxygen-carrier as bed material for combustion of biomass in a 12-MWth circulating fluidized-bed boiler.* Fuel, 2013. **113**: p. 300-309.

Winquist, F., et al., *Electronic Tongues and Combinations of Artificial Senses.* Sensors Update, 2002. **11**(1): p. 279-306.

Zevenhoven-Onderwater, M., et al., *Bed agglomeration characteristics of wood-derived fuels in FBC.* Energy & Fuels, 2006. **20**(2): p. 818-824.

MEASUREMENT OF SUPERCRITICAL FLUID FLOW UNIFORMITY IN PARALLEL TUBES BY A FLUID-TO-FLUID MODELLING METHOD

Yu Peng, Leming Cheng*, Qinhui Wang, Mengxiang Fang, Zhongyang Luo, Mingjiang Ni, Kefa Cen

Institute for Thermal Power Engineering, State Key Laboratory of Clean Energy Utilization,
Zhejiang University, Hangzhou, 310027, Zhejiang Province, P. R. China

* Email: *lemingc@zju.edu.cn*

Abstract

The flow uniformity in parallel tubes of the suspended superheaters and/or reheaters in the furnace of a circulating fluidized bed (CFB) boiler is one of the key issues. Considering the difficulty of conducting a measurement in a commercial boiler or a lab experiment with supercritical water, a novel method, fluid-to-fluid modelling of supercritical water is presented to investigate the supercritical fluid flow uniformity in parallel tubes of a suspended superheater at cold mode. This method was developed according to the fundamental principal of fluid-to-fluid modelling criteria for the supercritical water. Based on this theory, a supercritical flow experimental system was constructed using R134a as working fluid. The flow uniformity in parallel tubes may be determined by the temperatures and heat transfer coefficient on different tubes, which varies with gas velocity and solids suspension density in the CFB. The effects of fluid inlet temperature, inlet pressure, bed solid suspension density and two types of inlet modes of the working fluid on the mass flux distribution in parallel tubes were studied.

Key words: supercritical boiler, CFB, suspended heat transfer surface, flow uniformity

Introduction

Though a few supercritical circulating fluidized bed (CFB) boilers have been put into operation in the past years, the flow uniformity in parallel tubes of the suspended superheaters and/or reheaters in a CFB boiler is one of the key issues (Cheng et al., 2015). In a supercritical CFB boiler, the working fluid is at supercritical state. The physical parameters of working fluid at the critical point will change dramatically with the change of temperature and pressure, especially the specific heat capacity and thermal conductivity. It influences the heat transfer in tubes greatly. The flow uniformity in the parallel tubes will result in the tube bursting due to overtemperature. Therefore, the flow uniformity and heat transfer characteristics of the working fluid in the tubes have become one of the key points in the development of a supercritical CFB boiler. However, it is difficult to conduct a measurement in a commercial boiler or a lab test rig with supercritical water.

In this work, a novel method, fluid-to-fluid modelling of supercritical water is presented to investigate the supercritical fluid flow uniformity in parallel tubes of a suspended superheater at cold mode. The flow uniformity of working fluid in parallel tubes bundles under supercritical conditions was studied at different operation superficial velocity and solids suspension density. It was also investigated the flow uniformity at subcritical and supercritical states of the working fluid and two types of inlet modes of working fluids entering the parallel tubes.

Fluid-to-Fluid Modelling Method

The critical pressure of water is 22.06 MPa and the critical temperature is 647.1K. To do tests at supercritical state, a test system has to be operated at very high pressure and temperature. If one method could be developed to simulate the conditions at cold mode, it would bring great benefits to investigate the effect of different parameters on the flow uniformity in parallel tubes.

The object of the modelling is to do the simulation test at cold mode. The fundamental principal of fluid-to-fluid modelling criteria for the supercritical water may be applied for this purpose. It has been studied and developed for years. Researchers focus mainly on heat transfer modelling in supercritical working fluid tube with the supercritical working fluid-to-fluid modelling method. Represented by CHF(Critical Heat Flux) proposed by Barnett (Barnett et al.,1963), it has been developed with different methods, including Stevens-Kirby model (Stevens-Kirby et al.,1964), Ahmad model (Ahmad et al.,1973), Groeneveld model (Groeneveld et al.,1986) and Chen Changnian model (Chen et al.,2010). One of key issue is to select the test medium for the simulation at the designed test conditions, which many cases are at low pressure and temperature.

According to the fundamental principal of fluid-to-fluid modelling criteria, it requires the same dimensionless physical properties of fluids, system dimensionless time, equation constants and flow resistance coefficients between the actual facility and the model test system. The modelling coefficients and relationships may be obtained based on those principles. The size of the parallel tubes, the conditions and medium for tests can then be determined (Xu et al.,2017). The main calculation equations of the dimensionless number are given below.

(1) The dimensionless enthalpy $X_H = \frac{H_{pc,\ M}}{H_{pc,\ P}}$, where $H_{pc,\ M}$ and $H_{pc,\ P}$ represent the enthalpy at critical condition of the model and the prototype respectively. Temperature and pressure of the tests are determined by the equation.

(2) The dimensionless length $X_L = \left(\frac{G_M}{G_P}\frac{\rho_{pc,P}}{\rho_{pc,M}}\right)^2 = \frac{L_M}{L_P}$, where G is mass flow rate of the working fluid, ρ is flow density and L is the length of the tube. The length of the tubes is calculated by the equation.

(3) The dimensionless diameter $X_D = CX_L = \frac{d_M}{d_P}$, where C is friction coefficient, d is the diameter of the tube. The inside and outside diameter of the test tube are determined by the equation.

By the simulation, R-134a with low critical temperature and pressure was selected as the simulation medium. Table 1 gives the main modelling results.

Table. 1. Calculation results of experimental prototype and model

Item	Prototype, Water	Model, R-134a
Length (m)	23.5	1.1
The inner diameter (mm)	37	3
Thickness (mm)	10	1.2
Inlet temperature (K)	783	503
Pressure (MPa)	25.4	4.0
Mass flow rate (kg/m^2·s)	1400	500

Experimental System and Test Method

The experimental system was designed based on the modelling simulation results. Its diagram is shown in Fig. 1. The working fluid R-134a in its storage tank was first pressurized and heated to a test pressure and temperature by a pressure pump and an electric heater. It then enters the parallel tubes testing device shown in Fig. 2. Leaving from the testing device, the working fluid gathered together, released the pressure and returned to the recovery tank. Its mass flow rate was measured by a high-precision mass flow meter.

The parallel tubes testing device consists of 5 parallel tubes with same length and diameter. Each tube has a length of 1.1m, inner diameter of 3mm with 1.2mm thickness. Fives thermal-couples are installed on each tube to measure the temperature of tube wall as shown in Fig. 3. There are two types of flow inlet modes to simulate Z-type header (inlet 1 on Fig. 2) and L-type header (inlet 2 on Fig. 2) on the parallel tubes testing device.

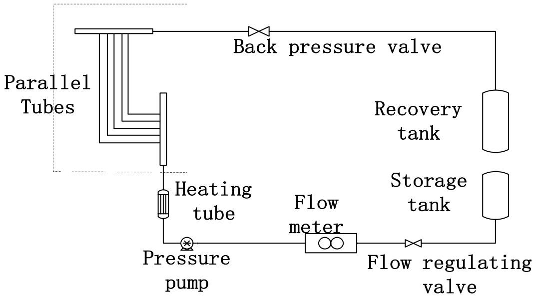

Fig. 1. Experimental system diagram

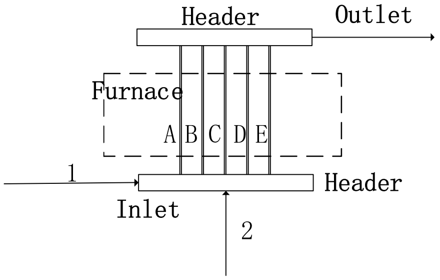

Fig. 2. The parallel tubes testing device

The parallel tubes testing device was located at the upper section of the CFB test rig, shown in Fig.4 (Zhou et al.,2012). Solids suspension density and superficial gas velocity were varied to investigate their influence on the flow uniformity in parallel tubes.

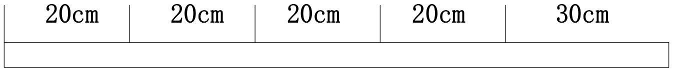

Fig. 3. Temperature measuring points on the testing device

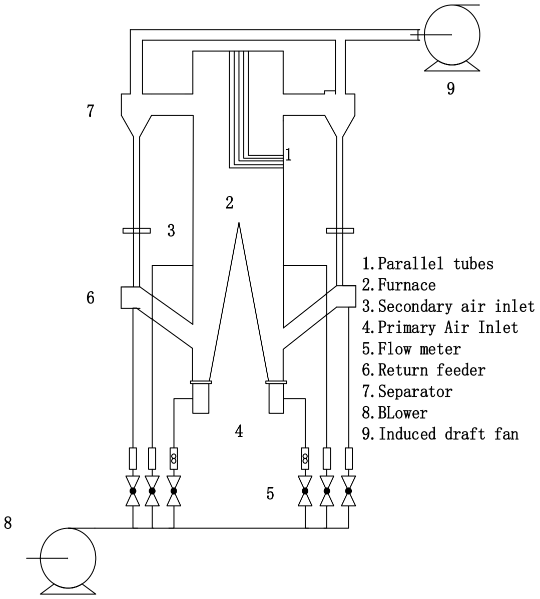

Fig. 4. CFB cold test rig

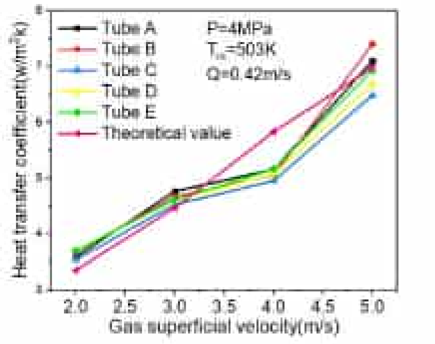

Fig. 5. Hear transfer coefficient of different tubes at only air running condition

The mass flow in each tube is calculated by Eq. (1).

$$c * m_i * (T_{in} - T_{out}) == h * A * (T_{air} - T_{surface}) \tag{1}$$

where c is specific heat of R-134a, $m_i = \rho S Q_i$ is mass flow rate of R-134a, T_{in}, T_{out} are the temperature of R-134a at the inlet and outlet of a tube. A is the heat transfer area. $T_{air}, T_{surface}$ are the temperature of the CFB and the surface of the tube.

h is the heat transfer coefficient between the tube and the bed. It is a function of solids suspension density, gas velocity and determined by the formula obtained in our previous work (Cheng, 1996)：

$$Nu_1 = 0.11 Ar^{0.12} Re^{-0.23} \left(\frac{\rho_s}{\rho_g}\right)^{-0.55} (1-\alpha)^{0.2} \left(\frac{D_a}{D_0}\right)^{-0.4} \tag{2}$$

where Ar is Archimedes number, Re is Reynolds number, ρ_s is solid suspension density, ρ_g is gas density, α is void fraction, H_a is height of parallel tubes and H_0 is the bed height.

The heat transfer coefficient between the working fluid and the tubes is determined by the formula (QT Zhou, 2009):

$$Nu_2 = 0.023Re^{0.8}Pr^{0.3} \tag{3}$$

where Pr is Prandtl number.

To study the flow uniformity in parallel tubes, a flow uniformity coefficient of each tube is defined by Eq. (4):

$$\varepsilon_i = \frac{Q_i}{Q_0}\left(i = A, B, C, D, E, Q_0 = \frac{1}{5}\sum_{i=A}^{E} Q_i\right) \tag{4}$$

Results and Discussion

The parallel tubes testing device was tested with only air at first to verify the accuracy of the experiment and measurement system. The heat transfer coefficient of the parallel tubes can be determined by the formula $Nu = 0.023Re^{0.8}Pr_{min}^{0.8}$ (Zhou.,2009) with measuring the temperatures on the tube wall and in the CFB bed. Fig. 5 shows the comparison of errors between the heat transfer coefficient measured and calculated. The errors are less than 15%. It proves that the test method is acceptable and the device performance is reliable.

Fig. 6 shows the flow uniformity coefficient of each tube varies with the fluid inlet temperature. It was done at the condition of 4MPa inlet pressure, 500kg/(m^2·s) mass flow rate of working fluid and 4.4kg/m^3 solid suspension density. The inlet temperature of the working fluid varies from 503K to 543K. Since the physical parameters of the working fluid, including thermal conductivity and viscosity coefficient change with fluid temperature, the heat transfer coefficient between the working fluid and the tubes are affected according to Eq. (3). Then the flow uniformity of the flow in the tubes varies.

Fig. 7 shows the flow uniformity coefficient variation of each tube with solid suspension density. As the solid suspension density increases, the heat transfer between the tubes and the CFB bed is enhanced. This results in increasing of the flow uniformity of the working fluid in the parallel tubes. When the solid suspension density increases from 3.9kg/m^3 to 10kg/m^3, the flow uniformity coefficients have greater changes compare to the suspension density below 10kg/m^3.

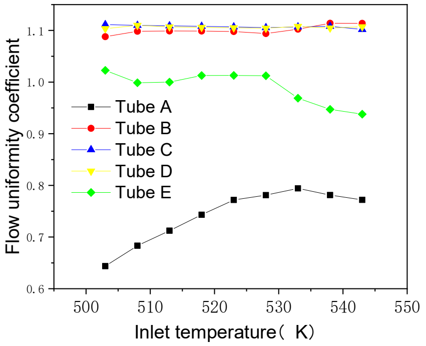

Fig. 6. Flow uniformity coefficient varies with inlet temperature of the fluid

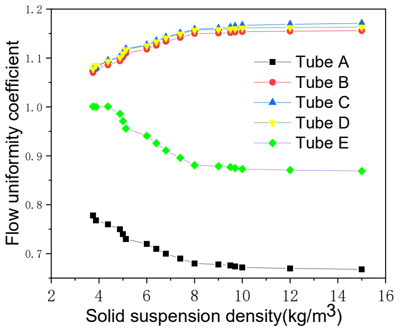

Fig. 7. Flow uniformity coefficient varies with solid suspension density

As shown in Fig.8, the flow uniformity decreases when the flow pressure increase from 3MPa to 4.3MPa. It should mentioned the R-134a is at subcritical state at 3MPa and supercritical state at 4.3MPa.When the fluid inlet pressure is at subcritical state, the influence of pressure on flow uniformity is more than that at supercritical state. When the inlet pressure is at supercritical state, the physical parameters of working fluid vary less with the increase of inlet pressure, which causing the flow uniformity varies less. This indicates the flow uniformity at supercritical state is closer to 1 compare to that at subcritical state.

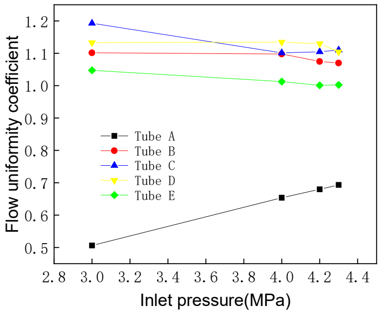

Fig. 8. The standard deviation of the flow uniformity coefficient at different pressures

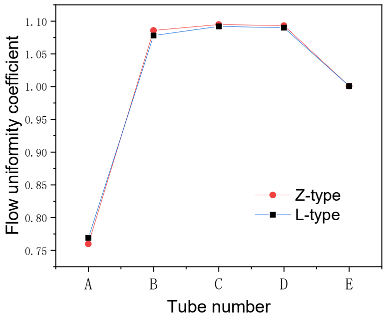

Fig. 9. The flow uniformity coefficient of different fluid inlet mode

Fig. 9 shows the comparison of the flow uniformity coefficient at two types of the fluid inlet mode, Z-type header and L-type header. Due to the symmetric flow in the L-type structure, the flow uniformity of L-type header is relatively uniform than that of Z-type header. The design of the flow for the panel is a important considering issure.

Conclusions

In this work, a novel measurement method to measure the superitical fluid flow uniformity in parallel tubes was developed based on a fluid-to-fluid modelling method. The following conclusions may be obtained through the work.

(1) The developed method based on a fluid-to-fluid modelling may be applied to investigate the superitical fluid flow uniformity in parallel tubes. In the fluid operating range of a supercritical CFB boiler, R-134a may be selected as the test working fluid to simulate the operation conditions;

(2) The main factors affecting the flow uniformity of the working fluid in the tubes include the heat transfer inside, outside of the tube and the pressure drop inside the tube;

(3) The flow uniformity of the tubes tends to 1 as the fluid inlet temperature increases and gradually leave 1 as the solid suspension density increases;

(4) The flow uniformity at supercritical state is closer to 1 compare to that at subcritical state;

(5) The flow uniformity coefficients of the tubes located at side were affected stronger. This suggests more attention should be paid to those tubes located at the side of the suspended panel.

(6) The flow uniformity of L-type header is relatively uniform than that of Z-type header. The design of the flow for the panel is a important considering issure.

Acknowledgements

This work is financially supported by the National Key Research & Development Program of China (No. 2016YFB0600202-2).

Notation

A	surface area, m^2	S	cross-sectional area, m^2
Ar	Archimedes number	T	temperature, K
C	friction coefficient	X_H,X_L,X_D	dimensionless number

c	specific heat capacity, kg/(kJ·K)	α	void fraction
D	height, m	ρ	density or concentration,kg/m^3
d	diameter, m	ε	flow uniformity coefficient
G	mass flow rate, kg/m$^{2\cdot}$s	$\sigma()$	standard deviation
g	gravitational acceleration, 9.81m/s^2	*Subscripts*	
H	enthalpy, kJ/kg	Air	environment
h	heat transfer coefficient, W/m^{2}k	i	tube number (i=A,B,C,D,E)
K	drag coefficient	in	inlet
L	length of tube, m	M	modeling parameters
m	mass flow rate, kg/s	min	minimum
Nu	Nusselt number	out	outlet
Pr	Prandtl number	0	average
△P	pressure difference, Pa	P	prototype parameters
Q	velocity, m/s	pc	critical point
Re	Reynolds number	surface	surface of tube

References

Ahmad S Y, Fluid to fluid modelling of critical heat flux:a compensated distortion model, International Journal of Heat and Mass Transfer, 1973, 16(3): 641-662.

Barnett P G, The scaling of forced convection boiling heat transfer, United Kingdom Atomic Energy Authority, Reactor Group, Atomic Energy Establishment, Winfrith, Dorset, England, 1963.

Chang Nian Chen, Ji-Tian H, Li S, et al., Extension of Fluid to Fluid Modeling Similarity Law for Critical Heat Flux, Atomic Energy Science and Technology, 2010, 44(5): 558-561.

LM Cheng., Heat transfer in a Circulating Fluidized Bed and a Pressurized Circulating Fluidized Bed, Zhejiang University, 1996: 51-55.

LM Cheng, LJ Xu, YF Xia, et al., Key Issues and Solutions in Development of the 600MW CFB Boiler, Proceedings of the CSEE, 2015, 35(21): 5520-5532.

Groeneveld D C, Cheng S C, Doan T, AECL-UO critical heat flux lookup table, Hear transfer Engineering,1986, 7(1-2): 46-62.

Stevens G F, Kirby G J, A quantitative comparison between burn-out data for water at 1000 Ib/in 2 and Freon 12 at 155 Ib/in 2(abs) uniformly heated round tubes, Vertical upflow, United Kingdom Atomic Energy Authority, 1964.

LJ Xu, Numerical model development of an ultra/supercritical circulating fluidized bed boiler, Ph D thesis, Zhejiang University, 2017.

QT Zhou, Principles of boiler, China Electric Power Press, 2009, Beijing.

XL Zhou, LM Cheng, QH Wang, ZY Luo, KF Cen, Non-uniform distribution of gas-solid through six parallel cyclones in a CFB system: an experimental study, Particuology, 2012, 10: 170-175

A NEW METHOD FOR CALIBRATION OF RADIOACTIVE PARTICLE TRACKING SYSTEMS USING COMPUTATIONAL FLUID DYNAMICS AND MONTE CARLO SIMULATION DATA

Guilherme Lindner[*], **Sanja Miskovic**

Norman B. Keevil Institute of Mining Engineering, University of British Columbia, Vancouver, Canada

**Email: glindner@student.ubc.ca*

Abstract

The Radioactive Particle Tracking (RPT) is a non-invasive flow monitoring technique used extensively in the past to monitor fluidized bed reactors. The accuracy of the RPT method is highly dependent on the size and quality of the calibration data, that can be obtained by using Monte Carlo (MC) simulations. However, in typical applications, the MC method does not consider fluidized bed media's dynamic behavior, where the gamma attenuation profile changes due to spatiotemporal variability of solids void fraction. A new method to augment the standard RPT calibration procedure by leveraging results of Computational Fluid Dynamics (CFD) simulations is proposed in this work. The new workflow aims to better capture the flow conditions of a gas-solid fluidized bed and enable a more accurate estimation of the tracer particle trajectory. In each time step, the particle positions from CFD simulation using the Multiphase particle-in-cell (MP-PIC) method are treated as the attenuation media in the MC simulation. The tracer position reconstruction is accomplished using calibration data from MC simulations and the Support Vector Regression algorithm. We show that the proposed method yields significantly better accuracy than the standard MC approach using the assumption of continuous attenuation media.

Introduction

Radioactive particle tracking is a non-invasive flow measurement technique that reconstructs a trajectory of a dynamic tracer particle carrying a gamma-emitting radionuclide. Initially developed by Lin et al. (1985), the technique has a distinct advantage of working with opaque media (Larachi et al., 1997). Using RPT, the tracer particle's Lagrangian path can be used to calculate many critical flow characteristics, such as mean and instantaneous velocities, turbulent properties, and high order statistics.

The basic principle of RPT comes from the fact that the radionuclides in the tracer element release their excess amount of energy by emitting alpha, beta, and gamma rays. The number of gamma rays recorded by a detector depends on the distance between the gamma source and the detector and the media's density between them. This particular feature is explored in RPT, where multiple scintillation detectors surrounding the monitored domain are used to discern the tracer's position as it is moving through the domain. The tracer's reconstructed position accuracy relies on the availability of the high-resolution calibration data, which must be generated each time the reactor design, detector type, or detector placement is changed. The calibration data is collected experimentally by placing the tracer at known locations within the monitored domain. In ideal conditions, the reactor must be operating during the calibration to capture the media's true attenuation profile. The manual calibration is, hence, time-consuming and limited by the geometry and operating conditions of the reactor.

Another method that can be applied to generate the calibration data is by running Monte Carlo (MC) gamma transport simulations using the technique proposed by Beam et al. (1978). The reactor materials and geometry can be modelled accurately using high energy physics software such as Geant4 or MCNP for multiple different source locations for a given detector array configuration. Once available, the calibration data can be used by many reconstruction algorithms.

To reduce the deviation between the true and the reconstructed trajectory, we propose a new method for the collection of accurate calibration data that considers attenuation media extracted directly from CFD simulations. The method enables simulation of true reactor's geometry, density profile, and dynamic behavior. The paper aims to briefly present the workflow of the new method and demonstrate its benefits.

Methodology

The proposed methodology for RPT calibration data collection and tracer position reconstruction can be divided into three main stages: (i) CFD simulation of the fluidized bed, (ii) MC simulation of gamma interaction with the matter, and (iii) experiments with a small number of calibration points followed by the RPT measurements in operating reactor. In the current work, the validation stage is done using numerical simulations, where experimental output (raw counts from the scintillation detectors) is replaced by the counts obtained from an independent MC simulation using a single particle trajectory of a randomly selected particle from the CFD simulation. A rectangular fluidized bed with dimensions of 0.23x0.076x1.2 m from the NETL's SSCP I challenge problem (Gopalan & Shaffer, 2012) is used as the study domain. The overview of the proposed methodology is shown in Fig. 1, where the blue, green and orange boxes represent the main input, process, and output tasks, respectively.

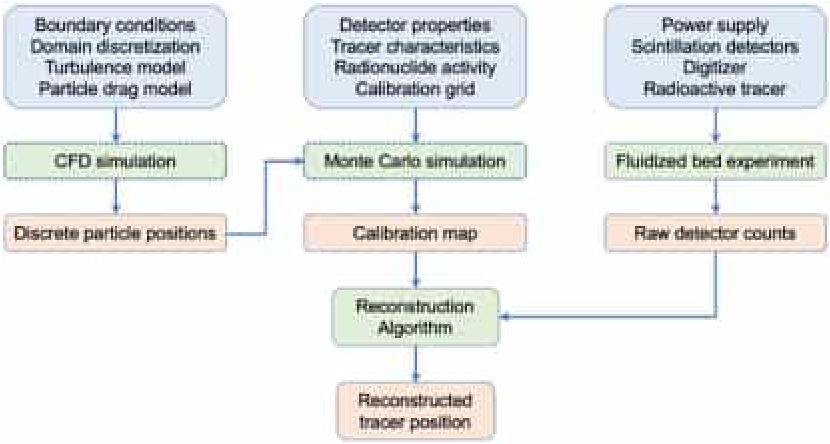

Fig. 1. Flowchart of the new RPT calibration data collection method using both CFD and MC simulations.

CFD Simulation - MPPIC

The CFD simulation is carried out using the MP-PIC method implemented in OpenFOAM that assumes an incompressible fluid phase and a Lagrangian framework for the solids phase. Here, the particle phase is described by a probability distribution function, $\phi(x, u_p, \rho_p, \Omega_p, t)$, which indicates the probability of finding a particle with a velocity u_p, particle density ρ_p, particle volume Ω_p at location x and time t. More details on the implementation of the model can be found in the work of Snider et al. (1998).

Gas-solid fluidization of 90350 glass spheres with 3 mm diameter at fluidization velocity of 2.17 m/s is modeled. A structured mesh with 80000 elements with no wall refinement was used.

MC Simulation – Calibration Data Generation Method

The MC simulation uses the same geometry as the CFD case with the addition of an array of 32 scintillator detectors positioned around the reactor and 6.35 mm thick acrylic walls. Each scintillation crystal is modelled as Thallium doped Sodium Iodide NaI(Tl). The detectors are identical with crystals' dimensions of 57 mm in length and 38 mm in diameter and 1 mm thin aluminum shield. Fig. 2 shows the modeled geometry with positioning of the detectors and fluidized glass beads.

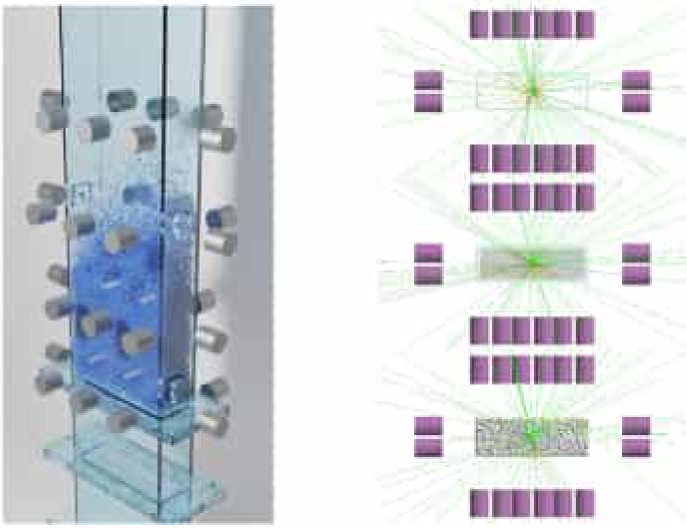

Fig. 2. Isometric view of the fluidized bed reactor geometry (left) and top view of raw output of the MC simulation for the air, glass and discrete media scenarios (right).

Three different calibration scenarios are compared: a) empty reactor (filled with air), b) solid glass media, and c) discrete media from CFD simulation. For all scenarios, the calibration grid consists of 3264 equally spaced points (15 mm apart; square array), which are placed inside the reactor. The gamma-emitting radionuclide chosen for the MC simulations is Sc-46. The activity of the source in each grid position is taken to be 2x10^6 Bq. The ground truth trajectory is comprised of 5000 source locations corresponding to an acquisition rate of 50Hz over the period of 100 seconds.

Fluidized Bed Experiment – Tracer Trajectory Reconstruction Method

A typical RPT experiment can last for more than 16 hours, which allows the radioactive tracer to travel through most of the domain improving the overall statistics and accuracy of the calculated flow properties. In our case, due to the numerical aspect of the work, the particle positions are collected over the period of 100 seconds at a rate of 50 Hz. The numerical setup uses the same reactor design as the calibration scenario c).

The SVR reconstruction algorithm, proposed by Yadav et al. (2019), is implemented and used to convert the counts collected by the detectors to spatial coordinates (x, y and z) of the tracer. In the current application, the calibration data serves as the training sample, while the dataset representing validation trajectory is used as the testing sample in the SVR model.

To investigate the influence of the type of the calibration maps on the accuracy of the reconstructed tracer positions, the mean Euclidian distance error (MEDE) is calculated and compared at *n* positions (Eq. 1), where index v represents the ground truth coordinate and r index represents the reconstructed coordinate.

$$MEDE = \frac{\sum_{i=1}^{n} \sqrt{(x_v^i - x_r^i)^2 + (y_v^i - y_r^i)^2 + (z_v^i - z_r^i)^2}}{n} \tag{1}$$

We also compare the standard deviation, σ, for each coordinate *k*, which is calculated as:

$$\sigma_k = \sqrt{\frac{1}{n}\sum_{i=1}^{n}(x_i - \bar{x})} \tag{2}$$

where $x_i = |k_v - k_r|$ representing the difference between the ground truth validation and the reconstructed value for each coordinate.

The sojourn time distribution (STD) for different regions of the reactor is also calculated. Following the methodology of Rammohan et al. (2000), the reactor volume containing glass beads is divided into five identical subdomains along the vertical axis. To create the STD curve, all particle positions are scanned and assigned to the correspondent subdomain. Each time the particle enters and leaves the subdomain is considered as a new occurrence, and the residence time is stored. The sojourn time of each occurrence is calculated as follows:

$$t_{soj} = N\Delta t \tag{3}$$

where N is the number of recordings of the tracer particle inside the specific subdomain and Δt is the length of the acquisition time step (0.02 s for 50Hz). The first moment of the STD is calculated for each subdomain, i, as described in Eq. 4. n_{max} refers to the maximum number of occurrences of the tracer particle in subdomain i, t_{soj_j} is the sojourn time for each passage j, and $E_i(t_{res\_j})$ is the probability density function (PDF) of the STD of the same subdomain.

$$\mu_i = \sum_{j=1}^{n_{max}} t_{\mathrm{soj}\_j} E_i(t_{res\_j})\,\Delta t \tag{4}$$

Results

Fig. 3 shows the glass beads distribution and their velocity magnitude at two different times: 5 and 10 seconds. The beads remain concentrated forming a dense bed at the lower part of the reactor over the full duration of the experiment, while the upper section is occupied by the fast-moving fluidized beads. To better visualize the dynamic changes of the density profile of the system, air void fraction in the mid plane of the reactor is also shown. It should be noted that this significant spatiotemporal variability of the fluidized bed density gradient is the crucial factor controlling the attenuation of the gamma rays during RPT experiments.

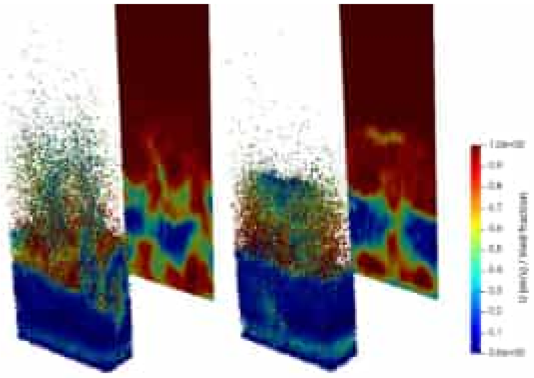

Fig. 3. Gas-solid fluidization of 90350 glass beads at two times minimal fluidization velocity (front) and centerline air void fraction (back) at 5 and 10 seconds.

The position of all glass beads in each time step is extracted and used as the attenuation media in MC simulations for the calibration scenario c). A single random particle is selected from the population and treated as the tracer for the validation case. The three distinct media scenarios, Air, Glass and Discrete Media, are simulated using the MC approach for 3264 calibration grid positions.

The trajectory reconstruction error for the three different calibration maps is shown in Table 1. The σ at all three directions and MEDE errors are both shown. The error using air or glass as continuous attenuation media is shown to be significantly higher than for the Discrete media scenario. An additional case was considered where the SVR model was trained using combined data from both Air and Glass MC simulations. Interestingly, the combined approach is shown to significantly improve the reconstruction error when compared with each individual base-case.

Table 1. MEDE and standard deviation of each calibration map.

Measure, mm	**Air**	**Glass**	**CFD**	**Air+Glass**
σ_x	2.65	3.02	0.62	1.52
σ_y	3.53	3.23	0.55	0.99
σ_z	5.23	5.61	1.02	5.77
MEDE	10.64	10.02	1.52	7.71

The ground truth (validation) and reconstructed trajectories for the Discrete media case are shown in Fig. 4. A small deviation between the two datasets can be observed. The greatest error is present at the reactor's extremities, where the distant detectors don't contribute much to the reconstruction. The trajectory at the center of the reactor, which has most detectors at the optimal distance, shows the lowest deviation from the true path. This conclusion can be further confirmed by observing the trend in σ for all three coordinates in Table 1. Here, σ_z is almost twice as large as σ_x and σ_y, which is due to concentrated placement of the detectors along XY planes only. Better distribution of the detectors along vertical direction could minimize the error, but generally, the reconstruction errors at the reactor extremes can be expected to be greater than in the middle of the reactor.

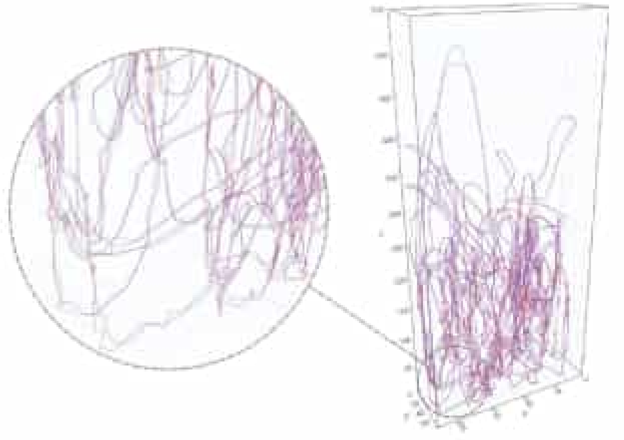

Fig. 4. Perspective view of the reconstructed trajectory (red line) compared to the real trajectory (blue line) using the Discrete media case over 100 s.

By calculating the probability density function (PDF) of the STD data for both ground truth and reconstructed trajectory (scenario c), we can notice that the previously reported reconstruction errors do not contribute significantly to the errors of the critical average statistics. In Fig. 5, the solid lines represent the PDF of STD calculated from the ground truth trajectory, while the dashed lines represent the same metric using the reconstructed trajectory data.

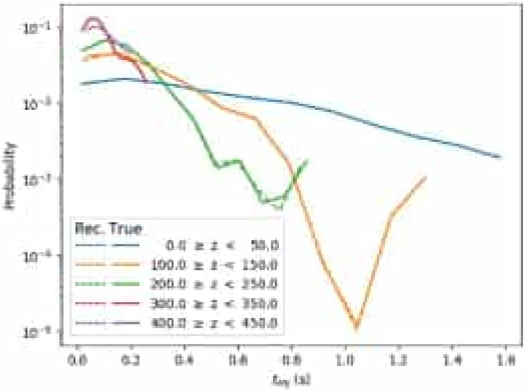

Fig. 5. Probability density functions of the STD in five distinct subdomains of the reactor. Dashed lines represent the reconstructed trajectory, while the solid lines represent the ground truth data.

Conclusion

A new method for calibration of RPT experiments is presented, which was shown to reduce the error of the standard calibration approach, where calibration data is collected experimentally in a simplified phase distribution or in an empty reactor over a sparse calibration grid. In typical RPT applications, the MC method does not consider fluidized bed media's dynamic behavior, where the gamma attenuation profile changes due to spatiotemporal variability of solids void fraction. This method was improved by using information from the CFD simulation, which is capable of capturing actual reactor's geometry, media density profile, and dynamic behavior of the gas-solid fluidization. We show that a better RPT calibration map can be created by considering the attenuation media's accurate profile.

In each time step, the particle positions from CFD simulation using the Multiphase particle-in-cell (MP-PIC) method are treated as the attenuation media in the MC simulation. The fluid velocity field information of the CFD simulation is not necessary for the MC method, reducing the need for a high-resolution flow description. Three limit cases of attenuation media are compared in this work: air, solid glass, and CFD-obtained fluidized bed media structure, to evaluate their effect on the accuracy of the reconstructed tracer position. The tracer position reconstruction is accomplished using calibration data from MC simulations and the Support Vector Regression (SVR) algorithm. The trajectory of a randomly selected particle from the CFD simulation is used for reconstruction error estimation. We show that the proposed method yields significantly better accuracy than the standard MC approach using the assumption of continuous attenuation media. The average statistics are not much affected by a small variation in the instantaneous tracer position, so identifying average flow and reactor properties, such as dead zones or short-circuiting, does not seem to be affected by the reconstruction error.

By combining both Air and Glass calibration data as a training set for the SVR reconstruction model, we demonstrated that it is possible to reduce reconstruction errors compared with the individual calibration set. The combined approach is still inferior to the case where MC simulations are run to collect calibration data considering discrete media obtained from CFD simulations.

References

Beam, G. B., Wielopolski, L., Gardner, R. P., & Verghese, K. (1978). Monte Carlo calculation of efficiencies of right-circular cylindrical NaI detectors for arbitrarily located point sources. *Nuclear Instruments and Methods*, *154*(3), 501–508.

Gopalan, B., & Shaffer, F. (2012). A new method for decomposition of high speed particle image velocimetry data. *Powder Technology*, *220*, 164–171.

Larachi, F., Chaouki, J., Kennedy, G., & Dudukovic, M. P. (1997). Chapter 11 - Radioactive particle tracking in multiphase reactors: Principles and applications. In J. Chaouki, F. Larachi, & M. P. Duduković (Eds.), *Non-Invasive Monitoring of Multiphase Flows* (pp. 335–406). Elsevier Science B.V. https://doi.org/10.1016/B978-044482521-6/50012-7

Lin, J. S., Chen, M. M., & Chao, B. T. (1985). A novel radioactive particle tracking facility for measurement of solids motion in gas fluidized beds. *AIChE Journal*, *31*(3), 465–473.

Rammohan, A. R., Kemoun, A., Al-Dahhan, M. H., & Dudukovic, M. P. (2000). A Lagrangian description of flows in stirred tanks via computer-automated radioactive particle tracking (CARPT). *Chemical Engineering Science*, *56*(8), 2629–2639.

Snider, D. M., O'Rourke, P. J., & Andrews, M. J. (1998). Sediment flow in inclined vessels calculated using a multiphase particle-in-cell model for dense particle flows. *International Journal of Multiphase Flow*, *24*(8), 1359–1382.

Yadav, A., Pant, H. J., & Roy, S. (2019). Velocity measurements in convective boiling flow using Radioactive Particle Tracking (RPT) technique. *AIChE Journal*, *0*(ja), e16782.

EFFCT OF NOISE IN ELECTRICAL CAPACITANCE TOMOGRAPHY MEASUREMENTS OF FLUIDIZED BED HYDRODYAMICS

Kai Huang[1,2], Shuanghe Meng[1], Jingjing Shen[1,2], Mao Ye[1,*] and Zhongmin Liu[1]

[1] *Dalian National Laboratory for Clean Energy and National Engineering Laboratory for MTO, Dalian Institute of Chemical Physics, Chinese Academy of Sciences, Dalian 116023, China*

[2] *University of Chinese Academy of Sciences, Beijing 100049, China*

*Email: *maoye@dicp.ac.cn*

Abstract

Electrical capacitance tomography (ECT) are widely used in the fluidized bed measurements and noise is inevitably happening during measurements. However, there were little researches focusing the evaluation of noise effect on measurements. In this study, noise distribution and effect on the reconstructed solid fraction by two representative algorithms (Linear Back Projection, Projected Landweber iteration) were studied. Benchmarks which based on the computation of correlation coefficients between solid fractions with different noises and solid fraction without noise were identified for these two algorithms, which can be regarded as a standard when designing an ECT sensor in the fluidized bed measurements.

Introduction

Gas-solid fluidized beds are widely used in chemical industry, such as methanol-to-olefins (MTO), fluidized catalytic cracking (FCC) and so on (Bai et al., 2018; Tian et al., 2010). Understanding the hydrodynamics of fluidized bed is important for the fluidized bed design, optimization and accurate simulation. Many methods have been used in the fluidized bed measurements which are classified into intrusive and non-intrusive measurements (Werther, 1999). Electrical capacitance tomography is one of the master non-intrusive methods which is widely used in the fluidized bed measurements (Makkawi and Wright, 2002). The principle of ECT measurements is attributed to solid fraction distribution variation which induces the variation of relative permittivity distribution and causes the variation of measurement capacitance. The measurement capacitance is then used to reconstruct the relative permittivity distribution which is converted to solid fraction distribution in fluidized bed through specific algorithms (Makkawi and Wright, 2002; Yang and Peng, 2003). It is well-known that number of elements of measured capacitance vector is much less than the number of reconstructed pixels in the measurement zone which is an ill-posed problem. For example, in a 12-electrodes sensor, the capacitance vector of 66 * 1 dimension is usually used to reconstruct relative permittivity distribution of 3228 *1 dimension in the measurement zone. Therefore a small variation of measurement capacitance vector will have significant effect on the reconstructed permittivity distribution. In ECT measurements, noise is inevitably happening which will cause measurement error during the reconstruction process. However, there were little researches talking about noise effect (Yang and Peng, 2003) and there was no research studying noise effect on the reconstruction of relative permittivity distribution.

Therefore, in this paper, noise effect on the reconstruction of relative permittivity distribution is studied and benchmarks which could ignore noise effect are identified for two representative algorithms. All measurement data are based on the fluidized bed measurements by a 12-eleoctrdes sensor.

Noise distribution

Fluidized bed measurements are first conducted in a 6.5 cm diameter fluidized bed from packed bed to slugging bed which could represent typical solid distributions in the fluidized bed as shown in Fig. 1(a). The noise distribution is measured from 20000 measurements of packed bed. Fig. 1(b) shows the noise distribution of a specific electrode-pair as an example. It is shown that noise distribution fits the Gaussian distribution and the bandwidth is related to signal-to-noise ratio which is used to measure the level of desired signal to the level of background noise. The definition is shown below,

$$SNR_m = 20\, log_{10} \sqrt{\frac{\sum_{i=1}^{Q} \lambda_{mi}^2}{\sum_{i=1}^{Q} (\lambda_{mi} - \overline{\lambda_m})^2}} \tag{1}$$

where λ_{mi} is the relative capacitance of i_{th} frame of m_{th} electrode pair, $\overline{\lambda_m}$ is the average normalized capacitance of all frames of the m_{th} electrode pair, Q is the number of frames, i.e. 20000. SNR_m is the SNR of the m_{th} electrode pair.

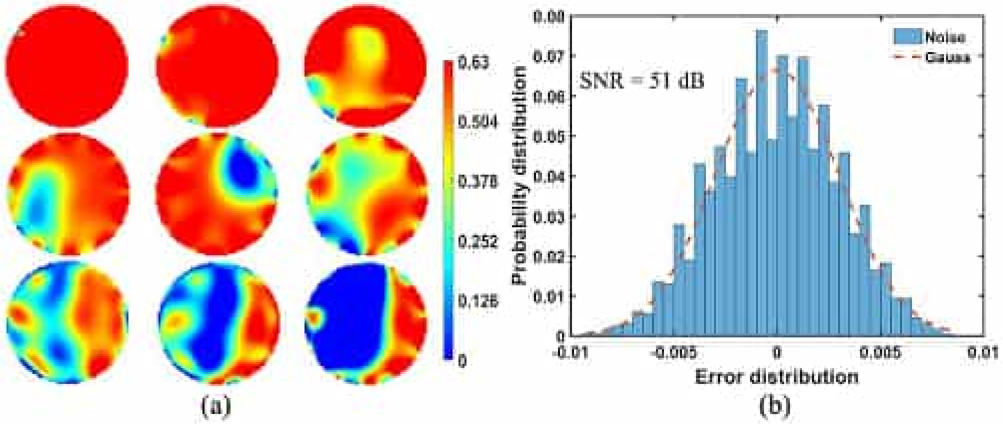

Fig. 1. (a) Typical solid fractions from fixed bed to slugging bed. (b) Noise distribution of one electrode pair.

Noise effect evaluation

As the noise distribution fits the Gaussian distribution very well, different SNR levels noises could be added to the measurement results. Then noise effect on the reconstructed relative permittivity (i.e. solid fraction) could be studied. The procedure to identify the noise effect is described below.

1. Data from fluidized bed measurements at different superficial velocities were added different SNR levels noises, from 10 dB to 70 dB.
2. Same algorithms were used to reconstruct solid fraction distributions from the data with different SNR levels noises.
3. Solid fraction distributions from the data with different SNR levels noises were compared using correlation coefficient to show noise effect.
4. Benchmarks were obtained from the statistical results of correlation coefficients of different algorithms.

The linear back-projection algorithm (LBP), which is suitable for real-time measurements and the projected Landweber iteration algorithm (Yang and Peng, 2003) which is suitable for off-time measurements and has higher accuracy are used to study noise effect on the reconstruction results. The LBP algorithm is shown in Eq. (2),

$$\hat{g} = S^T \lambda / S^T u_\lambda \tag{2}$$

where g is solids fraction, S is the sensitivity distribution matrix, λ is the relative capacitance and u_λ is an identity vector. The division of the two vectors is defined as one numerator component being divided by the corresponding denominator component. The Landweber iteration algorithm is shown in Eq. (3) – (5),

$$\widehat{g_0} = S^T\lambda \tag{3}$$

$$\widehat{g_{k+1}} = P[\widehat{g_k} - \alpha S^T(S\widehat{g_k} - \lambda)]$$

(4)

$$P[x] = \begin{cases} 0 & if \quad x < 0 \\ x & if \quad 0 \le x \le 1 \\ 1 & if \quad x > 1 \end{cases}$$

(5)

where α is relaxation factor, i.e. 2 in this study. P is the function operator and the property is defined in Eq. (5). The iteration number is set to 10. Correlation coefficients were used to compare between solid fractions reconstructed by data with different SNR levels noises. The definition is shown below.

$$r = \frac{\sum_{i=1}^{N}(g1_i - \overline{g1})(g2_i - \overline{g2})}{\sqrt{\sum_{i=1}^{N}(g1_i - \overline{g1})^2(g2_i - \overline{g2})^2}} \tag{6}$$

where g1, g2 are two different solid fraction distributions, r is the correlation coefficient between g1 and g2, N is the dimension of solid fraction distribution, i.e. pixel number in the measurement zone and the value is 3228. In the computation of correlation coefficients, solid fraction distribution obtained from data without noise is set as the base.

Fig. 2 shows the correlation coefficient distributions obtained from above mentioned algorithms in different noise levels. In each noise level, 260 data were presented although 50000 data were obtained.

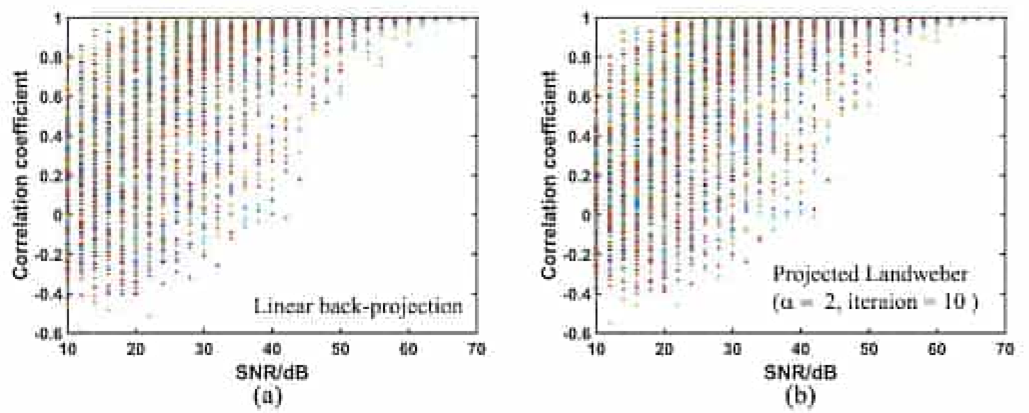

Fig. 2. (a) Correlation coefficient distributions of LBP algorithm in different SNR levels, (b) Correlation coefficient distributions of Projected Landweber algorithm ($\alpha = 2, iteraion = 10$) in different SNR levels.

It is obtained that correlation coefficients are converged to one with the increase of SNR (i.e. decrease of noise). Therefore, it is natural to study probability when correlation coefficient is bigger than set value in different noise levels. Before computing probabilities, sample number effect on the relative frequency should be studied.

Fig. 3 shows the variation of relative frequencies when correlation coefficient exceeds 0.99 of two algorithms with sample numbers in five SNR levels as an example. It is shown that when sample number is beyond 35000, the relative frequencies become stable and it can be regarded as the probability. Therefore 35000 sets of data were used to obtain the probability when the correlation coefficient is bigger than set value in different SNR levels. Besides as the probability when correlation coefficient exceeds set value is obtained, the benchmark of noise level could be assigned which depends on our requirement of accuracy. For example, if we want the probability which ensures correlation coefficient exceeds 0.995 is bigger than 0.995, the SNR value should exceed 58 dB for LBP algorithm. Therefore 58 dB can be regarded as the benchmark if the required probability which ensures correlation coefficient exceeds 0.995 is 0.995. If the benchmark is assigned as the required probability which ensures correlation coefficient exceeds 0.995 is 0.995, the results of SNR value for above algorithms can be seen in Table 1. It is obtained that SNR value is high if we want to maintain same solid fraction distribution with the value of noise free. In the next work, we will study noise effect on the fluidized bed hydrodynamics measurements.

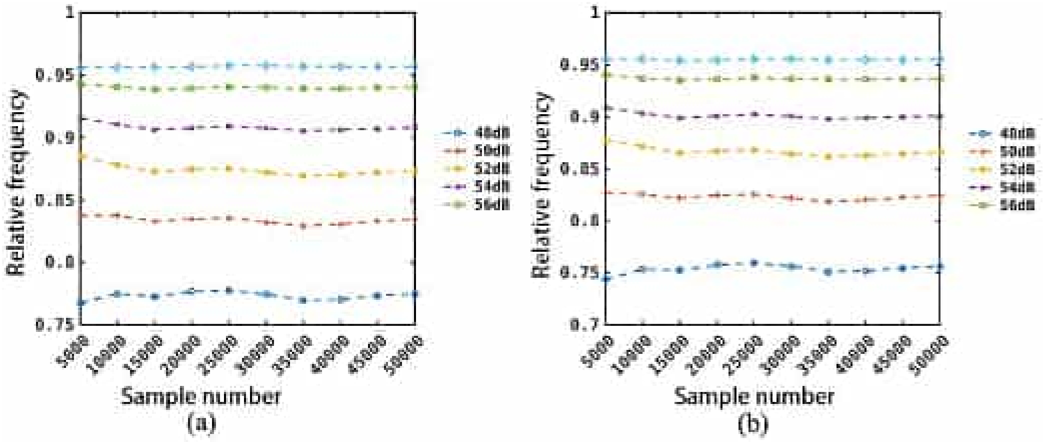

Fig 3. Variation of relative frequencies that ensure correlation coefficient exceeds 0.99 with different samples of (a) LBP algorithm, (b) Projected Landweber iteration ($\alpha = 2, iteraion = 10$) algorithm.

Table 1. Benchmarks (Probability > 0.995) that ensure correlation coefficient exceeds 0.995.

Algorithm	Benchmark/dB
LBP	58
Projected Landweber iteration($\alpha = 2, iteraion = 10$)	58

Conclusion

In this paper, noise distribution of ECT measurements which fitted the Gaussian distribution very well was first identified. Then Gaussian distribution noise is added to the ECT measurement results in different SNR levels and noise effect on solid fraction distributions based on two representative algorithms (LBP, Projected Landweber iteration) was studied. It is obtained that when sample number is bigger than 35000, results of relative frequency in different SNR levels can be regarded as probability value. The benchmark is assigned from our requirement of accuracy. An example of benchmarks of two algorithms was also presented.

Notation

S	normalized sensitivity matrix	g	solid fraction
λ	normalized capacitance vectors	α	relation factor, 2
N	number of pixels in measurement zone, 3228	P	Function operator
r	correlation coefficient	^	reconstructed value
-	Average value		

Acknowledgment

We are grateful to the National Key Research and Development Program of China (Grant No. 2018YFB0604904) and the National Natural Science Foundation of China (Grant No. 91834302).

References

Bai, P., Etim, U. J., Yan, Z., Mintova, S., Zhang, Z., Zhong, Z., Gao, X. Fluid catalytic cracking technology: current status and recent discoveries on catalyst contamination. Catal. Rev. 2018, 61, 333.

Makkawi, Y. T., Wright, P. C. Fluidization regimes in a conventional fluidized bed characterized by means of electrical capacitance tomography. Chem. Eng. Sci. 2002, 57, 2411.

Tian, P., Wei, Y., Ye, M., Liu, Z. Methanol to Olefins (MTO): From Fundamentals to Commercialization. ACS Catal. 2015, 5, 1922.

Werther, J. Measurement techniques in fluidized beds. Powder Technol. 1999, 102, 15.

Yang, W. Q., Peng, L. Image reconstruction algorithms for electrical capacitance tomography. Meas. Sci. Technol. 2003, 14, R1.

BUILDING A TRAINING DATABASE FROM NUMERICAL SIMULATIONS FOR ARTIFICIAL NEURAL NETWORK TO RECONSTRUCT ECVT IMAGES

Carlos Montilla[1], Anass Majji[2], Ranem Nadir[2], Renaud Ansart[1], Emmanuel Cid[1], David Simoncini[2], Stephane Negny[1]

[1]Laboratoire de Génie Chimique, Université de Toulouse, CNRS, INPT, UPS Toulouse. France
[2]IRIT UMR 5505-CNRS, Université de Toulouse. France.

*Email: carlos.montillaestrella@toulouse-inp.fr

Abstract

The electrical capacitance volume tomography (ECVT) is an experimental technique capable of reconstructing the 3D solid volume fraction distribution inside a sensing region. This technique has been extensively used in fluidized beds as it allows to have access to data that is very difficult to obtain using other experimental devices. Recently, artificial neural networks have been proposed as a new type of reconstruction algorithm for ECVT devices. One of the main drawbacks of neural networks is that they need a database containing previous reconstructed images to learn from. Previous works have used databases with very simple or limited configurations that might not be well adapted to the complex dynamics of fluidized bed configurations. In this work, a strategy to build a training database fit for fluidized bed configurations is proposed. The solid volume fraction inside a fluidized is obtained by accurate 3D numerical simulations. Then, a linear approximation is used to simulate the capacitance measurements associated with those distributions. Using this database, we trained a neural network to be able to reconstruct images from an ECVT system. The reconstructed images produced by the neural network approach were very similar to the expected images, and the ANN's performance was comparable to the already existing algorithms.

Introduction

Nowadays, fluidized beds play a major role in many industrial processes. They offer numerous advantages as a great gas-solid mixing and uniform conditions inside the reactor. These characteristics are, however, extremely dependent on the internal behavior and dynamics of the fluidized bed. Due to their nature, it is very difficult to obtain experimental information inside the reactor. Probes and pressure taps provide only local information and could be intrusive and disturb the internal dynamics. Optical techniques are more difficult to apply due to the opaque properties of most particles and their refraction index. Furthermore, they are very difficult to implement in a 3D reactor. The Electrical Capacitance Volume Tomography (ECVT) is a measurement technique that addresses all these problems (Wang et al. 2010). This device is capable of reconstructing the internal 3D solid volume fraction distribution using only capacitance sensors located externally at the walls of the reactor. Therefore, it is a fully non-intrusive and non-invasive technique that can provide valuable information to characterize the reactor and to even validate the CFD simulations and mathematical models (Weber et al. 2013; Holland et al. 2009). The key parameter of the ECVT system is the reconstruction algorithm used to obtain the 3D solid volume fraction distribution from the capacitance measurements. Several propositions can be found in the literature. Recently, an approach using machine learning and artificial neural networks has been studied and it has proven to be very performant (Lei et al. 2018). Because they do not rely on an iterative algorithm to reconstruct the 3D image, they are much faster than classical reconstruction approaches. This makes them suitable when we need to process data in real-time or when the amount of images to process is very large. However, the accuracy of these approaches is directly linked to the training database used. Previous works have used very limited or simple datasets to train their neural network as they were more interested in the reconstruction algorithm itself and not in their application to fluidized beds. In this work, we present an approach that will allow us to build a training database suitable for fluidized bed reactors. We use accurate 3D numerical simulations to simulate a fluidized bed with an ECVT system. This will enable us to obtain a great amount of data of fluidized-bed-like patterns that can be used to train our neural network.

Electrical capacitance tomography

The Electrical capacitance tomography is a non-invasive and non-intrusive device capable of mapping the 3D solid volume fraction distribution inside a sensing region. It consists of a series of capacitance sensors placed around the interest volume. By measuring the m inter-sensor capacitances between all pairs of sensors, we can obtain an approximation of the α_p in a series of n predefined voxels inside the volume. Using the sensitivity matrix approximation, we can establish the following relationship between the capacitance vector and the solid volume fraction vector:

$$S\alpha_p = C \tag{1}$$

Here S is called the sensitivity matrix. Because n is usually larger than m, equation 1 cannot be solved. This shows that the ECVT reconstruction problem is ill-posed.

Numerous approaches can be found in the literature trying to approximate a solution for equation 1. The first approaches studied consisted mainly of optimization problems that needed to be solved using iterative methods (Warsito et al. 2001). Although these methods could be very accurate, the iterative process can be computationally expensive. Especially, if we need to analyze a large number of images, or if we need to obtain results in real-time. For this reason, a new type of algorithm has been developed using machine learning techniques. These approaches train artificial neural networks so they can learn how to reconstruct images coming from an ECVT system.

Artificial neural network as image reconstruction technique

An artificial neural network (ANN) is a set of nodes, called neurons, organized in inter-connected layers. In a feed-forward ANN, a signal transits through the network from the input layer to the output layer. Each edge transforms the signal by multiplying its value by a weight. The network can be trained so that its last layer outputs a desired signal for a given input signal in the first layer. To do so, a training data set containing pairs of input and output vectors of values is used. An input vector is propagated through the network, and the error between the predicted and expected output vector is measured via a loss function. The weights of the networks are subsequently modified by back-propagation so that the error is minimized (figure 1). The objective is, therefore, to build an ANN that accepts the capacitance measurements as input and gives the solid volume fraction inside the sensing region as outputs.

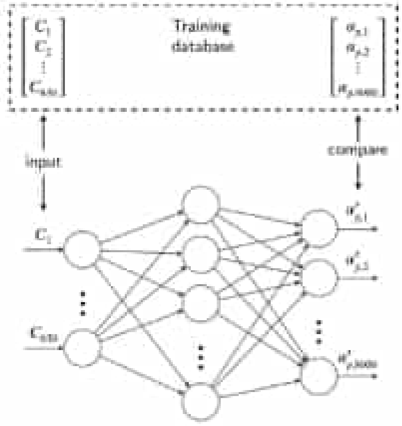

Fig. 1. Training algorithm scheme

To train a neural network, a training database containing different capacitance measurements and their corresponding 3D solid volume fraction distribution is required. This training database must contain information similar to the one we expect to reconstruct. Otherwise, the performance of the ANN might not be optimal. There are multiple ways to build this database. We could insert objects of known shape and solid volume fraction inside the sensing region of a real ECVT system and record the capacitance values. This would, however, be very time-consuming, and the database would be very limited in terms of object shape and solid volume fraction. Another option that has been used is to artificially generate 2D images with the most common flow patterns (stratified, annular, and core flows) and to simulate the capacitance measurements (Zheng et al. 2018). This allows us to generate a large number of different images to train our neural network. Nevertheless, we might not be able to accurately generate images corresponding to a 3D fluidized bed because the flow patterns are much more complex.

Here, a novel strategy to generate a training database for fluidized bed reactors is presented. Nowadays, our mathematical models and CFD software are very capable of accurately reproducing the global dynamics of a fluidized bed. The 3D solid volume fraction produced by these simulations can be extracted. Then equation 1 can be used to estimate the capacitance measurements associated with such distribution (figure 2). In this way, the high precision of the current software packages is used to generate a training dataset with images that correspond to the real complex dynamics of a fluidized bed.

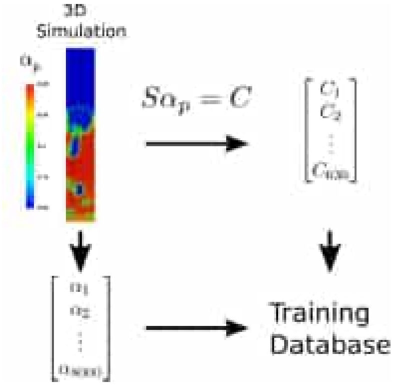

Fig. 2. Strategy to generate the training database for an ANN

For this study, the software NEPTUNE_CFD is used. This is a multiphase Euler-nfluid code developed in the framework of the NEPTUNE project financially supported by CEA, EDF, IRNS, and Framatome. This code has been extensively validated using very accurate experimental techniques (Ansart et al. 2017; Sabatier et al. 2020). A 1m height and 10cm diameter fluidized bed is simulated. The solid phase are glass beads of 250μm diameter and 2,700kg/m^3 The gas phase is air at ambient conditions. 4 different inlet velocities were tested; from $3U_{mf}$ to $7U_{mf}$, where U_{mf} is the minimum fluidization velocity given the Ergun's correlation. For each velocity, 30 seconds of physical time were simulated and the solid volume fraction distribution in a region between 6cm and 16cm from the bottom of the fluidized bed is saved each 0.01 seconds. In total, the final training database contained 12,000 different pairs of C / α_p. The sensitivity matrix used in this study comes from a real ECVT device acquired from Tech4Imaging. This tomograph has 36 capacitance plates and the sensing region is a cylinder of 10cm height and 10cm diameter. The reconstructed image is composed of 8,000 cubic voxels of 5mm in length. Finally, a feed-forward artificial neural network was built using the software Keras with Tensorflow as the backend. The neural network consists of one input layer of 630 neurons (one neuron per inter-plate capacitance value); three hidden layers of 1024, 2048, and 4096 neurons each; and one output layer of 8000 neurons (one neuron for each output voxel). The hidden layers used a ReLU activation function, while the output layer uses a scaled sigmoid function to ensure that the output is always bounded between 0 and 0.64.

Results

The neural network was trained using the database generated as described above. Before training, the database is split into 2 smaller sub-sets. A first subset, called the training set, on which we will apply the training algorithm. And a second subset, called the validation set, which will not be used to train the ANN, instead it will be used to quantify the accuracy of the ANN for data that has not been used for training. The training set consists of 80% of the original database, and the validation set is the remaining 20%. To monitor the convergence of the algorithm during the training phase, we monitor the root mean squared error (RMSE) between the predicted (α'_p) and the expected (α_p) solid volume fraction.

$$RMSE_{\alpha_p} = \frac{1}{8000}\sqrt{\sum_{i=1}^{8000}\left(\alpha_p - \alpha'_p\right)^2} \tag{2}$$

The training algorithm will iterate over each entry of the training database until a certain criteria is met or until the error converges to a value. When the algorithm reaches the end of the database it restarts from the first entry. The evolution of the error is shown in figure 3. As we can see, the error between the ANN prediction and the expected solid volume fraction decreases, for both the training and the validation set. This figure shows that the neural network is learning to accurately reconstruct images of an ECVT system. The fact that error in the validation dataset is also decreasing shows that the ANN generalizes well to data that is not being used for training purposes.

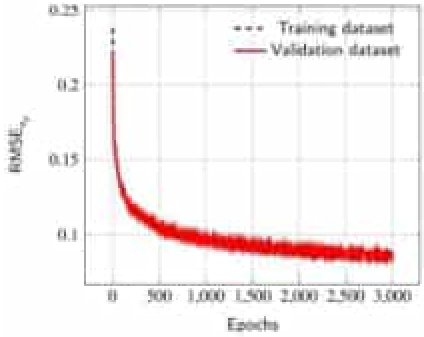

Fig. 3. Root mean square error during the training phase as a function of epochs (one epoch is defined as the iteration over all entries in the training database)

Once the training phase was completed, the ANN was fed with capacitance data coming from a different simulation that was not present in neither the training nor the validation subsets. In figure 4, the output of the neural network is compared to the CFD simulation at two different moments. We observe that the reconstructed images are very close to the expected images coming from the CFD simulation. This was the case for the majority of the images. This highlights that the neural network trained with CFD data is capable of accurately reconstruct images of an ECVT system. We also performed a quantitative analysis of these results. The RMSE of all images was calculated and compared to the RMSE when using already known algorithms found in the literature (Warsito et al. 2001). In particular, the following algorithms were tested: Linear BackProjection (LBP), Iterative LinearBackProjection (ILBP), Multi-Objective Image Reconstruction Technique (MOIRT). Figure 5 summarizes our findings. We remark that our ANN has a performance comparable to the classical approaches. The average of the RMSE is as good as the most performant algorithm. In addition, the standard deviation of the mean RMSE is the lowest for the ANN approach: 0.014; for the other algorithms, we had: 0.051 for LBP, 0.021 for ILBP, and 0.078 for the MOIRT. In our tests, the processing time for one image was: 45 milliseconds for LBP, 2.2 seconds for ILBP, and 25 minutes for the MOIRT. In comparison, the neural network approach took only 50 milliseconds to process one image. Which is 50 times faster than the ILBP algorithm and more than 40,000 times faster than the MOIRT.

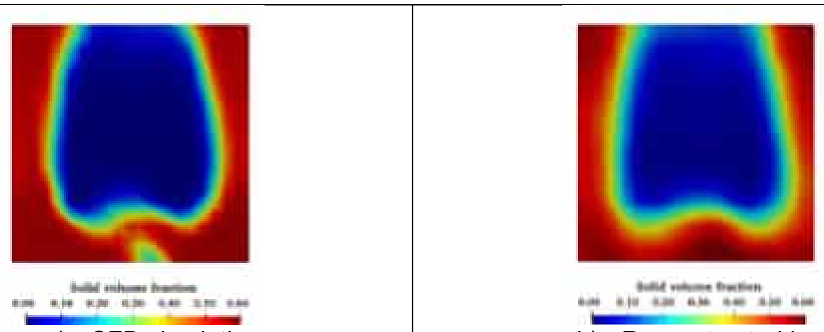

a) CFD simulation b) Reconstructed image

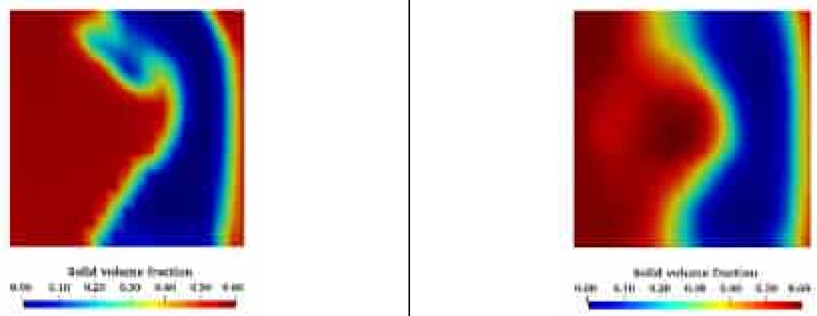

c) CFD simulation d) Reconstructed image

Fig. 4. Comparison at two different moments between the CFD simulation and the predicted reconstructed image

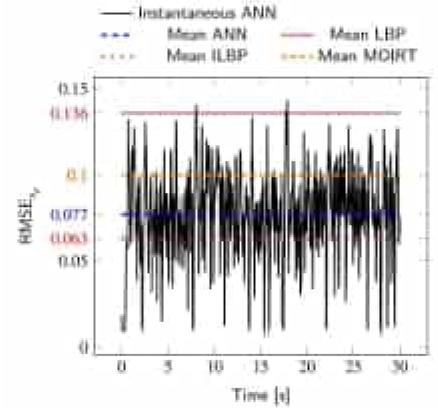

Fig. 5. Root mean square error of the predicted images generated by the ANN compared to the main reconstruction algorithms found in the literature.

Conclusion

In this work, we presented a novel strategy to build a training database for an artificial neural network to tackle the image reconstruction problem of an ECVT device. We showed that CFD simulations can be used and coupled with the sensitivity matrix approach to simulate the measurements of an ECVT system. This method allowed us to obtain enough data to build a training database for an artificial neural network aiming to reconstruct images of an ECVT system. This training database was used to train a simple artificial neural network built with Keras and Tensorflow. After the training phase was completed, we fed our neural network with a new set of simulated capacitance data that the neural network had not seen before. First, we compared visually the reconstructed images generated by the ANN to the CFD simulations. The results obtained showed an excellent agreement. The ANN was able to even reconstruct the most complex patterns present in a fluidized bed. We also performed a quantitative analysis comparing the error of the ANN approach to the different classical algorithms found in the literature. Our study showed that the artificial neural network was as accurate as the best algorithms found in the literature, however the ANN can process data much faster.

Notation

S	Sensitivity matrix	α_p	Solid volume fraction
C	Capacitance measurement		

References

Ansart, R., García-Triñanes, P., Boissière, B., Benoit, H., Seville, J. P., & Simonin, O. *Dense gas-particle suspension upward flow used as heat transfer fluid in solar receiver: PEPT experiments and 3D numerical simulations*. Powder Technology, 307, 25-36. 2017.

Holland, D. J., Marashdeh, Q., Muller, C. R., Wang, F., Dennis, J. S., Fan, L. S., & Gladden, L. F. *Comparison of ECVT and MR measurements of voidage in a gas-fluidized bed*. Industrial & Engineering Chemistry Research, 48(1), 172-181. 2009.

Lei, J., Liu, Q., & Wang, X. *Deep learning-based inversion method for imaging problems in electrical capacitance tomography*. IEEE Transactions on Instrumentation and Measurement, 67(9), 2107-2118. 2018.

Sabatier, F., Ansart, R., Zhang, H., Baeyens, J., & Simonin, O. *Experiments support simulations by the NEPTUNE_CFD code in an Upflow Bubbling Fluidized Bed reactor*. Chemical Engineering Journal, 385, 123568. 2020.

Wang, F., Marashdeh, Q., Fan, L. S., & Warsito, W. *Electrical capacitance volume tomography: Design and applications*. Sensors, 10(3), 1890-1917. 2010.

Warsito, W., & Fan, L. S. *Neural network based multi-criterion optimization image reconstruction technique for imaging two-and three-phase flow systems using electrical capacitance tomography*. Measurement Science and Technology, 12(12), 2198. 2001

Weber, J. M., Layfield, K. J., Van Essendelft, D. T., & Mei, J. S. *Fluid bed characterization using electrical capacitance volume tomography (ECVT), compared to CPFD software's barracuda*. Powder Technology, 250, 138-146. 2013.

Zheng, J., Li, J., Li, Y., & Peng, L. *A benchmark dataset and deep learning-based image reconstruction for electrical capacitance tomography*. Sensors, 18(11), 3701. 2018

ROTATING COIL–SHAPED SPIRAL GAS–SOLID REACTOR

Tadaaki Shimizu[1*], Liuyun Li[1], Heizo Kato[1], Akimichi Hatta[2],

Toshinori Kojima[3]

[1] Program of Chemistry and Chemical Engineering, Niigata University, 2-8050 Ikarashi, Niigata 950-2181, Japan

[2] CR-POWER LLC, 7-3-37 Place-Canada, Akasaka, Minato-ku, Tokyo 107-0052, Japan

[3] Seikei University, 3-3-1 Kichijoji-kitamachi, Musashino-shi, Tokyo 180-8633, Japan

*Email: *tshimizu@eng.niigata-u.ac.jp*

Abstract

A novel rotating coil-shaped spiral gas–solid contacting device was proposed, of which the spiral would be made of 180° elbows that are commercially produced as piping parts. Metal models and transparent cold models of the spiral structure were produced by combining 180° elbows. Spherical particles with different size and different density were used as solid materials. This article summarizes the authors' works to evaluate solid transportation rate, solid residence time distribution, pressure drop during gas feed, gas-solid contact efficiency, and heat transfer rate between reactor wall and solids. Also, preliminary results of the influence of scale-up on solid transportation rate and pressure drop are presented.

Introduction

Various types of continuous gas–solid contact devices, such as moving bed, fluidized bed, rotary drum, stoker, are available at present, but each has benefits and shortcomings. As a novel continuous gas–solid contacting device that can transport solids mechanically, attaining good gas–solid contact, and enabling external heating/cooling of solids through reactor wall, Hatta (2012), Ito et al. (2015), Iwasaki et al. (2015), and Takahashi et al. (2017) proposed a spiral reactor. Their spiral reactor consisted of a spiral screw plate fixed between two cylinders, as presented in Fig. 1-(a). It transports the solid layer formed at the bottom part of the cylinder by rotation. By maintaining the ratio of the rotation rate to the solid feed rate, the solid bed depth can be maintained at a suitable level so that the gas passes through the bed at the bottom and void above the bed alternately without gas bypassing. Heat can be transferred to the solids through the outer cylinder surface. However, an important difficulty of reactors of this type is that they are not easily manufactured. The screw plate and two cylinders must be welded without gas leakage, but it is difficult to find the leakage. With heating, non-uniform temperature formed among outer cylinder, screw, and inner cylinder may result in stress caused by the difference in thermal expansion.

To solve the difficulties related to the spiral reactor with the screw between two cylinders mentioned above, the authors proposed a novel continuous gas–solid contacting device to transport solids mechanically, attaining gas–solid contact, and enabling heat transfer through the reactor wall (Shimizu et al., 2019, 2020a, 2020b, 2020c, 2020d). An example of the design is presented in Fig. 1-(b). The reactor, a coil-shaped spiral, is formed by welding 180° elbows that are commercially produced as piping parts. When 180° long elbows of 50A size (o.d. 60.5 mm, JIS B2312) are connected alternately with an angle of 20° (one side), a nearly circular (204 mm × 213 mm) coil-shaped structure of pitch 104 mm can be formed. By rotating the coil-shaped reactor of this type, a solid bed, through which gas passes, is formed at the bottom part of the reactor, similarly to the screw reactor described above.

The salient benefits of coil-shaped reactors are summarized below.

- It is easy to manufacture and detect leakage because all welded parts are visible from the outside.
- Stable and reliable quality of the parts (elbows) is expected because they are produced according to industrial standards.
- A wider external heating area is available.
- Thermal expansion can be absorbed by the coil-shaped structure.

However, for the design of the reactors, basic properties of these reactors are necessary. Such design properties include solid transportation rate, pressure drop of the gas when gas is fed, gas-solid contact efficiency, and heat transfer between solids and wall. The authors have investigated the above-mentioned basic properties. This article summarizes the authors' findings about the properties of the coil-shaped reactor. Also larger model was made and the influence of reactor size on solid transportation and pressure drop was investigated.

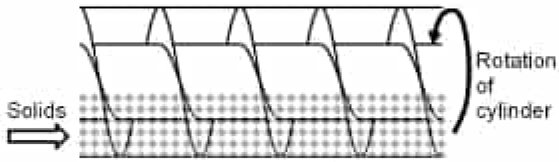

(a) Spiral reactor consisted of a screw between two cylinders (Hatta, 2012; Ito et al., 2015; Iwasaki et al., 2015; Takahashi et al., 2017)

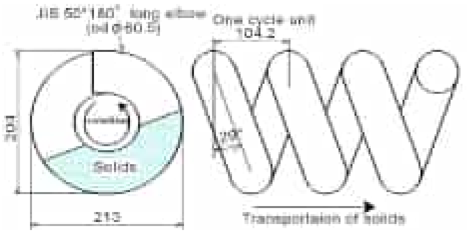

(b) Example of spiral reactor proposed in this work

Fig. 1. Spiral rotating reactors for solid transportation and gas–solid contact.

(a) JIS 180° 20 A long elbow (red) and half-octagonal 180° elbow

(b) Transparent 1.5-cycle cold model (ID 24mm)

(c) 20A size five-cycle metal model

Fig. 2. Japanese Industrial Standards (JIS) 180° long-elbow compared with half-octagonal 180° elbow, 1.5-cycle transparent cold-model, and five-cycle coil-shaped spiral structure made of metal elbows. (Shimizu et al., 2019, 2020c)

Experimental

(1) Metal models and transparent cold models of spiral structure made of 180° long elbows

Fig. 2(a) presents a design of a half-octagonal 180° elbow that simulates a JIS B2312 180° long elbow of 20A size. This "simulated elbow" was made of transparent plastic tube of 24 mm inner diameter. By combining three elbows, a 1.5-cycle cold model was made, as presented in Fig. 2-(b). This 1.5-cycle transparent model was driven by hand. In addition, a hand-driven 3/4-cycle model and motor-driven five-cycle model were made using transparent tubes. For metal models, a five-cycle model, which was driven continuously by a motor, was made as presented in Fig. 2-(c). For five-cycle model, solid inlet section and outlet section were attached. In the inlet section, a solid scraper was installed so that a sufficient quantity of solids could be fed to the inlet of the spiral. Then the particles were transported to the next cycle with the rotation. More particles were fed to the inlet than the amount which the spiral could transport. Therefore, the excess particles were dropped to the inlet section when the inlet opening became downward. Therefore, the transportation rate of particles was governed by the transportation capacity of the spiral, not by the feeding rate of solids to the inlet of the spiral. The transportation rate (by bulk volume) of the solids was measured using a measuring cylinder installed at the outlet of the spiral reactors. Evaluation of solid movement and mixing within a unit of spiral was also observed visually by placing tracer particles in the 3/4-cycle model and the 1.5-cycle model.

Both 1.5-cycle and five-cycle transparent models were used for pressure drop measurement (Shimizu et al., 2020a, 2020b). The particles were packed in the spiral to make a solid layer at the bottom. Fig. 3 presents examples of the solid bed formed in the apparatus. Air was fed to the spiral through a mass-flow controller. Then the pressure drop was measured. The pressure drop was measured for both counter-flow mode and co-current flow mode. The pressure drop of a uniformly packed bed was also measured using a straight tube of the same diameter (24 mm), thus the influence of solid bed shape on the pressure drop was discussed.

The 1.5-cycle transparent model was used to evaluate gas-solid contact efficiency (Shimizu et al., 2020d). Zeolite particles that irreversibly adsorb CO_2 were used. A pulse of CO_2 was injected into dry N_2 stream and the concentration of CO_2 was measured at the exit of the spiral. The removal of CO_2 was also measured using a uniformly-packed bed in a straight tube of the same diameter (24 mm). The influence of solid bed shape on gas-solid contact was discussed.

The five-cycle metal model was heated by flexible heaters and the metal surface temperature was regulated by controllers. The temperature of solids was measured at the inlet and the outlet, thus heat transfer rate was determined from the temperature rise, flow rate of solids, and specific heat of solids (Shimizu et al., 2020c).

In addition to ID 24 mm transparent models which have been used for the past works, a 1.5-cycle of ID 50 mm and a 1.5-cycle of ID 74 mm were newly made. Solid transportation rate and pressure drop was measured by use of this larger model.

(2) Particles

Spherical particles of different size and different density were employed for the experiments, as summarized in Table 1. For solid transportation rate measurement, glass beads and silica-gel particles were used (Shimizu et al., 2019). For pressure drop measurement, silica-gel, glass beads, and zirconia particles were employed (Shimizu et al., 2020a, 2020b). For heat transfer experiments, glass beads and zirconia particles (two different types) were employed (Shimizu et al., 2020c). Gas-solid contact efficiency was evaluated by measuring CO_2 removal (adsorption) efficiency by zeolite particles (Shimizu et al., 2020d).

Table 1 Spherical particles used for experiments

	Size	Bulk density ρ_b
Glass beads (GB)	1.2, 2.0, 3.1 mm	1.42 – 1.44 g/cm^3
Zirconia heavy (ZH)	2.0 mm	3.93 g/cm^3
Zirconia light (ZL)	2.0, 3.0 mm	2.38 – 2.45 g/cm^3
Silica gel (SG)	2.7 mm, 3.7 mm	0.95 – 0.96 g/cm^3
Zeolite	2.7 mm, 3.8 mm	(no data, used for gas-solid contact efficiency)

Results and Discussion

(1) Solid transportation rate and solid mixing in a spiral unit

When the five-cycle transparent model (ID 24 mm) was used, the rotation rate was varied from 2 rpm to 4 rpm, but the rotation rate did not affect the volume fraction (Shimizu et al. 2019). Fig. 3 presents examples of the solid bed formed in the 1.5-cycle models. Irrespective of the spiral size, analogous spiral formed analogous solid bed. The solid transportation rate per one rotation normalized by cube of diameter (D^3) was independent on the size (Fig. 4).

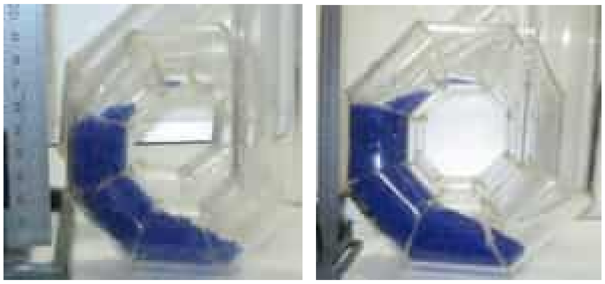

(a)ID 24 mm (Shimizu, 2020b) (b)ID 74 mm (This work)

Fig. 3. View of the solid bed formed in coil-shaped 1.5-cycle spiral (solids: Silica gel (blue)).

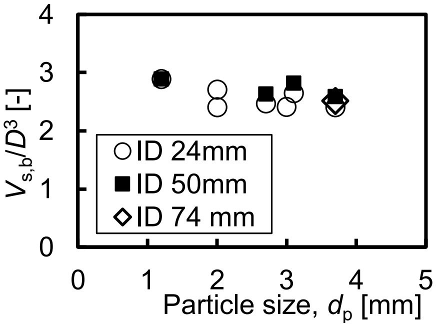

Fig. 4. Solid transportation rate per rotation (by bulk volume) normalized by cube of diameter

A similar solid bed was formed also in the 3/4-cycle model (Fig.5). Figs. 5(a)–(d) show solid movement with rotation of 3/4-cycle model. Tracer (blue) particles initially at the bottom (Fig. 5(a)) were carried upward with the counterclockwise rotation of the spiral because of the friction to wall. They finally reached the top of the bed (Fig. 5(b)). The tracer initially at the top (Fig. 5(c)) moved downward along the upper wall (Fig. 5-(d)). Such a circulation flow of solids produced good solid mixing within one unit of the spiral. Visual observation using the 1.5-cycle model revealed that the tracer particles were well mixed with the main body of the particles after one rotation. Consequently, in this coil-shaped spiral reactor, packets of well-mixed particles are transported, forming nearly plug flow (Shimizu et al., 2019).

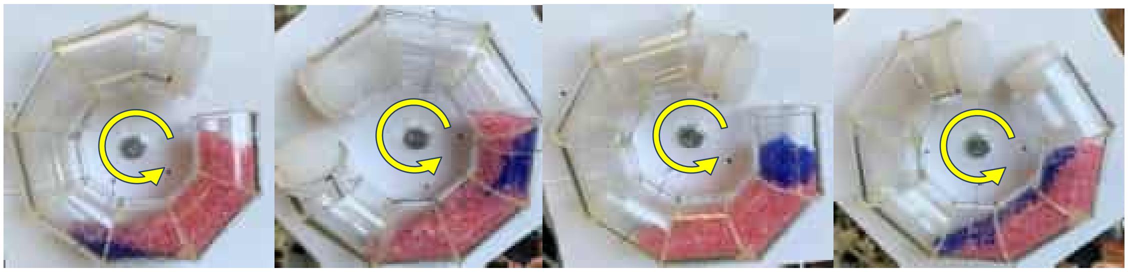

(a) tracer at bottom (b) after 3/8 rotation (c) tracer at top (d) after 1/8 rotation

Fig. 5. Solid movement in 3/4-cycle (ID 24mm) model with rotation (solids: SG small).

(2) Pressure drop of the solid bed and limit to maintain fixed bed in the spiral

Using the 1.5-cycle transparent models, the pressure drop of the solid bed formed in the coil-shaped reactor was measured by feeding air. Fig, 6-(a) shows typical changes in the pressure drop (ΔP) with increasing superficial gas velocity (U) in co-current direction. The pressure drop increased monotonically with the increase of the air flow rate to a certain value (threshold flow rate), but a further increase in air flow suddenly decreased the pressure drop. The phenomena observed when pressure drop decreased differed between the counter-current flow and co-current flow. For the counter-current flow, a part of the solids in the vertical zone started to fluidize. For the co-current flow, particles were pushed downstream by the gas flow. Consequently, gas bypassing the channel was formed in the solid bed (Shimizu et al., 2020b).

Comparing the results between ID 24 mm and ID 50 mm, it was found that the pressure drop normalized by the diameter (D) was not influenced by the size as far as fixed bed was stably maintained in the spiral (Fig, 6-(a)). As shown in Fig. 3, the form of the packed bed was analogous irrespective of the size, thus the length of gas flowing through the bed was proportional to the diameter. A difference was observed between ID 24 mm and ID 50 mm for the onset of gas bypassing (sudden decrease in pressure drop); gas bypassing started at lower gas velocity for ID 50 mm than ID 24 mm. This is attributable to the lower perimeter/cross sectional area ratio for larger size unit. The force to push the solid bed is proportional to the sectional area, namely proportional to square of diameter (D^2), whereas the friction force between solid and wall or between solids is considered to be proportional to diameter (D), as schematically illustrated in Fig.6-(b).

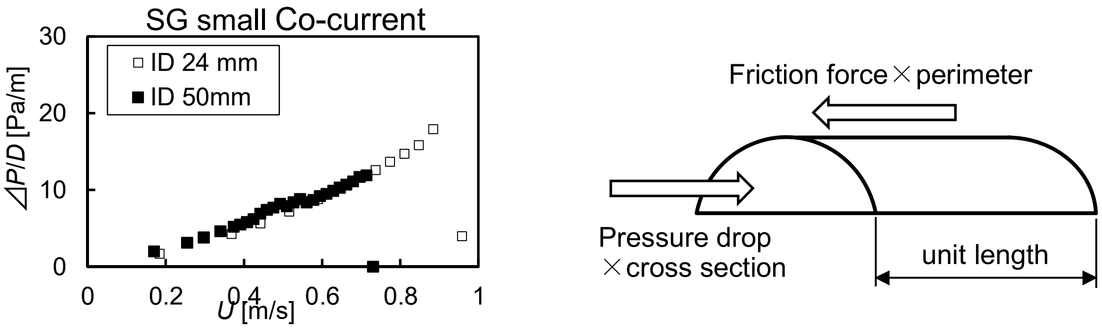

(a) Relationship between pressure drop and gas velocity U (b) Force balance to maintain fixed bed

Fig. 6. Pressure drop of the bed (normalized by diameter) in 1.5-cycle model with different size (Results for ID 24 mm: Shimizu 2020b; Results of ID 50 mm: This work).

(3) Gas-solid contact efficiency

Using the 1.5-cycle transparent model of ID 24 mm, gas contact efficiency of the fixed bed in the spiral was evaluated by measuring CO_2 capture by zeolite particles and comparing with that in a uniformly packed bed formed in a vertical straight tube of ID 24 mm (Shimizu et al., 2020d). The contact efficiency of the bed in the spiral was up to 30% lower than that in the uniformly-packed bed. This lower contact efficiency is attributable to the non-uniform shape of the bed in the spiral. The gas tends to flow through shorter path in the upper part of the bed in the spiral.

(4) Heat transfer

Using the motor-driven five-cycle metal model of 20 A size, heat transfer rate from wall to the solids was measured. (Shimizu et al., 2020c). Also thermal properties of the solids, specific heat C_p, bulk density ρ_b, and effective thermal conductivity of packed bed, k_e°, were measured. An empirical expression of the heat transfer coefficient h was obtained as:

$$h = 0.88(k_e^{\circ}\ \rho_b\ C_p/\tau)^{0.5} \qquad (1)$$

where τ is time for one rotation of spiral. This expression suggests that the heat transfer mechanism is similar to the packet renewal model of heat transfer. The influence of scale-up on heat transfer rate, however, has not yet been evaluated. This is a task of future work.

(4) Upward solid transportation (This work)

In many gas-solid continuous reactors, solid flows downward or horizontal, except for pneumatic transport systems (including circulating fluidized bed). One feature of the present spiral is enabling upward transportation of solids by inclining the axis. Fig. 7 shows the preliminary result of transportation of solids from lower position to the upper position. By rotation, particle were carried upward by inclining the rotation axis. Even when the rotation axis was inclined, solid bed was formed at the bottom which gas can pass through.

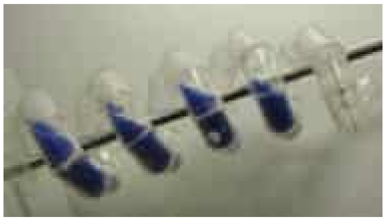

Fig. 7. Upward solid transportation using a five-cycle model (ID 24 mm, This work).

Conclusion

A novel coil-shaped spiral reactor was proposed. The authors' works about the properties of this reactor type, solid transportation rate, pressure drop, gas-solid contact, and heat transfer rate, are summarized. Preliminary results of scale-up was also presented.

Acknowledgments

The authors express their appreciation of the late Professor Daizo Kunii, Professor Emeritus of The University of Tokyo, for his encouragement. T. Shimizu received financial support from the Japan Science and Technology Agency (JST) [MIRAI; Grant Number JPMJMI17E4]

References

Hatta, A. Invention of a Waste-based Pyrolysis Power Generation Plant (in Japanese). Mater. Cycles Waste Manag. Res. 2012. 23, 239-243 DOI: 10.3985/mcwmr.23.239

Ito, T., H. Suganuma, S. Suzuki, S. Kato, A. Hatta, T. Kojima. Pressure Drop and Transfer Rate of Wood Powder Pellets in a Cold Model of a Horizontally Rotating Cylinder with Internal Screw Cylinders. Kagaku Kogaku Ronbunshu. 2015. 41, 1, 25-28 DOI: 10.1252/kakoronbunshu.41.25

Iwasaki, T., S. Kato, Y. Kodera, A. Hatta, M. Kikuzato, A. Yamasaki, T. Ito, S. Suzuki, T. Kojima. Thermal Decomposition of Woody Wastes Contaminated with Radioactive Materials using Externally Heated Horizontal Kiln. Kagaku Kogaku Ronbunshu. 2015. 41, 1, 62-66 DOI: 10.1252/kakoronbunshu.41.62

Shimizu, T., R. Adachi, L. Li, A. Hatta, T. Kojima. Solid transportation in coil-shaped rotating spiral gas–solid contacting device (in Japanese). Kagaku Kogaku Ronbunshu. 2019. 45, 5, 197-209 DOI: 10.1252/kakoronbunshu.45.197

Shimizu, T., R. Adachi, L. Li, A. Hatta, T. Kojima. Pressure Drop in a Coil-shaped Rotating Spiral Gas-Solid Contacting Device (in Japanese). Kagaku Kogaku Ronbunshu. 2020a, 1, 1-7 DOI: 10.1252/kakoronbunshu.46.1

Shimizu, T., R. Adachi, L. Li, A. Hatta, T. Kojima. Limiting Conditions for Maintaining a Fixed Bed within a Coil-Shaped Rotating Spiral Gas–Solid Contacting Device under Gas Feeding (in Japanese). Kagaku Kogaku Ronbunshu. 2020b, 3, 84-89 DOI: 10.1252/kakoronbunshu.46.84

Shimizu, T., R. Adachi, L. Li, A. Hatta, T. Kojima. Wall-to-Solids Heat Transfer in a Coil-Shaped Rotating Spiral Gas-Solid Contacting Device (in Japanese). Kagaku Kogaku Ronbunshu. 2020c, 3, 176-182 DOI: 10.1252/kakoronbunshu.46.176

Shimizu, T., R. Adachi, L. Li, A. Hatta, T. Kojima. Gas-Solid Contact Efficiency in a Coil-Shaped Rotating Spiral Gas-Solid Contacting Device (in Japanese). Kagaku Kogaku Ronbunshu. 2020d, 5, 200-206 DOI: 10.1252/kakoronbunshu.46.200

Takahashi, Y., T. Ito, A. Hatta, Y. Kodera, T. Kojima. Highly Efficient Gasification Process of Sewage Sludge using Horizontally Rotating Kiln with Screw Cylinders, in: L Juan (Eds.), Int. Proc. of Chemical Biological and Environmental Engineering. 2017. Vol.102, paper 15 DOI: 10.7763/IPCBEE.2017.V102.15

EXPERIMENTAL INVESTIGATION OF PROCESS BEHAVIOUR OF CONTINUOUS FLUIDIZED BED SPRAY AGGLOMERATION WITH INTERNAL CLASSIFICATION

Gerd Strenzke[1*], Robert Dürr[2], Andreas Bück[3], Achim Kienle[2,4], Evangelos Tsotsas[1]

[1] *Chair of Thermal Process Engineering, Institute of Process Engineering, Otto von Guericke University, Universitätsplatz 2, 39106, Magdeburg, Germany*

[2] *Process Synthesis and Process Dynamics, Max Planck Institute for Dynamics of Complex Technical Systems, Sandtorstrasse 1, 39106, Magdeburg, Germany*

[3] *Institute of Particle Technology, Friedrich-Alexander University Erlangen-Nuremberg, Cauerstraße 4, 91058, Erlangen, Germany*

[4] *Institute of Automation Engineering, Otto von Guericke University, Universitätsplatz 2, 39106, Magdeburg, Germany*

*Email: *gerd.strenzke@ovgu.de*

Abstract

Agglomerates are formed in industrial practice, e.g. pharmaceutical manufacturing and food processing. In case of fluidized bed productions, a solid-containing liquid, called binder, is sprayed on the particles and fluidization guarantees good mixing and high heat/mass transfer between particles, liquid and gas phase. Continuous operation provides additional benefits such as constant product throughput and quality. This work experimentally investigates the influence of the gas inlet temperature on the dynamics of continuous spray agglomeration for two different operation strategies (with and without bed mass control). For the experiments, glass beads and a solution of water and hydroxylpropylmethylcellulose (HPMC) are used as solid and binder, respectively. Focus is on analysis of the influence on the product quality, e.g. characteristic particle size, shape and apparent density.

Introduction

Agglomeration is a particle formulation process in which at least two primary particles are combined to form a new one. Fluidized bed agglomeration is an established process to modify the properties of the initial material (Litster et al., 2004; Mörl et al, 2007; Dadkhah et al., 2012) and is used in chemical, food and pharmaceutical industry (Bück et al., 2016; Palzer et al., 2011). In fluidized bed spray agglomeration, a solid-containing liquid, called binder, is sprayed on the particles. The growth of agglomerates depends on interactions of particles covered with wet spots that are generated by deposition of the binder droplets. Due to evaporation of water from the binder, liquid bridges between primary particles are transformed to solid bridges (Terrazas-Velarde et al., 2011). The advantages are good mixing and uniform high heat and mass transfer rates between particle, liquid and gas phase. In this study, the focus is on fluidized bed spray agglomeration process in continuous operation. Compared to batch operation the additional benefits of continuous processing are constant product quality and throughputs. However, the influence of process parameters, e.g. spray rate or gas inlet temperature, or operation strategies, e.g. with or without bed-mass control, on the product quality is not yet fully understood. Therefore, this contribution presents experimental results on the influence of different gas inlet temperature levels on agglomerate properties like particle size distribution (PSD) and agglomerate structure, which affect solubility or flowability of the agglomerate product. Furthermore, it is analysed if a bed mass controller (BMC) has beneficial effects on process dynamics.

Material and Methods

To carry out the experiments, a cylindrical pilot-scale fluidized bed is used. The particles are fluidized by heated air, which enters the fluidized bed chamber from the bottom through a distributor plate. The chamber of the fluidized bed has a diameter of 300 mm. The spray nozzle, which atomizes and sprays the solution in top-spray configuration, is installed at a distance of 420 mm above the distributor plate of the fluidized bed. An external pump supplies the binder feed. Additionally, primary particles are continuously fed to the process chamber by a rotary valve. During the process, particles having the target size are continuously discharged by internal classification through a classifying tube, which is centrally installed at the bottom of the fluidized bed. The classifying air can also be used to control the bed mass. For offline analysis representative samples are directly taken from the bed. The homogeneity of the samples is ensured by the common approach of a continuous stirred tank reactor (CSTR) for the fluidized bed.

The starting materials in the fluidized bed and the continuous feeding during the process are glass beads with a narrow PSD (Merkus, 2009). The primary particle fraction has a Sauter Mean Diameter (SMD) of 0.2 mm, which was optically measured by a Camsizer (Retsch Technologies GmbH, Germany). The $\mathrm{d}_{50,3} = 206\,\mu\mathrm{m}$ and a standard deviation of $\sigma = 22\,\mu\mathrm{m}$.The binder is a solution of water and hydroxylpropylmethylcellulose (HPMC). HPMC is also known as Pharmacoat and used in food and pharmaceutical industries. In the present work, the solution has a mass concentration of 4 wt% of HPMC and 96 wt% of water. Initially, 8 kg of primary particles are placed inside of the fluidized bed as starting material.

Six experiments were conducted to investigate the effects of a controlled bed mass and the influence of the fluidizing gas inlet temperature. The experiments were split by the temperature in three series, each with and without a controlled bed mass. The bed mass was calculated with the measured pressure drop over the bed and the Ergun equation (Ergun and Orning, 1949). Every experiment was carried out for at least 2h. The frequency of product sampling during the process was set to every 2 min for the first 30 minutes, every 5 min between 30 and 60 minutes and every 10 min after 60 minutes. The taken samples were all analysed offline with respect to size, shape and apparent agglomerate density. Product particles were analysed with the Camsizer. The measurement infers particle size and density via dynamic image analysis of each sample. The output data is the PSD, normalized with respect to the volume resulting in q_3-distribution of the particle collective for each sample.

Table 1: Experimental parameters

Parameter	Value
Inlet air temperature T_{inlet}	[80, 90, 100] °C
Inlet air mass flow rate $\dot{M}_{inlet}$	275 kg/h
Target feed rate $\dot{M}_{feed}$	15 kg/h
Sauter Mean Diameter of starting material	0.2 mm
Average binder spray rate $\dot{M}_{Spray}$	~ 2.7 kg/h
Binder content w	4 wt%

Bed Mass Controller

Control of bed mass can be advantageous to prevent over-/underfilling of the fluidizing chamber and as a basis for automatic control of particle properties (Neugebauer et al., 2019). As mentioned previously, the pressure drop over the bed is used as a surrogate measurement for the bed mass which represents a good approximation for constant fluidization conditions (Neugebauer et al., 2019). The bed mass is controlled by adjustment of the classifying gas mass flow. Proportional-Integral control (PI) is the most applied controller type in industrial processes due to easy implementation and favorable performance for a wide range of processes. Controller parameters are determined based on response of the bed mass on a step change in the gas mass flow. For the presented fluidized bed spray agglomeration process the Tyreus-Luyben tuning rule (Tyreus & Luyben, 1992) was applied and the following PI-parameters where obtained $KP = 90 \frac{l}{\min kg}$ and $KI = 0.45 \frac{l}{\min kg\, s}$. The control algorithm was connected via OPC to the process plant.

Results and Discussion

Results for all experiments are seen in Figure 1-3. For the three experiments without BMC, bed masses are decreasing immediately after the start of the experiment. The reason for this phenomenon is the fast agglomeration mechanism. A lower gas temperature ($T_{in} = 80°C$) leads to a lower evaporation rate of water in the binder. Following the wetted particle surface is sticky for a longer time than for higher temperatures and the probability of a successful collision of two wet primary particle surfaces increases proportional (Terrazas-Velarde et al., 2011; Rieck et al., 2016). Within the first ten minutes a significant part of the agglomerates become larger than the theoretical separation diameter of approx. 0.6 mm and will discharge, see Figure 1 right. Due to it the bed mass is decreasing rapidly. The comparison of the initial loss of bed mass for all experiments without BMC proof this temperature dependency. At higher temperatures the loss of bed mass starts later and the effect is smaller, see Figure 1-3 left. After reaching the stationary size, the bed masses start to increasing. Though, experimental data indicate convergence to a stationary value, no constant bed mass is reached after 2 h.

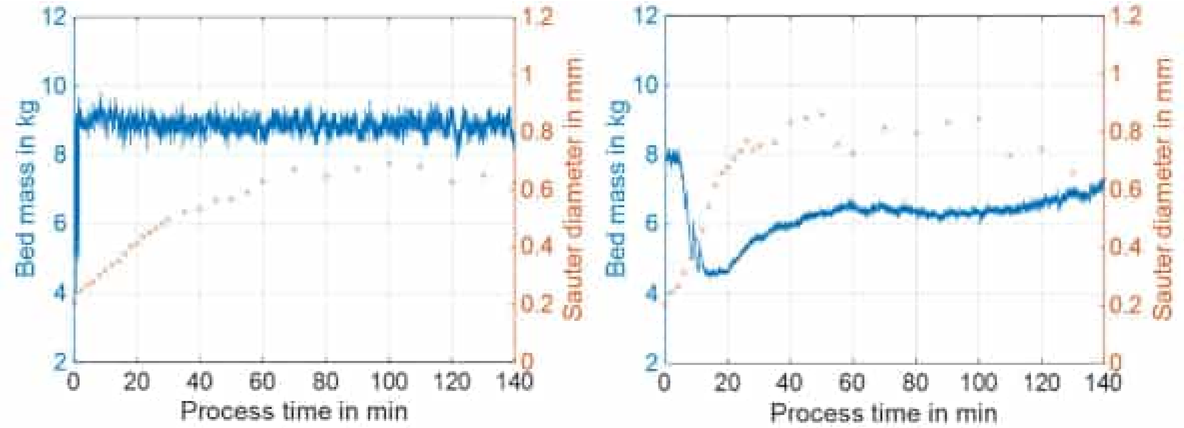

Figure 1: Bed mass and Sauter diameter for 80 °C with (left) and without (right) controlled bed mass

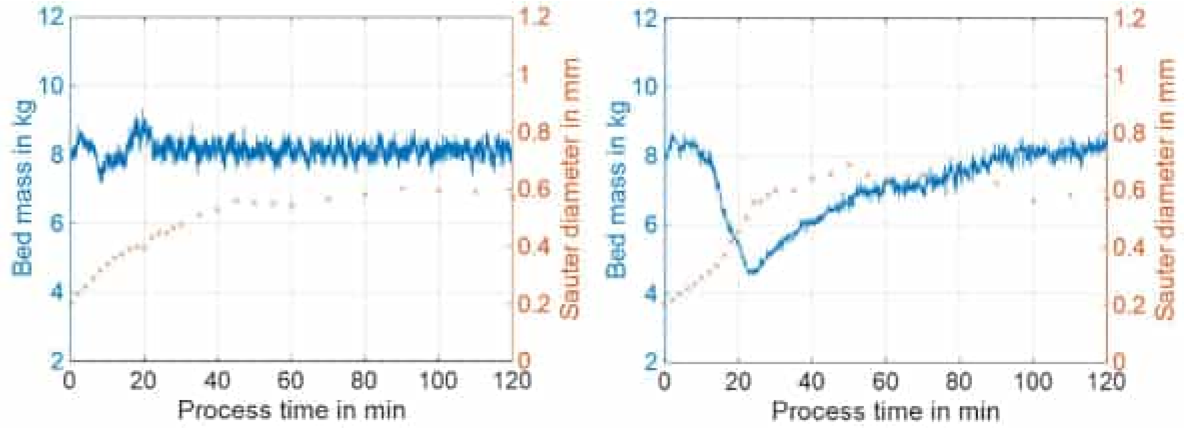

Figure 2: Bed mass and Sauter diameter for 90 °C with (left) and without (right) controlled bed mass

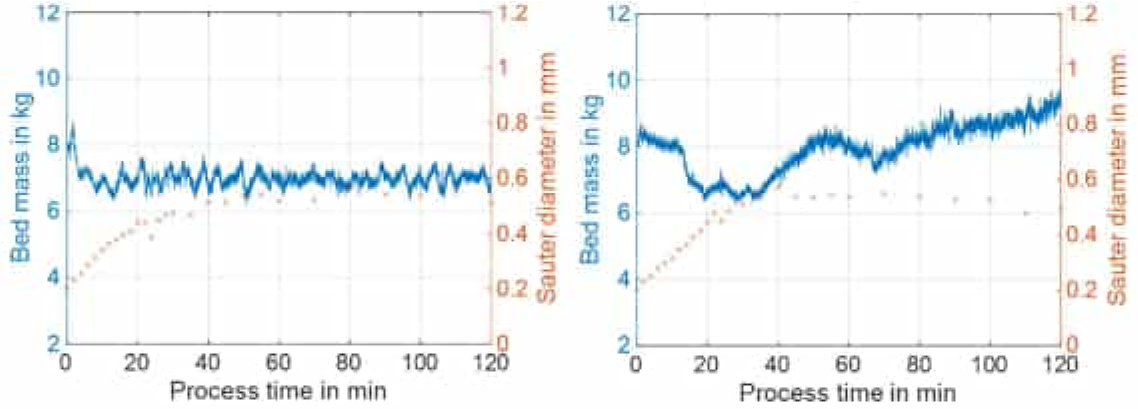

Figure 3: Bed mass and Sauter diameter for 100 °C with (left) and without (right) controlled bed mass

In contrast, with active BMC, the bed masses are kept constant within a narrow range as expected, see Figure 1-3 left. The results show a simultaneous reaching to steady states of size and bed mass is faster. However, it is also seen that bed mass control results in slower dynamics of the Sauter mean diameter (SMD) compared to the uncontrolled case. The reason for this phenomenon lies in the lower bed mass for the latter's initial phase: The lower amount of particles and the constant spray rate come along with a higher wet-to-dry particle ratio resulting in a faster growth rate of the characteristic SMD. However, the experimental results for T= 80 °C (Figure 1) and T= 90 °C (Figure 2) also indicate that for the process with active BMC the SMD dynamics are slightly smoother in both, transition phase as well as stationary phase. The comparison of the three temperature levels shows a dependency of the resulting agglomerate size on the temperature, see Figure 1-3. For a gas inlet temperature level of $T_{in} = 80°C$, the steady state SMD of the agglomerates is measured as approximately 0.8 mm while for $T_{in} = 90(100)°C$ it decreases to 0.6 (0.55) mm. This characteristic behavior is observed for both strategies and is again a result of the lower evaporation rate of the water in the binder at lower temperatures. Additional to the temperature dependency of the agglomerate size, the investigation has shown a faster transfer to the stationary SMD at higher temperatures, especially for the controlled bed mass strategy.

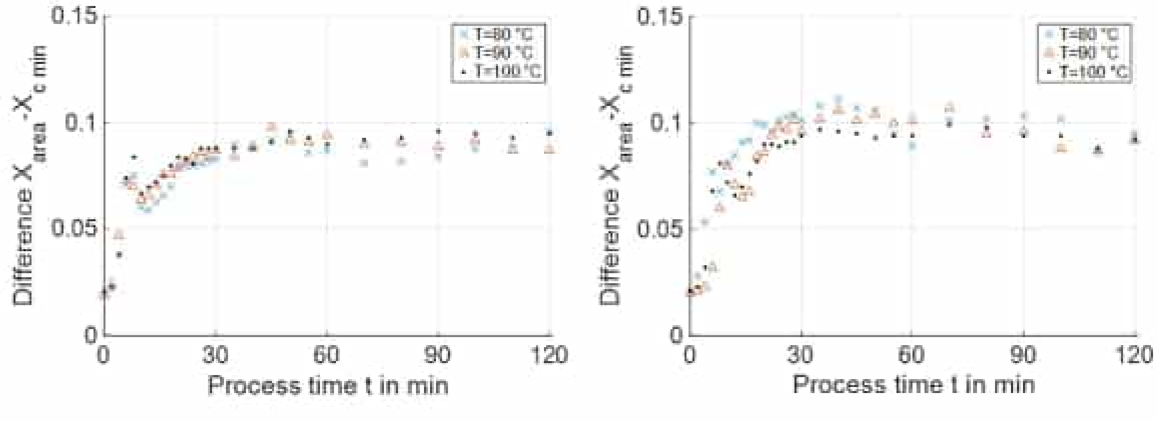

Figure 4: Temporal evolution of agglomerate shape during the process, with (left) and without BMC (right)

For all experiments, the difference was growing to a stable value until 30 minutes, see Figure 4. A trend to produce more spherical agglomerates with a controlled bed mass strategy is slightly visible, but an effect of different temperature on sphericity is observed in neither strategy.

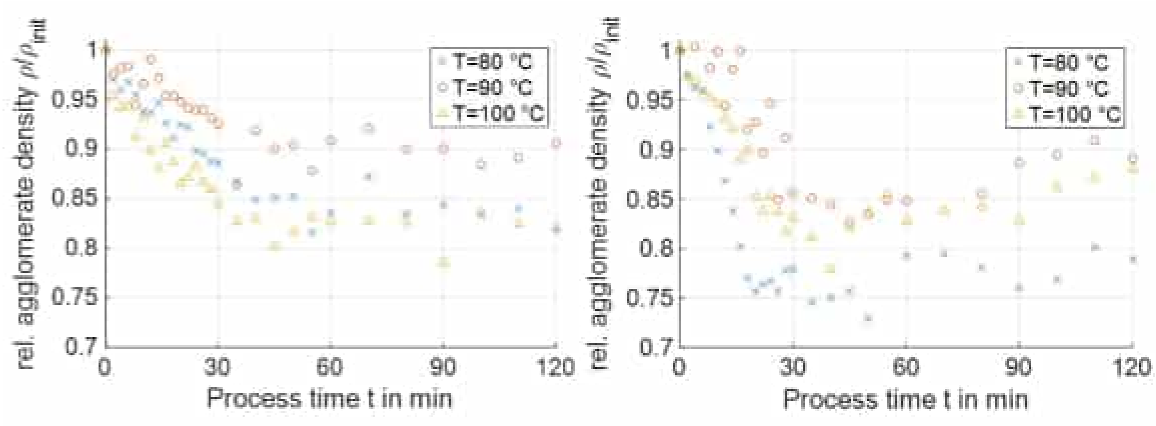

Figure 5: Temporal evolution of rel. agglomerate density during the process, with (left) and without BMC (right)

The temperature influence on density or porosity, as reported by Dadkhah et al. (2012), is not completely reproducible. Dadkhah et.al. wrote that the produced agglomerates will be denser for a higher temperature of the fluidization inlet air. In this contribution, the relative agglomerate density measurements show that a constant agglomerate density can be reached after approximately 50 min for all temperatures with active BMC while no steady state is observed without BMC after 120 min of experimental time, see Figure 5. However, a clear dependency of the density on the temperature is not visible. Without BMC, the lowest agglomerate density was measured at the lowest temperature (80 °C) but the densest agglomerates are produced at 90 °C, not at 100 °C. For the active BMC, the lowest agglomerate density was obtained at 100 °C and the densest particles were produced again at 90 °C.

Conclusion

The influence of the temperature and the effect of a bed mass controller on the product quality and the process dynamics were investigated. For the temperature, the results have shown an inverse dependency of the agglomerate size in terms of SMD on the temperature, which means that a lower temperature level leads to a larger agglomerate size. The comparison of the process strategies has shown a faster convergence to the stationary size without a controlled bed mass, yet simultaneous steady states of size and bed mass are reached faster for the bed mass controlled process. Moreover, the results indicate that BMC is beneficial for smooth dynamics of the process. Further improvement of the BMC performance may be obtained by applying PID or other advanced control laws. However, those controller types are generally more sensitive to measurement noise and require sophisticated and careful design. In future works, the investigation of the product properties, e.g. agglomerate density and porosity, will be extended. Furthermore, a feedback controller for desired product properties will be designed and experimentally verified.

Acknowledgement

The authors gratefully acknowledge the funding of this work by the Center of Dynamic Systems (CDS) and the EU-programme ERDF (European Regional Development Fund). Partially funded by the Deutsche Forschungsgemeinschaft (DFG, German Research Foundation) – Project-ID 61375930 – SFB 814 – “Additive Manufacturing” TP A02. We also thank Mr. Rajkumar Megaraj for his assistance in the conduction of the experiments and measurements.

References

Bück, A., Tsotsas, E., Encyclopedia of Food and Health., Vol.1., Oxford: Academic Press, Ch. Agglomeration, pp.73-81, 2016

Dadkhah, M., Peglow, M., Tsotsas, E., Characterization of the internal morphology of agglomerates produced in a spray fluidized bed by X-ray tomography, Powder Technology, 228 (2012), pp. 349-358

Ergun, S., Orning, A.A., Fluid flow through randomly packed columns and fluidized beds, Industrial and Engineering Chemistry, 41 (1949), 1179-1184

Litster, J., Ennis, B., The Science and Engineering of Granulation Processes, Kluwer Academic Publishers, Dordrecht, 2004

Merkus, H.G., Particle Size Measurements Fundamentals, Practice, Quality, Particle Technology Series, Springer Publishers, p. 2, 2009

Mörl, L., Heinrich, S., Peglow, M., Fluidized bed spray granulation, in Salman, A.D., Hounslow, M. J., Seville, J.P.K., (Eds.), Handbook of Powder Technology, Vol 11, Elsvier, 2007, pp. 21-188

Neugebauer, C., Diez, E., Bück, A., Palis, S., Heinrich, S., Kienle, A., On the dynamics and control of continuous fluidized bed layering granulation with screen-mill-cycle, Powder Technology, 354 (2019), pp. 765-778

Palzer, S., Agglomeration of pharmaceutical, detergent, chemical and food powders - Similarities and differences of materials and processes, Powder Technology, 206 (2011), pp. 2-17

Rieck, C., Bück, A., Tsotsas, E., Monte Carlo modeling of fluidized bed coating and layering processes, AiChE J., 62 (2016), pp. 2670-2680

Terrazas-Velarde, K., Peglow, M., Tsotsas, E., Kinetics of fluidized bed spray agglomeration for compact and porous particles, Chemical Engineering Science, 66(2011), pp 1866-1878

Tyreus, B. D. , Luyben, W. L., Tuning PI controllers for integrator/dead time processes, Industrial & Engineering Chemistry Research, 31(1992), pp. 2625-2628

ECONOMIC GAS CLEANING BY INLINE-PARTICLE-COLLECTORS

Ulrich Muschelknautz

MK Engineering - Dust Removal Technology
Heinrich-Fuchs-Str. 101, 69126 Heidelberg, Germany
Email: *um@mkengineering.de*

Abstract

The particle feed into a gas-particle separator like a fabric filter or an electrostatic precipitator (ESP) cleaning the flue gas of a fluidized bed reactor can be efficiently reduced by installing an array of parallel swirlers inline into the crude gas channel of that deduster. This measure significantly reduces the particle emission of the overall dedusting line and/or economizes its installation and operating costs. The swirler array can be applied in horizontal as well as in vertical duct segments. The collector cells are uniflow cyclones which have particles and gas streaming in only one direction providing several advantages over an array of parallel standard reverse flow cyclone cells with an axial inlet (swirl tubes): Besides their easy applicability as an inline separator they need less space and in addition they can achieve a higher efficiency per volume with low pressure drop than swirl tubes. Comprehensive studies of uniflow cyclones have strongly improved their understanding and led to approved design criteria and calculation methods. Applying this calculation model shows that a uniflow cyclone array significantly relieves subsequent fine dust collectors in a industrial fluidized bed reactor by separating fine particle feeds (d50 ca. 5-10 micron) from large gas volume flows at low pressure drops < 1000 Pa.

Introduction

Cyclones for separating solid particles from gases are applied preferably for reasons of high operational safety due to their simple and robust construction, usability for product recovery, stable and generally low pressure drops and, in many applications, comparable low investment and operating costs. In addition, they can operate under extreme conditions, including large gas volume flows and high solids concentrations, temperatures and pressures, which is a comparative advantage over other gas-solids separation technologies.

The minimum particle size that can be separated by a cyclone at a given pressure drop generally decreases with decreasing cyclone size. This is used in multicyclones consisting of many parallel cyclone cells in a common housing with a common hopper for solids discharge: Distributing the gas solids feed over many small cyclone cells instead of just one or few large cyclones increases the separation efficiency. By increasing the number of parallel cyclone cells while reducing their size, the efficiency of a multicyclone is improved without changing the flow cross-section and without affecting its pressure drop. The prerequisite for this is, however, that gas and solids can be evenly distributed to the cyclone cells and bypass flows through the solids discharge openings from one cyclone cell to the other can be avoided.

Usually, multicyclones use standard reverse flow cyclone cells with an axial inlet, also called swirl tubes. Fig. 1a shows a multicyclone consisting of 16 swirl tubes for separating a dilute gas solids flow streaming through the flue gas duct of a fluidized bed system in order to relieve the subsequent fine dust collector (Filter or ESP). By this measure particle emission into the atmosphere can be reduced and / or the operating costs of the final filter can be economized.

A competitive alternative for solving this problem is a multicylcone consisting of 16 horizontally aligned uniflow cyclone cells, Fig. 1b. This device can be installed inline in the duct see Fig. 1b, which leads to considerable cost savings.

Both cyclone types, the swirl tube and the uniflow cyclone, have axial inlets with swirl vane inserts for vortex generation. Their main difference is that in swirl tubes the gas flow reverses its direction and pure gas and collected particles are leaving the device at opposite sides, whereas uniflow cyclones have gas and particles passing through them in only one direction exiting at the same end of the device. Due to those design differences, uniflow cyclones can be built more compact and can easily be integrated into pipelines or ducts.

This point becomes relevant if space for a dedusting unit is limited. If saving of space is of high priority or if there is even only limited space available for purifying a given gas volume flow the question arises whether under the restriction of *limited space* a uniflow cyclone may be preferable over its standard reverse flow cyclone counterpart.

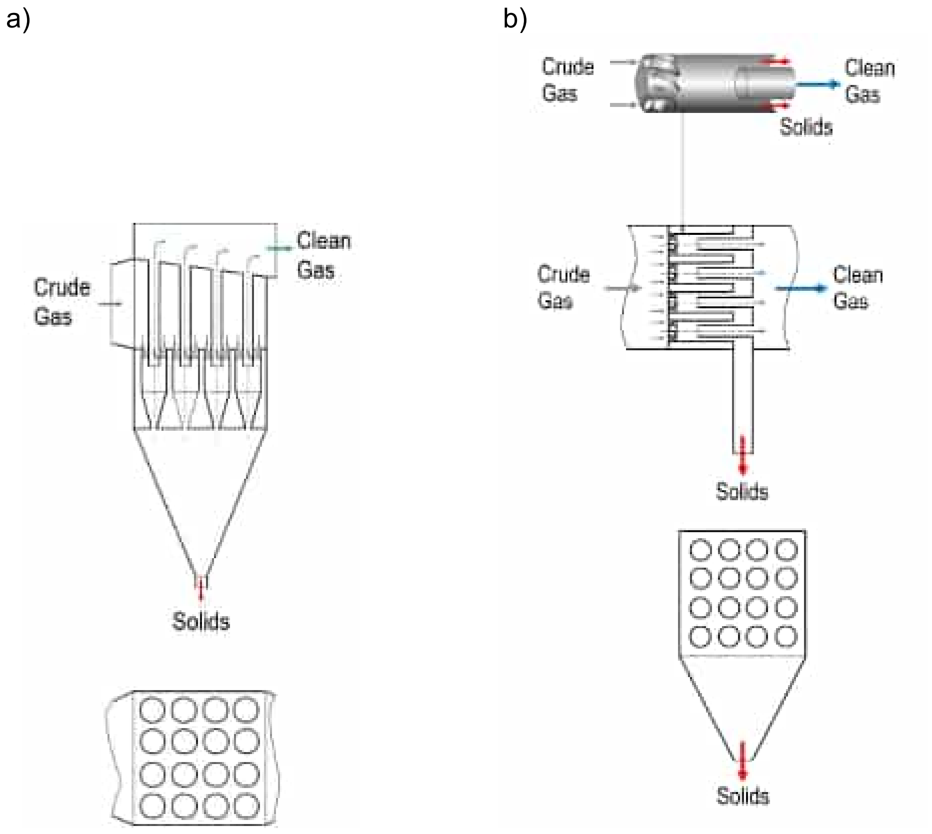

Fig. 1. Multicyclones with Swirl Tubes (a) and with horizontal Uniflow Cyclones (b) for separating a dilute gas solids, installed in a horizontal duct.

Calculation Method

The model for uniflow cyclones is based on the same physical concepts as the equilibrium orbit model for standard reverse flow cyclones described in Muschelknautz E, Greif V. (1997). The latter model has been validated by extensive experimental data (see e. g. Hoffmann, Stein (2008) and Muschelknautz (2021)) and has proven to be successful in a large number of industrial applications.

The model for uniflow cyclones calculates the separation efficiency η and the pressure drop Δp. It has been validated by extensive experimental data covering various cyclone sizes (diameters between 110 and 292 mm), geometries, as well as operating data including various solids feeds and types of solids, see Würtl (2007), Muschelknautz et al. (2011) and references cited in Muschelknautz (2019). An overview of the calculation of the separation efficiency is given below. The components of the separation process in uniflow cyclones are shown in Fig. 2.

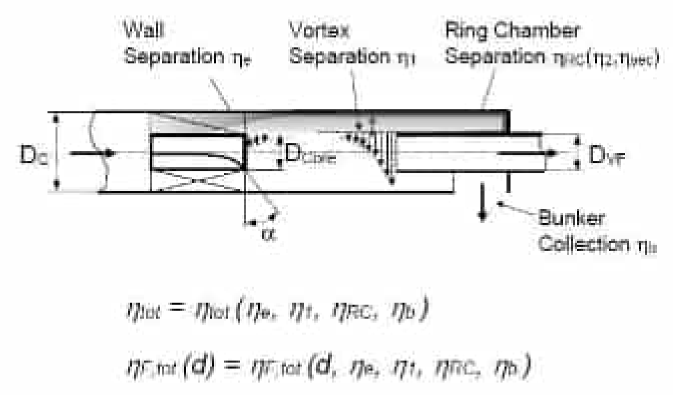

Fig. 2. Structure of the separation process in a uniflow cyclone.

In analogy to the calculation model for reverse-flow cyclones (Muschelknautz E., Greif V.) the gas entering the uniflow cyclone splits into a main flow and a secondary flow.

$$\dot{V} = \dot{V}_{main} + \dot{V}_{\sec} \qquad (1)$$

The secondary flow streams through the boundary layer along the cyclone wall towards the solids discharge opening. Particles transported with that secondary flow are discharged with the collection efficiency η_b of the discharge device. Particles which are not discharged are fed into the secondary flow streaming through the boundary layer along the cyclone roof towards the vortex finder and from there along the outer vortex finder wall into the gas exit. Particles are separated from that secondary flow by the efficiency $\eta_{\sec}$.

The main flow streams outside of that boundary layer through the cyclone. In contrast to standard cyclones the total main flow splits into two parts

$$\dot{V}_{main} = \dot{V}_1 + \dot{V}_2 \qquad (2)$$

with $\dot{V}_1$ streaming directly from the separation chamber into the vortex finder and $\dot{V}_2$ making a loop way through the ring chamber around the vortex finder before exiting the cyclone.

Analogous to the model for standard cyclones, the model for uniflow cyclones assumes that the main gas flow in the uniflow cyclone has a critical loading capacity splitting the separation process into two steps. The first separation takes place inside the swirl vane inserts for swirl generation and subsequently in the separation chamber due to exceeding the limited load ratio, $\mu_{\lim}$, of the uniflow cyclone. If the load ratio at the inlet μ exceeds the limited load ratio the excess mass fraction will be removed immediately after the gas jet enters the cyclone with the separation efficiency $\eta_e = 1 - \mu_{\lim} / \mu$, and only a small fraction, that is restricted by $\mu_{\lim}$, will undergo the centrifugal separation process in the inner vortex, Fig. 2. That particle fraction is separated from the two gas flows $\dot{V}_1$ and $\dot{V}_2$ by the efficiencies η_1 and η_2. Table 1 compares the flow structure and the efficiency equations of both cyclone types. Detailed information about the model is given in Muschelknautz (2019).

Table 1. Flow structure and separation efficiency of standard cyclones and uniflow cyclones.

	Standard Cyclones	Uniflow Cyclones
Flow structure	$\dot{V} = \dot{V}_{main} + \dot{V}_{\sec}$	$\dot{V} = \dot{V}_{main} + \dot{V}_{\sec}$ with $\dot{V}_{main} = \dot{V}_1 + \dot{V}_2$
Separation Efficiency	$\eta = [\eta_e + \eta_i\,(1-\eta_e)]\,\frac{\dot{V}_{main}}{\dot{V}} + \eta_{\sec}\,\frac{\dot{V}_{\sec}}{\dot{V}}$	$\eta = \frac{\eta_b}{1-\eta_{\sec}\,(1-\eta_b)} \left\{ \sum_{i=1}^{2} [\eta_e + \eta_i\,(1-\eta_e)]\,\frac{\dot{V}_i}{\dot{V}} + \frac{\dot{V}_{\sec}}{\dot{V}} \right\}$

Often multicyclones are operated with an underflow, i. e. a small portion of 1 to 3% of the inlet gas flow is withdrawn with the solids in order to improve the collection efficiency, Knowlton (2003). Here, underflow has not been considered.

Performance Comparison of Swirl Tubes and Uniflow Cyclones

Applying the calculation models for standard cyclones and for uniflow cyclones indicate in agreement with experiments that uniflow cyclones require significantly less space for separating a specified solids-gas mixture than standard cyclones but are generally also slightly less efficient, at least in their present state design, Muschelknautz (2017).

However, uniflow cyclones can achieve a higher efficiency per volume than standard cyclones if the available pressure drop is low (Muschelknautz 2021): Comparing calculated cut-off sizes d_c of swirl tubes with measured cut-off sizes of uniflow cyclones for separating the same gas-solids feed with the same pressure drop indicates that the efficiency of a standard reverse flow cyclone falls below that of its uniflow cyclone counterpart if its diameter approaches that of the uniflow cyclone and the pressure drop is low (Fig. 3a).

Fig. 3b compares both multicyclone types in terms of dimensionless numbers characterizing the cyclone performance, i. e. the cut-off size d_c in terms of the Stokes number

$$Stk(d_c) = \frac{\Delta\rho\, d_c^2\, v_z}{18\,\eta_g\, D_c} \tag{3}$$

and the pressure drop Δp in terms of the dimensionless Euler number

$$Eu = \frac{\Delta p}{\frac{1}{2}\rho_g\, v_z^2} \tag{4}$$

with the mean axial gas velocity through the cyclone $v_z = (4/\pi)\,\dot{V}/D_c{}^2$, the cyclone diameter D_c and the difference between particle and gas density $\Delta\rho = \rho_s - \rho_g$. In addition, the line resulting from the equation

$$Eu\,\sqrt{Stk(d_c)} = \sqrt{12} \tag{5}$$

is plotted in Fig. 3. This line provides a scaling rule for “well-designed” standard cyclones at low solids concentrations according to Peng et al (2004).

Fig. 3b shows that uniflow cyclones have *Stk*-*Eu*-values below the line for well-designed reverse flow cyclones according to Svarovsky, eq. (5), indicating that they achieve at least similar efficiencies per volume than optimally designed swirl tubes if the available pressure drop is low.

The courses of the cut-off sizes and the *Stk*-*Eu*-values shown in Fig. 3 lead one to expect that uniflow cyclones with even smaller pressure drops than designed in the experiments of

Schretter (2012) will have cut-off sizes below those of the compact swirl tubes (D_c=210mm) and *Stk*-*Eu*-values below those of the optimally designed swirl tubes.

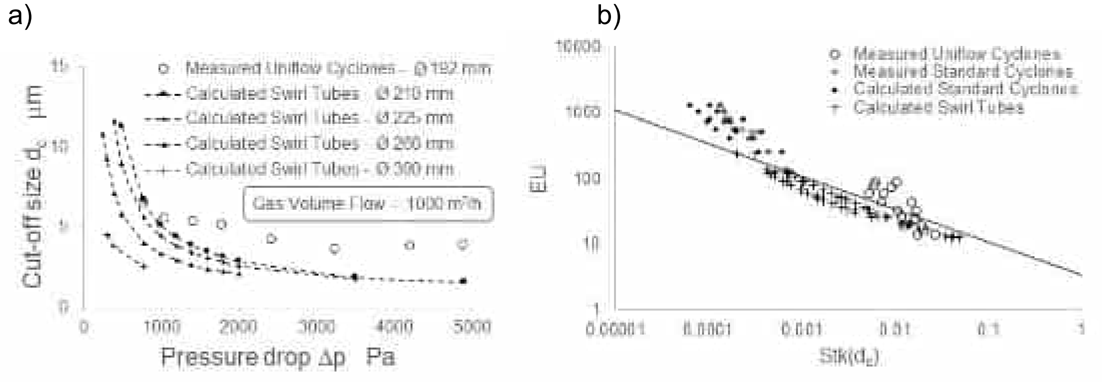

Fig. 3. a) Cut-off sizes d_c of swirl tubes with different diameters and of uniflow cyclones for separating the same gas-solids feeds as a function of cyclone pressure drop. b) *Stk-Eu*-values of uniflow cyclones, swirl tubes and standard cyclones. The solid line represents the line for well-designed reverse-flow cyclones according to Svarovsky (eq. (5)). Uniflow cyclone measurements by Schretter (2012), standard cyclone measurements by Neges (2013).

Application of Uniflow Multicyclones in Fluidized Bed Systems

Industrial application:

- Removal of 15 g/m^3 (actual) ash particles from hot gas (96% air, 4% steam) with an actual gas flow rate of 160,000 m^3/h at a temperature of 190°C.
- Particle density: 2500 kg/m^3, Range of PSDs see Fig. 4 right
- Gas density: 0.73 kg/m^3, Gas viscosity: $25.84 \cdot 10^{-6}$ Pa s)
- Installation in the flue gas duct of a fluidized bed reactor: Option a, see Fig. 4

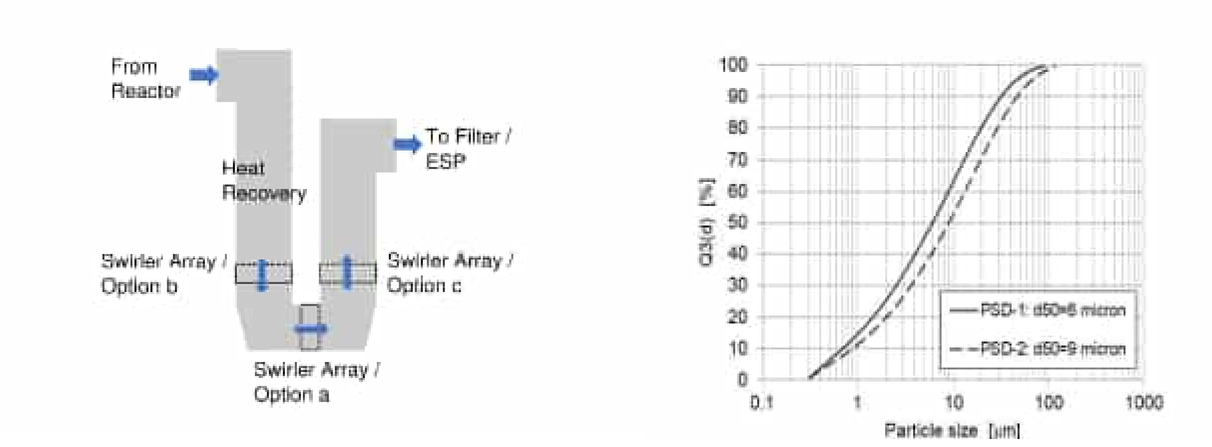

Fig. 4. Left: Options a, b (Fig. 1) and c for installing the swirler array in the flue gas duct of a fluidized bed reactor. Right: Range of particle size distributions of the feed into the swirler array.

In uniflow cyclones the collection efficiency of the solids bunker η_b has a stronger influence on the overall efficiency than in standard cyclones (Muschelknautz, 2019). The bunker collection efficiency depends significantly on the design of the cyclone and of the collection bunker. Furthermore, this efficiency is influenced by the operation data. In the calculation model according to Muschelknautz (2019) its value at the actual superficial gas velocity is derived from the value of η_b for v_z=10m/s. Typical values of η_b at v_z=10m/s vary between 70% and 80%. In the present case the calculations have been performed in addition for a lower bunker collection efficiency of 50% at v_z=10m/s. This takes conservatively into account disturbing effects on the bunker collection efficiency due to bypass flows through the solids discharge openings of neighboring cells.

Table 2. Design and performance data of the swirler array.

Number of swirlers (hexagonal packing)		280			
Total length of swirler array	mm	1000			
Cross section of duct	mm	2000 x 3900			
Diameter of swirler	mm	150			
Diameter of vortex finder	mm	91			
Diameter of core	mm	86			
Guide vane angle	°	35			
PSD of Feed		PSD-1		PSD-2	
Bunker collection efficiency $\eta_{b,0}$ at v_z=10m/s	%	50	70	50	70
Efficiency	%	48.6	60.8	58.2	70.6
Pressure drop	Pa	884	895	884	895

Conclusion

Installing an inline swirler array in the flue gas duct of fluidized bed reactors is appropriate to significantly reduce the particle load onto subsequent fine dust collectors. Depending on the PSD of the particle feed and on the arrangement of the swirlers fine particles (d50 ca. 5-10 micron) can be removed by efficiencies > 50% at low pressure drops < 1000 Pa.

References

Hoffmann, A. C., L. E. Stein. Gas cyclones and swirl tubes, 2nd ed., Springer. 2008.

Knowlton, T.M. Cyclone separators. In: Wen-Ching Yang (ed.) Handbook of Fluidization and Fluid-Particle Systems. Marcel-Dekker-Verlag. 2003.

Muschelknautz, E., V. Greif, Cyclones and other gas-solids separators, in Circulating Fluidized Beds (Eds: J. R. Grace, A. A. Avidan, T. M. Knowlton), Blackie Acad. & Profess., London. 1997. 181-213.

Muschelknautz, U., P. Pattis, M. Reinalter, M. Kraxner. Design criteria of uniflow cyclones for the separation of solid particles from gases, Proceedings of CFB-10, Sunriver, USA. 2011.

Muschelknautz, U. Performance comparison of uniflow cyclones and standard cyclones, Proceedings of CFB-12, Krakow. 2017. 421-428.

Muschelknautz, U. Design criteria for multicyclones in a limited space. Powder Technol. 2019. 2-20.

Muschelknautz, U. Comparing efficiency per volume of uniflow cyclones and standard cyclones, Chem. Ing. Tech. 2021. Vol. 93. No. 1-2. 1-18.

Neges, H. Experimentelle Untersuchungen zum Vergleich von Gleichstromzyklonen mit Gegenstromzyklonen. Bachelor Thesis, MCI Management Center Innsbruck, Austria. 2013.

Peng, W., A. C. Hoffmann, H. Dries. Separation Characteristics of Swirl-Tube Dust Separators, AIChE J. 50 (1). 2004. 87-96.

Schretter, P. Untersuchung optimaler Spiralgeometrien in Gleichstromzyklonen, Bachelor Thesis, MCI Management Center Innsbruck, Austria. 2012.

Würtl, R. Experimental investigation of uniflow cyclone performance, Diploma Thesis, MCI Management Center Innsbruck, Austria. 2007.

PRODUCT DESIGN OF POWDER FOR 3D PRINTING

J. Ruud van Ommen[1]*, Fuweng Zhang[1], Aris Goulas[1], Johan T. Padding[1], Riikka L. Puurunen[2], Gabrie M.H. Meesters[1]

[1]*TU Delft Process Technology Institute, Delft University of Technology, Van der Maasweg 9, Delft, 2629 HZ, the Netherlands*
[2]*Department of Chemical and Metallurgical Engineering, School of Chemical Engineering, Aalto University, Kemistintie 1, 02150 Espoo, Finland*

*Email: *J.R.vanOmmen@tudelft.nl*

Abstract

Atomic layer deposition in a fluidized bed is utilised for the coating of polyamide powders with thin films of silicon dioxide. By varying the number of exposure cycles the amount of deposited material can be precisely controlled, allowing for tailoring wetting, flowing, and melting behaviour of the powder. The favourable process operation characteristics enable a facile envisioning of scalable production in volumes complying with the demands of 3D printing applications.

Introduction

Additive manufacturing or 3D printing has attracted increasing interest in recent years, and is expected to make a large impact on various sectors of our society in coming years. It can be used for printing spare parts for machines, structured reactors, food structures, and even (parts of) constructing buildings and building ornaments for restoration purposes. An important class of 3D printing approaches, referred to as powder bed fusion techniques, relies on a powder as the starting material. The properties of the used powder are crucial for reaching high-quality printed products, *e.g.* with respect to resolution and strength.

Product design starts with specifying the functions of the final product. The next step is to come up with ideas to meet the needs that arise from these functions, after which the best ideas are selected. Finally, it is decided what form the product should take and how it can be manufactured as can be found in Cussler and Moggridge (2011). In order to come to high-quality powders to be used in 3D printing, it is crucial to possess tools by which one can tune powder properties such as flowability, wetting and melting behaviour. For several powder properties, it is crucial to have precise means to modify the surface. One way to tailor the surface properties of powders with high precision is to modify their surface *via* atomic layer deposition (ALD) in a fluidized bed reactor as can be found in Hakim et al. (2007). Fluidized bed ALD can provide particles with a film of just a few nm; this approach is both highly precise, versatile – in terms of both coating materials availability and ability to process different types of powder surfaces, including polyamide-based nanocomposites often used in 3D printing processes as Nevalainen et al. (2009) wrote – and scalable as can be found in van Ommen and Goulas (2019).

In the current research, we investigate the use of fluidized bed ALD technology in order to tune the wetting and melting behaviour of powders. In this way, we can optimize their performance in 3D printing approaches such as selective laser sintering. We also look into the powder flowability. Fluidization behaviour – especially in dense beds equipped with a stirrer – is a good predictor for the flowing performance of a powder in 3D printing applications. The particle size distribution and coating surface characteristics are optimized in order to maximize the flowability, as shown by measuring the angle of repose of the coated particles.

Experimental Part

A polyamide-based powder from Evonik Resource Efficiency GmbH (PA12, VESTOSINT® 3D 6644) was used as the substrate material. The ALD experiments were carried out in a home-built fluidized bed reactor operating at atmospheric pressure as can be found in Goulas and van Ommen (2013). The ALD chamber consists of a glass column (26 mm in internal diameter and 500 mm in height). Powder batches of up to 25 g were processed. The Si precursor (silicon(IV) chloride, Cl_4Si, 99% metals basis) and the co-reactant (demineralized water, H_2O) were contained in stainless steel bubblers kept at room temperature. The stainless steel tubing connecting the bubblers and the reactor were maintained at 50 °C to avoid precursor condensation. The reactor was heated by an infrared lamp placed parallel to the column with feedback control to maintain a constant temperature of 60 °C during ALD. The precursor and co-reactant vapours were transported to the reactor column by means of an inert gas flow (N_2, 99.999 vol.%) of 0.5 L min^{-1} (corresponding to a gas velocity of 1.6 cm s^{-1}). Prior to the deposition of the silicon dioxide (SiO_2) coatings the powders were initially fluidized with vibration assistance (at 36 Hz) at the reaction temperature for about 60 min. The ALD process consisted of sequential exposures of the powders to the Si precursor (10 s) and water (30 s), separated by purging steps (5 min) of inert gas. By repeating the exposure sequence, samples with 10, 20, 34 and 40 cycles were obtained.

Elemental analysis was carried-out by inductively coupled plasma optical emission spectroscopy (ICP-OES) using a PerkinElmer Optima 4300DV spectrometer. The angle of repose of the powders (AOR) was measured according to the Hosokawa powder testing method that can be found in de Campos and Ferreira (2013) and was used as an indicator of flowability. Wettability of the tested powders was measured using the sessile contact angle technique. A droplet of demineralized water is deposited on the powder surface bed and the dynamic angle between the solid surface and the tangent to the drop profile at the waterdrop edge is recorded using a CCD camera. The melting behaviour of the powders before and after coating is characterized according to the analysis that can be found in Valdesueiro et al. (2017). A fixed amount (0.2 g) of powder is placed on a silicon wafer which is heated to 180 °C by means of a hot plate equipped with a temperature control unit. A high definition camera with a light source is used to record the texture transitions of the powder during heating.

Results

Elemental analysis showed that the Si content of the coated powders increased with the number of ALD cycles in a relatively linear order as shown in Fig. 1. This resulted to Si loadings of up to 1.05 wt.% (for the sample coated with 40 ALD cycles).

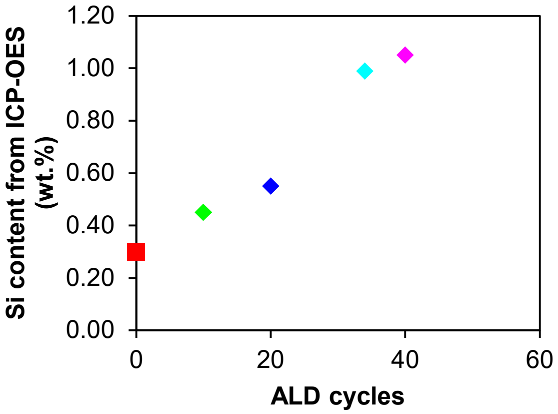

Fig. 1. Si content of the PA12 powders as a function of the ALD cycles.

The angle of repose measurements showed that the as-received (uncoated) powder has already satisfactory flow properties (Fig. 2). (“Good” with AOR at 31-35 degrees as can be found in Cheremisinoff and Cheremisinoff (1984).) However, coating the particles with an ultrathin film of SiO_2 already leads to a further increase in flowability as reflected by the observed decrease in their angle of repose. This is already the case even after only 10 ALD cycles, which corresponds to an expected SiO_2 film of only 0.5 nm as can be found in Guo et al. (2019). Increasing the number of cycles leads to further improvement of the flow properties, although these results are on the boundary of significance.

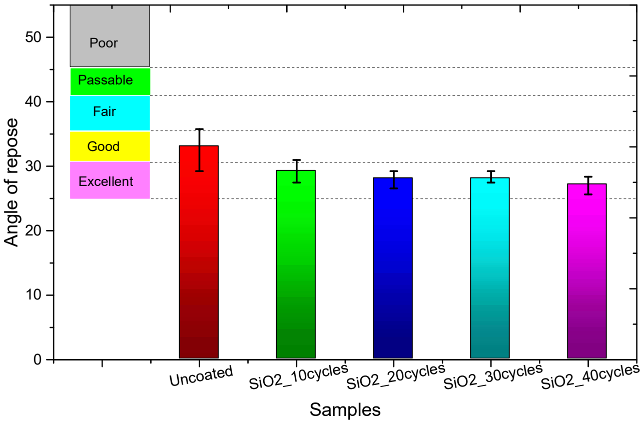

Fig. 2. Effect of SiO_2 ALD coating on the flowability of the PA12 powder.

Fig. *3* shows the effect of ALD coating on the powder wetting behaviour, indicated by the dynamic contact angle with water. The uncoated powder sample shows very hydrophobic behaviour with an average water contact angle of 125 degrees. Wettability is enhanced by depositing the ultrathin SiO_2 on the PA12 powder surface. The surface of the coated powder, after both 10 and 20 ALD cycles, became hydrophilic as the water droplet could fully penetrate into the powder layer. It can also be seen that there is a direct correlation of wettability with the number of film thickness from 10 to 20 cycles. For the powder coated with 10 cycles it takes around 180 s for water to fully spread into the powder bed, whereas it takes less than 2 s for the powder coated with 20 cycles.

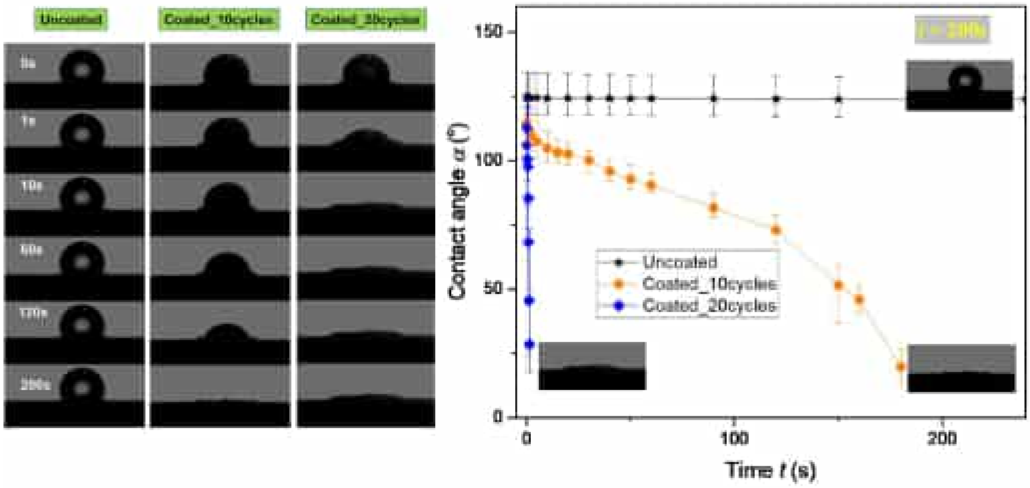

Fig. 3. Effect of SiO_2 ALD coating on water wettability of the PA12 powder. Left: images of water droplet spreading onto the powder surface as a function of time. Right: contact angle as a function of time after deposition of a water droplet onto the powder bed.

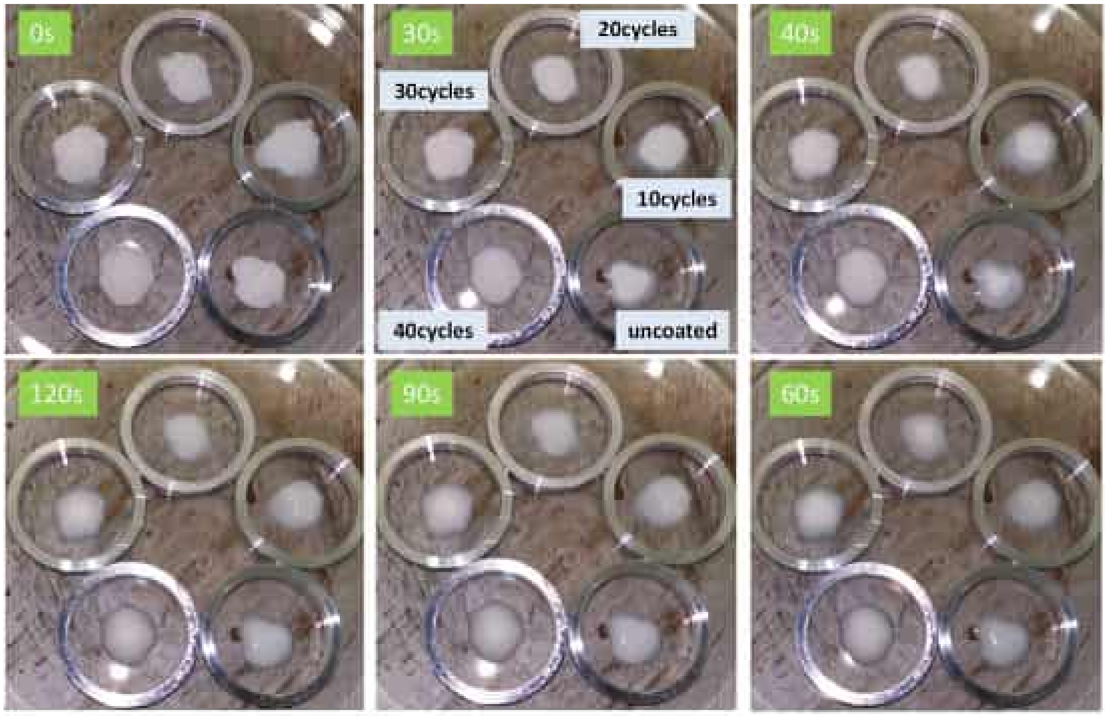

Fig. 4. The effect of ALD coating on the PA12 powder melting behaviour as a function of time.

The melting behaviour of different powder samples during an observation time of 2 min is shown in Fig. 4. The full melting of all particulate grains of the uncoated powder takes less than 60 s for the uncoated sample. However, for the powder coated with 40 cycles, there are quite a few grains that do not melt even after 10 min (Fig. 5). This indicates that the SiO_2 film on the powder surface is effectively delaying the melting process of the powder sample. It can also be clearly seen that for the same observation time, powder samples containing less Si lose more solid particles due to melting compared to powders with higher amounts of Si.

Fig. 5. The effect of ALD coating on the PA12 powder melting behaviour for 10 min under a heating temperature of 180 ^{o}C.

In this paper, we have shown that by coating a small amount of SiO_2 (Si < 1wt.%) the properties of particles used for 3D printing can be strongly influenced. This is very attractive when designing the optimum powder properties for 3D printing. First, we have shown that an ultrathin SiO_2 film enhances the flowability of the powder; this is a key property when 3D printing. Second, we have shown that the SiO_2 coating strongly improves the wettability of the powder. This is useful in 3D printing processes in which a carrying liquid is being used. Finally, we have shown that the coating can strongly influence the melting behaviour of the powder. This is in line with our earlier work on paint powder coating that can be found in Valdesueiro al. (2017). Tuning the melting behaviour can be especially important when combining multiple materials, e.g. 3D printing objects composed of both metal and polymer. Although the scope of this study was limited to a typically used ALD ceramic oxide, SiO_2, many more materials can be deposited using ALD as can be found in Miikkulainen et al. (2013). This provides an excellent addition to the toolbox for product design.

Conclusions

Atomic layer deposition (ALD) in a fluidized bed reactor is an attractive method to tune particle properties. We have demonstrated its ability to successfully modify the surface of polyamide-based powder, further optimizing the desirable powder characteristics. This study is a first step in demonstrating how ALD can be implemented in product design for 3D printing applications.

References

Cheremisinoff, N.P., P.N. Cheremisinoff, Hydrodynamics of gas-solids fluidization, 1984.

Cussler, E.L., G.D. Moggridge, Chemical Product Design, 2 ed., Cambridge University Press, Cambridge, 2011.

De Campos, M.M., M.d.C. Ferreira, A comparative analysis of the flow properties between two alumina-based dry powders, Advances in Materials Science and Engineering 2013 (2013) 7.

Goulas, A., J.R. van Ommen, Atomic layer deposition of platinum clusters on titania nanoparticles at atmospheric pressure, Journal of Materials Chemistry A 1 (2013) 4647-4650.

Guo, J., D. Benz, T.-T.D. Nguyen, P.-H. Nguyen, T.-L.T. Le, D.L. Zara, B. Liang, H.T.B. Hintzen, J.R.v. Ommen, H.V. Bui, submitted for publication, 2019.

Hakim, L.F., J.H. Blackson, A.W. Weimer, Modification of interparticle forces for nanoparticles using atomic layer deposition, Chemical Engineering Science 62 (2007) 6199-6211.

Miikkulainen, V., M. Leskelä, M. Ritala, R.L. Puurunen, Crystallinity of inorganic films grown by atomic layer deposition: Overview and general trends, Journal of Applied Physics 113 (2013) 021301:021301-021101.

Nevalainen, K., R. Suihkonen, P. Eteläaho, J. Vuorinen, P. Järvelä, N. Isomäki, C. Hintze, M. Leskelä, Mechanical and tribological property comparison of melt-compounded nanocomposites of atomic-layer-deposition-coated polyamide particles and commercial nanofillers, J. Vac. Sci. Technol. A 27 (2009) 929-936.

Valdesueiro, D., H. Hettinga, J.P. Drijfhout, P. Lips, G.M.H. Meesters, M.T. Kreutzer, J. R. van Ommen, Tuning roughness and gloss of powder coating paint by encapsulating the coating particles with thin Al2O3 films, Powder Technology 318 (2017) 401-410.

van Ommen, J.R., A. Goulas, Atomic layer deposition on particulate materials, Mater. Today Chem. 14 (2019) 100183.

SCALE-UP OF ROTATING FLUIDIZED BED REACTOR THROUGH NUMERICAL SIMULATIONS

Tingwen Li[1*], Sreekanth Pannala[1], Christoph Dittrich[2], and David West[1]

[1] *Corporate Technology & Innovation, SABIC, Houston TX, USA*
[2] *Technology & Innovation Chemicals, SABIC, Geleen, Netherlands*

*Email: *tingwen.li@sabic.com*

Abstract

A rotating fluidized bed reactor was proposed to enhance gas-solids contacting by imposing high centrifugal acceleration to form a dense annular bed with high gas-solids slip velocity. Significant benefits of process intensification through such a device have been reported in numerous studies. The current study focuses on scaling up a rotating fluidized bed from lab-scale to commercial-scale through computational fluid dynamics modeling. The numerical model was first validated using a lab-scale horizontal rotating fluidized bed setup with column diameter of 0.12 m available in the literature for predicting the general flow behavior. The device was then scaled up to 0.48 m and 1.92 m to investigate the general solids distribution and flow hydrodynamics at large scales. Major challenges for ensuring stable operation of rotating fluidized beds at large scales are discussed. The insights gained through this numerical scale-up exercise will be used to guide novel process development based on rotating fluidized beds.

Introduction

Fluidized beds, as found in numerous industrial applications, have many advantages as a gas–solids contacting device and solids handling equipment. However, there are certain limitations in the conventional fluidized bed technology, which tend to compromise the gas-solids contact at high gas velocity and restrain its capability of handling cohesive fine powders. A rotating fluidized bed (centrifugal fluidized bed in some references) was proposed to overcome some limitations of a conventional fluidized bed reactor by imposing a strong centrifugal force field to facilitate high gas-solids slip velocity in many studies (Fan 1978; Chen 1987; Qian et al. 2001; Nakamura et al. 2013). Rotating fluidized beds have been demonstrated with enhanced heat and mass transfer for different applications, including particle drying (Kang et al. 1995; Lim et al. 2010), fine powder granulation (Watano et al. 2003), filtration (Qian et al. 2004), and polymerization (Ahmadzadeh et al. 2008). The fluidization characteristics in a rotating fluidized bed have been studied experimentally and numerically for many small-scale facilities (Qian et al. 1998; Nakamura et al. 2007, 2013). However, one challenge that remains for the rotating fluidized bed technology is the difficulty to scale up the reactor for large-scale applications. So far, no systematic study on scaling up the concept for large-scale operation has been reported.

In the current study, numerical modeling is used to investigate limitations and challenges for scaling up the rotating fluidized bed. For this purpose, the numerical model is first validated against a lab-scale rotating fluidized bed experiment. Simulations are then conducted for rotating fluidized beds at different scales to understand the general flow behavior. Challenges encountered for ensuring the stable operation of a rotating fluidized bed at large scales are identified and factors affecting the current study are discussed.

Numerical Method

A rotating fluidized bed typically consists of a cylindrical vessel rotating along its axis to apply a centrifugal force field pushing particles toward the column wall forming a rotating dense annular bed (Qian et al. 2001). The rotating column wall, which is porous or perforated, serves as the gas distributor for introducing radial fluidizing gas to suspend the solids and enable gas-solids contact.

The rotating fluidized bed is simplified as a two-dimensional flow system normal to the axis of cylindrical column as shown in Fig. 1. The commercial software ANSYS Fluent is employed to carry out the numerical simulations using the kinetic theory based two-fluid model for gas-solids flow. The rotating column is simulated using the moving mesh approach and a no-slip boundary condition is assumed for both gas and solid phases at the moving wall. Uniform gas flow is introduced as a source in the cells next to the wall to fluidize the particle bed. The fluidizing gas then leaves through the central exit. During the numerical simulations, a dense annular bed with high rotation is initialized at the beginning. Gas flow is then introduced to fluidize the dense bed. Results are analyzed when the flow is fully developed.

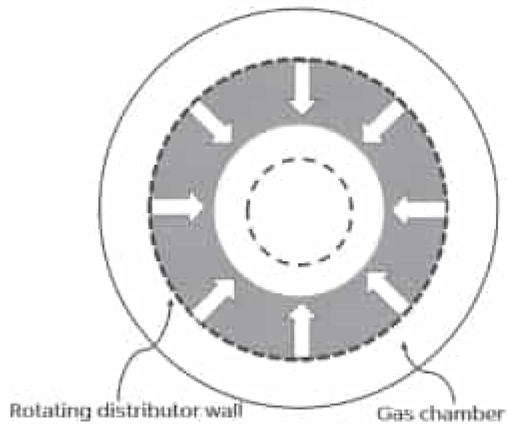

Fig. 1. Schematic of rotating fluidized bed

Small-scale Validation

A small-scale experimental setup is first simulated for validation. The experimental facility consists of a plenum chamber and a thin porous cylindrical air distributor made of stainless sintered mesh with 100μm opening and an inner diameter of 0.12 m (Nakamura and Watano, 2007). The horizontal cylinder rotates around its axis inside the plenum chamber. The bed has a length of 0.005 m and the front covers of the chamber and rotating air distributor are both made of transparent acrylic plastic to allow visual observation through a high-speed video camera. Detailed information on the experimental setup and testing results can be found in Nakamura and Watano (2007). Key parameters and physical properties used in the simulations are summarized in Table 1.

Table 1. Key numerical parameters and physical properties used for the simulations.

Parameter	Value	Parameter	Value
Vessel diameter	12 cm	Inner filter diameter	4 cm
Particle diameter	470 μm	Particle density	918 kg/m^3
Angle of repose	30 deg.	Restitution coefficient	0.9
Particle-particle friction	0.32	Particle-wall friction	0.34
Packing limit	0.63	Friction packing limit	0.61
Gas density	1.18 kg/m^3	Gas viscosity	1.8 e-5 Pa.s
Rotational speed	40.4 rad/s	Absolute pressure	1 atm
Bed inventory	9 g		

Snapshots of solids volume fraction from the current numerical simulations are shown in Fig. 2 for comparison with photos of particle flow at the top of the horizontal rotating fluidized bed taken by high-speed camera under different superficial gas velocities from the experiment as well as CFD-DEM simulations results in Nakamura and Watano (2007). With the fixed rotational speed of 40.4 rad/s, the imposed centrifugal acceleration is maintained at 10 times gravity acceleration. Both simulation and experiment show fixed bed, partial fluidization, partial bubbling, and bubbling regimes as the gas velocity increases. More vigorous bubbling can be observed at high gas velocities which leads to further bed expansion. The bubbling behavior predicted in the numerical simulations resembles the observations from high-speed videos of the experiment. In addition, the influence of gravity along the vertical direction can be clearly observed in the numerical simulations of horizontal rotating fluidized bed, which results in early incipient of fluidization, larger bubble size, and higher bed expansion near the top of the horizontal column away from the ground where the net centrifugal acceleration is the least.

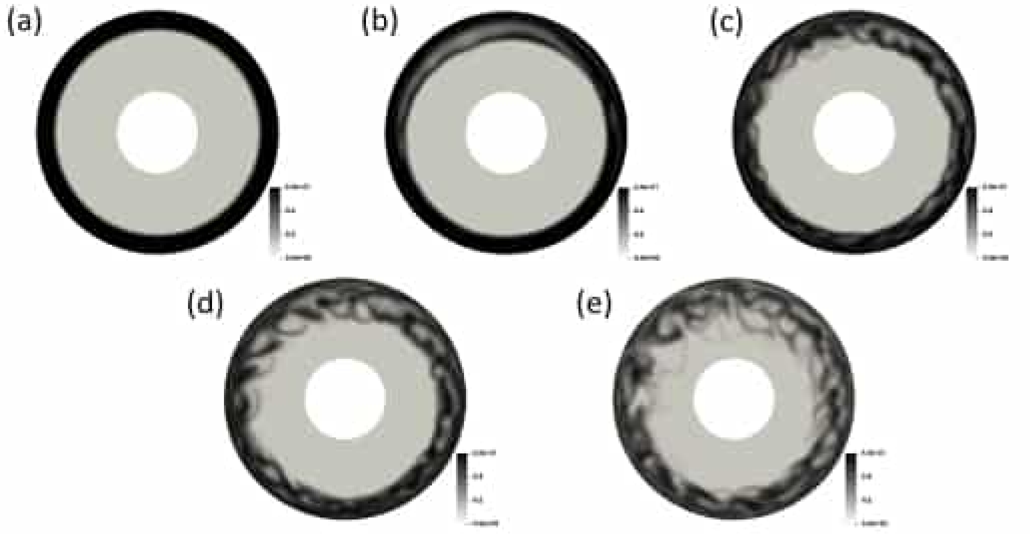

Fig. 2. Snapshots of solids distribution from numerical simulations at different superficial gas velocities (a) 0.30 m/s (b) 0.60 m/s (c) 0.88 m/s (d) 1.10 m/s (e) 1.47 m/s

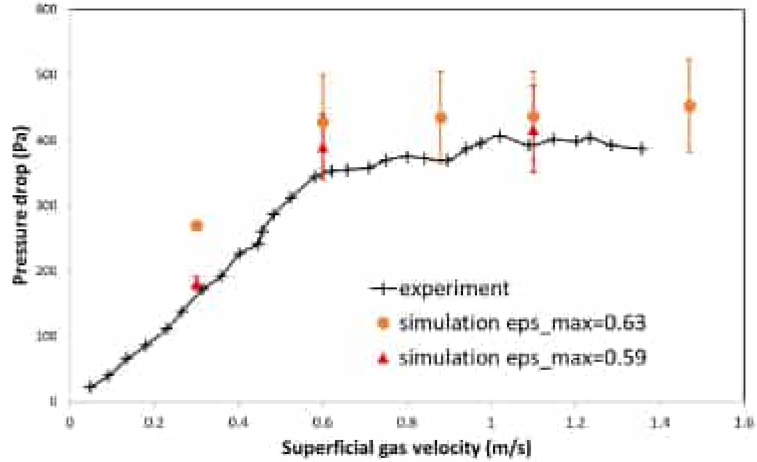

Fig. 3. Comparison of pressure drop between numerical simulations and experimental data

The simulated pressure drop through the bed under different superficial gas velocities is shown in Fig. 3 for comparison against the experimental measurements reported in Nakamura and Watano (2007). It should be noted that the pressure distribution along the distributor plate is non-uniform due to the presence of asymmetric flow behavior caused by gravity. The overall average is shown with an error bar indicating the standard deviation for pressure drop along different radial directions. The simulations predict the typical fluidization curve for rotating fluidized bed. However, the current simulations tend to over-predict the pressure drop especially in the fixed bed regime. The over-prediction is attributed to the high solids concentration under fixed bed condition, which is close to the maximum packing limit of 0.63, a typical value used for frictionless spherical particles. For frictional particles, it has been shown that the maximum packing is affected by the friction coefficient (Chialvo et al., 2012) and a value of 0.59 is then used which yields improved agreement especially for a fixed bed and partial fluidization regimes. Overall, the validation study demonstrates that the current numerical method is capable of capturing the general flow behavior of a rotating fluidized bed.

Scale-up Study

With reasonable confidence in the modeling tool, the lab-scale rotating fluidized bed setup by Nakamura and Watano (2007) is chosen as the starting point for scaling up to two larger scales. The general rule for scale-up followed in the current study is to maintain the same intensity of centrifugal acceleration at different scales. Two additional cases are considered by subsequently increasing the reactor scale by a factor of 4. Consequently, three different scales of small, medium, and large, corresponding to reactor diameter of 0.12 m, 0.48 m and 1.92 m respectively, are studied. Identical bed material and same superficial gas velocity are considered for all cases. As the centrifugal acceleration is imposed by the rotating wall at fixed angular velocity, the rotational speed of the column is reduced for large scale. Detailed operating conditions are summarized in Table 2.

Table 2. Detailed operating conditions considered for cases at different scales

Parameter\Case	**Small**	**Medium**	**Large**
Diameter (m)	0.12	0.48	1.92
Superficial gas velocity (m/s)	1.1	1.1	1.1
Rotation speed (rad/s)	40.4	20.2	10.1
Initial bed loading (kg)	1.816	29.05	465
Centrifugal acceleration (g)	10	10	10

Some transient snapshots of solids distribution are shown in Fig. 4 when the flow reaches a fully developed state. For all cases, an annular bubbling fluidized bed has been developed. Small bubbles originate from the outer gas distributor and grow into bigger ones towards the inner bed surface. Bubbles erupt at the bed surface and eject particles into the freeboard region. Depending on the relative strength of the drag and centrifugal forces, particles can escape through the inner outlet or return to the bed surface. It can be seen from the snapshots that the non-dimensional bed height (actual bed height divided by the reactor radius) tends to decrease as the reactor size is increased. This is especially evident in the bottom region, where the bed height can be measured about 0.012 cm, 0.031 cm, and 0.086 cm for small, medium, and large-scale cases respectively.

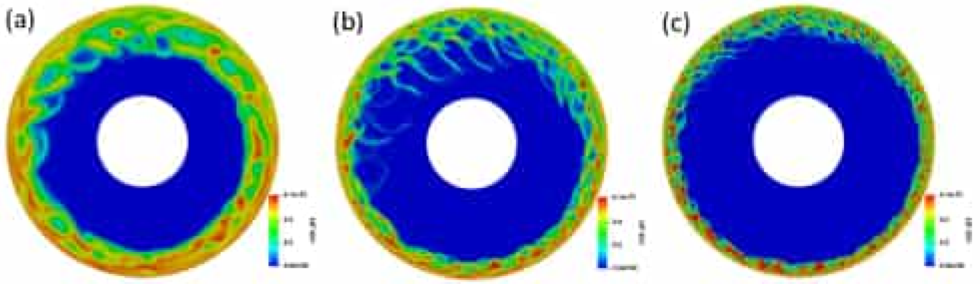

Fig. 4. Solids distribution in rotating fluidized bed at different scales (a) 0.12 m; (b) 0.48 m; (c) 1.92 m.

The time history of the solids inventory indicates that both medium- and large-scale cases tend to lose solids due to entrainment. Once the particles get entrained and escape from the central exit, they cannot return. After the initial significant solids entrainment, the bed reaches a fully developed state with only occasional mild solids entrainment and the bed inventory remains relatively stable. The bed inventory at fully developed state is about 66% and 48% of the target inventory based on the small-scale results. Clearly the reduced inventory compromises the objective of reactor scale-up and inevitably affects the reactor performance.

The strong solids entrainment is partially attributed to the asymmetric flow behavior caused by gravity. The effect of gravity can be minimized by imposing high centrifugal acceleration at extreme RPM or rotating the column along the gravity direction. Fig. 5 shows the transient results for small and large-scale cases without gravity. The flow demonstrates good axi-symmetric behavior. In addition, the solid entrainment has been substantially reduced and a much higher inventory can be maintained during stable operation for the large-scale case.

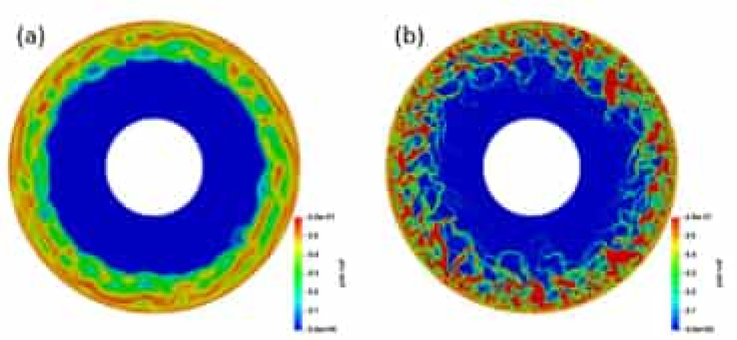

Fig. 5. Snapshots of solids distribution for different cases without gravity (a) 0.12 m; (b) 1.92 m

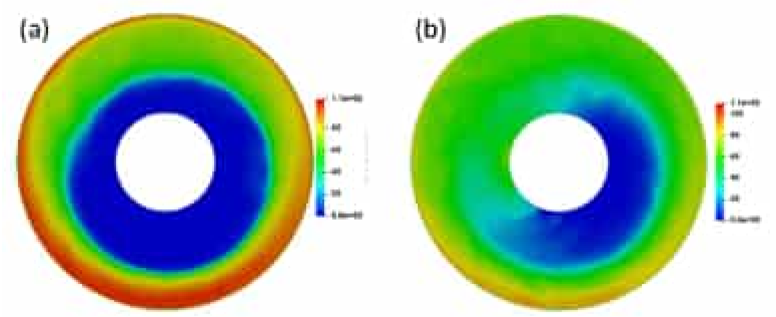

Fig. 6. Distribution of mean centrifugal acceleration for (a) no-slip wall; (b) partial-slip wall (unit: m/s^2)

In all simulations, a no-slip wall boundary is used which over-estimates the tangential momentum transfer from the moving wall to the annular bed. A more realistic partial-slip wall boundary condition by Johnson and Jackson (1987) is tested. With a specularity coefficient of 0.1, the limited tangential momentum transfer leads to non-negligible difference between particle tangential velocity and wall velocity. Fig. 6 shows a lower centrifugal acceleration from a partial-slip wall as compared to the no-slip wall condition. The low centrifugal acceleration fails to sustain the initial loading and the bed inventory reduces by about 25% due to entrainment. These results clearly indicate the important role of particle-wall interaction in the operation of rotating fluidized bed, as it determines how effectively the energy can be transferred to the solid bed to sustain high centrifugal force field. The particle-wall interaction poses two challenges when scaling up the rotating bed reactor. First, the increased wall velocity at large scale causes less effective tangential momentum transfer, i.e., high slip velocity at wall leads to small specularity coefficient (Li and Benyahia 2012). On the other hand, as the reactor size increases, the tangential motion of particles imparted by the rotating wall needs to propagate further inside to maintain high centrifugal acceleration throughout.

Conclusion

In this study, numerical simulations are conducted to study the hydrodynamics in a rotating fluidized bed with a focus on reactor scale-up. Numerical simulations of a lab-scale horizontal rotating fluidized bed is first conducted for validation against experimental observation and measurements. The reactor is then scaled up by a factor of 4 and 16 while keeping constant centrifugal force intensity. The solids distributions are examined for cases at different scales to understand the challenges associated with reactor scale-up.

The numerical results suggest increasing tendency of solids entrainment during the scale-up exercise which compromises the performance of large-scale reactor. Two factors affecting predicted flow behavior of the rotating fluidized bed are further investigated. It is found that gravity has significant impact on the flow behavior of a horizontal rotating fluidized bed. The role of particle-wall interaction is examined through a more realistic wall boundary condition. The rotating column wall becomes less effective to drive the annular bed for maintaining high centrifugal acceleration. An additional mechanism is needed to enhance tangential momentum transfer from the wall to the annular bed to aid scale-up of a rotating fluidized bed.

References

Ahmadzadeh, A., H. Arastoopour, F. Teymour, M. Strumendo. Population balance equations' application in rotating fluidized bed polymerization reactor, Chem Eng Res and Des. 2008. 86, 329-343.

Chen, Y., Fundamentals of a centrifugal fluidized bed, AIChE J. 1987, 33, 722-728.

Chialvo, S., J. Sun, S. Sundaresan. Bridging the rheology of granular flows in three regimes, Phys Rev E. 2012. 85, 021305.

Fan, L.T. Fluidized bed combustion in centrifugal field, Energ Commun. 1978. 4, 509.

Johnson, P.C., R. Jackson. Frictional collisional constitutive relations for antigranulocytes-materials, with application to plane shearing. J Fluid Mech.1987. 176, 67-93.

Kang, Y., J.S. Shim, M.J. Choi, K.W. Lee, S.D. Kim. Drying of fluidized materials in a centrifugal fluidized bed, Korean J Chem Eng. 1995. 12, 325-330.

Li, T., S. Benyahia. Revisiting Johnson and Jackson boundary conditions for granular flow, AIChE J. 2012. 58, 2058-2068.

Lim, H.O., J.J. Seo, K. Kang. Drying of thermally-weak organic powder in a centrifugal fluidized bed, Adv Powder Technol. 2010. 21, 131-135.

Nakamura, H., S. Watano. Numerical modeling of particle fluidization behavior in a rotating fluidized bed, Powder Technol. 2007. 171, 106-117.

Nakamura, H., T. Tokuda, T. Iwasaki, S. Watano. Numerical analysis of particle mixing in a rotating fluidized bed, Chem Eng Sci. 2007. 62, 3043-3056.

Nakamura, H., T. Kondo, S. Watano. Improvement of particle mixing and fluidization quality in rotating fluidized bed by inclined injection of fluidizing air, Chem Eng Sci. 2013. 91, 70-78.

Qian, G.H., I. Bagyi, R. Pfeffer, H. Shaw, J. Stevens. Soot removal from diesel engine exhaust using a rotating fluidized bed filter, Adv Env Res. 2004. 8, 387-395.

Qian, G.H., I. Bagyi, R. Pfeffer, H. Shaw, J. Stevens. A parametric study of a horizontal rotating fluidized bed using slotted and sintered metal cylindrical gas distributors, Powder Technol. 1998. 100, 190–199.

Qian, G.H., I. Bagyi, I.W. Burdick, R. Pfeffer, H. Shaw. Gas-solid fluidization in a centrifugal field, AIChE J. 2001. 47, 1022-1034.

Watano, S., Y. Imada, K. Hamada, Y. Wakamatsu, Y. Tanabe, R.N. Dave, R. Pfeffer. Micro granulation of fine powders by a novel rotating fluidized bed granulator. Powder Technol. 2003. 131, 250–255.

OPERATION CHARACTERISTICS OF A 90 T/H INDONESIAN COAL-FIRED CIRCULATING FLUIDIZED BED BOILER

Xiwei Ke[1], Jin Cai[2], Jianguang Liu[2], Lujian Chen[1], Man Zhang[1], Hairui Yang[1]*, Junfu Lyu[1], Jianchun Zhang[2]

[1] *Key Laboratory for Thermal Science and Power Engineering of Ministry of Education, State Key Laboratory of Power Systems, Department of Energy and Power Engineering, Tsinghua University, Beijing, 100084, China*

[2] *Shanxi Research Institute for Clean Energy, Tsinghua University, Taiyuan, 030032, China*

[2] *Taiyuan Boiler Group Co. Ltd., Taiyuan, 030021, China*

*Email: *yhr@mail.tsinghua.edu.cn*

Abstract

Due to the economic benefits and well-performed combustion characteristics, the Indonesian coal is increasingly popular in the market of coal power generation. To get better understanding on the operation characteristics of a CFB boiler burning such coal, one 90 t/h CFB boiler was tested. Although the coal ash content was very low, the boiler can maintain stable operation without injection of additional bed materials such as sand. Analyses showed that most of the coal ash particles were fine and mainly participated in the solid circulation. Because the slag cooler was closed during operation, the coarse particles can stay in the dense bed for a long time, and a fair number of them came from the initial bed materials which were added in boiler start-up stage. Moreover, with the help of two high efficiency cyclones, most fine particles can be separated and the $d_{0.5}$ of fly ash was only 5εm. These measures ensured sufficient bed inventory and thermal capacity inside furnace. Historical operation data indicated that this boiler had good load flexibility. Other than the operation strategy used by this 90 t/h CFB boiler, adding additional bed materials during operation or adopting bottom ash self-circulation can also help to improve the performance of a CFB boiler burning low ash content fuel.

Introduction

Due to the certain solid suspension density and high thermal capacity inside furnace, the CFB boilers have the advantages of load flexibility and fuel type adaptability. Normally, almost all solid fuel can be burned in CFB boilers including coal, coal gangue, oil shale, biomass, etc. However, He et.al. (2010) indicated that It is difficult to maintain enough high solid circulating rate of CFB boilers if they burn low ash content fuel. In these cases, the additional circulating materials such as sand are usually suggested in order to reach certain bed quality.

In recent years, the Indonesian coal is increasingly popular in the market of coal power generation because of its economic benefits and well-performed combustion characteristics (Drosatos, 2017), and some industrial CFB boilers start to select such coal as feeding fuel. For example, the 550 MW supercritical CFB boilers in Samcheok Power Plant, Korea, burn six different kinds of Indonesian coal alternately (Li, 2018). A 430 t/h Indonesian coal-fired CFB boiler located in Indonesia was also successfully put into operation in 2013 (Bao, 2014). It is interesting that both two CFB boilers can maintain stable operation without injection of additional bed materials (ABM), even this kind of coal has very low ash content (<10%). Regrettably, to date, there has been little investigation reported for the operation characteristics of such CFB boilers which burn Indonesian coal or other similar fuel only.

In this paper, one 90 t/h CFB boiler purely burning Indonesian coal in Dongguan Junye Paper Co., Ltd., China, was selected to study its combustion conditions, including fly/bottom ash properties and NOx emission. The variation of some operation parameters with boiler load was also discussed. Based on these analyses, several suggestions for the design and operation of a CFB boiler burning low ash content fuel were proposed.

Experimental Section

The Dongguan (DG) 90 t/h CFB boiler was designed by Taiyuan Boiler Group Co. Ltd. and came into use in 2018. This boiler adopted natural circulation with two drums, and had two high efficiency insulated cyclones. The SNCR and WFGD systems were designed to control the NOx and SO_2 emission. The main structure parameters of this boiler and layout of some measuring points were shown in Fig. 1. The design operation parameters were listed in Table 1.

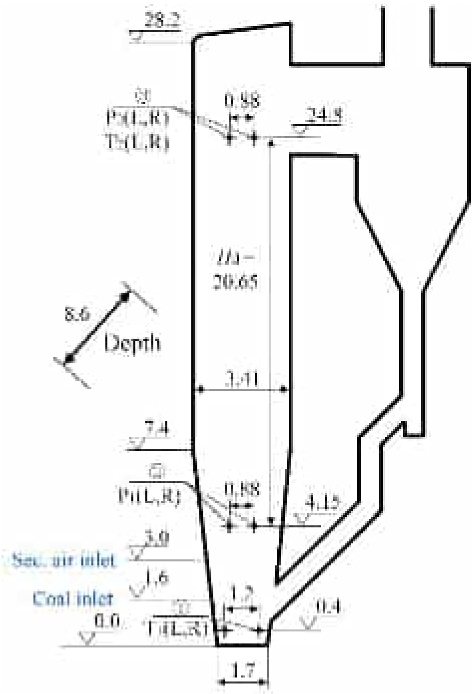

Fig. 1. Schematic diagram of the DG 90 t/h CFB boiler (Unit: m)
①-bottom bed temp. measuring points
②-differential pressure (Low) measuring points
③-upper furnace temp. and differential pressure (High) measuring points

Table 1. Design parameters of the DG 90 t/h CFB boiler

Item	Unit	Value
Boiler rated load (BRL)	$t{\cdot}h^{-1}$	90
Superheated steam temp. (T_s)	℃	540
Superheated steam pressure (P_s)	MPa	9.81
Drum steam pressure (P_{ds})	MPa	10.7
Boiler feed-water temp. (T_{fw})	℃	150
Exhaust gas temp. (T_{eg})	℃	135
Average bed temp. (T_b)	℃	873
Excess air coefficient (α)	-	Ò1.4
Primary air ratio (R_{sec})	-	~ 0.5
Boiler efficiency (q_b)	%	~ 90

One kind of Indonesian coal was selected as the only feeding fuel, whose ultimate and proximate analyses were listed in Table 2. The suggested feeding coal size range was 0~12mm, and the design coal particle size distribution (PSD) was listed in Table 3.

Table 2. The analysis of feeding coal

Proximate analysis / %				Ultimate analysis / %					$Q_{ar,net,p}$ / $MJ{\cdot}kg^{-1}$
M_{ar}	A_{ar}	V_{ar}	FC_{ar}	C_{ar}	H_{ar}	N_{ar}	S_{ar}	O_{ar}	
33.85	3.40	33.32	29.42	44.71	5.15	0.65	0.10	12.14	17.64

Table 3. Design feeding coal particle size distribution

Particle size / mm	0 ~ 0.5	0.5 ~ 3.0	3.0 ~ 8.0	8.0 ~ 12.0
Mass fraction / %	20.0	50.0	20.0	10.0

During the test, the fly ash was sampled directly in the ash outlet of precipitator. The slag discharging system of this boiler was a roller slag cooler without recovering the heat of cooling water, and the bottom ash can be collected in the outlet of slag cooler. The exhaust gas composition analyzing point was set at the outlet of desulfurization tower and the NOx /

SO2 concentrations can be read directly in DCS system. While the CO concentration was measured after precipitator by an electrochemical flue gas analyzer (Testo 340). Some operation parameters such as temperature, pressure, etc., were recorded once every 1 hour for purpose of analyzing the influence of boiler load. The entire record time was 466 hours.

Results and Discussion

1. Testing operation characteristics and mass balance

The main operation conditions under testing case was listed in Table 4. For this boiler, the initial bed materials (IBM), namely the river sand or other boilersô bottom ash, were just added in boiler start-up stage (it is a pity that the IBM were failed to be obtained during the field test). Under stable operation, ABM were not needed, which is similar with the two CFB boilers mentioned before. Meanwhile, the slag cooler was closed for most of time and no slag was discharged, so that the wind box pressure can be kept around 8 kPa. In other words, almost all ash escaped from the boiler as fly ash. It has once again proven that under specific conditions, the CFB boilers can maintain stable operation without using ABM even if the fuel ash content is too low.

Table 4. The operation condition of the DG 90 t/h CFB boiler under testing case

D_b / %	T_s / ℃	P_s / MPa	P_{ds} / MPa	α	R_{sec}	T_b / ℃	T_{fup} / ℃
70.9	464.2	4.9	5.59	1.24	0.49	791	816
T_{eg} / ℃	P_w / Pa	ΔP_d / Pa·m^{-1}	C_{CO} / mg·Nm^{-3}	Carbon content / %		C_{SO2} / mg·Nm^{-3}	C_{NOx} / mg·Nm^{-3}
				Bottom ash	Fly ash		
119	8304	42.6	1469	1.71	10.42	0.7	43.6

D_b ï boiler load, means the percentage of the current evaporation capacity accounts for BRL; T_{fup} ï temperature in upper furnace; P_w - static pressure of wind-box, which is equal to the sum of bed and distributor pressure drops; ΔP_d ï pressure drop per meter across dilute zone; C_{CO} ï CO concentration in flue gas after precipitator [6% O_2, basis]; C_{NOx} ï NOx concentration in flue gas after desulfurization tower [6% O_2, basis]; C_{SO2} ï SO_2 concentration in flue gas after desulfurization tower [6% O_2, basis]

In order to further analyze the mass balance of this CFB boiler, the slag cooler was opened for 10 minutes. The boiler load was kept around 71 t/h during the test.

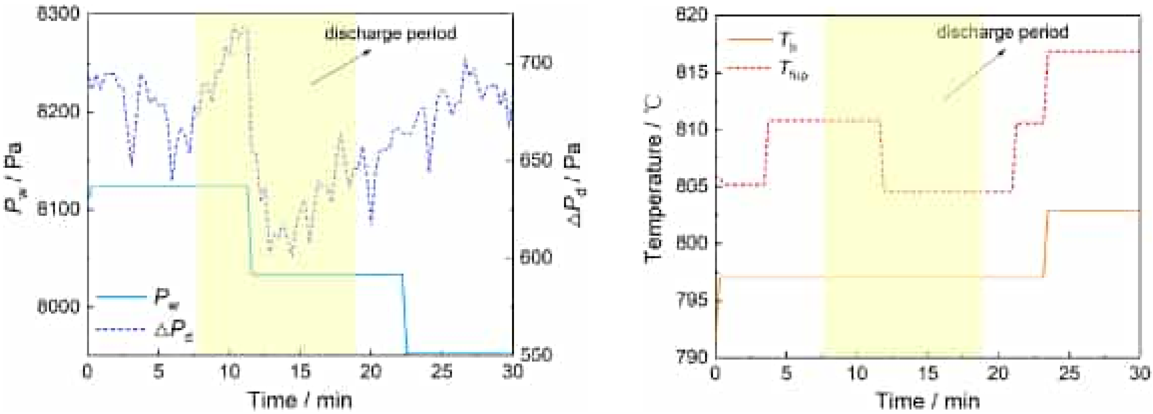

(a) Pressure variation (b) Temperature variation

Fig. 2. The variation of some pressure and temperature parameters during discharge

From Fig. 2, it can be seen that after some bottom ash was discharged, the P_w significantly decreased. The ΔP_d and T_{fup} also decreased due to the loss of some circulating materials, while the former trend was more obvious. When slag cooler was closed again, the ΔP_d and T_{fup} can return to the original level in short time. For P_w, however, it would take a very long time to recover if the operation state keeps stable. It implied that the particles stayed in bottom bed and the particles participated in solid circulation may be different in source of supplement, role, even compositions.

To test this, the properties of sampled fly ash and bottom ash were analyzed. In addition, the intrinsic ash particle size distribution (IAPSD) of this kind of Indonesian coal was also obtained by means of static combustion and cold sieving (SCCS), which was proposed by Yang et al. (2003). The PSD of fly ash and intrinsic ash were shown in Fig. 3.

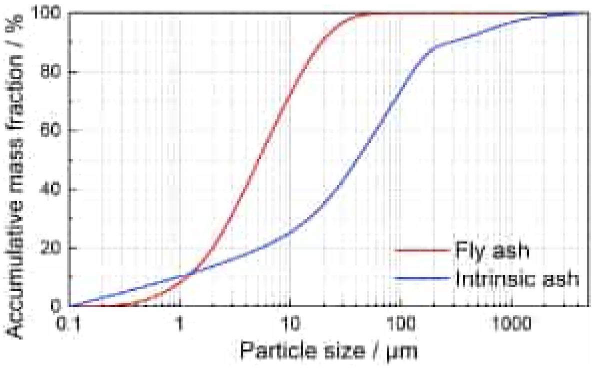

Fig. 3. Particle size distribution of fly ash and intrinsic ash

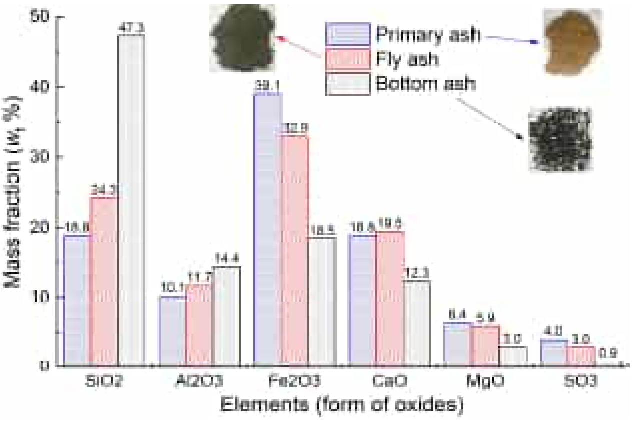

Fig. 4. Comparison of the chemical composition among fly ash, bottom ash and intrinsic ash

It can be seen that the fly ash was very fine with $d_{0.5}$ of 5εm. The SCCS experiment also showed that the intrinsic ash was quite fine ($d_{0.5}$ ≈ 40εm) and nearly no gangue exists. However, the sampled bottom ash was completely different from the fly ash or intrinsic ash in appearance, which was much larger and harder. The XRF and nitrogen adsorption tests results (Fig. 4 and Table 5) also revealed that the fly ash and bottom ash were different substances. The chemical and physical properties of fly ash was similar to that of intrinsic ash, while the other was closer to the IBM.

Table 5. The comparison of physical properties between fly ash and bottom ash

Sample	Apparent morphology	Specific area (m^2/g)	Porosity	Particle density (kg/m^3)	α_1 (%)	α_2 (%)	α_3 (%)
Fly ash	red-brown, clay-like	55.91	0.394	1836.8	4.27	23.48	72.25
Intrinsic ash	Khaki, clay-like	42.35	0.322	2670.5	2.64	27.25	70.11
Bottom ash	black, hard block	6.00	0.017	2969.6	1.32	11.46	87.22

α_1-microporous ratio (<2nm); α_2-mesoporous ratio (2~50nm); α_3-macroporous ratio (50~250nm)

Based on these phenomena, it can be inferred that how the DG 90 t/h CFB boiler maintained its mass balance. Due to the ash formation characteristics of Indonesian coal (Ke, 2019), most ash particles from coal combustion were fine and mainly participated in the solid circulation. While a fair number of particles in the bottom of furnace came from the IBM which were added in boiler start-up stage. Because the slag cooler was closed during operation, the coarse bed materials can stay in the dense bed for a long time. Though these coarse particles cannot be entrained by flue gas and seems invalid for circulation system, they ensured sufficient bed inventory and thermal capacity inside furnace, which is benefit for stable and uniform fluidization. Moreover, with the help of two high efficiency cyclones, the vast majority of bed materials were separated. Therefore, a certain amount of solid circulating rate can be formed.

As for pollution emission, it is interesting that the NOx concentration in exhaust gas was just around 50 mg/Nm^3 without running the SNCR system (listed in Table 4), which was unexpected compared to other CFB boilers burning high volatile coals. In contrast, the original NO_x emission of the 550 MW supercritical CFB boilers in Samcheok Power Plant was 120~200 ppm. There are three possible reasons for this. Firstly, the furnace temperature was relatively low (~805℃). Secondly, the incomplete combustion resulted in high CO concentration in flue gas and high char content in bed inventory, which was beneficial to the NO_x reduction (C_{CO} in exhaust gas was more than 1400 mg·Nm^{-3}, carbon content in fly ash was more than 10%). Thirdly, the small size of circulating ash and high solid suspension density (ΔP_d > 40 Pa·m^{-1}), namely high bed quality, can also help to reduce the NO_x emission of CFB boilers (Ke, 2018).

2. Variation of Operation Parameters with Boiler Load

A long-time historical data revealed that this 90 t/h CFB boiler can keep stable operation in a wide range of boiler load, which indicated that it had good load flexibility. The variation of pressure and temperature with boiler load was shown in Fig. 5.

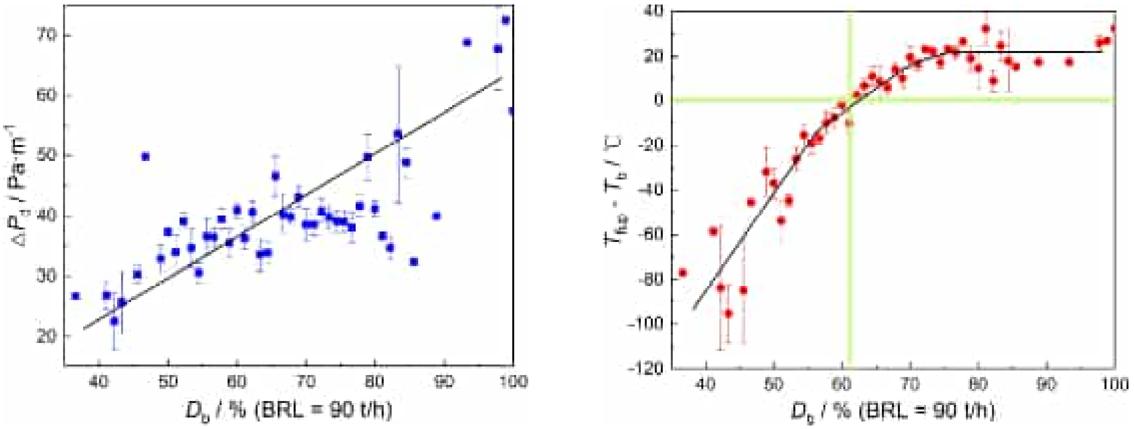

(a) D_b (b) T_{fup} - T_b

Fig. 4. The boiler load vs. some operation parameters

With the increase of boiler load, the circulating ash rate and solid hold-up in dilute zone increased, resulting in the increase of ΔP_d (Fig. 5(a)). As for temperature, within low boiler load range, the solid circulating rate was not high, therefore the T_{fup} was lower than T_b. When the load increased, the temperature difference was smaller and smaller, then the whole furnace temperature became nearly uniform in the load of 60% BRL. Further increasing the load, the T_{fup} was even higher than T_b, namely the temperature inversion occurred, though the variation trend was less obvious (Fig. 5(b)). The uniform temperature distribution can only be realized by the strong gas-solid mixing in axial direction. It was caused by the formation of clusters, namely the fast fluidization state in dilute zone was formed.

3. Technical routes of a CFB boiler burning low ash content fuel

To improve the performance of a CFB boiler burning low ash content fuel, according to the operation characteristics of the DG 90 t/h CFB boiler and some other industrial practices, following three technical routes were proposed for reference.

a) Adding the initial bed materials with suitable size and low attrition rate in the boiler start-up stage. During stable operation, reducing the amount of bottom ash discharged or even closing the discharge device to keep sufficient bed inventory.

b) During operation, the additional bed materials with suitable size such as sand can be added into furnace to increase the solid circulating rate. In this case, the discharge system can be run, while it should be adjusted to reach a well-performed mass balance. The practices in a 73.2 t/h CFB boiler verified the reliability of this method (He, 2010).

c) A little different from the route b), using part of the discharged bottom ash as the additional bed materials, which can be regarded as "bottom ash self-circulation". In practice, the recycled bottom ash can be crushed before re-entering furnace in order to obtain a suitable PSD. Other than the economic benefit (do not need to find other materials), the lime particles that are not fully sulfated in bottom ash are reused, which can potentially increase the residence time of lime. However, this method increases the complexity of boiler system. The 550 MW supercritical CFB boilers in Samcheok Power Plant adopted this technical route.

All three routes have one thing in common: high efficiency cyclone is suggested for keeping most bed materials staying in furnace, thus the sufficient bed inventory can be ensured.

Conclusions

In this paper, one 90 t/h CFB boiler burning Indonesian coal was tested to study its operation characteristics. Although the coal ash content was very low, the boiler can maintain stable operation without injection of additional bed materials. It was achieved by several conditions. Firstly, most of the coal ash particles were fine and mainly participated in the solid circulation. Secondly, the slag cooler was closed, thus the coarse particles can keep staying in dense bed, and a fair number of them came from the initial bed materials which were added in start-up stage. Thirdly, two high efficiency cyclones can separate most fine particles. These measures ensured sufficient bed inventory and thermal capacity inside furnace. In addition, the NOx emission of this boiler was just around 50 mg/Nm^3 without running the SNCR system. It may be attributed to low bed temperature, strong reducing atmosphere inside furnace and high bed quality. Besides, historical operation data indicated that this boiler had good load flexibility.

Other than the operation strategy used by the 90 t/h CFB boiler, adding additional bed materials during operation or adopting bottom ash self-circulation can also help to improve the circulating performance of a CFB boiler. This paper is valuable not only for the Indonesian coal, but also with some reference value for other types of low ash content fuel such as biomass.

Notation

C	gas component concentration, mg·Nm^{-3}	D_b	boiler load, %
P_{ds}	drum steam pressure, MPa	P_s	superheated steam pressure, MPa
P_w	static pressure of wind-box, Pa	R_{sec}	primary air ratio, -
T_{fw}	boiler feed-water temp., ℃	T_s	superheated steam temp., ℃
T_{eg}	exhaust gas temp., ℃	T_b	average bed temp., ℃
T_{fup}	temperature in upper furnace, ℃	q_b	boiler efficiency, %
α	excess air coefficient, -; or the ratio of specific size pore, %	ΔP_d	pressure drop per meter across dilute zone, Pa·m^{-1}

Acknowledgement

Financial supports of the National Natural Science Foundation of China (U1810126) are gratefully acknowledged.

References

He H.B., Hu N., Lyu J.F., etc., Analysis on additional sand size in low-ash fuel fired circulating fluidized bed boilers. J. Chin. Soc. Power Eng. 2010. 30(6), 409-414

Drosatos P., Muhiļ S., Rakopoulos D., etc., Numerical investigation of a coal-fired power plant main furnace under normal and reduced-oxygen operating conditions. J. Energy Eng. 2017. 143: 1ï 14

Li D.F., Kim S., Jeon C.H., etc., Mass Balance Study of a 550 MW Supercritical CFB Boiler with PAPSD Method. 23rd International Conference on Fluidized Bed Conversion. 2018

Bao S.L., Lyu Q.G., Na Y.J., etc., Design and operation of 430 t/h Indonesian coal-fired circulating fluidized bed boiler. Industrial Boilers, 2014(03): 13-16

Yang H.R., Wirsum M., Yue G.X., etc., A six-parameter model to predict ash formation in a CFB boiler. Powder Technol. 2003. 134(1), 117ï 122

Ke X.W., Li D.F., Zhang M., etc., Ash formation characteristics of two Indonesian coals and the change of ash properties with particle size. Fuel Process. Technol. 2019. 186, 73-80

Ke X.W., Cai R.X., Zhang M., etc., Application of ultra-low NOx emission control for CFB boilers based on theoretical analysis and industrial practices. Fuel Process. Technol. 2018. 181, 252-258

DEVELOPMENT AND APPLICATION OF TURBULENT FLUIDIZED BED FOR INCINERATION OF MULTIPLE WASTES

Kunlin Cong[1], Yanguo Zhang[1], Yongfeng Zhao[1,2], and Qinghai Li[1*]

[1]*Tsinghua University-University of Waterloo Joint Research Centre for Micro/Nano Energy & Environment Technology, Key Laboratory for Thermal Science and Power Engineering of Ministry of Education, Department of Energy and Power Engineering, Tsinghua University, Beijing 100084, P.R. China*

[2] *Beijing One-A Hi-tech Energy Technology Co., Ltd., Beijing 100085, P.R. China*

*Email: *liqh@tsinghua.edu.cn*

Abstract

Fluidized bed combustion technology is one of the commonly used technologies for solid waste incineration, which has better capacity reduction effect and higher combustion efficiency than fixed bed technology. However, fluidized bed combustion technology also has some problems, such as high ash concentration in flue gas, large power consumption, and poor combustion stability. With the elevation of the emission standards for nitrogen oxides, the advantage of low-nitrogen emission of fluidized bed has gradually weakened. In response to these problems, a new variant of circulating fluidized bed, called turbulent fluidized bed (TFB), was developed by physically reconfiguring the fluidization state in the dense zone. Along the direction of the airflow, the cross-sectional area of the dense zone in TFB furnace gradually diverged to a certain extent, and then rapidly converged. The special section of the furnace produced a larger velocity at the entrance, which effectively avoids the accumulation of material at the bottom of the furnace. The formed shoulder in the middle of the furnace strengthened the swirl disturbance and internal circulation, greatly enhanced the effect of heat and mass transfer, and achieved full pyrolysis and gasification of fuels with wide particle size distribution and different densities in the dense zone. Afterward, in combination with the air-staging supply, a process of pre-gasified combustion of composite fuels was realized. By regulating the temperature distribution of each zone in the furnace, the original emission of nitrogen oxides could be further reduced. At present, an industrial application of TFB incinerator has been implemented in Vietnam. TFB incinerator is used to dispose of rejects generated during the papermaking process, such as residues and sludge, to generate steam. The application results show that the TFB incinerator can efficiently burn a variety of complex fuels, and can also effectively inhibit the original emissions of pollutants.

Introduction

Energy and environment have always been two major themes related to the future of mankind. The higher rate of urbanization and economic development level has caused a snowballing generation of waste in the world. The World bank estimates that waste generation will increase from 550 million tonnes per day in 2016 to 930 million tonnes per day in 2050(Kaza et al., 2018). More than 33% of the waste is mismanaged today through open dumping or burning(Kaza et al., 2018), which not only pollutes the environment, but also causes great waste of energy.

Combustible waste incineration is an effective waste-to-energy (WTE) technology due to its generally recognized advantages in volume reduction and energy recovery(Cheng & Hu, 2010). However, the formation of dioxins and other carcinogens during incineration(Tuppurainen et al., 1998) and the discharge of heavy metal pollutants(Wang et al., 1999) have made this technology encounter tremendous challenges and resistance. The construction of waste incineration plants was often criticized by the public, and even triggered anti-incineration protests(Wong, 2016). In addition, due to the complexity of composition of the waste and the great differences in properties between different components(Zhou et al., 2015), it is difficult to burn the complex waste simultaneously in the same furnace and maintain a stable combustion. It leads to the low thermal conversion efficiency of traditional waste incineration.

Gasification is an oxidation reaction that is similar to combustion, but milder than combustion. The organic components in the waste are converted to combustible gases such as CO, H_2 and CH_4 under oxygen-deficient atmosphere(Arena, 2012). Compared to incineration technology, gasification is more conducive to the thermal disposal of complex waste. The lower reaction strength and temperature means that the energy required to maintain a stable gasification reaction is much lower than that of combustion, thus stabilizing the drastic fluctuation of the energy consumption of different waste components to maintain the reaction, and solving the problem of stable operation of industrial plants. The reducing atmosphere can also inhibit the generation of harmful substances such as dioxins, reduce the emission of nitrogen oxides, and also facilitate the recovery of metal resources in waste(Consonni & Viganò, 2012). At present, the commonly used gasification devices in industry include three main categories, fixed bed, entrained bed and fluidized bed. It is difficult to gasify CSW effectively in fixed bed and entrained bed because of its different morphology, complex composition and poor homogeneity. In contrast, the fluidized bed contains a large number of inert bed materials, with high heat capacity and small temperature fluctuation, which is conducive to the self-heating operation of gasification system. Moreover, the materials and waste in the fluidized bed are well mixed. The transfer process and chemical reaction in the fluidized bed are adequate enough for various types of solid waste gasification(Gómez-Barea & Leckner, 2010). However, fluidized bed gasification also has some shortcomings, such as high tar content and ash content in gas production(Bhattacharya, 2006).

At present, the developed fluidized bed waste incinerators are practically used to incinerate unitary waste or wastes with similar properties. There are few incineration technologies that can effectively dispose of multiple wastes. In recent years, Tsinghua University and Beijing One-A High-Tech Energy Technology Co., Ltd. jointly developed a novel fluidized bed incineration technology called Turbulent Fluidized Bed (TFB) for variety waste fuels, which changed the traditional one-stage direct incineration into two-stage. The first stage is a gasification process, and the second stage is gas phase combustion process. This paper aims at providing a basic principle of TFB boilers and explaining how could TFB boiler benefit from its novel configuration. The experiences for designing and operating are also presented.

Design Principle and Consideration

The schematic diagram of TFB and the real appearance of the gasification chamber of a pilot device are shown in **Fig. 1**. The TFB furnace can be divided into two parts, a gasification chamber and a combustion chamber. The gasification chamber is a spindle-shaped space with a divergent-convergent variable cross section. The lower part of dense zone of TFB boiler exhibits very complex hydrodynamics, caused by the divergent structure, which forms a variety of flow regimes, including fast bed, turbulent bed and bubbling bed, and a gradually decreased air velocity distribution with the increase of height. In this way, various components in the complex waste can simultaneously fully react in the spindle-shaped furnace, thereby improving the gasification efficiency. In addition, the lower air velocity in the upper part of the dense zone can effectively reduce the amount of fly ash that is carried out of the furnace, which is only one third that of a conventional CFB boiler. It can reduce the abrasion of heating surface in the back pass, and the difficulty of purifying the flue gas. The convergent structure of the upper dense zone can increase the air velocity in the dilute zone and ensure that the combustible gas generated from lower part is brought out at a certain speed. At the maximum cross section of the furnace, the structure is transformed from divergent to convergent to form a “shoulder”, in where local vortex flow will occur. The “shoulder” enhances the disturbance of the airflow to the material, strengthens the flow and heat transfer at the wall, avoids the formation of dead zones and local over-temperature, and reduces the risk of coking in the furnace. The “shoulder” also constructs an internal circulating condition different from the characteristics of high circulation rate and external circulation of CFB, which significantly enhances the solidification effect of alkali metals in the dense zone, greatly reduces the carrying amount of alkali metals in flue gas at the source, and avoids the problem of ash blockage in the rear heating surface.

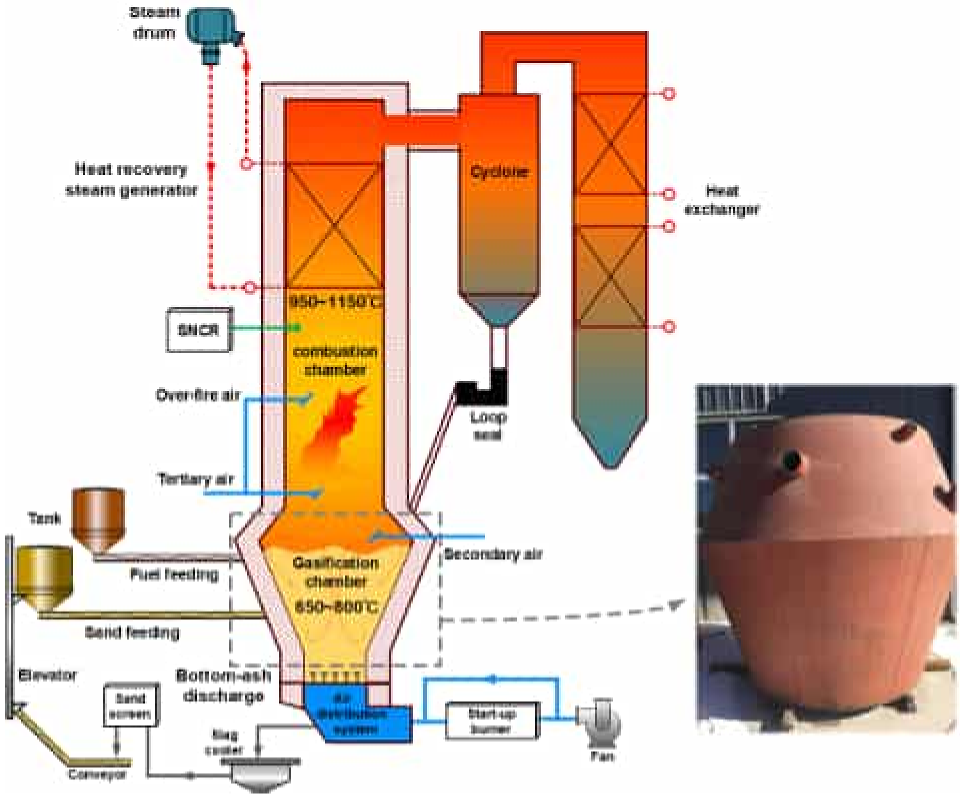

Fig. 1. Schematic diagram of TFB boiler and the spindle-shaped gasification chamber.

The TFB incinerator adopts a multi-stage air distribution form of “grading gasification + grading high-temperature combustion”. By controlling the air supply in the gasification chamber, the air-equivalent ratio of the primary air from the bottom is limited to 25% or less, and the secondary gasification air is supplemented to the upper part of the dense zone to form a step distribution of temperature in gasification chamber, and the temperature is controlled at 650 °C ~800 °C. The reducing atmosphere in the gasification chamber reduces the initial formation of dioxins at the source. Through the replenishment of the tertiary air and the over-fire air, the temperature of the combustion chamber is controlled at 950 °C~1150 ° C, and flue gas is fully retained in the combustion chamber to ensure the waste burnout and the full decomposition of dioxins. Due to the low content of alkali metal in flue gas, the necessary catalyst is lacking. The synthesis amount of dioxin at low temperature is effectively controlled. In addition, measures for flue gas quenching coupled with activated carbon adsorption are set up to ensure that the dioxin emissions meet the requirement.

The form of "grading gasification + grading high-temperature combustion" can precisely control the temperature of each area in TFB incinerator, so that the temperature can be distributed according to the needs of gasification and combustion, effectively avoiding the irrationality of local temperature that is too high or too low. The oxygen content in flue gas can be strictly controlled by 5 to 8%, which effectively reduces the heat loss of the flue gas, thereby improving the energy utilization efficiency of the system. The low-oxygen combustion effectively reduces the initial generation of NOx, and the incineration process will eliminate the need for additional Selective Catalytic Reduction (SCR) system, reducing investment and operating costs.

Engineering Implementation

TFB incineration technology and incinerators involve the cleaning dispose of multi-waste (including industrial, agricultural, forestry, domestic and hazardous waste), and can also be converted into chemical reactors, or widely used in rural towns and industrial parks for centralized heating, steam supply and cogeneration.

The technology has been successfully applied to the Vietnam Paper Mill Incinerator Plant of Chen Loong Corporation (CLVP) for the treatment of papermaking reject and sludge. The project has been in continuous operation. According to the purchase specification, the treatment requirement and characteristics are listed in **Table 1**.

Table 1. Treatment requirement and characteristics.

Sample	Paper Reject	Dry Sludge
Treatment requirement / t·d^{-1}	140	260
Bulk density / kg·m^{-3}	400~800	800~1200
Proximate analysis/mass%		
Moisture, ar	50	20~30
Ash, db	1-8	25~33
Volatile matter, db	-	40.8
Fixed carbon, db	-	3.33
Combustible materials, db	47.7	-
Ultimate analysis/mass%, db		
C	61.23	45.81
H	8.85	5.5
O (by difference)	27.71	48.89
N	0.41	2.3
S	0.32	0.49
Cl	0.5~1.5	0.01
Calorific value/kcal·kg^{-1}		
NCV, ad	2500~3400	1200~2500

ar, received basis. db, dry basis. daf, dry ash free basis. ad, air-dried basis. NCV, net calorific value.

An incinerator with capacity of 25 t/h mainly includes a gasification chamber, a combustion chamber, a radiant heat absorption zone, a medium-temperature separator, an HRSG, a spray quenching device and an external material circulation system. It is about 30 m high and the energy recovery efficiency of HRSG is more than 60%. The plot plan is shown in **Fig. 2**.

The wastes inlets are all arranged in the upper part of the dense zone. Different wastes are supplied into the furnace at different heights depending on the properties such as moisture, state and heating value. Adding CaO to the bottom of the gasification chamber near the air distribution plate partially removes sulfur and chlorine from the waste. The gasification chamber is designed for a temperature range of 700~800 °C. A secondary air is arranged at the outlet of the gasification chamber (also at the inlet of the combustion chamber), and the total amount of primary and secondary air satisfies the oxygen required for fuel combustion. A tertiary air is placed in the middle of the combustion chamber as a means of adjusting the temperature of the combustion chamber. The combustible gas generated in the gasification chamber entrains unburned carbon particles into the combustion chamber and burns rapidly. The temperature reaches 1050 °C, and the residence time of the flue gas in the combustion chamber is more than 2 seconds.

The furnace is surrounded by membrane water wall structure. Refractory material is cast on the fireside surface in the gasification chamber and constructs an insulated furnace to ensure stable gasification of waste with low calorific value (CV). The height of the refractory casting in the combustion chamber decreases as the CV of the waste increases. When the CV of the waste into the furnace does not meet the design requirements, it is necessary to add auxiliary fuel. A selective non catalytic reduction (SNCR) device is arranged in the middle and upper part of the combustion chamber. After passing through the radiant heat absorption zone, the temperature of flue gas drops to about 600 °C and then enters the separator. Some of the particles collected by the separator are sent back to the gasifier for circulation, some of which can be discharged directly and treated together with the bottom slag. In order to prevent the secondary synthesis of dioxins at low temperature, a quench tower is set at the outlet of the economizer. By spraying water into the flue gas, the flue gas is cooled from 550 °C to 180 °C within one second.

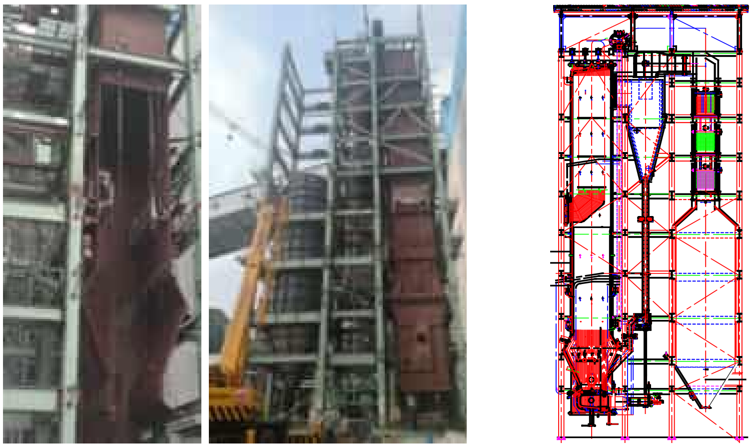

(a) Furnace under installation (b) Plot plan of TFB

Fig. 2. Configuration of TFB incinerator.

The emission requirements and the actual index achieved by TFB are listed in **Table 2**. The actual monitoring screen is shown in **Fig. 3**. Specific industrial measurement campaigns will be conducted according to the requirements of the proprietor.

Table 2. Emission requirements.

Pollutant	Emission Requirement	Reserved Expansion Capability	TFB Actual Index
Dust Content/ mg·Nm^{-3}	＜20	＜10	＜10
NOx/ mg·Nm^{-3}	＜400	＜60	＜100 (50 with SNCR)
SOx/ mg·Nm^{-3}	＜140	＜70	＜50
Dioxin/ ng-TEQ·Nm^{-3}	＜0.3	＜0.1	＜0.01
CO/ mg·Nm^{-3}	＜250		＜50

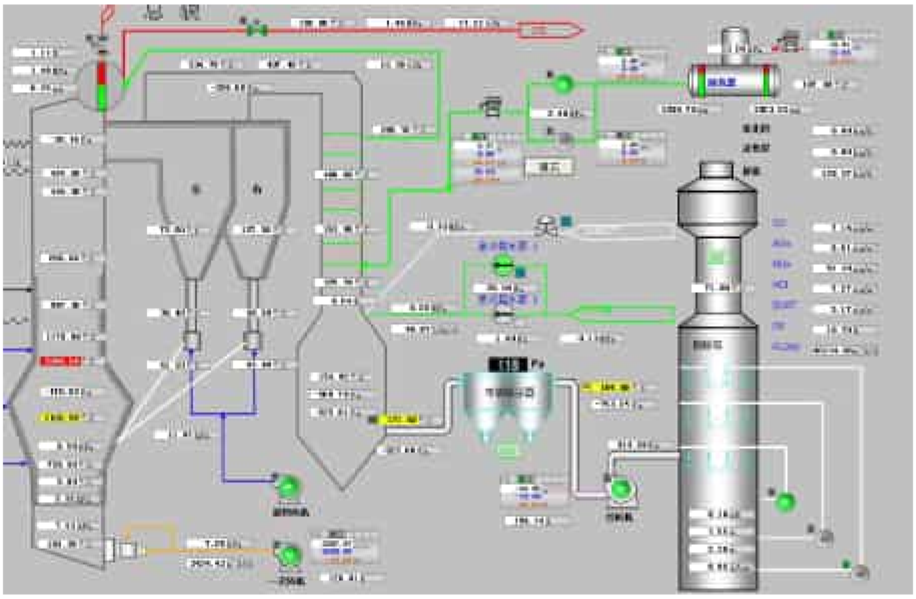

Fig. 3. Actual monitoring screen of TFB incinerator in CLVP.

Conclusion

The fuel adaptability of TFB incinerator is wide enough to dispose of solid, liquid and gaseous waste. It solves the problem of centralized treatment of combustible waste in the same furnace with multiple states, components and sorts. The combination of staged gasification and oxygen-deficient combustion can effectively inhibit the formation of NOx and dioxin, which endows TFB incinerator with excellent environmental protection performance. Furthermore, it has the advantages of remarkable energy-saving effect under stable and reliable operation.

The incinerator can be customizing designed according to the project requirements for different fuels, while meeting the industrial emissions requirement from *DIRECTIVE 2010/75/EU*. The promotion of TFB incinerator is of great significance for achieving efficient, energy-saving, clean and harmless disposal of combustible waste.

References

Arena, U., Process and technological aspects of municipal solid waste gasification. A review. Waste Management, 32(4), 625-639, 2012.

Bhattacharya, S.P., Gasification Performance of Australian Lignites in a Pressurized Fluidized Bed Gasifier Process Development Unit Under Air and Oxygen-enriched Air Blown Conditions. Process Safety and Environmental Protection, 84(6), 453-460, 2006.

Cheng, H., Hu, Y., Municipal solid waste (MSW) as a renewable source of energy: Current and future practices in China. Bioresource Technology, 101(11), 3816-3824, 2010.

Consonni, S., Viganò, F., Waste gasification vs. conventional Waste-To-Energy: A comparative evaluation of two commercial technologies. Waste Management, 32(4), 653-666, 2012.

Gómez-Barea, A., Leckner, B., Modeling of biomass gasification in fluidized bed. Progress in Energy and Combustion Science, 36(4), 444-509, 2010.

Kaza, S., Yao, L.C., Bhada-Tata, P., Van Woerden, F., What a Waste 2.0 : A Global Snapshot of Solid Waste Management to 2050 (English), World Bank Group, 2018. Washington, D.C. http://documents.worldbank.org/curated/en/697271544470229584/

Tuppurainen, K., Halonen, I., Ruokojärvi, P., Tarhanen, J., Ruuskanen, J., Formation of PCDDs and PCDFs in municipal waste incineration and its inhibition mechanisms: A review. Chemosphere, 36(7), 1493-1511, 1998.

Wang, K.-S., Chiang, K.-Y., Lin, S.-M., Tsai, C.-C., Sun, C.-J., Effects of chlorides on emissions of toxic compounds in waste incineration: Study on partitioning characteristics of heavy metal. Chemosphere, 38(8), 1833-1849, 1999.

Wong, N.W.M., Advocacy Coalitions and Policy Change in China: A Case Study of Anti-incinerator Protest in Guangzhou. VOLUNTAS: International Journal of Voluntary and Nonprofit Organizations, 27(5), 2037-2054, 2016.

Zhou, H., Long, Y., Meng, A., Li, Q., Zhang, Y., Classification of municipal solid waste components for thermal conversion in waste-to-energy research. Fuel, 145, 151-157, 2015.

OPERATIONAL CHALLENGES IN A BFB BOILER FIRING DEMOLITION WOOD WITH ADDITION OF AMMONIUM SULPHATE TO REDUCE SUPERHEATER CORROSION

Håkan Kassman[1]*, Tomas Leffler[1], Christer Forsberg[2], and Jinying Yan[1]

[1]*Vattenfall AB, Research & Development, SE-169 92 Stockholm, Sweden*
[2]*Vattenfall AB, Heat Nordic, Bolandsgatan 16, 753 23 Uppsala, Sweden*

*Email: *hakan.kassman@vattenfall.com*

Abstract

There are certain operational challenges during combustion of biomass with increased chlorine contents, such as demolition wood. They include increased superheater corrosion and fouling. This is due to the higher levels of alkali chlorides (hereafter referred to as KCl) in the flue gas. Various strategies can be applied to reduce the impact from such operational challenges. For instance, the superheaters can be replaced at more frequent intervals or more corrosion resistant materials can be used in combination with increased soot-blowing. Another strategy is to measure the corrosive species in the flue gas and adjust the flue gas chemistry accordingly so that the original superheater and soot blowing conditions are maintained. In this paper the latter strategy is applied with on-line measurements of KCl by IACM (In-situ Alkali Chloride Monitor), and the addition of a sulphate-containing additive (here ammonium sulphate, AS). This strategy is known as the ChlorOut concept. The AS is sprayed into the flue gases and converts the alkali chlorides into less corrosive alkali sulphates. In this paper operational experiences concerning superheater corrosion during combustion of demolition wood in a 63 MW_{th} Bubbling Fluidised Bed boiler are evaluated after five years with the addition of AS. An aspect of particular interest is also the recent installation of a flue gas condenser with a flue gas quench (FGQ). The FGQ water is recirculated back into the boiler, and it contains chlorine which could possibly alter the flue gas chemistry and have an impact on the superheater corrosion. Results have previously been presented after three years of operation but the last two years include the impact from recirculation of quench water back to the boiler. These experiences are compared to the situation before the ChlorOut concept was installed. The results after five years reveal the addition of AS drastically reduces high temperature corrosion and extends the life time of the final superheater by more than two times.

Introduction

Combustion of biomass with increased chlorine (Cl) contents such as recycled wood (RW) and demolition wood (DW) can result in several operational challenges. These challenges include increased superheater corrosion and fouling because of the higher levels of alkali chlorides (KCl and NaCl) in the flue gas. Various strategies can be applied to reduce the impact from such challenges (Kassman 2012, Kassman et al. 2018). For example, the superheaters can be replaced at more frequent intervals, or a more corrosion resistant material like stainless steel can be used for them in combination with increased soot-blowing. Another strategy is to monitor the corrosive species in the flue gas and adjust the flue gas chemistry accordingly, so that the original superheater and soot-blowing conditions are maintained. The latter strategy, with the application of on-line monitoring of alkali chlorides (hereafter referred to as KCl) by an IACM (In-situ alkali chloride monitor) and injection of a sulphate-containing additive, is known as the ChlorOut concept (Anderson 2006a, Andersson 2006b). The sulphate containing additive, often ammonium sulphate ($(NH_4)_2SO_4$, AS) is sprayed into the flue gases in an appropriate position prior to the superheaters, and it converts KCl into less corrosive alkali sulphate. AS is more effective than elemental sulphur for sulphation of gaseous KCl and can in addition be used for the selective non-catalytic reduction (SNCR) of NO (Kassman et al. 2010, Kassman and ¡ mand 2015, Kassman and ¡ mand 2017). Investigations in several boilers have shown that injection of AS reduces the content of KCl in the flue gases and also chlorides in the deposits, which both are measures for the risk for superheater corrosion (Kassman et al. 2011, Kassman et al. 2017).

The long-term operational experiences focusing on superheater corrosion during combustion of DW in a 63 MW_{th} Bubbling Fluidised Bed (BFB) boiler with the injection of AS after three years operation were compared with the corrosion caused before the AS injection system was installed in Kassman and Henderson (2018). There is a recent installation of a flue gas condenser (FGC) in the boiler. This included a flue gas quench (FGQ) after the bag house filter and prior to the FGC. A concept for sustainable emission reduction was achieved through a closed water loop (CWL) around the flue gas condensation system by reducing chemical dosing, minimizing waste streams and enhancing water recovering and reuse. Initial evaluation of the impacts of the CWL on boiler performance was conducted in terms of the characteristics of acidic components. The results indicated that there are no significant negative impacts on the accumulation of gaseous contaminants in the flue gas path (Galanopoulos et al. 2018). Measurements around the flue gas condensation system show a significant improvement in water recovering, internal water utilization, and reduction of emissions (Kylhammar 2018). Another concern is that the FGQ water contains chlorine, sulphur and other contaminants which are recirculated back into the boiler. This could possibly alter the flue gas chemistry and have an impact on the superheater corrosion.

In this paper operational challenges concerning superheater corrosion during combustion of demolition wood in the same BFB boiler are evaluated after five years with the addition of AS. Results have previously been presented after three years of operation but the last two years include the impact on the corrosion from recirculation of quench water back to the boiler. These experiences are compared to the situation before the ChlorOut concept was installed.

Experimental

Vattenfall owns and operates a BFB boiler in Jordbro, south of Stockholm, Sweden. The boiler was built by Metso Wärtsilä Power and commissioned in 2010. It produces a total of 65 MW_{th}, and 20 MW_{el} is produced in a turbine with steam data of 80 bar / 470°C for 100% demolition wood (DW). The properties of DW can vary significantly due to both origin and fuel supplier. Table 2 in Kassman and Henderson (2018) presents properties of three representative fuels which have been used in the boiler. Fig. 1 shows the BFB boiler with locations of importance for the present paper indicated. The superheaters are made of low alloyed carbon steels. The first section of the primary superheater SH1 is made of 16Mo3 and the remaining sections are made of 13CrMo4-5. The secondary superheater SH2 has the highest out-going steam temperature (470°C) and both sections are made of 10CrMo9-10. The risk for corrosion is often considered great at a molar ratio S/Cl less than 2.0 in the fuel mix although the content of chlorine in deposits is also a measure of the risk for corrosion. The molar ratio S/Cl ranged from 0.3 to 0.8 in Table 2 and consequently the fuel mix was considered corrosive. The boiler was initially operated without any additives to prevent corrosion at the conditions prevailing in the superheater region during combustion of DW, and the lower hottest part of SH2 were replaced after four years of operation in 2014.

A permanent ChlorOut installation was fully implemented in regular operation before replacing SH2 in 2014. It consisted of an IACM for measurement of gaseous KCl, and a dosage system for injection of ammonium sulphate which is further described in Kassman and Henderson (2018). The injection positions are in the upper part of the combustion chamber (Level L1) and in the upper part of the empty pass (Level L2). The boiler had a separate SNCR system for NH_3 before the injection system for AS was installed and it is still in operation. The injection levels for AS, ammonia (NH_3), and the location for IACM can be found in Fig. 1. The openings for IACM are located on the left and right side of the boiler wall.

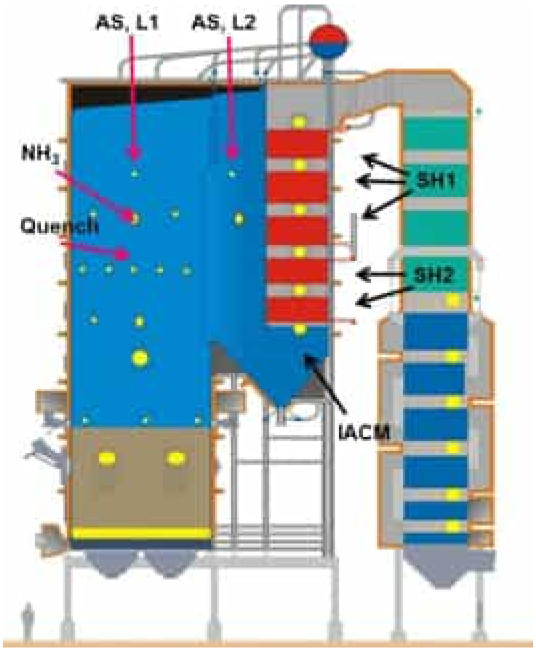

Fig. 1. The BFB boiler with superheaters SH1 and SH2, IACM and injection points for AS, NH_3 and FG quench water indicated.

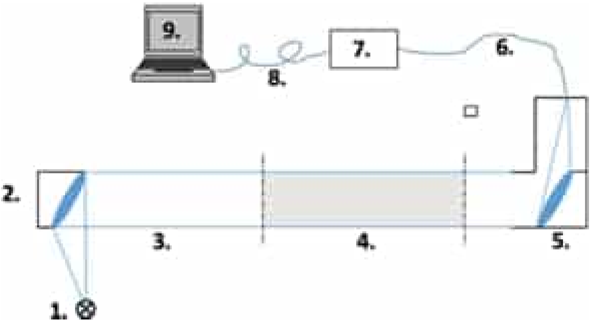

Fig. 2. Principle schematic diagram of the IACM instrument: 1. Xenon light source, 2. parabolic mirror, 3. collimated light beam, 4. measurement path (flue gas channel), 5. parabolic mirror connected to an optical fibre, 6. optical fibre, 7. spectrometer, 8. USB cable, and 9. computer.

The IACM (In-situ Alkali Chloride Monitor) is an optical instrument that measures the sum of gas-phase alkali chlorides (KCl and NaCl) in the flue gas channel prior to the superheater region. An additional feature of the IACM instrument is the possibility to simultaneously measure the sulphur dioxide (SO_2). IACM was initially developed by Vattenfall Research and Development AB (VRD) as an integrated part of the ChlorOut concept. Fig. 2 shows a principal schematic of the measurement set-up for IACM. Collimated UV-light from a Xenon lamp is transmitted from one side of the boiler wall over the flue gas channel (measurement path) to a receiver located on the opposite boiler wall. The receiver collects the collimated light from the transmitter and focuses it onto an optical fibre, which subsequently guides the light to a spectrometer. The spectrometer sends the spectrally resolved spectrum to a computer for evaluation and determination of the concentrations of KCl and SO_2 by means of Differential Optical Absorption Spectroscopy (DOAS). The result is expressed as the concentration of KCl and SO_2 respectively in ppm. IACM is a valuable measurement tool in several applications since the concentration of gaseous KCl is a measure to which extent a flue gas is corrosive. IACM is in Leffler et al. (2016) used for so-called on-line fuel quality control of the fuel-mix. A more detailed description of IACM can be found in Kassman (2012) and Leffler (2016).

Demolition wood (DW) is an inhomogeneous fuel and the reference level of KCl without any additive as well as the amount of additive required to reach a specific value of KCl varies significantly over time. The flow of AS or other additives can be controlled to a specific value of KCl by IACM measurements. This value is the so-called breaking point. It can be described as the greatest allowed level of gaseous KCl for complete reduction of chlorine in the deposits and corresponds to the minimal flow of AS for sufficient corrosion protection.

Fig. 3 shows the boiler and the main parts in the flue gas cleaning system which consists of a bag house filter, and a flue gas condenser (FGC). The FGC consists of three subprocesses i.e. flue gas quench (FGQ), two-stage condensation and droplet separation. The FGC produces 10 MW_{th} during full load. The bag house filter has three parallel sections which are in continuous operation and the additives are activated carbon and hydrated lime ($Ca(OH)_2$) for capture of HCl and SO_2. There is an accumulation of contaminants in the quench water and a certain amount of these salts must be removed from the water loop in order to maintain a proper salt balance. A part of the FGQ water is recirculated back to the combustion chamber where the salt water is evaporated after which the salts are precipitated together with ashes then collected by the baghouse filters. This results in a maintained salt balance in the flue gas cleaning system and also an enhanced water recovering and reuse by setting up a so-called closed water loop (CWL). A concern is that the recirculated quench water contains chlorine, which could possibly alter the flue gas chemistry and have an impact on the superheater corrosion. The condensate treatment from the FGC include several cleaning steps such as a CO_2-stripper, pre-treatment in sand filter, ultra-filter (UF), followed by reversed osmosis (RO) membrane modules in series. The reject flow from the RO modules contains sulphates and they are recirculated back to the boiler as a part of the quench water in Fig. 3.

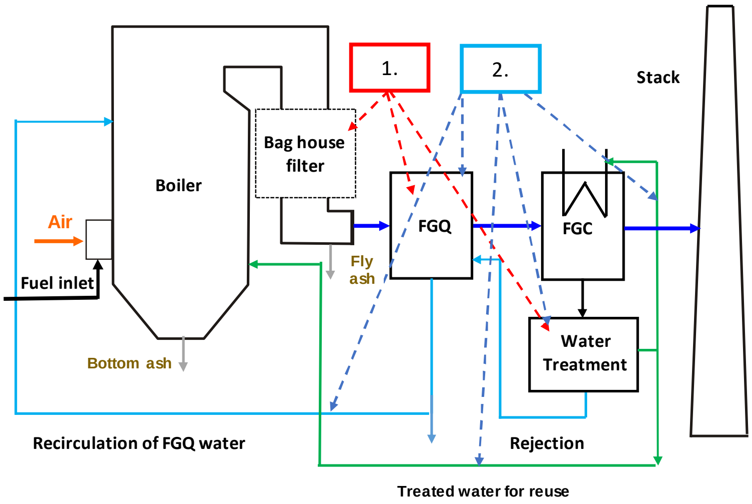

Fig. 3. Overview of the flue gas cleaning system with bag house filter, flue gas quench (FGQ) and flue gas condenser (FGC). 1. Reduced chemical dosing by using effective flue gas cleaning and physical separation. 2. Enhanced water recovering and reuse by setting up a closed water loop (CWL).

Results and Discussion

The installation of the flue gas quench (FGQ) and flue gas condenser (FGC) has had an impact on the operating parameters of the boiler. It was necessary to reduce the emissions of SO_2, HCl as well as the NH_3-slip below the emission limit values (ELV) in the raw gas after the bag house filter prior to the installation was made. These emissions are collected in the FGQ and/or FGC enabling higher concentrations in the raw gas after the filter. Another aspect is the recirculation of contaminants with the FGQ. Table 1 shows an analysis of selected salt concentrations in the FGQ water and reversed osmosis reject water (ROR).

Table 1. Analysis of salt concentrations in the FGQ water and reversed osmosis reject (ROR), molar flow of recirculated components calculated at a total quench water flow of 500 litres/h.

Contaminant	Quench water (QW)		Concentrated contaminant	
	Concentration mg/l	QW molar flow* mol/h	ROR** mg/l	QW/ROR (mg/l:mg/l)
Chlorine, Cl	11000	155	35	314
Sulphur, S	7800	122	590	13
NH_4-N	7300	243	14	521
Cromium, Cr	0.057	0.0005	0.0005	108
Zinc, Zn	1.2	0.0092	0.0150	80
Lead, Pb	0.16	0.0004	0.0024	67
Nickel, Ni	0.021	0.0002	0.0006	34

Notes: *QW flowrate 500 l/h, ** Salts from the ROR are the major contaminants of FG quench stage. FGQ water is recirculated from the water loop into the boiler, QW/ROR- concentrate factor of the ROR in the FGQ.

The recirculated flow of quench water (QW) into the combustion chamber of the boiler is approximately 500 litres/h and the molar flows of S and Cl are calculated based on this flow. Table 4 in Kassman and ¡ mand (2017) presented experimental parameters such as the molar ratios S/Cl and molar flows of S and Cl for different flows of AS in litres/MWh. Primary data from that table and Table 1 are compared in Table 2. The comparison is made between the molar flows of S and Cl from the FGQ water and from injection of AS. Table 2 reveals that the molar ratio S/Cl and consequently the corrosivity of the chemical environment at the superheater region is similar between two reference cases (Ref, Ref CLW) without any injection of AS before and after recirculation of the quench water according to the close water loop (CWL) concept. The flow of AS was often between 0.50 and 0.75 l/MWh before introducing the CLW and it is now somewhat higher and typically close to 0.75.

Table 2. Experimental parameters obtained from Kassman and ¡ mand 2017 before installation of the FG quench and FGC and after recirculation of quench water (close water loop, CWL)

Case	AS (l/MWh)	S^{AS}/Cl molar ratio	S^{tot}/Cl molar ratio	$Sulphur^{tot}$ mol/MWh	Chlorine mol/MWh
Ref	0.0	0	0.51	4.0	7.9
AS-0.5	0.50	0.24	0.74	5.9	7.9
AS-0.75	0.75	0.35	0.86	6.8	7.9
AS-1.0	1.00	0.47	0.97	7.7	7.9
Ref CLW	0.0	0	0.58	6.0	10.3
AS-+ CLW	0.75	0.27	0.85	8.8	10.3

S^{AS}/Cl = Molar ratio based on added S from AS. S^{tot}/Cl = Molar ratio based on added S from fuel, CWL and AS.

Parts of SH2 were replaced after four years of operation without any additives to prevent corrosion in 2014 and tube samples were taken for analysis. The wall thickness of the tubes was as an average value 4.2 mm and as a minimum 3.3 mm (S_{min} = 3.5 mm). This resulted in a nominal average corrosion rate of 0.52 mm/year and a maximum of 0.75 mm/year for a nominal value S_{Nom} of 6.3 mm. The appearance of the tubes in the lower part of SH2 were also investigated during the revision after two years of operation with injection of AS. Results from these two investigations are described in Kassman et al. (2017). The appearance of SH2 was again studied after three years of operation with injection of AS during the regular revision in 2017 and these results are described in Kassman and Henderson (2018).

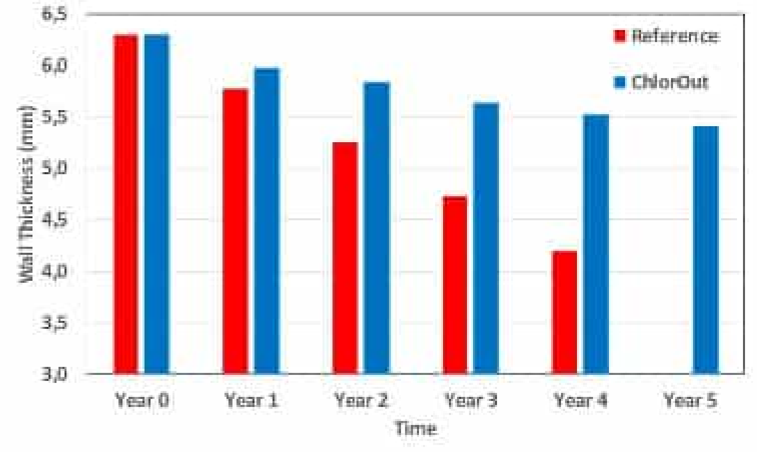

Fig. 4. Tube wall thickness versus time. Injection of AS (ChlorOut) and without AS (Reference).

The appearance of SH2 is once more inspected after another two years during the regular revision in 2019. There was a particular interest during this inspection since it included the impact from recirculation of quench water. Spot checks of the wall thickness were taken during the inspection. The overall average corrosion after five years of operation was approximately 0.9 mm. The wall thickness was reduced from a nominal 6.3 mm to an average of 5.4 mm giving a nominal average corrosion rate of less than 0.20 mm/year. Fig. 4 shows a bar chart with the wall thickness versus time for the first four years without an additive in red, the three years with AS injection only followed by the last two years with AS and CWL are all in blue. The impression is that the corrosion rate is equal or somewhat lower during the last two years with AS and CWL compared to the first three years with the ChlorOut concept. The overall corrosion rate during the last five years with injection of AS is between a half and a third of it without any additive.

Conclusion

The long-term experiences and operational challenges during combustion of demolition wood in a BFB boiler with addition of ammonium sulphate and the recirculation of quench water into the combustion chamber can be summarised as follows:

The corrosion rate was approximately 0.5 mm/year before the installation of the ChlorOut concept and parts of SH2 was replaced after four years of operation.

The superheater corrosion was significantly reduced by injection of AS and the overall corrosion rate after five years of operation was approximately 0.2 mm/year.

The recirculation of quench water according to the CWL concept had no negative impact on the corrosion rate of SH2 when it was combined with injection of AS.

Acknowledgements

This paper is a part of the project KME-802 *Increased fuel flexibility and performance for boilers with challenging fuels*. KME 802 is funded by the Swedish Energy Agency.

References

Andersson C, European Patent EP 1221036, 2006a.

Andersson C, European Patent EP 1354167, 2006b.

Galanopoulos C, J Yan, H Li, L Liu. Impacts of acidic gas components on combustion of contaminated biomass fuels. Biomass and Bioenergy 111 2018. pp. 263-277.

Kassman H, L Bäfver L, LE ¡ mand. The importance of SO_2 and SO_3 for sulphation of gaseous KCl ï An experimental investigation in a biomass fired CFB boiler, Combust. Flame 157 2010. pp. 1649-1657.

Kassman H, M Broström, M Berg, LE ¡ mand, Measures to reduce chlorine in deposits: Application in a large-scale circulating fluidised bed boiler firing biomass. Fuel 90 2011. pp. 1325-1334.

Kassman H, Strategies to reduce gaseous KCl and chlorine in deposits during combustion of biomass in fluidised bed boilers, Dep Energy & Environment, Chalmers University of Technology, PhD thesis, 2012.

Kassman H, LE ¡ mand, Aspects on the flue gas chemistry of KCl, NO and CO during injection of ammonium sulphate ï An experimental approach, Proc 22nd Int Conf on Fluidized Bed Conversion, ¡ bo, Finland, 2015. pp. 583-593.

Kassman H, LE ¡ mand, Simultaneous reduction of NO and KCl during injection of ammonium sulphate in a biomass fired BFB boiler, Proc 12th Int Conf on Fluidized Bed Techn, CFB-12, Krakow Poland, 2017. p. 1093-1101.

Kassman H, C Forsberg, P Henderson, Reduced superheater corrosion by injection of ammonium sulphate in a biomass fired BFB boiler, Proc 12th Int Conf on Fluidized Bed Techn, CFB-12, Krakow Poland, 2017 p. 1103-1110.

Kassman H, P Henderson, Mitigation of Superheater Corrosion with Addition of Ammonium Sulphate in a BFB boiler Firing Demolition Wood, Proc 23rd Int Conf on Fluidized Bed Conversion, Seoul, Korea, 2018 p. 29-38.

Kylhammar K, Comparative evaluation of membrane based flue gas condensate treatment systems for biomass-fired CHP plants. MSc thesis, Dep Chemical Engineering, Lund University, 2018.

Leffler T, Development and application of optical diagnostics of alkali vapours for solid fuel combustion, Dep Physics, Lund University, PhD thesis, 2016.

Leffler T, C Brackmann, M Berg, ZS Li, M Aldén, On-line alkali measurement for fuel quality control in biomass operated boilers, Journal of IFRF, Article 201601, 2016.

STUDY ON UNIFORM AIR DISTRIBUTION SYSTEM FOR LARGE-SIZE CIRCULATING FLUIDIZED BED BOILERS

Dajun Wang[1*], Liyong Wang[2], Eric Eddings[3]

[1]*Sichuan Electric Power Industry Commission and Testing Institute, No.24 Qinghua Road, Chengdu, Sichuan province, China, 610072*
[2]*Power Works, LLC，299 South Main Suite 1300 in Salt Lake City, Utah, 84111*
[3]*The University of Utah, 55 South Central Campus Drive, Salt Lake City, Utah, 84112*

*Email: *928969159@qq.com, liyongw@gmail.com, eric.eddings@utah.edu*

Abstract

In this paper, it is studied that the boiler air distribution system of 300MW-600MW circulating fluidized bed (CFB) boiler has a genetic defect in boiler design, because the air flow is non-uniform distributed on the grid, the phenomenon of channeling, produces some high temperature areas, resulting in high nitrogen oxide emissions, low combustion efficiency, chaotic internal loop, also non-uniform results in a high primary air flow rate during CFB boiler operation in the low and medium loads. Power Works LLC provides users with a new design concept and technology, the wind box partition, parallel accurate distribution of air flow rate, the use of a new static or dynamic drag coefficient variable air nozzle, matching the grid dynamic background pressure map of CFB boiler operation. The new technology can provide uniform and stable fluidization for CFB boiler, realize uniform low heat flux and high-efficiency combustion mode, improve combustion and desulfurization efficiency, and reduce pollutant emissions, significantly improves the performance of CFB boilers over the entire range of operation, the CFB boiler reliability, and reduces operating and maintenance costs.

Introduction

Fluidized bed combustion (FBC) is one of the most popular coal combustion technologies (Duan et al., 2019; Hanisková et al., 2016; Kang & Choi, 2018; KuŦnia et al., 2019; Leckner, 2016; Urciuolo et al., 2012), which have been applied to coal power generation worldwide. Many CFBs were commercialized in China, and quite a few Chinese scientists were involved in these efforts (Lee et al., 2011; Lin et al., 1999; Man et al., 2010; Tang et al., 2019; Wu et al., 2018). Also, some scientists had been studying key mechanisms (e.g., SO_2 formation, NO_x formation, ash formation, and fluidization, etc.) and their applications (Duan et al., 2015; Engin et al., 2019; Niemi & Kallio, 2018; Pettersson et al., 2008; Skrifvars et al., 1998). Theoretically, fluidization is an excellent approach to mix fuel and air in a specific proportion, which can rapidly be mixed to ensure uniform temperature. Thus, FBC can be used for heat generation with various fuels (e.g. municipal waste, sewage plant sludge, biomass, agricultural waste, and other high moisture fuels, etc.).

However, a lot of hot spots occur in most commercial CFBs. Hot spots can cause a high amount of NO_x emissions, bed agglomeration (Li et al., 2007; Liu et al., 2019; Qi et al., 2018), and de-fluidization, etc. Uniform airflow is key to minimize those hot spots. Thus, it is a considerable challenge to get uniform flow through distribution grids, especially for large-scale wind boxes. In order to distribute airflow evenly through a long pipe (Lu & Ozoe, 2006; Matarrese et al., 2014; Yeoh et al., 2012) or distribution grids (Yaµci et al., 2014; Yaµci et al., 2016), several researchers have developed mathematical & computational models, as well as experimental facilities, during the last several decades. However, there are not many reports dealing with methods for determining the optimal geometry of the wind box. The new homogeneous air distribution system discussed here can provide a significant improvement for the existing CFB boilers, to achieve better combustion efficiency and to reduce pollution emissions.

Research on Non-Uniform Problems of Existing Air Distribution Systems

In order to study the non-uniform of air distribution system, it is necessary to know more deeply about the principle of circulating fluidized bed boiler and the actual wind box and nozzle structural design. We would compare, analyze and study on the genes of boilers. In fact, inhomogeneous air distribution result in some regions of the grid plate to achieve channeling and dead zones. The channeling will lead to local strong fluidization, high temperatures, particles redistribution non-uniform, and high NO_x formation in this area. In contrast, the dead zone has poor fluidization, whereby the heat exchange and mixing processes progress less effectively. It directly affects the combustion and emission performance of the CFB boilers. After a lot of cold testing and thermal operation data validation, we can draw the following conclusions:

1) Primary air (PA) will be freely distributed in the large space of the wind box, the nonuniform velocity results in big pressure gradients, the structural design is unacceptable.
2) Every nozzle has a different pressure drop between the wind box and the background pressure, which leads to different air flow rates and local presence of channeling.
3) The existing air distribution system is designed to use several fixed drag coefficient air nozzles arrangement, which It does not effectively compensate for the effects of background pressure.
4) The difference velocities among nozzles will also result in a horizontal flow and redistribution of particles on the grid, and some the local circulation results in complex final background pressure distribution, and unpredictable chaos of solid flow and bottom ash discharge.

Operation and Modeling Analysis of Three Types of Existing Air Distribution Systems

CFD Analysis and condition

This paper uses CFD modeling analysis to evaluate existing air distribution system designs and provide optimization and troubleshooting analysis, the CFD modeling conditions are as follows:

1) Geometry: 3-dimensional
2) Mesh technique: polyhedral mesh, prism layer mesh, surface re-meshing
3) Selected model technique: turbulent model, realizable k-epsilon two-layer, segregated flow, Reynolds-average Navier-Stokes, steady-state
4) PA Inlet condition: mass flow inlet
5) Outlet condition: pressure out

The first type of wind box: double grid, double wind box, and PA inlet from rear wall

During the commissioning and operation of the ALSTOM 300MW and DONGFANG 600MW CFB boilers, the following phenomena occur:

1) The cold test shows that the solids in the front wall area of the furnace are strongly fluidized and the solids in the rear wall area of the furnace is poorly fluidized;
2) The front wall of the furnace is burning strongly, and more O_2 causes higher NO_x emission, the opposite is true of the rear wall of the furnace;
3) During boiler running, in order to keep the bed temperature distribution as uniform as possible, the operators had to supply a small amount of coal in the front wall of the furnace, and a many amount of coal in the rear wall to hold high load;
4) The amount of returning solids near the front wall separator is more massive, and the amount of returning solids near the rear wall separator is smaller;
5) The discharge bottom ash particle size and flow rate near the front wall of the furnace is larger, and near the rear wall of the furnace is small;

Fig. 1. One of double grid, double wind box, and rear wall independent inlet modes)

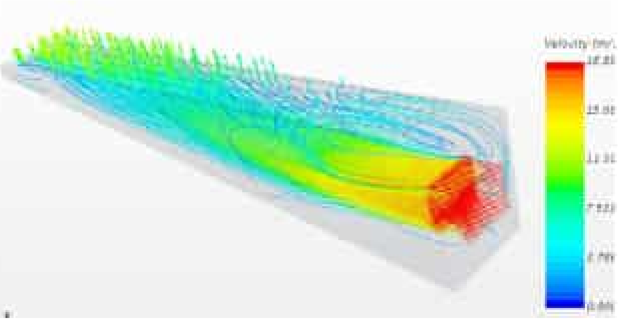

Fig. 2. Velocity distribution of model in one of double box

We used CFD technology to check the flow characteristics for such wind box, the results showed that the deflection distribution of airflow on the grid on a single wind box was consistent with the distribution on the actual operating grid, as shown in Figs. 1 and 2.

The second type of wind box: single grid, single air wind box, and PA inlet from dual side inlet

The following phenomena occur in the CFB boiler during a cold test and operation:

1) The cold flow test shows that the solids in the middle area between left and right inlet have powerful fluidization, and the solids at two side area are poorly fluidized;
2) The middle area between left and right inlet is burning strongly, and more O_2 and high temperature results in higher NO_x emission. The combustion on the two sides is relatively weak, and the lower supplied O_2 and temperature results in lower NO_x;
3) During boiler running, in order to keep the bed temperature distribution as uniform as possible, the operators had to supply a small amount of coal into the middle of the furnace, and a large amount of coal into two sides;
4) In the middle of the separator, the solid return is large. At the same time, the solid return flow of the separator on both sides of the furnace is relatively small.
5) The discharge bottom ash particle size and flow rate in the middle area of the furnace is larger, and near both sides of the furnace is small;

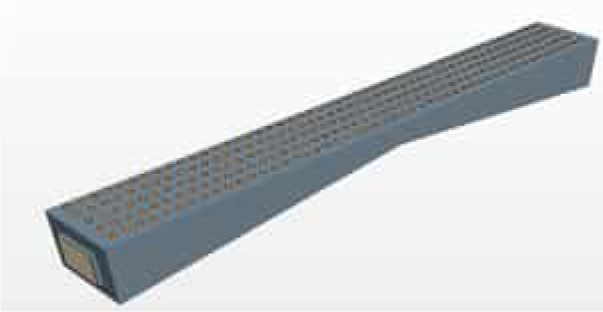

Fig. 3. Single grid, single air wind box, double side air inlet modes

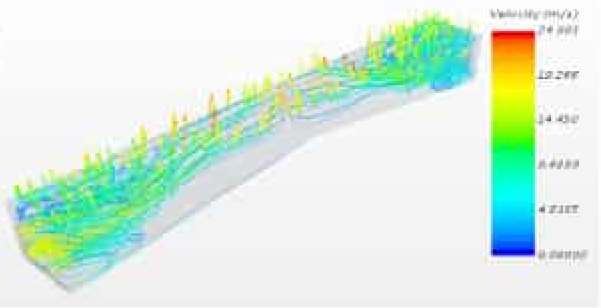

Fig. 4. Velocity distribution of model

We used CFD technology to check the flow characteristics of such boilers, and the results showed that the deflection distribution of airflow on the grid was consistent with the distribution on the actual operating grid, as shown in Figs. 3 and 4.

The third type of wind box: single grid, single wind box, and PA inlet from rear wall four-duct

The following phenomena occur in the CFB boiler during a cold test and hot operation:

1) The cold test shows that the fluidization of the solids in the front wall of the furnace is strong. Also, the fluidization of the solids in the back wall of the furnace is weak;
2) When adopting a uniform coal feeding method on the front wall, the coal particle burning can absorb the heat to reduce the temperature of the front wall bed. And the burning coal solids move to the rear wall. The primary airflow rate of the rear wall is small, and the bed

temperature is high. The bed temperature distribution in the grid area of the furnace is relatively uniform;

3) The combustion at the front wall area of the furnace is intense. The more O_2, the higher NO_x formation will be. The burning at the rear furnace wall is weak. The O_2 is low, and the furnace temperature is relatively uniform, which could make NO_x lower than the former two structures;
4) In the middle of the separator, the solid return is large. At the same time, the solid return flow of the separator on both sides of the furnace is relatively small.
5) The discharge bottom ash particle size and flow rate in the middle area of the furnace is larger, and near both sides of the furnace is small;

Fig. 5. Single grid, single air wind box, double side air inlet modes

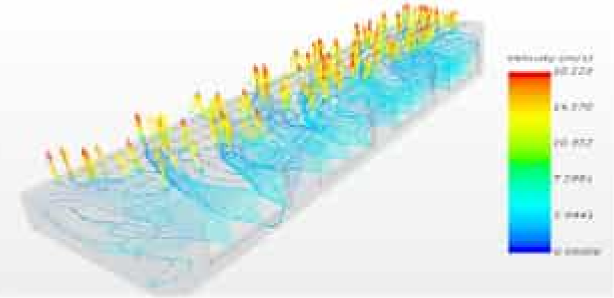

Fig. 6. Velocity distribution of the model

We used CFD technology to check the flow characteristics of such boilers, and the results showed that the deflection distribution of airflow on the grid was consistent with the distribution on the actual operating grid, as shown in Figs. 5 and 6.

Existing Nozzle Design Defects

At present, there are many types of existing nozzle structures, but their coefficient of resistance is completely fixed, because there are still some errors in the manufacture of nozzles, the inevitable performance of the new nozzle is different. When the boiler is running for a long time, the nozzle is eroded and damaged. Sometimes new nozzles need to be replaced, and the fluidization of air distribution system will become nonuniform due to the different drag coefficients between the old and new nozzles. In severe cases, the user must replace all old nozzles, which require longer construction cycles and higher maintenance costs.

New Homogeneous Air Distribution System Design

The new air distribution system was developed by POWER WORK ® LLC to provide users with the best package solution, it includes a new wind box design, a new type nozzle and a background pressure compensation technology.

The new homogeneous air distribution system has the following features:

1) The structure and symmetric design of water wall are used in the wind box;
2) According to the calculation, a certain number of parallel independent space is set in the wind box, PA will be evenly distributed and controlled;
3) Each independent space is set to high temperature, wear corrosion, adjustable area of PA inlet;
4) Each independent space upper outlet, installation of a new static or dynamic resistance coefficient adjustable air nozzle;
5) Pre-adjust the air nozzle resistance distribution map to match the actual operation background pressure distribution of the grid plate.

New Type Nozzle Design

A large number of investigations and studies have found that users urgently need new nozzles with the following properties:

1) The first type of new nozzle with adjustable static resistance coefficient, non-destructive installation, and disassembly. This is the first time to achieve new and old nozzles with

the same performance matching replacement, and background pressure map pre-superimposed correction. Non-destructive disassembly can significantly reduce maintenance costs;

2) The second type of new nozzle with adjustable static drag coefficient, variable dynamic drag coefficient, non-destructive installation, and disassembly. This is the first type of nozzle upgrade to improve the low and medium load performance of CFB boilers.

New Air Distribution System Technology Benefit

The new air distribution system can significantly reduce the occurrence of boiler in the trench flow phenomenon, greatly improve the uniformity of the air distribution grid, and help CFB boilers achieve the following goals:

1) At low heat flux, uniform fluidization, combustion and heat transfer are achieved;
2) Reduce the primary air ratio and the auxiliary power consumption rate.
3) Reduce the carbon content of fly ash and bottom ash to improve boiler combustion efficiency;
4) Improve the desulfurization efficiency, reduce the consumption of limestone powder, and reduce the catalytic effect of limestone powder on producing more NO$_x$;
5) Decreased thermal NO$_x$ can reduce the amount of ammonia required for SNCR, ammonia slip, and ammonium hydrogen sulfate (NH_4HSO_4) formation. This in turn will significantly reduce the risk of blockage and corrosion damage of air preheaters, bag filters, induced draft fans, and other equipment.
6) Extend the safe running time of the CFB boiler unit.

Conclusion

In recently the comprehensive technology research of large-scale CFB boiler uniform air distribution system has made great progress. The new large-size grid air distribution technology first realized the wind box partition and the precise control of mass flow, provided two type new nozzle of resistance coefficients that can be adjusted statically or dynamically, and used the grid thermal background pressure map matching technique for the first time to ensure uniform speed profile and pressure gradient of air flow in the wind box. The uniform and stable flow of CFB boilers is realized in the entire operating range, the uniform low heat flux and efficient combustion mode are realized, the combustion and desulfurization efficiency is improved, the pollutant emissions are reduced, the performance of CFB boilers is significantly improved in the whole operating range, the reliability of equipment, and the operating and maintenance costs are reduced.

References

Duan, L., Duan, Y., Sarbassov, Y., Li, Y., Anthony, E.J. 2015. SO3 formation under oxy-CFB combustion conditions. International Journal of Greenhouse Gas Control, 43, 172-178.

Duan, L., Li, L., Liu, D., Zhao, C. 2019. Fundamental study on fuel-staged oxy-fuel fluidized bed combustion. Combustion and Flame, 206, 227-238.

Engin, B., Atak¿l, H., Ünl¿, A., Olgun, Z. 2019. CFB combustion of low-grade lignites: Operating stability and emissions. Journal of the Energy Institute, 92(3), 542-553.

Hanisková, D., Bartoníļ ková, E., Koplík, J., Opravil, T. 2016. The Ash from Fluidized Bed Combustion as a Donor of Sulfates to the Portland Clinker. Procedia Engineering, 151, 394-401.

Kang, Y.H., Choi, Y.C. 2018. Development of non-sintered zero-OPC binders using circulating fluidized bed combustion ash. Construction and Building Materials, 178, 562-573.

KuŦnia, M., Magiera, A., Pielichowska, K., ZiŃbka, M., Benko, A., Szatkowski, P., Jerzak, W. 2019. Fluidized bed combustion fly ash as filler in composite polyurethane materials. Waste Management, 92, 115-123.

Leckner, B. 2016. Fluidized Bed Combustion. in: Reference Module in Chemistry, Molecular Sciences and Chemical Engineering, Elsevier.

Lee, J.M., Kim, D.W., Kim, J.S. 2011. Characteristics of co-combustion of anthracite with bituminous coal in a 200-MWe circulating fluidized bed boiler. Energy, 36(9), 5703-5709.

Li, D., Zhong, F., Guo, Q., Lu, J., Zhang, J., Yue, G. 2007. Properties of flash hydrated and agglomerated particles of CFB fly ashes. Fuel Processing Technology, 88(3), 215-220.

Lin, W., Weinell, C.E., Hansen, P.F.B., Dam-Johansen, K. 1999. Hydrodynamics of a commercial scale CFB boiler-study with radioactive tracer particles. Chemical Engineering Science, 54(22), 5495-5506.

Liu, Z., Li, J., Wang, Q., Lu, X., Zhang, Y., Zhu, M., Zhang, Z., Zhang, D. 2019. An experimental investigation into mineral transformation, particle agglomeration and ash deposition during combustion of Zhundong lignite in a laboratory-scale circulating fluidized bed. Fuel, 243, 458-468.

Lu, S.-S., Ozoe, H. 2006. Application of multiple magnetic coils to drive the airflow in a long pipe. International Journal of Heat and Mass Transfer, 49(23), 4536-4542.

Man, Z., Rushan, B., Zezhong, Y., Xiaoguo, J. 2010. Heat flux profile of the furnace wall of a 300MWe CFB boiler. Powder Technology, 203(3), 548-554.

Matarrese, P., Gaetano, A., Airaghi, S., Montorfano, D., Barbato, M.C., Ambrosetti, G., Pedretti, A. 2014. Performance Analysis of a Novel Air-based Cavity Receiver. Energy Procedia, 49, 438-446.

Niemi, T., Kallio, S. 2018. Modeling of conversion of a single fuel particle in a CFD model for CFB combustion. Fuel Processing Technology, 169, 236-243.

Pettersson, A., Zevenhoven, M., Steenari, B.-M., ¡ mand, L.-E. 2008. Application of chemical fractionation methods for ultimately of biofuels, waste derived fuels and CFB co-combustion fly ashes. Fuel, 87(15), 3183-3193.

Qi, X., Song, G., Yang, S., Yang, Z., Lyu, Q. 2018. Exploration of effective bed material for use as slagging/agglomeration preventatives in circulating fluidized bed gasification of high-sodium lignite. Fuel, 217, 577-586.

Skrifvars, B.-J., Backman, R., Hupa, M., Sfiris, G., ¡ byhammar, T., Lyngfelt, A. 1998. Ash behaviour in a CFB boiler during combustion of coal, peat or wood. Fuel, 77(1), 65-70.

Tang, G., Zhang, M., Gu, J., Wu, Y., Yang, H., Zhang, Y., Wei, G., Lyu, J. 2019. Thermal-hydraulic calculation and analysis on evaporator system of a 660;MWe ultra-supercritical CFB boiler. Applied Thermal Engineering, 151, 385-393.

Urciuolo, M., Solimene, R., Chirone, R., Salatino, P. 2012. Fluidized bed combustion and fragmentation of wet sewage sludge. Experimental Thermal and Fluid Science, 43, 97-104.

Wu, H., Yang, C., He, H., Huang, S., Chen, H. 2018. A hybrid simulation of a 600;MW supercritical circulating fluidized bed boiler system. Applied Thermal Engineering, 143, 977-987.

Yaµci, W., Ghorab, M., Entchev, E. 2014. 3D CFD analysis of the effect of inlet airflow maldistribution on the fluid flow and heat transfer performances of plate-fin-and-tube laminar heat exchangers. International Journal of Heat and Mass Transfer, 74, 490-500.

Yaµci, W., Ghorab, M., Entchev, E. 2016. 3D CFD study of the effect of inlet airflow maldistribution on plate-fin-tube heat exchanger design and thermalï hydraulic performance. International Journal of Heat and Mass Transfer, 101, 527-541.

Yeoh, G.H., Cheung, S.C.P., Tu, J.Y. 2012. On the prediction of the phase distribution of bubbly flow in a horizontal pipe. Chemical Engineering Research and Design, 90(1), 40-51.

DRYING OF PHARMACEUTICAL GRANULES IN A PULSED FLUIDIZED BED

Chen Li[1], Carter Blocka[1], Lifeng Zhang[1*]

[1]*Department of Chemical and Biological Engineering, University of Saskatchewan, 57 Campus Dr, Saskatoon, SK S7N 5A9*

*Email: *lifeng.zhang@usask.ca*

Abstract

Drying behaviour of pharmaceutical granules has been studied in a pulsed fluidized bed dryer with the pulsation frequency ranging from 0.75 to 3 Hz, superficial gas velocity of 4 to 5.6U_{mf}, and an inlet gas temperature of 40 to 50 ℃. Results show that superficial gas velocity has the most important influence on the drying time. Increasing the drying gas velocity results in a longer drying time. Higher drying air temperature also decreases the drying time as expected. The effect of pulsation on drying is influenced by the gas velocity. Pulsation is more effective to eliminate channeling and enhance drying at higher superficial gas velocity. There is no enhanced drying effect found for a pulsed fluidized bed operated at low gas flow rate. A lower pulsation frequency, namely 0.75 Hz, is more favorable to decrease the drying time. A pulsed fluidized bed at a high frequency is similar to a conventional fluidized bed.

Introduction

Solid oral dosage (SOD) forms offer enhanced physical and chemical stability, relatively easy preparation, and low manufacturing costs. Among different types of SOD forms, tablet is the most common in pharmaceutical market due to its ease of use and high throughput (Davies, 2001). Wet granulation is the most popular method used to manufacture tablets in the pharmaceutical industry. In a typical wet granulation method, active pharmaceutical ingredients (APIs) and excipients need to be well mixed , and then a liquid binder is added to form granules (Gad, 2008). Afterwards, the moisture needs to be removed by a drying process. Fluidized bed drying is one of the most commonly used method due to its large heat transfer area and high heat transfer efficiency. During the drying operation, because of the tendency of wet pharmaceutical powders to form agglomerates, channeling phenomenon may occur. Using pulsed flow in fluidized bed drying is reported to be an effective method to eliminate channeling (Ali and Asif, 2012; Godoi et al., 2011; Jia et al., 2017). Pulsed air flow can also deagglomeration of pharmaceutical particles (Sosnowski et al., 2014). However, this enhanced effect has not been investigated with pharmaceutical granules, particularly, when APIs are included.

Materials and Methods

Materials

Pre-determined compositions powders, as shown in Table 1, were sieved through a screen with an opening size of 0.2 mm, and then mixed in a 250 W low-shear granulator (Kitchen-Aid class mixer) for 2 minutes at the lowest speed (setting 1). Water was gradually added during the following 5 minutes at a rate of 60 ml/min followed by a higher speed (setting 2) mixing for 2 minutes. Afterward, the initial mixture was sieved with a 3.36 mm screens. This process was repeated 3 times to get 3 kg of wet pharmaceutical granules. The API and its concentration in the formulation is based on regular strength TYLENOL tablets. Every tablet (1.75 g) contains 325 mg acetaminophen. The presence of moisture in the pharmaceutical powders can have a significant effect on the minimum fluidization velocity (U_{mf}). U_{mf} at the initial moisture content 30 wt.% (wet basis) is 0.45 m/s, and U_{mf} at the final moisture content 5 wt.% (wet base) is 0.08

m/s. An average value of 0.25 m/s was taken among values measured at four moisture contents as the minimum fluidization velocity.

Table 1. Wet granule formulation

Function	Component	Percentage by mass (dry basis)	Supplier
API	Acetaminophen	18%	Hebei Jiheng Pharmaceutical
Filler	Lactose Monohydrate (LMH)	40%	Foremost Farms
Filler	Microcrystalline Cellulose (MCC)	36%	FMC BioPolymers
Binder	Hydroxypropyl Methylcellulose (HPMC)	4%	DOW Chemical Company
Disintegrant	Croscamellose Sodium	2%	FMC BioPolymers
Liquid binder	Water	42%	

Fluidized bed setup and instrumentation

Drying experiments were performed in an acrylic fluidized bed as shown in Fig. 1. A batch of 3 kg of wet granules was loaded in the product bowl. The air distributor was made of aluminum plate with 2 mm opening and 5.6% open air ratio. The pulsed air was supplied from a surge tank connected with building air. The continuous air supply was provided by a blower. The continuous air was used to maintain the wet granules fluidized, and pulsed air can enhance the pulsation and oscillation inside the fluidized bed to break agglomerates. The pulsed air was supplied through a solenoid valve. The two air streams were mixed and heated before entering the wind box. An air bag filter was installed at the top of the column to collect fine particles.

Throughout the drying process, data was simultaneously collected from the thermocouples and RH meters located at the inlet and outlet of the fluidized bed dryer, as shown in Fig. 1. The pressure transducers are located at the product bowl and the free board to measure the pressure. The pressure drop was used to determine minimum fluidization velocity of the pharmaceutical powders.

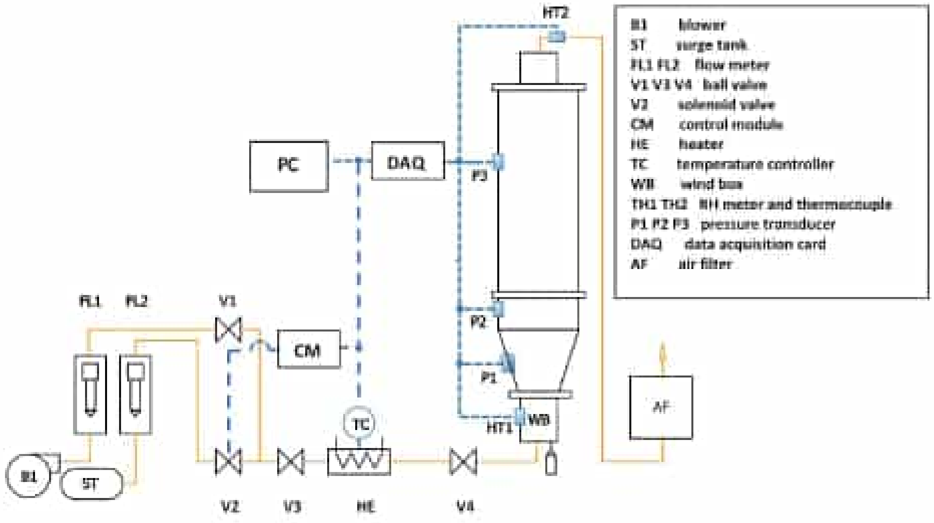

Fig. 1. Pulsed fluidized bed dryer set-up

Results and Discussion

Comparison between continuous fluidized bed and pulsed fluidized bed

At a low superficial gas velocity 1 m/s ($4U_{mf}$), the drying time of pulsed fluidized bed is longer than a fluidized bed with a continuous gas flow. When the control factor of the drying process is superficial gas velocity, applying pulsed air didnôt decrease drying time. The ñoffò period then decreased the total air flow rate and significantly increased the drying time. The low pulsation amplitude with low flow rate cannot overcome the strong inter-particle forces in wet pharmaceutical granules, and cannot enhance mass and heat transfer between air and wet granules.

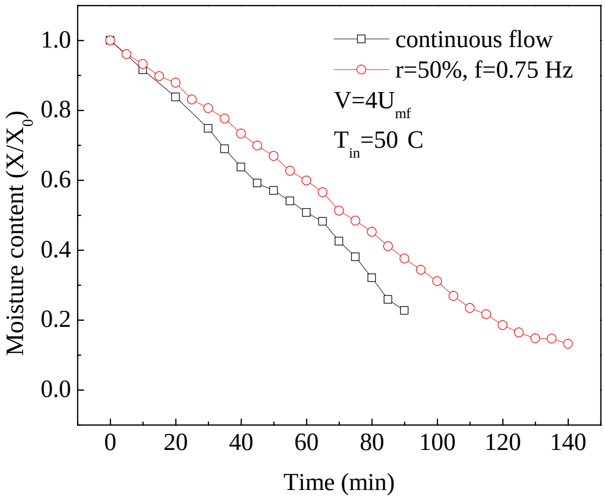

Fig. 3. Effect of pulsation on drying at V = $4U_{mf}$

Under a higher superficial gas velocity 1.4 m/s ($5.6U_{mf}$), the pulsed fluidized bed has a shorter drying time than a conventional fluidized bed, as shown in Fig. 4, which is different from the lower superficial gas velocity ($4U_{mf}$). For the pulsed fluidized bed, 50% of the total air flow was pulsed and the other 50% was continuous. At the lower superficial gas velocity, 50% of the continuous air was not enough to keep bed at minimum fluidized status. The fluctuation induced by pulsed air cannot effectively break agglomerates. The ñoffò period of pulsed air decreased the total air flow rate. When increasing the superficial gas velocity from $4U_{mf}$ to $5.6U_{mf}$, 50% continuous air flow can keep the bed continually fluidized, and the other 50% pulsed air can enhance mixing and eliminate channeling at the beginning of the drying process.

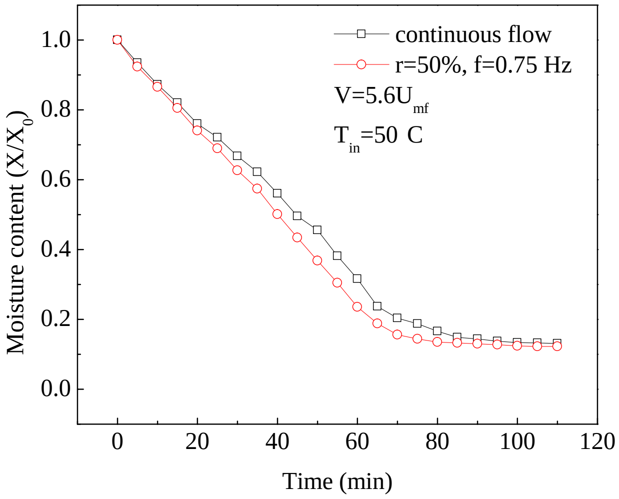

Fig. 4. Effect of pulsation on drying at V = $5.6U_{mf}$

Effect of pulsation frequency

The hydrodynamic properties, including mixing efficiency, bubble size and velocity, is significantly influenced by pulsation frequency. The mass and heat transfer in pulsed bed is affected correspondingly. Batch drying tests were conducted at the pulsation frequencies 0.75, 1.5, and 3 Hz to study the effect of pulsation frequency on drying of pharmaceutical granules in a fluidized bed dryer. The moisture content curves of pharmaceutical granules during drying are shown in Figs. 5 and 6. At 5.6U_{mf} as shown in Fig. 5, decreasing the pulsation frequency increases the drying rate. The ĩonòand ĩoffòperiods of a pulsation cycle are equal. During the ĩoffò period, the solenoid valve is closed, and the pressure started to accumulate. The accumulated pressure was released when the solenoid valve opened at the beginning of ĩonò period. The instantaneous pressure release can cause a peak pressure. The pressure drop was increased from 1 kPa to 2.2 kPa. This high pressure and the following oscillation can overcome the large inter-particle forces between wet pharmaceutical granules. The pulsed air can reach higher peak pressure with longer ĩoffòperiod.

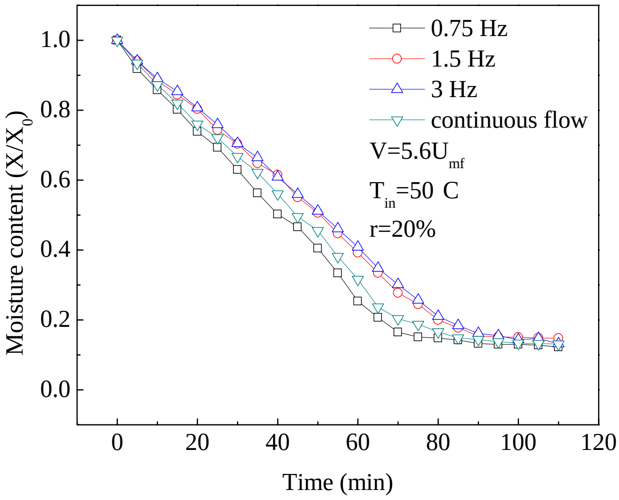

Fig. 5. Effect of pulsation on drying at V = 5.6U_{mf}

At a lower superficial gas velocity (4U_{mf}), drying with higher pulsation frequency has faster drying rate than lower frequency. During the ĩoffò period, the pressure accumulated can increase the instantaneous air flow rate when valve opens. When pulsation frequency is high, the ĩoffòperiod of solenoid valve is shorter. The high frequency switching of valve results in many similarities with conventional fluidized bed. While, with lower frequency, longer ĩoffò period caused reduced air flow rate. The drying time is significantly influenced by air flow rate. Under low air flow rate, lower frequency has longer drying time compared with high frequency pulsation.

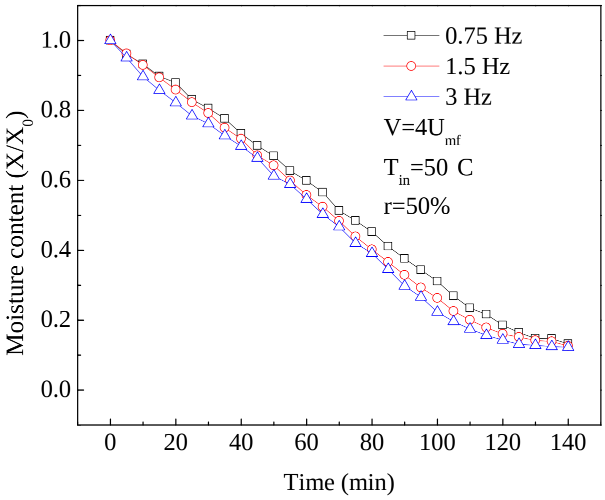

Fig. 6. Effect of pulsation on drying at V = 4U$_{mf}$

Conclusion

Our experimental results show that the superficial gas velocity has the most important influence on the drying time. The effect of pulsation on the drying performance depends on the gas flow rate. Pulsed gas flow is more effective to eliminate channeling and enhance drying at a higher superficial gas velocity. A lower pulsation frequency, namely 0.75 Hz, is found to be more favorable to enhance the drying rate. The overall drying performance at a high frequency is similar to that in a conventional fluidized bed.

References

Ali, SS., Asif, M., 2012. Fluidization of nano-powders: Effect of flow pulsation. Powder Technology 225, 86-92.

Davies, P., 2001. Oral solid dosage forms. Pharmaceutical preformulation and formulation. Boca Raton: Interpharm/CRC, 379-458.

Gad, SC., 2008. Pharmaceutical manufacturing handbook: production and processes. John Wiley & Sons.

Godoi, FC., Pereira, NR., Rocha, SCS., 2011. Analysis of the drying process of a biopolymer (poly-hydroxybutyrate) in rotating-pulsed fluidized bed. Chemical Engineering and Processing: Process Intensification 50, 623-629.

Jia, D., Bi, X., Lim, CJ., Sokhansanj, S., Tsutsumi, A., 2017. Gas-solid mixing and mass transfer in a tapered fluidized bed of biomass with pulsed gas flow. Powder Technology 316, 373-387.

Sosnowski, TR., GiŨyŒska, K., ł ywczyk, Ğ, 2014. Fluidization and break-up of powder particle aggregates during constant and pulsating flow in converging nozzles. Colloids and Surfaces A: Physicochemical and Engineering Aspects 441, 905-911.

A PERSPECTIVE ON ELECTROSTATICS IN GAS-SOLID FLUIDIZED BEDS: CHALLENGES AND FUTURE RESEARCH NEEDS

Farzam Fotovat[1*], **Xiaotao T. Bi**[2], **John R. Grace**[2]

[1]*I Department of Chemical and Petroleum Engineering, Sharif University of Technology, Azadi Avenue, P.O. Box 11365-9465, Tehran, Iran*
[2] *Department of Chemical and Biological Engineering, University of British Columbia, Vancouver V6T 1Z3, Canada*

*Email: *Fotovat@sharif.edu*

Abstract

This paper provides a perspective on the current knowledge and potential areas of future research related to electrostatics in fluidized beds. Aspects addressed include characterization techniques, interplay between electrostatics and hydrodynamics, charge control methods, applications of tribo-electrostatic fluidization systems, and computational simulations which account for electrostatic forces, as well as other forces. This is a complex research field involving fluid mechanics, powders, and electrical physics.

Introduction

Gas-solid fluidized beds are characterized by intense solids mixing, uniform temperature profiles, and efficient heat transfer. These features have made fluidization widely used in many physical and chemical processes dealing with particulate systems. Fluidization of solid particles, by its nature, involves intense and frequent collisions of solid particles with each other and with vessel walls, causing tribo-electrification. Although tribo-electrification is a ubiquitous phenomenon known for centuries, current understanding of the underlying mechanisms is still limited. Intrinsic complexity of particle motion and contacts in fluidized beds results in complex charge generation and dissipation phenomena, far from being well understood. Due to the electrostatic interactions, charged particles in fluidized beds are prone to aggregation by adhering to vessel walls (wall sheeting) (Hendrickson, 2006) and/or to other particles, leading to formation of agglomerates. In addition, the electrostatic charges on particles and vessel walls, as well as high-voltage electrical fields arising from them, can affect the motion of particles and fluids, interfering with sensors and bed internals, leading to malfunction of instruments and operation. Due to these effects, electrostatic charges in commercial gas-solid fluidized bed facilities, especially in fluidized bed polymerization reactors, cause several operational problems such as the formation of undesired byproducts (Cheng, Lau, Guan, Fushimi, Tsutsumi and Wang, 2012), production losses (Hendrickson, 2006), and problematic product handling (Chen, Bi and Grace, 2003). Moreover, unintentional charge accumulation and resultant hazardous discharges can cause sparks, fires, and even explosions, affecting process performance and endangering operators. On the other hand, the tribo-charging propensity of fluidized beds and its impact on the particle motion has been exploited in some industrial processes such as powder coating (Yang et al., 2016) and coal beneficiation. Electrostatic fields have also been proven to be effective in modifying hydrodynamics of bubbling fluidized beds (Lepek *et al.*, 2010) and in enhancing fluidization of nanoparticles (Espin *et al.*, 2009).

This paper provides an outlook of the measurement, characterization, control, applications, and simulation of electrostatics in fluidized beds, highlighting areas needing further research and development for advanced and effective control and exploitation of electrostatics in commercial fluidized beds.

When Does Electrostatics Play an Important Role in Fluidized Beds?

While electrostatic charges are generated in a wide range of fluidized bed systems, they only play an important role when the resulting electrical forces are appreciable, relative to the weight-minus-buoyancy of at least some of the particles. In particular, electrostatics are most likely to influence hydrodynamic behavior when:

- At least some of the particles are relatively small, e.g. Ò100 µm
- Particle dielectric constants are intermediate in magnitude such that particles are able to gain and retain electrical charges
- Superficial gas velocities are high enough to cause vigorous particle motion
- Relative humidity is low, e.g. Ò10%
- Pressure is high, e.g. Ó3 bar
- Temperature is low, e.g. Ò50°C
- The difference between work functions of the column wall and particles is large, and the wall surface-area-to-reactor-volume ratio is high.

Characterization of Electrostatics in Fluidized Beds

Detailed characterization of electrostatics in fluidized beds relies strongly on accurate, online, and local measurement techniques. Electrostatic charges can be measured directly using Faraday cups, or indirectly extracted from signals registered by electrostatic probes of three major types: capacitance probes, collision probes, and induction probes/sensors.

By measuring the net charge of a given mass of particles, Faraday cups can directly provide particle mass charge density, i.e. particle charge-to-mass ratio. Faraday cups are generally used offline, measuring the charge density of particles withdrawn from different locations of the fluidized bed. Due to the difficulties associated with particle sampling and utilization of Faraday cups in large-scale industrial processes operating at elevated pressures and temperatures, it is desirable to use electrostatic probes to measure local particle charge densities online. The output of an electrostatic probe is in the form of an induced charge signal, current signal or voltage signal from which the local charge level in a gas-solid fluidized bed is extracted. For example, a capacitance probe inside the fluidized bed connected to an electrometer measures the potential of a section of the bed located between the probe and a grounded reference (reactor wall, metal distributor or another metal probe). Collision, or so-called ball probes, most commonly used electrostatic probe in industry, receive both charges transferred from particles colliding with the probe surface and charges induced when particles pass the probe. The average magnitude of electrical current/potential from collision probes depends on the charge density and velocity of particles colliding with the probe and the collision frequency or particle concentration.

Non-contacting induction sensors are independent of net charge transfer, encountered by contacting probes, and have the advantage of not disturbing the flow since they are not directly exposed to the fluidized media. However, they may not be suitable for obtaining local particle charging information since particle-wall interactions, rather than particle-probe interactions, may dominate the induction signals when there is a strong charge buildup on the column wall. Due to non-uniform charge distributions in the fluidized bed, bulk measurements relying on the assumption of uniform spatial charge distribution are unable to capture the local charging characteristics. Therefore, simultaneous acquisition of signals from small collision or induction probes installed at different locations of the fluidized bed, in conjunction with advanced signal analysis and reconstruction methods, are needed to map charge distributions in fluidized beds and to unveil the underlying charging mechanisms. Online and automated measurement techniques would also be helpful for early detection of the detrimental effects of electrostatic charges so that timely actions can be carried out to offset them.

Relationship Between Electrostatic Phenomenon and Hydrodynamics in Fluidized Beds

Influence of fluidized bed hydrodynamics on electrostatics

The probability, intensity, and frequency of particle-particle and particle-wall collisions are related to the hydrodynamic characteristics of fluidized beds. On the other hand, when electrostatic forces are comparable in magnitude to hydrodynamic forces, they can affect the motion of particles and consequently the hydrodynamics of fluidized beds.

There is a general consensus that the degree of electrification, e.g. particle charge density, increases with increasing superficial gas velocity in the bubbling and turbulent fluidization flow regimes, presumably because the enhanced particle-particle interactions result in augmented charge generation. Fluidized bed polyolefin reactors, especially vulnerable to electrostatic-induced problems, operate at elevated pressures, up to 3000 kPa. Experimental studies have generally shown an increase in the degree of electrification and wall fouling with increasing pressure of operation for polymer particles, probably due to increased bubble rise velocity, bubble frequency, and bubble phase volume fraction (Moughrabiah et al., 2009; Song et al., 2016). Moughrabiah et al. (2009) and Alsmari et al. (2014; 2015) reported a decrease in electrostatic current and even a reversal in charge polarity as the bed temperature increased from 20 to 75°C, likely due to increased charge dissipation at higher temperatures.

The size distribution of particles also influences the electrostatic characteristics of fluidized beds. Experiments conducted on particles with wide size distributions have shown that the particle charge-to-mass ratio increases with decreasing mean particle size. This explains the increase observed in the degree of wall fouling with increasing fraction of fine particles in mixtures of fine and coarse polyethylene particles. Addition of fine particles to a fluidized bed containing coarse granules of the same chemical composition could increase or decrease the electrostatic potential of the bed, depending on the amount added. This has been attributed to the role of fine particles in altering the contact mode between coarse particles and in affecting the generation, transfer and neutralization of electrostatic charges. As the particle size distribution may vary in industrial fluidized beds with time due to chemical reactions, entrainment of fines, and/or attrition/ agglomeration of particles, these findings imply that the degree of electrification is subject to change during the operation of fluidized systems, a topic that needs further investigation.

Influence of electrostatics on hydrodynamics of fluidized beds

Experimental and numerical studies suggest that the frequency, size and rising velocity of bubbles generally decrease because of electrostatic interactions in fluidized beds. Computational simulations have also shown elongation of bubbles which tend to rise more towards the axis of the column in the presence of charged particles. Highly charged particles can delay fluidization by increasing the minimum fluidization velocity. The tendency of strong electrostatic forces to restrain particle motion and decrease particle impact velocities results in less vigorous fluidization (Rokkam, 2012), decreased solids mixing (Lim, 2013), and greater likelihood of wall sheeting and particle agglomeration. Size segregation in fluidized beds can be suppressed by bipolar electrostatic charges, since small and large particles having opposite polarities are likely to attract each other and form agglomerates (Yang et al. 2017). Further investigations are required to understand the interplay between electrostatics and mixing/segregation in fluidized beds. The entrainment rate of charged fines from fluidized beds is lower than that of uncharged fines (Fotovat. 2017a;. 2017b; 2017c) , since electrostatic forces hinder the free movement of fines and promote agglomeration of bipolarly charged coarse and fine particles, making them less likely to be entrained (Fotovat et al., 2017d).

The interrelationship between electrostatics and hydrodynamics complicates characterization, operation and scale-up of gas-solid fluidized beds hydrodynamics and particle charging behavior. Interaction between non-homogenous flow structures of fluidized beds and non-uniform charge distribution in the bed requires advanced techniques, capable of measuring local electrostatic and hydrodynamic parameters simultaneously.

Electrostatic Charge Control

Electrostatic charges in fluidized beds are controlled by charge generation rate reduction, charge dissipation rate enhancement and charge neutralization (Hendrickson, 2006). The generation rate is decreased by reducing the difference in work function between wall and bed materials, e.g. by treating or coating the reactor inner wall, decreasing the contact surface area, e.g. by adding fines, or by changing the operating conditions, e.g. decreasing bed pressure. Increasing the relative humidity [23] and adding antistatic agents, such as graphite, Larostat 519 and ionic gases (SO_2), as well as increasing the bed temperature are effective in enhancing charge dissipation rates. Charge inducing agents such as solid metal oxides [109] and static modifier-catalysts (e.g. titanium-based catalyst) and charge neutralizing ions, e.g. from an in-situ corona charge eliminator, have been adopted to neutralize electrostatic charges in fluidized beds. Injection of ions into fluidized bulk material through a supersonic nozzle has been effective to control electrostatic charges in the presence of sufficient humidity (Taillet, 1993). However, charge elimination with ionization of the air injected into a fluidized bed has reportedly been ineffective (Revel et al., 2003). Further work is needed to determine the efficacy of charge control methods in large-scale fluidized beds operating in the bubbling and turbulent fluidization flow regimes at elevated pressure and temperature.

Applications

The ability of fluidized beds to tribo-charge particles has been exploited in a number of industrial applications such as powder coating and solids separation. In powder coating, uniform coating of layers thicker than 250 µm can be achieved when charged fine powders adhere to a grounded work-piece. Bipolar charging of the components of a solid particulate mixture provides favorable conditions for solids separation when freely flowing tribo-charged particles are exposed to an external electrical field, deflecting particles with one polarity towards an electrode of opposite polarity. For instance, opposite polarities of coal particles and accompanying impurities charged in a fluidized bed can be exploited to separate them according to the magnitude and polarity of their charges during free-fall through an electrical field. A similar technique has been developed to separate mixed plastic waste granules or mixtures of protein- and carbohydrates-rich particles.

Electric fields can also be implemented to modify hydrodynamics of fluidized beds. For example, polarized semi-insulating particles can be arranged in chains along the external electric field direction, leading to bubble deformation. Controlling bubble size and spatial distribution can facilitate reactor scale-up and increase gas-solids contact efficiency. Non-uniform fluidization of nanopowders, caused by formation of highly porous agglomerates hundreds of microns in diameter, can be enhanced in an external electric field with optimal oscillation frequencies of tens to hundreds of Hertz, resulting in mobilization of dispersed agglomerates (Quintanilla et al., 2012).

Simulations Including Electrostatic Charges

The most crucial issue when simulating electrostatics in fluidized beds is the lack of a precise model to predict dynamic charge generation, accumulation and dissipation as a function of the hydrodynamics, operating conditions, and particle properties. In the absence of such a model, incorporating the electrostatic effects in computational studies of fluidized beds is generally based on the simplifying assumption of uniform and constant charge density of the particles. The hydrodynamics of tribo-charged fluidized beds with a charge distribution is not completely captured by simulations in which all particles are assumed to carry the same charge (Kolehmainen, 2016b). However, fixed charge simulations can predict hydrodynamics accurately for a given particle charge distribution. According to Kolehmainen et al. (2016a), Eulerianï Eulerian simulations using Poissonôs equation to model the electrostatic effects can capture the electrostatic field fairly accurately for large systems consisting of similarly charged particles, whereas Eulerian–Lagrangian techniques are more appropriate for simulating reactors of all sizes with oppositely charged particles. The main challenge to develop an effective simulation approach, which can be used as a predictive tool, is to determine the charge polarity and distribution a priori. To overcome this challenge, detailed tribo-charging models based on underlying charge generation and dissipation mechanisms coupled with the hydrodynamics of the reactor system still need to be developed.

References

Alsmari, T.A. (2014) Effect of operating conditions and particle properties on electrostatics and entrainment in gas-solid fluidized beds, Ph.D. dissertation. University of British Columbia, Vancouver, Canada.

Alsmari, T.A., Grace, J.R. and Bi, X.T. (2015) ‘Effects of superficial gas velocity and temperature on entrainment and electrostatics in gas–solid fluidized beds’, Chemical Engineering Science. Elsevier, 123, pp. 49–56.

Chen, A., Bi, H.T. and Grace, J.R. (2003) ‘Measurement of particle charge-to-mass ratios in a gas-solids fluidized bed by a collision probe’, Powder Technology, 135–136, pp. 181–191. doi: 10.1016/j.powtec.2003.08.014.

Cheng, Y., Lau, D.Y.J., Guan, G., Fushimi, C., Tsutsumi, A. and Wang, C.H. (2012) ‘Experimental and numerical investigations on the electrostatics generation and transport in the downer reactor of a triple-bed combined circulating fluidized bed’, Industrial and Engineering Chemistry Research, 51(43), pp. 14258–14267. doi: 10.1021/ie3011879.

Colver, G.M. (1977) ‘Bubble control in gas-fluidized beds with applied electric fields’, Powder Technology, 17(1), pp. 9–18. doi: 10.1016/0032-5910(77)85038-9.

Espin, M.J., Valverde, J.M., Quintanilla, M.A.S. and Castellanos, A. (2009) ‘Electromechanics of fluidized beds of nanoparticles’, Physical Review E - Statistical, Nonlinear, and Soft Matter Physics, 79(1), pp. 1–7. doi: 10.1103/PhysRevE.79.011304.

Fotovat, F., Alsmari, T.A., Grace, J.R. and Bi, X.T. (2017a) ‘The relationship between fluidized bed electrostatics and entrainment’, Powder Technology, 316, pp. 157–165.

Fotovat, F., Grace, J.R. and Bi, X.T. (2017b) ‘Particle entrainment from gas-solid fluidized beds: conductive vs. dielectric fines’, AIChE Journal, 63(4), pp. 1194–1202.

Fotovat, F., Gill, K., Grace, J.R. and Bi, X.T. (2017c) ‘Impact of column material on electrostatics and entrainment of particles from gas-solid fluidized beds’, Chemical Engineering Science, 167, pp. 120–134.

Fotovat, F., Grace, J. R. and Bi, X. T. (2017d) ‘Electrostatics in gas-solid fluidized beds: a review’, Chemical Engineering Science, 173, pp. 303-334.

Hendrickson, G. (2006) ‘Electrostatics and gas phase fluidized bed polymerization reactor wall sheeting’, Chemical Engineering Science, 61(4), pp. 1041–1064. doi: 10.1016/j.ces.2005.07.029.

Kashyap, M., Gidaspow, D. and Driscoll, M. (2008) ‘Effect of electric field on the hydrodynamics of fluidized nanoparticles’, Powder Technology, 183(3), pp. 441–453. doi: 10.1016/j.powtec.2008.01.010.

Kolehmainen, J., Ozel, A., Boyce, C.M. and Sundaresan, S. (2016a) ‘A hybrid approach to computing electrostatic forces in fluidized beds of charged particles’, AIChE Journal, 62(7). doi: 10.1002/aic.

Kolehmainen, J., Ozel, A., Boyce, C.M. and Sundaresan, S. (2016b) ‘Triboelectric charging of monodisperse particles in fluidized beds’, AIChE Journal. Wiley Online Library, pp. 1–20.

Lepek, D., Valverde, J.M., Pfeffer, R. and Dave, R.N. (2010) ‘Enhanced nanofluidization by alternating electric fields’, AIChE Journal. Wiley Subscription Services, Inc., A Wiley Company, 56(1), pp. 54–65. doi: 10.1002/aic.11954.

Lim, E.W.C. (2013) ‘Mixing behaviors of granular materials in gas fluidized beds with electrostatic effects’, Industrial and Engineering Chemistry Research, 52(45), pp. 15863–15873. doi: 10.1021/ie402511p.

Moughrabiah, W.O., Grace, J.R. and Bi, X.T. (2009) ‘Effects of pressure, temperature, and gas velocity on electrostatics in gas-solid fluidized beds’, Industrial & Engineering Chemistry Research, 48, pp. 320–325. doi: 10.1021/ie800556y.

Quintanilla, M.A.S., Valverde, J.M., Castellanos, A., Lepek, D., Pfeffer, R. and Dave, R.N. (2008) óNanofluidization as affected by vibration and electrostatic fieldsô, Chemical Engineering Science, 63(22), pp. 5559ï 5569. doi: 10.1016/j.ces.2008.08.012.

Quintanilla, M.A.S., Valverde, J.M., Espin, M.J. and Castellanos, A. (2012) óElectrofluidization of silica nanoparticle agglomeratesô, Industrial and Engineering Chemistry Research, 51(1), pp. 531ï 538. doi: 10.1021/ie200538v.

Revel, J., Gatumel, C., Dodds, J.A. and Taillet, J. (2003) óGeneration of static electricity during fluidisation of polyethylene and its elimination by air ionisationô, Powder Technology, 135ï 136, pp. 192ï 200. doi: 10.1016/j.powtec.2003.08.015.

Rokkam, R.G. (2012) Computational fluid dynamics simulation of fluidized bed polymerization reactors, Ph.D. dissertation. Iowa State University, Ames, Iowa, USA.

Rokkam, R.G., Fox, R.O. and Muhle, M.E. (2010a) óCFD modeling of electrostatic forces in gas-solid fluidized bedsô, Journal of Computational Multiphase Flows, 2(4), pp. 189ï 205.

Rokkam, R.G., Fox, R.O. and Muhle, M.E. (2010b) óComputational fluid dynamics and electrostatic modeling of polymerization fluidized-bed reactorsô, Powder Technology. Elsevier B.V., 203(2), pp. 109ï 124. doi: 10.1016/j.powtec.2010.04.002.

Song, D., Salama, F., Matta, J. and Mehrani, P. (2016) óImplementation of Faraday cup electrostatic charge measurement technique in high-pressure gas-solid fluidized beds at pilot-scaleô, Powder Technology. Elsevier B.V., 290, pp. 21ï 26. doi: 10.1016/j.powtec.2015.05.049.

Taillet, J. (1993) óElimination of static charges in the processing of bulk materialô, Journal of Electrostatics, 30, pp. 181ï 189.

Valverde, J.M., Quintanilla, M.A.S., Espin, M.J. and Castellanos, A. (2008) óNanofluidization electrostaticsô, Physical Review E. APS, 77(3), p. 31301.

Valverde, J. M. and Castellanos, A. (2007) óFluidization, bubbling and jamming of nanoparticle agglomeratesô, Chemical Engineering Science. Elsevier, 62(23), pp. 6947ï 6956.

van Willigen, K.F., van Ommen, J.R., van Turnhout, J. and van den Bleek, C.M. (2005) óBubble size reduction in electric-field-enhanced fluidized bedsô, Journal of Electrostatics, 63(6ï 10), pp. 943ï 948. doi: 10.1016/j.elstat.2005.03.065.

Yang, Q., Ma, Y., Zhu, J., Chow, K. and Shi, K. (2016) óAn update on electrostatic powder coating for pharmaceuticalsô, Particuology. Chinese Society of Particuology, 31, pp. 1ï 7. doi: 10.1016/j.partic.2016.10.001.

Yang, Y., Zi, C., Huang, Z., Wang, J., Lungu, M. and Liao, Z. (2017) óCFD-DEM investigation of particle elutriation with electrostatic effects in gas-solid fluidized bedsô, Powder Technology. Elsevier B.V., 308, pp. 422ï 433. doi: 10.1016/j.powtec.2016.12.032.

IMPACT OF AN ELECTROSTATICALLY CHARGED SILICA POWDER PNEUMATICALLY INJECTED INTO A POLYETHYLENE FLUIDIZED BED AT DIFFERENT FLUIDIZATION TIMES

Milad Taghavivand, Mohsen Isaac Nimvari, Andrew Sowinski, Poupak Mehrani*

Department of Chemical and Biological Engineering, University of Ottawa, 161 Louis-Pasteur, K1N 6N5 Ottawa, Ontario, Canada

**Email: poupak.mehrani@uottawa.ca*

Abstract

This work investigated the effect of injecting a silica powder, electrostatically charged due to pneumatic conveying, on the degree of polyethylene fluidized bed wall fouling. The silica powder used was as a typical catalyst support in polyethylene production. A 5 m stainless steel tube (4.75 mm ID) curved with a 1 m radius bend was used to convey 0.1 g of the silica into a 1 kg bed of polyethylene and was fluidized in a 0.1 m diameter stainless steel atmospheric fluidized bed. The results were compared for when the powder was injected into the fluid bed at different stages of a one-hour fluidization period. This included the powder injection prior to fluidization of polyethylene particles as well as injections after 15 and 30 minutes of fluidization. To calculate electrostatic charge of powders upon entering the fluidized bed, the electric current data generated by powders in the conveying line was measured. Overall, it was observed that the wall fouling either did not change significantly or increased as a result of silica powder injection.

Introduction

Electrostatic charge generation due to continuous interparticle and particle-vessel wall contacts, which occurs during particle handling, transport (e.g., pneumatic conveying) and processing (e.g., gas-solid fluidized beds), is a phenomenon that can result in severe problems such as particle-wall adhesion, electrostatic discharge, and particle segregation. Gas-solid polyethylene (PE) fluidized bed reactors are examples where the high electrostatically charged polyethylene resin and catalyst particles adhere to the reactor wall, resulting in poor removal of the heat of the exothermic polymerization reaction in the wall regions. This in turn results in melting of the fouled particles and forming sheets that can grow and break off of the reactor wall, causing long reactor shut down periods and ultimately a significant economic loss (Hagerty et al., 2011).

The majority of the works studying electrostatic charge generation in relation to PE fluidized bed reactors have considered PE resin as the only particle present in such reactors (Mehrani et al., 2017). Whereas, in the commercial PE reactors, catalyst particles also exist which necessitates studying their contribution on the degree of fluidized bed electrification. In commercial PE processes, catalyst particles are injected into the reactor in either slurry or dry solid form. However, problems such as uneven distribution of catalyst particles inside the reactor after the injection, need for additional slurry making equipment and procedure, as well as possible impacts on catalyst activity make slurry feeding less favorable compared to dry solid feeding (Rao et al., 2019). In dry feeding systems, catalyst particles are pneumatically conveyed to the reactor through narrow and long tubes (typically 4.57 mm stainless steel in diameter). It is important to realize that, in general, pneumatic conveying systems are known to generate the largest amount of electrostatic charge among all gas-solid processes (Klinzing, 2018). Thus, in relation to the polyethylene process, catalyst particles are anticipated to be electrostatically charged upon entering the reactor. The attractive image forces formed due to the induction charging between the fluidized bed wall and pneumatically injected charged catalyst particles, as well as attractive electrostatic forces between the fouled particles and newly injected catalyst are then suspected to contribute in the formation/promotion of reactor wall fouling (Song and Mehrani, 2017).

Due to the fact that a major portion of the catalyst particles (typically 90 to 99 wt. %) is occupied by their support (Cann et al., 2019; Hoff, 2018; Rao et al., 2019), it is probable that the catalyst support shows a dominant effect on catalyst charging tendency. One of the common supports used for chromium-based (e.g., Phillips type), Metallocene and Ziegler-Natta catalysts in polyethylene production is silica powder, which also becomes electrostatically charged during pneumatic conveying. The aim of this work was to study the effect of pneumatically injecting a predetermined mass of charged silica powder at different stages of fluidization (prior to and after fluidization onset) on the degree of a PE fluidized bed wall fouling.

Materials and Methods

Fig. 1 shows the schematic diagram of the gas-solid fluidization system along with the horizontal powder conveying line used in this work.

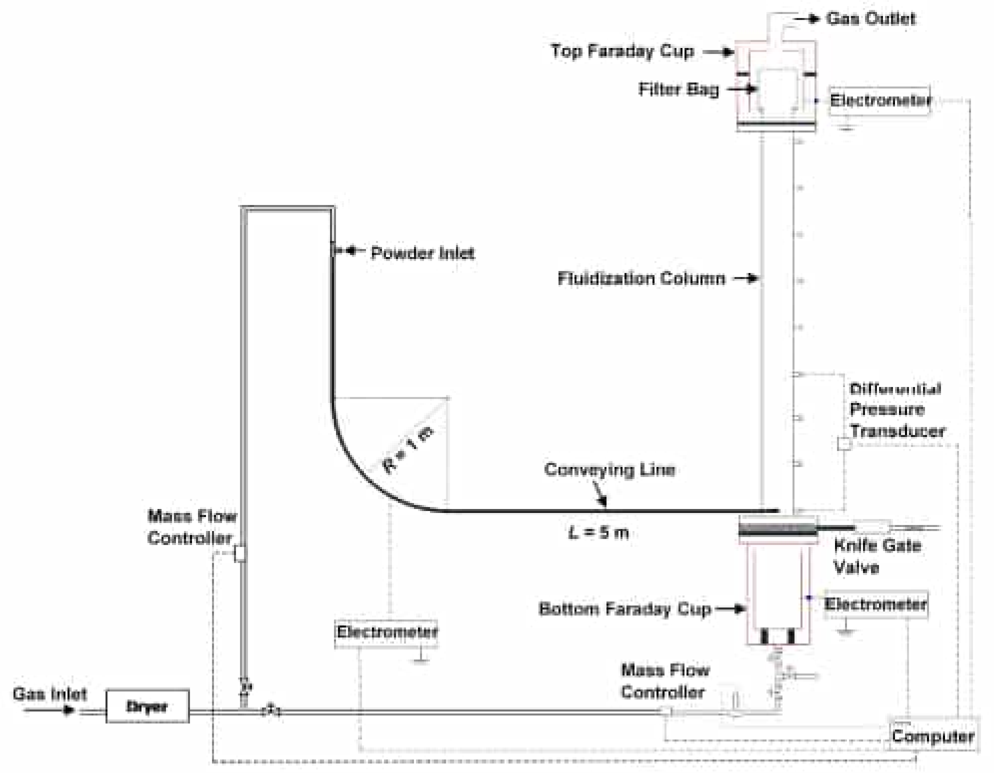

Fig. 1. Schematic diagram of the fluidization system along with the horizontal conveying line directly connected to the fluidized bed.

Details of the fluidization column and its compartments can be found elsewhere (Sowinski et al., 2009). The apparatus consisted of a 0.1 m in diameter stainless steel fluidization column connected to two Faraday cages which allowed the measurement of the charge, mass, and size distribution of the particles in the bulk of the bed (referred to as ñDroppedò), those attached to the column wall (referred to as ñWallò) and those entrained from the column (referred to as ñFinesò). Both Faraday cages were connected to Keithley 6514 digital electrometers. The top Faraday cage housed a filter bag to contain the entrained fines for their mass and charge measurements. A modified knife gate valve acted as the distributor plate (perforated type) and also allowed the collection of the bed particles without any particle handling at the end of the fluidization run for their charge and mass measurement. A stainless steel tube with an inner diameter of 4.57 mm and a length of 5 m with a smooth 1 m radius bend was used as the pneumatic conveying line to replicate the commercial catalyst conveying lines used in PE processes. The exit of the conveying line was situated approximately 0.025 m above the distributor plate. It is important to note that the silica powder's conveying pathway (i.e., addition of bends to the straight tubing) was proven to have no significant affect on their charge magnitude.

The fluidizing particles were PE resin directly received from a commercial plant having a wide size distribution (35 to 1300 micron) with a volume-based mean diameter of 560 micron and a density of 915.6 kg/m^3.The conveyed powder was silica which was the base of the catalyst used for producing the same PE resin and had a volume-based mean diameter of 43 micron. The amount of the injected silica powder was determined based on the catalyst productivity of 10,000 g-PE/g-catalyst. Since the mass of the fluidizing polyethylene in this work was set at 1 kg, the proportional mass of the silica powder was calculated to be 0.1 g.

To determine the influence of the conveyed silica powder on the degree of PE resin wall fouling, it was paramount to know the electrostatic charge of the 0.1 g injected silica powder upon entering the bed. The charge of the powder was found by converting the electrical current signal measured from the conveying tube. As can be seen in Fig. 1 the conveying line was directly connected to a Keithley 6514 digital electrometer to measure the current. The details of such measurement are presented in earlier work (Taghavivand et al., 2019).

During preliminary testing, it became evident that the silica powder fouls inside the conveying tube. However, multiple consecutive injections (up to 6 or 7) showed a reduction on the extent of the powder loss due to fouling. Thus, the experiments were split into two segments. The first segment was to consecutively inject 0.1 g of the silica powder into a filter bag housed inside a Faraday cage (Fig. 2) until the conveying line fouling reached a saturation level. Ten injections were found adequate to achieve approximately 98-100 wt.% recovery of the injected mass. The conveying gas was air with a velocity set at 15 m/s which is a typical velocity used for catalyst injection in PE production. Upon the completion of the 10th injection, the conveying line was disconnected from the Faraday cage and connected to the fluidized bed.

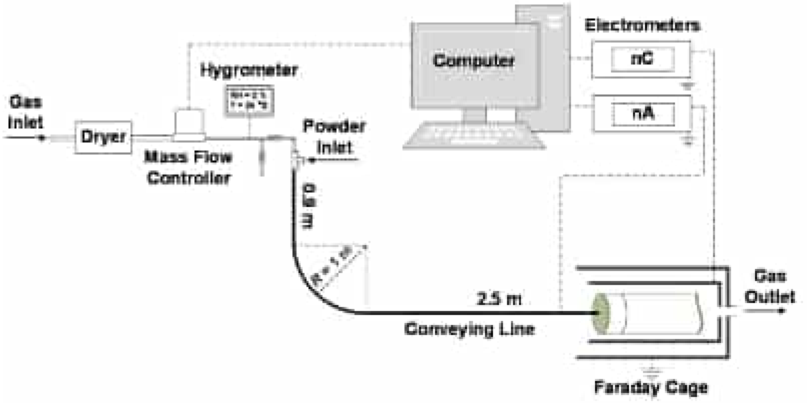

Fig. 2. Schematic diagram of horizontal pneumatic conveying apparatus.

The second segment of the experiment consisted of the 11th injection of the 0.1 g silica powder into the bed of PE, at different time intervals. The conveying gas velocity was set at 15 m/s. The fluidizing gas was supplied from the same source as for the pneumatic conveying line and was dried to approximately 0% relative humidity. The superficial gas velocity was 1.5 times the minimum fluidization velocity to represent the bubbling flow regime and the system was operated at the ambient temperature and atmospheric pressure.

The fluidization runs were carried out for a period of 60 minutes. The depth conveying line exit inside the column varied depending on the injection time. The injections were performed at 0 minutes (prior to fluidization), as well as 15 and 30 minutes into the fluidization. If the injection time was at 0 minutes, the exit of the conveying line was located at the center of the column and after the injection the conveying line was made flush to the column wall and the fluidization was carried out for 60 minutes. In case the injection time was at 15 or 30 minutes, the conveying line was made flush to the column followed by gradually increasing the fluidizing gas and carrying out the fluidization for 15 or 30 minutes. During this period, the conveying gas of 15 m/s passed through the conveying line to prevent any tube blockage. It needs to be mentioned that the conveying gas flow rate was 15% of the fluidizing gas flow rate and therefore had minimal effect on the fluidization velocity of PE particles. After 15 or 30 minutes, the conveying line was gradually pushed towards the center of the bed and both the fluidizing gas and conveying gas were stopped. Then, the injection was performed, the conveying line was retracted, and the fluidization was proceeded for an additional 45 or 30 minutes. All experiments were repeated at least two times to ensure the reproducibility of results. In each trial, the initial charge of the polyethylene particles as well as the silica powder were measured in a bench-scale Faraday cage prior to placing the particles inside the column.

Results and Discussion

In addition to the fluidization runs in the presence of silica powder, runs of 15, 30 and 60 minutes of pure polyethylene were also performed to provide a point of reference when comparing the wall fouling at different conditions. These runs also provided information on the amount of time needed for wall fouling to grow and reach a steady level.

The initial net specific charge (*Q/m*) of polyethylene and silica particles were −0.01 ± 0.03 εC/kg and -16.6 ± 0.2 εC/kg, respectively. The specific charge of the silica powder upon entering the fluidized bed was found to be quite large at −431 ± 153 εC/kg. Upon the completion of the one-hour fluidization period for pure PE, the net charges of the ñFinesò, ñDroppedò and particles covering the top section of the column (ñWall ï Topò) were observed to be negative (*Q/m* of -140.5 ± 47 εC/kg), positive (*Q/m* of 0.33 ± 0.12 εC/kg) and negative (*Q/m* of -491 ± 156 εC/kg), respectively. These sections are illustrated in Fig. 3.

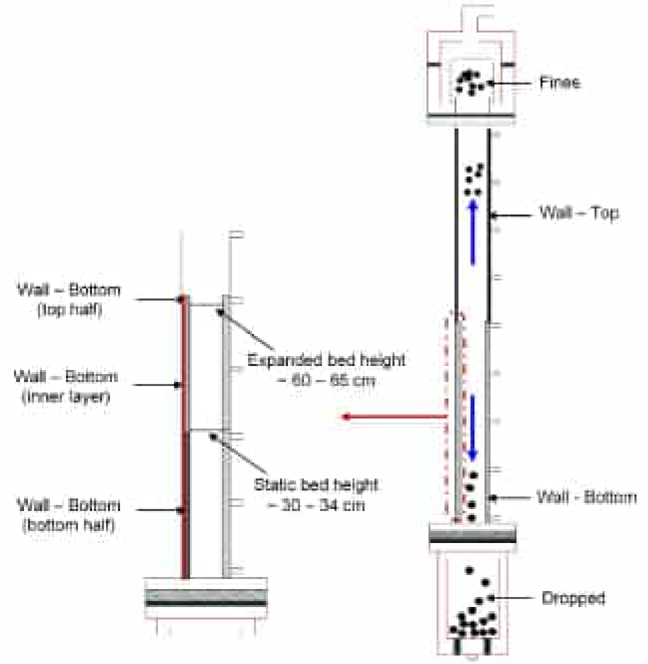

Fig. 3. Location of the particles within the fluidization column.

Compressed air was passed through a narrow long tube which was inserted into the bed to dislodge the particles attached to the column wall and measure their mass and charge. It was found that the ñWall ï Bottomòparticles had different polarities depending on their location. As a result, three sublayers were identified for this layer which are shown in Fig. 3.

The particles covering the top half of this layer which were referred as ñWall ï Bottom (top half)òwere negatively charged (*Q/m* of -35 ± 16 εC/kg). Particles covering the bottom section of the ñWall ï Bottomò, referred as ñWall ï Bottom (bottom half)ò, at times had positive (*Q/m* of 79 ± 49 εC/kg) or negative (*Q/m* of -66 ± 29 εC/kg) charges. The third sublayer belonged to those particles which were attracted to the wall and formed the very first coating layer on the wall. These particles which were referred as ñWall ï Bottom (Inner layer)ò were negatively charged (-461 ± 359 εC/kg). Comparing the effective work function of the PE with the stainless steel, it is clear that PE must gain negative charges when contacting the stainless steel (Song and Mehrani, 2017). Observing a net of positively charged particles in the ñDroppedò region could be due to the contacts between the polyethylene particles and occurrence of the bipolar charging inside the column where smaller particles carry negative charges whereas larger particles which are mostly accumulated at the bottom carry positive charges. Existence of positively charged particles on the wall layer can be related to the attractive electrostatic forces between the negatively charged inner layer and positively charged bulk particles (Song and Mehrani, 2017). As well, the repulsive electrostatic forces between the positively charged bulk particles can promote the migration of PE particles towards the wall.

Fig. 4 presents the total mass of particles collected from the wall region of the bed (i.e., wall fouling) and those entrained at various fluidization times for runs in the absence of silica powder. This figure also provides a comparison on the influence of silica powder presence and its injection time on the mass of Fines and Wall. The red dashed lines represent the average value for 60 minutes fluidization of pure PE.

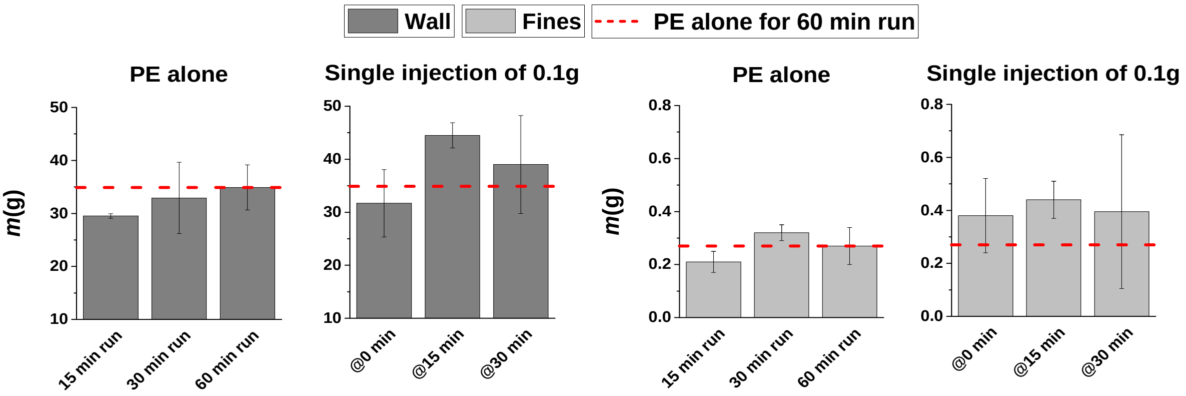

(a) (b)

Fig. 4. Effect of injecting silica powder on the mass of (a) Wall, and (b) Fine particles.

From Fig. 4(a) it is clear that 15 minutes of fluidization was sufficient to form a substantial layer of fouling. It can also be seen in this figure that injecting the silica powder prior to fluidization onset did not statistically affect the wall fouling magnitude, whereas, an increase in the fouling was observed when the silica was injected 15 minutes after the fluidization onset. On average, injection at 30 minutes into the fluidization period showed an increase in the wall fouling mass, but no statistically significant change was observed in the fouled mass on the wall. At the fluidization onset, the pneumatically injected negatively charged silica powder can migrate towards the wall due to the image forces and form a negative layer. This layer in turn, can prevent some of the PE particles from contacting the wall. Additionally, silica powders can coat some of the PE particles in the bulk and lower their positive charge by introducing negative charge. The *Q/m* of the ñDroppedòparticles was 0.29 ± 0.1 εC/kg, which is lower on average compared to that of the pure PE. This in turn results in reducing the magnitude of repulsive forces between the particles of the bulk region. The increase in the fouling magnitude by injecting silica powder at 15or 30 minutes after fluidization onset can again be related to silica powdersôhigh magnitude charge. Even though a portion of the injected silica can coat the PE resin in the bulk and thus decrease the *Q/m* (0.3 ± 0.1 εC/kg), a portion of the negatively charged silica powder can also migrate towards the positively charged PE particles sitting on the wall owing to the attractive electrostatic forces. The negatively charged silica powders on the wall, in turn, can attract more of the positively charged PE particles from the bulk and these migrations could promote the wall fouling. It should be noted that since the smallest PE particle size used was 35 microns, the influence of the Van der Waals force is assumed negligible.

Looking at the mass of entrained particles in Fig. 4(b), it can be seen that on average more particles left the column when silica powder was injected. It is probable that a small portion of the silica powder was entrained along with PE fines. The *Q/m* of the ñFinesòwhen silica powder was injected prior to fluidization as well as 15 minutes or 30 minutes into fluidization period statistically remained the same (-73.8 ± 29.3 εC/kg, -96.8 ± 8.8 εC/kg and -98.1 ± 27.4 εC/kg, respectively).

Conclusion

The influence of the injection of a silica powder (i.e., catalyst base) at different fluidization times on the degree of the PE fluidized bed wall fouling was investigated. Overall, it was found that the wall fouling mass either did not change or increased after injection of silica powder. The increase in the mass wall fouling was attributed to the image forces as well as the electrostatic forces formed between the silica particles and the column wall as well as the polyethylene particles.

Acknowledgement

Financial support from Univation Technologies, LLC (USA) and The Natural Sciences and Engineering Research Council of Canada (NSERC) is acknowledged with gratitude.

References

Cann, K.J., JH Moorhouse, PA Khokhani, TT Tamargo, KR Gross, MG Goode. Chromium-based catalyst compositions for olefin polymerization. US 10266618 B2. 2019.

Hagerty, R.O., ME Muhle, AK Agapiou, C-TI Kuo, MG Goode, FD Hussein, RB Pannell, JF Szul. Method for controlling sheeting in gas phase reactors. US 7985811 B2. 2011.

Hoff, R. Handbook of transition metal polymerization catalysts, Second Edition, John Wiley & Sons, Hoboken, 2018

Klinzing, G.E. A review of pneumatic conveying status, advances and projections. Powder Technol. 2018. 333, 78ï 90

Rao, Y., P Cai, KJ Cann, FD Hussein, WR Mariott, PA Cao. Supported catalyst with improved flowability. US 10280283. 2019.

Song, D., P Mehrani. Mechanism of particle build-up on gas-solid fluidization column wall due to electrostatic charge generation. Powder Technol. 2017. 316, 166ï 170

Sowinski, A., F Salama, P Mehrani. New technique for electrostatic charge measurement in gas-solid fluidized beds. J. Electrostat. 2009. 67, 568ï 573

Taghavivand, M., B Elchamaa, A Sowinski, P Mehrani. Study of electrostatic charging of single particles during pneumatic conveying. Powder Technol. 2019. 355, 242ï 250

SEPARATION OF POLYVINYL CHLORIDE AND SILICA GLASS IN A PULSED FLUIDIZED BED WITH THE AID OF AN ELECTRIC FIELD

Yong Yang*[1,2,*]*, Yusheng Deng*[2,*]*, Yaqun He*[3]*, Xiaotao Bi*[4]*, John R Grace*[4]*,
***Haifeng Wang*[3]**

[1] *Guangzhou Key Laboratory Environmental Catalysis and Pollution Control, Guangdong Key Laboratory of Environmental Catalysis and Health Risk Control, School of Environmental Science and Engineering, Institute of Environmental Health and Pollution Control, Guangdong University of Technology, Guangzhou 510006, China*

[2] *SINOPEC Maoming Petrochemical Co.,Ltd., Guangdong Maoming 525011, China*

[3] *School of Chemical Engineering and Technology, China University of Mining and Technology, Xuzhou, Jiangsu 221116, China*

[4] *Department of Chemical and Biological Engineering, University of British Columbia, Vancouver V6T 1Z3, Canada*

*Email: *Yong Yang*, yangyong65.mmsh@sinopec.com

Yusheng Deng, dengysh.mmsh@sinopec.com

ABSTRACT

The binary mixture of polyvinyl chloride (PVC) and silica glass (SG) was experimentally studied to obtain the optimum operating conditions required to promote triboelectric separation. Results show that the optimum separation result could be reached when the pulsation frequency comes near to the natural frequency of the bed. The pulsed fluidized bed with the assistance of an external electric field has proven to be appropriate for the separation of PVC/SG mixture. The highest segregation index of 41.05 was obtained at average pulse velocity 0.75 U_{mf}, pulsation frequency of 2.0 Hz, and electric field strength of 0.39 kV/cm.

Keywords: triboelectric separation; pulsating fluidized bed; external electric field.

INTRODUCTION

The segregation phenomenon in the gas-solid fluidized bed is of great interest in mineral processing, particularly in dry beneficiation technologies, such as coal and fly ash beneficiation, granular plastic waste separation, etc. In fluidized bed, triboelectrification is inevitable due to the continuous particle-particle, particle-wall, and particle-gas interactions and rotations(Bi 2005). Since the motion of charged particles could be affected by electric forces, the utilization of electrostatics in bed could be effective in the triboelectric separation process(Kiewiet et al. 1978). The separation efficiency depends on the ability to control triboelectrostatic charging(Inculet, Castle, and Brown 1998), which highly relies on the hydrodynamics in the fluidized bed(Zhang et al. 2012). The present study is aimed at enhancing the separation of PVC/SG mixture using a pulsed fluidized bed with the assistance of an external electric field. The effects of pulsation frequency and electric field strength on fluidization hydrodynamics and separation performance were investigated.

EXPERIMENTAL APPARATUS AND PROCEDURE

As shown in Fig.1, the Plexiglas (PMMA) vessel shows a rectangular cross-section of 150 mm×100 mm and a height of 250 mm. The vertical electric field was generated between two parallel perforated aluminum plates, each with the L×W×H dimensions of 180×120×2 mm. The interelectrode distance was fixed at 7 inches (177.8 mm). The upper plate was ground and was used as the negative electrode. The bottom plate was connected to a high voltage DC power supply (Matsusada Precision Inc., Japan), and was used both as the positive plate and the air distributor.

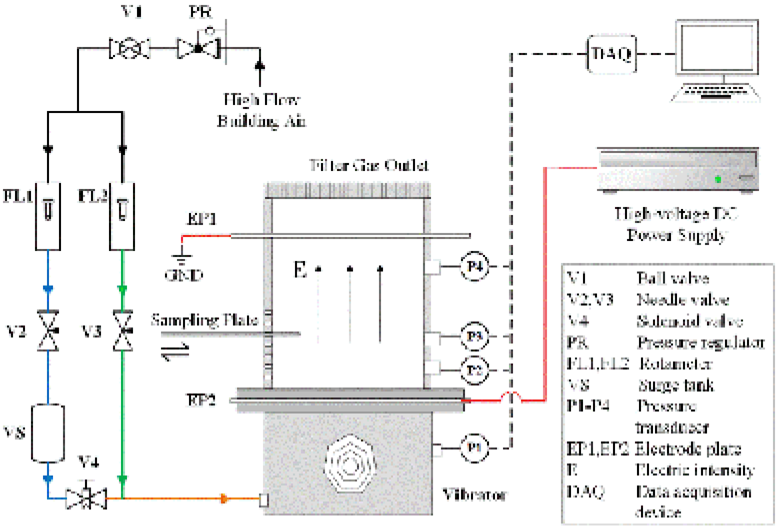

Fig.1. Schematic of the fluidization and tribo-electrostatic separation unit

The binary mixture used in the tests is shown in Tab.1. The separation time is fixed at ten minutes. After separation, the fluidizing air was immediately shut down, bed materials were drawn out layer by layer through an absorbing vacuum. The segregation degree was evaluated by:

$$S = \sqrt{\frac{\sum_1^n (x_i - x_0)^2}{n}} \tag{1}$$

where S is the segregation degree, a larger value of S means a better separation performance; x_i is the weight fraction of one particular component of *i*th sampling layer; x_0 is the initial weight fraction of the particular component; n is the sampling layers (n = 4).

Tab.1. Properties of PVC and SG particles

Material	Size range, mm	Mean size, mm	True density, g/cm^3	Weight, g
PVC	3.0-3.7	3.4	1.4	773.96
SG	1.44-1.77	1.6	2.5	771.32

PRESSURE FLUCTUATIONS AND GAS-SOLID FLOW BEHAVIOR

To recognize the link between the pressure fluctuations and the flow behaviors in the pulsed fluidized bed, time traces of the pressure-drop and video snapshots are presented in this section. Velocities of the rectangular pulse were kept constant in all tests and were high enough to eliminate channeling or defluidization. The pressure-drop profiles for six pulsation frequencies are shown in Fig.2. It can be seen that each pulse includes a distinct “Gas-On” and “Gas-Off” period with a duty cycle of 50%. Referring to the curve in Fig2 (c1), a sharp dominant peak (point B) occurs shortly as the solenoid valve was switched open (A-B). This is due to a relatively high-pressure build-up in the surge tank during the “Gas-off” period. The instant gas enters the bed at the highest velocity when each pulsation cycle begins, which fluidizes the bed immediately. According to the screenshots shown in Fig.3 (d1-d2), a homogeneous pattern was just formed at point B. Particles' motion was denoted by red arrows in the pictures. Soon particles underwent the upcasting motion with high amplitudes of bed expansion. As seen in Fig.3 (d3-d5), lots of by-passing of gas went through the bed in form of slug chains, resulting in the quick release of gas pressure in Fig.2 (c1): B-C. As the slug chains passed, particles started to descend and accumulate at the lower section of the bed, denoted by the red frame in Fig.3 (d5-d6), which induced the increase of the bed pressure drop (Fig.2 (c1): C-D). Point D is the time when particles in the top section fall back to the bed surface. After that, the bed would secondly expend slightly to take up a loose-packed arrangement (Fig.3 (d7)) and the pressure drop gradually rose to the secondary peak (Fig.2 (c1): E). Then, as illustrated in Fig.3 (d7-d8), a stable fluidizing state was formed corresponding to a nearly constant pressure drop (Fig.2 (c1): E-F), which is consistent with the pressure characteristics of a normal fluidized bed. At point F, the solenoid valve was turned off and the bed remained stationary during the "Gas-off" period as shown in Fig.2 (c1): F-H and Fig.3 (d9).

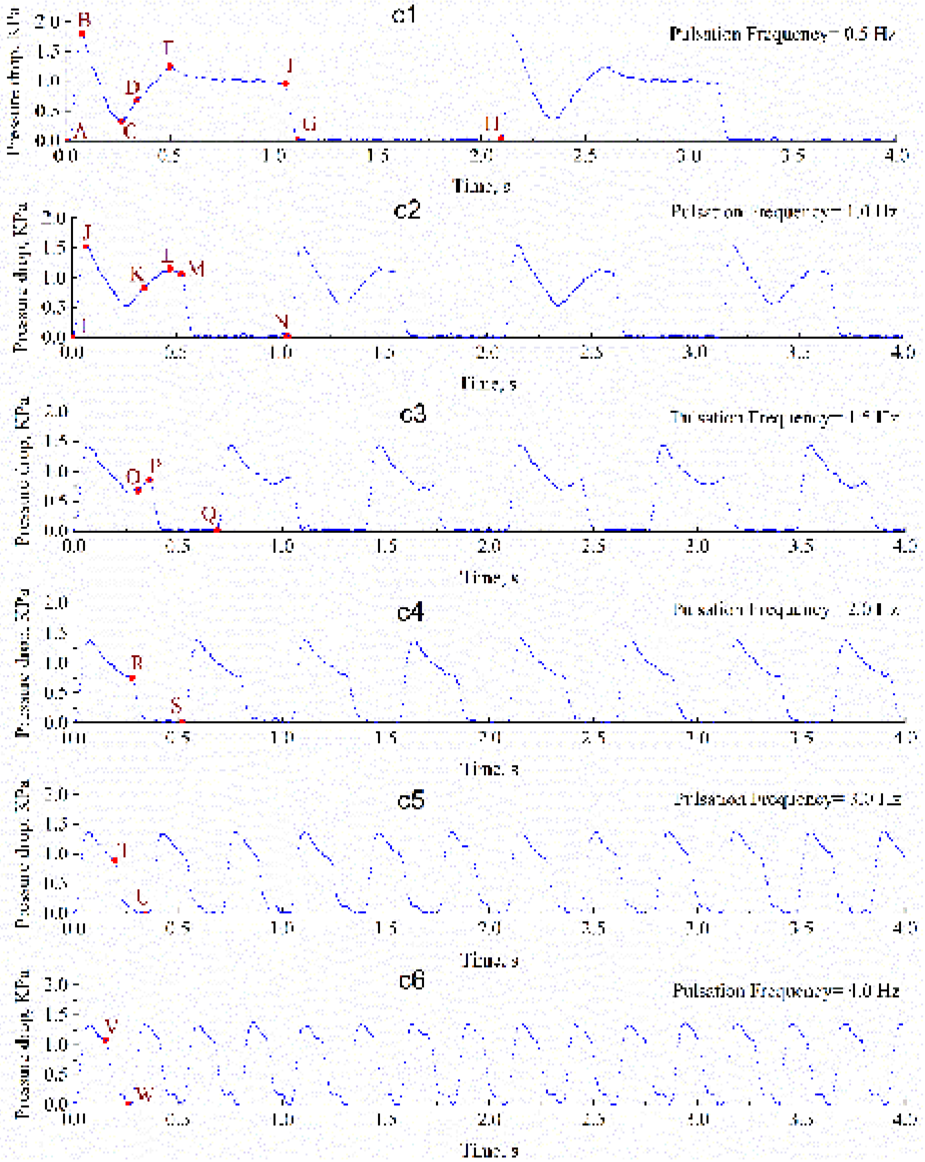

Fig.2. Pressure fluctuations plotted against time for various pulsation frequencies.

Similar pressure fluctuations and flow patterns can be observed at higher frequencies. It should be pointed that at higher pulsation frequency, the intensity of the pulsation became weaker due to the diminished pressure build-up during the shortened “Gas-Off” period. However, special attention should be paid to the pulsation frequency of 2.0 Hz and 3.0 Hz as their proximity to the natural frequency f_n=2.6 Hz of the bed calculated using the equation derived by Verloop and Heertjes(Verloop and Heertjes 1974):

$$f_n = \frac{1}{2\pi}\sqrt{\frac{g\cdot(2-\varepsilon)}{H_{mf}\cdot\varepsilon}} \tag{2}$$

where f_n (Hz) is the natural frequency, g (m/s^2) is gravity, ε (%) is the bed voidage, and H_{mf} (m) is the initial bed height at minimum fluidization. Increasing the pulsation frequency from 2.0 Hz to 3.0 Hz, the “Gas-Off” stationary state gradually began to disappear as the pulsation frequency came to and exceeded the natural frequency of the system, bed materials were lifted again before particles in the higher section could descend to the bed surface. This agrees with the disappearance of zero pressure drop values shown in Fig.2 (c5). At 4.0 Hz, the flow behavior was similar to that at 3.0 Hz, except for the less bed expansion. Unfortunately, owing to the adhesion of particles on the observation wall, the hydrodynamics of the pulsed fluidized bed under the external electrostatic field could not be observed and discussed here.

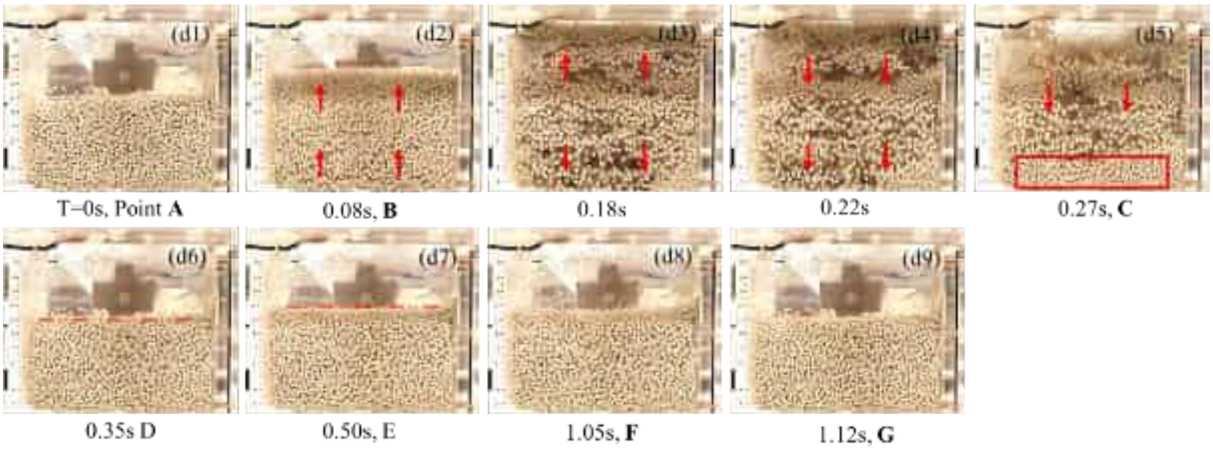

Fig.3. Synchronized video snapshots for pulsation frequency of 0.5 Hz.

CHARACTERISTICS OF SEGREGATION INDEX

In general,the pulsed fluidized bed could be operated at an average gas velocity lower than the minimum fluidization velocity(Jia et al. 2015). Fig.4(a) depicts the inverted “V” curves of the segregation index as a function of pulsation frequency for different average gas velocities. At the lower pulse, the prolonged gas storage induced higher volume and velocity of air entering the bed and caused greater bed expansion and turbulence, hence promoting the particles to mix. By increasing the pulsation frequency, the intensity of the pulse flow was reduced. This reduction also caused less expansion amplitude and reduced turbulent effect(Aziz et al. 2019). The optimum segregation result could be reached as the pulsation frequency came around the natural frequency of the bed. This agrees with the result in the literature (Mukherjee et al. 2006). Once the frequency increased over the certain value, the damped pulse flow was insufficient to lift the whole bed and particle motion was less vigorous, thereby reducing the segregation performance. The optimum pulsation frequency for particle segregation was 2.0 Hz for the average gas velocity of 0.75 U_{mf}, and the segregation index was 3.51. Fig.4(b) shows the triboelectric separation results carried out on the average pulse velocity of 0.75 U_{mf} and pulsation frequency of 2.0 Hz, presenting a significant improvement in the separation performance. The segregation index undergoes a sharp increase and reaches the highest value of 41.05 when the electric field strength is 0.39 kV/cm. The electric field strength cannot be set higher, otherwise, it will cause air breakdown sparks.

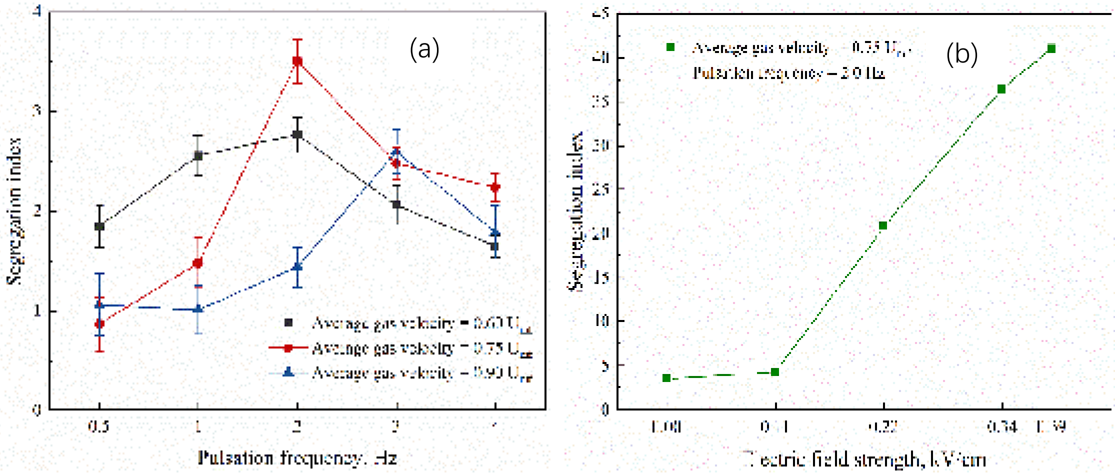

Fig.4. Segregation indexes of the pulsating fluidized bed, (a)without electric field, (b) with electric field.

SEPARATION MECHANISM

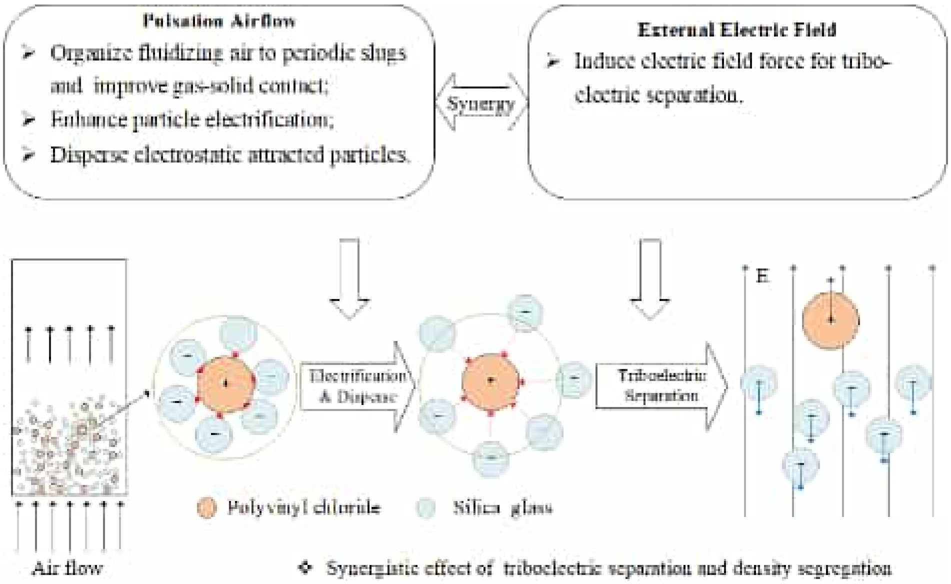

Fig.5. Schematic of mechanism of triboelectric separation in pulsed fluidized bed.

In the gas-solid fluidization system, PVC/SG mixture tends to mix easily as their small physical disparity in particle size/density. The generation of particle electrification will cause particle-particle electrostatic attraction and particle movement is restricted, thereby reducing the segregation tendency. Increasing the fluidizing air velocity is a feasible way both to disperse the heteroaggregation of oppositely charged particles and to improve the degree of particle electrification. Pulsating airflow has proven to be effective at organizing fluidizing air into periodic slugs which improving gas-solid and solid-solid contact. Especially, when pulsation frequency comes to the natural frequency of the bed, the formation and growth of slug chains become smaller and the stationary contact state begins to disappear, which are favorable for density segregation. Fig.5 illustrates the separation mechanism of triboelectric separation in the pulsation fluidized bed. Under the synergy of pulsation airflow and external electric field, a significant improvement in the separation of PVC/SG mixture could be achieved through the combined effect of density segregation and triboelectric separation.

CONCLUSION

(1) Pulsating air has proven to be effective in promoting gas distribution and organizing the fluidizing gas into periodic slugs, which increases particle motion and electrification. The optimum separation result could be reached when the pulsation frequency comes near to the natural frequency of the bed.

(2) Effective separation of PVC/SG mixture in the pulsed fluidized bed with the assistance of the external electric field can be achieved under the synergistic effect of triboelectric separation and density segregation. The highest segregation index of 41.05 was obtained at average pulse velocity 0.75 U_{mf}, pulsation frequency 2.0 Hz, and electric field strength 0.39 kV/cm.

ACKNOWLEDGEMENTS

This work was supported by the National Natural Science Foundation of China (No. 51674257).

REFERENCES

Aziz, M. A.A., K. Md Isa, N. J. Miles, and R. A. Rashid. 2019. “Pneumatic Jig: Effect of Airflow, Time and Pulse Rates on Solid Particle Separation.” *International Journal of Environmental Science and Technology* 16 (1): 11–22.

Bi, Hsiaotao T. 2005. “Electrostatic Phenomena in Gas-Solids Fluidized Beds.” *China Particuology* 3 (6): 395–99.

Inculet, I. I., G. S.P. Castle, and J. D. Brown. 1998. “Electrostatic Separation of Plastics for Recycling.” *Particulate Science and Technology* 16 (1): 91–100.

Jia, Dening, Océane Cathary, Jianghong Peng, Xiaotao Bi, C. Jim Lim, Shahab Sokhansanj, Yuping Liu, Ruixu Wang, and Atsushi Tsutsumi. 2015. “Fluidization and Drying of Biomass Particles in a Vibrating Fluidized Bed with Pulsed Gas Flow.” *Fuel Processing Technology* 138: 471–82.

Kiewiet, Charel W, Maurice A Bergougnou, James D Brown, and Ion I Inculet. 1978. “Electrostatic Separation of Fine Particles in Vibrated Fluidized Beds.” *IEEE Transactions on Industry Applications* IA-14 (6): 526–30.

Matsusaka, S., H. Maruyama, T. Matsuyama, and M. Ghadiri. 2010. “Triboelectric Charging of Powders: A Review.” *Chemical Engineering Science* 65 (22): 5781–5807.

Mukherjee, A. K., D. Bhattacharjee, and B. K. Mishra. 2006. “Role of Water Velocity for Efficient Jigging of Iron Ore.” *Minerals Engineering* 19 (9): 952–59.

Verloop, J., and P. M. Heertjes. 1974. “Periodic Pressure Fluctuations in Fluidized Beds.” *Chemical Engineering Science* 29 (4): 1035–42.

Zhang, Lifeng, Jiangtian Hou, Xiaotao T. Bi, John R. Grace, Travis Janke, and Claudio Arato. 2012. “Fluidization Characteristics and Charging Behavior of Fly Ash in a Vibro-Fluidized Bed.” *Powder Technology* 215–216: 235–41.

EFFECT OF TEMPERATURE ON POLYETHYLENE ELECTROSTATIC CHARGING IN AN ATMOSPHERIC GAS-SOLID FLUIDIZED BED

Mohsen Isaac Nimvari, Andrew Sowinski, Poupak Mehrani*

Department of Chemical and Biological Engineering, University of Ottawa, 161 Louis-Pasteur, K1N 6N5 Ottawa, Ontario, Canada

**Email: poupak.mehrani@uottawa.ca*

Abstract

This study investigated the influence of operating temperature on the degree of electrostatic charge generation and particles reactor wall fouling in a pilot plant atmospheric gas-solid fluidized bed. The fluidized bed was a stainless-steel column with an inner diameter of 0.15 m and a total height of 5 m (2.5 m fluidization section) containing a perforated distributor plate. Polyethylene (PE) resin received from commercial reactors was fluidized for 60 min at 23-53ºC. Two Faraday cages at top and bottom of the fluidization column were used to measure the charge of entrained particles as well as those in the bed, and those fouled on the column wall, respectively. The amount of wall fouling and net specific charge of the particles were found to be directly proportional to the operation temperature such that at elevated temperatures, the amount of fouling and net specific charge of fluidizing particles in the bulk of the bed were reduced.

Introduction

One of the problems in commercial polyethylene fluidized bed reactors is the adhesion of particles (PE, and/or catalysts) to the column wall as the result of particles triboelectrification. In such reactors, the numerous contacts between the fluidizing particles build up electrostatic charge on the surface of catalyst and polyethylene particles making them to migrate and adhere to the reactor wall. Melting of the fouled particles due to the inadequate removal of the heat of reaction then results in formation of ñ*wall sheets*ò in various locations of the reactor (Hendrickson, 2006). Wall sheeting could cause a reduction in fluidization quality and in some cases reactor shutdown for cleaning. Studies have been performed to investigate different parameters that could affect electrostatic charge generation in polyethylene fluidization system such as operating pressure, fluidizing gas velocity, humidity, size/type of the fluidized particles and column material (Alsmari et al., 2015; Guardiola et al.,1996; Mehrani et al., 2017; Moughrabiah et al., 2009; Song and Mehrani, 2017a, 2017b; Song et. al., 2016; Sowinski et al., 2012). Commercial polyethylene reactors are typically operated at 75-110ºC (Goode et al., 1989); however, the influence of the operating temperature on the degree of bed electrification has received minimal attention. Only two temperature effect studies have been found in open literature (Alsmari et al., 2015; Moughrabiah et al., 2009). Moughrabiah et al. (2009) used collision ball probes to measure the cumulative charge of 600 µm linear low-density polyethylene (LLDPE) particles at different axial location inside a stainless-steel fluidization column. At the operating condition of 60°C and 379 kPa, their results showed that the degree of charge generation for LLDPE particles was significantly less than that at 20ºC. The same team in their second work (Alsmari et al., 2015), evaluated the electrostatic charging of a mixture of fine (25-50 µm) and large (425-600 µm) glass beads at 414 kPa while varying the temperatures from 20°C to 75°C. They showed that by increasing temperature, electrostatic charge measured at different locations of the bed decreased, and for temperatures above 70°C, a polarity change was observed. In the same study, the authors also observed that the charge of entrained glass beads declined as the temperature increased while the particles mass flux did not have a noticeable change.

Overall, there is limited knowledge available about the effect of temperature on solids charging behaviour especially in relation to fluidization systems. In works by Moughrabiah et al. (2009) and Alsmari et al. (2015), collision ball probes were used for particles electrostatic charge measurement which not only provide a very local measurement but also do not provide any information concerning the fluid bed wall fouling generated due to the charged fluidizing particles. Hence, in this study we aimed at investigating the effect of temperature on the degree of electrostatic charge build-up by measuring the mass and the net charge of particles fouled on the fluidization column, as well as the net specific charge of the particles in the bulk of the bed and those entrained. Here, we are presenting preliminary results of the study at atmospheric operating pressure. Our future work will include the same measurement at elevated pressures of 2600 kPa.

Materials and Methods

In this work, a pilot plant fluidization system was utilized. The detailed description of the system is presented elsewhere (Song and Mehrani, 2017). The fluidized bed was a stainless-steel column with an inner diameter of 0.15 m and fluidization length 2.5 m. The apparatus was modified for this work to enable heating of the fluidizing gas to temperatures up to 65ºC (Fig. 1a). To achieve this temperature, several band heaters were wrapped around the inlet pipes to the fluidization column and around the fluidization column up to the expanded bed height. To monitor the operating temperature during each run, two thermocouples were used, one located below distributor plate (T_1) and one at 0.60 m above the distributor plate (T_2). Building air at a relative humidity (RH) of 8% was used as fluidizing gas while its flow rate was measured by an orifice place meter. Minimum fluidization velocity was determined experimentally by measuring the pressure drop across the bed at various superficial gas velocities. The fluidization was conducted at 1.5 times the minimum fluidization velocity (i.e., bubbling flow regime) and each condition was carried out 2-4 times. To determine the particles electrostatic charge, two Faraday cages were used, located at the top and bottom of the fluidization column, and both directly connected to digital *Kiethley Model 6514* electrometers. The top Faraday cage measured the charge of the entrained particles (referred to as “*Fines*”) which were captured by a filter bag at its center. After a fluidization period of 60 minutes, the filter bag was removed to measure mass of the *Fines*. To determine the charge and mass of the fluidizing particles (referred to as “*Bulk*”), the distributor plate was opened allowing the particles to drop into the bottom Faraday cage. At this point, the inner surface of the column was inspected for any particle accumulation on the wall and images were taken from the fouled layer. Then, a ¼ in. tube was inserted into the column from the top and a very small air flow was used to gradually dislodge the particles accumulated on wall (referred to as “*Fouling*”) to the bottom Faraday cage to measure their mass and net charge.

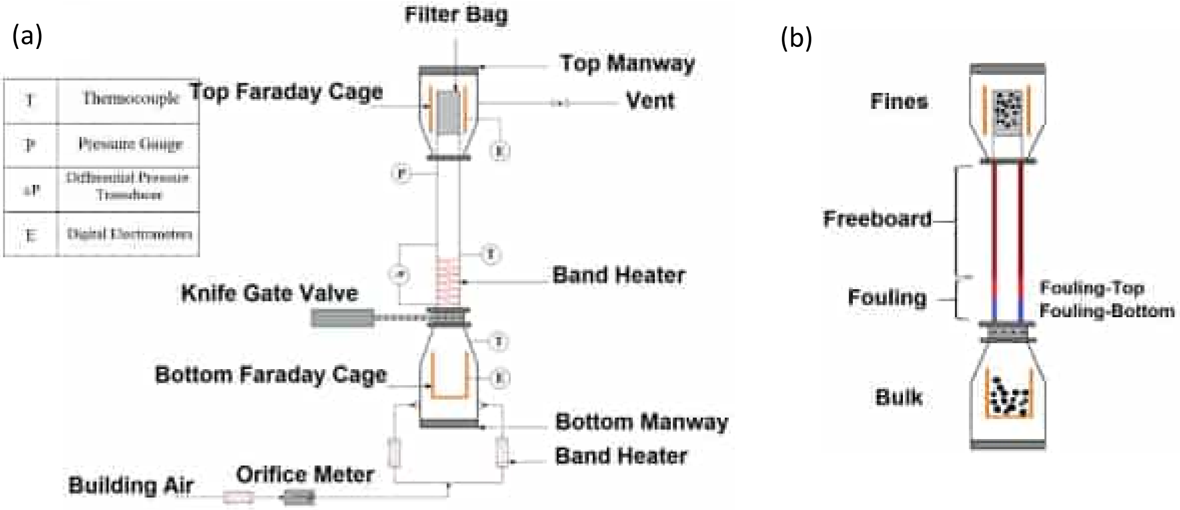

Fig. 1. a) Schematic of the pilot-scale fluidization system, b) A schematic illustration of regions of particle accumulation and collection.

At the start of each run, all heaters were turned on to warm up the system for 30 minutes. Then, particles which were kept in oven overnight were poured into the column to a static bed height of approximately 30 cm. This was followed by mounting the top Faraday cage and closing the top manway. The fluidization period was then initiated by increasing the fluidizing gas velocity to 1.5 times the minimum fluidization velocity. Fig. 2. shows an example of temperature profile measured by thermocouples T_1 and T_2. The operating temperature in fluidizing section (T_{Opr}) was considered as the average of temperatures read by these two thermocouples from 5 min into the fluidization and the end of fluidization.

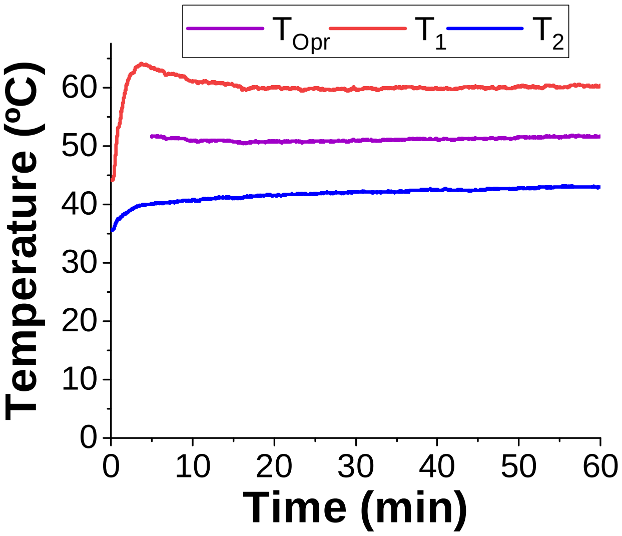

Fig. 2. An example of temperature-profile of thermocouples before (T_1) and after (T_2) distributor plate and the average operating temperature of fluidization region (T_{Opr}).

In this work, Linear Low-Density Polyethylene (LLDPE) resin received from commercial reactors, was fluidized. The properties of the particles and minimum fluidization velocity are summarized in Table 1.

Table 1. Properties of the fluidizing PE particles

Property	**Value**
Density (kg/m^3)	917
Particle Size Distribution (µm)	20-2000
Mean Particle Diameter (µm)	820
Minimum Fluidization Velocity (m/s)	0.15

Results and Discussion

For all the operating temperatures tested, accumulation of polyethylene resin on the fluidization column wall was observed. Fig. 3 shows the results for the total mass of the *Fouling* and its distribution on the column wall at various temperatures. Results illustrate that higher temperatures resulted in lower amount of particles adhesion on the column wall which was mostly due to the change in mass of *Fouling-Bottom* region where the most particle accumulation took place. A significant finding was obtained in this study in which a similar trend was observed for the charge-to-mass ratio (Q/m) of the *Bulk* of the particles as shown in Fig. 4 indicating a clear relationship between the degree of particles net specific charge in the bulk of the bed and their tendency to migrate and accumulate on the column wall.

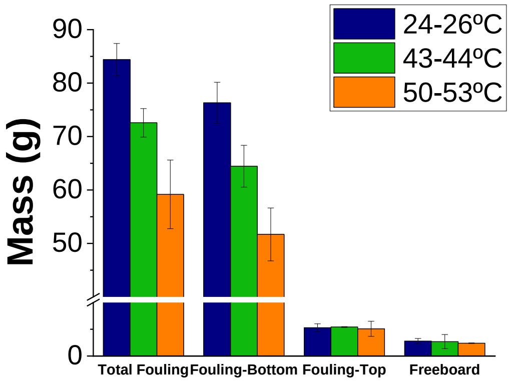

Fig. 3. Total fouling and its distribution in the column at various operating temperatures.

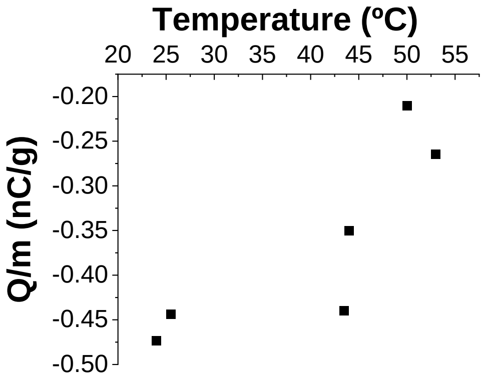

Fig. 4. Charge-to-mass ratio of *Bulk* particles at various operating temperatures.

Table 2 shows the mean particle diameter (d_{50}) of fouled particles in different region of the bed indicating that particles smaller than 400 micron had higher net specific charge and thus migrated to the wall.

Table 2. Mean particle size of particles at different regions of the fluidized bed

Property	**Mean particle size ((µ)**
Bulk	600
Fouling-Bottom	350
Fouling-Top	400
Freeboard	400
Fines	80

The mechanism for formation of wall fouling can be explained by the attractive and repulsive forces caused by image and Coulomb forces between the electrostatically charge fluidizing particles and the metallic column wall (Song and Mehrani, 2017). Since the work function of the stainless-steel column is less than the PE particles, therefore, PE particles gained a negative polarity in contact with the wall. This net negative polarity in the fluidizing particles in turn resulted in accumulation of these particles on the wall which is evident from results in Fig. 5. Consequently, the Coulomb forces originated by the first layer on the wall, attract or repel the particles in the *Bulk* with an opposite or same polarity, respectively. Thus, promoting or mitigating the extent of particles fouling on the column wall. Results also showed that the polarity of *Fouling-Top* and *Freeboard* regions was positive. Bipolar charging of PE particles in the *Bulk* due to particle-particle collisions was inevitable. Therefore, it can be interpreted that the repulsive force, resulted from positively charged PE particles in the *Bulk* and the positive image charge on the wall, was greater than the attractive Coulomb force resulted from negatively charged *Fouling-Bottom* and positively charged PE particles in the *Bulk*.

Forasmuch as the net specific charge of the *Bulk* particles declined at higher temperatures, it can be concluded that less image force was induced on the wall, and this in turn caused fewer fouled particles. Fig. 5 also illustrates that the Q/m of the *Fouling* at different regions on the wall was not affected by temperature. It is visible from the results that temperature affected the mass of fouling by changing the net specific charge of *Bulk* particles.

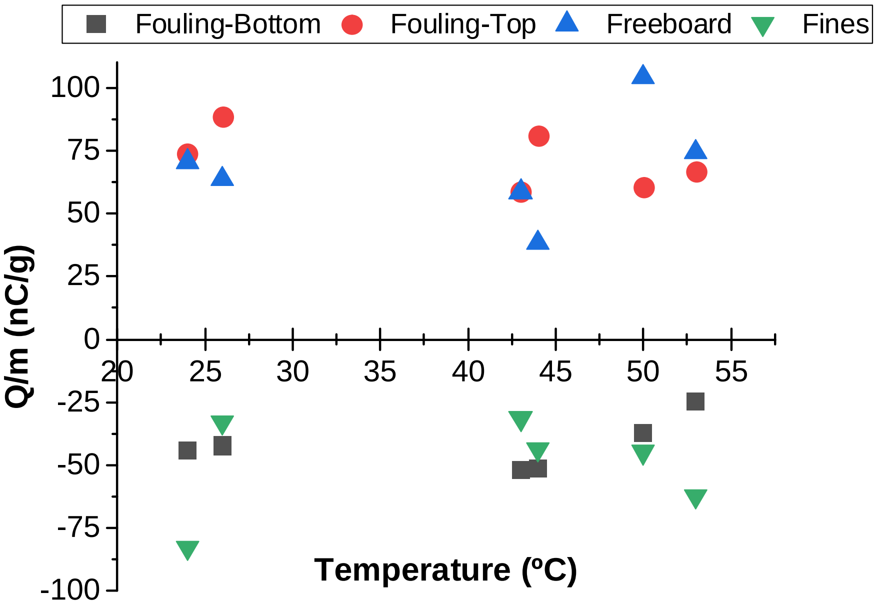

Fig. 5. Charge-to-mass ratio of particles in various regions of the bed at different operating temperatures.

One of the parameters that can explain the temperature influence is the change in volume resistivity (i.e., electrical property) of PE particles. Dennison and Brunson (2008) measured volume resistivity of LDPE in a temperature range of -40ºC to 50ºC and found that volume resistivity declined at greater temperatures. Smaller volume resistivity or, in other words, higher conductivity could result in a faster charge dissipation, and consequently decrease electrostatic charge of the surface of particles. Bench-scale contact electrification (a metal ball with different insulators) experiments conducted at temperatures between 10-30°C also revealed that at higher temperatures, less electrostatic charge generated (Greason, 2000). Another mechanism proposed by Lin et al. (2019) while conducting bench scale AFM testing to explain this effect is the excitation of electrons at higher temperatures, facilitating the transfer of electrons from one surface to another. In future studies, we plan to further investigate the reasons behind the influence of operating temperature on the particle properties including volume resistivity.

Conclusion

Preliminary experimental results pertaining to the influence of operating temperature on the degree of contact electrification in a pilot-scale fluidized bed was presented for LLDPE particles. It was found that temperature affects the electrostatic charge generation in the fluidized bed and consequently influences the mass of fouled particles on the column wall. Results showed that at elevated temperatures, net specific charge of fluidizing particles in the bulk of the bed dropped which is a clear indication of effect of temperature on particles degree of contact electrification. This in turn reduced the extent of particles migration and fouling on the column wall. Our future work will focus on determining the potential reasons behind the decline of the particles net specific charge at elevated temperatures as well as operations at elevated pressures of 2500 kPa (similar to commercial gas-phase PE processes)

Acknowledgement

The authors are grateful for the financial support from Univation Technologies, LLC (USA) and The Natural Sciences and Engineering Research Council of Canada (NSERC).

References

Alsmari, Turki A., JR Grace, and XT Bi. 2015. ñEffects of Superficial Gas Velocity and Temperature on Entrainment and Electrostatics in Gas-Solid Fluidized Beds.ò Chemical Engineering Science 123: 49ï 56.

Dennison, John R., and J Brunson. 2008. ñTemperature and Electric Field Dependence of Conduction in Low-Density Polyethylene.ò IEEE Transactions on Plasma Science 36(5): 2246ï 52.

Fotovat, Farzam, TA Alsmari, JR Grace, and XT Bi. 2017. ñThe Relationship between Fluidized Bed Electrostatics and Entrainment.ò Powder Technology 316: 157ï 65.

Goode, Mark G., DM Hasenberg, TJ Mcneil, and TE Spriggs. 1987. ñMethod for Reducing Sheeting During Polymerization of Alpha-Olefns, United Stated Patent, No. 4803251.ò

Greason, William D. 2000. ñInvestigation of a Test Methodology for Triboelectrification.ò Journal of Electrostatics 49(3ï 4): 245ï 56.

Guardiola, Jesús, V Rojo, and G Ramos. 1996. ñInfluence of Particle Size, Fluidization Velocity and Relative Humidity on Fluidized Bed Electrostatics.ò Journal of Electrostatics 37(1ï 2): 1ï 20.

Hendrickson, Gregory. 2006. ñElectrostatics and Gas Phase Fluidized Bed Polymerization Reactor Wall Sheeting.ò Chemical Engineering Science 61(4): 1041ï 64.

Lin, Shiquan, L Xu, W Tang, XG Chen, and ZL Wang. 2019. ñElectron Transfer in Nano-Scale Contact Electrification: Atmosphere Effect on the Surface States of Dielectrics.ò Nano Energy 65: 103956.

Moughrabiah, Wajeeh O., JR Grace, and XT Bi. 2009. ñEffects of Pressure, Temperature, and Gas Velocity on Electrostatics in Gas-Solid Fluidized Beds.ò Ind. Eng. Chem. Res. 45: 320ï 25.

Moughrabiah, Wajeeh O., JR Grace, and XT Bi. 2012. ñElectrostatics in Gas-Solid Fluidized Beds for Different Particle Properties.ò Chemical Engineering Science 75: 198ï 208.

Song, Di, and P. Mehrani. 2017a. ñComparison of Electrostatic Charge Generation in Gas-Solid Fluidized Beds in Turbulent versus Pre-Turbulent Flow Regime.ò Powder Technology 319: 426ï 33.

Song, Di, and P. Mehrani. 2017b. ñMechanism of Particle Build-up on Gas-Solid Fluidization Column Wall Due to Electrostatic Charge Generation.ò Powder Technology 316: 166ï 70.

Song, Di, F Salama, J Matta, and P Mehrani. 2016. ñImplementation of Faraday Cup Electrostatic Charge Measurement Technique in High-Pressure Gas-Solid Fluidized Beds at Pilot-Scale.ò Powder Technology 290: 21ï 26.

Sowinski, Andrew, A Mayne, and P Mehrani. 2012. ñEffect of Fluidizing Particle Size on Electrostatic Charge Generation and Reactor Wall Fouling in Gas-Solid Fluidized Beds.ò Chemical Engineering Science 71: 552ï 63.

FLUIDIZED BED CALCINATION OF MAGNESITE AND ITS CHEMICAL AND MORPHOLOGICAL CHANGES

Zhennan Han[1*], Cong Sun [1], Wenqian Hao [1], Xuejing Liu[1], Junrong Yue[2], Guangwen Xu[1,2*]

[1] Institute of Industrial Chemistry and Energy Technology, Shenyang University of Chemical Technology, Shenyang 110142, Liaoning, China
[2] State Key Laboratory of Multi-Phase Complex Systems, Institute of Process Engineering, Chinese Academy of Sciences, Beijing 100190, China

*Email: hanzhennan1989@163.com; *gwxu @ipe.ac.cn*

Abstract

In this study, the reaction kinetic of magnesite calcination in air atmospheres was measured in micro fluidized bed reaction analyzer (MFBRA) and TGA. The complete decomposition time of magnesite in TGA is above 4 min at heating rate of 40 °C /min, but it is just a few seconds (3-5 s) in MFBRA above 750 °C. The activation energy measured in MFBRA and TGA are 125 kJ/mol and 236 kJ/mol respectively, showing a good suitability of MFBRA for rapid reaction in fluidized bed at a specific temperature. Besides, a pilot-scale plant with a capacity of 1 kg/h was established to analysis the effect of temperature, particle size and calcination times on the characteristic of magnesite calcination in transport bed. For powder magnesite with particle sizes of 0.05-0.15 mm, it just needs 1.5-2.3 s to complete the calcination reaction as temperature is above 800 °C. However, with the calcination times exceeding 4 times or residence time exceeding 3 seconds, the recrystallization or sintering will lead to a large grain size of MgO crystal and a dense particle structure with a smaller surface area and a low reactivity.

Introduction

Magnesite (mainly composed of magnesium carbonate, $MgCO_3$) is rich in resources in China, accounting for about 25% of the world's magnesite reserves. It is a main raw material in magnesium and refractory industry and widely used for production of building materials, chemical, paper, aerospace, automobile, and environmental protection (Zhao, 2007; Demir, 2008). Generally, magnesite calcination for producing magnesium oxide is the initial step for its utilization. The reaction equation of magnesite calcination reaction is listed as follow:

$$\mathrm{MgCO_3} \overset{\Delta}{\rightarrow} \mathrm{MGO} + \mathrm{CO_2} \qquad \Delta\mathrm{H} = 100.59\ \mathrm{kJ/mol}$$

According to the calcination temperature, the products can be divided into light burned magnesium oxide (calcined at 650-1100 °C) and dead burned magnesium oxide (calcined at 1200-1400 °C). The light burned MgO with a better reactivity and large specific surface area is widely used in production of chemical materials, adsorbent, catalyst and magnesium cement (Yang, 2018; Creamer, 2018; Stefanidis, 2016). However, there is a remarkably large difference in the physiochemical property of MgO produced at different calcination conditions. Zhu (??) studied the morphological changes of calcined magnesite and found that the size of MgO grain continuously increases with calcination temperature. Industrial magnesium oxide is typically produced by using reflective kiln or shaft kiln. In order to promise a good breathability and a small pressure drop in particle bed, the block magnesite with particle size of 30-50 mm is adopted as material, thus leading to a long calcination time (up to 3-5 hours), low product activity, poor material adaptability, high energy consumption and so on.

Recently, a novel process named transport bed flash calcination (TBFC) with powder magnesite as material was developed by Shenyang University of Chemical Technology (SYUCT) to solve those problems existed in traditional technology. And basic kinetics data of magnesite thermal decomposition is significance and necessary for the design of this novel reactor. In this study, a micro fluidized bed reaction analyzer (MFBRA) and a pilot-scale transport bed calcinator were used to investigate the characteristic of magnesite calcination in fluidized bed as well as morphological and physiochemical changes of calcined magnesite.

Method

1. Reaction kinetic analysis

The kinetic of magnesite calcination was analyzed by using MFBRA and TG (Thermal gravity). TG analysis of magnesite decomposition was conducted at different heating rates (10-40 °C/min), and Flynn-Wall-Ozawa and Coats-redfern methods (Bagchi, 1981) was used to calculate the kinetic data measured. The schematic diagram of the MFBRA is shown in **Figure 1**. This system consists of electric heating furnace, a quartz reactor with a diameter of 20 mm, mass spectrometry (Ametek Dycor LC-D 100) for analyzing the concentration of CO_2 in gas product and the online feeding device. Quartz sand of 100−150 μm (about 3 g) was used as the fluidization medium, and the fluidized gas is air with a flow rate of 400 ml/min. After the desired temperature and stable fluidization of quartz sand was reached by air, about 20 mg of magnesite reactant was instantaneously injected into the reaction zone of the MFB reactor to initiate decomposition reaction. Based on the change in concentration of CO_2, the kinetic data was calculated by the isothermal kinetic equation (Yu, 2010).

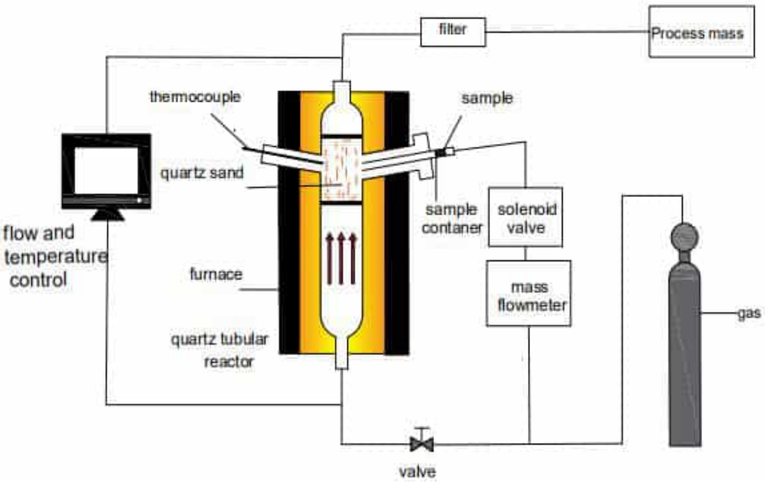

Fig. 1. Schematic diagram of the micro fluidized bed reaction analyzer (MFBRA).

2. Magnesite calcination in transport bed

Figure 2 shows the flowsheet of the pilot-scale plant with a height of 10 m and a capacity of 1 kg/h magnesite. This plant is consisted of gas combustor, transport bed calcinator, product collector (cyclone), bag filer and induced draft fan.

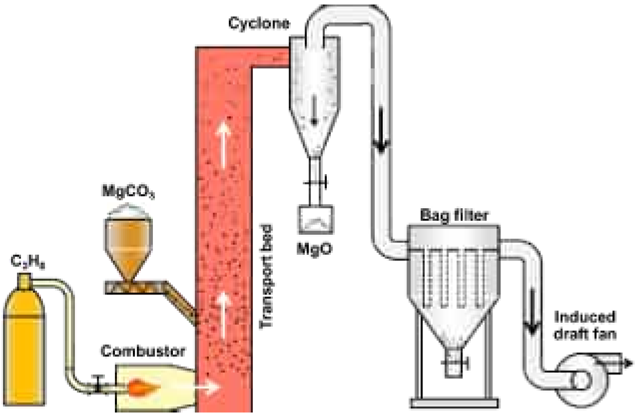

Fig. 2. Pilot-scale plant of transport bed calcinator

During test, C_3H_8 is adopted as the fuel. The hot-temperature flue gas generated from combustion can heat powder magnesite rapidly and then carry the calcined magnesite sample out of reactor. The particle sizes of samples are range from 0.05mm to 0.15mm. As the residence time of particle in calcinator is just 0.75 seconds, the calcination of every magnesite sample is repeated 8 times to simulate a long-time process. And the dynamic changes in the composition and micro-structure of products with different calcination times were analyzed by using TG, XRD and SEM.

The magnesite decomposition ratio are calculated by Eq. (1) based on TGA of calcinated magnesite samples. Where X is decomposition ratio; w% and 46.2% are the weight of calcinated magnesite sample and magnesite material at 750 °C in TG, respectively.

$$\mathrm{X} = (1 - \frac{1 - 46.2\%}{1 - w\%})/46.2\% \tag{1}$$

Results and discussion

1. Reaction kinetic of magnesite decomposition

As shown in **Figure 3**, we can clearly see that the complete decomposition time of magnesite in TG is above 4 min at heating rate of 40 °C/min, but it is just a few seconds (3-5 s) in MFBRA above 750 °C. Hence, compared to TG, MFBRA is more suitable for rapid gas-solid reaction and can reappear. As shown in **Table 1**, the activation energy measured using TG and MFBRA are 236.6 and 124.16 kJ/mol, indicating that MFBRA can enhance mass transfer and effectively reduce the effect of external diffusion on the reaction.

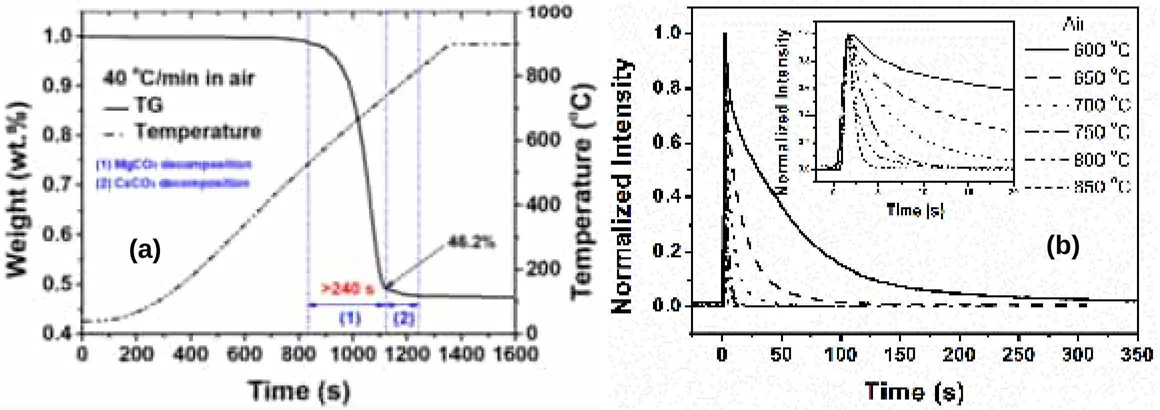

Fig. 3. Magnesite calcination in TG (a) and MFBRA (b).

Table 1. Kinetics parameters of magnesite calcination in air measured using TG and MFBRA

Analyzer	E (kJ/mol)	lg A (s^{-1})	G(x)
TG (Air)	236.60	15.81	-ln(1-x)
MFBRA(Air)	124.16	5.69	-ln(1-x)

2. Characterization of calcined magnesite produced in transport bed

Figure 4 shows the $MgCO_3$ decomposition ratio against calcination times, and the decomposition ratios are calculated by Eq. (1) based on TGA of calcinated magnesite samples. For the magnesite samples with a particle size of 0.05-0.15 mm, the decomposition ratios both reach up to 98% after 3 calcination times, indicating $MgCO_3$ can decompose almost completely as residence time above 2.25 seconds. And this phenomenon is consistent with the MFBRA result.

As shown in **Figure 5**, the XRD pattern demonstrates that the MgO is the dominant mineral phase in the samples produced from magnesite with particle size of 0.05-0.075 mm. The intensities of MgO diffraction peaks are enhanced with calcination times increases, which is consistent with **Figure 4**. The grain size of MgO crystal in those calcined magnesite samples are also calculated by Scherrer formula, shown in Eq. (2), based on the half-peak width of peak at $2\theta=42.5^{o}$.

$$\mathrm{D} = \frac{K\gamma}{B\cos\theta} \tag{2}$$

Where D is grain size of MgO crystal (nm); K is Scherrer constant (0.89); γ is X-Ray wavelength (0.154056 nm); B is half-peak width of peak at $2\theta=42.5^{o}$; Θ is diffraction Angle. As shown in Table 2, the grain size of MgO crystal continuously increases after multiple calcination due to recrystallization at high temperature.

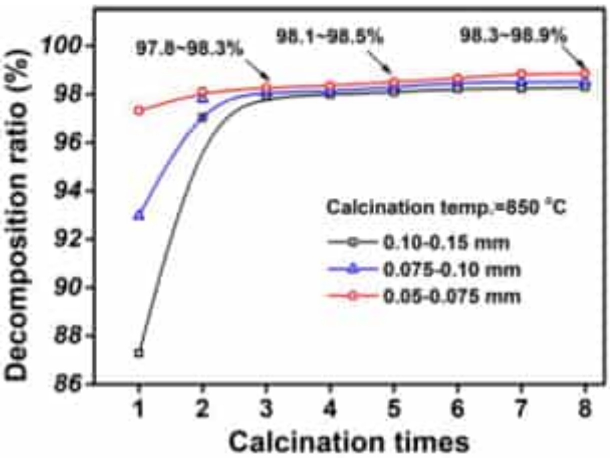

Fig. 4. $MgCO_3$ decomposition ratio of calcined magnesite samples with different calcination times

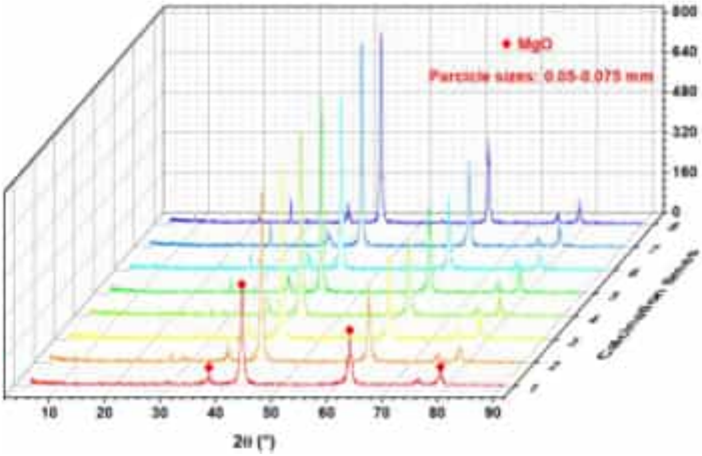

Fig. 5. XRD pattern for calcined magnesite samples with different calcination times

Table 2. Half-peak width of peak at $2\theta=42.5^{o}$ in XRD pattern and grain size of MgO crystal.

Parameters	Calcination times							
	1	2	3	4	5	6	7	8
B	0.737	0.517	0.481	0.444	0.427	0.399	0.379	0.379
D (nm)	12.0	17.7	18.3	20.6	21.3	21.4	22.9	24.0

B-Half-peak width of peak at $2\theta=42.5^{o}$; D-Grain size of MgO crystal.

Morphological characterization of calcined magnesite samples is performed to observe changes in the solid structure after calcination. As shown in **Figure 6**, the surface of the samples with 3-4 calcination times is porous and rough. With calcination times increasing, the granular shape continuously disappears and the surface becomes considerably smoother. A previous study of Eubank (1951) indicated that calcination of magnesite included two distinct steps: (1) loss of gases and (2) recrystallization or sintering. Therefore, the loss of gases leaves a very porous structure with a large internal surface area and a great reactivity for the products with less calcination times or residence time. However, excessive calcination times or residence time will inevitably lead to recrystallization or sintering and a dense particle structure with a smaller surface area and a lower reactivity.

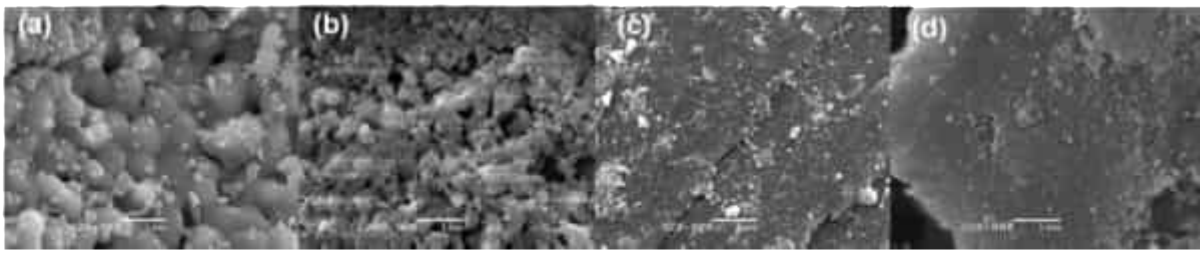

Fig. 6. SEM images of calcined magnesite samples with different calcination times
(a) 3 times, (b) 4 times, (c) 5 times and (d) 7 times

Conclusion

The complete decomposition time of magnesite in TGA is above 4 min at heating rate of 40 ^{o}C /min, but it is just a few seconds (3-5 s) in MFBRA above 750 ^{o}C. The activation energy measured in MFBRA and TGA are 125 kJ/mol and 236 kJ/mol respectively, showing a good suitability of MFBRA for rapid reaction in fluidized bed at a specific temperature. For powder magnesite with particle sizes of 0.05-0.15 mm, it just needs 1.5-2.3 s to complete the calcination reaction as temperature is above 800 ^{o}C in pilot-scale reactor. However, with the calcination times exceeding 4 times or residence time exceeding 3 seconds, the recrystallization or sintering will lead to a large grain size of MgO crystal and a dense particle structure with a smaller surface area and a low reactivity.

References

Bagchi, TP, KP Sen. Combined differential and integral method for analysis of non-isothermal kinetic data. Thermochimica Acta. 1981. 51, 175-189

Creamer, AE. Biomass-facilitated production of activated magnesium oxide nanoparticles with extraordinary CO_2 capture capacity. Chemical Engineering Journal. 2018. 334, 81-88

Demir, F., B Dönmez. Optimization of the dissolution of magnesite in citric acid solutions. International Journal of Mineral Processing. 2008. 87 (1-2), 60-64

Eubank, WR. Calcination studies of magnesium oxides. Journal of the American Ceramic Society. 1951. 34, 225−229

Stefanidis, S. Natural magnesium oxide (MgO) catalysts: a cost-effective sustainable alternative to acid zeolites for the in situ upgrading of biomass fast pyrolysis oil. Applied Catalysis B: Environmental. 2016. 196, 155-173

Yang, N. MgO-based adsorbent achieved from magnesite for CO_2 capture in simulate wet flue gas. Journal of the Taiwan Institute of Chemical Engineers. 2018. 86, 73-80

Yu, J., JR Yue, ZE Liu. (2010). Kinetics and Mechanism of Solid reactions in Micro Fluidized Bed Reactor. AIChE Journal. 2010. 56, 2905-2912

Zhao, Y., G Zhu. Thermal decomposition kinetics and mechanism of magnesium bicarbonate aqueous solution. Hydrometallurgy. 2007. 89 (3), 217-22

BIOMASS CATALYTIC PYROLYSIS FOR BTX PRODUCTION: A STUDY OF ZSM-5 MODIFICATION

Xianhua Wang*, **Qingfeng Che**, **Qing Yang**, **Haiping Yang**, **Yingquan Chen**, **Hanping Chen**

State Key Laboratory of Coal Combustion, Huazhong University of Science and Technology, 1037 Luoyu Road, Wuhan, Hubei 430074, PR China
*Email: *wangxianhua@hust.edu.cn*

Abstract

Biomass can be converted into valuable aromatic hydrocarbons (benzene, toluene and xylene, BTX) through fast pyrolysis in a fluidized bed reactor, combined with a zeolite (ZSM-5) catalytic process. Currently, the main constraints to this process are the rapid deactivation of catalyst and low BTX yield. Volatiles from biomass pyrolysis contain a large amount of oxygen containing organic compounds, such as sugars and branched phenols, which can not directly enter the channels of ZSM-5 but are adsorbed on the surface and accumulated to block the pores of the catalyst. In addition, the inappropriate acidity of the catalyst also leads to serious coke deposition and low catalyst activity. Therefore, we have redesigned the pore structure and acidity of ZSM-5 catalyst to improve the BTX production from biomass catalytic pyrolysis. Firstly, a meso-microporous structured ZSM-5 catalyst was prepared by hydrothermal synthesis using green templates (sucrose, cellulose, and starch). The results showed that the catalysts prepared using the sucrose and cellulose templates only exhibited a slight increase in their micropore volumes, while the mesopore volume of the catalyst modified with the starch template rose significantly and reached up to 0.359 cm^3/g. This increase promoted the cracking of bulky oxygenates and suppressed the polymerization reaction on the ZSM-5 surface, thereby producing a greater number of aromatic products. Moreover, the BTX yields exhibited a positive correlation with the catalyst mesopore volume, and the highest BTX yield of 91.84 mg/g was obtained by using the mesoporous ZSM-5 catalyst prepared with 10% starch/SiO_2 ratio. Then, the ZSM-5 catalyst was modified with various metals (Zn, Fe, Ca, Ce, and La) to adjust the acidity, and the relationship between the physicochemical properties of catalysts and the BTX products were also investigated. It was found that the BTX yield was positively correlated with the strong acid sites content. Appropriate loading amount (0.5-4 wt.%) of Zn species increased the strong acid sites content of ZSM-5 catalyst as well as BTX products yield, and the highest BTX yield was observed under 2 wt.% loading amount of Zn. While excessive metal loading amount (10 wt.%) decreased both the acidity and the physical properties of the catalyst, resulting in poor diffusion of reactants and products inside the catalyst and decreased the BTX yield.

Introduction

Biomass is the only carbon-containing renewable energy source, and as such, the bio-oil produced from fast pyrolysis of biomass is expected to be an important source for fuels and chemicals in the future. However, Liu et al. (2014) wrote that the complex component of bio-oil in addition to its corrosiveness, low calorific value, and high oxygen content render its application difficult in the existing petroleum-based infrastructure. Thus, the upgrading of bio-oil to high-grade fuels through a one-step catalytic pyrolysis process is considered to be a promising route for the high-value utilization of biomass. ZSM-5 is a widely employed catalyst in the petrochemical and petroleum refining industries, the high thermal and hydrothermal stability render it a suitable catalyst for the catalytic fast pyrolysis (CFP) of biomass, especially using a fluidized bed reactor, where lignocellulosic biomass can be effectively converted into valuable aromatic hydrocarbons (benzene, toluene and xylene, BTX). Wang et al. (2014) found that the oxygenates from pyrolysis undergo a series of deoxygenation and aromatization reactions within the catalyst channels, with the released products including benzene, toluene, xylene, naphthalene, ethylene, and propylene, where oxygen is removed in the form of CO_2, CO, and H_2O. In addition, Du et al. (2013) found that a solid carbonaceous residue known as coke is generated during this process, and is deposited either on the catalyst surface or inside the pores, resulting in catalyst deactivation with a long-term use. Currently, the biggest problems with this biomass to BTX process are the rapid deactivation of catalyst and low conversion rate due to the narrow pore size and the inappropriate acidity of the catalyst. In this study, the methods of template and metal loading will be adopted to modify the pore structure and acidity of ZSM-5 catalyst so as to improve the conversion efficiency of biomass to BTX.

Methods

Three green templates (sucrose, starch, and cellulose) with different molecular sizes were selected for preparation of meso-microporous ZSM-5 catalysts. The synthesized ZSM-5 catalysts with the template to SiO_2 mass ratio of 10% were denoted as ZSM-SU (sucrose), ZSM-CE (cellulose), and ZSM-ST (starch), while the starch-modified ZSM-5 catalysts with different ratios of 5%, 15%, and 20% were denoted as ZSM-5%ST, ZSM-15%ST, and ZSM-20%ST, respectively. The catalyst prepared without any template was denoted as ZSM-5, and a commercial microporous ZSM-5 catalyst was denoted as ZSM-5 (con.). The acidity of ZSM-5 catalyst was modified by loading different metals (Zn, Fe, Ca, Ce, and La) with 2wt.% amount using impregnation method, and the different loading amounts (0.5, 4, 10wt.%) of Zn were also investigated.

The acidity of the catalyst was quantitatively analyzed using the NH_3-TPD method (ChemiSorb 2720, Micromeritics), and the structural properties of the catalyst were measured using nitrogen isothermal adsorption at 77 K with an accelerated surface area and porosimetry system (ASAP 2020, Micromeritics). The catalytic fast pyrolysis experiments of sawdust were conducted using a CDS Pyroprobe 5250 pyrolyser. The sawdust and catalyst were separately loaded at the middle of the quartz tube (2 mm in internal diameter and 38 mm in length) using the loose quartz wool (CDS Analytical Inc.) as carrier platform. In a typical CFP experiment, 0.3 mg sawdust and 1.2 mg catalyst were used. The samples were heated to 600 °C at a rate of 20 °C/ms and held for 15 s to decompose completely. After CFP, the vapors were promptly swept into GC/MS (7890B/5977A, Agilent) with He (purity ≥ 99.999%) via a heated transmission pipe (280 °C). The GC/MS injector hold temperature of 280 °C, and the spilt rate was 80:1. The GC column used was an Agilent Technologies, HP-5MS capillary column (30 m×0.25 mm×0.25 μm). The products were identified according to the NIST library and quantitatively analyzed using an external standard method. Each experiment was repeated 3–5 times under the same conditions, and the results were averaged.

Results and Discussion

Characterization of mesoporous catalysts

The textural properties of the various ZSM-5 catalysts are listed in Table 1, where it is apparent that the synthesized ZSM-5 catalysts have higher BET surface area, mesoporous pore volume, and average pore size in comparison with ZSM-5(con.). In terms of the template-modified ZSM-5 catalysts, ZSM-SU, ZSM-CE and ZSM-5%ST have higher BET surface area and micropore volume than ZSM-5. The addition of starch created more mesopore, and the highest mesopore volume reached up to 0.370 cm^3/g with the starch to SiO_2 mass ratio of 5%, while adding sucrose or cellulose does not have such effect. Besides, the starch-modified catalysts have larger average pore diameter and a maximum value of 4.901 nm was also obtained for ZSM-5%ST. The mesoporous volume and average pore size of the starch-modified catalyst decreased gradually upon increasing the amount of added starch.

Table 1. Textural properties of various ZSM-5 catalysts

Catalyst	S_{BET} (m^2/g)	V_{Total} (cm^3/g)	V_{Micro} (cm^3/g)	V_{Meso} (cm^3/g)	D (nm)
ZSM-5(con.)	404.57	0.185	0.164	0.021	1.832
ZSM-5	423.11	0.418	0.166	0.252	3.983
ZSM-SU	452.96	0.394	0.177	0.217	3.519
ZSM-CE	441.21	0.402	0.171	0.231	3.694
ZSM-ST	423.07	0.522	0.163	0.359	4.508
ZSM-5%ST	447.19	0.541	0.171	0.370	4.901
ZSM-15%ST	428.22	0.506	0.166	0.340	4.461
ZSM-20%ST	432.94	0.412	0.168	0.254	3.872

Table 2 details the parameters of each catalyst, including the acidity, acid site distribution, and the temperature corresponding to the center of each peak. As shown, the ZSM-5(con.) has the highest acidity of 887.1 μmol/g, which is significantly higher than that of every synthesized ZSM-5 catalyst. Compared with ZSM-5, the acidity of the catalyst increased slightly with the addition of sucrose and starch, and decreased with the addition of cellulose. For the starch-modified catalysts, the acidity increased first and then decreased with increase of the starch/SiO_2 ratio, and the highest value was obtained for ZSM-ST (10%). The template also has a great effect on the acid site distribution of the catalyst. Specifically, ZSM-ST, ZSM-CE and ZSM-20%ST have the highest content of strong acid, medium acid and weak acid sites, respectively. While ZSM-CE, ZSM-20%ST and ZSM-5 (con.) have the lowest content of strong acid, medium strong acid and weak acid sites, respectively.

Table 2. Acidity of various ZSM-5 catalysts

Catalysts	Acid amount (μmol/g)	Acid sites content (%)			Peak position (℃)		
		Weak	Medium	Strong	Weak	Medium	Strong
ZSM-5(con.)	887.1	28.17	19.08	52.74	204.6	254.7	415.7
ZSM-5	594.2	40.90	14.60	44.48	229.8	304.7	444.1
ZSM-SU	623.3	40.21	16.15	43.62	234.9	322.1	447.3
ZSM-CE	574.6	43.18	26.87	29.93	233.8	367.0	456.8
ZSM-ST	613.8	48.17	4.05	47.76	237.3	338.8	444.3
ZSM-5%ST	602.5	45.60	10.64	43.74	233.3	338.6	444.8
ZSM-15%ST	593.4	47.57	9.92	42.50	237.7	348.1	450.8
ZSM-20%ST	572.7	51.41	2.31	46.26	234.6	342.7	439.4

Catalytic effect with mesoporous catalysts

Fig. 1. shows the BTX yields from sawdust catalytic pyrolysis using different ZSM-5 catalysts and the correlation between the mesopore volume of the ZSM-5 catalyst and the BTX yield. It can be seen from Fig. 1. (a) that the BTX yields from the synthesized and modified mesoporous catalysts are much higher than that of ZSM-5 (con.), and the highest BTX yield of 91.84 mg/g was obtained with the ZSM-ST catalyst. The Fig. 1. (b) shows that the BTX yield is positively correlated with the mesoporous volume of the catalyst. The catalysts containing lower mesopore content (i.e. ZSM-5, ZSM-CE, and ZSM-20%ST) lead to lower BTX yield. In contrast, an optimal starch/SiO_2 ratio (10%) causes a higher mesoporous pore

volume, thereby resulting in a higher BTX yield. Besides, the mesopore volume of the catalyst gradually decreased with the starch/SiO_2 ratio increased, and the lowest yield of BTX products was obtained at the starch to SiO_2 mass ratio of 20%, which is equivalent to the catalytic effect of the catalyst without template modification (ZSM-5).

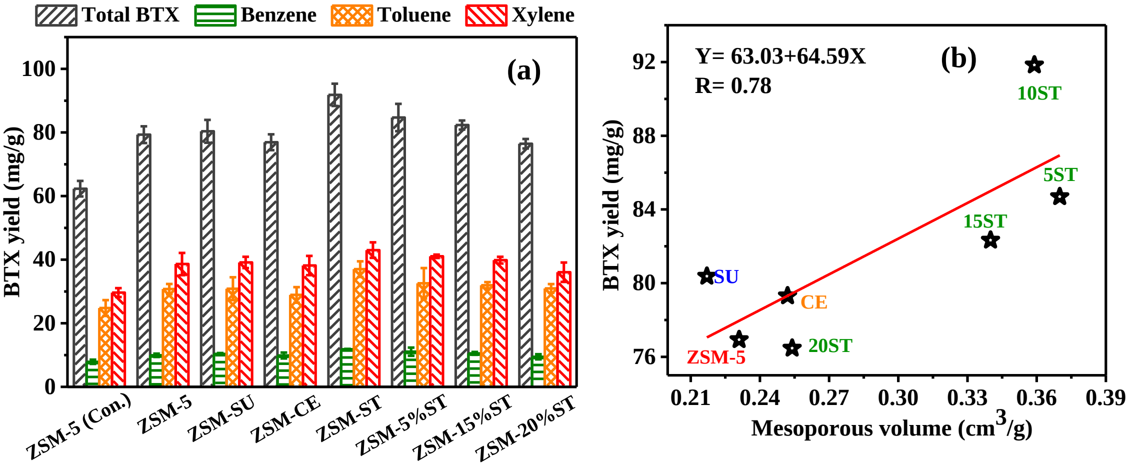

Fig. 1. Catalytic pyrolysis with various mesoporous catalysts

(a) BTX yield, (b) Correlation between mesoporous volume and BTX yield

Table 1 shows that the ZSM-5(con.) catalyst has a limited number of mesopores, which results in the polymerization of the bulky oxygenates from biomass pyrolysis to form coke on the surface of the catalyst, thereby preventing the reactants entering the micropores. In contrast, the synthesized ZSM-5 catalyst is composed of small particle crystals with rich mesopores, thereby facilitating the conversion of pyrolysis volatiles inside the catalyst. Upon modification with starch, the space between the crystal particles is further enlarged to form additional mesopores, which results in the higher yields of BTX. In contrast, the addition of sucrose and cellulose only caused a small increase in the micropore volume, with no obvious promoting effect on BTX formation. Similarly, when the starch/SiO_2 ratio gradually increased from 10% to 20%, the mesoporous volume of the catalyst declined from 0.359 to 0.254 cm^3/g, resulting in a sharp decrease in BTX yield. It is worth noting that ZSM-5%ST has the highest mesopore volume of 0.370 cm^3/g, but its BTX yield is lower than that of ZSM-ST. Indeed, the NH_3-TPD results show that the strong acid content of ZSM-5%ST is 43.74%, which is lower than that of ZSM-ST (47.76%), thereby the poor catalytic effect of ZSM-5%ST may be attributed to its lower strong acid content, as strong acid sites are effective sites for biomass catalytic pyrolysis conversion. These results indicate that both the acidity and pore structure of the catalyst play important roles in the catalytic pyrolysis of biomass, but the pore structure, and in particular the mesoporous volume, seems to be a key parameter. Thus it can be concluded that increasing the mesopore volume of the ZSM-5 catalyst can effectively improve the activity of the catalyst when the acid amount is sufficient. Meanwhile, increasing the acid amount is a better choice when the mesopores volume reaches a limit (i.e. 0.359 cm^3/g).

Characterization of metal modified catalysts

In order to get an insight of the acidity of ZSM-5 catalyst on the catalytic pyrolysis efficiency, the catalyst was modified with metal loading method. The acidity parameters of the modified ZSM-5 catalysts are listed in Table 2. The acid amount decreased with metal incorporation, Ca/ZSM-5 had the lowest acid amount of 195.1 μmol/g, which was 32.1 % less than raw ZSM-5, while Fe showed the least effect on the acid of catalyst. The acid sites distribution was changed significantly with the incorporation of metals. La and Ca decreased the content of strong acid sites from 49.9 % for raw ZSM-5 to 23.3 % and 28.8 %, respectively, while Zn increased the content of strong acid sites to 53 %. La/ZSM-5 had the highest content of medium acid sites while Ce/ZSM-5 had the highest content of weak acid sites. Besides, the content of both weak and strong acid sites first increased and then decreased with the increase of Zn loading amount, and reached the maximum values at the Zn loading amount of 2 wt.%. The acidity change of the metal modified catalysts can be mainly attributed to the coverage of the acidic sites on the external surface, and the reaction of metal species with protonic acid or other groups on the external surface or inside the channels. Niu et al. (2014) found that the reaction between metal species and protonic acid would convert the strong acid into medium or weak acid.

Table 3. Acidity of various metal modified ZSM-5 catalysts

Catalysts	Acid amount (μmol/g)	Acid sites content (%)			Peak position (℃)		
		Weak	Medium	Strong	Weak	Medium	Strong
ZSM-5	287.6	10.9	39.2	49.9	181.9	233.4	379.2
Fe/ZSM-5	272.3	11.4	38.5	50.1	182.2	236.1	385.1
Ca/ZSM-5	195.1	20.5	50.7	28.8	192.7	254.4	340.9
Ce/ZSM-5	216.7	24.2	35.2	40.6	193.4	252.2	383.1
La/ZSM-5	234.6	22.6	54.1	23.3	219.7	303.6	444.2
Zn/ZSM-5	242.5	23.1	23.9	53.0	193.5	254.5	364.7
0.5%Zn/ZSM-5	259.6	20.8	28.5	50.7	185.4	246.9	375.7
4%Zn/ZSM-5	226.1	22.6	30.5	46.9	191.3	252.7	368.3
10%Zn/ZSM-5	228.7	19.3	40.5	40.2	194.0	252.1	361.5

Catalytic effect of metal modified catalysts

Fig. 2. shows that the BTX yield is positively correlated with the strong acid sites content of ZSM-5 catalyst, except for the data point of 10 wt.% Zn loading. It can be seen that the loading with 2 wt.% Zn significantly increased the yield of BTX from 71.81 mg/g of ZSM-5 to 85.66 mg/g of Zn/ZSM-5. Fe almost have no contribution in promoting the BTX formation, while Ca, Ce and La reduced the BTX yield. Studies have shown that strong acid sites play a greater role in the catalytic reaction, such as C-O bond cleavage, hydrogen transfer and aromatization. That is, the catalyst with a higher content of strong acid sites may be more favorable for the deoxygenation and aromatization of biomass pyrolysis volatiles. When the Zn loading is excessive (10 wt.%), the metal altered both the acidity and the physical properties of the catalyst effectively. The ZnO species accumulated in micropores and mesopores, and caused a sharp decrease in pore volume and pore size of the ZSM-5 catalyst. This would result in poor diffusion of reactants and products in the channels of catalyst. Therefore, it can be inferred that a higher content of the strong acid sites could enhance the yield of BTX when the metal loadings were in proper range. Furthermore, excessive loading would lead to a decrease in catalytic performance of the catalyst, thereby inhibiting the formation of BTX.

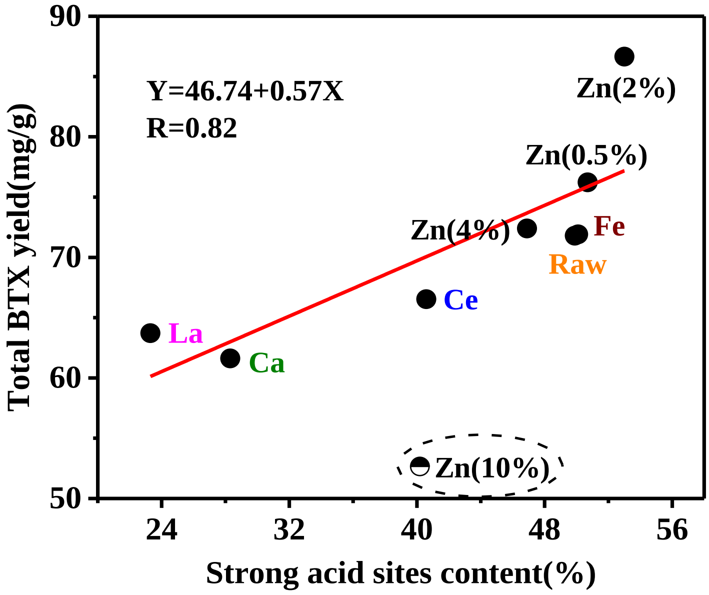

Fig. 2. Correlation between BTX yield and strong acid sites content

Conclusion

The conversion efficiency of biomass catalytic pyrolysis for BTX production can be improved by adjusting the pore structure and acidity of ZSM-5 catalyst. The usage of starch as a template to prepare mesoporous catalyst can improve the transportion characteristics of biomass pyrolysis volatiles, while Zn modified ZSM-5 catalyst can increase the content of strong acid of the catalyst, thereby increasing the catalytic activity of the catalyst. A starch to SiO_2 mass ratio of 10% and a Zn loading amount of 2wt.% is the optimal condition for adjusting pore structure and acidity.

References

Du, S., J.A. Valla and G.M. Bollas. Characteristics and origin of char and coke from fast and slow, catalytic and thermal pyrolysis of biomass and relevant model compounds. Green Chem. 2013. 15, 3214-3229

Liu, C., H. Wang, A.M. Karim, J. Sun and Y. Wang. Catalytic fast pyrolysis of lignocellulosic biomass. Chem. Soc. Rev. 2014. 43, 7594-7623

Niu, X., J. Gao, Q. Miao, M. Dong, G. Wang, W. Fan, Z. Qin and J. Wang. Influence of preparation method on the performance of Zn-containing HZSM-5 catalysts in methanol-to-aromatics. Microporous Mesoporous Mat. 2014. 197, 252-261

Wang, K.G., K.H. Kim and R.C. Brown. Catalytic pyrolysis of individual components of lignocellulosic biomass. Green Chem. 2014. 16, 727-735

MEASUREMENT OF RESIDENCE TIME DISTRIBUTION OF SAWDUST IN A HORIZONTAL FLUIDIZED BED WITH GAS PULSATION

Ruixu Wang[1], Ziliang Wang[1], Xiaotao Bi[1]*, C. Jim Lim[1] and Shahabaddine, Sokhansanj[1], Chang Soo Kim[2]

[1]*Clean Energy Research Centre and Department of Chemical and Biological Engineering, University of British Columbia, 2360 East mall, Vancouver BC, V6T1Z3, Canada*

[2]*Korea Institute of Science and Technology, 39-1 Hawolgok-dong, Seongbuk-gu, Seoul 136-791, Korea*

*Email: *tony.bi@ubc.ca*

Abstract

A prototype horizontal fluidized bed reactor with gas pulsation is designed and built for continuous production of torrefied biomass. By choosing a shallow bed with a length to width ratio of 10:3, biomass particle transport along the reactor length is close to a plug flow with back-mixing induced by gas-bubbles. A narrower solid residence time distribution (RTD) than that of a vertical tall fluidized bed is achieved, which consequently leads to an improved product uniformity.

In present study, RTD of sawdust particles was measured by a pulse injection method. Dedicated tracers were prepared by impregnating sawdust with sodium chloride solution followed by drying at 105°C for 24h. Conductivities of solutions of discharged products were determined, which were proportional to the concentrations of the tracer. Effects of operating conditions, such as biomass feed rate, gas pulsation frequency, and gas velocity on solid RTD were experimentally investigated.

Introduction

Fluidized beds have been widely used in particulate processes due to its good mass and heat transfer rates. Biomass processing also can benefit from fluidization technologies if the issue of poor fluidization quality of unconventional biomass particles is properly addressed. Jia et al. (2015) successfully dried biomass particles in a batch pulsed fluidized bed without inert bed materials, showing the potential application of pulsed fluidized beds to the thermochemical conversion, such as torrefaction, pyrolysis, and gasification of biomass particles. A horizontal pulsed fluidized bed reactor with continuous feeding of biomass at up to 4 kg/h for torrefaction has been designed and built to prove the concept. As the operation moves from batch to continuous production, a spread in solid residence time is inevitable and undesirable, leading to variable degrees of conversion and, ultimately, an uneven product quality. A shallow bed with a length to width ratio of 10:3 is thus chosen, with biomass particles flow horizontally, to achieve a narrower solid RTD than that of a vertical tall fluidized bed. As a result, improved mass and heat transfer in fluidized beds (Jia et al. 2017a, 2017b) and the narrow solid RTD would reduce the reactor volume to treat bulky biomass and hence enable a reduction in capital cost at large scale.

RTD measurement is an essential tool to determine the reaction time and reactor behavior of a continuously operated reactor (Levenspiel 1999; Fogler 2017). As energy derived from biomass has grown rapidly over recent years (IEA 2017), studies of various continuous reactors employed for biomass treatments have been recently published. RTD of biomass particles in screw-type reactors (Chamberlin et al. 2018; Nachenius et al. 2015; Youssef et al. 2017; Sievers et al. 2016), rotary drums (Bongo Njeng et al. 2015; Colin et al. 2015; Renström 2008), horizontal stirred bed reactor (Xi et al. 2015a), horizontal tube reactor (Sievers and Stickel 2018), and horizontal fluidized bed reactor (Chen et al. 2018) has been tested. Influences of operating conditions (degree of inclination, rotation speed, feed rate, gas velocity), design parameters (exit dam height, lifter shape, blade number, blade angle), and flowability of the test materials on residence time control have been investigated. In particulate systems, solid RTD data reflect the transport of particles and the intensity of solids mixing. Axial dispersion model (ADM) is one of the commonly used models to describe a solids flow close to plug flow (Bongo Njeng et al. 2015; Colin et al. 2015; Nachenius et al. 2015; Sievers et al. 2016; Xi et al. 2015b). The back-mixing extent is then quantified by the fitted dispersion coefficient or Peclet number. Particularly in a shallow horizontal fluidized bed with or without baffles tested by Kong et al. (2018), RTD curves of cristobalite powder were fitted to tank-in-series model, ADM and non-ideal compartment model, and ADM appeared to give the best fit within tested range with Peclet number over 25.

Comprehensive information of RTD of the novel fluidized bed reactor in the present study for sawdust particles is therefore imperative for evaluating the torrefaction performance. This paper presents the solid RTD technique developed for the specific reactor and typical results.

Experiments

Biomass tested in this study was hemlock sawdust acquired directly from a sawmill of Teal-Jones Group, BC, Canada. Hemlock sawdust was grounded by a hammermill with a 3.175 mm screen and then dried at 105 °C for 24 h. Particle size distribution was determined by sieving and shown in Fig. 1. Grounded sawdust has a tapped bulk density of 173 kg/m^3 with a Sauter mean diameter of 0.70 mm.

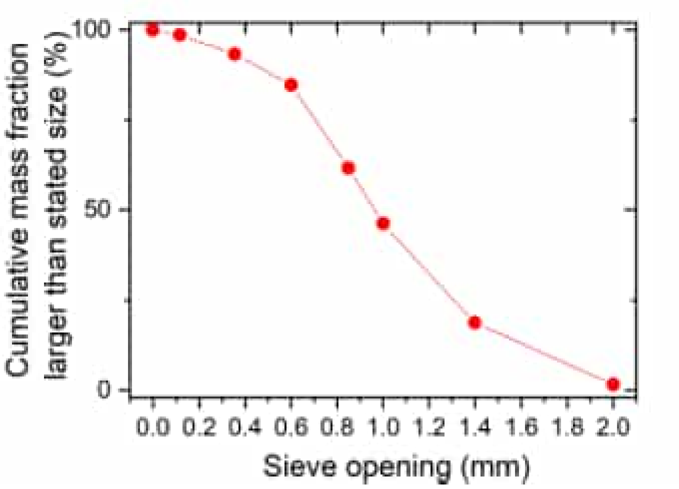

Fig. 1. Particle size distribution of grounded hemlock sawdust.

The pulsed fluidized bed reactor used for RTD tests is depicted in Fig. 2. Dimensions of the reactor were 635×372×76.2 mm (Height×Length×Width). Compressed air was used as fluidizing gas. Gas pulsation was generated by a solenoid valve (customized, Xi'An Aoxin Technology Co., Ltd., China). A 75.7 L buffer tank was positioned before the solenoid valve to stabilize the reading at rotameter and to sustain the gas supply for pulsation. Sawdust was fed from one side by a screw feeder, slowly traveled along the length of the reactor, contacted with gas, and finally exited by passing an overflow weir at the opposite end. The bed length was 254 mm, and weir height was 63.5 mm. Particles overflowed from the weir and passed through a 381 mm long discharge leg before fell into a sample collection bag. Fine particles entrained were captured by a filter bag installed at the gas exit of the reactor. A camera was placed on top inside the reactor to monitor and record the bed behavior to ensure proper tracer injection.

Tracer was prepared by impregnating dried sawdust with solutions containing 30 g sodium chloride per 100 mL deionized water and then dried at 105°C for 24h. Preliminary tests showed impregnated sawdust generally gained around 18% of the original weight and roughly remained the same size distribution. Therefore, the physical property of the dedicated tracer was close to that of the raw material.

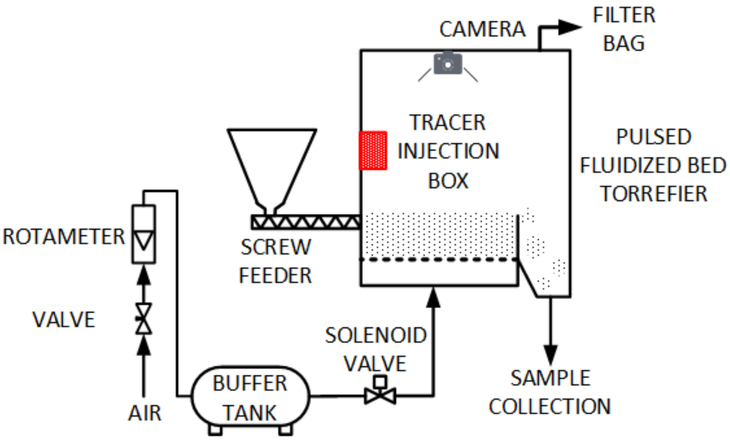

Fig. 2. Schematic of the pulsed fluidized bed unit for biomass torrefaction.

Once both gas and solid flow reached steady-state under testing conditions, 20 g of tracer was poured onto the top of the feeding end of the bed by flipping the tracer box. Discharged samples were collected starting at the exact moment of injection and continuing at a regular time interval. Detailed sampling schemes for different feed rates are summarized in Table 1. Conductivities of solutions of collected samples subtracting a base conductivity originated from the same amount of raw sample without tracer were determined afterward by a conductivity transmitter (CDTX90 with CDCE-90-01 sensor, Omega Engineering, Inc. USA). Corrected conductivities were proportional to the concentrations of the tracer.

Table 1. Solid RTD sampling schemes.

F, kg/h	**N_{total}**	**Quick sampling**			**Slow sampling**		
		Duration	Interval, s	Number	Duration	Interval, s	Number
1	49	1-18min	40	27	19-40min	60	22
1.5, 2	40	1-13min	30	26	14-27min	60	14

Effects of feed rate, gas velocity, and pulsation frequency have been investigated. All tested experimental conditions are listed in Table 2. For each condition, two experiments were conducted to check reproducibility.

Table 2. Operating conditions of solid RTD tests.

#	**F, kg/h**	**f_p, Hz**	**U, m/s**
1	1.05±0.03	1	0.172
2	1.03±0.01	2	0.170
3	1.03±0.03	4	0.170
4	1.49±0.04	1	0.169
5	1.47±0.02	2	0.170
6	1.46±0.04	3	0.170
7	1.44±0.01	4	0.169
8	1.51±0.02	2	0.140
9	1.50±0.01	2	0.202
10	1.45±0.00	2	0.240
11	2.02±0.00	1	0.170
12	2.01±0.01	2	0.172
13	2.03±0.01	4	0.172

Results and Discussions

Fig. 3 shows the RTD at different operating conditions. Normalized tracer concentrations were plotted against averaged time over sampling period. One typical result was adopted for each case. In general, one distinct peak can be spotted for each run for most of the runs. Only for pulsation frequency of 3 or 4 Hz, or gas velocity as low as 0.14 m/s, where the bed behaved unsteadily due to poor fluidization, multiple peaks or substantial fluctuations were detected in RTD curves. All RTD curves in Fig. 3 displayed pronounced tailing, implying the existence of a stagnant zone or relatively inactive part of the bed. The rectangular cross-section of the bed naturally creates dead-zones along corners. The fact was also confirmed by Jia et al. (2017a) by improved drying performance in a batch reactor with a tapered column section to reduce dead-zones in the unmodified rectangular cross-section column. In the other situation, for instance, if particles of different sizes tend to be segregated in the bed, large tracer particles might be trapped and come out much later.

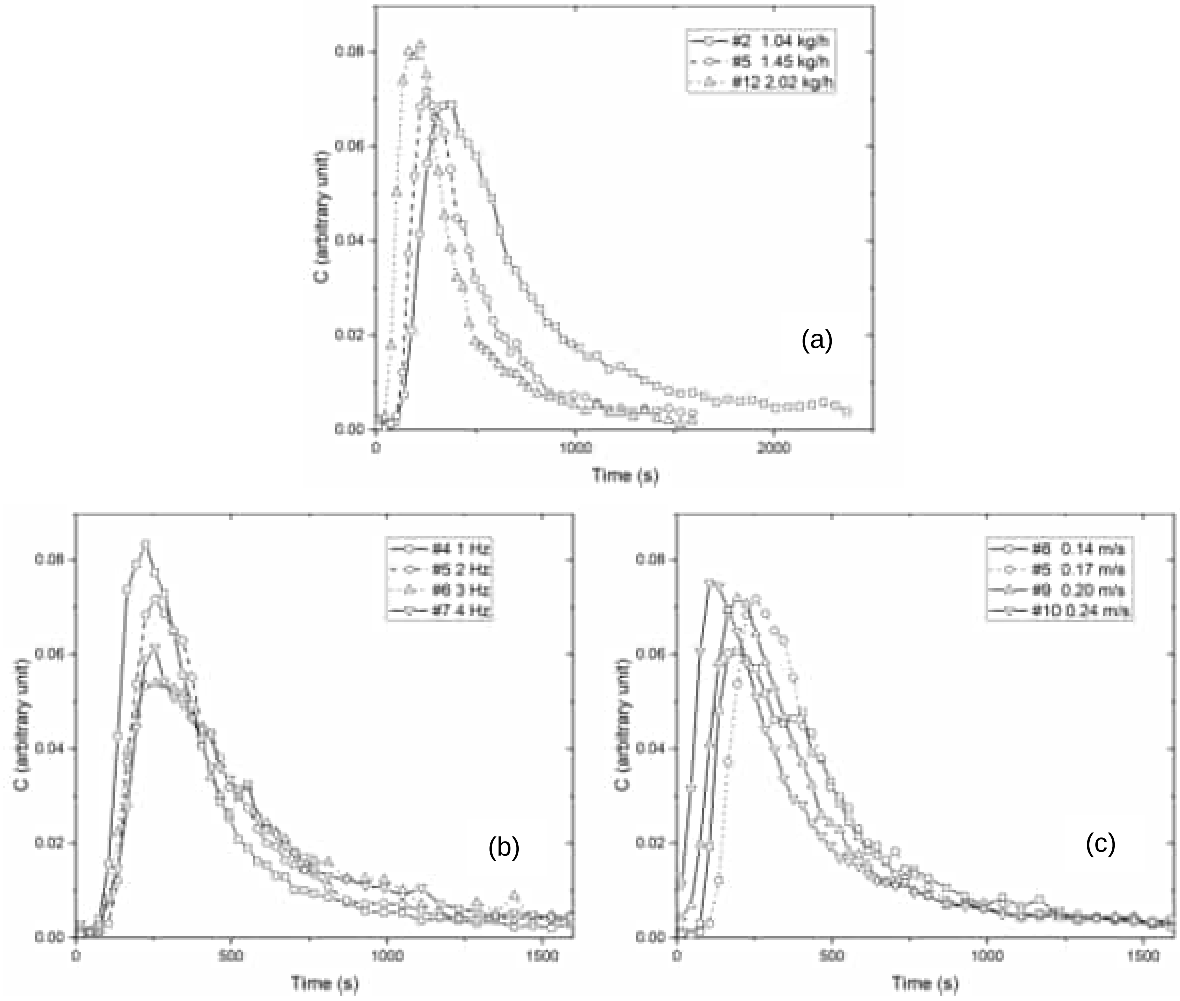

Fig. 3. Solid RTD curves at different operating conditions (a. U= 0.17 m/s, f_P= 2 Hz, b. U= 0.17 m/s, F~ 1.5 kg/h, c. f_P= 2 Hz, F~ 1.5kg/h).

In Fig. 3a, feed rates of 1 kg/h, 1.5 kg/h, and 2 kg/h were tested. The peak time shifted left as feed rate increased, resulting from faster biomass traveling through the bed. Peaks also became sharper and less spread at a higher feed rate, indicating a lower back-mixing level at higher feed rate. RTD curves at pulsation frequency of 1 Hz, 2 Hz, 3 Hz, and 4 Hz are presented in Fig. 3b. Peak time decreased slightly with the decrease of pulsation frequency, because the lower the pulsation frequency, the higher the instantaneous gas velocity, and eventually, leading to lower bed solid hold-up. Curves of 3 Hz and 4 Hz were spread broader with more oscillations than these of 1 Hz and 2 Hz, implying less stable particle movement. Effect of gas velocity is shown in Fig. 3d. All curves had similar shapes except for the case of a gas velocity of 0.14 m/s. The peak appeared earlier at higher gas velocity, because of higher bed expansion and thus lower solids hold-up.

The experimental mean residence time for a pulse injection of tracer can be determined following the method given by Fogler (2017):

$$E(t) = \frac{C(t)}{\int_0^\infty C(t)dt} \tag{1}$$

$$t_m = \frac{\int_0^\infty tE(t)dt}{\int_0^\infty E(t)dt} = \int_0^\infty tE(t)dt \tag{2}$$

On the other hand, theoretical mean residence time was calculated by:

$$\tau = \frac{\text{Bed mass}}{\text{Mass feed rate}} \tag{3}$$

Another important measure of the RTD curves is the peak time, denoted by t_{peak}. It is closely linked to the solid flow condition and is highly sensitive to the impacts of operating conditions, as discussed above.

Fig. 4 compares t_m and t_{peak} with τ of all runs, respectively. The experimental mean residence times were observed to be slightly lower than theoretical ones. The difference could be caused by the existence of internal circulation or less active zones. Note that t_m was affected by the cut-off time because of the long tailing of the RTD curves. On the contrary, peak times were much smaller than the mean residence time, which can be resulting from a stagnant volume or the short circuit of some fast-moving tracer particles at the bed surface considering that bed was subjected to a vertical velocity profile.

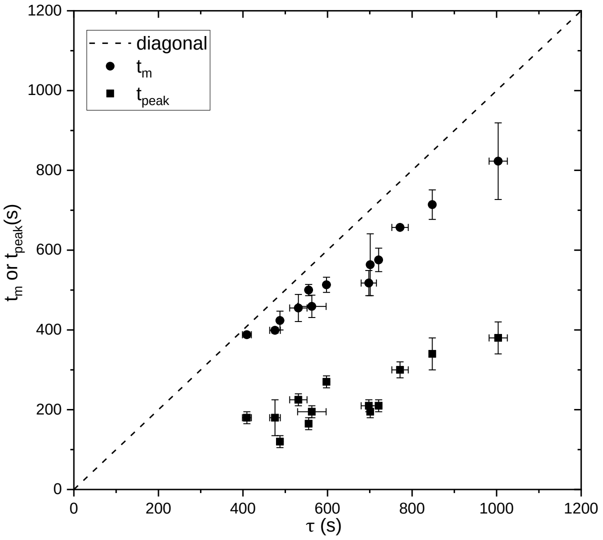

Fig. 4. Comparison of mean residence time by experimental mean residence time t_m with theoretical mean residence time τ, and peak time t_{peak} with τ. Error bars of t_{peak} are errors in repeats or uncertainty in peak time, whichever is larger.

Effects of pulsation frequency and gas velocity on back-mixing and mean residence time are too complicated to be directly inferred from the RTD curves alone, and the mean residence time does not provide direct information on particle spreading/mixing. A dispersion model should be developed and fitted to the experimental data to extract dispersion parameters to interpret solid flow behavior and provide more insights on particle transport and mixing.

Conclusion

Solid RTDs under different operating conditions have been measured in a horizontal fluidized bed reactor for biomass torrefaction. It is shown that the solid RTD is significantly impacted by operating conditions. An RTD model based on the axial dispersion model is needed to characterize the solids mixing so as to better understand the effects of pulsation frequency and gas velocity. The proposed model eventually can be incorporated in an overall reactor model for the design, improvement, and scale-up of such reactors.

Notation

τ	theoretical residence time, s	N_{total}	total number of samples
C	tracer concentration, dimensionless	t	time, s
E	RTD function, dimensionless	t_m	calculated mean residence time, s
F	feed rate, kg/h	t_{peak}	peak time, s
f_P	pulsation frequency, Hz	U	gas velocity, m/s

References

Bongo Njeng, A. S., S. Vitu, M. Clausse, J. L. Dirion, and M. Debacq. 2015. 'Effect of lifter shape and operating parameters on the flow of materials in a pilot rotary kiln: Part I. Experimental RTD and axial dispersion study', Powder Technology, 269: 554-65.

Chamberlin, Charles, David Carter, and Arne Jacobson. 2018. 'Measuring residence time distributions of wood chips in a screw conveyor reactor', Fuel Processing Technology, 178: 271-82.

Chen, K., P. Bachmann, A. Bück, M. Jacob, and E. Tsotsas. 2019. 'CFD simulation of particle residence time distribution in industrial scale horizontal fluidized bed', Powder Technology. 345: 129-139.

Colin, B., J. L. Dirion, P. Arlabosse, and S. Salvador. 2015. 'Wood chips flow in a rotary kiln: Experiments and modeling', Chemical Engineering Research and Design, 98: 179-87.

Fogler, H. Scott. 2017. Essentials of chemical reaction engineering (Prentice Hall).

IEA. 2017. 'Technology Roadmap Delivering Sustainable Bioenergy'.

Jia, Dening, Xiaotao Bi, C. Jim Lim, Shahab Sokhansanj, and Atsushi Tsutsumi. 2017a. 'Gas-solid mixing and mass transfer in a tapered fluidized bed of biomass with pulsed gas flow', Powder Technology, 316: 373-87.

Jia, Dening, Xiaotao Bi, C. Jim Lim, Shahab Sokhansanj, and Atsushi Tsutsumi. 2017b. 'Heat Transfer in a Pulsed Fluidized Bed of Biomass Particles', Industrial & Engineering Chemistry Research, 56: 3740-56.

Jia, Dening, Océane Cathary, Jianghong Peng, Xiaotao Bi, C. Jim Lim, Shahab Sokhansanj, Yuping Liu, Ruixu Wang, and Atsushi Tsutsumi. 2015. 'Fluidization and drying of biomass particles in a vibrating fluidized bed with pulsed gas flow', Fuel Processing Technology, 138: 471-82.

Levenspiel, Octave. 1999. Chemical Reaction Engineering (3rd Edition). John Wiley & Sons.

Nachenius, R. W., T. A. van de Wardt, F. Ronsse, and W. Prins. 2015. 'Residence time distributions of coarse biomass particles in a screw conveyor reactor', Fuel Processing Technology, 130: 87-95.

Renström, Roger. 2008. 'Mean Residence Time and Residence Time Distribution When Sawdust Is Dried in Continuous Dryers', Drying Technology, 26: 1457-63.

Sievers, David A., Erik M. Kuhn, Jonathan J. Stickel, Melvin P. Tucker, and Edward J. Wolfrum. 2016. 'Online residence time distribution measurement of thermochemical biomass pretreatment reactors', Chemical Engineering Science, 140: 330-36.

Sievers, David A., and Jonathan J. Stickel. 2018. 'Modeling residence-time distribution in horizontal screw hydrolysis reactors', Chemical Engineering Science, 175: 396-404.

Xi, Yingtao, Qun Chen, and Changfu You. 2015a. 'Flow characteristics of biomass particles in a horizontal stirred bed reactor: Part I. Experimental measurements of residence time distribution', Powder Technology, 269: 577-84.

Xi, Yingtao, Qun Chen, and Changfu You. 2015b. 'Flow characteristics of biomass particles in a horizontal stirred bed reactor: Part II. Modeling studies on particle residence time distribution and axial mixing', Powder Technology, 269: 585-95.

Youssef, Ziad, Fabrice Ducept, Hamdi Bennaceur, Barbara Malinowska, Giana Almeida, Patrick Perre, and Denis Flick. 2017. 'Residence time distribution in a biomass pretreatment reactor: Experimentation and modeling', Chemical Engineering Research and Design, 125: 233-44.

EFFECT OF MIXING QUALITY ON AGGLOMERATE FORMATION IN A FLUID COKING REACTOR

Francisco Sanchez Careaga[1], Cedric Briens[1*], Jennifer McMillan[2]

[1] Institute for Chemicals and Fuels from Alternative Resources, Western University, 22312 Wonderland Rd. North RR#3, Ilderton, ON, N0M 2A0, Canada

[2] Syncrude Canada Ltd, Edmonton Research Centre, 9421 17th Ave., Edmonton, AB, T6N 1H4, Canada

*Email: *cbriens@uwo.ca*

Abstract – Fluid Coking^{TM} is a process used to upgrade heavy oils, such as bitumen from the oil sands, through thermal cracking. Oil is sprayed in a downward-flowing fluid bed of hot coke particles, where the heavy oil heats up and thermally cracks into smaller vapor molecules. The down-flowing coke particles are then conveyed to a fluid bed burner where they are reheated and conveyed back into the Coker reactor. Not all the liquid that is injected into the Coker is instantaneously vaporized, a portion of the liquid form agglomerates. Agglomerate formation in the Coker needs to be minimized to have better mass and heat transfer. The objective of this study was to determine the impact of fluidization quality and agitation on agglomerate formation and breakup. The research was conducted with a 7.62 cm [3 in] diameter pilot scale Fluid Coking Reactor (FCR). The bed was fluidized with nitrogen (7.87 cm/s) and for some cases, mixed with a very effective mechanical agitator. 1.5 liters of Vacuum Tower Bottoms (VTB) at 220 °C atomized with nitrogen was sprayed into a fluidized bed of 2 kg of sand particles at 530 °C. The bitumen flowrate was around 900 ml/hr. The reactor pressure was controlled at a gauge pressure of 68.9 kPa [10 psig]. At the end of each run the bed of coke and sand was collected; the liquid products were collected and analyzed; and the non-condensable gases were vented. The instantaneous flow of organic vapors leaving the reactor was estimated by measuring the temperature drop along the reactor exhaust pipe, upstream of the condenser. This method was verified and calibrated by varying the VTB flowrate. Increasing the bitumen flowrate reduced the temperature drop. With poor bed agitation, e.g. low fluidization velocity and no mechanical mixing, large deposits would form on the wall and reactor internals, hindering fluidization; furthermore, poor mixing resulted in low liquid yields (around 71 wt.%). For cases where the mechanical agitator was activated during the experimental run, higher liquid yields (77 wt. %) were achieved.

INTRODUCTION

Fluid Coking^{TM} is a process used in industry to crack heavy oils into more useful liquid products. As shown in Fig. 1, oil is sprayed in a downward-flowing fluidized bed of hot coke particles, where it heats up and cracks into smaller vapor molecules (Speight 2006). The down-flowing coke particles are then transported to a fluid bed burner where they are reheated.

Oil vapors are recovered from the downflowing coke particles with steam stripping before the coke particles are conveyed to the burner.

Although the coking reactions are typically fast (Gray et al. 2004), the liquid needs to reach the reactor temperature, and most of the injected liquid is initially trapped

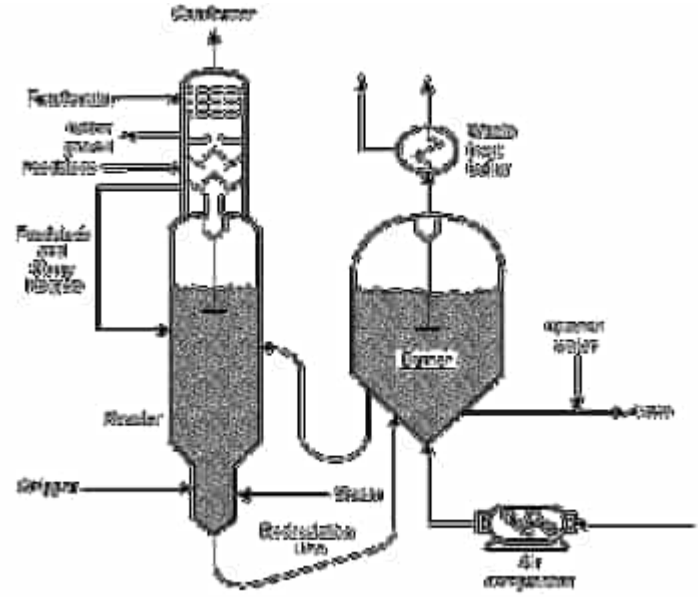

Fig. 1. Schematic diagram of Fluid Coking process

(Farkhondehkavaki 2012) within wet agglomerates ranging from 1 to 20 mm (Gray 2002; Weber et al. 2006; Ali et al. 2010). Because thermal cracking is endothermic, the effective reaction rate of the liquid trapped is dramatically reduced due to heat transfer limitations through the agglomerates (Gray et al. 2004; Peter K. House, Mohammad Saberian, Cedric L. Briens and Chan 2004).

Previous research had shown that enhancing the mixing quality improves the liquid yield in thermal cracking processes and that agglomerate formation in a fluidized bed is detrimental to liquid yields (Stanlick 2014). Widespread formation of agglomerates can lead to fouling of the reactor internals and can cause premature shutdown of the reactor (Sanchez Careaga et al. 2018). Raising the Coker temperature reduces stripper fouling by speeding up the cracking reactions, but also reduces the yield of valuable liquid product, as there is over-cracking of hydrocarbon vapors to permanent gases.

The objective of this study is to monitor the instantaneous hot vapor flow coming out of the reactor, and determine how fluidization quality and agitation affects agglomerates, liquid yield, and liquid quality.

EQUIPMENT, MATERIAL AND METHODS

The study was conducted with a 7.62 cm [3 in] diameter, 59.4 cm [23 ⅜ in] high pilot scale Fluid Coking Reactor (FCR). A schematic of the FCR is shown in Fig. 2.

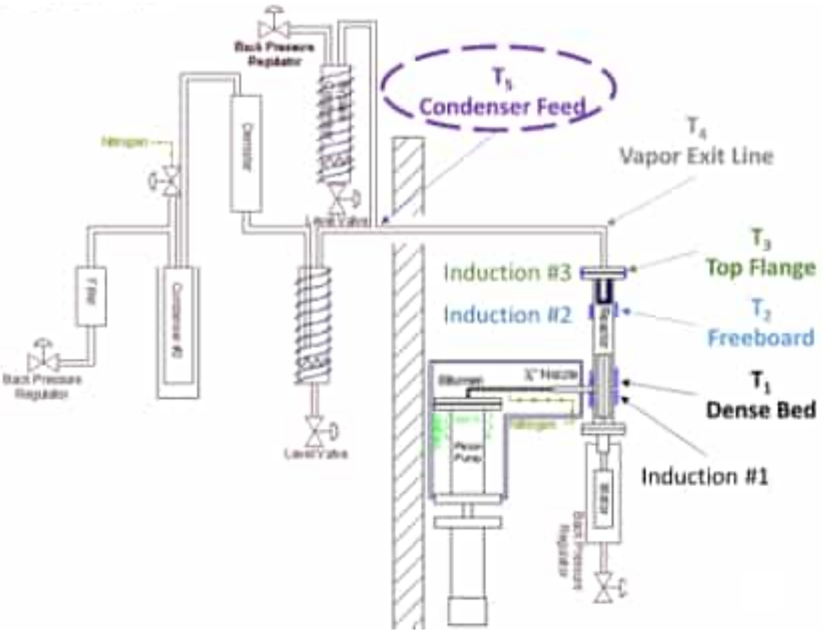

Fig. 2. Fluid coking pilot plant

A bed of sand (2 kg of silica sand with a particle density of 2650 kg/m^3 and a Sauter mean diameter of 190 µm) was fluidized with nitrogen (at a superficial velocity of 4.68 or 7.87 cm/s). In some cases, the bed was mixed with a mechanical agitator that operated 3 s counterclockwise and 3 s clockwise at 120 RPM; preliminary experiments showed that this mode of mixing was very effective. Three induction heaters (2 x 15 kW and 1 x 1 kW) kept the whole reactor at a constant temperature of 530 °C, as measured with Thermocouples T_1, T_2 and T_3 in Fig. 2). 1.5 liters of Vacuum Tower Bottoms (VTB bitumen, provided by Syncrude Canada) was pre-heated in an oven at 220 °C and injected by a displacement pump into the reactor at a maximum feedrate of 1 l/h. A primary condenser condensed most of the vapors, a demister captured any mist entrained by the gas stream and a secondary condenser collected any leftover condensate; finally, a cold filter cleaned the non-condensable gas stream which was vented outside the building. The whole system operated at a constant pressure of 169 kPa [10 psig] controlled with back pressure regulators.

Monitoring the flow of hot vapors exiting the FCR was extremely challenging as the measuring equipment needed to operate at a very high temperature and condensed vapors tended to cause fouling. A simple, fouling-resistant temperature measuring technique was therefore developed and calibrated. It measured the temperature drop along the vapor exit line connecting the reactor exit to the 1st condenser inlet (Fig. 2). Fig. 3 illustrates its principle. Because of the large temperature difference, of about 400 °C, between the vapor coming out of the reactor and the room, there were significant heat losses. Equations (1) and (2) show how the gas and vapor flowrate F can be estimated from the temperature difference ΔT between T_4 and T_5, where C_p is the specific heat capacity. Because the controlling thermal resistance was between the external line wall and the room, heat losses along the pipe can be assumed to be constant.

$$(Heat\ Loses) \approx F\ C_p\ \Delta T \tag{1}$$

$$F \approx f(1\ /\ \Delta T) \tag{2}$$

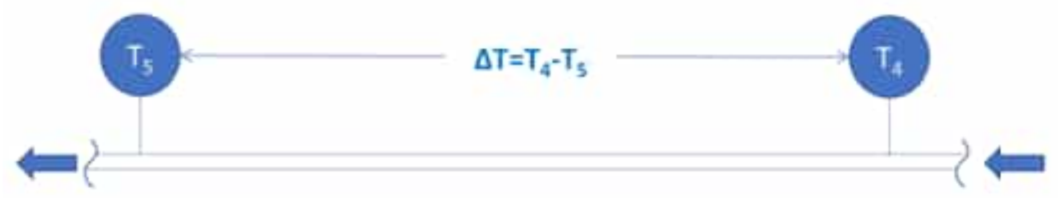

Fig. 3. Vapor flow measurement schematic of the reactor's vapor exit line.

RESULTS AND DISCUSSION

Liquid/Solid Contact and Vapor Measurements

The temperature profile graph of the dense bed (T_1), vapor exit line (T_4) and condenser feed (T_5) are presented in Fig. 4-a. This temperature profile clearly shows that:

- The dense bed could be maintained at a constant temperature for the duration of the run.
- The temperature difference (ΔT) between vapor exit line (T_4) and condenser feed (T_5) clearly increased when the flow of bitumen was reduced from 880 mL/h to 420 mL/h.

Using the temperature difference (ΔT) between vapor exit line (T_4) and condenser feed (T_5) when a steady state in (T_5) was reached (about halfway into each sub-run), a correlation can be made between the flowrate of bitumen fed into the FCR and ΔT as shown in Fig. 4-b). Not all bitumen liquid injected into the FCR converted to vapors, as a significant amount (10-20 wt. %) was transformed into coke that remained in the dense bed of the fluidized reactor. Nevertheless, a very good correlation between the bitumen feedrate and the temperature change was obtained, as shown by Fig. 4-b.

When a large agglomerate was formed, it stored liquid that reacted slowly. When the agglomerate broke up, its liquid was released, reacted and vaporized suddenly, resulting in a momentary increase or "puff" of vapor that was detected by the temperature drop along the condenser line. The formation of larger and wetter agglomerates resulted in larger temperature fluctuations, as such agglomerates tended to survive longer. Fig. 5-a shows that, as the bitumen feed was reduced from 880 mL/h to 420 mL/h, the fluctuations of the condenser feed temperature (T_5) became more pronounced. The variability in T_5 was quantified with its coefficient of variation as presented in Fig. 5-b. As the bitumen feedrate was increased, the superficial velocity of the gas and vapors increased, providing better mixing within the fluidized bed and reducing the formation of large wet agglomerates, which resulted in a smaller coefficient of variation of the condenser inlet temperature.

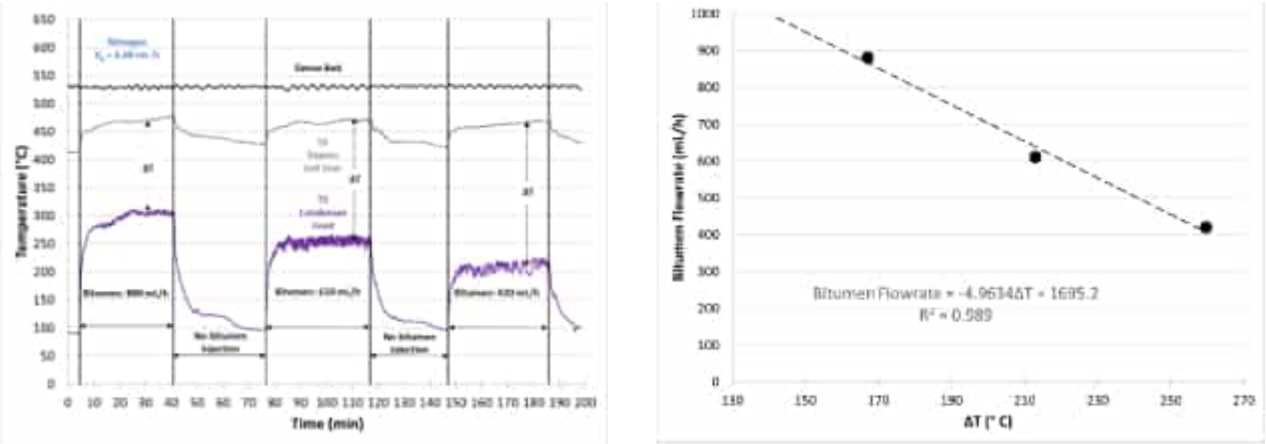

a) b)

Fig. 4.a) Temperature profile in time as a function of bitumen flowrate. b) VTB flowrate as a function of ΔT. Nitrogen V_g = 4.68 cm/s, with three bitumen flowrates 880 mL/h, 610 mL/h and 420 mL/h

$$Bitumen\ Flowrate \approx -4.9634\Delta T + 1695.2 \tag{3}$$

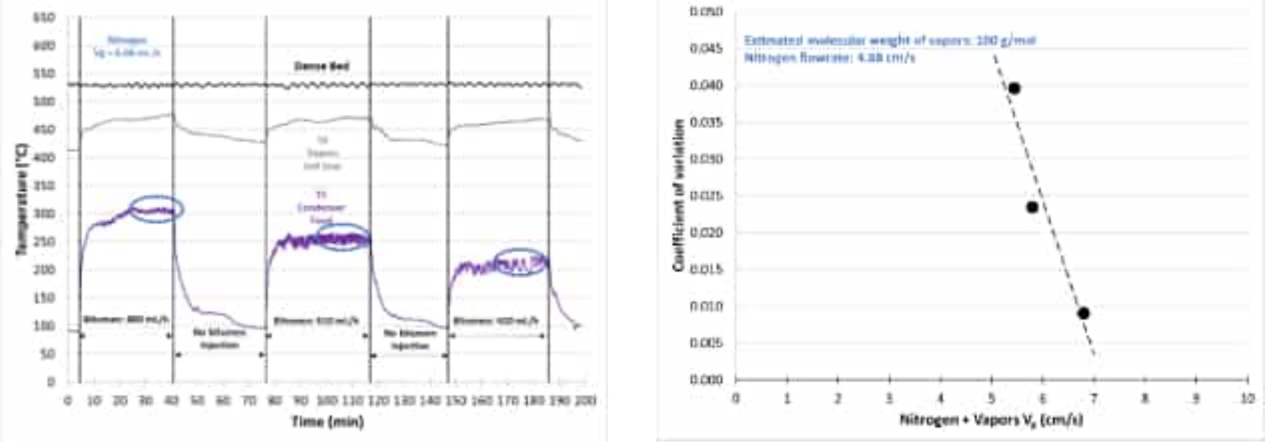

a) b)

Fig. 5 a) Temperature profile in time as a function of bitumen flowrate. b) Coefficient of variation of T_5 as a function of V_g. Nitrogen V_g = 4.68 cm/s, with three bitumen flowrates 880 mL/h, 610 mL/h and 420 mL/h

Effect of Mixing Quality

This section used a mechanical mixer to determine the impact of mixing in the bed on liquid yield and quality.

For both experimental runs in this section, 1530 mL of bitumen was injected into the FCR over about 98 minutes (98.9 minutes when the mixer was ON and 97.5 minutes when the mixer was OFF). The temperature profiles for the condenser feed (T_5) measurements for both operational runs, with the mixer ON and with the mixer OFF are presented in Fig. 6. When the mixer was ON, the temperature T_5 reached steady state smoothly and quickly when compared to the run with the mixer OFF. When the mixer was OFF, there were also strong of fluctuations in the temperature T_5 at the beginning of the run, indicating that large, wet agglomerates were formed until the extra fluidization that the thermal cracking process generated, stabilized the bed and a steady state T_5 was reached, after about 25 minutes.

At steady state, for times greater than 25 minutes, there was an average condenser inlet temperature difference of 7 °C between the two runs (Fig. 6) that, according to Eq. (3), corresponds to a reduction of 35 mL/h (3.4 wt.%) in vapor flowrate when no mixer was used (Table 1).

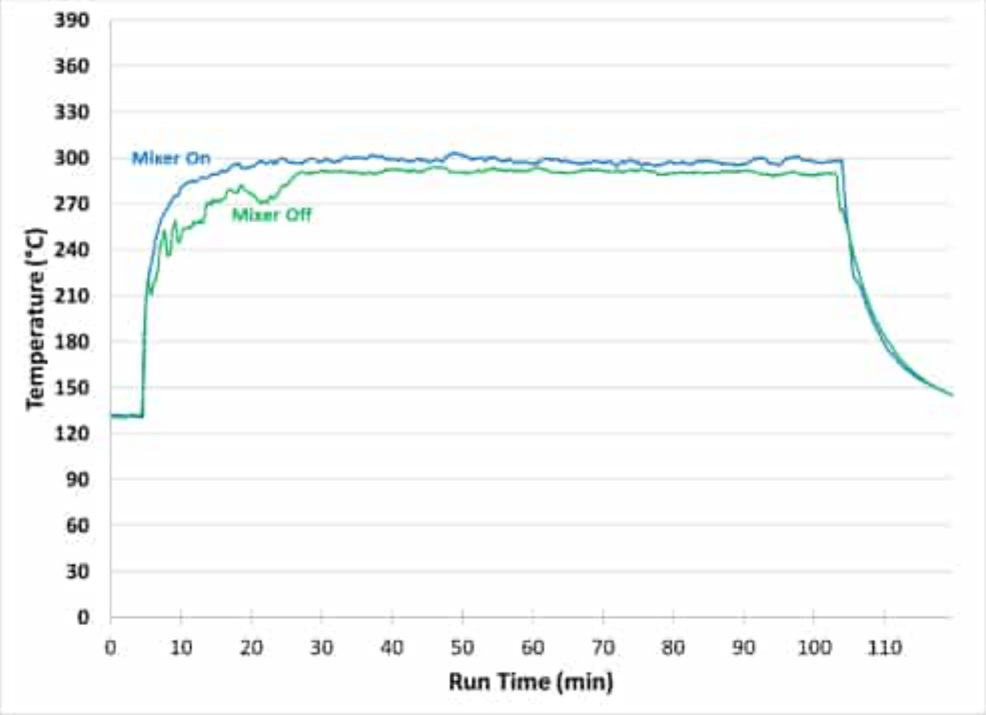

Fig. 6. Condenser feed temperature profile (T_5) comparison between mixer on and mixer off. Nitrogen V_g=7.87 cm/s, bitumen flowrate of 928 mL/h when mixer is ON, and bitumen flowrate of 940 mL/h when mixer is OFF

The liquid yields and viscosity of the runs with and without agitation are presented in Table 1. There is 3.6 wt.% less liquid being collected when the mixer is OFF, which corresponds to the estimate obtained from the difference in condenser inlet temperature. Surprisingly, although more liquid was obtained when the mixer was ON, its liquid was of lower quality than when the mixer was OFF. Liquid vaporization is limited by heat transfer from the hot regions of the bed to the colder, wet regions; the mixer speeded up vaporization by bringing hot particles to the wet regions of the bed. Delaying vaporization allows for additional thermal cracking in the liquid phase.

Table 1. Measured liquid yield and quality as a function of mixing quality

	Liquid Yield (wt. %)	Viscosity (cSt)
Mixer ON	75.6	154
Mixer OFF	72.9	89

It can also be concluded that the 35 mL/h of injected liquid that was not leaving the FCR when the mixer was OFF transformed to solid coke, as it was not detected by the condenser feed temperature thermocouple T_5. Future work involves analyzing the non-condensable gases and solid coke residue to verify these results.

CONCLUSION

The quality of the liquid/solid contact inside the reactor bed can be estimated from the fluctuations in the flow of product vapor, which can be evaluated from the temperature drop along the line connecting the reactor to its condenser.

Improving liquid/solid contact in the fluidized bed resulted in a higher yield of valuable liquid. The liquid was, however, of lower quality.

ACKNOWLEDGMENTS

The authors thank the entire group at the Institute for Chemicals and Fuels from Alternative Resources (ICFAR) at Western University. Special thanks to the University Machine Services (UMS) at Western University. The authors gratefully acknowledge financial support from the NSERC/Syncrude Industrial Research Chair in Fluid Coking Technologies.

NOTATION

F	Flow of vapor, mL/h	T_1	Dense bed temperature, °C
C_p	Specific heat capacity of the vapor, kJ/(kg K)	T_2	Free board temperature, °C
V_g	Superficial gas velocity, cm/s	T_3	Top flange temperature, °C
ΔT	Temperature difference (T4-T5), °C	T_4	Vapors exit line temperature, °C
		T_5	Condenser feed temperature. °C

REFERENCES

Ali M, Courtney M, Boddez L, Gray M. 2010. Coke yield and heat transfer in reaction of liquid-solid agglomerates of Athabasca vacuum residue. Can J Chem Eng. 88(1):48–54. doi:10.1002/cjce.20242.

Farkhondehkavaki M. 2012. Developing Novel Methods to characterize Liquid Dispersion in a Fluidized bed. University of Western Ontario. http://ir.lib.uwo.ca/etd/444.

Gray MR. 2002. Fundamentals of bitumen coking processes analogous to granulations: A critical review. Can J Chem Eng. 80(3):393–401. doi:10.1002/cjce.5450800308. isi:000179832300008.

Gray MR, McCaffrey WC, Huq I, Le T. 2004. Kinetics of Cracking and Devolatilization during Coking of Athabasca Residues. Ind Eng Chem Res. 43(18):5438–5445. doi:10.1021/ie030654r.

Peter K. House, Mohammad Saberian, Cedric L. Briens FB, Chan and E. 2004. Injection of a Liquid Spray into a Fluidized Bed: Particle−Liquid Mixing and Impact on Fluid Coker Yields. Ind Eng Chem Res. 43(18):5663–5669. doi:10.1021/ie034237q.

Sanchez Careaga FJ, Briens C, Berruti F, McMillan J, Gray M. 2018. Agglomerate behavior in a recirculating fluidized bed with sheds: Effect of sheds. Adv Powder Technol. 29(7):1758–1770. doi:10.1016/j.apt.2018.04.011. https://doi.org/10.1016/j.apt.2018.04.011.

Speight JG. 2006. The chemistry and technology of petroleum. Boca Raton: CRC Press/Taylor & Francis.

Stanlick C. 2014. Effects of mixing and vapor residence time on the thermal cracking performance of fluidized beds. The University of Western Ontario. https://ir.lib.uwo.ca/etd/2435/.

Weber S, Briens C, Berruti F, Chan E, Gray M. 2006. Agglomerate stability in fluidized beds of glass beads and silica sand. Powder Technol. 165(3):115–127. doi:10.1016/j.powtec.2006.03.006.

MITIGATION OF FOULING IN A FLUID COKER^{TM}: INFLUENCE OF COLUMN GEOMETRY, INTERNALS AND OPERATING CONDITIONS ON GAS AND PARTICLE BEHAVIOURS IN A COLD FLUIDIZED BED WITH DOWNWARD SOLIDS CIRCULATION

Yohann Cochet[1], Cedric Briens[1*], Franco Berruti[1], Francisco Sanchez Careaga[1], Jennifer McMillan[2]

[1]Institute for Chemicals and Fuels from Alternative Resources, Chemical and Biochemical Engineering, Western University, 22312 Wonderland Rd., Ilderton, ON, N0M 2AO, Canada.
[2]Edmonton Research Centre, Syncrude Canada Ltd., 9421 17th Ave., Edmonton, AB, T6N 1H4, Canada.

*Email: *cbriens@uwo.ca*

Abstract

This paper proposes a new model to infer the hydrocarbon liquid losses in the bottom part of an industrial Fluid Coker by using a room-temperature pilot unit. In Cokers, wet agglomerates that trapped injected bitumen carry unreacted liquid to the stripper. In this study, the effect of lateral bitumen injections, and their impact on superficial gas velocity were simulated with 5 banks of 8 lateral gas injectors, issuing into a fluidized bed with the flux of recirculating coke particles that matched that of the commercial unit. Radioactive simulated agglomerates were tracked to obtain agglomerate trajectories in the bed. O_2 sensors were used to detect the gas Residence Time Distribution (RTD) and the local concentration of a N_2 tracer. These experimental results were used in the model developed to estimate the liquid losses happening in the commercial unit with the hydrodynamic properties studied. The first results obtained highlight the importance of agglomerate rewetting and initial agglomerate properties in order to model properly commercial units. The next stage of the study will be to use the model to quantify how much lateral redistribution of bitumen injection and the addition of a ring baffle can help to mitigate fouling.

Introduction

Fluid Coking^{TM} (Pfeiffer, 1959) provides non-catalytic thermal upgrading of heavy hydrocarbons into distillate products. As shown in Fig. 1(a), Fluid Coking includes two vessels, with coke providing heat for the cracking process by circulating between a fluidized bed reactor and a fluidized bed burner. In the reactor, the distribution of the bitumen injection points along the height leads to a cumulative contribution of the vapors created by cracking. Consequently, the average superficial velocity of the rising gases and vapors ranges from 0.30 m/s to 0.91 m/s (Pfeiffer et al., 1959). Coke particles move down the reactor then circulate, first to the stripper section, and then back to the burner. Fluid Coking^{TM} and its Flexicoking^{TM} variant (Saxton, 1972), upgrade 700 to 750 Thousand Barrels Per Day (kbd) worldwide (Giove and Sciarrabba, 2019 and Chitnis et al., 2013). A major issue in industrial Fluid Cokers is the formation of wet agglomerates of coke particles. Some agglomerates carry liquid to the stripper, causing fouling of stripper sheds (Kamienski et al., 2013) and losses of highly valuable hydrocarbons to the

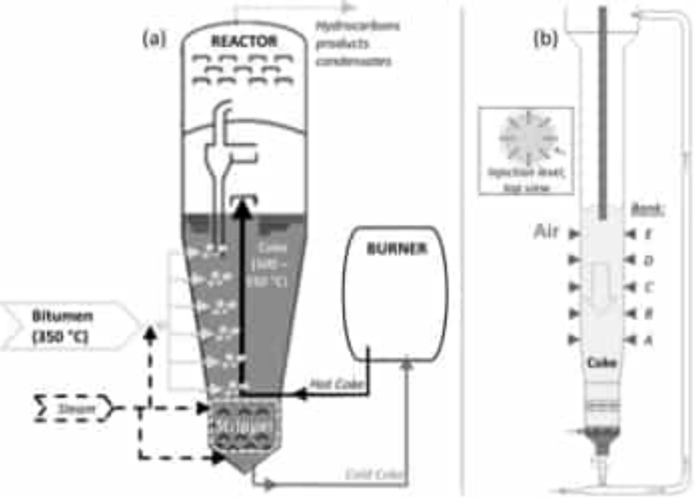

Fig. 1. Fluid coker unit
(a) Industrial unit, (b) Cold model unit

burner. In many cokers, stripper fouling sets the frequency of costly, major maintenance shut-downs. Minimizing liquid carryover to the stripper is a critical process improvement goal.

The objective of this study is to develop a model based on experimental results obtained in a cold scaled-down Fluid Coker model to estimate the liquid content that reaches the stripper in a Fluid Coker and thus develop methods to improve Fluid Coker operation.

Experimental Setup and Measurement Tools

Measurements were performed in a recirculated fluidized bed with a circular cross-section shown in Fig. 1(b). Fluid Coke with a 140 µm Sauter mean diameter and an apparent particle density of 1470 kg/m^3 was used as fluidization media (Sanchez Careaga, 2013). Air fluidized the bed through a sparger located at the bottom of the unit, to simulate the vapors formed by thermal cracking of the injected bitumen (Song et al., 2006) and to recirculate the coke by pneumatic transport. The bed design matched key parameters of industrial Fluid Cokers such as: five banks of eight injectors, a bed height/diameter ratio of 6.33, a tapered geometry and optional baffles located just below an injection bank. As in a typical Coker, the superficial gas velocity increased from 0.30 m/s (through sparger) to 0.91 m/s from bottom to bed surface, through lateral gas injector located along bed height. Phase holdups and velocities are not too sensitive to change in gas and particle properties, so that coke could be used for these room temperature experiments (Song et al, 2006 and Xing et al., 2019). The solids recirculation was set at 0.55 kg/s to match the industrial flux.

The main experimental tool of this study was Radioactive Particle Tracking (RPT). The 14 mm diameter tracer particle was made of radioactive scandium ^{46}Sc coated with epoxy resin. Two different tracers were based on agglomerates recovered commercial Fluid Coker: a “heavy tracer” with a density of 1100 kg/m^3 to simulate wet agglomerates (Sanchez Careaga, 2013) and a “light tracer” with a density of 910 kg/m^3 to simulate the emulsion phase (Tebianian et al., 2015). Twelve NaI(T1) scintillation detectors capture radioactive counts every 12 ms to 25 ms. They were arranged in three layers of four detectors around the bed.

Overview of Proposed Model

The proposed model of a Fluid Coker includes three zones: the jets, the stripper, and the rest of the bed. Agglomerates are formed at the tip of the gas-liquid spray jets (Weber, 2009). The RPT detects the passage of the simulated agglomerate in each formation zone. The initial agglomerate diameter d_{Agg} and liquid to solid ratio $(L/S)_0$ was based on previous measurements (Weber, 2009 and Bhatti, 2017). RPT provided the position of the moving agglomerate at any time, t. Since solid fluxes and gas velocities matched the industrial Coker values, the dimensionless time t/θ was used as scale-up factor, where θ is the mean solids residence time. A shrinking core model predicted bitumen cracking and vaporization (Sanchez Careaga, 2013). In this model, the agglomerate size was assumed constant while the liquid to solid ratio (L/S) decreased as the reaction front progressed inside the agglomerate. From the initial agglomerate properties d_{Agg} and $(L/S)_0$, this model provided the liquid to solid ratio $(L/S)_{St}$ when the agglomerate reached the stripper.

Many agglomerates break up before they reach the stripper, as they interact with gas bubbles (Weber, 2009). The agglomerate breaks up if its yield strength τ_{Agg} is smaller than τ_{Agg}^*. An empirical equation Eq. (1) developed for the pendular state was used to estimate the agglomerate yield strength (Weber, 2009). This might lead to a moderate underestimation, since the agglomerate saturation S_{Agg}, defined as the pore volume occupied by liquid divided by the total void volume of the agglomerate (Sherrington and Oliver, 1980), reached a maximal value of around 60%, equivalent to the funicular state. The equation Eq. (2) to obtain τ_{Agg}^* used a critical Stokes deformation number $St_{def}^* = 0.2$ for wet agglomerates (Tardos et al., 1997).

$$\tau_{Agg} = 8.5\ 10^{12}\ (1000\ \mu_L)^{0.9}\ \left(S_{Agg}\right)^{0.35}\ \left(\pi\ d_{p,SM}\ \gamma_L\right)^2 \tag{1}$$

$$\tau_{Agg}{}^* = \frac{\rho_{Agg}}{8\ St_{def}{}^*}\left(d_{Agg}\ \frac{4.5\ q_b\ d_b}{s_b{}^2}\right)^2 \tag{2}$$

This study used a bitumen viscosity of 3.0 10^{-3} Pa.s and a surface tension of 2.2 10^{-2} N/m (Weber, 2009).

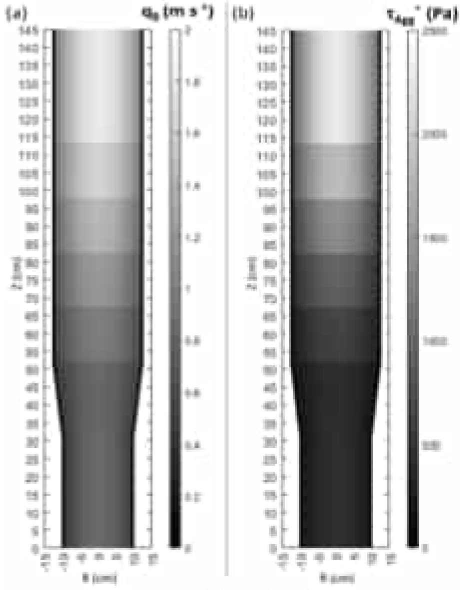

Fig. 2. Empirical bed maps
(a) q_b map, (b) τ_{Agg}^* map

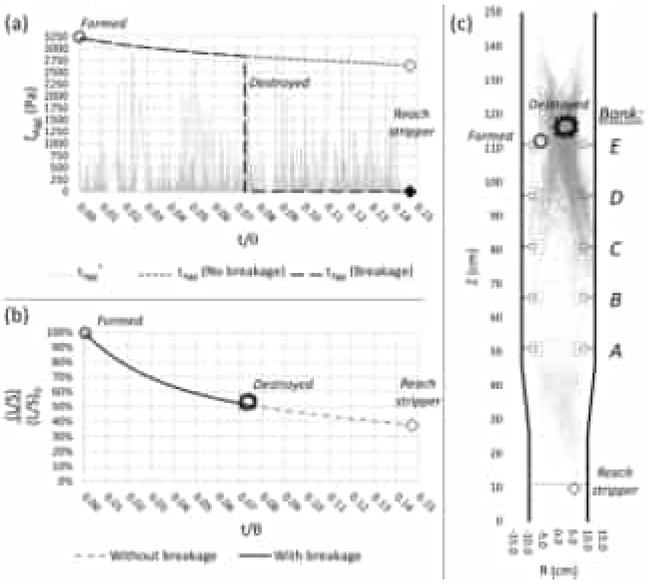

Fig. 3. Model results (with breakage)
(a) Breakage, (b) Liquid content, (c) Trajectory

Due to the high gas velocity used, most of the bed was in the turbulent regime. Consequently, the bubble diameter d_b was assumed to be constant and equal to the maximum bubble size at any point in the bed. Radial profile of bubble gas flux q_b was calculated using typical shape of voidage radial profile (Song et al., 2006) combined with pressure and linear radiation transmission measurements to determine the maximum to minimum voidage ratio at each height. This ratio varies from 1.76 at the bottom to 1.97 at the top. Average flux at a given height was obtained using cross-sectional gas velocity at a given height (from gas mass balance). Bubble separation s_b was calculated by assuming that bubbles in the turbulent regime were locally distributed in a uniform cube geometry.

Fig. 2(a) shows an example of the q_b map obtained and Fig. 2(b) shows the corresponding τ_{Agg}^* map. Variations along the vertical axis are caused by the increase in gas flowrate resulting from lateral gas injections. CFD modeling is being developed to confirm the radial variations (Xing et al., 2019).

Fig. 3 shows the results obtained with the model for a typical agglomerate trajectory. The agglomerate was formed from bank E (Fig. 3c). Fig. 3a shows two curves for this agglomerate: the grey curve shows τ_{Agg}* at each location where the agglomerate is at time t/θ, while the black curve represents τ_{Agg}, and decreases with time as the agglomerate progressively loses liquid due to reaction and vaporization (Fig. 3b shows how the agglomerate liquid content changes with time). According to Fig. 3a, this agglomerate would have reached the stripper if it had not broken up at t/θ of about 0.07, when τ_{Agg} first became smaller than τ_{Agg*} (Fig. 3(a & b)). As shown in Fig. 3(c), the agglomerate first travelled up and down. It was finally carried up to a region of high bubble intensity just above bank E: by then, the agglomerate had lost enough liquid that it could be broken up. In a Coker, an agglomerate

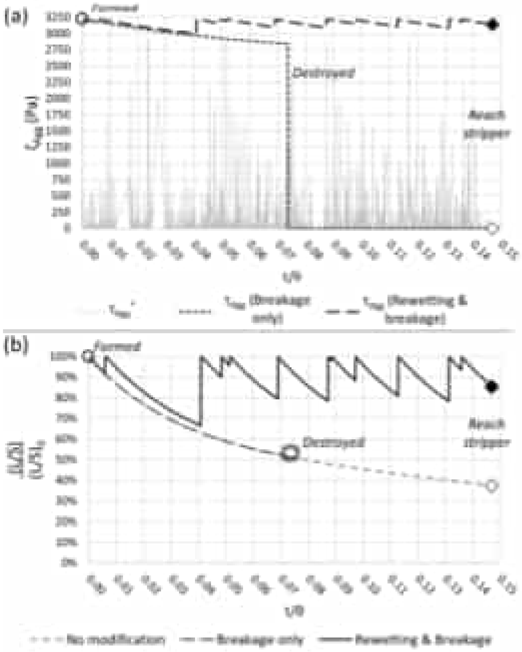

Fig. 4. Model with breakage
(a) Breakage test, (b) Liquid content

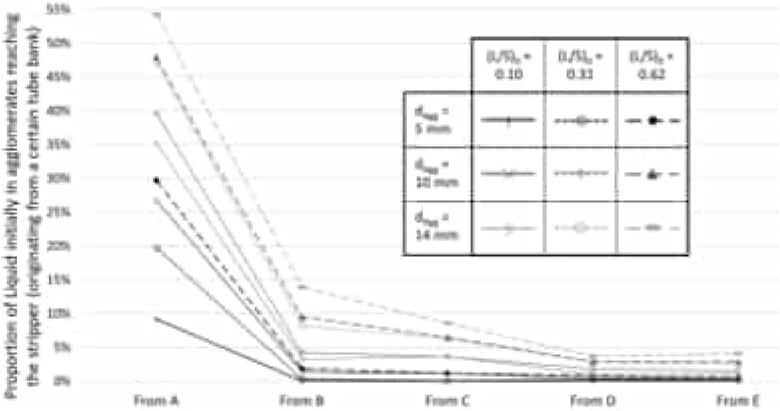

Fig. 5. Weight fraction of liquid initially present agglomerate formed at a certain tube bank with reach the stripper

formed from a jet can enter the same jet or another jet and be rewetted. Using RPT with a heavy tracer, the multiple entries of an agglomerate in jets can be detected in the cold model equipment. Using empirical results from a previous study, rewetting modifies the agglomerate properties: the agglomerate diameter is not modified but the liquid content goes back to its initial $(L/S)_0$ value (Pardo Reyes, 2015). Fig. 4 updates the results shown in Figs. 2 and 3 by considering possible rewetting. Fig. 4(b) shows that rewetting is frequent and has a significant impact on the evolution of the agglomerate liquid content. Another local bed characteristic that can affect agglomerate liquid content is the vapor concentration. The shrinking core model considers only heat transfer and does not include any mass transfer limitations. Yet, in a Fluid Coker, the local concentration of vapor impacts the rate of which the product liquid can evaporate from agglomerates. At this point in the study, only local saturation is not considered. Its study would require the measurement of four parameters: the bubble-emulsion exchange, the radial mixing of bubble gas, the radial mixing of emulsion and the local bubble flux. Item 1 & 2 could be obtained using a nitrogen tracer and oxygen sensors (Yamada, 1992) to measure both the overall bed residence time and the local concentration in the bed. Item 3 & 4 can be obtained using RPT with a light tracer.

Analysis of Results

The unit was operated without a baffle and with the five lateral injection banks injecting the same flowrate of gas. The velocity profile varied between 0.3 m/s and 0.9 m/s as described previously. Fig. 5 shows the effect on the proportion of injected liquid that reaches the stripper of initial agglomerate properties, d_{Agg} and $(L/S)_0$, within the range of these parameters of expected values (Weber, 2009 and Bhatti, 2017). Three agglomerate diameters d_{Agg} are investigated: 5 mm, 10 mm & 14 mm. Three Initial Liquid to Solid Ratios $(L/S)_0$ are also investigated: 0.1, 0.31 & 0.62. Fig. 5 shows that most of the liquid reaching the stripper zone originates from the lowest injection bank (Bank A). As expected, decreasing either the initial liquid content $(L/S)_0$ or the agglomerate size (d_{Agg}) leads to less liquid reaching the stripper.

However, the results presented in Fig. 5 assumed that each bank produced agglomerates with the same range of properties. In practice, initial agglomerate properties are not constant. Past studies (Li, 2016) studied the impact of local bed hydrodynamics on how much of injected liquid is captured by an agglomerate of size d_{Agg}. Table 1 shows these experimental results.

Table 1. Weight fraction of liquid injected captured by agglomerates, for a given U_g below the jet.

		U_g below the jet (m/s)				
		Bank A	***Bank B***	***Bank C***	***Bank D***	***Bank E***
		0.20	***0.34***	***0.48***	***0.63***	***0.77***
d_{Agg} (mm)	***14***	*1.3%*	*1.0%*	*0.7%*	*0.5%*	*0.4%*
	10	*2.5%*	*2.0%*	*1.4%*	*1.0%*	*0.8%*
	5	*15.4%*	*13.8%*	*11.7%*	*12.1%*	*9.6%*

The same study showed that $(L/S)_0$ does not vary with d_{Agg} or the local bed hydrodynamics in the range used in our work. After correcting experimental results obtained for sand-water to apply them with coke-bitumen, the results of Fig. 5 were updated and combined. The resulting Fig. 6 shows the overall liquid for the bed, for $(L/S)_0 = 0.22$ (chosen to match corrected experimental data from Li et al., 2016) and 3 agglomerate sizes combined (d_{Agg} = 5, 10 & 14 mm). The impact of bank A on the overall liquid losses becomes even more critical.

Fig. 7 shows the impact of agglomerate size and initial liquid content on the resistance to breakage. Fig. 7(a) shows that decreasing agglomerate size from 14 mm to 10 mm does not impact breakage, but decreasing the agglomerate size from 10 mm to 5 mm increases breakage dramatically. It is not due to shear, but to the much faster reaction rate with the smallest diameter, leading to full drying of the agglomerate before it can be rewetted in a jet. Fig 7(b) shows that decreasing $(L/S)_0$ promote breakage, as drier agglomerates are easier to break up.

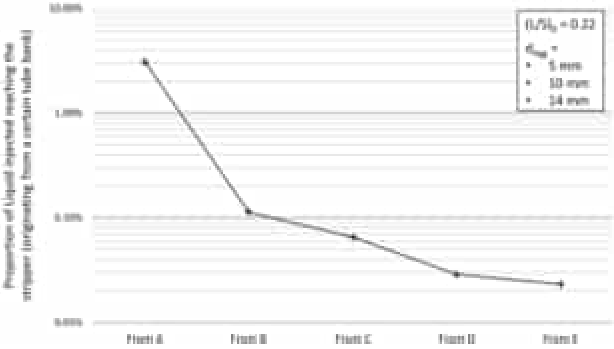

Fig. 6. Weight fraction of liquid injected in a certain tube bank which reach the stripper

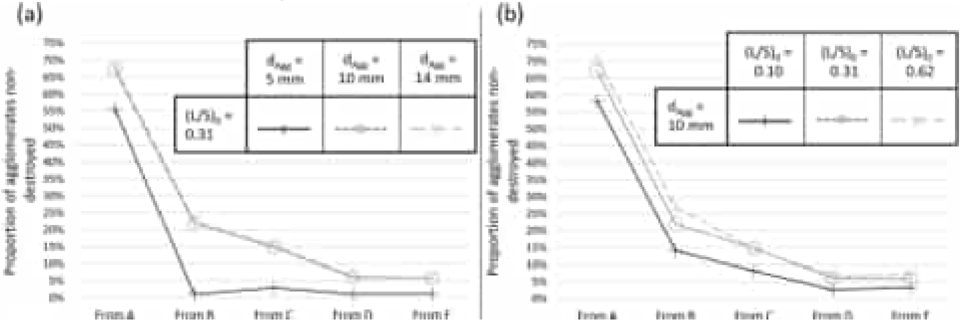

Fig. 7. Initial agglomerate property effect on agglomerate breakage
(a) Effect of d_{Agg}, (b) Effect of $(L/S)_0$

The impact of rewetting was investigated: when included in the model, the overall liquid losses to stripper are multiplied by 1.5. Fig. 8 shows the repartition of the liquid losses to stripper as a function of the original formation bank and the last rewetting location. Bank A, the lowest bank, is the main source of last rewetting before agglomerates reach the stripper: agglomerates formed in higher banks carry liquid to the stripper only due to this rewetting. It suggests that optimizing jets performances in this bank is crucial to mitigate the amount of liquid recaptured by rewetting.

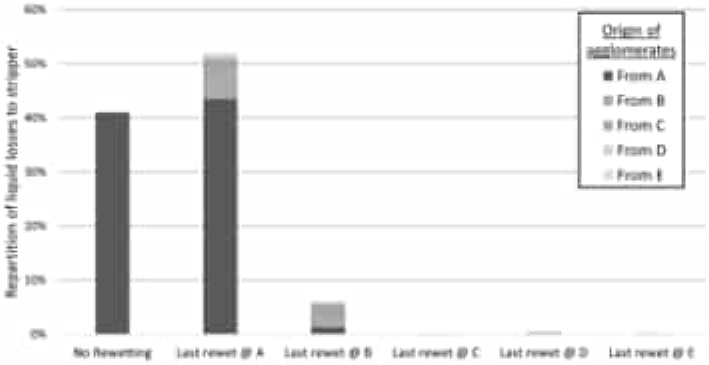

Fig. 8. Repartition of liquid losses to stripper: impact of rewetting from each tube bank

Conclusion

The empirical model presented in this study used experimental results obtained in a cold pilot unit to predict the amount of liquid reaching the stripper of industrial Fluid Cokers. The results show how the initial properties of the agglomerates formed in spray jets can affect the amount of liquid reaching the stripper. It demonstrates the critical importance of lower bank spray jets in liquid losses. Moreover, rewetting proved to be crucial: more than half of the liquid losses go through rewetting (mostly in the lower bank spray jets).

This study suggests that the amount of liquid reaching the stripper could be reduced by focusing on the agglomerates formed in the lowest banks. This could be achieved by rerouting atomization gas to improve liquid distribution from these nozzles or reducing the flowrate of liquid to these banks. Local bed hydrodynamics could also be modified with internals or rerouting of liquid between banks to promote agglomerate breakup and/or reduce bypassing of agglomerates from the lower banks to the stripper. These possible solutions will be investigated in the cold model and, eventually, verified in a hot pilot plant.

Notation

d_{Agg}	Agglomerate diameter, m	t_0	Agglomerate formation time, s
d_b	Bubble diameter, m	t_C	Agglomerate full conversion time, s
$d_{p,Sm}$	Coke Sauter-mean diameter, m	T_B	Fluidized bed temperature, K
C_p	Bitumen heat capacity, J kg^{-1} K^{-1}	T_R	Reaction front temperature, K
k	Coke thermal conductivity, W m^{-1} K^{-1}	u_b	Local bubble velocity, m s^{-1}
(L/S)	Liquid to dry solid mass ratio	V_{loc}	Local volume, m^3
$(L/S)_0$	(L/S) @ formation	γ	Liquid surface tension, N m^{-1}
$(L/S)_{Rw}$	(L/S) after rewetting	$\dot{\gamma}$	Local fluidized bed shear rate, s^{-1}
$(L/S)_{St}$	(L/S) @ stripper	$\varepsilon_{L,Agg}$	Agglomerate liquid volume fraction
m_L	Mass of liquid in agglomerate, kg	$\varepsilon_{S,Agg}$	Agglomerate solid volume fraction
m_S	Mass of solid in agglomerate, kg	ΔH_{Liq}	Liq. vaporization enthalpy @ T_B, J kg^{-1}
N_b	Local number of bubbles	Δt_{F-S}	Agg. formation-to-stripper time, s
P_V	Local vapor pressure^2, Pa	η	Normalized reaction front radius
P_V^{Sat}	Local saturated vapor pressure, Pa	θ	Mean solids residence time in unit, s
q_b	Local flux of bubbles, m_{GAS}^3 s^{-1} m^{-2}	μ_L	Liquid (Bitumen) viscosity, Pa s
r_{Agg}	Agglomerate diameter, m	ρ_{Agg}	Agglomerate density, kg m^{-3}
r_b	Bubble radius, m	ρ_S	Solid (Coke) density, kg m^{-3}
S_{Agg}	Agglomerate saturation	ρ_L	Liquid (Bitumen) density, kg m^{-3}
s_b	Bubble separation distance, m	τ_{Agg}	Agglomerate yield strength, Pa
St_{def}^*	Critical Stokes deformation number	τ_{Agg}^*	Critical agglomerate yield strength, Pa

Acknowledgements

The author gratefully acknowledges funding from the NSERC/Syncrude Industrial Research Chair in Fluid Coking Technologies.

References

Bhatti. 2017. Study of motion of Agglomerates through a Fluidized Bed. Western University.

Chitnis, Brady, et al. 2013. Flexicoking^{TM} Resid Upgrading Technology. In: Refining India. New Delhi, India.

Giove, Sciarrabba. 2019. Bitumen & Heavy Oil Upgraders - Bitumen Production. Oil Sands Mag. *https://www.oilsandsmagazine.com/projects/bitumen-upgraders* [07/05/2019].

Kamienski, Zhao, et al. 2013. Flexicoking^{TM} Resid. Upgrading Technology. In: 11th International BBTC Conference. Dubrovnik, Croatia.

Li. 2016. Effect of Local Bed Hydrodynamics on the Distribution of Liquid in a Fluidized Bed. Western University .

Pardo Reyes. 2015. Effect of Temperature and Successive Sprays on Liquid Distribution in Fluidized Beds. Western University .

Pfeiffer, Borey, et al. 07 /04/1959. Fluid coking of heavy hydrocarbons. *US 2881130 A*.

Sanchez Careaga. 2013. Hydrodynamics in Recirculating Fluidized Bed Mimicking the Stripper Section of the Fluid Coker. Western University.

Saxton. 09/05/1972. Fluid coking process incorporating gasification of product ore. *US 3661543 A*.

Sherrington, Oliver. 1980. Granulation. John Wiley & Sons, Ltd. (Monographs in Powder Science and Technology). ISBN: *9780471260196*.

Song, Grace, et al. 2006. Experimental Simulation of the Reactor Section of Fluid Cokers : Comparison of FCC and Fluid Coke Particles. Can J Chem Eng. 84(2):161–169. doi:*10.1002/cjce.5450840203*.

Tardos, Khan, et al. 1997. Critical parameters and limiting conditions in binder granulation of fine powders. Powder Technol. 94(3):245–258. doi:*10.1016/S0032-5910(97)03321-4*.

Tebianian, Dubrawski, et al. 2015. Investigation of particle velocity in FCC gas-fluidized beds based on different measurement techniques. Chem Eng Sci. 127:310–322. doi:*10.1016/j.ces.2015.01.049*.

Weber. 2009. Agglomerate stability in fluidized beds. Western University.

Xing, Briens, et al. 2019. Effects of the distributor and baffle on the hydrodynamic performance of a bubbling fluidized bed. In: Fluidization XVI.

MODELING OF SORBENT ENHANCED GASIFICATION UTILIZING WASTE-DERIVED FUEL

Antti Pitkäoja[1], Jouni Ritvanen[1], Selina Hafner[2], Timo Hyppänen[1] and G¿nter Scheffknecht[2]

[1] *LUT School of Energy Systems, Lappeenranta-Lahti University of Technology,*
Yliopistonkatu 34, PO. Box 20, FI-53851 Lappeenranta, Finland
[2] *Institute of Combustion and Power Plant Technology (IFK), University of Stuttgart,*
Pfaffenwaldring 23, 70569 Stuttgart, Germany

*Email: *antti.pitkaoja@lut.fi*

Abstract

EU strategy for transition to a low-carbon economy sets out a framework and mechanisms to address climate change. A target of 14% renewable fuels usage in the transportation sector by 2030 has been set and, consequently, there is a pressing need to develop effective and cost-efficient ways to produce transportation fuels from renewable sources. Efficient use of existing resources such as a low value waste reduces needs of fresh resources and reduces consumption of non-renewable sources. Dimethyl ether (DME) is an alternative fuel for the transportation sector, when the DME is produced from the renewable feedstock. Sorbent enhanced gasification (SEG) is a promising technology for replacing conventional gasification processes on DME production. Operating conditions of the SEG reactor can be altered by adjusting bed material CO_2 capture in the reactor, which enhances the water-gas shift reaction to yield more H_2. The adjustable CO_2 capture enable altering the process conditions in such way that the producer gas of the reactor is directly suitable for the DME synthesis, which allows reducing the number of post-refining steps compared to the conventional DME production line. The SEG process has been demonstrated at pilot scale. A 1D bubbling fluidized bed (BFB) gasification reactor model developed for the pilot SEG process is utilized for simulation of waste-derived fuel. Empirical equations for local gas-solid interaction and gasification chemistry have been employed in the model. Process conditions at the bubbling bed and the freeboard sections of the gasification reactor are estimated with the developed model. The modeling results compared against experimental investigations of $200kW_{th}$ dual fluidized bed facility are with good agreement. The conducted model validation improved understanding of bed material behavior, gasification chemistry and hydrodynamics and their role in SEG reactors under waste gasification conditions.

Introduction

The Paris climate agreement sets out a framework for EU strategy to transition to low-carbon economy to address climate change. The aim of the EU strategy is to keep average global warming below 2°C compared to the pre-industrial temperatures (Delbeke and Vis, 2016). A target of 14% renewable fuels usage in the transportation sector by 2030 has been set and, consequently, there is a pressing need to develop effective and cost-efficient ways to produce transportation fuels from renewable sources. Efficient use of existing resources such as a low value waste reduces needs of fresh resources and reduces consumption of non-renewable sources. Greenhouse gas emissions from transportation account for almost one quarter of Europeôs greenhouse gas emissions and transportation is the main source of air pollution in European cities (European commission, 2016). The majority of emissions from traditional liquid fuels comprises CO_2, NO_X and small particulate emissions. However, gaseous fuels such as dimethyl ether (DME) are free from small particle emissions, which makes them as attractive alternative.

Indirect gasification comprises two interconnected reactors with continuous exchange of material flows. In sorbent enhanced gasification (SEG) reactive bed material is circulated between the reactors. Limestone is commonly used as the bed material and the limestone is carbonated in the gasifier with CO_2 formed in the gasification process and calcined in the combustion reactor. The producer gas of the gasifier can be tailored by changing CO_2 capture of the bed, which influences the yield of the water-gas shift reaction at lower operating temperatures. Typical operation range for the SEG reactor is between 600-800°C. Feedstock gas of DME synthesis requires certain composition from the producer gas that can be achieved with a certain operating temperature. The capability to tailor the producer gas facilitates flexible use of various solid feedstocks with varying properties.

A 1D BFB gasification model for biomass SEG process has been developed in Pitkäoja et al. (2020). The previously published model is improved to take into account heavy hydrocarbons. The improved model is used to simulate SEG process operating with waste-derived fuel. The purpose of model validation is to provide a better understanding of phenomena and their role in the SEG process, which can be applied for predicting operation of process under different conditions. The validation of the model is carried out with steady-state simulations against experimental data published by Hafner et al. (2020) from a dual fluidized bed facility located at the Institute of Combustion and Power Plant Technology (IFK) of the University of Stuttgart.

Model Description

The model frame for the BFB SEG process has been developed based on a semi-empirical 1D-approach in Pitkäoja et al. (2020). Fundamental conservation equations for mass and energy for gas and solid phases are implemented in the gasification model frame. The model frame is implemented in Matlabôs Simulink environment, where reactor code is resolved using Simulinkôs embedded computational engine. Spatial derivatives of the reactor model are discretized using a first order upwind scheme for convection terms and time derivatives are resolved using an explicit solver in Simulink. A hydrodynamic model was previously derived in Pitkäoja et al. (2020) based on Kunii and Levenspiel (1991). Heavy hydrocarbons ñTarsò were not included in this previous model frame. To model appropriate elemental distribution of the producer gas, it is important to also consider the heavy hydrocarbons. In the current study, the existing model frame is further developed to take into account the heavy hydrocarbon fractions by using a model component. Additional balance was added in the model for the heavy hydrocarbons. The model component for the heavy fractions was selected as C_8H_{10} and C_2H_4 for the light hydrocarbons based on biomass studies. The hydrocarbons (C_2 and C_8) are assumed to be inert gas species only affecting the elemental distribution. The decomposition of the fuel as permanent gases and hydrocarbons is according to following chemical equation:

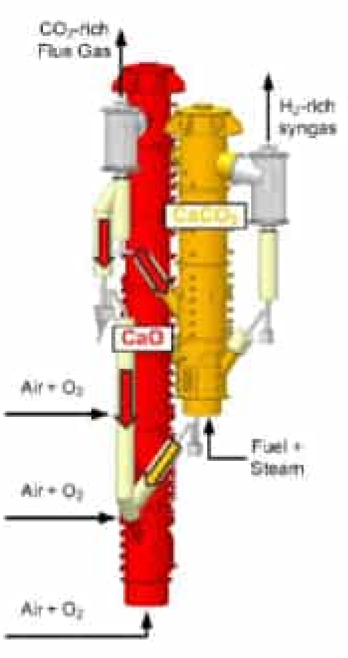

Fig. 1. 200 kWth dual fluidized bed facility at IFK, University of Stuttgart (Hafner et al., 2018).

$$FUEL \rightarrow NH_3 + H_2S + CO + CO_2 + CH_4 + C_2H_4 + C_8H_{10} + H_2 \tag{1}$$

Chemical reactions are modeled according to Table 1. A detailed discussion about the chemical reactions is provided in Pitkäoja et al. (2020).

Modelling Setup

Modelling setup is done based on the specification of the pilot gasifier. Only the gasifier is modelled. The facility including gasifier (yellow) and combustor (red) is shown in Fig. 1. For modelling, the gasifier is divided into 40 discrete elements from which 3 were placed on the conical bottom.

Experimental investigations were conducted by Hafner et al. (2020). Two similar batches of waste pellets were used in experiments and characterization of the fuel is provided in Table 2. The gasifier was operated with constant operational parameters that are summarized in Table 3. Simulation boundary conditions, which are summarized in Table 3, were determined from online process measurements and samples of solid material extracted from loop seals. Maximum solid conversion for calcium carbonate is selected as 30m-% based on previous studies on calcium looping process (Ylätalo, 2013).

Table 1. Chemical reactions.

Reaction	Chemical equation	*H* (at 25°C) [J/kg]	Ref
Boudouard	$C(s)+CO_2(g) \rightarrow 2CO(g)$	172400	van den Aarsen et al. (1985)
Water-gas	$C(s)+H_2O(g) \rightarrow H_2(g)+CO(g)$	131300	Nandi and Onischak (1985)
Methanation	$C(s)+2H_2(g) \rightarrow CH_4(g)$	-75000	Hejazi et al. (2017)
Water-gas shift	$CO(g)+H_2O(g) \rightleftharpoons CO_2(g)+H_2(g)$	-41100	Biba et al. (1978)
Steam methane reforming	$CH_4(g)+H_2O(g) \rightleftharpoons CO(g)+H_2(g)$	206200	Jones and Lindstedt (1988)
Calcination	$CaCO_3(s) \rightarrow CaO(s)+CO_2(g)$	178300	Martinez (2012)
Carbonation	$CaO(s)+CO_2(g) \rightarrow CaCO_3(s)$	-178300	Alonso et al. (2009), Shimizu et al. (1999)
Sulphation	$CaO(s)+SO_2(g)+0.5O_2(g) \rightarrow CaSO_4(s)$	-502100	Rajan and Wen (1980)
De-sulphation	$CaSO_4(s)+CO(g) \rightarrow CaO(s)+SO_2(g)+CO_2(g)$	219200	Myöhänen (2011)
Direct sulphation	$CaCO_3(s)+SO_2(g)+0.5O_2(g) \rightarrow CaSO_4(s)+CO_2(g)$	-323800	Myöhänen (2011)

Table 2. Chemical composition of two batches of pellets used in experimental investigations of the SEG process.

Batch	Proximate analysis				Ultimate analysis					
	Moisture	Ash	Volatiles	Fixed carbon	C	H	N	S	Cl	LHV
	m-%, ar	m-%, ds			m-%, daf					MJ/kg, ar
1	8.0	33.2	60.2	6.7	53.9	6.4	2.5	0.6	1.0	11.6
2	10.7	26.2	65.4	8.4	51.6	6.7	2.6	0.6	1.0	12.7

Simulation Results

Validation of the developed reactor model was conducted by introducing the measured operation parameters into the model with appropriate model equations for physical and chemical phenomena. Model equations for chemical reactions were used according to Table 1. Hydrocarbons that were measured from the gasifier were mainly assumed to form during devolatilization (Neves et al., 2011). The devolatilization yield for hydrocarbons were set according to this assumption. Heaviest hydrocarbons were set according to tar measurement (Hafner et al., 2020) and light hydrocarbons according to CH_4 yield of the gasifier. Hydrodynamics scheme is described in details in Pitkäoja et al. (2020). The hydrodynamics scheme was set against pressure measurements of the reactor.

Experimental and simulated temperature profiles are shown in Fig. 2 a). Good match was gained between the simulations and experimental temperatures. A heat source term was applied for the reactor bed to match local temperatures. The heat balance adjustment according to Table 3 is applied for the bed of the gasifier. A constant heat loss was applied at the freeboard in each simulations case. The freeboard heat loss is included in the energy balance adjustment. The approach was used to compensate impacts of uncertainties, such as devolatilization process, solid flow measurement and temperature measurements in the energy balance. A suitable match for temperatures between the simulations and measurements in the bed section is important for model validation, since chemical kinetics are influenced by the local temperature.

The measured producer gas composition against simulation results is shown in Fig. 2 b)-f). Good agreement between the measured producer gas composition and the simulation was achieved at higher temperatures. The model prediction capability on the higher temperatures is more important, since optimal gas composition for DME synthesis is achieved at higher operating temperatures. The relation of gas species is described with module:

$$M = (y_{H_2} - y_{CO_2})/(y_{CO} + y_{CO_2}) \tag{2}$$

The optimal value of the module for DME synthesis is 2 (Hafner et al., 2018), which is achieved at operating temperatures similar to OP 1.3, which is shown in Fig. 2 g).

Table 3. Experimental operation conditions and simulation boundary conditions.

Parameter	OP 1.1	OP 1.2	OP 1.3
Experimental operation conditions			
Fuel feed [kg/h]	45	30	30
Primary gas [kg/h]	30	20	20
Primary gas temperature [°C]		146	
S/C [mol/mol]		1.5	
Fuel batch	1	2	2
Solid make-up to gasifier/combustor [kg/h]	20/0	0/20	0/20
Simulation boundary conditions			
Solid flow from combustor [kg/h]	430	370	520
Temperature of solid flow [°C]	760	770	810
Solid make-up to gasifier ($CaCO_3$)	20	0	0
Material mass fractions at circulation inlet [%]			
CaO	85.4	84.0	65.7
$CaCO_3$	0.5	0.3	0.0
$CaSO_4$	0.0	0.0	0.0
Ash	14.1	15.8	34.3
Solid heat capacity [J/(kg K)]	1000		
Heat balance adjustment [kW/kW_{fuel}]	14.1	15.8	15.8
Heat loss of freeboard [kW/m]	1.5	1.2	1.2

Common for steam gasification processes such as SEG is a low wet CO_2 partial pressure in the reactor. The SEG reactor is operated as carbonator, where the CO_2 is captured by the CaO of the bed material. The low CO_2 partial pressure with reactive bed material produces special operation characteristics for the SEG process, where the gasification process is enhanced by the reactive bed material. The bed material carbonation was measured for each operation point from the pilot process, and in Fig. 2 h), the simulated carbonation is compared against the measurement. Thermodynamic reaction equilibrium according to Stanmore and Gilot (2005) was shifted towards calcination 22°C according to limestone equilibrium modification of Pitkäoja et al (2020). Actual limestone does not follow exactly the theoretical reaction equilibrium in real process conditions because of impurities of the limestone. This remark can be determined from measurements of Hajaligol et al.(1988). The reaction equilibrium plays an important role in the pilot reactor, since the bed of the pilot reactor operates close by the equilibrium, which causes the temperature to govern the carbonation reaction in the bed. Four solid material fractions (CaO, $CaCO_3$, $CaSO_4$ and ash) were included in simulations and material fraction profiles were modelled for each fraction with separate balances for wake and emulsion in the bed. In the pilot reactor high in-bed solid mixing is induced by pilot reactor design, which evens differences in the solid material fractions on vertical direction of the dense bed, which is shown in Fig. 2 i) for $CaCO_3$. The high mixing of solids causes the bed to behave as ideally mixed bed without significant material fraction differences.

Conclusions

Validation of the 1D BFB gasification model was done at steady-state conditions for a waste-derived fuel. The model was able to capture the most important characteristics of the SEG process and an influence of hydrocarbons to the elemental distribution was considered. The improved model was capable of predicting temperature profiles, bed material conversion and producer gas composition at higher operating temperatures, which is more important than prediction capability of lower operating temperatures, since producer gas composition at higher temperatures is favourable for DME synthesis.

Model validation provided detailed information regarding different phenomena. The current understanding of bed material behaviour in the reactor was improved. Reaction kinetics and reaction equilibrium were included in the model to take into account reversibility of carbonation and calcination. The reaction equilibrium between the two reactions played an important role, since the bed of the gasifier operated close by the reaction equilibrium. At particular operation conditions the process temperature was governing the quantity of carbonation.

The modeling results compared against the measurements show a good agreement. However, further refinement and comprehensive validation of the gasification model with additional data from the pilot reactor is required.

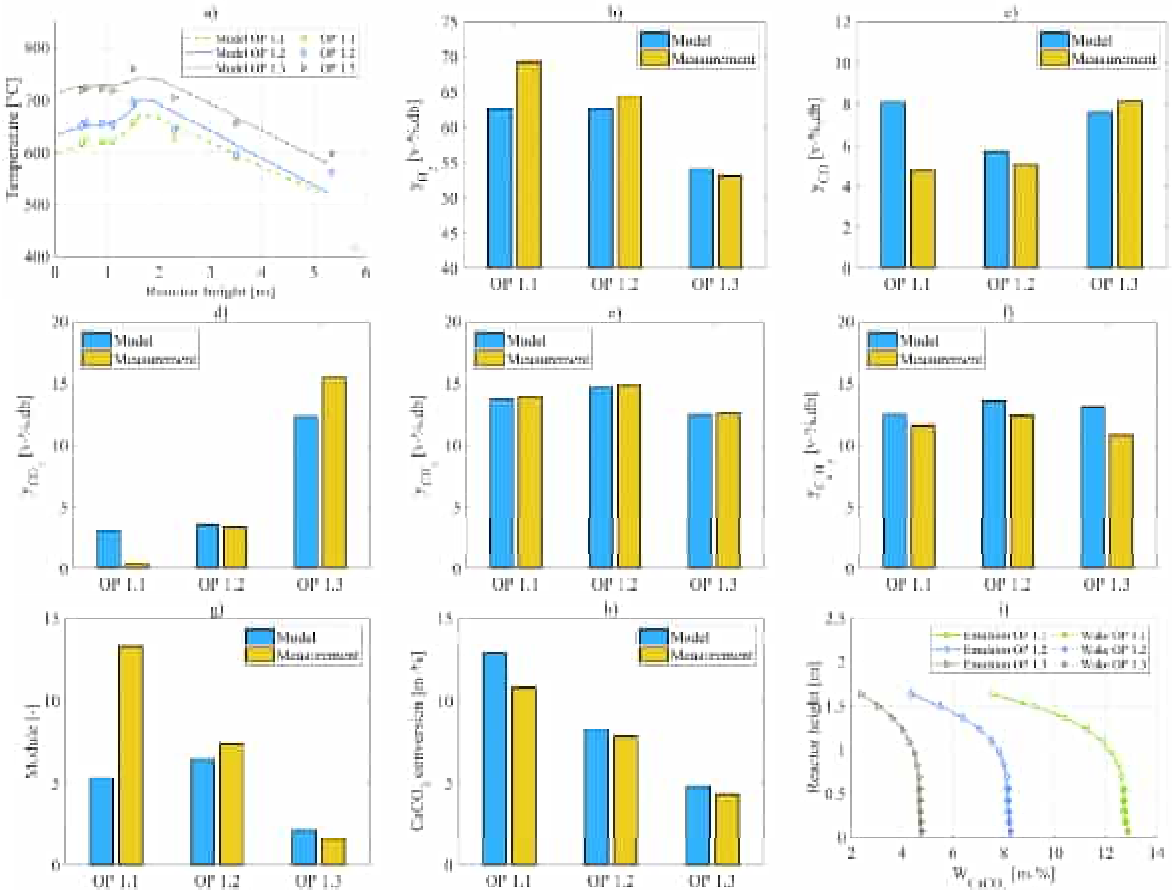

Fig. 2. Simulation results. (a) Simulated temperature profiles and process measurements from the pilot gasifier, (b) H_2, (c) CO, (d) CO_2, (e) CH_4, and (f) C_xH_y volume fractions of producer gas are shown, (g) Module of producer gas is shown. Producer gas volume fractions are presented as N_2, NH_3, H_2S and tar free and dry basis, (h) Bed material conversion in the gasifier from CaO to $CaCO_3$ is shown. The bed material conversion was determined from solid samples extracted from loop seals. The conversion is calculated as difference of $CaCO_3$ mass fractions, (i) Local material fractions for $CaCO_3$ below bed material feeding point is shown.

Acknowledgement

This work in FLEDGED project has received funding from the European Unionôs Horizon 2020 research and innovation programme under grant agreement No 727600.

References

Alonso, M., Rodríguez, N., Grasa, G., Abanades, J.C., 2009. Modelling of a fluidized bed carbonator reactor to capture CO2 from a combustion flue gas. Chem. Eng. Sci. 64, 883ï 891. https://doi.org/10.1016/J.CES.2008.10.044

Biba, V., Macák, J., Klose, E., Malecha, J., 1978. Mathematical Model for the Gasification of Coal under Pressure. Ind. Eng. Chem. Process Des. Dev. 17, 92ï 98.

Delbeke, J., Vis, P., 2016. EU climate policy explained [WWW Document]. URL https://ec.europa.eu/clima/sites/clima/files/eu_climate_policy_explained_en.pdf

European commission, 2016. A European Strategy for Low-Emission Mobility [WWW Document]. URL https://ec.europa.eu/transparency/regdoc/rep/1/2016/EN/1-2016-501-EN-F1-1.PDF

Hafner, S., Schmid, M., Scheffknecht, G., 2020. Investigation of the Sorption Enhanced Gasification Process in a Dual Fluidized Bed Pilot Plant Using a Waste-Derived Fuel. Proceeding 13th Int. Conf. Fluid. Bed Technol.

Hafner, S., Spörl, R., Scheffknecht, G., 2018. Sorption Enhanced Gasification;: Process validation and investigations on the syngas composition in a 200 kW th dual fluidized bed facility. 23rd Int. Conf. Fluid. Bed Convers. 826ï 832.

Hajaligol, M.R., Longwell, J.P., Sarofim, A.F., 1988. Analysis and Modeling of the Direct Sulfation of CaCO3. Ind. Eng. Chem. Res. 27, 2203ï 2210.

Hejazi, B., Grace, J.R., Bi, X., Mahecha-Botero, A., 2017. Kinetic Model of Steam Gasification of Biomass in a Bubbling Fluidized Bed Reactor. Energy and Fuels 31, 1702ï 1711.

Jones, W.P., Lindstedt, R.P., 1988. Global reaction schemes for hydrocarbon combustion. Combust. Flame 73, 233ï 249. https://doi.org/10.1016/0010-2180(88)90021-1

Kunii, D., Levenspiel, O., 1991. Fluidization engineering, 2nd ed. Butterwoth-Heinemann.

Martínez, I., Grasa, G., Murillo, R., Arias, B., Abanades, J.C., 2012. Kinetics of calcination of partially carbonated particles in a Ca-looping system for CO2 capture. Energy and Fuels 26, 1432ï 1440. https://doi.org/10.1021/ef201525k

Myöhanen, K., 2011. Modelling of Combustion and Sorbent Reactions in Three-Dimensional Flow Environment of a Circulating Fluidized Bed Furnace. Acta Universitatis Lappeenrantaensis. Doctoral Dissertation, Lappeenranta.

Nandi, S.P., Onischak, M., 1985. Gasification of Chars Obtained from Maple and Jack Pine Woods, in: Overend, R.P., Milne, T.A., Mudge, L.K. (Ed.), Fundamentals of Thermochemical Biomass Conversion. Springer, Dordrecht, p. 1159.

Neves, D., Thunman, H., Matos, A., Tarelho, L., Gómez-Barea, A., 2011. Characterization and prediction of biomass pyrolysis products. Prog. Energy Combust. Sci. 37, 611ï 630.

Pitkäoja, A., Ritvanen, J., Hafner, S., Hyppänen, T., Scheffknecht, G., 2020. Simulation of a sorbent enhanced gasification pilot reactor and validation of reactor model. Energy Convers. Manag. 204, 112318. https://doi.org/10.1016/j.enconman.2019.112318

Rajan, R.R., Wen, C.Y., 1980. A comprehensive model for fluidized bed coal combustors. AIChE J. 26, 642ï 655. https://doi.org/https://doi.org/10.1002/aic.690260416

Shimizu, T., Hirama, T., Hosoda, H., Kitano, K., Inagaki, M., Tejima, K., 1999. A Twin Fluid-Bed Reactor for Removal of CO2 from Combustion Processes. Chem. Eng. Res. Des. 77, 62ï 68. https://doi.org/10.1205/026387699525882

Stanmore, B.R., Gilot, P., 2005. Reviewð calcination and carbonation of limestone during thermal cycling for CO2 sequestration. Fuel Process. Technol. 86, 1707ï 1743.

van den Aarsen, F., Beenackers, A., van Swaaij, W., 1985. Wood pyrolysis and carbon dioxide char gasification kinetics in a fluidized bed, in: Overend, R.P., Milne, T.A., Mudge, L.K. (Ed.), Fundamentals of Thermochemical Biomass Conversion. Springer, Dordrecht, p. 1159. https://doi.org/https://doi.org/10.1007/978-94-009-4932-4_36

Ylätalo, J., 2013. Model Based Analysis of the Post- Combustion Calcium Looping Process for Carbon Dioxide Capture. Acta Universitatis Lappeenrantaensis. Doctoral Dissertation, Lappeenranta.

INVESTIGATION OF THE SORPTION ENHANCED GASIFICATION PROCESS IN A DUAL FLUIDIZED BED PILOT PLANT USING A WASTE DERIVED FUEL

Selina Hafner[1*], Max Schmid[1], G¿nter Scheffknecht[1]

[1]*Institute of Combustion and Power Plant Technology (IFK), University of Stuttgart, Pfaffenwaldring 23, 70569 Stuttgart, Germany*

*Email: *Selina.Hafner@IFK.uni-stuttgart.de*

Abstract

SEG is carried out in a dual fluidized bed system using CaO as active bed material. In the gasifier, biomass is gasified with steam as gasifying agent. The CO_2 that is formed during gasification is absorbed by CaO, shifting the water-gas-shift reaction towards the product side, leading to an enhanced hydrogen output. By adjusting the operational parameters (e.g. gasification temperature, steam-to-carbon ratio), the syngas composition can be adjusted in such a way, that it is tailored for the following downstream synthesis process. This leads to a significant reduction of the necessary post-processing steps and costs.

In this paper results obtained from SEG in a 200 kW_{th} dual fluidized bed facility using a municipal waste-derived fuel are presented. Results are presented comprehensively focusing on the syngas composition and yields considering standard gases (H_2, CO, CO_2, CH_4), hydrocarbons (C_2 - C_4) and tars. It is shown that the facility can be operated stably with the waste-derived fuel as feedstock achieving hydrogen concentrations between 53 ï 70 vol%,db for gasification temperatures between 625 and 723 °C, underlining the flexibility of SEG regarding the adjustment of the syngas composition for downstream synthesis processes.

Introduction

Transition to a circular and low-carbon economy will be necessary to reach the climate targets of the European Union as well as the Sustainable Development Goals set by the United Nations in 2015 (United Nations, 2015). To fulfill those aims, new processes for the production of basic chemicals and transport fuels (e.g. Dimethyl Ether) from renewable sources and waste streams instead of fossil fuels, are of main importance. One promising way for the production of the gas mixture that serves as feedstock for the synthesis of a variety of chemicals and transport fuels is the sorption enhanced gasification (SEG) process. In this process, different biomasses as well as bio-based waste-derived fuels (e.g. from municipal waste) can be used as solid feedstock, supporting the transition to a circular and low-carbon economy.

The basic principle of the sorption enhanced gasification process is shown in Fig. 1. In the gasifier, biomass is gasified with steam acting as both fluidizing and gasification agent, producing a syngas that mainly consists of the gases H_2, CO, CO_2 and CH_4. Limestone as CaO based sorbent is used as bed material. CO_2 that is formed during gasification reacts according to equation (1) with CaO to $CaCO_3$ (Wilcox, 2012). Therefore the water-gas-shift reaction (see equation (2) (Kaltschmitt et al., 2009)) is shifted towards the product side, leading to an enhanced hydrogen output. The energy that is required for the gasification is supplied by the sensible heat of circulating bed material coming from the calciner and by the exothermic carbonation reaction. In the calciner, $CaCO_3$ coming from the gasifier is calcined (i.e. regenerated) to CaO at temperatures above 850 °C and then recirculated back into the gasifier. The energy that is required for this endothermic reaction is supplied by combustion of char particles from the gasifier and additional biomass (if required).

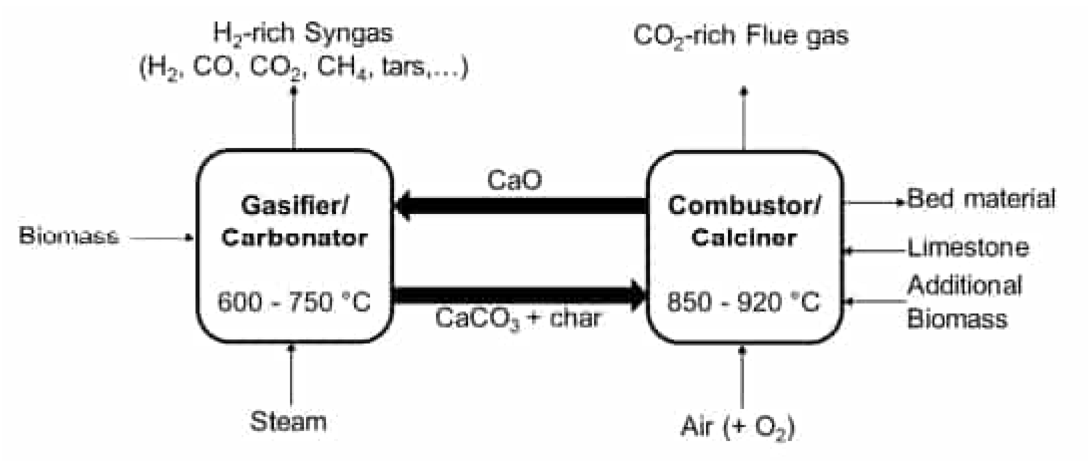

Fig. 1. Scheme of the Sorption Enhanced Gasification (SEG) process

$$CaO_{(s)} + CO_{2\,(g)} \rightleftharpoons CaCO_{3\,(s)} \qquad \Delta H_R(298\,K) = -179\ kJ/mol \tag{1}$$

$$CO_{(g)} + H_2O_{(g)} \rightleftharpoons CO_{2\,(g)} + H_{2\,(g)} \qquad \Delta H_R(298\,K) = -41\ kJ/mol \tag{2}$$

As the CaO/CaCO$_3$ equilibrium is strongly temperature dependent under atmospheric conditions, the gasification temperature is an important process parameter that mainly influences the syngas composition. This influence enables the production of a tailored syngas for different downstream processes.

Experimental setup

Investigations of the SEG process have been conducted in a 200 kW$_{th}$ dual fluidized bed facility at the Institute of Combustion and Power Plant Technology (IFK) at the University of Stuttgart. The facility consists of two refractory lined reactors that are connected to each other. The gasifier has a height of 6 m and an inner diameter of 0.33 m and is operated as bubbling fluidized bed. The calciner is a circulating fluidized bed reactor with a height of 10 m and an inner diameter of 0.2 m. Biomass is gravimetrically fed via rotary valve and screw feeder to the gasifier. Steam that is acting as fluidizing and gasification agent, enters the gasifier via two gas spargers at the bottom of the reactor. The reactor is equipped with two cyclones. One for separation and internal recirculation of entrained bed material and char particles and a second one for further reduction of the particle concentration in the product gas. After the cyclones the gas is sampled and analyzed for standard gas components such as H$_2$, CO, CO$_2$, O$_2$ and CH$_4$ and for lower hydrocarbons (C2-C4) C$_2$H$_4$, C$_2$H$_6$, C$_3$H$_6$, C$_3$H$_8$ and C$_4$H$_{10}$. Tars are measured wet chemically according to the tar protocol (German Institute for Standardisation (DIN) 2006).

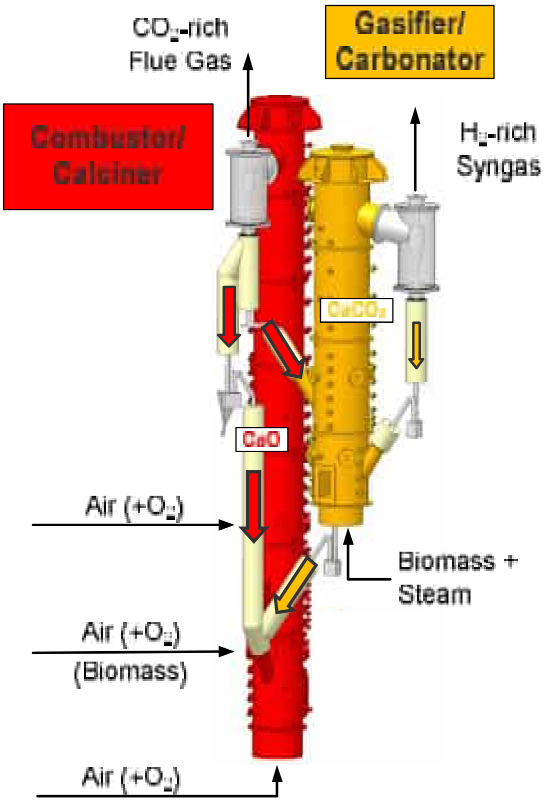

Fig. 2. Scheme of the 200 kW$_{th}$ dual fluidized bed facility at IFK, University of Stuttgart

In the calciner, char particles coming from the gasifier are combusted with oxygen enriched air together with additional biomass (if required). In the pilot facility oxygen enriched air is used to maintain the required heating power while not exceeding a certain gas velocity. In the primary cyclone of the calciner, solids are separated from the flue gas and partly transferred back to the gasifier via screw conveyor. The remaining solids flow back via a loop seal to the calciner.

For further particle reduction in the flue gas, the calciner is equipped with a secondary cyclone and a bag filter.

Experiments presented in this paper were conducted with limestone with a nominal particle size distribution of 100 ï 300 µm as bed material. Two batches of pellets made out of a waste derived fuel were used as feedstock. Batch 1 was used for the experiments with a gasification temperature of 625 °C, while batch 2 was used for the experiments at all other investigated gasification temperatures. The chemical compositions of the waste-derived fuel and the bed material are presented in

Table 1 and Table 2. x_{CO2} in Table 2 refers to the mass fraction of the limestone sample that is released as CO_2, when the sample is decomposed to CaO.

During the experiments, the gasification temperature has been increased by increasing the mass flow between the two reactors. The influence of the gasification temperature has been investigated for temperatures between 625 and 723 °C. The calcination temperature was kept constant at 919±5°C. For maintaining a certain CO_2 carrying capacity of the bed material and for compensation of losses due to attrition, fresh limestone was continuously fed to the combustor. The ratio between fresh CaO and fuel-C (into the gasifier) was kept constant at 0.16 mol_{Ca}/mol_{C}.

Table 1. Chemical composition of the waste derived fuel used for the experimental investigations

	Proximate analysis				Ultimate analysis					
Batch	$ɔ_{H2O}$	$ɔ_{ash}$	$ɔ_{V}$	$ɔ_{FC}$	$ɔ_{C}$	$ɔ_{H}$	$ɔ_{N}$	$ɔ_{S}$	$ɔ_{Cl}$	H_u
	wt%,ad	wt%,db	wt%,daf							MJ/kg
1	8.0	33.2	90.0	10.0	53.9	6.4	2.5	0.6	1.0	11.6
2	10.7	26.2	88.7	11.3	51.6	6.7	2.6	0.6	1.0	12.7

Table 2. Chemical composition of the limestone used as bed material

	x_{CaO}	x_{MgO}	x_{SiO2}	x_{Al2O3}	x_{others}	x_{CO2}
	wt%, db					
Limestone	55.1	0.7	0.4	0.1	0.2	43.5

Results and Discussion

In Fig. 3, the N_2-free gas volume fractions on dry basis for H_2, CO, CO_2 and CH_4 are plotted vs. the gasification temperature. The highest H_2-content with 70 % was measured at a gasification temperature of 625 °C. It decreases with increasing gasification temperature while the CO and CO_2-contents are increasing. This is due to the $CaO/CaCO_3$ equilibrium, which is temperature dependent resulting in a reduced CO_2 capture at higher temperatures. The C2-C4 content was between 11 and 12 % and much higher compared to concentrations of 2 ï 3 % that were obtained during SEG with wood pellets. Hydrogen concentrations on the other hand were lower for SEG with the waste-derived fuel compared to SEG with wood pellets (Hafner et al. 2018).

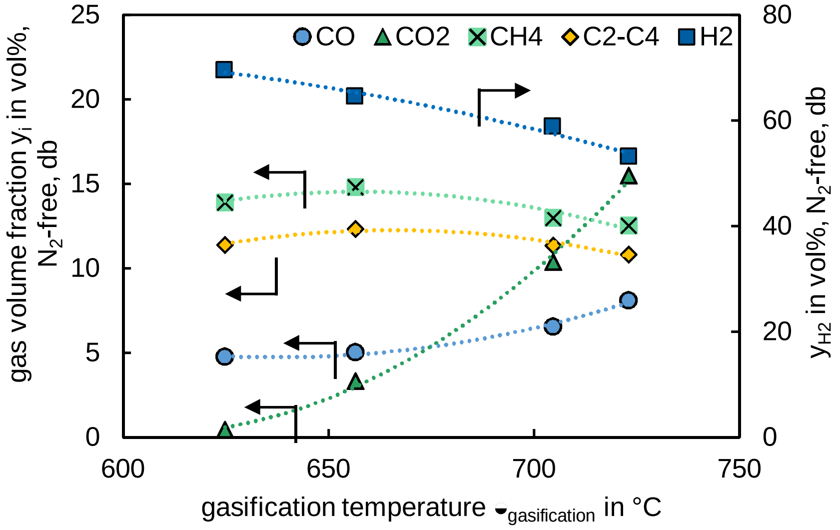

Fig. 3. Gas volume fractions of the syngas (N_2-free, db) at gasification temperatures between 625 and 723 °C

Fig. 4 presents the influence of the gasification temperature on the M-module, which is calculated based on the gas volume fractions from Fig. 3 according to equation (3). Within the investigated temperature range, M-modules between 2 and 13 have been achieved underlining the high flexibility of the SEG process. According to the experiments a gasification temperature of about 697 °C would be necessary for a M-module of 3 that is required for CH_4 synthesis while a gasification temperature of about 715 °C would be necessary for a module M of 2 that is suitable for the production of both methanol and dimethyl ether.

$$M = \frac{y_{H2} - y_{CO2}}{y_{CO} + y_{CO2}} \qquad (3)$$

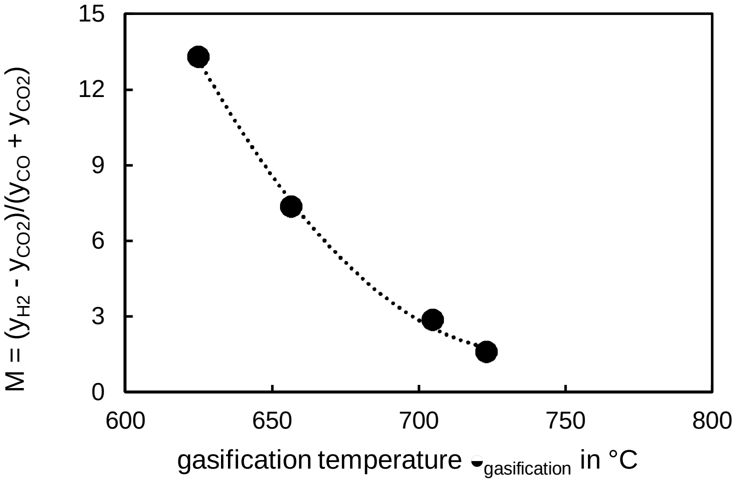

Fig. 4. Module M calculated based on gas volume fractions from Fig. 3 vs. gasification temperature

The gas yields for the main syngas components for gasification temperatures of 625 and 657 °C are presented in Fig. 5. The gas yield refers to a dry, nitrogen free syngas and dry and ash free fuel. It can be noted that an increasing gasification temperature leads to higher gas yields due to a better conversion of the waste-derived fuel. For gasification temperatures of 625 and 657 °C, syngas yields of 0.3 and 0.6 m^3/kg at STP, daf were achieved.

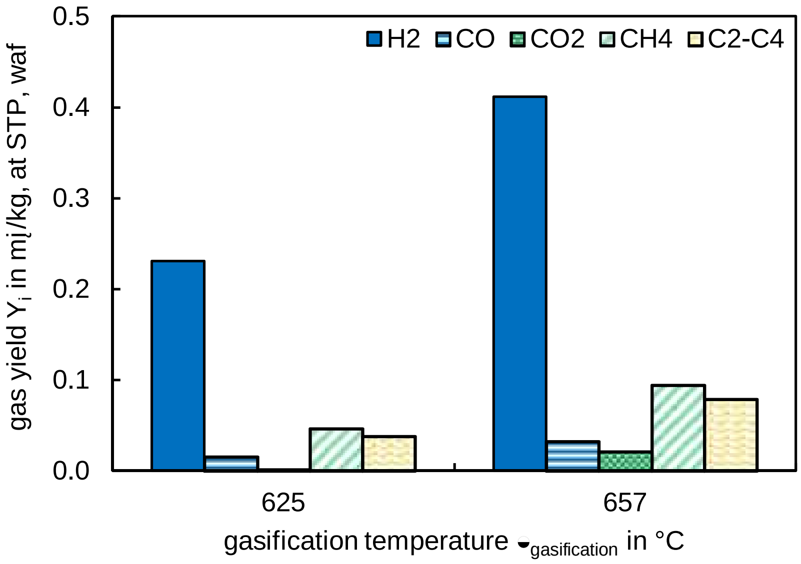

Fig. 5. Gas yields for SEG at gasification temperatures between 625 and 723 °C

Fig. 6 presents the gravimetric tar concentration for gasification temperatures between 657 and 723 °C. At 657 °C a tar concentration of 62 g/mį at STP has been measured. By increasing the gasification temperature to 723 °C, the gravimetric tar concentration could be decreased significantly to 35 g/mį at STP.

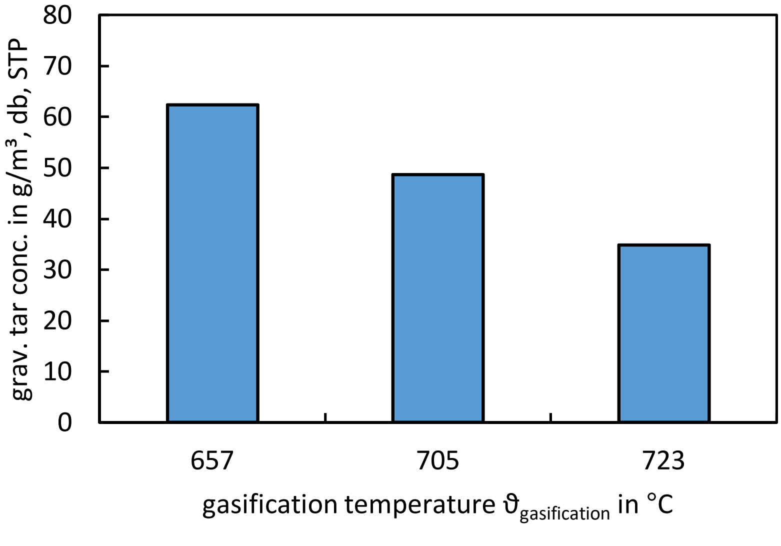

Fig. 6. Gravimetric tar concentration for gasification temperatures between 657 and 723 °C

Conclusion

The sorption enhanced gasification process has been investigated in a 200 kW$_{th}$ dual fluidized bed pilot scale facility using a waste-derived fuel. It has been demonstrated that it is possible to operate the facility stably for gasification temperatures between 625 and 723 °C. Results regarding the syngas composition within this temperature range have been presented. Hydrogen concentrations of up to 70 % have been achieved during the experiments. The module M could be varied in a range between 2 and 13 demonstrating the high flexibility of the process on behalf of the production of a syngas that is tailored for different downstream processes. The tar concentration could be decreased to 35 g/mį at a gasification temperature of 723 °C.

Notation

ΔH_R	specific reaction enthalpy, kJ/mol
ad	air dried
$c_{tar,grav.}$	Gravimetric tar concentration, g/mį at STP
daf	dry ash free
db	dry basis
FC	fixed carbon
H_u	net calorific value, MJ/kg
M	M-module = $(y_{H2} - y_{CO2})/(y_{CO} + y_{CO2})$
SEG	Sorption Enhanced Gasification
STP	Standard temperature and pressure (0°C, 101.3 kPa)
V	volatiles
x	mass fraction, wt%
y	gas concentration, vol%
Y	Gas yield, mį/kg at STP, daf
ɔ	mass fraction in the fuel, wt%
◒	temperature, °C

Acknowledgement

The FLEDGED project has received funding from the European Unionôs Horizon 2020 research and innovation program under grant agreement No 727600 .

References

German Institute for Standardisation (DIN) 2006. Biomass Gasificationð Tar and Particles in Product Gasesð Sampling and Analysis. Beuth Verlag, Berlin.

Hafner, S., Spörl, R., Scheffknecht, G. Sorption Enhanced Gasification: Process validation and investigations on the syngas composition in a 200 kWth dual fluidized bed facility, in: , 23rd International Conference on Fluidized Bed Conversion 2018, pp. 826ï 832.

United Nations, 2015. Paris Agreement. URL: <https://unfccc.int/sites/default/files/english_paris_agreement.pdf>. Accessed 23 September 2019.

LABORATORY STUDY OF INTERACTIONS BETWEEN BIOMASS ASH AND ALKALI-FELDSPAR BED MATERIAL

Robin Faust[1*], Pavleta Knutsson[1]

[1]*Department of Chemistry and Chemical Engineering, Chalmers University of Technology, Kemigården 4, SE-41296 Gothenburg, Sweden*

*E-mail: *faust@chalmers.se*

Abstract

Bed material reactivity and lifetime are dependent on the materials' interactions with biomass ash. Literature on reactions between feldspar and ash elements is scarce, as it is a relatively new bed material and therefore less established. To gain a better understanding on the mechanism behind the observed activity of feldspar, and thereby increase the viability of its industrial application, a mixture of Na- and K-rich feldspar was exposed in a lab-scale furnace under fixed bed conditions. Ash interactions were mimicked by adding major biomass ash elements, such as Ca and K. The interaction of the particles with ash components in terms of layer formation and agglomeration were studied using SEM-EDS and compared to thermodynamic modelling calculations with FactSage. Microscopic analysis of the synthetically formed surface layers revealed similarities to ash layers formed on alkali-feldspar during biomass gasification. Ca reacted with feldspar forming a Ca-rich layer of about 10 µm thickness after 24 hours exposure. It could be shown that Na-feldspar reacts with KOH to form K-feldspar by expelling Na from the particles structure which accumulated in the surface layer. From the laboratory exposures it was further found that fresh feldspar particles tend to agglomerate when exposed to KOH from the beginning. By pre-exposing the particles to a Ca-salt and thereby forming a Ca-rich layer on the particles' surface prior to the exposure to KOH, the agglomeration tendency could be mitigated due to the higher melting point of the elemental composition present in the Ca-rich layer. Pre-exposure to $CaCl_2$ was therefore found to be an effective method against agglomeration.

Introduction

The application of suitable bed material can mitigate the generation of larger aromatic hydrocarbons ("tars"), which are unwanted side products during gasification in dual fluidized bed units. Furthermore, prolonged retention time of bed material particles leads to the development of a surface layer rich in elements native in biomass ash. At the same time as this surface layer develops on the bed material particles, an increase in activity towards tar cracking has been found. This has been attributed to the presence of K and Ca on the particles' surface and their catalytic activity as shown by Knutsson et al (2018). However, despite the observed beneficial activation by alkali and alkaline earth metals, the interaction of bed material and ash could also eventually lead to agglomeration and thus defluidization of the bed material. Agglomeration is caused mainly by the formation of low melting K-silicates and is therefore dependent on the interaction potential of K originating from the fuel and the Si present as an inherent component of most bed materials (Grimm et al. (2012)).

Different naturally occurring minerals have been tested regarding their applicability as bed materials for fluidized bed gasification of biomass such as quartz, olivine and alkali-feldspar. Quartz (SiO_2) was found to have minor activity towards reduction of the unwanted tar species from the product gas, and readily reacts with K from biomass ash which consequently leads to the formation of agglomerates. Olivine ($(Mg, Fe)_2SiO_4$) has shown suitable resistance towards agglomeration due to a slower reaction with the released K. Furthermore, olivine used as bed material was previously shown to mitigate tar formation. The observed activity was associated to the Fe content of the olivine by Rapagnà (2000), which is considered to be further enhanced by the previously mentioned ash layer formation. Even though pointed as one of the most suited materials based on its activity and low agglomeration potential, a major disadvantage of olivine is its Cr content which causes problems when disposing the used material.

Therefore, recent research has focused on the use of alkali-feldspar ((Na, K)$AlSi_3O_8$) which is one of the most common minerals in the earth's crust. Feldspar has shown promising results when utilized as bed material for biomass gasification regarding tar cracking, as can be found in Berguerand (2017) and Wagner (2019). Apart from the described activity, feldspar does not contain any Cr and neither does it show significant tendency to form agglomerates. Furthermore, similar to olivine, a positive impact towards tar cracking due to prolonged retention time and thus ash layer formation was found for feldspar.

Different studies on the effect of ash elements have associated the presence of different elements with the enhanced tar cracking ability of bed material. While it is widely established that the Ca-rich layer plays a major role, Knutsson et al. (2018) have discussed the interplay of K and Ca, whereas Arnold et al. (2019) discusses K, Na, Ca, Mg and heavy metals as catalytically active for gasification.

Due to the variety of elements present in biomass ash, and the complexity of the formed system, the interactions of bed material and ash are challenging to interpret. The aim of this study is therefore to specifically focus on the interactions of alkali-feldspar particles with solely the main ash components. Thermodynamic modelling was used in connection with the performed material characterization in order to suggest a possible mechanism responsible for the ash layer formation.

Experimental

Alkali-feldspar particles were provided by SIBELCO Nordic and consist of both K- and Na-feldspar (48 wt.% and 40 wt.%) and minor amounts of quartz and Ca-feldspar (6 wt.% each). To simulate biomass ash and to study its interaction with feldspar, the samples were exposed to $CaCl_2$, K_2CO_3 and KOH. Previous experiments by Faust et al. (2018) with $CaCO_3$ and Ahlgren et al. (2019) with CaO had shown only limited interaction with feldspar. The exposures were conducted for 24 h at 820 °C in air under fixed bed conditions. K_2CO_3 and $CaCl_2$ were provided by mechanical mixing of powder with feldspar particles in a crucible prior to exposure. The exposure to KOH was done by placing two alumina crucibles next to each other in a tubular furnace. As KOH is in gaseous state at 820 °C, a heterogenic gas-solid reaction with the feldspar sample is expected. A schematic of the different exposures is shown in Fig. 1.

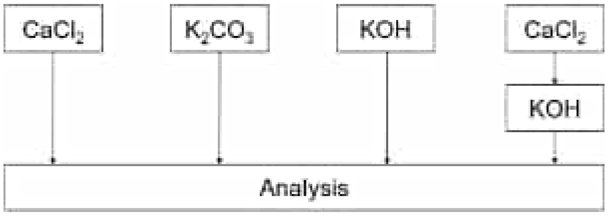

Fig. 1. Schematic of the conducted exposures. Each of the five exposures was done for 24 h at 820 °C in air. $CaCl_2$ and K_2CO_3 were supplied to the feldspar particles as powder and the exposures were conducted under fixed bed conditions. KOH pellets were placed in a separate crucible adjacent to the feldspar during the exposure.

The analysis was done with Phenom ProX scanning electron microscope (SEM) equipped with an energy dispersive X-ray spectroscope (EDS). The obtained elemental compositions were studied with FactSage 7.2 using the Equilib module. As conditions, 820 °C and 1 atm were applied and FactPS and FToxid were used as databases.

Results and Discussion

$CaCl_2$ Exposure

The interaction of $CaCl_2$ powder with feldspar lead to the development of an about 10 µm thick Ca-rich layer on Na-feldspar and about 7 µm thick layer on K-feldspar. As Ca-rich layers around bed material particles are suggested to increase the material's activity towards tar cracking, this can be considered beneficial when utilizing such particles for gasification of biomass. A similar effect was found by Berguerand et al. (2017) when exposing alkali feldspar particles to biomass ash, however, another element found by the authors in the surface layer was K. Hence, in the present study, to imitate the layer formation mechanism, different K-compounds were added to the particles to form a K-rich surface layer.

K_2CO_3 Exposure

Exposing the particles to K_2CO_3 powder had no impact on K-feldspar or Na-feldspar. No formation of an interaction layer could be seen. This contradicts the accumulation of K in the surface layer when K_2CO_3 was added to the process as observed by Knutsson et al. (2018). Therefore, a K-compound with lower melting point was utilized.

KOH Exposure

The exposure of feldspar particles to KOH lead to the development of thick K-rich layers. As the development of a K-rich layers was reported already by Berguerand et al. (2017), it is most likely that KOH and not K_2CO_3 is the K-containing phase which reacts with bed material particles. It can therefore be suggested that, when K_2CO_3 is added to the gasification process (as done by Berdugo Vilches et al. (2018)), conversion of K_2CO_3 to KOH precedes the interactions with the bed material.

Furthermore, the formation of several large agglomerates was found (see Fig. 2). Two EDS point analysis were conducted on the collected samples as pointed on the micrograph, where point 2 (in the darker area) resembles the composition of pure K-feldspar. In point 1, however, which was collected on the brighter area, a high concentration of K and Na could be found where the sum of the K and Na concentrations is as high as the concentration of Si, suggesting the formation of mixed K- and Na-silicates.

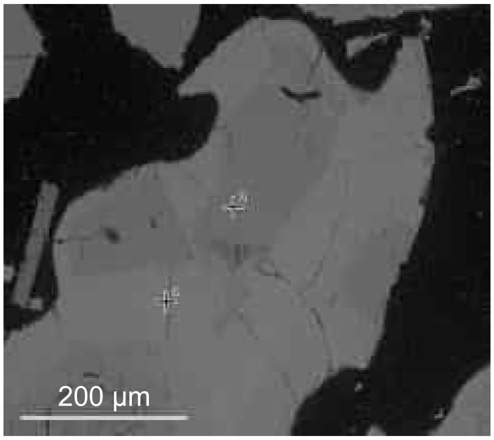

	Si	Al	K	Na
Point 1 [at. %]	42 (±2)	16 (±2)	31 (±3)	11 (±3)
Point 2 [at. %]	59 (±0.3)	18 (±0.3)	22 (±0.4)	1 (±0.4)

Fig. 2. Back-scattered electron (BSE) image of a cross-section of the particles exposed for 24 h at 820 °C to KOH. EDS spectra were recorded on two representative points (as shown on the micrograph) and the elemental composition in these points is shown in the table on the right. The values were calculated on an oxygen-free basis as an average from 5 different point analysis recorded on similar areas, and the standart deviation between the points is shown. Point 1 was chosen as a representative for the area brighter in contrast, whereas Point 2 - as representative for the darker area, where the composition resembles fresh K-feldspar.

EDS-maps were recorded on the surface of a typical particle and are shown in Fig. 3. It can be seen from the contrast in the electron image that a layer of about 50 – 80 µm thickness has formed around the exposed particles as a result of the interaction. Compared to the fresh particle, the layer is enriched in K and Na. Locations rich in Na are poor in Al and vice-versa. The composition in the layer is comparable to the one collected from Point 1 in Fig. 2 and the composition in Point 2 resembles the composition of the phase formed underneath the Na-rich layer.

Similar findings were made by Hannl et al. (2019) and Faust et al. (2019) where alkali-feldspar bed material was exposed to biomass in a DFB gasifier for prolonged intervals of time. After 143 hours of exposure, a thick Na-rich layer had formed on particles which were originally Na-feldspar, where the core of these particles resembled the composition of K-feldspar. However, no agglomeration was reported by the authors. This suggests that in the experimental setup of the present study higher amount of KOH was allowed to interact with the particles. This can further be confirmed by the K-feldspar particles investigated by Hannl and Faust. In their study, K-feldspar particles still had Na dissolved in the particles' cores and only showed minor amounts of Na in the ash layer, whereas in the present study, no distinction between particles could be made, as all were covered by a layer rich in Na.

The compositions measured in the points representative for the different phases, point 1 and 2, were further investigated to obtain information about melt formation of the respective phases. It could be shown that for the composition present in Point 1, almost 99 % of the components are present as melt with only a small fraction of solid $KAlSiO_4$. Point 2 on the other hand, consists mostly of solid K-feldspar with a smaller fraction of melt, consisting mostly of melted SiO_2, as SiO_2 forms a eutectic melt with K_2O.

This means that even though alkali-feldspar has not previously shown any major agglomeration tendency during biomass gasification exposures, problems might be expected when utilizing fuels rich in K. Furthermore, providing additional Al (either by fuel rich in Al or as an additive) would be stabilizing for the solid phase.

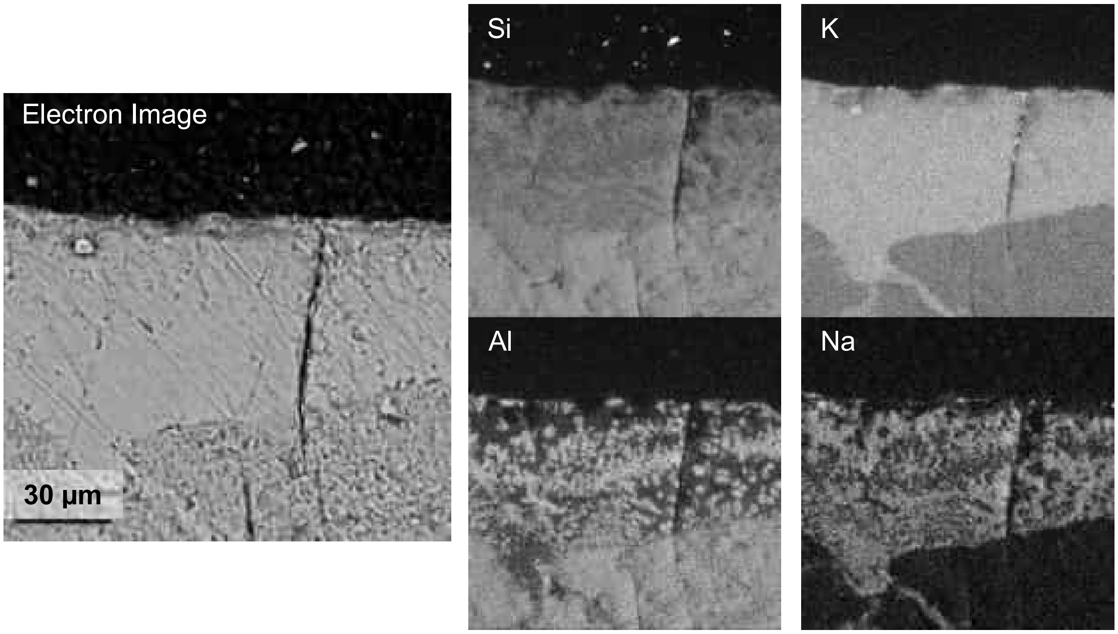

Fig. 3. Back-scattered electron (BSE) image and a selection of EDS maps recorded on the sample exposed for 24 h at 820 °C to KOH. The analysis was done on a cross-section of the exposed particles where the morphology and composition of the surface can be also followed. In the upper area of the image the black phase represents the epoxy resin used for embedding of the particles. In the center of the image, the area rich in K and Na can be found. In the bottom of the image a composition similar to fresh K-feldspar could be measured.

$CaCl_2$ with subsequent KOH exposure

A stepwise exposure of alkali-feldspar to $CaCl_2$ powder followed by exposure to KOH in gaseous state significantly changed the layer formation on the particles (as can be seen in Fig. 4). While K could still diffuse through the Ca-layer which had formed after the initial exposure to $CaCl_2$, no large agglomerates could be found as it was seen in the case without the pre-formed Ca-layer. This observation could explain why in the study by Berguerand et al. (2017) no signs of agglomeration could be found. It could be speculated that in the mentioned study all particles were covered by a Ca-rich layer, which was protecting the particles from agglomerating. One possible explanation for this protective effect is the thermodynamic stability of the phases present in the Ca-layer towards melt formation. A point analysis in the Ca-layer shows a high concentration of Al in the layer (see **Error! Not a valid bookmark self-reference.**). Thermodynamic modelling of the layer composition shows predominance of solid $KAlSiO_4$ and Ca-silicates such as $Ca_3Si_2O_7$ and Na_2CaSiO_4. Thus, both the presence of Al and Ca can stabilize K and Si at higher temperatures and thereby avoid melt formation.

Table 1. Elemental composition (in at. %) of the Ca-layer formed on the sample exposed for 24 h at 820 °C to $CaCl_2$ and subsequently to $KOH_{(g)}$ for 24 hours at 820 °C. The values were obtained from SEM-EDS point analysis of several locations in the layer. The larger standard-deviation compared to the point analysis in Fig. 2 is a result of the less homogeneous elemental composition of the layer.

	Si	Al	Ca	K	Na
Ca-layer [at. %]	32 (±4)	14 (±5)	15 (±7)	36 (±5)	3 (±1)

The morphology of the Ca-layer is similar in both exposures (with and without subsequent $KOH_{(g)}$) with a thickness of about 10 µm. This indicates that during the interaction of feldspar with KOH, it can freely diffuse through the formed Ca-rich layer and react with the feldspar underneath. This ability of the material to absorb K can be beneficial from a corrosion protection point of view as the presence of K in the fuel can increase the risk for corrosion which could be mitigated with an appropriate bed material.

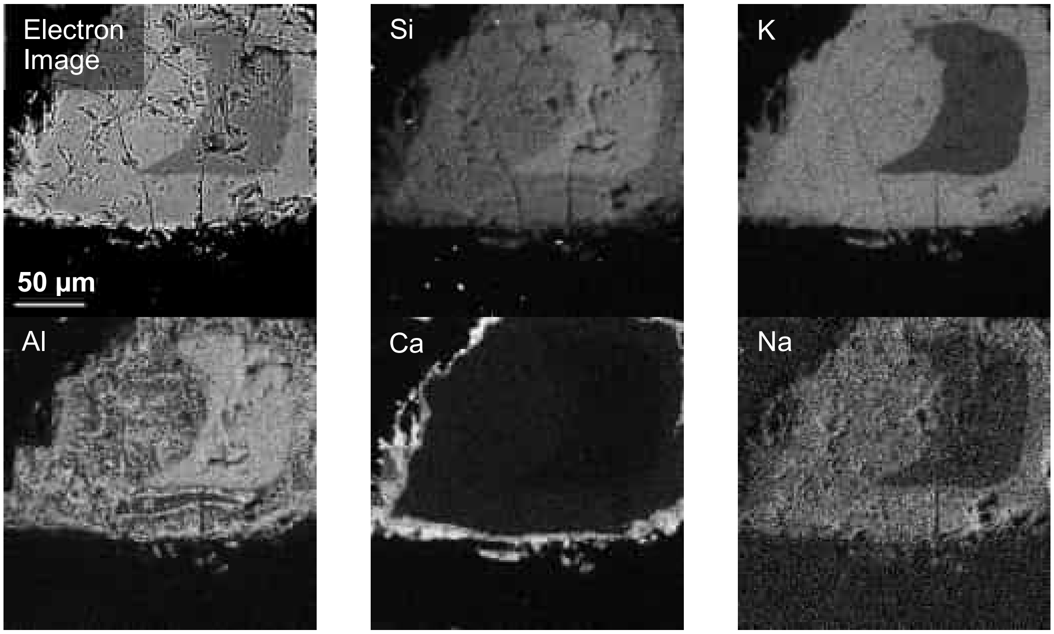

Fig. 4. Back-scattered electron (BSE) image and a selection of EDS maps recorded on the sample exposed first for 24 h at 820 °C to $CaCl_2$ and then for 24 h at 820 °C to gaseous KOH. The analysis was done on a cross-section, where the morphology and the elemental composition of the surface of the particle is shown. The image shows a particle surrounded by a Ca-rich layer. Closer to the core, a layer rich in K and Na is visible with a composition similar to point 1 in Fig. 2. The core has an elemental composition similar to that of K-feldspar.

Conclusion

Alkali-feldspar was exposed to different salts, representative for the main ash components of woody biomass ash, thereby imitating the conditions present during thermal conversion of biomass. It was found that the exposure to gaseous KOH leads to the formation of a thick K- and Na-rich layer with a low melting point. This can lead to agglomeration of the particles. Pre-exposure of the particles to $CaCl_2$ can mitigate this effect due to the formation of a Ca-rich layer around the particles with a high melting point and thus low tendency for agglomeration. The results are in agreement with studies on feldspar from industrial plants. Furthermore, feldspar readily absorbs K which can be beneficial from a corrosion point of view.

Acknowledgement

Special thanks to Jon Ahlgren, Liam Hultén, Clara Lindqvist, Emmy Mäkitalo, Benjamin Storm and Pontus Wageborn for helping me with both experiments and analysis for the article.

References

Ahlgren, Jon, Liam Hultén, Clara Lindqvist, Emmy Mäkitalo, Benjamin Storm, and Pontus Wageborn. 2019. “Lageruppbyggnad Runt Alkalifältspat Vid Exponering Av Askkomponenter - En Undersökning Av Fältspat Som Bäddmaterial Vid Förgasning Av Biomassa.” Chalmers University.

Arnold, R. A. and J. M. Hill. 2019. “Catalysts for Gasification: A Review.” *Sustainable Energy and Fuels* 3(3):656–72.

Berdugo Vilches, Teresa, Jelena Maric, Pavleta Knutsson, Daniel C. Rosenfeld, Henrik Thunman, and Martin Seemann. 2018. “Bed Material as a Catalyst for Char Gasification: The Case of Ash-Coated Olivine Activated by K and S Addition.” *Fuel* 224:85–93.

Berguerand, Nicolas and Teresa Berdugo Vilches. 2017. “Alkali-Feldspar as a Catalyst for Biomass Gasification in a 2-MW Indirect Gasifier.” *Energy and Fuels* 31(2):1583–92.

Faust, Robin, Thomas Karl Hannl, Teresa Berdugo Vilches, Matthias Kuba, Pavleta Knutsson, Martin Seemann, and Marcus Öhman. 2019. “Layer Formation on Feldspar Bed Particles during Indirect Gasification of Wood. 1. K-Feldspar.” *Energy & Fuels* 33(8):7321–32.

Faust, Robin, Jelena Maric, Teresa Berdugo Vilches, Britt-marie Steenari, Martin Seemann, and Pavleta Knutsson. 2018. “Role of K and Ca for Catalytic Activation of Bed Material during Biomass Gasification.” in *23rd International Conference on Fluidized Bed Conversion*. Seoul.

Grimm, Alejandro, Marcus Öhman, Therése Lindberg, Andreas Fredriksson, and Dan Boström. 2012. “Bed Agglomeration Characteristics in Fluidized-Bed Combustion of Biomass Fuels Using Olivine as Bed Material.” *Energy and Fuels* 26(7):4550–59.

Hannl, Thomas Karl, Robin Faust, Matthias Kuba, Pavleta Knutsson, Teresa Berdugo Vilches, Martin Seemann, and Marcus Öhman. 2019. “Layer Formation on Feldspar Bed Particles during Indirect Gasification of Wood. 2. Na-Feldspar.” *Energy & Fuels* 33(8):7333–46.

Knutsson, Pavleta, Valentina Cantatore, Martin Seemann, Pui Lam Tam, and Itai Panas. 2018. “Role of Potassium in the Enhancement of the Catalytic Activity of Calcium Oxide towards Tar Reduction.” *Applied Catalysis B: Environmental* 229(November 2017):88–95.

Rapagnà, S., N. Jand, A. Kiennemann, and P. U. Foscolo. 2000. “Steam-Gasification of Biomass in a Fluidised-Bed of Olivine Particles.” *Biomass and Bioenergy* 19(3):187–97.

Wagner, Katharina, Gustav Häggström, Anna Magdalena Mauerhofer, Matthias Kuba, Nils Skoglund, Marcus Öhman, and Hermann Hofbauer. 2019. “Layer Formation on K-Feldspar in Fluidized Bed Combustion and Gasification of Bark and Chicken Manure.” *Biomass and Bioenergy* 127(October 2018):105251.

HYDRODYNAMIC BEHAVIOUR OF A DUAL FLUIDIZED BED DESIGNED FOR HIGH ASH COAL GASIFICATION

Saurabh Gupta, Santanu De*

Combustion and Energy Conversion Systems Laboratory, Department of Mechanical Engineering, Indian Institute of Technology Kanpur, Kanpur, Uttar Pradesh, 208016, India

*Email: *sde@iitk.ac.in*

Abstract

Cold flow hydrodynamic performance of a dual fluidized bed (DFB) gasifier has been examined which is specifically designed for gasification of high-ash coal. The DFB consists of a riser and a bubbling fluidized bed (BFB) connected by solids recycle valves and a cyclone separator. The total airflow rate of the riser is split into primary aeration (PA) inducted through the bottom distributor plate and secondary aeration (SA) injected tangentially at a height of 300 mm from the bottom of the riser. Two different operations of riser have been investigated, in which a fast fluidized bed (FFB) regime is obtained by PA only, and a combination of PA and SA. In the second case, PA is kept below the particle terminal velocity to maintain a BFB state in the lower portion of the riser, and subsequently, SA is used to entrain solid particles. The effects of aeration rates through loopseal, potseal, BFB, and riser are examined on pressure distribution in the riser and the global solids circulation rate ($\boldsymbol{G_s}$) under low solids flux conditions. The results indicate the influence of riser PA on resulting pressure distribution along with the riser height, whereas SA has a localized effect in the bottom riser section only. For the same total aeration rate in the riser, $\boldsymbol{G_s}$ decreases significantly when SA is used in conjunction with PA compared to PA only operation. Both solids circulation rate and riser pressure distribution increase significantly with an increase in aeration rate in BFB. A maximum solids circulation rate is achieved for an optimum value of fluidization rates in solids recycle valves keeping other operating parameters unchanged.

Introduction

Fluidized bed (FB) reactors are widely used for gasification of solid fuels, such as coal, biomass, and solid wastes to produce syngas, which may be subsequently used to produce valuable chemicals, thermal energy or electricity. FB gasifiers provide several advantages, such as good gas/solids mixing, effective heat and mass transfer, fuel-flexibility, uniform temperature distribution, etc (Karmakar and Datta (2011)). External heat required to sustain endothermic gasification reactions may be provided by partial oxidation of the feedstock which is the most conventional way. Air assisted partial oxidation lowers the calorific value of syngas by dilution of nitrogen whereas oxygen assisted combustion requires an additional air separation unit. Recently, dual fluidized bed (DFB) technology has been used successfully for steam gasification of solid fuels to produce syngas with the heating value in the range of 15-18 MJ/Kg (Göransson et al. (2011). In the DFB gasification system, separate reactors are used for combustion and gasification and the bed material is circulated between them to transport heat. It is demonstrated that the application of fast fluidized bed (FFB) as the combustor and bubbling fluidized bed (BFB) as the gasifier enhances the carbon conversion and lowers the tar yield (Goo et al. (2008)). Solids feedstock is fed in the gasifier where it reacts with the steam, producing a mixture of combustible gases. Unconverted char with the bed material is transferred to the combustor where char is combusted and simultaneously heats the bed material. Hot solids leaving the combustor are segregated from the flue gas in the cyclone separator and conveyed to the gasifier. Important hydrodynamic parameters such as solids distribution, pressure balance, and solids circulation rate influence the heat and mass transfer profile of the DFB gasifier and the gasification efficiency of the DFB gasification system. Therefore, a proper understanding of complex gas-solid hydrodynamics is crucial for scale-up, design and process optimization of FB reactors. In practice, scaled cold flow models are developed to examine parameters such as solids holdup, solids circulation rate, gas leakage, etc. which are otherwise difficult to measure during the hotbed operation. Fluidization conditions in the DFB reactor not only affect the local gas-solids flow dynamics but also the global solids circulation rate. Static pressure measurement is a reliable method that has been used widely in circulating fluidized bed systems to estimate the solids holdup in different parts of the reactor.

In previous studies on circulating fluidized beds, it has been shown that the operating conditions like fluidization velocity, solids inventory, particle diameter, solids circulation rate, etc. Influence the pressure balance of the system (Shrestha et al. (2016)). Rhodes and Laussmann (1992) determined that the riser pressure drop is directly proportional to the ratio of mean solids flux and riser superficial velocity whereas it is least affected by variation in the global solids inventory. Basu and Cheng (2000) studied the effect of loop seal operation on the solids circulation characteristics and pressure balance of the circulating fluidized bed where they concluded that the loopseal aeration increased solids flow rate keeping other operating conditions constant. Further, it was found that the smaller standpipe cross-section area and smaller particle size augmented loop seal aeration effect on solids flow rate while slit height in loop seal did not have any considerable influence. Wang et al. (2014) examined the effect of particle size on the hydrodynamic behavior of the CFB for Geldart B type particles. They illustrated that finer particles attained a higher solid circulating rate and a better material seal against gas leakage. The global distribution of solids in the full loop reactor can also be influenced by providing additional aeration ports along with the reactor height or implementing extra design features. Penthor et al. (2016) installed extruded obstacles on the fuel reactor walls to improve gas-solids interactions which increased solids concentration in the upper reactor region and caused more homogeneous solids distribution along with the reactor height. Lim et al. (2012) utilized a diffuser section in the upper region of the riser along with a secondary air injection port which augmented gas-particle interactions and particle residence time as a result of enhanced particle recirculation in the wall annular region.

Various designs and configurations of DFB reactors have been proposed by researchers in order to optimize the process yield and efficiency for a particular application. Gas-solids flow characteristics in a DFB system designed for any specific application is very complex and needs to be examined thoroughly for continuous reliable operation under various operating conditions. In this work, we investigate the hydrodynamic characteristics of the dual fluidized bed designed for high ash coal gasification to determine the operational flexibility for different operating conditions. Indian sub-bituminous high ash coal has a good amount of fixed carbon and volatiles (around 25-30% each) with less than 1% sulphur and a high ash content (around 40-50%). Effect of fluidization rates in bubbling bed, pot seal, recycle and supply chambers of the loop seal, riser on riser pressure profile and solids circulation characteristics in the reactor is studied.

Experimental Setup and Procedure

Fig. 1 shows the schematic diagram of the DFB cold flow model which is made of transparent acrylic material. The cold model test rig consists of a fast fluidized bed (riser), a bubbling fluidized bed (BFB), a cyclone separator, a pot seal and a loop-seal. The riser is designed as the combustor with the internal diameter and the total height as 50 mm and 2250 mm respectively. Fast fluidized bed regime promotes better gas-particle contact however in order to get higher solid fuel conversion, riser height is to be kept several meters high. Alternatively, a short riser is employed with the arrangement of primary and secondary aeration flow to increase the particle residence time. Operation of the lower riser region in the bubbling/turbulent bed regime and the upper section of the riser in the fast fluidized bed regime increases particle residence time, minimizes gas leakage to the BFB and decreases NOx formation.

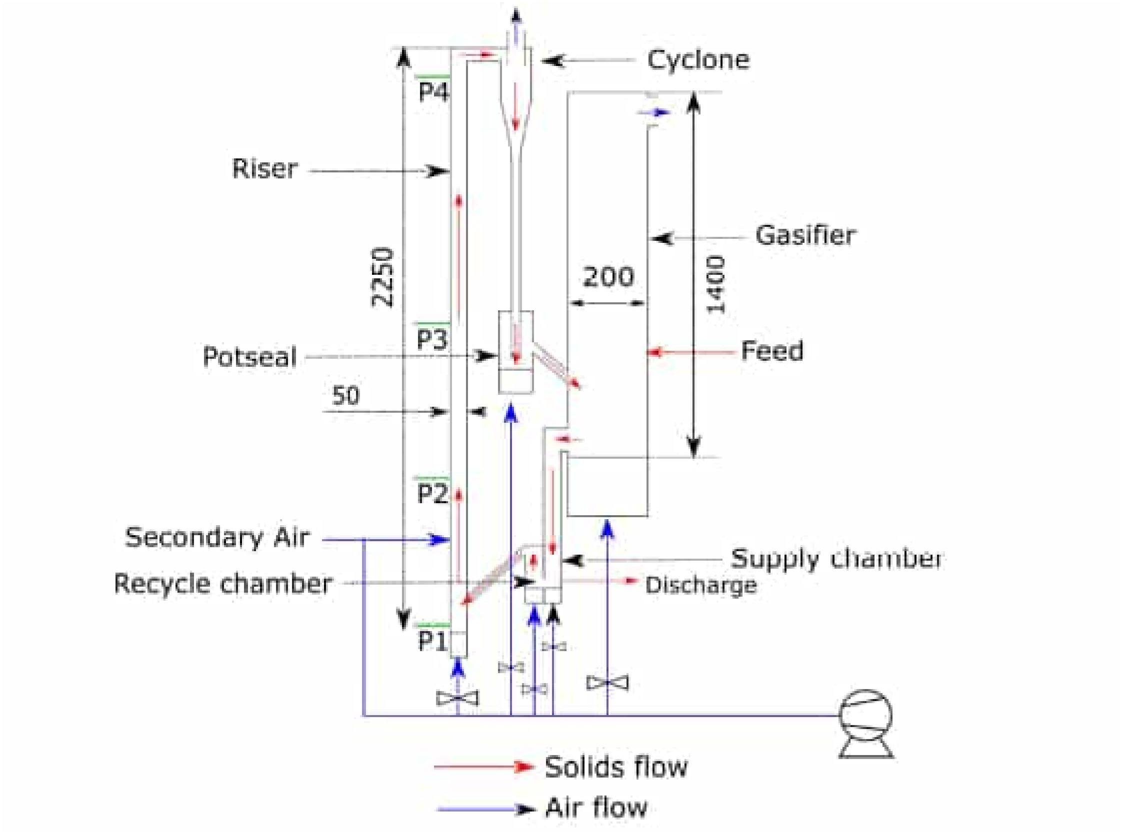

Fig.1. Schematic diagram of the DFB cold flow model

Primary air is introduced from the bubble cap type distributor plate and a secondary air injection port is provided at the height of 250 mm above the riser bottom. Bed material is introduced from an on-bed feeding hopper attached to the BFB, conveyed to the riser via the loopseal. Bed material leaves the BFB through a rectangular aperture into the supply chamber of the loop seal. Loop seal has two chambers i.e. recycle chamber and supply chamber, each having the square cross-section of area 50×50 mm^2. Bed material is transferred from supply chamber to the recycle chamber and then to the riser transported by the fluidizing air from the bottom distributor plate of the loopseal. Bed material exit from riser through a rectangular opening and enters into the cyclone separator where solids are segregated from the carrier air and slides down into the potseal. Potseal is continuously fluidized by the air which transfers solids into the BFB and thereby completes the solids circulation loop. Pressure transmitters are used to measure static pressure at different locations in the riser of the DFB as shown in Fig. 1. Pressure transmitters send signals to the NI current input module which is connected to the computer by the *CompactDAQ* Chassis, LAN and the Labview software. Solids circulation rate (G_s) is measured by abruptly stopping potseal fluidization and observing the time interval in which solids get accumulated up to a certain height in the standpipe. Solids circulation rate is estimated based on the expression, $G_s = \rho_b \left(\frac{A_d}{A_r}\right)\frac{h_{ac}}{\Delta t}$. Here, A_d and A_r are cross-sectional areas of the downer and the riser, respectively. Bulk density, ρ_b and Accumulation height, h_{ac} are known parameters, whereas filling time Δt is recorded during the experiment. Experiments are performed at standard atmospheric pressure and temperature condition. Silica sand having particle density of 2500 kg/m^3 and mean particle diameter of 314 μm is used as the circulating bed material, with the Geldart B type classification. Minimum fluidization velocity and terminal velocity are calculated as 0.9 m/s and 1.66 m/s respectively. Air is used as the fluidizing medium where rotameters fitted with needle/ball valves are used to regulate the airflow rates to various aeration ports.

Results and Discussion

The main objectives of this work are to determine the operational flexibility and the optimum range of the fluidization rates in different components of the DFB for stable and sustainable operation. Solids circulation rate which dictates the char transfer rate from the gasifier to the combustor and the riser solids holdup are the major influencing parameters responsible for the heat production in the combustor. Therefore, solids circulation characteristics and pressure distribution in the riser are analyzed for different values of aeration rates in riser (Q_{par}, Q_{sar}), BFB (Q_{bfb}), potseal (Q_{pot}), and loopseal (Q_{lr}, Q_{ls}) for which cold flow model achieved reliable and continuous operation under low solids flux conditions.

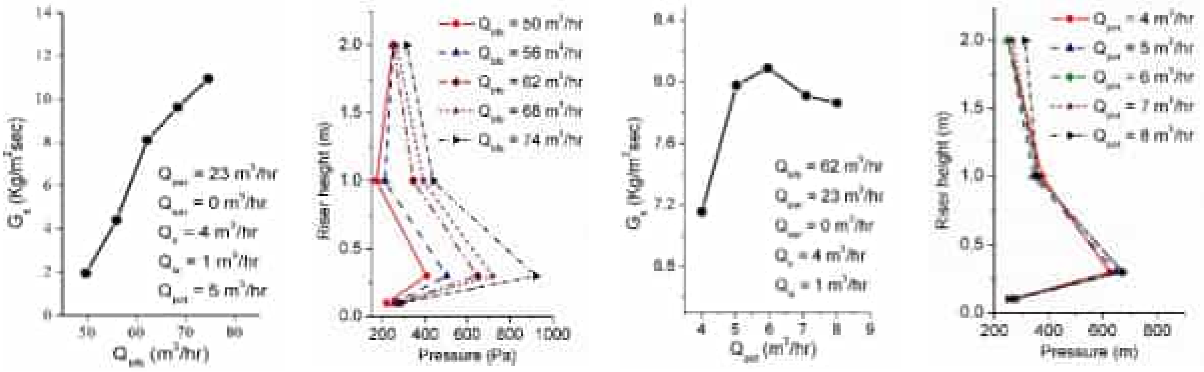

(a) (b)

Fig. 2. The influence of aeration rates on the solids circulation rate and riser pressure distribution in (a) low-velocity fluidized bed, and (b) potseal.

It can be deduced from Fig. 2(a) that the solids circulation rate is increased monotonously with the increase in fluidization rate in the BFB. Higher aeration rates in BFB increase fluidization intensity which promotes vigorous solids movement and gas-solids mixing. Consequently, particles move with higher momentum in the lateral direction and exert higher collision force on the BFB walls. Therefore, at higher fluidization rates, more solids inventory leaves the BFB to the supply chamber through the outlet port located on the sidewall. It was observed that as long as the supply chamber of the loopseal has the capacity to accommodate incoming solids flux from the BFB, increasing BFB fluidization rate is likely to increases the solids circulation rate. The pressure distribution profile in the riser for different BFB aeration rates also validates that the higher BFB aeration rates transfer more solids inventory to the riser. Fig. 2(b) shows the effect of potseal fluidization rates on the G_s and riser pressure drop. Potseal is located between cyclone separator and the BFB where it aids the solids flow from cyclone into the BFB while preventing any gas flow in the reverse direction. It can be observed that the potseal aeration has less pronounced effect on the G_s where greater fluidizing effect increases G_s in a limited range. Excess potseal fluidization ($Q_{pot} = 8\,\mathrm{m}^3/\mathrm{hr}$) reduces the solids circulation rate and impede the solids flow from riser to the cyclone which can be verified by the increased pressure values near to the riser exit. In Fig. 3(a) effect of air injection rate in the recycle chamber of the loopseal on the solids circulation rate demonstrates that the solids circulation rate is increased up to an optimal value by increasing Q_{lr}; thereafter enhanced fluidization rates have no significant influence. Riser pressure profile also demonstrates that the augmentation in the riser solids inventory is considerable up to the value of $Q_{lr} = 4\,\mathrm{m}^3/\mathrm{hr}$ only. Supply chamber of the loopseal acts as a solids inventory reservoir which provides extra sealing effect against the gas leakage from riser to the BFB. Fig. 3(b) shows that the optimum solids circulation rate is attained when supply chamber aeration rate is varied from no fluidization to minimum fluidization state and beyond that, no further considerable effect is discerned. Also, aeration rates in the supply chamber increase riser solids inventory up to the value of $Q_{ls} = 2\ \mathrm{m}^3/\mathrm{hr}$ thereafter, it has insignificant contribution.

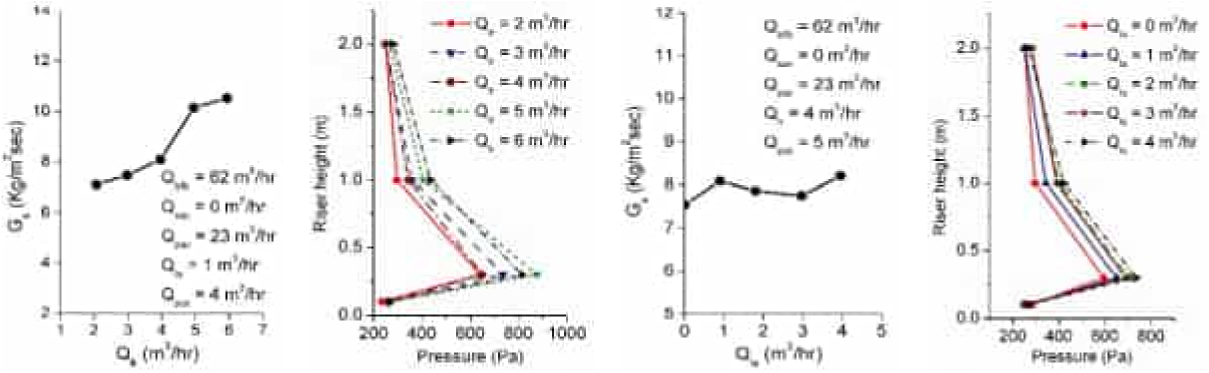

(a) (b)

Fig. 3. The influence of aeration rates on the solids circulation rate and riser pressure distribution in (a) recycle chamber, and (b) supply chamber of the loopseal.

Proper solids circulation rate must be maintained along with the adequate solids holdup in the riser to maintain heat balance of the reactor, therefore, particle-laden flow dynamics in the riser is investigated for primary riser aeration alone and primary aeration aided by secondary aeration. In the latter case, primary aeration (Q_{par}) is used to fluidize bottom riser section below terminal velocity whereas secondary aeration (Q_{sar}) is utilized to entrain solids from the riser.

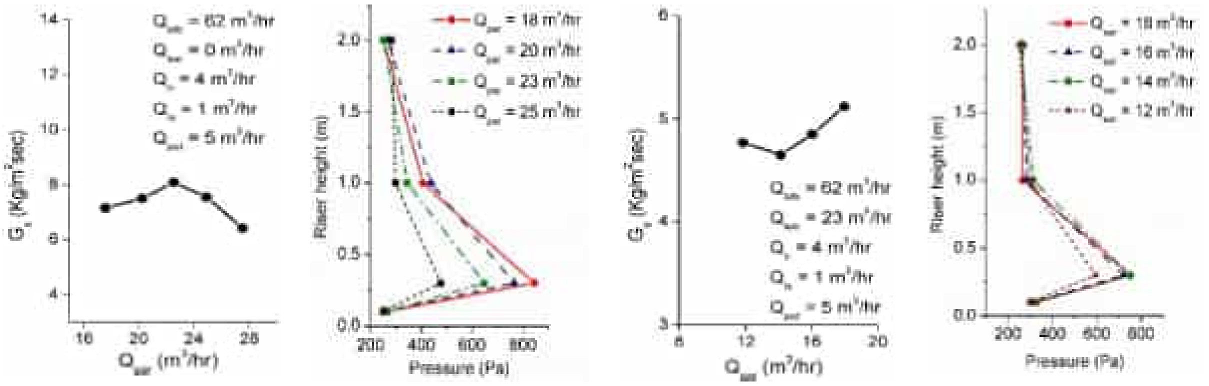

(a) (b)

Fig. 4. The influence of (a) primary riser aeration rates, and (b) secondary riser aeration rates on the solids circulation rate and riser pressure distribution.

Fig. 4(a) depicts the variation in solids circulation rate for different primary aeration rates, operating riser into the fast fluidized regime with no additional secondary air injection. It can clearly be noticed from the plot that G_s rises at higher rate by increasing Q_{par} however further increase in Q_{par} suddenly drops the G_s drastically. Visual observations during the experiments suggested that the high primary aeration rates in the riser create more resistance for solids flow from loopseal to the riser. Riser pressure profile shows that increasing the Q_{par} values dilute the gas-solids fluidized regime along the riser height. Higher primary aeration rates in the riser increase the particle entrainment rate and decrease particle residence time owing to the larger drag imparted by gas flow on the particles. Fig.

4(b) demonstrates the effect of varying secondary aeration rates in riser and primary aeration rates such that the total airflow rate (Q_{totr}) in the riser is maintained at $23\ \mathrm{m^3/hr}$. It can be discerned from the figure that G_s is reduced by a significant margin as compared to the G_s achieved from the same total airflow rate obtained from the primary aeration only (Fig. 4(a)). Riser pressure profile denotes that the increasing Q_{sar} increases solids holdup in the lower section of the riser whereas constant pressure drop in the upper riser section signifies similar solids loading.

Conclusions

An experimental investigation of the hydrodynamics has been conducted in a cold flow model of a DFB designed for high-ash coal. The effect of aeration rates through various ports of the gasifier is examined on the hydrodynamics parameters including solids circulation rate and riser pressure profile. In riser, SA is introduced along with PA. A short riser with the provision of secondary aeration port is utilized to alter the solids loading along with the height with different airflow rates. Hydrodynamics of the riser is examined for two cases; one where riser is operated in fast fluidized regime with only primary aeration and other where fluidization velocity through the primary aeration port is kept below the terminal velocity and secondary air injection is used to entrain solids out of the riser. It is found out that the fluidization rates in BFB, riser, loopseal recycle chamber exert the most significant impact whereas loopseal supply chamber, potseal fluidization rates only has a minor impact. At low primary aeration rates, a distinctly visible dense zone is formed which becomes dilute upon increasing fluidization rate through primary air injection port. The use of secondary aeration increases the solids entrainment rate above the secondary air injection port and dilutes the gas-solids flow. For the same total airflow rate in the riser, secondary air injection reduced the solids circulation rate whereas increased solids hold up in the lower riser region.

References

Basu, P., L Cheng. An analysis of loop seal operations in a circulating fluidized bed. Chem Eng Res Des. 2000. 78(7), 991-998.

Goo, J. H., MW Seo, DK Park, SD Kim, SH Lee, JG Lee, BH Song. Hydrodynamic properties in a cold-model dual fluidized-bed gasifier. J Chem Eng Jpn. 2008. 41(7), 686-690.

Göransson, K., U Söderlind, J He, W Zhang. Review of syngas production via biomass DFBGs. Renewable Sustainable Energy Rev. 2011. 15(1), 482-492.

Karmakar, M., A Datta. Generation of hydrogen rich gas through fluidized bed gasification of biomass. Bioresour. Technol. 2011. 102(2), 1907-1913.

Lim, M.T., S Pang, J Nijdam. Investigation of solids circulation in a cold model of a circulating fluidized bed. Powder Technol. 2012. 226, 57-67.

Penthor, S., M Stollhof, T Pröll, H Hofbauer. Detailed fluid dynamic investigations of a novel fuel reactor concept for chemical looping combustion of solid fuels. Powder Technol. 2016. 287, 61-69.

Rhodes, M., P Laussmann. A study of the pressure balance around the loop of a circulating fluidized bed. Can J Chem Eng. 1992. 70(4), 625-630.

Shrestha, S., BS Ali, MDB. Hamid. Cold flow model of dual fluidized bed: a review. Renewable Sustainable Energy Rev. 2016. 53, 1529-1548.

Wang, P., X Yao, H Yang, M Zhang. Impact of particle properties on gas solid flow in the whole circulating fluidized bed system. Powder Technol. 2014. 267, 193-200.

THE STUDY OF CO-PRODUCTION OF COAL GAS AND POWDERED ACTIVATED COKE BASED ON FLUIDIZED BED

Binxuan Zhou, Tao Wang*, Cheng Li, Zhanlong Song, Chunyuan Ma*

National Engineering Laboratory for Reducing Emissions from Coal Combustion, Engineering Research Center of Environmental Thermal Technology of Ministry of Education, Shandong Key Laboratory of Energy Carbon Reduction and Resource Utilization, School of Energy and Power Engineering, Shandong University, Jinan, Shandong, 250061, China

*Email: *wtao@sdu.edu.cn; chym@sdu.edu.cn*

Abstract

In this paper, a process of co-production of coal gas and powdered activated coke (PAC) is proposed, which adopts a U-shaped two-stage fluidized bed reactor. With the Shengli lignite from Inner Mongolia as the raw material, a drop-tube reactor is used to study the preparation of PAC in the low-temperature zone of the reactor. The effect of water vapor concentration in the gas on the preparation of PAC was studied, and the results show that the presence of water vapor significantly improves the pore structure and the SO_2 adsorption capacity of PAC; however, the burn-off rate also increases. And as the vapor concentration increases, the pore structure parameters (the surface area and the total pore volume), the SO_2 adsorption capacity and the burn-off rate increase, but not significantly. The activation reaction of H_2O tends to reach equilibrium when the water vapor concentration is higher than 30%. For the high-temperature zone, a gasification simulation of 1000 kg/h coal feed was studied using the Aspen Plus software. Combined the results of the experiment and simulation, the final results show that the calorific value of gas increases from 1265 kcal/Nm^3 to 1459 kcal/Nm^3, and the co-production of the PAC is 359 kg/h.

Introduction

Carbon-based materials, such as activated coke (Li et al., 2008), activated carbon (Ma et al., 2003) and activated carbon fiber (Mochida et al., 2000 and Gaur et al., 2006), have so far been proven as clean and effective adsorbents for the removal of SO_2 from flue gas. Among these materials, low-cost activated coke has attracted more and more attention. So, how to prepare activated coke at low cost is a hot research topic at present. Over the last dozen years, Shandong University has been committed to the research of the rapid preparation of PAC under the flus gas atmosphere. Previous research has shown that the mixture of oxygen and water vapor in flue gas is very beneficial to the rapid preparation of PAC, which can promote pore development during the preparation process and increase the SO_2 adsorption capacity of the PAC (Zhen et al., 2015 and 2016). By now, this technology has completed a 30~50 kg/h PAC pilot test and achieved preliminary success (Zhen et al., 2016). Although the rapid preparation of PAC under flue gas atmosphere can reduce production cost, and the PAC prepared using it has a relatively high SO_2 adsorption capacity, there are still an unavoidable problem: the gas after PAC preparation has low calorific value, only 200~300 kcal/Nm^3 (Ke et al., 2017), and the effective use of the gas is difficult.

The above problem can be solved by using gasification gas instead of flue gas to prepare PAC, that is, the rapid preparation of the PAC depends solely on the activation of water vapor in the gasification gas. Thus, a U-shaped two-stage fluidized bed reactor is proposed to fulfill the task, as shown in Fig. 1 (a). The high-temperature zone is a downdraft entrained bed, which is used to realize pulverized coal gasification, and the gas outlet temperature is about 1500 ℃ so as to achieve liquid slag draining. Then, spraying water at the ash hopper, in order to reduce the gas temperature and improve the concentration of water vapor in the gas, aims to obtain suitable preparation conditions for the PAC. Then, the gas carries the pulverized coal fed at the bottom of the low-temperature zone up together, the rapid preparation of PAC is completed in 3~5 seconds. Finally, through the gas-solid separator, the PAC and the gas are obtained respectively. During this preparation process, compared with the rapid preparation under flus gas atmosphere, the SO_2 adsorption performance of the PAC will decline to some extent, but the calorific value of gas is greatly improved.

In this paper, the Shengli lignite from Inner Mongolia is used as the raw material. For the low-temperature zone, a drop-tube reactor (as shown in Fig. 1 (b)) is used to study the preparation of PAC under different concentrations of water vapor. Effect of water vapor in the gas was investigated by analyzing the pore structure, the SO_2 adsorption capacity, the burn-off rate as well as the gas yields. For the high-temperature zone, the gasification simulation was carried out using the Aspen Plus software. Combined the results of the experiment and simulation, the basic balance parameters of the process are obtained, and the results of this research would provide some guidance to the optimization and design of this process in the future.

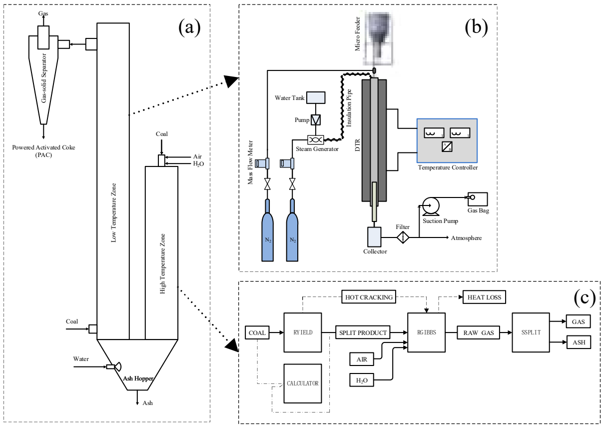

Fig. 1. (a) Diagram of two-stage reactor, (b) Drop-tube reactor system, (c) Aspen plus flow chart.

Experimental Section

Experimental materials

In this study, Shengli lignite (SL) from Inner Mongolia was used as the experimental materials to prepare the PAC. The proximate and ultimate analysis of the SL are given in Table 1. The experimental materials were dried at 105℃ for 8 h, then crushed, ground, and sieved to obtain a particle size of 60~90 μm.

Table 1. Proximate and Ultimate Analysis of the SL.

Sample	Proximate (wt. %)			Ultimate (wt. %)				
	V_d	A_d	FC_d	C_{daf}	H_{daf}	O_{daf}	N_{daf}	S_{daf}
SL-coal	40.58	13.18	46.24	81.13	5.23	12.00	1.14	0.50

Preparation of PAC

A drop-tube reactor (DTR) system was used to prepare the PAC, as shown in Fig. 1. (b). The system consists of five parts: gas system, micro feeder, DTR, PAC collector and vent treatment system. The micro feeder was used to continuously feed the pulverized coal into the DTR, and N_2 was used as carrier gas with a flow rate of 6 L/min. The water vapor comes from a steam generator, and the pipe after steam generator maintains 120℃ with heating tape to avoid steam condensation. The DTR is a stainless steel tube with an inner diameter of 80 mm and a length of 2000 mm. The maximum temperature that DTR can reach is 1200 ℃, and the length of constant temperature zone is 1200 mm. The PAC was collected

Table 2. Design of experimental conditions

Experimental conditions	Parameters				
	Reaction temperature (℃)	Coal-feeding flow rate (g/min)	N_2 flow rate for carrying coal (L/min)	N_2 flow rate for balance (L/min)	Water vapor flow rate (g/min)
0% H_2O	950.00	2.17	6.00	9.89	0.00
10% H_2O				8.30	1.28
20% H_2O				6.71	2.55
30% H_2O				5.13	3.83
40% H_2O				3.54	5.11

in a container at the bottom of the DTR through a water-cooled sampling tube. After filtering, the gas was exhausted into the atmosphere. And in the exhaust line, some gas is extracted by a suction pump and stored in the sealed air bag for gas samples analysis. The detailed experimental parameters are shown in the Table 2.

Characterization and Testing

SO_2 adsorption capacity of PAC

The SO_2 adsorption experiments were carried out in a fixed bed reactor using 1 g of sample at 75℃. The experimental system consists of a tubular reactor (inner diameter is 17 mm, wall thickness is 1.5 mm), placed in a vertical furnace, with a system of valves and mass flow controllers in order to control the flow rate and the composition of the inlet gas. The gas volumetric composition used in experiments was: SO_2, 1500 ppm; O_2, 6%; water vapor, 8%; N_2, balance. The SO_2 concentration was continuously monitored with an on-line Fourier transform infrared gas analyzer (GASMET-DX4000, Finland) for 2 hours. The amount of SO_2 removed expressed in mg SO_2 g^{-1} PAC was calculated by integration of SO_2 conversion versus time curves (Izquierdo et al., 2003 and Zhu et al., 2011).

Pore structure of PAC

The pore structure characteristics of samples were determined by N_2 adsorption at 77K using Autosorb-IQ fully automatic surface and pore size distribution analyzer. The BET surface area was calculated from the isotherm using the Brunauer Emmett Teller equation, and the total pore volume was calculated by the analysis software at relative pressure larger than 0.97 (Hu et al., 2008).

Determination of burn-off rate

The burn-off rate (R) is calculated according to the ash balance method, that is, assuming that the absolute amount of ash does not change before and after the reaction, as shown in the Eq. (1).

$$R = 1 - \frac{A_{\text{coal}}}{A_{\text{PAC}}} \times 100\% \tag{1}$$

Where, A_{coal} and A_{PAC} are the dry base ash mass fraction (%) in raw coal and PAC respectively.

Gas products analysis

In the preparation of PAC, the yield of each component in gas products are calculated according to the N_2 balance method, that is, assuming that the absolute amount of N_2 does not change before and after the reaction, as shown in the Eq. (2).

$$y_{\mathrm{i}} = \frac{\frac{\varphi_{\mathrm{i}}}{\varphi_{\mathrm{N_2}}} \times V_{\mathrm{N_2}}^0 - V_{\mathrm{i}}^0}{m} \tag{2}$$

Where, y_i is the yield of the i gas (L/g), V_{i}^0, $V_{\mathrm{N_2}}^0$ are the volume flow rate of the i gas and the nitrogen in the carrier gas (L/min), φ_{i}, φ_{N_2} are the volume fraction of the i gas and the nitrogen detected by the refinery gas analyzer (%), and *m* is the mass flow rate of the coal (g/min).

Experimental Results and Discussion

SO_2 adsorption capacity

Fig. 2 shows the SO_2 adsorption capacity of the PACs prepared in these experiments. It can be seen that the SO_2 adsorption capacity of the PAC is very low without the activation of water vapor, only 60 mg/g. When there's 10% water vapor, the SO_2 adsorption performance of the PAC is significantly improved, it increases to 85 mg/g, that's up 42 %. As the steam concentration increases to 20 %, the adsorption performance of the PAC further improves, it increases from 85 to 94 mg/g, that's up 11 %. As the concentration of water vapor continues to increase, the adsorption performance is increased, but not significantly.

The possible reason for the above trend is that, during the preparation of the PAC, the presence of water vapor has a good activation effect: improving the pore structure of the PACs. Fig. 3 shows the pore structure information of the PACs prepared in these experiments. It can be seen that, as the addition of water vapor, the pore structure of the PAC improves significantly. In detail, the surface area (S_{BET}) and total pore volume (V_{tot}) are greatly increased. However, as the water vapor concentration increases to more than 10%, the pore structure of the PACs improve slightly.

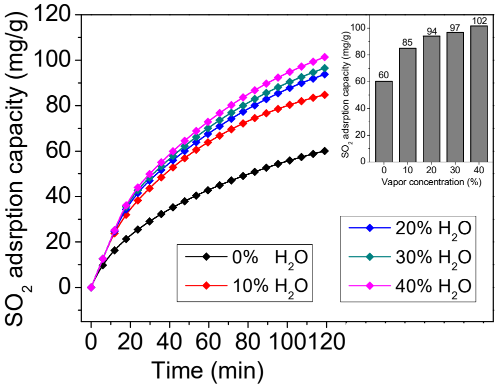

Fig. 2. The SO_2 adsorption capacity of the PACs.

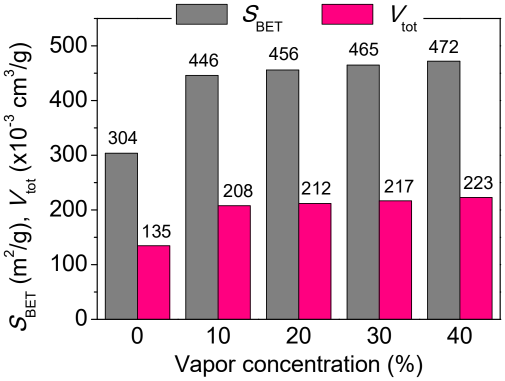

Fig. 3. Pore structure information of the PACs.

Burn-off rate and Gas products analysis

Fig. 4 shows the change of burn-off rate, and Fig. 5 shows the yield of gas products. From Fig. 4, the burn-off rate is 42.35% without water vapor during the preparation of the PAC, which increases with the addition of water vapor, and at 10% of vapor concentration, it increases to 49.07%. As the concentration of water vapor continues to increase, the burn-off rate is increased, but not significantly. From Fig. 5, the yield of H_2, CO_2 and CH_4 all increase with the increase of water vapor, while that of CO decreases. It indicates that the increase of water vapor promotes the reaction between H_2O and CO. Because the rate of decrease of CO is significantly lower than the rate of increase of H_2, or CO_2, the reaction between C and H_2O also happens, so the pore structure of PACs improve and the burn-off rate of PACs increase.

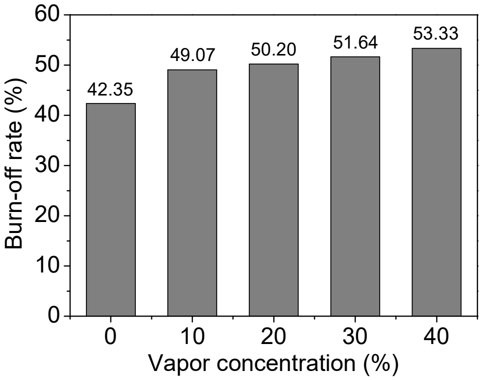

Fig. 4. The burn-off rate

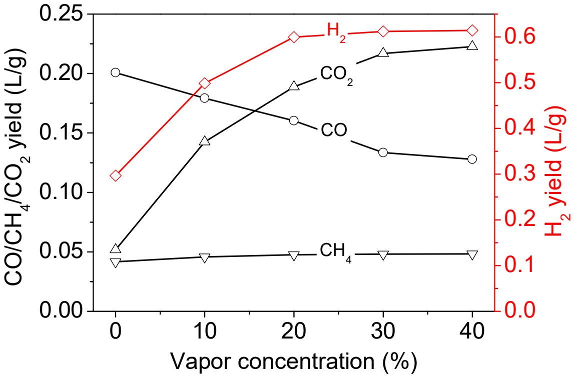

Fig. 5. The yield of gas products

Aspen Simulation Section

Model development

The coal gasification simulation model is developed in Aspen Plus based on Gibbs free energy minimization approach, which is a well-known technique for performance analysis of gasification process (Adnan. et al., 2017 and T. et al., 2012). Fig. 1. (c) shows the flow-sheet of the gasification model. The ultimate and proximate analysis of coal for gasification are shown in Table 1. As a complement, the moisture content of coal is 10 %, and the dry base calorific value of coal is 28369 kJ/kg. More details about the simulation process can be found elsewhere (Peng et al., 2016). In this study, a 1000 kg/h of feed stock is used in the simulation run. The detailed simulation parameters are tabulated in Table 3.

Table 3. Operating parameters used in the simulation.

Coal-feeding flow rate	1000 kg/h
Coal-feeding temperature	100 ℃
Steam flow rate	steam/coal[a] = 0.11
Steam temperature	150 ℃
Air flow rate	O/C[b] = 1.0
Air temperature	600 ℃
Pressure	0.1 MPa

a: steam /coal is the mass ratio of water vapor to coal, kg/kg;
b: O/C is the mole ratio, mol/mol.

Simulation results and discussion

Table 4 shows the simulation results of the design condition in Table 3. The gas composition and heating value are on the dry basis. As observed, the outlet temperature of the gasification section (high temperature zone) is 1495 ℃, which ensures the ash is molten, thus reducing the fly ash content.

Table 4. Gasification results from Aspen Plus simulation.

Gas composition (dry basis, vol. %)					Calorific value of gas (dry basis, kcal/Nm^3)	Outlet temperature (℃)
N_2	H_2	CO	CO_2	H_2S		
54.66	13.30	30.44	1.53	0.07	1265	1495

Combination of Experiment and Simulation

Temperature and quality control of gas

In Fig. 1 (a), the Aspen simulation results show that the outlet gas temperature of high-temperature zone is 1495 ℃, and the gas at such a high temperature directly enters into the low-temperature zone to prepare PAC, which will have the following problems:

1. Too high temperature is not conducive to the preparation of PAC and seriously affects its pore structure.
2. Endothermic reactions occur in the low-temperature zone, and the temperature gradually decreases, inevitably resulting in coking and slagging.

The above problems can be well solved by setting water nozzles at the joint part of high and low temperature zone, that is the ash hopper as shown in Fig. 1 (a). Spraying water can reduce the gas temperature and improve the concentration of steam in the gas, which are beneficial to the preparation of PAC. In addition, water can chill the high temperature ash residue (1495 ℃, in this study), so that they can be removed from the bottom of the ash hopper, so as to avoid them into the low temperature zone, and affect the performance of PAC. Table 5 shows the gas information after spraying water.

Table 5. Gas parameters after spraying water.

Spray water flow rate (kg/h)	Gas temperature (℃)	Gas composition (vol. %)					
		H_2O	N_2	H_2	CO	CO_2	H_2S
505.71	1100	16.41	45.69	11.12	25.45	1.28	0.06

Summary results of two sections

Considering the actual heat loss and reaction heat consumption, the gas temperature is adjusted to 1100 ℃, as shown in Table 5. In the low-temperature zone, the coal feed is determined according to the steam-coal ratio, and 1.0 is taken here, so it is 722 kg/h. According to the yield of gas products in Fig. 5, the final summary results of the two sections are shown in Table 6. Compared with Table 4, H_2 concentration increases significantly, and CH_4 is produced because of the presence of low-temperature zone. The final result of after combining with these two zones is that the calorific value of gas increases from 1265 to 1459 kcal/Nm^3, and there are 359 kg/h of PAC prepared at the same time.

Table 6. Summary results of two sections.

Gas composition (dry basis, vol. %)						Calorific value of gas	PAC production
N_2	H_2	CO	CO_2	CH_4	H_2S	(dry basis, kcal/Nm^3)	(kg/h)
45.69	21.00	28.09	4.39	0.78	0.06	1459	359

Conclusions

1. Water vapor is very beneficial to the preparation of PAC. As the concentration of water vapor increases from 0 to 10%, the surface area and total volume of the PAC increase 46.7% and 54.1%, respectively; the SO_2 adsorption capacity increases 41.7%, while the burn-off rate also increases 15.9%.

2. As the concentration of water vapor increases to more than 20%, the pore structure parameters (the surface area and the total pore volume), the SO_2 adsorption capacity and the burn-off rate all increase, but not significantly.

3. Under the setting condition, the calorific value of gasification gas is 1265 kcal/Nm^3, while combined with the experiment and the simulation, the calorific value of final gas increases to 1459 kcal/Nm^3, and the co-production of the PAC is 359 kg per 1722 kg coal (Gasification, 1000 kg; Preparation of PAC, 722 kg).

References

Adnan, M. A., Susanto, H., Binous, H., Muraza, O., Hossain, M.M., Feed compositions and gasification potential of several biomasses including a microalgae: a thermo dynamic modeling approach. Int. J. Hydrogen Energy. 2017. 42, (27), 17009-17019.

Gaur, V., Asthana, R., Verma, N., Removal of SO_2 by activated carbon fibers in the presence of O_2 and H_2O. Carbon. 2006. 44, (1), 46-60.

Hu, Q., Lu, Y., Meisner, G. P., Preparation of Nanoporous Carbon Particles and Their Cryogenic Hydrogen Storage Capacities. The Journal of Physical Chemistry C. 2008. 112, (5), 1516-1523.

Izquierdo, M. T., Rubio, B., Mayoral, C., Andres, J. M., Low cost coal-based carbons for combined SO_2 and NO removal from exhaust gas. Fuel. 2003. 82, 147-151.

Ke, L., Experimental study on preparation of powder activated coke and by-product pyrolysis gas by rapid pyrolysis of pulverized coal. Shandong University. 2017.

Li, J., Kobayashi, N., Hu, Y., The activated coke preparation for SO_2 adsorption by using flue gas from coal power plant. Chemical Engineering and Processing: Process Intensification. 2008. 47, (1), 118-127.

Ma, J., Liu, Z., Liu, S., Zhu, Z., A regenerable Fe/AC desulfurizer for SO_2 adsorption at low temperatures. Applied Catalysis B: Environmental. 2003. 45, (4), 301-309.

Mochida, I., Korai, Y., Shirahama, M., Kawano, S., Hada, T., Seo, Y., Yoshikawa, M., Yasutake, A., Removal of SO_x and NO_x over activated carbon fibers. Carbon. 2000. 38, (2), 227-239.

Peng, B., Farahani, M. R., Gao, W., Aspen Plus simulation of steam-gasification of different crude oils: A detailed comparison. Pet. Sci. Technol. 2017, 35, (4), 332-337.

T. Renganathan, M.V. Yadav, S. Pushpavanam, R.K. Voolapalli, Y.S. Cho, CO_2 utilization for gasification of carbonaceous feedstocks: a thermodynamic analysis. Chem. Eng. Sci. 2012, 83, 159.

Zhu, Y., Gao, J., Li, Y., Sun, F., Gao, J., Wu, S., Qin, Y., Preparation of activated carbons for SO_2 adsorption by CO_2 and steam activation. Journal of the Taiwan Institute of Chemical Engineers. 2012, 43, (1), 112-119.

Zhen, Z., Tao, W., Tai, F., Chunyuan, M., Influence of Steam and Oxygen on Pore Structure Evolution of Active Semi-Char. Journal of Combustion Science and Technology. 2015, 21, (4), 318-323.

Zhen, Z., Tao, W., Ke, L., Xiqiang, Z., Chunyuan, M., Powder-Activated Semicokes Prepared from Coal Fast Pyrolysis: Influence of Oxygen and Steam Atmosphere on Pore Structure. Energy & Fuels. 2016, 30, (2), 896-903.

INVESTIGATION OF OCAC USING CANADIAN ILMENITE ORE IN A CIRCULATING FLUIDIZED BED COMBUSTOR

Margarita De Las Obras Loscertales*[1]*, Dennis Y. Lu*[1], Lin Li*[1,2]*, and Robin W. Hughes*[1]**

[1] *Natural Resources Canada, CanmetENERGY, 1 Haanel Drive, Ottawa, Ontario K1A 1M1, Canada;*

[2] *Key Laboratory of Energy Thermal Conversion and Control of Ministry of Education, School of Energy and Environment, Southeast University, Nanjing, 210096, China*;

*Email: Dennis.Lu@canada.ca

Abstract

Oxygen carrier aided combustion (OCAC) in fluidized bed combustors is a novel process that consists of replacing, totally or partially, the inert bed material by an active oxygen carrying material such as ilmenite ore. The use of these materials may enhance the combustion efficiency and reduce hot spots in the combustor by its oxygen buffering ability. During the fuel combustion, the oxygen carrier is reduced providing oxygen in oxygen lean zones and oxidized/regenerated in oxygen rich zones.

In this research work, experimental tests in a circulating fluidized bed combustor (CFBC) have been performed using a torrefied hardwood biomass and an ilmenite ore as fuel and bed material, respectively. The effects of the temperature and the excess oxygen on the OCAC process were evaluated. Olivine sand was also used as bed material for comparison purposes. An improved combustion performance was observed when ilmenite was used as bed material. Lower CO and hydrocarbon emissions in the freeboard were detected. In addition, ilmenite was found to be a suitable material to operate at lower excess oxygen values. These results suggest that ilmenite may be a promising material to be used as bed material in OCAC processes.

Introduction

Currently, most commercial fluidized bed combustors (FBCs) operate with an excess of oxygen in order to improve combustion efficiency, but even this measure is not enough to completely eliminate reducing areas generated in the combustor. Working with an excess of oxygen results in larger boiler sizes and higher power consumption for equipment such as blowers or fans, causing an increase in capital and operating expenses. Therefore, it is desirable to decrease the excess of oxygen fed to the combustor while maintaining the same level of high fuel conversion.

The most common bed materials used in FBCs, which act largely as inert solids from the perspective of combustion, are silica and olivine sands. Recently, research studies have been carried out to investigate the partial or total replacement of sands by materials with oxygen carrying properties including ilmenite and manganese ores (Corcoran et al., 2014; Hanning et al., 2018; Kajnäs et al., 2019; Lind et al., 2017; Thunman et al., 2013; Wang et al., 2017; Zhao et al., 2014). This novel technique is referred to as OCAC.

The concept of using an oxygen carrier as bed material comes from the carbon capture technology called chemical looping combustion (CLC) (Adanez et al., 2012; Hossain et al., 2008; Lyngfelt, 2014). In this process, an oxygen carrier is used to transfer oxygen from the air reactor to the fuel reactor, thus allowing combustion without direct contact between the air and the fuel. Among the different oxygen carriers (OCs), ilmenite ore, a natural mineral composed of iron-titanium oxides, has gained special attention due to its low cost and relatively high attrition resistance. It has been observed that ilmenite demonstrates a reasonably high reactivity towards CO and H_2, but lower reactivity with CH_4. This fact makes ilmenite a suitable OC for use in FBCs; especially when burning solid fuels with high volatiles content such as low-rank coals (lignite) or biomass. As a result of the combustion of gaseous fuel components in the dense bed via reaction with the oxygen carrier, less excess oxygen is needed to meet emission restrictions, suggesting that OCAC is a promising technology to broadly improve the performance of FBCs (Rydén et al., 2016).

In the research work presented here, the performance of ilmenite as bed material in a CFBC has been studied at CanmetENERGY in Ottawa, Canada. To do so, experiments were performed in which biomass was burned in a CFBC at firing rates of around 15 kW_{th} using ilmenite ore as bed material at different temperatures and at various excess oxygen rates. Experiments using olivine sand as bed material were carried out for comparison with the ilmenite ore.

Experimental Method

Raw Materials

The minerals used in this work as bed materials are UKTO ilmenite ore (Hughes et al., 2017) supplied by Rio Tinto Iron & Titanium, Quebec, Canada and olivine sand provided by Olimag Sand Inc, Quebec, Canada. Ilmenite is a titanium-iron oxide mineral and olivine sand is a magnesium iron silicate. Torrefied hardwood biomass from Airex Energy's Bécancour plant in Canada with a particle size below 869 micron was used as fuel. XRF, ultimate and proximate analyses of ilmenite and the biomass, are shown in Table 1 and Table 2, respectively.

Table 1. UKTO ilmenite and torrefied biomass ash composition via XRF analysis

XRF	UKTO Ilmenite	Torrefied Biomass
SiO_2 wt%	1.03	4.75
Al_2O_3 wt%	0.96	0.96
Fe_2O_3 wt%	58.67	2.01
TiO_2 wt%	35.91	0.13
P_2O_5 wt%	0.02	2.490
CaO wt%	0.23	36.00
MgO wt%	2.61	5.79
SO_3 wt%	0.10	1.81
Na_2O wt%	<0.2	0.42
K_2O wt%	0.02	15.48
Ba (ppm)	<250	2762
Sr (ppm)	<50	1515
V (ppm)	1611	<50
Ni (ppm)	199	141
Mn (ppm)	1071	13083
Cr (ppm)	892	238
Cu (ppm)	81	191
Zn (ppm)	49	1235
LoF (%)	0.0	28.25

Table 2. Ultimate and proximate analysis of the torrefied hardwood biomass (a.r.)

Torrefied Biomass Analysis	
Proximate (wt.%)	
Moisture	3.68
Ash	1.12
Volatile	74.03
Fixed Carbon	21.17
Ultimate (wt.%)	
Carbon	51.4
Hydrogen	5.77
Nitrogen	0.16
Sulphur	0.05
Oxygen (by diff.)	37.86
Chlorine ($\mu g/g_{db}$)	16
HHV (MJ/kg)	19.98
Ash Fusion Temperature Oxidizing Atmosphere (ºC)	>1485
Ash Fusion Temperature Reducing Atmosphere (ºC)	>1485

Description of the Pilot Plant

The CFBC operates under atmospheric pressure and is equipped to perform test work in both air-fired and oxy-fired modes (Hughes et al., 2017). A process flow diagram of the facility is shown in Fig 1. Table 3 provides the independent variables selected for the operation of the CFBC. The conditions selected in the upper part of the table were picked to investigate the effect of temperature, while the conditions selected in the lower portion of the table were picked to investigate the effect of excess oxygen.

Table 3. Pilot plant test matrix

Bed material	Bed (kg)	U/U_{mf}	Temperature (°C)	O_2 flue gas (vol%$_{db}$*)
Ilmenite ore	14	75	**800-850-900**	2.5
Olivine sand	9	75	**800-850-900**	2.5
Ilmenite ore	14	75	850	**5-2.5-1.5**
Olivine sand	9	75	850	**5-2.5-1.5**

*vol%$_{db}$: volume concentration in dry basis

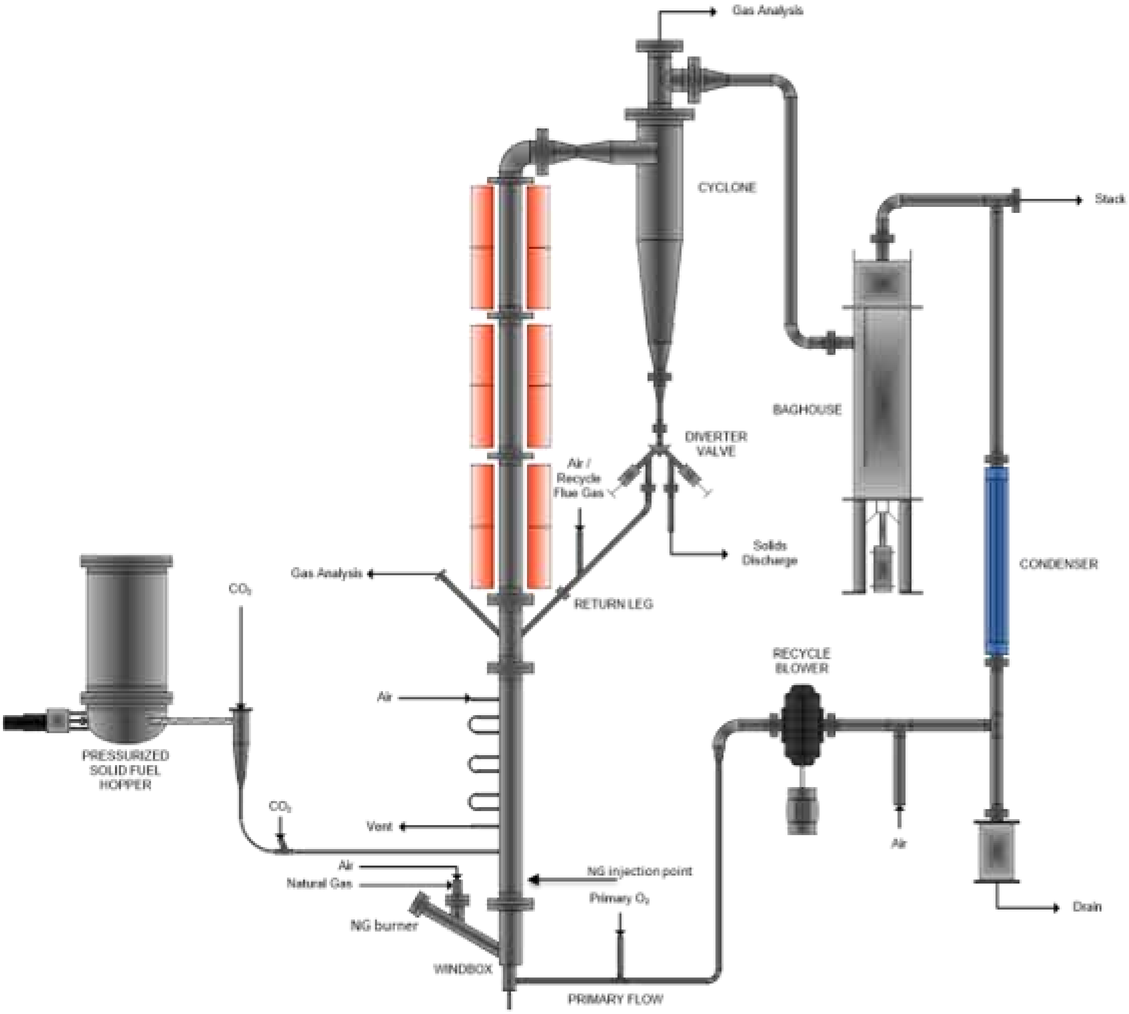

Fig 1. CFBC system flow diagram

Bed Materials

CLC studies have noted that fresh ilmenite reacts slowly during reduction with both syngas and methane and that the reactivity for both reduction and oxidation increases substantially over a number of cycles (Adanez et al., 2010; Cuadrat et al., 2012). Therefore, for this experimental campaign to be representative of long term operations, ilmenite was activated in the CFBC system. Prior to activation the ilmenite bed material was subjected to a calcination process in the CFBC in order to prevent agglomeration and to obtain consistent characteristics.

The calcination temperature selected was 820 °C. The heat supply to reach this bed temperature came from the combustion of 0.71 kg/h of natural gas (NG) with air in the NG burner located at the windbox. In addition, a primary air flow rate of 17 kg/h was fed to the combustor in order to keep the temperature in the windbox within safe limits (below 1000 °C). A total fluidizing gas (primary air and burner flue gas) of around 36 kg/h entered the combustor through the distributor plate to heat and oxidize the bed material. The total calcination time in the CFB was 2 hours. Ilmenite samples were taken at 30 min intervals from the cyclone and subsequently tested in a TGA in order to determine the time necessary to obtain a complete calcination of the material. After 2 hours of calcination the samples were considered fully oxidized with a mass gain of 0.32 wt%.

As mentioned above, the reactivity of ilmenite with syngas and CH_4 increases with the number of redox cycles. Activation of the ilmenite was achieved by injecting natural gas into the fluidized bed while fluidizing the bed with air. The NG burner was turned off and the transition from NG burner to NG injection into the fluidized bed was performed smoothly while maintaining combustion. This resulted in a reducing zone being present at the fuel injector located at ≈ 8 cm above the distributor plate, an oxidizing zone being present at the distributor and combustion occurring within the fluidized bed. A NG flow rate of 15 SLPM was injected into the bed. Jet penetration calculations considering geometry and operating conditions indicate that no NG jet would have been formed, but instead a plume of NG would rise along the wall of the combustor which burned as it passed through the CFBC. After reaching steady state conditions, the conditions were maintained for different times, 4 and 14 hours, in order to assess the evolution of the activation degree of ilmenite particles. The operating temperature was 900 °C with a superficial gas velocity of around 1.7 m/s.

During the activation process bed material samples were extracted from the bottom of the fluidized bed and subsequently evaluated in a TGA in order to establish if the material had in fact been activated. It was determined that the ilmenite was activated after 14 hours of treatment.

In addition to ilmenite ore, OCAC tests with olivine sand were carried out for comparison purposes. Given the difference in density of the two bed materials, 14 kg ilmenite ore and 9 kg of olivine were used in order to maintain a similar expanded bed height, and consequently similar solids circulation rates. Mean particle sizes of 250 and 310 micron were selected for ilmenite and olivine sand, respectively, to obtain similar minimum fluidization velocities (U_{mf}). A U/U_{mf} ratio of 75 was set for each test, with U calculated based on the average molar flow of the inlet and outlet gas streams.

Results

Effect of Temperature on Combustion Performance for the Two Bed Materials

The effect of the temperature between 800°C and 900°C was determined for both bed materials; olivine sand and ilmenite. For this set of tests an excess of oxygen corresponding to 2.5 vol% O_2 in the flue gas was maintained and flow rates were adjusted to provide a U/U_{mf} ratio of 75. Depending on the operating conditions, biomass fuel flow rates ranged between 2.4 and 2.9 kg/h. Fig 2 shows the effect of the temperature on combustion performance (i.e. CO concentration above the dense bed) with the two bed materials. As can be noted, there is a downward trend in CO concentration above the dense bed with temperature. In comparing the slope of the lines for CO concentration above the dense bed we can see that the effect of temperature is greater for ilmenite than for olivine. Two conclusions can be drawn from this 1) combustion of CO is not strongly affected by temperature in the case of the olivine, therefore it appears that combustion of CO is mass transfer limited in this case, 2) combustion of CO is more strongly affected by temperature with ilmenite, so it would appear that kinetics may play a greater role in combustion and we can then infer that the additional combustion is the result of the reaction between ilmenite and CO. In addition to lower CO concentration, lower H_2 and hydrocarbon concentrations were detected when ilmenite was used as bed material.

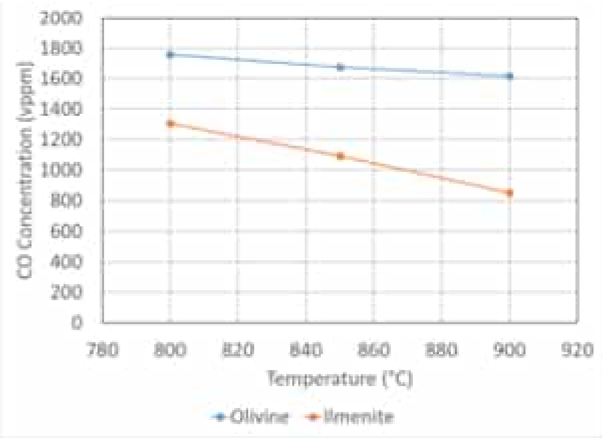

Fig 2. Effect of the temperature on combustion performance (i.e. CO at concentration above the dense bed) with the two bed materials.

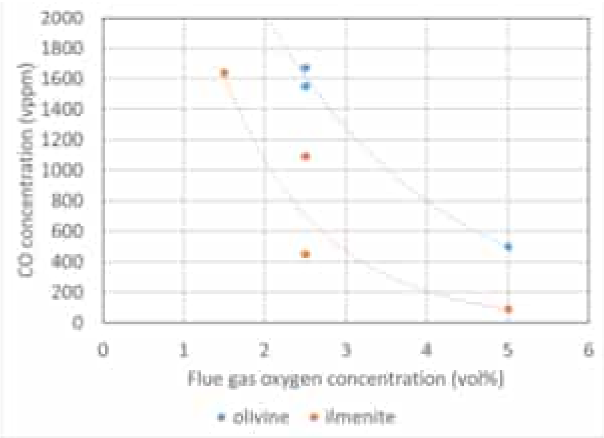

Fig 3. Effect of excess oxygen on combustion performance (i.e. CO at concentration above the dense bed) with the two bed materials.

Effect of Excess of Oxygen on Combustion Performance for the Two Bed Materials

In this research study, different excess oxygen rates corresponding to 5.0, 2.5 and 1.5 vol% O_2 in the flue gas with a U/U_{mf} ratio of 75 at 850°C were tested in the CFBC. Fuel flow rates corresponding to these operating conditions ranged between 2.2 and 2.7 kg/h. As was expected, a decrease in the excess oxygen led to higher CO emissions. Fig 3 shows the effect of excess oxygen on combustion performance (i.e. CO concentration above the dense bed) with the two bed materials. As can be seen, for a similar CO concentration in the freeboard, it is possible to operate at lower excess oxygen with ilmenite ore as bed material.

Conclusions

An assessment of ilmenite ore performance as an oxygen carrier for OCAC has been carried out in a circulating fluidized bed combustor. To do so, the effects of temperature and excess O_2 were analyzed. Olivine sand was also tested for comparison purposes. The main conclusions reached through this study are the following:

- Ilmenite ore can improve combustion performance when it is used as bed material; lower CO and hydrocarbon emissions compared to olivine sand were found above the dense bed of the combustor.
- Lower excess oxygen is required to meet CO specifications when using ilmenite ore as bed material in comparison to olivine sand.

Acknowledgements

This research was sponsored and funded by the Program for Energy Research and Development (PERD) at Natural Resources Canada, Government of Canada.

References

Adanez, J., A Cuadrat, A Abad, P Gayan, LF de Diego, F Garcia-Labiano. Ilmenite Activation during Consecutive Redox Cycles in Chemical-Looping Combustion. Energy and Fuels 2010, 24, 1402-1413.

Adanez, J., A Abad, F Garcia-Labiano, P Gayan, LF de Diego. Progress in chemical-looping combustion and reforming technologies.Progress in Energy and Combustion Science 2012, 38, 215-282.

Corcoran, A., J Marinkovic, F Lind, H Thunman, P Knutsson, M Seemann . Ash properties of ilmenite used as bed material for combustion of biomass in a circulating fluidized bed boiler. Energy and Fuels 2014, 28, 7672-7679.

Cuadrat, A., A Abad, J Adánez, LF de Diego, F García-Labiano, P Gayán. Behavior of ilmenite as oxygen carrier in chemical-looping combustion. Fuel Processing Technology 2012, 94, 101-112.

Hanning, M., A Corcoran, F Lind, M Rydén. Biomass ash interactions with a manganese ore used as oxygen-carrying bed material in a 12 MWth CFB boiler. Biomass and Bioenergy 2018, 119, 179-190.

Hossain, M.M., HI de Lasa. Chemical-looping combustion (CLC) for inherent CO_2 separations-a review. Chemical Engineering Science 2008, 63, 4433-4451.

Hughes, R.W., DY Lu, RT Symonds. Improvement of Oxy-FBC Using Oxygen Carriers: Concept and Combustion Performance. Energy and Fuels 2017, 31, 10101-10115.

Kajnäs, C., M Hedberg, H Leion. The Effect of Iron- and Manganese-Based Oxygen Carriers as Bed Materials in Oxygen Carrier Aided Combustion. Energy Technology 2019. DOI: 10.1002/ente.201900321

Lind, F., A Corcoran, H Thunman. Validation of the oxygen buffering ability of bed materials used for OCAC in a large scale CFB boiler. Powder Technology 2017, 316, 462-468.

Lyngfelt, A. Chemical-looping combustion of solid fuels - Status of development. Applied Energy 2014, 113, 1869-1873.

Rydén, M., M Hanning, A Corcoran, F Lind. Oxygen carrier aided combustion (OCAC) of wood chips in a semi-commercial circulating fluidized bed boiler using manganese ore as bed material. Applied Sciences 2016 (Switzerland), 6, 1-19.

Thunman, H., F Lind, C Breitholtz, N Berguerand, M Seemann. Using an oxygen-carrier as bed material for combustion of biomass in a 12-MWth circulating fluidized-bed boiler. Fuel 2013, 113, 300-309.

Wang, P., H Leion, H Yang. Oxygen-Carrier-Aided Combustion in a Bench-Scale Fluidized Bed. Energy Fuels 2017, 31, 6463−6471.

Zhao, D., G Schwebel, NM Pour, H Leion, F Lind, H Thunman. Laboratory fluidized bed testing of ilmenite as bed material for oxygen carrier aided combustion (OCAC). CFB-11: Proceedings of the 11th International Conference on Fluidized Bed Technology 2014, 721-726.

PREDICTION OF THE BED TEMPERATURE OF A CFB BOILER AFTER A SUDDEN POWER CUT

Yuge Yao, Ling Jiang, Huiren Xiao, Boyu Deng, Man Zhang*, Yang Zhang, Hairui Yang, Junfu Lyu

Key Laboratory for Thermal Science and Power Engineering of Ministry of Education, Department of Energy and Power Engineering, Tsinghua University, Beijing 100084, China

*Email: *zhangman@tsinghua.edu.cn*

Abstract

When the power supply of a circulating fluidized bed (CFB) boiler is suddenly cut off, the massive bed materials will accumulate at the bottom of the furnace. Then a large amount of heat will be continuously transferred from the stationary bed materials to the tubes of the heating surfaces arranged in the furnace, which may result in metal failure and tube burst accidents. In this process, the bed temperature is a key parameter of the heat transfer. To predict the bed temperature of a CFB boiler after a sudden power cut, the heat transfer of the stationary bed materials is numerically simulated in this study which is confirmed by a real accident in a 170 t/h CFB boiler. The absolute deviations between the simulation results and the accident data are always within 20 ^{o}C, verifying the reliability of this simulation. The average bed temperature is also predicted to reach 645.6 ^{o}C at the 8th hour after the sudden power cut. The total heat loss of the stationary bed materials is estimated to be 1.1×10^{6} kJ.

Introduction

The unplanned sudden power cut is a common accident in the power plant boiler. Once the power supply of a circulating fluidized bed (CFB) boiler is suddenly cut off, the boiler will lose all the wind supply. As a result, the circulation of the bed materials in the main loop will be halted and then the bed materials accumulate at the bottom of the furnace. Although the coal combustion is suppressed due to the loss of the wind supply, there is still a large amount of heat stored in the stationary bed materials and continuously transferred by radiation and conduction to the heating surfaces arranged in the furnace. Absorbing too much heat, the heating surfaces may face the risk of metal failure and tube burst accidents (Duarte et al., 2017). Consequently, compared to a pulverized coal boiler, an unplanned sudden power cut may have a greater impact on the safety of a CFB boiler.

The bed temperature is a key parameter of the heat transfer in the furnace according to Arjunwadkar et al. (2016) and Yue et al. (2017). It can also directly reflect the heat dissipation process of the stationary bed materials after a sudden power cut. It is also an important parameter for the estimation of the heat transferred to the heat exchanger and the evaporation of the working fluid. Therefore, the accurate prediction of the bed temperature after a sudden power cut is significant to the safe operation of a CFB boiler.

However, few published studies have focused on heat transfer during this process. Only Deng et al. (2019) have predicted the temperature and pressure inside the water wall tube in a 350 MW supercritical CFB boiler after a sudden power cut while the validation of the prediction was proved by experimental data of a CO_2 experimental system. Meanwhile, it is not easy to find the data of the sudden power cut accidents in a CFB boiler. To fill this blank and predict the stationary bed temperature, a numerical simulation of the heat transfer in the furnace after a sudden power cut is conducted in this study based on and confirmed a real accident in a 170 t/h CFB boiler. Compared with the operation data obtained in that accident, the simulation results are proved to be reliable for further analysis. These results are significant to the safety assessment of the sudden power cut accident in a CFB boiler.

Numerical Simulation

Simulation object

The numerical simulation in this study is based on and confirmed by a real sudden power cut accident that happened in a 170t/h natural circulation CFB boiler of the Wendeng Power Plant located in Weihai, Shandong Province, China. The simulation object, a 1:1 model of a quarter of the bottom part of that furnace is shown in Fig. 1 and 2. As shown in Fig. 2, the simulation object consists of five parts: the bed materials (in brown), the refractory materials (in gray), the membrane tubes of the front wall (in green), the membrane tubes of the sidewall which extend to the bottom (in orange) and the working fluid inside the tubes. The stationary bed dissipated heat by radiation through its top surface and by conduction through the other surfaces contacted with the refractory materials. To help the understanding of the simulation object, the refractory materials and the membrane tubes of the sidewall are also shown in Fig. 3.

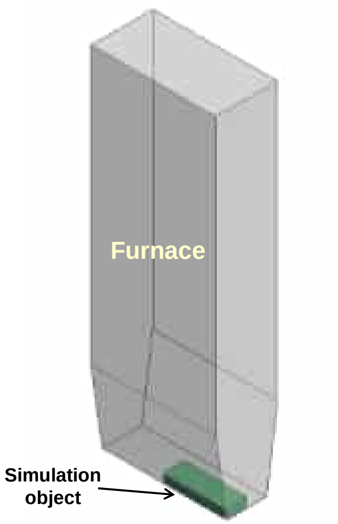

Fig. 1. The simulation object in the furnace.

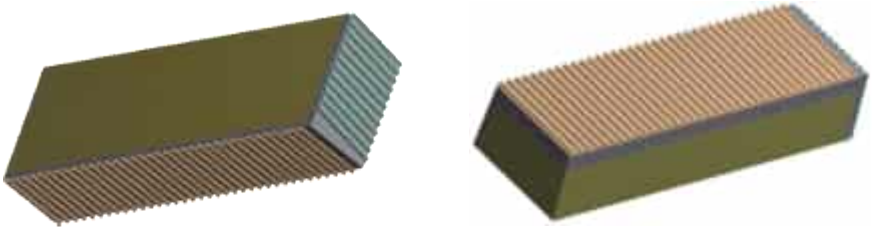

(a) (b)

Fig. 2. The simulation object in two different views.

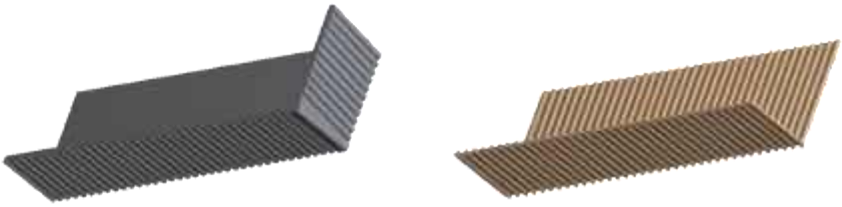

(a) Refractory materials (b) Membrane tubes of the sidewall

Fig. 3. Two parts of the simulation object in the same view as Fig. 2(a).

Assumptions

To simplify the complicated actual situation, some assumptions are adopted in this numerical simulation.

As shown in Fig. 2, several assumptions are made to simplify the simulation object:

a) The bottom part of that furnace is perfectly symmetrical, therefore only a quarter of the furnace is chosen as the simulation object.

b) The stationary bed materials have a flat top surface.

c) The backside of the membrane tubes and refractory materials is insulated, as a result, they are not concluded in the simulation object.

In addition, there are also a few assumptions made for the heat transfer process:

d) All the outer surfaces except the top surface of the simulation object shown in Fig. 2 are seen to be ideally insulated.

e) The stationary bed materials radiate heat to ambient with a constant temperature.

f) The bed materials have a uniform initial temperature of 850 ^{o}C according to the operation records.

g) The contact thermal resistance between the bed materials and refractory materials is neglected.

h) The combustion stops at once as the sudden power cut happens due to the sudden cut of all the wind supply, which means there is no initial heat source inside the bed materials in this study.

i) The heat transfer in the simulation object at the initial time is steady-state due to the stable operation before the sudden power cut.

j) The working fluid inside the tubes is always regarded as saturated water.

Settings

The settings of the numerical simulation based on a sudden power cut accident on Feb 23, 2018, in the CFB boiler mentioned in Section 2.1. The power supply to the boiler was unplanned cut off at 9:58 am, which is chosen as the initial time and restored at 12:35 pm. According to the operation data, at the initial time, the pressure inside the heat exchangers was 5.32 MPa and therefore the initial temperature of the working fluid is set to be 268 ^{o}C. The main steam temperature was 472 ^{o}C at the initial time, the tube wall temperature of the superheater is suggested to be 522 ^{o}C according to Yao et al. (2019), which is also selected to be the ambient temperature of the radiation. The height of the stationary bed materials is 600 mm according to the operation records.

Combined with the assumptions listed in section 2.2, the numerical simulation in this study can be implemented using ANSYS Workbench 18.2 software.

Results and Discussion

Validation of the simulation results

To verify the reliability of this simulation, the simulation results need to be compared with the accident data measured by three thermocouples inserted vertically from the front wall of the furnace. The locations of the measuring points are listed in Table 1.

Table 1. Locations of the measuring points.

Location	Point *A*	Point *B*	Point *C*
Distance from the central plane / mm	0	400	800
Insertion depth / mm	150	150	150
Submerged depth / mm	15	10	5

The temperature curves recorded by thermocouples and the simulation results of the three measurement points in the first 160 minutes are presented in Fig. 4. The simulation results are consistent well with the accident data and the absolute deviations between the simulation results and the accident data are always within 20 °C, which can prove that the simulation results are reliable for bed temperature prediction and further analysis.

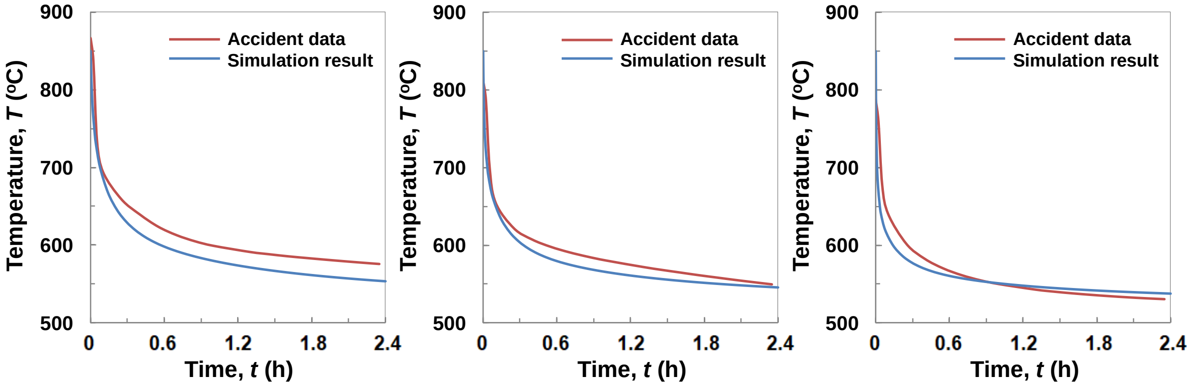

(a) Point *A* (b) Point *B* (c) Point *C*

Fig. 4. Comparison between the accident data and the simulation results.

Prediction of the stationary bed temperature

The average bed temperature directly reflects the overall heat dissipation trend of the stationary bed materials. The simulation result of the average bed temperature in 8 hours is present in Fig. 5. As shown in Fig. 5, the average temperature of the stationary bed materials has a sharp decrease at the initial time and then decreases slowly and steadily. At the time when the power supply restored, namely, 156 minutes after the sudden power cut, the average bed temperature decreased to 730.8 °C. This temperature is much higher than the ignition temperature of the designed coal of the CFB boiler mentioned in Section 2.1, which is about 550~650 °C reported by Yang et al. (2005) and Chao et al. (2016). That implies the unburned coal in the stationary bed materials will burn spontaneously after the restoration of the power and the wind supply, which is consistent with the operation records on that day and significant to the safe and stable operation of the CFB boiler. If the power supply keeps failed for a long period of time, the average bed temperature will decrease to 645.6 °C at the 8th hour after the sudden power cut.

As the decrease of the average temperature, the stationary bed materials continuously dissipate heat and the total heat loss is also presented in Fig. 5. It is estimated that the stationary bed materials dissipate 1.1×10^6 kJ in total during these 8 hours.

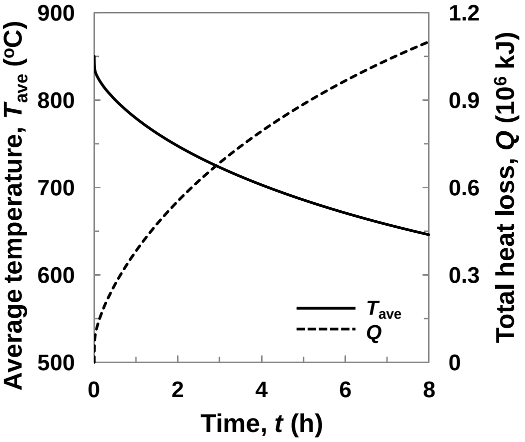

Fig. 5. The average temperature and total heat loss of the stationary bed materials.

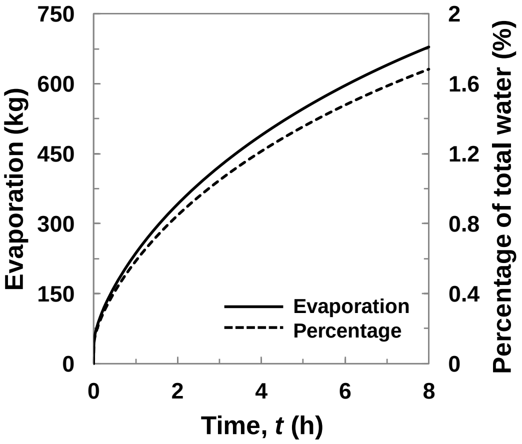

Fig. 6. The evaporation of the working fluid.

Assuming that all the heat dissipated from the bed materials is absorbed by the working fluid, the evaporation of the working fluid can be estimated, see Fig. 6. The working fluid keeps evaporating inside the tubes of the heat exchangers. However, up to the 8th hour, only less than 700 kg water has evaporated. In practice, partial heat dissipated from the bed materials is absorbed by the tube wall and the refractory materials, therefore the actual evaporation must be below the results shown in Fig. 6. The sudden power cut has a very small impact on the working fluid and the parameters such as pressure and temperature inside the tubes in this CFB boiler, indicating that the tubes of the heating exchangers will be safe for a long time after a sudden power cut.

Conclusion

A sudden power cut in a CFB boiler may lead to greater risk compared to a pulverized coal boiler. To predict the bed temperature of a CFB boiler after a sudden power cut, the heat transfer of the stationary bed materials is numerically simulated in this study based on a real accident in a 170 t/h CFB boiler. The simulation results are consistent well with the accident data, proving the reliability of this numerical simulation. The stationary bed materials continuously dissipate heat after a sudden power cut and the average bed temperature is predicted to be 645.6 ^{o}C 8 hours later, which indicates that the unburned coal in the stationary bed materials will burn spontaneously after the restoration of the wind supply, consistent with the operation records. Even assuming that the working fluid absorbs all the heat dissipated from the bed materials, only less than 700 kg water can evaporate in these 8 hours. That indicates the sudden power cut has a very small impact on the temperature and pressure inside the tubes and also the safety of the tubes in this CFB boiler. However, only one specific accident in a 170 t/h CFB boiler is considered in this work, the influencing factors that affect the heat transfer process after a sudden power cut and the restart-up performance also need to be known.

Acknowledgment

This research was supported by National Key Research and Development Program of China (2019YFE0102100) and Key Science and Technology Program of Shanxi Province (2018110200).

References

Arjunwadkar, A., Basu, P., Acharya, B. A review of some operation and maintenance issues of CFBC boilers. Applied Thermal Engineering. 2016. 102, 672-694

Chao, J., Yang, H., Wu, Y., et al. The investigation of the coal ignition temperature and ignition characteristics in an oxygen-enriched FBR. Fuel. 2016. 183, 351-8

Deng, B., Zhang, M., Lyu, J., et al. Safety analysis on the water wall in the 350 MW supercritical CFB boiler under sudden electricity failure. Energy. 2019. 189, 116364

Duarte, C.A., Espejo, E., Martinez, J.C. Failure analysis of the wall tubes of a water-tube boiler. Engineering Failure Analysis. 2017. 79, 704-713

Yang, H., Lu, J., Zhang, H. Coal ignition characteristics in CFB boiler. Fuel. 2005. 84, 1849-1853

Yao, Y., Cai, R., Zhang, Y., et al. A method to measure the tube-wall temperature in CFB boilers. Applied Thermal Engineering. 2019. 153, 493-500

Yue, G., Cai, R., Lu, J., et al. From a CFB reactor to a CFB boiler - the review of R&D progress of CFB coal combustion technology in China. Powder Technology. 2017. 316, 18-28

FORMATION OF NH_4Cl AND ITS ROLE ON COLD-END CORROSION IN CFB COMBUSTION

Emil Vainio*, Patrik Yrjas, Leena Hupa, Mikko Hupa

Johan Gadolin Process Chemistry Centre, Åbo Akademi University, Turku 20500, Finland

*Email: *emil.vainio@abo.fi*

Abstract

There is an increased demand to operate CFB boilers at various loads to cope with changes in energy demand. The combination of load changes and the use of additives to mitigate emissions has been shown to have dramatic effects on cold-end deposits and corrosion. Ammonium chloride (NH_4Cl) may form in the cold-end of the flue gas channel if NH_3 and HCl are present in the flue gases. During low load operation of a CFB boiler, some NH_3 released from the fuel nitrogen in the furnace may remain unreacted in the cooled flue gases. Furthermore, an NH_3 slip may form when using ammonia injection for NO_X mitigation. Ammonium chloride can cause corrosion and deposit build-up in the cold-end, e.g. corrosion of economizers, air-preheaters, and flue gas cleaning equipment. In this work, the conditions where NH_4Cl is stable were determined by thermodynamic calculations. The hygroscopic properties of NH_4Cl was determined in controlled conditions with a chronoamperometric setup for flue gas conditions to evaluate the corrosiveness of the salt at lower temperatures. Additionally, corrosion experiments with NH_4Cl on carbon steel and austenitic stainless steel were performed at 80-160 °C. SEM-EDX analyses of the corrosion products were performed to understand the corrosion mechanism. The results of this work can be used to optimize material temperatures and avoid corrosion caused by NH_4Cl.

Introduction

Optimization of energy recovery and efficient use of the energy in flue gases as well as the desire for reliable operation are of highest importance for the economy of power plants. Problems with corrosion and deposit build-up on heat transfer tubes and flue gas cleaning equipment in the cold-end may be an issue, however, the reason for this is not always clear. Generally, corrosion in the cold-end in power plants may be caused by dew point corrosion and hygroscopic deposits. Recently it has been shown that challenges related to corrosion and operational issues in the cold-end of the flue gas channel utilizing biomass fuels is mainly caused by hygroscopic salts and deposits:

- Corrosion of heat-exchangers (air preheaters and economizers), flue gas walls, and flue gas cleaning equipment (Brunner et al. 2017, Herzog et al. 2014, Lindau and Goldschmidt 2008, Retschitzegger et al. 2015, Vainio et al. 2014 and 2016)
- Deposit build-up by formation of wet and sticky deposits leading to a decrease in heat transfer and plugging of flue gas equipment (Herzog et al. 2014), e.g., by forming dense filter cakes in baghouse filters
- Down-time corrosion (Bakker 2004 and Jones et al. 2016)

Many salts that are formed in thermal conversion of biomass and waste are deliquescent, i.e., at a certain relative humidity, the salt will absorb enough water to fully dissolve in the absorbed water. This critical humidity is called the deliquescence relative humidity or DRH. Deliquescent salts may cause corrosion at surface temperatures well above 100 °C (Vainio et al. 2016 and 2019). The formation of deliquescent salts and deposits in energy conversion is influenced by the ash composition of the fuel, additives used (e.g., ammonia, limestone, lime), conversion technology, boiler operation, and flue gas composition. In a study in a large-scale bituminous coal fired CFB, Vainio et al. 2017 showed that changes in the operational mode had dramatic effects on cold-end deposits. At full load, no chlorine was detected in the cold-end deposits, whereas, during low load the deposit consisted mainly of NH_4Cl. Ammonium chloride was formed due to the presence of HCl and NH_3. The HCl in this case originated from the Cl in the coal burned. The NH_3 was obviously residues of the fuel nitrogen released in the CFB furnace but not fully converted there. Ammonium chloride is a hygroscopic salt and it has been reported to cause corrosion of economizers, at temperatures as high as 160 °C (Herzog et al. 2014). However, very high concentrations of NH_3 and HCl are needed for NH_4Cl to be stable at 160 °C (Fig. 2).

The purpose of this work was to learn more about the hygroscopic and corrosion properties of NH_4Cl at conditions relevant to CFB combustion flue gases. The hygroscopic properties of NH_4Cl were studied by measuring the conductivity of the salt using chronoamperometry. The corrosivity of NH_4Cl on test coupons of carbon and austenitic steels, respectively, in the temperature range of 80-160 °C.

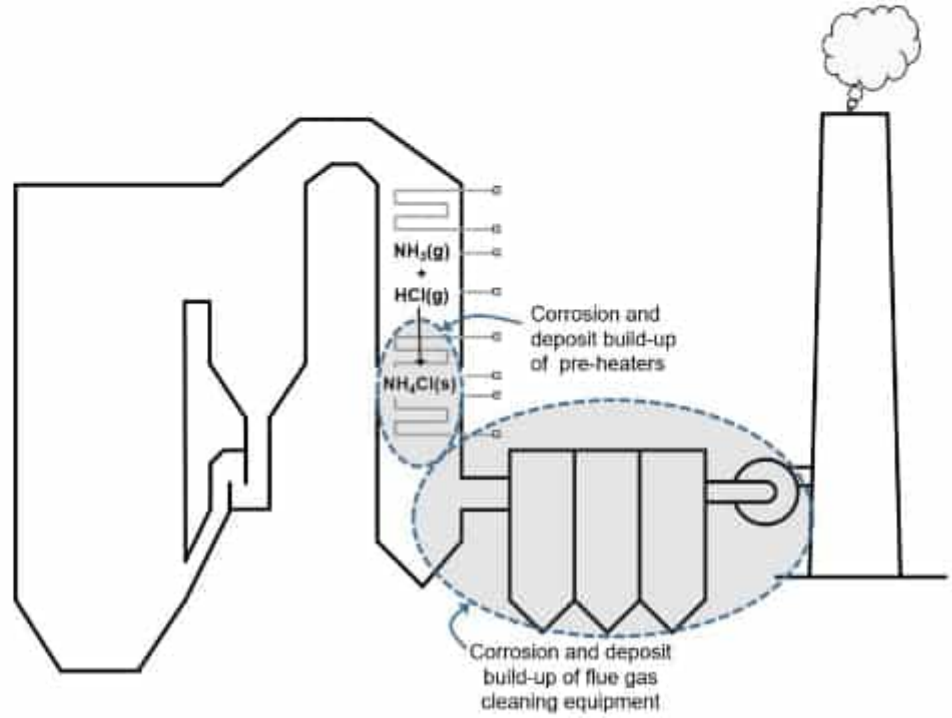

Fig. 1. Challenges caused by hygroscopic and deliquescent salts/deposits in CFB combustion.

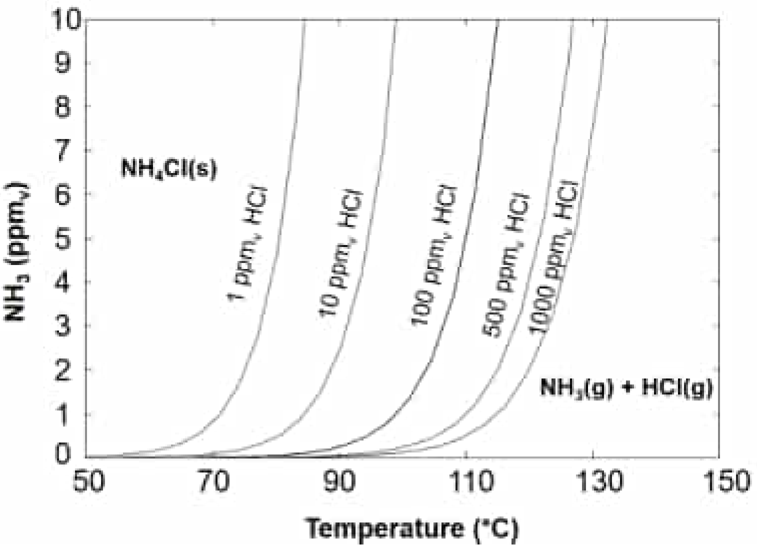

Fig. 2. Thermodynamic stability of $NH_4Cl(s)$ as calculated with FactSage 7.3.

Experimental

Corrosion tests

Two steel qualities were used in the corrosion tests: carbon steel (P235GH) and austenitic stainless steel (AISI 347). The corrosion experiments were done with 20 mm x 20 mm x 5 mm steel coupons. The coupons were first polished in ethanol with a 320 grit silicon carbide paper and then with a 1000 grit paper, and finally with a 2500 grit paper. Then, the coupons were washed in an ultrasound bath in ethanol. About 100 mg of NH_4Cl was placed on top of each of the coupons. The experimental setup is shown in Fig. 3. Three coupons were used in each experiment and were placed on a sample tray. The experiments were conducted in a gas atmosphere with 25 vol% water vapor at three temperatures: 80, 120, and 160 °C. The coupons were first heated in a nitrogen atmosphere to the desired temperature. When the temperature was stable, water vapor and oxygen were added to the gas. The total flow was 2 Nl/min and the O_2 concentration was 5 vol%. The exposure time was 24h. After exposure, one coupon was cast in epoxy, cut, and polished to reveal the cross-section. The metal surface was analyzed by means of scanning electron microscopy with energy dispersive X-ray spectroscopy (SEM-EDX), LEO Gemini 1530 with a Thermo Scientific UltraDry Silicon Drift Detector (SDD) and the mean corrosion layer thickness was determined. Additionally, the weight change of the coupon before and after the exposure was determined. After the exposure, the salt and corrosion products were rubbed off with a paper towel under water and then dried with acetone before weighing. The remaining corrosion products were removed by citric acid and the samples were weighed again.

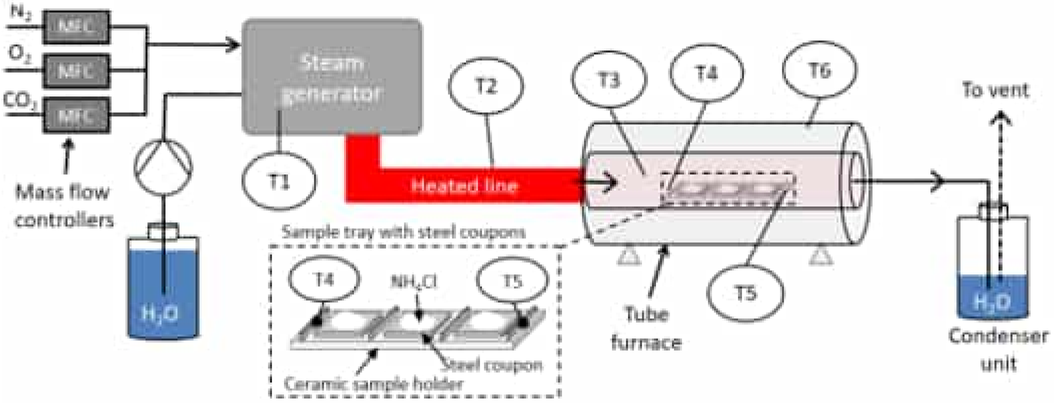

Fig. 3. Experimental setup in the corrosion experiments. T1-T6 indicate temperature measurements.

Measurements with Chronoamperometry

To determine the hygroscopic properties of NH_4Cl, the conductivity of the salt was measured at various water vapor concentrations. Two-electrode chronoamperometry (CA) was used to detect water uptake by the salt. The conductivity was measured using an EmStat portable potentiostat. One of the electrodes was employed as the working electrode and the other as the counter/reference electrode. Titanium electrodes were used, which were Teflon-coated, apart from the measuring tips, to avoid any disturbance of the signal from water condensation at the cold-end of the tube furnace used in the experiments. The voltage between the electrodes was set to 1000 mV. A more detailed description of the method can be found in Vainio et al. 2018.

Results

The weight change after exposure to 25 vol% H_2O for 24h at the various temperatures are shown in Fig. 4 and photographs of the steel coupons after both exposure, washing, and removing of corrosion products are shown in Table 1. At 80 °C the carbon steel corroded substantially and a clear weight gain was observed (11.0 mg). An iron oxide/hydroxide layer had formed which could not be removed in the water washing procedure. After removing the corrosion products with citric acid, a clear weight loss could be measured. The 27 mg weight loss corresponds to an average material loss of about 10 mm. An SEM image of the cross-section of the sample is shown in Fig. 5. The mean corrosion layer thickness was 74 µm over the corroded area. The corrosion product is mainly iron oxide/hydroxide. Some chlorine could be detected at the steel surface, which impplies the formation of iron chloirdes. The formation of iron chloride will lead to the acidification at the steel surface by the hydrolysis of the iron chlorides, which may accelrate the corrosion. At 120 °C some weight loss (0.2 mg) was observed and at 160 °C the weight loss was higher (2.3 mg). In the tests with the austenitic steel no clear corrosion was observed in the weight loss measurements.

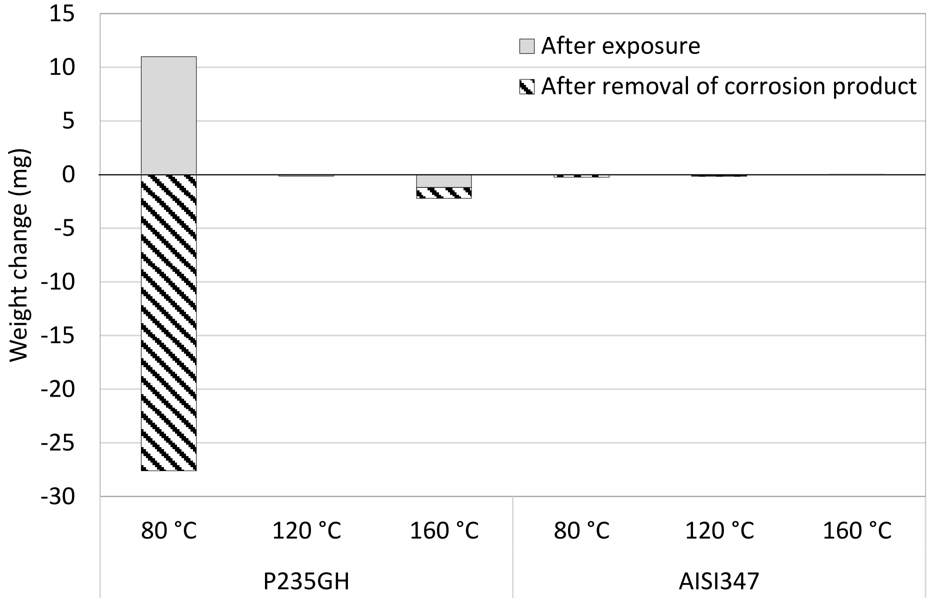

Fig. 4. Weight changes after exposure and after removing the corrosion products with citric acid. The two steel qualities were exposed to 25 vol% H_2O and 5 vol% O_2 at three temperature for 24 h.

Although no clear weight change was seen in the experiments with AISI 347, some discoloration of the steel coupon can be seen in Table 1. Longer exposures would be needed to clarify the corrosion resistance. At 120 °C the discoloration is around the salt and could be attributed to the dissocation of NH_4Cl to NH_3(g) and HCl(g) leading to a corrosive environment, while at 160 °C most of the salt has dissociated due to no NH_3(g) and HCl(g) in the inlet gas.

Table 1. Photos of the steel coupons after exposure and washing.

Test temp.	P235GH			AISI347		
	After exposure	After washing	After acid wash	After exposure	After washing	After acid wash
80 °C						
120 °C						
160 °C						

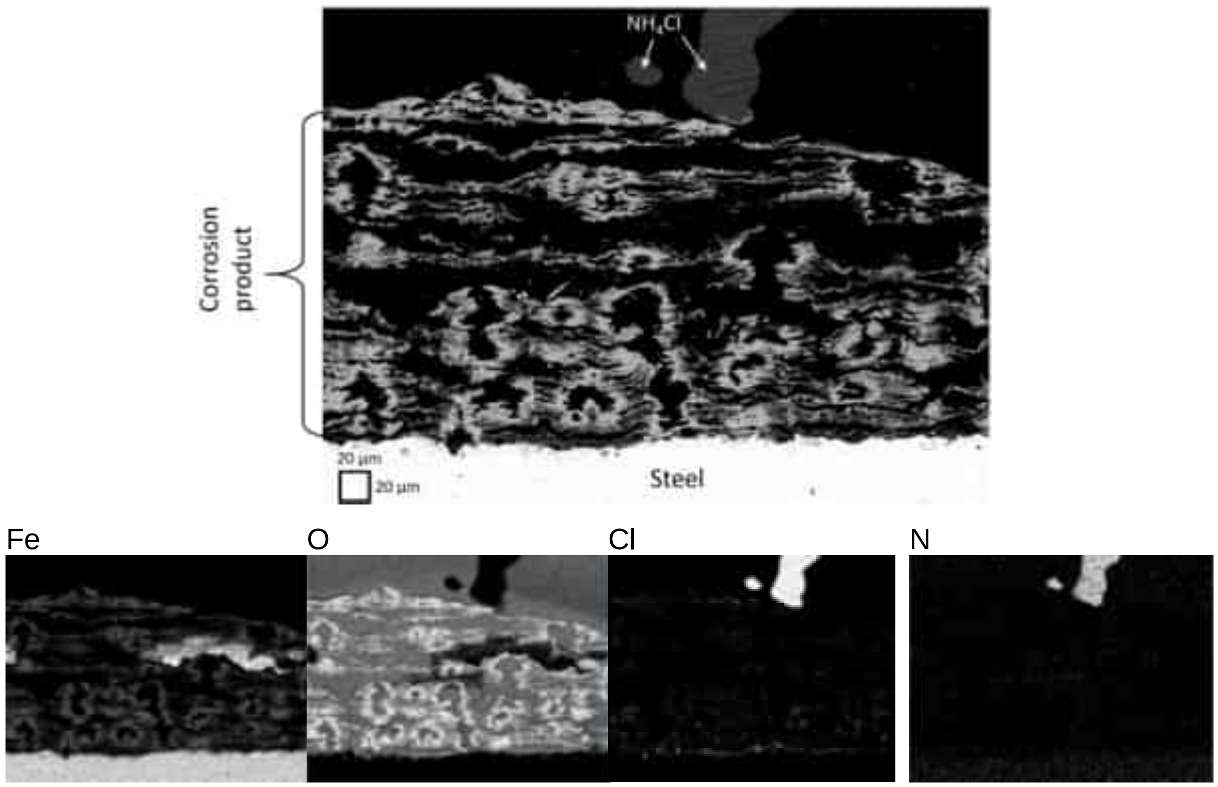

Fig. 5. SEM image of the cross-section's mid part of P235GH after exposure to 80 °C and 25 vol% H_2O, and x-ray maps of Fe, O, Cl, and N.

Results from the measurements of water uptake by NH_4Cl at 25 vol% by measuring the conductivity of the salt are shown in *Fig. 6*. In the beginning of the tests, the current reading is close to zero as the salt is dry. Water uptake by NH_4Cl starts when the temperature is decreased below about 91 °C, as can be seen from the increase in the current signal. Hence, the heavy corrosion seen at 80 °C in the case with carbon steel is caused by the salt absorbing water and resulting in a highly corrosive environment. However, from Table 1 it can be seen that the salt is not deliquescent at these conditions, instead only some water has been absorbed by the salt. The corrosion seen at 160 °C for the carbon steel cannot however be explained by the hygroscopic properties of the salt.

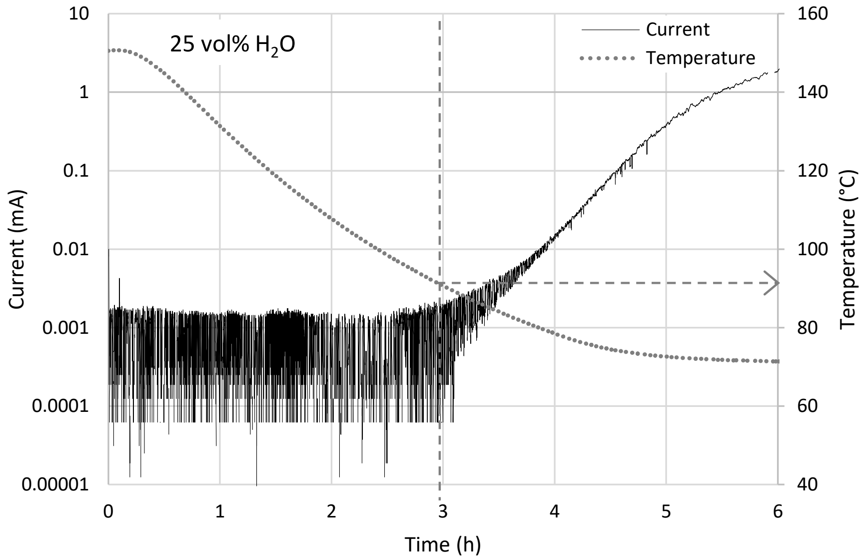

Fig. 6. Current and temperature readings in the experiment with NH_4Cl at 25 vol% H_2O. Water uptake starts at 91 °C.

Summary and Conclusions

Ammonium chloride can form in the cold-end of CFB boilers if $NH_3(g)$ and HCl(g) are present. The work revealed that NH_4Cl is highly corrosive on carbon steel if the salt absorbs water. At 80 °C and 25 vol% H_2O a thick (on average 74 µm in 24h) corrosion layer was formed implying extremely rapid corrosion (several mm/y). At these conditions, NH_4Cl absorbed some water, but did not deliquesce. The temperature for water uptake by NH_4Cl depends on the water vapor concentration in the flue gases. The ability of NH_4Cl to absorb moisture from the flue gas was further studied with chronoamperometry; with a water vapor concentration of 25 vol%, the salt started to absorb water at about 91 °C. Corrosion of carbon steel was also observed at higher temperatures. At 160 °C, a clear weigh loss of the carbon steel was observed. Ammonium chloride does not absorb water at 160 °C, however corrosion could be caused by the dissociation products of NH_4Cl ($NH_3(g)$ and HCl(g)). The austenitic stainless steel did not show clear signs of corrosion at any of the experimental conditions, even in the cases when water was absorbed by the salt. To avoid heavy corrosion of carbon steel by NH_4Cl, the material temperatures have to be maintained above the water uptake temperature for NH_4Cl. The formation of NH_4Cl may also be avoided by controlling the $NH_3(g)$ slip and HCl(g) in the flue gas. In this case, the measurement should be done at a position where NH_4Cl is not yet formed, i.e. at flue gas temperatures of about 100-140 °C depending on the $NH_3(g)$ and HCl(g) concentrations.

Acknowledgements

This work is part of the project Clean and efficient utilization of demanding fuels (CLUE), with support from the industrial partners: ANDRITZ, Fortum, International Paper, UPM-Kymmene Corporation, and Valmet Technologies Oy. The work was financed by Academy of Finland (Decision No. 289869 and 333917) and is gratefully acknowledged. We also want to thank Linus Silvander for carrying out the SEM/EDXA analyses and Jaana Paananen for helping out with experimental work.

References

Bakker, W. High Temperature Corrosion in Gasifiers, Materials Research 2004; 7(1): 53-59.

Brunner T, Reisenhofer E, Obernberger I, et al. Low-Temperature Corrosion in Biomass-Fired Combustion Plants - Online Measurement of Corrosion Rates, Acid Dew Points and Deliquescence Corrosion, 25th European Biomass Conference and Exhibition 2017.

Herzog T, Müller W, Spiegel W, et al. Corrosion caused by dewpoint and deliquescent salts in the boiler and flue gas cleaning VGL: KG Thome-Kozmiensky og M. Beckmann: Energie aus Abfall Band 9 Neuruppin: TK Verlag 2012; 429–460.

Jones F, Ryde D, Hjörnhede A.Down-time corrosion in boilers, Fuel Processing Technology 2016; 141:276-284.

Lindau L and Goldschimdt B. Low temperature corrosion in bark fueled, small boilers. Värmeforsk Services AB, 2008; M9–835.

Retschitzegger S, Brunner T, Obernberger I. Low-Temperature Corrosion in Biomass Boilers Fired with Chemically Untreated Wood Chips and Bark. Energy Fuels 2015; 29(6): 3913–3921.

Vainio E, DeMartini N, Hupa L, Åmand L-E, Richards T, Hupa M. Hygroscopic Properties of Calcium Chloride and its Role on Cold-End Corrosion in Biomass Combustion, Energy & Fuels 2019, 10.1021/acs.energyfuels.9b02731

Vainio E, Kinnunen H, Laurén T, et al. Low-Temperature Corrosion in Co-Combustion of Biomass and Solid Recovered Fuels, FUEL 2016; 184: 957-965.

Vainio E, Laurén T, DeMartini N, et al. Understanding low-temperature corrosion in recovery boilers: risk of sulphuric acid dew point corrosion? J-FOR 2014; 4(6):14–22.

SORBENT-ENHANCED BIOCHAR-DIRECT CHEMICAL LOOPING PROCESS FOR HYDROGEN PRODUCTION WITH CO_2 CAPTURE

Zezhong John Li[1], Long Bill Cheng[1*], Arian Ebneyamini[1], Jun Young Kim[1], John R. Grace[1], C. Jim Lim[1], and Naoko Ellis[1]

[1]*Department of Chemical and Biological Engineering, University of British Columbia*
2360 East Mall, Vancouver, BC, V6T 1Z3, Canada

*Email: lcheng96@chbe.ubc.ca

ABSTRACT

A novel sorbent-enhanced biochar-direct chemical looping process is introduced for hydrogen production utilizing steam-iron reaction. ASPEN simulation was employed, performing a preliminary equilibrium analysis on the sorbent-enhanced biochar-direct iron oxide reduction. The effects of biochar and sorbent addition on the iron oxide reduction and reactor heat duty were investigated at different reactor temperatures. It is predicted that co-feeding of biochar and lime-based sorbents can significantly enhance the extent of iron reduction, while producing H_2-rich syngas under a limited range of operating conditions. It was also observed that the proposed process can offer nearly autothermal iron oxide reduction at reactor temperature range of 650-700°C.

Introduction

Chemical Looping Hydrogen Production (CLHP) is a novel technology for hydrogen generation using metal-based oxygen carriers (OC) (Chiesa et al., 2008). This process involves OC reduction in a fuel reactor, followed by OC re-oxidation in the presence of steam. Steam oxidation of the reduced OC produces a substantial amount of hydrogen, which can be purified by condensing the steam content of the oxidizer off-gas. One of the key challenges of the CLHP process is the low OC reduction extent in the fuel reactor. *In situ* CO_2 removal using CaO-based sorbents has been previously reported by Kim et al. (2019) to enhance the metal oxide reduction extent in fuel reactors.

Biomass gasification is a renewable fuel production route, generating syngas of higher heating value, mainly composed of H_2, CO, CO_2, CH_4 and steam. Such syngas is a strong reductant medium, which could be used in CLHP fuel reactors. Nevertheless, biomass-derived syngas contains undesirable contaminants (tar and sulfur compounds), and therefore, requires pre-treatment prior to the CLHP application (Abdelouahed et al., 2012). Biochar, a by-product of the biomass gasification, can also be a promising reducing agent. In fact, reducing metal oxides with solid carbon sources (e.g., coal, biochar) has been widely applied through the carbothermic reaction. However, solid-solid carbothermic reactions are challenging due to a restricted mass transfer in fluidized bed reactors, a major concern for practical applications. This imposes a challenge for integrating carbothermic reaction with the CLHP process, which would normally be conducted in dual fluidized bed reactors.

Fig. 1 demonstrates a general schematic of the proposed biochar-direct sorbent enhanced CLHP (BD-SE-CLHP) process, including a fuel reactor (FR), hydrogen generator (HG) and steam calciner. This process combines the merits of CLHP and carbothermic reaction by co-feeding syngas and biochar into the fuel reactor. It is postulated that syngas would act as a transferring agent, carrying oxygen from oxygen carrier to biochar and consequently, replacing the solid-solid reaction by conventional gas-solid reactions. This scheme is believed to enhance the overall reduction extent of the OC in the fuel reactors, decreasing the mass transfer limitations for the carbothermic reaction. CaO-based sorbents can also be fed into the fuel reactor, capturing the CO_2 generated for further metal oxide reduction. The exothermic carbonation may also be able to supply the energy required for the endothermic reduction and gasification within the fuel reactor. In addition, considering the fact that CaO-based, iron-based and biochar-based materials have been widely used as syngas cleaning catalysts (Han et al., 2011), the use of iron oxide as OC with CaO as CO_2 sorbents and biochar could potentially demonstrate an economically feasible route to reform undesirable syngas contaminants within the BD-SE-CLHP process.

Assuming complete biochar consumption, a mixture of the reduced OC and carbonated lime leaves the FR toward the hydrogen generator (HG) where the reduced OC is oxidized to Fe_3O_4 in the presence of steam. Given the low temperature of the steam-iron process (below 500°C), the limestone calcination might not occur in the HG reactor as reported by Chiesa et al. (2008). Hence, the resulting solid is directed to a steam calciner, regenerating the spent CaO sorbent prior to recirculation. To the best of authors' knowledge, this is the first study on the co-feeding of syngas, biochar and CO_2 sorbents into a CLHP fuel reactor. ASPEN PLUS V.10 was employed to investigate the equilibrium performance of the proposed fuel reactor at different operating conditions. The effects of biochar addition and *in situ* CO_2 capture on the iron oxide reduction and reactor heat duty were studied at different operating temperatures.

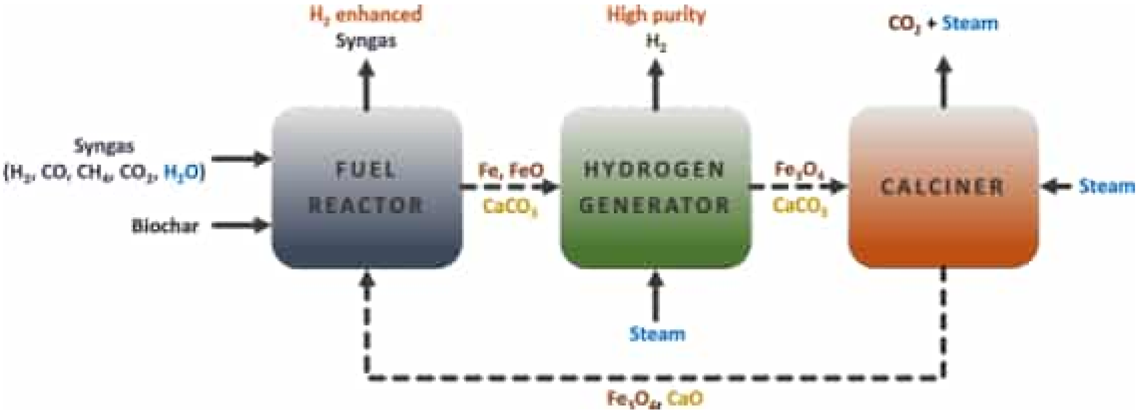

Fig. 1. Schematic diagram of the SE-BD-CLHP process

Simulation Setup

The equilibrium performance of the fuel reactor in the BD-SE-CLHP process was studied by means of ASPEN Plus simulation. The FR was modeled as an isothermal RGibbs reactor, while four preheaters increased the feed (syngas, Fe_3O_4, biochar, and CaO) temperatures to the reactor temperature. The Peng-Robinson equation of state was applied, with biochar being represented by elemental carbon (graphite phase). The syngas feed flow rate (1 kmol/h) and composition (Table 1) were fixed for the simulation. The Fe_3O_4 feed flow rate was also maintained at 2.5 kmol/h, sufficiently high for incomplete iron oxide reduction for the range of operating conditions studied. The FR reduction performance and heat duty was tracked at different reactor temperatures and biochar feeding ratios. The effect of *in situ* CO_2 capture on the reactor performance was also studied by feeding excess CaO into the reactor. A summary of the applied simulation basis and ranges is presented in Table 2.

Table 1. Syngas composition for ASPEN simulation (Li et al., 2018)

Composition	H_2	CO	CO_2	CH_4	Ar	H_2O
mol. %	17.5%	25.1%	8.8%	7.0%	1.6%	40.0%

Table 2. Simulation parameters and range of FR

Parameter	Range of Values
Reactor pressure (atm)	1
Reactor temperature (°C)	600-800
Syngas feed (kmol/h)	1
Fe_3O_4 feed (kmol/h)	2.5
Biochar feed (kmol/h)	0-3
CaO feed (kmol/h)	0 and 4

Results and Discussions

A number of reactions are considered in order to understand the variation of the FR performance at different biochar-to-syngas molar feed ratios (BSR) and reactor temperatures. Char gasification by CO_2 (Boudouard reaction) and steam are the major mechanisms for converting biochar into CO and H_2, respectively. Hereafter for simplicity, these two reactions are collectively referred to as char gasification. The two iron oxide phases present in this simulation, Fe_3O_4 and FeO, are reduced in the presence of H_2 and CO, either generated via biochar gasification or fed as syngas. Subsequently, iron oxide reduction generates CO_2 and steam, resulting in further biochar gasification within the reactor. It appears that the syngas transfers oxygen from the iron oxide to biochar, leading to a higher iron oxide reduction extent in the FR reactor. Implementation of the CaO sorbent can also lower the CO_2 concentration through the carbonation reaction, thereby enhancing the extent of iron oxide reduction in the FR reactor.

Fig. 2 plots the Fe_3O_4 reduction performance (Fe_3O_4 conversion and product Fe/FeO ratio) with varying BSR and reactor temperature, in the presence or absence of CaO. Increasing BSR leads to increased CO and H_2 generation by biochar gasification, resulting in enhanced Fe_3O_4 reduction. The equilibrium conversion of the Fe_3O_4 increases linearly upon reaching a BSR value of roughly 1, corresponding to 100% conversion of the Fe_3O_4 to FeO. The reaction temperature was observed to have a limited impact on the Fe_3O_4 conversion within the temperature range of this study. Neither does the presence of CaO noticeably change the Fe_3O_4 conversion for BSR less than unity.

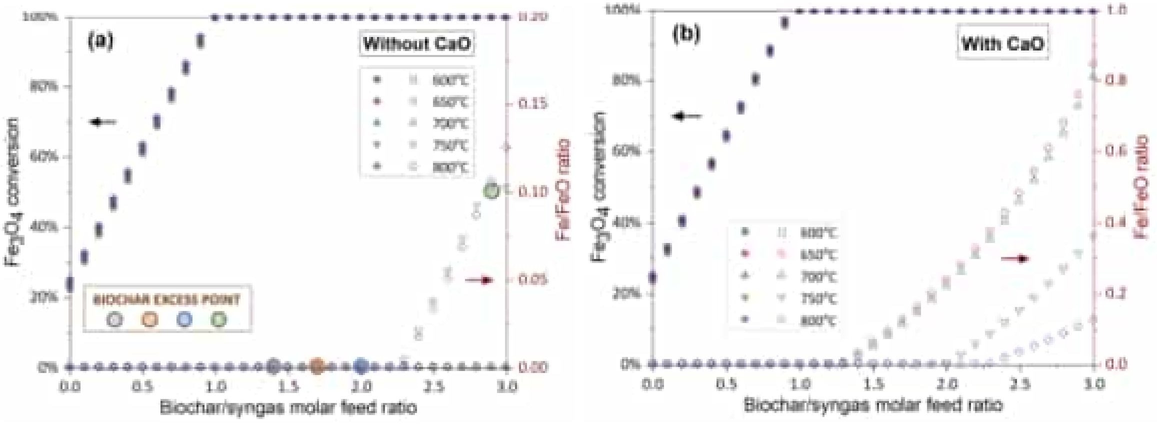

Fig. 2. Effect of biochar to syngas molar ratio on Fe_3O_4 conversion and Fe/FeO ratio in reduced OC: (a) without CaO; (b) with excess CaO addition

The simulation predictions presented in Fig. 2 also demonstrate that FeO can be further reduced into metallic iron at elevated BSR values. This is due to the higher required concentration of the reducing species (H_2, CO, and CH_4) for initiation of FeO to Fe conversion, mainly owing to the higher reduction potential of Fe^{3+} than Fe^{2+} ions (Cheng et al., 2016). Indeed, further addition of biochar might convert the steam and CO_2 content of the gaseous mixture to highly reductive H_2 and CO, increasing the reducibility of the FR gaseous medium and, hence, reducing the FeO to metallic iron.

Furthermore, the simulation results indicated that the metallic iron production depends strongly on the reactor temperature and the absence/presence of CaO sorbents. Increasing the BSR in a sorbent-free reactor does not affect the extent of iron reduction at low reactor temperature (< 750°C), but leads to excess biochar due to thermodynamic limitations. Incomplete biochar conversion is practically undesirable since additional biochar removal would need to be implemented prior to transferring the solid mixture to the steam-iron reactor. A minimum BSR of 2.3 is predicted to initiate metallic iron production at sorbent-free reactor temperatures exceeding 750°C. Interestingly, the addition of CO_2 sorbent resulted in significant Fe generation at reduced BSR values, even at reactor temperatures below 750°C. This could be due to the positive impact of CO_2 removal on the reducibility of the FR gaseous mixture. Note that atmospheric lime carbonation only occurs if the CO_2 partial pressure is higher than the $CaO/CaCO_3$ equilibrium value, with the equilibrium CO_2 partial pressure increasing with reactor temperature as reported by Stanmore and Gilot (2005). Therefore, the reduction enhancement by CaO addition is hindered by reactor temperature, with an operating temperature of 600-700°C being optimal at atmospheric pressure.

Fig. 3 shows the variation of the FR reactor heat duty with operating conditions similar to those in Fig. 2. It is found in Fig. 3(a) that increasing the BSR ratio leads to higher reactor heat duty in the absence of CaO-based sorbents. This is due to a larger extent of biochar gasification, resulting in more reactor endothermicity at elevated BSR ratios. Note that exceeding a certain BSR ratio results in incomplete biochar conversion at lower temperatures (< 750°C) and therefore, thermodynamic equilibrium insensitive to the biochar addition. Furthermore, it was found in Johnsen et al. (2006) that the reactor heat duty at 600°C differs largely from other temperatures owing to less favoured biochar gasification at reduced reactor temperatures. In addition, increasing BSR at reactor temperatures > 700°C results in a higher extent of biochar gasification, ultimately reducing FeO to Fe. Accordingly, the reactor heat duty continues to grow as the BSR ratio is increased at elevated reactor temperatures.

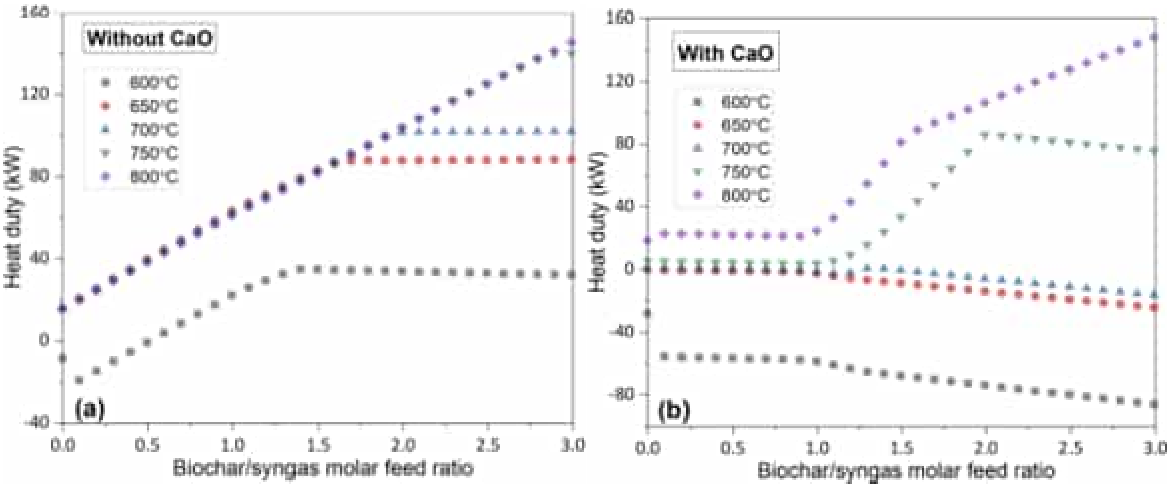

Fig. 3. Effect of biochar to syngas ratio on reactor heat duty: (a) without CaO; (b) with excess CaO

On the other hand, as depicted in Fig. 3(b), the addition of CaO-based sorbents resulted in reducing the reactor heat duty in most cases. This is mainly due to the highly exothermic lime carbonation, resulting in a substantial release of energy within the reactor (Ebneyamini et al., 2019). As mentioned above, the carbonation extent depends strongly on the CO_2 partial pressure and the reactor temperature. Lime carbonation is extremely favoured at 600°C, resulting in more exothermicity compared to the sorbent-free fuel reactor. The simulation results demonstrate a stable reactor heat duty at a BSR ratios of less than unity, with the system becoming more exothermic as the BSR ratio is increased further. This might be due to less endothermicity of the FeO reduction (compared to Fe_3O_4 to FeO conversion), resulting in a slightly exothermic reaction due to lime carbonation.

Fig. 3(b) also indicates that the FR reactor can be operated at nearly autothermal conditions with reactor temperatures of 650-700°C, while the reactor heat duty slightly reduced if a BSR ratio of unity is exceeded. This is similar to the results obtained at 600°C, with the difference of a higher extent of biochar gasification, leading to higher reactor heat duty at elevated reactor temperatures. In fact, the energy released by exothermic CaO carbonation balances the heat required by the endothermic reduction and gasification at reactor temperatures of 650-700°C. Given the preference of autothermal metallic iron production, a BSR ratio >1.3 and reactor temperature of 650-700°C would be optimal for this fuel reactor configuration. A further increase of the reactor temperature would lead to less lime carbonation, resulting in less impact of CaO addition on the iron oxide reduction behaviour (Fig. 2(b)) and FR heat duty (Fig. 3(b)). Note that the optimal operating conditions might be sensitive to the syngas compositions. More investigations are required to improve the current knowledge of this novel fuel reactor configuration.

The simulation results in Fig. 3(b) further show a multi-stage variation of the reactor heat duty at reactor temperatures exceeding 700°C. This is mainly due to the lower impact of lime carbonation at elevated reactor temperatures. Increasing the BSR did not significantly change the reactor heat duty for a BSR of less than unity. This is similar to other reactor temperatures, and is mainly due to competitive behaviour of Fe_3O_4 reduction, biochar gasification and lime carbonation. For a BSR ratio of 1 to nearly 2, the iron remains in the FeO phase while the biochar is further gasified, utilizing CO_2 and steam from the gaseous medium. Reducing the CO_2 partial pressure inside the reactor leads to a lower carbonation extent and therefore, more endothermicity. FeO starts to reduce into metallic iron at BSR of nearly 2, resulting in enhanced CO_2 generation. The increased CO_2 concentration increases the lime carbonation extent, and therefore the system becomes less endothermic with further increases of the BSR. Note that the lime carbonation is more favoured at 750°C and, hence, the effect of carbonation on reactor heat duty is more pronounced compared to a FR temperature of 800°C.

Conclusion

A novel configuration of the chemical looping hydrogen production process is introduced, implementing gasification-derived biochar and CaO-based sorbent inside a fuel reactor. Co-feeding of biochar and lime results in enhanced iron reduction at reduced reactor temperatures. In addition, the exothermic lime carbonation can release a substantial amount of energy within the reactor, resulting in a nearly autothermal reactor at operating temperatures of 650 to 700°C. Further studies are being undertaken on the feasibility and limitations of the proposed process when the reaction kinetics and reactor hydrodynamics are considered.

Abbreviations

BD-SE	Biochar Direct – Sorbent Enhanced
BSR	Biochar to Syngas Ratio
CLHP	Chemical Looping Hydrogen Production
FR	Fuel Reactor
HG	Hydrogen Generator
OC	Oxygen Carrier

References

Abdelouahed, L., O. Authier, G. Mauviel, JP Corriou, G. Verdie, A. Dufour. Detailed modeling of biomass gasification in dual fluidized bed reactors under Aspen plus. Energy & Fuels. 2012. 26, 3840–55

Cheng, Z., L. Qin, M. Guo, JA Fan, D. Xu, LS Fan. Methane adsorption and dissociation on iron oxide oxygen carriers: the role of oxygen vacancies. Phys Chem Chem Phys. 2016. 18, 16423-35

Chiesa, P., G. Lozza, A. Malandrino, M. Romano, V. Piccolo. Three-reactors chemical looping process for hydrogen production. Int J Hydrogen Energy. 2008. 33, 2233–45

Ebneyamini, A., JR Grace, CJ Lim, N. Ellis, SSEH Elnashaie. Simulation of limestone calcination for calcium looping: potential for autothermal and hydrogen-producing sorbent regeneration. Ind Eng Chem Res. 2019. 58, 8636–55.

Li, YH, Z. Chen, AP Watkinson, XT Bi, JR Grace, CJ Lim, N. Ellis. A novel dual-bed for steam gasification of biomass. Biomass Convers Biorefinery. 2018. 8, 357–67.

Han, L., Q. Wang, Y. Yang, C. Yu, M. Fang, Z. Luo. Hydrogen production via CaO sorption enhanced anaerobic gasification of sawdust in a bubbling fluidized bed. Int J Hydrogen Energy. 2011. 36, 4820–29

Johnsen, K., JR Grace, SSEH Elnashaie, L. Kolbeinsen, D. Eriksen. Modeling of sorption-enhanced steam reforming in a dual fluidized bubbling bed reactor. 2006. 45, 16423-35

Kim, JY, N. Ellis, CJ Lim, JR Grace. Attrition of binary mixtures of solids in a jet attrition unit. Powder Technol. 2019. 352, 445–52.

Stanmore, BR, P. Gilot. Review: calcination and carbonation of limestone during thermal cycling for CO_2 sequestration. Fuel Process Technol. 2005. 86, 1707-43

CFD SIMULATION OF GAS PARTICLE FLOWS IN A CFB CARBON CAPTURE UNIT USING SOLID SORBENTS

Farnaz Esmaeili Rad[*], **Javad Abbasian**, **Hamid Arastoopour**

Department of Chemical and Biological Engineering, Illinois Institute of Technology,
Wanger Institute for Sustainable Energy Research (WISER), Illinois Institute of Technology,
Chicago, IL 60616

*Email: *fesmaeil@hawk.iit.edu*

Abstract

The significance of this study is the use of computational fluid dynamics (CFD) approach to simulate entire a circulating fluidized bed (CFB) loop that was designed by the National Energy Technology Laboratory (NETL) for carbon capture using solid sorbents. The kinetic theory based granular flow model along with frictional stress and viscosity for dense solid flow regimes were used in this study. The solid flow rate was calculated at different locations of the CFB system. Our simulation predicted steady solid circulation and pressure balance in the entire CFB loop. Calculated pressure drop using our CFD across the system components compared well with NETL experimental pressure profile data. It is observed that the neglection of granular temperature diffusion and convection terms in the granular temperature equation results in over prediction of solids flow rate in the CFB loop.

Introduction

There are increasing concerns over the emission of greenhouse gases, particularly CO_2. One of the major sources of CO_2 is fossil-fuel-fired power plants. Amine-based aqueous solutions have been used to capture carbon dioxide from gas streams. This CO_2 capturing method suffers from a high energy penalty because of the energy required to heat water during CO_2 recovery. Therefore, amine-based solid sorbents have been considered as a promising alternative to amine aqueous solutions (Gray et al. 2009),(Yang and Hoffman 2009). Amine-covered solid sorbents have high capacity and selectivity and can be operated in temperature and pressure swing systems (Spenik et al. 2015). They can adsorb CO_2 at lower temperature and desorb it at higher temperature; they also require less energy during regeneration which makes them more economically feasible. Supported amine-solid materials are practically effective for CO_2 capture at relatively low CO_2 partial pressure in flue gas exiting fossil-fuel-fired power plants.

NETL has designed a small-scale circulating fluidized bed to evaluate the performance and hydrodynamics of solid sorbents in an adsorption and regeneration system (Breault et al. 2016). The circulating fluidized bed consists of four fluidized beds (see Fig. 1). The injected gas from the bottom of the first fluidized bed carries solids along the riser pipe. After the gas and solid passes the crossover, the gas goes out at the cyclone and particles exit from the bottom of the cyclone and fill the dip-leg. Then, the particles move through the upper loop-seal and overflow into the second fluidized bed. In the second fluidized bed, the solids move downward and pass into the stand pipe. At the horizontal part of the L-valve, particles move into the lower loop-seal. The solids overflow from the top of the lower loop-seal into fluidized bed 1 and complete the solid circulation loop. CFD simulation of this system provides the essential tools for scale up of such carbon capture units. This paper is focused on simulation of the hydrodynamics of the entire circulating fluidized bed (CFB) loop designed by NETL.

Mathematical Modeling

In this study, the Eulerian-Eulerian two-fluid model (TFM) was used to perform CFD simulations of a circulating fluidized bed. Continuity and momentum conservation equations were solved for both phases. The kinetic theory of granular flow was used to close the governing equations (Arastoopour, Gidaspow, and Abbasi 2017),(Arastoopour 2001). In addition, granular temperature diffusion and convection terms were neglected in the granular temperature conservation equation to reduce computational time. To consider the formation of clusters in the solid phase, the EMMS (energy minimization multi-scale) drag model was used (Lu, Wang, and Li 2011). For the gas phase, a no-slip and non-penetrating wall boundary condition was considered. For the solid phase, the Johnson and Jackson slip boundary condition with a specularity coefficient of 0.5 was considered (Johnson and Jackson 1987).

Initial bed heights and particle properties are shown in Table 1. Gas and solid velocities initially were set to be zero throughout the entire system and the solid volume fraction was assumed to be 0.5 in all four fluidized beds. Uniform gas velocity injections were applied to all beds. Pressure at the outlet of the cyclone and fluidized bed 2 were set to be at atmospheric pressure.

The FLUENT 16.1 was used to perform the simulations. The EMMS drag model was compiled using the User-Defined Function (UDF). The governing equations were discretized using a second-order upwind scheme. A time step of 5×10^{-5} was chosen to avoid divergence. The convergence criterion for all variables' scaled residual was set at 10^{-3}.

Table 1. Initial and Boundary Conditions

Properties	**Values**
Particle size	115 μm
Particle density	910 kg/m^3
Gas density	1.225 kg/m^3
Gas viscosity	1.789$\times 10^{-5}$ kg/m.s
Inlet gas velocity	
Fluidized bed 1	0.032 m/sec
Loopseal 1	0.01 m/sec
Fluidized bed 2	0.01 m/sec
Loop-seal 2	0.01 m/sec
Aerations at L-valve	0.0003 m/sec
Initial bed height	
Fluidized bed 1	0.375 m
Loop-seal 1	0.25 m
Fluidized bed 2	0.4 m
Loop-seal 2	0.25 m

Results and Discussion

Simulation results of the solid circulation rate in a CFB, sensitivity of the system to the gas flow rates, and gas injections at different parts of the unit are presented in this section.

Fig. 1 shows the simulation of solid flow in the entire CFB system after 36 seconds of operation. Gas is injected from the bottom of fluidized bed 1 to fluidize the solids. Fluidized bed 1 operates relatively at dense regime. Our simulation demonstrated that the particles that were at the top part of the bed mixed more rigorously and the particles close to the riser entrance were pushed into the riser by the gas in this section. Because the riser entrance was initially inside of the bed, our simulation showed that we initially had high solid flow to the riser. Then, the bed height leveled off to the riser entrance level. Our simulation showed that, due to the gas suction at this section, the particles at the top of the bed formed a cone. At the center of the cone, which is in line with the entrance of the riser, the average solid volume fraction is much lower in comparison with the average volume fraction of the bed.

Our simulation showed heterogeneous gas-solid distribution and cluster formations at the riser and at the horizontal part of the crossover, some particles deposit and gas pushes out a pile of solids that have stacked together. Therefore, the solid circulation rate calculation at the outlet of the riser to the cyclone showed more fluctuation compared to the top part of the riser (see Fig. 2). The average particles flow at the outlet of the riser is the same as the solids flow rate at the L-valve.

At the dip-leg, the flow regime was almost moving packed bed. Particles have moved downward and entered into the upper loop-seal. Gas injection from the bottom of loop-seal 1 was one centimeter per second, twice the minimum fluidization velocity. Therefore, the average solid volume fraction was higher than that of fluidized bed 1, and less fluctuation was calculated at the top of the bed. Together, the dip-leg and loop-seal 1 are damping down the solid flow rate fluctuations from the riser outlet.

The flow regime at fluidized bed 2 is denser than fluidized bed 1 due to low gas injection. There is small mixing of solids and the general movement of particles is downward toward the stand pipe.

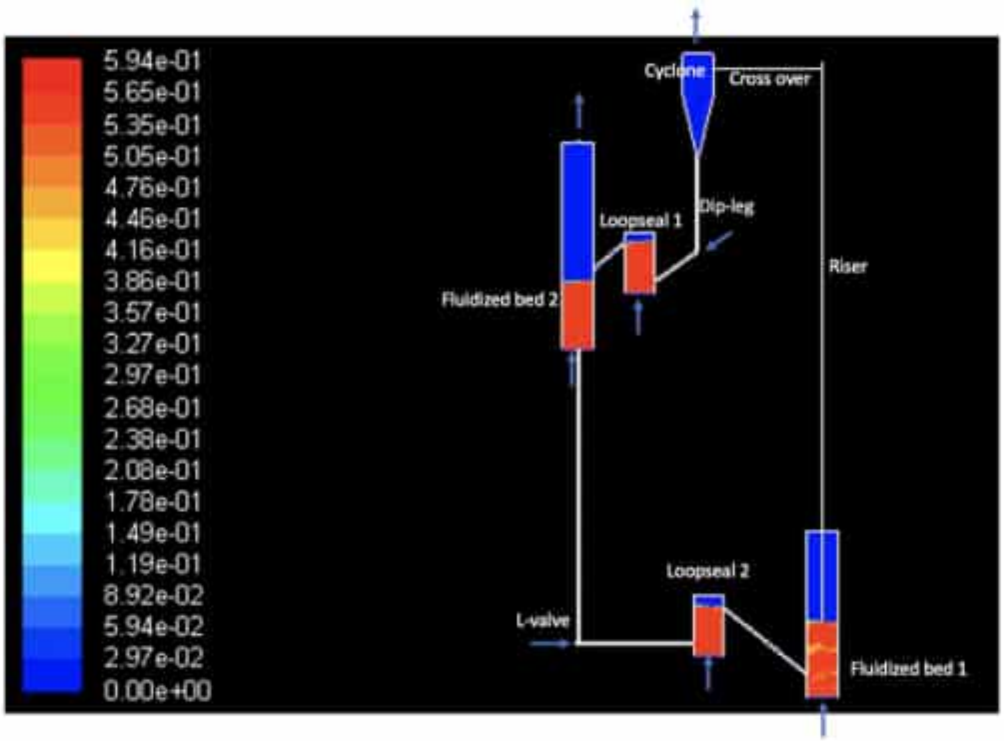

Fig. 1. Contour of solid volume fraction at CFB

The moving packed bed of solids goes down into the stand pipe and the horizontal part of the L-valve. The aeration gases at the bending part push the solids along the pipe to enter the lower loop-seal. At loop-seal 2, the gas injection was twice the minimum fluidization velocity. Our simulation showed this helped the particles smoothly overflow into the pipe that links the loop-seal top to the bottom of fluidized bed 1.

Fig. 2 shows our calculated solid circulation rate at the outlet of the riser, loop-seal 1 to fluidized bed 2, loop-seal 2 to fluidized bed 1 and close to the end of the horizontal part of the L-valve. Gas injection from the bottom of fluidized bed 1 and aerations at the bending part of the L-valve control the overall solid circulation rate in the whole system at a stable condition. Therefore, the solid circulation rates at the outlet of the riser and the end part of the L-valve are directly impacted by two main gas injections to the unit. At the L-valve, the average solid volume fraction and solid velocity experience only small fluctuations around their average values. Our numerical CFD simulation results showed that the solid circulation rate at the outlet of the riser and the horizontal part of the L-valve reached the stable condition. The particle flow rates at the other parts of the loop were regulated by the flow rate of these two main sections.

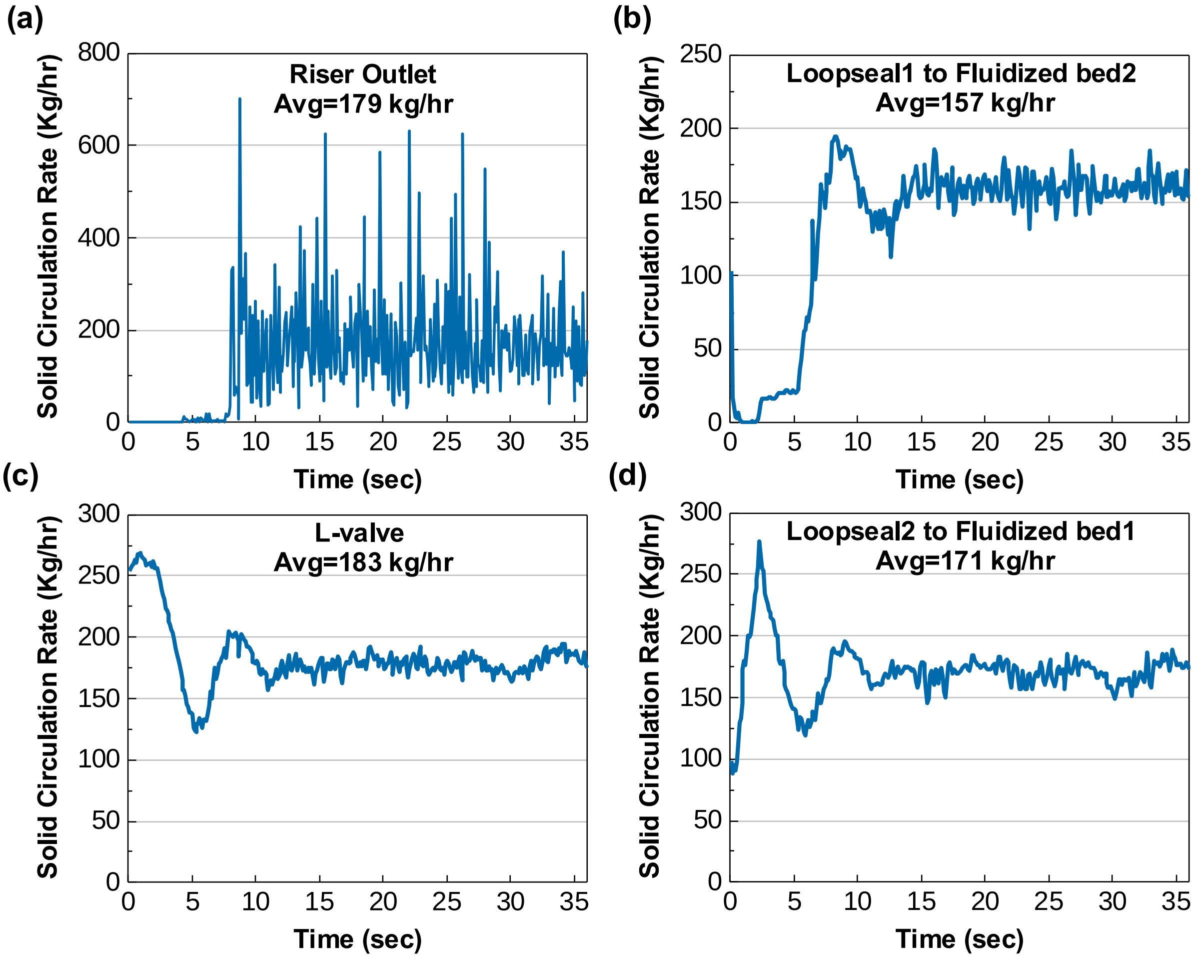

Fig. 2. Solid circulation rate calculated from two-dimensional CFD simulation of CFB

Our simulation also showed steady solid circulation in the loop, but the circulation rate was six times higher than 30 kg/hr., which was reported from the 3D experiments. Elimination of granular temperature diffusion and convection terms limited the particles fluctuation and, as a result, they circulated with a higher rate. Even increasing the specularity coefficient and decreasing the restitution coefficient could not compensate this simplification. Particles may have had different velocities immediately after the collision, but they regressed quickly toward the mean value prior to the next collision. Therefore, the number of collisions and the dissipation of energy due to the collisions were restricted, which caused a higher circulation rate of solids in the CFB loop. Therefore, to continue the study, CFD simulation of the system should be performed by considering all terms of the granular temperature conservation equation. This requires more computational time.

Pressure Balance of the System

The simulated contour of the pressure balance of the whole system is shown in Fig. 3. Pressure decreases from the bottom of fluidized bed 1 (a), along its bed (b), in the riser (c), and, at the cyclone outlet, reaches to atmospheric pressure. At fluidized bed 2, the pressure increases from the top of the bed (d), to the bottom of the bed (e). The increase continues along the stand pipe and the L-valve (f). The pressure map of the loop resulting from the simulation (shown in Fig. 3), supported particle circulation in the CFB. Calculated Pressure drop in the fluidized beds 1 and 2, riser and L-valve were compared with experimental data reported by NETL at the same operating conditions. As a result of the higher solid circulation rate in the loop, pressure drops across the CFB components increased.

Conclusion

In this study, the hydrodynamics of the entire circulating fluidized bed were successfully simulated. Results of our simulation predicted the same average solid circulation rate in the two main parts of the system: the outlet of the riser and the L-valve. Our simulation is capable of predicting steady solid circulation in the entire CFB system. Neglecting granular temperature diffusion and convection terms in the granular temperature equation result in the over-prediction of solid circulation in the CFB. A higher solid circulation rate caused a higher pressure drop across the system components compared to the NETL experimental data.

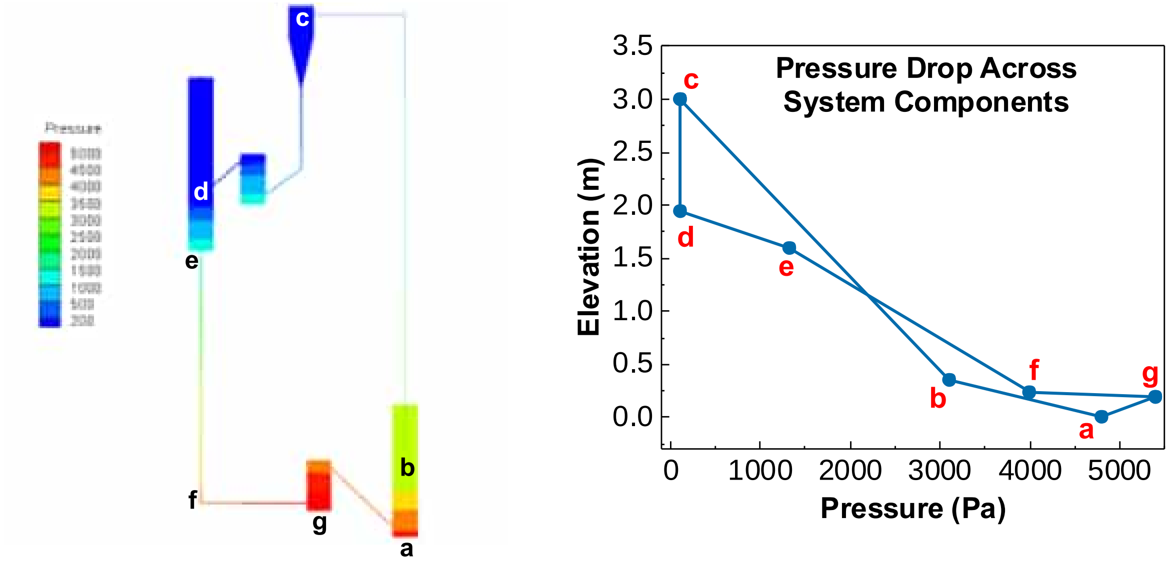

Fig. 3. Pressure balance of the CFB loop

Table 2. Pressure drops across system components

	Carbonation section (a-c)	Regeneration section (d-g)
CFD Simulation	4.82 kPa	5.42 kPa
Experimental	3.75 kPa	4.32 kPa

References

Arastoopour, Hamid. 2001. “Numerical Simulation and Experimental Analysis of Gas/Solid Flow Systems: 1999 Fluor-Daniel Plenary Lecture.” *Powder Technology* 119 (2–3): 59–67.

Arastoopour, Hamid, Dimitri Gidaspow, and Emad Abbasi. 2017. *Computational Transport Phenomena of Fluid-Particle Systems*. Mechanical Engineering Series. Cham: Springer International Publishing.

Breault, Ronald W, James L Spenik, Lawrence J Shadle, James S Hoffman, McMahan L Gray, Rupen Panday, and Richard C Stehle. 2016. “Carbon Capture Test Unit Design and Development Using Amine-Based Solid Sorbent.” *Chemical Engineering Research and Design* 112: 251–62.

Gray, M. L., J. S. Hoffman, D. C. Hreha, D. J. Fauth, S. W. Hedges, K. J. Champagne, and H. W. Pennline. 2009. “Parametric Study of Solid Amine Sorbents for the Capture of Carbon Dioxide †.” *Energy & Fuels* 23 (10): 4840–44.

Johnson, P. C., and R. Jackson. 1987. “Frictional–Collisional Constitutive Relations for Granular Materials, with Application to Plane Shearing.” *Journal of Fluid Mechanics* 176 (1): 67.

Lu, Bona, Wei Wang, and Jinghai Li. 2011. “Eulerian Simulation of Gas–Solid Flows with Particles of Geldart Groups A, B and D Using EMMS-Based Meso-Scale Model.” *Chemical Engineering Science* 66 (20): 4624–35.

Spenik, James L, Lawrence J Shadle, Ronald W Breault, James S Hoffman, and McMahan L Gray. 2015. “Cyclic Tests in Batch Mode of CO2 Adsorption and Regeneration with Sorbent Consisting of Immobilized Amine on a Mesoporous Silica.” *Industrial & Engineering Chemistry Research* 54 (20): 5388–97.

Yang, Wen-Ching, and James Hoffman. 2009. “Exploratory Design Study on Reactor Configurations for Carbon Dioxide Capture from Conventional Power Plants Employing Regenerable Solid Sorbents.” *Industrial & Engineering Chemistry Research* 48 (1): 341–51.

NETL private communication on experimental Data. 2017.

EXPERIMENTS ON CO_2 ABSORPTION PERFORMANCE OF NEW CALCIUM BASED ABSORBENT MODIFIED WITH HIGH-ALUMINA CEMENT

Qinhui Wang*, Yi Feng, Yang Yang, Chengdong Ying, Leming Cheng, Zhongyang Luo

State Key Laboratory of Clean Energy Utilization, Institute for Thermal Power Engineering Zhejiang University, Hangzhou, 310027, China

*Email: *qhwang@zju.edu.cn*

Abstract

The carbon dioxide capture technology based on Calcium-based adsorbent for chemical-looping gasification is attracting more and more attentions due to low energy consumption, reasonable price and abundant resources. However, the natural limestone, which is utilized as the calcium based absorbent, has many disadvantages, such as low sintering resistance and low mechanical strength. In response to this problem, a potential approach for calcium-based absorbent treatment was proposed and investigated in this paper. It was found that the calcium-based absorbent modified by hydration treatment and citric acid sol-gel method shows a superior CO_2 adsorption capacity during the cycles of carbonation and calcination reaction and hydration treatment is considered to be more appropriate for industrial application. The absorbents doped with high-alumina cement shows supreme CO_2 adsorption capacity. After 10 cycles, the CO_2 absorptivity is about 12% higher than that of natural lime. Calcium-based absorbents doped with high- alumina cement by 2.5wt%, 5wt%, 10wt%, 15wt%, respectively, were investigated and the calcium-based absorbent doped with 5wt% high-alumina cement has maintained a CO_2 adsorption rate up to 51.8% after 20 cycles, which is 14.7% higher than that of natural lime.

Introduction

With the demand of energy increasing, the natural resources are consumed in great quantities and the abundant CO_2 was produced in the process. The Calcium based Chemical looping gasification technology is an attractive option to convert solid fuel into hydrogen-rich syngas and separate the by-product CO_2 economically and appropriately coupling with the circulation fluidized bed reactor, which is shown in Fig.1. In the process, CaO can remove CO_2 from the fuel gases generated by solid fuel gasification and meanwhile the present of CaO increase the decomposition of tar. Due to the selective removal of CO_2 during gasification, the water-gas shift reaction, steam methane reforming and other hydrogen production reactions are enhanced because of the equilibrium law. After then, the generated $CaCO_3$ is transported into the air reactor to regenerate CaO. By the carbonation and calcination reaction of calcium-based absorbent, the capture of CO_2 and the regeneration of absorbent are realized. However, the sintering of Calcium-based absorbent was noticed by many researchers and it has been proved that the sintering will lead to a sharply decrease of the absorption efficiency.

To solve these problems, plenty of research works were down the predecessors. It can be found in Broad M. et al. (2012) and Syrah M. et al. (2013), the sintering situation of the Calcium-based absorbent is greatly improved when the natural limestone was doped with different alkali metal or alkali earth metal compounds. It can be found in Florin N. et al. (2010), the limestone was doped with $Al(NO_3)_3 \cdot 9H_2O$ as precursor. After 30 cycles, 0.22 germs of CO_2 is captured by the Calcium-based absorbent, which is 3 times higher than that of natural limestone. Similar results can be also found in Yu C T et al. (2014) and Sayyah M. et al. (2013). The Influence of different doping additive ratios can be found in Chang P. et al. (2011). It is found that when the percentage of CaO and Al_2O_3 was 88.5% and 11.5%, the best CO_2 capture capacity can be reached.

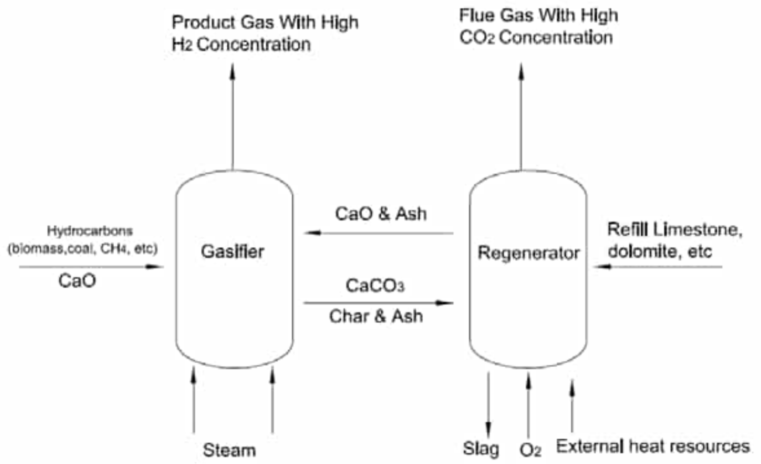

Fig. 1. Chemical looping gasification of CaO schematic diagram

However, the methods in these works to modified the natural limestone were expensive and complicate. An economical and simple method is urgently in need when expanded to Industrial application. In this paper, the influence of different doping methods and different additive species for the Calcium-based adsorbent modification were investigated.

Experimental Details

The limestone used in this paper was Hunan limestone, and the XRF composition analysis was shown in Table.1. The sorbent sample was prepared by calcinated in a tube furnace at 900°C for 1h. A stream of N_2 was introduced into the furnace during the preparation. The composition of the four additives were shown in Table 2.

The calcium-based adsorbents were prepared by different methods. For direct mixing method, 10g of natural limestone was uniformly mixed with a certain amount of additive mechanically. Then the mixture was calcinated in a tube furnace under 850°C for 2h. Meanwhile a stream of N_2 was introduce into the furnace as inert gas. For hydration treatment, 10g of limestone and a certain amount of additive was injected into deionized water and stirred uniformly. Then the mixture was placed in a muffle under 100°C to remove the moisture. At last, the sample was calcinated in the tube furnace under the same conditions as direct mixing method. For citric acid sol-gel method, the citric acid solution and the deionized water was introduced into the mixture of 10g of natural limestone and a certain amount of additive. The ratio of citrate ion to metal ion was 1:1, and the ratio of metal ion to water was about 1:30. After dried in the muffle, the particles were grounded and calcinated in the tube furnace under the same conditions.

The experimental campaign was carried out in a tube furnace system. The samples was introduced into the tube furnace and calcinated under 850°C for 15 min. The calcination process was conducted under N_2 atmosphere. After calcination, the temperature was set to 700°C. After the temperature was reached, CO_2 and N_2 were introduced into the furnace in a ratio of 1:4. After carbonated for 20 min, the sample was cooled down and weighted. The calcination and carbonation process was repeated until certain cycles was reached. The absorption efficiency was defined as the amount of CO_2 absorbed by 1 molar of CaO during carbonation.

Table 1. Composition analysis of Hunan limestone.

Component	$CaCO_3$	MgO	Al_2O_3	SiO_2	Others
Content,wt%	73.0	5.1	2.3	4.9	14.7

Table 2. Composition analysis of different additives.

Component	$CaCO_3$	MgO	Al_2O_3	SiO_2	Others
High-alumina Cement	17.3%	Trace	80.2%	Trace	2.5%
Feldspar Powder	51.7%	2.1%	13.2%	3.1%	29.9%
Dolomite	28.8%	19.4%	3.2%	2.1%	46.5%
Composite Cement	64.0%	3.1%	4.6%	20.0%	3.8%

Results and Discussion - Preparation Method Comparison

The absorption efficiency of the adsorbents prepared by different methods were shown in Fig.2. The hydration treatment and citric acid sol-gel method greatly improved the absorption efficiency of natural lime in multiple cycles. This was because the microscopical pore structure of the limestone was improved. When the lime was dissolved in water or acid, Ca and Al were uniformly mixed by ions, and after calcination, a uniform and stable mixture was formed. Microscopically speaking, Al became the skeleton of Ca, which greatly enhanced the strength of natural limestone pores.

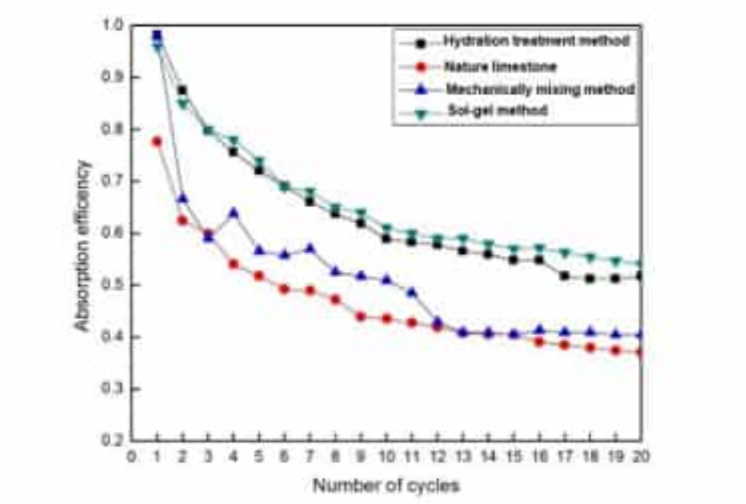

Fig. 2. Characteristics of absorption efficiency of calcium-based absorbents prepared by different methods with the number of carbonization/calcination cycles.

Results and Discussion - Doping Additive Comparison

As shown in Fig.3, highest absorption efficiency was reached by the sorbent doped with the high-aluminum cement. After 10 cycles, the absorption efficiency was 26.7% higher than that of natural limestone. The strength of the multiple pore structure of the calcium-based absorbent was greatly enhanced by addition of Al_2O_3. In contrast, as can be seen in Fig.3, the absorption efficiency of sorbent doped with dolomite was almost the same to that of natural limestone. After 10 cycles, the absorption efficiency was only 1% higher than that of natural lime. Similar result also can be found in Sayyah et al. (2013). According to the study, the MgO mass percent of 41% in doping additive was need to provide enough MgO for the molecular skeleton construction, while the mass percent of MgO in dolomite was only 19.5%. The calcium-based absorbent prepared by adding composite cement and feldspar powder had lower absorption efficiency than natural limestone after 10 cycles. It is because of the exist of the fusible salts content, which exacerbated the coking of the calcium-based absorbent. In summary, high-alumina cement was chosen as the best additive.

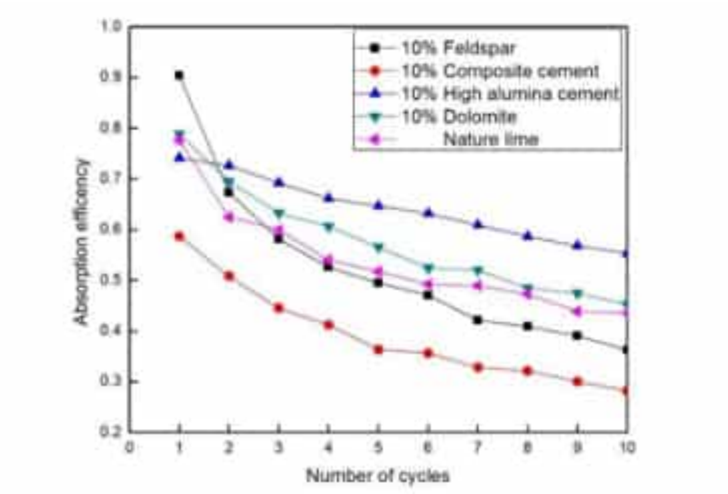

Fig. 3. Characteristics of absorption cycle efficiency of calcium-based absorbents prepared by adding different materials with the number of carbonization/calcination cycles.

Results and Discussion - Doping Ratio Comparison

As shown in Fig.4, as the number of cycles increased, the absorption efficiency of the natural limestone decreased significantly. Yet the absorption efficiency of the calcium-based absorbent doped with the high-alumina cement was higher than that of natural limestone. It could be seen that the absorption efficiency of the calcium-based absorbent prepared by high-aluminum cement (2.5wt%, 5wt%, 10wt%, 15wt%) after 20 cycles was 0.43, 0.51, 0.46, and 0.44, respectively. The highest absorption efficiency of calcium-based absorbent modified by high-alumina cement was reached when the mass percentage of high-alumina cement was 5%.

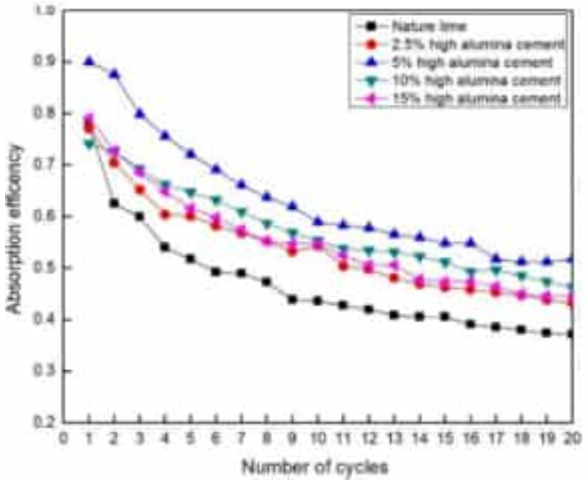

Fig. 4. Characteristics of absorption cycle efficiency of calcium-based absorbents prepared by adding different proportions of high-alumina cement with the number of carbonization/calcination cycles.

Fig.5 shows the microscopic pore structure of four new calcium absorbents. During the carbonization/calcination cycles, the diffusion of CO_2 is mainly depended on the pore structure. Compared with the natural limestone, relatively stronger pore structure was found from the sorbent modified by high-alumina cement after 20 cycles. Meanwhile, with the increase of high-alumina percentage, the pores observed on the surface were becoming less and less.

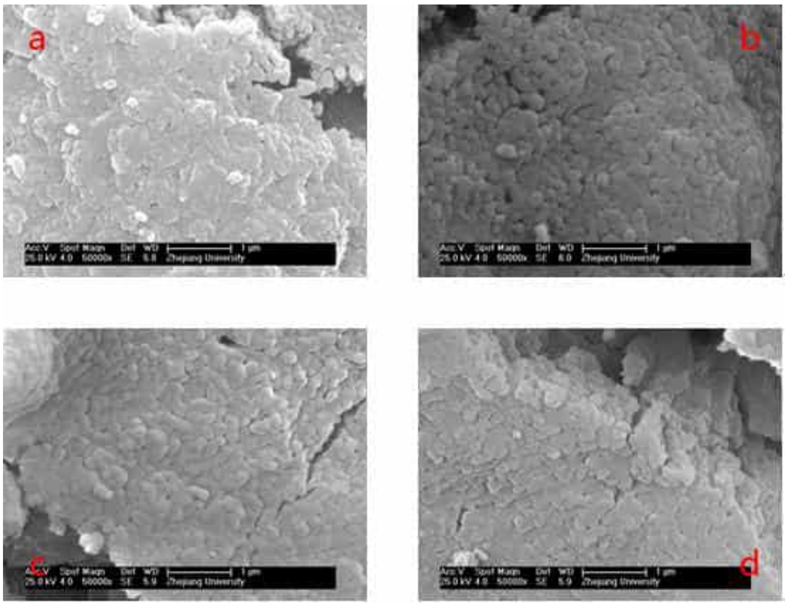

Fig. 5. SEM image of calcium-based absorbent and natural lime prepared by adding high-aluminum cement after 20 cycles (a. natural limestone; b. 5wt% of high-aluminum cement; c. 10wt% of high-alumina cement; d. 15wt% of high-alumina cement)

The pore distribution of the sample was measured by a nitrogen absorber. The pores with size ranged from 2 nm to 200 nm were detected and the results were shown in Fig.6. It can be seen from Fig.6a that at the pore size range of 20 nm to 70 nm, the calcium-based absorbent prepared by adding 5wt% high-alumina cement was significantly higher than other samples; in Fig.6b, at the pore size range of 20nm to 70 nm, the calcium-based absorbent, which was doped with high-alumina cement of 5wt% and 10wt%, was much higher than the others. It was indicated that the strongest pore structure in the pore size range of 20-70 nm was reached by the calcium-based absorbent doped with 5wt% high-aluminum cement.

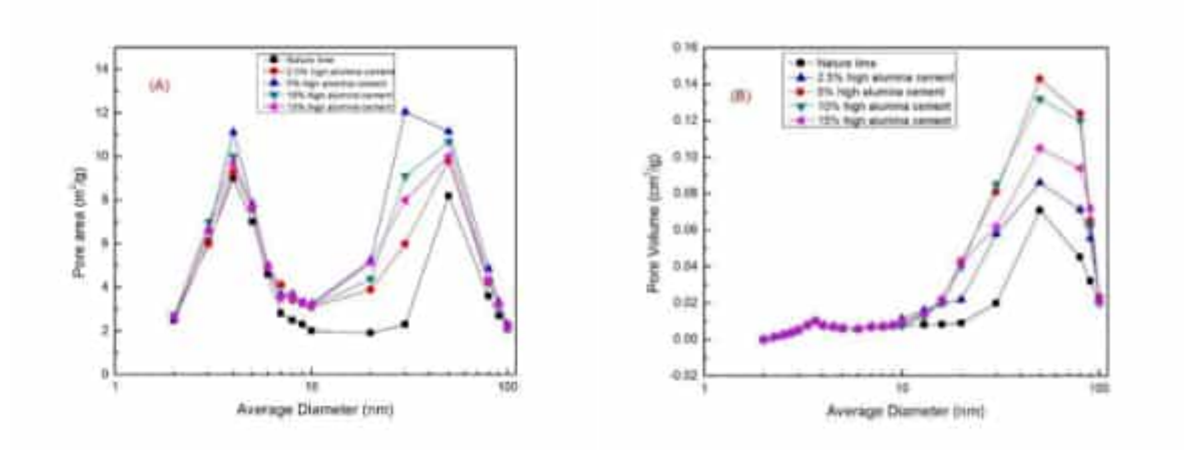

Fig. 6. Pore structure distribution of calcium-based absorbent particles (a. pore area; b. pore volume)

The results of XRD analysis of the calcium-based absorbent were shown in Fig.7. it is observed that the Al_2O_3 molecules were distributed among CaO molecules. The oxide of calcium and aluminum $Ca_{12}Al_{14}O_{33}$, for an example, formed under high temperature proved the sorbent with a stronger pore structure and higher anti-sintering capacity.

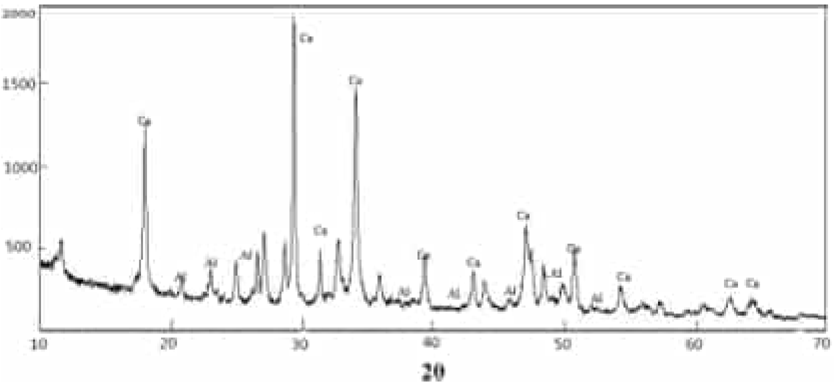

Fig. 7. XRD analysis of Ca/Al distribution of new calcium-based absorbents prepared by adding 5wt% high-alumina cement

In this experiment, the content of Al_2O_3 in high-alumina cement was 80%. It was calculated that after adding 5wt% of high-alumina cement to natural lime, the Ca/Al ratio of the new calcium-based absorbent was 6.7:1. Similar result was found in Chang P. H. et al. (2014) that the optimal Ca/Al ratio was 7:1.

Conclusions

In this paper, the natural limestone was modified with different preparation methods, additives and doping proportions. By comparing the results with another, conclusions are showed below:

1) Compared with other methods, the highest absorption efficiency was reached by the direct mixing method and the citric acid sol-gel method. Among them, hydration treatment was considered to be the best modification method in this experiment due to its low price and simple process.
2) Among the four additives, high-alumina cement had the best effect on the improvement of calcium-based adsorbent after multiple cycles.
3) The highest absorption efficiency was reached by the calcium based adsorbent modified by adding 5wt% of high-alumina cement. A larger surface area, stronger pore volume and average pore size were found on the modified sorbent.

References

Broda M, Christoph R Müller. Synthesis of Highly Efficient, Ca-Based, Al_2O_3-Stabilized, Carbon Gel-Templated CO_2 Sorbents[J]. Advanced Materials, 2012, 24(22):0-0.

Caplow, Michael. Kinetics of carbamate formation and breakdown [J]. Journal of the American Chemical Society, 1968, 90(24):6795-6803.

Chang P H, Chang Y P, Chen S Y, et al. Ca-Rich Ca-Al-Oxide, High-Temperature-Stable Sorbents Prepared from Hydrotalcite Precursors: Synthesis, Characterization, and CO_2, Capture Capacity[M]// ChemSusChem. :1844-1851.

Przepiórski J, Czyżewski A, Pietrzak R, et al. MgO/CaO-loaded porous carbons for carbon dioxide capture[J]. Journal of Thermal Analysis & Calorimetry, 2013, 111(1):357-364.

Sayyah M, Lu Y, Masel R I, et al. Mechanical Activation of CaO-Based Adsorbents for CO_2 Capture[J]. ChemSusChem, 2013, 6(1).

Sayyah M, Lu Y, Masel R I, et al. Mechanical Activation of CaO-Based Adsorbents for CO_2 Capture [J]. Chemsuschem, 2013, 6(1):193.

Yu C T, Kuo H T, Chen Y M. Manufacturing of the High-temperature CO_2, Sorbents from Titanic Nanoparticles Doped Calcium Aluminate Carbonates [J]. Energy Procedia, 2014, 61:1952-1956.

EQUILIBRIUM ANALYSIS OF PRESSURIZED SORBENT REGENERATION BY COMBINING METHANE REFORMING, COMBUSTION AND CALCINATION

Arian Ebneyamini*, **Bill Long Cheng, Jun Young Kim, Zezhong John Li, John Grace, Jim Lim, and Naoko Ellis**

Department of Chemical and Biological Engineering, University of British Columbia, 2360 East Mall, Vancouver, BC, Canada, V6T 1Z3

*Email: *aebneyam@mail.ubc.ca*

Abstract

The equilibrium performance of limestone calcination combined with methane reforming and combustion is studied at elevated reactor pressures. A correlation is developed to estimate the required gaseous feed composition for autothermal, complete and coke-free limestone calcination at different operating conditions. Proper ranges of reactor temperature, pressure and $CaCO_3$/total gas molar feed ratio are also assessed for this novel sorbent regeneration process. The effects of varying operating conditions on the system performance (e.g. sorbent conversion, H_2 yield) are also investigated for isothermal and adiabatic reactor configurations. The results provide guidance on sorbent regenerator design for calcium looping technologies.

Introduction

Lime is a well-known sorbent for CO_2 capture in high-temperature applications, including sorbent-enhanced steam methane reforming. The sorbent-enhanced reforming process can be conducted in fluidized bed reactors, integrated with a parallel sorbent regeneration unit, calciner (Aloisi et al., 2017; Johnsen, 2006). Limestone calcination is highly endothermic, with both the rate and extent of reaction depending on the operating temperature and CO_2 partial pressure. The calcination reaction can occur in the presence of non-CO_2 gaseous media (e.g. air and steam), or oxy-fuel feedstock (Sakadjian, Iyer, Gupta, & Fan, 2007; Ylätalo, Parkkinen, Ritvanen, Tynjälä, & Hyppänen, 2013). Non-CO_2 media produce diluted CO_2 off-gas while also requiring external heating. Although steam calcination can produce a highly concentrated dry CO_2 off-gas, steam generation is energy-consuming, reducing the thermal efficiency of the overall integrated process. In contrast, oxy-fuel calciners offer *in situ* heat generation, while producing the substantial amount of CO_2 inside the reactor. The generated CO_2 inhibits the calcination reaction and, therefore, higher reactor temperature than those in non-CO_2 media is required for oxy-fuel sorbent regenerators (Ebneyamini, Grace, Lim, Ellis, & Elnashaie, 2019).

We recently proposed a novel sorbent regeneration configuration, combining exothermic methane combustion with endothermic reforming and calcination, called the MRC-CAL process (Ebneyamini, Grace, Lim, Ellis, & Elnashaie, 2019). This process utilizes concentrated methane feed balanced with enriched-air, resulting in methane conversion toward both combustion and reforming reactions. After rapid combustion and reforming stages, limestone decomposes to CaO, with the released CO_2 entering the reactor gaseous medium. Simultaneously, a portion of the desorbed CO_2 is consumed by the formerly generated hydrogen during the reforming stage (reverse water-gas shift reaction), increasing the driving force for limestone calcination. In addition, the energy required for the limestone decomposition and methane reforming can be balanced with the heat released from the exothermic methane combustion, eliminating the need for external heating supply.

This paper employs Aspen simulation to investigate the equilibrium performance of the MRC-CAL process at elevated reactor pressures. The simulation results are used to develop an empirical correlation for estimating the required gaseous feed composition for autothermal, coke-free and complete sorbent regeneration. Variation of sorbent conversion, reactor heat duty, methane conversion and hydrogen yield with the operating pressure and $CaCO_3$/total gas molar feed ratio are also assessed. The reactor is also simulated for adiabatic operation, demonstrating the potential non-isothermal performance of this novel sorbent regeneration process under near-equilibrium conditions.

Aspen Simulation Setup

Aspen Plus software (V10.0) was applied in order to investigate the equilibrium performance of the MRC-CAL process at different operating conditions. Fig. 1 shows the Aspen process flowsheet, applied to evaluate the system performance for different scenarios. An isothermal Gibbs reactor was used as the MRC-CAL reactor. Feed temperatures were fixed at 25°C, while two heaters increased their temperatures to the reactor temperature (isothermal operation). The enriched-air (95% O_2 balanced with N_2, (Ebneyamini, Grace, Lim, Ellis, & Elnashaie, 2019)) molar feed flow rate was fixed at 0.15 $mol.s^{-1}$ and different gaseous feed compositions were achieved by varying the methane inlet flow rate. A gas splitter was placed next, maintaining a 0.2 $mol.s^{-1}$ gaseous feed flow rate for all simulation tests. Different $CaCO_3$/total gas molar feed ratios were then obtained by varying the $CaCO_3$ feed flow rate into the reactor. A similar process flowsheet was applied to the adiabatic simulation, assuming an MRC-CAL reactor with zero heat duty. Summaries of streams and blocks properties are provided in Tables 1 and 2, respectively.

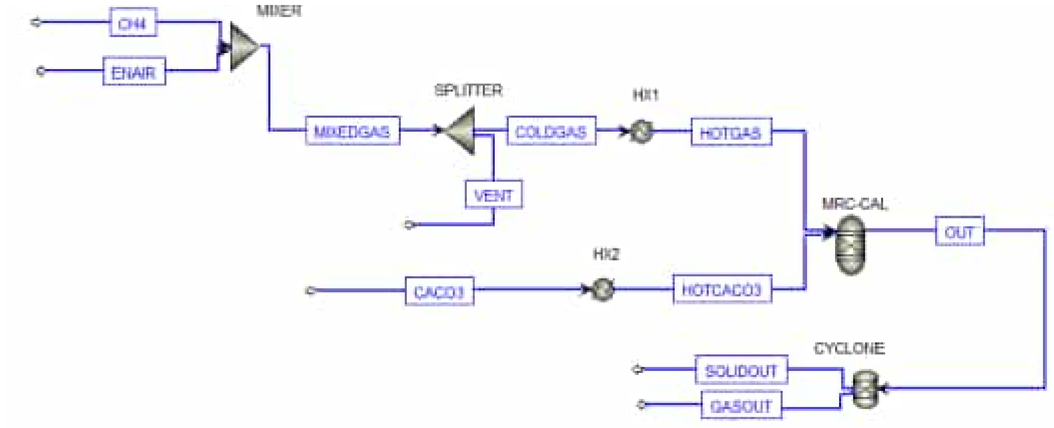

Fig. 1. Aspen process flowsheet.

Table 1. Stream properties for Aspen Plus simulations[1]

Stream	Composition	Flow Rate ($mol.s^{-1}$)
CH_4	100% CH_4	0.075-0.3[2]
EN-AIR	95% O_2 + 5% N_2	0.15
$CaCO_3$	100% $CaCO_3$	0.05-0.3[3]

Table 2. Block properties for Aspen Plus simulations

Block	Properties
MRC-CAL	• Gibbs reactor • Pressure range: 1-5 bars • Temperature range for isothermal operation: 800-900°C
HX 1 & 2	• Isothermal MRC-CAL: Increase the feed temperatures to the reactor temperature • Adiabatic MRC-CAL: Increase the feed temperatures to 850°C

---

[1] Streams pressures of identical to the of reactor pressure

[2] Corresponding to CH_4/Enriched-Air molar feed ratio of 0.5 (oxy-fuel combustion) to 2

[3] Corresponding to $CaCO_3$/total gas molar feed ratio of 0.05 to 1.5

Correlation Development

Fig. 2(a) demonstrates the methane/enriched-air molar feed ratio (β) required for autothermal sorbent regeneration at different $CaCO_3$/total gas molar feed ratios (maximum error of ± 0.4%). These results indicate that increasing the $CaCO_3$/total gas molar feed flow ratio (α) results in lower methane feed concentration for autothermal MRC-CAL operation. The methane/enriched air molar feed ratio in the MRC-CAL process exceeds 0.5, resulting in oxygen being the limiting reactant for the exothermic combustion. Accordingly, higher enriched-air feed concentration is needed if more energy has to be supplied in the reactor. Increasing α (e.g. by increasing the $CaCO_3$ feed flow rate) leads to greater reactor endothermicity and hence, lower methane/enriched-air molar feed ratio (β) required for autothermal MRC-CAL operation (Ebneyamini, Grace, Lim, Ellis, & Elnashaie, 2019).

Eq. (1) shows a previously proposed correlation to estimate β for autothermal operation of the atmospheric MRC-CAL reactors (Ebneyamini, Grace, Lim, Ellis, Elnashaie, et al., 2020). This equation indicates that β (corresponding to autothermal MRC-CAL) is only a function of the $CaCO_3$/total gas molar feed ratio. However, Fig. 2(a) shows that the Eq. (1) underestimates the simulation results at low α ($R^2 = 0.9443$), especially for elevated reactor pressures and reduced temperatures. Accordingly, a new correlation (Eq. (2)) is proposed in this study, estimating the required gaseous feed composition for autothermal MRC-CAL sorbent regeneration at reactor pressures of 1-5 bars. Fig. 2(a) confirms the excellent predictions by Eq. (2) ($R^2 = 0.982$), while inevitable deviations still exist for α < 0.3.

$$\beta = 2e^{-0.97\alpha} \qquad 800°C \le T \le 900°C \ \& \ P = 1\,bars \tag{1}$$

$$\beta = 0.275 + 1.903e^{-\alpha/0.716} \qquad 800°C \le T \le 900°C \ \& \ P = 1-5\,bars \tag{2}$$

Fig. 2(b) demonstrates the critical operation limits for autothermal, complete and coke-free limestone calcination using MRC-CAL process. The previous work showed that exceeding an upper α limit results in incomplete/endothermic sorbent regeneration, while reducing α increases the chance of coke-formation (Ebneyamini, Grace, Lim, Ellis, Elnashaie, et al., 2019). Accordingly, the above-mentioned three criteria are only attainable within a certain range of $CaCO_3$/total gas molar feed ratios. Fig. 2(b) shows that increasing the reactor pressure results in a narrowing of the range of applicable α for proper MRC-CAL operation (area between upper and lower limits). This is due to reduced calcination driving force and enhanced carbon formation (e.g. by CO hydrogenation) at elevated pressures, in agreement with Le Chatelier's principal. On the other hand, increasing the reactor temperature leads to a wider range of applicable α, as also observed in our previous work (Ebneyamini, Grace, Lim, Ellis, Elnashaie, et al., 2020).

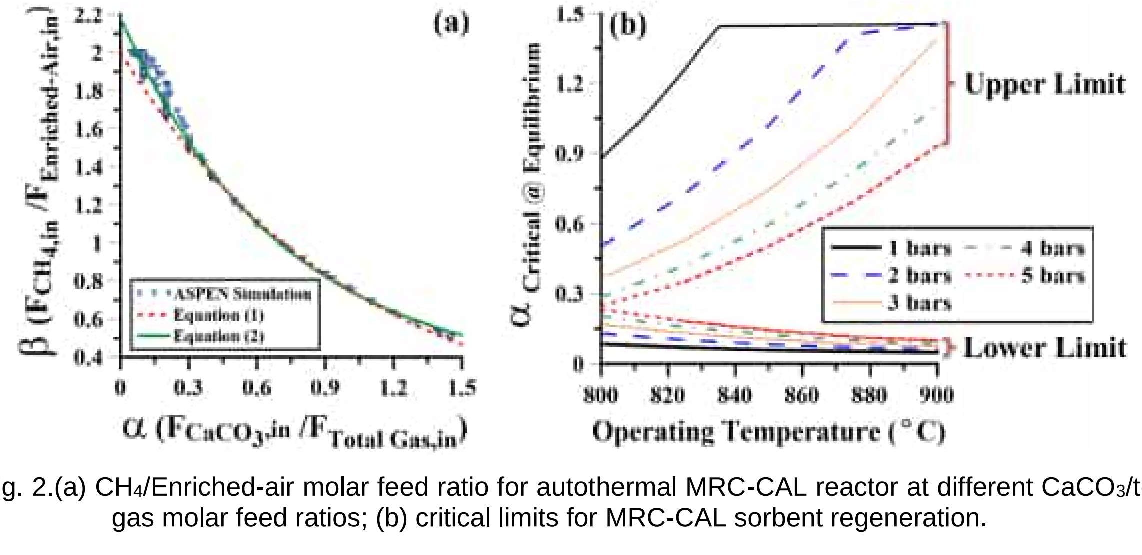

Fig. 2.(a) CH_4/Enriched-air molar feed ratio for autothermal MRC-CAL reactor at different $CaCO_3$/total gas molar feed ratios; (b) critical limits for MRC-CAL sorbent regeneration.

Performance Analysis for Isothermal Operation

Fig. 3 shows effects of reactor pressure and $CaCO_3$/total gas feed ratio, α, on the MRC-CAL sorbent conversion and heat duty. The gaseous feed compositions for these runs were obtained based on Eq. (2). Fig. 3(a) shows that incomplete sorbent conversion occurs when exceeding a certain reactor pressure at $\alpha > 0.5$. In addition, the maximum reactor pressure for complete limestone calcination decreases with increasing the $CaCO_3$/total gas molar feeding ratio, in agreement with Fig. 2(b). Fig. 3(b) shows that the MRC-CAL heat duty is roughly zero when $\alpha_{\text{Upper-limit}} > \alpha$. Larger deviations are observed at low α, owing to less precision for $\alpha < 0.3$ (Fig. 2(a)). In addition, exceeding the α upper limit results in incomplete sorbent conversion and, thus, lower energy consumption by the limestone calcination. Accordingly, the isothermal reactor tends toward exothermicity when the $CaCO_3$/total gas molar feed ratio exceeds the α upper limit, in agreement with Fig. 3(b).

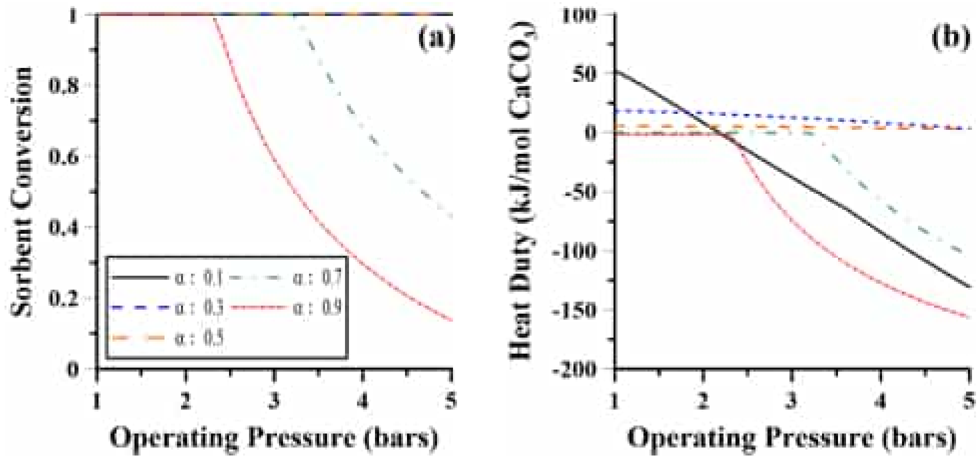

Fig. 3. Effect of operating pressure on: (a) sorbent conversion; (b) MRC-CAL heat duty at fixed temperature of 850°C and different $CaCO_3$/total gas molar feed ratios.

Fig. 4 compares the methane conversion and hydrogen yield of the MRC-CAL process with identical operating conditions to those applied in Fig. 3. Fig. 4(a) demonstrates that the MRC-CAL process offers relatively high methane conversion; while, increasing reactor pressure and reducing α ($CaCO_3$/total gas molar feed ratio) result in lower methane conversion. Increasing the reactor pressure reduces the extent of methane reforming, in agreement with Le Chatelier's principal. On the other hand, reducing the $CaCO_3$/total gas molar feed ratio leads to higher methane/enriched-air molar feed ratio needed for autothermal operation (Fig. 2(a)). Accordingly, reducing α lowers the oxygen feed concentration and, hence, results in higher methane conversion toward reversible methane reforming. Lower methane combustion also results in less initial steam and CO_2 generation, inhibiting methane reforming. Hence, lower methane conversion is expected when the $CaCO_3$/total gas molar feed ratio decreases, in agreement with the results in Fig. 4(a). Note that the low methane conversion for $\alpha < 0.3$ could be also responsible for observed deviations between the simulation results and predictions in Fig. 2(a).

Fig. 4(b) demonstrates that increasing the reactor pressure results in slightly less hydrogen yield for $\alpha < \alpha_{\text{Upper-limit}}$. This can be explained by the means of reduced methane conversion observed at elevated reactor pressures (Fig. 4(a)). In addition, exceeding the upper $CaCO_3$/total gas molar feed ratio limit results in incomplete sorbent conversion (Fig. 3(a)) and consequently, lower hydrogen consumption by the reverse water-gas shift reaction. This enhances the MRC-CAL hydrogen yield, confirmed by the results in Fig. 4(b). Fig. 4(b) also shows that increasing α substantially reduces the hydrogen yield of the process. According to Fig. 2(a), a lower methane/enriched-air molar feed ratio is needed for autothermal operation at elevated $CaCO_3$/gas molar feed ratios. Hence, a smaller portion of the methane feed content participates in the reforming and consequently, lower hydrogen production is achieved.

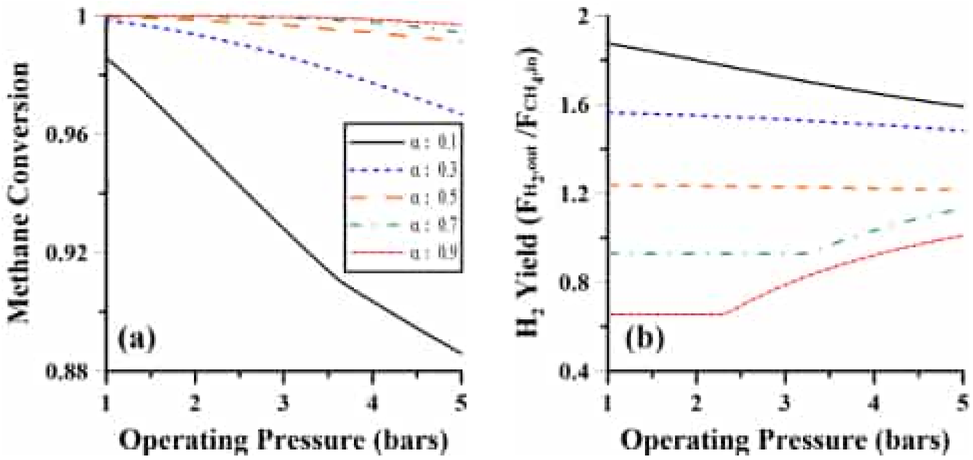

Fig. 4. Effect of operating pressure at fixed reactor temperature of 850°C and different $CaCO_3$/total gas molar feed ratios on the MRC-CAL: (a) CH_4 conversion; (b) H_2 yield.

Performance Analysis for Non-Isothermal Operation

Fig. 5 compares the sorbent conversion and off-gas temperature of a well-insulated MRC-CAL reactor at different reactor pressures and $CaCO_3$/total gas molar feed ratios (α). The feed streams enter the reactor at 850°C with the reactor heat duty set to zero. The results show that the MRC-CAL off-gas temperature is roughly similar to the feed temperature at $\alpha < \alpha_{Upper\text{-}limit}$. However, exceeding the upper α limit leads to a rapid jump in the reactor off-gas temperature, accompanied by slight reduction of the extent of limestone calcination. According to Fig. 3, exceeding the upper α limit results in a lower calcination extent and higher heat duty of the isothermal MRC-CAL reactor. However, the excess energy due to incomplete sorbent calcination leads to elevating the reactor temperature in the adiabatic operation, enhancing the sorbent calcination driving force. In fact, the adiabatic MRC-CAL reactor offers promising thermal-adaptability to maximize the limestone calcination by naturally increasing the reactor temperature.

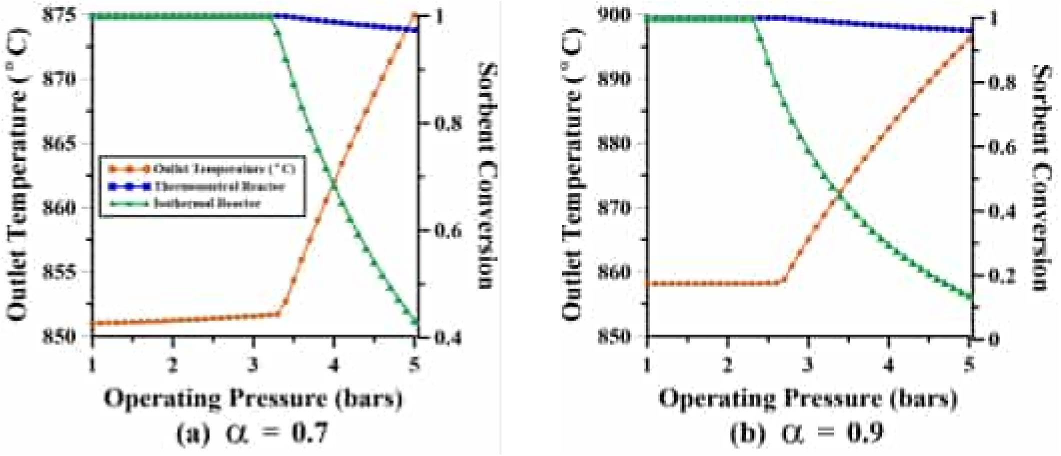

(a) α = 0.7 (b) α = 0.9

Fig. 5. Adiabatic and isothermal performance of MRC-CAL with different operating pressures at: (a) α=0.7 and (b) α=0.9. Solid and gas enter the reactor at 850°C.

Note that the feed streams in practice enter the calciner at low temperatures (e.g. solid circulates from/to a lower temperature reformer/carbonator). Therefore, the excess energy due to incomplete sorbent conversion can be used to provide a portion of the feed heating energy within the reactor. In addition, the higher heating value MRC-CAL off-gas can be partially burned inside or outside the calciner, providing energy for thermal processing. The former case potentially reduces the sorbent conversion since *in situ* syngas combustion increases the CO_2 concentration within the reactor. On the other hand, burning the syngas outside the MRC-CAL reactor results in lower heating efficiency as well as a greater radial temperature gradient. Further investigations are important to study the non-isothermal performance of this novel sorbent regeneration process, when integrated with sorbent-enhanced steam methane reformers.

Conclusion

The performance of a process which combines methane combustion, reforming and calcination is evaluated at elevated reactor pressures. A single correlation is developed to estimate the required gaseous feed composition at different operating conditions, satisfying complete, autothermal and coke-free sorbent regeneration criteria. The proposed correlation agrees well with Aspen simulation results, with larger deviations at low $CaCO_3$/total gas molar feed ratios. The applicable ranges of $CaCO_3$/total gas molar ratio for proper MRC-CAL operation are shown to narrow as the reactor pressure increases and temperature decreases. The simulation results show a relatively high hydrogen yield, with higher hydrogen production at lower $CaCO_3$/total gas molar feed ratios. The hydrogen yield was nearly insensitive to the reactor pressure, unless the critical limit for complete limestone calcination is exceeded. Reactor performance is also assessed for adiabatic operation, demonstrating promising thermal adaptivity of this novel sorbent regeneration process. Future studies will concentrate on the kinetic simulation of the MRC-CAL reactor, evaluating the feasibility of pressurized sorbent regeneration based on the proposed regeneration technology.

References

Aloisi, I., Di Giuliano, A., Di Carlo, A., Foscolo, P. U., Courson, C., & Gallucci, K. Sorption enhanced catalytic steam methane reforming: Experimental data and simulations describing the behaviour of bi-functional particles. Chemical Engineering Journal. 2017. 314, 570–582. https://doi.org/10.1016/j.cej.2016.12.014

Ebneyamini, A., Grace, J. R., Lim, C. J., Ellis, N., & Elnashaie, S. S. E. H. Simulation of limestone calcination for calcium looping: Potential for autothermal and hydrogen-producing sorbent regeneration. Industrial & Engineering Chemistry Research. 2019. 58(20), 8636–8655. https://doi.org/10.1021/acs.iecr.9b00668

Ebneyamini, A., Grace, J. R., Lim, C. J., Ellis, N., Elnashaie, S. S. E. H., & Mahecha-Botero, A. Simulation of autothermal hydrogen-producing limestone calcination for calcium looping in turbulent fluidized bed reactors. Chemical Engineering Science. 2020. 212, 115353. https://doi.org/https://doi.org/10.1016/j.ces.2019.115353

Johnsen, K. Sorption-enhanced steam methane reforming in fluidized bed reactors. Norwegian University of Science and Technology. Ph. D. Thesis. 2006

Sakadjian, B. B., Iyer, M. V., Gupta, H., & Fan, L. S. Kinetics and structural characterization of calcium-based sorbents calcined under subatmospheric conditions for the high-temperature CO_2 capture process. Industrial and Engineering Chemistry Research. 2007. 46(1), 35–42. https://doi.org/10.1021/ie060214a

Ylätalo, J., Parkkinen, J., Ritvanen, J., Tynjälä, T., & Hyppänen, T. Modeling of the oxy-combustion calciner in the post-combustion calcium looping process. Fuel. 2013. 113, 770–779. https://doi.org/10.1016/j.fuel.2012.11.041

PERFORMANCE OF DIFFERENT H_2O SORBENTS FOR FLUIDIZED BED SORPTION-ENHANCED METHANATION

Antonio Coppola[1], Fiorella Massa[1], Piero Salatino[1,2] and Fabrizio Scala[1,2*]

[1]Dipartimento di Ingegneria Chimica, dei Materiali e della Produzione Industriale, Università degli Studi di Napoli Federico II, 80125 Napoli, Italy;
[2]Istituto di Ricerche sulla Combustione, Consiglio Nazionale delle Ricerche, 80125 Napoli, Italy

*Email: *fabrizio.scala@unina.it*

Abstract

In this work a CaO, derived from natural limestone, and two commercial zeolites (3A and 4A) were tested as sorbent materials for H_2O capture in a new configuration for the sorption-enhanced methanation, based on the concept of chemical looping in dual interconnected fluidized bed systems. The experimental campaign was aimed at studying the sorbent performance in terms of hydration and dehydration cycles at different operating conditions relevant for catalytic methanation. The results showed that CaO has a good capacity to capture and release steam in the temperature range of interest. Unfortunately, even at the lowest temperatures tested, the sorbent was affected by the presence of CO_2, which worsened its performance in terms of H_2O capture capacity. The zeolites had a more stable behavior than CaO with the number of cycles under all investigated conditions. Comparing the performance of the three materials, the zeolites on average had better asymptotic capture capacity than CaO, and were not affected by deactivation during the cycles.

Introduction

Methane is an important energy carrier, which features a well-developed distribution and storage infrastructure in many countries, and a massive utilization in the automotive, household and industrial sectors. Nowadays, natural gas is the main source of methane; however, the increasing dispute on global warming related to the exploitation of fossil fuels has moved the interest to alternative and renewable technologies for methane production, such as catalytic and biological processes (Seifert et al., 2014).

Specifically, catalytic methanation (Sabatier and Senderens, 1902), via CO (Eq.1) or CO_2 (Eq.2) hydrogenation, has several features that makes it very interesting if combined with the concepts of solar fuels, chemical storage and CO_2 utilization. Indeed, methane could act as chemical storage carrier of solar energy (Götz et al., 2015), initially used to convert water into hydrogen by electrolysis (Smestad and Steinfeld, 2012). Moreover, CO_2 methanation could be considered as a process for CO_2 utilization in the framework of Carbon Capture and Utilization (CCU) technologies (Cuéllar-Franca and Azapagic, 2015). On the other hand, the production of methane from CO could represent the final step after coal or biomass gasification into syngas.

$$3H_2 + CO \rightleftharpoons CH_4 + H_2O \qquad (-206 kJ\, mol^{-1} \;\; @298\mathrm{K}) \tag{1}$$

$$4H_2 + CO_2 \rightleftharpoons CH_4 + 2H_2O \qquad (-164 kJ\, mol^{-1} \;\; @298\mathrm{K}) \tag{2}$$

The typical catalysts able to promote methanation are based on different metals such as Ru, Ni, Co, Fe, and Mo (Mills and Steffgen, 1974), though Ni-based catalysts are considered to provide the best compromise among activity, selectivity and low price (Panagiotopoulou et al., 2009).

Commercial methanators consist of fixed beds, typically operated at high pressure to obtain high methane yields, and arranged in series in order to carry out intermediate cooling steps and recycles to manage the temperature of the process (due to the high exothermicity of the reaction) (Seifert et al., 2014). In particular, the temperature management represents the main issue for the process because it may lead to the deactivation of the catalyst (Bartholomew, 2001). In addition, the high temperature can promote carbon deposition on the catalyst surface due to the Boudouard reaction (Seemann, 2006). In the last years, many research groups have proposed new solutions, based also on new reactor designs (fluidized bed reactors, three-phase reactors), to improve the current methanation process with the main goal to have a better temperature control (Götz et al., 2015).

Recently, Borgschulte et al. (2013) and Walspurger et al. (2014) investigated the possibility to enhance the methane production by the application of the concept of Sorption-Enhanced Methanation (SEM), where the steam, produced by the methanation reaction, is continuously removed from the reaction environment by means of a suitable regenerable sorbent material, e.g. a zeolite. These studies demonstrated in lab scale fixed beds that the SEM process has the potential for high-grade methane production at relatively low pressure using commercial materials, with the consequence of a relevant energy saving for the entire process. Based on these promising outcomes, in this work an innovative configuration for the SEM process is proposed. In particular, this configuration takes advantage of chemical looping concept where in the main reactor (the methanator) catalytic methanation occurs simultaneously with the hydration of a suitable sorbent, so as to drive the equilibrium towards product formation, while the regeneration of the sorbent takes place in another reactor (dehydrator). The two reactors are connected each other in a dual-interconnected fluidized beds configuration as shown in Fig. 1.

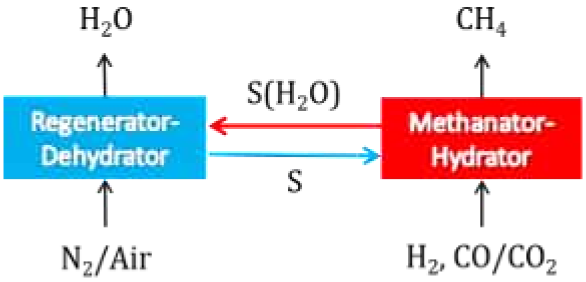

Fig. 1. Scheme of the Chemical Looping Sorption-Enhanced Methanation concept.

This scheme has the advantage of a steady operation of the plant, thus avoiding the unsteady cyclic operation necessary for sorbent regeneration in fixed bed reactors. In addition, the use of fluidized bed reactors appears to be particularly suitable to achieve an accurate temperature control for highly exothermic reactions like methanation.

In this work, three potential sorbents were tested for their steam capture potential in a lab-scale dual bed fluidized bed apparatus: CaO, derived from natural limestone, and two commercial zeolites. The main aim was to evaluate the sorbent performance in terms of hydration and dehydration cycles at different operating conditions relevant for catalytic methanation.

Experimental

Three materials were tested as sorbents for SEM: a CaO and two zeolites. CaO was obtained by calcination of an Italian limestone named Massicci: the material was prepared in a lab-scale fluidized bed (40mm-ID) at 850°C with air and at a fluidization velocity of 0.5m/s for 20min. The zeolites were spherically shaped commercial 3A- and 4A-Zeolites. The experimental apparatus used for the tests, called Twin Beds, consisting of two identical lab-scale bubbling fluidized beds, is a specifically designed device for studying chemical looping processes. A systematic description of the operating principle of the TB system is reported elsewhere

(Coppola et al., 2017). The two reactors were employed as hydrator and dehydrator respectively. The experimental campaign was aimed at evaluating the suitability of the sorbents to capture and release water at different temperatures and reaction environments relevant for methane production. The main operating conditions were: hydration with 10% steam (balance air) and dehydration in air. A sensitivity analysis on temperature was carried out varying both the hydration and the dehydration temperature. The temperature range investigated for hydration was 200-300°C, while that for dehydration was 300-450°C. As an example, the acronym M-H25A-D35A is a typical name used to identify one test where the first letter specifies the sorbent (M=Massicci lime; Z3=3A-zeolite and Z4=4A-zeolite), H25A indicates the hydration step at 250°C in air, while D35A indicates the dehydration step at 350°C in air. Table 1 indicates the different temperature conditions adopted for each sorbent.

Table 1. Temperature Conditions in °C adopted in the tests

		Hydration Temperature		
		200	**250**	**300**
Dehydration Temperature	**300**	M/Z3*	M/Z3	M/Z3/Z4
	350	M/Z3	M/Z3	M/Z3/Z4
	400	M/Z3	M/Z3	M/Z3
	450	M/Z3	M/Z3	M/Z3

*M=Massicci lime; Z3=3A-Zeolite; Z4=4A-Zeolite

The experimental campaign was planned in two stages: in the first stage a deep investigation on the effect of the temperature on the sorbent performance was dedicated to CaO and 3A-Zeolite; afterwards, based on the results of these first tests, the most interesting conditions, in terms of chemical performance and industrial interest, were adopted for the 4A-Zeolite tests.
The progress of hydration and dehydration reactions was followed during the tests by measuring the steam concentration at the outlet of the reactors by means of a calibrated humidity sensor (Sensirion - SHT75 Humidity and Temperature Sensor IC). Each test consisted of 10 complete cycles, with a fluidization velocity fixed at 0.5m/s, while the time of each hydration or dehydration step was fixed at 10 min.

Results and Discussion

Steam capture tests for Massicci CaO. Figure 2 (A-C) reports the steam capture capacity of the sorbent with the number of cycles, expressed as grams of captured H_2O per gram of initial CaO, for all the conditions investigated. In general, the performance of CaO tends to decay with the number of cycles, and to reach an asymptotic value after the 6th-7th cycle. Moreover, the 2nd cycle typically presents a higher value of steam capture than the 1st cycle. This trend is most likely due to the different molar density between calcium hydroxide and calcium oxide, with a consequent swelling of the particle during the 1st hydration. This, in turn, entails an alteration of the sorbent microstructure with the formation of a highly porous CaO after the 1st dehydration step (Coppola et al., 2015). The decay after the 2nd cycle is the consequence of two effects. The first one is the occurrence of particle attrition, which implies the removal of sorbent material leaving as fines from the reactor with the outlet gas. The second effect is caused by carbonation of CaO with the CO_2 contained in the air, consuming active CaO from the sorbent. This reaction is irreversible in the temperature range used in the tests.

In Fig. 2-A the results of the tests M-H20A-D40A, M-H25A-D40A and M-H30A-D40A are reported, at a fixed dehydration temperature of 400°C, and for three different hydration temperatures (200, 250 and 300°C). The steam capture capacity decreases with the hydration temperature and this difference is evident during the first cycles and tends to vanish with the number of cycles. This behavior is related to the higher hydration (and carbonation) kinetics which determines the formation of a plugging layer of $Ca(OH)_2$ (and $CaCO_3$) hindering the diffusion of steam into the core of the particles. The asymptotic capacity values are quite similar among the samples and range around 0.008-0.019 g/g.

The effect of the dehydration temperature was investigated setting two different hydration temperatures of 250 and 300°C and varying the dehydration temperature (300, 350, 400 and 450°C). These results are shown in Figs. 2-B and 2-C. In general, the increase of the regeneration (dehydration) temperature improves the steam capture capacity but these differences are only significant during the first cycles and tend to disappear with the increase of the cycle number. Probably, this behavior may be explained by the fact that faster dehydration (at higher temperatures) determines overpressures inside particle that induce a more severe breakage of the particles with the formation of new surface for the subsequent hydration step (Scala et al., 1997). However, these effects appear to be more relevant at the highest hydration temperature, during the first cycles (compare Figs. 2-B and 2-C).

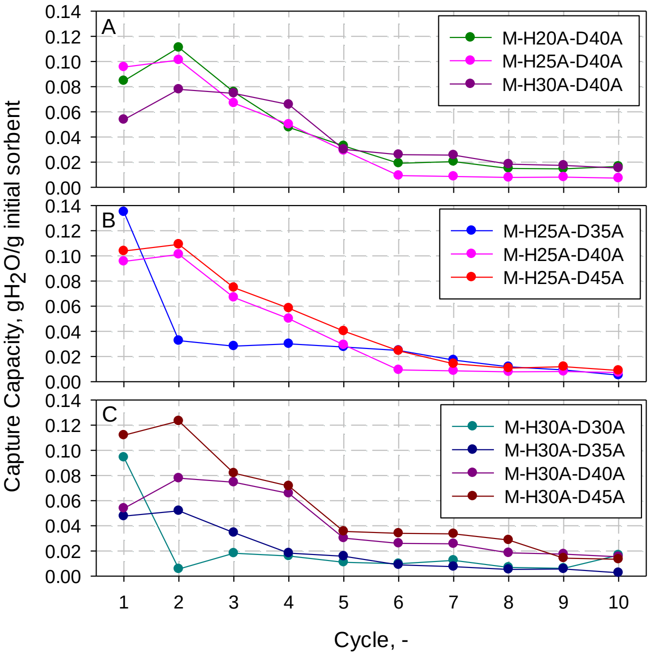

Fig. 2. H_2O capture capacity of the sorbent with the number of cycles for Massicci CaO.

Steam capture tests for 3A-Zeolite. Figure 3(A-C) reports the steam capture capacity of the sorbent with the number of cycles, expressed as grams of captured H_2O per gram of initial zeolite, for all the condition investigated. In general, the behavior of the zeolite is quite stable along the cycles with a slight increase of the capture capacity during the first cycles that indicates a sort of feeble activation. Similar to CaO, the influence of the hydration temperature was studied fixing the dehydration temperature at 400°C and varying the hydration temperature at 200, 250 and 300°C (Fig. 3-A). It is possible to note a slight negative influence of hydration temperature, in particular for the test Z3-H30A-D40A, which shows an average capture value of about 0.022 g/g, compared to 0.044 and 0.049 g/g for Z3-H20A-D400A and Z3-H25A-D40A, respectively. This effect is due to the worsening of physical absorption of H_2O on the sorbent surface at higher temperatures. In Figs. 3-B and 3-C the effect of the dehydration temperature was examined (300, 350, 400 and 450°C) for two different hydration temperatures (250 and 300°C). In particular, when the hydration temperature was set to 250°C (Fig. 3-B), the increase of the dehydration temperature had a limited effect until 400°C (average values of 0.046 and 0.049 g/g for Z3-H25A-D35A and Z3-H25A-D40A, respectively), while the capture capacity significantly decreased at 450°C (average value of 0.22 g/g for Z3-H25A-D45A). This behavior is most likely caused by the chemical degradation of the sorbent at 450°C, probably related to the release of water contained in the zeolite structure. When the hydration temperature was 300°C, the steam capture capacity recorded a relevant decay for all investigated dehydration temperatures. As matter of fact, the average capacity values were 0.017, 0.018, 0.022 and 0.024 g/g for the tests Z3-H30A-D30A, Z3-H30A-D35A, Z3-H30A-D40A and Z3-H30A-D45A, respectively. Probably, the hydration temperature limits from a thermodynamic point of view the physisorption of water as detected for the tests at different hydration temperatures (see figure 3-A), and this effect is more pronounced when the difference between hydration temperature and dehydration decreases.

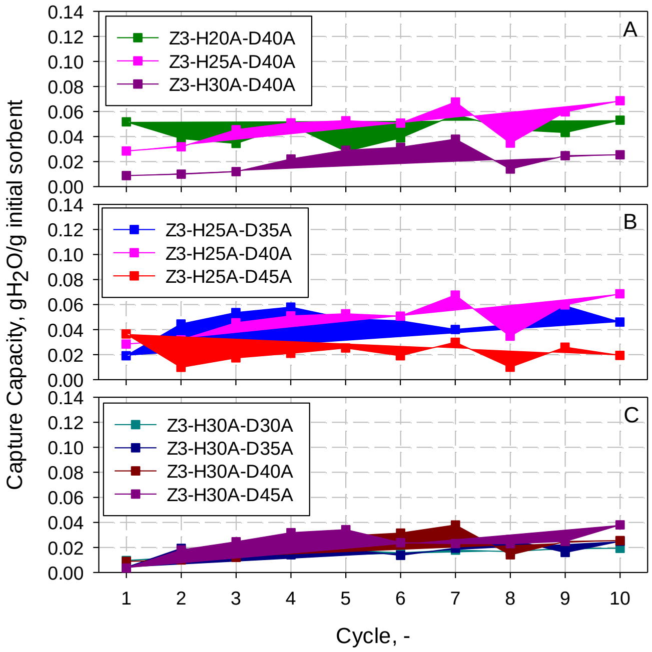

Fig. 3. H_2O capture capacity of the sorbent with the number of cycles for 3A-zeolite.

Steam capture tests for 4A-Zeolite. Figure 4 reports the steam capture capacity of the sorbent with the number of cycles, expressed as grams of captured H_2O per gram of initial zeolite, for the conditions Z4-H30A-D30A and Z4-H30A-D35A. The following considerations clarify the choice to investigate only these two conditions: i) the commercial Ni-based catalyst starts to be active at about 300°C and this determines the minimum methanation temperature; ii) the regenerator reactor needs energy, due to the endothermicity of dehydration reaction, hence operation at low temperature involves a lower energy consumption for the system. Moreover, these considerations are supported by the fact that at the hydration temperature of 300°C, the effect of dehydration temperature on the 3A-Zeolite is unimportant, meaning that an increase in the regeneration temperature implicates no tangible benefits (see Fig. 3-C). The 4A-Zeolite shows a very stable behavior and the average value of H_2O capture is slightly higher than that of the 3A-Zeolite: indeed, for the tests Z4-H30A-D30A and Z4-H30A-D35A values of about 0.022 and 0.021 g/g were recorded, respectively, while for the Z3-H30A-D30A and Z3-H30A-D35A these were 0.017 and 0.018 g/g, respectively.

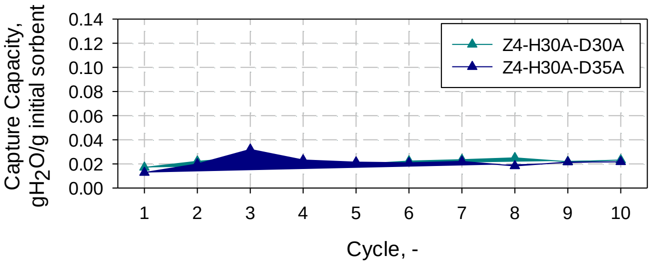

Fig. 4. H_2O capture capacity of the sorbent with the number of cycles for 4A -zeolite.

Conclusions

In general, CaO presents a decay of the steam capture capacity with the number of cycles in all conditions investigated. This decay is likely determined by the combination of chemical deactivation, induced by the irreversible carbonation of the sorbent with CO_2, and the elutriation of fine particles generated by attrition. The increase of the hydration temperature entails a negative effect during the first cycles, which tends to vanish with the increase of the cycle number. This behavior is probably due to the formation of a plugging external layer of $Ca(OH)_2$ (and $CaCO_3$) induced by faster reactions. Conversely, higher dehydration temperatures promote particle breakage with the formation of new surface with the consequent increase of the steam capture capacity. On the other hand, the zeolites have a more stable behavior than CaO in all conditions investigated, and present a slight activation during the first cycles. However, higher hydration temperatures have a similar effect as for CaO, determining a decrease of the steam capture capacity. The explanation of this trend is due to the less favorable physisorption with the increasing temperature. Contrary to CaO, the influence of the dehydration temperature on the zeolites seems to be related to the hydration temperature. At low hydration temperature, a negative effect could be observed only at the highest dehydration temperature, probably induced by a modification of the structure of the zeolite. Instead, at higher hydration temperature the steam capture was principally limited by the thermodynamics of physisorption during the hydration stage. Comparing the performance of the three materials, the zeolites on average have a better asymptotic capture capacity (0.017-0.049 g/g) than CaO (0.006-0.025 g/g), and furthermore they are not affected by deactivation during the cycles. However, this is not the only parameter to be considered for the choice of the best sorbent for the sorption-enhanced methanation, because other features could be important, such as the different cost of the sorbent, which is in favor of CaO. In addition, another important factor is the attrition resistance of the sorbent in a fluidized bed environment, which will be the subject of future experimental tests.

Acknowledgment

Mr. Alessandro Esposito, Mr. Claudio De Giacomo and Mr. Antonio Russo are gratefully acknowledged for their contribution in performing the experiments.

References

Bartholomew, C.H. Mechanisms of catalyst deactivation. Appl Catal A 2001. 212, 17–60

Borgschulte, A., N Gallandat, B Probst, R Suter, E Callini, D Ferri, et al. Sorption enhanced CO_2 methanation. Phys. Chem. Chem. Phys. 2013. 15, 9620-9625

Coppola, A., F Scala, L Gargiulo, P Salatino. A twin-bed test reactor for characterization of calcium looping sorbents. Powder Technol. 2017. 316, 585-591

Coppola, A., L Palladino, F Montagnaro, F Scala, P Salatino, Reactivation by Steam Hydration of Sorbents for Fluidized-Bed Calcium Looping. Energy & Fuels 2015. 29, 4436-4446

Cuéllar-Franca, R.M., A Azapagic. Carbon capture, storage and utilisation technologies: A critical analysis and comparison of their life cycle environmental impacts”, Journal of CO_2 Utilization 2015. 9, 82–102

Götz, M., J Lefebvre, F Mörs, A McDaniel Koch, F Graf, S Bajohr, et al. Renewable Power-to-Gas: A technological and economic review. Renew. Energy 2015. 85, 1371-1390

Mills, G.A., FW Steffgen. Catalytic methanation”, Catal Rev 1974. 8, 159–210

Panagiotopoulou, P., DI Kondarides, XE Verykios. Selective methanation of CO over supported Ru catalysts. Appl Catal B 2009. 88, 470–478

Sabatier, P., JB Senderens. New methane synthesis”, J. Chem. Soc. 1902. 82, 333-337

Scala, F., A Cammarota, R Chirone, P Salatino. Comminution of limestone during batch fluidized-bed calcination and sulfation. AIChE J. 1997. 43, 363–373

Seemann, M. Methanation of biosyngas in a fluidized bed reactor –development of a one-step synthesis process, featuring simultaneous methanation, watergas shift and low temperature tar reforming, PhD thesis. ETH Zurich. 2006

Seifert, A.H., S Rittmann, C Herwig. Analysis of process related factors to increase volumetric productivity and quality of biomethane with Methanothermobacter marburgensis. Appl. Energy 2014. 132, 155–162

Smestad, G.P., A Steinfeld. Review: Photochemical and Thermochemical Production of Solar Fuels from H_2O and CO_2 Using Metal Oxide Catalysts. Ind. Eng. Chem. Res. 2012. 51, 11828−11840

Walspurger, S., GD Elzinga, JW Dijkstra, M Saric, WG Haije. Sorption enhanced methanation for substitute natural gas production: Experimental results and thermodynamic considerations. Chem. Eng. J. 2014. 242, 379–386

THE ATTRITION BEHAVIOUR OF A LIMESTONE-BASED SORBENT FOR SORPTION-ENHANCED GASIFICATION IN DUAL FLUIDISED BEDS

Antonio Coppola[1], Aida Sattari[2], Fabio Montagnaro[2*], Fabrizio Scala[1,3], Piero Salatino[1,3]

[1] Dipartimento di Ingegneria Chimica, dei Materiali e della Produzione Industriale, Università degli Studi di Napoli Federico II, 80125 Napoli, Italy
[2] Dipartimento di Scienze Chimiche, Università degli Studi di Napoli Federico II, 80126 Napoli, Italy
[3] Istituto di Ricerche sulla Combustione, Consiglio Nazionale delle Ricerche, 80125 Napoli, Italy

*Email: *fabio.montagnaro@unina.it*

Abstract

The behaviour of a commercial sorbent for CO_2 capture in a dual interconnected fluidised bed looping process under simulated sorption-enhanced gasification conditions was investigated in a lab-scale apparatus. Each test consisted of ten calcination/carbonation cycles plus an eleventh calcination stage. Calcination was carried out at 850°C in 10% CO_2. Carbonation was carried out under six different test conditions, by varying temperature (600–700°C) and in absence/presence of 10% steam. CO_2 concentration was set at 10% as well. CO_2 capture capacity, elutriation rate and sorbent particle size distribution were obtained, and the results were discussed as a function of the operating parameters.

Overview

The Sorption-Enhanced Gasification (SEG) concept relies on the use of Ca-based sorbents during gasification of a fuel, to remove CO_2 from the syngas thus enriching it in H_2 (in percentages up to 80% by vol.; Florin and Harris, 2008). This can be achieved as, upon CO_2 sorption, the equilibrium of the water-gas shift reaction ($CO+H_2O=CO_2+H_2$) results pushed towards the products. Moreover, the presence of Ca in the gasification environment can also have a catalytic role (Sutton et al., 2001) in converting, by reforming, fuel-derived tar towards less harmful products (e.g. CO, CO_2) and H_2. The SEG process can borrow the concept of "calcium looping", a post-combustion technique to remove CO_2 from flue gas. In calcium looping, by means of a system of Dual Interconnected Fluidised Beds (DIFB), limestone sorbent is cycled between a carbonator (where it captures CO_2 from flue gas) and a calciner (where it releases CO_2 in a concentrated stream, to be further stored or re-utilised, so regenerating itself for another cycle), under proper operating conditions (Erans et al., 2016; Coppola et al., 2017a). DIFB configuration is an optimal choice for carrying out SEG (Göransson et al. 2011; Kirnbauer and Hofbauer, 2011), due to the need of: (i) carrying out heterogeneous reactions, both involving the sorbent and the fuel (if solid as, e.g., coal/biomass); (ii) transferring a stream of solid particles from one reaction environment to the other, as illustrated in Fig. 1 where a SEG conceptual scheme is reported. In the gasifier-carbonator, operated at circa 600–700°C, the solid fuel is fed with steam to give rise to the common gasification reactions yielding syngas. At the same time, the reactor is fed with a stream of CaO: CO_2 capture from syngas occurs via carbonation reaction ($CaO+CO_2=CaCO_3$), active in this temperature range. Thus, from this reactor one obtains: (i) a gaseous stream rich in H_2 (other main species being, as usual, CO and CO_2 d.b.); (ii) a solid stream of carbonated sorbent (plus unconverted CaO) and gasified solid fuel, still containing carbon. The latter stream is sent to the combustor-calciner, fed with air and, if needed, additional fuel. This reactor is operated around 800–900°C, a temperature range where the calcination reaction ($CaCO_3=CaO+CO_2$) occurs so to obtain again CaO, to be sent back to the carbonator for another cycle. The combustion allows: (i) the operation of the reactor at a higher temperature than the other one, also considering that limestone calcination is endothermal; (ii) the stream of regenerated sorbent to act as heat carrier, so to sustain the conditions in the gasifier-carbonator (gasification reactions are mostly endothermal). The flue gas exiting the combustor will result enriched in CO_2. Two main aspects are worthy of concern when dealing with looping processes of solid sorbents in DIFB systems (Coppola et al., 2019a): deactivation (i.e. decay of CO_2 capture capacity) over cycling, due to thermal sintering and, in SEG, possible "poisoning" by SO_2, tar, solid fuel; and loss of material by elutriation following attrition/fragmentation. These are aspects that, in addition, require continuous purge of spent sorbent and make-up of fresh one (Fig. 1) to compensate for both losses, i.e. in material reactivity ("chemical" loss) and that by elutriation ("physical" loss). The aim of this work is to carry out an investigation on these aspects, using a commercial limestone in a DIFB apparatus operated under typical SEG conditions. Moreover, the effect of both temperature and steam presence in the carbonator was addressed.

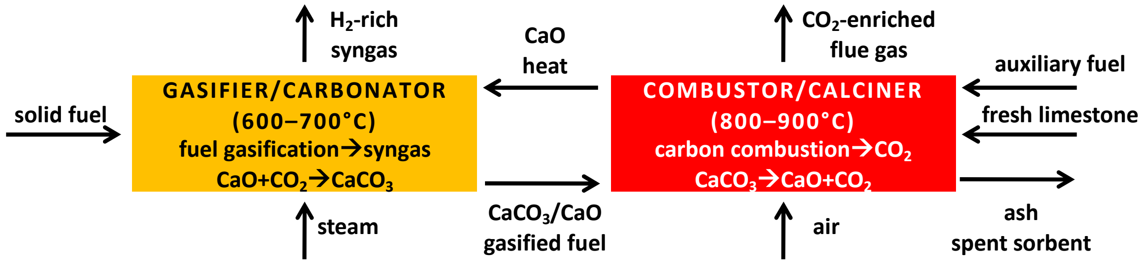

Fig. 1. Conceptual scheme of a sorption-enhanced gasification process in dual interconnected fluidised beds configuration.

Experimental Details

The experimental campaign was carried out in a lab-scale twin interconnected FB reactor, purposely designed for looping tests. The apparatus, named "twin beds", consists of two identical bubbling fluidised beds that can be operated as calciner and carbonator, respectively. The two reactors are electrically-heated and have an inner diameter of 40 mm. They are divided in three sections: a wind box (0.66 m height) also used as gas preheater; a fluidised bed (1.0 m height), separated from the wind box by a perforated plate; at the top, a gas exit duct that leads to a two-exit valve with two compartments housing sintered steel filters for elutriated fines collection (whose filtration efficiency is >99% for >10 µm particles). A steel hopper for solid feeding to the bed is connected sideways to each reactor. Both reactors operate separately in batch mode but they are connected to each other by a duct (inner diameter of 10 mm), partially immersed in the beds, used for fast pneumatic conveying of the sorbent between the two reactors. Transfer of sorbent is accomplished by using a valve system arranged along the duct and at the outlet of the reactors. The key advantage of this experimental setup is that it is able to reproduce a realistic particle thermal, chemical and mechanical history, while keeping the experimental complexity still much lower than for a full continuous looping system. A complete description of the apparatus is reported by Coppola et al. (2017b), while details on the experimental procedure now follow:

- the sorbent was an Italian limestone, "Massicci" (>97% $CaCO_3$ wt.). Cylinders of CO_2 and N_2, and a steam generation system (Bronkhorst CEM - Controlled Evaporator and Mixer), equipped with a flow meter controller, were used to generate surrogate flue gases to simulate realistic SEG conditions;
- a "test" consisted of ten complete cycles of calcination/carbonation, plus an eleventh calcination stage (total number of stages=twenty-one);
- the initial amount of limestone was 10 g, sieved in the size range 0.4–0.6 mm. At the beginning of the test, the sorbent was fed to the calciner. Silica sand (size 0.85–1 mm) was used in both reactors as ballast material, to limit temperature oscillations due to

chemical reactions and reactor temperature variations as the sorbent is conveyed from one reactor to the other. Sand proved to be chemically inert and with negligible contribution to attrition/fragmentation of sorbent;

- for all the tests (Table 1), calcination was operated at T=850°C fluidising the bed with a stream of 10% (v.) CO_2 (rest, air to simulate oxidising conditions in the combustor);
- in the carbonation stage, the temperature was varied in the range 600–700°C and the CO_2 concentration was set up to the value of 10%. Carbonation was carried out either in absence or in presence of steam (when present, at 10% concentration level – a value able to increase the sorbent efficiency, as seen in previous works by this research group; rest is always N_2 in this case, to simulate reducing conditions in a gasifier). Six different test conditions were designed, labelled so as to remind the two carbonation operating variables, i.e. temperature and steam concentration (see Table 1);
- each calcination or carbonation stage lasted for 10 min. Both the beds were fluidised with a flow rate able to allow a superficial velocity of 0.5 m/s.

Table 1. Operating conditions, in terms of temperature and gaseous atmosphere, for simulated DIFB-SEG tests. Carbonation conditions have been labelled T*xy*, where *x* is the temperature (600, 650, 700°C) and *y* is D when under "dry" conditions and W when under "wet" conditions.

	Calcination	**Carbonation**					
		T600D	**T600W**	**T650D**	**T650W**	**T700D**	**T700W**
Temperature, °C	850	600	600	650	650	700	700
CO_2, % v.	10	10	10	10	10	10	10
Air, % v.	90	–	–	–	–	–	–
H_2O, % v.	–	–	10	–	10	–	10
N_2, % v.	–	90	80	90	80	90	80

During each carbonation stage, the CO_2 concentration at the exhaust was continuously monitored by a NDIR analyser and the uptake of CO_2 was calculated by time-integration of the outlet CO_2 profile. The CO_2 specific capture capacity ξ was assessed as the mass of CO_2 captured in a stage per mass of initial sorbent. The attrition rate of the sorbent was investigated by collecting the fines elutriated at the exhaust. A quantity E (specific elutriation rate) is here defined as the mass of sorbent fines cumulatively collected over a stage (calcination or carbonation) divided by the initial mass of sorbent and by the total time length of the stage itself. The material (sand+sorbent) was retrieved from the apparatus at the end of each test (namely, after the eleventh calcination), and the sorbent was separated from sand using a 0.71 mm-sieve. The exhaust sorbent was then sieved, using sieves of different sizes, to obtain the Particle Size Distribution (PSD) and to assess in-bed particle fragmentation. The PSD was used to calculate the mean Sauter diameter d_S and the value of the quantity f_{FR}, defined as the fraction of in-bed sorbent fragments, i.e. the particles finer than 0.4 mm (the lower limit of the initial size range) but that remained un-elutriated after the eleventh calcination.

Results and Discussion

CO_2 Capture Capacity

Fig. 2 reports, for simulated DIFB-SEG tests (Table 1), the values for ξ vs. N (number of carbonation stages). The effect of thermal sintering in determining the decline of ξ is evident as long as N increases, and particularly relevant for the first cycles. If we use T600D as the reference base-case, for which $\xi(N=1)=0.199$ g/g, i.e. carbonation conversion degree X=45.2%, and $\xi(N=10)=0.030$ g/g (X=6.8%), we can observe the effect of temperature by comparing this case with T650D (where $\xi(N=1)=0.210$ g/g, i.e. X=47.7%, and $\xi(N=10)=0.059$ g/g, i.e. X=13.4%) and T700D (where $\xi(N=1)=0.198$ g/g, i.e. X=45.0%, and $\xi(N=10)=0.070$ g/g, i.e. X=15.9%). Also the visual inspection of the trends in Fig. 2 allows to notice a general positive effect of temperature T, at least under the adopted operating conditions (being true that, for even higher T-values, the exothermal carbonation process would reach the equilibrium), due to the complex superimposition of kinetic and diffusive aspects generally occurring in a gas-solid reaction. Apparently, in this temperature range, the increase in the kinetic and diffusive coefficients as T rises has a major role respect to aspects concerning thermodynamics (equilibrium-related) and change from kinetics- to diffusion-controlled regime. In presence of steam at 600°C and 650°C, it is confirmed that T has a positive effect, as for T600W it is $\xi(N=1)=0.207$ g/g ($X=47.0\%$), and $\xi(N=10)=0.048$ g/g ($X=10.9\%$), while for T650W it is $\xi(N=1)=0.224$ g/g ($X=50.8\%$), and $\xi(N=10)=0.084$ g/g ($X=19.1\%$). Moreover, steam is able to help the diffusion of CO_2 inside the porous network of the sorbent particle (Arias et al., 2012; Zhang et al., 2015; Coppola et al., 2019a, 2019b; Yang et al., 2018, 2019), as inferred by comparing, respectively, the results for T600W with T600D, and T650W with T650D. On the other hand, at higher temperature, H_2O can promote sorbent sintering phenomena (Borgwardt, 1989; Agnew et al., 2000), and this could explain why T700W ($\xi(N=1)=0.200$ g/g, i.e. $X=45.4\%$, and $\xi(N=10)=0.057$ g/g, i.e. $X=12.9\%$) did not show the best results among the tests. As a matter of fact (Fig. 2), the highest and lowest values for ξ were those under T650W and T600D conditions, respectively. It is finally observed that, if we compare these data with those obtained under “classical” calcium looping conditions (Coppola et al., 2019b), apart from minor differences in operating conditions of the carbonation stage, the more severe calcination temperature (940°C) of the other work lead to enhanced sintering and markedly lower values for ξ.

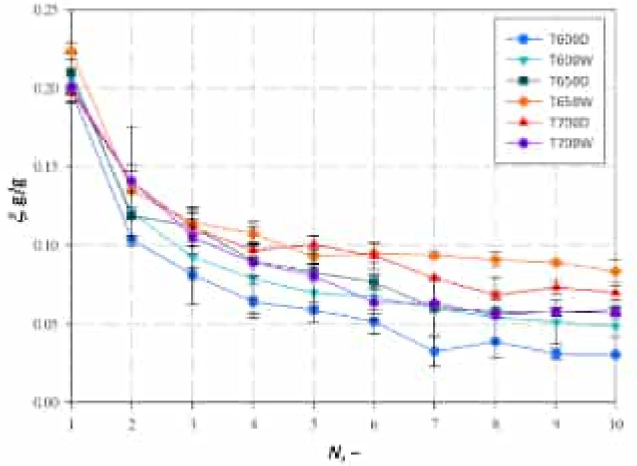

Fig. 2. Values for the specific CO_2 capture capacity ξ as a function of the number N of carbonation stage. Operating conditions reported in Table 1. Each experiment has been repeated three times.

Attrition and Fragmentation

Through capture of elutriated fines, the specific elutriation rate E (average value over the twenty-one stages constituting a test) resulted in the range $0.017–0.038\times10^{-3}$ min^{-1} (Table 2), translating into a percentage of fines lost by elutriation (per stage, average value) in the range 0.017–0.038%, as a function of the test conditions. Carbonation carried out under conditions favouring CO_2 capture gave rise to sorbent samples that, in their lifetime, experience a larger fraction of $CaCO_3$. As the latter, mechanically harder than CaO, prevailingly concentrates in the outer periphery of the particle (namely, the zone more exposed to surface wear due to the motion of rising bubbles under fluidised conditions), following a core-shell reaction path, the cases that showed larger values for ξ were, generally, also those with lower values for E (Fig. 3).

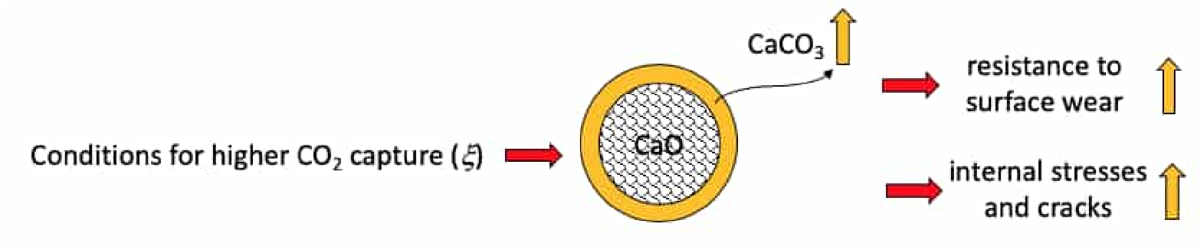

Fig. 3. A sketch showing the possible interrelation among CO_2 capture capacity, elutriation and fragmentation tendency. Higher CO_2 capture yields more resistant particle $CaCO_3$-rich shell (→lower elutriation tendency) and more fractured particle CaO-rich core (→higher in-bed fragmentation tendency).

Fig. 4 reports the absolute particle size distributions for the sorbent samples retrieved from the system at the end of each of the six different tests. It is seen that most of the particles remain in the feed size range (0.4–0.6 mm), but the presence of finer fragments (with a peak around 0.35 mm) can be clearly detected. These are fragments that, remaining un-elutriated from the system, concur to the CO_2 capture. From the quantitative point of view, the Sauter diameter d_S ranged from 0.384 to 0.407 mm, and the fraction of fragments was f_{FR}=24–30% (at the end of the whole test), see Table 2. The effect of the test conditions was substantially reversed with respect to what discussed about elutriation. Namely, the larger the CO_2 capture, the less resistant the material to in-bed fragmentation. As recently speculated (Coppola et al., 2019b), a larger Ca conversion to carbonate might induce more compact structures and, in turn, larger internal stresses which enhanced the formation of cracks in the particles during their processing in the fluidised beds (Fig. 3).

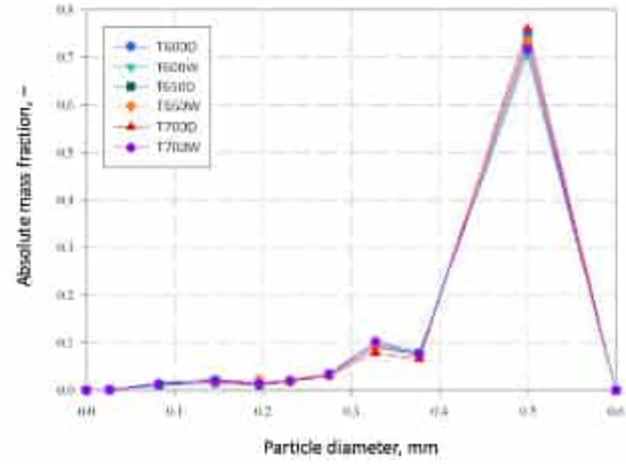

	T600D	T600W	T650D	T650W	T700D	T700W
$E\times10^1$, min^{-1}	0.038	0.028	0.030	0.017	0.032	0.022
d_S, mm	0.407	0.384	0.392	0.390	0.400	0.388
f_{FR}, –	0.25	0.30	0.27	0.26	0.24	0.28

Fig. 4 (left). Absolute particle size distributions for sorbent samples retrieved from the DIFB system after each of the six tests. Table 2 (right). Mean value (over twenty-one stages) of the specific elutriation rate, and mean Sauter diameter and fraction of fragments for sorbent particle population retrieved from the DIFB system after each of the six tests (operating conditions in Table 1).

Conclusions

Results of simulated SEG tests carried out in a DIFB system showed values for the carbonation conversion degree of a commercial limestone from circa 7% to 50% per cycle, as a function of the number of carbonation stage in the looping process, and of the adopted operating conditions. In particular, both increasing temperature and the presence of steam determined a better kinetic-diffusive scenario for the CaO carbonation process, even if, at 700°C, steam promoted sorbent sintering phenomena. Attrition/fragmentation studies allowed to observe that the operating conditions allowing a higher CO_2 capture are also those determining a more resistant particle shell (→lower elutriation tendency) and a more fractured particle core (→higher in-bed fragmentation tendency). The percentage of fines lost by elutriation was, per stage and in average, never higher than 0.038%, while the amount of fragments (particles finer than 0.4 mm) remained un-elutriated at the end of each test (twenty-one stages) was between 24% and 30% as a function of the test conditions. The analysis of data of CO_2 capture during the carbonation stage, contextually investigating the loss of material by elutriation and the changes in the particle size distribution of sorbent samples, is important for the correct design of a DIFB-SEG process, that must take into account both sorbent deactivation, need of make-up of fresh material and residence time distribution of sorbent particles.

References

Agnew, J., E Hampartsoumian, JM Jones, W Nimmo. The simultaneous calcination and sintering of calcium based sorbents under a combustion atmosphere. Fuel 2000. 79, 1515–1523.

Arias, B., G Grasa, JC Abanades, V Manovic, EJ Anthony. The effect of steam on the fast carbonation reaction rates of CaO. Ind. Eng. Chem. Res. 2012. 51, 2478–2482.

Borgwardt, R.H. Calcium oxide sintering in atmospheres containing water and carbon dioxide. Ind. Eng. Chem. Res. 1989. 28, 493–500.

Coppola, A., M Allocca, F Montagnaro, F Scala, P Salatino. The effect of steam on CO_2 uptake and sorbent attrition in fluidised bed calcium looping: the influence of process conditions and sorbent properties. Sep. Purif. Technol. 2017a. 189, 101–107.

Coppola, A., F Scala, L Gargiulo, P Salatino. A twin-bed test reactor for characterization of calcium looping sorbents. Powder Technol. 2017b. 316, 585–591.

Coppola, A., A Esposito, F Montagnaro, M Iuliano, F Scala, P Salatino. The combined effect of H_2O and SO_2 on CO_2 uptake and sorbent attrition during fluidised bed calcium looping. Proc. Comb. Inst. 2019a. 37, 4379–4387.

Coppola, A., A Esposito, F Montagnaro, G De Tommaso, F Scala, P Salatino. Effect of exposure to SO_2 and H_2O during the carbonation stage of fluidised bed calcium looping on the performance of sorbents of different nature. Chem. Eng. J. 2019b. In press, published on-line, doi.org/10.1016/j.cej.2018.12.086.

Erans, M., V Manovic, EJ Anthony. Calcium looping sorbents for CO_2 capture. Appl. Energy 2016. 180, 722–742.

Florin, N.H., AT Harris. Enhanced hydrogen production from biomass with in situ carbon dioxide capture using calcium oxide sorbents. Chem. Eng. Sci. 2008. 63, 287–316.

Göransson, K., U Söderlind, J He, W Zhang. Review of syngas production via biomass DFBGs. Renew. Sust. Energy Rev. 2011. 15, 482–492.

Kirnbauer, F., H Hofbauer. Investigation on bed material changes in a dual fluidized bed steam gasification plant in Güssing, Austria. Energy Fuels 2011. 25, 3793–3798.

Sutton, D., B Kelleher, JRH Ross. Review of literature on catalysts for biomass gasification. Fuel Process. Technol. 2001. 73, 155–173.

Yang, P., L Duan, H Tang, T Cai, Z Sun. Explaining steam-enhanced carbonation of CaO based on first principles. Greenh. Gases Sci. Technol. 2018. 8, 1110–1123.

Yang, P., Z Sun, L Duan, H Tang. Mechanism of steam-declined sulfation and steam-enhanced carbonation by DFT calculations. Greenh. Gases Sci. Technol. 2019. In press, published on-line, doi.org/10.1002/ghg.1905.

Zhang, L., B Zhang, Z Yang, M Guo. The role of water on the performance of calcium oxide-based sorbents for carbon dioxide capture: a review. Energy Technol. 2015. 3, 10–19.

NO AND SO$_2$ EMISSION CHARACTERISTICS OF COAL GANGUE AND SUNFLOWER STALK CO-COMBUSTION IN BUBBLING FLUIDIZED BED

Xiangru Jia*, Zhihui Shi, Guofang Yang, Yabin Zhao, Changzhong Song

College of Energy and Power Engineering, Inner Mongolia University of Technology,
Hohhot 010051, China

*Email: *jxr0818@163.com*

Abstract

Energy is the basis for the survival and development of human society. With the global energy shortage and environmental degradation, countries around the world are paying more and more attention to renewable clean energy and solid waste energy. Using the bubbling fluidized bed and flue gas analysis equipment, NO and SO$_2$ emission characteristics in the process of coal gangue combustion and co-combustion of coal gangue and sunflower stalk were researched. The results showed that NO and SO$_2$ emissions changed in the process of coal gangue combustion when the volume of the primary air and feeding air changed. When the volume of the primary air changed, NO and SO$_2$ emissions also changed in the process of co-combustion of coal gangue blended with sunflower stalk in a 4:1 ratio. NO and SO$_2$ emissions of coal gangue combustion alone were more than that of coal gangue and sunflower stalk co-combustion.

Key words： biomass; coal gangue; fluidized bed combustion; co-combustion

1. INTRODUCTION

Biomass energy refers to the energy that plant chlorophyll converts solar energy into chemical energy stored in biomass. Biomass has high volatile matter, low ash, is renewable, and low pollution (Font, 2012; Demirbas, 2005). Biomass energy development and utilization prospects are very wide. Coal gangue is a carbonaceous rock abandoned during coal mining and coal washing. Coal gangue has the characteristics of low volatile matter, high ash, low calorific value and difficult combustion. Fluidized bed combustion technology has wide fuel adaptability and high combustion efficiency. Therefore, by using the complementarity of coal gangue and biomass combustion characteristics, biomass and coal gangue utilization efficiency can be improved while affecting gaseous pollutant emissions when they are burned in a fluidized bed.

The literature reports on the mixed burning of coal gangue and agricultural and forestry biomass mainly have the following contents. Zhang et al. (1995) discussed the promoting effect of biomass on coal gangue combustion. Chen (2007) studied on the characteristics of mixed combustion of various biomass and coal gangue. The results showed that, the combustion characteristics of the mixture depend on the content of each substance in the mixture proportion. Pu et al. (2009) used a thermogravimetric analyzer to study the characteristics of co-combustion of coal gangue and corn stalk, and kinetic parameters such as activation energy of combustion were obtained by kinetic analysis. Zhou et al. (2014, 2015, 2017) studied the distribution of trace elements in flue gas, fly ash and ash during the mixed combustion of coal gangue and biomass using a fixed bed. Zhou et al. (2014, 2015, 2017) also studied the occurrence mechanism and migration law of trace elements in the process of co-combustion of various biomass and coal gangue in a laboratory-scale circulating fluidized bed. Zhang et al. (2016) used thermal analysis to study the interaction of coal gangue and pine sawdust in high temperature and low temperature stages under different conditions. Yang (2016) analyzed the data obtained from the mixed pyrolysis and combustion of coal gangue and biomass by thermogravimetric analysis. It is considered that the combustion process of the mixture is more stable and the combustion performance is better.

In this paper, the typical agricultural biomass and coal gangue in Inner Mongolia were used to study the NO and SO_2 gas emission characteristics of coal gangue combustion and the co-combustion of biomass and coal gangue by using a small bubbling fluidized bed.

2. MATERIALS AND METHODS

2.1 Material

The selected materials were coal gangue (CG) and sunflower stalk (SS) in Inner Mongolia. The coal gangue had a particle size of 0.5-0.6 mm (30-40 mesh) and a density of 2800 kg/m^3; while, the sunflower stalk had a particle size of 0.87-1.9 mm (10-20 mesh) and a density of 500 kg/m^3. Proximate and ultimate analysis values are shown in Table 1.

Table 1. Proximate and ultimate analysis of samples

Samples	**Proximate analysis, ad (wt%)**				**Ultimate analysis, ad (wt%)**					**$Q_{net,\ ad}$ (kJ·kg^{-1})**
	M	*A*	*VM*	*FC*	C	H	O	N	S	*Q*
SS	1.45	4.43	72.89	21.2	45.8	6.21	42.6	0.55	0.15	16351.64
CG	1.93	55.55	19.68	22.8	38.2	2.61	3.63	0.48	0.89	10349.18

2.2 Experimental equipment

The main test equipment used for the investigation was a small fluidized bed combustion system, as shown in Fig. 1. The system included a combustion furnace, a feeding system, an air delivery system, a smoke exhaustion system, and a furnace electric heating system. The equipment had an electrical heating power of 36 kW, a furnace height of 2.5 m and a diameter of 0.05 m.

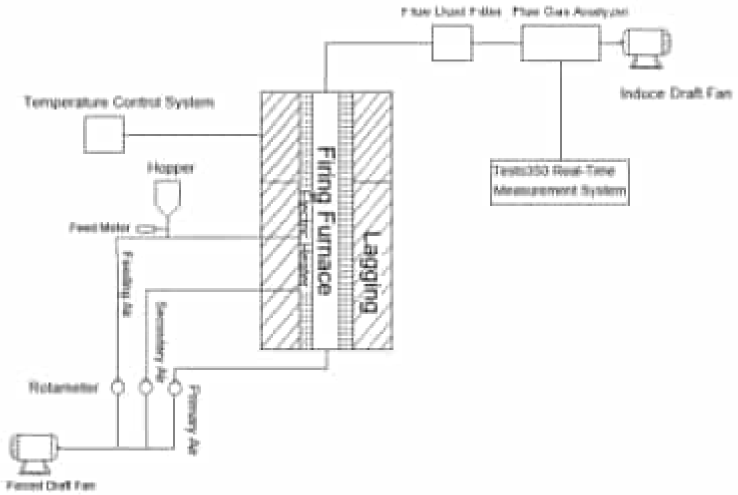

Fig. 1. The fluidized bed combustion test system

During the test, the Testo350 flue gas measurement system was used to measure the content of pollutant gases such as NO, SO_2 and CO online. The flue gas sampling point was located behind the pipeline after the flue gas was cooled and dedusted. The testo350 real-time measurement software was used to collect the flue gas data at intervals of 1 s.

2.3 Experimental scheme

Before the start of the test, the ash at the bottom of the fluidized bed was cleaned with a primary air, and coal gangue was used as bed material to be fed into the fluidized bed from the feeding system. Turn on the electric heating device to heat the furnace. When the temperature reached 900°C, the test material particles were fed through the hopper. During the test, the furnace temperature was kept at 900°C, the feeding amount was 2.8 g/min, and burning time was 2 h. The test conditions are shown in Table 2.

Table 2. Fluidized bed combustion test conditions

Samples	**Particle diameter (mesh)**	**Feeding air ($m^3 \cdot h^{-1}$)**	**Primary air ($m^3 \cdot h^{-1}$)**	**Secondary air ($m^3 \cdot h^{-1}$)**
CG	30-40	1.8	1, 1.5, 1.8	1.5
CG	30-40	1, 1.5,1.8	1.5	1.5
SS:CG=1:4	SS: 10-20 ; CG: 20-40	1.5	1, 1.5	1.5

3. RESULTS AND DISCUSSION

3.1 Pollutant emission characteristics of coal gangue combustion

3.1.1 Effect of primary air volume on NO, SO_2 and CO emission characteristics

The fluidization parameters at 900°C were calculated. When the coal gangue particle size is 0.5 to 0.6 mm, the minimum fluidization velocity (u_{mf}) is 0.095 to 0.137 m/s.

The NO, SO_2 and CO emissions were compared When the feeding air volume was 1.8 m^3/h, the secondary air volume was 1.5 m^3/h, and the primary air volume was 1, 1.5, 1.8 m^3/h (u, 0.142, 0.212 and 0.256 m/s). The effects of primary air volume on NO, SO_2 and CO emissions are shown in Figs. 2, 3 and 4.

The average value was selected as the representative value. The release of NO, SO_2 and CO changed with the change of primary air volume. When the total air volume was 4.3, 4.8 and 5.1 m^3/h, the average release amount of NO was 52, 42 and 41 ppm, respectively; the average actual release amount of SO_2 was 230, 188 and 164 ppm, respectively; the average actual release amount of CO was 264, 201 and 190 ppm, respectively, as shown in Fig. 2, 3 and 4. After conversion, CO, SO_2 and CO emissions per unit time are shown in Figure 5.

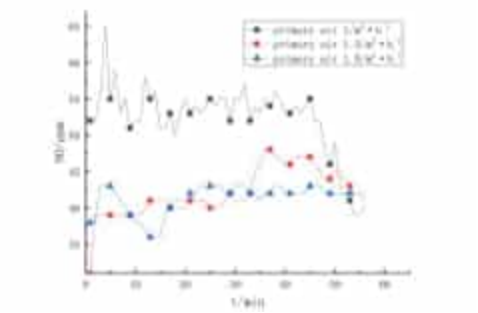

Fig. 2. NO emission curve with primary air

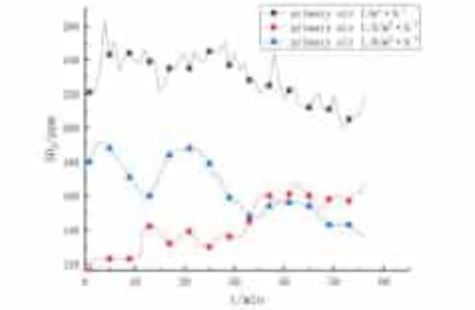

Fig. 3. SO_2 emission curve with primary air

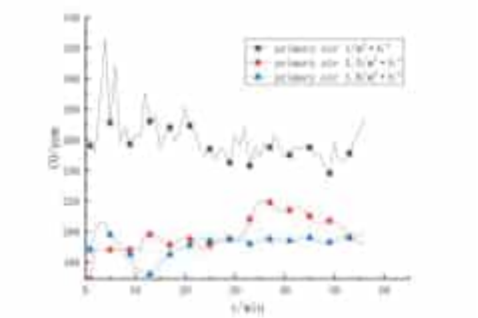

Fig. 4. CO emission curve with primary air

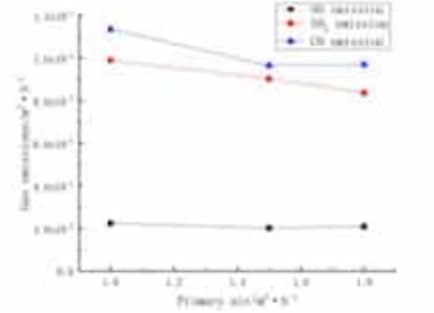

Fig. 5. Gas emission trend with primary air

It can be seen from Fig. 5 that with the increase of primary air volume, the release of NO, SO_2 and CO gradually decreased. When the primary air volume was 1 m^3/h, the flow rate was small, and very few particles could enter the lean-phase zone of the fluidized bed. The particles mainly burned in the dense-phase zone of the fluidized bed, and the combustion was insufficient, so the CO release amount was the largest in the combustion process. When the primary air volume was increased, more particles entered the lean-phase zone and continued to burn, so the combustion was sufficient. At the same time, NO generated in the dense-phase zone of the fluidized bed entered the lean-phase zone and reacted with the small particles therein due to an increase in the amount of air. The reduction reaction of NO occurred, and the amount of NO gas was reduced. For SO_2, the SO_2 gas generated in the dense-phase zone reacted with the minerals in the lean-phase zone to fix sulfur, so the release of SO_2 gas was reduced.

3.1.2 Effect of feeding air volume on NO, SO_2 and CO emission characteristics

The NO, SO_2 and CO emissions were compared when the primary air volume was 1.5 m^3/h, the secondary air volume was 1.5 m^3/h, and the feeding air volume was 1, 1.5, and 1.8 m^3/h. The average value was selected as the representative value. The release amount of NO, SO_2 and CO changed with the change of feeding air. When the total air volume was 4, 4.5, 4.8 m^3/h, the average release amount of NO was 6.04, 2.21 and 2.02×10^{-4} m^3/h, respectively; the average release amount of SO_2 was 9.36, 7.43 and 9.02×10^{-4} m^3/h, respectively; the average release amount of CO was 13.96, 14.8 and 9.65×10^{-4} m^3/h, respectively, as shown in Fig. 6.

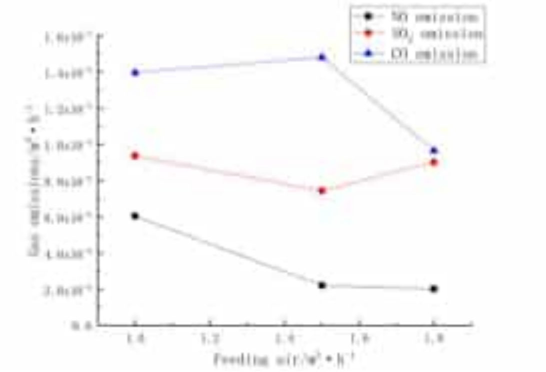

Fig. 6. Gas emission trend with feeding air

The feeding air mainly plays the role of conveying materials, and its tuyere was located in the middle and lower part of the furnace. Therefore, it had little influence on the dense-phase zone in the fluidized bed, and mainly affected the combustion of coal gangue particles in the lean-phase zone. It can be seen from Fig. 6 that when the feeding air was 1 m^3/h, the NO and SO_2 emissions were the largest; when the feeding air volume increased, the NO and SO_2 emissions changed greatly. For NO, as the feeding air volume increased, many small particles were carried into the lean-phase zone and the separator. There were “reburning” phenomenon in some parts of the lean-phase zone and “post-combustion” phenomenon in some parts of the separator, and reducing atmosphere was formed in these locations, which reduced NO and caused its release to decrease. At the same time, SO_2 formed in the dense-phase zone entered the lean-phase zone and the separator, and reacted with the mineral or inorganic substances (such as alkali metals) in the small particles forming solid sulfides, so the release of SO_2 was reduced. When the feeding air volume was increased to 1.8 m^3/h, the main reason for the increase in the release of SO_2 may be that the sulfur fixation reaction was weakened as gas phase residence time decreased.

3.2 Pollutant emission characteristics of coal gangue and sunflower stalk co-combustion

3.2.1 Effect of primary air volume on NO, SO_2 and CO emission characteristics

The NO, SO_2 and CO emissions were compared when the feeding air volume was 1.5 m^3/h, the secondary air volume was 1.5 m^3/h, and the primary air volume was 1 and 1.5 m^3/h. When the total air volume was 4 and 4.5 m^3/h, the average value of the actual release of NO was 1.92×10^{-4} and 1.67×10^{-4} m^3/h, respectively; the average value of the actual release of SO_2 was 4.44×10^{-4} and 3.56×10^{-4} m^3/h, respectively; and the average value of the actual release of CO was 11.84×10^{-4} and 9.09×10^{-4} m^3/h, respectively, as shown in Fig. 7. It can be seen from the figure that the average value decreased when the primary air volume increased. When the total air volume increased to 4.5 m^3/h, the corresponding wind speed was 2.55 m/s, which was close to the fluidization terminal speed (2.81 m/s) of the small size sunflower stalk particle (0.87 mm), so "post-combustion" phenomenon occurred in the lean-phase zone and separator, in which a strong reducing atmosphere was formed. NO underwent a reduction reaction in the lean-phase zone and the separator, and the release amount of NO decreased. At the same time, the alkali metal element contained in the sunflower stalk reacted with SO_2 to form alkaline-earth sulphates reducing the amount of SO_2 released.

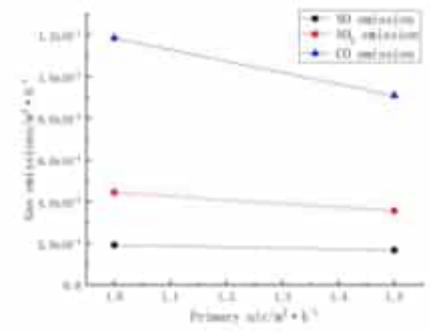

Fig. 7. Gas emission trend of primary air change

3.2.2 *Comparison of NO, SO_2 and CO emission characteristics of coal gangue separate combustion and co-combustion*

When the primary air volume, the secondary air volume and the feeding air volume were all 1.5 m^3/h, NO, SO_2 and CO emissions of coal gangue separate combustion were compared with that of co-combustion. The results are shown in Figs. 8, 9 and 10.

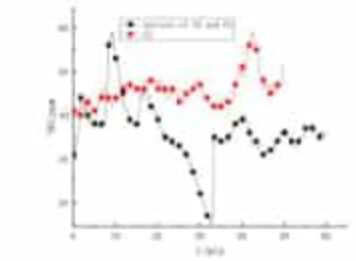

Fig.8 The comparison of NO emissions

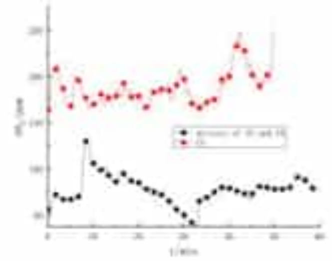

Fig.9 The comparison of SO_2 emissions

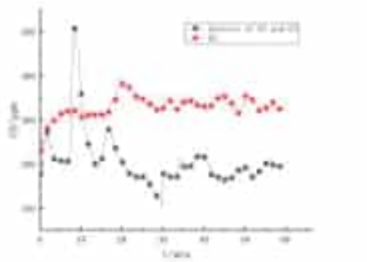

Fig.10 The comparison of CO emissions

When the total air volume was 4.5 m^3/h, the actual emissions of NO SO_2 and CO in the coal gangue separate combustion process were 49, 165 and 326 ppm, respectively, and the actual emissions of NO, SO_2 and CO in the co-combustion of coal gangue and sunflower stalk were 37, 79 and 202 ppm, respectively. Because the feed rate was constant, the amount of coal gangue in co-combustion was 80% of the separate combustion per unit time. The release of NO, SO_2 and CO during the separate combustion of coal gangue is multiplied by 80%, and the values are 39, 132 and 261 ppm, respectively. Therefore, the actual release of NO, SO_2 and CO during the combustion of coal gangue and sunflower stalk was less than that of NO, SO_2 and CO during the combustion of coal gangue.

The release of NO and CO of coal gangue and sunflower stalk co-combustion was lower than that of coal gangue separate combustion. This was mainly due to the strong reducing atmosphere formed in the lean-phase zone and the high volatile content of sunflower stalk during co-combustion. The NO produced could be quickly reduced to N_2. Therefore, the release of NO during the co-combustion was lower. The high volatile content of sunflower stalk could promote coal gangue burning.

The release of SO_2 of coal gangue and sunflower stalk co-combustion was lower than that of coal gangue separate combustion also. Because there was very little sulfur in sunflower stalk, SO_2 in the process of co-combustion mainly comes from coal gangue. This indicates that sunflower stalk inhibits the release of SO_2 from coal gangue, thus reducing the release of SO_2.

The main reason is that the alkali metals contained in the sunflower stalk can convert SO_2 into solid sulfides.

4. CONCLUSIONS

(1) The emission amount of NO, SO_2 and CO during the coal gangue combustion in a fluidized bed decreased as the primary air volume increased.

(2) As the feeding air volume increased, the release of NO decreased during the coal gangue combustion. When the feed air volume was 1 m^3/h, the maximum amount of SO_2 was released.

(3) When the sunflower stalk and coal gangue were mixed and burned in a fluidized bed in a ratio of 1:4, the emission of NO and SO_2 decreased as the primary air volume increased.

(4) When the primary air volume, secondary air volume and feeding air volume were all 1.5 m^3/h, the co-combustion of coal gangue and sunflower stalk was compared with the combustion of coal gangue alone. It was found that the release of NO and SO_2 of co-combustion was less than that of gangue separate combustion. The sunflower stalk can inhibit the release of NO and SO_2 during the combustion of coal gangue. The main reason may be that the alkali metals contained in the sunflower stalk can convert SO_2 into solid sulfides.

ACKNOWLEDGEMENTS

This work was supported by Research Program of Science and Technology at Universities of Inner Mongolia Autonomous Region (No. NJZY18082).

REFERENCES

Chen, Y. Experimental study on co-pyrolysis and co-combustion characteristic of biomass and coal residue. Chongqing: Chongqing University, 2007

Demirbas, A. Potential applications of renewable energy sources, biomass combustion problems in boiler power systems and combustion related environmental issues. Prog. Energy Combust. Sci. 2005. 31(2), 171-192

Font, O, P Cordoba, C Leiva, et al. Fate and abatement of mercury and other trace elements in a coal fluidized bed oxy combustion pilot plant. Fuel, 2012. 95, 272-281

Pu, G, L Zhang, J Wang, et al. Experimental study on co-combustion characteristics of biomass and coal residue. Journal of Engineering Thermophysics. 2009. 30(2), 333-335

Yang, F. Experimental Study on Mixed Pyrolysis and Combustion Characteristics of Biomass and Coal Gangue. Hohhot: Inner Mongolia University of Technology, 2016

Zhang, B, Q Zhang, S Liu. Experimental study on the characteristics of gangue briquetting combustion in industrial boilers. Coal Science and Technology, 1995. 24(2), 1645-1648

Zhang, Y, Z Zhang, M Zhu, et al. Interactions of coal gangue and pine sawdust during combustion of their blends studied using differential thermogravimetric analysis. Bioresource Technology, 2016a. 214(8), 396-40

Zhang, Y. The study of combustion characteristic and influence mechanism of coal gangue. Taiyuan: Shanxi University, 2016b

Zhou, C, G Liu, S Cheng, et al. Thermochemical and trace element behavior of coal gangue, agricultural biomass and their blends during co-combustion. Bioresource Technology, 2014. 166(8), 243-251

Zhou, C, G Liu, T Fang, et al. Investigation on thermal and trace element characteristics during co-combustion biomass with gangue coal. Bioresource Technology, 2015. 175(1), 454-462

Zhou, C, G Liu, Z Xu, et al. The retention mechanism, transformation behavior and environmental implication of trace element during co-combustion coal gangue with soybean stalk. Fuel, 2017. 189(2), 32-38

EXPERIMENTAL STUDY ON THE INFLUENCE OF EXCESS AIR RATIO IN THE FURNACE OF A CFB WITH POST-COMBUSTION ON NO_X EMISSIONS

Yuan Xiao[12], Guoliang Song[123*], Zhao Yang[12] and Qinggang Lyu [123]

[1] *Institute of Engineering Thermophysics, Chinese Academy of Sciences,*
Beijing 100190, China
[2] *University of Chinese Academy of Sciences, Beijing 100049, China*
[3] *Dalian National Laboratory for Clean Energy, Dalian 116023, China*

*Email:*songgl@iet.cn*

Abstract

The study explored the influence of the combustion temperature and the excess air ratio in the furnace on the nitrogen oxides (NO_x) emission during combustion in a circulating fluidized bed (CFB) test platform. The test platform was composed of a CFB and a post-combustion chamber (PCC). The combustion and NO_x emission characteristics of Shenmu semi-coke were investigated with the condition of the post-combustion. In comparison to conventional CFB combustion, the post-combustion is a new combustion technology that could effectively control NO_x initial emission. The experiment results showed that NO_x emission of Shenmu semi-coke decreases with the increase of combustion temperature when the excess air ratio in the furnace (λ_{CFB}) was 1.2. But NO_x emission increased with the combustion temperature increased while λ_{CFB} was 0.8 under the post-combustion conditions. In the case of post-combustion, NO_x emission increases when the λ_{CFB} increased. The post-combustion with the λ_{CFB} of 0.8 was able to bring the conventional concentration of NO_x emission to 156 mg/m^3 (at 6% O_2), only 16.6% of conventional CFB combustion. When the temperature decreases and the excess air ratio increases, CO emission and carbon content in fly ash decrease under all the experiment conditions, which means higher combustion efficiency. The results show that the post-combustion technology is a very effective method to decrease NO_x initial emission and guarantee the combustion efficiency. The operation parameters obtained have certain guiding significance for industrial applications of post-combustion.

Introduction

Nitrogen oxides (NO_x) is one of the environmental issues which have attracted widespread attention in recent years, and thermal power plants as the main source of NO_x emission are subjected to increasingly strict environmental regulation. Low-rank coals account for more than 55% of the coal reserves in China. In the past few decades, low-rank coals were mainly directly combusted in power plants, which not only has relatively low energy use efficiency, but also increases the difficulty of NO_x removal. Grade utilization of coals is believed as the most clean and efficient utilization method of low-rank coals. At first, the low-rank coal was pyrolysis, and pyrolysis gas and tar are used as high-grade products, while the low-grade product semi-coke can be combusted in power plants. Because of excellent fuel feasibility, the circulating fluidized bed (CFB) boilers can be used to achieve the effective utilization of semi-coke.

Some related studies about low nitrogen combustion operation have been published. Hayhurst, A (1996) wrote that N concentration in the coal was dominant parameter to predict the NO_x emission from a large-scale CFB boiler. Tourunen, A (2009) wrote that NO emissions above the dense bed decrease with furnace atmosphere which was the change in oxygen concentration. With the combustion temperature increasing, the concentration of NO_x gradually increases was found by Luis F (1996) and Gungor A et al (2009). In addition to the above studies, Yao et al (2015a, 2015b) found that O_2 concentration profile is the major factor affecting NO emission, the lower O_2 concentration led to the generation of lower initial NO. Zhou T et al (2015, 2017) wrote that post-combustion which means lean oxygen combustion in a CFB with excess oxygen in a post-combustion chamber (PCC) is an effective approach of enhanced control initial NO_x emission for CFB boilers. The influence of combustion temperatures and excess air ratio on the post-combustion characteristics of Shenmu semi-coke were investigated on a pilot platform of a 0.75kW CFB test rig with a post-combustion chamber in this study.

Experimental

The combustion and NO_x emission characteristics of Shenmu semi-coke were investigated on a CFB test platform. The test platform which is composed of a circulating fluidized bed (CFB), a post-combustion chamber (PCC) and an auxiliary system is demonstrated in Fig 1. CFB furnace diameter is 150 mm and length is 5000 mm. The CFB connected with the post-combustion chamber through a flue duct of 80 mm in diameter. The post-combustion chamber is 120mm and length is 3000mm. There is a post-combustion air (PCA) spout arranged at the flue duct between CFB and the post-combustion chamber. At the one side of the furnace, there were cyclone separator and a loop seal, forming a recirculation loop. Primary air without preheat is fed into the furnace at the bottom through the air distribution plate. There are six temperature measurement points (T1-T6) and three temperature measurement points (T8-T10) along the CFB furnace and the post-combustion chamber, respectively. Another temperature measurement point (T7) was arranged on the flue duct between the CFB furnace and the post-combustion chamber. Sampling point after the PCC is used for collecting fly ash and monitoring the flue gas for each experimental condition. The sampled flue gas is dried, filtered, and then analyzed online with a Gasmet FTIR DX-4000 analyzer. A CY-IS-G zirconia oxygen analyzer is used to monitor the oxygen concentration in flue gas at the tail-end flue duct.

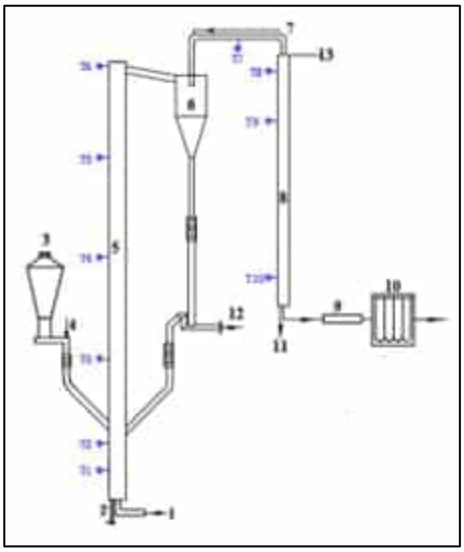

Fig1. Schematic diagram of the CFB system 1- Primary air 2- Slag discharging pipe 3- Coal hopper 4- Coal spreading air 5- CFB furnace 6-Cyclone 7- Post-combustion air 8- Post-combustion chamber 9- Flue gas cooler 10- Gas filter 11- Sampling point 12- Recirculation air 13.Top of the post-combustion chamber

Shenmu semi-coke is the low-grade product of slow pyrolysis of Shenmu coal between 500 and 700 ℃. Before experiment, the Shenmu coal was sieved into particular particle size between 0.1 and 1 mm. Proximate and ultimate analyses of Shenmu semi-coke were listed in Table 1.

Table 1: Proximate and Ultimate Analysis (wt %)

Moisture^a	Volatile Matter^b	Fixed Carbon^a	Ash^a	Low Heating Value^a(MJ/kg)	Carbon^a	Hydrogen^a	Oxygen^a	Nitrogen^a	Sulfur^a
14.60	9.89	66.72	11.36	23.32	68.31	0.85	4.01	0.58	0.30

a As received basis; b Dry and ash-free basis

Experimental Conditions

Experimental variables include bed temperature, the excess air ratio in furnace (λ_{CFB}) and total excess air ratio (λ). Operation conditions of the experiment were listed in table 2. The excess air ratio in the PCC was λ_{PCC}, and $\lambda=\lambda_{CFB} + \lambda_{PCC}$. In this article, NO_x (dry, at 6% O_2) was defined as the total of NO and NO_2. The gas was sampled and analyzed through sampling point. Combustion temperature meant the highest temperature in the CFB furnace. For case 1-3, combustion temperatures were 900, 940 and 980℃ respectively. The PCA injected from the cyclone outlet in all of the post-combustion cases.

Table 2. Operation Conditions of the Experiments

Case	Unit	1				2				3			
		1.1	1.2	1.3	1.4	2.1	2.2	2.3	2.4	3.1	3.2	3.3	3.4
Combustion Temperature	℃	900	898	898	905	939	945	940	937	988	979	983	978
λ_{CFB}		1.0	0.8	1.0	1.2	1.0	0.8	1.0	1.2	1.0	0.8	1.0	1.2
λ_{PCC}		-	0.4	0.2	-	-	0.4	0.2	-	-	0.4	0.2	-
λ		1.0	1.2	1.2	1.2	1.0	1.2	1.2	1.2	1.0	1.2	1.2	1.2
Primary Air	m^3/h	25.6	25.6	25.7	27.8	30.2	39.0	30.2	39.1	23.6	35.5	23.6	42.2
Coal Feeding Rates	Kg/h	5.0	7.4	5.0	5.1	7.4	11.2	7.4	6.6	4.4	8.1	4.4	6.8

Results and Discussion

Combustion Characteristic of Shenmu Semi-coke

The temperature distributions along the CFB furnace for experimental conditions were displayed in Fig 2 (a). In all the experimental conditions, the furnace temperature first increased and then decreased. The injection of the primary air and circulating ash into the bottom of the furnace resulted in a low temperature. The temperature reached its highest at approximately 1.5 m above the air distributor and then decreased gradually because of the presence of the water cooling tube in the dilute region. But in case 3.1, 3.3 and 3.4, descending trends were not obvious as other cases, because water cooling tube was not used in above-mentioned cases. Case 1.1, 1.3 and 1.4 had same fuel feeding rate, but the temperature in the dilute region of case 1.4 was higher than that in Cases 1.1. This phenomenon was caused by the fact that less heat was released owing to the incomplete combustion of fuel in the furnace under the low oxygen combustion. Besides, under low oxygen combustion, some endothermic reactions such as char particle react with CO_2 or H_2O could also contribute to the endotherm effect. By comparing case 1.1 and case 1.3, it can be found that post-combustion had little influence on temperature distribution in the CFB furnace.

Fig 2 (b) revealed the temperature distributions in the cyclone and along the PCC under all of the experimental cases. In the Fig 2(b), the word “Cyclone” represented the temperature between the cyclone and post-combustion chamber, while others were temperatures measured in places having different distances from the top of the post-combustion chamber. The top of post-combustion chamber was marked as “13” in Fig 1. In all of the cases, temperature gradually decreased with the distance from the top of PCC increasing. In the cases without post-combustion, the temperature of the first measurement point of PCC was lower than the temperature of cyclone. In the post-combustion cases, the temperature of the first measurement point of PCC was higher than the temperature of cyclone, because unburned carbon in fly ash and CO started burning with the injection of PCA. This phenomenon was more obvious with a lower λ_{CFB}, which resulted in a decrease in the combustion ratio in the CFB furnace and a corresponding increase of the combustion ratio in PCC, thus the temperature in the PCC increased.

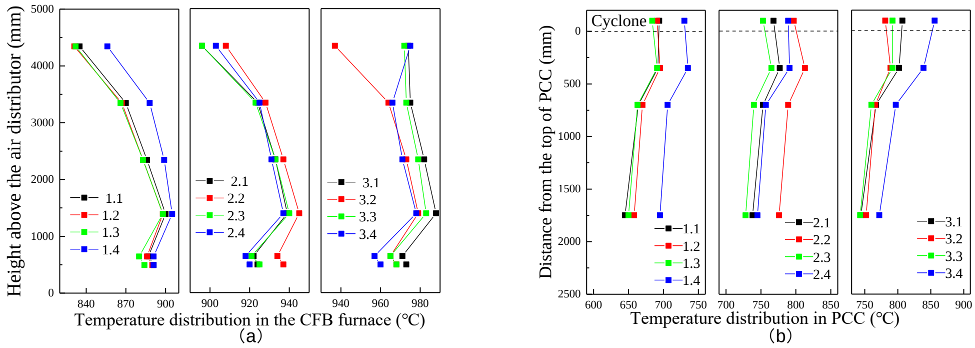

(a)

(b)

Fig 2. Temperature distribution of the test platform system

The carbon content in fly ash collected after the PCC was shown in Fig 3. Carbon content of fly ash in conventional CFB combustion cases were below 10%. Moreover, the temperature in the CFB furnace had significant influence on the carbon content of fly ash, which can be concluded that the higher temperature resulted in lower the carbon content of fly ash. The carbon content of fly ash in low oxygen combustion was 34.1% at 900℃. But when temperature reaches 980℃, the carbon content of fly ash was reduced to 8.8%. In conclusion, temperature was the key point to guarantee fly ash burning out, especially in low oxygen combustion cases.

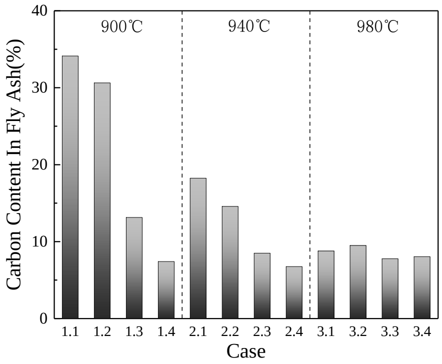

Fig 3. Carbon content in fly ash in different cases

In comparison to cases 1.1, 2.1 and 3.1, cases 1.3, 2.3 and 3.3 has lower carbon content in fly ash. In other words, after post-combustion in the PCC, the carbon content in fly ash decreased significantly. λ_{CFB} was another crucial variable to cut down the carbon content of fly ash in post-combustion cases. The higher temperature and λ_{CFB} were, the lower carbon content of fly ash was.

NO_x Emission Characteristic of Shenmu Semi-Coke

Fig 4 exhibited the relationship between the combustion temperature and NO_x emission concentration in the flue gas. Except to the combustion temperature, the other operational conditions were same in cases which were in same color. Black points represented the cases mentioned above had same λ_{CFB} and λ of 1.0. Other cases had same λ of 1.2, but λ_{CFB} of red, blue and green points were 0.8, 1.0 and 1.2 respectively. In a conventional CFB combustion of Shenmu semi-coke, NO_x emission decreased with an increase in the combustion temperature. It could be seen in Fig 3 that NO_x emission concentration reduced from 940 mg/m^3 to 655 mg/m^3 with the temperature increasing from 900 to 980 ℃. When the λ_{CFB} and λ were 1.0 and 1.2, respectively. NO_x emission has similar trend with the conventional CFB combustion of Shenmu semi-coke. But NO_x emission of black points increased with an increase in the combustion temperature. It means that NO_x emission trend of low oxygen combustion of Shenmu semi-coke was opposite to the NO_x emission trend of the conventional CFB combustion of Shenmu semi-coke. From Fig 3, it was evident that the NO_x emission in red points increased from 156 mg/m^3 to 224 mg/m^3 with the temperature increasing.

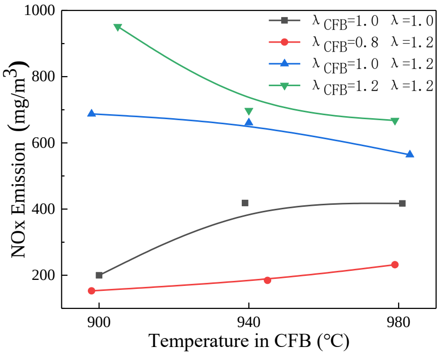

Fig 4. NO_x emission at different temperature

Excess air ratios also had significant influence on NO_x emission. Fig 5 revealed the effect of excess air ratio on NO_x and CO emission. Every 4 cases in a group had same combustion temperature. The first case in every group was low oxygen combustion. And the λ of remaining 3 cases were 1.2, and λ_{CFB} were 0.8, 1.0 and 1.2 in turn.

By comparison the first and fourth case in every group, it was obvious that no matter what temperature it was, NO_x emission concentration increased with λ increasing. NO_x emission increased from 249 mg/m^3 to 940 mg/m^3 with λ increasing from 1.0 to 1.2 at 900℃. On the other hand, as temperature increased, the effect of λ on NO_x emission was weakened. When the temperature was 900℃, NO_x emission of low oxygen combustion was only 16.1% of conventional CFB combustion. The ratios of NO_x emission of low oxygen combustion to conventional CFB combustion raised 34.7 % when the combustion temperature was 980℃. Comparing case 1.2, 1.3 and 1.4, it was evident that NO_x emissions had a significant relation with λ_{CFB}. The NO_x emission concentration of above cases were 156, 669 and 940 mg/m^3 respectively. Therefore, NO_x emission was reduced with the λ_{CFB} decreasing. When temperature increased, NO_x emission also had same regular.

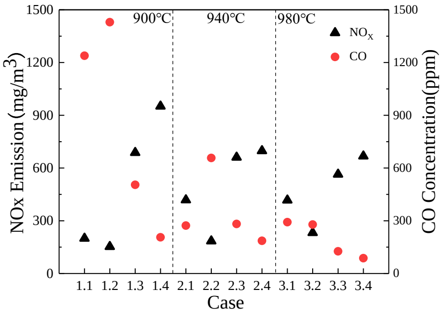

Fig 5. NO_x and CO emission concentration in flue gas

Although the injection of the post-combustion air can reduce nitrogen oxide emissions while maintaining the λ. In fact, the effects of post-combustion chamber did not include reducing NO_x. In low oxygen combustion cases, furnace maintained weak reducing atmosphere, and then NO_x formation could be inhibited effectively. The approach of oxygen-poor combustion in the furnace provided a possible way to control NO_x emission, but required post-combustion air for burning out. For example, according to case 3.1 and 3.3, the NO_x emission increases but CO concentration decreased with the injection of post-combustion air. The CO concentration in the flue gas showed a trend opposite to that of the NO_x concentration. Gong et al (2016) found that in the combustion process, a large amount of NO_x was reduced by high CO concentration and high carbon content in fly ash, which depended on the λ_{CFB}. The CO concentration decreased with the increase of λ_{CFB} and operation of post-combustion.

Conclusion

(1) Increasing temperature could decrease content of fly ash and CO emission. NO_x emission of Shenmu semi-coke conventional combustion decreased with the temperature increasing. While NO_x emission increased with the temperature increasing in post-combustion cases.

(2) λ_{CFB} and λ had same influence on NO_x and CO emission. Lower λ_{CFB} and λ result in lower NO_x emission concentration and higher CO emission concentration.

(3) The results show that the post-combustion technology is a very effective method to decrease NO_x initial emission and guarantee the combustion efficiency. In optimum condition, NO_x original emission can be reduced to only 16.6% of conventional CFB combustion.

Acknowledgement

This work was financially supported by the National Key Research & Development Program of China, Grant No. 2018YFB0605002 and "Transformational Technologies for Clean Energy and Demonstration", Strategic Priority Research Program of the Chinese Academy of Sciences, Grant No.XDA21040100.

References

Gong Z., T Zhou, Q Lu et al. Combustion and NO_x Emission Characteristics of Shenmu Char in a Circulating Fluidized Bed with Post-combustion. Energy & Fuels 2016. 30. 31-38.

Gungor, A. Prediction of SO2 and NOx emissions for low-grade Turkish lignites in CFB combustors. Chemical Engineering Journal 2009. 146. 388-400.

Gungor, A. Simulation of NO_x Emission in Circulating Fluidized Beds Burning Low-grade Fuels. Energy & Fuels 2009. 23. 2475-2481.

Hayhurst, AN, AD Lawrence. The amounts of NO_x and N_2O formed in a fluidized bed combustor during the burning of coal volatiles and also of char. Combustion & Flame 1996. 105. 341-357.

Luis F., CA Londono, XS Wang et al. Influence of operating parameters on NO_x and N_2O axial profiles in a circulating fluidized bed combustor. Fuel 1996. 75. 971-978.

Tourunen, A., J Saastamoinen, H Nevalainen. Experimental trends of NO in circulating fluidized bed combustion. Fuel 2009. 88. 1333-1341.

Yao Y., J Zhu, Q Lu et al. Experimental Study on Preheated Combustion of Pulverized Semi-coke. Journal of Thermal Science 2015. 24. 370-377.

Yao Y., J Zhu, Q Lu et al. Experimental Study on Nitrogen Transformation in Combustion of Pulverized Semi-coke Preheated in a Circulating Fluidized Bed. Energy & Fuels 2015. 29. 3985-3991.

Zhou T., Z Gong, Q Lu et al. Experimental Study on Enhanced Control of NO_x Emission from Circulating Fluidized Bed Combustion. Energy & Fuels 2015. 29. 3634-3639.

Zhou T., Q Lu, Y Cao et al. Study on the Combustion and NO_x Emission Characteristics of Low Rank Coal in a Circulating Fluidized Bed with Post-combustion. The Canadian Journal of Chemical Engineering 2017. 95.

STUDY ON EMISSION CHARACTERISTICS OF NO_X AND N_2O FROM CFB BOILERS

Miao Miao, Man Zhang, Boyu Deng, Junfu Lyu, Hairui Yang*

Key Laboratory for Thermal Science and Power Engineering of Ministry of Education,
State Key Laboratory of Power Systems, Department of Energy and Power Engineering,
Tsinghua University, Beijing 100084, China

*Email: *yhr@mail.tsinghua.edu.cn*

Abstract

In order to explore the emission characteristics of pollutants from boilers and to study the changes of NO_X and N_2O emissions during the combustion process of circulating fluidized bed (CFB) boilers, the off-design tests were carried out on three CFB boilers in China. This paper recorded the emission of NO_X and N_2O under different test conditions and described the reasons for the variation of their emissions. The influencing factors of boiler pollutants emission were studied and the key points of relevant control technology were analyzed. The emission of NO_X and N_2O is closely related to the type of coal, volatile, furnace temperature and oxygen content. By the tests, reliable experience for the low emission design and operation of CFB boilers are accumulated.

Introduction

With the rapid development of China's economy and the electricity industry, coal-fired pollutants are increasing. Under the increasingly strict environmental protection in China, the control of nitrogen oxides, which are the main air pollutants, is becoming more and more stringent. According to Ministry of Ecology and Environment (MEE) of China (2012), the total NO_X emissions in China in 2010 were 18.524 million tons, including coal-fired utility boilers, accounting for 79.1% of industrial NO_X emissions, becoming the main source of NO_X. Because the nitrogen oxides produced by coal combustion are harmful to the environment, the control of their emissions has attracted worldwide attention. Most countries and regions have formulated strict emission control laws and standards. Thermal power plants are facing serious pressure of emission reduction. MEE of China (2011) revised the Air Pollutant Emission Standard for Thermal Power Plants, requiring new power plants to meet the emission standard of 100 mg/m^3 of NO_X (in terms of NO_2, converted to dry base with oxygen volume fraction of 6%). Li et al. (2013) reviewed that in order to control the coal-fired utility boilers to meet the emission standards of nitrogen oxides, it was of great practical significance to have a thorough understanding of the emission characteristics of NO_X from boilers.

Compared with conventional coal-fired boilers, circulating fluidized bed (CFB) boilers had the advantages of good fuel adaptability, strong peak-shaving ability, high combustion efficiency and easy utilization of ash (Yue et al. 2017). Therefore, this technology has been rapidly promoted in China and now it has become one of the most successful clean coal combustion technologies in commercial applications (Lyu et al. 2005). CFB boilers have advantages of low nitrogen oxides emission due to their low-temperature combustion (800-900 ^oC) and a strong reduction atmosphere. However, Yin et al. (2003) found the N_2O emission of CFB boilers was more than that of conventional pulverized coal-fired boilers, even 100 times higher than that of ordinary pulverized coal-fired boilers. As the main greenhouse gas, N_2O has harmful effect on the environment. Li et al. (2016) reported that furnace temperature and oxygen content were important factors affecting N_2O emission.

For emission characteristics, previous studies mainly focused on mechanism research, lacking the actual data of power plants as support. Because of the complexity of boilers, the results of laboratory research are difficult to match with the actual situation of power plants. Therefore, the field test data from the CFB power plants can help to deepen the understanding of pollutant emission rules of large boilers and effectively guide the follow-up research work. This paper further explores the emission characteristics of NO_X and N_2O from several CFB boilers, including 150 MW CFB boiler in Ruiping Power Plant (boiler 1), 440 t/h CFB boiler in Yima Power Plant (boiler 2) and 220 t/h CFB boiler in Xiangyuan Power Plant (boilers 3), through pollutant emission regularity test, material sampling balance test and boiler temperature field test.

Industry and Element Analysis

The primary and ultimate analysis results of coal samples in three CFB boilers are listed in Table 1. Comparably, in boiler 1, the contents of carbon, volatile and nitrogen are low and the content of ash is high. In boiler 2, the content of volatile is high and the content of nitrogen is moderate. In boiler 3, the content of carbon is high and the content of nitrogen is moderate.

Table 1. Primary and Ultimate Analysis of Coal Samples in Three Boilers

Categories (Wt. /%)	C_{ad}	H_{ad}	N_{ad}	S_{ad}	O_{ad}	A_{ad}	M_{ad}	V_{ad}	FC_{ad}	LHV/MJ·kg^{-1}
1	24.95	1.74	0.35	0.47	7.47	63.75	1.27	14.12	20.86	8.39
2	43.93	2.88	0.62	0.51	11.5	36.16	4.76	27.24	31.84	15.81
3	45.74	2.24	0.67	0.29	5.85	43.58	1.63	11.07	43.72	16.40

Temperature and Oxygen Analysis

The concentration of flue gas pollutants was measured under the steady operating conditions in boiler 1, especially the emission of NO_X and N_2O, as listed in table 2. Ke et al. (2018) reported that the emission of NO_X and N_2O could be affected by limestone desulfurization, thus it should be emphasized that all the values in Fig.1 were measured under the condition without limestone desulfurization in the furnace. The interference of limestone on the generation of NO_X and N_2O can be eliminated.

From Fig. 1, it can be seen that the coal type of boiler 1 can achieve the emission standard because the lower volatile content of coal and lower furnace temperature can reduce overall NO_X emission. With the increase of furnace temperature and oxygen concentration, the emission of NOx increases generally, but the sensitivity is low and the majority is below 70 mg/m^3. The emission value of N_2O is higher than that of NO_X and increases significantly with the decreasing of furnace temperature and the increasing of oxygen content, which indicates that N_2O may one potential consideration in nitrogen-containing pollutants for CFB boilers with lower combustion temperature in the furnace. The national standard aimed at pulverized coal-fired boilers, which have high temperature and almost have no N_2O emission problem, has no strict regulation for N_2O emission so far, while in the future, N_2O emission in CFB boiler can't be ignored.

Table 2. Gas Measuring Value and Working Conditions in Boiler 1

Numbers	Furnace load/MW	Furnace temperature/°C			Oxygen content/%	NO_x converted value /mg·m^{-3}	N_2O converted value /mg·m^{-3}
		Lower part	Central section	Upper part			
1	108	909.9	863.9	804.7	3.7	55.6	111.7
2	108	878.7	853.4	768.6	4.6	66.3	170.8
3	108	878.9	828.3	773.1	5.9	69.4	237.8
4	124	873.2	846.0	800.1	3.1	52.3	139.4
5	124	866.3	845.8	792.4	3.8	65.0	128.3
6	135	889.7	875.6	824.6	2.6	68.5	74.2
7	135	902.7	874.9	852.4	1.9	54.6	59.1

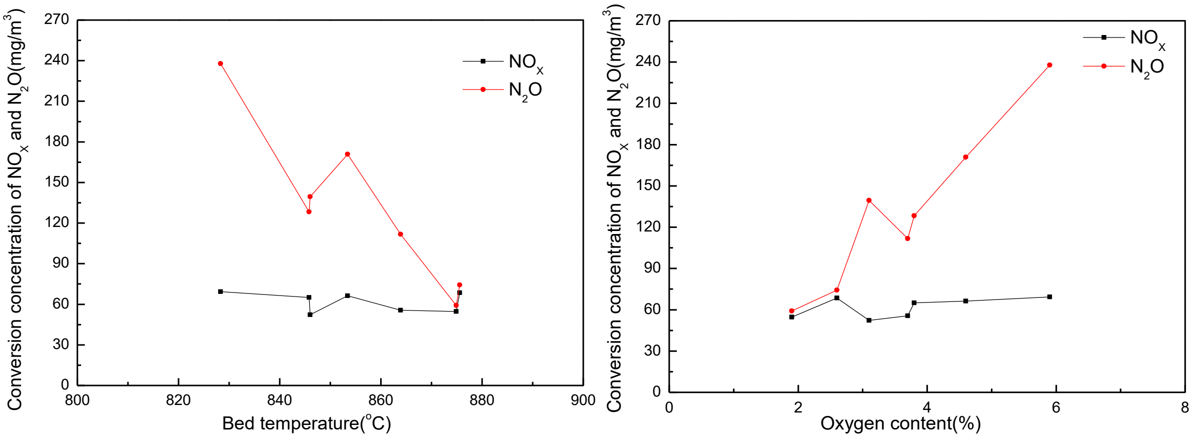

Fig. 1. Test results of NO_X and N_2O varying with temperature and oxygen content in power plant 1

Although the content of nitrogen element is moderate in boiler 2, the conversion rate of fuel nitrogen to nitrogen oxide is higher due to the higher volatile content, which even reaches more than 300 mg/m^3, far exceeding the national standard of 100 mg/m^3. From Tables 3 and 4, the emission of NO_X increases with the increasing of furnace temperature and oxygen content, but the degree is different. Because of the higher furnace temperature, the emission of N_2O can be neglected.

The increasing of furnace temperature has little effect on the emission of nitrogen oxides. From the change of working conditions 2 to 3, when the oxygen content is kept at about 4%, the furnace temperature decreases by about 30 °C, and the range of NO_X emission decreased by 50 mg/m^3.

Table 3. Flue Gas Measuring Conditions of Boiler 2

Working conditions	Furnace load/ t·h^{-1}	Furnace temperature /°C		Pressure/kPa		
		Lower part	Central section	Lower part	Central section	Upper part
1	271.5	922.83	904.59	6.69	0.89	-0.36
2	255.5	919.34	893.79	6.88	1.04	-0.22
3	249.0	889.22	860.65	6.84	1.00	-0.23

Table 4 Flue Gas Compositions of Boiler 2

Working conditions	CO /mg·m^{-3}	SO_2 /mg·m^{-3}	H_2O /%	O_2 /%	NO_x converted value /mg·m^{-3}	N_2O converted value /mg·m^{-3}
1	16.9	1903.9	2.5	2.4	223.3	2.4
	16.9	1903.9	2.5	2.4	222.3	2.3
	16.9	1969.0	2.5	2.4	219.2	2.3
2	14.6	431.1	2.3	4.6	346.8	11.2
	14.6	421.3	2.4	4.7	358.8	12.0
	13.4	395.6	2.4	4.7	366.0	13.3
3	10.9	725.8	2.7	4.3	310.5	17.9
	10.9	720.0	2.9	4.4	310.3	16.7
	10.9	755.6	2.9	4.2	302.4	15.0

As shown in Fig. 2, the emission of NO_X increases rapidly with the increase of oxygen content. When the furnace temperature is about 900 °C and the oxygen content increases from 2% to 4%, the emission of NO_X rapidly increases from 220 mg/m^3 to more than 340 mg/m^3, and the variation range is more than 100 mg/m^3. On the contrary, the N_2O emission does not change significantly. According to the absolute emissions of NOx and N_2O, for the boiler with NOx as the main pollutant, the influence of oxygen and temperature on NOx is more obvious while the influence on N_2O is not obvious.

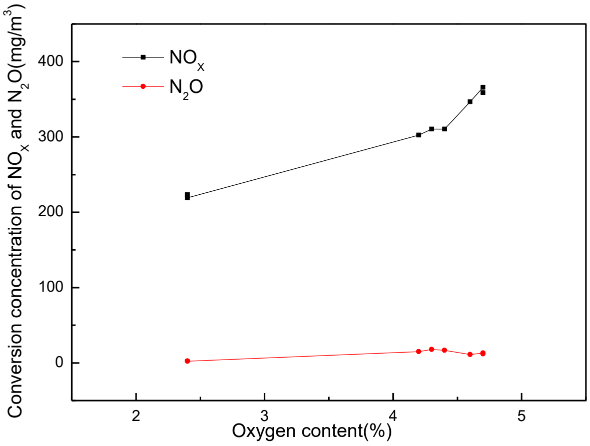

Fig. 2. Test results of NO_X and N_2O varying with oxygen content in boiler 2

Measuring conditions and results of flue gas in boiler 3 are listed in Tables 5 and 6. As shown in Fig. 3, boiler 3 can basically meet the emission standard of 100 mg/m³. With the increase of load, although the furnace temperature increases greatly, the NO_X emission of the boiler decreases slightly due to the decreasing of oxygen content, which fully proves the key role of oxygen content in the formation of NO_X. Because of the effects of oxygen reduction and the temperature rising, the reduction of N_2O is inevitable.

Table 5. Flue Gas Measuring Conditions of Boiler 3

Working conditions	Furnace load/ t·h⁻¹	Furnace temperature/ °C			Pressure/ kPa		
		Lower part	Central section	Upper part	Lower part	Central section	Upper part
1	198.01	884.7	870.3	913.4	2.823	0.21	-0.364
2	221.05	899.7	904.5	951.9	2.642	0.4	-0.504

Table 6. Flue Gas Compositions of Boiler 3

Working conditions	CO /mg·m⁻³	SO_2 /mg·m⁻³	H_2O /%	O_2 /%	NO_x converted value /mg·m⁻³	N_2O converted value /mg·m⁻³
1	293.9	544.0	2.9	3.9	90.4	35.4
	295.1	546.8	3.0	4.3	91.6	36.1
	289.3	485.4	3.5	4.4	93.0	34.3
	294.0	538.9	3.3	3.8	86.5	35.0
2	403.0	663.1	4.3	2.5	85.1	15.5
	393.5	688.9	4.4	2.7	85.4	14.8
	387.5	698.8	4.5	2.7	85.9	12.7
	379.2	714.7	4.5	2.5	86.0	12.6

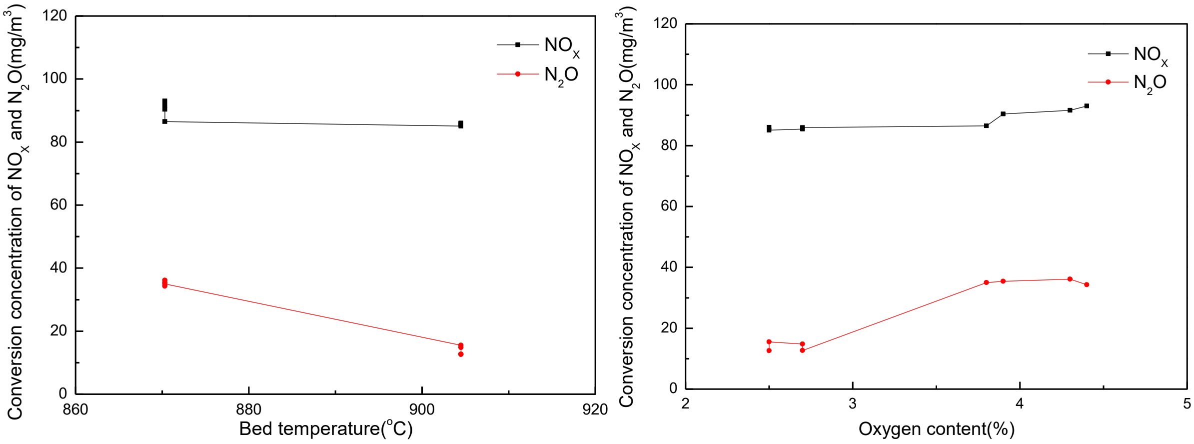

Fig. 3. Test results of NO_X and N_2O varying with temperature and oxygen content in power plant 3

Conclusions

In this paper, by analyzing the coal samples and ash slag of three CFB boilers, the effects of oxygen content and furnace temperature on the emission of NO_X and N_2O were discussed, which accumulates low emission experience of NO_X and N_2O and provides some references for the future operation of CFB boilers. The main conclusions are as follows:

1. Coal type is the most critical factor to determine the emission of NO_X and N_2O in CFB boilers, which lays a foundation for boiler emission. Boiler operation must first ensure the stability and efficiency of combustion, so the adjustment range is limited. When the coal type is fixed and the boiler operating parameters change, the emission concentration of NO_X and N_2O can only be adjusted within a certain range.

2. Volatile content is an important factor affecting the emission of nitrogen oxides. Volatile content determines the conversion rate of fuel nitrogen to nitrogen oxides in CFB boilers. Generally, the higher the volatile matter is, the more nitrogen oxides are discharged from the boiler when the difference of nitrogen content of coal is small. When the volatile content is low and the furnace temperature is low, the emission level of nitrogen oxides is low.

3. Furnace temperature and oxygen content are the key operating parameters affecting the emission of NO_X and N_2O from CFB boilers. With the increasing of furnace temperature and oxygen content, the emission of nitrogen oxides increases. The emission of NO_X is less sensitive to furnace temperature, and the reasons need to be explored. Because of its instability, N_2O is highly sensitive to temperature. When the furnace temperature is higher than 920 °C, its emission can be neglected, while, the emission is greatly increased when the furnace temperature is lower than 870 °C.

4. Under the current strict emission limitation of nitrogen oxides, it is of great significance to study the emission characteristics of NO_X and N_2O from CFB boilers, especially the latter one.

Acknowledgements

This study was financial supported by C9 League Science and Technology Cooperation Project(201903D421009) and Huaneng Group science and technology research project(HNKJ20-H50) KTHT- U20GJJS06.

References

Ke, X., Cai, R., Zhang, M., et al. Application of ultra-low NOx emission control for CFB boilers based on. theoretical analysis and industrial practices. Fuel Processing Technology. 2018. 181, 252-258

Li, J., Yang, H., Lv, J., et al. Analysis of low nitrogen oxide. emissions from energy-saving circulating fluidized bed boilers. Combustion Science and Technology. 2013. 19(04), 293-298 (in Chinese)

Li, S., Xu, M., Jia, L., et al. Influence of operating parameters on N_2O emission in O_2/CO_2 combustion with high oxygen concentration in circulating fluidized bed. Applied Energy. 2016. 173, 197-209

Lv, J., Yue, G., Zhang, J., et al. Operation and Maintenance of Circulating Fluidized Bed Boiler, China Water & Power Press, Beijing, 2005 (in Chinese)

Ministry of Ecology and Environment of the People's Republic of China. Air Pollutant Emission Standard for Thermal Power Plants, China Environmental Science Press, Beijing, 2011 (in Chinese)

Ministry of Ecology and Environment of the People's Republic of China. 2010 Annual Statistic Report on Environment in China, China Environmental Science Press, Beijing, 2012 (in Chinese)

Yin, L., Yan, W., Ye, X., et al. Formation mechanism and emission. reduction control of N_2O in CFB boiler combustion. Boiler Manufacturing. 2003. 01, 7-9(in Chinese)

Yue, G., Cai, R., Lv, J., et al. From a CFB reactor to a CFB boiler - the review of R&D progress of CFB coal combustion technology in China. Powder Technology. 2017. 316, 18-28

NO AND ULTRAFINE PARTICLES FORMATION DURING THE COMBUSTION OF SINGLE BIOMASS PARTICLES UNDER FBC CONDITIONS

Iliyana Naydenova[1], Ognyan Sandov[1], Florian Wesenauer [2], Thomas Laminger [2], Franz Winter [2*]

[1] *Technical University of Sofia, College of Energy and Electronics, 8 Kliment Ochridski Blvd., 1000 Sofia, Bulgaria*

[2] *Technische Universität Wien, Institute of Chemical, Environmental & Bioscience Engineering, Getreidemarkt 9, 1060 Vienna, Austria*

*Email: *franz.winter@tuwien.ac.at*

Abstract

The present study aims at investigating key pollutants (gaseous and particulates), identified in the single particle combustion of three different types of biomass. The biomass was characterized through the following chemical analyses: proximate, ultimate and ash analyses. The higher heating values were obtained with calorimetric analyses.

The experiments were carried out at atmospheric pressure (p), varying the following operating parameters: temperature (T), inflow oxygen partial pressure (p_{O2}) and initial mass of a single fuel particle/sample ($m_{fuel,0}$). In focus were the emissions of NO and particulate matter (PM). The NO emissions were dependent on the fuel bound nitrogen content and this was the reaction mechanism assumed to dominate the NO formation in the flue gases. Ultrafine PM of submicron size were measured in the highest concentration for all types of biomass. The size of the fuel particles and their chemical composition were assumed to affect the PM emissions. However, these effects need detailed investigation.

Introduction

Biomass residue is annually available in significant quantity from different economic sectors. Its conversion for power generation has been largely promoted within the European Union (EU). However, there is a serious environmental concern. For instance, Nyström R (2016) wrote that controlling the operation of any combustion system is of major importance for improving the burning condition and suppressing the emissions of harmful products (e.g. greenhouse gases, soot, particulates and many other). The same author stressed that biomass combustion delivers about 70% of all organic particulate matter (PM) in the ambient air of Europe. It can be found in Bulgaria's IIR (2019) that in 2017 about 50 % of the PM_{10} and about 80 % of the $PM_{2.5}$, measured in the ambient air, are emitted from the NFR source category residential: stationary combustion. Bulgaria is an EU Member State, lacking compliance with Directive 2008/50/EC concerning the emissions of PM_{10}, $PM_{2.5}$ and SO_2. At some municipalities NO_X was also exceeded in the past. Improving the quality of fuels or replacing the combustion appliances with highly efficient are measures envisaged for lowering the emissions from the sector, see e.g. OPE (2014-2020).

The present work was focused on the emissions of NO and PM in the flue gasses during single particle combustion of three different types of biomass: *softwood (SW) pellets*, *coffee residue (CR)*, and *cherry stones (CS)*, burnt under FBC conditions. In addition, the primary gaseous products (CO, CO_2) and the SO_2 were experimentally measured; and the rate of carbon (C) conversion was estimated. Thus, the influence of a few key operating parameters on the measured pollutants was investigated.

Materials and methods

Experimental setup

The SW pellets and the CS are available at the Bulgarian energy market*:* The manufacturer certifies that the SW pellets contain corps SW plus up to 10 % residue and bark and are produced with no additives. The CR was delivered as biomass residue from the food industry. The samples were prepared in line with ISO 18135:2017 Solid Biofuels – Sampling. The CS is also food-industry residue. It was burned as received, the way it is utilized in many combustion appliances, used for residential heating.

The fuels were burnt in a fluidized bed reactor, which is described in detail in Winter F. et al. (1999) and Wartha C.C.et al. (2000). The reactor was electrically heated and a fluidized bed was used to achieve conditions with constant temperature and pressure around the fuel particle. This FRU operates at atmospheric p and pre-set steady state conditions, with air flow rate of 15 l/min. The maximum applicable bed T is 1000 ^{o}C and the p_{O2} can be varied between 0 and 21 kPa.

The applied experimental conditions were: T between 700 and 900 °C; p_{O2}: 21 - 5 vol. % and $m_{fuel,0}$: 0.1 ÷ 0.5 g. For validation reasons the series of experiments were repeated between 4 and 10 times each.

Emissions of primary gaseous products

The concentrations of the gaseous products were measured shortly after the fuel particle combustion, in line with Winter F. et al.(1999) and Wartha C. et all (2000). For that purpose non-dispersive infrared spectrometer (NDIR) of type “EasyLine Continuous Gas Analyzers Model EL3020” was used to measure the CO_2, CO, NO, SO_2 and an electrochemical cell – for the excess of O_2 (detection limits: O_2: 0-25%, CO: 0-10000 ppm, SO_2: 0-2000 ppm, CO_2: 0-20%, NO: 0-2000 ppm).

PM emissions

Sampling and analysis procedure was implemented, for PM measurement in the exhaust in parallel with the gas phase products. Aerosol spectrometer analyzer (Welas Digital 2000) allowed measuring the PM size (128 particle size channels (0.1 ÷ 10 µm)) and concentration (1 and 10^6 particles/cm^3), at constant p and sampling flow rate of 5 l/min. The PM bypass flow was diluted (1:10) with compressed air, while controlling the pressure of the carrier gas.

Estimated kinetic parameters

The instantaneous rate of carbon (C)-conversion was calculated through the equation:

$$\frac{\partial X_{C,fuel}}{\partial t} = \frac{m_{C,burnt}(\Delta t)}{m_{C,0}} = \left(\frac{m_{C,burnt}(\Delta t)}{\xi_C \cdot m_{fuel,0}\,\Delta t}\right), \tag{1}$$

where, $m_{c,burnt}(\Delta t)$ is the mass balance of C in the burnt fuel particle per detection interval, which was derived from the measured CO_2 and CO concentrations in the exhaust gas; ξ_C is the fraction of C, based on the ultimate analysis; $m_{fuel,0}$ is the initial mass of a single fuel particle sample.

In addition, the cumulative conversion rate was estimated by integrating the instantaneous rate from time 0 to the instantaneous time τ:

$$\mathrm{X_{C,fuel}}(\tau) = \sum_{j=0}^{j=\tau} \frac{\mathrm{m_{C,burnt}}(t_j)}{\xi_C \cdot \mathrm{m_{fuel,o}}}. \tag{2}$$

Results and discussion

Biomass characterization

Table 1 presents the major chemical features of the investigated biomass, based on the proximate, ultimate and ash analyses. The fuel's higher heating value (HHV) was obtained with calorimetric bomb or estimated from Differential Scanning Calorimetry (DSC) analysis.

Table 1. Chemical parameters of the biomass.

Measured parameter	***SW***	***CR***	***CS***	***Measured parameter***	***SW***	***CR***	***CS***
Proximate analyses (wt %, as analyzed)				***Ash analysis (wt %, dry basis)***			
Moisture	6.89	7.78	9.98	SiO_2	2.74	1.78	3.58
Ash	0.65	1.52	1.13	Al_2O_3	5.37	0.60	0.43
Volatile compounds	78.77	83.98	81.12	Fe_2O_3	1.72	0.47	0.43
Fixed carbon (by dif.)	13.69	7.66	7.76	*MnO*	1.60	0.22	0.05
Ultimate analysis (wt%, as analyzed)				*CaO*	33.29	17.75	13.00
Carbon	47.77	56.52	54.29	*MgO*	7.44	9.75	10.57
Hydrogen	6.48	8.52	7.90	*BaO*	0.18	0.02	0.01
Sulfur	0.02	<0.05	<0.05	Na_2O	0.98	0.75	0.8
Nitrogen	0.14	4.07	4.40	K_2O	15.76	31.24	24.16
Chlorine	*not analyzed*	<0.10	<0.10	Cr_2O_3	<0.01	<0.01	<0.01
Oxygen (by dif.)	38.05	21.44	22.15	TiO_2	0.32	0.15	0.14
Higher heating value, (MJ/kg, dry basis)				*ZnO*	0.93	0.12	0.08
HHV	19.38	20.7*	23.62	*CuO*	0.03	0.18	0.07
				SrO	0.01	0.03	0.03
				P_2O_5	5.78	17.96	26.65

* *Estimated from DSC analysis*.

Fig. 1 (a) – (c) shows an example of the effects of $m_{fuel,0}$ on the maximum concentration of the primary gaseous and the PM (averaged for all samples with equal $m_{fuel,0}$), which were experimentally measured during single particle combustion of SW pellets, varying just the $m_{fuel,0}$ between 0.3 and 0.5 g. Apparently, the maximum CO_2 (a), CO (b) and NO (b) concentration and the PM (c) number density increased with increasing the $m_{fuel,0}$, while the opposite trend (even though being minor) was observed for the instantaneous rate (d). A slight shift to the right was found for all peaks when increasing the $m_{fuel,0}$. The concentration of SO_2 was within the detection limit, thus excluded from the figure. The effect of $m_{fuel,0}$ was negligible regarding the time history of the cumulative rates of carbon conversion (Fig. 1(d)).

In Nyström (2016) it is stated that the smallest particles (ultrafine) have the highest number density, but scarcely contributing to the total PM mass, while the coarse particles are having the opposite influence. In the present experiment mainly particles of submicron size were measured in all fuels. The highest number density was obtained in the CS combustion. Fig. 2 shows an example of the effect of p_{O2} on of the mass normalized particle number density, plotted versus the mean particle diameter. The results were obtained during CS combustion at T = 800 °C and three different p_{O2} and the values were averaged over all T (700; 750; 800; 850; 900 °C) per given p_{O2}. The emission at p_{O2} = 21 kPa were about an order of magnitude higher than those at p_{O2} = 13 kPa.

Fig. 3 (a) shows the temperature dependence of the maximum NO concentration, obtained for all studied types of biomass. Considering the combustion conditions in the FRU and the measurement approach, it was assumed that the NO was the major product of nitrogen conversion, generated mainly by the oxidation of the fuel bound nitrogen as described in

Winter F. et al.(1999) and Wartha C.C. et all (2000). Preliminary studies show that the biomass containing kernel or cereal typically has high fuel bound N-content, which leads to higher NO emissions, see e.g. Obernberger I. (2006). This effect was confirmed by the current experiment.

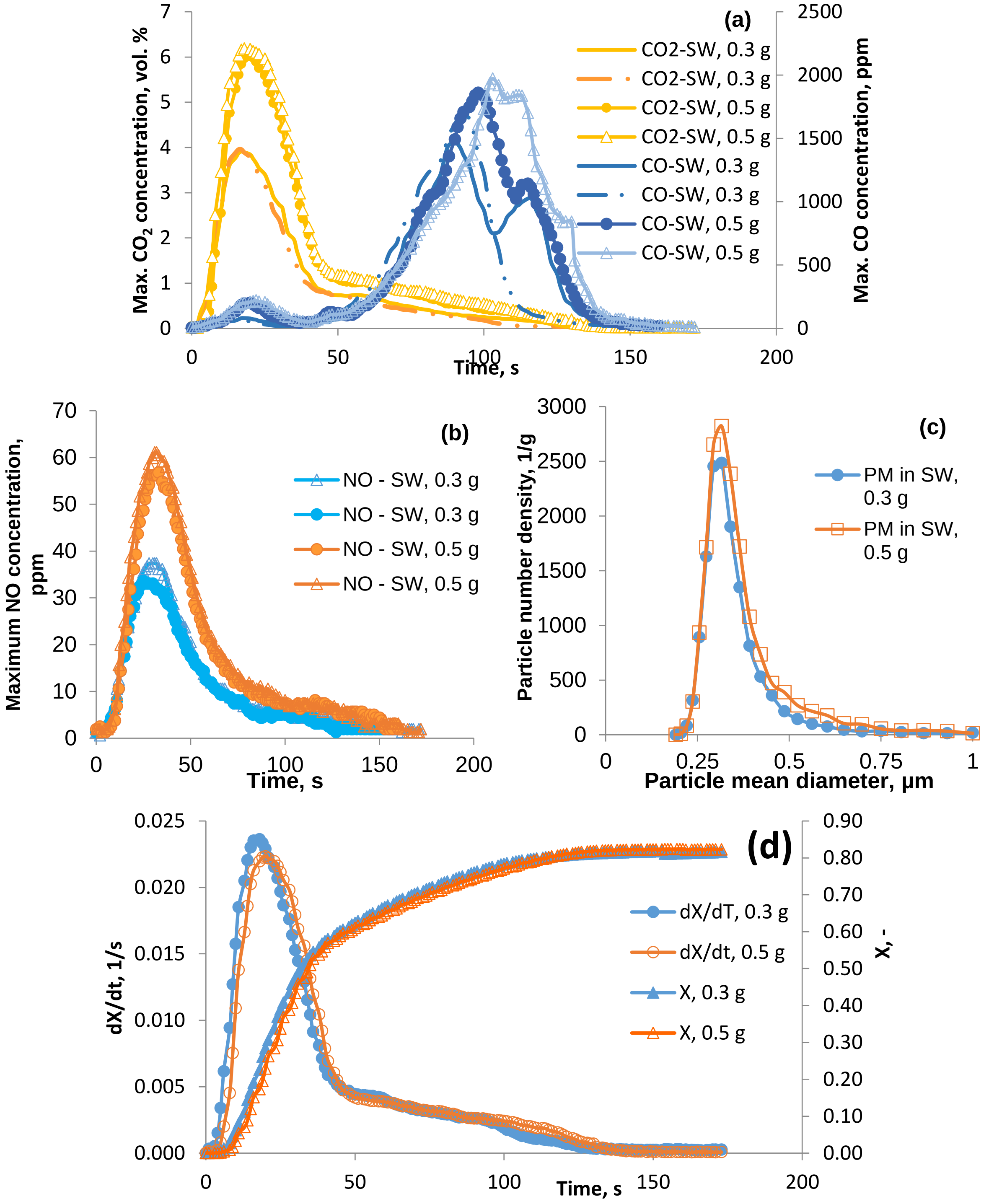

Fig. 1. Time history of the experimentally measured pollutants: (a) CO_2, CO, (b) NO and (c) PM, and (d) the instantaneous (*dX/dt*) rate and the cumulative (*X*) C-conversions during SW oxidation at: *p* = atmospheric; *T* = 800 °C; p_{O2} = 21 kPa; $m_{fuel,0}$ = 0.3 and 0.5 g.

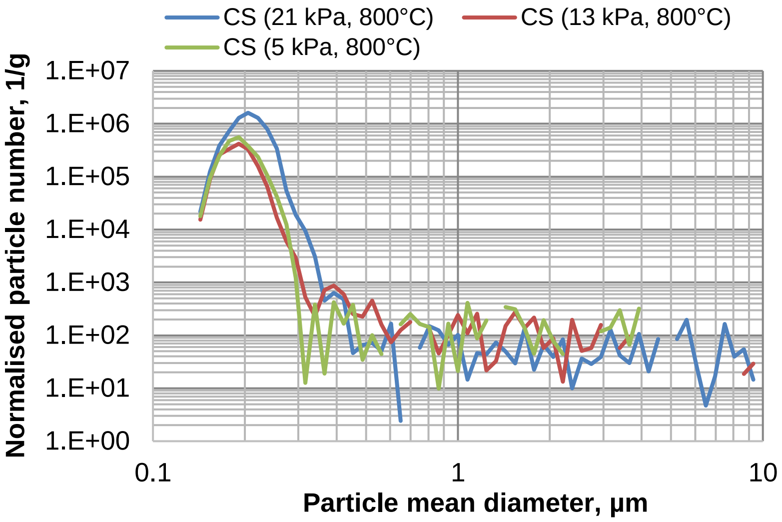

Fig. 2. Experimentally measured mass normalized particle number density during CS oxidation under FBC conditions at: p = atmospheric; T = 800 ºC; p_{O2} = 21, 13 and 5 kPa; $m_{fuel,0}$ = 0.2 ÷ 0.5 g. The values were averaged for all samples, obtained at given p_{O2}.

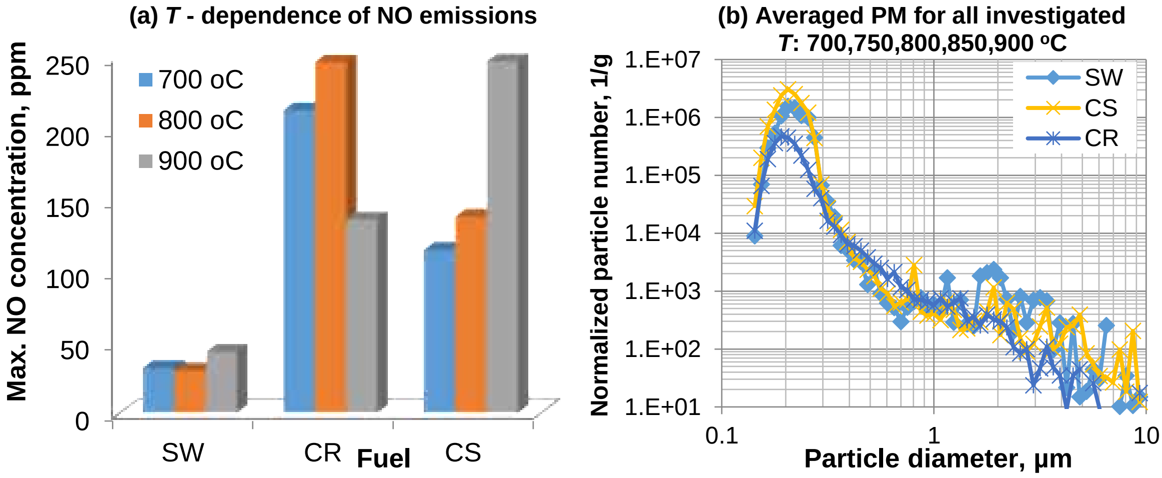

Fig. 3. Experimentally measured (a) maximum NO concentration and (b) mass normalized particle number concentration for three different biomass fuels at: p = atmospheric; T = 700 - 900 ºC; p_{O2} = 21 kPa and $m_{fuel,0}$ = 0.2 g.

Fig. 3 (b) presents the mass normalized particle number density obtained in the oxidation of SW, CR and CS at p_{O2} = 21 kPa. The maximum PM was measured in the CS oxidation. Although, the CR had the highest content of volatile compounds (Table 1) and was expected to have high PM emission, it showed the lowest PM concentration. However, this type of biomass was burnt “as received” in powder, which may have affected the overall combustion conditions and PM emissions. The authors Branco et al. (2017) studied the effect of particle size on the burnout and the emissions of PM. The role of the fuel particle size and its chemical composition needs additional investigation.

Conclusions

The following general conclusions can be summarized from the recently obtained results:

- The effects of $m_{fuel,0}$, bed T, and p_{O2} were not identical for the experimentally measured products and the estimated rate of conversion of all fuels. The maximum concentration of the measured primary gaseous and PM products in the flue gases increased with increasing the $m_{fuel,0}$. This parameter had minor influence on the cumulative C-conversion rate in SW combustion, while the instantaneous rate was decreasing with the larger $m_{fuel,0}$. Bed T of 900 °C caused higher maximum NO concentration in the combustion of SW and CS, while in the case of CR - NO showed its lowest value. The p_{O2} significantly influenced the PM emissions. The lowest mass normalized PM number density, measured in the exhaust of CS, was obtained at T = 800 °C and p_{O2} = 13 kPa, while the highest one – at p_{O2} = 21 kPa.

- As expected, the reaction mechanism of NO formation through the oxidation of the fuel bound nitrogen played the major role. The biomass containing kernel/cereal (CS and CR) had about four times higher N-content than the SW. The NO concentration, measured in the flue gases had similar ratio for the CR (700 and 800 °C) and for the CS (900 °C) in comparison with the NO from the SW combustion.
- In this experiment the submicron size (ultrafine) particulates (125 and 325 nm), were the major portion of the measured PM. In a parallel study, a relation between the availability of volatile compounds and the PM number density was observed, which was not directly confirmed with the current results. Thus, investigation of the effect of fuel particle size and its chemical composition on the PM under FBC conditions is required.

Acknowledgement

This work was supported by COST Action CM 1404 SMARTCATs and NSF at the Ministry of Education and Science (MES) of Bulgaria: National co-funding contract No ДКОСТ 01/13, and by the National Science Program “Environmental Protection and Reduction of Risks of Adverse Events and Natural Disasters”, approved by the Resolution of the Council of Ministers No 577/17.08.2018 and supported by the MES, Bulgaria (Agreement No D01-230/06.12.2018).

References

Branco V., Costa M., Effect of particle size on the burnout and emissions of particulate matter from the combustion of pulverized agricultural residues in a drop tube furnace, Energy Conversion and Management 149 (2017) 774–780.

Bulgaria’s Informative Inventory Report 2019 (IIR), Submission under the UNECE Convention on Long-Range Transboundary Air Pollution (http://eea.government.bg/bg/dokladi/clrtap и https://www.ceip.at/ms/ceip_home1/ceip_home/status_reporting/2019_submissions/).

Directive 2008/50/EC of the European Parliament and of the Council of 21 May 2008 on ambient air quality and cleaner air for Europe, ELI: http://data.europa.eu/eli/dir/2008/50/2015-09-18.

Nyström R., Particle emissions from residential wood and biodiesel combustion, Doctoral Thesis, Umeå University, 2016, Swedish Copyright Legislation (Act 1960:729) ISBN: 978-91-7601-605-3, Printed by: UmU Print Service, Umeå University, Dec. 2016 Umeå, Sweden, 2016.

Obernberger I., Brunner T., Baernthaler G., Chemical properties of solid biofuels - significance and impact, Biomass and Bioenergy 30 (2006) 973–982, http://dx.doi.org/10.1016/j.biombioe.2006.06.011.

Operational Programme Environment (OPE) 2014 – 2020, https://www.eufunds.bg/en/opos.

Wartha C., Winter F., Hofbauer H., The Trade-Off Between N2, NO, and N2O Under Fluidized Bed Combustor Conditions. ASME. J. Energy Resour. Technol, 122(2), 2000, 94-100, https://doi.org/10.1115/1.483169.

Winter F., Krobath P., Hofbauer H., Comparison of a circulating fluidized bed combustor with a stationary fluidized bed combustor, 13th Int. Conf. FBC, Orlando, 1995.

Winter F., Wartha C., Hofbauer H., NO and N2O Formation during the Combustion of Wood, Straw, Malt Waste and Peat, Bioresource Technology, 70, 1999, 39-49. https://doi.org/10.1016/S0960-8524(99)00019-X.

NO_X AND N_2O EMISSIONS DURING OXY-FUEL COMBUSTION OF BITUMINOUS COAL AND LIGNITE IN A CIRCULATING FLUIDIZED BED COMBUSTOR

Monika Kosowska-Golachowska[1*], Adam Luckos[2], Tomasz Musiał[1], Agnieszka Kijo-Kleczkowska[1], Krzysztof Wolski[1], Katarzyna Środa[1]

[1]*Czestochowa University of Technology, Institute of Thermal Machinery*
Armii Krajowej 21, 42-201 Czestochowa, Poland
[2]*University of the Witwatersrand, School of Chemical and Metallurgical Engineering*
Braamfontein Campus East, Johannesburg, South Africa

*Email: *kosowska@imc.pcz.czest.pl*

Abstract

Oxy-fuel combustion of Polish bituminous coal and lignite were carried out in the 12-kW bench scale CFB combustor and emissions of NO and NO_2 (NO_x) and N_2O were measured. Combustion tests were conducted at temperature of 850°C in air (base case) and O_2/CO_2 mixtures with oxygen concentrations 21, 30 and 40%vol. Concentrations of NO, NO_2, N_2O and precursors of the nitrogen oxide emissions, such as NH_3 and HCN in the flue gas leaving the combustor were measured on-line by a FTIR spectrometer. The effects of oxygen concentration in oxidizing atmosphere and fuel type on gaseous emissions are evaluated. The fractional conversions of fuel-N to NO_x and N_2O are calculated and compared for both fuels.

Introduction

Despite of increasing contribution from renewable energy (solar and wind), electricity and heat generation are the largest sources of greenhouse gas emissions accounting for more than 40% of the global total. Nowadays, carbon capture and storage (CCS) is critical to stabilize the concentration of greenhouse gases in the atmosphere and to prevent climate change.

Oxy-fuel combustion is a promising CCS technique because it uses oxygen instead of air and, therefore, generates almost pure stream of CO_2 that can be easily captured and stored. Oxy-combustion of coal in pulverized coal (PC) systems has been extensively studied in the last decade and several reviews have been published. Oxy-combustion in bubbling fluidized-bed and, in particular, in circulating fluidized-bed (CFB) combustors is relatively new with little information available in the open literature. Recently Mathekga et al. (2016) and Singh and Kumar (2016) reviewed the status of fluidized-bed oxy-combustion. According to the authors, there is only one demonstration CFB plant in the world, the 30-MW_{th} facility at CIUDEN in Spain. The most available information on the performance of CFB oxy-combustion systems comes from studies conducted in laboratory-scale reactors.

The well-known advantages of CFB combustion include fuel flexibility, relatively low NO_x emissions and *in situ* SO_2 capture. In the context of oxy-combustion, Jia et al. (2010) mentioned one more advantage namely the use of external solid heat exchangers to remove heat from the combustion process. This results in a significant reduction of the recycled flue gas and allows using higher initial O_2 concentrations in the combustor.

The influence of the initial O_2 concentration on NO_x formation in oxy-fuel CFB combustion has been investigated by several researches. Czakiert et al. (2006) and Czakiert et al. (2010) studied the conversion of C, S and N during combustion in air, O_2-enriched air and O_2/CO_2 mixtures. Tests with lignite and bituminous coal were conducted in a lab-scale (0.05 m ID, 1.7 m tall) CFB reactor and a small-scale pilot CFB plant (0.1 m ID, 5 m tall) at temperatures 700–860°C and initial O_2 concentrations 21, 40 and 60%. Tests with lignite in the lab-scale CFB reactor revealed that the conversion of fuel-N to NO_x was lower in oxy-combustion than in air combustion (Czakiert et al., 2006). However, the opposite trend was observed during combustion of bituminous coal in the pilot-scale CFB reactor (Czakiert et al., 2010); the conversion of fuel-N to NO_x increased with increasing O_2 concentration in the O_2/CO_2 mixture. Nevertheless, the fuel-N conversion to NO_x was below 20% for all tested O_2/CO_2 mixtures.

Jia et al. (2010) investigated oxy-combustion of bituminous coal and petroleum coke with limestone addition in a mini-CFB reactor. They found that NO_x emissions were lower or similar to those in air combustion. In the case of coal, the conversion of fuel-N to NO_x was 1.5–1.8% compared to 6.2% in air combustion.

Duan et al. (2011) studied oxy-combustion of bituminous coals in a 50-kWth CFB plant. They found that NO emissions in O_2/CO_2 atmosphere (with no flue gas recirculation and limestone addition) were similar to those in air combustion. However, at the same O_2 concentrations in in the oxidizing atmospheres, the NO emissions in air were higher than those in $21\%O_2/79\%CO_2$ atmosphere. In the subsequent study with flue gas recirculation, Duan et al. (2014) observed significantly lower fuel-N conversions to NO in oxy-combustion than in air combustion; they were 6.2–9.4% and 26.8–27.1% respectively.

Hofbauer et al. (2014) investigated oxy-combustion of bituminous coal in a 150 kW_{th} pilot CFB facility with flue gas recirculation. Tests were conducted at 880°C in air and in O_2/recirculated flue gas mixtures with 26 and 36% O_2. The lowest NO_x concentration (in mg/m^3) was recorded during combustion in air; it increased with increasing O_2 concentration in the oxidizing atmosphere. On the other hand, the fuel-N conversion to NO_x was lower in oxy combustion than in air combustion for all investigated cases. The values of fuel-N conversion were small; they did not exceeded 2.5%.

Li et al. (2017) studied combustion of a Chinese bituminous coal in air and O_2/dry recycled flue gas mixtures (with 30, 40 and 50% O_2 concentrations) in a 1 MW_{th} CFB pilot plant. The authors found that in O_2/recycled flue gas atmospheres the NO emissions were much lower than those in air combustion. On the other hand, the N_2O emissions were higher in oxy combustion; they were at the level similar to the corresponding NO emissions. The conversions of fuel-N to NO and N_2O were in the ranges from 10.3% (30% O_2) to 20% (air) and from 9.7% (air) to 17.8% (30% O_2) respectively.

In this study, the influence of the oxidizing atmosphere on the NO_x and N_2O emissions during combustion of lignite and bituminous coal in a bench-scale oxy-CFB reactor is investigated. The results for air combustion and oxy-combustion with different inlet O_2 concentrations are presented and compared with results obtained by other researchers.

Experimental

Air and oxy-fuel combustion tests were conducted in a 12-kW bench-scale CFB combustor shown schematically in Fig. 1. A detailed description of the test facility can be found in Kosowska-Golachowska et al (2011). The experiments were carried out at temperature 850°C in air (base case) and mixtures of O_2/CO_2 with oxygen concentrations of 21, 30 and 40% vol. For each test, a 0.5-g sample of fuel was dropped into the combustion chamber and burnt in the bed of silica sand particles. No sorbent was used to capture SO_2 during experiments. Concentrations of NO, NO_2, N_2O and precursors of the nitrogen oxide emissions, such as NH_3 and HCN in the flue gas leaving the combustor were measured on-line by a FTIR spectrometer (Gasmet DX-4000). Sampling frequency for all mentioned gases was 1 Hz. Each test was carried out three times to check and confirm repeatability of results.

Polish bituminous coal and lignite were used in this study. Table 1 shows proximate, ultimate and higher heating value (HHV) analyses of these fuels. Moisture, ash and volatile matter contents in lignite are higher than those in bituminous coal. The nitrogen content in lignite is much lower than that in bituminous coal whereas its oxygen content is significantly higher than that in bituminous coal.

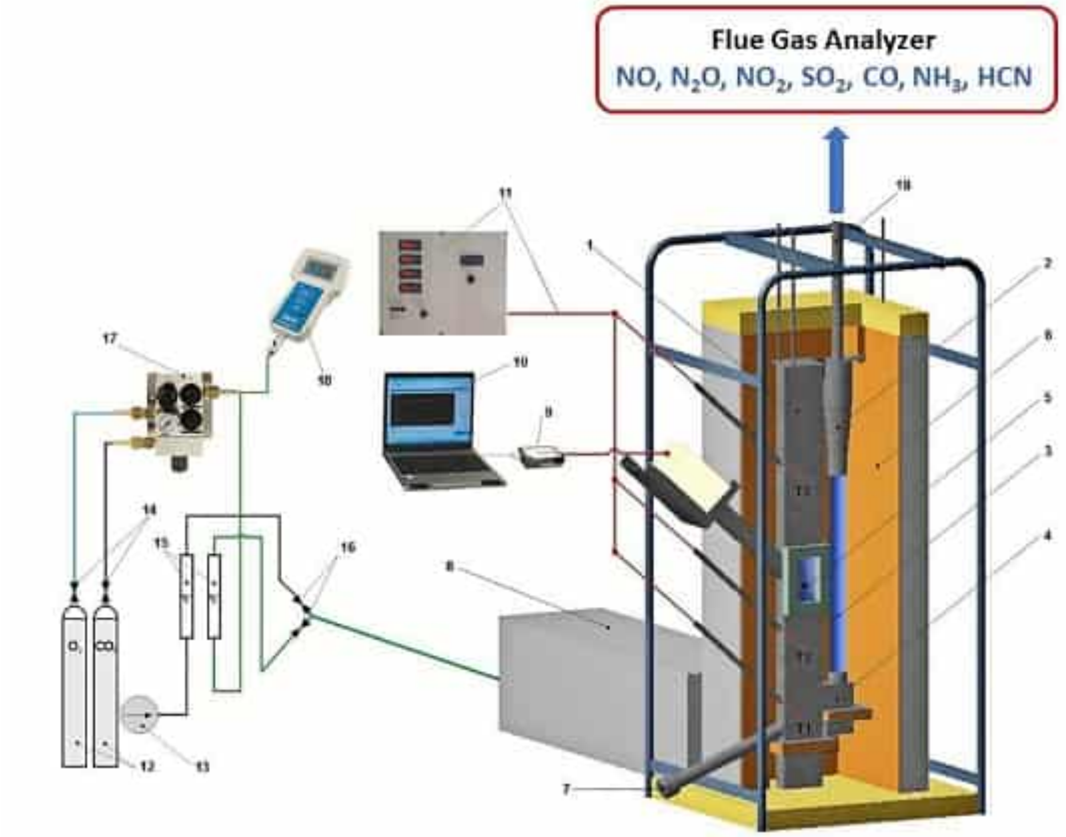

Fig. 1. Schematic diagram of the experimental apparatus for oxy-CFB combustion

1 - combustion chamber, 2 - cyclone, 3 - downcomer, 4 - loop seal, 5 - fuel sample, 6 - insulation, 7 - drain valve, 8 - preheater, 9 - card, 10 - computer, 11 - temperature measurement and control system, 12 - gas cylinders, 13 - air compressor, 14 - pressure regulators, 15 - rotameters, 16 - valves, 17 - mixer, 18 - gas analyser, 19 - ventilation duct, T1–T3 - S-type thermocouples

Table 1. Proximate and ultimate analyses of the tested fuels, wt.%.

Coal	**Lignite**	**Bituminous coal**
Proximate analysis (%, air-dry basis)		
Moisture	13.3	8.7
Ash	22.4	18.9
Volatile matter	39.1	26.8
Fixed carbon (by difference)	25.2	45.6
HHV, MJ/kg	17.33	22.75
Ultimate analysis (%, dry, ash-free basis)		
Carbon	64.4	73.3
Hydrogen	5.5	4.3
Nitrogen	0.6	1.1
Sulphur	0.9	2.3
Oxygen (by difference)	28.6	19.0

Results and discussion

The time-resolved NO concentrations during air and oxy-combustion of lignite and bituminous coal are shown in Fig. 2. Both maximum and average values of NO concentration are higher for lignite than for bituminous coal. On the other hand, the NO release time is slightly shorter for lignite. Because lignite contains 46% more volatiles than bituminous coal, this observation suggests that more NO is formed through faster homogeneous reactions involving O$_2$ and volatile-N than through slower heterogeneous reactions of O$_2$ with char-N. During air-combustion, the average NO concentrations were 18.7 ppm and 26.4 ppm for bituminous coal and lignite respectively. In the case of oxy-combustion, concentrations of NO increase with increasing O_2 content in the O_2/CO_2 mixture. The average concentrations of NO in the 21% O_2 + 79% N_2 mixture were 12.0 ppm and 24.4 ppm for bituminous coal and lignite respectively. They were lower than the corresponding concentrations in the air-combustion case owing to lower temperatures of fuel particles.

The lowest values of fuel-N conversion to NO, 25.6% for bituminous coal and 46.2% for lignite, were found in the case of combustion in air (see Table 2). In the oxy-combustion mode, the conversions of fuel-N to NO were in the range 36.1–36.5% for bituminous coal and 52.6–58.4% for lignite.

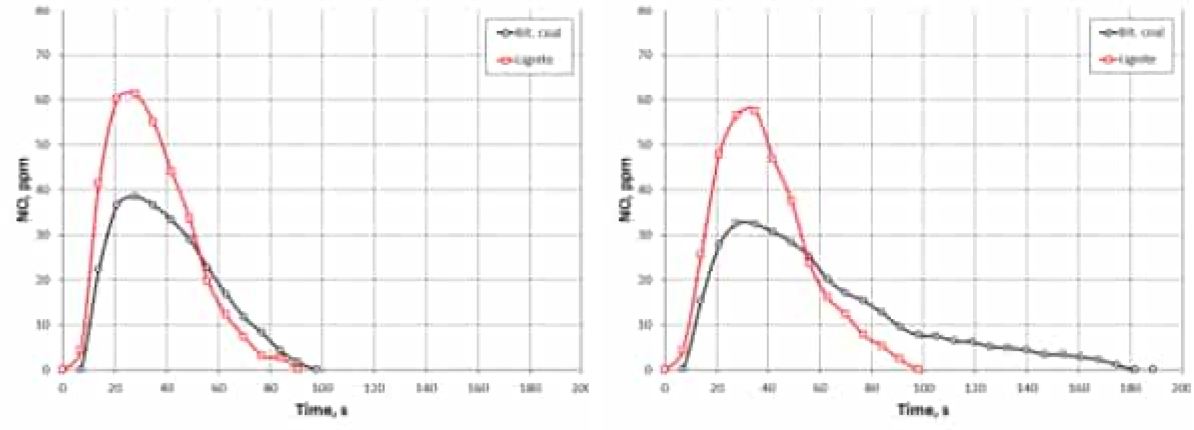

a) Air

b) 21% O_2+79% CO_2

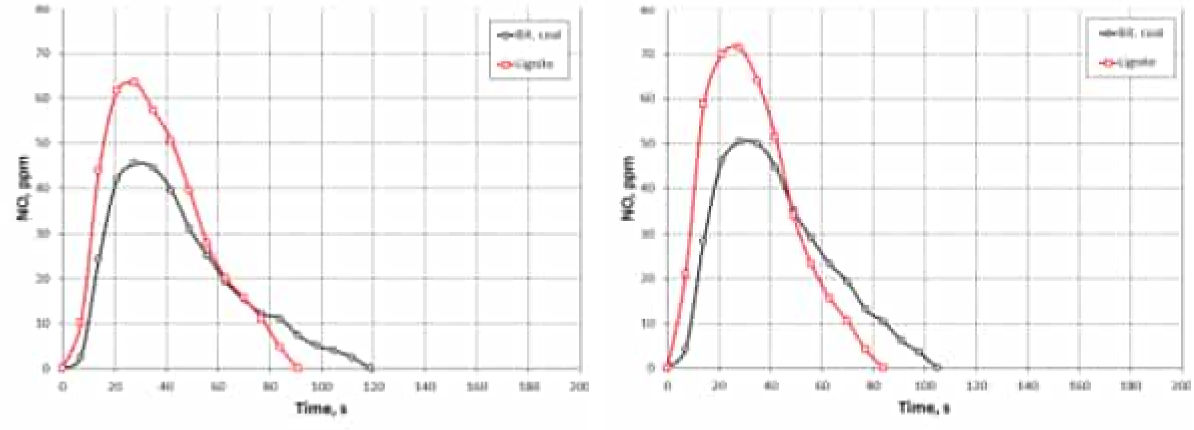

c) 30% O_2+70% CO_2

d) 40% O_2+60% CO_2

Fig. 2. Time-resolved NO concentrations for combustion in different atmospheres

Fig. 3 shows time-resolved N_2O concentrations during air and oxy-combustion of tested coals. As expected, the maximum and average concentrations of N_2O for both coals are much lower than those for NO. For both coals, the instantaneous N_2O concentrations reached their maximum values after approximately 20 s. In the case of lignite, the total N_2O release time was 80–100 s whereas in the case of bituminous coal this time was in the range from 130 to 280 s. The characteristic feature of N_2O release curve during bituminous coal combustion was a long “wake” with instantaneous concentration below 2 ppm, stretching from approximately 100 s to more than 200 s, with one exception in the case of 40% O_2 + 60% CO_2 mixture. Because bituminous coal contains much more fixed carbon these “wakes” in N_2O release can be attributed to the oxidation of char-N to N_2O.

In the case of lignite, conversions of fuel-N to N_2O (Table 2) in oxy-combustion decreased with increasing concentrations of O_2 in the O_2/CO_2 mixture and were significantly lower than that in the air-combustion mode. In the case of bituminous coal, conversions of fuel-N to N_2O were similar to those for lignite in all atmospheres but one. In the 21% O_2 + 79% CO_2 mixture, the conversion of fuel-N to N_2O was two times higher compared to lignite. The total conversion of fuel-N to NO and N_2O was higher for lignite in all atmospheres tested.

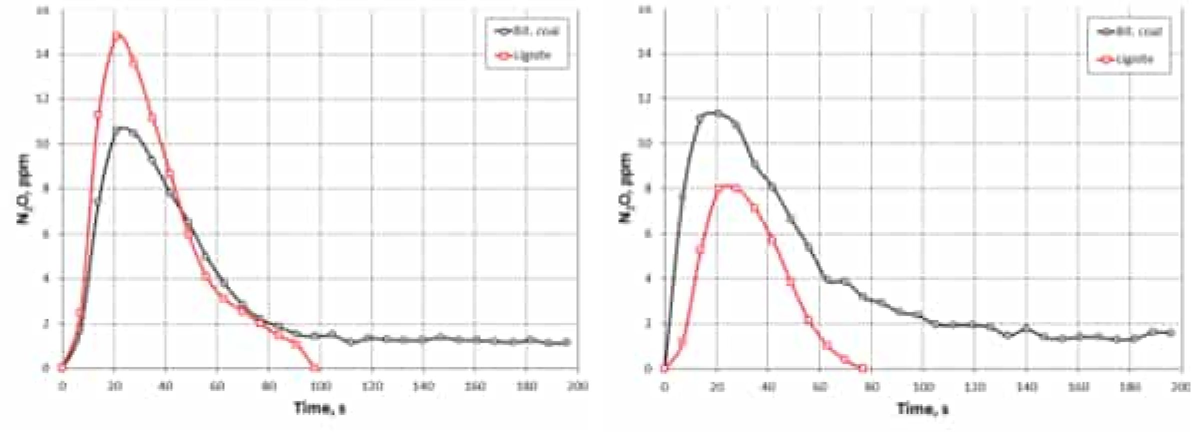

a) Air

b) 21% O_2+79% CO_2

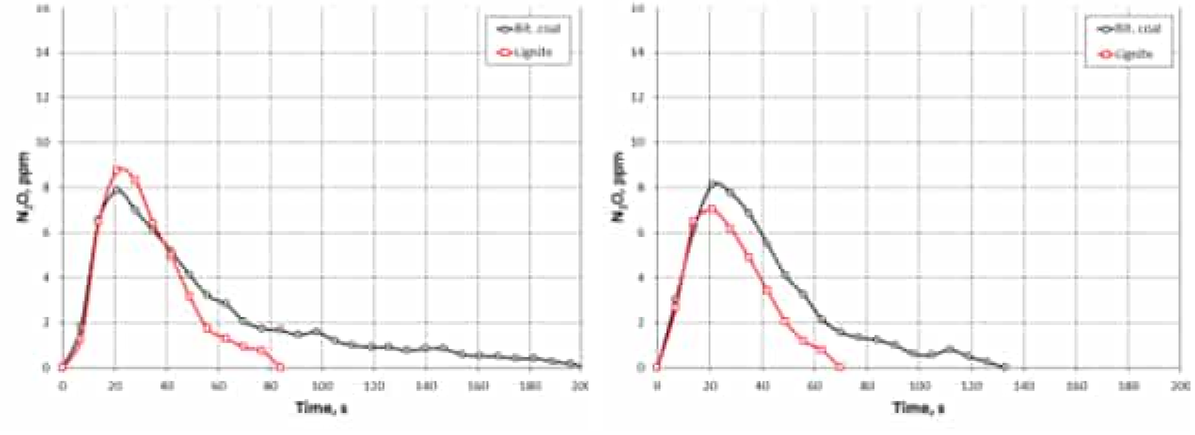

c) 30% O_2+70% CO_2

d) 40% O_2+60% CO_2

Fig. 3. Time-resolved N_2O concentrations for combustion in different atmospheres

Table 2. Conversion of fuel-N to nitrogen oxides, wt.%.

Atmosphere	**Air**	**21% O_2+79% CO_2**	**30% O_2+70% CO_2**	**40% O_2+60% CO_2**
Conversion of fuel-N to NO				
Lignite	46.2	52.6	57.4	58.4
Bituminous coal	25.6	36.1	36.3	36.5
Conversion of fuel-N to N_2O				
Lignite	22.1	13.1	12.5	9.6
Bituminous coal	19.9	26.2	12.9	11.0
Total conversion of fuel-N to nitrogen oxides				
Lignite	68.3	65.7	69.9	68.0
Bituminous coal	45.5	62.3	49.2	47.5

Measurements of flue gas composition reveal the presence of NO_2, NH_3 and HCN. However, concentrations of these species were very low so that they can be considered as traces.

For both tested fuels, conversions of fuel-N to NO were higher in the oxy-combustion mode than in the air-combustion mode. Our results for lignite combustion contradict those presented by Czakiert et al. (2006). Also, our values of fuel-N conversion to NO are significantly higher than those reported by Czakiert et al. (2006), Czakiert et al. (2010), Jia et al. (2010), Duan et al. (2011), Hofbauer et al. (2014) and Li et al. (2017).

In the oxy-combustion, the contribution of thermal-NO_x to the total NO_x emission is eliminated because there is no free nitrogen present in the oxidizing agent and NO_x are only formed via the oxidation of fuel-N. Temperature in the vicinity of burning coal particles is a key parameter that determines the conversion of fuel-N to NO_x. With an increase in the combustion temperature, volatiles content and oxygen concentration in the O_2/CO_2 mixture, emissions of NO also increase wheras emissions of N_2O decrease for tested coals.

Conclusions

Instantaneous emissions of NO for the combustion of lignite in all atmospheres were higher than those for bituminous coal owing to higher concentration of volatiles in lignite. The lowest NO emissions were measured in 21% O_2+79% CO_2 atmosphere for both coals, owing to lower temperatures of fuel particles. With increase in temperature, volatiles content in fuel and concentration of oxygen in the O_2/CO_2 mixture emissions of NO increase whereas emissions of N_2O decrease.

Our results show that for both tested coals, conversions of fuel-N to NO were higher in the oxy-combustion mode than in the air-combustion mode. Our values of fuel-N conversion to NO in all atmospheres are also higher, in some cases significantly, than those presented by other researchers. On the other hand, we have found that the conversion of fuel-N to N_2O is lower in the oxy-combustion mode than in the air-combustion mode for both coals except bituminous coal burned in the 21% O_2 + 79% CO_2 mixture. The total conversion of fuel-N to NO and N_2O was higher for lignite in all atmospheres tested.

References

Czakiert, T, Z Bis, W Muskala, W Nowak. Fuel conversion from oxy-fuel combustion in a circulating fluidized bed. Fuel Proc. Technol. 2006, 87, 531–38

Czakiert, T, K. Sztekler, S Karski, D Markiewicz, W Nowak. Oxy-fuel circulating fluidized bed combustion in a small pilot-scale test rig. Fuel Proc. Technol. 2010, 91, 1617–23

Duan, L, C Zhao, W Zhou, C Qu, X Chen. O_2/CO_2 coal combustion in a 50 kW_{th} circulating fluidized bed. Int. J. Greenhouse Gas Contr. 2011, 5, 770–776

Duan, L, H. Sun, C Zhao, W Zhou, X Chen. Coal combustion characteristics on an oxy-fuel circulating fluidized bed combustor with warm flue gas recycle. Fuel 2014, 127, 47–51

Hofbauer, G, T Beisheim, H Dieter, G. Scheffknecht. Experiences of oxy-fuel combustion of bituminous coal in a 150 kW_{th} circulating fluidized bed pilot facility. Energy Procedia 2014, 51, 24–30

Jia, L., Y Tan, EJ Anthony. 2010. Emissions of SO_2 and NO_x during oxy-fuel CFB combustion tests in a mini-circulating fluidized bed combustion reactor. Energy&Fuels 2010. 24, 910–915

Kosowska-Golachowska, M, A Luckos, K Kłos, T Musiał. Oxy-combustion of different coals in a circulating fluidized bed, in: T Knowlton (Ed.), CFB-10, ECI, New York, 2011

Li S, H Li, W Li, M Xu, EG Eddings, Q Ren, Q Lu. Coal combustion emission and ash formation characteristics at high oxygen concentration in a 1 MW_{th} pilot scale oxy-fuel circulating fluidized bed. Applied Energy 2017, 197, 203–211

Mathekga, HI, BO Oboirien, BC North. A review of oxy-fuel combustion in fluidized bed reactors. International Journal of Energy Research, 2016.

Singh RI, R Kumar. Current status and experimental investigation of oxy-fired fluidized bed. Renewable and Sustainable Energy Reviews 2016. 61, 398–420

ATTRIBUTES OF AN ECCENTRICALLY POSITIONED VORTEX FINDER ON PRIMARY CYCLONES

Ray A. Cocco[1], Ulrich Muschelknautz[2], Ben Freireich[1], S. B. Reddy Karri[1] and Ted Knowlton[1],

[1]Particulate Solid Research, Inc. 4201 W. 36th Street, Building A, Chicago, IL 60632 USA
[2]MK Engineering, Heinrich-Fuchs-Str. 101, 69126 Heidelberg, Germany
Email: ray.cocco@psri.org

Abstract

With fluidized bed, circulating fluidized bed (CFB) and even pneumatic conveying operations, reverse-flow cyclones are a critical component in a successful process. Although the designing principle for cyclones is straightforward, the hydrodynamics in these units are not. This poor understanding of the hydrodynamics has limited improved cyclone operations which is why cyclone designs has not changed significantly in 150 years.

This is especially true with the symmetrical design of the cyclone. With the exception of the inlet, everything else on a cyclone is symmetric. For example, the gas outlet tube (also called the vortex finder) immersed into the cyclone, also called the vortex finder, is located concentrically, i.e. its axis coincides with the axis of the cyclone. However, it has been shown in numerous recirculating cyclones of CFB power plants that eccentric positioning of the vortex finder axis improves the cyclone efficiency without affecting the pressure drop [Muschelknautz and Muschelknautz, 1999; Ispen, et al., 2014]. By modifying the vortex finder, the circulating material became finer and its quantity increased resulting in a considerable improvement of the boiler performance, the heat transfer in the combustion chamber, improved the optimum combustion temperature to ~900°C, and reduced the amount of unburnt filter ash. In addition, this optimization led to cost savings of operational costs.

Trefz [1992] gave a qualitative explanation of the positive effect of eccentrically shifting the vortex finder axis on the cyclone efficiency based on flow measurements in cyclones. At the top of the cyclone barrel region, there is a secondary flow through the boundary layer of about 10% of the total flow carrying particles towards the center. The vortex finder forces this secondary flow around the tube down to the opening allowing to remove particles from that flow by centrifugal force. In cyclones with a tangential inlet and a concentric vortex finder, however, this separation is not optimal. The axis of the vortex flow is pushed away from the geometrical center of the cyclone by the incoming gas flow and as a consequence the tangential velocity of the flow around the vortex finder is not symmetrical. In the section of the vortex finder surface which is closer to the cyclone axis, the tangential velocity stagnates and the secondary flow streams vertically downwards with practically no circumferential velocity. In this section, the particle separation is poor. By shifting the vortex finder axis into the “eye” of the vortex a more uniform flow around the vortex finder is achieved and its separation efficiency improves considerably.

Recently, numerical granular-fluid simulations of high loaded cyclones with a concentric and with an eccentric vortex finder have been performed by applying the CFD code Barracuda Virtual Reactor® of CPFD, LLC. The CFD results confirmed that eccentrically shifting the vortex finder results in a better collection efficiency without compromising the pressure drop. The calculations were compared with measurement data from commercial high loaded cyclones in CFB boilers and the origin of the improvement due to the eccentric shifting the vortex finder was studied.

Introduction

Usually, the gas outlet tube, also called the vortex finer, immersed into the cyclone separator, also called the vortex finder, is located concentrically at the center (i.e. its axis coincides with the axis of the cyclone barrel). However, it has been shown in numerous recirculating cyclones in CFB power plants that eccentric positioning of the vortex finder axis improves the cyclone efficiency without affecting the pressure drop [Muschelknautz and Muschelknautz, 1999; Ispen, et al., 2014]. Eccentric outlet tubes on primary cyclones resulted in the material circulating back to the unit to be finer. The finer particles suggest a reduced the amount of fly ash, improved heat transfer in the combustion chamber, and provided better fluidization in the fluidized bed cooler. In other words, the eccentric vortex finder resulted in improved collection efficiency by way of smaller cut sizes. Thus, the optimization of the vortex finder or outlet tube position can lead to a higher boiler efficiency and cost savings. In the case of circulating fluidized bed (CFB) combustors, the optimized cyclone configurations led to an increased thermal efficiency, a reduction in silica sand, and a reduction of fly ash build up in the electrostatic precipitators.

Barracuda Virtual Reactor® (CPFD, LLC) simulations were used to study high-loaded cyclones with a concentric and with an eccentric vortex finder. The CFD results confirm that eccentrically shifting the vortex finder results in a better collection efficiency without compromising the pressure drop. The calculations were used to understand how moving the vortex finder or outlet tube off-axis resulted in better performance.

Procedure

Cyclone Designs

Figure 1 provides the cyclone dimensions which is a standard reverse flow cyclone with a concentric outlet. Figure 2 shows a similar cyclone design but the vortex finder was skewed in the 210° direction away from the inlet. This skewing of the vortex finder resulted in a shift of 15 mm in the X direction and 4 mm downward in the Y direction.

Computational Domains

Barracuda Virtual Reactor® reads stereo-lithography files for grid generation. Figure 3 shows the CADs for a cyclone with a concentric (Case A) and eccentric (Case B) vortex finder or outlet tube. The computational domain consisted of a cyclone, a dipleg with a splash plate and a fluidized bed. The fluidized bed was added to better model the hydrodynamics in the diplegs with the realization that a uniform boundary condition at the bottom of a dipleg is not an acceptable assumption. With the addition of a fluidized bed, a realistic exit condition can be simulated for the dipleg exit.

The gas exit boundary conditions for the fluidized beds are two outlets with a uniform pressure boundary condition. It was believed that a uniform boundary condition in this region would have a minimal effect on the cyclone performance or on the results of the simulations.

Simulations were done using Barracuda Virtual Reactor® version 17.1, which is a Lagrangian-Eulerian hybrid code employing the multiphase particle-in-cell (MP-PIC) numerical method [Andrew,et al.; Snider,et al.].

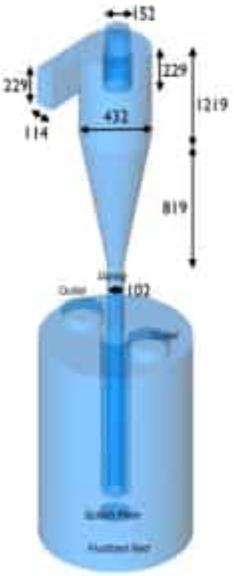

Figure 1: Standard cyclone design. All units are in mm.

Physical Properties

The fluid phase was air with a density of 1.1 kg/m^3 (0.68 lb$_m$/ft^3) and a viscosity of 0.0000188 kg/m-sec (0.0000126 lb$_m$/ft-sec) which corresponds to a temperature of 25°C (77°F) and 101,325 Pa (14.7 psia). The particulate phase was FCC eCat with a particle density of 1,480 kg/m^3 (92.5 lb$_m$/ft^3), a median particle size (d_{p50}) of 64 microns and a fines level of 15% (where fines are defined as particles smaller than 44 microns). The particle size distribution and loading were based on an entrainment rate calculation using the PSRI proprietary entrainment rate correlation for a 0.9-m (3-ft) diameter by 1.2-m (4-ft) tall fluidized bed of FCC eCat at a superficial gas velocity of 0.9 m/sec (3 ft/sec).

Boundary and Initial Conditions

All simulations had the same inlet and boundary conditions. The cyclone started with stagnant air (0 ft/sec), and with no solids at a temperature of 25°C (77°F) and pressure of 101,325 Pa (14.7 psia). All simulations were isothermal. The fluidized bed started with 260 kg of FCC catalyst powder in a static packed bed. The particle close pack volume fraction, *(1-ε)*, was set to 0.63.

The cyclone inlet velocity boundary condition for the gas was set to 18 m/sec (59 ft/sec) at 25°C (77°F) and 180,000 Pa (26.1 psia) after one second of simulation time. The solids inlet feed rate was set at 9.2 kg/sec (20.2 $\mathrm{lb_m}$/sec) for Cases 1 and 2, and 18.5 kg/sec (40.7 $\mathrm{lb_m}$/sec) for Cases 3 and 4 after the first second of simulation time. Table 1 provides a depiction of the differences associated with each case.

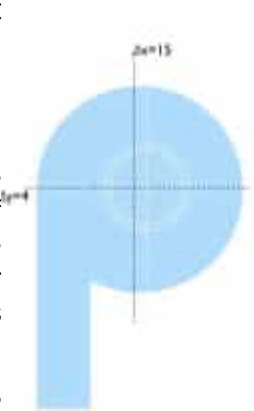

Figure 2: Cyclone design with eccentric vortex finder skewed at 210°. All units are in mm.

The outlets pressure boundary conditions for the cyclone exit and the fluidized bed exits were set as unrestricted pressure outlets at a pressure of 101,325 Pa (14.7 psia). Any particle that reached the outlet was allowed to exit in the simulation.

Table 1: Boundary Conditions and Vortex Finder Configurations

Case Number	**Vortex Finder**	**Inlet Velocity**	**Solids Flow Rate**	**Mass Ratio**
1	Concentric	18 m/sec (59 ft/sec)	9.24 kg/sec (20.3 $\mathrm{lb_m}$/sec)	10
2	Eccentric	18 m/sec (59 ft/sec)	9.24 kg/sec (20.3 $\mathrm{lb_m}$/sec)	10
3	Concentric	18 m/sec (59 ft/sec)	18.5 kg/sec (41 $\mathrm{lb_m}$/sec)	20
4	Ecentric	18 m/sec (59 ft/sec)	18.5 kg/sec (41 lbm/sec)	20

Results and Discussion

Grade Efficiency

Figure 3 shows the grade efficiency curves and cut sizes for each case. In both the high and low loading cases, the asymmetric configurations trend with higher collection efficiency than the symmetric ones. For the lower solids loading at the inlet, differences were only observed for particles smaller than 12 microns with the eccentric configuration having a better collection efficiency. Cut fractions for Cases 1 and 2 were different but only to a small extent. For the higher loadings, Cases 3 and 4, the differences between the two cyclone designs were significant. For the small particles with less than 99% collection efficiency, the cyclone with the eccentric vortex finder (Case 4) showed a 35% better collection efficiency (61% vs. 45%) for particles smaller than 17 microns. The cut size was also reduced from 13 to 12 microns.

Gas and Solid Hydrodynamics

One issue with tangential cyclones, and to a lesser extent, volute cyclones, is that the swirling gas and solids flow comes back around and interacts with the incoming gas and solids at the cyclone inlet. This interaction cause the inlet solids stream to fluctuate. If not designed correctly, this fluctuation can cause the inlet solids stream to collide with the outer wall of the

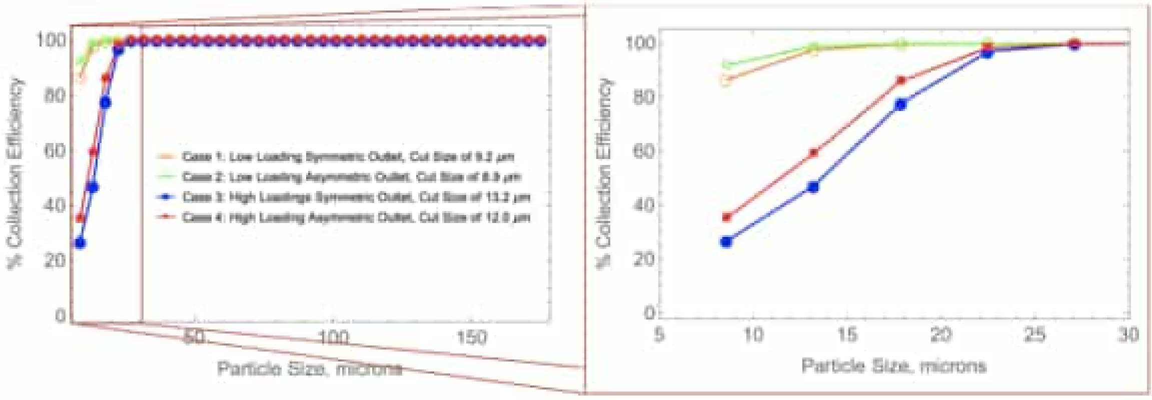

Figure 3: Grade efficiency curves for high and low solids loadings to the inlet for concentric and eccentric vortex finder tubes (outlet tubes).

vortex finder, which would impact the collection efficiency and promote erosion of the vortex finder tube.

Yet, the outlet tube offers other complications that has to be addressed. The outlet tube can cause recirculation of the gas and solids swirl that results in additional scattering of particles and leakage into the vortex finder [Cocco, 2006]. This scattering can be seen by tracking the number and severity of particle collisions with the wall in the cyclone barrel region near the cyclone inlet, as shown in Figure 4. More wall collisions were observed for the concentric vortex finder configuration at both low and high solids loadings. The grid resolution was similar for all cases.

This secondary swirl near the inlet region is the result of a lower pressure region on the back side of the vortex finder or outlet tube. The swirling flow around the vortex finder causes the lower pressure region on the back side of this tube, as the gas can no longer adhere to the vortex finder tube wall [Muschelknautz & Muschelknautz, 1999]. This behavior is similar to what occurs with an airplane wing or a sail on a sailboat.

Pressure Drop

The pressure drops from the inlet to the outlet, the inlet to the dipleg, and across the dipleg showed to be dependent on solids loading. There was only a minimal effect of the outlet tube position on the cyclone pressure drop. The eccentric vortex finder did provide a slightly lower pressure drop from the inlet to the gas outlet. Negligible differences were observed in the pressure drop from the inlet to the dipleg suggesting no significant difference with the two cyclone designs.

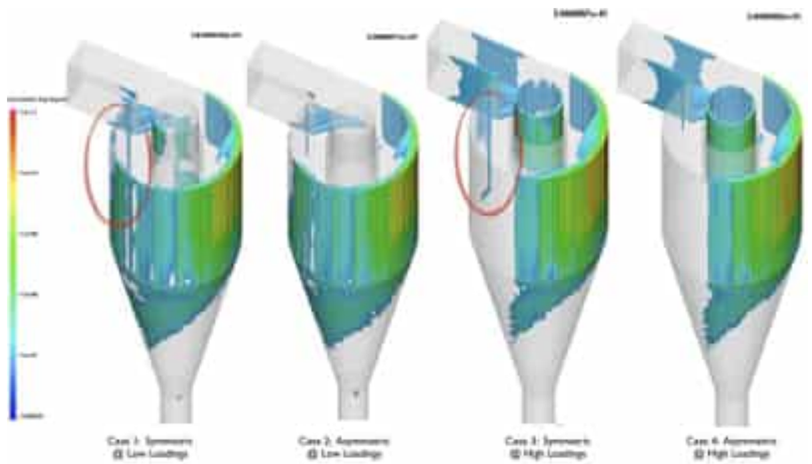

Figure 4: Particle wall collisions for all cases as mapped from the impact summation (by particle count) function of $\sum\theta\ m_p^{1.5}v^{3.5}$ where θ is a PDF function associated with erosion of ceramic or glass material (max at 90°).

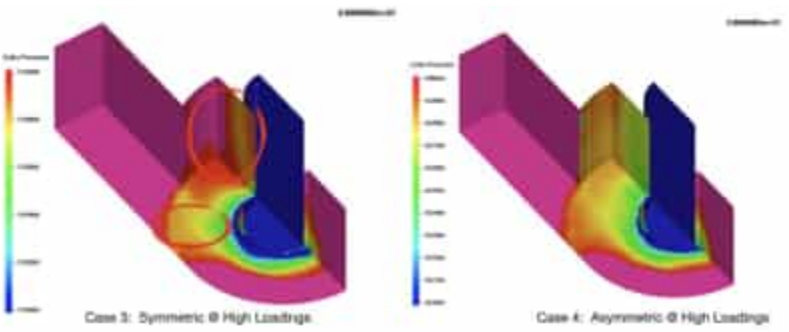

Figure 5: Instantaneous pressure profiles (at 20 simulated seconds) in upper cyclone barrel region for high loading cases.

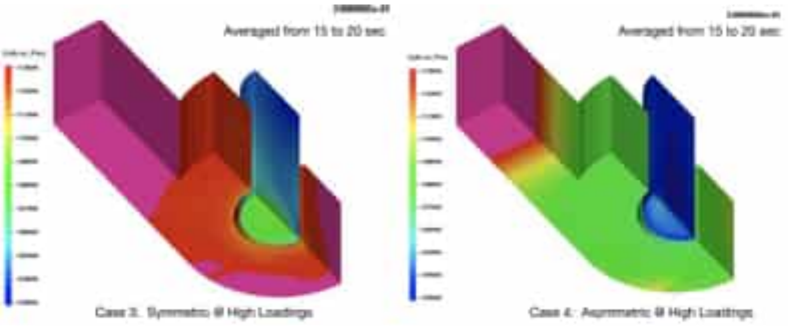

Figure 6: Average pressure profiles (15 to 20 simulated seconds) in upper cyclone barrel region for high loading cases.

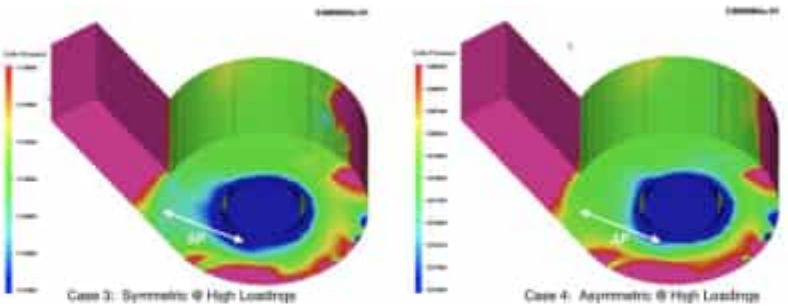

Figure 7: Instantaneous pressure profiles (at 20 simulated seconds) in upper cyclone barrel region for high loadings cases with emphasis on the pressure differences rather than the absolute pressure.

However, the pressure profiles within the cyclones were not similar. For most cyclones, a lower pressure pocket does not provide lift but a suction region that causes a secondary swirl from near the inlet region. This suction region can be seen in Figure 5 where the pressure is mapped on the upper barrel region for the high loading cases of the cyclone simulations at 20 seconds simulation time. Two features are notable. First, the lower pressure region extends into the bottom of the inlet for the concentrical cyclone case (i.e., Case 3). This is similar to that proposed by Muschelknautz & Muschelknautz except they presumed this low pressure extension to be 90° counter clockwise to what is shown in Figure 5. Second, the pressure in the upper barrel region is higher for the concentric vortex finder position than the case with the eccentric vortex finder position. It is about 0.3 kPa higher for the concentric vortex finder case.

Figure 6 shows the averaged pressure profile in the upper barrel region. The pressure difference in the upper barrel region between the two cases is still significant suggesting that this difference is not due to a single to several transient fluctuations in the pressure. Figure 6 also shows how the concentric vortex finder position affects the pressure profile in the vortex finder. The pressure profile for the eccentric outlet tube is nearly concentric.

The driving forces for estimated leakage across the vortex finder are more evident by comparing the pressure differences between the bottom of the inlet to the bottom of the vortex stabilizer near the inlet (i.e., near the region of estimated leakage). Figure 7 shows a more refined pressure profile where the pressure range is similar but the absolute pressure on the color scale has been changed to account for the higher pressure observed in Case 3. For the concentric vortex finder case, Case 3, the pressure drop was 750 Pa (0.11 psi) whereas for the eccentric vortex finder case the pressure drop was only 500 Pa (0.07 psi). This higher pressure drop appears to skew the lower pressure region around the vortex finder more towards the inlet region for the concentric vortex finder case.

Conclusions

CFD results using the Barracuda Virtual Reactor® CFD package showed that cyclones with an eccentric vortex finder (Case 4) showed 35% better collection efficiency for particles smaller than 17 microns. The eccentric vortex finder configuration results in a reduction of the cut size from 13.2 to 12 microns. The increase in the collection efficiency had little impact on the pressure drop.

In addition, CFD results confirm the findings of Muschelknautz and Muschelknautz [1999] that an eccentric vortex finder configuration reduces the lower pressure pocket on the back side of the vortex finder which diminishes the secondary swirling flow. All of which results in a higher collection efficiency, especially for higher loading cyclones. This reduction in the secondary swirling flow may also affect the hydrodynamics further down in the cyclone which could also impact the collection efficiency.

Reverse flow cyclones have been in use for over 100 years, but little has changed in their basic design. The outlet tube has remained concentric with respect to the barrel. The findings of Muschelknautz and Muschelknautz [1999] and the above-noted CFD findings suggest that design criteria for the vortex finder positioning and perhaps for other cyclones parameters, in general, should be questioned.

Selected References

Andrews, M.J., O'Rourke, P.J. 1996. The multiphase particle-in-cell (MP-PIC) method for dense particulate flows. International Journal of Multiphase Flow, 22, 379-402.

Cocco, R., Jacob, K., Understanding gas residence times in reverse flow cyclones, 5th World Congress in Particle Technology, Orlando, FL, USA, April 23, 2006.

Hoffmann, A.C., Stein, L.E., Gas Cyclones and Swirl Tubes, 1st Ed. Springer, Berlin, 2001.

Ipsen C, Roschek D, Muschelknautz U (2014) Optimierung eines Zyklonabscheiders einer zirkulierenden Wirbelschichtfeuerung. VGB PowerTech 4/2014:75-79

Muschelknautz U, Muschelknautz E (1999). Separation efficiency of recirculating cyclones in CFB combustions. VGB PowerTech 4/1999, 48-53.

Snider, D., O'Rourke, P.J., Andrews, M.J., Sediment flow in inclined vessels calculated using a multiphase particle-in-cell model for dense particle flows. International Journal of Multiphase Flow, 24, (1998) 1359-1382.

Snider, D., An incompressible three-dimensional multiphase particle-in-cell model for dense particle flows. Journal of Computational Physics, 170, (2001) 523–549.

Trefz M (1992). Die verschiedenen Abscheidevorgänge im höher und hoch beladenen Gaszyklon unter besonderer Berücksichtigung der Sekundärströmung. VDI-Fortschr.-Ber., VDI-Verlag, Düsseldorf, Reihe 3, No. 295.

Trefz, M., and Muschelknautz, E., Extended cyclone theory for gas flow with high solids concentration. Chem. Eng. Technol. 16 (1993), pp. 153 – 165.

EXPERIMENTAL INVESTIGATION OF SEGREGATION DIRECTION AND LAYER INVERSION IN LIQUID FLUIDIZED BEDS

Alberto Di Renzo[1*], Giacomo Rito[1], Francesco P. Di Maio[1]

[1]*Università della Calabria, Via P. Bucci, Cubo 45a, 87036 Rende (CS), Italy*

*Email: alberto.direnzo@unical.it

Abstract

Multi-component liquid-fluidized beds are encountered in a variety of industrial processes and technologies. Rather often, segregation severely affects the performance of the process unit. Unfortunately, size-driven and density-driven separation processes may occur with a complex interplay, showing prevailing mechanisms that change with the operating conditions. For example, when the solids exhibit contrasting differences in size and density, even the *direction of segregation*, e.g. the component that tends to separate towards the surface, can turn out hard to predict, giving rise for some systems to the so-called “layer inversion phenomenon.” In the present contribution, the reliability of a model for predicting the segregation direction of fluidized binary beds (the Particle Segregation Model, PSM) is examined and discussed on the basis of a systematic experimental investigation of binary beds with different size and density ratios and at different bed composition. By measurements of the solids’ concentration at the surface, expansion/segregation properties and the inversion voidage are compared with the PSM predictions, offering a direct means of model validation.

Introduction

Multi-component liquid-fluidized beds are encountered in a variety of industrial processes and technologies, including mineral ore dressing, sorting/classification, coal beneficiation, separation in plastic waste recycling and in biochemical reactors (Epstein N., 2003). Rather often, segregation severely affects the performance of the process unit. Unfortunately, size-driven and density-driven separation processes may occur with a complex interplay, showing prevailing mechanisms that change with the operating conditions. For example, when the solids exhibit contrasting differences in size and density (like in many applications cited above), some mixtures can give rise to the so-called “layer inversion phenomenon” (Vivacqua et al., 2012, Di Felice et al., 1988) (see Fig. 1). In such systems even the direction of segregation, i.e. which one component tends to separate towards the surface and which one to sink to the bottom, can turn out hard to predict. Among the various analytical models proposed in the literature, the approach recently introduced by Di Maio and Di Renzo (2016) (Particle Segregation Model, PSM) was shown theoretically capable of predicting both the segregation direction and the layer inversion voidage, starting with the information on the solids properties and bed composition. Based on the hypothesis of bed uniformity and the knowledge of a model for the drag force in size-polidisperse systems, it has been proved possible to analytically predict the segregation tendency of different types of particles in the liquid-fluidized bed. In the present work, a set of binary mixtures specifically assorted to emphasize the role of the solids’ sizes and densities have been analyzed experimentally. The results of the inversion voidage are compared to the PSM calculations in an attempt to assess the predicting capabilities.

Prediction of the Inversion Voidage: the Particle Segregation Model (PSM)

The Particle Segregation Model approach follows from the force equilibrium on one particle immersed in the mixture (Di Maio and Di Renzo, 2016) and is shortly summarized here. Considering a binary mixture composed of a smaller and denser component with a bigger and less dense component, without loss of generality, we denote the former as species 1 and the latter as species 2.

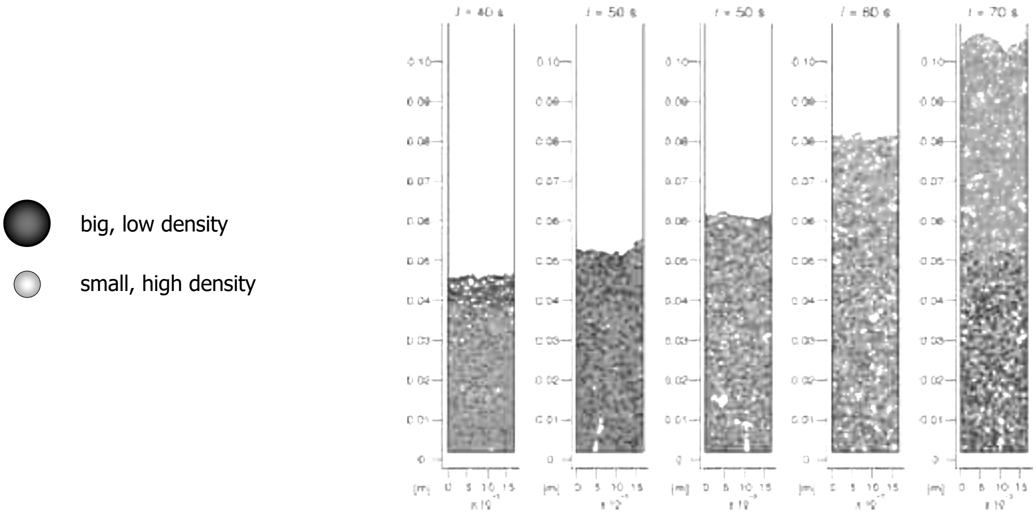

Fig. 1. Simulations of the segregation and layer inversion in liquid fluidized bed (Di Renzo et al., 2011)

The mixture average properties are defined as follows:

$$\overline{D} = \left(\frac{x_1}{D_1} + \frac{1-x_1}{D_2}\right)^{-1} , \tag{1}$$

$$\overline{\rho} = \rho_1 x_1 + \rho_2 (1 - x_1) \tag{2}$$

where D and ρ denote the particle diameter and density, respectively, and x_1 is the volume fraction of solid species 1 over the total solid volume.

Since the mixed bed is in the fluidized state – so the pressure gradient equals the apparent bed weight per unit volume – the generalized buoyancy force acting on a particle of species 2 can be calculated by

$$V_2 \nabla p = \frac{\pi}{6} D_2^3 (\overline{\rho} - \rho_f)(1 - \varepsilon) g , \tag{3}$$

where V is the particle volume, ρ_f is the fluid density and ε is the voidage.

The drag force acting on species 2 in a fully mixed bed can be expressed as the product of a species dependent coefficient and the average value of the force (van der Hoef et al., 2005), i.e.

$$F_2 = y_2^2 \overline{F} , \tag{4}$$

where the polydispersion index y_i is

$$y_i = \frac{D_i}{\overline{D}} \tag{5}$$

and $\overline{F}$, the average drag force in the system, can be expressed by

$$\overline{F} = \sum_i \frac{x_i}{y_i^3} F_i . \tag{6}$$

If the mixture is fully fluidized, the average force is the value necessary to balance the apparent weight of an average particle. So, it can be more conveniently expressed as:

$$\overline{F} = \varepsilon\left(\overline{\rho} - \rho_f\right) \frac{\pi}{6} \overline{D}^3 g \ . \tag{7}$$

The force balance on species 2 reads

$$\rho_f \frac{\pi}{6} D_2^3 g + V_2 \nabla p + F_2 = \rho_2 \frac{\pi}{6} D_2^3 g , \tag{8}$$

which, upon substitution of the generalized buoyancy force (Eq. 3) and drag force (Eq. 4), can be rearranged to lead to the following prediction formula:

$$\varepsilon_{inv} = \frac{1-\bar{s}}{1-\bar{d}} \,. \tag{9}$$

In Eq. (9) the following definitions of the average size and net density ratios appear:

$$\bar{d} = \frac{\bar{D}}{D_2} \tag{10}$$

and

$$\bar{s} = \frac{\rho_2-\rho_f}{\bar{\rho}-\rho_f} \tag{11}$$

It shall be noted that the voidage value obtained by the Particle Segregation Model, Eq. (9), named the force balance on species 2 under the assumption of a fluidized and fully mixed binary mixture, can interpreted as the inversion condition voidage, hence the subscript *inv*. Indeed, a condition arises, for which the species 2 particles are in equilibrium within a system that is globally at equilibrium (suspended), i.e. there is no drive to internal segregation during fluidization. As a result of total bed equilibrium, Species 1 is also at force equilibrium individually, and the full mixture remains mixed. On the contrary, at voidage values different than ε_{inv} some segregation occurs, in the "direction" that depends on the sign of the prevailing force. A map like the one in Figure 2 can be drawn.

Differently from other macroscopic models in which the inversion conditions of voidage and velocity are strongly coupled, Eq. (9) leads to the direct prediction of the inversion voidage and lends itself to a relatively easy experimental verification.

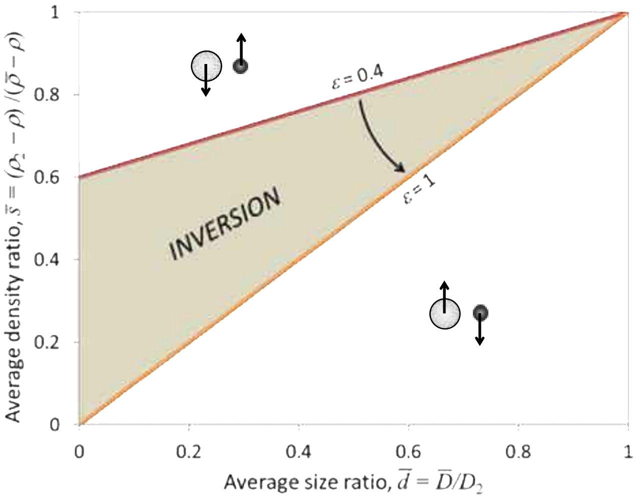

Fig. 2. Layer inversion zone in the average density vs. average diameter ratio map.

Experimental Set-up and Materials

Different binary mixtures potentially exhibiting layer inversion have been tested in a water fluidization rig. The experimental facility is composed of a 10-cm diameter, 1.75-m height fluidization column with a perforated plate distributor, inserted in a water recirculation loop, as illustrated in Fig. 3a. Water flow-rate is measured by rotameters and bed height is acquired by direct observation of the liquid level and three meter tapes attached to the column. Average bed voidage is then computed based on the bed height and the known solids mass and density. Solids volume fraction at the surface is evaluated by collecting a sample of solids from the fluidized bed surface, using a cup shaped device as shown in Fig. 3b, sieving and weighing the solids.

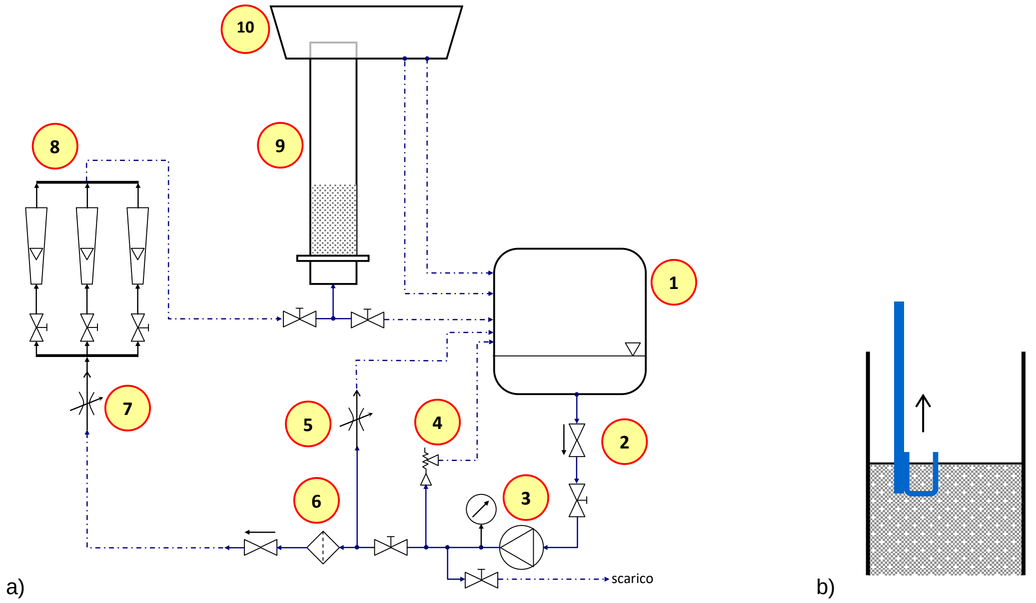

Fig. 3. Experimental water-fluidization rig (a). 1. Tank, 2. check valve, 3. Pump, 4. overpressure valve, 5. by-pass valve, 6. Filter, 7. fine regulation valve, 8. Rotameters, 9. fluidization column (10 cm ID, 1.75 m height), 10. collection tank. Sketch of the withdrawal device and procedure (b).

Table 1. Glass beads (GB) and calibrated plastic spheres (PS) properties

Code	**Density (kg/m^3)**	**Nominal size (mm)**	**Average size (mm)**
GB1	2500	0.60 - 0.81	**0.87**
GB2	2500	1.40 – 2.0	**2.12**
GB3	2500	2.40 - 2.90	**2.80**
GB4	2500	2.85 - 3.45	**3.18**
GB5	2500	3.80 - 4.40	**4.21**
PS1	**1451**	5.95	5.95
PS2	**1632**	5.95	5.95
PS3	**1814**	5.95	5.95
PS4	**2086**	5.95	5.95
PS5	**2267**	5.95	5.95

Fig. 4. Low velocity fluidization of plastic-on-glass beads binary mixture

To investigate the role of particle size and density in the mixture, spherical particles are used as bed materials, including different size cuts of glass beads and bigger, calibrated particles made of different density copolymers. The codes and properties of the mixture components are listed in Table 1. A typical fluidized, strongly segregated mixture with the plastic spheres at the top is shown in Fig. 4. Pairs are denoted by a string representing the codes of the plastic spheres, the glass beads and the volume fraction of the latter, e.g. PS*x*_GB*y*_X1_*z.zz*.

Results and Discussion

Solids volume fraction of the uppermost layer can be compared with the nominal volume fraction of the overall mixture at different superficial velocities. Under the commonly observed hypothesis that segregation manifests with two layers of different concentrations of the two solids, if the top layer concentration profile at some degree of expansion equals the nominal mixture value then the fluidized bed will be fully mixed. That peculiar condition corresponds to the layer inversion point, at which the full system is mixed.

Figure 5 shows two examples of mixture whose profile of the top layer volume fraction with voidage is compared with the nominal mixture concentration (red horizontal arrow). Based on the measurements, the mixture PS3_GB4_X1_0.42 does not exhibit a cross point (Fig. 5a), indicating no inversion conditions (not in the expansion range technically observable), and the mixture PS5_GB5_X1_0.48 exhibits layer inversion (Fig. 5b), as witnessed the intersection between the volume fraction profile and the nominal concentration.

For the systems exhibiting layer inversion, the voidage is determined as the abscissa value of the intersection point. Generally, the average value of multiple runs is taken, for example collecting data at increasing and decreasing velocity (see Fig. 6). The variability on ε_{inv} associated with these tests was limited to 8%. Despite the combination of sizes and densities, not all mixtures are predicted by the PSM to exhibit layer inversion, as shown by the mixture points on the density vs. size ratio map in Fig. 7.

The comparison of predicted and measured inversion voidage is reported in Fig. 8. The match for presence/absence of the layer inversion occurred is for 11 out of 14 systems. The average discrepancy on $\boldsymbol{\varepsilon_{inv}}$ is 5% and the maximum is 18%.

Conclusions

Prediction of the voidage at layer inversion conditions using the Particle Segregation Model has been tested by a systematic experimental campaign on binary liquid-fluidized beds. The model is able to capture the influence of solids' properties and mixture concentration, allowing parameter-free analytical prediction of the inversion voidage, irrespective of the corresponding velocity.

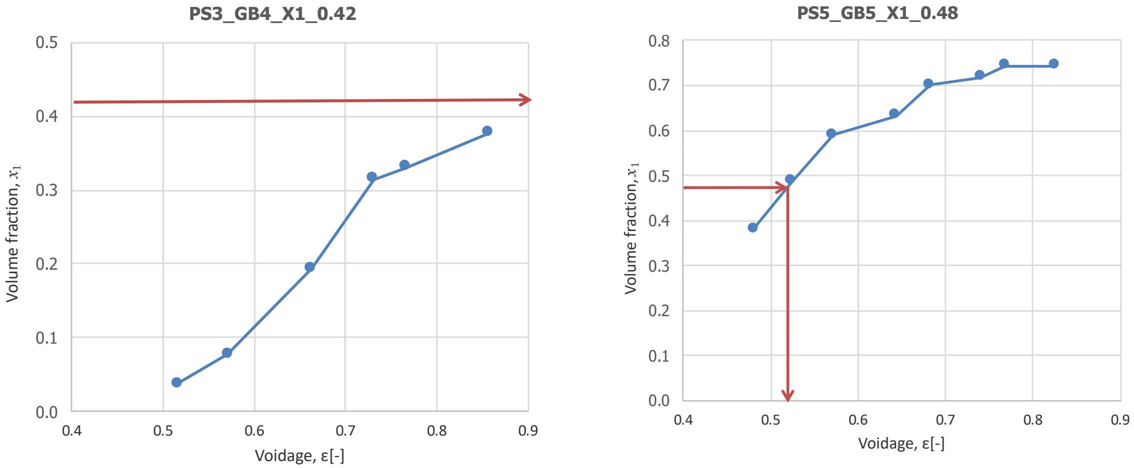

a) b)

Fig. 5. Concentration of the uppermost layer as a function of the expansion voidage. System not reaching the inversion condition (red arrow) (a) and system reaching layer inversion (b).

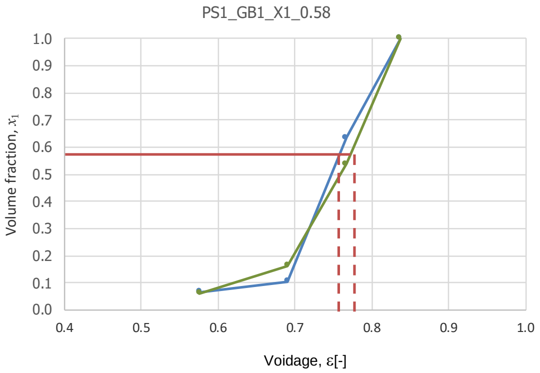

Fig. 6. Determination of the experimental inversion voidage.

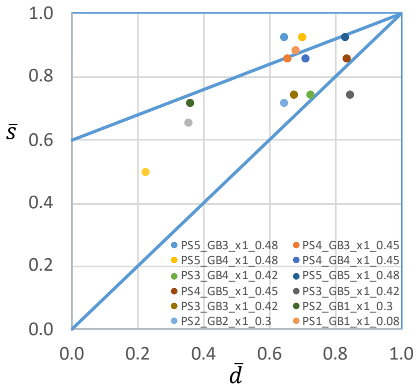

Fig. 7. Representative points for the mixtures on the density vs. size ratio map (see Fig. 2).

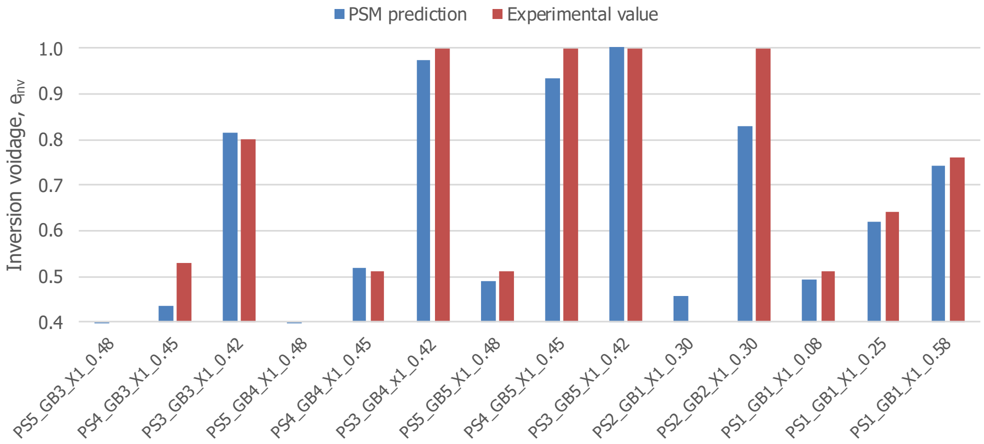

Fig. 8. Predicted vs. experimentally determined inversion voidage for all considered systems. Solids properties available in Table 1.

Experimental determination of the surface solid concentration allowed volume fraction *vs.* average voidage plots to be obtained for 14 different mixtures involving 5 cuts of glass beads and 5 calibrated plastic spheres with different densities. Despite the simple procedure to determine the concentration, repeatability tests showed reproducibility of the voidage to within 8%. PSM ability to capture of the occurrence of layer inversion phenomena appeared reliable both for exhibiting and non-exhibiting systems (11 out of 14). Quantitative agreement, with an average of 5% and a maximum of 18%, appears encouraging, particularly considering the simplicity of the PSM model formulation.

Notation

D	diameter, m
$\bar{d}$	average-to-species 2 diameter ratio, -
ε	voidage, -
F	force, N
g	gravitational acceleration, m/s^2
p	pressure, Pa
$\bar{s}$	species-2-to-average net density ratio, -
x	volume fraction

y	polydispersion index, -
ρ	density, kg/m^3
V	volume, m^3

Subscripts

1,2	referring to species
f	fluid
inv	inversion

References

Epstein N., Liquid-solids Fluidization. In: Yang W-C, ed. Handbook of Fluidization and Fluid-Particle Systems. New York: Marcel Dekker Inc.; 2003.

Vivacqua V., S Vashisth, G Hébrard, JR Grace, N Epstein, Characterization of fluidized bed layer inversion in a 191-mm-diameter column using both experimental and CPFD approaches. Chem Eng Sci. 2012. 80, 419-428.

Di Felice R., LG Gibilaro, PU Forscolo, On the inversion of binary-solid liquid fluidised beds. Chem Eng Sci. 1988. 43(4), 979-981.

Di Renzo A., F Cello, FP Di Maio, Simulation of the layer inversion phenomenon in binary liquid--fluidized beds by DEM–CFD with a drag law for polydisperse systems. Chem Eng Sci. 2011. 66(13), 2945-2958.

Di Maio F.P., Di Renzo A, Direct modeling of voidage at layer inversion in binary liquid-fluidized bed. Chem Eng J. 2016. 284, 668-678.

van der Hoef M.A., R Beetstra, JAM Kuipers, Lattice-Boltzmann simulations of low-Reynolds-number flow past mono- and bidisperse arrays of spheres: results for the permeability and drag force. J Fluid Mech. 2005. 528(1), 233-254.

NOVEL TECHNIQUE FOR COATING OF FINE PARTICLES USING FLUIDIZED BED AND AEROSOL ATOMIZER

Rongyi Zhang* , Torsten Hoffmann , Evangelos Tsotsas

Department of Thermal Process Engineering,
Otto von Guericke University, Universitätsplatz 2, 39106 Magdeburg, Germany

*Email: *Rongyi.zhang@ovgu.de*

Abstract

This work contributes to the development of the fine dispersed particles coating process by combining the fluidized bed with a micro-spray atomizer (fog generator). The feasibility of the operation is based on and demonstrated by the application of the fog generator. In our experimental studies, sodium benzoate-water solution will be firstly atomized into very small droplets through the fog generator. Therefore, the further coating process is conducted through the contact between the fog droplet (diameter less than 1µm) and the small particle in a fluidized bed. The experiment result of novel particle coating system was compared regarding the coating rate and coating layer microstructure. In addition, scanning electron microscope (SEM) and CAMSIZER were carried out to characterizing the product. The quality of fine disperses particle coating-products can be guaranteed depending on the process.

Introduction

In coating and granulation processes, a suspension or solution is sprayed on the carrier particles, and the liquid film is created on the surface of every single particle. By evaporation of the liquid new solid layers are formed, which results in the growth of the particles. Regarding these particle formation processes, several process technologies are available; for example, fluidized beds installed with a spray nozzle. Normally, the above coating method without severe agglomeration is typically limited particle sizes that are appreciably larger than 100µm. For fine-disperse particles, which are smaller than 70µm [1], the use of traditional spray fluidized bed process gets increasingly difficult. Mainly because of the large size of spray droplets reaching tens of microns leads to the onset of the cohesive behavior of the particles. Thus, smaller particles are more likely to cause the formation of agglomerates. The reason for this is that the attractive microscopic forces between the particles increase with decreasing particle size. The smaller the particles, the more they are likely to cause the formation of agglomerates: lumping of two or more individual particles into one more massive structure [2]. If such a composition is coated and breaks up afterward, defects in the coating layer develop, which may significantly reduce product quality.

At the same time, fine-disperse particles coating process of particulates are of interest for many applications, e.g., for producing precious catalyst layers with no more than the necessary use of the rare and expensive active ingredient, for manufacturing core-shell and encapsulated particles in pharmaceutical, biochemical and biomedical industries, and others. The aim of this study was thus to investigate a novel fine-disperse particle coating system, in which the micro-spray (ultra-fine droplet aerosol), instead of typically used spraying, the generated micro-spray was supplied into the chamber of laboratory-scale fluidized bed from the one side. For that aim, recently developed liquid atomization method and the atomizer device design [3] were used to produce and supply micro-spray (fog) on the fluidized bed. The working hypothesis was that the application of very fine droplets, with diameters 10-100 times smaller than in regular sprays, would be expected suitable for fine particles, enable considerably uniform coating layers and lower process temperatures than traditional spray-fluidized bed particle coating systems.

Material and Methods

A simple and reliable technique for the generation of micro-spray was recently developed and investigated by Mezhericher et al. [3, 4]. Compare to traditional liquid atomization technologies [5]. This method is based on shear-driven disintegration by gas jets of thin liquid films formed by gas bubbles on the liquid surface. The central part of the device was an elastic rubber tube which was perforated with orifices along the tube circumference at several axial positions. The tube was horizontally oriented and partially submerged into a vessel filled with coating solution: the lower portion of the tube was immersed in the liquid, and the upper portion of the tube was exposed to the environment, see Fig. 1a. The tube was connected to a source of compressed air, and the supplied air was discharged through the perforated orifices. Ensembles of small bubbles which caused by compressed air occurred in the lower part of the tube, then came up to the liquid surface and created a froth - ensembles of thin spherical liquid films in the vicinity of the tube upper part. Subsequently, the air discharged through the upper orifices broke and disintegrated these liquid films into micro-spray, as schematically illustrated in Fig. 1b. In this study, we adopted the fog generator described previously developed by Mezhericher [3, 6], Droplet size between 0.1 µm and 20 µm (volume based) and 99 % are smaller than 1 µm (number based) [4].

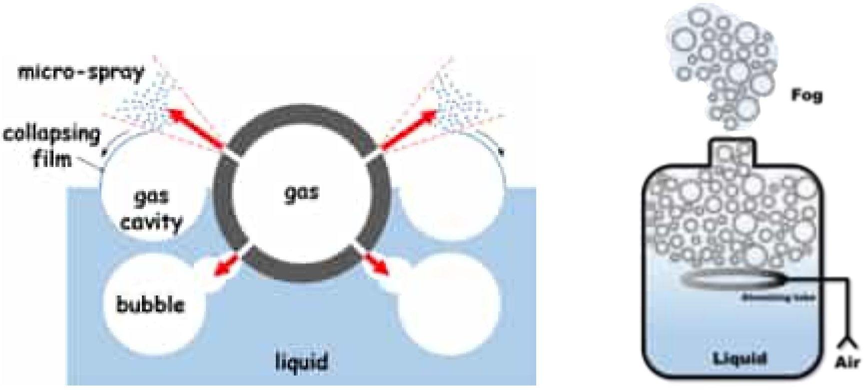

Fig. 1. A-sketch of the new atomization method [3]; b- Schematic of fog generator enabling generation of micro-spray using innovative liquid atomization method.

The droplet size distributions produced by the fog generator for different atomizing air pressures were characterized separately by means of a laser diffraction system (Particle Analyzer LA-960, Retsch Technologies GmbH, Haan, Germany), the measurement was also worked for different coating solution composition or concentration. After a series of pre-tests, the pressure of the compressed air was determined to be 5.5 bar. The liquid flow rates of atomized solution were determined by the weighing method using the procedure described in [4]. For the actual mass of the sodium benzoate solution supplied to the particle coating, it is equal to the mass of the peristaltic pump pumped into the container throughout the experiment. In order to support the solution initial level in the middle of the fog generator cross section stays the same during the experiment.

This work contributes to the development of a coating process of finely dispersed particles by combining the fluidized bed with a fog generator. Laboratory-scale setup (GPCG 1, Glatt GmbH, Weimar, Germany) was modified to incorporate a side inlet into the chamber providing the inflow of micro spray and mixing with the fluidized particles, as schematically shown in Fig. 2. For the coating experiments, two types of particles were utilized, glass beads (Sigmund Lindner GmbH, Germany) with a mean diameter of 195µm and 66µm. These two types of particles represent the normal small particle and fine dispersed particle. The coating solution is the aqueous solution of sodium benzoate and HPMC (hydroxypropyl methylcellulose) with different concentration. During the coating process, the fluidized particles contact with micro-spray of the coating solution, and drying of the solution deposited on the particles by the high-temperature fluidizing air.

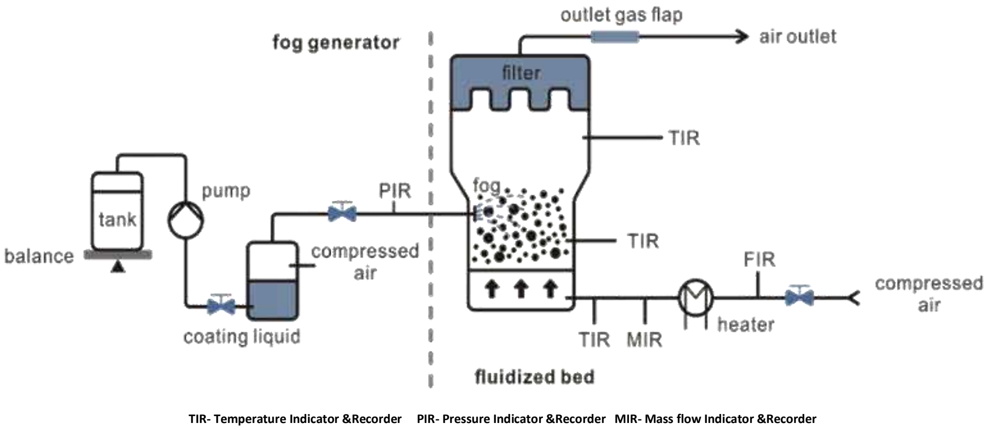

Fig. 2. Scheme of experiment setup.

Particle size and coating structure influences many properties of particulate materials and is a valuable indicator of quality and performance. Particle size distribution and microstructure of products at different times were tested to characterize the coating layer quality versus time. During the process of coating, samples were taken in a defined period; for our process, it was 20 minutes. A constant number of samples are collected using a "sample taker" device in the fluidized bed. Sampling time is usually less than 10 seconds, so it does not affect normal fluidization To perform the analysis of particle size distribution and coating layer microstructure, we randomly picked several coated particles from the samples and investigated that using particle measuring device (CAMSIZER, Retsch Technology GmbH, Germany) scanning electron microscopy (SEM, model Phenom G2 Pro & model Jeol JSM-5410).

Table 1. Main parameters of the particle coating process.

Parameter	Value Group A	Value Group B	Unit
Mean particle initial diameter	195	66	μm
Diameter of fluidized bed chamber	150	150	mm
Initial mass of particle bed	1	1	kg
Mass flow rate of fluidization air	23	10	kg/h
Temperature of fluidization air	90	90	°C
Pressure of atomizing air	5.5	5.5	bar

To study the influence of process parameters, two series in total eight experiments were carried out, denoted by No.A1-A4 and No.B1-B4, see table 1. For the experiment, the process temperature was controlled at 90℃ and pressure of atomizing air is 5 bar. For Group A and Group B experiments, Mass flow rate of fluidization air was set to 23kg/h and 10kg/h, respectively. Each experiment was performed three times, and the average of the three experiments was taken as the result. The influence of coating solution was studied by running experiments with different composition and concentration, see Table 2.

To start the experiments, Fluidized bed containing an initial feed of 1 kg of glass beads needs to warm up till the desired temperature. Fog generator is not still connected in this stage. Starting the coating process, the fluidized bed needs to be in a temperature balance. When the temperature reached the desired point, the next stage starts. The fog generator is initiated after the airflow and temperature reach a steady state. Samples were collected from the bed by sample taker periodically and used for analysis. The processing time in each experiment was 360 min.

Table 2. Coating solution plans for experiments.

	NaB (wt.%)	HPMC (wt.%)		NaB (wt.%)	HPMC (wt.%)
A1	30	0	B1	30	0
A2	30	1	B2	30	1
A3	30	1.5	B3	30	1.5
A4	30	2	B4	30	2

Experiment Results

Figure 3a represents an increase in D50 of the particles of the group A. The trend of increase in particle size is not constant, and its fluctuations intensify when having more concentrations of HPMC for coating. However, the general trend shows that particle size increases from the first minutes of coating, and it stays constant at a specific time in which the particle is fully coated with the coating material. For group B, the regime of increasing particle size in a period of coating is different with bigger particles. As particles become smaller, the first coating layer plays a significant role in determining the final particle size. Figure 3b shows that in most cases, increasing in particle size happens in the first hour of the coating process. Since then, the trend of increasing the particle size slows down, but coating continues on the surface of glass particles.

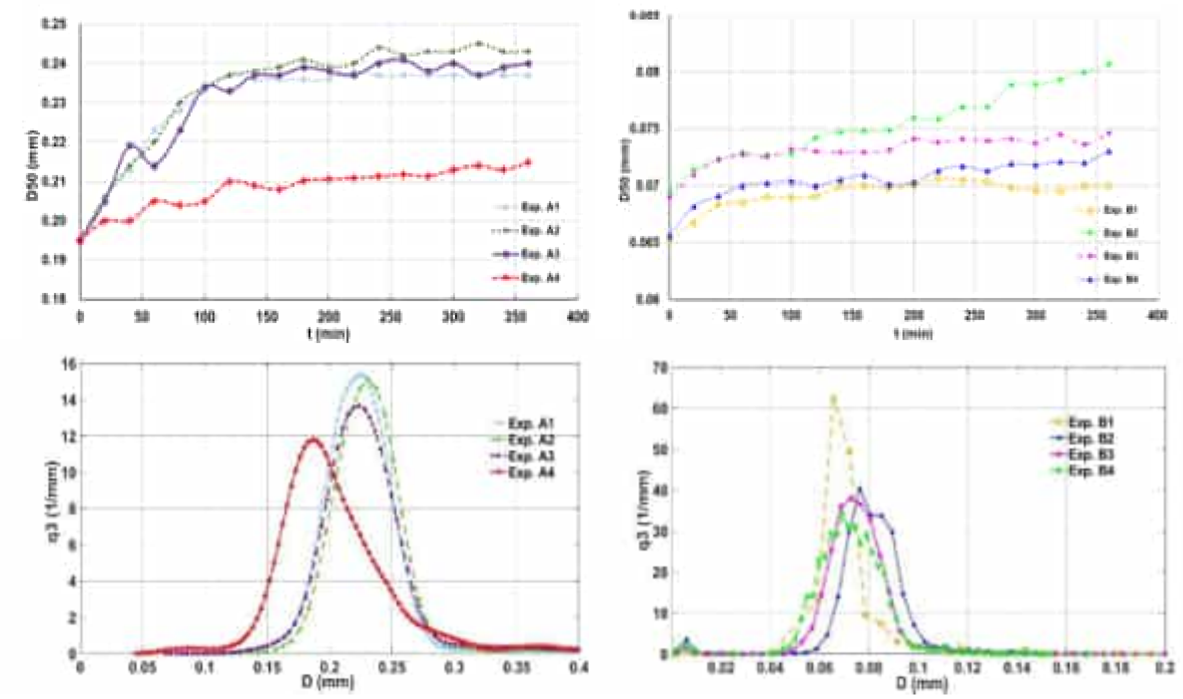

Fig. 3. D50 versus time in different experiments. A1-A4 (left, top), B1-B4 (right, top) & particle size distribution of resulted samples of experiments A1-A4 (left, bottom) and B1-B4 (right, bottom).

As Fig. 3 displays, the most significant growth rate of coating processes was obtained at the experiment A2 and B2 when HPMC is 1wt.%. The rate of the coating was relatively slow when HPMC is not added, but when the HPMC concentration continues to increase to 2wt.%, the coating rate was decreased, and 1wt.% is determined to be the suitable concentration.

From the SEM measuring results, the novel particle coating system is working for normal small particles (group A). These observations also practically confirmed the results revealed by particle size analysis of CAMSIZER. Figure 4a shows that the experiment A1 has a good layer of the coating after 360 minutes.

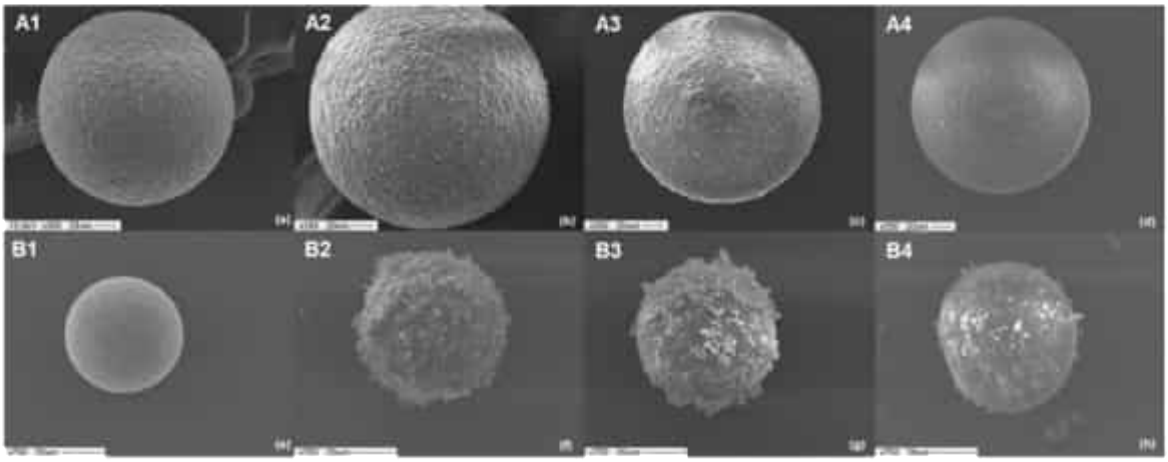

Fig. 4 SEM picture of coatings in the 360th minute from experiments group A (top, a b c d) and group B (bottom, e f g h).

For the fine particles in group B, SEM results showed different microstructure results by using the fog generator coating system. Figure 4e shows that the coating quality for small particles being coated just with Sodium Benzoate is acceptable, the coating is uniform and covers all outer surface of the glass particle, but still not as uniform as A1. When HPMC added, In the experiment B2, the resulted coated glass beads show a different regime of the coating. Unlike normal small particles (group A), finely dispersed particles being coated with HPMC have a severe non-uniform surface which can be seen in Figure 4f, 4g, and 4h. This effect might not be realized from CAMSIZER analysis, but SEM images can reveal the difference. For the fine disperse particles, the solution with HPMC by itself produces considerable foam inside the fog generator. As the foam could quickly enter the fluidized bed., it deposited much easier on the surface of the fine particle from the beginning of the coating process, and therefore most of the increase in particle size happens in this time.

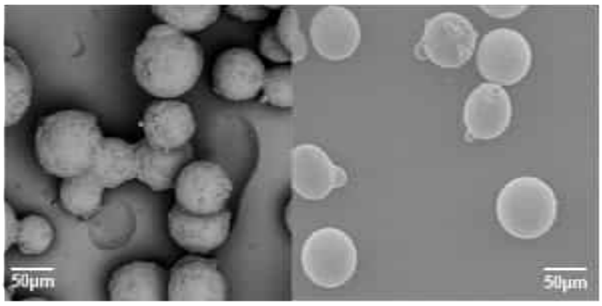

Fig. 5 SEM picture of coatings in spray fluidized bed (left) and fluidized bed with fog generator (right).

From the analysis of SEM images of particle coatings, it follows that the size of utilized spray droplets may have an influence not only on the coating results but also on agglomeration. According to Dewettinck and Huyghebaert, spray fluidized bed coating without severe agglomeration is typically limited to particle sizes that are appreciably larger than100µm [1]. Therefore, in group A, the mean diameter of the particle is 195µm. When the novel particle coating system in this study which has smaller particle size spray droplet was used, no agglomeration occurred as expected.

Moreover, SEM analysis didn't show visible signs of agglomeration between fine particles in group B experiments. Figure 5 reveals the agglomeration performance of the same particles in a conventional spray fluidized bed and the new coating device of the present study. It can be seen that this study solves the agglomeration problem in the coating of small particles to some extent.

At the same time, the observation about difference in coating microstructure generated by the micro-spray is supported by the literature, e.g., Rieck et al. [7] and Tsotsas [8] demonstrated that in spray fluidized bed granulation, fast-drying led to compact and smooth whereas slow drying resulted in porous and rough particle microstructures it is also applicable for the fluidized bed with fog generator. In addition, the different ratio between the droplet evaporation and crystallization timescales for submicron and regular micron-sized droplets might explain the visible difference in the microstructure. As it was reported in the literature [9], fine droplets have a smaller ratio of timescales of droplet evaporation and crystallization, and thus tend to produce more amorphous structures on their evaporation. Hence, a detailed comparison between the microstructure, porosity of the obtained fine coating layers for different size particles is a question for further study.

Conclusions

this work, a new system for particle coating is presented and investigated. The micro spray droplets are utilized to produce coating on particles in a laboratory-scale fluidized bed. Sodium benzoate-water solution was atomized by recently developed fog generator into very small droplets with mean diameter less than 1µm to coat 195µm 66µm glass particles. The microscopic analysis of coating layer distribution demonstrated the ability of the new system to produce coating layers for both normal small particle and fine dispersed particle with out severe agglomeration. In future work, coating solution will be improved to eliminate the effect of foam produced by HPMC on coating roughness. In addition, the experimental results obtained in different types of fluidized beds (e.g. Wurster bed) will be compared. To describe the continuous spray agglomeration, process a stochastic modelling approach based on a Monte Carlo method will be developed and compared with the experimental results.

Nomenclature

D50,3	particle size Q3(d50) =0.5, µm	HPMC	hydroxypropyl methylcellulose
T	temperature, °C	t	time, min

References

[1] N. Hampel, E. Roydeva, A. Bück, E. Tsotsas, 2018. Coating of finely-dispersed particles by means of two-fluid nozzle, Particuology 38, 80-93.

[2] B. Ennis, G. Tardos, R. Pfeffer. A microlevel-based characterization of granulation phenomena, Powder Technology 1991. 65, 257–272.

[3] M. Mezhericher, I. Ladizhensky, I. Etlin, Atomization of liquids by disintegrating thin liquid films using gas jets, Int J Multiphas Flow 2017, 88, 99-115.

[4] M. Mezhericher, N. Razorenov, G. Mazor, Y. Ju, H.A. Stone, Submicron aerosols of liquid fuels: Method of production, experimental characterization and a semi-empirical model, Appl-Energ 2019, 235, 1651-1663.

[5] A.H. Lefebvre, V.G. McDonell, Atomization and Sprays, 2nd ed., Taylor & Francis, CRC Press, Boca Raton, 2017.

[6] M. Mezhericher, J.K. Nunes, J.J. Guzowski, H.A. Stone, Aerosol-assisted synthesis of submicron particles at room temperature using ultra-fine liquid atomization, Chemical Engineering Journal 2018, 346, 606-620.

[7] C. Rieck, T. Hoffmann, A. Bück, M. Peglow, E. Tsotsas, Influence of drying conditions on layer porosity in fluidized bed spray granulation, Powder Technol 2015, 272, 120-131.

[8] E. Tsotsas, Influence of drying kinetics on particle formation: a personal perspective, Dry Technol 2012, 30, 1167-1175.

[9] E. Amstad, M. Gopinadhan, C. Holtze, C.O. Osuji, M.P. Brenner, F. Spaepen, D.A. Weitz, Production of amorphous nanoparticles by supersonic spray-drying with a microfluidic nebulator, Science 2015, 349, 956-960.

THE ROLE OF OPERATING PARAMETRS ON THE PERFORMANCE OF THE CATALYTIC HIGH TEMPERATURE FISCHER-TROPSCH SYNTHESIS IN FLUIDIZED BED REACTOR

Mahdi Sharifian[1*], Francesco Rossi[2], Federico Galli[1], Gregory S. Patience[1]

[1]Department of chemical engineering, Polytechnique Montreal, 2500 chemin de PolytechniqueMontréal (Québec) H3T 1J4, Canada
[2]Forney Hall of Chemical Engineering, Purdue University, 480 Stadium Mall Drive, West Lafayette, IN 47907-2100, United States

*Email: *mahdi.sharifian@polymtl.ca*

Abstract

Converting shale gas into long chain hydrocarbons is an attractive economic and environmental alternative to venting and flaring. Catalytic partial oxidation coupled with Fischer-Tropsch synthesis (FTS) convert remote natural gas to transportable liquid hydrocarbons. Here we selected a kinetic model to simulate a FTS fluidized bed reactor with Aspen plus software and compared the results with available experimental data. We calculated the effect of reaction temperature, pressure, and superficial velocity of syngas feed on the yield of gasoline (C_5 fraction). Pressure increases leads to higher production of gasoline while temperature increase up to 300^{0}C converts the syngas to lighter hydrocarbons. Moreover, increasing the superficial velocity has a negative impact on gasoline production as it reduces the residence time inside the reactor and eventually we estimated the optimum conditions to maximize the yield of gasoline by using the optimizer subroutine of Aspen plus as few investigations have been previously done in order to optimize production of specific products.

Introduction

Fischer-Tropsch synthesis (FTS) is demonstrated as a feasible way for production of liquid to fuels from coal, natural gas and biomass via synthesis gas, Zhang et al (2018). Synthetic fuels have a superior quality due to the absence of aromatics, sulfur, and nitrogen compounds, Zhang (2018) and Rahimpour (2010). FTS technology is one of the notable alternatives for liquid fuels in case of oil deficiency, de Deugd (2013).

Many studies have been done on the kinetics of the Fischer-Tropsch reaction using various iron catalysts and many kinetic models have been proposed, Montazer-Rahmati (2001). Each of these models agree with experimental results in a narrow range and cannot be applied to a wide range of conditions. The complex fluid dynamics of a fluidized bed reactor (gas bubbles and solids circulation) makes kinetics analysis challenging. Also, catalyst synthesis and reactor design—grid configuration, cyclones, and filters, require more attention according to Menéndez and Patience (2019). Most of studies have been accordingly carried out in fixed bed or slurry phase, Montazer-Rahmati (2001) and Zimmerman (1990), and rare cases investigated the modeling of fluidized bed reactors Kazemeini (2001), Fernandez (2006) and Nabipoor (2012).

The objective of this work is to select a suitable kinetic model proposed for FT synthesis and optimize its parameters so that has a good agreement with the available experimental data given by Fernandes (2005), (2006) and Chang (2007) in order to use for our pilot plant unit in future. The impact of temperature, pressure and synthesis gas ratio on the Fischer-Tropsch synthesis using this model was also investigated and the operating parameters to optimize the gasoline yield in the product were specified as well.

Process Simulation

In this study, the main goal is simulation of Fischer-Tropsch synthesis to convert the Syngas $(H_2 + CO)$ into hydrocarbons in high temperature and high pressure fluidized bed reactor. As the temperature is high enough (higher than 250ºC), the reaction is expected to carry out completely in gas phase condition over iron catalyst as mentioned by Rahimpour (2010) and Dry (1999). The ranges of operating conditions has been considered as 250°C-300ºC, 10 bar - 20 bar and syngas molar ratio (H_2/CO) of 0.5-2. In order to assign the reactions and hydrodynamic properties of fluidized bed reactor, a plug flow reactor was applied as a proper set in Aspen Plus version 8.4. Figure 1 shows the schematic of process flow.

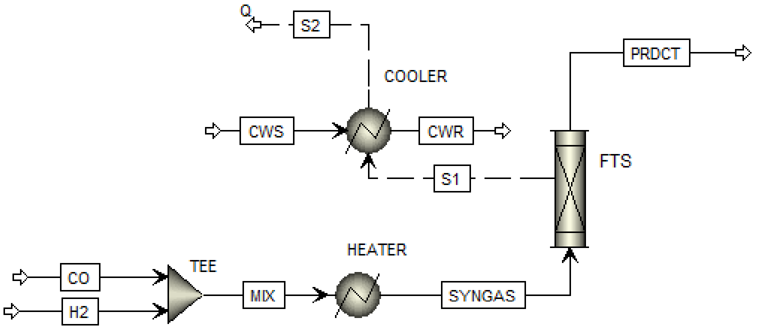

Fig.1. Process flow diagram of Fischer-Tropsch synthesis in Aspen Plus

Kinetic Model

FTS reaction may be viewed as a methylene polymerization reaction where the methylene monomer unit $(-CH_2)$ is not initially present. Fernandes (2006) mentioned that hydrogenation of CO generates the methylene monomer in situ, and polymerization occurs through addition of methylene units in the growing hydrocarbon chain. The FT synthesis is a surface polymerization reaction and reactants, CO and H_2, absorb and dissociate at the surface of the catalyst and react to from chain initiator (CH_3), methylene (CH_2) monomer and water according to Nabipoor (2012). The Fischer–Tropsch synthesis over iron catalyst can be approximated as simultaneous series–parallel reactions for the FT reaction and the water gas shift (WGS) that can be found in Rafiee (2012):

$$\mathrm{nCO + 2nH_2 \rightarrow n(-CH_2-) + nH_2O} \qquad (\Delta H_r)_{FT} = -172\ \mathrm{kJmol^{-1}} \tag{1}$$

$$\mathrm{CO + H_2O \leftrightarrow CO_2 + H_2} \qquad (\Delta H_r)_{WGS} = 39.89\ \mathrm{kJmol^{-1}} \tag{2}$$

To adjust the kinetic model in Aspen Plus simulator, we applied 8 sets of reactions proposed in literature for FT and WGS, Zimmerman (1990), Van der lann (2000), Fernandes (2006), and then tried to compare the simulation results of CO conversion to the experiments reported in Fernandes (2006), Chang (2007) and Kang (2011). According to our simulation results, we selected the model given by Van der Lann and Beenackers (2000) giving closer component fractions to those obtained by experiments:

$$r_{FT} = k_{FT}\frac{P_{H_2}P_{CO}}{1 + a_{FT}P_{CO} + b_{FT}P_{H_2O}} \tag{3}$$

$$r_{WGS} = k_{WGS}\frac{P_{CO}P_{H_2O} - \frac{P_{H_2}P_{CO_2}}{K_P}}{\left(1 + a_{WGS}P_{CO} + b_{WGS}P_{H_2O}\right)^2}\ , \qquad K_P = e^{\left(\frac{4578}{T} - 4.33\right)} \tag{4}$$

Table 1. Coefficients of Fischer-Tropsch Kinetic

	$\boldsymbol{k_{0,i}\ (mol/s.kg.Pa)}$	$\boldsymbol{E_i\ (kJ/mol)}$	$\boldsymbol{a_i\ (Pa^{-1})}$	$\boldsymbol{b_i\ (Pa^{-1})}$
FT reaction	7.79×10^{-14}	1	5.36×10^{-7}	3.227×10^{-5}
WGS reaction	1.77×10^{-12}	1	2.1×10^{-6}	2.419×10^{-5}

In the simulation procedure, we considered a once through FT reactor to the process and we lumped the reaction products. Hence, in addition to CO , $\mathrm{CO_2}$, $\mathrm{H_2}$ and $\mathrm{H_2O}$, a “Pseudocomponent” was defined in the software as a mixture product of hydrocarbons from $\mathrm{C_1}$ to $\mathrm{C_{30}}$. The product distributions tend to obey the Anderson-Shultz-Flory (ASF) chain-length statistics Fernandes (2006) and Rafiee (2012). Here we assume that α_{ASF} is the same for paraffins and olefins, Rafiee (2012):

$$W_n = n(1-\alpha_{ASF})^2\alpha_{ASF}^{n-1} \tag{5}$$

In which n is the number of carbon atoms and W_n is the weight fraction of hydrocarbon with n carbon atoms. We utilized the chain growth probability, α_{ASF} as calculated based on the correlation developed by Lox and Froment (1993a, 1993b) and Rafiee (2012). (Table 2)

$$\alpha_{ASF} = \frac{K_1P_{CO}}{K_1P_{CO} + K_2P_{H2} + K_3} \tag{6}$$

Table 2. Model coefficients for calculation of α_{ASF}

Parameter	$\boldsymbol{K_i(T_0)}$	$\boldsymbol{E_i}$
$\boldsymbol{K_1}$	1.22×10^{-6}	0
$\boldsymbol{K_2}$	1.05×10^{-6}	94.5
$\boldsymbol{K_3}$	2.36×10^{-6}	132.3

We used the process and reactor specifications of Fernandes (2006) and adapted according to the data given by Chang et al (2007).

Results and discussion

Figure 2 shows the graph of calculated values in simulation versus experimental data by Chang (2007). AAD representing average absolute deviation percentage, was defined to compare the simulation results of CO conversion to experiment and it was 7.8% which is highly acceptable comparing to the previous results reported in Chang (2007) and Kazemeini (2012).

$$AAD = \frac{1}{n}\sum_{i=1}^{n}\left|\frac{X_{CO}^{cal} - X_{CO}^{exp}}{X_{CO}^{exp}}\right| \times 100 \tag{7}$$

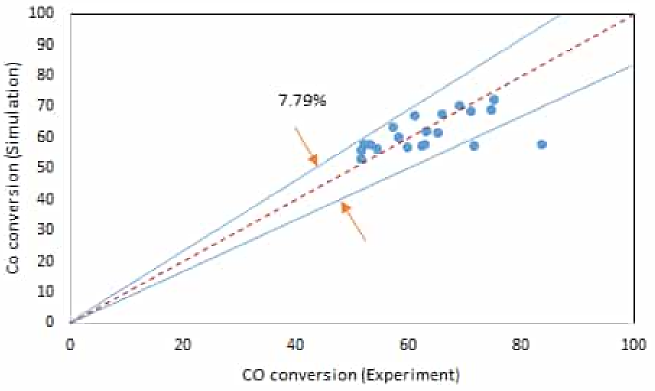

Fig.2. CO conversion, simulation versus experiment by Chang (2007).

We also set the specification of the reactor to those considered by Fernandes and Sousa (2006) to compere our simulation results to their data. These specification of the FTS can be found in Fernandes (2006). For instance, Fernandes considered the superficial gas velocity 0.4 - 0.6 m/s to make sure that it is sufficiently higher than the minimum fluidization velocity of the catalytic bed. Figure 3 shows a comparison between syngas conversion as well as gasoline weight fraction. In this case, pressure and temperature are 20 bar and 270°C respectively as $U_0 = 0.6\, m$.

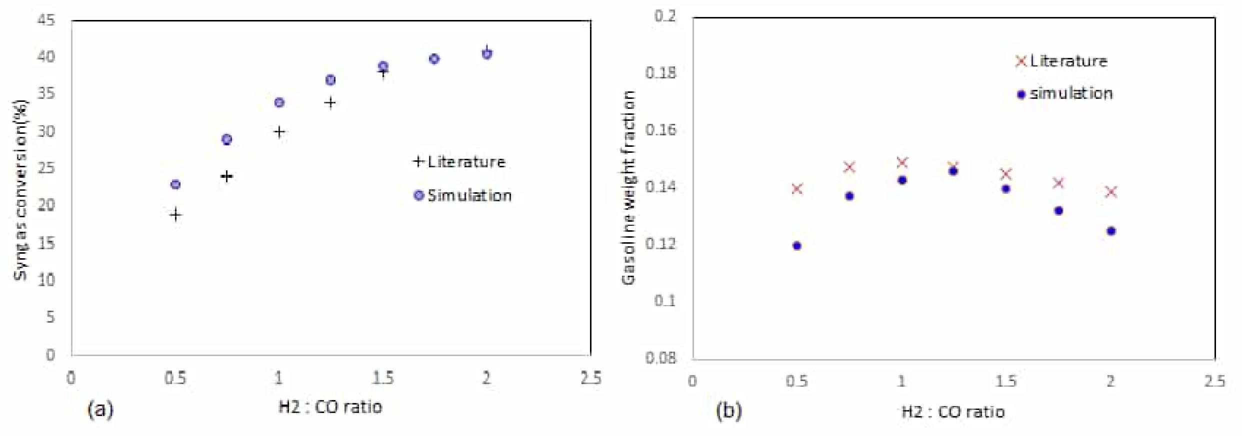

Fig.3. Simulation results versus Fernandes data; Syngas conversion to hydrocarbon (a), gasoline fraction (b) at 20 bar and 270°C

The kinetic model well predicts the increasing conversion of CO to hydrocarbon by increasing the syngas ratio as the ratio is going towards the stoichiometry of the reaction. The gasoline weight fraction in the outlet product is also increased by the ratio and further increasing of hydrogen ($\mathrm{H2{:}CO} > 1.25$) will decrease the gasoline fraction since hydrogen acts as the terminator of the reaction and prevents the forming of long chain hydrocarbons in range of gasoline, diesel and heavier products.

Figure 4 shows the effect of varying the reaction temperature and pressure on the yield of gasoline in the simulation. Increasing the temperature, the gasoline production rate decreases since the catalyst promotes the methane production and deactivates faster due to sintering and coking. Increasing the pressure from 10 bar to 20 bar, on the other hand, has not a substantial impact on the production rate according to our simulation and the data given by Fernandes (2006).

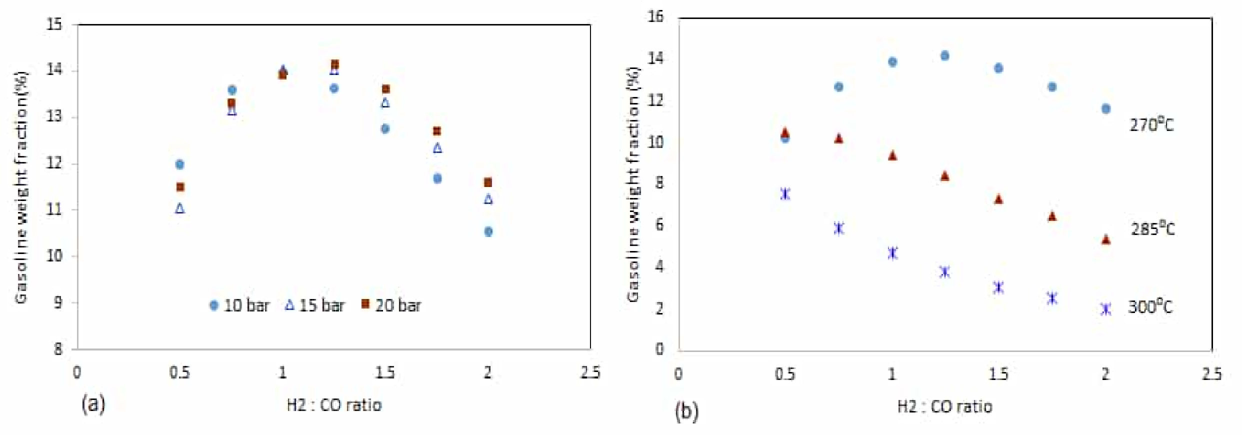

Fig.4 Gasoline weight fraction in the product vs molar ratio at (a) 270°C and 10-20 bar, and at (b) 20 bar and 270-300°C

We also investigated the influence of the superficial syngas velocity on the syngas conversion as well as the gasoline production (Figure 5). As the operating pressure and temperature did not change and only the syngas velocity decreased from 0.6 to 0.4 m/s, the residence time inside the reactor increased. At molar ratio $(\mathrm{H2}/\mathrm{CO})$ higher than 1.5, the impact of syngas velocity is negligible. Instead the flow rate has an influence on the product distribution with the better result for 0.4 m/s (at 20 bar and 270ºC).

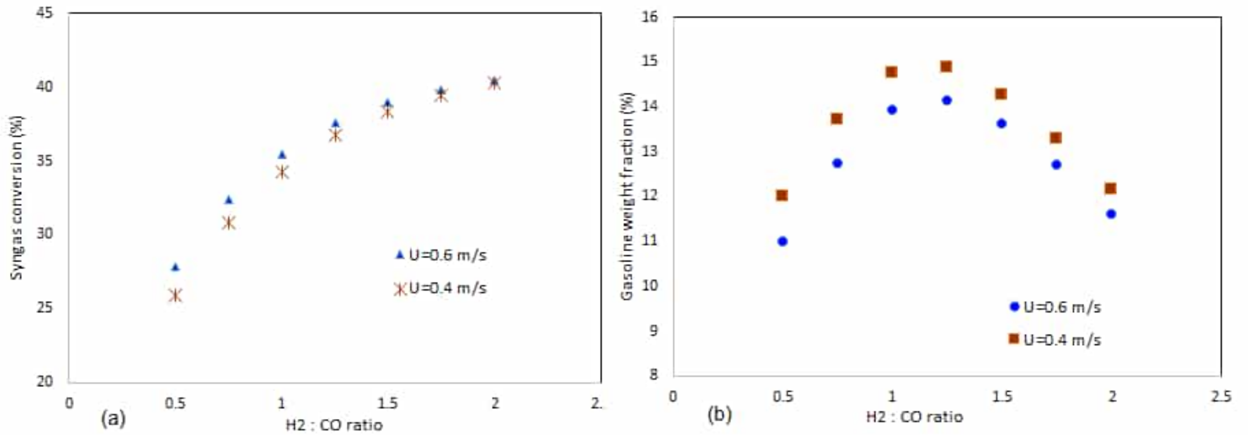

Fig. 5. Syngas conversion to hydrocarbon (a) and gasoline fraction in product (b) at different superficial gas velocities

Optimization

In order to find the operating parameters to maximize the yield of gasoline in the product stream of FT reactor, we used the optimizer module of Aspen Plus and applied some codes in its FORTRAN environment to compute the gasoline weight fraction as the cost function. We also added a constrain for CO conversion $(X_{CO} \geq 0.75)$ to provide a reasonable conversion of carbon monoxide through the reaction (Table 3).

Table 3. Optimum operating conditions for gasoline production

$T(^0C)$	$P\ (bar)$	$U(m/s)$	$H_2 : CO\ ratio$	$CO\ conversion\%$	$Gasoline\ wt\%$
266	20	0.4	1.5	0.78	14.6

Conclusion

The FTS process in a fluidized bed reactor was simulated using Aspen Plus simulator and selecting a proper set of kinetic model among eight models of Fischer-Tropsch synthesis from literature to fit the simulation results to the experimental data at the same condition. Then, the effect of temperature and pressure on the gasoline yield as the target value was investigated and the optimized operating conditions based on this simulation were computed using the optimizer subroutine of Aspen plus software. In the next step, we intend to start our pilot set-up which has been designed for High temperature FTS to compare our experimental data to the model, improve the kinetic reaction parameters and develop a mathematical model which is going to be verified by experiment.

Notation

ΔH_r	Heat of reaction, kJ/mol	T	Reaction temperature, K
E	Activation energy, kJ/mol	r_{FT}	reaction rate of Fischer-Tropsch, $mol.kg^{-1}.s^{-1}$
P_i	Partial pressure of component i, Pa	r_{WGS}	reaction rate of water gas shift, $mol.kg^{-1}.s^{-1}$

W_n Weight fraction of hydrocarbon with n carbon atoms

α Chain growth probability of hydrocarbons

References

J. Chang, L. Bai, B-T. Teng, R.-L. Zhang, J. Yang, Y.-Y. Xu, H.-W. Xiang, Y.-W. Li, Kinetic modeling of Fischer-Tropsch synthesis over Fe-Cu-K-SiO2 Catalyst in slurry phase reactor,

Chem. Eng. Sci. 62 (2007) 4983-4991

R.M. de Deugd, F. Kapteijn, J.A. Moulijn, Trends in Fischer–Tropsch reactor technology—Opportunities for structured reactors, Top. Catal. 26 (1–4) (2013) 29–39.

Mark E. Dry, Fischer–Tropsch reactions and the environment, Applied Catalysis A: General 189 (1999) 185–190.

F.A.N. Fernandes, Polymerization Kinetics of Fischer-Tropsch Reaction on Iron Based Catalysts and Product Grade Optimization, Chem. Eng. Technol. 28 (2005) 930-938

Fabiano A. N. Fernandes and Elida M. M. Sousa, Fischer-Tropsch Synthesis Product Grade Optimization in a Fluidized Bed Reactor, American Institute of Chemical Engineers AIChE J, 52 (2006) 2844–2850.

S-H Kang, J. W. Bae, J-Y Cheon, Y-J Lee, K-S Ha, K-W Jun, D-H Lee, B-W Kim, Catalytic performance on iron-based Fischer–Tropsch catalyst in fixed-bed and bubbling fluidized-bed reactor, Applied Catalysis B: Environmental 103 (2011) 169–180.

Mohammad Kazemeini, Reza Maleki, Moslem Fattahi, Modelling of Fischer-Tropsch Synthesis in a Fluidized Bed Reactor, Advanced Materials Research Vol. 586 (2012) 274-281.

Lox, E. S., & Froment, G. F. Kinetics of the Fischer–Tropsch reaction on a precipitated promoted iron catalyst. 2. Kinetic modelling. Industrial & Engineering Chemistry Research, 32 (1993a) 71–82.

Lox, E. S., & Froment, G. F. Kinetics of the Fischer–Tropsch reaction on a precipitated promoted iron catalyst. 1. Experimental procedure and results. Industrial & Engineering Chemistry Research, 32 (1993b) 61–70.

Miguel Menéndez, Javier Herguido, Ariane Bérard and Gregory S. Patience, Experimental Methods in Chemical Engineering: Reactors—Fluidized Beds, Canadian Journal of Chemical Engineering, Volume 97, 2019.

Montazer-Rahmati, Mohammad Mehdi and Mehdi Bargh-Soleimani, Rate equations for Fischer-Tropsch reaction on a promoted iron catalyst, Canadian Journal of Chemical Engineering, Volume 79, 2001.

Mojtaba Nabipoor Hassankiadeh, Ali Khajehfard, and Morteza Golmohammadi, Kinetic and Product Distribution Modeling of Fischer-Tropsch Synthesis in a Fluidized Bed Reactor, International Journal of Chemical Engineering and Applications, Vol. 3, No. 6, 2012.

Ahmad Rafiee, Magne Hillestad, Staging of the Fischer–Tropsch reactor with an iron based catalyst, Computers and Chemical Engineering 39 (2012) 75– 83.

M.R. Rahimpour, M.H. Khademi, A.M. Bahmanpour, A comparison of conventional and optimized thermally coupled reactors for Fischer–Tropsch synthesis in GTL technology, Chem. Eng. Sci. 65 (23) (2010) 6206–6214.

Van der Laan, G.P. and A.A.C.M. Beenackers, Intrinsic kinetics of the gas–solid Fischer–Tropsch and water gas shift reactions over a precipitated iron catalyst. Applied Catalysis A: General, 193 (1–2) (2000) 39-53.

Xiaolai Zhang, Weixin Qian, Haitao Zhang, Qiwen Sun, Weiyong Ying, Effect of the operation parameters on the Fischer–Tropsch synthesis in fluidized bed reactors, Chinese Journal of Chemical Engineering 26 (2018) 245–251.

Zimmerman, W. H., & Bukur, D. B. Reaction kinetics over iron catalysts used for Fischer–Tropsch synthesis. The Canadian Journal of Chemical Engineering, 68 (1990) 292–301.

USING MACHINE LEARNING TO ELUCIDATE THE KINETICS OF CRACKING REACTIONS IN A DOWN FLOW REACTOR SYSTEM

Qi Xu*, Aaron Akah, Musaed Ghrami, Abdennour Bourane, Ibrahim Abba

Research and Development Center, Saudi Aramco, Dhahran, Saudi Arabia, 31311
*Email: *Qi.Xu@aramco.com*

Abstract

Use of machine learning (ML) to aid innovation in the chemical and refining industry is becoming ubiquitous. In this study, machine learning was employed to elucidate the kinetics of olefins production from the direct cracking of crude oil feedstock in a dual-downer high severity fluidized bed system. The reactions considered include both catalytic and thermal cracking chemistries. First, many sets of experimental data were produced in a lab-scale microdowner reactor, which were then used to train the ML algorithm to: (a) enable prediction of olefins and (b) guide retro-synthesis, through innovative combinations of operating conditions, catalyst properties and reactor geometry. Second, predictions from the trained model were compared with those from our conventional 5-lump kinetic model, and they showed good agreement. Finally, using the ML-based kinetic model, results from this study provided deeper insights into the important role of thermal and catalytic cracking as competing mechanisms in the direct cracking of crude oil under high-severity operating conditions. Specifically, the study elucidated the dominance of thermal cracking mechanism at high temperatures representative of high-severity operating conditions. Thermal cracking mechanism is comparatively negligible at lower temperatures representative of conventional FCC conditions, where the catalytic cracking mechanism is dominant.

Introduction

The demand for light olefins, such as ethylene and propylene in the petrochemicals industry continues to grow, and the direct conversion of whole crude oil is expected to bridge the gap between demand and supply. It was reported by Tullo (2019) that by 2030, the demand for gasoline and other fuels will be on the decline while the petrochemical sector, in contrast, will grow. The growth in demand for petrochemicals acts as an incentive for refiners to reconfigure their fluid catalytic cracking (FCC) units to increase yield of light olefins, especially propylene.

Since the first commercial FCC plant began processing petroleum oil with a capacity of 13,000 barrels per day in 1942, many improved FCC design and catalysts have been developed over time, enabling refineries to meet requirements of evolving environmental regulations and increasing demand for liquid fuels and petrochemicals. Most recently, a high severity fluid catalytic cracking (HSFCC™) technology was developed by an alliance comprising Saudi Aramco, JX Nippon Oil & Energy Corp.(JX), King Fahd University of Petroleum and Minerals (KFUMP). This alliance culminated in a 76,000 BPD HSFCC™ commercial unit, which has been in operation since 2019 in Onsan refinery complex in Ulsan, South Korea. Compared to conventional FCC process, the HSFCC™ technology features higher reaction temperature (550-650 °C), large catalyst-to-oil ratio (20-30), short contact time (0.5-1.0 second), and a down flow reactor design, and is able to produce high light olefin yields from vacuum gas oil (VGO) as reported in Fujiyama et al. (2007), or a wide range boiling feed such as whole crude.

The complex nature of FCC feeds such as whole crude oil, makes it extremely difficult to study the inherent kinetics at a molecular level. One strategy for kinetic models is to group the complex mixtures into pseudo-components, or lumps, with similar behavior, and these are used to derive a number of kinetic equations. The first lumping model proposed was a three-lump model advanced by Weekman et al. (1970) that consisted of heavy feed lump, gasoline lump, and the remaining hydrocarbon lump (gases + coke). Since then, the lumping model has been widely used to study catalytic cracking processes and the number of lumps has been consistently increasing to obtain a more detailed understanding of the reaction mechanism and the prediction of the product distribution. Most of the work on kinetic modelling of FCC is based on VGO as feed and other heavy fractions, but does not address the contribution of thermal cracking. Recently, Corma et al. (2018) and Usman et al. (2017) have studied the direct catalytic cracking of crude oil to petrochemicals via kinetic modelling, but there is not enough data in the literature quantifying the thermal cracking contribute to the overall process.

The main objective of the present study is to gain a fundamental understanding of thermal and catalytic cracking as competing mechanisms in the direct cracking of crude oil under high-severity operating conditions, using the power of machine learning algorithm together with a conventional five-lump kinetic model for both thermal and catalytic cracking. This study will determine the contribution from thermal cracking to the conversion of whole crude oil to petrochemicals, based on the down flow HSFCC™ technology. The HSFCC™ operates at high temperatures (550-650 °C), and at these temperatures the contribution of thermal cracking cannot be ignored. Hence, a better understanding of the contribution from thermal cracking in the HSFCC process is desirable to optimize the light olefins yields.

Experimental

Experiments in this work were carried out using a Microdowner (MD) unit. This unit is a laboratory scale transported bed unit (downer) which was designed primarily for catalytic cracking testing. Main features of the unit comprise a catalyst preheater where the catalyst is stored before the test and preheated to typical regenerator temperatures, a once-through tubular reactor, where the feed and the preheated catalyst are contacted continuously at a short residence time (0.3-5 s), and a stripper in which catalyst is separated from hydrocarbons before regeneration.

In the present study, feed rate was generally set at 2.5 g/min with catalyst flows between 20 and 120 g/min. As a result, the catalyst-to-oil ratio was varied between 8 and 40. Run time was maintained between 60 and 90 s, so that injected feed mass was between 2.5 and 4 g per test, enough to perform good mass balances. Feed density was determined at pumping conditions at 0.811 g/cm^3. Detailed description of the unit and experimental conditions are described in the work by Corma et al. (2013; 2018).

Gas products were analyzed in an Agilent 3000A fast micro gas chromatograph equipped with three thermal conductivity detectors. The GC was calibrated with a standard gas mixture prior to product analysis. Liquid products were analyzed by simulated distillation method ASTM D-2887 using Shimadzu GC 2010 Plus equipped with a flame ionization detector. The analytical results were combined to obtain the detailed product yield patterns and information on the ability of cracking crude oils.

Modeling Approach

A regression machine learning (ML) model based on artificial neural network (ANN) with three layers was created using Keras Deep Learning Library in Python to predict the olefins yields. Keras was chosen for its efficient access to numerical computation libraries Theano and TensorFlow and its capabilities allowing users to define and train neural network models with minimum programming need.

Three features are considered in the developed ML model, including temperature, catalyst-to-oil ratio, and residence time. Potentially more features could be included in the ML model but was not considered because of the focus of the present study and availability in the experimental data. The output from the ML model are five lumps, which are heavy cycle oil (HCO), light cycle oil (LCO), gasoline, gas (C1-C4), and coke. The HCO lump represents heavy liquid hydrocarbons of boiling point higher than 343 °C. The LCO lump represents light liquid hydrocarbons of boiling point between 221 and 343 °C. Gasoline lump represents the liquid hydrocarbons of boiling point less than 221 °C. Gas lump represents the hydrocarbons in the gas phase under normal conditions. Coke lump represents both kinetic coke and metal coke formed from the cracking reactions and deposited on the catalyst. The average molecular weight of the lumps ranks from high to low in the following order: HCO > LCO > Gasoline > Gas, which corresponds to the ranking of boiling point range. In addition to the five lumps, the ML model output also includes the light olefins such as ethylene and propylene.

After the ML model was developed, it was trained and cross-checked using the experimental data from the MD unit. Then the model is used to make predictions of the light olefin yields, not only at the conditions same as the experimental setup, but also at the other conditions that are not measured in the experiments. By doing this, it is made possible by using this ML model to provide deeper insight in the cracking process by providing the optimum conditions for optimum propylene yield.

The same five lumps were used to build a kinetic model for both the thermal cracking and catalytic cracking. A reaction network was set up, starting from the heaviest lump HCO, cascades through the lighter lumps, and ending with Gas and Coke lumps, as shown in Fig.1.

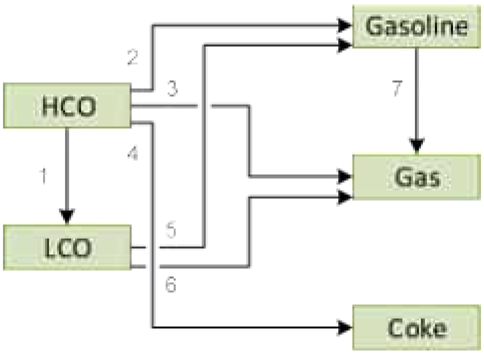

Fig. 1. Schematic diagram of the reaction network for a five-lump kinetic model

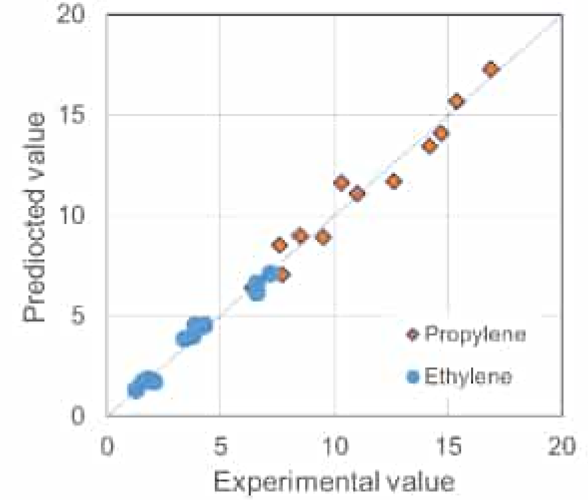

Fig. 2. Light olefin yields comparison between the experimental and predictions by the ML model.

Mathematical models have been developed to describe the system of five-lump reaction network with the following assumptions:

- Homogeneous distribution of gas and solid mixture
- Ideal plug flow reactor for the mixture of gas and solid
- Isothermal reactor
- Coke contribution from heaviest lump is considered
- Irreversible reactions
- Second order for HCO and LCO lumps and first order for all other lumps
- Nonselective catalyst deactivation as a function of coke concentration

The behavior of catalyst activity is derived from an activity function considering the effects of pore blocking and activity site blockage due to coke formation on the catalyst.

The reaction rates for thermal cracking are governed by Eqs. (1) - (5). The reaction rates for catalytic cracking are governed by Eqs. (6) - (11). Both thermal cracking and catalytic cracking are contributing to the rate of change of each lump in the kinetic model. The reaction rate constant for each k_i in Eqs. (1) through (10) is given by the Arrhenius equation, Eq. (12).

Results and Discussions

The predictive ML model was able to make accurate predictions of the light olefins and lumps after being trained by the experimental data, as made clear in Fig. 2 by the good agreement between the experimental data and predictions made by the ML model. The square norm of the residual, or resnorm, is used to measure the accuracy of the mathematical model. This value is 0.0083 for ML model and 0.015 for the kinetic model when they are used to predict the five lumps in the cracking reactions. Then the trained Ml model was used to explore the operational parameter space to predict the propylene yield with the purpose of identifying the optimum conditions for the maximum propylene yield, as shown in Fig. 3. It is shown in Fig. 3 that the propylene yield is optimized at high temperature, high residence time, and high catalyst-to-oil ratio (CTO). Since propylene is an intermediate product in the cracking reactor, Fig. 3 provides the operational direction where it is possible to further increase its yield from the whole crude feed under the given conditions. It confirms that the propylene yield will be enhanced by the higher severity conditions in the HSFCC process.

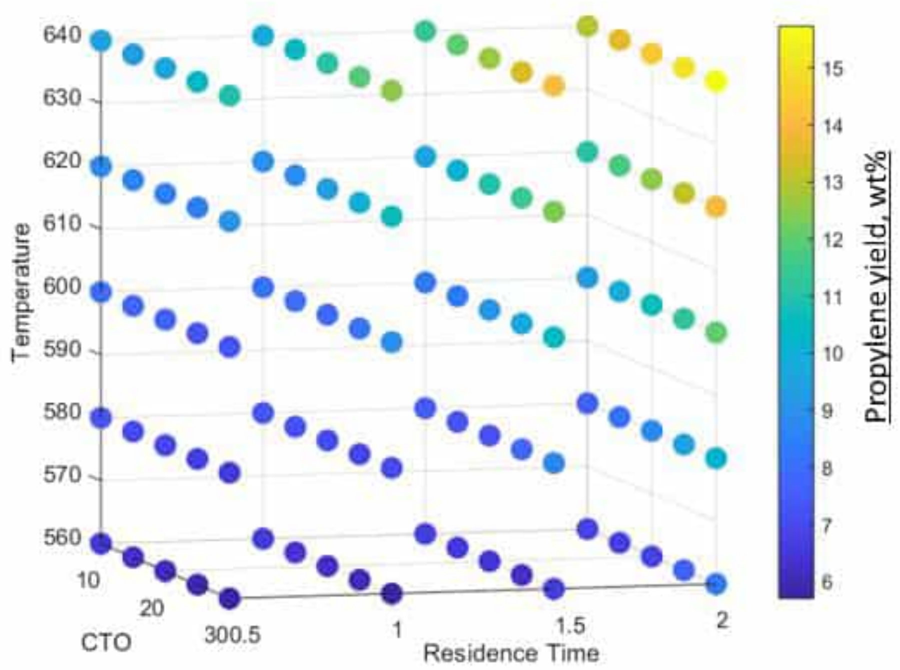

Fig. 3. A 4-D plot to show the propylene yield predicted by the ML model as a function of reaction temperature, residence time, and CTO.

As both thermal cracking and catalytic cracking reactions compete in the HSFCC™ process due to the presence of catalyst at high temperature, the first step to a better understanding of the contribution from thermal cracking in the HSFCC™ process starts with the knowledge of their activation energies. Therefore, the reaction activation energies for both thermal cracking and catalytic cracking reactions were obtained by fitting 21 sets of experimental data at 560, 600, and 640 °C, as shown in Table 1, using the 5-lump kinetic model. The predictions from the 5-lump model shows good agreement with the ML model and experimental data, as shown in Fig.4.

Table 1. Activation energies (kJ/mol) for thermal and catalytic cracking reactions

Reaction	Thermal cracking	Catalytic cracking
HCO to LCO	175.0	19.8
HCO to gasoline	180.0	25.0
HCO to gas	195.4	47.6
HCO to coke	142.9	60.0
LCO to gasoline	180.2	35.0
LCO to gas	200.8	67.2
Gasoline to gas	220.0	80.0

Table 1 shows that the calculated apparent activation energies for thermal cracking reactions are in the range of 140 to 220 kJ/mol, in line with a previous study by Corma *et al.* (2018). On the other hand, the calculated activation energies for catalytic cracking reactions are in the range of 20 to 80 kJ/mol. It is made obvious that the activation energies for catalytic cracking are lower than the activation energies for thermal cracking. This implies that the thermal cracking would make more significant contributions to the overall cracking when temperature is high compared to the case at low temperature.

The light olefins are produced from the heavier hydrocarbons through both catalytic cracking and thermal cracking. The ethylene production is mainly attributed to the thermal cracking while the propylene yield is largely due to the catalytic cracking reactions. To illustrate the contribution from thermal cracking during the HSFCC™ process, the rate of change of Gas lump in the 5-lump kinetic model is traced in time for three experiments, as shown in Fig. 5. For each time instance, the contributions to the rate of change from the thermal cracking and catalytic cracking are calculated individually from the kinetic reaction rate equation. When T=560 °C (low temperature case), Fig. 5 shows that the thermal cracking contribution is insignificant, lower than 5% at time 0 and about 20% at t=2 second. When T=640 °C (high temperature case), Fig. 5 shows that the thermal cracking accounts for close to 20% of gas production in the beginning and more than 50% after t = 0.5 second, making a much sensible impact on the production of Gas lump, which includes the light olefins. Therefore, it is made clear that the thermal cracking prevails at higher temperature and longer residence time.

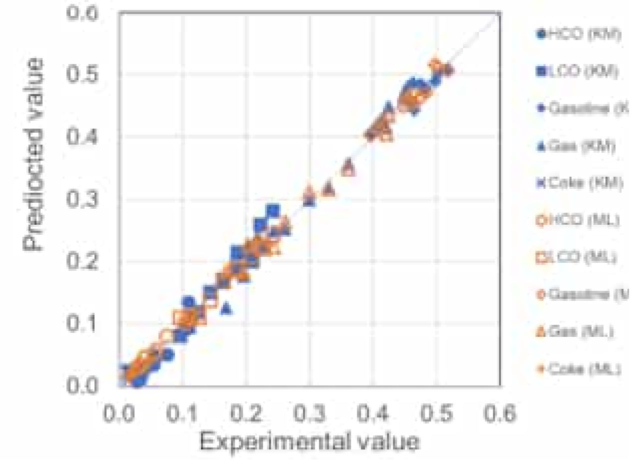

Fig. 4. Yields comparison of the experimental value and predicted value. KM: from 5-lump kinetic model; ML: from ML model based on ANN.

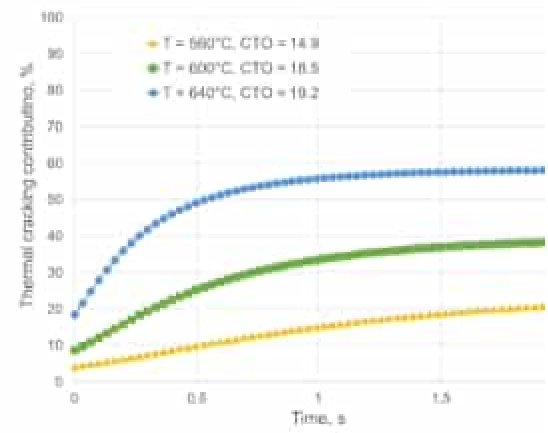

Fig. 5. The contribution of thermal cracking to the rate of change of Gas lump at each time instance.

Table 2 shows the accumulative contribution of the thermal cracking to the overall production of Gas lump during the cracking process at different temperatures and catalyst-to-oil ratio. At the same temperature, the thermal cracking contribution is reduced by addition of more catalyst (at high catalyst-to-oil ratio). This provides a strategy to use in order to increase the propylene yield in HSFCC™ because propylene yield is enhanced with higher degree of catalytic cracking.

Table 2: The time average rate of change of Gas lump due to thermal cracking (weight percent).

T(°C)	560	560	560	560	600	600	600	600	640	640	640	640
CTO	8.3	11.2	11.8	14.9	12.2	18.5	19.2	31.3	19.2	29.2	30.9	42.6
t=0.5 s	10.6	8.7	8.4	7.4	22.2	18.4	18.1	14.9	39.1	33.7	33.0	29.1
1.0 s	13.1	11.3	11.1	10.0	28.2	24.2	23.8	19.5	46.0	39.5	38.6	33.4
1.5 s	15.6	13.8	13.5	12.4	32.6	27.9	27.4	21.9	49.5	42.0	41.0	34.9
2.0 s	17.9	15.9	15.6	14.2	35.8	30.3	29.8	23.2	51.4	43.3	42.2	35.6

Conclusions

In the present study, a predictive ML model was created to elucidate the kinetics of light olefins production from the direct cracking of crude oil feedstock in a dual-downer high severity fluidized bed system. This is coupled with a conventional 5-lump kinetic model that considers both catalytic and thermal cracking chemistries. Through using the ML-based model and the kinetic model, this study provides deeper insights into the important role of thermal and catalytic cracking as competing mechanisms in the direct cracking of crude oil under high-severity operating conditions. Specifically, the present study further quantified the thermal cracking contribution, confirmed the dominance of thermal cracking mechanism at high temperatures representative of high-severity operating conditions and that thermal cracking mechanism is comparatively negligible at lower temperatures representative of conventional FCC conditions, where the catalytic cracking mechanism is dominant.

The present study showed that thermal cracking prevails at high temperature and longer residence time, which might lead to undesirable over cracking and excessive production of ethylene instead of propylene. The guidance on the operating conditions can be proposed based on the present study. First, it is recommended to use shorter catalyst contact time to reduce the effect from thermal cracking. Second, catalyst should be carefully chosen based on better selectivity of propylene at higher temperature. Third, higher catalyst-to-oil ratio should be employed in HSFCC™ for more catalytic cracking to counteract the significant impact of thermal cracking.

Equations

$$r_1 = \frac{dy_1}{\mathrm{d}t} = -(k_1 + k_2 + k_3 + k_4) * y_1^2 \qquad (1)$$

$$r_2 = \frac{dy_2}{\mathrm{d}t} = (k_1 * y_1^2 - (k_5 + k_6) * y_2^2) \qquad (2)$$

$$r_3 = \frac{dy_3}{\mathrm{d}t} = (k_2 * y_1^2 + k_5 * y_1^2 - k_7 * y_3) \qquad (3)$$

$$r_4 = \frac{dy_4}{\mathrm{d}t} = (k_3 * y_1^2 + k_6 * y_1^2 + k_7 * y_3) \qquad (4)$$

$$r_5 = \frac{dy_5}{dt} = k_4 * y_1^2 \qquad (5)$$

$$r_1 = \frac{dy_1}{\mathrm{d}t} = -(k_1 + k_2 + k_3 + k_4) * y_1^2 * a_c \qquad (6)$$

$$r_2 = \frac{dy_2}{dt} = (k_1 * y_1^2 - (k_5 + k_6) * y_2^2) * a_c \qquad (7)$$

$$r_3 = \frac{dy_3}{dt} = (k_2 * y_1^2 + k_5 * y_1^2 - k_7 * y_3) * a_c \qquad (8)$$

$$r_4 = \frac{dy_4}{dt} = (k_3 * y_1^2 + k_6 * y_1^2 + k_7 * y_3) * a_c \qquad (9)$$

$$r_5 = \frac{dy_5}{dt} = k_4 * y_1^2 * a_c \qquad (10)$$

$$a_c = \frac{B+1}{B + exp\,(A * y_5)} \qquad (11)$$

$$k_i = F_i \cdot exp\,(-\frac{Eai}{R}(\frac{1}{T_i} - \frac{1}{Tr})) \qquad (12)$$

Notation

r_i	reaction rate for lump i, s^{-1}
y_i	yield for lump i, unitless
t	time, s
k_i	reaction rate constant for i^{th} reaction
F_i	pre-exponential factor
Ea_i	activation energy, kJ/mol
T_i	reaction temperature, K

References

Corma, A., and Sauvanaud, L. (2013). "FCC testing at bench scale: New units, new processes, new feeds." Catalysis Today, 218–219, 107-114.

Corma, A., Sauvanaud, L., Mathieu, Y., Al-Bogami, S., Bourane, A., and Al-Ghrami, M. (2018). "Direct crude oil cracking for producing chemicals: Thermal cracking modeling." Fuel, 211, 726-736.

Fujiyama, Y., Al-Tayyar, M. H., Dean, C. F., Aitani, A., and Redhwi, H. H. (2007). "Chapter 1 Development of high-severity FCC process: an overview." Studies in Surface Science and Catalysis, 166, 1-12.

Tullo, A. H. (2019). "The future of oil is in chemicals, not fuels." C&EN Global Enterprise, 97(8), 26-29.

Usman, A., Aitani, A., and Al-Khattaf, S. (2017). "Catalytic Cracking of Light Crude Oil: Effect of Feed Mixing with Liquid Hydrocarbon Fractions." Energy & Fuels, 31(11), 12677-12684.

Weekman, V. W., and Nace, D. M. (1970). "Kinetics of catalytic cracking selectivity in fixed, moving, and fluid bed reactors." AIChE Journal, 16(3), 397-404.

FLUIDIZED BED MACHINING OF METAL OBJECTS PRODUCED BY ADDITIVE MANUFACTURING

Maurizio Troiano[1*], Andrea El Hassanin[1], Alessia Teresa Silvestri[1,2], Fabio Scherillo[1], Fabrizio Scala[1], Roberto Solimene[3], Antonino Squillace[1], Piero Salatino[1]

[1]Dipartimento di Ingegneria Chimica, dei Materali e della Produzione Industriale, Università degli Studi di Napoli Federico II, P.le V. Tecchio 80, 80125, Napoli, Italy
[2]Dipartimento di Ingegneria Gestionale, dell'Informazione e della Produzione, Università degli Studi di Bergamo, viale Marconi 5, 24044, Bergamo, Italy
[3]Istituto di Ricerche sulla Combustione, Consiglio Nazionale delle Ricerche, P.le V. Tecchio 80, 80125, Napoli, Italy

*Email: *maurizio.troiano@unina.it*

Abstract

Fluidized bed surface finishing of objects made by additive manufacturing technology has been investigated. Surface roughness is a crucial parameter for parts made with additive manufacturing technology, since it affects the dimensional accuracy and mechanical, tribological and corrosion resistance. Fluidized Bed Machining can be a suitable method for finishing parts with high geometrical complexity due to the high particles mobility. In this study, an experimental campaign has been carried out in a lab-scale fluidized bed apparatus with Aluminium alloy samples made by selective laser melting technology. Surface finishing has been evaluated in terms of wear and roughness under bubbling fluidization conditions while varying the sample orientation. Furthermore, the main mechanisms of particle removal are under investigation. In particular, inertial and frictional mechanisms are considered for the surface finishing process of metal parts in fluidized bed. Results show that the sample orientation affects the wear rate and the resulting roughness. Furthermore, energy dissipation models could be able to describe the finishing process of metal parts in fluidized beds.

Introduction

Additive manufacturing (AM) technology is one of the rapidly developing advanced manufacturing techniques in the world. In contrast to conventional, subtractive manufacturing methods, AM is based on the material incremental manufacturing. It implies layer-by layer shaping and consolidation of feedstock, usually powder materials, to arbitrary geometries, normally using a computer-controlled laser as the energy resource. The full vision of AM includes the production of complex, composite and hybrid structures with precision and control that cannot be made through traditional manufacturing routes. AM advantages include improved resource efficiency during both the production and use phases, extended product life and reduction up to 80% of production time from the designed to the finished part, as reported by Tofail et al. (2018) and Ford et al. (2016).

AM methods can be classified on the basis of the nature and the aggregate state of the feedstock as well as by the binding mechanisms between the building layers, as reported by Herzog et al. (2016). Vock et al. (2019) reported that the most widespread Additive Manufacturing technologies for metals, i.e. *Selective Laser Melting*, *Electron Beam Melting* and *Laser Metal Deposition*, use powders as the material feedstock. *Selective Laser Melting* (SLM) utilizes a bed of powder metal that is 'selectively' melted via a laser, while *Electron Beam Melting* and *Laser Metal Deposition* involve the deposition of metal powders and their simultaneous or subsequent melting via an energy source.

One of the main reasons that hampers the expected high employment of these technologies is the high surface roughness of the as-built parts, as reported by Strano et al. (2013), due to the well-known *stairstep effect* and the *balling effect*, resulting in rough surfaces with overhangs and sintered powders. The presence of such superficial defects affects the dimensional accuracy and the mechanical, tribological and corrosion resistance of the produced parts. As a consequence, objects produced by AM technologies need to be further worked with post-process surface finishing techniques. The most common finishing methods such as CNC machining, shot peening, electrochemical polishing and laser polishing are limited to objects with low geometrical complexity, while in principle, fluidized bed finishing (Fluidized Bed Machining) can be suitable also for parts with complex geometries, thanks to the mobility of fluidized particles and flowability of the emulsion phase, as can be found in Du et al. (2016), AlMangour et al. (2016), Rosa et al. (2015), Yang et al. (2016).

In this study, the employment of the Fluidised Bed Machining technology is investigated, that consists in dipping the part in a suspension of an abrasive material using air fluidizing gas. Barletta (2009) reported that the presence of fluidized particles could promote a homogeneous abrasive machining effect on complex parts. The prediction of surface finishing of metal objects in fluidized bed is not a trivial task. The inertial and frictional forces responsible for surface finishing are needed to be quantitatively assessed, starting from the previous literature on the subject and on the extensive cumulated experience on erosion of internals in fluidized beds. Models reported in the literature can be classified in single-particle models, dense phase fluidized bed models and power/energy dissipation models, as reported by Lyczkowski and Bouillard (2002). Single-particle and dense phase models are developed considering the interaction of a single particle and many particles with a planar wall, respectively. For both the models, the finishing process can be in purely ductile mode, purely brittle mode or failure-fatigue mode. On the other hand, energy dissipation models are based on the concept that energy dissipation of particles impinging on a surface gives rise to deformation wear.

This study deals with the investigation of the Fluidised Bed Machining technology for the treatment of flat samples produced via Selective Laser Melting technology, using one of the most widespread materials for Additive Manufacturing, i.e. the AlSi10Mg aluminum alloy. Experiments have been carried out with a static sample under bubbling fluidization conditions for different sample orientations. Roughness prior and after the tests has been measured by means of profilometry. The surface morphology of the samples has been characterized by scanning electron microscopy. Results are analysed in the light of the fluidized bed machining models.

Experimental

The experimental apparatus and one of the SLM samples used for the experiments are reported in Fig.1. The fluidized bed apparatus consists in a Plexiglas reactor (inner diameter: 0.21 m) which comprises a windbox zone and an upper section 1.4 m high where the abrasive is located. Fluidization air is fed at the bottom of the column and it flows through a steel bubble caps distributor before entering the upper section of the column. Alumina irregular shaped particles (Vickers Hardness: 2300 HV), with an average size of 650 µm, were used as abrasive material. The carrier gas is controlled by a mass flow meter (*Bronkhorst EL-Flow Select*) with a maximum operating flow rate of 200 Nm^3/h (corresponding to a superficial gas velocity of 1.6 m/s). The fluidized bed is equipped with a purposely designed fixture that allows the sample positioning at any height and tilt angle with respect to the horizontal direction. 20 x 20 x 2 mm^3 square flat samples of AlSi10Mg aluminum alloy were used (Vickers Hardness: approx. 120 HV). The samples were produced in collaboration with MBDA Italia S.p.A using an EOS M280 Selective Laser Melting machine. Samples were built in the vertical direction in respect to the building plate, adopting also a contour strategy to optimize the as-built surface roughness. The detailed set of process parameters is not reported due to restrictions imposed by MBDA Italia S.p.A. Experiments were carried out placing the samples at a pre-set distance from the distributor of 150 mm and with three impact angles: 0°, 90° and 25°. The latter value was investigated because, according to the literature, it could maximize the contribution of all the different surface/abrasive interaction mechanisms, i.e. micro-peening, micro-cutting, micro-fatigue and micro-cracking, as reported by Barletta (2009). Each sample was treated for a total time of 24h, at a superficial gas velocity of 1.22 m/s, i.e. under bubbling fluidization conditions of the abrasive (U_{mf}=0.42 m/s), according to the flow regime diagram reported by Kunii and Levenspiel (1991). Evaluations of the morphological evolution, surface roughness and weight loss were carried out by dividing the process time into several steps, observing the results every 30 min for the first 2h. After each treatment step, samples were cleaned in ultrasonic bath for 15 min using ethanol and then dried.

For all the conditions investigated, weighing measurements were performed, before and after the treatment, right after the samples cleaning in order to avoid the influence of any residues or dirt. Subsequently, a qualitative evaluation of the surface improvement was carried out by means of a Hitachi TM3000 Scanning Electron Microscope, while the surface texture analysis was carried out by means of a Leica DCM3D Confocal Microscope. As far as this latter characterization is concerned, from each sample an 8x8 mm^2 area was investigated and, according to the ISO 25178-2 standard (2012), surface texture was analyzed through the parameter Sa (mean surface roughness).

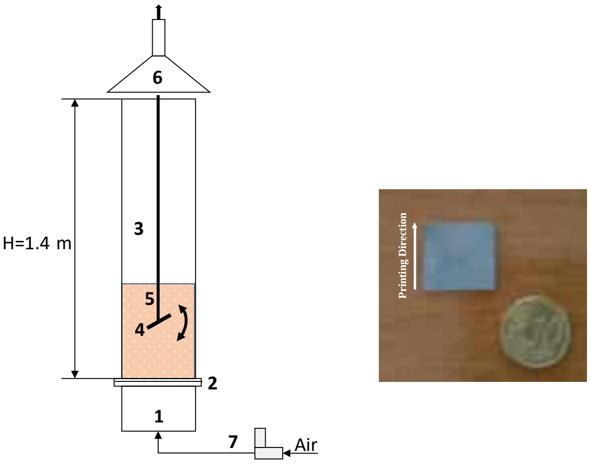

(**1**) Windbox; (**2**) Gas distributor; (**3**) Fluidization column; (**4**) Sample;
(**5**) Sample holder; (**6**) Extractor fan; (**7**) Digital mass flow meters.

Fig. 1. Fluidized bed apparatus and inset image of the AlSi10Mg sample, with a coin as a scale marker.

Results and discussion

Graphs of the temporal evolution of material removal and average roughness are reported in Fig. 2 (a) and (b), respectively. Results show that the wear increases with the treatment time for the first three hours (Fig. 2(a)), then it is about constant with time for all the inclinations considered. Furthermore, the material removal has not a monotonic trend with the sample inclination. As matter of fact, the highest wear is obtained for an impact angle of 25° from the horizontal position, while the lowest wear is obtained for a horizontal position of the sample (0°). In Fig. 2(b), the average roughness decreases with the machining time for all the experimental conditions. In particular, the sample treated with a 25° impact angle experienced, although slight, the highest reduction of Sa of about 1.5 µm, while for the other two cases the roughness reduction is lower. These results can be explained taking into account that, for all the investigated conditions, the impact energy transferred from the abrasive particles to the plate surfaces is low. Under these conditions, particle-to-surface impact can induce just a partial removal of the sintered powders appearing as peaks on plate surface and, therefore, only a slight roughness reduction can be obtained. However, the high hardness ratio between the abrasive particles and the substrate could also promote indenting effects on the surfaces counteracting the smoothening effect of the treatment and resulting in surface with less rounded edges.

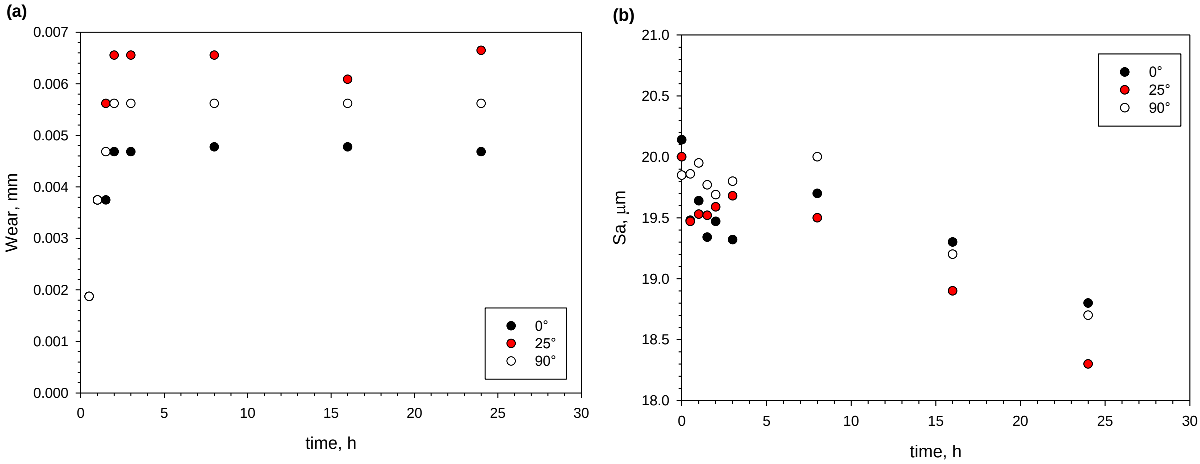

Fig. 2. Effect of the sample orientation on the temporal evolution of (a) material removal; (b) average roughness.

Fig. 3 reports the surface morphology of the samples treated with an impact angle equal to 25°, before and after 3 h, 8 h and 16 h of treatment (Fig. 3 a), b), c) and d), respectively). The SEM micrographs show that small sintered particles are removed from the surface after 3 h of treatment. Further machining (to 8 h and 16 h) does not result in additional wear, but it only slightly influences the surface roughness as an effect of plastic deformations.

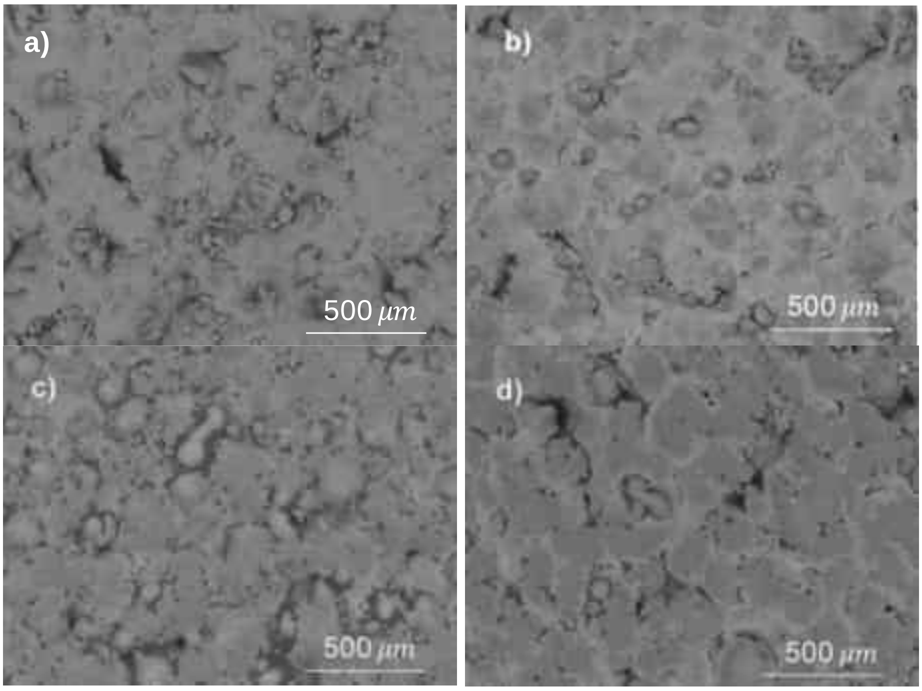

Fig. 3. SEM images for the sample orientation of 25°: a) un-treated sample, b) after 3 h, c) after 8 h, d) after 16 h of treatment.

Several semiempirical and analytical models of erosion rate in fluidized beds are reported in the literature. Finnie (1960) was the first to derive a single-particle erosive cutting model. The model expresses the material removal as the result of the cumulative action of individual particles. Finnie (1960) related the material removal to the impact velocity, impact angle and mechanical properties of the impinged material. One of the drawbacks of the single-particle models is that they can not be used to calculate the erosion rate a priori. Furthermore, Finnie's model predicts no erosion at 0 and 90°. Lyczkowski and Bouillard (2002 "a", "b") developed an energy dissipation model for the calculation of an average erosion rate in fluidized beds. In particular, the simplified closed form of the monolayer kinetic energy dissipation model

(SCFMED) was developed by Lyczkowski and Bouillard as a simplified version of the monolayer kinetic energy dissipation (MED) model for erosion of tubes in fluidized beds. The erosion rate $\dot{E}$ is expressed as:

$$\dot{E} = f(\varepsilon)(1 + 0.01167Re)\dot{E}_0 \tag{1}$$

where the fluidization Reynolds number, $Re = \varphi_s d_p \rho_p U/\mu_g$ and:

$$f(\varepsilon) = \frac{(1-\varepsilon)\left(\varepsilon - \varepsilon_{mf}\right)}{\varepsilon^2} \tag{2}$$

represents the porosity dependence in the fluidized bed. The erosion group $\dot{E}_0$ is expressed as:

$$\dot{E}_0 = (1 - e^2)\frac{75\mu_g g x_d}{\varphi_s d_p E_{sp}} \tag{3}$$

The units of $\dot{E}_0$ are in terms of velocity, usually expressed in mm/1000 h. e represents the particle-surface coefficient of restitution, which is the ratio of particle rebound to particle impact velocities, and x_d an acceleration distance, which in this work has been taken equal to the distance of the eroding surface from the gas distributor. μ_g is the gas dynamic viscosity at ambient conditions, g the gravitational acceleration, φ_s the sphericity of the particles, d_p the particle size. E_{sp} is the specific energy of the eroding material, related to its hardness.

The British Coal Corporation (BCC) (1989) proposed an empirical model for tube erosion in fluidized beds on the basis of data on several fluidized bed combustors which was expressed as:

$$\dot{E} = 1.873 \cdot 10^{-9} U^2 D^{0.6} L_s^{1.33}(1 + 0.1P) \tag{4}$$

Where $\dot{E}$ is the erosion rate in mm/h, D is the characteristic length of the eroding piece in mm, L_s is the bed height before fluidization in mm and P is the tube inclination.

The average erosion rate has been calculated for both the MED and BCC models for the experimental case. In particular, for the MED model, the average removal rate was equal to 0.39 mm/1000h, while using the BCC correlation it was equal to 0.048, 0.17 and 0.48 mm/1000h for an inclination P equal to 0, 25 and 90°, respectively.

The comparison of the experimental wear data with the average removal rate from the energy dissipation model and BCC correlation highlights that there is a roughly good agreement between the experimental wear and the average value calculated by the MED model. Comparing the experimental results with the BCC correlation it is noteworthy that Eq. (4) predicts erosion rates to increase with the object inclination, P. In particular, a 10-fold increase in erosion is predicted for P =90° (vertical orientation) over P =0° (horizontal position), while a non-monotonic trend of the removed material over time is obtained by the experimental results at different object inclinations.

The experimental results highlight that for all the investigated sample orientations, after about three hours, the removal rate is very slow. This outcome reveals that if very rough surfaces need to be smoothed, very long machining time are required, under the experimental investigated conditions. Also, in terms of average roughness, after about three hours the roughness reached about a constant value. For longer times, the reduction in the roughness is to be attributed to a rearrangement of the surface morphology due to plastic modifications rather than to material removal.

On the basis of the experimental and calculations results, in order to have an efficient and fast finishing of objects made by additive manufacturing technologies, it is possible to conclude that the enhancement of shear and friction could improve the surface finishing of metal objects, as they are responsible for higher energy dissipation. For this reason, future experiments will report the results obtained by setting minimum fluidization conditions and imparting rotation to the sample. Furthermore, the effect of different abrasive materials will be investigated.

Conclusions

Fluidized bed surface finishing of AlSi10Mg samples made by Selective Laser Melting technology was investigated. Surface finishing was evaluated in terms of wear and roughness under bubbling fluidization conditions while varying the sample orientation. The experimental results highlighted that wear increased for the first three hours of treatment. For longer treatment time, the wear was almost constant for all the conditions under investigation. The mean surface roughness, on the other side, decreased of about 1 μm over 24 hours of treatment. The best results in terms of wear and surface roughness were obtained for an impact angle equal to 25°. The analysis of erosion model based on single/multiple impacts and energy deformation concept indicated that the energy deformation model could be more suitable for the description of material removal during finishing process in fluidized bed. Further investigation will be carried out in order to assess the role of different abrasive materials and relative motion between the sample and the fluidized particles on the finishing process.

References

AlMangour, B., J-M Yang. Improving the surface quality and mechanical properties by shotpeening of 17-4 stainless steel fabricated by additive manufacturing. Materials & Design. 2016. 110, 914-924

Barletta, M. Progress in abrasive fluidized bed machining. J. Mat. Proc. Tech. 2009. 209, 6087-6102

British Coal Corporation, Coal research establishment. Minimizing erosion in coal-fired boilers. Commission of the European Communities Report EUR 1236OEN, (Directorate-General) Telecommunications, Information Industries and Innovation, Luxembourg, 1989

BS EN ISO 25178-2. Geometrical product specifications (GPS) — Surface texture: Areal Part 2: Terms, definitions and surface texture parameters. British Standards Institution (2012)

Du, W., Q Bai, B Zhang. A Novel Method for Additive/Subtractive Hybrid Manufacturing of Metallic Parts. Procedia Manufacturing. 2016. 5, 1018-1030

Finnie, I. Erosion of surfaces by solid particles. Wear. 1960. 3, 87-103

Ford, S., M Despeisse. Additive manufacturing and sustainability: an exploratory study of the advantages and challenges. J. Clean Prod. 2016. 137, 1573-1587

Herzog, D., V Seyda, E Wycisk, C Emmelmann. Additive manufacturing of metals. Acta Mater. 2016. 117, 371-392

Kunii, D., O Levenspiel. Fluidization engineering, second ed., Butterworth-Heinemann, Boston, 1991

Lyczkowski, R.W., JX Bouillard. Scaling and guidelines for erosion in fluidized beds. Powder Technol. 2002. 125, 217-225

Lyczkowski, R.W., JX Bouillard. State-of-the-art review of erosion modeling in fluid/solids systems. Prog. Energ. Combust. 2002. 28, 543-602

Rosa, B., P Mognol, J-Y Hascoët. Laser polishing of additive laser manufacturing surfaces. J. Laser Appl. 2015. 27, S2

Strano, G., L Hao, RM Everson, KE Evans. Surface roughness analysis, modelling and prediction in selective laser melting. J. Mat. Proc. Tech. 2013. 213, 589-597

Tofail, S.A.M., EP, Koumoulos, A Bandyopadhyay, S Bose, L O'Donoghue, C Charitidis. Additive manufacturing: scientific and technological challenges, market uptake and opportunities. Mater. Today. 2018. 21, 22-37

Vock, S., B Klöden, A Kirchner, T Weißgärber, B.Kieback. Powders for powder bed fusion: a review. Progress in Additive Manufacturing. 2019, 1-15

Yang, L., Y Wu, A Lassell, B Zhou. Electropolishing of Ti6Al4V Parts Fabricated by Electron Beam Melting. Proceedings of the 26th Annual International Solid Freeform Fabrication Symposium (2016) 1333-1344

Author Index

CFB13

HOSTED BY FRC ONLINE IN
VANCOUVER, CANADA

MAY 10-14, 2021